

Fuqin XIONG

Digital

Modulation

Techniques

Digital Modulation Techniques

For a listing of recent titles in the *Artech House Telecommunications Library*, turn to the back of this book.

Digital Modulation Techniques

Fuqin Xiong



Artech House
Boston • London

Library of Congress Cataloging-in-Publication Data

Xiong, Fuqin.

Digital modulation techniques / Fuqin Xiong.

p. cm. - (Artech House telecommunications library)

Includes bibliographical references and index.

ISBN 0-89006-970-0 (alk. paper)

1. Digital modulation. I. Title. II. Series.

TK5103.7.X65 2000

621.3815'36 - dc21

99-058091

CIP

British Library Cataloguing in Publication Data

Xiong, Fuqin

Digital modulation techniques. - (Artech House telecommunications library)

1. Digital modulation

I. Title

621.3'81536

ISBN 0-89006-970-0

Cover design by Igor Valdman

© 2000 ARTECH HOUSE, INC.

685 Canton Street

Norwood, MA 02062

All rights reserved. Printed and bound in the United States of America. No part of this book may be reproduced or utilized in any form or by any means, electronic or mechanical, including photocopying, recording, or by any information storage and retrieval system, without permission in writing from the publisher.

All terms mentioned in this book that are known to be trademarks or service marks have been appropriately capitalized. Artech House cannot attest to the accuracy of this information. Use of a term in this book should not be regarded as affecting the validity of any trademark or service mark.

International Standard Book Number: 0-89006-970-0

Library of Congress Catalog Card Number: 99-058091

10 9 8 7 6 5 4 3 2 1

Contents

Preface	xiii
Chapter 1. Introduction	1
1.1 Digital Communication Systems	1
1.2 Communication Channels	4
1.2.1 Additive White Gaussian Noise Channel	4
1.2.2 Bandlimited Channel	6
1.2.3 Fading Channel	7
1.3 Basic Modulation Methods	7
1.4 Criteria of Choosing Modulation Schemes	9
1.4.1 Power Efficiency	10
1.4.2 Bandwidth Efficiency	10
1.4.3 System Complexity	11
1.5 Overview of Digital Modulation Schemes	12
References	15
Chapter 2. Baseband Modulation (Line Codes)	17
2.1 Differential Coding	18
2.2 Description of Line Codes	22
2.2.1 Nonreturn-to-Zero Codes	25
2.2.2 Return-to-Zero Codes	25
2.2.3 Pseudoternary Codes (including AMI)	26
2.2.4 Biphasic Codes (including Manchester)	27
2.2.5 Delay Modulation (Miller Code)	27
2.3 Power Spectral Density of Line Codes	28
2.3.1 PSD of Nonreturn-to-Zero Codes	30
2.3.2 PSD of Return-to-Zero Codes	34
2.3.3 PSD of Pseudoternary Codes	35
2.3.4 PSD of Biphasic Codes	37
2.3.5 PSD of Delay Modulation	40

2.4 Bit Error Rate of Line Codes	43
2.4.1 BER of Binary Codes	44
2.4.2 BER of Pseudoternary Codes	49
2.4.3 BER of Biphasic Codes	54
2.4.4 BER of Delay Modulation	57
2.5 Substitution Line Codes	57
2.5.1 Binary N-Zero Substitution Codes	58
2.5.2 High Density Bipolar n Codes	60
2.6 Block Line Codes	62
2.6.1 Coded Mark Inversion Codes	63
2.6.2 Differential Mode Inversion Codes	69
2.6.3 mBnB Codes	71
2.6.4 mB1C Codes	74
2.6.5 DmB1M Codes	76
2.6.6 PFmB(m+1)B Codes	77
2.6.7 kBnT Codes	78
2.7 Summary	81
References	83
Chapter 3. Frequency Shift Keying	87
3.1 Binary FSK	87
3.1.1 Binary FSK Signal and Modulator	87
3.1.2 Power Spectral Density	92
3.2 Coherent Demodulation and Error Performance	95
3.3 Noncoherent Demodulation and Error Performance	98
3.4 M-ary FSK	102
3.4.1 MFSK Signal and Power Spectral Density	102
3.4.2 Modulator, Demodulator, and Error Performance	104
3.5 Demodulation Using Discriminator	115
3.6 Synchronization	121
3.7 Summary	121
References	122
Chapter 4. Phase Shift Keying	123
4.1 Binary PSK	123
4.2 Differential BPSK	129
4.3 M-ary PSK	136
4.4 PSD of MPSK	146
4.5 Differential MPSK	148
4.6 Quadrature PSK	154

4.7 Differential QPSK	160
4.8 Offset QPSK	167
4.9 $\pi/4$-QPSK	170
4.10 Synchronization	179
4.10.1 Carrier Recovery	179
4.10.2 Clock Recovery	183
4.10.3 Effects of Phase and Timing Error	186
4.11 Summary	187
4.12 Appendix 4A	190
References	192
Chapter 5. Minimum Shift Keying and MSK-Type Modulations	195
5.1 Description of MSK	196
5.1.1 MSK Viewed as a Sinusoidal Weighted OQPSK	196
5.1.2 MSK Viewed as a Special Case of CPFSK	201
5.2 Power Spectrum and Bandwidth	203
5.2.1 Power Spectral Density of MSK	203
5.2.2 Bandwidth of MSK and Comparison with PSK	204
5.3 Modulator	207
5.4 Demodulator	210
5.5 Synchronization	214
5.6 Error Probability	216
5.7 Serial MSK	219
5.7.1 SMSK Description	219
5.7.2 SMSK Modulator	221
5.7.3 SMSK Demodulator	223
5.7.4 Conversion and Matched Filter Implementation	227
5.7.5 Synchronization of SMSK	231
5.8 MSK-Type Modulation Schemes	231
5.9 Sinusoidal Frequency Shift Keying	236
5.10 Simon's Class of Symbol-Shaping Pulses	240
5.11 Rabzel and Pathupathy's Symbol-Shaping Pulses	247
5.12 Bazin's Class of Symbol-Shaping Pulses	250
5.13 MSK-Type Signal's Spectral Main Lobe	254
5.14 Summary	256
References	257
Chapter 6. Continuous Phase Modulation	259
6.1 Description of CPM	260
6.1.1 Various Modulating Pulse Shapes	261
6.1.2 Phase and State of the CPM Signal	265

6.1.3 Phase Tree and Trellis, State Trellis	269
6.2 Power Spectral Density	272
6.2.1 Steps for Calculating PSDs for General CPM Signals	274
6.2.2 Effects of Pulse Shape, Modulation Index, and A Priori Distribution	276
6.2.3 PSD of CPFSK	277
6.3 MLSD for CPM and Error Probability	279
6.3.1 Error Probability and Euclidean Distance	281
6.3.2 Comparison of Minimum Distances	285
6.4 Modulator	286
6.4.1 Quadrature Modulator	286
6.4.2 Serial Modulator	292
6.4.3 All-Digital Modulator	295
6.5 Demodulator	297
6.5.1 Optimum ML Coherent Demodulator	297
6.5.2 Optimum ML Noncoherent Demodulator	301
6.5.3 Viterbi Demodulator	311
6.5.4 Reduced-Complexity Viterbi Demodulator	317
6.5.5 Reduction of the Number of Filters for LREC CPM	320
6.5.6 ML Block Detection of Noncoherent CPM	325
6.5.7 MSK-Type Demodulator	326
6.5.8 Differential and Discriminator Demodulator	330
6.5.9 Other Types of Demodulators	333
6.6 Synchronization	337
6.6.1 MSK-Type Synchronizer	337
6.6.2 Squaring Loop and Fourth-Power Loop Synchronizers	340
6.6.3 Other Types of Synchronizer	341
6.7 Gaussian Minimum Shift Keying	342
6.8 Summary	346
References	347
 Chapter 7. Multi-h Continuous Phase Modulation	 351
7.1 MHPM Signal, Phase Tree, and Trellis	351
7.2 Power Spectral Density	361
7.3 Distance Properties and Error Probability	366
7.4 Modulator	382
7.5 Demodulator and Synchronization	382
7.5.1 A Simple ML Demodulator for Multi-h Binary CPFSK	382

7.5.2 Joint Demodulation and Carrier Synchronization of Multi-h CPFSK	388
7.5.3 Joint Carrier Phase Tracking and Data Detection of Multi-h CPFSK	392
7.5.4 Joint Demodulation, Carrier Synchronization, and Symbol Synchronization of M-ary Multi-h CPFSK	393
7.5.5 Synchronization of MHPM	398
7.6 Improved MHPM Schemes	399
7.6.1 MHPM with Asymmetrical Modulation Indexes	400
7.6.2 Multi-T Realization of Multi-h Phase Codes	401
7.6.3 Correlatively Encoded Multi-h Signaling Technique	401
7.6.4 Nonlinear Multi-h CPFSK	403
7.7 Summary	403
7.8 Appendix 7A	404
References	408
Chapter 8. Quadrature Amplitude Modulation	411
8.1 M-ary Amplitude Modulation	411
8.1.1 Power Spectral Density	412
8.1.2 Optimum Detection and Error Probability	414
8.1.3 Modulator and Demodulator for Bandpass MAM	418
8.1.4 On-Off Keying	421
8.2 QAM Signal Description	422
8.3 QAM Constellations	426
8.3.1 Square QAM	429
8.4 Power Spectral Density	432
8.5 Modulator	434
8.6 Demodulator	436
8.7 Error Probability	438
8.8 Synchronization	441
8.9 Differential Coding in QAM	448
8.10 Summary	454
8.11 Appendix 8A	455
References	457
Chapter 9. Nonconstant-Envelope Bandwidth-Efficient Modulations	459
9.1 Two-Symbol-Period Schemes and Optimum Demodulator	460
9.2 Quasi-Bandlimited Modulation	465
9.3 QORC, SQORC, and QOSRC	471
9.4 IJF-OQPSK and TSI-OQPSK	478

9.5 Superposed-QAM	490
9.6 Quadrature Quadrature PSK	498
9.7 Summary	515
References	515
Chapter 10. Performance of Modulations in Fading Channels	517
10.1 Fading Channel Characteristics	518
10.1.1 Channel Characteristics	518
10.1.2 Channel Classification	521
10.1.3 Fading Envelope Distributions	524
10.2 Digital Modulation in Slow, Flat Fading Channels	527
10.2.1 Rayleigh Fading Channel	527
10.2.2 Rician Fading Channel	531
10.3 Digital Modulation in Frequency Selective Channels	533
10.4 $\pi/4$ -DQPSK in Fading Channels	544
10.5 MHPM in Fading Channels	548
10.6 QAM in Fading Channels	554
10.6.1 Square QAM	555
10.6.2 Star QAM	558
10.7 Remedial Measures Against Fading	560
10.8 Summary	563
References	564
Appendix A. Power Spectral Densities of Signals	567
A.1 Bandpass Signals and Spectra	567
A.2 Bandpass Stationary Random Process and PSD	569
A.3 Power Spectral Densities of Digital Signals	572
A.3.1 Case 1: Data Symbols Are Uncorrelated	574
A.3.2 Case 2: Data Symbols Are Correlated	576
A.4 Power Spectral Densities of Digital Bandpass Signals	577
A.5 Power Spectral Densities of CPM Signals	580
References	586
Appendix B. Detection of Signals	589
B.1 Detection of Discrete Signals	589
B.1.1 Binary Hypothesis Test	589
B.1.2 Decision Criteria	590
B.1.3 M Hypotheses	594
B.2 Detection of Continuous Signals With Known Phases	596
B.2.1 Detection of Binary Signals	596
B.2.2 Decision of M-ary Signals	608

B.3 Detection of Continuous Signals With Unknown Phases	615
B.3.1 Receiver Structure	615
B.3.2 Receiver Error Performance	621
References	625
Glossary	627
About the Author	631
Index	633

Preface

Digital modulation techniques are essential to many digital communication systems, whether it is a telephone system, a mobile cellular communication system, or a satellite communication system. In the past twenty years or so, research and development in digital modulation techniques have been very active and have yielded many promising results. However, these results are scattered all over the literature. As a result, engineers and students in this field usually have difficulty locating particular techniques for applications or for research topics.

This book provides readers with complete, up-to-date information of all modulation techniques in digital communication systems. There exist numerous textbooks of digital communications, each of them containing one or more chapters of digital modulation techniques covering either certain types of modulation, or only principles of the techniques. There are also a few books specializing in certain modulations. This book presents principles and applications information of all currently used digital modulation techniques, as well as new techniques now being developed. For each modulation scheme, the following topics are covered: historical background, operation principles, symbol and bit error performance (power efficiency), spectral characteristic (bandwidth efficiency), block diagrams of modulator, demodulator, carrier recovery (if any), clock recovery, comparison with other schemes, and applications. After we fully understand the modulations and their performances in the AWGN channel, we will discuss their performances in multipath-fading channels.

Organization of the book

This book is organized into 10 chapters. Chapter 1 is an introduction for those requiring basic knowledge about digital communication systems, and modulation methods.

Chapter 2 is about baseband signal modulation that does not involve a carrier.

It is usually called baseband signal formatting or line coding. Traditionally the term *modulation* refers to “impression of message on a carrier,” however, if we widen the definition to “impression of message on a transmission medium,” this formatting is also a kind of modulation. Baseband modulation is important not only because it is used in short distance data communications, magnetic recording, optical recording, etc., but also because it is the front end of bandpass modulations.

Chapters 3–4 cover classical frequency shift keying (FSK) and phase shift keying (PSK) techniques, including coherent and noncoherent. These techniques are currently used in many digital communication systems, such as cellular digital telephone systems, and satellite communication systems.

Chapters 5–7 are advanced phase modulation techniques which include minimum shift keying (MSK), continuous phase modulation (CPM), and multi-*h* phase modulation (MHPM). These techniques are the research results of recent years, and some of them are being used in the most advanced systems, for example, MSK has been used in NASA's Advanced Communications Technology Satellite (ACTS) launched in 1993, and the others are being perfected for future applications.

Chapter 8 is about quadrature amplitude modulation (QAM). QAM schemes are widely used in telephone modems. For instance, CCITT (Consultative Committee for International Telephone and Telegraph) recommended V.29 and V.33 modems use 16- and 128-QAM, reaching speeds of 9600 bps and 14400 bps respectively, over four-wire leased telephone lines.

Chapter 9 covers nonconstant-envelope bandwidth-efficient modulation schemes. We will study eight schemes, namely, QBL, QORC, SQORC, QOSRC, IJF-OQPSK, TSI-OQPSK, SQAM and Q^2 PSK. These schemes improve the power spectral density with little loss in error probability. They are primarily designed for satellite communications.

Chapter 10 first briefly introduces characteristics of channels with fading and multipath propagation. Then all modulations discussed in Chapters 2–8 are examined under the fading-multipath environment.

Appendixes A and B are basic knowledge of signal spectra and classical signal detection and estimation theory.

This book can be used as a reference book for engineers and researchers. It also can be used as a textbook for graduate students. The material in the book can be covered in a half-year course. For short course use, the instructor may select relevant chapters to cover.

Acknowledgments

First I would like to thank the reviewers and editors at Artech House, Ray Sperber, Mark Walsh, Barbara Lovenvirth, and Judi Stone, whose many critiques and suggestions based on careful reviews contributed to the improvement of the manuscript.

I would like to thank Cleveland State University and Fenn College of Engineering for granting me the sabbatical leave in 1997 during which I wrote a substantial part of the book. I am grateful for the support and encouragement from many colleagues at the Department of Electrical and Computer Engineering.

I am grateful to NASA Glenn Research Center for providing me with several research grants. Particularly, the grant for investigating various modulation schemes that resulted in a report which was well received by NASA engineers and researchers. Encouraged by their enthusiastic response to the report, I published the tutorial paper “Modem Techniques in Satellite Communications” in the *IEEE Communication Magazine*, August 1994. Further, encouraged by the positive response to the tutorial paper, I developed the idea of writing a book detailing all major modulation schemes.

I would like to thank Professor Djamal Zeglache of the Institut National des Telecommunications of France for his support and encouragement to the book.

I would like to thank the Department of Electronics, City University of Hong Kong (CUHK), and the Department of Electronics, Tsinghua University, Beijing, China for supporting my sabbatical leave. Particularly, I would like to thank Professor Li Ping of CUHK for his suggestions to the book and Professor Cao Zhigang of Tsinghua for his support of the book writing.

I am very grateful to the excellent education that I received from Tsinghua University and the University of Manitoba, Canada. Particularly, I would like to thank my doctoral program advisor, Professor Edward Shwedyk of the Department of Electrical and Computer Engineering, University of Manitoba, and Professor John B. Anderson of Electrical, Computer and Systems Engineering Department, Rensselaer Polytechnic Institute, who served in my doctoral dissertation committee, for their guidance and encouragement.

I also appreciate the support and suggestions from my graduate students during the past a few years.

Finally, the support and help for the book from my family are also deeply appreciated.

Fuqin Xiong

Chapter 1

Introduction

In this chapter we briefly discuss the role of modulation in a typical digital communication system, basic modulation methods, and criteria for choosing modulation schemes. Also included is a brief description of various communication channels, which will serve as a background for the later discussion of the modulation schemes.

1.1 DIGITAL COMMUNICATION SYSTEMS

Figure 1.1 is the block diagram of a typical digital communication system. The message to be sent may be from an analog source (e.g., voice) or from a digital source (e.g., computer data). The analog-to-digital (A/D) converter samples and quantizes the analog signal and represents the samples in digital form (bit 1 or 0). The source encoder accepts the digital signal and encodes it into a shorter digital signal. This is called source encoding, which reduces the redundancy hence the transmission speed. This in turn reduces the bandwidth requirement of the system. The channel encoder accepts the output digital signal of the source encoder and encodes it into a longer digital signal. Redundancy is deliberately added into the coded digital signal so that some of the errors caused by the noise or interference during transmission through the channel can be corrected at the receiver. Most often the transmission is in a high-frequency passband, the modulator thus impresses the encoded digital symbols onto a carrier. Sometimes the transmission is in baseband, the modulator is a baseband modulator, also called formator, which formats the encoded digital symbols into a waveform suitable for transmission. Usually there is a power amplifier following the modulator. For high-frequency transmission, modulation and demodulation are usually performed in the intermediate frequency (IF). If this is the case, a frequency up-converter is inserted between the modulator and the power amplifier. If the IF is too low compared with the carrier frequency, several stages of carrier frequency conversions are needed. For wireless systems an antenna is the final stage of the trans-

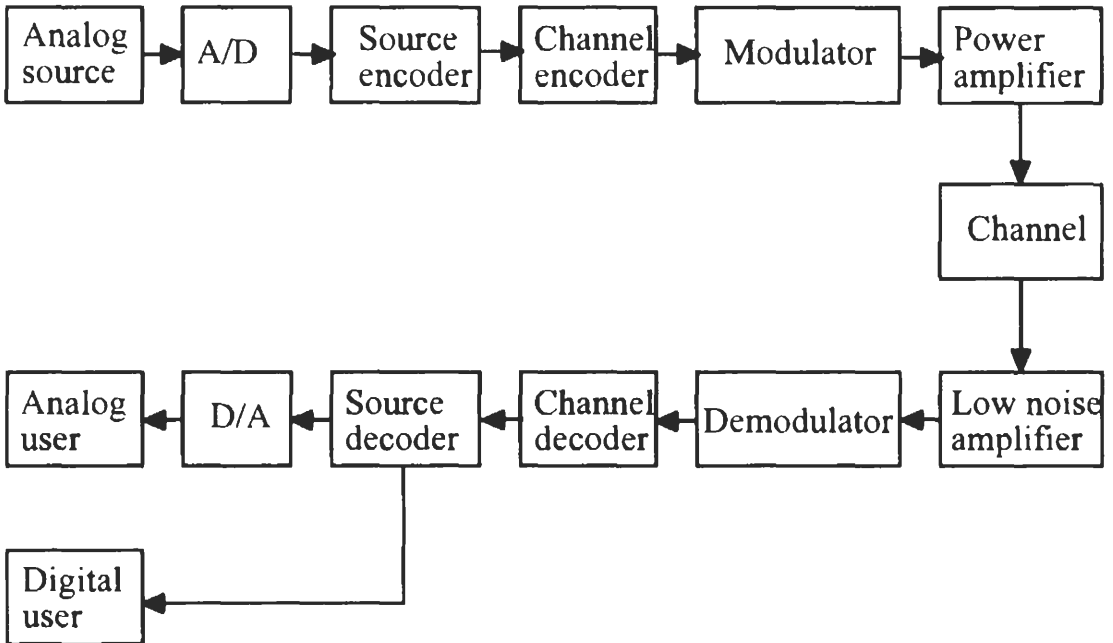


Figure 1.1 Block diagram of a typical digital communication system.

mitter. The transmission medium is usually called the channel, where noise adds to the signal and fading and attenuation effects appear as a complex multiplicative factor on the signal. The term noise here is a wide-sense term which includes all kinds of random electrical disturbance from outside or from within the system. The channel also usually has a limited frequency bandwidth so that it can be viewed as a filter. In the receiver, virtually the reverse signal processing happens. First the received weak signal is amplified (and down-converted if needed) and demodulated. Then the added redundancy is taken away by the channel decoder and the source decoder recovers the signal to its original form before being sent to the user. A digital-to-analog (D/A) converter is needed for analog signals.

The block diagram in Figure 1.1 is just a typical system configuration. A real system configuration could be more complicated. For a multiuser system, a multiplexing stage is inserted before modulator. For a multistation system, a multiple access control stage is inserted before the transmitter. Other features like frequency spread and encryption can also be added into the system. A real system could be simpler too. Source coding and channel coding may not be needed in a simple system. In fact, only the modulator, channel, demodulator, and amplifiers are essential in all communication systems (with antennas for wireless systems).

For the purpose of describing modulation and demodulation techniques and an-

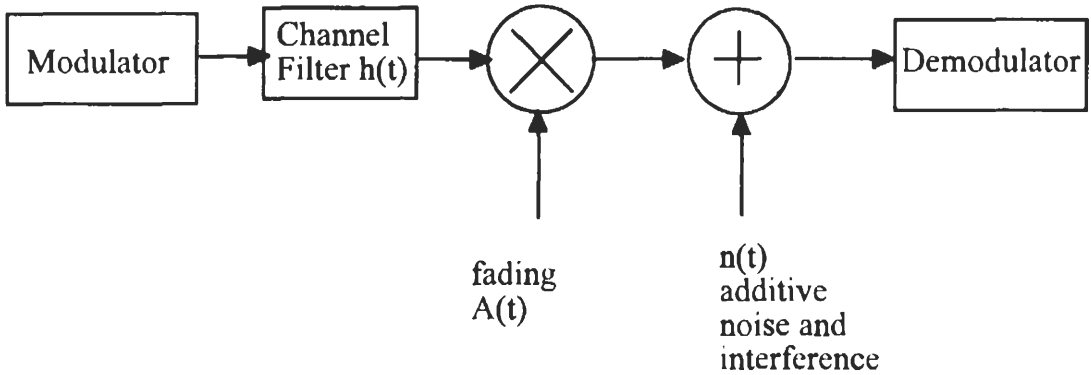


Figure 1.2 Digital communication system model for modulation and demodulation

analyzing their performance, the simplified system model shown in Figure 1.2 will be often used. This model excludes irrelevant blocks with regard to modulation so that relevant blocks stand out. However, recently developed modem techniques combine modulation and channel coding together. In these cases the channel encoder is part of the modulator and the channel decoder is part of the demodulator. From Figure 1.2, the received signal at the input of the demodulator can be expressed as

$$r(t) = A(t) [s(t) * h(t)] + n(t) \quad (1.1)$$

where $*$ denotes convolution. In Figure 1.2 the channel is described by three elements. The first is the channel filter. Because of the fact that the signal $s(t)$ from the modulator must pass the transmitter, the channel (transmission medium) and the receiver before it can reach the demodulator, the channel filter therefore is a composite filter whose transfer function is

$$H(f) = H_T(f)H_C(f)H_R(f) \quad (1.2)$$

where $H_T(f)$, $H_C(f)$, and $H_R(f)$ are the transfer function of the transmitter, the channel, and the receiver, respectively. Equivalently, the impulse response of the channel filter is

$$h(t) = h_T(t) * h_C(t) * h_R(t) \quad (1.3)$$

where $h_T(t)$, $h_C(t)$, and $h_R(t)$ are the impulse responses of the transmitter, the channel, and the receiver, respectively. The second element is the factor $A(t)$ which is generally complex. This factor represents fading in some types of channels, such as mobile radio channel. The third element is the additive noise and interference term $n(t)$. We will discuss fading and noise in more detail in the next section. The channel

model in Figure 1.2 is a general model. It may be simplified in some circumstances, as we will see in the next section.

1.2 COMMUNICATION CHANNELS

Channel characteristic plays an important role in studying, choosing, and designing modulation schemes. Modulation schemes are studied for different channels in order to know their performance in these channels. Modulation schemes are chosen or designed according to channel characteristic in order to optimize their performance. In this section we discuss several important channel models in communications.

1.2.1 Additive White Gaussian Noise Channel

Additive white Gaussian noise (AWGN) channel is a universal channel model for analyzing modulation schemes. In this model, the channel does nothing but add a white Gaussian noise to the signal passing through it. This implies that the channel's amplitude frequency response is flat (thus with unlimited or infinite bandwidth) and phase frequency response is linear for all frequencies so that modulated signals pass through it without any amplitude loss and phase distortion of frequency components. Fading does not exist. The only distortion is introduced by the AWGN. The received signal in (1.1) is simplified to

$$r(t) = s(t) + n(t) \quad (1.4)$$

where $n(t)$ is the additive white Gaussian noise.

The whiteness of $n(t)$ implies that it is a stationary random process with a flat power spectral density (PSD) for all frequencies. It is a convention to assume its PSD as

$$N(f) = N_o/2, \quad -\infty < f < \infty \quad (1.5)$$

This implies that a white process has infinite power. This of course is a mathematical idealization. According to the Wiener-Khinchine theorem, the autocorrelation function of the AWGN is

$$\begin{aligned} R(\tau) &\triangleq E\{n(t)n(t-\tau)\} = \int_{-\infty}^{\infty} N(f)e^{j2\pi f\tau} df \\ &= \int_{-\infty}^{\infty} \frac{N_o}{2} e^{j2\pi f\tau} df = \frac{N_o}{2} \delta(\tau) \end{aligned} \quad (1.6)$$

where $\delta(\tau)$ is the Dirac delta function. This shows the noise samples are uncorrelated

no matter how close they are in time. The samples are also independent since the process is Gaussian.

At any time instance, the amplitude of $n(t)$ obeys a Gaussian probability density function given by

$$p(\eta) = \frac{1}{\sqrt{2\pi\sigma^2}} \exp\left\{-\frac{\eta^2}{2\sigma^2}\right\} \quad (1.7)$$

where η is used to represent the values of the random process $n(t)$ and σ^2 is the variance of the random process. It is interesting to note that $\sigma^2 = \infty$ for the AWGN process since σ^2 is the power of the noise, which is infinite due to its “whiteness.”

However, when $r(t)$ is correlated with a orthonormal function $\phi(t)$, the noise in the output has a finite variance. In fact

$$r = \int_{-\infty}^{\infty} r(t)\phi(t)dt = s + n$$

where

$$s = \int_{-\infty}^{\infty} s(t)\phi(t)dt$$

and

$$n = \int_{-\infty}^{\infty} n(t)\phi(t)dt$$

The variance of n is

$$\begin{aligned} E\{n^2\} &= E\left\{\left[\int_{-\infty}^{\infty} n(t)\phi(t)dt\right]^2\right\} \\ &= E\left\{\int_{-\infty}^{\infty} \int_{-\infty}^{\infty} n(t)\phi(t)n(\tau)\phi(\tau)dtd\tau\right\} \\ &= \int_{-\infty}^{\infty} \int_{-\infty}^{\infty} E\{n(t)n(\tau)\}\phi(t)\phi(\tau)dtd\tau \\ &= \int_{-\infty}^{\infty} \int_{-\infty}^{\infty} \frac{N_o}{2}\delta(t-\tau)\phi(t)\phi(\tau)dtd\tau \\ &= \frac{N_o}{2} \int_{-\infty}^{\infty} \phi^2(t)dt = \frac{N_o}{2} \end{aligned} \quad (1.8)$$

Then the probability density function (PDF) of n can be written as

$$p(n) = \frac{1}{\sqrt{\pi N_o}} \exp\left\{-\frac{n^2}{N_o}\right\} \quad (1.9)$$

This result will be frequently used in this book.

Strictly speaking, the AWGN channel does not exist since no channel can have an infinite bandwidth. However, when the signal bandwidth is smaller than the channel bandwidth, many practical channels are approximately an AWGN channel. For example, the line-of-sight (LOS) radio channels, including fixed terrestrial microwave links and fixed satellite links, are approximately AWGN channels when the weather is good. Wideband coaxial cables are also approximately AWGN channels since there is no other interference except the Gaussian noise.

In this book, all modulation schemes are studied for the AWGN channel. The reason of doing this is two-fold. First, some channels are approximately an AWGN channel, the results can be used directly. Second, additive Gaussian noise is ever present regardless of whether other channel impairments such as limited bandwidth, fading, multipath, and other interferences exist or not. Thus the AWGN channel is the best channel that one can get. The performance of a modulation scheme evaluated in this channel is an upper bound on the performance. When other channel impairments exist, the system performance will degrade. The extent of degradation may vary for different modulation schemes. The performance in AWGN can serve as a standard in evaluating the degradation and also in evaluating effectiveness of impairment-combatting techniques.

1.2.2 Bandlimited Channel

When the channel bandwidth is smaller than the signal bandwidth, the channel is bandlimited. Severe bandwidth limitation causes intersymbol interference (ISI) (i.e., digital pulses will extend beyond their transmission duration (symbol period T_s)) and interfere with the next symbol or even more symbols. The ISI causes an increase in the bit error probability (P_b) or bit error rate (BER), as it is commonly called. When increasing the channel bandwidth is impossible or not cost-efficient, channel equalization techniques are used for combatting ISI. Throughout the years, numerous equalization techniques have been invented and used. New equalization techniques are appearing continuously. We will not cover them in this book. For introductory treatment of equalization techniques, the reader is referred to [1, Chapter 6] or any other communication systems books.

1.2.3 Fading Channel

Fading is a phenomena occurring when the amplitude and phase of a radio signal change rapidly over a short period of time or travel distance. Fading is caused by interference between two or more versions of the transmitted signal which arrive at the receiver at slightly different times. These waves, called multipath waves, combine at the receiver antenna to give a resultant signal which can vary widely in amplitude and phase. If the delays of the multipath signals are longer than a symbol period, these multipath signals must be considered as different signals. In this case, we have individual multipath signals.

In mobile communication channels, such as terrestrial mobile channel and satellite mobile channel, fading and multipath interference are caused by reflections from surrounding buildings and terrains. In addition, the relative motion between the transmitter and receiver results in random frequency modulation in the signal due to different Doppler shifts on each of the multipath components. The motion of surrounding objects, such as vehicles, also induces a time-varying Doppler shift on multipath component. However, if the surrounding objects move at a speed less than the mobile unit, their effect can be ignored [2].

Fading and multipath interference also exist in fixed LOS microwave links [3]. On clear, calm summer evenings, normal atmospheric turbulence is minimal. The troposphere stratifies with inhomogeneous temperature and moisture distributions. Layering of the lower atmosphere creates sharp refractive index gradients which in turn create multiple signal paths with different relative amplitudes and delays.

Fading causes amplitude fluctuations and phase variations in received signals. Multipath causes intersymbol interference. Doppler shift causes carrier frequency drift and signal bandwidth spread. All these lead to performances degradation of modulations. Analysis of modulation performances in fading channels is given in Chapter 10 where characteristics of fading channels will be discussed in more detail.

1.3 BASIC MODULATION METHODS

Digital modulation is a process that impresses a digital symbol onto a signal suitable for transmission. For short distance transmissions, baseband modulation is usually used. Baseband modulation is often called line coding. A sequence of digital symbols are used to create a square pulse waveform with certain features which represent each type of symbol without ambiguity so that they can be recovered upon reception. These features are variations of pulse amplitude, pulse width, and pulse position. Figure 1.3 shows several baseband modulation waveforms. The first one is the non-return to zero-level (NRZ-L) modulation which represents a symbol 1 by a positive

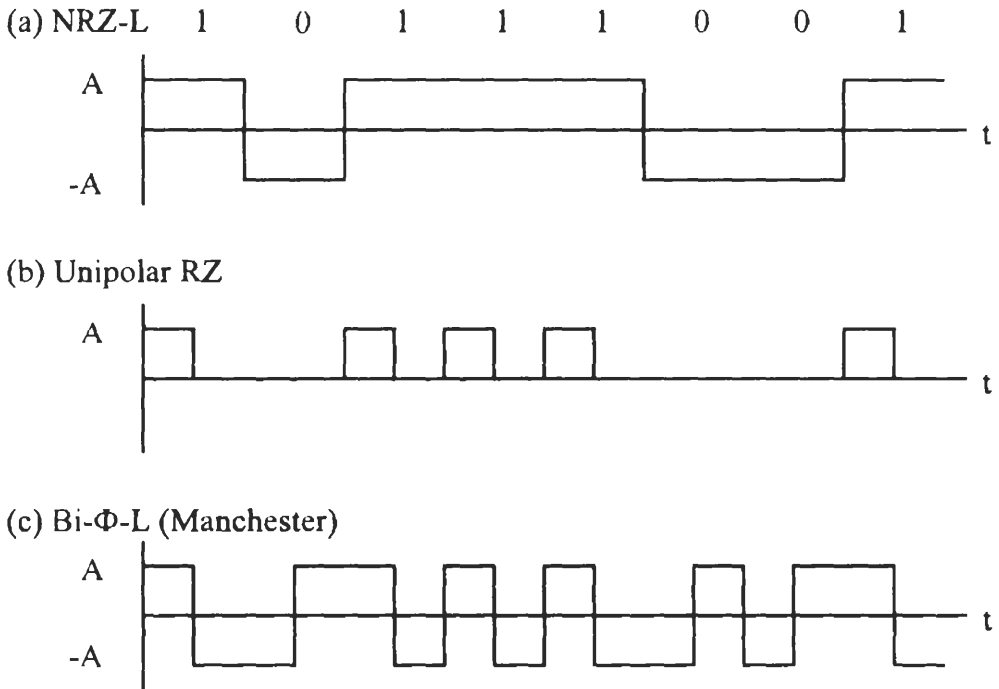


Figure 1.3 Baseband digital modulation examples.

square pulse with length T and a symbol 0 by a negative square pulse with length T . The second one is the unipolar return to zero modulation with a positive pulse of $T/2$ for symbol 1 and nothing for 0. The third is the biphas level or Manchester, after its inventor, modulation which uses a waveform consisting of a positive first-half T pulse and a negative second-half T pulse for 1 and a reversed waveform for 0. These and other baseband schemes will be discussed in detail in Chapter 2.

For long distance and wireless transmissions, bandpass modulation is usually used. Bandpass modulation is also called carrier modulation. A sequence of digital symbols are used to alter the parameters of a high-frequency sinusoidal signal called carrier. It is well known that a sinusoidal signal has three parameters: amplitude, frequency, and phase. Thus amplitude modulation, frequency modulation, and phase modulation are the three basic modulation methods in passband modulation. Figure 1.4 shows three basic binary carrier modulations. They are amplitude shift keying (ASK), frequency shift keying (FSK), and phase shift keying (PSK). In ASK, the modulator puts out a burst of carrier for every symbol 1, and no signal for every symbol 0. This scheme is also called on-off keying (OOK). In a general ASK scheme, the amplitude for symbol 0 is not necessarily 0. In FSK, for symbol 1 a higher frequency burst is transmitted and for symbol 0 a lower frequency burst

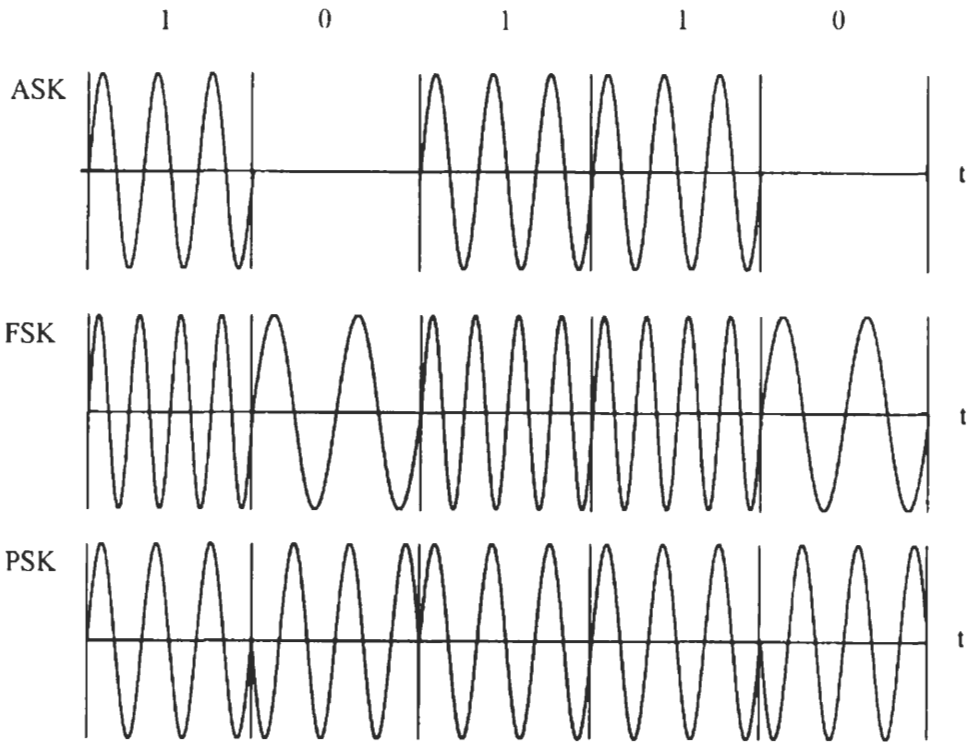


Figure 1.4 Three basic bandpass modulation schemes.

is transmitted, or vice versa. In PSK, a symbol 1 is transmitted as a burst of carrier with 0 initial phase while a symbol 0 is transmitted as a burst of carrier with 180° initial phase.

Based on these three basic schemes, a variety of modulation schemes can be derived from their combinations. For example, by combining two binary PSK (BPSK) signals with orthogonal carriers a new scheme called quadrature phase shift keying (QPSK) can be generated. By modulating both amplitude and phase of the carrier, we can obtain a scheme called quadrature amplitude modulation (QAM), etc.

1.4 CRITERIA OF CHOOSING MODULATION SCHEMES

The essence of digital modem design is to efficiently transmit digital bits and recover them from corruptions from the noise and other channel impairments. There are three primary criteria of choosing modulation schemes: power efficiency, bandwidth

efficiency, and system complexity.

1.4.1 Power Efficiency

The bit error rate, or bit error probability of a modulation scheme is inversely related to E_b/N_o , the bit energy to noise spectral density ratio. For example, P_b of ASK in the AWGN channel is given by

$$P_b = Q\left(\sqrt{\frac{2E_b}{N_o}}\right) \quad (1.10)$$

where E_b is the average bit energy, N_o is the noise power spectral density (PSD), and $Q(x)$ is the Gaussian integral, sometimes referred to as the Q-function. It is defined as

$$Q(x) = \int_x^\infty \frac{1}{\sqrt{2\pi}} e^{-u^2} du \quad (1.11)$$

which is a monotonically decreasing function of x . Therefore the power efficiency of a modulation scheme is defined straightforwardly as the required E_b/N_o for a certain bit error probability (P_b) over an AWGN channel. $P_b = 10^{-5}$ is usually used as the reference bit error probability.

1.4.2 Bandwidth Efficiency

The determination of bandwidth efficiency is a bit more complex. The bandwidth efficiency is defined as the number of bits per second that can be transmitted in one Hertz of system bandwidth. Obviously it depends on the requirement of system bandwidth for a certain modulated signal. For example, the one-sided power spectral density of an ASK signal modulated by an equiprobable independent random binary sequence is given by

$$\Psi_s(f) = \frac{A^2 T}{4} \text{sinc}^2 [T(f - f_c)] + \frac{A^2}{4} \delta(f - f_c)$$

and is shown in Figure 1.5, where T is the bit duration, A is the carrier amplitude, and f_c is the carrier frequency. From the figure we can see that the signal spectrum stretches from $-\infty$ to ∞ . Thus to perfectly transmit the signal an infinite system bandwidth is required, which is impractical. The practical system bandwidth requirement is finite, which varies depending on different criteria. For example, in Figure 1.5, most of the signal energy concentrates in the band between two nulls, thus a null-to-null bandwidth requirement seems adequate. Three bandwidth efficiencies

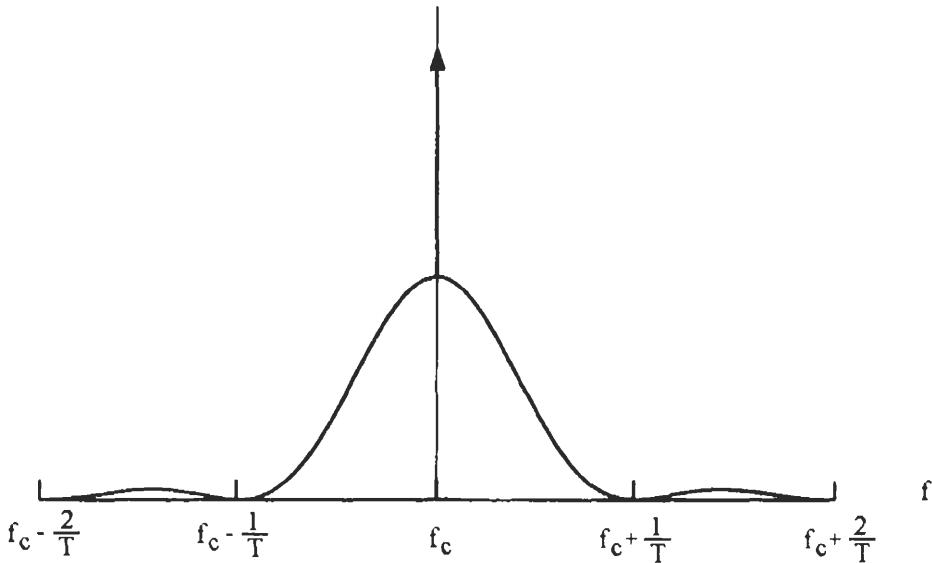


Figure 1.5 Power spectral density of ASK.

used in the literature are as follows:

Nyquist Bandwidth Efficiency—Assuming the system uses Nyquist (ideal rectangular) filtering at baseband, which has the minimum bandwidth required for intersymbol interference-free transmission of digital signals, then the bandwidth at baseband is $0.5R_s$, R_s is the symbol rate, and the bandwidth at carrier frequency is $W = R_s$. Since $R_s = R_b/\log_2 M$, $R_b =$ bit rate, for M -ary modulation, the bandwidth efficiency is

$$R_b/W = \log_2 M \quad (1.12)$$

Null-to-Null Bandwidth Efficiency—For modulation schemes that have power density spectral nulls such as the one of ASK in Figure 1.5, defining the bandwidth as the width of the main spectral lobe is a convenient way of bandwidth definition.

Percentage Bandwidth Efficiency—If the spectrum of the modulated signal does not have nulls, as in general continuous phase modulation (CPM), null-to-null bandwidth no longer exists. In this case, energy percentage bandwidth may be used. Usually 99% is used, even though other percentages (e.g., 90%, 95%) are also used.

1.4.3 System Complexity

System complexity refers to the amount of circuits involved and the technical difficulty of the system. Associated with the system complexity is the cost of manu-

facturing, which is of course a major concern in choosing a modulation technique. Usually the demodulator is more complex than the modulator. Coherent demodulator is much more complex than noncoherent demodulator since carrier recovery is required. For some demodulation methods, sophisticated algorithms like the Viterbi algorithm is required. All these are basis for complexity comparison.

Since power efficiency, bandwidth efficiency, and system complexity are the main criteria of choosing a modulation technique, we will always pay attention to them in the analysis of modulation techniques in the rest of the book.

1.5 OVERVIEW OF DIGITAL MODULATION SCHEMES

To provide the reader with an overview, we list the abbreviations and descriptive names of various digital modulations that we will cover in Table 1.1 and arrange them in a relationship tree diagram in Figure 1.6. Some of the schemes can be derived from more than one “parent” scheme. The schemes where differential encoding can be used are labeled by letter D and those that can be noncoherently demodulated are labeled with a letter N. All schemes can be coherently demodulated.

The modulation schemes listed in the table and the tree are classified into two large categories: constant envelope and nonconstant envelope. Under constant envelope class, there are three subclasses: FSK, PSK, and CPM. Under nonconstant envelope class, there are three subclasses: ASK, QAM, and other nonconstant envelope modulations.

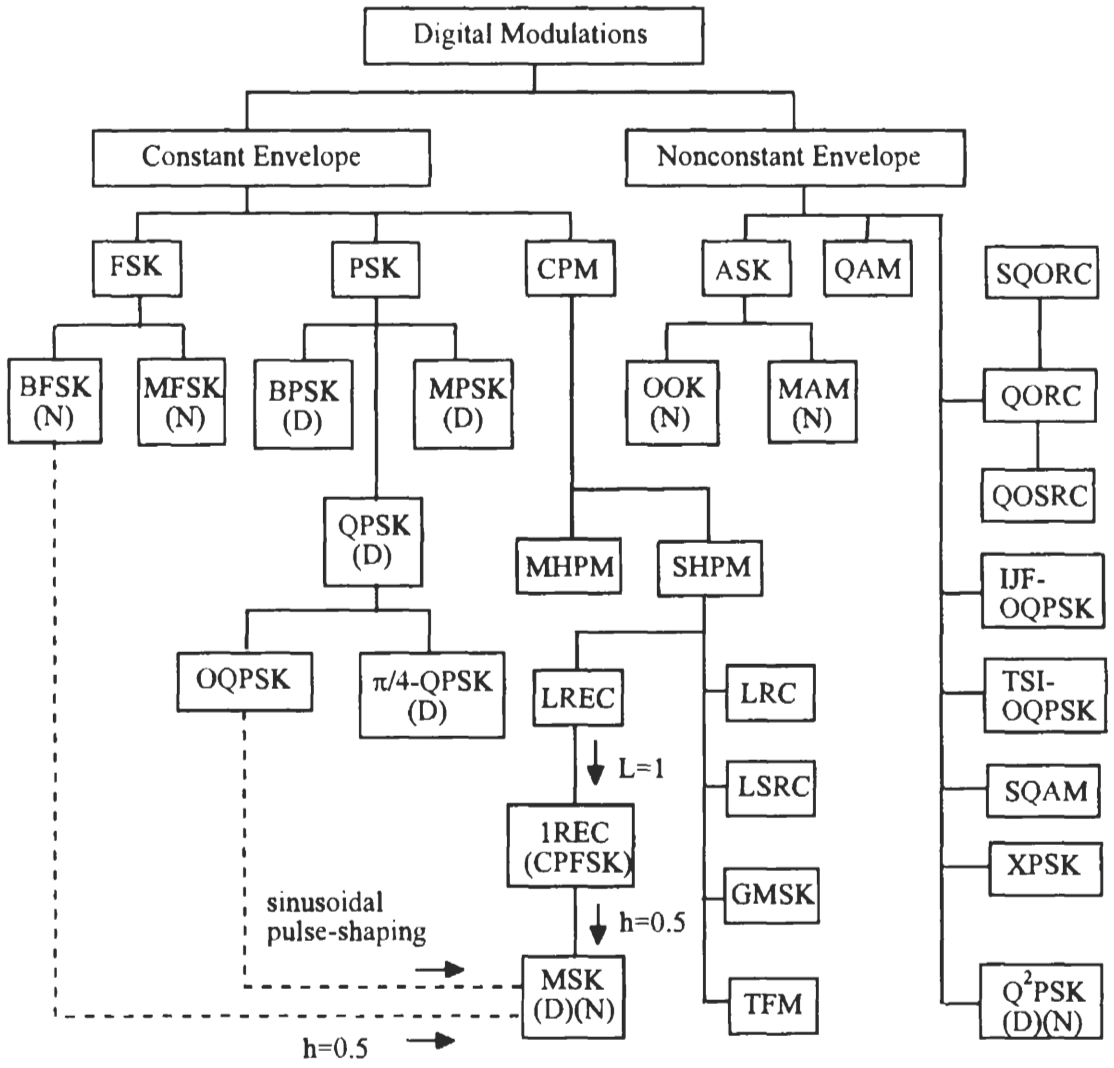
Among the listed schemes, ASK, PSK, and FSK are basic modulations, and MSK, GMSK, CPM, MHPM, and QAM, etc. are advanced schemes. The advanced schemes are variations and combinations of the basic schemes.

The constant envelope class is generally suitable for communication systems whose power amplifiers must operate in the nonlinear region of the input-output characteristic in order to achieve maximum amplifier efficiency. An example is the TWTA (traveling wave tube amplifier) in satellite communications. However, the generic FSK schemes in this class are inappropriate for satellite application since they have very low bandwidth efficiency in comparison with PSK schemes. Binary FSK is used in the low-rate control channels of first generation cellular systems, AMPS (advance mobile phone service of US.) and ETACS (European total access communication system). The data rates are 10 Kbps for AMPS and 8 Kbps for ETACS. The PSK schemes, including BPSK, QPSK, OQPSK, and MSK have been used in satellite communication systems.

The $\pi/4$ -QPSK is worth special attention due to its ability to avoid 180° abrupt phase shift and to enable differential demodulation. It has been used in digital mobile cellular systems, such as the United States digital cellular (USDC) system.

Abbreviation	Alternate Abbr.	Descriptive name
Frequency Shift Keying (FSK)		
BFSK	FSK	Binary Frequency Shift Keying
MFSK		M-ary Frequency Shift Keying
Phase Shift Keying (PSK)		
BPSK	PSK	Binary Phase Shift Keying
QPSK	4PSK	Quadrature Phase Shift Keying
OQPSK	SQPSK	Offset QPSK, Staggered QPSK
$\pi/4$ -QPSK		$\pi/4$ Quadrature Phase Shift Keying
MPSK		M-ary Phase Shift Keying
Continuous Phase Modulations (CPM)		
SHPM		Single-h (modulation index) Phase Modulation
MHPM		Multi-h Phase Modulation
LREC		Rectangular Pulse of Length L
CPFSK		Continuous Phase Frequency Shift Keying
MSK	FFSK	Minimum Shift Keying, Fast FSK
SMSK		Serial Minimum Shift Keying
LRC		Raised Cosine Pulse of Length L
LSRC		Spectrally Raised Cosine Pulse of Length L
GMSK		Gaussian Minimum Shift Keying
TFM		Tamed Frequency Modulation
Amplitude and Amplitude/Phase modulations		
ASK		Amplitude Shift Keying (generic name)
OOK	ASK	Binary On-Off Keying
MASK	MAM	M-ary ASK, M-ary Amplitude Modulation
QAM		Quadrature Amplitude Modulation
Nonconstant Envelope Modulations		
QORC		Quadrature Overlapped Raised Cosine Modulation
SQORC		Staggered QORC
QOSRC		Quadrature Overlapped Squared Raised Cosine Modulation
Q ² PSK		Quadrature Quadrature Phase Shift Keying
IIF-OQPSK		Intersymbol-Interference/Jitter-Free OQPSK
TSI-OQPSK		Two-Symbol-Interval OQPSK
SQAM		Superposed-QAM
XPSK		Crosscorrelated QPSK

Table 1.1 Digital modulation schemes (Abbr.=Abbreviation).



- Solid lines indicate “can be derived from”
- - - - - Dashed lines indicate “alternatively can be derived from”
- (D) Can be differentially encoded and decoded
- (N) Can be noncoherently detected

Figure 1.6 Digital Modulation Tree. After [4].

The PSK schemes have constant envelope but discontinuous phase transitions from symbol to symbol. The CPM schemes have not only constant envelope, but also continuous phase transitions. Thus they have less side lobe energy in their spectra in comparison with the PSK schemes. The CPM class includes LREC, LRC, LSRC, GMSK, and TFM. Their differences lie in their different *frequency pulses* which are reflected in their names. For example, LREC means the frequency pulse is a rectangular pulse with a length of L symbol periods. MSK and GMSK are two important schemes in CPM class. MSK is a special case of CPFSK, but it also can be derived from OQPSK with extra sinusoidal pulse-shaping. MSK has excellent power and bandwidth efficiency. Its modulator and demodulator are also not too complex. MSK has been used in NASA's Advanced Communication Technology Satellite (ACTS). GMSK has a Gaussian frequency pulse. Thus it can achieve even better bandwidth efficiency than MSK. GMSK is used in the US cellular digital packet data (CDPD) system and European GSM (global system for mobile communication) system.

MHPM is worth special attention since it has better error performance than single- h CPM by cyclically varying the modulation index h .

The generic nonconstant envelope schemes, such as ASK and QAM, are generally not suitable for systems with nonlinear power amplifiers. However QAM, with a large signal constellation, can achieve extremely high bandwidth efficiency. QAM has been widely used in modems used in telephone networks, such as computer modems. QAM can even be considered for satellite systems. In this case, however, back-off in TWTA's input and output power must be provided to ensure the linearity of the power amplifier.

The third class under nonconstant envelope modulation includes quite a few schemes. These are primarily designed for satellite applications since they have very good bandwidth efficiency and the amplitude variation is minimal. All of them except Q^2 PSK are based on $2T_s$ amplitude pulse shaping and their modulator structures are similar to that of OQPSK. The scheme Q^2 PSK is based on four orthogonal carriers.

References

- [1] Proakis, J., *Digital Communication*, New York: McGraw-Hill, 1983.
- [2] Rappaport, T., *Wireless Communications: Principles and Practice*. Upper Saddle River, New Jersey: Prentice Hall, 1996.
- [3] Siller, C., "Multipath propagation," *IEEE Communications Magazine*, vol. 22, no.2, Feb. 1984, pp. 6-15.
- [4] Xiong, F., "Modem techniques in satellite communications," *IEEE Communications Magazine*, vol. 32, no.8, August 1994, pp. 84-98.

Selected Bibliography

- Feher, K., editor. *Advanced Digital Communications*. Englewood Cliffs, New Jersey: Prentice Hall, 1987.
- Proakis, J., and M. Salehi. *Communication Systems Engineering*. Englewood Cliffs, New Jersey: Prentice Hall, 1994.
- Sklar, B., *Digital Communications, Fundamentals and Applications*, Englewood Cliffs, New Jersey: Prentice Hall, 1988.

Chapter 2

Baseband Modulation (Line Codes)

Baseband modulation is defined as a direct transmission without frequency transform. It is the technology of representing digital sequences by pulse waveforms suitable for baseband transmission. A variety of waveforms have been proposed in an effort to find ones with some desirable properties, such as good bandwidth and power efficiency, and adequate timing information. These baseband modulation waveforms are variably called *line codes*, *baseband formats* (or *waveforms*), *PCM waveforms* (or *formats*, or *codes*). PCM (pulse code modulation) refers to the process that a binary sequence representing a digitized analog signal is coded into a pulse waveform. For a data signal PCM is not needed. Therefore the terms line code and baseband format (or waveform) are more pertinent and the former one is more often used. Line codes were mainly developed in the 1960s by engineers at AT&T, IBM or RCA for digital transmission over telephone cables or digital recording on magnetic media [1–5]. Recent developments in line codes mainly concentrate on fiber optic transmission systems [6–11].

In this chapter we first introduce differential coding technique which is used in the later part of the chapter in constructing line codes. Then we describe various basic line codes in Section 2.2. Their power spectral densities are discussed in Section 2.3. The demodulation of these waveforms is in effect a detection problem of signals in noise. In Section 2.4 we first describe optimum detection of binary signals in additive white Gaussian noise (AWGN) and then apply the resultant general formulas to obtain expressions for bit error probabilities or bit error rates (BER) of various line codes. The general results can be used for any binary signal, including bandpass signals which will be described in later chapters. It also should be pointed out that practical detectors for line codes are often not optimum in order to simplify circuitry. However, the performance of an optimum detector can always serve as a reference for comparison. Substitution codes and block line codes are more complicated codes with improved performance over basic line codes. They are discussed in Sections 2.5 and 2.6. Section 2.7 summarizes this chapter. Intersymbol interference (ISI)

phenomena and equalization techniques, including duobinary signaling technique, are important topics in baseband signaling techniques, whether bandpass modulation is followed or not. An in-depth coverage of these topics requires a large number of pages and is therefore not included in this book which is intended for modulation schemes. For introductory knowledge of ISI and equalization the reader can refer to any text book on digital communications.

2.1 DIFFERENTIAL CODING

Since some of the baseband binary waveforms use a technique called *differential encoding*, we need become familiar with this simple yet important baseband technique. This technique is not only used in baseband modulation but also in bandpass modulation where it is used to encode the baseband data before modulating it onto a carrier. The benefit of using differential coding will become clear when we discuss the schemes that use it. We now study this technique and it will be used throughout the rest of the book.

Let $\{a_k\}$ be the original binary data sequence, then a differentially encoded binary data sequence $\{d_k\}$ is produced according to the rule

$$d_k = a_k \oplus d_{k-1} \quad (2.1)$$

where \oplus indicates *modulo-2 addition*. Modulo-2 addition is also called *exclusive-OR (XOR)*. The modulo-2 addition rules are $0 + 0 = 0$, $0 + 1 = 1$, $1 + 0 = 1$, and $1 + 1 = 0$. From (2.1) and the modulo-2 rules we can see that the current output bit of the encoder is determined by the current input bit and the previous output bit. If they are different the output bit is 1, otherwise the output bit is 0. This gives the name differential encoding.

To perform differential encoding an initial bit is needed and it is called a reference bit. For example, if $\{a_k\}$ and $\{d_k\}$ both start with $k = 1$, then we need a d_0 as the reference bit. Since d_0 could be chosen as 0 or 1, then $\{a_k\}$ can be encoded into two different data sequences. They are complementary to each other.

The decoding rule is

$$\hat{a}_k = \hat{d}_k \oplus \hat{d}_{k-1} \quad (2.2)$$

where the hat indicates the received data at the receiver. The received $\{\hat{d}_k\}$ could be the same as or different from $\{d_k\}$. For example channel noise might have altered some of the bits in $\{d_k\}$ when it is received. Even if noise is light so that no bits have been altered by noise, the polarity reversals in various stages of the transmitter and receiver might have reversed the polarity of the entire sequence. One of the

Encoding													
a_k		1	0	1	1	0	0	0	1	1	1	0	0
$\hat{d}_k = a_k \oplus d_{k-1}$	0	1	1	0	1	1	1	1	0	1	0	0	0
Decoding													
\hat{d}_k (correct polarity)	0	1	1	0	1	1	1	1	0	1	0	0	0
$\hat{a}_k = \hat{d}_k \oplus \hat{d}_{k-1}$		1	0	1	1	0	0	0	1	1	1	0	0
Decoding													
\hat{d}_k (reversed polarity)	1	0	0	1	0	0	0	0	1	0	1	1	1
$\hat{a}_k = \hat{d}_k \oplus \hat{d}_{k-1}$		1	0	1	1	0	0	0	1	1	1	0	0

Table 2.1 Examples of differential coding.

important uses of differential coding is to eliminate the effect of polarity reversal. This is clear from (2.2) since the decoder output depends on the difference of the two consecutive received bits, not their polarities. When the polarity of the entire sequence is altered, the difference between two consecutive bits remains the same. Table 2.1 is an example which illustrates the encoding and decoding processes with or without polarity reversal. The results are the same. Note that no errors caused by noise are assumed in the example. The first bit of $\{d_k\}$ is the reference bit which is 0 in the example.

Figure 2.1 shows the block diagrams of the differential encoder and decoder defined by (2.1) and (2.2).

The probability distribution of the differentially encoded sequence is of interest. It is useful when the autocorrelation function of the coded sequence is calculated later in the chapter. Assume the data sequence $\{a_k\}$ is stationary, its bits are independent and with a distribution of (p_0, p_1) , where $p_0 = \Pr(0)$ and $p_1 = \Pr(1)$, $p_0 + p_1 = 1$. Assume the distribution of the k th bit of the coded sequence $\{d_k\}$ is $(q_0^{(k)}, q_1^{(k)})$, where $q_0^{(k)} = \Pr(0)$ and $q_1^{(k)} = \Pr(1)$, $q_0^{(k)} + q_1^{(k)} = 1$. According to (2.1) we have

$$q_0^{(k)} = p_0 q_0^{(k-1)} + p_1 q_1^{(k-1)} \quad (2.3)$$

and

$$q_1^{(k)} = p_0 q_1^{(k-1)} + p_1 q_0^{(k-1)} \quad (2.4)$$

Since an initial bit is specified when encoding, $q_0^{(0)}$ and $q_1^{(0)}$ are known. They are either 0 or 1, depending on what is chosen. For instance, if the reference is 0, then $q_0^{(0)} = 1$, $q_1^{(0)} = 0$. It is easy to verify that if $p_0 = p_1 = 1/2$, then $q_0^{(k)} = q_1^{(k)} = 1/2$, for all k . That is, differential encoding does not change data distribution for equally likely data. However, when the distribution of the original data is not equal, differential encoding does change the data distribution. Further we can show that

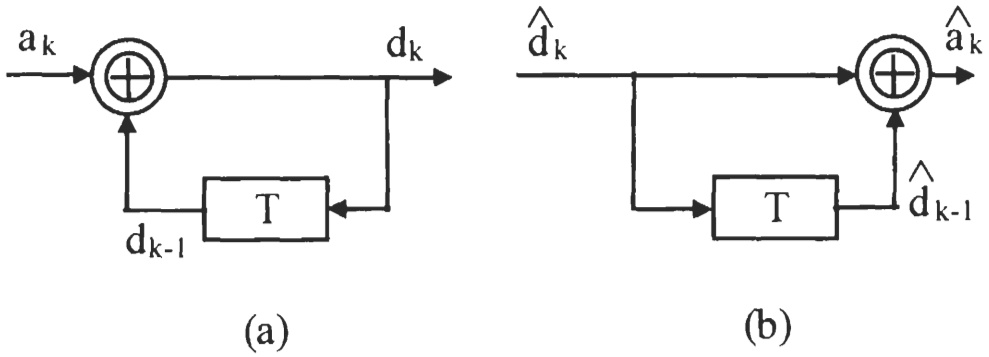


Figure 2.1 Differential encoder (a), and decoder (b).

$q_0^{(k)} = q_1^{(k)} = 1/2$ asymptotically regardless of values of p_0 and p_1 .

We start with any one of the above two equations, say (2.3), from which we have

$$q_0^{(k)} = (1 - p_0) + (2p_0 - 1)q_0^{(k-1)}$$

Taking a z -transform of both sides of the above equation, we obtain

$$Q_0(z) = \frac{1 - p_0}{(1 - z^{-1})} + (2p_0 - 1)z^{-1}Q_0(z)$$

where $Q_0(z)$ is the z -transform of sequence $\{q_0^{(k)}\}$. Rearranging terms we have

$$Q_0(z) = \frac{1 - p_0}{(1 - z^{-1})[1 - (2p_0 - 1)z^{-1}]}$$

Using the final-value theorem we obtain the limit of $q_0^{(k)}$ as

$$\begin{aligned} \lim_{k \rightarrow \infty} q_0^{(k)} &= \lim_{z \rightarrow 1} [(1 - z^{-1})Q_0(z)] \\ &= \lim_{z \rightarrow 1} \frac{1 - p_0}{1 - (2p_0 - 1)z^{-1}} = \frac{1}{2} \end{aligned}$$

Thus we can conclude that regardless of the distribution of the original data, the distribution of the differentially encoded data is always asymptotically equal.

To see how fast $q_0^{(k)}$ converges to $1/2$, we define two ratios as

$$r_k = q_1^{(k)} / q_0^{(k)}$$

$$l = p_1 / p_0$$

and substituting (2.3) and (2.4) into the r_k expression we have

$$r_k = \frac{l + r_{k-1}}{1 + lr_{k-1}} \quad (2.5)$$

Next we define the ratio difference as

$$\Delta r_k = r_k - r_{k-1}$$

If $\Delta r_k \rightarrow 0$, then $r_k \rightarrow r_{k-1}$, solving (2.5) will give $r_k = 1$ (i.e., $q_1^{(k)} = q_0^{(k)}$ for $k \rightarrow \infty$).

Calculations show that for $p_0 = 0.3$ and 0.1 , $q_1^{(k)}$ virtually equals $q_0^{(k)}$ ($\Delta r_k < 0.001$) at $k = 10$ and 38 , respectively. For a very skewed distribution (e.g., $p_0 = 0.01$), to reach $\Delta r_k < 0.001$, 411 iterations are needed. All these k values are small when compared with numbers of data in practical systems. Thus we can see that the distribution of the differentially encoded data becomes virtually equal very quickly, regardless of the distribution of the original data,

Differential encoding can also be done by taking the binary complement of the modulo-2 adder as the output, that is

$$d_k = \overline{a_k \oplus d_{k-1}} \quad (2.6)$$

where \bar{x} denotes a binary complement of x . Again this second rule can generate two complementary sequences with the two different choices of the reference bit. The corresponding decoding rule is

$$\hat{a}_k = \overline{\hat{d}_k \oplus \hat{d}_{k-1}} \quad (2.7)$$

which is also capable of correcting polarity reversals. The block diagrams of the encoder and the decoder defined by this set of rules are similar to that in Figure 2.1 except that an inverter is needed at the output of both encoder and decoder.

The above argument about distribution also applies to data encoded this way since this coded sequence is just a complement of the previous one.

Another type of differential encoding is

$$d_k = a_{k-1} - a_k \quad (2.8)$$

which produces a three-level sequence $(-1, 0, +1)$. An arbitrary initial reference bit a_0 must be specified. It is obvious that the distribution of d_k is

$$d_k = \begin{cases} 1, & q_1 = p_1 p_0, & \text{for } a_{k-1} = 1 \text{ and } a_k = 0 \\ -1, & q_{-1} = p_0 p_1, & \text{for } a_{k-1} = 0 \text{ and } a_k = 1 \\ 0, & q_0 = p_0^2 + p_1^2, & \text{for } a_{k-1} = a_k = 0 \text{ or } 1 \end{cases} \quad (2.9)$$

Decoding can be done as follows. First $\{\widehat{d}_k\}$ is converted to unipolar $\{\widehat{u}_k\}$ by full-wave rectification, then $\{\widehat{a}_k\}$ is recovered from $\{\widehat{u}_k\}$ by XOR operation:

$$\widehat{a}_k = \widehat{a}_{k-1} \oplus \widehat{u}_k \quad (2.10)$$

where the initial $\widehat{a}_0 = a_0$ is known. This coding scheme is also immune from polarity inversion-ambiguity problem since after full-wave rectification, the waveform would be the same.

2.2 DESCRIPTION OF LINE CODES

Many binary line codes have been proposed in the literature and some of them have been used in practical systems [1–11]. Basic codes can be classified into four classes: *nonreturn-to-zero (NRZ)*, *return-to-zero (RZ)*, *pseudoternary (PT)*, and *biphase*. NRZ and RZ classes can be further divided into *unipolar* and *polar* subclasses. Advanced codes include *substitution codes* and *block codes*. There are some other codes which do not belong to any of the classes. Some codes may belong to more than one class. Figure 2.2 is a quite complete collection of waveforms of various basic line codes. Each of them will be studied in detail shortly. Figure 2.2 does not include substitution codes and block codes. They will be studied separately in the latter part of this chapter.

The reason for the large selection of line codes is because of their differences in performance which will lead to different applications. The features to look for in choosing a line code are as follows. For a particular application, some of the features may be important while others may be not.

- (1) *Adequate timing information.* Bit or symbol timing are usually recovered from the received data sequence. This requires that the line code format provides adequate transition density in the coded sequence. Formats with higher transition density are preferable since the timing recovery will have fewer problems with these kinds of signals. A long string of binary 1s and 0s in the data should not cause a problem in timing recovery.
- (2) *A spectrum that is suitable for the channel.* For example, line codes with no dc component and small near-dc components in their power spectral density (PSD) are desirable for magnetic recording systems, ac coupled channels, or systems using transformer coupling which have very poor low frequency responses. In addition the PSD of the line code should have sufficiently small bandwidth compared with the channel bandwidth so ISI will not be a problem.
- (3) *Narrow bandwidth.* The bandwidth of the line code should be as narrow

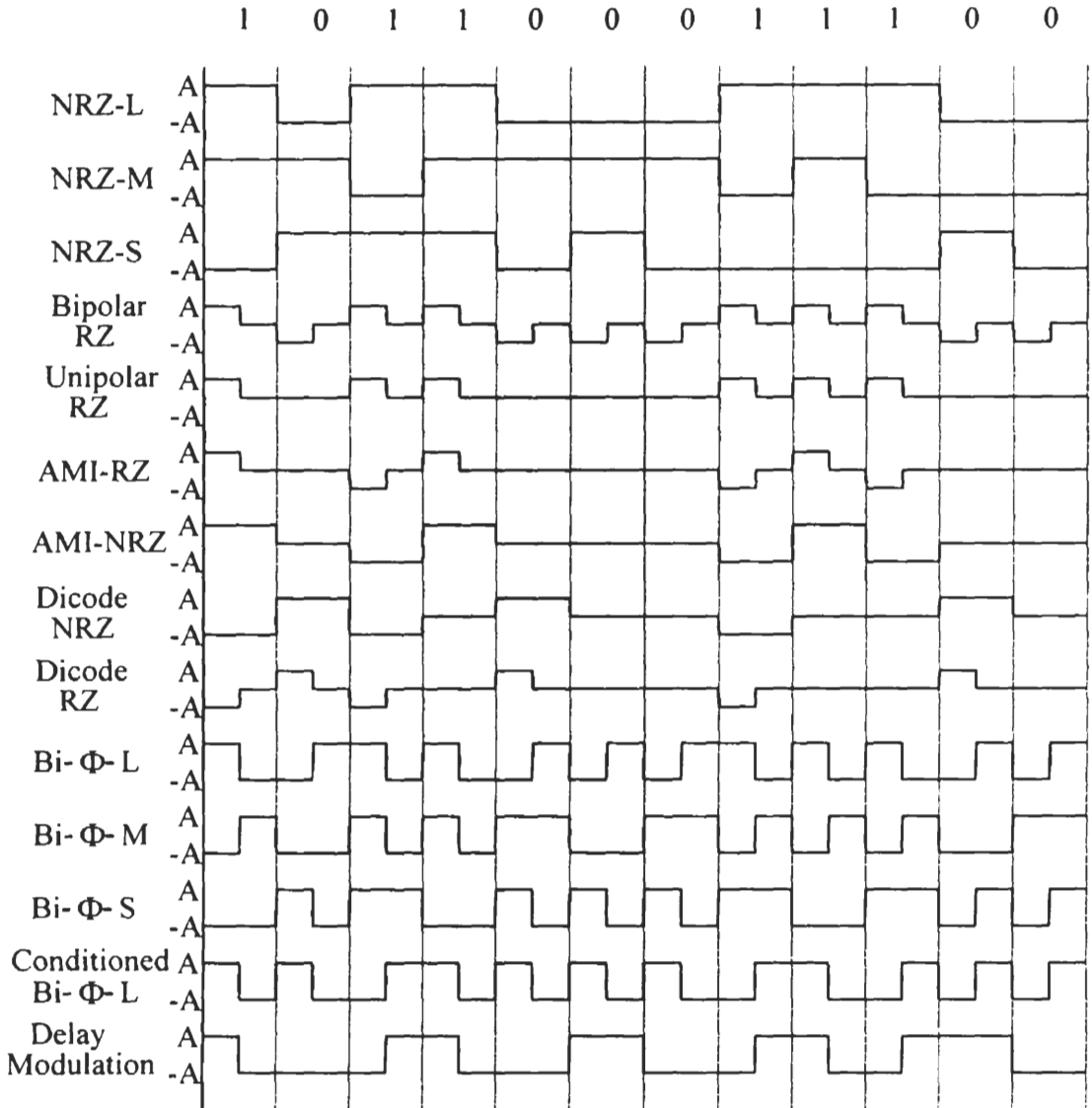


Figure 2.2 Line codes. After [12].

as possible. The transmission bandwidth may be reduced by filtering and multilevel transmission schemes. The penalty is an increase in P_b due to an increase in ISI and a decrease in signal-to-noise ratio. Some line codes may suffer less degradation than others.

- (4) *Low error probability.* The line code can be recovered with low bit error probability (P_b) from noise and/or ISI corrupted received signal. The ones with lower P_b for the same average bit energy are usually preferable, but consideration should be given to other characteristics, such as bandwidth and self-timing capability.
- (5) *Error detection capability.* Some schemes have the capability of detecting errors in the received sequence without introducing extra bits like in channel coding schemes. This error detection capability can be used as a means of performance monitoring. However error correction is not possible, which can only be achieved through channel coding techniques or automatic retransmission schemes.
- (6) *Bit sequence independence (transparency).* The line code must be able to encode any data sequence from any source and the decoder must be able to decode it back to original data. In other words, attributes of the code are independent of the source statistics.
- (7) *Differential coding.* This feature is useful since differentially coded sequences are immune from polarity inversion as we studied in the previous section. However, if differential coding is not inherent in the line code itself, a separate differential coding scheme can be incorporated in the system.

In the following we describe the various line codes basically in groups. But some of the line codes are singled out due to their importance or unique features. When we study these codes the above criteria should be kept in mind, and we will refer to them from time to time.

We put emphases on coding rules and characteristics. We generally omit coder and decoder implementations. Simple codes can be implemented by simple combinational and sequential digital circuits, while complex codes can be implemented by digital signal processing techniques. A comprehensive coverage on coder and decoder implementation is not necessary and also is beyond the page limit of this book. Interested readers may refer to listed references for circuits. However many reported circuits are obsolete already, new circuits should be designed based on new products of IC chips.

2.2.1 Nonreturn-to-Zero Codes

The nonreturn-to-zero group includes the first three codes in Figure 2.2. Two levels ($\pm A$) of the pulse amplitude are used to distinguish binary 1 and 0 in the *NRZ-L* format. This waveform has no dc component for an equiprobable binary data sequence. In the *NRZ-M* format a level change (A to $-A$ or $-A$ to A) is used for a mark (1) in the binary sequence and no change for a space (0). The *NRZ-S* waveform is similar except that the level change is used to indicate a space (0). Both *NRZ-M* and *NRZ-S* are differentially encoded waveforms. They can be produced by modulating the differentially encoded binary sequence using *NRZ-L* format. The *NRZ-M* waveform is generated with the encoding rule of (2.1) and the *NRZ-S* waveform with the encoding rule of (2.6). The reference bit is 0. The corresponding coded sequence for *NRZ-M* is already given in Table 2.1.

Recovery of *NRZ-L*¹ from *NRZ-M* or *NRZ-S* is accomplished by differential decoding.

The main advantage of *NRZ-M* and *NRZ-S* over *NRZ-L* is its immunity to polarity reversals owing to the differential coding.

All the above three formats can be made *unipolar* by changing the lower level $-A$ to level 0. For a binary sequence with equally likely 1s and 0s, which is the usual assumption, the unipolar waveforms have a dc component at a level of $A/2$, whereas the polar ones do not.

Since a string of 1s in *NRZ-S*, a string of 0s in *NRZ-M*, and a string of 1s or 0s in *NRZ-L* does not contain any transitions, this class of waveforms may not provide adequate timing information for data with long strings of 1s and 0s. Solutions to this shortcoming include precoding the data sequence to eliminate long strings of 1s and 0s or transmission of a separate synchronizing sequence.

NRZ-L is used extensively in digital logic as we all know. *NRZ-M* is used primarily in magnetic tape recording. In telecommunication, *NRZ* format applications are limited to short-haul links due to its timing characteristic.

2.2.2 Return-to-Zero Codes

The lack of timing information of the *NRZ* formats can be overcome by introducing more transitions into the waveform. This leads to the *RZ* formats shown in Figure 2.2. However, the bandwidth of an *RZ* format is wider than that of an *NRZ* format, as we will see shortly.

In the *unipolar RZ* format, a binary 1 is represented by a positive pulse for a half-bit period then returning to zero level for the next half period, resulting in a transition

¹ Since *NRZ-L* waveform is the most common waveform in the digital circuit, it is chosen as the ultimate decoding result of line codes in our discussion.

in the middle of the bit. A binary 0 is represented by the zero level for the entire bit period. Since there are no transitions in a string of 0s, precoding or scrambling are needed to eliminate long strings of 0s. This format also has a dc component since it is unipolar.

In the *polar RZ* format, 1 and 0 are represented by positive and negative half-period pulses, respectively. This waveform ensures two transitions per bit. It has no dc component.

2.2.3 Pseudoternary Codes (including AMI)

This group of line codes use three levels $\pm A$ and 0. *AMI* (alternative mark inversion) codes are in this group. They are often called *bipolar codes* in the telecommunication industry. In *AMI-RZ* (return-to-zero AMI) format, a 1 is represented by an RZ pulse with alternative polarities if 1s are consecutive. A 0 is represented by the zero level. In *AMI-NRZ* (nonreturn-to-zero AMI), the coding rule is the same as AMI-RZ except that the symbol pulse has a full length of T. They have no dc component but like unipolar RZ their lack of transitions in a string of 0s may cause a synchronization problem. Therefore AMI codes with zero extraction (substitution codes) are proposed as will be discussed later in this chapter.

Recovery of NRZ-L from the AMI-NRZ code is accomplished by simple full-wave rectification [1]. Similarly AMI-RZ code can be full-wave rectified to form RZ-L waveform which can be easily converted to NRZ-L waveform.

These formats are used in baseband data transmission and magnetic recording. The AMI-RZ format is most often used in telemetry systems. It is used by AT&T for T1 carrier systems.

Other members of this group include the *dicode NRZ* and *dicode RZ*. Dicode formats are also called *twinned binary* in the literature [1,2]. In dicode NRZ the 1 to 0 or 0 to 1 transition changes the pulse polarity, a zero level represents no data transition. In dicode RZ, the same coding rule is used except that the pulse is only half-bit wide (i.e., it returns to zero for the second half bit).

Dicodes and AMI codes are related by differential coding [2]. If data sequence $\{a_k\}$ is the sequence used directly to construct a dicode, then sequence $\{d_k\}$, where $d_k = a_{k-1} - a_k$, can be used to construct an AMI code which is a dicode to the original sequence $\{a_k\}$. This can be seen from the example in Figure 2.2. Assuming $a_0 = 0$, we convert $\{a_k\} = (1, 0, 1, 1, 0, 0, 0, 1, 1, 1, 0, 0)$ to $\{d_k\} = (-1, 1, -1, 0, 1, 0, 0, -1, 0, 0, 1, 0)$. Using $\{d_k\}$ and AMI rules we can construct exactly the dicodes in the figure (with replacements A and $-A$ for 1 and -1 , respectively).

Dicodes can be decoded as follows. First $\{\hat{d}_k\}$ is converted to unipolar $\{\hat{u}_k\}$ by full-wave rectification, then $\{\hat{a}_k\}$ is recovered from $\{\hat{u}_k\}$ by modulo-2 summation: $\hat{a}_k = \hat{a}_{k-1} \oplus \hat{u}_k$ ($\hat{a}_0 = a_0$). Readers can easily verify this using the above example.

2.2.4 Biphasic Codes (including Manchester)

This group of line codes uses half-period pulses with different phases according to certain encoding rules in the waveform. Four waveforms of this group are shown in Figure 2.2.

The $Bi-\Phi-L$ (biphase-level) format is better known as *Manchester*, and is also called *diphase*, or *split-phase*. In this format, a 1 is represented as a pulse with first half bit at a higher level and the second half bit at a lower level. A 0 is represented as a pulse with the opposite phase (i.e., a lower level for the first half bit and a higher level for the second half bit). Of course, the pulse shapes for 1 and 0 can be exchanged.

The $Bi-\Phi-M$ (biphase-mark) format requires that a transition is always present at the beginning of each bit. A 1 is coded as a second transition in the middle of the bit and a 0 is coded as no second transition in the bit. This results in representing a 1 by one of the two phases of the pulse. In the $Bi-\Phi-S$ (biphase-space) format the opposite coding rules are applied to 1 and 0. The above three biphase formats ensure that there is at least one transition in a bit duration, thus providing adequate timing information to the demodulator.

The fourth format in this group is the *conditioned Bi- Φ -L*. In fact it is a differentially encoded $Bi-\Phi-L$ (i.e., the data sequence used for modulation is generated from the original binary sequence with differential encoding). Like NRZ-M and NRZ-S, this format is immune from polarity inversions in the circuit.

Biphase formats are used in magnetic recording, optical communications, and in some satellite telemetry links. Manchester code has been specified for the IEEE 802.3 standard for baseband coaxial cable using carrier sense multiple access and collision detection (CSMA/CD) (i.e., Ethernet [13, 14]). It has also been used in MIL-STD-1553B, which is a shielded twisted-pair bus system designed for high-noise environments [14]. Differential Manchester has been specified for the IEEE 802.5 standard for token ring, using either baseband coaxial cable or twisted-pair. Because it uses differential coding, differential Manchester is preferred for a twisted-pair channel.

2.2.5 Delay Modulation (Miller Code)

Delay modulation (DM) [3] or *Miller code* also can be classified into the biphase group since there are two phases in the waveform. However, it has some unique features. A 1 is represented by a transition in the midpoint of the bit. A 0 is represented by no transition unless it is followed by another 0. Then a transition is placed at the end of the first 0 bit. This format has a very small bandwidth, and most importantly, very small dc component as we will see shortly. This makes it suitable for magnetic recording since magnetic recorders have no dc response [3].

2.3 POWER SPECTRAL DENSITY OF LINE CODES

In this section we first present a general formula for power spectral density (PSD) calculation for digitally modulated baseband waveforms. It can be used for most of the binary line codes. Therefore for most of the time we will simply apply this formula to various codes in the rest of this section. However, this formula is not applicable to some codes so other methods to calculate the PSD will be discussed.

We know that most signals like voice signal and image signal are essentially random. Therefore digital signals derived from these signals are also random. Data signals are also essentially random.

Assume the digital signal can be represented by

$$s(t) = \sum_{k=-\infty}^{\infty} a_k g(t - kT) \quad (2.11)$$

where a_k are discrete random data bits, $g(t)$ is a signal of duration T (i.e., nonzero only in $[0, T]$). Let us name $g(t)$ as *symbol function*. It could be any signal with a Fourier transform. For example it could be a baseband symbol shaping pulse or a burst of modulated carrier at passband. The random sequence $\{a_k\}$ could be binary or nonbinary.

In Appendix A (A.16) we show that the power spectral density of $s(t)$ is

$$\Psi_s(f) = \frac{|G(f)|^2}{T} \sum_{n=-\infty}^{\infty} R(n) e^{-jn\omega T} \quad (2.12)$$

where $\omega = 2\pi f$. $G(f)$ is the Fourier transform of $g(t)$ and $R(n)$ is the autocorrelation function of random sequence $\{a_k\}$, defined as $R(n) = E\{a_k a_{k+n}\}$, where $E\{x\}$ is the probabilistic average of x . Equation (2.12) shows that the PSD of a digitally modulated signal is not only determined by its symbol function but also is affected by the autocorrelation function of the data sequence.

In the following we always assume that the original binary data sequence has 1s and 0s equally likely. That is, $p_0 = Pr(0) = p_1 = Pr(1) = 1/2$. However, in order to write the modulated waveform in the form of (2.11), sequence $\{a_k\}$ of (2.11) is usually not the original sequence, rather it is derived from the original. Therefore its probability distribution needs to be calculated.

For uncorrelated sequence $\{a_k\}$,

$$R(n) = \begin{cases} \sigma_a^2 + m_a^2, & n = 0 \\ m_a^2, & n \neq 0 \end{cases} \quad (2.13)$$

where σ_a^2 is the variance and m_a is the mean of the sequence $\{a_k\}$. Using the Poisson sum formula, the PSD expression can be written as (see Appendix A, (A.17))

$$\Psi_s(f) = \frac{|G(f)|^2}{T} \left[\sigma_a^2 + m_a^2 R_b \sum_{n=-\infty}^{\infty} \delta(f - nR_b) \right] \quad (2.14)$$

where $R_b = 1/T$ is the data bit rate.

For line codes with $R(n) = 0$ for $n \neq 0$, (2.12) is more convenient. For line codes with $R(n) \neq 0$ for $n \neq 0$, (2.14) is more convenient.

Among baseband modulated signals, NRZ-L, NRZ-M, NRZ-S, RZ (polar or unipolar), AMI-RZ, AMI-NRZ, Bi- Φ -L, and dicode (RZ or NRZ) can be written in the form of (2.11). Therefore their PSD can be found quite easily using the above series of equations. However, there are some digital signals which can not simply be represented by (2.11). Among the line codes, Bi- Φ -M, Bi- Φ -S, DM, and the substitution codes and block codes (which will be described later) belong to this group. If the signal is wide sense stationary (WSS), to find their PSD, the approach is to find their autocorrelation $R(\tau)$ first, then take the Fourier transform to find the PSD (Wiener-Khintchine theorem). If the signal is cyclostationary, then $R(\tau)$ is the time average of the time-dependant $R(t, \tau)$ in a period. The Wiener-Khintchine theorem is still applicable when time average of $R(t, \tau)$ is used for a nonstationary (including cyclostationary) process.

Some coded sequence, like Bi- Φ -M and delay modulation, can be described as a first order Markov random process. Their $R(\tau)$ can be found by using the method provided in [3]. We will use this method when we encounter the calculation of PSDs of Bi- Φ -M and delay modulation.

For more complex coded sequences one can use the general formula given by [15, 16]:

$$\Psi_s(f) = \frac{1}{T} \sum_i \sum_j G_i(-f) G_j(f) [p_i U_{ij}(f) + p_j U_{ji}(f) - p_i \delta_{ij}] \quad (2.15)$$

where $G_i(f)$ is the Fourier transform of the state i pulse waveform², T is the pulse width, and δ_{ij} is the Kronecker delta function. p_i is the state i steady-state occurrence probability, and $U_{ji}(f)$ is the transform probability of state j occurring after state i . Probability p_i is found by taking residues of $U_{ji}(f)$ at its poles when $f = 0$. The $U_{ji}(f)$ is calculated by a signal flow graph and Mason's formula [17]. We do not attempt to use this method in this chapter in order not to make our discussion too

² A state of a coded sequence is determined by the symbols representing an information bit. For example, Manchester code has two states: 10 or 01, corresponding to the two half-positive and half-negative pulses.

mathematical.³ Instead, results obtained using this method may be quoted when necessary. Or we may use the computer Monte-Carlo simulation to find the $R(\tau)$ and PSD.

Now we are ready to discuss the PSDs of the binary line codes described in the previous section.

2.3.1 PSD of Nonreturn-to-Zero Codes

Recall that NRZ-M and NRZ-S are generated by NRZ-L modulation with differentially encoded data sequences. Assume that original binary data are equally likely. Then according to Section 2.1, the differentially encoded sequences with (2.1) or (2.6) are also equally likely. In other words, the statistic properties of the sequences used directly for modulation are the same for NRZ-L, NRZ-M, and NRZ-S. And their symbol functions are also the same. *As a result their PSDs are the same.*

NRZ formats' symbol function is a square pulse with amplitude A in the interval $[0, T]$, which can be expressed as

$$g(t) = \begin{cases} A, & 0 \leq t \leq T \\ 0, & \text{elsewhere} \end{cases} \quad (2.16)$$

Its Fourier transform can be easily found as

$$\begin{aligned} G(f) &= AT \left(\frac{\sin \pi f T}{\pi f T} \right) e^{-j\pi f T} \\ &= AT \text{sinc}(\pi f T) e^{-j\pi f T} \end{aligned} \quad (2.17)$$

where $\text{sinc}(x) = \sin(x)/x$ is the *sinc function*. Next we need to find the autocorrelation function $R(n)$ of the binary data sequence $\{a_k\}$. For this waveform

$$a_k = \begin{cases} 1, & \text{for binary 1, } p_1 = 1/2 \\ -1, & \text{for binary 0, } p_0 = 1/2 \end{cases} \quad (2.18)$$

Thus

$$R(n) = \begin{cases} p_1(1)^2 + p_0(-1)^2 = 1, & n = 0 \\ (p_0)^2(1)^2 + (p_1)^2(1)^2 + 2p_0p_1(1)(-1) = 0, & n \neq 0 \end{cases} \quad (2.19)$$

³ We also do not expect the reader to be able to use this method by just reading this formula. This is to provide a reference in case the reader is interested in finding out the PSD of a complex coded sequence.

Substitute expressions of $G(f)$ and $R(n)$ into (2.12) we have,

$$\Psi_s(f) = A^2 T \left(\frac{\sin \pi f T}{\pi f T} \right)^2, \quad (\text{NRZ}) \quad (2.20)$$

Figure 2.3(a) shows the plot of $\Psi_s(f)$ and the plot of the fractional out-of-band power, $P_{ob}(B)$, defined as⁴

$$P_{ob}(B) = 1 - \frac{\int_{-B}^B \Psi_s(f) df}{\int_{-\infty}^{\infty} \Psi_s(f) df} \quad (2.21)$$

In the figure $P_{ob}(B)$ is in dB, the horizontal axis is normalized frequency $fT = f/R_b$. In the figure we set $A = 1$ and $T = 1$ for unity symbol pulse energy. This PSD is a squared sinc function with its first null at $fT = 1$. The signal energy concentrates near 0 frequency and the null bandwidth is $B_{null} = 1.0R_b$, 90% energy bandwidth is $B_{90\%} \approx 0.85R_b$ and the 99% bandwidth is $B_{99\%} \approx 10R_b$.

We mentioned that all three NRZ waveforms can be made unipolar. Assume the pulse amplitude is A , then there is a dc component of $A/2$ in the signals and it appears as an impulse function with strength of $A^2/4$ at 0 frequency in the power spectral density as we will show next. In this case the pulse function is still the one in (2.16), and the data is

$$a_k = \begin{cases} 1, & \text{for binary 1, } p_1 = 1/2 \\ 0, & \text{for binary 0, } p_0 = 1/2 \end{cases} \quad (2.22)$$

From this we have

$$m_a = E\{a_k\} = p_1(1) + p_0(0) = 1/2 \quad (2.23)$$

and

$$\sigma^2 = E\{(a_k - m_a)^2\} = p_1(1 - 1/2)^2 + p_0(0 - 1/2)^2 = 1/4 \quad (2.24)$$

Substitute expressions of $G(f)$, m_a , and σ^2 into (2.14) we have,

$$\Psi_s(f) = \frac{A^2 T}{4} \left(\frac{\sin \pi f T}{\pi f T} \right)^2 + \frac{A^2}{4} \delta(f), \quad (\text{unipolar NRZ}) \quad (2.25)$$

For unity average symbol energy we must set $A = \sqrt{2}$. This PSD has the same shape of that of the polar NRZs. The only difference is the impulse at the 0 frequency. The

⁴ $\Psi_s(f)$ may be singular. For instance, $\Psi_s(f)$ may contain $\delta(f)$. In these cases we must integrate the singular part separately. $\int_{-\infty}^{\infty} \Psi_s(f) df$ will equal unity when $\Psi_s(f)$ is normalized. In this book $P_{ob}(B)$ is evaluated by numerical integration.

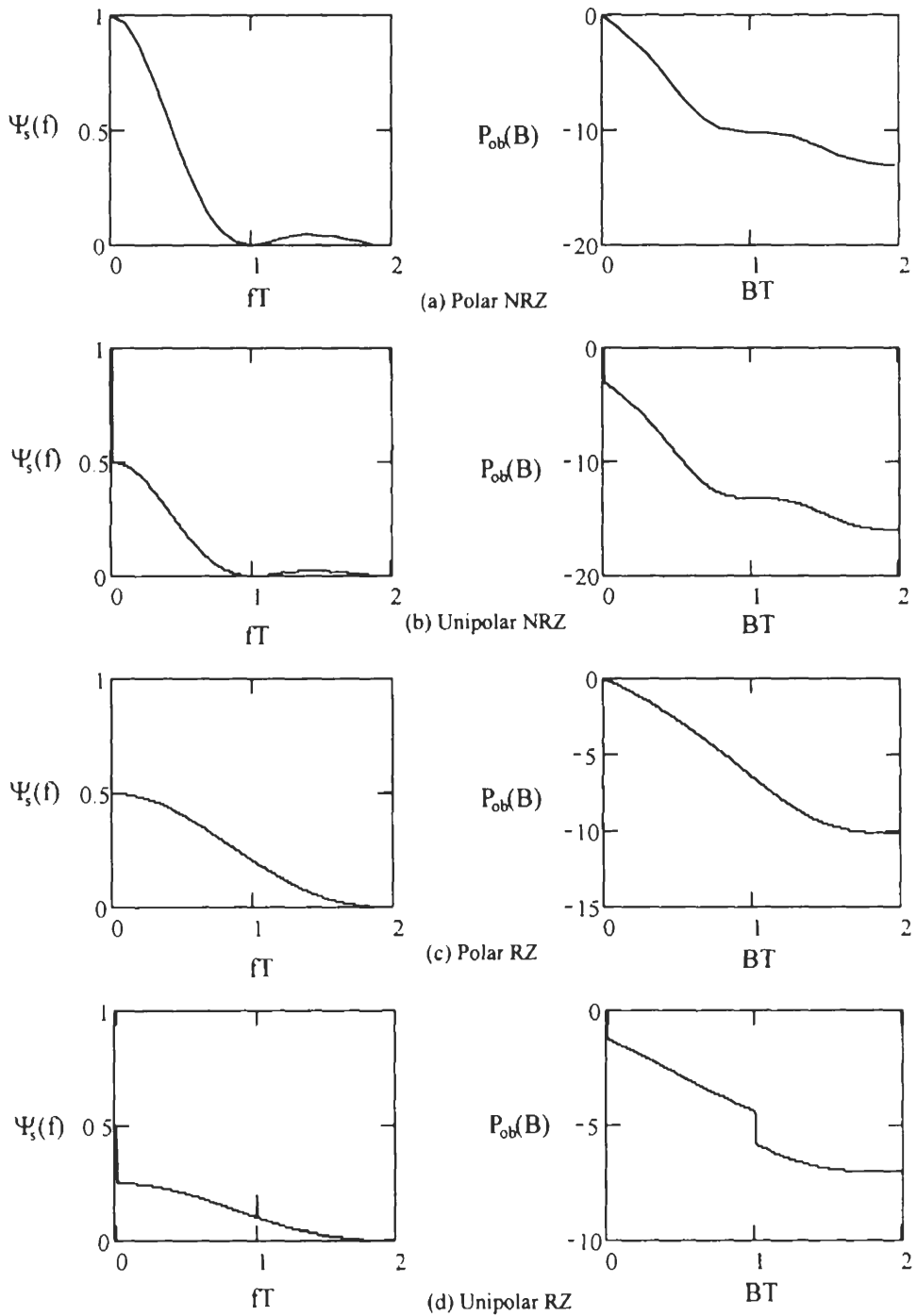


Figure 2.3 PSD of line codes ($P_{ob}(B)$ is in dB).

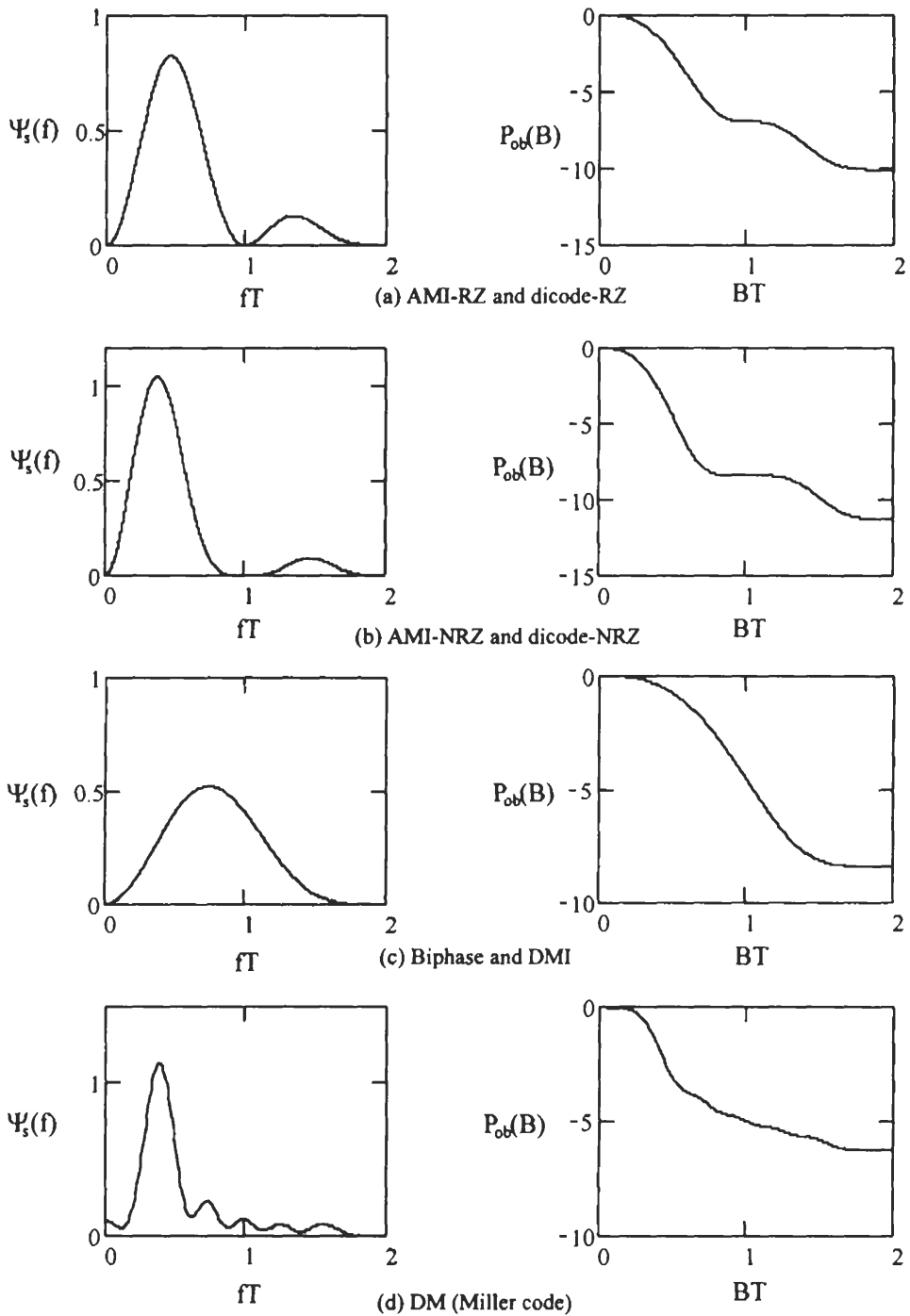


Figure 2.4 PSD of line codes ($P_{ob}(B)$ is in dB) (continued).

PSD and the out-of-band power are shown in Figure 2.3(b). The bandwidths are $B_{null} = 1.0R_b$, $B_{90\%} \approx 0.54R_b$, and $B_{99\%} \approx 5R_b$.

2.3.2 PSD of Return-to-Zero Codes

For RZ formats, the pulse function is a square pulse with half-bit duration

$$g(t) = \begin{cases} A, & 0 \leq t \leq \frac{T}{2} \\ 0, & \text{elsewhere} \end{cases} \quad (2.26)$$

The corresponding Fourier transform is

$$G(f) = \frac{AT}{2} \left(\frac{\sin \pi fT/2}{\pi fT/2} \right) e^{-j\pi fT/2} \quad (2.27)$$

For *polar RZ* waveform

$$a_k = \begin{cases} 1, & \text{for binary 1, } p_1 = 1/2 \\ -1, & \text{for binary 0, } p_0 = 1/2 \end{cases} \quad (2.28)$$

which is the same as polar NRZ. Thus

$$R(n) = \begin{cases} 1, & n = 0 \\ 0, & n \neq 0 \end{cases} \quad (2.29)$$

Substituting (2.27) and (2.29) into (2.12), the result is

$$\Psi_s(f) = \frac{A^2T}{4} \left(\frac{\sin \pi fT/2}{\pi fT/2} \right)^2, \quad (\text{Polar RZ}) \quad (2.30)$$

For unity average symbol energy we must set $A = \sqrt{2}$. The PSD and the out-of-band power are shown in Figure 2.3(c). Compared with the PSD of NRZ format, this PSD is a stretched version with frequency axis scaled up twice. Therefore all its bandwidths are double that of NRZ. The bandwidths are $B_{null} = 2.0R_b$, $B_{90\%} \approx 1.7R_b$, and $B_{99\%} \approx 22R_b$.

For *unipolar RZ* format the symbol pulse is the same as in (2.26). The data sequence, its mean and variance are the same as those of unipolar NRZ as given in (2.22), (2.23) and (2.24). Substituting $G(f)$ in (2.27), m_a and σ_a^2 into (2.14) we have

$$\Psi_s(f) = \frac{A^2T}{16} \left(\frac{\sin \pi fT/2}{\pi fT/2} \right)^2 \left[1 + R_b \sum_{k=-\infty}^{\infty} \delta(f - nR_b) \right], \quad (\text{unipolar RZ}) \quad (2.31)$$

For unity average symbol energy we must set $A = 2$. The PSD and the out-of-band power are shown in Figure 2.3(d). From the figure we can see that besides the continuous spectrum resembling the PSD of polar RZ, there are spikes at all odd integer frequencies. Their strengths are determined by the second term of (2.31) and are given by

$$\frac{A^2}{16} \left(\frac{\sin \pi n/2}{\pi f n/2} \right)^2$$

For $A = 2$, the strengths of the components form $f = 0, R_b, 3R_b, 5R_b, 7R_b$, and $9R_b$ are: 0.25, 0.101, 0.011, 0.004, 0.002, and 0.001 in the two-side spectrum. All discrete harmonics add up to 0.5 and the rest of energy (0.5) is in the continuous part of the spectrum.

The bandwidths are $B_{null} = 2.0R_b$, $B_{90\%} \approx 1.6R_b$, and $B_{99\%} \approx 22R_b$, which are almost the same as those of the polar RZ format.

2.3.3 PSD of Pseudoternary Codes

For *AMI* codes the data sequence $\{a_k\}$ takes on three values:

$$a_k = \begin{cases} 1, & \text{for binary 1, } p_1 = 1/4 \\ -1, & \text{for binary 1, } p_{-1} = 1/4 \\ 0, & \text{for binary 0, } p_0 = 1/2 \end{cases} \quad (2.32)$$

We can find $R(0)$ as follows

$$R(0) = E\{a_k^2\} = \frac{1}{4}(1)^2 + \frac{1}{4}(-1)^2 + \frac{1}{2}(0)^2 = \frac{1}{2}$$

Adjacent bits in $\{a_k\}$ are correlated due to the alternate mark inversion. The adjacent bit pattern in the original binary sequence must be one of these: (1,1), (1,0), (0,1), and (0,0). The possible $a_k a_{k+1}$ products are -1, 0, 0, 0. Each of them has a probability of 1/4. Thus

$$R(1) = E\{a_k a_{k+1}\} = \frac{1}{4}(-1) + \frac{1}{4} \cdot 0 + \frac{1}{4} \cdot 0 + \frac{1}{4} \cdot 0 = -\frac{1}{4}$$

For $n > 1$, a_k and a_{k+n} are not correlated. The possible $a_k a_{k+n}$ products are $\pm 1, 0, 0, 0$. Each case occurs with a probability of 1/4. Thus

$$R(n > 1) = E\{a_k a_{k+n}\} = \frac{1}{8}(1) + \frac{1}{8}(-1) = 0$$

Summarizing above results we have

$$R(n) = \begin{cases} \frac{1}{2}, & n = 0 \\ -\frac{1}{4}, & |n| = 1 \\ 0, & |n| > 1 \end{cases}$$

Substitute this $R(n)$ and the symbol pulse spectrum of (2.27) into (2.12), we have the PSD of AMI-RZ code:

$$\begin{aligned} \Psi_s(f) &= \frac{1}{T} |G(f)|^2 \left(\frac{1}{2} - \frac{1}{4} e^{j\omega T} - \frac{1}{4} e^{-j\omega T} \right) \\ &= \frac{1}{T} |G(f)|^2 \left(\frac{1}{2} - \frac{1}{2} \cos(\omega T) \right) \\ &= \frac{A^2 T}{4} \left(\frac{\sin \pi f T / 2}{\pi f T / 2} \right)^2 \sin^2 \pi f T, \quad (\text{AMI-RZ}) \quad (2.33) \end{aligned}$$

The PSD is shown in Figure 2.4(a) where we set $A = 2$ to normalize the PSD. The bandwidths are $B_{null} = 1.0R_b$, $B_{90\%} \approx 1.71R_b$, and $B_{99\%} \approx 20R_b$, which are narrower than those of other RZ formats, especially the null bandwidth is only half of the others.

The PSD of AMI-NRZ can be obtained by replacing $T/2$ with T in $G(f)$ of AMI-RZ (2.27) since both of them have the same coding rules and the only difference is the pulse width. Thus the PSD of AMI-NRZ is given as

$$\Psi_s(f) = A^2 T \left(\frac{\sin \pi f T}{\pi f T} \right)^2 \sin^2 \pi f T, \quad (\text{AMI-NRZ}) \quad (2.34)$$

The PSD is shown in Figure 2.4(b) where we set $A = \sqrt{2}$ to normalize the PSD. The bandwidths are $B_{null} = 1.0R_b$, $B_{90\%} \approx 1.53R_b$, and $B_{99\%} \approx 15R_b$ which are narrower than those of AMI-RZ.

The PSDs of other members of this group (i.e., *dicode NRZ* and *dicode RZ* (or *twinned binary codes*)) are derived in the following. As we described before that the dicodes can be constructed using AMI rules and a differentially coded sequence, that is, the dicodes can be written in the form of (2.11) as

$$s(t) = \sum_{k=-\infty}^{\infty} d_k g(t - kT) \quad (2.35)$$

where,

$$d_k = a_{k-1} - a_k = \begin{cases} 1, & p_1 = 1/4 \\ -1, & p_{-1} = 1/4 \\ 0, & p_0 = 1/2 \end{cases}$$

Sequence $\{d_k\}$ is a pseudoternary sequence derived from the original binary data sequence $\{a_k\}$. Its probability distribution is exactly the same as that of AMI (2.32). Therefore the PSDs of dicodes are the same as those of AMI codes and bandwidths are also the same as those of corresponding AMI codes.

2.3.4 PSD of Biphasic Codes

For *Bi-Φ-L (Manchester)*, the symbol function is half-positive and half-negative pulse defined by

$$g(t) = \begin{cases} A, & 0 \leq t \leq \frac{T}{2} \\ -A, & \frac{T}{2} \leq t \leq T \\ 0, & \text{elsewhere} \end{cases} \quad (2.36)$$

The Fourier transform of $g(t)$ is

$$G(f) = AT \left(\frac{\sin \pi fT/2}{\pi fT/2} \right) (\sin \pi fT/2) j e^{-j\omega T/2} \quad (2.37)$$

The data probability distribution is

$$a_k = \begin{cases} 1, & \text{for binary 1, } p_1 = 1/2 \\ -1, & \text{for binary 0, } p_0 = 1/2 \end{cases}$$

which is the same as that of NRZ. We have shown that $R(n) = 1$ for $n = 0$ and $R(n) = 0$ for $n \neq 0$ (2.19). Using (2.12) we obtain

$$\Psi_s(f) = A^2 T \left(\frac{\sin \pi fT/2}{\pi fT/2} \right)^2 \sin^2 \pi fT/2. \quad (\text{Bi-}\Phi\text{-L}) \quad (2.38)$$

This PSD is shown in Figure 2.4(c) where we set $A = 1$ for unity symbol energy.

The PSD of the conditioned Bi-Φ-L is the same as that of the Bi-Φ-L since it is merely a differentially encoded Bi-Φ-L, and differential encoding does not change the probability distribution of the equally likely data.

It is obvious that Bi-Φ-M and Bi-Φ-S have the same PSD since the marks and spaces are equally likely in an equiprobable data sequence. We also observe that their waveforms are very similar to that of Bi-Φ-L in terms of pulse shapes and number of transitions. We therefore may intuitively guess that their PSD is the same as that of Bi-Φ-L. In fact this guess is right. We will prove it in the following.

We will use the method used in deriving the PSD of the delay modulation or Miller code whose PSD will be discussed in the next subsection [3]. We will base our derivation on Bi-Φ-M and the result is applicable to Bi-Φ-S as we mentioned already.

The coding rule of Bi- Φ -M can be described as a first-order Markov random process. Each bit interval can be divided into two half-bit intervals, then each bit interval can be described by the levels occurring in the two half-bit intervals. Temporarily assume the amplitude A to be 1, then the two levels are $+1$ and -1 . There are four types of bit intervals or states that can occur in a bit interval: $(-1, +1)$, $(+1, -1)$, $(-1, -1)$, and $(+1, +1)$. They are equally likely (i.e., $p_i = 1/4$, $i = 1, 2, 3, 4$). A state of a bit interval depends only on the state of the previous bit interval. This is a first-order Markov process. The process is then completely described by $P = [p_{ij}]$, the probability-of-transition matrix, in which an element $p_{ij} = p(j/i)$ equals the conditional probability of the state j occurring after a given state i has occurred in the previous bit interval. For Bi- Φ -M, from the coding rules we can find the transition matrix as

$$P = \begin{bmatrix} 0.5 & 0 & 0.5 & 0 \\ 0 & 0.5 & 0 & 0.5 \\ 0 & 0.5 & 0 & 0.5 \\ 0.5 & 0 & 0.5 & 0 \end{bmatrix}$$

which is defined in Figure 2.5(a).

The autocorrelation function $R(\tau)$ at $\tau = nT$ ($n = 0, 1, 2, \dots$) is [3]⁵

$$\begin{aligned} R(nT) &= \sum_{i,j} p(j/i, n) p_i \int_0^T g_i(t) g_j(t) dt / T \\ &= \frac{1}{4} \text{trace}[P^n W^T] \end{aligned} \quad (2.39)$$

where

$g_i(t)$ = waveform of state i .

$p(j/i, n)$ = probability of occurrence of state j at $t = nT$, given state i at $t = 0$,

which is equal to ij th element of the matrix P^n .

W = a matrix with elements $w_{ij} = \int_0^T g_i(t) g_j(t) dt / T$, W^T is the transpose of W .

The integral $w_{ij} = \int_0^T g_i(t) g_j(t) dt / T = \int_{nT}^{(n+1)T} g_i(t) g_j(t) dt / T$ accounts for "time averaging" the time-varying $R(nT, t)$ over a bit interval in order to obtain $R(nT)$. Based on the waveforms of the states, we can find W as

$$W = \begin{bmatrix} 1 & -1 & 0 & 0 \\ -1 & 1 & 0 & 0 \\ 0 & 0 & 1 & -1 \\ 0 & 0 & -1 & 1 \end{bmatrix}$$

⁵ The transpose of W is missing in the reference [3].

which is defined in Figure 2.5(b), where shaded areas are areas of integration. Substituting P and W into (2.39), the result is

$$R(nT) = \begin{cases} 1, & n = 1 \\ 0, & n \neq 0 \end{cases}$$

Similarly we can find the autocorrelation for $\tau = (n + 1/2)T$ as follows

$$\begin{aligned} R((n + 1/2)T) &= \sum_{i,j} p(j/i, n) p_i \int_0^{T/2} g_i(t) g_j(t + \frac{T}{2}) dt / T \\ &\quad + \sum_{i,j} p(j/i, n + 1) p_i \int_{T/2}^T g_i(t) g_j(t + \frac{T}{2}) dt / T \\ &= \frac{1}{4} \text{trace}[P^n W_1^T] + \frac{1}{4} \text{trace}[P^{n+1} W_2^T] \end{aligned} \quad (2.40)$$

where

$$W_1 = \begin{bmatrix} -0.5 & 0.5 & 0.5 & -0.5 \\ 0.5 & -0.5 & -0.5 & 0.5 \\ -0.5 & 0.5 & 0.5 & -0.5 \\ 0.5 & -0.5 & -0.5 & 0.5 \end{bmatrix}$$

and

$$W_2 = \begin{bmatrix} -0.5 & 0.5 & -0.5 & 0.5 \\ 0.5 & -0.5 & 0.5 & -0.5 \\ 0.5 & -0.5 & 0.5 & -0.5 \\ -0.5 & 0.5 & -0.5 & 0.5 \end{bmatrix}$$

which are defined in Figure 2.5(c, d). The results for $n \geq 0$ are

$$R((n + 1/2)T) = \begin{cases} -0.5, & n = 0 \\ 0, & n > 0 \end{cases}$$

Due to symmetry of the $R(\tau)$, it is clear that $R(-T/2) = -0.5$ and $R(nT/2) = 0$ for all $n < -1$. The autocorrelation at intermediate values of τ is obtained exactly by joining these points. $R(\tau)$ of Bi- Φ -M is shown in Figure 2.5(e). By taking the Fourier transform of $R(\tau)$, the PSD is easily found as

$$\Psi_s(f) = A^2 T \left(\frac{\sin \pi f T / 2}{\pi f T / 2} \right)^2 \sin^2 \pi f T / 2, \quad (\text{Bi-}\Phi\text{-M and S}) \quad (2.41)$$

which is exactly the same as that of Bi- Φ -L or Manchester.

The bandwidths of all biphasic codes are $B_{null} = 2.0R_b$, $B_{90\%} \approx 3.05R_b$, and $B_{99\%} \approx 29R_b$.

2.3.5 PSD of Delay Modulation

The spectral analysis of delay modulation is also based on first-order Markov process [3]. The autocorrelation $R(nT)$ and $R((n + 1/2)T)$ are also given by (2.39) and (2.40).

The probability-of-transition matrix is

$$P = \begin{bmatrix} 0 & 0.5 & 0 & 0.5 \\ 0 & 0 & 0.5 & 0.5 \\ 0.5 & 0.5 & 0 & 0 \\ 0.5 & 0 & 0.5 & 0 \end{bmatrix}$$

which is defined in Figure 2.6(a). The W matrices are

$$W = \begin{bmatrix} 1 & 0 & 0 & -1 \\ 0 & 1 & -1 & 0 \\ 0 & -1 & 1 & 0 \\ -1 & 0 & 0 & 1 \end{bmatrix}$$

$$W_1 = \begin{bmatrix} 0.5 & -0.5 & 0.5 & -0.5 \\ 0.5 & -0.5 & 0.5 & -0.5 \\ -0.5 & 0.5 & -0.5 & 0.5 \\ -0.5 & 0.5 & -0.5 & 0.5 \end{bmatrix}$$

$$W_2 = \begin{bmatrix} 0.5 & 0.5 & -0.5 & -0.5 \\ -0.5 & -0.5 & 0.5 & 0.5 \\ 0.5 & 0.5 & -0.5 & -0.5 \\ -0.5 & -0.5 & 0.5 & 0.5 \end{bmatrix}$$

All of them are defined in Figure 2.6.

By using these matrices we can determine $R(\tau)$ for $\tau = nT$ and $(n + 1/2)T$. The intermediate $R(\tau)$ is obtained exactly by joining these points. In addition it can be easily verified that for DM, $P^4W = -\frac{1}{4}W$ and $P^4W_i = -\frac{1}{4}W_i$, $i = 1, 2$. Therefore

$$R(\tau + 4T) = -\frac{1}{4}R(\tau), \quad \tau > 0 \quad (2.42)$$

Thus, the first eight values of $R(\tau)$ from $R(0)$ to $R(3.5T)$ given in Figure 2.6(e) completely specifies $R(\tau)$. Taking the Fourier transform of $R(\tau)$, using (2.42), and

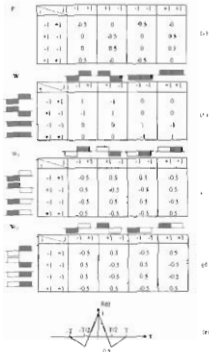


Figure 2.5. (a) \mathbf{P} - \mathbf{Q} - \mathbf{M} matrices, (b) the probability-of-transition matrix, (c) the matrix \mathbf{W}_1 , (d) the matrix \mathbf{W}_2 , (e) the matrix \mathbf{W}_3 , (f) autocorrelation $R(r)$.

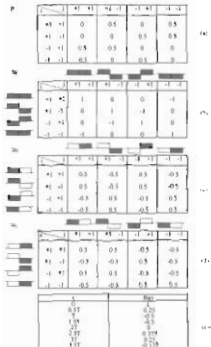


Figure 2.6. DTM matrices: (a) the probability-of-transition matrix, (b) the matrix W , (c) the matrix W_1 , (d) the matrix W_2 , (e) autocorrelation $R(\tau)$.

the relation that $\Psi_s(-f) = \Psi_s^*(f)$, where * indicates conjugate, the PSD of DM is

$$\begin{aligned}\Psi_s(f) &= \int_{-\infty}^{\infty} R(\tau)e^{-j2\pi f\tau} d\tau \\ &= 2 \operatorname{Re} \left[\int_0^{\infty} R(\tau)e^{-j2\pi f\tau} d\tau \right] \\ &= 2 \operatorname{Re} \left[\frac{1}{1 + \frac{1}{4}e^{-j2\pi f(4T)}} \int_0^{4T} R(\tau)e^{-j2\pi f\tau} d\tau \right]\end{aligned}$$

where Re indicates real part. The integral is easily, though tediously, evaluated [3]:

$$\begin{aligned}\Psi_s(f) &= \frac{2A^2}{(2\pi f)^2 T(17 + 8 \cos \theta)} (23 - 2 \cos \theta - 22 \cos 2\theta \\ &\quad - 12 \cos 3\theta + 5 \cos 4\theta + 12 \cos 5\theta + 2 \cos 6\theta \\ &\quad - 8 \cos 7\theta + 2 \cos 8\theta), \quad (\text{DM or Miller}) \quad (2.43)\end{aligned}$$

where $\theta = \pi fT$. The PSD is shown in Figure 2.4(d) where we set $A = 1$ for unity symbol energy. The PSD has a peak at $f = 0.4R_b$, and it has a very narrow main lobe bandwidth of about $0.5R_b$. However, it converges to zero very slowly. As a result its energy within a bandwidth of $2R_b$ is only 76.4% and within $250R_b$ is only 83.7%.

2.4 BIT ERROR RATE OF LINE CODES

In this section we discuss optimum detection of line codes transmitted through an AWGN channel and their error probabilities. We should keep in mind that the AWGN channel model implies that the channel frequency response is flat and has infinite bandwidth. The only distortion is introduced by the additive white Gaussian noise. This of course is not accurate for many practical channels. However, it is a reasonably accurate model as long as the signal bandwidth is much narrower than that of the channel. It is also important to note that the optimum receiver might not be the practical solution. Other nonoptimum receivers might be just as good as the optimum one in certain circumstances (e.g., high signal-to-noise ratio) and their structures are simpler. Nonetheless the error probability in the AWGN channel serves as a reference for performance comparison.

We start with the binary codes and will progress to pseudoternary codes and other complex codes. The fundamental theory of detection and estimation of signals in noise is provided in Appendix B. Here we will first present the signal model and

use the corresponding results in Appendix B to obtain the error probabilities of the line codes.

2.4.1 BER of Binary Codes

A binary line code consists of two kinds of signals, or from the point of view of detection theory, we have two hypotheses:

$$\begin{aligned} H_1 &: s_1(t), \quad 0 \leq t \leq T, \quad \text{is sent with probability of } p_1 \\ H_2 &: s_2(t), \quad 0 \leq t \leq T, \quad \text{is sent with probability of } p_2 \end{aligned}$$

where p_1 and p_2 are called *a priori probability*. The energy of the two signals are

$$E_1 = \int_0^T s_1^2(t) dt$$

and

$$E_2 = \int_0^T s_2^2(t) dt$$

In general these two signals may be correlated. We define

$$\rho_{12} = \frac{1}{\sqrt{E_1 E_2}} \int_0^T s_1(t) s_2(t) dt \quad (2.44)$$

as the *correlation coefficient* of $s_1(t)$ and $s_2(t)$. $|\rho_{12}| \leq 1$. The received signal is

$$r(t) = s_i(t) + n(t), \quad i = 1, 2$$

where the noise $n(t)$ is the AWGN with zero mean and a two-sided spectral density of $N_o/2$.

The optimum receiver consists of a correlator or a matched filter matched to the difference signal (see Appendix B)

$$s_d(t) = s_1(t) - s_2(t)$$

These two forms of receiver are shown in Figure 2.7(a, b) and they are equivalent in terms of error probability. The decision regions of binary signal detection is shown in Figure 2.7(c) where $\mu_i = \mu_i(T)$, $i = 1, 2$.

The threshold detector compares the integrator or sampler output $z = z(T)$ to

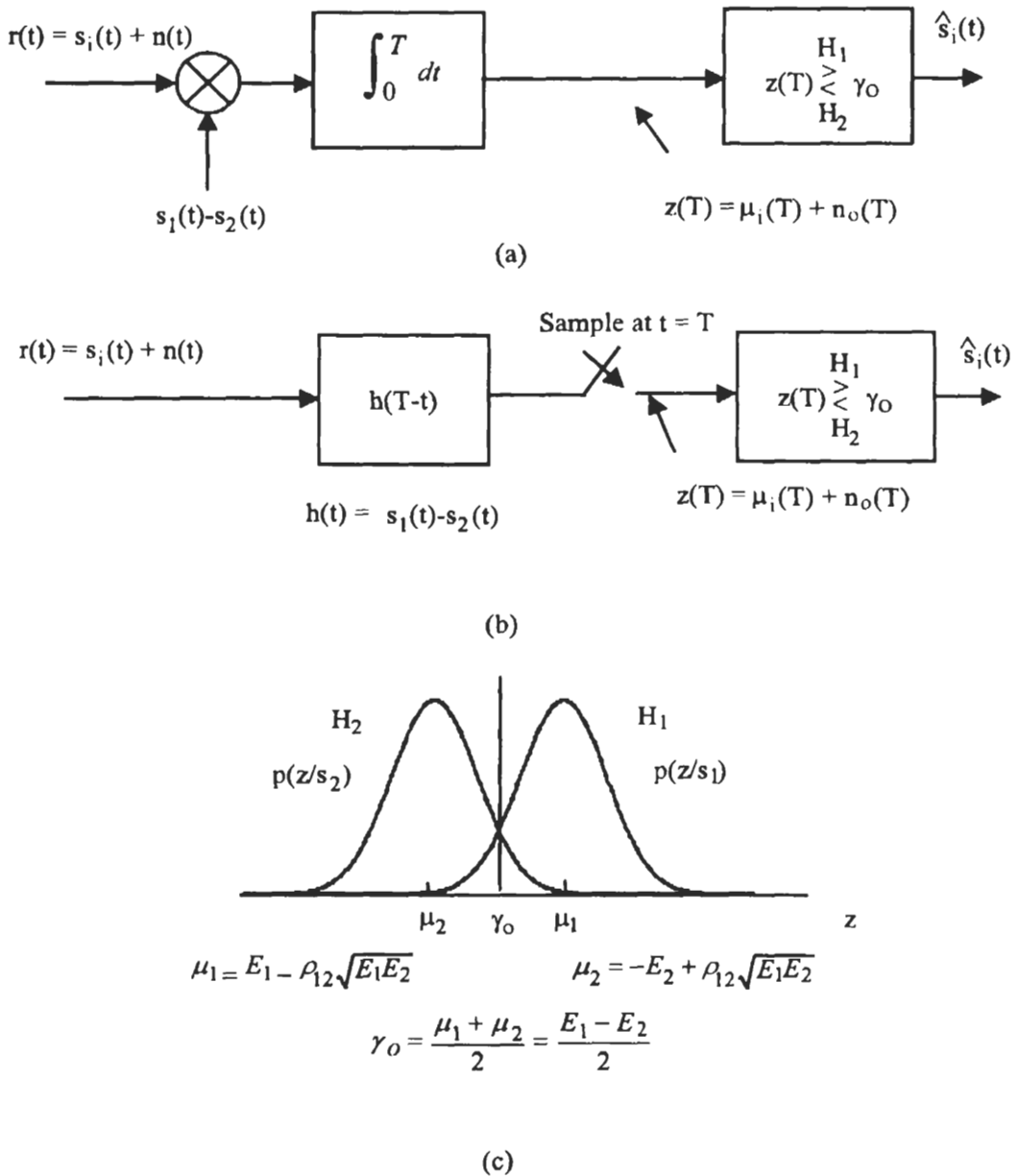


Figure 2.7 Optimum receiver for binary signals: (a) correlator. (b) matched filter. (c) decision regions.

threshold γ_o and decide which hypothesis is true, that is, the decision rule is

$$z \underset{H_2}{\overset{H_1}{\gtrless}} \gamma_o$$

For *minimum error probability criterion* and $p_1 = p_2$, the threshold is chosen as (see Appendix B, (B.22))

$$\gamma_o = \frac{E_1 - E_2}{2} \quad (2.45)$$

The bit error probability is given by

$$P_b = Q \left(\sqrt{\frac{E_d}{2N_o}} \right) \quad (2.46)$$

where

$$\begin{aligned} E_d &= \int_0^T s_d^2(t) dt \\ &= E_1 + E_2 - 2\rho_{12}\sqrt{E_1 E_2} \end{aligned}$$

is the energy of the difference signal, and $Q(x)$ is the Q-function, which we have defined in Chapter 1 already (see (1.11)).

Expression (2.46) shows that the larger the distance (E_d) between the two signals $s_1(t)$ and $s_2(t)$, the smaller the P_b . This is intuitively convincing since the larger the distance, the easier for the detector to distinguish them. In terms of each signal's energy, the above P_b expression becomes

$$P_b = Q \left(\sqrt{\frac{E_1 + E_2 - 2\rho_{12}\sqrt{E_1 E_2}}{2N_o}} \right) \quad (2.47)$$

This expression indicates that P_b depends not only on the individual signal energies, but also on the correlation between them. It is interesting to discover that when $\rho_{12} = -1$, P_b is the minimum. Binary signals with $\rho_{12} = -1$ are called *antipodal*. When $\rho_{12} = 0$, the signals are *orthogonal*.

2.4.1.1 BER of Nonreturn-to-Zero Codes

NRZ-L. The NRZ-L is antipodal with

$$s_1(t) = A, \quad 0 \leq t \leq T$$

$$s_2(t) = -A, \quad 0 \leq t \leq T$$

and

$$s_d(t) = 2A, \quad 0 \leq t \leq T$$

Then $\rho_{12} = -1$, $E_1 = E_2 = A^2T$, and $E_b = (E_1 + E_2)/2 = A^2T$. From (2.47) its P_b is

$$P_b = Q\left(\sqrt{\frac{2A^2T}{N_o}}\right) = Q\left(\sqrt{\frac{2E_b}{N_o}}\right). \quad (\text{NRZ-L}) \quad (2.48)$$

which is plotted in Figure 2.8. The optimum threshold is

$$\gamma_o = \frac{E_1 - E_2}{2} = 0, \quad (\text{NRZ-L})$$

Unipolar NRZ. For unipolar NRZ,

$$\begin{aligned} s_1(t) &= A, & 0 \leq t \leq T \\ s_2(t) &= 0, & 0 \leq t \leq T \end{aligned}$$

and

$$s_d(t) = A, \quad 0 \leq t \leq T$$

Thus $E_1 = A^2T$, $E_2 = 0$, $E_b = A^2T/2$, and $\rho_{12} = 0$. Its error probability is

$$P_b = Q\left(\sqrt{\frac{A^2T}{2N_o}}\right) = Q\left(\sqrt{\frac{E_b}{N_o}}\right), \quad (\text{unipolar-NRZ}) \quad (2.49)$$

which is plotted in Figure 2.8. The optimum threshold is

$$\gamma_o = \frac{A^2T}{2}, \quad (\text{unipolar-NRZ})$$

NRZ-M or S. They are modulated by differentially coded data sequence. To the coded sequence the optimum receiver produces an error probability of (2.48) with $\gamma_o = 0$. After detection the coded sequence is differentially decoded back to the original data sequence. The present bit and the previous bit of the coded sequence are used to produce the present bit of the original sequence (see (2.2)). Therefore error probability is

$$\begin{aligned} P'_b &= \Pr(\text{present bit correct and previous bit incorrect}) \\ &\quad + \Pr(\text{present bit incorrect and previous bit correct}) \end{aligned}$$

$$\begin{aligned}
 &= (1 - P_b)P_b + P_b(1 - P_b) \\
 &= 2(1 - P_b)P_b \\
 &\approx 2P_b, \quad \text{for small } P_b
 \end{aligned}$$

That is

$$P_b \approx 2Q \left(\sqrt{\frac{2A^2T}{N_o}} \right) = 2Q \left(\sqrt{\frac{2E_b}{N_o}} \right), \quad (\text{NRZ-M or S}) \quad (2.50)$$

which is plotted in Figure 2.8.

2.4.1.2 BER of Return-to-Zero Codes

Polar RZ. The signals are antipodal with

$$\begin{aligned}
 s_1(t) &= \begin{cases} A, & 0 \leq t \leq \frac{T}{2} \\ 0, & \text{elsewhere} \end{cases} \\
 s_2(t) &= -s_1(t)
 \end{aligned}$$

and

$$s_d(t) = \begin{cases} 2A, & 0 \leq t \leq \frac{T}{2} \\ 0, & \text{elsewhere} \end{cases}$$

Then $\rho_{12} = -1$, $E_1 = E_2 = A^2T/2$, and $E_b = (E_1 + E_2)/2 = A^2T/2$. From (2.47) its P_b is

$$P_b = Q \left(\sqrt{\frac{A^2T}{N_o}} \right) = Q \left(\sqrt{\frac{2E_b}{N_o}} \right). \quad (\text{polar-RZ}) \quad (2.51)$$

which is the same as that of NRZ-L in terms of E_b/N_o and the optimum threshold γ_o is also 0. P_b is plotted in Figure 2.8.

Unipolar RZ. The signals are

$$\begin{aligned}
 s_1(t) &= \begin{cases} A, & 0 \leq t \leq \frac{T}{2} \\ 0, & \text{elsewhere} \end{cases} \\
 s_2(t) &= 0, \quad 0 \leq t \leq T
 \end{aligned}$$

and

$$s_d(t) = \begin{cases} A, & 0 \leq t \leq \frac{T}{2} \\ 0, & \text{elsewhere} \end{cases}$$

Then $\rho_{12} = 0$, $E_1 = A^2T/2$, $E_2 = 0$, and $E_b = (E_1 + E_2)/2 = A^2T/4$. From (2.47) its P_b is

$$P_b = Q\left(\sqrt{\frac{A^2T}{4N_o}}\right) = Q\left(\sqrt{\frac{E_b}{N_o}}\right), \quad (\text{unipolar-RZ}) \quad (2.52)$$

which is plotted in Figure 2.8. This is the same as that of unipolar NRZ in terms of E_b/N_o and optimum threshold γ_o is $A^2T/4$. Note that for the E_b of unipolar-RZ to be the same as that of unipolar-NRZ, its amplitude must be $\sqrt{2}$ times that of unipolar-NRZ. This will make their thresholds the same when their E_b s are the same. However, if the amplitude is fixed, the unipolar-NRZ pulse will have twice the energy of the unipolar-RZ pulse, thus the error probability is lower. From this discussion we can see that different conclusions will be drawn for different comparison basis. In the following, our comparison is always based on the same E_b/N_o . However, the reader should be aware of different conclusions if comparison is based on the same amplitude.

2.4.2 BER of Pseudoternary Codes

According to the results of the detection theory in Appendix B ((B.37), see also [18, Chapter 4]), for M-ary signals, the *minimum error probability* receiver computes

$$l_j = \ln P_j - \frac{1}{N_o} \sum_{i=1}^N (r_i - s_{ij})^2, \quad j = 1, 2, \dots, M \quad (2.53)$$

and chooses the largest, where

$$r_i = \int_0^T r(t)\phi_i(t)dt, \quad i = 1, 2, \dots, N$$

r_i are statistically independent Gaussian random variables with variance of $N_o/2$. Their mean values depend on hypotheses, that is,

$$\begin{aligned} s_{ij} &= E\{r_i/H_j\} = \int_0^T s_j(t)\phi_i(t)dt \\ i &= 1, 2, \dots, N; j = 1, 2, \dots, M \end{aligned}$$

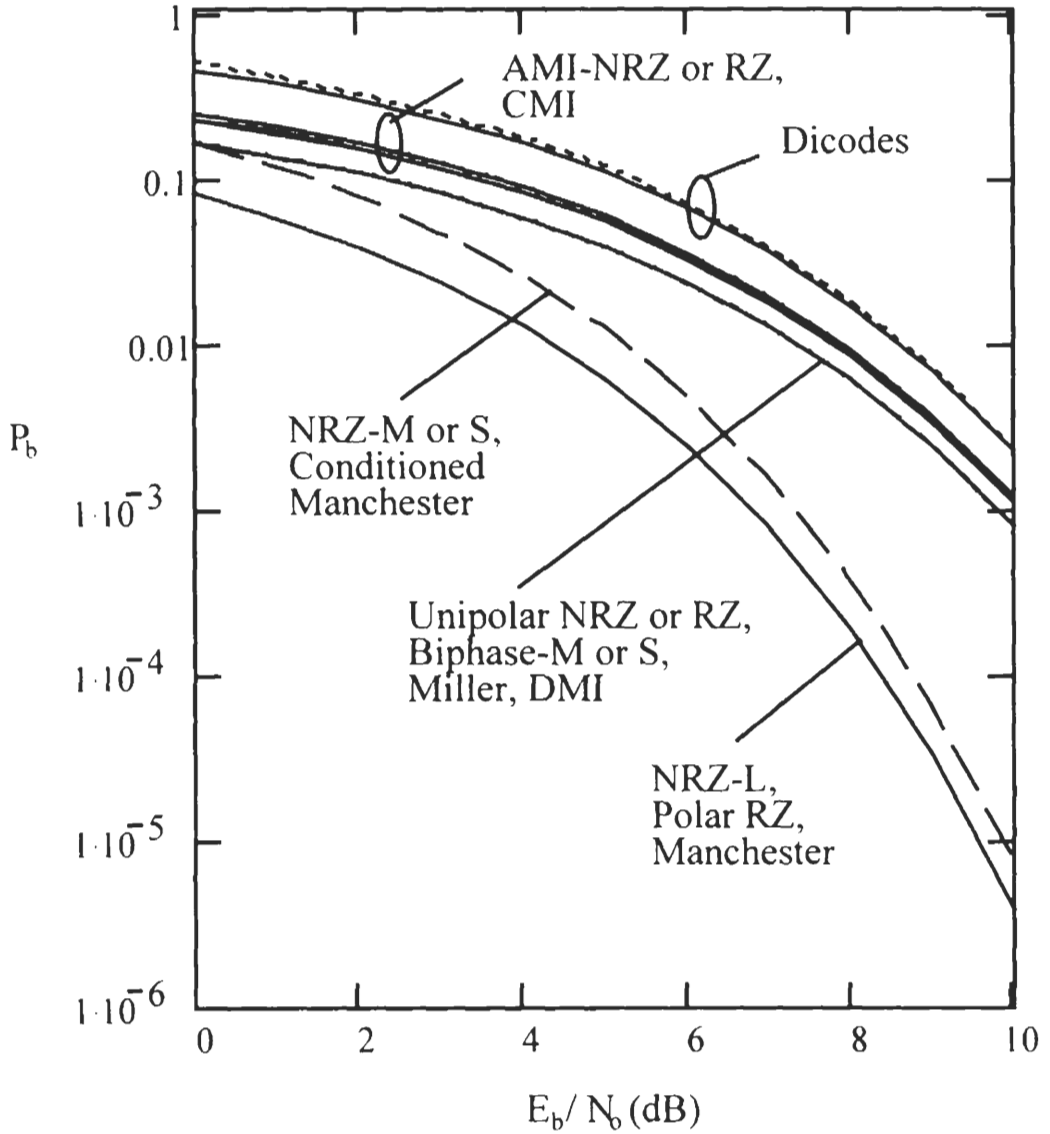


Figure 2.8 Bit error probabilities of some line codes.

$\phi_i(t)$ are the orthonormal coordinates for projecting $r(t)$ onto them. N is the dimension of the vector space spanned by $\phi_i(t)$.

AMI-NRZ codes consist of three types of signals, or we have three hypotheses:

$$\begin{aligned} H_1 &: s_1(t) = A, & 0 \leq t \leq T, & p_1 = \frac{1}{4} \\ H_2 &: s_2(t) = -A, & 0 \leq t \leq T, & p_2 = \frac{1}{4} \\ H_3 &: s_3(t) = 0, & 0 \leq t \leq T, & p_3 = \frac{1}{2} \end{aligned}$$

We choose $\phi_1(t) = s_1(t)/\sqrt{E_1} = s_1(t)/A\sqrt{T}$, and the rest of signals are linearly related to it. Therefore $N = 1$ in this case and the optimum receiver consists of one correlator and a threshold detector. The detection rule (2.53) reduces to

$$\begin{aligned} l_1 &= \ln \frac{1}{4} - \frac{1}{N_o} (r - \sqrt{E_1})^2 \\ l_2 &= \ln \frac{1}{4} - \frac{1}{N_o} (r + \sqrt{E_1})^2 \\ l_3 &= \ln \frac{1}{2} - \frac{1}{N_o} r^2 \end{aligned}$$

The decision rule is to choose the largest. For l_1 to be the largest we must have $l_1 > l_2$ and $l_1 > l_3$, from these relations we can deduce that

$$H_1 \text{ is true if } r > \frac{N_o \ln 2 + E_1}{2\sqrt{E_1}} \triangleq \gamma_{13}$$

Similarly we can deduce that

$$H_2 \text{ is true if } r < -\gamma_{13} \triangleq \gamma_{23}$$

and

$$H_3 \text{ is true if } \gamma_{13} > r > \gamma_{23}$$

Therefore there are two thresholds and three decision regions as shown in Figure 2.9. The optimum receiver consists of just one correlator and a threshold detector with two thresholds as shown in Figure 2.9.

Using $\Pr(e/s_i)$ to denote the probability of error when signal $s_i(t)$ is transmitted, the average bit error probability can be calculated as follows:

$$P_b = p_1 \Pr(e/s_1) + p_2 \Pr(e/s_2) + p_3 \Pr(e/s_3)$$

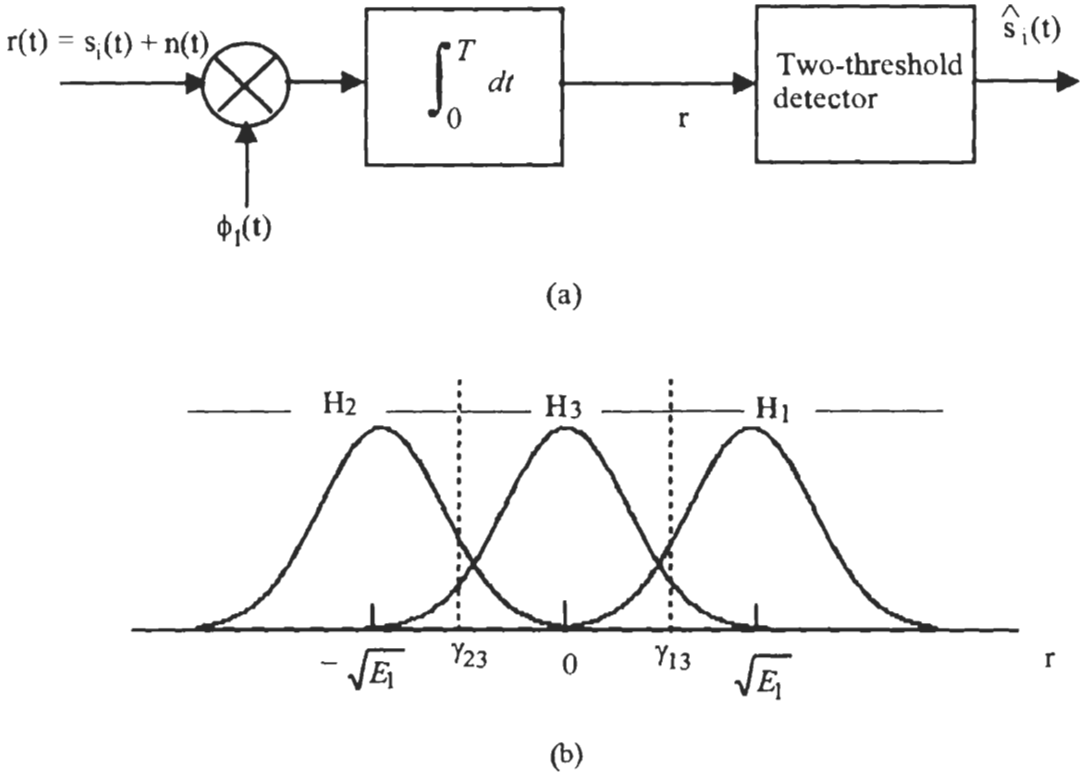


Figure 2.9 Optimum receiver (a), and decision regions (b), of AMI signals.

$$\begin{aligned}
 &= p_1 \int_{-\infty}^{\gamma_{13}} p(r/s_1) dr + p_2 \int_{\gamma_{23}}^{\infty} p(r/s_2) dr + 2p_3 \int_{\gamma_{13}}^{\infty} p(r/s_3) dr \\
 &= 2p_1 \int_{-\infty}^{\gamma_{13}} p(r/s_1) dr + 2p_3 \int_{\gamma_{13}}^{\infty} p(r/s_3) dr \\
 &= \frac{1}{2} Q \left(\frac{E_1 - N_o \ln 2}{\sqrt{2N_o E_1}} \right) + Q \left(\frac{E_1 + N_o \ln 2}{\sqrt{2N_o E_1}} \right) \quad (2.54)
 \end{aligned}$$

Given $E_1 = A^2 T$ and $E_b = 0.5E_1$ we have

$$\begin{aligned}
 P_b &= \frac{1}{2} Q \left(\frac{A^2 T - N_o \ln 2}{A \sqrt{2N_o T}} \right) + Q \left(\frac{A^2 T + N_o \ln 2}{A \sqrt{2N_o T}} \right) \\
 &= \frac{1}{2} Q \left(\frac{2E_b/N_o - \ln 2}{2\sqrt{E_b/N_o}} \right) + Q \left(\frac{2E_b/N_o + \ln 2}{2\sqrt{E_b/N_o}} \right). \quad (\text{AMI-NRZ}) \quad (2.55)
 \end{aligned}$$

This is the bit error probability of the optimum reception.

However, when signal-to-noise ratio is high, then $N_o \ln 2 \ll E_1$, the thresholds can be set in the midway between signals with very little loss of error performance. That is, $\gamma_{13} \approx \sqrt{E_1}/2$ and $\gamma_{23} \approx -\sqrt{E_1}/2$. Thus the BER expression (2.55) reduces to

$$P_b \approx \frac{3}{2}Q \left(\sqrt{\frac{E_b}{N_o}} \right), \quad (\text{AMI-NRZ}) \quad (2.56)$$

which is 3/2 times that of unipolar NRZ. Both accurate and approximate values of P_b for AMI-NRZ are plotted in Figure 2.8, where the upper curve is the approximation. It can be seen that they are very close, even at low signal-to-noise ratios.

For AMI-RZ whose $E_1 = A^2T/2$ and average $E_b = A^2T/4$, the BER can be found from (2.54)

$$\begin{aligned} P_b &= \frac{1}{2}Q \left(\frac{A^2T/2 - N_o \ln 2}{A\sqrt{N_oT}} \right) + Q \left(\frac{A^2T/2 + N_o \ln 2}{A\sqrt{N_oT}} \right) \\ &= \frac{1}{2}Q \left(\frac{2E_b/N_o - \ln 2}{2\sqrt{E_b/N_o}} \right) + Q \left(\frac{2E_b/N_o + \ln 2}{2\sqrt{E_b/N_o}} \right), \quad (\text{AMI-RZ}) \quad (2.57) \end{aligned}$$

and

$$P_b \approx \frac{3}{2}Q \left(\sqrt{\frac{E_b}{N_o}} \right), \quad (\text{AMI-RZ}) \quad (2.58)$$

which is the same as that of AMI-NRZ in terms of E_b/N_o .

Since recovery of NRZ-L from AMI codes is accomplished by simple full-wave rectification, the bit error probability of the final recovered data sequence remains the same.

Dicodes and AMI codes are related by differential coding. As described in Section 2.2.3, data sequence $\{\hat{a}_k\}$ is recovered from $\{\hat{u}_k\}$ using modulo-2 addition: $\hat{a}_k = \hat{a}_{k-1} \oplus \hat{u}_k$, where $\{\hat{u}_k\}$ is the unipolar sequence recovered from the dicode $\{\hat{d}_k\}$ by full-wave rectification. The P_b of $\{\hat{d}_k\}$ is the same as AMI and so is the P_b of $\{\hat{u}_k\}$. \hat{a}_k is incorrect when either \hat{a}_{k-1} or \hat{u}_k is incorrect. This is the same situation as we discussed for NRZ-M or NRZ-S codes in Section 2.4.1. Therefore the bit error probability of $\{\hat{a}_k\}$ is two times the bit error probability of their AMI counterparts. Using (2.58) we have

$$P_b \approx 3Q \left(\sqrt{\frac{E_b}{N_o}} \right), \quad (\text{Dicodes}) \quad (2.59)$$

which is shown in Figure 2.8.

2.4.3 BER of Biphase Codes

Bi-Φ-L (Manchester) signals are antipodal binary with

$$\begin{aligned} s_1(t) &= \begin{cases} A, & 0 \leq t \leq \frac{T}{2} \\ -A, & \frac{T}{2} \leq t \leq T \end{cases} \\ s_2(t) &= -s_1(t) \end{aligned} \quad (2.60)$$

Bi-Φ-L signals can be detected using the optimum receiver in Figure 2.7. The correlation coefficient between them is $\rho_{12} = -1$. The signal energies are

$$\begin{aligned} E_1 &= E_2 = A^2T = E_b \\ E_d &= E_1 + E_2 - 2\rho_{12}\sqrt{E_1E_2} \\ &= 4A^2T = 4E_b \end{aligned}$$

Thus the bit error probability is

$$P_b = Q\left(\sqrt{\frac{2A^2T}{N_o}}\right) = Q\left(\sqrt{\frac{2E_b}{N_o}}\right). \quad (\text{Bi-}\Phi\text{-L (Manchester)}) \quad (2.61)$$

which is the same as that of NRZ-L. This is not surprising since they have the same bit energy and both are antipodal.

Conditioned Bi-Φ-L has a bit error probability of about two times that of Bi-Φ-L since it is just differentially coded Bi-Φ-L. This is to say that conditioned Bi-Φ-L has the same BER as that of NRZ-M or S.

Bi-Φ-M and *Bi-Φ-S* have the same error probability. So it suffices to consider Bi-Φ-M. There are four signals in Bi-Φ-M:

$$\begin{aligned} s_1(t) &= A, & 0 \leq t \leq T, & \quad p_1 = \frac{1}{4} \\ s_2(t) &= \begin{cases} A, & 0 \leq t \leq \frac{T}{2} \\ -A, & \frac{T}{2} \leq t \leq T \end{cases}, & \quad p_2 = \frac{1}{4} \\ s_3(t) &= -s_1(t), & 0 \leq t \leq T, & \quad p_3 = \frac{1}{4} \\ s_4(t) &= -s_2(t), & 0 \leq t \leq T, & \quad p_4 = \frac{1}{4} \end{aligned}$$

Each of them has energy of $E = A^2T$. So average bit energy is also the same. We can choose $\phi_1(t) = s_1(t)/\sqrt{E}$ and $\phi_2(t) = s_2(t)/\sqrt{E}$ as basis functions. Thus

from (2.53) we have

$$l_j = \ln P_j - \frac{1}{N_o} \sum_{i=1}^2 (r_i - s_{ij})^2$$

where

$$\begin{aligned} s_{11} &= \sqrt{E}, & s_{21} &= 0 \\ s_{12} &= 0, & s_{22} &= \sqrt{E} \\ s_{13} &= -\sqrt{E}, & s_{23} &= 0 \\ s_{14} &= 0, & s_{24} &= -\sqrt{E} \end{aligned}$$

The decision rule is to choose the largest l_j . Since P_j are equal for all j , the above rule becomes computing

$$d_j = \sum_{i=1}^2 (r_i - s_{ij})^2$$

and choosing the minimum. Thus the optimum receiver is as shown in Figure 2.10(a) and the decision space is two-dimensional as shown in Figure 2.10(b). Since the problem is symmetrical, it is sufficient to assume that $s_1(t)$ is transmitted and compute the resulting $\Pr(e/s_1)$ which is equal to average P_b . We also can see that the answer would be invariant to a 45 degree rotation of the signal set because the noise is circularly symmetric. Thus we can use the simple diagram in Figure 2.10(c) to calculate the BER.

$$\begin{aligned} P_b &= \Pr(e/s_1) = 1 - \int \int_{Z_1} p(r_1, r_2/s_1) dr_1 dr_2 \\ &= 1 - \left[\int_0^\infty \frac{1}{\sqrt{\pi N_o}} \exp\left(-\frac{(r_1 - \sqrt{E}/2)^2}{N_o}\right) dr_1 \right]^2 \end{aligned}$$

where the two-dimensional integral is converted to the squared one-dimensional integral because r_1 and r_2 are independent identical Gaussian variables. Changing variables we have

$$\begin{aligned} P_b &= 1 - \left[\int_{-\sqrt{E/N_o}}^\infty \frac{1}{\sqrt{2\pi}} \exp\left(-\frac{x^2}{2}\right) dx \right]^2 \\ &= 1 - Q\left(-\sqrt{\frac{E}{N_o}}\right) \end{aligned}$$

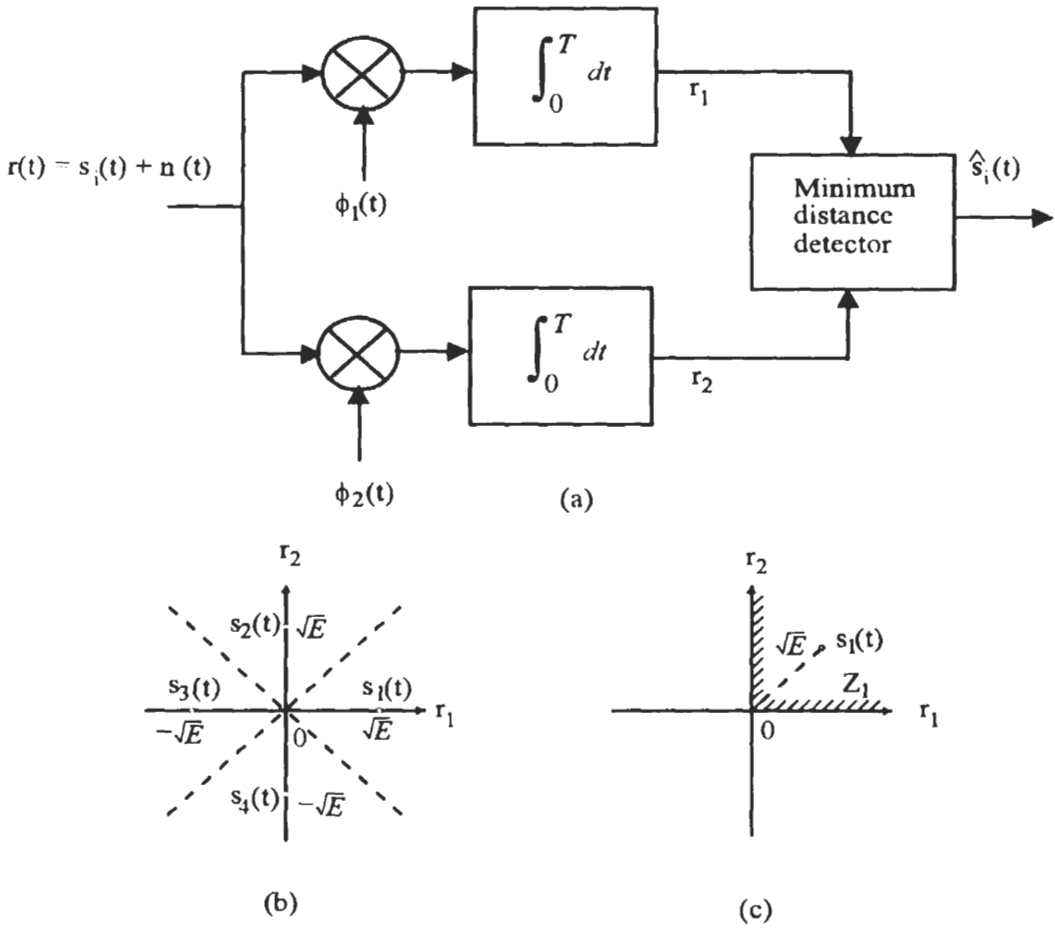


Figure 2.10 Optimum receiver and decision regions of Bi- Φ -M signals.

$$= Q\left(\sqrt{\frac{E}{N_o}}\right) = Q\left(\sqrt{\frac{E_b}{N_o}}\right), \quad (\text{Bi-}\Phi\text{-M,S}) \quad (2.62)$$

The BER of Bi- Φ -M is identical to that of unipolar codes and is 3 dB worse than that of NRZ-L or polar-RZ. This BER is plotted in Figure 2.8.

2.4.4 BER of Delay Modulation

The four symbol signals in delay modulation are the same as those of the Bi- Φ -M, and their probability distribution is also the same. Therefore the BER of delay modulation is the same of that of Bi- Φ -M

$$P_b = Q\left(\sqrt{\frac{E_b}{N_o}}\right), \quad (\text{DM or Miller}) \quad (2.63)$$

Like Bi- Φ -M, the BER of delay modulation is identical to that of unipolar codes and is 3 dB worse than that of NRZ-L or polar-RZ.

2.5 SUBSTITUTION LINE CODES

The AMI code is a preferable choice due to its many advantages. It has a narrow bandwidth and no dc component. It has error detection capability due to its alternate mark inversion. The occurrence of consecutive positive or negative amplitudes indicates transmission errors and is called a *bipolar violation*. Synchronization is made easier due to transitions in each binary 1 bit.

Even though synchronization of AMI code is better than that of NRZ code, it is still not satisfactory. A string of 0s will result in a long period of zero level which will cause loss of synchronization. In the T1 system, by eliminating the all-zero code word from the 8-bit source encoder, the maximum number of consecutive zeros is limited to 14. However, for data signals even this is impractical. A solution to this is to substitute the block of N consecutive zeros with a special sequence with intentional bipolar violations. These violations enable the zero-substitution sequence to be identified and replaced by spaces (zeros) at the receiving end of the line. The pulse density is at least $1/N$. This will improve bit timing recovery. Two popular zero substitution codes are the *binary N -zero substitution (BNZS)* and the *high density bipolar n (HDB n)* codes.

2.5.1 Binary N-Zero Substitution Codes

BNZS code was proposed by Johannes et al in 1969 [4]. It is the most popular substitution code which replaces a string of N 0s in the AMI waveform with a special N -bit waveform with at least one bipolar violation. All BNZS formats are dc free and retain the balanced feature of AMI, which is achieved by choosing the substitution sequences properly so that the conditioned sequences have an equal number of positive and negative pulses.

There are two kinds of BNZS codes. One is called *nonmodal code* in which two substitution sequences are allowed and the choice between them is based solely on the polarity of the pulse immediately preceding the zeros to be replaced.

For balance purposes, substitution sequences for nonmodal codes must contain an equal number of positive and negative pulses. They also may contain zeros, and the total number of zeros may be odd. The last pulse in the substitution sequences must have the same polarity as the pulse immediately preceding the sequence. If this property is not fulfilled, a unipolar pattern consisting of one, N zeros, a one, N zeros, and so on, would be converted to a sequence consisting of a + (say) for the one, the substitution sequence, another + (to follow alternate polarity rule),⁶ the same substitution sequence, and so on, and since the substitution sequence is balanced the signal would have a dc component. A sequence of two opposite polarity pulses would satisfy the above requirements. However, it would include no bipolar violations by which it may be recognized at the receiving end, so it is necessary to add another two pulses. Thus for nonmodal codes, N must be at least 4. Table 2.2 shows some practical nonmodal codes: B6ZS and B8ZS. All of them are balanced and the last pulse is the same as the preceding pulse.

Another substitution code is called *modal code* in which more than two substitution sequences are provided, and the choice of sequence is based on the polarity of the pulse immediately preceding the zeros to be replaced as well as the previous substitution sequence used. For modal codes, N can be two or three. Modal code substitution sequences need not be balanced, and balance is achieved by properly alternating the sequences. To illustrate this, we refer to Table 2.2 where B3ZS is a modal code (also see Figure 2.11). Let B represent a normal bipolar that conforms to the AMI rule, V represent a bipolar violation, and 0 represent no pulse. Then in the B3ZS code, a block of 000 is replaced by B0V or 00V. The choice of B0V or 00V is made so that the number of B pulses between two consecutive V pulses is odd. Thus if we consider the contribution to dc component by the signal segment since last substitution, there will be two "extra" pulses that contribute to the dc component due to

⁶ This bit would be a – if the coding rule is to simply replace the N -zero sequence. However, to make more transitions in the signal, it is better to follow the alternate polarity rule right after the substitution sequence.

(a) B3ZS		
Number of B pulses since last substitution		
Preceding pulse	odd	even
—	00—	+0+
+	00+	--0--

(b)B6ZS	
Preceding pulse	Substitution sequence
—	0—+0+—
+	0+—0--+

(c)B8ZS	
Preceding pulse	Substitution sequence
—	000—+0+—
+	000+—0—+

(d)HDB3		
Number of B pulses since last substitution		
Preceding pulse	odd	even
—	000—	+00+
+	000+	--00--

Table 2.2 Substitution codes. From [19]. Copyright © 1993 Kluwer. Reprinted with permission.

the bipolar violation. However, the polarity of these two pulses will be alternating since it depends on the polarity of the preceding pulse and whether the number of B pulses since last substitution is odd or even. All these conditions happen equally likely in a random sequence. Therefore in a long time average these “extra” pulses will cancel each other so that there will be no dc component.

B3ZS and B6ZS are specified for DS-3 and DS-2 North American standard rates, respectively, and B8ZS is specified as an alternative to AMI for the DS-1 and DS-1C rates. Figure 2.11 shows examples of some substitution codes.

Spectrum calculation of BNZS codes is based on a flow graph of the pulse states and is quite involved. The spectrum obviously depends on the substitution sequence used and the statistical property of the data sequence. Refer to [4] for detail. Figure 2.12 shows spectra of some substitution codes [4], where F/F_{bit} is the frequency normalized to the bit rate F_{bit} .

No results of bit error probability of BNZS codes are available in the literature. Since they are conditioned AMI codes we may conjecture that their bit error rates at the detector must be very close to those of AMI codes. However, there are more errors due to failures to recognize the substitution sequences in the decoder.

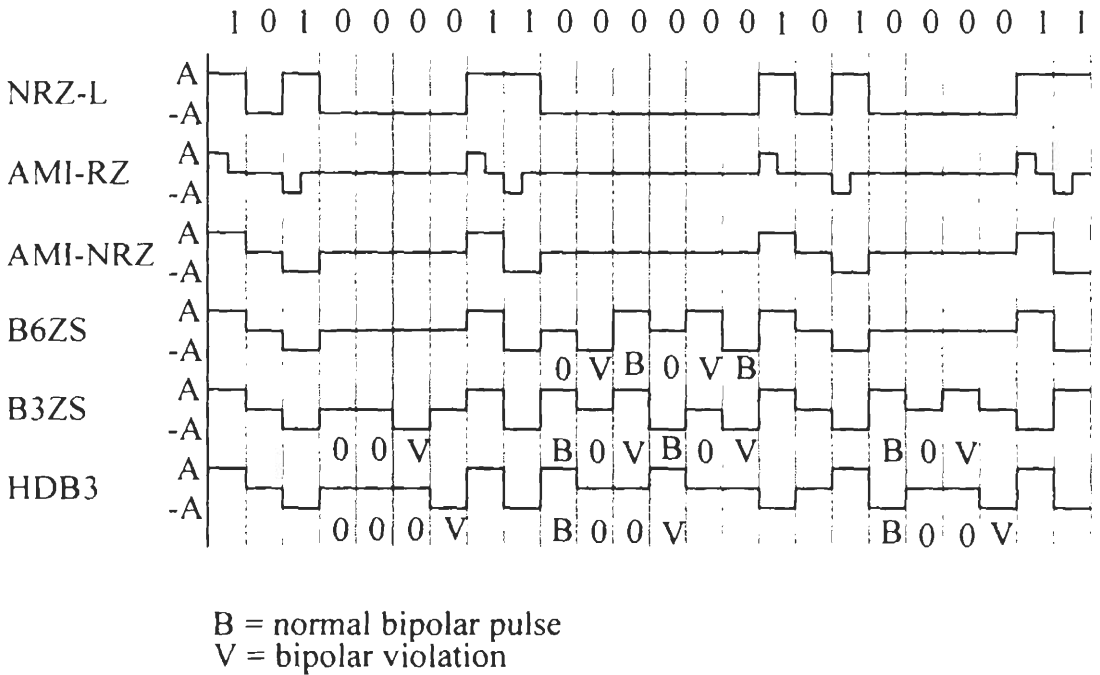


Figure 2.11 Substitution codes. From [19]. Copyright © 1993 Kluwer. Reprinted with permission.

2.5.2 High Density Bipolar n Codes

Croisier proposed HDB n code and *compatible high density bipolar n (CHDB n)* code in 1970 [2]. CHDB n may be considered as an improved version of HDB n since CHDB n coding and decoding hardware is somewhat simpler [2].

The common feature of these two codes is that they limit the number of consecutive 0s to n by replacing the $(n+1)$ th 0 by a bipolar violation. In addition, to avoid dc component, they are made modal. That is, they each have more than one possible substitution sequence. The substitution sequences are:

$$\begin{array}{ll} \text{HDB} & B 0 0, \dots, 0 V \quad \text{or} \quad 0 0 0, \dots, 0 V \\ \text{CHDB} & 0 0, \dots, 0 B 0 V \quad \text{or} \quad 0 0, \dots, 0 0 0 V \end{array}$$

where bits omitted are all zeros. There are total n zeros in each of the sequences.

The choices of the sequences must be such that the number of B pulses between two consecutive V pulses is always odd. It can be easily verified that the polarity of V pulses will always alternate so that a long sequence will produce virtually no dc

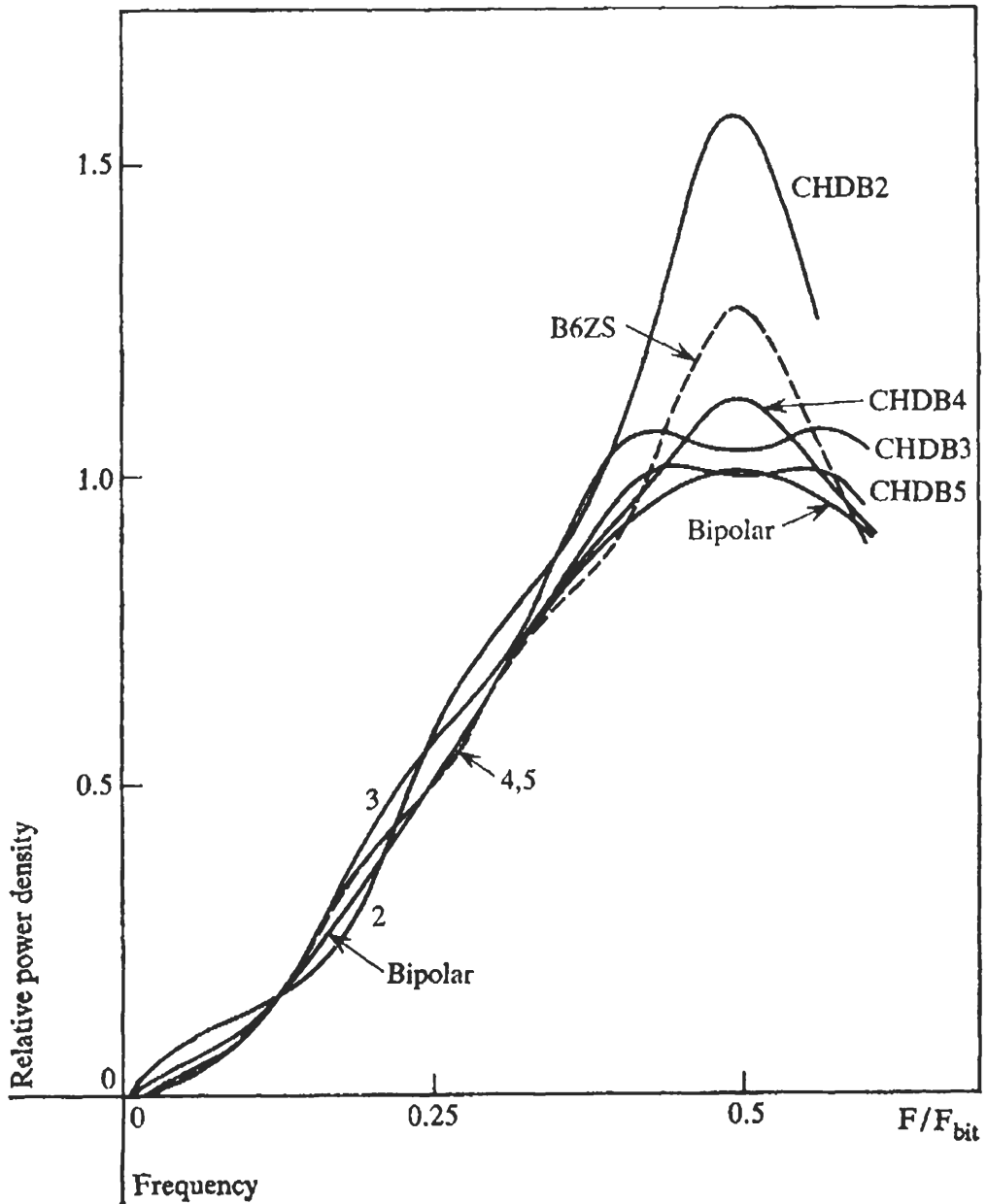


Figure 2.12 PSDs of some substitution codes. From [2]. Reprinted by permission from IBM Journal of Research and Development, copyright 1970 by International Business Machines Corporation.

component.

Two commonly used HDBn codes are HDB2 and HDB3. HDB2 is identical to B3ZS. HDB3 is used for coding of 2.048 Mbps, 8.448 Mbps, and 34.368 Mbps multiplex within the European digital hierarchy [20]. Its substitution rules are shown in Table 2.2(d). An example of HDB3 is shown in Figure 2.11.

2.6 BLOCK LINE CODES

So far the codes we discussed are bit-by-bit codes, in which each input bit is translated one at a time to an output symbol. In a *block code* input bits are grouped into blocks and each block is translated into another block of symbols. The purpose of using block codes is to introduce redundancy in order to meet one or more of the desired attributes of a line code as we stated at the beginning of this chapter. Two basic techniques used in block coding are (1) insertion of additional binary pulses to create a block of n binary symbols that is longer than the number of information bits m , or (2) translation of a block of input bits to a block of output symbols that uses more than two levels per symbol. The first technique is mainly used in optical transmission where modulation is limited to two-level (on-off) but is relatively insensitive to a small increase in transmission rate since optical fiber has a very wide bandwidth. The second technique applies to cases where bandwidth is limited but multilevel transmission is possible, such as metallic wires used for digital subscriber loops.

All basic line codes described in Section 2.2 can be viewed as special cases of block codes.

There are some technical terms which should be defined before we describe various block codes. Some of them are also used for nonblock codes, but some are only used in describing block codes.

Digital sum (DS) of a digital sequence is defined as the numerical sum of the symbols in the sequence. Digital sum is also called *disparity*. To suppress the dc component of a coded sequence, the sequence should have a zero digital sum or disparity. Because in many cases the DS decreases as the sequence gets longer, therefore long-term DS tends to be zero even though short-term DS varies with time. It is important to know the maximum *digital sum variation* (DSV) which leads to *dc wander*. When a sequence has a finite DSV, it is said to be *balanced*, otherwise it is *unbalanced*.

A block code which chooses symbols from more than one alphabet is called *alphabetic*, otherwise it is *nonalphabetic*.

The *efficiency* of a code is defined as [21]

$$\eta = \frac{\text{actual information rate}}{\text{theoretical maximum information rate}} \times 100\%$$

For example, NRZ codes encode 1 bit into 1 binary symbol, the efficiency is

$$\eta = \frac{\log_2 2}{\log_2 2} = 100\%$$

AMI codes encode 1 bit into 1 ternary symbol, the efficiency is

$$\eta = \frac{\log_2 2}{\log_2 3} = 63.09\%$$

The Manchester code encodes 1 bit into 2 binary symbols, the efficiency is

$$\eta = \frac{\log_2 2}{2 \log_2 2} = 50\%$$

2.6.1 Coded Mark Inversion Codes

Fiber optical communication systems use baseband modulation, not bandpass modulation, since the transmission of a symbol is represented by the intensity of the light of the optical source, namely the laser diode. Even though AMI has been widely used in digital coaxial or pair cable systems due to its merit described before, it can not be used in fiber optical systems since it uses three levels⁷ and thus suffers from nonlinearity of the laser diode. A promising solution for avoiding this difficulty is to replace the zero level of AMI with two-level waveforms. This leads to two-level AMI codes including coded mark inversion (CMI) scheme and differential mode inversion (DMI) scheme.

CMI was first proposed by Takasaki et al in 1976 [6] for optical fiber systems. CMI uses A or $-A$ for a binary 1 for a full-bit period. The levels A and $-A$ are alternated for each occurrence of 1. The 0s are represented by a pulse with level A for the first half bit and $-A$ for the second half bit, or vice versa. CMI can be also viewed as 1 bit to 2 bits coding (1B2B) with $1 \rightarrow 00$ or $1 \rightarrow 11$, alternatively and $0 \rightarrow 01$ only (or $0 \rightarrow 10$ only). An example of CMI is shown in Figure 2.13.

CMI improves the transition density significantly. It also has error detection feature through the monitoring of coding rule violation. Decoding is done by comparing the second half bit with the first half bit so that it is insensitive to polarity reversals. Compared with AMI codes, the disadvantage of this code is that the transmission rate is twice that of the binary input signal.

CMI is chosen for the coding of the 139.246-Mbps multiplex within the European digital hierarchy [20].

⁷ A negative 1 corresponds to laser diode off, zero to 1/2 intensity, and positive 1 to full intensity.

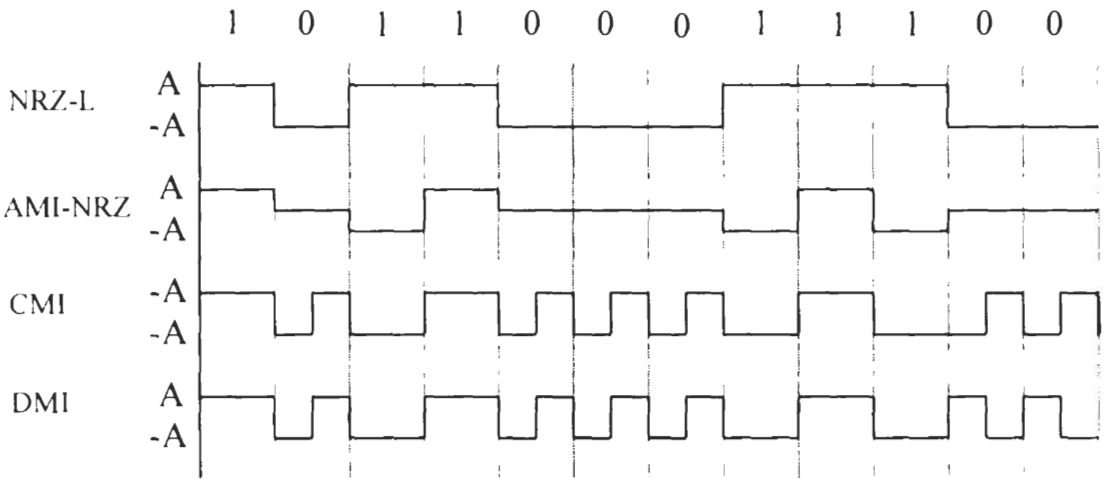


Figure 2.13 CMI and DMI waveforms.

The signal format of CMI cannot be described by (2.11) since it uses two waveforms (1,1) or (-1,1) for each bit. Nor can it be described by first-order Markov process since the mark is alternately inverted which implies that the current bit state may depend on a bit state long before the current one. Therefore its $R(\tau)$ is found by a computer Monte Carlo simulation as shown in Figure 2.14(a). Also shown is the $R(\tau)$ (Figure 2.14(b)) found by approximating CMI by first-order Markov process, which is quite close to the simulated one. The simulated $R(\tau)$ can be decomposed into two parts as shown in Figure 2.14 (c, d), where (d) is periodical. By taking the Fourier transforms of (c) and (d) analytically the PSD is given by

$$\Psi_s(f) = A^2 \frac{6 - 4 \cos(\pi f T) - 3 \cos(2\pi f T) + \cos(4\pi f T)}{8\pi^2 f^2 T} + A^2 \sum_{k=-\infty}^{\infty} \frac{1}{\pi^2 (2k+1)^2} \delta\left(f - \frac{2k+1}{T}\right). \quad (\text{CMI}) \quad (2.64)$$

which is plotted in Figure 2.14(e), where $A = 1$ for unity average bit energy. The periodical part of $R(\tau)$ manifests itself as a series of impulses at odd multiples of data rate in the spectrum. The sudden drop in the $P_{ob}(B)$ curve is due to the impulse at $f = R_b$ in the PSD. The bandwidths are $B_{null} = 2.0R_b$, $B_{90\%} \approx 2.92R_b$, and $B_{99\%} \approx 28R_b$.

Note that the above spectrum of CMI is calculated with two levels of $\pm A$, that is, the code waveform is bipolar. For optical transmission these two levels would be A and 0 , that is, the code waveform is unipolar. This level shift will not change the

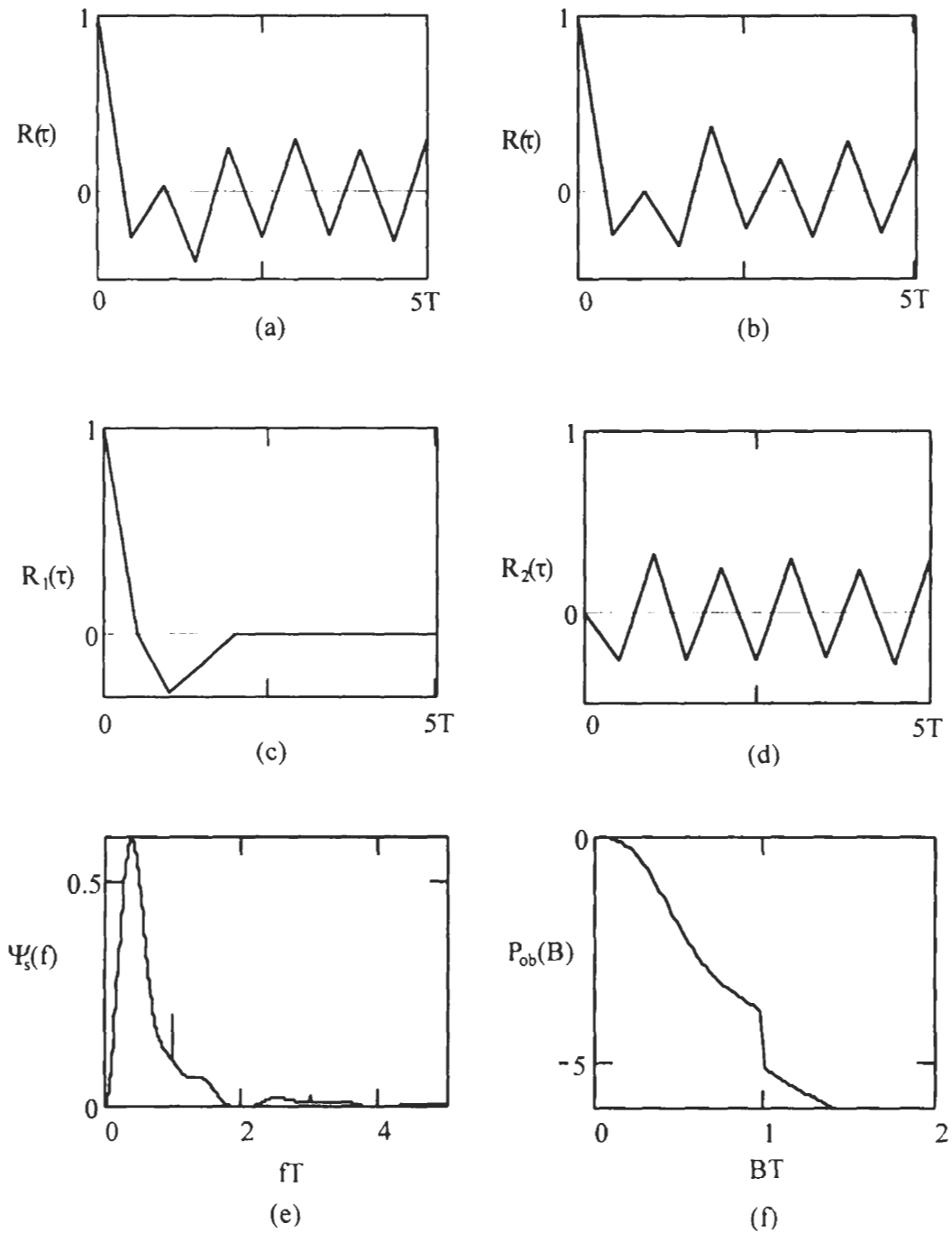


Figure 2.14 CMI correlations and spectrum: (a) simulated $R(\tau)$, (b) approximate $R(\tau)$, (c) nonperiodical part of the simulated $R(\tau)$, (d) periodical part of the simulated $R(\tau)$, (e) PSD, (f) out-of-band power.

spectral shape, but only causes the spectrum to have a dc component which can be represented by $\frac{1}{2}\delta(f)$, and the continuous part must be multiplied by a factor of $\frac{1}{2}$. The null bandwidth $B_{null} = 2.0R_b$. The energy within bandwidth R_b is 79.4% and just above R_b is 99.7% due to the jump caused by $0.101\delta(f)$ at $f = R_b$. Therefore $B_{90\%}$ and $B_{99\%}$ cannot be found.

We calculate the BER of CMI for the bipolar case which can be used in metallic wired systems. We will discuss the unipolar case for optical systems where CMI finds its primary use shortly. In the bipolar case, CMI is a ternary signal with

$$\begin{aligned} s_1(t) &= A, & 0 \leq t \leq T, & & p_1 &= \frac{1}{4} \\ s_2(t) &= \begin{cases} -A, & 0 \leq t \leq \frac{T}{2} \\ A, & \frac{T}{2} \leq t \leq T \end{cases} & & & p_2 &= \frac{1}{2} \\ s_3(t) &= -A, & 0 \leq t \leq T, & & p_3 &= \frac{1}{4} \end{aligned} \quad (2.65)$$

All three signals have the same energy: $E = A^2T$. $s_2(t)$ is orthogonal to $s_1(t)$ and $s_3(t)$. So we can choose $\phi_1(t) = s_1(t)/\sqrt{E}$ and $\phi_2(t) = s_2(t)/\sqrt{E}$ as the basis functions. The third signal $s_3(t) = -\sqrt{E}\phi_1(t)$. Thus from (2.53) we have

$$l_j = \ln P_j - \frac{1}{N_o} \sum_{i=1}^2 (r_i - s_{ij})^2$$

where

$$\begin{aligned} s_{11} &= \sqrt{E}, & s_{21} &= 0 \\ s_{12} &= 0, & s_{22} &= \sqrt{E} \\ s_{13} &= -\sqrt{E}, & s_{23} &= 0 \end{aligned}$$

Thus the decision space is two-dimensional as shown in Figure 2.15. The decision rule is to choose the largest. For l_1 to be the largest we must have $l_1 > l_2$ and $l_1 > l_3$, from these relations we can deduce that

$$H_1 \text{ is true if } r_1 > 0 \text{ and } r_1 > r_2 + \beta$$

where

$$\beta = \frac{N_o \ln 2}{2\sqrt{E}}$$

similarly we can deduce that

$$H_2 \text{ is true if } -(r_2 + \beta) < r_1 < (r_2 + \beta)$$

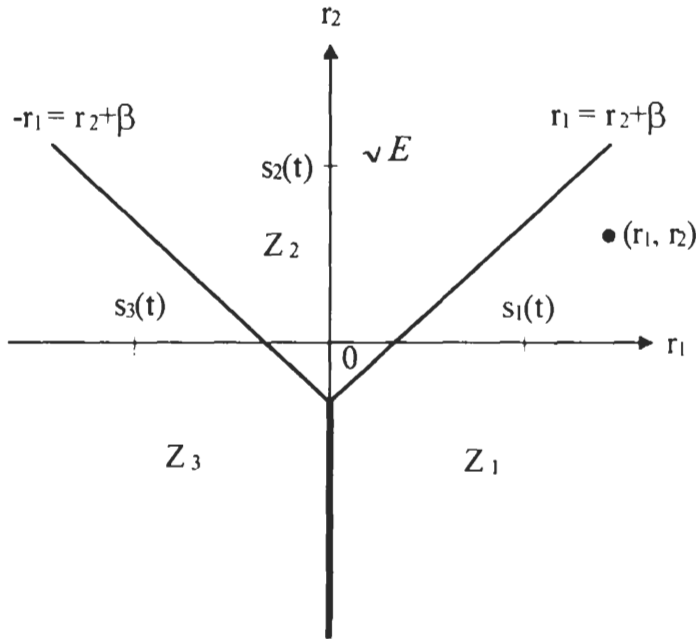


Figure 2.15 CMI decision space.

and

$$H_3 \text{ is true if } r_1 < 0 \text{ and } r_1 < -(r_2 + \beta)$$

Therefore there are three decision boundaries as shown in Figure 2.15. The optimum receiver consists of two correlators for computing r_1 and r_2 (see Figure 2.10(a)).

The average bit error probability is

$$\begin{aligned} P_b &= p_1 \Pr(e/s_1) + p_2 \Pr(e/s_2) + p_3 \Pr(e/s_3) \\ &= p_1 [1 - \int_{Z_1} \int p(r_1, r_2/s_1) dr_1 dr_2] + p_2 [1 - \int_{Z_2} \int p(r_1, r_2/s_2) dr_1 dr_2] \\ &\quad + p_3 [1 - \int_{Z_3} \int p(r_1, r_2/s_3) dr_1 dr_2] \end{aligned}$$

Due to the geometrical symmetry of decision regions Z_1 and Z_3 and the fact that

$p_3 = p_1$, we have

$$P_b = 2p_1 \left[1 - \int_{z_1} \int p(r_1, r_2/s_1) dr_1 dr_2 \right] + p_2 \left[1 - \int_{z_2} \int p(r_1, r_2/s_2) dr_1 dr_2 \right]$$

Integrating and omitting detail, the P_b is found as

$$P_b = 1 - \frac{1}{2} \int_{-\alpha}^{\infty} \frac{1}{\sqrt{2\pi}} \exp\left(-\frac{x^2}{2}\right) Q\left(\frac{\ln 2}{\alpha} - \alpha - x\right) dx \\ - \int_0^{\infty} \frac{1}{\sqrt{2\pi}} \exp\left(-\frac{x^2}{2}\right) Q\left(-\frac{\ln 2}{\alpha} - \alpha + x\right) dx, \quad (\text{CMI}) \quad (2.66)$$

where

$$\alpha = \sqrt{\frac{2E_b}{N_o}}$$

If we ignore the boundary bias for high SNR and set boundaries as bisectors between signals, then we can get the approximate P_b by replacing $\ln 2$ with 0 in the above expression:

$$P_b \approx 1 - \frac{1}{2} \int_{-\alpha}^{\infty} \frac{1}{\sqrt{2\pi}} \exp\left(-\frac{x^2}{2}\right) Q(-\alpha - x) dx \\ - \int_0^{\infty} \frac{1}{\sqrt{2\pi}} \exp\left(-\frac{x^2}{2}\right) Q(-\alpha + x) dx, \\ (\text{CMI, for high SNR}) \quad (2.67)$$

Moreover, if we ignore the error probability between s_1 and s_3 , then only error probability between s_1 and s_2 or s_3 and s_2 is considered. Thus P_b can be approximated as

$$P_b \approx Q\left(\sqrt{\frac{E_b}{N_o}}\right), \quad (\text{CMI, approximation}) \quad (2.68)$$

which is the same as that of unipolar codes. Expressions (2.66) and (2.67) are numerically evaluated. They are plotted in Figure 2.8 under the same label of AMI codes since they are very close to each other and are indistinguishable.

For optical transmission, the $-A$ level in the CMI signal set would be 0. Not only are the pulses unipolar, but also many other factors that are particular to optical systems must be considered in calculating the BER. The required power p_o to achieve a desired error rate has been studied in [22] for straight binary formats (unipolar NRZ-

L). It can be expressed as

$$p_o = EZ^{\frac{x}{2+2x}} \Sigma^{\frac{1}{1+r}} \Gamma(x, r) \quad (2.69)$$

where

$$\Gamma(x, r) = \Gamma_1(x, r)^{\frac{x}{2+2x}} \Gamma_2(x, r)^{\frac{2+x}{1+r}}$$

$$\Gamma_1(x, r) = \frac{-(2-r) + \sqrt{(2-r)^2 + 16(1+x)x^{-2}(1-r)}}{2(1-r)}$$

$$\Gamma_2(x, r) = \sqrt{\Gamma_1^{-1}(x, r) + 1 - r} + \sqrt{\Gamma_1^{-1}(x, r) + 1}$$

$$r = I_o/\Sigma$$

and where

E = constant that depends on the error rate and bit rate,

Z = thermal noise contribution,

I_i = shot noise contribution that would be caused by the optical pulse in the i th time slot ($i = 0$ corresponds to the time slot under decision),

Σ = total shot noise contribution,

x = excess noise factor for APD (avalanche photodiode).

Takasaki et al [6] showed that a slight modification of the above expressions provides the required optical power for other pulse formats, including CMI and DMI. For CMI and DMI the following substitutions in (2.69) will provide the required optical power for direct transmission

$$\left. \begin{array}{l} \Sigma_1 \rightarrow \Sigma + I_{-1/2} \\ I_1 \rightarrow I_o - I_{1/2} \\ Z \rightarrow Z \end{array} \right\} \quad (2.70)$$

The BER of edge-detected CMI data transmission over the AWGN channel was given in [23] as

$$P_b \approx \frac{BT}{4\sqrt{3}} \exp\left(\frac{-E_b/N_o}{2BT}\right)$$

where B is the equivalent noise bandwidth of the receiver low-pass filter.

2.6.2 Differential Mode Inversion Codes

DMI is another two-level AMI scheme proposed by Takasaki et al in 1976 [6] for optical fiber systems. Its coding rule for binary 1s is the same as that of CMI. Its

coding rule for binary 0s is different: $0 \rightarrow 01$ or $0 \rightarrow 10$ so that no pulses in a sequence have pulse widths wider than T , the bit duration. An example of DMI is shown in Figure 2.13. For optical applications, the DMI code is unipolar. If DMI is used for metallic applications, it could be made bipolar.

The PSD of the unipolar DMI was found using a code flow graph method by Yoshikai in 1986 [16] as

$$\Psi_s(f) = \frac{|G(f)|^2}{T_l} \cdot \frac{2p(1-p)(1 - \cos 4\pi f T_l)(1 - \cos 2\pi f T_l)}{4p^2 - 6p + 3 - 4(p-1)^2 \cos 4\pi f T_l + (1-2p) \cos 8\pi f T_l}$$

where $G(f)$ is the Fourier transform of the line pulse waveform which has the width of $T_l = T/2$ and p is the occurrence probability of mark. For equiprobable data sequence, $p = 0.5$, the above expression reduces to

$$\Psi_s(f) = \frac{|G(f)|^2}{T/2} \sin^2 \pi f T/2$$

For the rectangular pulse (NRZ pulse) with amplitude A , it becomes

$$\begin{aligned} \Psi_s(f) &= \frac{1}{T/2} \left(\frac{AT \sin \pi f T/2}{2 \pi f T/2} \right)^2 \sin^2 \pi f T/2 \\ &= \frac{A^2 T}{2} \left(\frac{\sin \pi f T/2}{\pi f T/2} \right)^2 \sin^2 \pi f T/2, \end{aligned}$$

(continuous part of the PSD of the unipolar DMI) (2.71)

The energy under the PSD curve is only half of the bit energy. This implies that the above PSD expression is the continuous part of the PSD of the unipolar DMI. Another half of the energy is in the dc component which can be represented by a delta function $\frac{1}{2}\delta(f)$. It has the first null at $fT = 2$. The bandwidths are $B_{null} = 2.0R_b$, $B_{90\%} \approx 1.27R_b$, and $B_{99\%} \approx 15R_b$.

When DMI is bipolar, then (2.71) should be multiplied by a factor 2 to represent the entire PSD. In this case its PSD has the same form of the PSD of biphasic codes (2.41). It has the first null at $fT = 2$. The bandwidths are $B_{null} = 2.0R_b$, $B_{90\%} \approx 3.05R_b$, and $B_{99\%} \approx 29R_b$.

It is not surprising that the PSD of the bipolar DMI is the same as that of biphasic codes. In fact bipolar DMI is the same code as Bi- Φ -S code even though their coding rules are presented differently. One can easily verify this claim by simply coding a sample sequence using their rules. DMI is also called frequency shift code (FSC) in a paper by Morris [24], where other simple codes for optical transmission are also presented.

Since bipolar DMI code is equal to Bi- Φ -S code, we can therefore detect it using

Figure 2.10(a) and use (2.62) for its BER calculation. For unipolar DMI which is used primarily in optical systems we can use (2.69) and (2.70) to calculate required optical power for a given BER and bit rate.

2.6.3 mBnB Codes

CMI and DMI can be interpreted as two special cases of a larger family of block codes called *mBnB* codes. An *mBnB* code converts m binary digits into n binary digits with $m < n$. CMI and DMI are 1B2B codes. Biphasic codes are also 1B2B codes.

When $n = m + 1$, the codes are *mB(m+1)B* codes which are popular in high speed-fiber optical transmission. Besides CMI, DMI and biphasic codes which belong to this class, there are other *mB(m+1)B* codes. CMI and DMI have a poor efficiency. CMI and DMI encode logic 1 into a binary symbol and a logic 0 into two binary symbols; the efficiency is

$$\eta = \frac{\log_2 2}{\frac{1}{2} \log_2 2 + 2 \times \frac{1}{2} \log_2 2} \times 100\% = 66.7\%$$

To increase the efficiency, a larger m must be chosen.

Following is a rather complete collection of *mBnB* codes proposed in literature.

2.6.3.1 Carter Code

Carter proposed a code in 1965 for PCM systems [5]. It is an *mB(m+1)B* code. The coding rules are as follows. The eight-digit character of a PCM channel is transmitted either unchanged or with the digits inverted (i.e., marks for spaces and spaces for marks), depending on which condition will reduce the total disparity since transmission commenced. Thus there will never be any continually increasing disparity, and the dc component will be zero over a long period. In order to indicate to the receiver whether the character is to be passed to the PCM terminal unchanged or re-inverted, the encoder at the transmitter precedes the character by a parity-control digit, the polarity of which gives this information. Thus this Carter code is an 8B9B code. Its efficiency is 94.64%. It is clear that this code can also apply to characters of any length. To apply it to an input having no character structure, the only additional thing to do is to define "characters" or blocks.

With Carter code, completely unrestricted binary input digits can be transmitted. This is not strictly true for the AMI codes since synchronization will be lost if long strings of zeros or marks are present. However, the substitution codes proposed later (1969) [4], described in Section 2.5, can also overcome the problem of AMI.

m+1	Words having disparity of					
	0	+2	+4	+6	+8	+10
2	2	1				
4	6	4	1			
6	20	15	6	1		
8	70	56	28	8	1	
10	252	210	120	45	10	1

Table 2.3 Number of code words with various disparities. From [25]. Copyright © 1969 IEE.

2.6.3.2 Griffiths Code

This code is a type of $mB(m+1)B$ codes. It was proposed by Griffiths (1969) [25] as an improvement on the Carter code in which strings of similar digits of length $2m+2$ may still occur for a block length of m . Griffiths checked numbers of possible code words with various lengths and disparities. If m is odd, the number of zero-disparity words of length $m+1$ is $\binom{m+1}{\frac{(m+1)}{2}}$ and the number of words having positive disparity is $2^m - \binom{m+1}{\frac{(m+1)}{2}}/2$. There are the same number having negative disparity. If words of opposite disparity are paired for transmission of alternate disparity words, there will be a total of $2^m + \binom{m+1}{\frac{(m+1)}{2}}/2$ words and pairs available. This is sufficient to translate a block of m binary digits, leaving $\binom{m+1}{\frac{(m+1)}{2}}/2$ code words spare. The number of code words for the first several values of m are listed in Table 2.3.

For $m+1$ equals two, there are two zero-disparity words (i.e., 0 and 1 may be translated to 01 and 10). This is in fact the Manchester code. The bit rate is doubled after coding.

Particular attention is drawn to the cases in which $m+1$ equals four and six. In both cases, translation may be achieved using only zero-disparity words and double-disparity words. For $m+1 = 6$ (i.e., 5B6B code), we can use all zero-disparity words and only those double-disparity words not having four same successive digits. The coding rules are shown in Table 2.4. For a block of five digits containing two ones, transmit it followed by a one. For a block containing three ones, transmit it followed by a zero. Twenty of the 32 possible blocks may be transmitted this way with zero disparity. The remaining 12 blocks are translated into double-disparity words. On alternate occasions, these double-disparity words are transmitted inverted. Words of opposite sign are sent alternatively. Thus the dc component of the line signal will be

11000	} transmitted as × × × × × 1	00111	} transmitted as × × × × × 0	
10100		01011		
10010		01101		
10001		01110		
01100		10011		
01010		10101		
01001		10110		
00110		11001		
00101		11010		
00011		11100		
11111	} transmitted as	111010	000101	} alternately
11110		110110	001001	
11101		101110	010001	
11011		111001	000110	
10111		110101	001010	
01111		101101	010010	
10000		011101 or	100010	
01000		110011	001100	
00100		101011	010100	
00010		011011	100100	
00001		100111	011000	
00000		010111	101000	

Table 2.4 Translation table for 5B6B Griffiths code. From [25]. Copyright © 1969 IEE.

zero. This code never has more than six consecutive digits of the same type. The rate increase is only 20%.

When this method is used to encode blocks of three bits (i.e., 3B4B), a set of suitable translation rules is shown in Table 2.5. The increase of transmission rate is 33%, higher than that of 5B6B Griffiths code. Similarly seven bits may be encoded into eight. However, use of quadruple-disparity words would have to be made to provide sufficient translations. In general, the complexity of higher-order encoders would appear to be excessive.

2.6.3.3 PAM-PPM Code

This code was proposed by Bosotti and Pirani (1978) [26] for optical communications. Coded bits 00, 10, and 01 are mapped to signals a, b, and c with one corresponding to a positive pulse for a duration of θT ($0 < \theta < 1$) and zero corresponding to zero level for $(1 - \theta)T$. Each of them is a pulse-amplitude and pulse-position modulated

001	}	transmitted as $\times \times \times 1$			
010					
100					
110	}	transmitted as $\times \times \times 0$			
101					
011					
000	}	transmitted as	0100	1011	alternately
111			0010	1101	

Table 2.5 Translation table for 3B4B Griffiths code. From [25]. Copyright © 1969 IEE.

signal, hence the name. The coding rules are shown in Table 2.6. This is in fact a 3B4B code with 0 and 1 in code words occupying different lengths.

The PSD of this code with $\theta = 1/2$ has the first null at $f = 2R_b$, which is the same as a straight PAM signal with pulse width of $T/2$. However, the PSD shows strongly reduced low-frequency components. The rectified PAM-PPM pulse train contains an abundant timing frequency component. The longest time interval without signal level change is $3T$.

2.6.3.4 2B3B dc-Constrained Code

This code was proposed by Takasaki et al (1976) [6]. Conventional codes try to suppress the dc component [5]. It is shown in [27] that such codes cannot provide the capability of error monitoring, since they use up most of the redundancy in suppressing the dc component. The 2B3B dc-constrained code uses a different approach. It constrains the dc component instead of suppressing it and thus makes it possible to use the redundancy for error detection also. Table 2.7 shows the translation rules. The data bits 1 and 0 are converted to + and -, respectively. Then a third symbol + or - is added to make combinations of one + and two -s (mode 1). The data pair 11 can not meet this requirement. Therefore modes 1 and 2 are used alternately for this pair to produce one + and two -s on the average. This code produces a dc component of $-1/3$. However, it does not suffer from dc wander since the dc component is constant regardless of data pattern. In terms of timing information, the average number of changes of levels per block ranges from 1 to 2. The longest succession of same levels is 7.

2.6.4 mB1C Codes

This code belongs to a class of codes called *bit insertion codes* which are popular in high-speed optical transmission.

Binary signal	PAM-PPM signal
000	a c = 0001
001	a b = 0010
010	c a = 0100
011	b a = 1000
100	c c = 0101
101	c b = 0110
110	b c = 1001
111	b b = 1010

Table 2.6 PAM-PPM code. From [26]. Copyright © 1978 IEE.

Binary	2B3B code	
	Mode 1	Mode 2
00	--+	
01	-+-	
10	+--	
11	++-	---

Table 2.7 2B3B dc-constrained code. From [6]. Copyright © 1983 IEEE.

The *mBIC* code was proposed by Yoshikai et al for optical fiber transmission in 1984 [8] in order to raise the speed limit achieved by CMI, DMI, and mBnB codes. In the coding process, the speed of input signal is increased by $(m + 1)/m$, then a complementary bit is inserted at the end of every block of m information bits. The inserted bit is complementary to the last bit of the m information bits. The coding rule is very simple therefore sophisticated electronic circuits at high speed required by mBnB codes can be avoided. The increase in code rate is smaller, only $1/m$, when compared with CMI and DMI which require a code rate twice as fast as the information rate.

With the mBIC code the maximum number of consecutive identical symbols is $m + 1$ which occurs when the inserted bit and the m succeeding bits are the same. In-service error can be monitored using an XOR applied to the last information bit and the complementary bit. This code has been adopted in a Japanese 400 Mbps optical system in the form of 10BIC.

The spectral of this code contains continuous part and discrete components. If the mark rate in the information sequence is $1/2$, only a dc component exists. The dc component is due to the fact that the code is unipolar. If the mark rate deviates from $1/2$, the PSD contains harmonic spectra with a fundamental component of $1/(m + 1)T$. The harmonic spectra are caused by the fact that when mark rate is not $1/2$, the occurrence probability for a mark in the C bit is also not $1/2$; instead it is inversely proportional to that in the information bit. The harmonic spectra cause jitter. A scrambler can be used to scramble the mBIC coded sequence hence suppress these harmonics.

2.6.5 DmBIM Codes

Differential m binary with 1 mark insertion (DmBIM) code is proposed by Kawanishi and Yoshikai et al (1988) for very high-speed optical transmission [9]. The coding rule is rather simple. In the coding process, the speed of input signal (P) is increased by $(m + 1)/m$, then a mark bit is inserted at the end of every block of m information bits. The mark-inserted signal (Q) is converted to the DmBIM code (S) by the following differential encoding equation:

$$S_k = S_{k-1} \oplus Q_k$$

where S_k and Q_k denote the k th signal bit of S and Q , respectively. The symbol \oplus denotes XOR. A C bit (complementary bit) is generated automatically in the coding process. This can be seen as follows (the inserted bit Q_{m+1} is always equal to 1):

$$S_{m+1} = S_m \oplus Q_{m+1} = S_m \oplus 1 = \overline{S_m}$$

That is, the $(m + 1)$ th bit is always complementary to the m th bit. So the S sequence is an mB1C code. Decoding is accomplished by equation

$$Q_k = S_k \oplus S_{k-1}$$

and the original signal P is then recovered through mark deletion and $m/(m + 1)$ speed conversion.

Like mB1C code, DmB1M limits the maximum length of consecutive identical digits to $(m + 1)$ and provides error detection through monitoring of the inserted bit every $(m + 1)$ bits. Unlike mB1C code, however, it can be shown that the mark probability of the coded sequence is always $1/2$ regardless of the mark probability of the information sequence [9]. Thus there are no jitter-causing discrete harmonics in the spectrum except the dc component.

When m is small, the continuous part of the spectra of both mB1C code and DmB1M code are similar to that of AMI, which ensures that high-frequency and low-frequency components are suppressed. As the block length m increases, however, the spectrum flattens and assumes the shape of the spectrum of a random signal, having nonzero components near the zero frequency. The problem of spectrum control in mB(m+1)B codes can be solved by adding further coding [10] or using scrambling techniques [11]. And the PFmB(m+1)B code described next can overcome the spectrum problem to some extent.

2.6.6 PFmB(m+1)B Codes

This partially flipped code or *PFmB(m+1)B* code was proposed by Krzymien (1989) [10]. It is balanced, with minimum rate increase $(1/m)$, and easy to encode and decode. Thus it is suitable for high-speed optical systems.

The coding process of a PFmB(m+1)B code consists of two stages: precoding and balanced coding. In the precoding stage the input binary sequence $\{B_i\}$ is grouped into blocks of m bits (m is an odd number) to which an additional bit B_{m+1} is added according to the rule

$$B_{m+1} = \begin{cases} 1 & \text{if } \sum_{i=1}^m B_i < \frac{m}{2} \\ 0 & \text{if } \sum_{i=1}^m B_i > \frac{m}{2} \end{cases} \quad (2.72)$$

The added bit B_{m+1} will serve a check bit in decoding as will be seen shortly.

In the second stage, the precoded input words $\mathbf{B} = [B_1, B_2, \dots, B_{m+1}]$ are mapped into the binary codewords $\mathbf{C} = [C_1, C_2, \dots, C_{m+1}]$ according to the rule

$$C_i = \begin{cases} B_i & \text{if } D(n) \times \text{WRDS}(n-1) \leq 0 \\ \bar{B}_i & \text{if } D(n) \times \text{WRDS}(n-1) > 0 \\ & \text{for } i = 1, 2, \dots, m \end{cases} \quad (2.73)$$

and

$$C_{m+1} = B_{m+1}$$

where

\overline{B}_i is the complement of B_i .

$D(n)$ is the disparity of the n th precoded word \mathbf{B}_n , which is determined by assigning -0.5 to a binary zero and 0.5 to a binary one and summing them up.

$\text{WRDS}(n-1)$ is the value of the running digital sum (total disparity) at the end of the $(n-1)$ th precoded word \mathbf{B}_{n-1}

$$\text{WRDS}(n-1) = \sum_{k=-\infty}^{n-1} D(k)$$

From (2.73) we have the following observations. If the total disparity and the disparity of the current precoded word have the same sign, the precoded word \mathbf{B} is partially flipped, only leaving the last bit unchanged because it will serve as a check bit in decoding. Otherwise the precoded word \mathbf{B} is copied to \mathbf{C} without any change. This will balance the total disparity or running digital sum.

Block synchronization in the receiver is accomplished by checking whether the received coded sequence $\{\hat{C}_i\}$ satisfies the coding rules (2.72) and (2.73). High rate of code rule violations indicates that the system is out of synchronism. After block synchronism is established, decoding is performed by checking a received block $\hat{\mathbf{C}}$ against the code rule (2.72) (with B_i replaced by \hat{C}_i). If (2.72) is satisfied, no inversion of the bits of $\hat{\mathbf{C}}$ is necessary. Otherwise, bits of $\hat{\mathbf{C}}$ have to be inverted to yield \mathbf{B} .

There are error extension cases in decoding this PFmB(m+1)B code. However, this extension is very small. An example given in [10] is 0.3 dB deterioration of SNR for $m = 7$, a crossover probability of 10^{-9} in an AWGN channel. The digital sum variation (DSV) is bounded and is $(3m-1)/2$. The maximum number of consecutive like bits is also bounded and is $2(m+1)$. The spectrum of the code has a roll-off to zero at zero frequency and $f = R_b$. However, when input data probability is unbalanced sharp peaks appear at the both edges of the band. This disadvantage can be eliminated by scrambling.

2.6.7 kBnT Codes

A class of codes using three levels is called $kBnT$ codes where k binary bits are coded into n ($n < k$) ternary symbols. AMI can be considered as a 1B1T code. The most important codes of this class are 4B3T type and 6B4T type. Their efficiencies are 84.12% and 94.64%, respectively.

Binary	Ternary transmitted when total disparity is		
	Negative (-3, -2, -1)	Positive (0, 1, 2)	Word disparity
0000	+0-	+0-	0
0001	-+0	-+0	0
0010	0-+	0-+	0
0011	+ - 0	+ - 0	0
0100	++0	--0	± 2
0101	0++	0--	± 2
0110	+0+	-0-	± 2
0111	+++	---	± 3
1000	++-	--+	± 1
1001	-++	+--	± 1
1010	+ - +	- + -	± 1
1011	+00	-00	± 1
1100	0+0	0-0	± 1
1101	00+	00-	± 1
1110	0+-	0+-	0
1111	-0+	-0+	0

Table 2.8 Translation table for 4B3T. From [21]. Copyright © 1983 International Journal of Electronics.

2.6.7.1 4B3T Code

The code proposed by Waters [21] is the simplest of the 4B3T class. The translation table is shown in Table 2.8, where disparities are calculated by assigning a weight of 1 to a positive mark and a weight of -1 to a negative mark. This is an alphabetic code since two alphabets are used.

There are $27 (3^3)$ possible combinations of three ternary digits. In order to maintain bit sequence independence, 000 is not used. All other combinations are used. We can allocate six binary four-bit blocks to the six zero disparity words. The remaining ten are allocated both a positive disparity word and its negative disparity inverse. During translation, a count is kept of the total disparity. When this is negative, positive disparity words are selected for transmission and vice versa. This ensures that the transmitted code has zero dc content. The disparity is bounded and at the end of a word only six values of total disparity are possible ($-3, -2, -1, 0, 1$ and 2 , where 0 is counted as positive). Total disparity $+3$ is not possible despite that word disparity could be $+3$, since the word of $+3$ disparity is sent only when total disparity is negative.

Binary	Ternary transmitted when total disparity is		
	-2	-1 or 0	+1
0000	+++	-+-	-+-
0001	++0	00-	00-
0010	+0+	0-0	0-0
0011	0-+	0-+	0-+
0100	0++	-00	-00
0101	-0+	-0+	-0+
0110	-+0	-+0	-+0
0111	-++	-++	--+
1000	+--	+--	---
1001	00+	00+	--0
1010	0+0	0+0	-0-
1011	0+-	0+-	0+-
1100	+00	+00	0--
1101	+0-	+0-	+0-
1110	+ -0	+ -0	+ -0
1111	+- -	+- -	+- -

Table 2.9 Translation table for MS43. From [21]. Copyright © 1968 ATT. All rights reserved. Reprinted with permission.

2.6.7.2 MS43 Code

MS43 code proposed by Franaszek (1968) [28] is also a 4B3T code. It has a more sophisticated three-alphabet translation table as shown in Table 2.9.

The word disparities range from -3 to $+3$. There are only four possible total disparity states at the end of a word: -2 , -1 , 0 , or 1 . In the -2 state, only zero or positive disparity words are sent; in the $+1$ state, only zero or negative disparity words; and in the 0 or -1 states, only zero and unit disparity words. This allocation reduces the low-frequency content compared with 4B3T, making it more tolerant to ac coupling [29].

2.6.7.3 6B4T Code

This code was proposed by Catchpole in 1975 [30]. The translation table is shown in Table 2.10. It is similar in concept to 4B3T, using two alphabets with both the zero and unit disparity words uniquely allocated to 50 of 64 possible six-bit binary blocks. Disparity control is achieved by pairing the ± 2 and ± 3 disparity words

+-+- -+--+ +0-0 ++-- +00- -00+ +0+- ++-0 ++0- +000 -0-+ --+0 --0+ -000	} And 3 cyclic shifts of each	} 18 zero disparity and 32 unit disparity ternary words always selected
+0+0 0+0+ ++00 0++0 00++ +00+ -+++ +-++ ++-+ +++-		
This set is inverted when the total disparity is positive		

Table 2.10 Translation table for 6B4T. From [21]. Copyright © 1975 IEE.

allocated to the other 14 binary combinations. This code is more efficient than the 4B3T codes, but has unbounded total disparity. However, it can be shown that with practical values of low frequency cut at the repeaters, this does not significantly affect the transmission performance provided a scrambler is used [21].

2.7 SUMMARY

In this chapter we first described the differential coding technique often used in line codes. Then before discussing various line codes we presented a list of line coding criteria. They include timing information, spectral characteristic, bandwidth, error probability, error detection capability, bit sequence independence, and use of differ-

ential coding. Armed with these criteria we took a close look at the classical line codes, including NRZ, RZ, PT, biphase and delay modulation.

NRZ codes include NRZ-L, NRZ-M, and NRZ-S. NRZ-M and NRZ-S are differentially encoded forms of NRZ-L. They are the simplest in terms of coding rules and have a narrow bandwidth ($B_{null} = R_b$), but lack most of the other desired characteristics. All NRZ codes have a similar BER with NRZ-L's the lowest and NRZ-M's and NRZ-S's slightly higher.

RZ codes increase the density of transitions which is good for timing recovery, but their bandwidth is doubled ($B_{null} = 2R_b$). Polar-RZ has the same BER as that of NRZ-L. Both unipolar-NRZ and unipolar-RZ have the same BER which is 3 dB inferior than that of NRZ-L. Spectra of NRZ and RZ codes have major energy near dc, which is not suitable for ac-coupled circuits.

PT codes include AMI (NRZ and RZ), and dicodes (NRZ and RZ). AMI codes have a narrow bandwidth ($B_{null} = R_b$), and most importantly, have no dc frequency component and near-dc components are also small. This makes AMI codes suitable for ac-coupled circuits. However, the three-level signaling of AMI codes makes BER performance about 3 dB worse than polar NRZ codes. Dicodes are related to AMI by differential encoding. So they have the same spectra as those of AMI codes and their BER performance is also close to but slightly higher than that of AMI codes. The lack of transitions in a string of 0s in AMI codes and dicodes may cause synchronization problems. Thus AMI codes with zero extraction were proposed to overcome this disadvantage.

Biphase codes include Bi- Φ -L, or Manchester, Bi- Φ -M, Bi- Φ -S, and conditioned (differential) Manchester. All of them have the same spectrum which has a $B_{null} = 2R_b$. However, the spectral shape is better than RZ's in that the dc and near-dc components are eliminated. In terms of BER, Manchester and conditioned Manchester are similar. The BER of Manchester is identical to that of NRZ-L. The BER of conditioned Manchester is slightly higher. The BER performance of Bi- Φ -M and Bi- Φ -S are the same, which is 3 dB worse than that of Manchester. Biphase codes always have at least one transition in a symbol, thus timing information is adequate. Due to its superb merit, Manchester code, especially the differential form, is widely used.

From the above discussion we see that AMI and Manchester have stood out as two most favorite codes. Both have small near-dc components. Manchester is 3 dB better than AMI in terms of BER. But AMI requires only half of the bandwidth required by Manchester. Manchester also provides better timing information than AMI.

Delay modulation has a very narrow bandwidth with a main lobe of about $0.5R_b$. However, its BER performance is 3 dB worse than that of NRZ-L. Its timing information is not as much as that of biphase codes, but is more than what other codes can provide. It is a potential competitor to AMI and Manchester, even though its

practical use has not been reported in literature.

In the rest of this chapter we discussed more complex codes, including substitution codes and block codes. Substitution codes are designed for suppression of long all-zero strings. Two important substitution codes, BNZS and HDBn (including CHDBn) are discussed. All of them are based on AMI codes. By suppressing consecutive zeros, the lack of timing information of original AMI codes are overcome. Thus these codes are very competitive against Manchester, especially in bandlimited systems.

Block codes are designed to introduce redundancy to meet one or more of the desirable characteristics of a code. Their drawback is the increase in the transmission rate. They are widely used in optical fiber transmission system where wide bandwidth is available. There are a great number of block codes. Important codes which are used in practical systems include the following codes: CMI and DMI which are two-level AMI codes, are designed to replace AMI in optical fiber system. A general class of binary block codes which can replace AMI are the mBnB codes. For high-speed optical transmission, simple coder and decoder are desirable and rate increase should be kept at minimum, thus simple codes in the class, like mB(m+1)B, mB1C, and DmB1M are proposed. All of them only add one redundant bit to the original bit block, thus keep the rate increase at the minimum. All of them have simple coding and decoding rules, thus high speed can be achieved.

Block codes are not limited to binary. Multiple-level block codes can increase the efficiency of the line codes. Popular multiple-level codes are ternary codes such as 4B3T, MS43, and 6B4T. They are designed to have a zero or constant dc component and bounded disparity. They may not be used for optical system due to multiple-level signaling.

References

- [1] Aaron, M. R., "PCM transmission in the exchange plant," *Bell System Technical Journal*, vol. 41, no. 99, January 1962.
- [2] Croisier, A., "Introduction to pseudoternary transmission codes," *IBM J. Res. Develop.*, July 1970, pp. 354-367.
- [3] Hecht, M., and A. Guida, "Delay modulation," *Proc. IEEE*, vol. 57, no. 7, July 1969, pp. 1314-1316.
- [4] Johannes, V. I., A. G. Kaim, and T. Walzman, "Bipolar pulse transmission with zero extraction," *IEEE Trans. Comm. Tech.* vol. 17, 1969, p. 303.
- [5] Carter, R. O., "Low disparity binary coding system," *Electron. Lett.*, vol. 1, no. 3, 1965, p. 67
- [6] Takasaki, Y. et al., "Optical pulse formats for fiber optic digital communications," *IEEE Trans. Comm.* vol. 24, April 1976, pp. 404-413.
- [7] Takasaki, Y. et al., "Two-level AMI line coding family for optic fiber systems," *Int. J. Electron.*

- vol. 55, July 1983, pp. 121-131
- [8] Yoshikai, N., K. Katagiri, and T. Ito, "mBIC code and its performance in an optical communication system," *IEEE Trans. Comm.* vol. 32, no.2, 1984, pp. 163-168.
 - [9] Kawanish, S. et al. "DmBIM code and its performance in a very high-speed optical transmission system," *IEEE Trans. Comm.* vol. 36, no.8, August 1988, pp. 951-956.
 - [10] Krzymien, W., "Transmission performance analysis of a new class of line codes for optical fiber systems," *IEEE Trans. Comm.* vol. 37, no.4, April 1989, pp. 402-404.
 - [11] Fair, I. J. et al. "Guided scrambler: a new line coding technique for high bit rate fiber optic transmission systems," *IEEE Trans. Comm.* vol. 39, no.2, Feb. 1991, pp. 289-297
 - [12] Sklar, B., *Digital Communications, Fundamentals and Applications*. Englewood Cliffs, New Jersey: Prentice Hall, 1988.
 - [13] Killen, H., *Fiber optic communications*, Englewood Cliffs, New Jersey, Prentice Hall, 1991.
 - [14] Stallings, W., "Digital signaling techniques," *IEEE Communications Magazine*, vol. 22, no.12, Dec. 1984, pp. 21-25.
 - [15] Tsujii, S., and H. Kasai, "An algebraic method of computing the power spectrum of coded pulse trains," *Electron. Commun. Japan*, vol. 51-A, no. 7, 1968.
 - [16] Yoshikai, N. "The effects of digital random errors on the DMI code power spectrum," *IEEE Trans. Comm.* vol. 34, July 1986, pp. 713-715.
 - [17] Huggins, W. H., "Signal-flow graphs and random signals," *Proc. IRE*, vol. 45, January 1957, pp. 74-86.
 - [18] Van Trees, H. L., *Detection, Estimation, and Modulation Theory; Part I*. New York: John Wiley & Sons, Inc., 1968.
 - [19] Smith, D. R., *Digital Transmission Systems*, 2nd Ed., New York, Van Nostrand Reinhold, 1993.
 - [20] CCITT yellow book, vol. III.3 *Digital Networks—Transmission systems and multiplexing equipment*, Geneva, ITU, 1981.
 - [21] Waters, D. B., "Line codes for metallic systems," *Int. J. Electron.*, vol. 55, July 1983, pp. 159-169
 - [22] Personick, S. D., "Receiver design for digital fiber optic communication systems. I-II," *Bell Syst. Tech. J.*, vol. 52, July-August 1973, pp. 843-886.
 - [23] Chew, Y. H. and T. T. Tjhung, "Bit error rate performance for edge-detected CMI data transmission," *IEEE Trans. Comm.* vol. 41, June 1993, pp. 813-816.
 - [24] Morris, D. J., "Code your fiber-optic data for speed, without losing circuit simplicity," *Electronic Design*, vol. 22, October 1978, pp. 84-91.
 - [25] Griffiths, J. M., "Binary code suitable for line transmission," *Electron. Lett.*, vol. 5, Feb. 1969, p. 79.
 - [26] Bosotti, L., and G. Pirani, "A new signaling format for optical communications," *Electronics Letters*, vol. 14, no. 3, 1978, pp. 71-73.
 - [27] Takasaki, Y et al. "Line coding plans for fiber optic communication systems," *Proc. Int. Conf. Commun.*, 1975, paper 32E.

- [28] Franaszek, P. A., "Sequence state coding for digital data transmission," *Bell Syst. Tech. J.*, vol. 47, 1968, pp. 143-157.
- [29] Buchner, J. B., "Ternary line codes," *Philips Telecommun. Rev.*, vol. 34, 1976, pp. 72-86.
- [30] Catchpole, R. J., "Efficient ternary transmission codes," *Electronics Letters*, vol. 11, 1975, pp. 482-484.

Selected Bibliography

- Brooks, R. M. and Jessop A., "Coding for optical systems," *Int. J. Electron.*, vol. 55, July 1983, pp. 81-120.
- "Binary line codes for digital transmission on optical fibers," *CCITT contrib. Study Group XVIII*, no. 291, 1979.
- Couch II, L. W., *Digital and Analog Communication Systems*, 3rd Ed., New York: Macmillan, 1990.
- Haykin, S., *Digital Communications*, New York: John Wiley & Sons, Inc., 1988.

Chapter 3

Frequency Shift Keying

We have seen in chapter one that there are three basic forms of digital bandpass modulations: amplitude shift keying (ASK), frequency shift keying (FSK), and phase shift keying (PSK). FSK is probably the earliest type of digital modulation used in the communication industry. In this chapter we first describe in Section 3.1 binary FSK signal, modulator, and its power spectrum density. Then we present the coherent demodulator and error probability in Section 3.2. Next we discuss noncoherent demodulation and error probability in Section 3.3. M-ary FSK (MFSK) is given in Section 3.4. Section 3.5 discusses FSK demodulators using conventional discriminator and other simple techniques. Section 3.6 is a brief discussion of synchronization. Finally we summarize the chapter with Section 3.7.

3.1 BINARY FSK

3.1.1 Binary FSK Signal and Modulator

In its most general form, the binary FSK scheme uses two signals with different frequencies to represent binary 1 and 0.

$$\begin{aligned} s_1(t) &= A \cos(2\pi f_1 t + \Phi_1), & kT \leq t \leq (k+1)T, & \text{ for } 1 \\ s_2(t) &= A \cos(2\pi f_2 t + \Phi_2), & kT \leq t \leq (k+1)T, & \text{ for } 0 \end{aligned} \quad (3.1)$$

where Φ_1 and Φ_2 are initial phases at $t = 0$, and T is the bit period of the binary data. These two signals are not coherent since Φ_1 and Φ_2 are not the same in general. The waveform is not continuous at bit transitions. This form of FSK is therefore called *noncoherent* or *discontinuous* FSK. It can be generated by switching the modulator output line between two different oscillators as shown in Figure 3.1. It can be noncoherently demodulated.

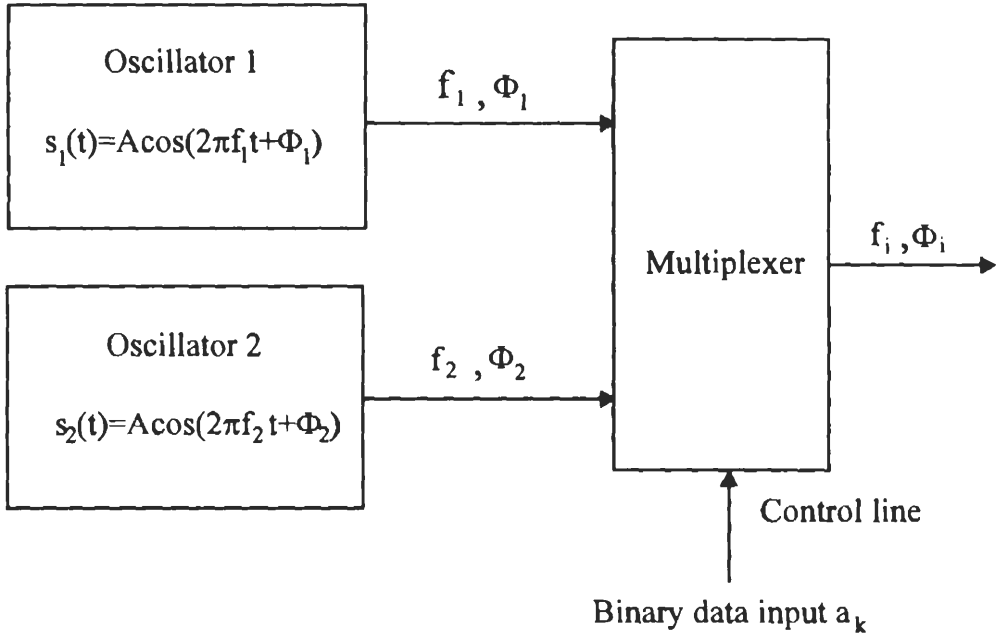


Figure 3.1 Noncoherent FSK modulator.

The second type of FSK is the *coherent* one where two signals have the same initial phase Φ at $t = 0$:

$$\begin{aligned} s_1(t) &= A \cos(2\pi f_1 t + \Phi), & kT \leq t \leq (k+1)T, & \text{for } 1 \\ s_2(t) &= A \cos(2\pi f_2 t + \Phi), & kT \leq t \leq (k+1)T, & \text{for } 0 \end{aligned} \quad (3.2)$$

This type of FSK can be generated by the modulator as shown in Figure 3.2. The frequency synthesizer generates two frequencies, f_1 and f_2 , which are synchronized. The binary input data controls the multiplexer. The bit timing must be synchronized with the carrier frequencies. The detail will be discussed shortly. If a 1 is present, $s_1(t)$ will pass and if a 0 is present, $s_2(t)$ will pass. Note that $s_1(t)$ and $s_2(t)$ are always there regardless of the input data. So when considering their phase in any bit interval $kT \leq t \leq (k+1)T$, the starting point of time is 0, not kT .

For coherent demodulation of the coherent FSK signal, the two frequencies are so chosen that the two signals are orthogonal:

$$\int_{kT}^{(k+1)T} s_1(t)s_2(t)dt = 0$$

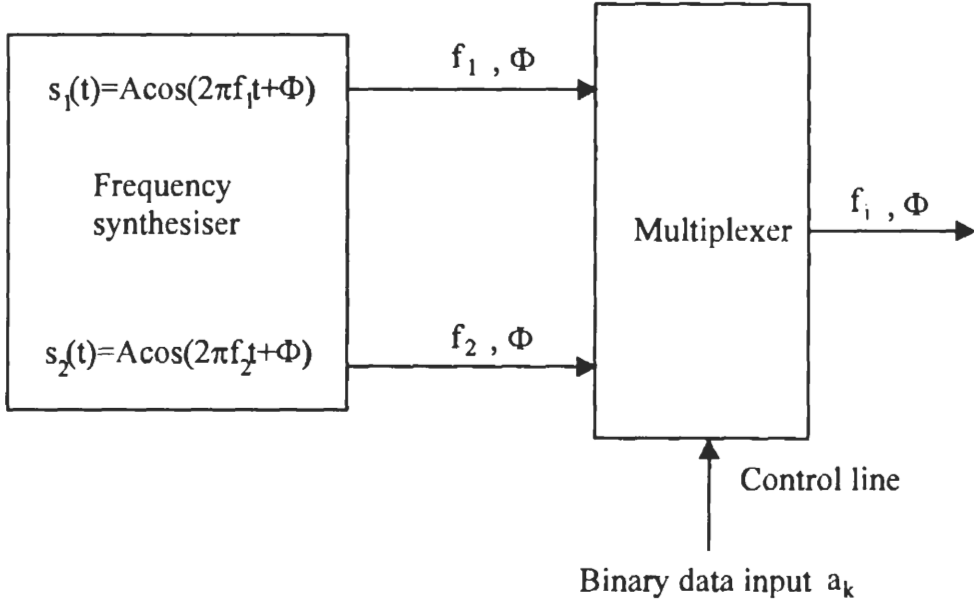


Figure 3.2 Coherent FSK modulator.

That is

$$\begin{aligned}
 & \int_{kT}^{(k+1)T} \cos(2\pi f_1 t + \Phi) \cos(2\pi f_2 t + \Phi) dt \\
 = & \frac{1}{2} \int_{kT}^{(k+1)T} [\cos[2\pi(f_1 + f_2)t + 2\Phi] + \cos 2\pi(f_1 - f_2)t] dt \\
 = & \frac{1}{4\pi(f_1 + f_2)} [\cos 2\Phi \sin 2\pi(f_1 + f_2)t + \sin 2\Phi \cos 2\pi(f_1 + f_2)t] \Big|_{kT}^{(k+1)T} \\
 & + \frac{1}{4\pi(f_1 - f_2)} \sin 2\pi(f_1 - f_2)t \Big|_{kT}^{(k+1)T} \\
 = & 0
 \end{aligned}$$

This requires that $2\pi(f_1 + f_2)T = 2n\pi$ and $2\pi(f_1 - f_2)T = m\pi$, where n and m are integers. This leads to

$$f_1 = \frac{2n + m}{4T}$$

$$f_2 = \frac{2n - m}{4T}$$

$$2\Delta f = f_1 - f_2 = \frac{m}{2T}$$

Thus we conclude that for orthogonality f_1 and f_2 must be integer multiple of $1/4T$ and their difference must be integer multiple of $1/2T$. Using Δf we can rewrite the two frequencies as

$$f_1 = f_c + \Delta f$$

$$f_2 = f_c - \Delta f$$

$$f_c = \frac{f_1 + f_2}{2} = \frac{n}{2T}$$

where f_c is the nominal (or apparent) carrier frequency which must be integer multiple of $1/2T$ for orthogonality.

When the separation is chosen as $1/T$, then the phase continuity will be maintained at bit transitions, the FSK is called *Sunde's FSK*. It is an important form of FSK and will be discussed in detail in this chapter. As a matter of fact, if the separation is k/T , where k is an integer, the phase of the coherent FSK signal of (3.2) is always continuous.

Proof: at $t = nT$, the phase of $s_1(t)$ is

$$\begin{aligned} 2\pi f_1 nT + \Phi &= 2\pi(f_2 + k/T)nT + \Phi \\ &= 2\pi f_2 nT + 2\pi kn + \Phi \\ &= 2\pi f_2 nT + \Phi \text{ (Modulo-}2\pi) \end{aligned}$$

which is exactly the phase of $s_2(t)$. Thus at $t = nT$, if the input bit switches from 1 to 0, the new signal $s_2(t)$ will start at exact the same amplitude where $s_1(t)$ has ended.

The minimum separation for orthogonality between f_1 and f_2 is $1/2T$. As we have just seen above, this separation cannot guarantee continuous phase. A particular form of FSK called minimum shift keying (MSK) *not only* has the minimum separation *but also* has continuous phase. However, MSK is much more than an ordinary FSK, it has properties that an ordinary FSK does not have. It must be generated by methods other than the one described in Figure 3.2. MSK is an important modulation scheme which will be covered in Chapter 5.

Figure 3.3(a) is an example of Sunde's FSK waveform where bit 1 corresponds to a higher frequency f_1 and bit 0 a lower f_2 . Since f_1 and f_2 are multiple of $1/T$, the ending phase of the carrier is the same as the starting phase, therefore the waveform has continuous phase at the bit boundaries. Sunde's FSK is a continuous phase FSK.

A coherent FSK waveform might have discontinuous phase at bit boundaries. Figure 3.3(b) is an example of such a waveform, where $f_1 = 9/4T$, $f_2 = 6/4T$. and

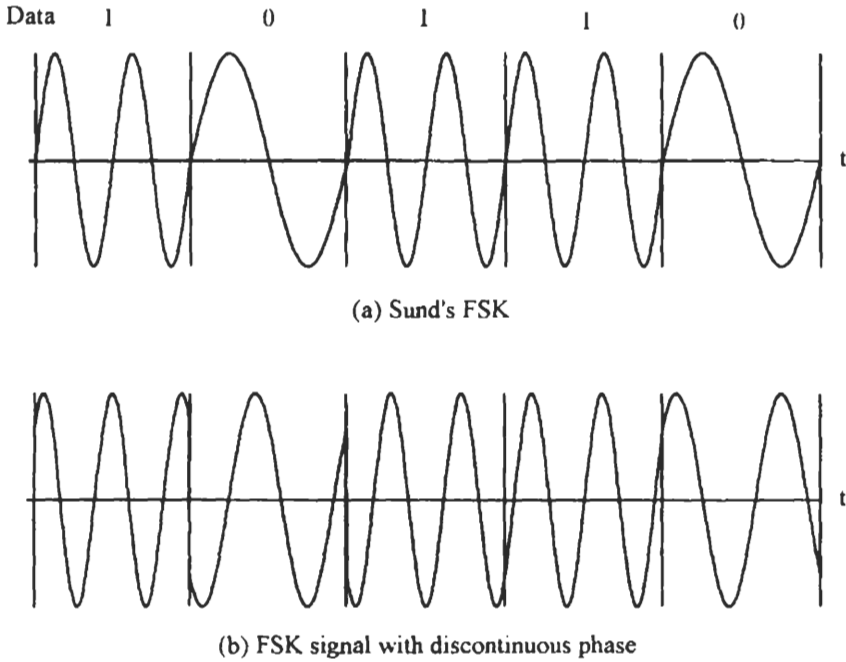


Figure 3.3 FSK waveforms: (a) Sunde's FSK, $f_1 = 2/T$, $f_2 = 1/T$, $2\Delta f = 1/T$, (b) FSK with discontinuous phase, $f_1 = 9/4T$, $f_2 = 6/4T$, $2\Delta f = 3/4T$.

the separation is $2\Delta f = 3/4T$.

Discontinuity in waveform will broaden the signal bandwidth. Therefore the third type of FSK, continuous phase FSK (CPFSK), is desired. To ensure continuous phase in the FSK, the signal must be in the form

$$s(t) = A \cos\left(2\pi f_c t + \frac{\pi h a_k (t - kT)}{T} + \pi h \sum_{i=0}^{k-1} a_i\right), \quad kT \leq t \leq (k+1)T \quad (3.3)$$

where h is called modulation index, $a_k = \pm 1$ is the k th data bit. Logic 0 and 1 correspond to binary data $+1$ and -1 , respectively. In the parenthesis, the second term represents the linearly changing phase or a constant frequency deviation required by an FSK signal. The third term represents the accumulated phase. Since the phase increment is proportional to $\Delta t = t - kT$, the phase is continuous in $(kT, (k+1)T)$. When $t = (k+1)T$, the phase accumulation is increased by $\pi h a_k$ and as t increases further, the phase changes continuously again. The frequency deviation is the deriv-

ative of the second term divided by 2π : $\Delta f = |ha_k/2T| = h/2T$. Thus

$$h = 2\Delta f T = \frac{2\Delta f}{R_b}$$

which is the ratio of frequency separation over the bit rate $R_b = 1/T$. The two frequencies are $f_1 = f_c - h/2T$, $f_2 = f_c + h/2T$. When $h = 1$, it becomes Sunde's FSK.

We will revisit CPFSK in Chapter 6 where it will be described from a perspective of continuous phase modulation (CPM). In this chapter we will concentrate on simple coherent and noncoherent FSK schemes. In the following we always assume that the initial phase $\Phi = 0$. This will simplify derivations without loss of generality.

3.1.2 Power Spectral Density

Now we proceed to find the power spectrum of the Sunde's FSK signal. We expand the Sunde's FSK signal as

$$\begin{aligned} s(t) &= A \cos 2\pi(f_c + a_k \frac{1}{2T})t \\ &= A \cos(a_k \frac{\pi t}{T}) \cos(2\pi f_c t) - A \sin(a_k \frac{\pi t}{T}) \sin(2\pi f_c t) \\ &= A \cos(\frac{\pi t}{T}) \cos(2\pi f_c t) - A a_k \sin(\frac{\pi t}{T}) \sin(2\pi f_c t) \\ kT &\leq t \leq (k+1)T \end{aligned} \quad (3.4)$$

where the last expression is derived using the fact that $a_k = \pm 1$. The inphase component $A \cos(\frac{\pi t}{T})$ is independent of the data. The quadrature component $A a_k \sin(\frac{\pi t}{T})$ is directly related to data. The inphase and quadrature components are independent of each other.

In Appendix A we have shown that the PSD of a bandpass signal

$$s(t) = \text{Re}[\tilde{s}(t)e^{j2\pi f_c t}]$$

is the shifted version of the equivalent baseband signal or complex envelope $\tilde{s}(t)$'s PSD $\Psi_{\tilde{s}}(f)$

$$\Psi_s(f) = \frac{1}{2}[\Psi_{\tilde{s}}(f - f_c) + \Psi_{\tilde{s}}^*(-f - f_c)]$$

where $*$ denotes complex conjugate. Therefore it suffices to determine the PSD of the equivalent baseband signal $\tilde{s}(t)$. Since the inphase component and the quadrature component of the FSK signal of (3.4) are independent of each other, the PSD for the

complex envelope is the sum of the PSDs of these two components.

$$\Psi_{\bar{s}}(f) = \Psi_I(f) + \Psi_Q(f)$$

$\Psi_I(f)$ can be found easily since the inphase component is independent of data. It is defined on the entire time axis. Thus

$$\Psi_I(f) = |\mathcal{F}\{A \cos(\frac{\pi t}{T})\}|^2 = \frac{A^2}{4} [\delta(f - \frac{1}{2T}) + \delta(f + \frac{1}{2T})]$$

where \mathcal{F} stands for Fourier transform. It is seen that the spectrum of the inphase part of the FSK signal are two delta functions.

To find $\Psi_Q(f)$, refer to (A.19) of Appendix A. It shows that the PSD of a binary, bipolar (± 1), equiprobable, stationary, and uncorrelated digital waveform is just equal to the energy spectral density of the symbol shaping pulse divided by the symbol duration. The shaping pulse here is $A \sin(\frac{\pi t}{T})$, therefore

$$\begin{aligned} \Psi_Q(f) &= \frac{1}{T} |\mathcal{F}\{A \sin(\frac{\pi t}{T})\}|^2, \quad 0 \leq t \leq T \\ &= \frac{1}{T} \left(\frac{2AT[\cos \pi T f]}{\pi[1 - (2Tf)^2]} \right)^2 \end{aligned}$$

The complete baseband PSD of the binary FSK signal is the sum of $\Psi_I(f)$ and $\Psi_Q(f)$:

$$\Psi_{\bar{s}}(f) = \frac{A^2}{4} [\delta(f - \frac{1}{2T}) + \delta(f + \frac{1}{2T})] + T \left(\frac{2A[\cos \pi T f]}{\pi[1 - (2Tf)^2]} \right)^2 \quad (3.5)$$

Figure 3.4(a,b) shows the baseband PSD of this Sunde's FSK for positive frequency only, where we set $A = \sqrt{2}$ in (3.5) for a unity signal energy. So the total energy under the PSD curve is 1 in one side and 2 in two sides. A spectral line arises at $fT = 0.5$. This means the passband spectrum should have spectral lines at $f = f_c \pm \frac{1}{2T}$ which are the two frequencies of binary FSK. The null bandwidth is $B_{null} = 1.5R_b$ in baseband, thus the null-to-null bandwidth at f_c is $3R_b$. Figure 3.4(c) is the out-of-band power, P_{ob} (dB), which is defined in Chapter 2. The abscissa of Figure 3.4(c) is the two-sided bandwidth normalized to data rate. The abrupt drop in P_{ob} is due to the delta function in the spectrum. The two-sided bandwidths at carrier frequency are $B_{90\%} \approx 1.23R_b$ and $B_{99\%} \approx 2.12R_b$. The transmission bandwidth thus is usually set as $B_T = 2R_b$.

The general spectral expression of CPFSK for index values other than 1 is more difficult to determine. It will be given in Section 3.4 for arbitrary index values and even M values for M -ary FSK. The derivation will be given in Chapter 6 in the context of continuous phase modulation.

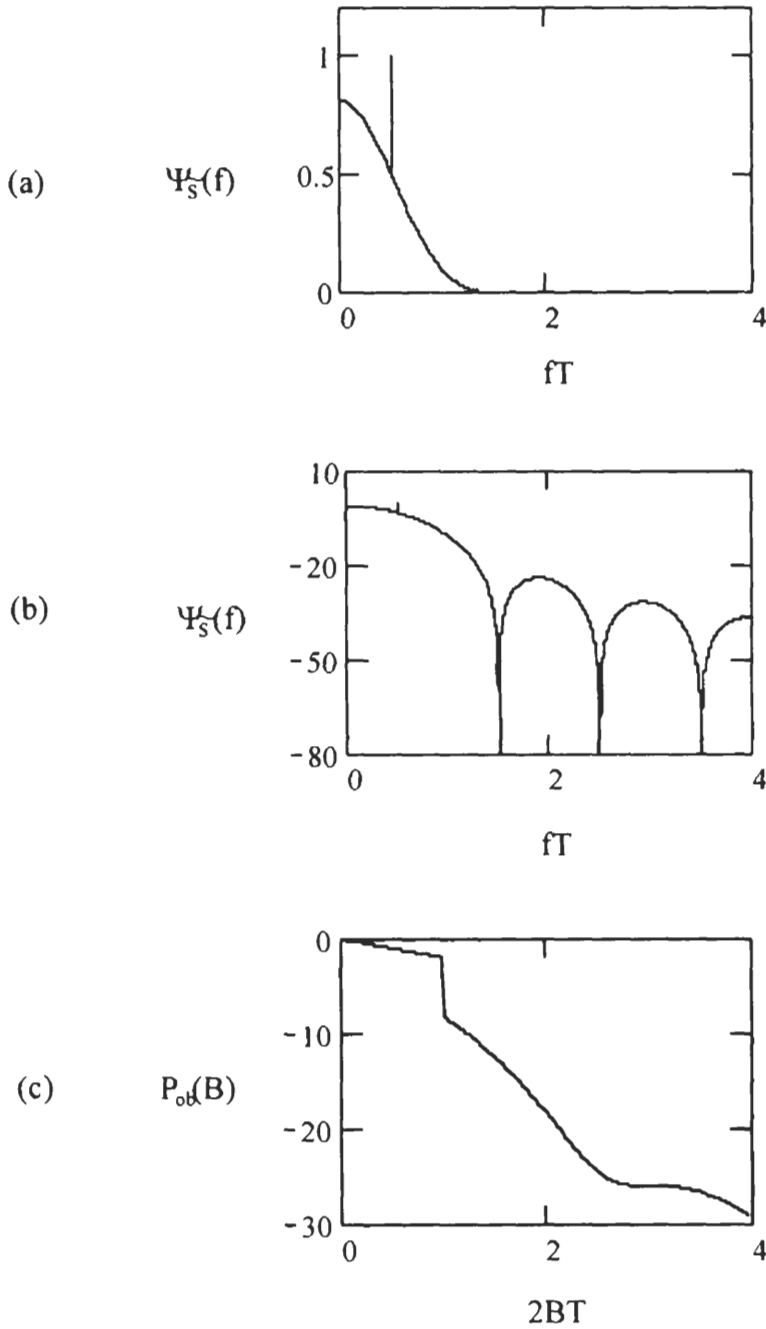


Figure 3.4 PSD of Sunde's FSK: (a) linear scale, (b) logarithmic scale (dB), (c) out-of-band power (dB).

3.2 COHERENT DEMODULATION AND ERROR PERFORMANCE

The coherent demodulator for the coherent FSK signal falls in the general form of coherent demodulators described in Appendix B. The demodulator can be implemented with two correlators as shown in Figure 3.5, where the two reference signals are $\cos(2\pi f_1 t)$ and $\cos(2\pi f_2 t)$. They must be synchronized with the received signal. The receiver is optimum in the sense that it minimizes the error probability for equally likely binary signals. Even though the receiver is rigorously derived in Appendix B, some heuristic explanation here may help understand its operation. When $s_1(t)$ is transmitted, the upper correlator yields a signal l_1 with a positive signal component and a noise component. However, the lower correlator output l_2 , due to the signals' orthogonality, has only a noise component. Thus the output of the summer is most likely above zero, and the threshold detector will most likely produce a 1. When $s_2(t)$ is transmitted, opposite things happen to the two correlators and the threshold detector will most likely produce a 0. However, due to the noise nature that its values range from $-\infty$ to ∞ , occasionally the noise amplitude might overpower the signal amplitude, then detection errors will happen.

An alternative to Figure 3.5 is to use just one correlator with the reference signal $\cos(2\pi f_1 t) - \cos(2\pi f_2 t)$ (Figure 3.6). The correlator in Figure 3.6 can be replaced by a matched filter that matches $\cos(2\pi f_1 t) - \cos(2\pi f_2 t)$ (Figure 3.7). All implementations are equivalent in terms of error performance (see Appendix B).

Assuming an AWGN channel, the received signal is

$$r(t) = s_i(t) + n(t), \quad i = 1, 2$$

where $n(t)$ is the additive white Gaussian noise with zero mean and a two-sided power spectral density $N_o/2$. From (B.33) the bit error probability for any equally likely binary signals is

$$P_b = Q \left(\sqrt{\frac{E_1 + E_2 - 2\rho_{12}\sqrt{E_1 E_2}}{2N_o}} \right)$$

where $N_o/2$ is the two-sided power spectral density of the additive white Gaussian noise. For Sunde's FSK signals $E_1 = E_2 = E_b$, $\rho_{12} = 0$ (orthogonal), thus the error probability is

$$P_b = Q \left(\sqrt{\frac{E_b}{N_o}} \right) \quad (3.6)$$

where $E_b = A^2 T/2$ is the average bit energy of the FSK signal. The above P_b is plotted in Figure 3.8 where P_b of noncoherently demodulated FSK, whose expression

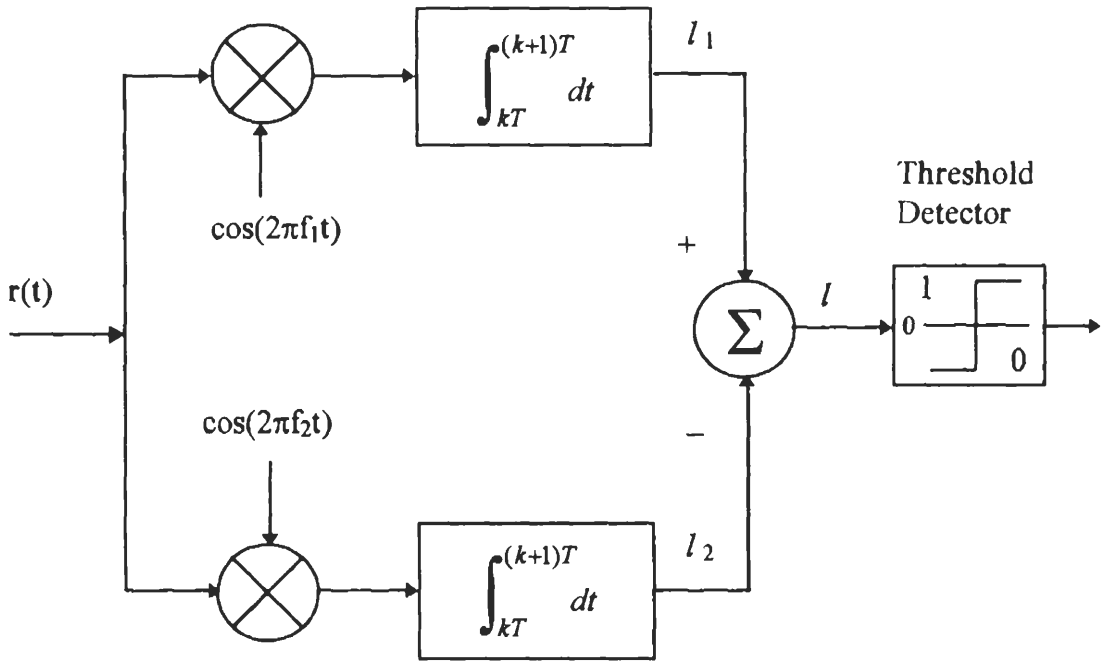


Figure 3.5 Coherent FSK demodulator: correlator implementation.

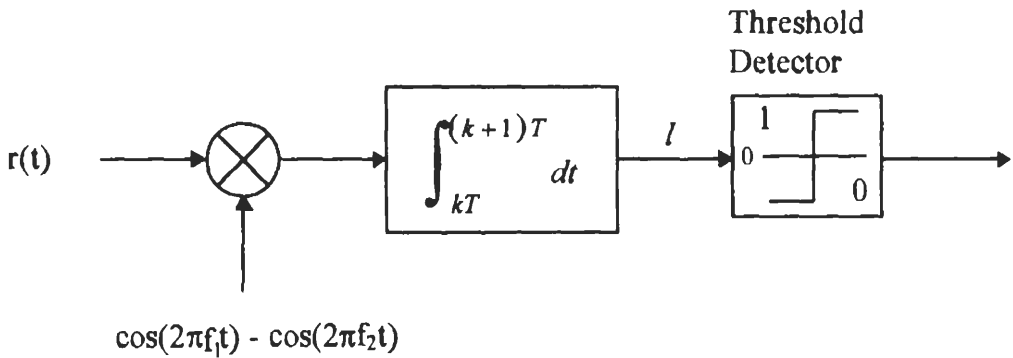


Figure 3.6 Coherent FSK demodulator: one correlator implementation.

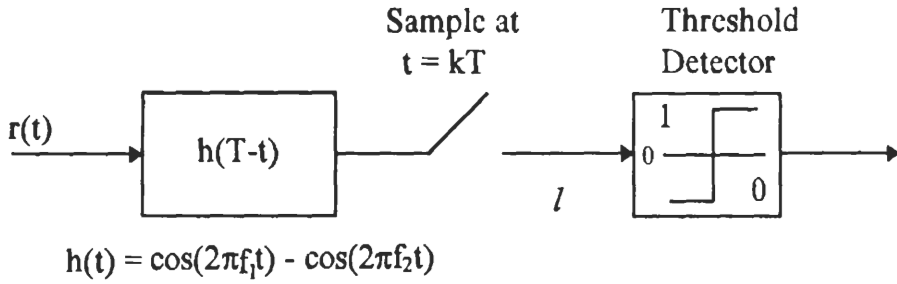
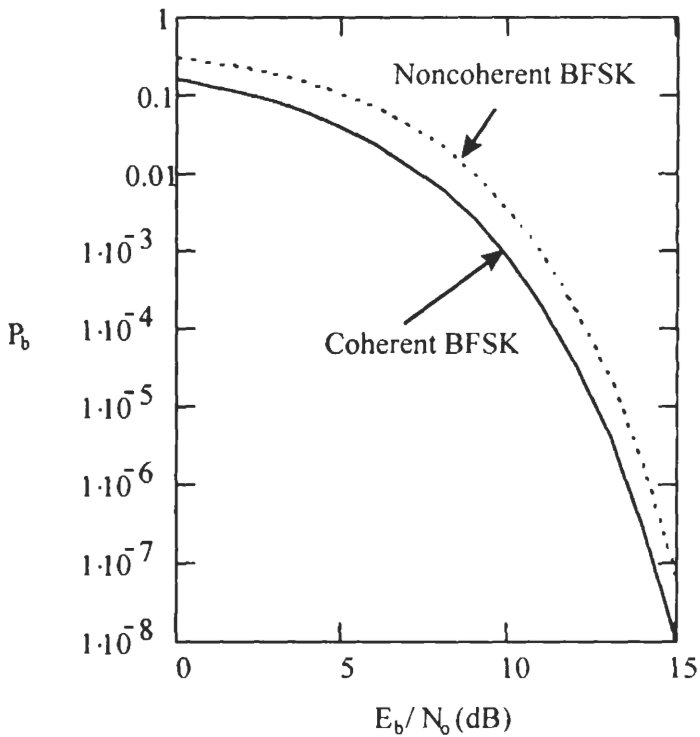


Figure 3.7 Coherent FSK demodulator: matched filter implementation.

Figure 3.8 P_b of coherently and noncoherently demodulated FSK signal.

will be given shortly, is also plotted for comparison.

3.3 NONCOHERENT DEMODULATION AND ERROR PERFORMANCE

Coherently FSK signals can be noncoherently demodulated to avoid the carrier recovery. Noncoherently generated FSK can only be noncoherently demodulated. We refer to both cases as noncoherent FSK. In both cases the demodulation problem becomes a problem of detecting signals with unknown phases. In Appendix B we have shown that the optimum receiver is a quadrature receiver. It can be implemented using correlators or equivalently, matched filters.

Here we assume that the binary noncoherent FSK signals are equally likely and with equal energies. Under these assumptions, the demodulator using correlators is shown in Figure 3.9. Again, like in the coherent case, the optimality of the receiver has been rigorously proved (Appendix B). However, we can easily understand its operation by some heuristic argument as follows.

The received signal (ignoring noise for the moment) with an unknown phase can be written as

$$\begin{aligned} s_i(t, \theta) &= A \cos(2\pi f_i t + \theta), \quad i = 1, 2 \\ &= A \cos \theta \cos 2\pi f_i t - A \sin \theta \sin 2\pi f_i t \end{aligned}$$

The signal consists of an inphase component $A \cos \theta \cos 2\pi f_i t$ and a quadrature component $A \sin \theta \sin 2\pi f_i t$. Thus the signal is *partially* correlated with $\cos 2\pi f_i t$ and *partially* correlated with $\sin 2\pi f_i t$. Therefore we use two correlators to collect the signal energy in these two parts. The outputs of the inphase and quadrature correlators will be $\frac{AT}{2} \cos \theta$ and $\frac{AT}{2} \sin \theta$, respectively. Depending on the value of the unknown phase θ , these two outputs could be anything in $(-\frac{AT}{2}, \frac{AT}{2})$. Fortunately the squared sum of these two signals is not dependent on the unknown phase. That is

$$\left(\frac{AT}{2} \cos \theta\right)^2 + \left(\frac{AT}{2} \sin \theta\right)^2 = \frac{A^2 T^2}{2}$$

This quantity is actually the mean value of the statistics l_i^2 when signal $s_i(t)$ is transmitted and noise is taken into consideration. When $s_i(t)$ is not transmitted the mean value of l_i^2 is 0. The comparator decides which signal is sent by checking these l_i^2 .

The matched filter equivalence to Figure 3.9 is shown in Figure 3.10 which has the same error performance. For implementation simplicity we can replace the matched filters by bandpass filters centered at f_1 and f_2 , respectively (Figure 3.11). However, if the bandpass filters are not matched to the FSK signals, degradation to

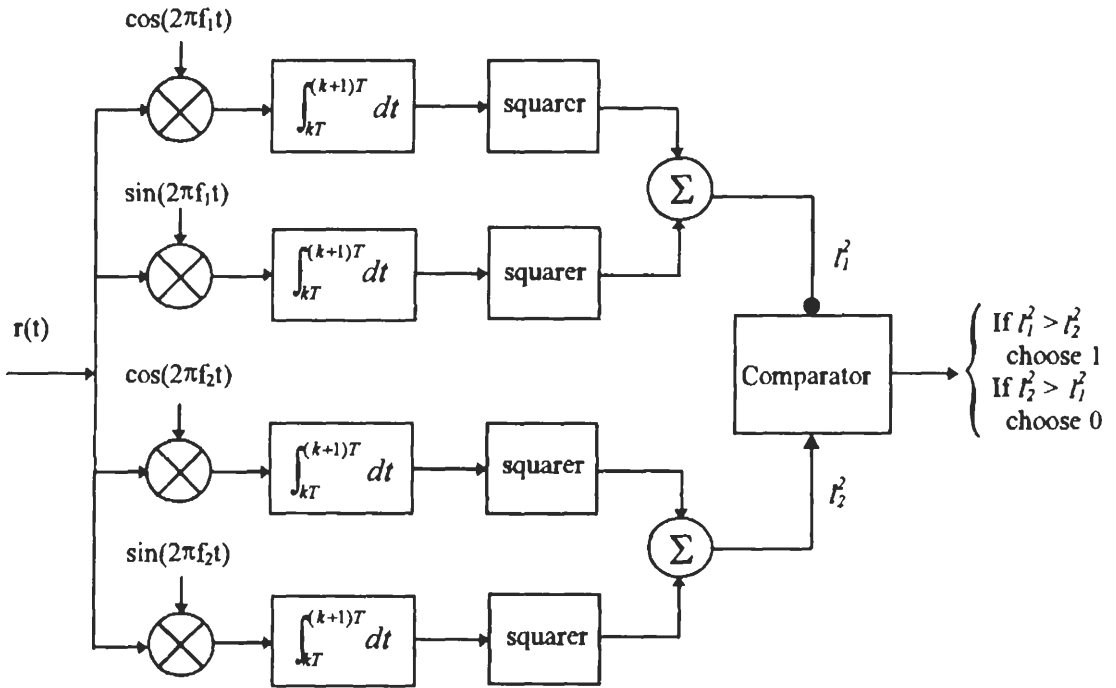


Figure 3.9 FSK noncoherent demodulator: correlator implementation.

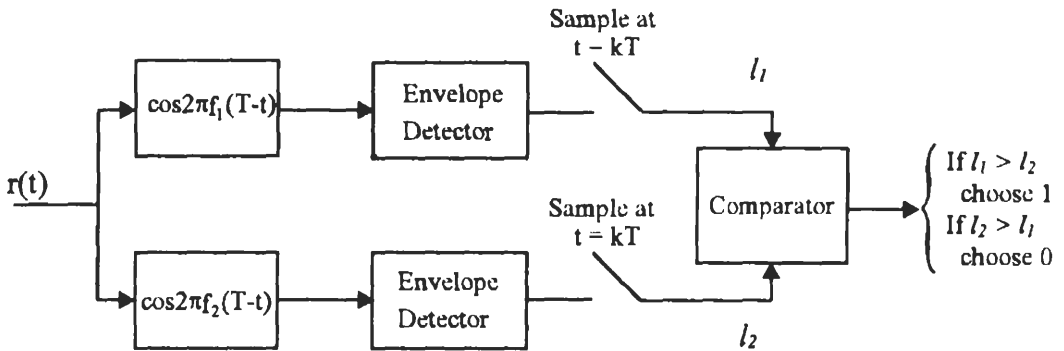


Figure 3.10 FSK noncoherent demodulator: matched filter implementation.

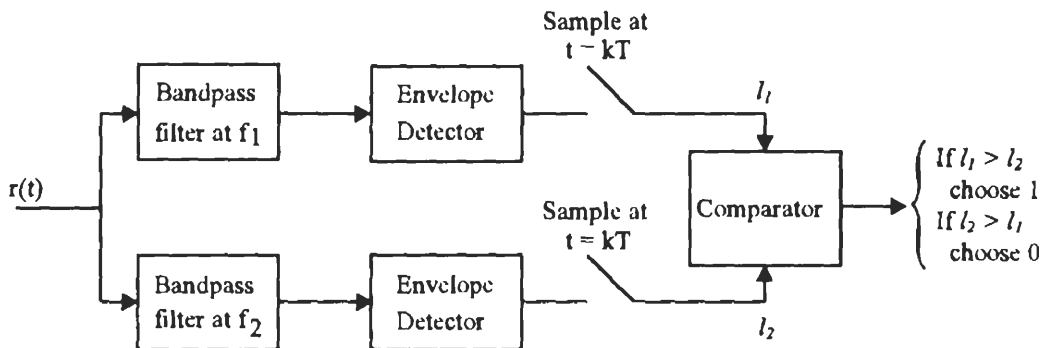


Figure 3.11 FSK noncoherent demodulator: bandpass filter implementation.

various extents will result.

The bit error probability can be derived using the correlator demodulator (Appendix B). Here we further assume that the FSK signals are orthogonal, then from Appendix B the error probability is

$$P_b = \frac{1}{2} e^{-E_b/2N_o} \quad (3.7)$$

The plot is shown in Figure 3.8. It is seen that the noncoherent FSK requires, at most, only 1 dB more E_b/N_o than that for coherent FSK for $P_b \leq 10^{-4}$. The noncoherent FSK demodulator is considerably easier to build since coherent reference signals need not be generated. Therefore in practical systems almost all of the FSK receivers use noncoherent demodulation.

It is worth reiterating that the demodulators in Figures 3.9 through 3.11 are good for equiprobable, equal-energy signals. They do not require the signals to be orthogonal. However, the P_b expression (3.7) is only applicable for orthogonal, equiprobable, equal-energy, noncoherent signals. If the noncoherent FSK signals are not equiprobable, equal-energy, then the demodulators need be slightly modified. See Appendix B for the more general demodulators.

We have shown in Section 3.1 that the minimum frequency separation for coherent FSK signals is $1/2T$. We now show that the minimum separation for noncoherent FSK signals is $1/T$ instead of $1/2T$. The two noncoherent FSK signals are $s_1(t) = \cos 2\pi f_1 t$ and $s_2(t) = \cos(2\pi f_2 t + \Phi)$. For them to be orthogonal, we need

$$\int_{kT}^{(k+1)T} \cos 2\pi f_1 t \cos(2\pi f_2 t + \Phi) dt = 0$$

That is

$$\begin{aligned} & \cos \Phi \int_{kT}^{(k+1)T} \cos 2\pi f_1 t \cos 2\pi f_2 t dt \\ & - \sin \Phi \int_{kT}^{(k+1)T} \sin 2\pi f_2 t \cos 2\pi f_1 t dt = 0 \\ \\ & \cos \Phi \int_{kT}^{(k+1)T} [\cos 2\pi(f_1 + f_2)t + \cos 2\pi(f_1 - f_2)t] dt \\ & - \sin \Phi \int_{kT}^{(k+1)T} [\sin 2\pi(f_1 + f_2)t - \sin 2\pi(f_1 - f_2)t] dt = 0 \\ \\ & \cos \Phi \left[\frac{\sin 2\pi(f_1 + f_2)t}{2\pi(f_1 + f_2)t} + \frac{\sin 2\pi(f_1 - f_2)t}{2\pi(f_1 - f_2)t} \right]_{kT}^{(k+1)T} \\ & + \sin \Phi \left[\frac{\cos 2\pi(f_1 + f_2)t}{2\pi(f_1 + f_2)t} - \frac{\cos 2\pi(f_1 - f_2)t}{2\pi(f_1 - f_2)t} \right]_{kT}^{(k+1)T} = 0 \end{aligned}$$

For arbitrary Φ , this requires that the sums inside the brackets be zero. This, in turn, requires that $2\pi(f_1 + f_2)T = k\pi$ for the first term and $2\pi(f_1 - f_2)T = l\pi$ for the second term in the first bracket, that $2\pi(f_1 + f_2)T = 2m\pi$ for the first term and $2\pi(f_1 - f_2)T = 2n\pi$ for the second term in the second bracket, where k, l, m and n are integers and $k > l, m > n$. The $k\pi$ and $l\pi$ cases are included in the $2m\pi$ and $2n\pi$ case, respectively. Therefore, all these requirements can be satisfied if and only if

$$2\pi(f_1 + f_2)T = 2m\pi$$

$$2\pi(f_1 - f_2)T = 2n\pi$$

This leads to

$$f_1 = \frac{m + n}{2T}$$

$$f_2 = \frac{m - n}{2T}$$

$$f_1 - f_2 = \frac{n}{T}$$

This is to say that for two noncoherent FSK signals to be orthogonal, the two frequencies must be integer multiple of $1/2T$ and their separation must be multiple of $1/T$. When $n = 1$, the separation is the $1/T$, which is the minimum. Comparing with coherent FSK case, the separation of noncoherent FSK is double that of FSK. Thus more system bandwidth is required for noncoherent FSK for the same symbol rate.

3.4 M-ARY FSK

3.4.1 MFSK Signal and Power Spectral Density

In an M-ary FSK modulation, the binary data stream is divided into n-tuples of $n = \log_2 M$ bits. We denote all M possible n-tuples as M messages: m_i , $i = 1, 2, \dots, M$.¹ There are M signals with different frequencies to represent these M messages. The expression of the i th signal is

$$s_i(t) = A \cos(2\pi f_i t + \Phi_i), \quad kT \leq t \leq (k+1)T, \text{ for } m_i \quad (3.8)$$

where T is the symbol period which is n times the bit period.

If the initial phases are the same for all i , the signal set is coherent. As in the binary case we can always assume $\Phi_i = 0$ for coherent MFSK. The demodulation could be coherent or noncoherent. Otherwise the signal set is noncoherent and the demodulation must be noncoherent.

From the discussion of binary FSK, we know that in order for the signals to be orthogonal, the frequency separations between any two of them must be $m/2T$ for coherent case and m/T for noncoherent case. Thus the minimum separation between two adjacent frequencies is $1/2T$ for orthogonal case and $1/T$ for noncoherent case. These are the same as those of the binary case. Usually a uniform frequency separation between two adjacent frequencies is chosen for MFSK.

The derivation of the power spectral density of MFSK schemes is much more complicated than that for the binary case [1]. Now we quote the PSD expression of the complex envelope of the MFSK with the following parameters: (1) The frequency separations are uniform but arbitrary, which is denoted as $2\Delta f$. We express the separation in terms of modulation index $h = 2\Delta f T$. (2) The M-ary messages are

$$\begin{aligned} m_i &= 2i - (M + 1), \quad i = 1, 2, \dots, M \\ &= \pm 1, \pm 3, \dots, \pm(M - 1) \end{aligned}$$

and the M-ary signals are

$$s_i(t) = A \cos(2\pi f_c t + m_i h \frac{\pi}{T}(t - kT) + \Phi_i), \quad kT \leq t \leq (k+1)T, \text{ for } m_i$$

where A is the signal amplitude and all signals have equal energies. For *equiprobable*

¹ M may be odd in some applications. Then n can be set as the nearest integer greater than $\log_2 M$. Some of the m_i must not be used.

messages, the PSD expression is given in [1] as

$$\Psi_{\bar{s}}(f) = \frac{A^2 T}{M} \sum_{i=1}^M \left[\frac{1}{2} \frac{\sin^2 \gamma_i}{\gamma_i^2} + \frac{1}{M} \sum_{j=1}^M A_{ij} \frac{\sin \gamma_i}{\gamma_i} \frac{\sin \gamma_j}{\gamma_j} \right] \quad (3.9)$$

Other parameters are defined as

$$A_{ij} = \frac{\cos(\gamma_i + \gamma_j) - C_a \cos(\gamma_i + \gamma_j - 2\pi fT)}{1 + C_a^2 - 2C_a \cos 2\pi fT}$$

$$\gamma_i = (fT - m_i h/2)\pi, \quad i = 1, 2, \dots, M$$

$$C_a = \frac{2}{M} \sum_{i=1}^{M/2} \cos[h\pi(2i - 1)]$$

We have plotted curves for $h = 0.5$ to 1.5 for $M = 2, 4$, and 8 in Figures 3.12, 3.13, and 3.14, respectively, where each abscissa is normalized frequency fT [1]. Curves are presented for various h values to show how the spectral shape changes with h . Figure 3.12 is for binary FSK where $h = 1$ is a special case that an impulse arises at $fT = 0.5$, that is, at the two FSK frequencies. This is the Sunde's FSK. We have calculated and plotted its PSD in Section 3.1.2. Figures 3.13 and 3.14 are for 4-ary and 8-ary MSK, respectively. The multilevel cases show considerable similarity to the binary ones. For small values of h , the spectra are narrow and decrease smoothly towards zero. As h increases towards unity the spectrum widens and spectral power is increasingly concentrated around $fT = 0.5$ and its odd multiples. These are the frequencies of the M signals in the scheme. At $h = 1$, spectral lines arise at these frequencies. As h increases further the concentration is again broadened and reduced in intensity. For coherent orthogonal case, $h = 0.5$, most spectral components are in a bandwidth of $\frac{M}{2T}$. Thus the transmission bandwidth can be set as $B_T = \frac{M}{2T}$. Similarly for noncoherent orthogonal case, $h = 1.0$, then $B_T = \frac{M}{T}$. This can be easily seen from the curves.

In some applications, M is *odd* and/or messages are *not equiprobable*. For this case the PSD expression in (3.9) is still applicable except that the parameter C_a must be in its original form as [1]

$$C_a = \sum_{i=1}^M P_i \exp\{jh\pi m_i\}$$

where P_i is the a priori probability of message m_i .

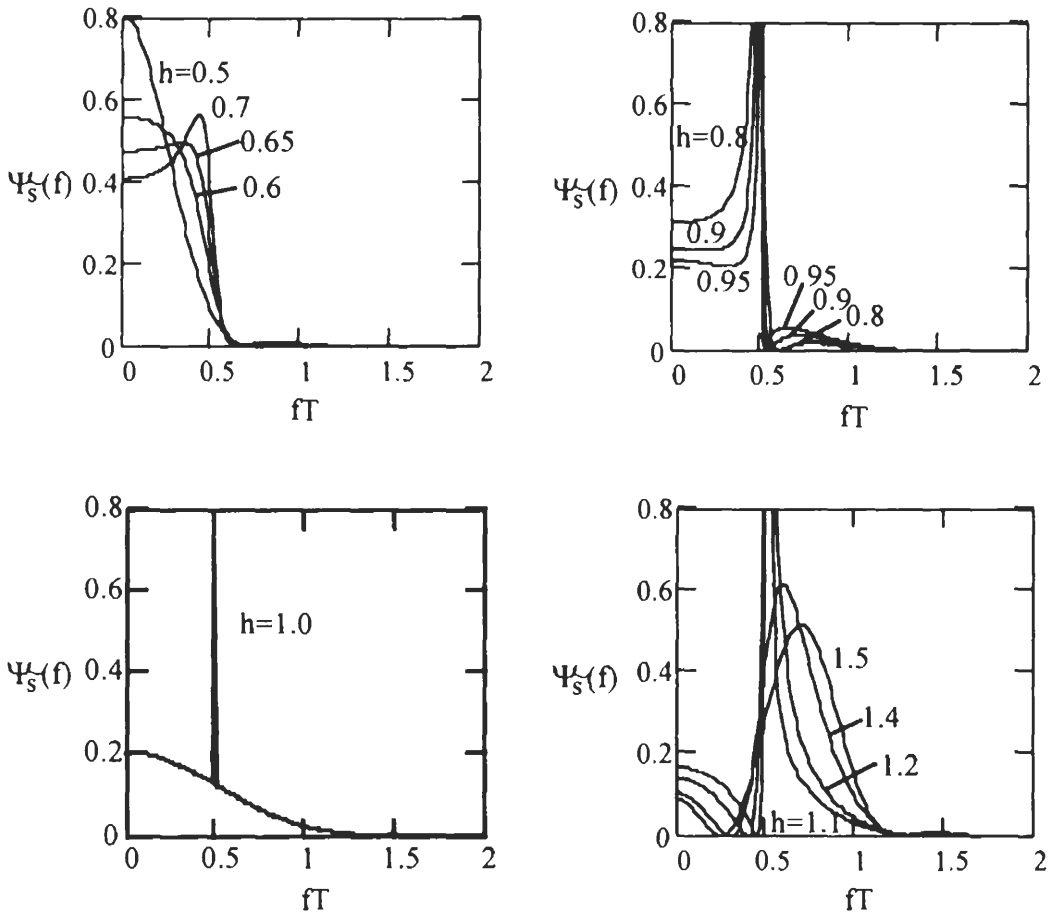


Figure 3.12 PSD of MFSK: $M = 2$. After [1].

3.4.2 Modulator, Demodulator, and Error Performance

The noncoherent modulator for binary FSK in Figure 3.1 can be easily extended to noncoherent MFSK by simply increasing the number of independent oscillators to M (Figure 3.15). The coherent modulator for binary FSK in Figure 3.2 can also be extended to MFSK (Figure 3.16). Then the frequency synthesizer generates M signals with the designed frequencies and coherent phase, and the multiplexer chooses one of the frequencies, according to the n data bits.

The coherent MFSK demodulator falls in the general form of detector for M -ary equiprobable, equal-energy signals with known phases as described in Appendix B. The demodulator consists of a bank of M correlators or matched filters (Figure 3.17 and 3.18). At sampling times $t = kT$, the receiver makes decisions based on

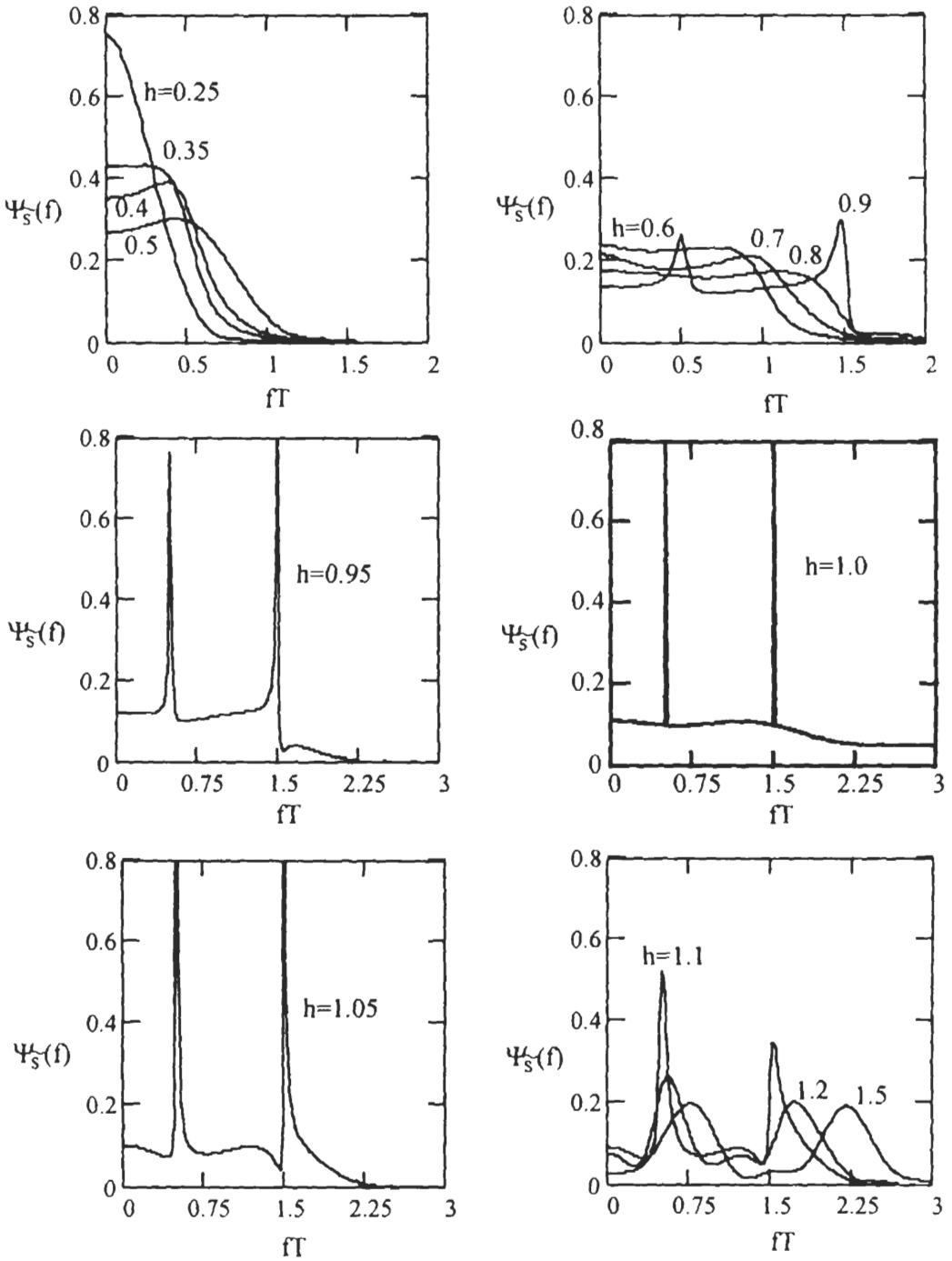


Figure 3.13 PSD of MFSK: $M = 4$. After [1].

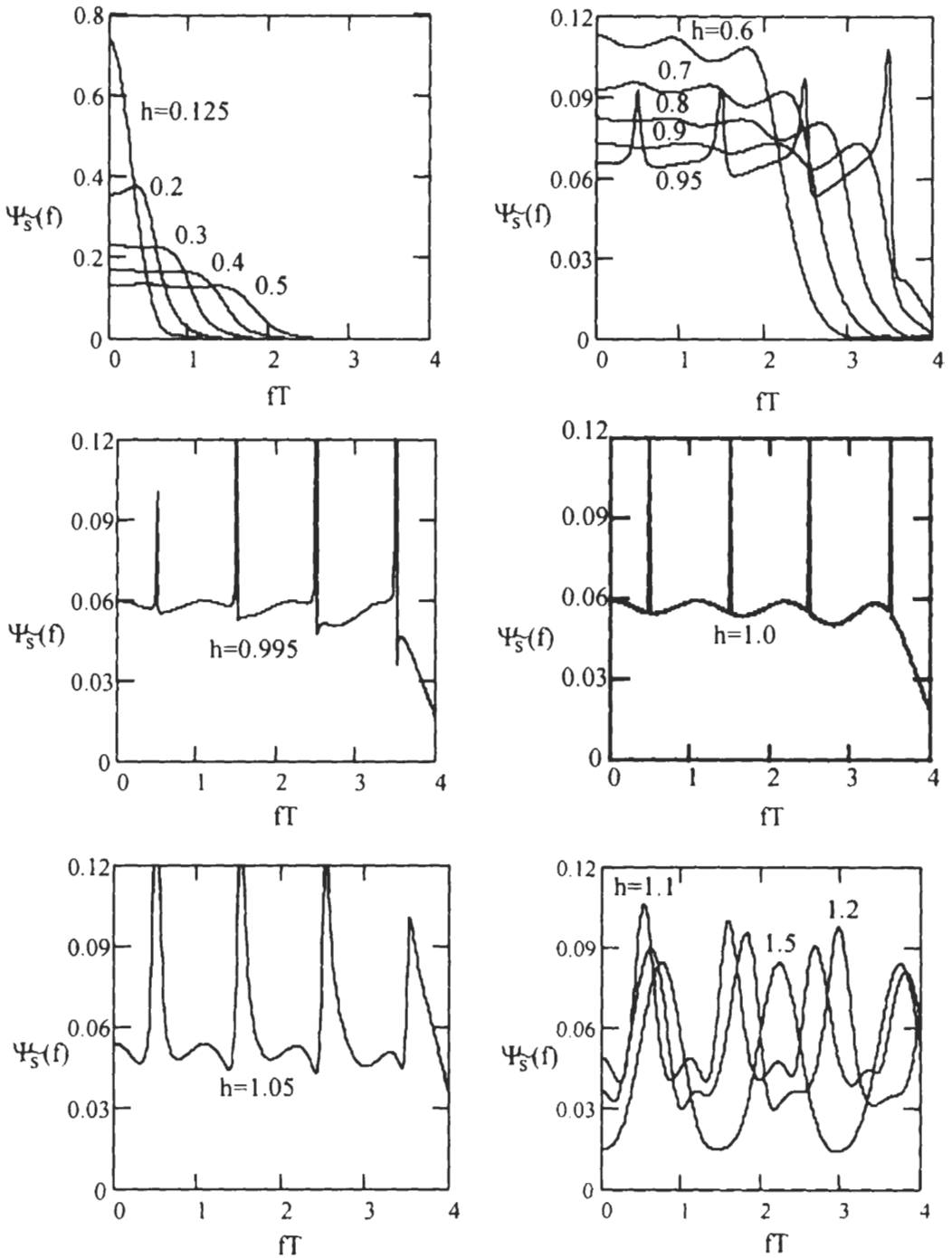


Figure 3.14 PSD of MFSK: $M = 8$. After [1].

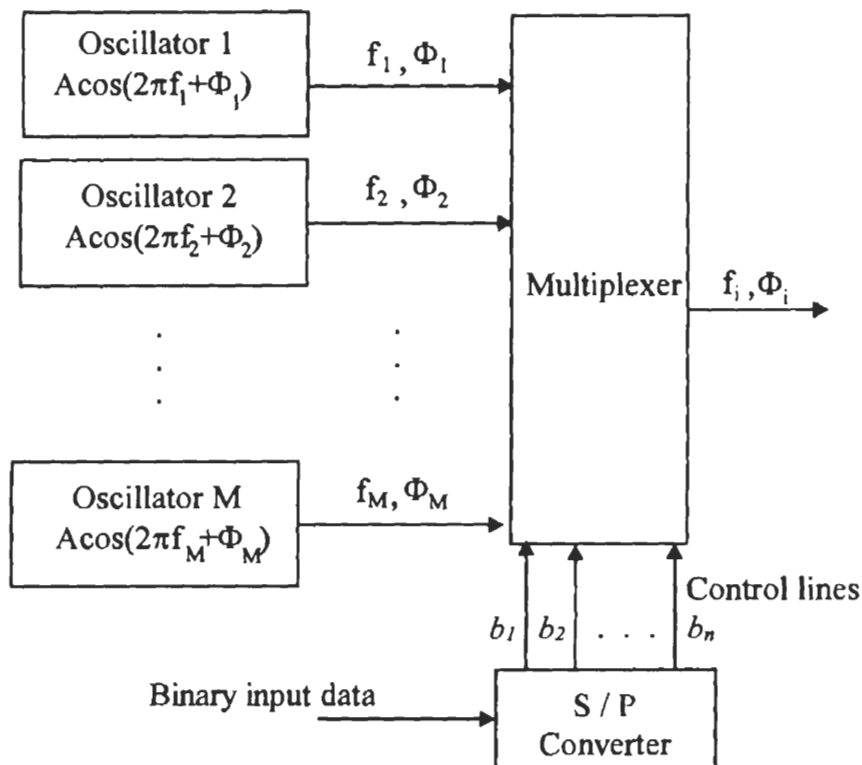


Figure 3.15 Noncoherent MFSK modulator.

the largest output of the correlators or matched filters. We have to point out that the coherent MFSK receivers in Figures 3.17 and 3.18 only require that the MFSK signals be equiprobable, equal-energy, and do not require them be orthogonal. For more general cases where the M-ary signal set is not equiprobable and/or not equal in energy, a bias term

$$B_i = \frac{N_o}{2} \ln P_i - \frac{1}{2} E_i$$

must be included in the sufficient statistics l_i in the receiver (see Figures B.6 and B.7).

The exact expression for the symbol error probability for symmetrical signal set (equal-energy, equiprobable) have been given in Appendix B (B. 42) as

$$P_s = 1 - \int_{-\infty}^{\infty} dx \frac{1}{\sqrt{2\pi}} \exp\left\{-\frac{(x - \sqrt{2E_s/N_o})^2}{2}\right\} [1 - Q(x)]^{M-1} \quad (3.10)$$

This expression does not require the signal set be orthogonal. This expression can

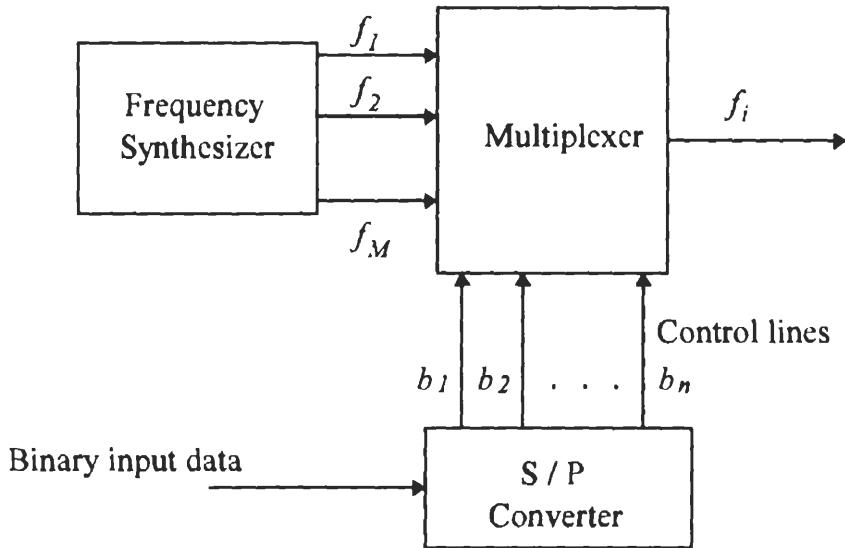


Figure 3.16 Coherent M-ary FSK modulator.

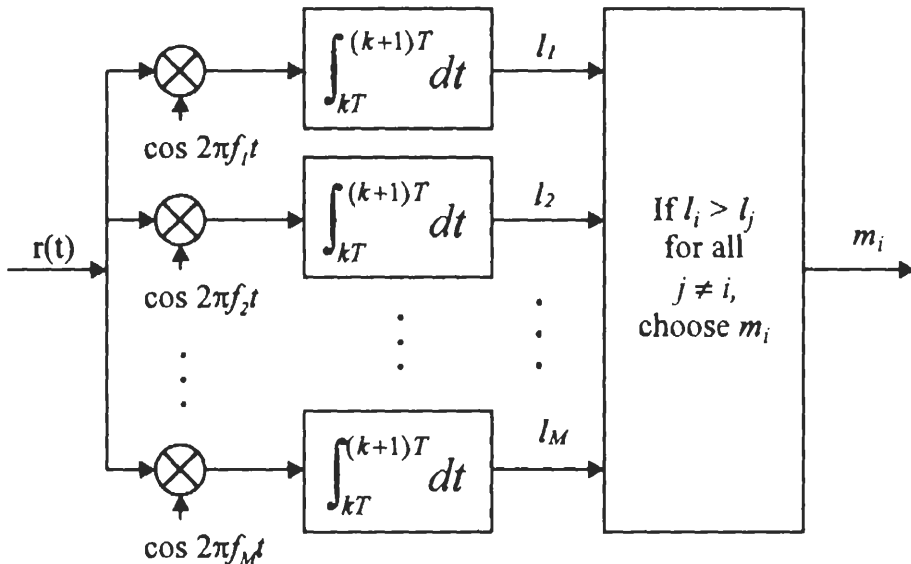


Figure 3.17 Coherent M-ary FSK demodulator: correlator implementation.

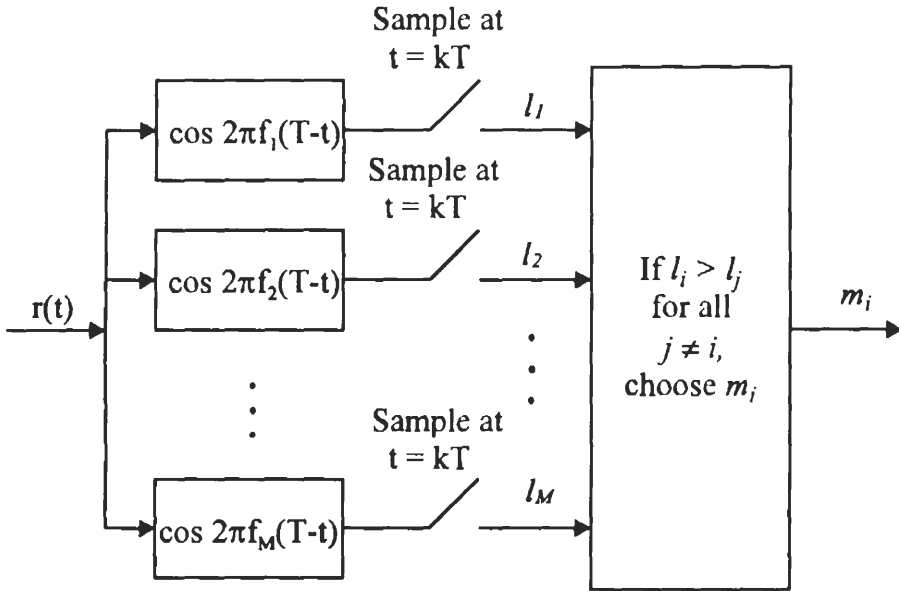


Figure 3.18 Coherent M-ary FSK demodulator: matched filter implementation.

not be analytically evaluated.

If the signal set is not symmetrical, an upper bound has been obtained in Appendix B (B. 43) as

$$P_s \leq \sum_{j \neq i} Q \left(\frac{d_{ij}}{\sqrt{2N_o}} \right)$$

If the signal set is equal-energy and orthogonal (not necessarily equiprobable), all distances between any two signals are equal. The distance $d = \sqrt{2E_s}$, and the upper bound becomes

$$P_s \leq (M - 1)Q \left(\sqrt{\frac{E_s}{N_o}} \right) \tag{3.11}$$

For fixed M this bound becomes increasingly tight as E_s/N_o is increased. In fact, it becomes a good approximation for $P_s \leq 10^{-3}$. For $M = 2$, it becomes the exact expression.

If the signaling scheme is such that each signal represents $n = \log_2 M$ bits, as we stated in the very beginning of this section, then the P_s can be expressed as a function of $E_b = E_s / \log_2 M$.

At this point we need to derive a relation between bit error probability P_b and symbol error probability P_s . For binary signals P_b is simply equal to P_s . For equally

likely orthogonal M-ary signals, all symbol errors are equiprobable. That is, the demodulator may choose any one of the $(M - 1)$ erroneous orthogonal signals with equal probability:²

$$\frac{P_s}{M - 1} = \frac{P_s}{2^n - 1}$$

There are $\binom{n}{k}$ ways in which k bits out of n bits may be in error. Hence the average number of bit errors per n -bit symbol is

$$\sum_{k=1}^n k \binom{n}{k} \frac{P_s}{2^n - 1} = n \frac{2^{n-1}}{2^n - 1} P_s$$

and the average bit error probability is just the above result divided by n . Thus

$$P_b = \frac{2^{n-1}}{2^n - 1} P_s \quad (3.12)$$

For large values of M , $P_b \approx \frac{1}{2} P_s$.

If M is odd then $M \neq 2^n$. If the M messages are still equiprobable, the above expression is modified as

$$P_b = \frac{2^{n-1}}{M - 1} P_s$$

P_s and P_b for coherently demodulated, *equal-energy, equiprobable, and orthogonal* MFSK are shown in Figures 3.19 and 3.20, respectively. The solid lines are accurate error curves and the dotted lines are upper bounds. Note that the curves in these two figures are very close at high SNRs, but the differences are clear at low SNRs. It can be seen that the upper bound is very tight for E_b/N_o over about 5 dB. We also observe that for the same E_b/N_o error probability reduces when M increases, or for the same error probability the required E_b/N_o decreases as M increases. However, the speed of decrease in E_b/N_o slows down when M gets larger.

The noncoherent demodulator for M-ary FSK falls in the general form of detector for M-ary equiprobable, equal-energy signals with unknown phases as described in Appendix B. The demodulator can be implemented in correlator-squarer form or matched filter-squarer or matched filter-envelope detector form (Figures 3.21, 3.22, 3.23). They are the extensions of their binary counterparts. Their operations are the same except for the increase of number of signals. Therefore we do not repeat the description here.

² This is, however, not true for M-ary PSK signals since they are not orthogonal. Therefore the P_b versus P_s relation is different, as we will see in Chapter 4.

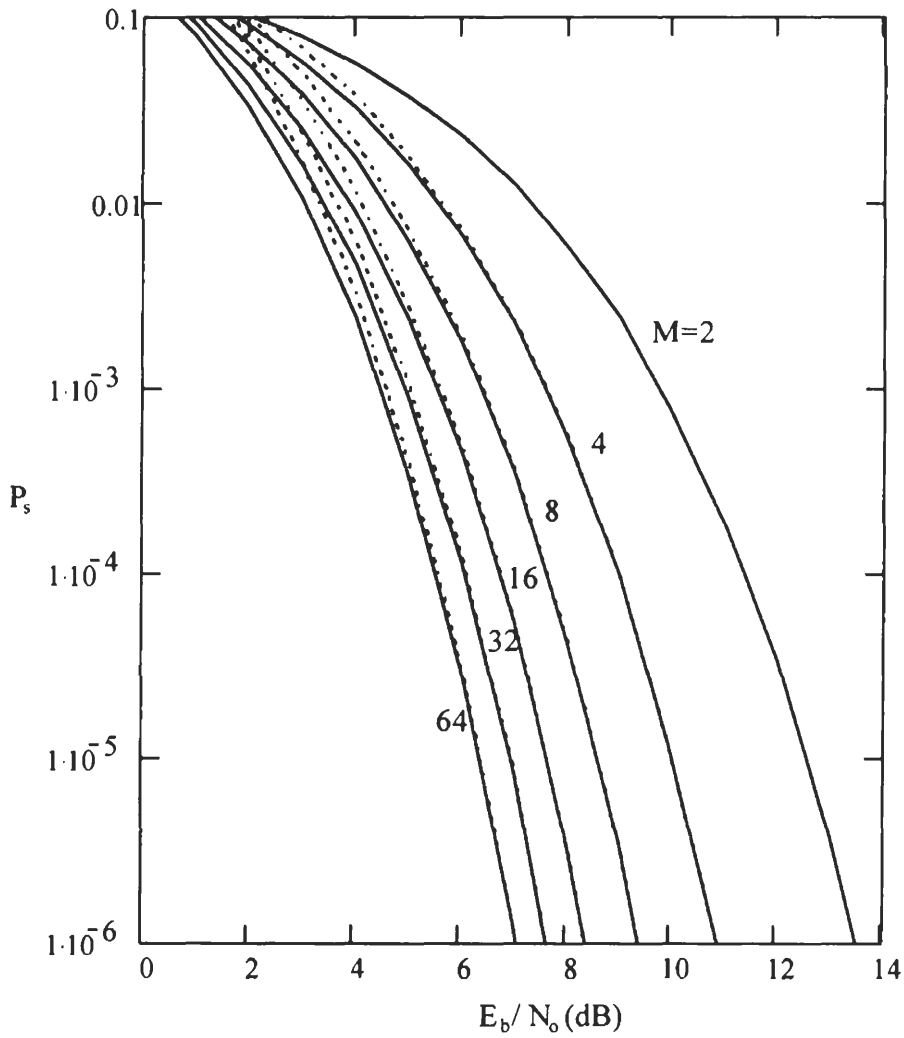


Figure 3.19 P_s of coherently demodulated, equiprobable, equal-energy, and orthogonal MFSK (dotted line: upper bound).

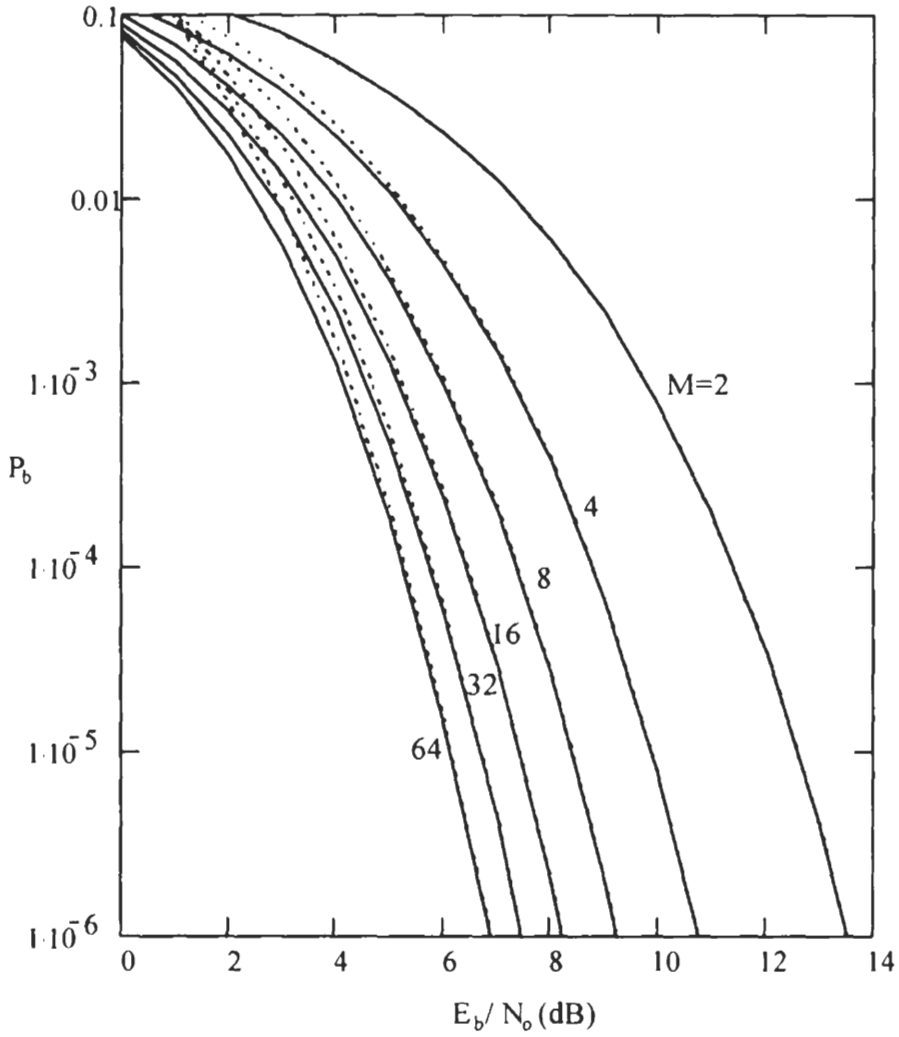


Figure 3.20 P_b of coherently demodulated, equiprobable, equal-energy, and orthogonal MFSK (dotted line: upper bound).

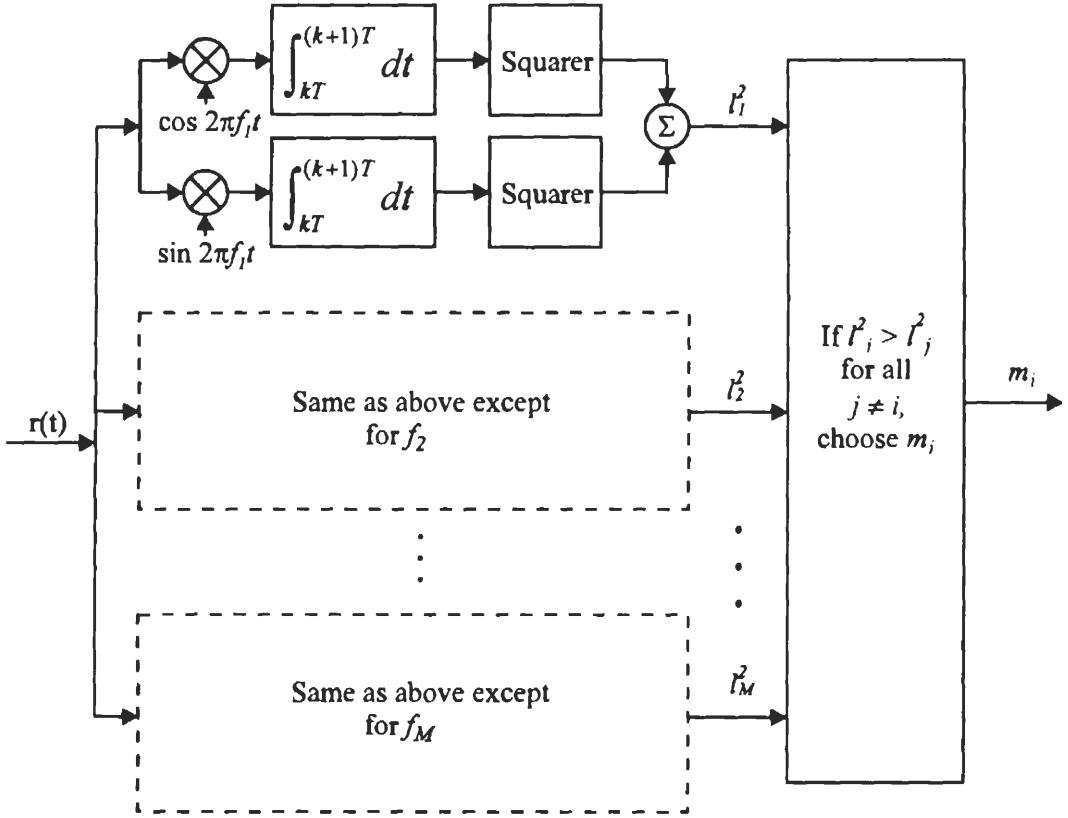


Figure 3.21 Noncoherent MFSK demodulator: correlator-squarer implementation.

Symbol error probability expression for noncoherently demodulated, *equiprobable, equal-energy, and orthogonal* MFSK has been given in Appendix B (B.57) as

$$P_s = 1 - P(c/H_1) = \sum_{k=1}^{M-1} \frac{(-1)^{k+1}}{k+1} \binom{M-1}{k} \exp\left[-\frac{kE_s}{(k+1)N_o}\right] \quad (3.13)$$

where $\binom{M-1}{k}$ is the binomial coefficient, defined by

$$\binom{M-1}{k} = \frac{(M-1)!}{(M-1-k)!k!}$$

The first term of the summation in (3.13) provides an upper bound (B.58) as

$$P_s \leq \frac{M-1}{2} \exp\left[-\frac{E_s}{2N_o}\right] \quad (3.14)$$

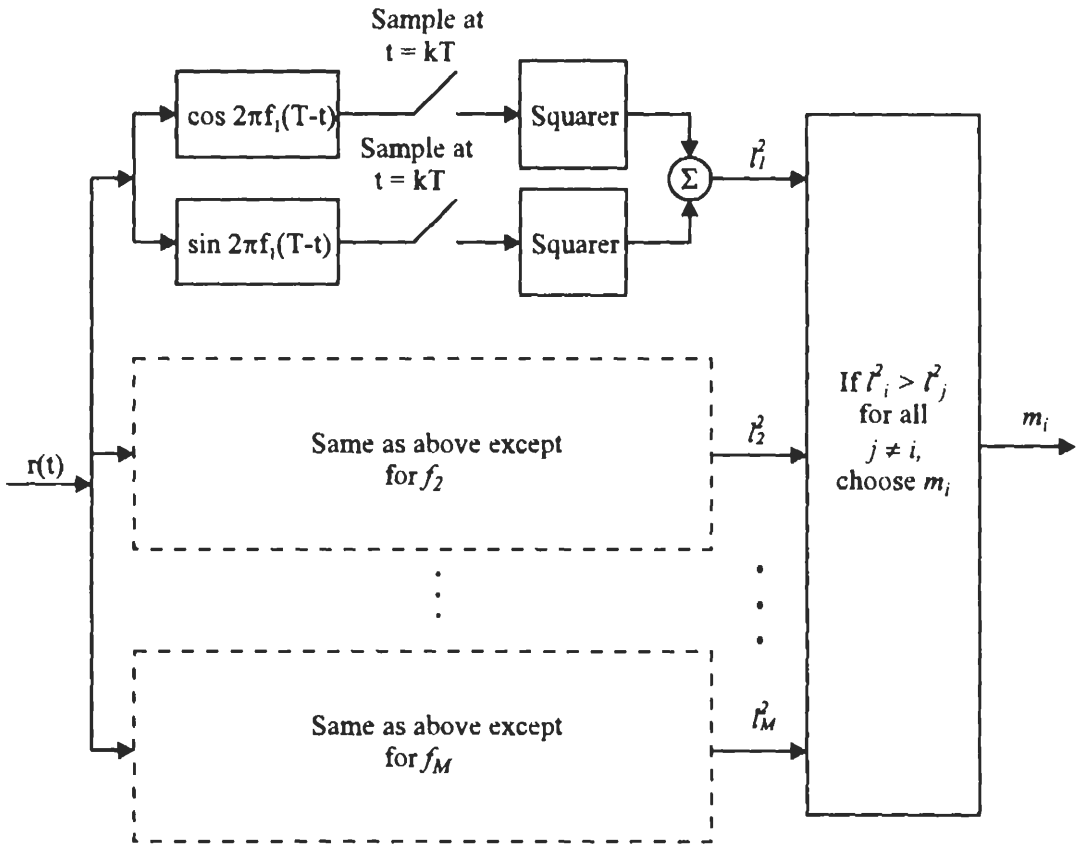


Figure 3.22 Noncoherent MFSK demodulator: matched filter-squarer detector implementation.

For fixed M this bound becomes increasingly close to the actual value of P_s as E_s/N_o is increased. In fact when $M = 2$, the upper bound becomes the exact expression.

Figures 3.24 and 3.25 show P_s and P_b for noncoherently demodulated, equiprobable, equal-energy, and orthogonal MFSK for $M = 2, \dots, 32$. Note that the curves in these two figures are very close at high SNRs, but the differences are clear at low SNRs. Like the coherent case, again the P_b versus P_s relation is given by (3.12). The behavior of the curves with values of M is very similar to that of the coherent case. The only difference is that the noncoherent one requires slightly more E_b/N_o for the same error probability. The increase of E_b/N_o is only a fraction of a dB for $P_b \leq 10^{-4}$ for all values of M and becomes smaller as M becomes larger.

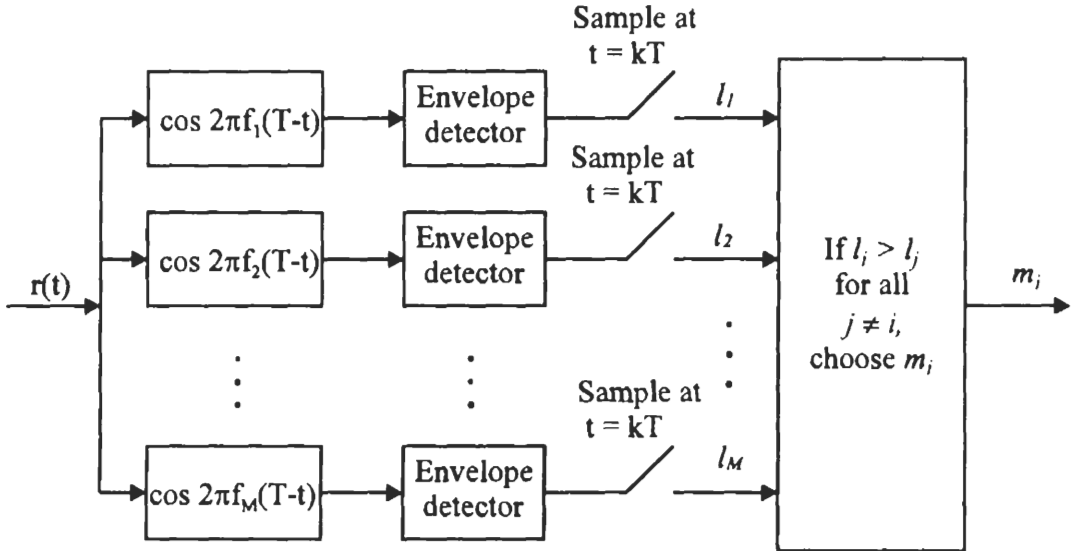


Figure 3.23 Noncoherent MFSK demodulator: matched filter-envelope detector implementation.

3.5 DEMODULATION USING DISCRIMINATOR

In comparison with other modulation schemes, such as PSK and QAM, the most important advantage of FSK is that demodulation can be very simple. We already have seen that FSK can be noncoherently demodulated and the error performance degradation is less than 1 dB in a meaningful range of bit error rate. Demodulation can be even simpler by using the conventional frequency discriminator which is widely used in analog FM demodulation.

Figure 3.26 is the block diagram of a typical binary FSK demodulator using limiter-discriminator detection and integrate-and-dump post-detection filtering. The IF filter is a narrow-band filter, with a frequency response $H(f)$ centered at f_c . This filter is to reject the out-of-band noise and restrict the frequency band of the signal. Although this filter is shown in Figure 3.26 as a part of the receiver, it should be considered as the overall filtering characteristic of the transmitter filter, channel, and receiver for analysis purposes. The demodulation is done by the limiter-discriminator combination which for the purpose of analysis is assumed to have an ideal characteristic, that is, the output is proportional to the angle of the input signal. The post-detection filter is an integrate-and-dump filter with an integration time of T . At the end of each bit interval the output of the integrate-and-dump filter is sampled and the polarity of the sample determines whether a 1 or 0 was sent.

For a narrow-band IF filter, a set of expressions for bit error probability was first published in [2]. The results in [2] show that for both the Gaussian and rectangular

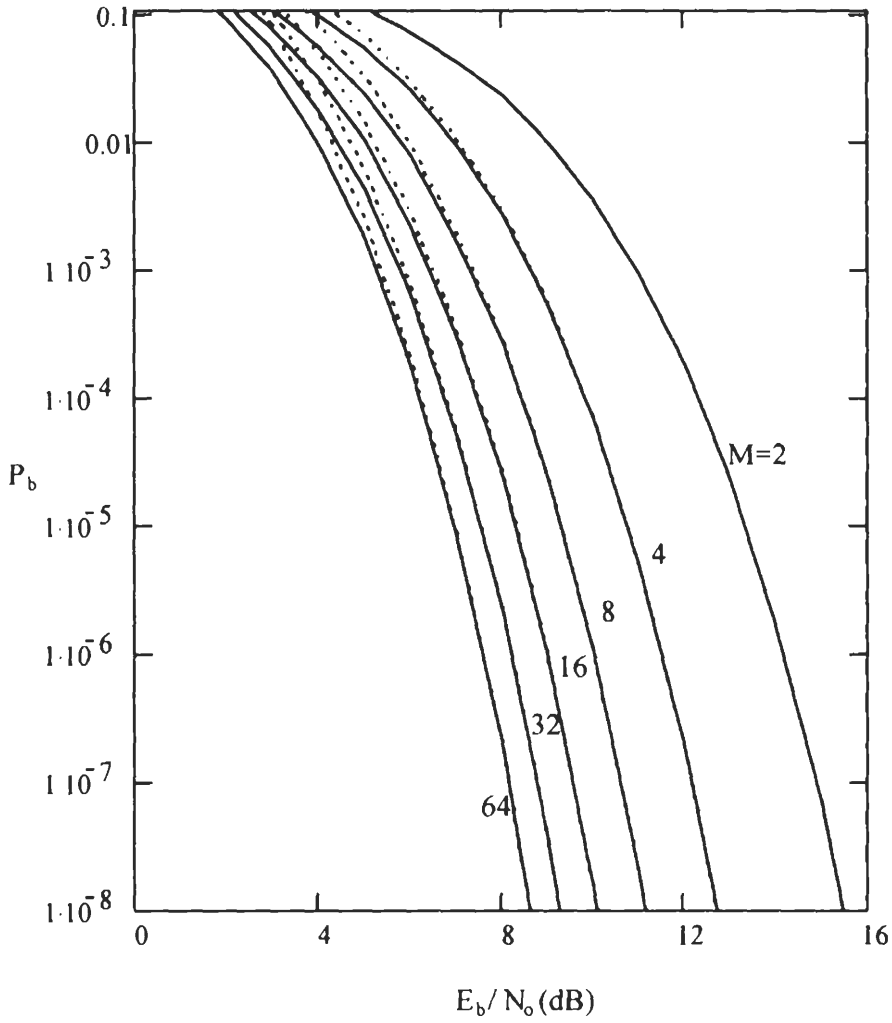


Figure 3.24 P_b of noncoherently demodulated, equiprobable, equal-energy, and orthogonal MFSK (dotted line: upper bound).

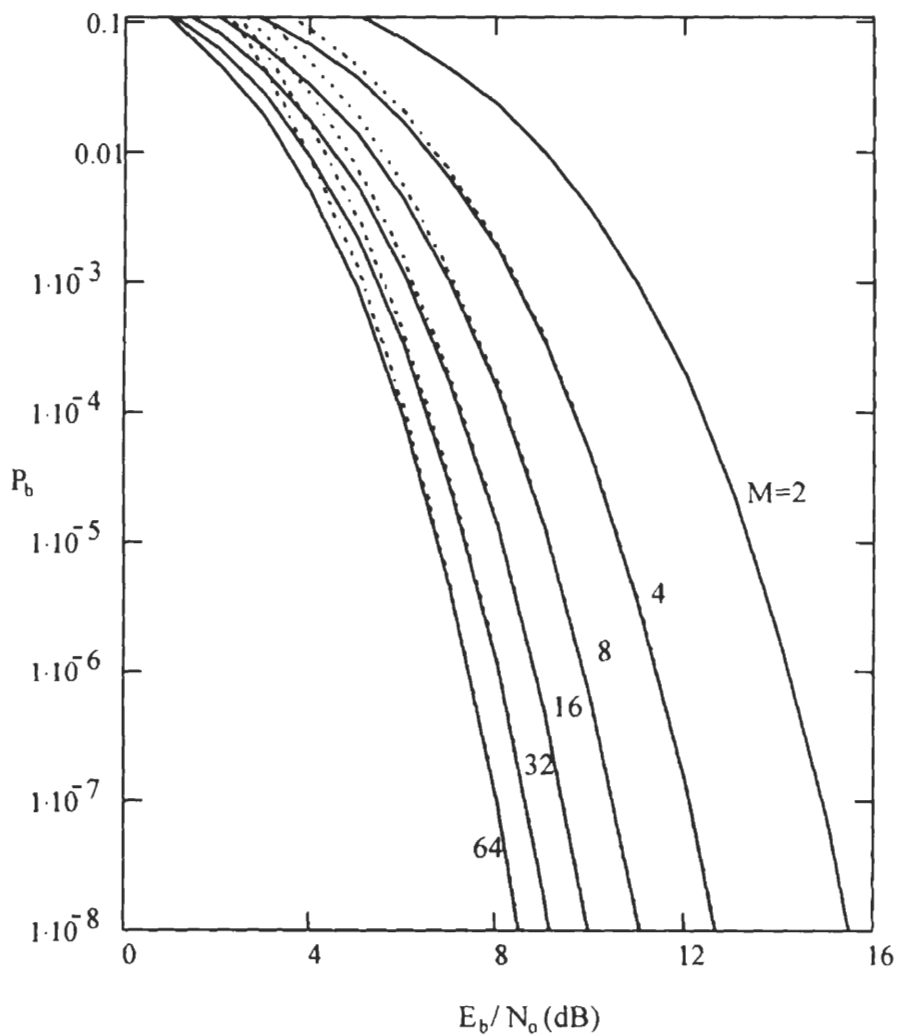


Figure 3.25 P_b of noncoherently demodulated, equiprobable, equal-energy, and orthogonal MFSK (dotted line: upper bound).

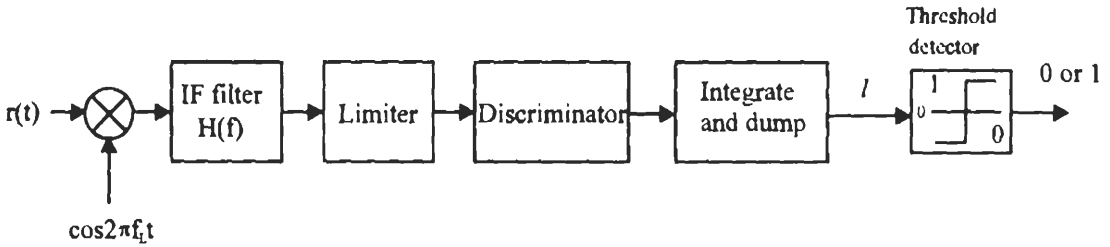


Figure 3.26 Binary FSK demodulator using limiter-discriminator detection and integrate-and-dump post-detection filtering

bandpass filters, the system with a modulation index of $h = 0.7$ is the best in that it requires the least signal energy in a given noise environment to achieve a 10^{-4} bit error rate for bandwidths ranging from $BT = 0.8$ to 3.0 , where B is the *equivalent noise bandwidth*.³ For a given SNR and modulation index there is a bandwidth that gives a minimum probability of error. It might be argued heuristically that as the bandwidth is increased more noise power is accepted and errors increase. On the other hand, as the bandwidth is reduced below a certain point, error arising out of the distortion of the signal increases. In general it appears that a bandpass filter bandwidth of about $B = 1/T$ gives a minimum probability of error. The precise value would depend on the shape of the filter, the modulation index, and the SNR. The theoretical results were generally in good agreement with experiment results reported in [2].

The work in [3] provided a set of simpler expressions by restricting the noise equivalent bandwidth B of the IF filter in the range of $1 \leq BT \leq 3$ and the frequency deviation ratio $h < 1.5$. Also the SNR is assumed large ($\geq 6dB$). However, even the simpler expressions are too complicated to be included here. Instead we present the curves from [3] in Figure 3.27 for several IF filter characteristics. They are the Gaussian filter, the six-element Butterworth filter, and two-stage synchronously tuned filters. Their characteristics are respectively

$$H(f) = e^{-\pi f^2 / 2B^2}, \quad (\text{Gaussian})$$

$$H(f) = \frac{2}{1 + (1 + j\sqrt{8}f/B)^2}, \quad (\text{Butterworth})$$

³ The equivalent noise bandwidth of a filter $H(f)$ is defined as

$$B = \frac{1}{|H(0)|} \int_{-\infty}^{\infty} |H(f)|^2 df$$

$$H(f) = \frac{2}{(1 + jf/\alpha)^2}, \quad \alpha = \frac{B/2}{\sqrt{\sqrt{2} - 1}}$$

(two-stage synchronously tuned)

Figure 3.27 shows the curves for the optimum index $h = 0.707$, and the optimum bandwidth $BT = 1$ for all three filters. The BER curves with the Gaussian and Butterworth filters are shown as a single curve since there is only a few percent difference in the performance with the Gaussian filter being slightly better. The performance of the synchronously tuned IF filters is about 0.75dB inferior to the Gaussian IF filter. Also shown in the figure for comparison is the performance curve for noncoherent orthogonal FSK which is about 0.75dB inferior to the synchronously tuned IF filters. These results are in consistence with those reported in [2]. We would expect that the error performance of the optimum noncoherent FSK be better than the narrow-band demodulator. However, the above results show the opposite. The reason why this happens was not given either in [2] or in [3]. Recall that for noncoherent demodulation, the optimum demodulator consists of matched filters followed by envelope detectors (or equivalently, correlators). It is optimum in the sense that the matched filter will give a maximum SNR. But this optimization is based on the assumption that the filter is linear. In the narrow-band demodulator, the discriminator is a nonlinear device. What is optimum for linear filters may not be optimum for nonlinear filters. This might explain why the error performance of the “optimum” noncoherent FSK is inferior to the narrow-band discriminator demodulator with the best set of parameters ($BT = 1$ and $h = 0.707$).

If the IF filter's bandwidth is sufficiently broad so that distortion of the signal can be ignored, and the post-detection low-pass filter is approximated by an ideal integrator with an integration time of T , then a simple expression of the symbol error probability for M -ary orthogonal FSK signals demodulated by the discriminator is given in [4] as

$$P_s = \left[\frac{1}{2} + \frac{1}{4} \left(\frac{M}{2} + 1 \right) \right] \exp\left(-\frac{2 E_s}{M N_o}\right) \quad (3.15)$$

When compared with the optimum noncoherent receiver whose error rate behaves as $\exp[-E_s/2N_o]$ (see (3.14)) we have lost a factor of $M/4$ in the error exponent by substituting discriminator detection for matched filter detection. When $M \leq 4$, there is actually no loss, rather there is a gain in symbol error performance. When $M = 2$, (3.15) becomes $\exp(-E_s/N_o)$ which is better by 3dB than the matched filter case. And it is 1.5dB better than the Gaussian filter case shown in Figure 3.27. The previous reasoning that explains why narrow-band discriminator detection performs better than optimum noncoherent detection can also be applied here to explain why the wide-band discriminator performs better.

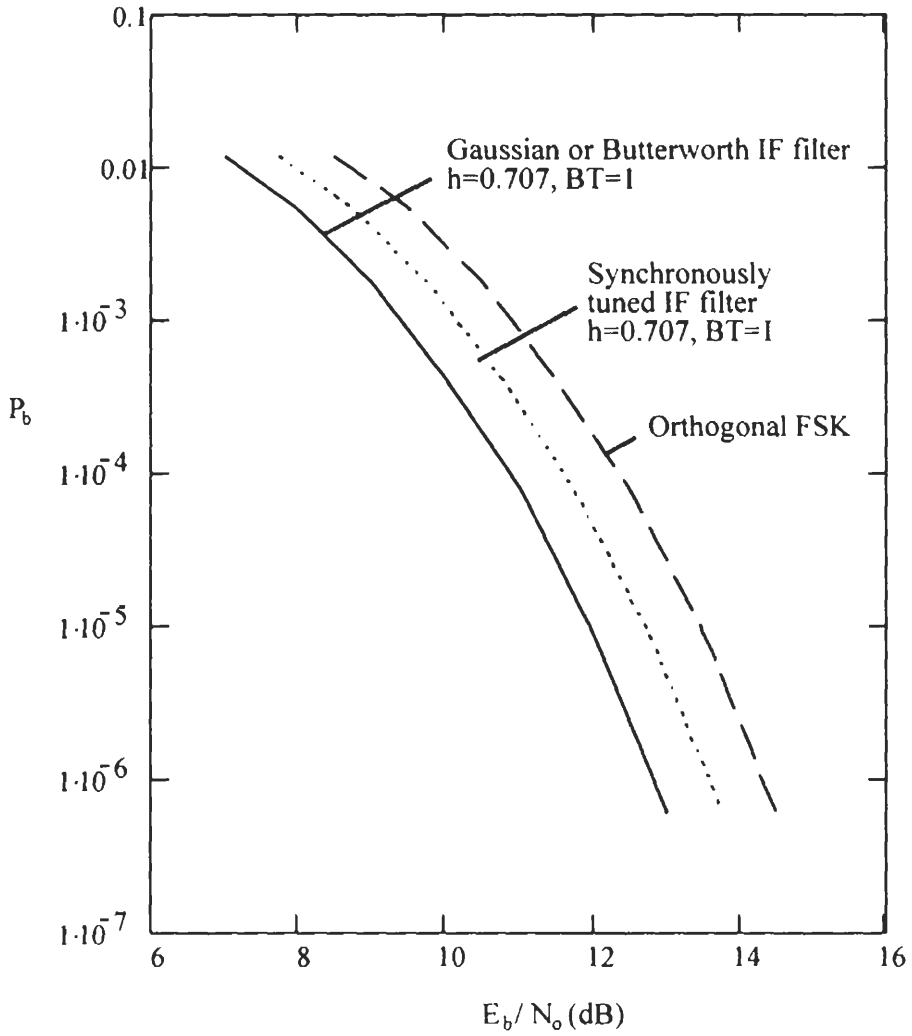


Figure 3.27 P_b of FSK demodulated by limiter-discriminator detection and integrate-and-dump post-detection filtering.

3.6 SYNCHRONIZATION

For coherent detection of the FSK signal the reference signals $\cos 2\pi f_i t$, $i = 1, 2$ and the bit timing signal must be recovered from the received signal. However, since practical systems never use coherent demodulation, there are no carrier recovery schemes found in the literature. For the usual Sunde's FSK, since the signal has two strong spectral components at f_1 and f_2 , two phase lock loops may be used to extract f_1 and f_2 from the FSK signal.

For noncoherent demodulation, only symbol synchronization is needed. Symbol timing can be achieved by generating the symbol clock signal using an early/late-gate circuit. Since symbol timing recovery problem is common to FSK and PSK modulation schemes, we leave it to be discussed at the end of the next chapter on PSK.

3.7 SUMMARY

In this chapter we have discussed coherent and noncoherent binary FSK and M-ary FSK schemes. For both cases we looked into the conditions for phase continuity and signal orthogonality. For phase continuity of coherent FSK (including MFSK), we found that the sufficient condition is that the frequency separation is an integer multiple of $1/T$. However, this is not necessary since there is a special form of binary FSK, namely MSK, which has a separation of $1/2T$. MSK is an important modulation scheme which is covered in great detail in Chapter 5. For orthogonality of the coherent FSK (including MFSK) the signal frequencies must be integer multiple of $1/4T$ and the separation must be integer multiple of $1/2T$. The phase of noncoherent FSK signal is not continuous and its orthogonality requires that the frequency separation be integer multiple of $1/T$. So the minimum separation for noncoherent FSK is double that of the coherent one.

The power spectral densities of FSK, both binary and M-ary, in the form of expressions or curves, were presented in this chapter.

We also presented modulators and demodulators, both coherent and noncoherent, binary and M-ary, in this chapter. The coherent demodulators consist of correlators or equivalently, matched filters and samplers. They require reference signals that are synchronized with the transmitted signals. The noncoherent demodulators consist of correlators and squarers, or equivalently, matched filters and envelope detectors. They do not require that reference signals be synchronous to the transmitted signals. Therefore additional squarers or envelope detectors are used to eliminate the adverse effect of random phase difference between the reference signals and the received signals. Since circuits of generating synchronous reference signals are very

costly, most of FSK receivers use noncoherent demodulation.

It is expected that the error performance of the noncoherent receivers is inferior to that of the coherent ones. However, the degradation is only a fraction of a dB. The expressions and curves for the error probabilities are also presented in great detail.

Finally we explored other possible demodulations. The discriminator demodulator is simple and efficient. It is even better than the noncoherent optimum demodulator for BFSK.

References

- [1] Anderson, R. R., and J. Salz, "Spectra of digital FM," *Bell System Technical Journal*, vol. 44, July-August, 1965, pp.1165-1189.
- [2] Tjhung, T. T., and P. H. Wittke, "Carrier transmission of binary data in a restricted band," *IEEE Trans. Comm. Tech.*, vol. 18, no. 4, August 1970, pp. 295-304.
- [3] Pawula, R. F., "On the theory of error rates for narrow-band digital FM," *IEEE Trans. Comm.*, vol. 29, no. 11, Nov. 1981, pp. 1634-1643.
- [4] Mazo, J. E., "Theory of error rates for digital FM," *Bell System Technical Journal*, vol. 45, Nov. 1966, pp. 1511-1535.

Selected Bibliography

- Couch II, L. W., *Digital and Analog Communication Systems*, 3rd Ed., New York: Macmillan, 1990.
- Haykin, S., *Digital Communications*, New York: John Wiley & Sons, Inc., 1988.
- Salz, J., "Performance of multilevel narrow-band FM digital communication systems," *IEEE Trans. Comm. Tech.*, vol. 13, no.4, Dec. 1975, pp. 420-424.
- Sklar, B., *Digital Communications, Fundamentals and Applications*, Englewood Cliff, New Jersey: Prentice Hall, 1988.
- Smith, D. R., *Digital Transmission Systems*, Second Edition, New York: Van Nostrand Reinhold, 1993.
- Sunde, E. D., "Ideal binary pulse transmission by AM and FM," *Bell System Technical Journal*, vol. 38, Nov. 1959, pp. 1357-1426.
- Van Trees, H. L., *Detection, Estimation, and Modulation Theory. Part I*, New York: John Wiley & Sons, Inc., 1968.

Chapter 4

Phase Shift Keying

Phase shift keying (PSK) is a large class of digital modulation schemes. PSK is widely used in the communication industry. In this chapter we study each PSK modulation scheme in a single section where signal description, power spectral density, modulator/demodulator block diagrams, and receiver error performance are all included. First we present coherent binary PSK(BPSK) and its noncoherent counterpart, differential BPSK (DBPSK), in Sections 4.1 and 4.2. Then we discuss in Section 4.3 M-ary PSK (MPSK) and its PSD in Section 4.4. The noncoherent version, differential MPSK (DMPSK) is treated in Section 4.5. We discuss in great detail quadrature PSK (QPSK) and differential QPSK (DQPSK) in Sections 4.6 and 4.7, respectively. Section 4.8 is a brief discussion of offset QPSK (OQPSK). An important variation of QPSK, the $\pi/4$ -DQPSK which has been designated as the American standard of the second-generation cellular mobile communications, is given in Section 4.9. Section 4.10 is devoted to carrier and clock recovery. Finally, we summarize the chapter with Section 4.11.

4.1 BINARY PSK

Binary data are represented by two signals with different phases in BPSK. Typically these two phases are 0 and π , the signals are

$$\begin{aligned} s_1(t) &= A \cos 2\pi f_c t, & 0 \leq t \leq T, & \text{ for } 1 \\ s_2(t) &= -A \cos 2\pi f_c t, & 0 \leq t \leq T, & \text{ for } 0 \end{aligned} \quad (4.1)$$

These signals are called *antipodal*. The reason that they are chosen is that they have a correlation coefficient of -1 , which leads to the minimum error probability for the same E_b/N_o , as we will see shortly. These two signals have the same frequency and energy.

As we will see in later sections, all PSK signals can be graphically represented

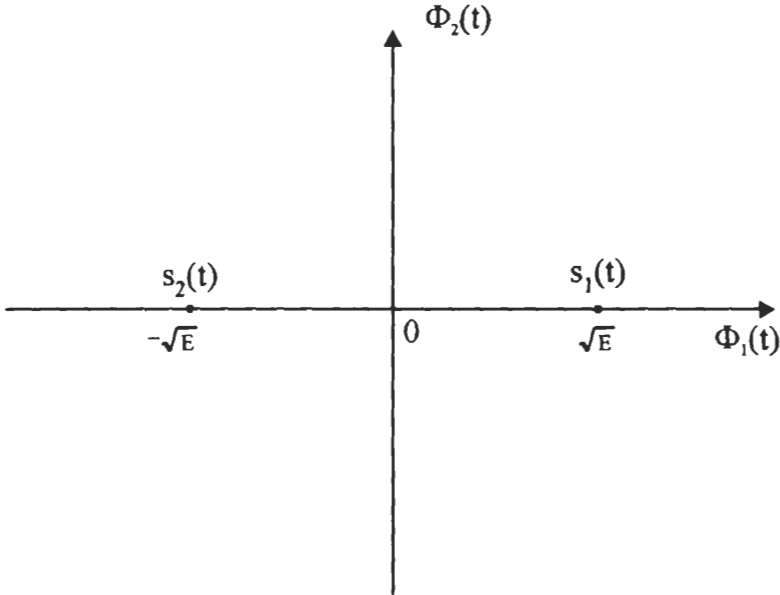


Figure 4.1 BPSK signal constellation.

by a *signal constellation* in a two-dimensional coordinate system with

$$\phi_1(t) = \sqrt{\frac{2}{T}} \cos 2\pi f_c t, \quad 0 \leq t \leq T \quad (4.2)$$

and

$$\phi_2(t) = -\sqrt{\frac{2}{T}} \sin 2\pi f_c t, \quad 0 \leq t \leq T \quad (4.3)$$

as its horizontal and vertical axis, respectively. Note that we deliberately add a minus sign in $\phi_2(t)$ so that PSK signal expressions will be a sum instead of a difference (see (4.14)). Many other signals, especially QAM signals, can also be represented in the same way. Therefore we introduce the signal constellation of BPSK here as shown in Figure 4.1 where $s_1(t)$ and $s_2(t)$ are represented by two points on the horizontal axis, respectively, where

$$E = \frac{A^2 T}{2}$$

The waveform of a BPSK signal generated by the modulator in Figure 4.3 for a data stream $\{10110\}$ is shown in Figure 4.2. The waveform has a constant envelope like FSK. Its frequency is constant too. In general the phase is not continuous at

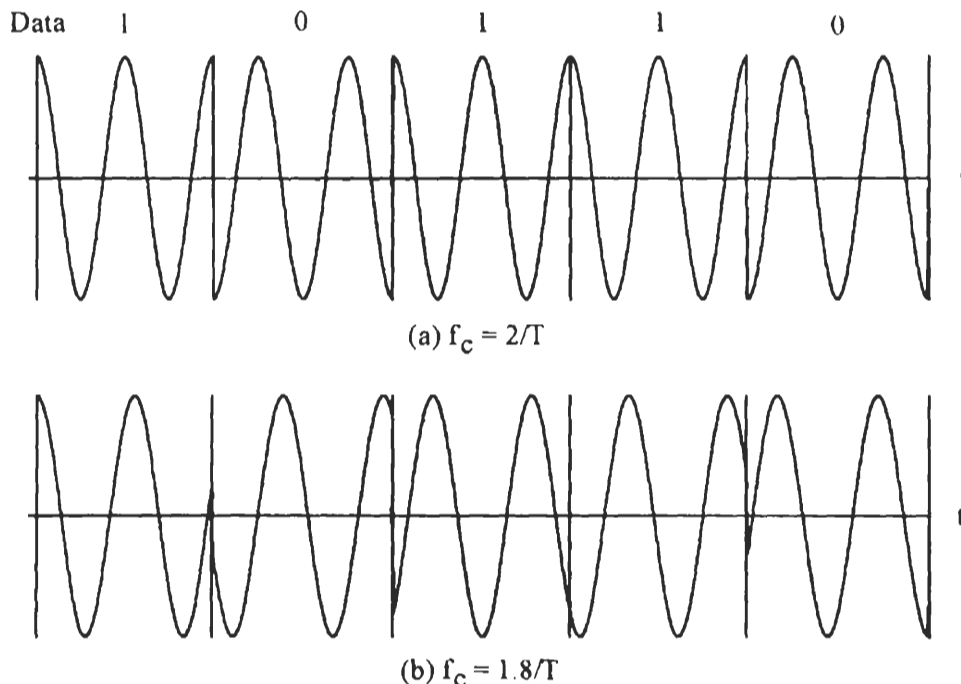


Figure 4.2 BPSK waveforms.

bit boundaries. If the $f_c = m R_b = m/T$, where m is an integer and R_b is the data bit rate, and the bit timing is synchronous with the carrier, then the initial phase at a bit boundary is either 0 or π (Figure 4.2(a)), corresponding to data bit 1 or 0. However, if the f_c is not an integer multiple of R_b , the initial phase at a bit boundary is neither 0 nor π (Figure 4.2(b)). In other words, the modulated signals are not the ones given in (4.1). We will show next in discussion of demodulation that condition $f_c = m R_b$ is necessary to ensure minimum bit error probability. However, if $f_c \gg R_b$, this condition can be relaxed and the resultant BER performance degradation is negligible.¹

The modulator which generates the BPSK signal is quite simple (Figure 4.3 (a)). First a bipolar data stream $a(t)$ is formed from the binary data stream

$$a(t) = \sum_{k=-\infty}^{\infty} a_k p(t - kT) \quad (4.4)$$

¹ This is true for all PSK schemes and PSK-derived schemes, including QPSK, MSK, and MPSK. We will not mention this again when we discuss other PSK schemes.

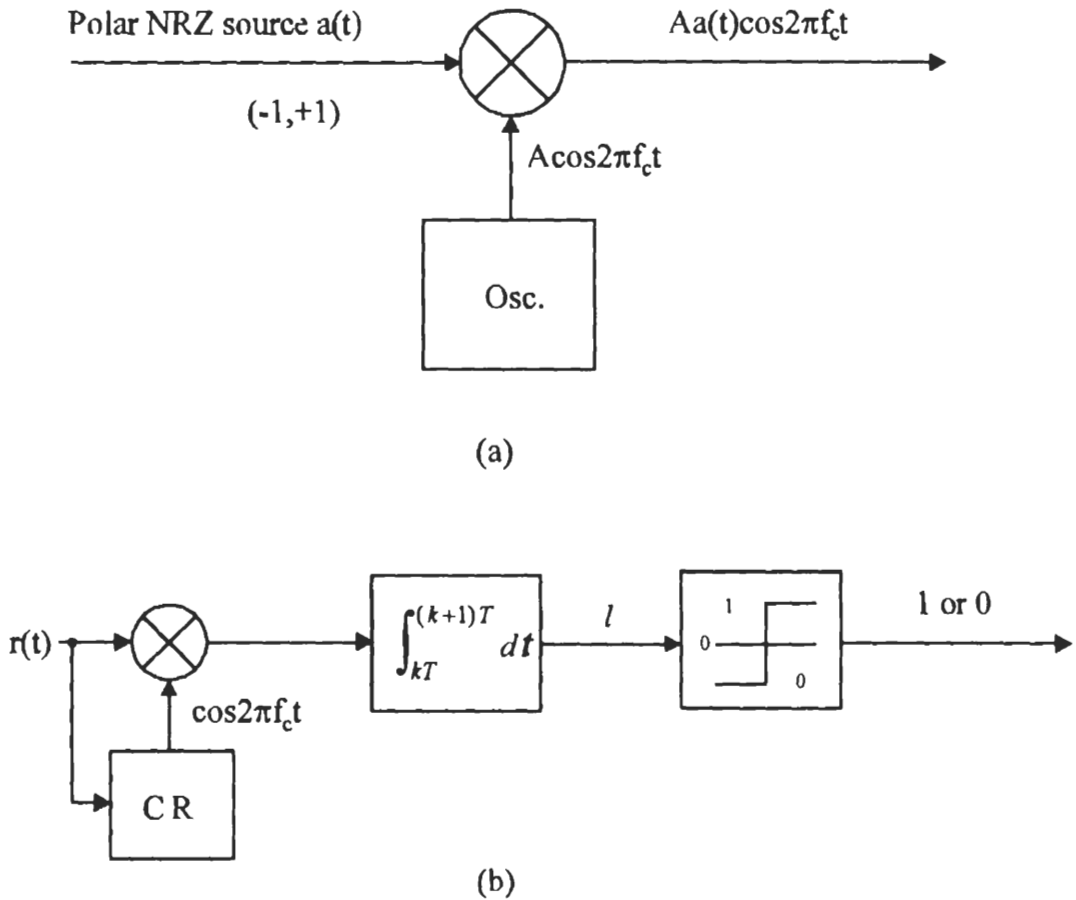


Figure 4.3 BPSK modulator (a), and coherent BPSK demodulator (b).

where $a_k \in \{+1, -1\}$, $p(t)$ is the rectangular pulse with unit amplitude defined on $[0, T]$. Then $a(t)$ is multiplied with a sinusoidal carrier $A \cos 2\pi f_c t$. The result is the BPSK signal

$$s(t) = Aa(t) \cos 2\pi f_c t, \quad -\infty < t < \infty \quad (4.5)$$

Note that the bit timing is not necessarily synchronous with the carrier.

The coherent demodulator of BPSK falls in the class of coherent detectors for binary signals as described in Appendix B. The coherent detector could be in the form of a correlator or matched filter. The correlator's reference signal is the difference signal ($s_d(t) = 2A \cos 2\pi f_c t$). Figure 4.3(b) is the coherent receiver using a correlator where the reference signal is the scaled-down version of the difference signal. The reference signal must be synchronous to the received signal in frequency and phase.

It is generated by the carrier recovery (CR) circuit. Using a matched filter instead of a correlator is not recommended at passband since a filter with $h(t) = \cos 2\pi f_c(T-t)$ is difficult to implement.

In the absence of noise, setting $A = 1$, the output of the correlator at $t = (k+1)T$ is

$$\begin{aligned} & \int_{kT}^{(k+1)T} r(t) \cos 2\pi f_c t dt \\ &= \int_{kT}^{(k+1)T} a_k \cos^2 2\pi f_c t dt \\ &= \frac{1}{2} \int_{kT}^{(k+1)T} a_k (1 + \cos 4\pi f_c t) dt \\ &= \frac{T}{2} a_k + \frac{a_k}{8\pi f_c} [\sin 4\pi f_c (k+1)T - \sin 4\pi f_c kT] \end{aligned}$$

If $f_c = m R_b$, the second term is zero, thus the original signal $a(t)$ is perfectly recovered (in the absence of noise). If $f_c \neq m R_b$, the second term will not be zero. However, as long as $f_c \gg R_b$, the second term is much smaller than the first term so that its effect is negligible.

The bit error probability can be derived from the formula for general binary signals (Appendix B):

$$P_b = Q \left(\sqrt{\frac{E_1 + E_2 - 2\rho_{12}\sqrt{E_2 E_1}}{2N_o}} \right)$$

For BPSK $\rho_{12} = -1$ and $E_1 = E_2 = E_b$, thus

$$P_b = Q \left(\sqrt{\frac{2E_b}{N_o}} \right), \text{ (coherent BPSK)} \quad (4.6)$$

A typical example is that, at $E_b/N_o = 9.6$ dB, $P_b = 10^{-5}$. Figure 4.4 shows the P_b curve of BPSK. The curves of coherent and noncoherent BFSK are also shown in the figure. Recall the P_b expression for coherent BFSK is $P_b = Q \left(\sqrt{\frac{E_b}{N_o}} \right)$ which is 3 dB inferior to coherent BPSK. However, coherent BPSK requires that the reference signal at the receiver to be synchronized in phase and frequency with the received signal. This will be discussed in Section 4.10. Noncoherent detection of BPSK is also possible. It is realized in the form of differential BPSK which will be studied in the next section.

Next we proceed to find the power spectral density of the BPSK signal. It suf-

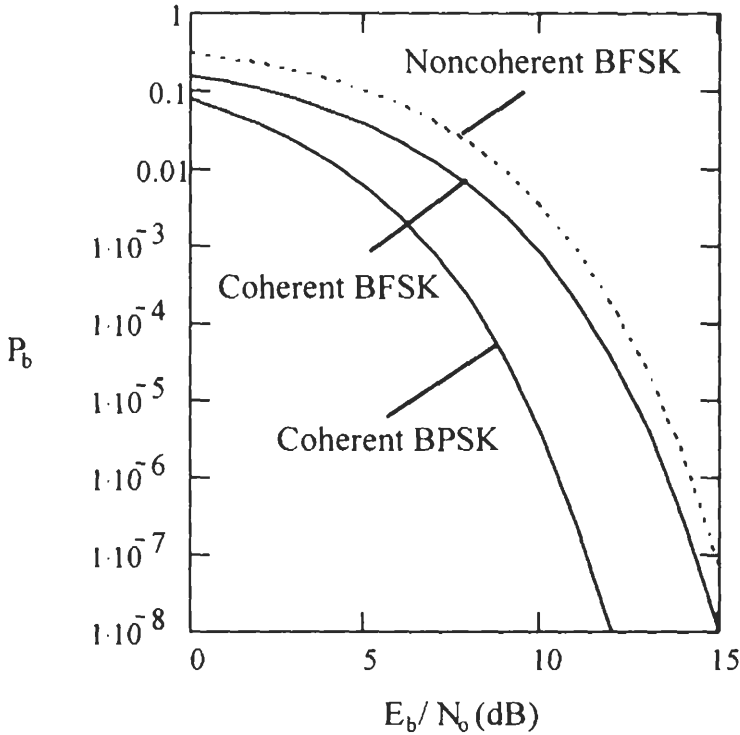


Figure 4.4 P_b of BPSK in comparison with BFSK.

fices to find the PSD of the baseband shaping pulse. As shown in Appendix A, the PSD of a binary, bipolar, equiprobable, stationary, and uncorrelated digital waveform is just equal to the energy spectral density of the pulse divided by the symbol duration (see (A.19)). The basic pulse of BPSK is just a rectangular pulse²

$$p(t) = \begin{cases} A, & 0 < t < T \\ 0, & \text{otherwise} \end{cases} \quad (4.7)$$

Its Fourier transform is

$$G(f) = AT \frac{\sin \pi f T}{\pi f T} e^{-2\pi f T/2}$$

Thus the PSD of the baseband BPSK signal is

$$\Psi_s(f) = \frac{|G(f)|^2}{T} = A^2 T \left(\frac{\sin \pi f T}{\pi f T} \right)^2, \quad (\text{BPSK}) \quad (4.8)$$

² The bipolarity of the baseband waveform of BPSK is controlled by the bipolar data $a_k = \pm 1$.

which is plotted in Figure 4.5. From the figure we can see that the null-to-null bandwidth $B_{null} = 2/T = 2R_b$. (Keep in mind that the PSD at the carrier frequency is two-sided about f_c .) Figure 4.5(c) is the out-of-band power curve which is defined by (2.21). From this curve we can estimate that $B_{90\%} \approx 1.7R_b$ (corresponding to -10 dB point on the curve). We also calculated that $B_{99\%} \approx 20R_b$.

4.2 DIFFERENTIAL BPSK

In Chapter 2 we first introduced differential encoding and decoding of binary data. This technique can be used in PSK modulation. We denote differentially encoded BPSK as DEBPSK. Figure 4.6 (a) is the DEBPSK modulator. DEBPSK signal can be coherently demodulated or differentially demodulated. We denote the modulation scheme that uses differential encoding and differential demodulation as DBPSK, which is sometimes simply called DPSK.

DBPSK does not require a coherent reference signal. Figure 4.6(b) is a simple, but suboptimum, differential demodulator which uses the previous symbol as the reference for demodulating the current symbol.³ The front-end bandpass filter reduces noise power but preserves the phase of the signal. The integrator can be replaced by an LPF. The output of the integrator is

$$l = \int_{kT}^{(k+1)T} r(t)r(t-T)dt$$

In the absence of noise and other channel impairment,

$$l = \int_{kT}^{(k+1)T} s_k(t)s_{k-1}(t)dt = \begin{cases} E_b, & \text{if } s_k(t) = s_{k-1}(t) \\ -E_b, & \text{if } s_k(t) = -s_{k-1}(t) \end{cases}$$

where $s_k(t)$ and $s_{k-1}(t)$ are the current and the previous symbols. The integrator output is positive if the current signal is the same as the previous one, otherwise the output is negative. This is to say that the demodulator makes decisions based on the difference between the two signals. Thus information data must be encoded as the difference between adjacent signals, which is exactly what the differential encoding can accomplish. Table 4.1 shows an example of differential encoding, where an arbitrary reference bit 1 is chosen. The encoding rule is

$$d_k = \overline{a_k \oplus d_{k-1}}$$

³ This is the commonly referred DPSK demodulator. Another DPSK demodulator is the optimum differentially coherent demodulator. Differentially encoded PSK can also be coherently detected. These will be discussed shortly.

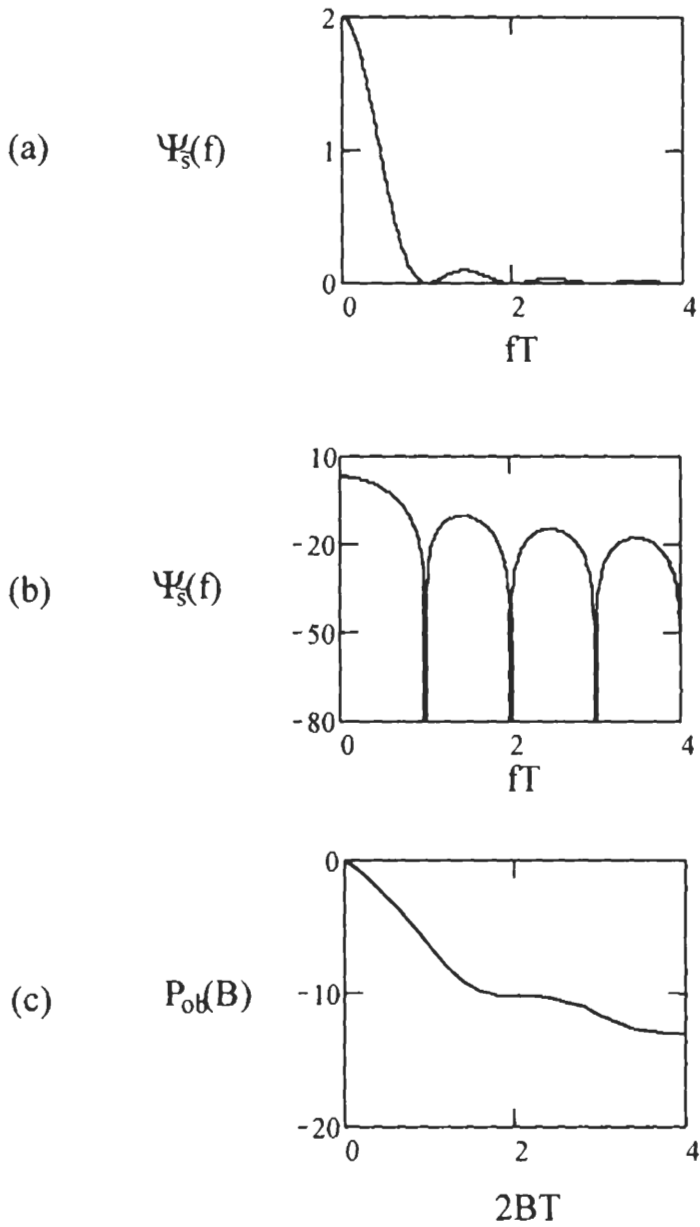


Figure 4.5 Power spectral density of BPSK: (a) linear, (b) logarithmic, (c) out-of-band power.

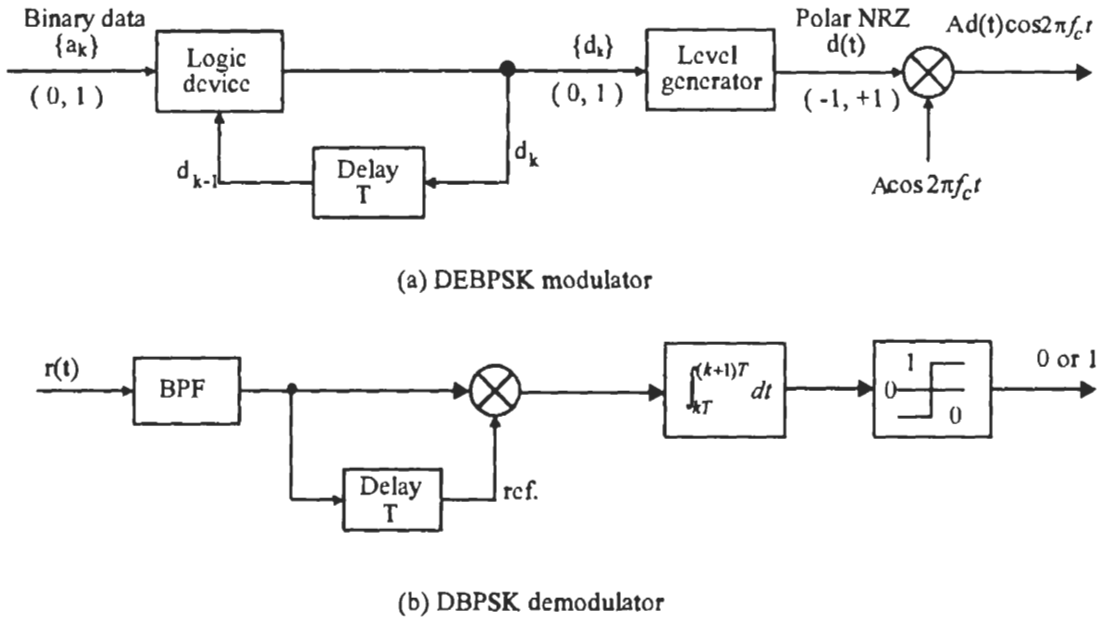


Figure 4.6 DBPSK modulator (a), and demodulator (b).

Inversely we can recover a_k from d_k using

$$a_k = \overline{d_k \oplus d_{k-1}}$$

If d_k and d_{k-1} are the same, then they represent a 1 of a_k . If d_k and d_{k-1} are different, they represent a 0 of a_k . This can be verified by comparing sequences $\{d_k\}$ and $\{a_k\}$ in the table. The sequence $\{d_k\}$ is modulated onto a carrier with phase 0 or π . In the absence of noise and other channel impairment, the demodulator output \hat{a}_k is identical to the message sequence.

The preceding receiver is suboptimum, since the reference signal is the previous symbol which is noisy. The optimum noncoherent, or differentially coherent, demodulation of DEBPSK is presented now. As discussed above, a message bit is represented by two modulated symbols. If the transmitted bit is 1, the two symbols are the same. Thus we can define a signal with a duration of $2T$ as follows to represent binary 1

$$\xi_1(t) = \begin{cases} A \cos 2\pi f_c t, & 0 \leq t \leq T \\ A \cos 2\pi f_c t, & T \leq t \leq 2T \end{cases}, \quad \text{for binary 1}$$

Modulation	ref.									
Message a_k										
Encoding $d_k = a_k \oplus d_{k-1}$	1	1	0	0	0	1	0	1	1	1
Signal phase θ	0	0	π	π	π	0	π	0	0	0
Demodulation										
$\frac{l}{E_b} = \frac{1}{E_b} \int_{kT}^{(k+1)T} s_k(t) s_{k-1}(t) dt$	1	-1	1	1	-1	-1	-1	1	1	1
Demodulator output \hat{a}_k	1	0	1	1	0	0	0	1	1	1

Table 4.1 Examples of differential coding.

If the transmitted bit is 0, the two symbols are different. Thus we can define

$$\xi_2(t) = \begin{cases} A \cos 2\pi f_c t, & 0 \leq t \leq T \\ -A \cos 2\pi f_c t, & T \leq t \leq 2T \end{cases}, \quad \text{for binary 0}$$

Note that in the modulated signal stream, the $2T$ -symbols are overlapped by T seconds.

Since we desire an optimum noncoherent demodulation, the DBPSK receiver may be implemented in the general forms for signals with unknown phases as depicted in Appendix B. However, a simpler form is possible due to the special property of the signals. The simpler form avoids the squarers or matched filters. We derive this receiver starting from (B.55). Assuming the received signal is $r(t)$, the sufficient statistic for $\xi_1(t)$ is

$$\begin{aligned} l_1^2 &= \left(\int_0^{2T} r(t) \xi_1(t) dt \right)^2 + \left(\int_0^{2T} r(t) \xi_1(t, \frac{\pi}{2}) dt \right)^2 \\ &= \left(\int_0^{2T} r(t) A \cos 2\pi f_c t dt \right)^2 + \left(\int_0^{2T} r(t) A \sin 2\pi f_c t dt \right)^2 \\ &= (w_0 + w_1)^2 + (z_0 + z_1)^2 \end{aligned}$$

where

$$w_0 \triangleq \int_0^T r(t) A \cos 2\pi f_c t dt$$

$$w_1 \triangleq \int_T^{2T} r(t) A \cos 2\pi f_c t dt$$

$$z_0 \triangleq \int_0^T r(t) A \sin 2\pi f_c t dt$$

$$z_1 \triangleq \int_T^{2T} r(t) A \sin 2\pi f_c t dt$$

Similarly, the sufficient statistic for $\xi_2(t)$ is

$$l_2^2 = (w_0 - w_1)^2 + (z_0 - z_1)^2$$

The decision rule is

$$l_1^2 \stackrel{1}{\geq} l_2^2$$

Substituting expressions for l_1^2 and l_2^2 into the above expression and cancelling like terms, we obtain

$$x \triangleq w_1 w_0 + z_1 z_0 \stackrel{1}{\geq} 0$$

For the k th symbol period, this rule is

$$x_k \triangleq w_k w_{k-1} + z_k z_{k-1} \stackrel{1}{\geq} 0 \quad (4.9)$$

This rule can be implemented by the receiver shown in Figure 4.7. The reference signals are locally generated since phase synchronization between $r(t)$ and the reference signals is not required. However, the frequency of the reference signals must be the same as the received signal's. This can be maintained by using stable oscillators, such as crystal oscillators, in both transmitter and receiver. However, in the case where Doppler shift exists in the carrier frequency, such as in mobile communications, frequency tracking is needed to maintain the same frequency. In this case the local oscillator must be synchronized in frequency to the received signal. The reference signals' amplitude A is set as 1 in Figure 4.7. In fact A could be any value since its value will not affect the decision rule in (4.9). The correlators produce w_k and z_k . The x_k is calculated by the delay-and-multiply circuits or differential decoders.

To derive the error probability of the optimum demodulator, we observe that two DBPSK symbols are orthogonal over $[0, 2T]$ since

$$\int_0^{2T} \xi_1(t) \xi_2(t) dt = \int_0^T (A \cos 2\pi f_c t)^2 dt - \int_T^{2T} (A \cos 2\pi f_c t)^2 dt = 0$$

In other words DBPSK is a special case of noncoherent orthogonal modulation with $T_s = 2T$ and $E_s = 2E_b$. Hence using the result of Appendix B (B.56) we have the

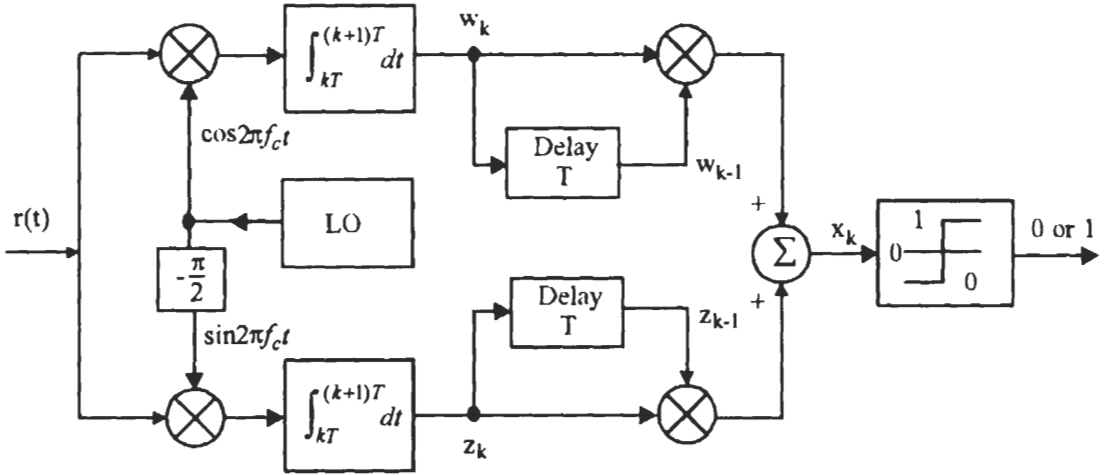


Figure 4.7 Optimum demodulator for DBPSK.

bit error probability

$$P_b = \frac{1}{2} e^{-E_b/N_o}, \quad (\text{optimum DBPSK}) \quad (4.10)$$

Note that the demodulator of Figure 4.7 does not require phase synchronization between the reference signals and the received signal. But it does require the reference frequency be the same as the received signal. Therefore the suboptimum receiver in Figure 4.6(b) is more practical, and indeed it is the usual-sense DBPSK receiver. Its error performance is slightly inferior to that of the optimum given in (4.10).

The performance of the suboptimum receiver is given by Park in [1]. It is shown that if an ideal narrow-band IF filter with bandwidth W is placed before the correlator in Figure 4.6(b), the bit error probability is

$$P_b = \frac{1}{2} e^{-0.76E_b/N_o}, \quad \text{for } W = 0.5/T$$

or

$$P_b = \frac{1}{2} e^{-0.8E_b/N_o}, \quad \text{for } W = 0.57/T$$

which amounts to a loss of 1.2 dB and 1 dB, respectively, with respect to the optimum.

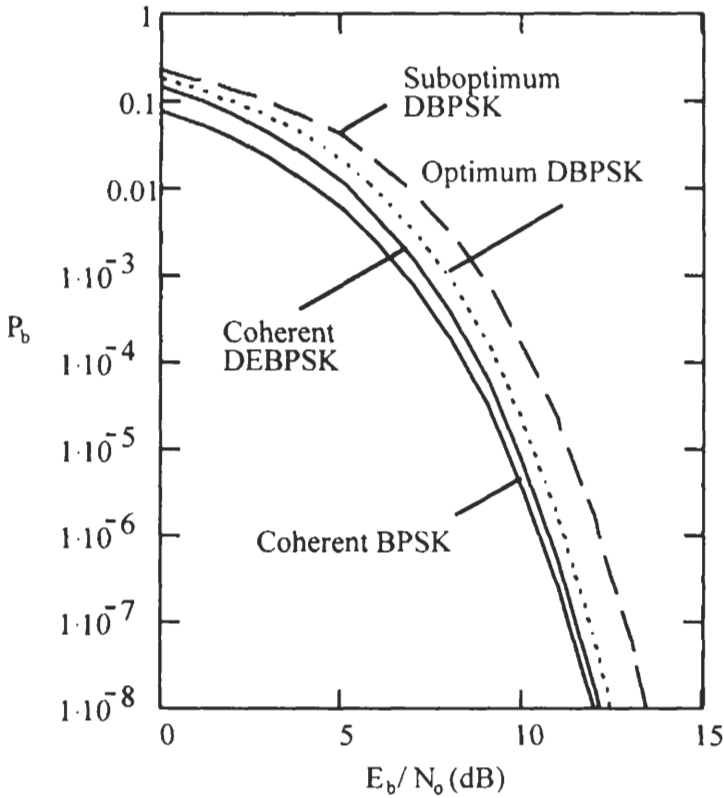


Figure 4.8 P_b of differential BPSK in comparison with coherent BPSK scheme.

If an ideal wide-band IF filter is used, then

$$P_b \approx Q\left(\sqrt{\frac{E_b}{N_o}}\right), \quad \text{for } W > 1/T$$

$$\approx \frac{1}{2\sqrt{\pi}\sqrt{E_b/2N_o}} e^{-E_b/2N_o}, \quad \text{for } W > 1/T, \text{ (Suboptimum DBPSK)}$$

Typical value of W is $1.5/T$. If W is too large or too small the above expression does not hold [1]. The P_b for the wide-band suboptimum receiver is about 2 dB worse than the optimum at high SNR. The bandwidth should be chosen as $0.57/T$ for the best performance. P_b curves of DBPSK are shown in Figure 4.8.

A differentially encoded BPSK signal can also be demodulated coherently (denoted as DEBPSK). It is used when the purpose of differential encoding is to eliminate phase ambiguity in the carrier recovery circuit for coherent PSK (see Section

4.10). This is not usually meant by the name DBPSK. DBPSK refers to the scheme of differential encoding and differentially coherent demodulation as we have discussed above.

In the case of DEBPSK, the bit error rate of the final decoded sequence $\{\hat{a}_k\}$. P_b is related to the bit error rate of the demodulated encoded sequence $\{\hat{d}_k\}$, $P_{b,d}$, by

$$P_b = 2P_{b,d}(1 - P_{b,d}) \quad (4.11)$$

as we have shown in Section 2.4.1 of Chapter 2. Substituting $P_{b,d}$ as in (4.6) into the above expression we have

$$P_b = 2Q\left(\sqrt{\frac{2E_b}{N_o}}\right) \left[1 - Q\left(\sqrt{\frac{2E_b}{N_o}}\right)\right], \quad (\text{DEBPSK}) \quad (4.12)$$

for coherently detected differentially encoded PSK. For large SNR, this is just about two times that of coherent BPSK without differential encoding.

Finally we need to say a few words of power spectral density of differentially encoded BPSK. Since the difference of differentially encoded BPSK from BPSK is differential encoding, which always produces an asymptotically equally likely data sequence (see Section 2.1), the PSD of the differentially encoded BPSK is the same as BPSK which we assume is equally likely. The PSD is shown in Figure 4.5. However, it is worthwhile to point out that if the data sequence is not equally likely the PSD of the BPSK is not the one in Figure 4.5, but the PSD of the differentially encoded PSK is still the one in Figure 4.5.

4.3 M-ARY PSK

The motivation behind MPSK is to increase the bandwidth efficiency of the PSK modulation schemes. In BPSK, a data bit is represented by a symbol. In MPSK, $n = \log_2 M$ data bits are represented by a symbol, thus the bandwidth efficiency is increased to n times. Among all MPSK schemes, QPSK is the most-often-used scheme since it does not suffer from BER degradation while the bandwidth efficiency is increased. We will see this in Section 4.6. Other MPSK schemes increase bandwidth efficiency at the expenses of BER performance.

M-ary PSK signal set is defined as

$$s_i(t) = A \cos(2\pi f_c t + \theta_i), \quad 0 \leq t \leq T, \quad i = 1, 2, \dots, M \quad (4.13)$$

where

$$\theta_i = \frac{(2i - 1)\pi}{M}$$

The carrier frequency is chosen as integer multiple of the symbol rate, therefore in any symbol interval, the signal initial phase is also one of the M phases. Usually M is chosen as a power of 2 (i.e., $M = 2^n$, $n = \log_2 M$). Therefore binary data stream is divided into n -tuples. Each of them is represented by a symbol with a particular initial phase.

The above expression can be written as

$$\begin{aligned} s_i(t) &= A \cos \theta_i \cos 2\pi f_c t - A \sin \theta_i \sin 2\pi f_c t \\ &= s_{i1} \phi_1(t) + s_{i2} \phi_2(t) \end{aligned} \quad (4.14)$$

where $\phi_1(t)$ and $\phi_2(t)$ are orthonormal basis functions (see (4.2) and (4.3)), and

$$s_{i1} = \int_0^T s_i(t) \phi_1(t) dt = \sqrt{E} \cos \theta_i$$

$$s_{i2} = \int_0^T s_i(t) \phi_2(t) dt = \sqrt{E} \sin \theta_i$$

where

$$E = \frac{1}{2} A^2 T$$

is the symbol energy of the signal. The phase is related with s_{i1} and s_{i2} as

$$\theta_i = \tan^{-1} \frac{s_{i2}}{s_{i1}}$$

The MPSK signal constellation is therefore two-dimensional. Each signal $s_i(t)$ is represented by a point (s_{i1}, s_{i2}) in the coordinates spanned by $\phi_1(t)$ and $\phi_2(t)$. The polar coordinates of the signal are (\sqrt{E}, θ_i) . That is, its magnitude is \sqrt{E} and its angle with respect to the horizontal axis is θ_i . The signal points are equally spaced on a circle of radius \sqrt{E} and centered at the origin. The bits-signal mapping could be arbitrary provided that the mapping is one-to-one. However, a method called Gray coding is usually used in signal assignment in MPSK. Gray coding assigns n -tuples with only one-bit difference to two adjacent signals in the constellation. When an M -ary symbol error occurs, it is more likely that the signal is detected as the adjacent signal on the constellation, thus only one of the n input bits is in error. Figure 4.9 is the constellation of 8-PSK, where Gray coding is used for bit assignment. Note that

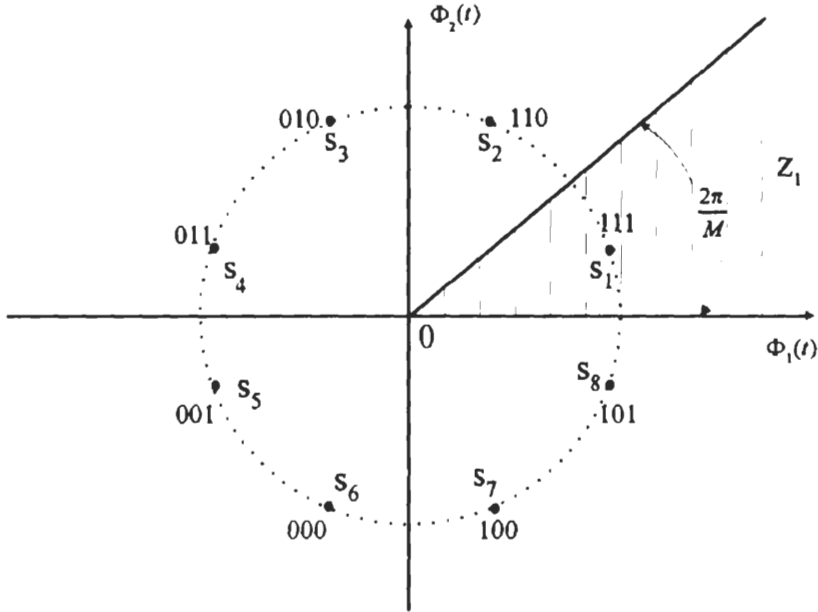


Figure 4.9 8-PSK constellation with Gray coded bit assignment.

BPSK and QPSK are special cases of MPSK with $M = 2$ and 4 , respectively. On the entire time axis, we can write MPSK signal as

$$s(t) = s_1(t) \cos 2\pi f_c t - s_2(t) \sin 2\pi f_c t, \quad -\infty < t < \infty \quad (4.15)$$

where

$$s_1(t) = A \sum_{k=-\infty}^{\infty} \cos(\theta_k) p(t - kT) \quad (4.16)$$

$$s_2(t) = A \sum_{k=-\infty}^{\infty} \sin(\theta_k) p(t - kT) \quad (4.17)$$

where θ_k is one of the M phases determined by the input binary n -tuple, $p(t)$ is the rectangular pulse with unit amplitude defined on $[0, T]$. Expression (4.15) implies that the carrier frequency is an integer multiple of the symbol timing so that the initial phase of the signal in any symbol period is θ_k .

Since MPSK signals are two-dimensional, for $M \geq 4$, the modulator can be implemented by a quadrature modulator. The MPSK modulator is shown in Figure 4.10. The only difference for different values of M is the level generator. Each n -tuple of the input bits is used to control the level generator. It provides the I-

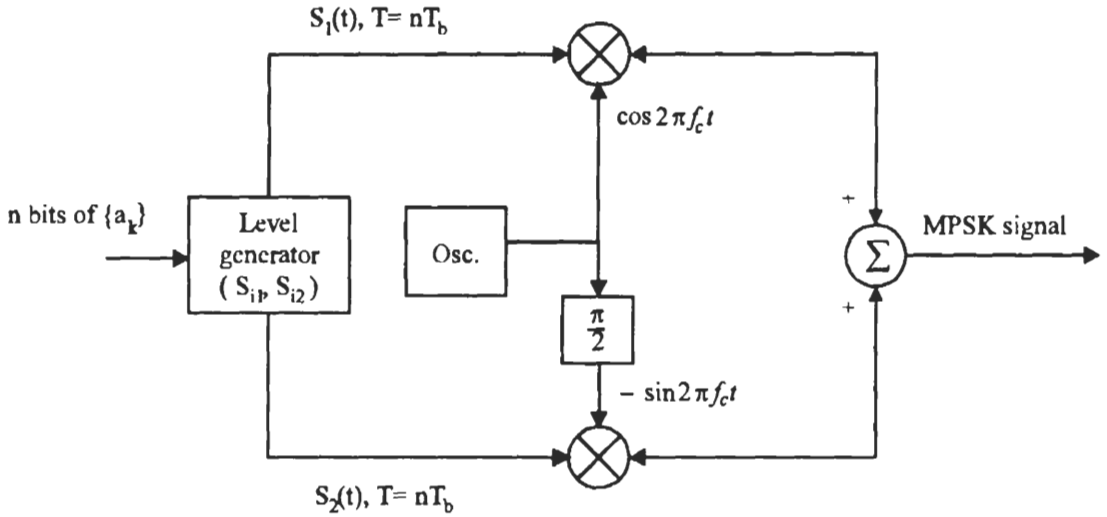


Figure 4.10 MPSK modulator.

and Q-channels the particular sign and level for a signal's horizontal and vertical coordinates, respectively. For QPSK, the level generator is particularly simple, it is simply a serial-to-parallel converter (see Section 4.6).

Modern technology intends to use completely digital devices. In such an environment, MPSK signals are digitally synthesized and fed to a D/A converter whose output is the desired phase modulated signal.

The coherent demodulation of MPSK could be implemented by one of the coherent detectors for M-ary signals as described in Appendix B. Since the MPSK signal set has only two basis functions, the simplest receiver is the one that uses two correlators (Figure B.8 with $N = 2$). Due to the special characteristic of the MPSK signal, the general demodulator of Figure B.8 can be further simplified. For MPSK the sufficient statistic is

$$\begin{aligned}
 l_i &= \int_0^T r(t) s_i(t) dt = \int_0^T r(t) [s_{i1} \phi_1(t) + s_{i2} \phi_2(t)] dt \\
 &= \int_0^T r(t) [\sqrt{E} \cos \theta_i \phi_1(t) + \sqrt{E} \sin \theta_i \phi_2(t)] dt \\
 &= \sqrt{E} [r_1 \cos \theta_i + r_2 \sin \theta_i]
 \end{aligned} \tag{4.18}$$

where

$$r_1 \triangleq \int_0^T r(t) \phi_1(t) dt = \int_0^T [s(t) + n(t)] \phi_1(t) dt = s_{i1} + n_1$$

$$r_2 \triangleq \int_0^T r(t)\phi_2(t)dt = \int_0^T [s(t) + n(t)]\phi_2(t)dt = s_{i2} + n_2$$

are independent Gaussian random variables with mean values s_{i1} and s_{i2} , respectively. Their variance is $N_o/2$.

Let

$$r_1 = \rho \cos \hat{\theta}$$

$$r_2 = \rho \sin \hat{\theta}$$

then

$$\rho = \sqrt{r_1^2 + r_2^2} \quad (4.19)$$

$$\hat{\theta} \triangleq \tan^{-1} \frac{r_2}{r_1} \quad (4.20)$$

$$\begin{aligned} l_i &= \sqrt{E}[\rho \cos \hat{\theta} \cos \theta_i + \rho \sin \hat{\theta} \sin \theta_i] \\ &= \sqrt{E}\rho \cos(\theta_i - \hat{\theta}) \end{aligned}$$

In the absence of noise, $\hat{\theta} = \tan^{-1} r_2/r_1 = \tan^{-1} s_{i2}/s_{i1} = \theta_i$. With noise, $\hat{\theta}$ will deviate from θ_i . Since ρ is independent of any signal, then choosing the largest l_i is equivalent to choosing the smallest $|\theta_i - \hat{\theta}|$. This rule is in fact to choose signal $s_i(t)$ when $\mathbf{r} = \begin{bmatrix} r_1 \\ r_2 \end{bmatrix}$ falls inside the pie-shape decision region of the signal (see Figure 4.9). Figure 4.11 is the demodulator based on the above decision rule where subscript k indicates the k th symbol period and CR stands for carrier recovery. Note that the amplitude of the reference signals can be any value, which is $\sqrt{2/T}$ in the figure, since the effect of the amplitude is cancelled when computing $\hat{\theta}_k$.

The symbol error probability can be derived as follows. Given $s_i(t)$ is transmitted (or hypothesis H_i is true), the received vector $\mathbf{r} = \begin{bmatrix} r_1 \\ r_2 \end{bmatrix}$ is a point in the $\phi_1(t) - \phi_2(t)$ plane. Its joint probability density function is two-dimensional.

$$p(\mathbf{r}/H_i) = \frac{1}{\pi N_o} \exp\left\{-\frac{1}{N_o}[(r_1 - \sqrt{E} \cos \theta_i)^2 + (r_2 - \sqrt{E} \sin \theta_i)^2]\right\}$$

Geometrically, the PDF is a bell-shape surface centered at $\mathbf{s}_i = \begin{bmatrix} s_{i1} \\ s_{i2} \end{bmatrix}$ (Figure 4.12).

An error occurs when \mathbf{r} falls outside the decision region Z_i (see Figure 4.9).

Thus

$$P_s = 1 - \int_{Z_i} p(\mathbf{r}/H_i) d\mathbf{r}$$

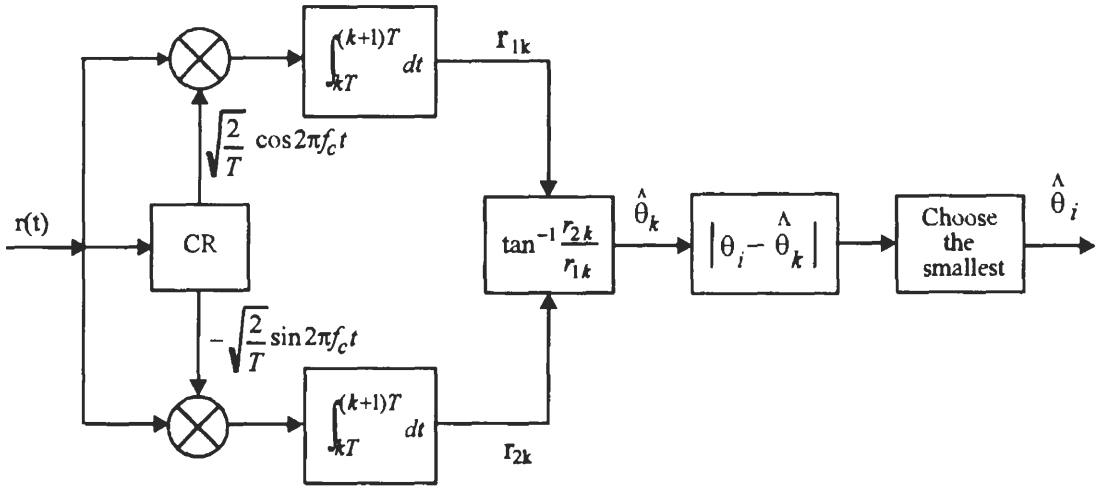


Figure 4.11 Coherent MPSK demodulator using two correlators.

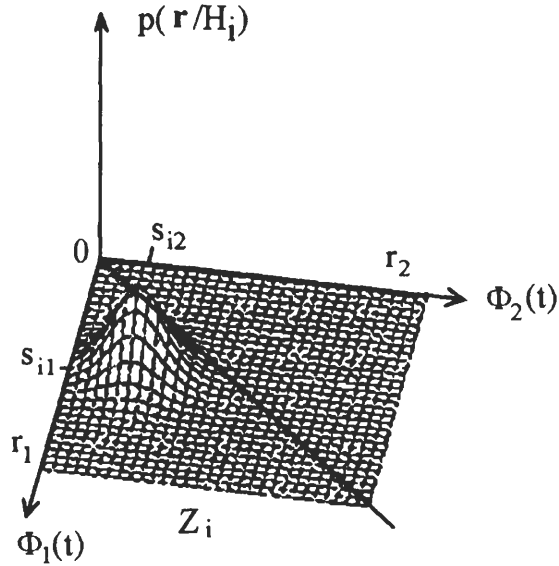


Figure 4.12 Joint PDF of \mathbf{r} given $s_i(t)$ is transmitted.

Using (4.19) and (4.20) we can transform the above into polar coordinates.⁴

$$\begin{aligned} P_s &= 1 - \int_{Z_i} \frac{1}{\pi N_o} \exp\left\{-\frac{1}{N_o}[\rho^2 + E - 2\rho\sqrt{E} \cos(\theta_i - \hat{\theta})]\right\} \rho d\rho d\theta \\ &= 1 - \int_{Z_i} p(\rho, \hat{\theta}/H_i) d\rho d\theta \end{aligned}$$

where

$$p(\rho, \hat{\theta}/H_i) = \frac{\rho}{\pi N_o} \exp\left\{-\frac{1}{N_o}[\rho^2 + E - 2\rho\sqrt{E} \cos(\theta_i - \hat{\theta})]\right\}$$

is the joint probability density of ρ and θ . We define $\varphi = \hat{\theta} - \theta_i$, which represents the phase deviation of the received signal from the transmitted one. Integrating both sides of the above with respect to ρ yields the PDF of $\varphi \in [-\pi, \pi]$ (see Appendix 4A for derivation).

$$\begin{aligned} p(\varphi/H_i) &= \frac{e^{-E/N_o}}{2\pi} \left\{ 1 + \sqrt{\frac{\pi E}{N_o}} (\cos \varphi) e^{(E/N_o) \cos^2 \varphi} \right. \\ &\quad \cdot \left. \left[1 + \operatorname{erf} \left(\sqrt{\frac{E}{N_o}} \cos \varphi \right) \right] \right\} \\ &= p(\varphi) \end{aligned}$$

where

$$\operatorname{erf}(x) \triangleq \frac{2}{\sqrt{\pi}} \int_0^x e^{-t^2} dt$$

is the *error function*. Note the distribution of φ is independent of index i . This is intuitively correct since φ is the phase deviation, not the absolute phase.

The symbol error probability is the probability that $\hat{\theta}$ is outside the decision region, or the deviation φ is greater than π/M in absolute value.

$$P_s = 1 - \int_{-\pi/M}^{\pi/M} p(\varphi) d\varphi \quad (4.21)$$

When $M = 2$ (BPSK) and $M = 4$ (QPSK) this integration results in the formulas given by (4.6) and (4.37). For $M > 4$, this expression cannot be evaluated in a closed form, the symbol error probability can be obtained by numerically integrating (4.21).

⁴ Note that $dr_1 dr_2 = \rho d\rho d\hat{\theta}$.

Another form of P_s is given in [2, p. 209]. The derivation is very complicated and is omitted here. The result is

$$P_s = \frac{M-1}{M} - \frac{1}{2} \operatorname{erf} \left[\sqrt{\frac{E}{N_o}} \sin \frac{\pi}{M} \right] - \frac{1}{\sqrt{\pi}} \int_0^{\sqrt{E/N_o} \sin \pi/M} e^{-y^2} \operatorname{erf}(y \cot \frac{\pi}{M}) dy \quad (4.22)$$

This again can only be numerically evaluated for $M > 4$.

Figure 4.13 shows P_s curves for $M = 2, 4, 8, 16$, and 32 given by the exact expression (4.22). Beyond $M = 4$, doubling the number of phases, or increasing one bit in the n -tuples represented by the phases, requires a substantial increase in SNR. For example, at $P_s = 10^{-5}$, the SNR difference between $M = 4$ and $M = 8$ is approximately 4 dB, the difference between $M = 8$ and $M = 16$ is approximately 5 dB. For large values of M , doubling the number of phases requires an SNR increase of 6 dB to maintain the same performance.

For $E/N_o \gg 1$, we can derive an approximation of the P_s expression. First we can use the approximation⁵

$$\operatorname{erf}(x) \approx 1 - \frac{e^{-x^2}}{\sqrt{\pi}x}, \quad x \gg 1$$

to obtain the approximation of the PDF of the phase deviation

$$p(\varphi/H_i) \approx \sqrt{\frac{E}{\pi N_o}} (\cos \varphi) e^{-(E/N_o) \sin^2 \varphi} \quad (4.23)$$

Finally substituting (4.23) into (4.21) we arrive at the result

$$\begin{aligned} P_s &\approx \operatorname{erf} c \left(\sqrt{\frac{E}{N_o}} \sin \frac{\pi}{M} \right) \\ &= 2Q \left(\sqrt{\frac{2E}{N_o}} \sin \frac{\pi}{M} \right), \quad (\text{coherent MPSK}) \end{aligned} \quad (4.24)$$

where

$$\operatorname{erf} c(x) = 1 - \operatorname{erf}(x) = 2Q(\sqrt{2}x)$$

⁵ In fact $1 - \frac{e^{-x^2}}{\sqrt{\pi}x}$ is a lower bound of $\operatorname{erf}(x)$, however they are extremely close for $x \gg 1$.

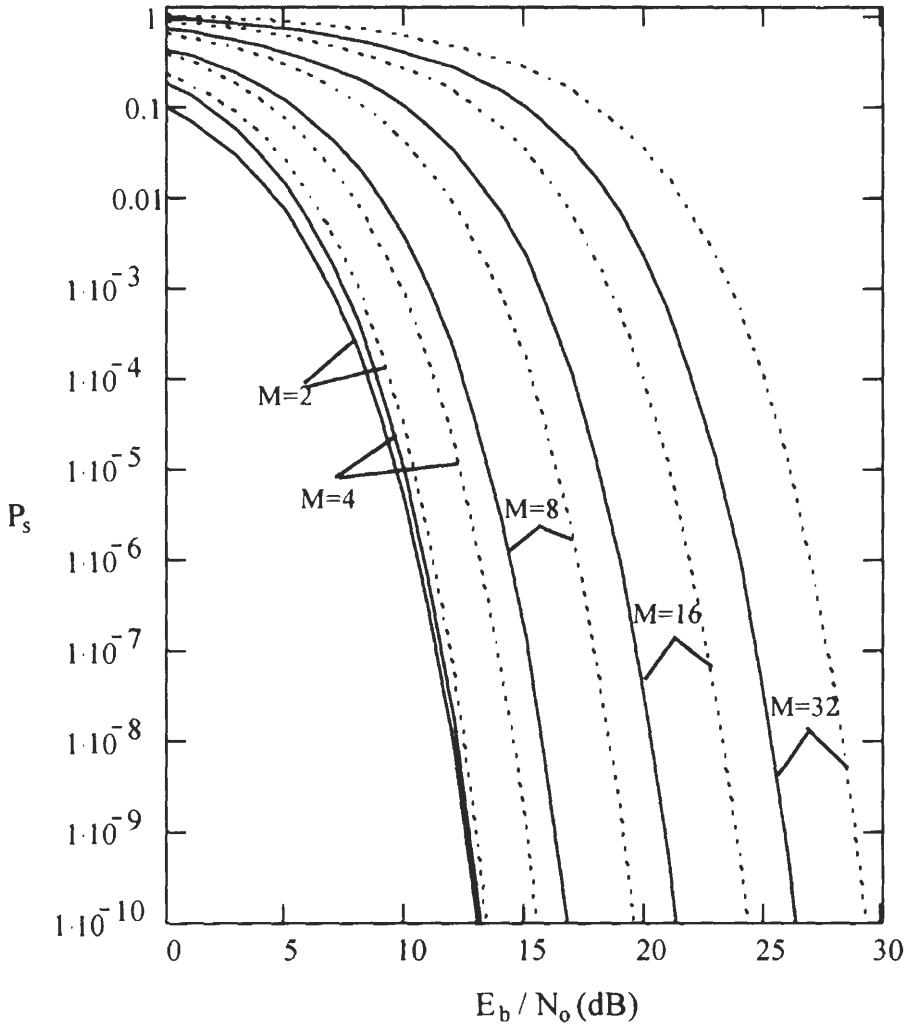


Figure 4.13 P_s of MPSK (solid lines) and DMPSK (dotted lines).

is the *complementary error function*. Note that only high signal-to-noise ratio assumption is needed for the approximation. Therefore (4.24) is good for any values of M , even though it is not needed for $M = 2$ and 4 since precise formulas are available.

Expression (4.24) can be derived geometrically. Consider Figure 4.14. Due to symmetry of the signal constellation, P_s is equal to the error probability of detecting s_1 , which is the probability that the received signal vector \mathbf{r} does not fall in the decision region Z_1 . This is bounded below and above as follows

$$\Pr(\mathbf{r} \in A_1) \leq P_s < \Pr(\mathbf{r} \in A_1) + \Pr(\mathbf{r} \in A_2) = 2 \Pr(\mathbf{r} \in A_2)$$

where the equal sign on the left part of the inequality accounts for the case of $M = 2$. The distance from s_1 to the nearest signal is

$$d_{12} = d_{18} = 2\sqrt{E} \sin \frac{\pi}{M}$$

Since white Gaussian noise is identically distributed along any set of orthogonal axes [3, Chapter 3], we may temporarily choose the first axis in such a set as one that passes through the points s_1 and s_2 , then for high SNR

$$\begin{aligned} \Pr(\mathbf{r} \in A_1) &= \Pr(\mathbf{r} \in A_2) \approx \Pr(s_2/H_1) \\ &= \int_{-\infty}^{-d_{12}/2} \frac{1}{\sqrt{\pi N_o}} \exp\left\{-\frac{x^2}{N_o}\right\} dx = Q\left(\sqrt{\frac{2E}{N_o}} \sin \frac{\pi}{M}\right) \end{aligned}$$

Thus

$$Q\left(\sqrt{\frac{2E}{N_o}} \sin \frac{\pi}{M}\right) \leq P_s \lesssim 2Q\left(\sqrt{\frac{2E}{N_o}} \sin \frac{\pi}{M}\right)$$

Since the lower and upper bounds differ only by a factor of two, which translates into a very small difference in term of SNR, these bounds are very tight.

The bit error rate can be related to the symbol error rate by

$$P_b \approx \frac{P_s}{\log_2 M} \quad (4.25)$$

for Gray coded MPSK signals since most likely the erroneous symbols are the adjacent signals which only differ by one bit.

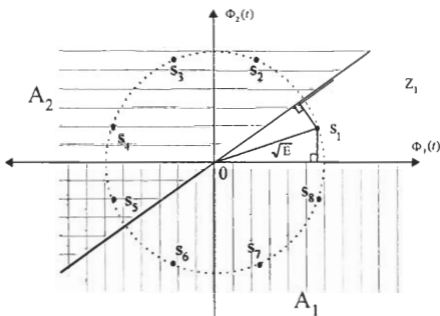


Figure 4.14 Decision regions for bounding P_s of MPSK signals.

4.4 PSD OF MPSK

The PSD of MPSK is similar to that of BPSK except that the spectral is narrower on a frequency scale normalized to the bit rate. As for all carrier modulated signals, it suffices to find the PSD of the complex envelope (Appendix A).

Substituting (4.16) and (4.17) into (4.15), we can write the MPSK signal as

$$s(t) = \text{Re} \left\{ \left[\sum_{k=-\infty}^{\infty} A \exp(j\theta_k) p(t - kT) \right] \exp(j2\pi f_c t) \right\}$$

Thus the complex envelope of MPSK is

$$\begin{aligned} \tilde{s}(t) &= \sum_{k=-\infty}^{\infty} A \exp(j\theta_k) p(t - kT) \\ &= \sum_{k=-\infty}^{\infty} A \cos \theta_k p(t - kT) + j \sum_{k=-\infty}^{\infty} A \sin \theta_k p(t - kT) \end{aligned}$$

where

$$\cos \theta_k \in \left(\cos \frac{(2i-1)\pi}{M}, i = 1, 2, \dots, M \right)$$

is a random variable which has $M/2$ different values with equal probabilities ($\frac{2}{M}$). Refer to the example of 8-PSK in Figure 4.9. We can see that $\cos \theta_k = \cos \frac{\pi}{8}$ or $\cos \frac{3\pi}{8}$ or $\cos \frac{5\pi}{8}$ or $\cos \frac{7\pi}{8}$, which is $\cos \theta_k = 0.924$ or 0.383 or -0.383 or -0.924 . These values are symmetrical about zero. Thus the mean value is zero. The mean square value is

$$\sigma^2 = \sum_{i=1}^{M/2} \frac{2}{M} \cos^2 \frac{(2i-1)\pi}{M} = \frac{1}{2}$$

Note that the mean square value is always $\frac{1}{2}$ for $M = 2^n$, $n > 1$. The distribution of $\sin \theta_k$ is the same.

Thus the complex envelope can be written as

$$\tilde{s}(t) = \sum_{k=-\infty}^{\infty} x_k p(t - kT) + j \sum_{k=-\infty}^{\infty} y_k p(t - kT)$$

where $\{x_k = \cos \theta_k\}$ and $\{y_k = \sin \theta_k\}$ are independent, identically distributed random sequences with zero means and a mean square value of $1/2$. The PSD of this type of complex envelope has been derived in Appendix A. The result (A.21) can be directly used here.

Since $\sigma_x^2 = \sigma_y^2 = \sigma^2 = 1/2$ and

$$|P(f)| = \left| AT \frac{\sin \pi f T}{\pi f T} \right|$$

then from (A.21) we have

$$\begin{aligned} \Psi_{\tilde{s}}(f) &= 2\sigma^2 A^2 T \left(\frac{\sin \pi f T}{\pi f T} \right)^2 \\ &= A^2 T \left(\frac{\sin \pi f T}{\pi f T} \right)^2 \\ &= A^2 n T_b \left(\frac{\sin \pi f n T_b}{\pi f n T_b} \right)^2, \text{ (MPSK)} \end{aligned} \quad (4.26)$$

where $n = \log_2 M$. This is exactly the same as that of BPSK in terms of symbol rate. However, in terms of bit rate the PSD of MPSK is n -times narrower than the

BPSK. Figure 4.15 is the PSDs ($A = \sqrt{2}$ and $T_b = 1$ for unit bit energy: $E_b = 1$) for different values of M where the frequency axis is normalized to the bit rate (fT_b).

Since the passband minimum (Nyquist) bandwidth required to transmit the symbols is $1/T$, the maximum bandwidth efficiency is

$$\frac{R_b}{B_{\min}} = \frac{(\log_2 M)/T}{1/T} = \log_2 M$$

4.5 DIFFERENTIAL MPSK

In Section 4.2 we discussed DBPSK, which is in fact a special case of differential MPSK (DMPSK). The term DMPSK refers to “differentially encoded and differentially coherently demodulated MPSK.” The differentially coherent demodulation is in fact noncoherent in the sense that phase coherent reference signals are not required. It is used to overcome the adversary effect of the random phase in the received signal.

Differentially encoded MPSK can also be coherently demodulated (denoted as DEMPSK). In this case, the purpose of differential encoding is to eliminate phase ambiguity in the carrier recovery process. This is not usually meant by the term DMPSK.

In both cases, the modulation processes are the same. In other words, the transmitted MPSK signals are the same. Only demodulations are different.

In the modulator the information bits are first differentially encoded. Then the encoded bits are used to modulate the carrier. In a DEMPSK signal stream, information is carried by the phase difference $\Delta\theta_i$ between two consecutive symbols. There are M different values of $\Delta\theta_i$, each represents an n -tuple ($n = \log_2 M$) of information bits.

For $M = 2$ and 4, encoding, modulation, and demodulation are simple, as we have seen in Section 4.2 for DBPSK and will see shortly for differentially encoded QPSK.

In light of the modern digital technology, DEMPSK signals can be generated by digital frequency synthesis technique. A phase change from one symbol to the next is simply controlled by the n -tuple which is represented by the phase change. This technique is particularly suitable for large values of M .

In DMPSK scheme, the DEMPSK signal is demodulated by a differentially coherent (or optimum noncoherent) demodulator as shown in Figure 4.16.

The derivation of the demodulator is similar to that of binary DPSK. In DEMPSK a message m_i of $n = \log_2 M$ bits is represented by the phase difference of two consecutive symbols. In other words, m_i is represented by a symbol with two symbol

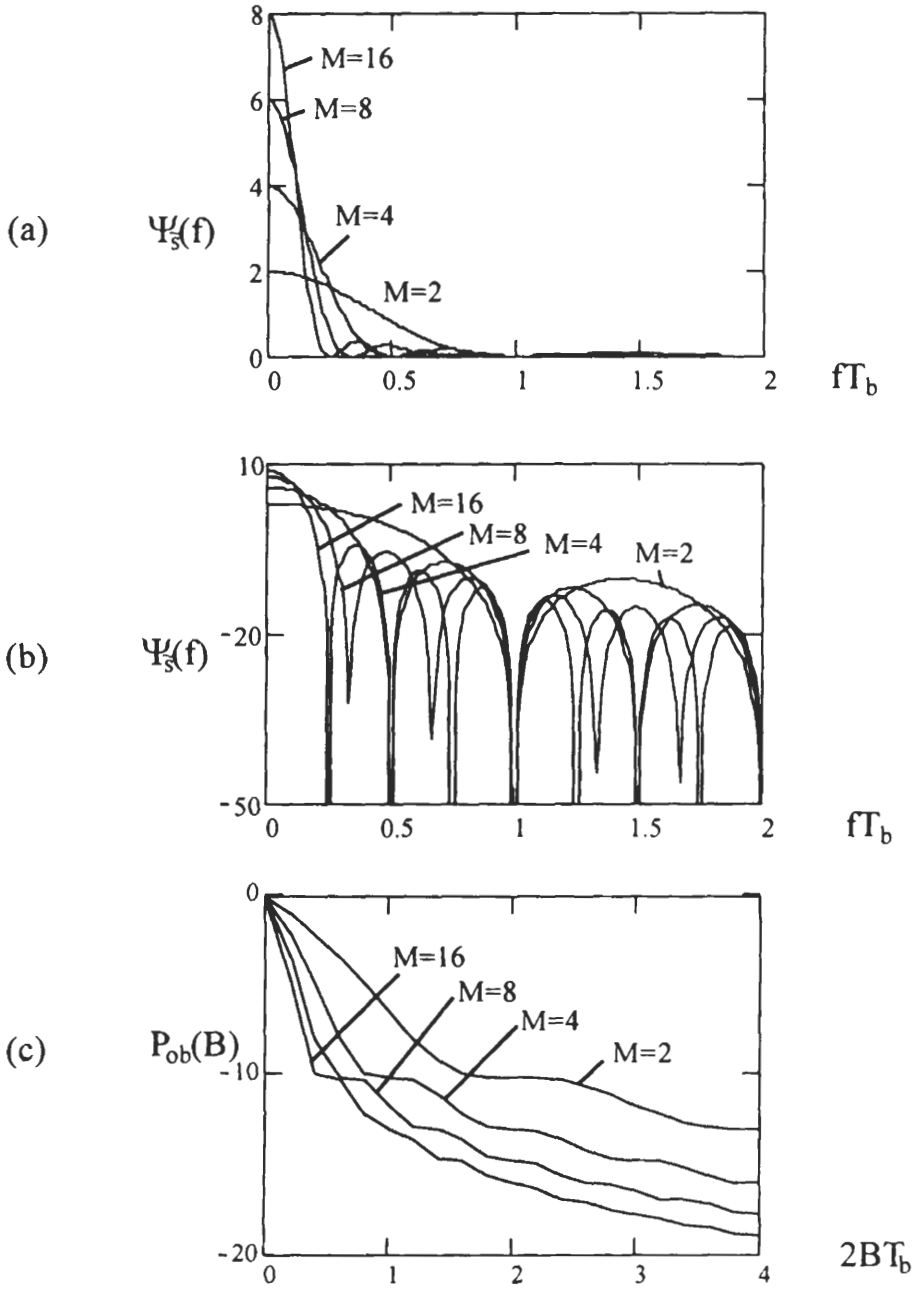


Figure 4.15 PSDs of MPSK: (a) linear, (b) logarithmic, (c) out-of-band power.

periods defined as

$$\xi_i(t) = \begin{cases} A \cos [2\pi f_c t + \Phi_0], & 0 \leq t \leq T \\ A \cos [2\pi f_c t + \Phi_0 + \Delta\theta_i], & T \leq t \leq 2T \end{cases}$$

where $\Delta\theta_i = \frac{2(i-1)\pi}{M}$, $i = 1, 2, \dots, M$. The received signal $r(t)$ has an unknown phase θ introduced by the channel and is corrupted by AWGN. Consider the first two symbol durations $[0 \leq t \leq 2T]$, from (B.55), the sufficient statistic for detecting $\xi_i(t)$ is

$$l_i^2 = \left(\int_0^{2T} r(t)\xi_i(t)dt \right)^2 + \left(\int_0^{2T} r(t)\xi_i(t, \frac{\pi}{2})dt \right)^2 \quad (4.27)$$

the first integral is

$$\begin{aligned} & \int_0^{2T} r(t)\xi_i(t)dt \\ = & \int_0^T r(t)A \cos(2\pi f_c t + \Phi_0)dt \\ & + \int_T^{2T} r(t)A \cos(2\pi f_c t + \Phi_0 + \Delta\theta_i)dt \\ = & \int_0^T r(t)A [\cos 2\pi f_c t \cos \Phi_0 - \sin 2\pi f_c t \sin \Phi_0] dt \\ & + \int_T^{2T} r(t)A [\cos 2\pi f_c t \cos(\Phi_0 + \Delta\theta_i) - \sin 2\pi f_c t \sin(\Phi_0 + \Delta\theta_i)] dt \\ = & w_0 \cos \Phi_0 + z_0 \sin \Phi_0 + w_1 \cos(\Phi_0 + \Delta\theta_i) + z_1 \sin(\Phi_0 + \Delta\theta_i) \end{aligned}$$

where

$$\begin{aligned} w_0 & \triangleq \int_0^T r(t)A \cos 2\pi f_c t dt \\ z_0 & \triangleq - \int_0^T r(t)A \sin 2\pi f_c t dt \\ w_1 & \triangleq \int_T^{2T} r(t)A \cos 2\pi f_c t dt \\ z_1 & \triangleq - \int_T^{2T} r(t)A \sin 2\pi f_c t dt \end{aligned}$$

and the second integral is

$$\begin{aligned}
 & \int_0^{2T} r(t)\xi_i(t, \frac{\pi}{2})dt \\
 = & \int_0^T r(t)A \sin(2\pi f_c t + \Phi_0)dt + \int_T^{2T} r(t)A \sin(2\pi f_c t + \Phi_0 + \Delta\theta_i)dt \\
 = & -z_0 \cos \Phi_0 + w_0 \sin \Phi_0 - z_1 \cos(\Phi_0 + \Delta\theta_i) + w_1 \sin(\Phi_0 + \Delta\theta_i)
 \end{aligned}$$

Then substituting these two integrals into (4.27), expanding the squares, discarding squared terms since they are independent of transmitted signals, dropping a factor of two, we have the following new sufficient statistic

$$L_i = (w_1 w_0 + z_1 z_0) \cos \Delta\theta_i + (z_1 w_0 - w_1 z_0) \sin \Delta\theta_i$$

For the k th symbol duration this is

$$\begin{aligned}
 L_i &= \underbrace{(w_k w_{k-1} + z_k z_{k-1})}_{x_k} \cos \theta_i + \underbrace{(z_k w_{k-1} - w_k z_{k-1})}_{y_k} \sin \theta_i \\
 &= x_k \cos \Delta\theta_i + y_k \sin \Delta\theta_i
 \end{aligned} \tag{4.28}$$

The decision rule is to choose the largest. Or we can write (4.28) as

$$\begin{aligned}
 L_i &= A \cos \Delta\hat{\theta}_k \cos \Delta\theta_i + A \sin \Delta\hat{\theta}_k \sin \Delta\theta_i \\
 &= A \cos(\Delta\theta_i - \Delta\hat{\theta}_k)
 \end{aligned}$$

where

$$\Delta\hat{\theta}_k = \tan^{-1} \frac{y_k}{x_k}$$

Thus the decision rule is to choose the smallest $|\Delta\theta_i - \Delta\hat{\theta}_k|$. Figure 4.16 implements this rule. As we stated in the binary DPSK case, the local oscillator output must have the same frequency, but not necessarily the same phase, as the received signal. The amplitude of the reference signals can be any value, which is unit in the figure, since the effect of the amplitude is cancelled when computing $\Delta\hat{\theta}_k$.

The symbol error probability is given by [2]

$$P_s = \frac{\sin \frac{\pi}{M}}{2\pi} \int_{-\pi/2}^{\pi/2} \frac{\exp\{-\frac{E}{N_o} [1 - \cos \frac{\pi}{M} \cos x]\}}{1 - \cos \frac{\pi}{M} \cos x} dx \tag{4.29}$$

which can be evaluated in a closed form for $M = 2$ (see (4.10)). For other values of M , it can only be numerically evaluated. Many approximate expressions have been

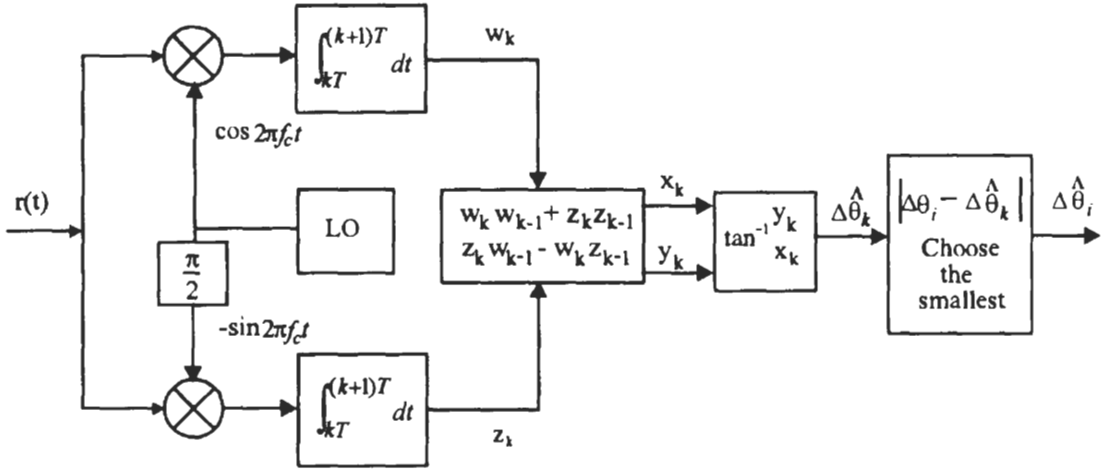


Figure 4.16 Differentially coherent demodulator for differentially encoded MPSK signals.

found [2.4], a simple one is

$$P_s \approx 2Q \left(\sqrt{\frac{2E}{N_o}} \sin \frac{\pi}{\sqrt{2M}} \right), \text{ (optimum DMPSK)} \quad (4.30)$$

for large SNR. The exact curves as obtained from (4.29) are given in Figure 4.13 together with those of coherent MPSK. Compared with coherent MPSK, asymptotically the DMPSK requires 3 dB more SNR to achieve the same error performance. This also can be quite easily seen by comparing the arguments of the Q-function in (4.30) and (4.24), using $\sin(x) \approx x$ for small x .

For the purpose of phase ambiguity elimination, the DEMPSK signal is coherently demodulated. The optimum demodulator is shown in Figure 4.17 which is similar to Figure 4.11, the demodulator for coherent MPSK, except that a differential decoder is attached as a final stage. This is intuitively convincing since at carrier frequency the DEMPSK signal is the same as MPSK signal, thus the correlator part is the same as that of coherent MPSK. The additional differential decoder recovers the differential phase $\Delta\theta_i$ from phases of two consecutive symbols. The $\Delta\theta_i$ then is mapped back to the corresponding n -tuple of bits. Rigorous derivation of this optimum demodulator and its equivalent forms can be found in [2.4].

The symbol error probability of coherently demodulated DEMPSK is given by [2.4]

$$P_s = 2P_{s-MPSK} \left[1 - \frac{1}{2}P_{s-MPSK} - \frac{1}{2} \frac{\sum_{i=1}^{M-1} P_i(C)}{P_{s-MPSK}} \right]. \text{ (DEMPSK)} \quad (4.31)$$

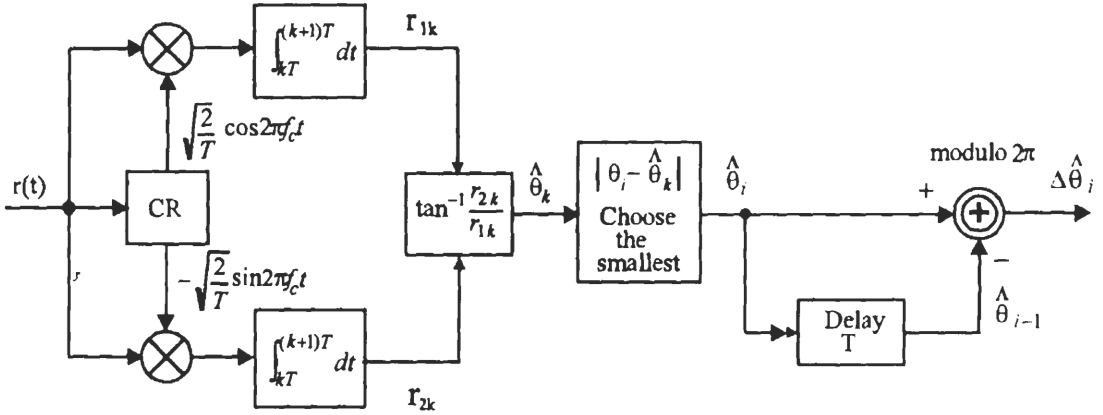


Figure 4.17 Coherent demodulation of differentially encoded MPSK signals.

where P_{s-MPSK} is the symbol error probability for MPSK without differential encoding and is given by (4.21), and

$$P_i(C) = \left[\int_{(2i-1)\pi/M}^{(2i+1)\pi/M} \int_0^\infty \frac{r}{\pi} \exp \left\{ - \left[r^2 - 2r \sqrt{\frac{E}{N_o}} \cos \Theta + \frac{E}{N_o} \right] \right\} dr d\Theta \right]^2$$

For $M = 2$, we have coherent detection of differentially encoded BPSK for which (4.31) reduces to (4.12). For $M = 4$, it reduces to

$$P_s = 4Q \left(\sqrt{\frac{E}{N_o}} \right) - 8 \left[Q \left(\sqrt{\frac{E}{N_o}} \right) \right]^2 + 8 \left[Q \left(\sqrt{\frac{E}{N_o}} \right) \right]^3 - 4 \left[Q \left(\sqrt{\frac{E}{N_o}} \right) \right]^4 \tag{4.32}$$

For large SNR, the second, third, and fourth terms can be ignored. Thus the above is just about two times that of coherent QPSK without differential encoding. In fact for any value of M when the SNR is large, the terms in the bracket of (4.31) is close to one, thus the P_s of the coherently demodulated DEMPSK is about two times that of coherent MPSK without differential encoding. This translates to 0.5 dB or less degradation in SNR. This is the price paid for removing the phase ambiguity.

A DEMPSK signal's PSD would be the same as its nonencoded counterpart if the encoding process does not change the statistic characteristic of the baseband data, since the final signal from the modulator is just MPSK signal. We always assume that the original data have an equally likely distribution. This results in that the

distribution of $\Delta\theta_i$ is equally likely too. In turn the absolute phases of the DEMPSK signals are also equally likely. This satisfies the condition for deriving (4.26). Thus the PSD of DEMPSK is the same as that of MPSK given in (4.26) for an equally likely original data sequence.

As we have proved in Chapter 2 and mentioned in Section 4.2, that differential encoding in DEBPSK always produces an equally likely data sequence asymptotically regardless of the distribution of the original data. This leads to a PSD given by (4.8) for DEBPSK even if the original data is not evenly distributed.

4.6 QUADRATURE PSK

Among all MPSK schemes, QPSK is the most often used scheme since it does not suffer from BER degradation while the bandwidth efficiency is increased. Other MPSK schemes increase bandwidth efficiency at the expenses of BER performance. In this section we will study QPSK in great detail.

Since QPSK is a special case of MPSK, its signals are defined as

$$s_i(t) = A \cos(2\pi f_c t + \theta_i), \quad 0 \leq t \leq T, \quad i = 1, 2, 3, 4 \quad (4.33)$$

where

$$\theta_i = \frac{(2i - 1)\pi}{4}$$

The initial signal phases are $\frac{\pi}{4}, \frac{3\pi}{4}, \frac{5\pi}{4}, \frac{7\pi}{4}$. The carrier frequency is chosen as integer multiple of the symbol rate, therefore in any symbol interval $[kT, (k+1)T]$, the signal initial phase is also one of the four phases.

The above expression can be written as

$$\begin{aligned} s_i(t) &= A \cos \theta_i \cos 2\pi f_c t - A \sin \theta_i \sin 2\pi f_c t \\ &= s_{i1} \phi_1(t) + s_{i2} \phi_2(t) \end{aligned} \quad (4.34)$$

where $\phi_1(t)$ and $\phi_2(t)$ are defined in (4.2) and (4.3),

$$s_{i1} = \sqrt{E} \cos \theta_i$$

$$s_{i2} = \sqrt{E} \sin \theta_i$$

and

$$\theta_i = \tan^{-1} \frac{s_{i2}}{s_{i1}}$$

Dibit	Phase θ_i	$s_{i1} = \sqrt{E} \cos \theta_i$	$s_{i2} = \sqrt{E} \sin \theta_i$
11	$\pi/4$	$+\sqrt{E/2}$	$+\sqrt{E/2}$
01	$3\pi/4$	$-\sqrt{E/2}$	$+\sqrt{E/2}$
00	$-3\pi/4$	$-\sqrt{E/2}$	$-\sqrt{E/2}$
10	$-\pi/4$	$+\sqrt{E/2}$	$-\sqrt{E/2}$

Table 4.2 QPSK signal coordinates.

where $E = A^2T/2$ is the symbol energy. We observe that this signal is a linear combination of two orthonormal basis functions: $\phi_1(t)$ and $\phi_2(t)$. On a coordinate system of $\phi_1(t)$ and $\phi_2(t)$ we can represent these four signals by four points or vectors: $\mathbf{s}_i = \begin{bmatrix} s_{i1} \\ s_{i2} \end{bmatrix}$, $i = 1, 2, 3, 4$. The angle of vector \mathbf{s}_i with respect to the horizontal axis is the signal initial phase θ_i . The length of the vectors is \sqrt{E} .

The signal constellation is shown in Figure 4.18. In a QPSK system, data bits are divided into groups of two bits, called dibits. There are four possible dibits, 00, 01, 10, and 11. Each of the four QPSK signals is used to represent one of them. The mapping of the dibits to the signals could be arbitrary as long as the mapping is one to one. The signal constellation in Figure 4.18 uses the Gray coding. The coordinates of signal points are tabulated in Table 4.2.

In the table, for convenience of modulator structure, we map logic 1 to $\sqrt{E/2}$ and logic 0 to $-\sqrt{E/2}$. We also map odd-numbered bits to s_{i1} and even-numbered bits to s_{i2} . Thus from (4.34) the QPSK signal on the entire time axis can be written as

$$s(t) = \frac{A}{\sqrt{2}}I(t) \cos 2\pi f_c t - \frac{A}{\sqrt{2}}Q(t) \sin 2\pi f_c t, \quad -\infty < t < \infty \quad (4.35)$$

where $I(t)$ and $Q(t)$ are pulse trains determined by the odd-numbered bits and even-numbered bits, respectively.

$$I(t) = \sum_{k=-\infty}^{\infty} I_k p(t - kT)$$

$$Q(t) = \sum_{k=-\infty}^{\infty} Q_k p(t - kT)$$

where $I_k = \pm 1$ and $Q_k = \pm 1$, the mapping between logic data and I_k or Q_k is $1 \rightarrow 1$ and $0 \rightarrow -1$. $p(t)$ is a rectangular pulse shaping function defined on $[0, T]$.

The QPSK waveform using the signal assignment in Figure 4.18 is shown in Figure 4.19. Like BPSK, the waveform has a constant envelope and discontinuous

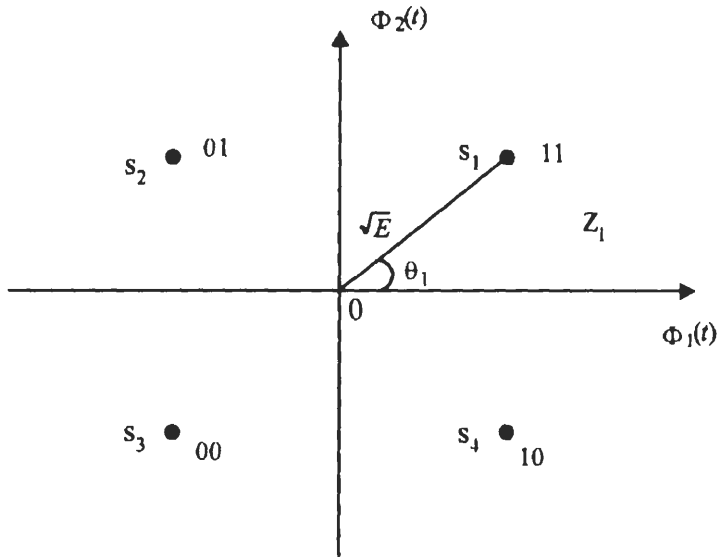


Figure 4.18 QPSK signal constellation.

phases at symbol boundaries. But unlike BPSK, the symbol interval is $2T_b$ instead of T_b . If the transmission rate of the symbols is the same in QPSK and BPSK, it is intuitively clear that QPSK transmits data twice as fast as BPSK does. Also we observe that the distance of adjacent points of the QPSK constellation is shorter than that of the BPSK. Does this cause the demodulator more difficulty, in comparison with BPSK, to distinguish those symbols, therefore symbol error performance is degraded and consequently bit error rate is also degraded? Surprisingly, it turns out that even though symbol error probability is increased, the bit error probability remains unchanged, as we will see shortly.

The modulator of QPSK is based on (4.35). This leads to the modulator in Figure 4.20(a). The channel with cosine reference is called inphase (I) channel and the channel with sine reference is called quadrature (Q) channel. The data sequence is separated by the serial-to-parallel converter (S/P) to form the odd-numbered-bit sequence for I-channel and the even-numbered-bit sequence for Q-channel. Then logic 1 is converted to a positive pulse and logic 0 is converted to a negative pulse, both have the same amplitude and a duration of T . Next the odd-numbered-bit pulse train is multiplied to $\cos 2\pi f_c t$ and the even-numbered-bit pulse train is multiplied to $\sin 2\pi f_c t$. It is clear that the I-channel and Q-channel signals are BPSK signals with a symbol duration of $2T_b$. Finally a summer adds these two waveforms together to produce the final QPSK signal. (see Figure 4.19 for waveforms at various stages.)

Since QPSK is a special case of MPSK, the demodulator for MPSK (Figure

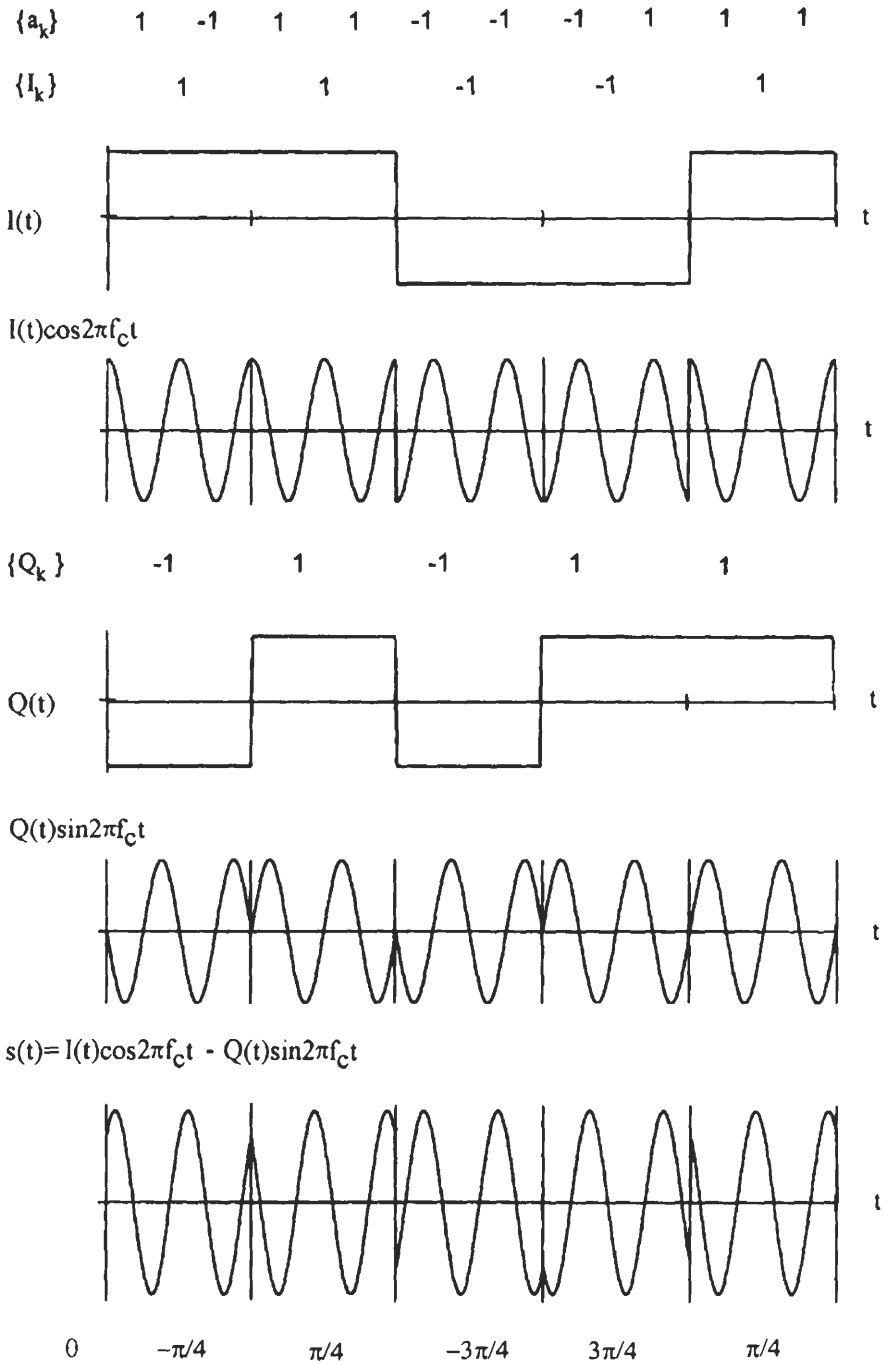
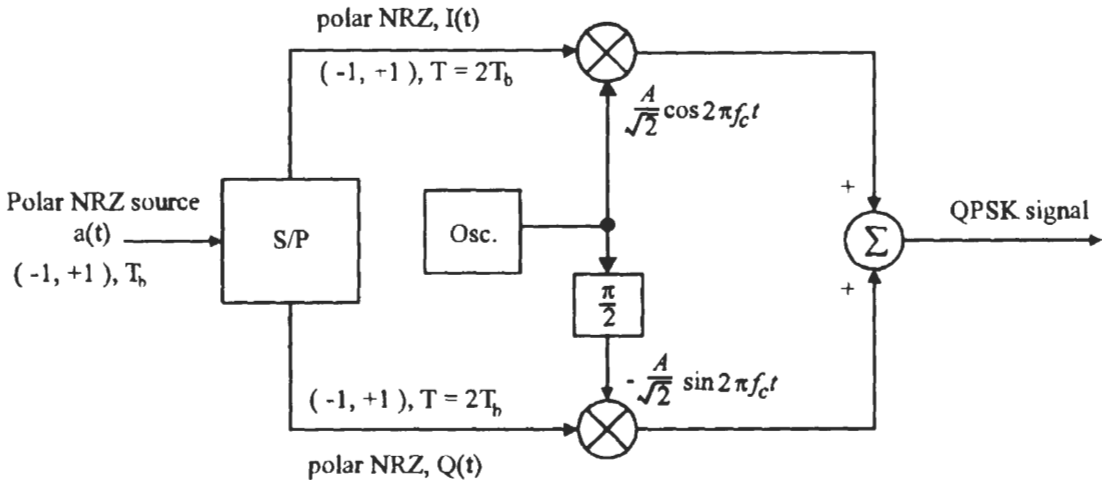
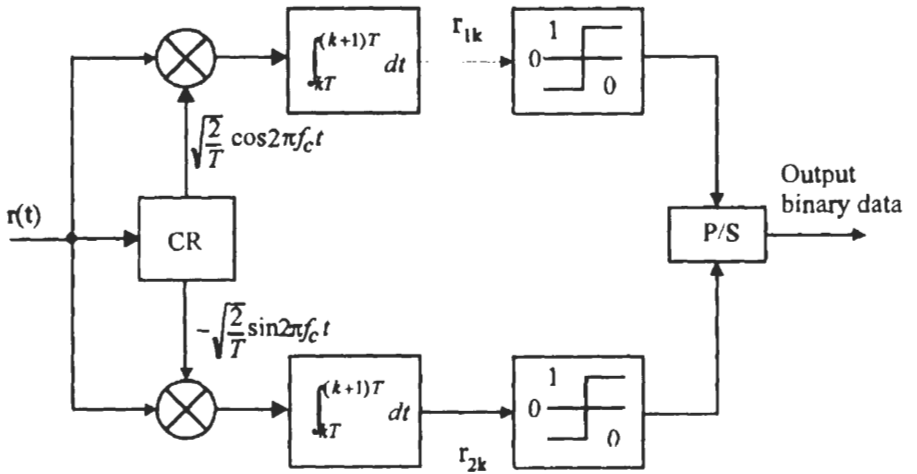


Figure 4.19 QPSK waveforms.



(a)



(b)

Figure 4.20 (a) QPSK modulator. (b) QPSK demodulator.

4.11) is applicable to QPSK. However, due to the special property of the QPSK constellation, a simpler demodulator is possible. It is shown in Figure 4.20(b) which is equivalent to Figure 4.11. I- and Q-channel signals are demodulated separately as two individual BPSK signals. A parallel-to-serial converter (P/S) is used to combine two sequences into a single sequence. This is possible because of the one-to-one correspondence between data bits and I- and Q-channel signals and their orthogonality. For $M > 4$, the optimum receiver can only be the form in Figure 4.11, since the signal in the I-channel or Q-channel does not correspond to a single bit, as we have seen in Section 4.3.

The bit error probability of the optimum demodulators can be derived using the demodulator of Figure 4.20. Since $E\{r_j\}$, $j = 1, 2$, is either $\sqrt{E/2}$ or $-\sqrt{E/2}$, corresponding to a bit of 1 or 0 (Table 4.2), the detection is a typical binary detection with a threshold of 0. The average bit error probability for each channel is

$$\begin{aligned}
 P_b &= \Pr(e/1 \text{ is sent}) = \Pr(e/0 \text{ is sent}) \\
 &= \int_0^\infty \frac{1}{\sqrt{\pi N_o}} \exp\left[-\frac{(R_j + \sqrt{E/2})^2}{N_o}\right] dR_j \\
 &= \int_{\sqrt{\frac{E}{N_o}}}^\infty \frac{1}{\sqrt{2\pi}} \exp\left[-\frac{x^2}{2}\right] dx \\
 &= Q\left(\sqrt{\frac{E}{N_o}}\right) = Q\left(\sqrt{\frac{2E_b}{N_o}}\right), \text{ (coherent QPSK)} \quad (4.36)
 \end{aligned}$$

The final output of the demodulator is just the multiplexed I- and Q-channel outputs. Thus the bit error rate for the final output is the same as that of each channel. A symbol represents two bits from the I- and Q-channels, respectively. A symbol error occurs if any one of them is in error. Therefore the symbol error probability is

$$\begin{aligned}
 P_s &= 1 - \Pr(\text{both bits are correct}) \\
 &= 1 - (1 - P_b)^2 \\
 &= 2P_b - P_b^2 \\
 &= 2Q\left(\sqrt{\frac{E}{N_o}}\right) - \left[Q\left(\sqrt{\frac{E}{N_o}}\right)\right]^2 \quad (4.37)
 \end{aligned}$$

The above symbol error probability expression can also be derived from the general formula in Section 4.3 for MPSK(4.21). Then the bit error probability expression can be derived in another way as follows. First for large SNR, the second term in (4.37) can be ignored. Second, for Gray coding and large SNR, a symbol error most likely causes the symbol being detected as the adjacent symbol which is only one bit

different out of two bits. Thus

$$P_b \approx \frac{1}{2} P_s \approx Q \left(\sqrt{\frac{2E_b}{N_o}} \right)$$

This expression is derived by approximations. But it is the same as the one obtained by the accurate derivation. We have made approximations twice. The first is to ignore the second term in (4.37). This increases the estimate of P_b slightly. The second is to ignore the symbol errors caused by choosing the nonadjacent symbols which may cause two bit errors for a symbol error. This decreases the estimate of P_b slightly. The fact that the final estimate is exactly equal to the accurate one shows that these two approximations happen to cancel each other. It is purely a coincidence.

The P_b curve of QPSK is shown in Figure 4.21, which is the same as that of BPSK. The P_s curve of QPSK is shown in Figure 4.13 together with other MPSK schemes.

The PSD of QPSK is similar to that of BPSK except that the spectral is narrower on a frequency scale normalized to the bit rate. From (4.26) we have

$$\Psi_{\bar{s}}(f) = 2A^2 T_b \left(\frac{\sin 2\pi f T_b}{2\pi f T_b} \right)^2, \quad (\text{QPSK}) \quad (4.38)$$

Figure 4.22(a, b) are the PSD curves of the QPSK. The null-to-null bandwidth $B_{null} = 1/T_b = R_b$. Figure 4.22(c) is the out-of-band power curve from which we can estimate that $B_{90\%} \approx 0.75R_b$. We also calculated that $B_{99\%} \approx 8R_b$.

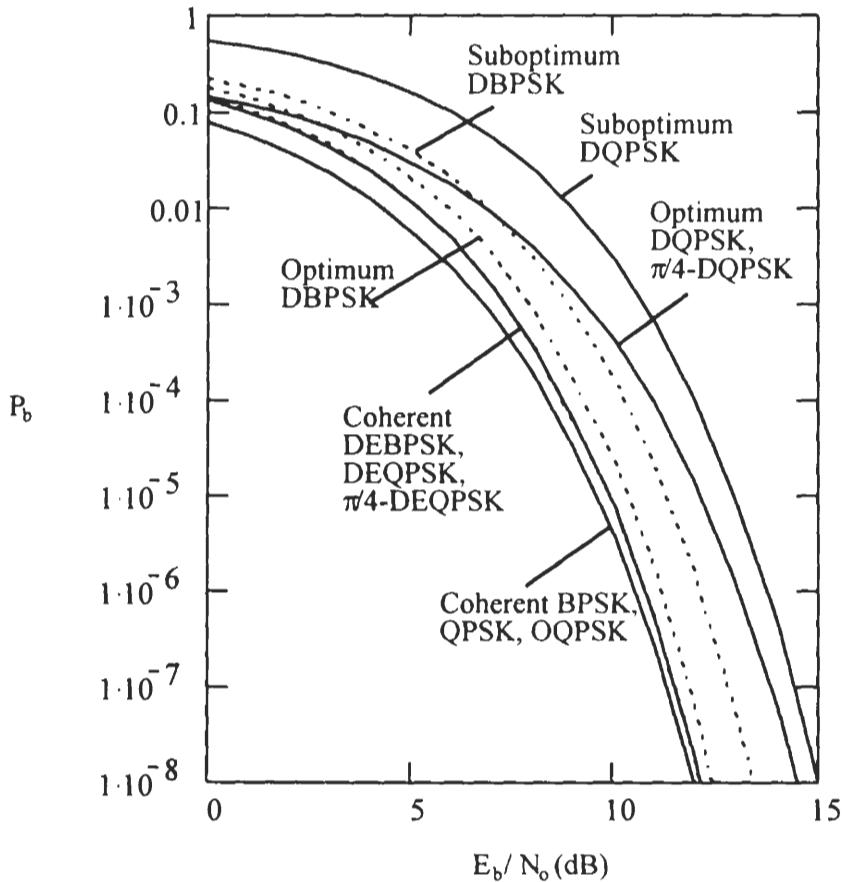
4.7 DIFFERENTIAL QPSK

Now we study an important special case of DEMPSK, the DEQPSK. In DEQPSK information dibits are represented by the phase differences $\Delta\theta_i$ from symbol to symbol. There are different phase assignments between $\Delta\theta_i$ and logic dibits. A possible phase assignment is listed in Table 4.3. Our discussion in this section is based on this phase assignment choice (later when we study $\pi/4$ -QPSK, the phase assignment is different). An example for this choice is shown in Table 4.4.

The coding rules are as follows [4].

$$\begin{aligned} u_k &= \overline{(I_k \oplus Q_k)}(I_k \oplus u_{k-1}) + (I_k \oplus Q_k)(Q_k \oplus v_{k-1}) \\ v_k &= (I_k \oplus Q_k)(Q_k \oplus v_{k-1}) + (I_k \oplus Q_k)(I_k \oplus u_{k-1}) \end{aligned} \quad (4.39)$$

where \oplus denotes exclusive OR operation. $I_k \in (0, 1)$ and $Q_k \in (0, 1)$ are odd-numbered and even-numbered original information bits, respectively; $u_k \in (0, 1)$

Figure 4.21 P_b of QPSK and DQPSK.

and $v_k \in (0, 1)$ are coded I-channel and Q-channel bits, respectively. Pairs (I_k, Q_k) and (u_{k-1}, v_{k-1}) are used to produce pair (u_k, v_k) which is used to control the absolute phase of the carrier. The resultant signal is a QPSK signal as shown in Figure 4.18 for (u_k, v_k) , but it is a DEQPSK signal for (I_k, Q_k) . Therefore the modulator is basically the same as the QPSK modulator (Figure 4.20) except that two differential encoders must be included in each channel before the carrier multiplier. The modulator is shown in Figure 4.23.

When DEQPSK is differentially coherently demodulated, the scheme is DQPSK. The optimum DQPSK demodulator can be derived from Figure 4.16 as a special case of $M = 4$. The symbol error probability is given by (4.29) or (4.30). The bit error

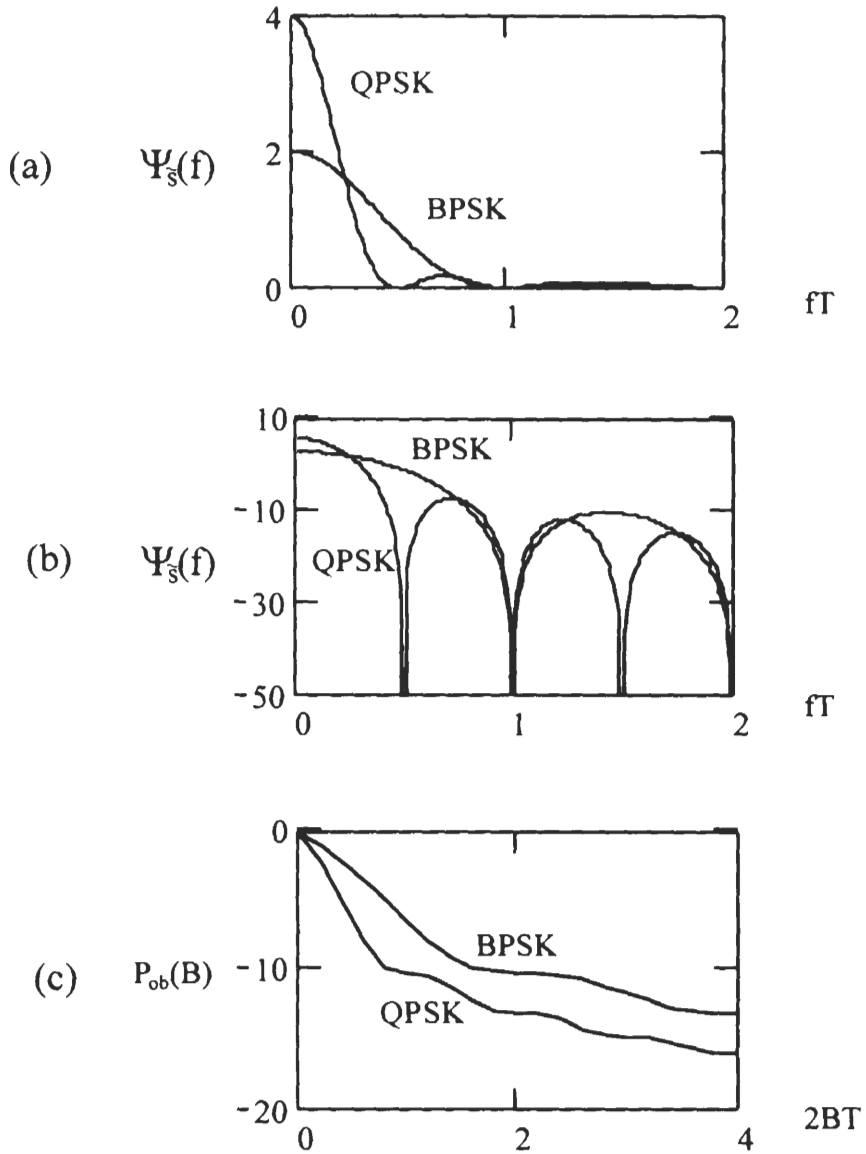


Figure 4.22 PSD of QPSK in comparison with BPSK: (a) linear, (b) logarithmic, (c) out-of-band power.

Dibit	$\Delta\theta_i$	$\cos \Delta\theta_i$	$\sin \Delta\theta_i$
00	0	1	0
01	$\pi/2$	0	1
10	$-\pi/2$	0	-1
11	π	-1	0

Table 4.3 DEQPSK signal phase assignment.

Modulation	ref.									
Information sequence	I_k		1	0	1	0	1	1	0	1
	Q_k		0	1	0	1	1	0	0	1
Encoded sequence	u_k	1	1	1	1	1	0	0	0	1
	v_k	1	0	1	0	1	0	1	1	0
Transmitted absolute phases		$\frac{\pi}{4}$	$\frac{7\pi}{4}$	$\frac{\pi}{4}$	$\frac{7\pi}{4}$	$\frac{\pi}{4}$	$\frac{5\pi}{4}$	$\frac{3\pi}{4}$	$\frac{3\pi}{4}$	$\frac{7\pi}{4}$

Table 4.4 Differential coding for DEQPSK.

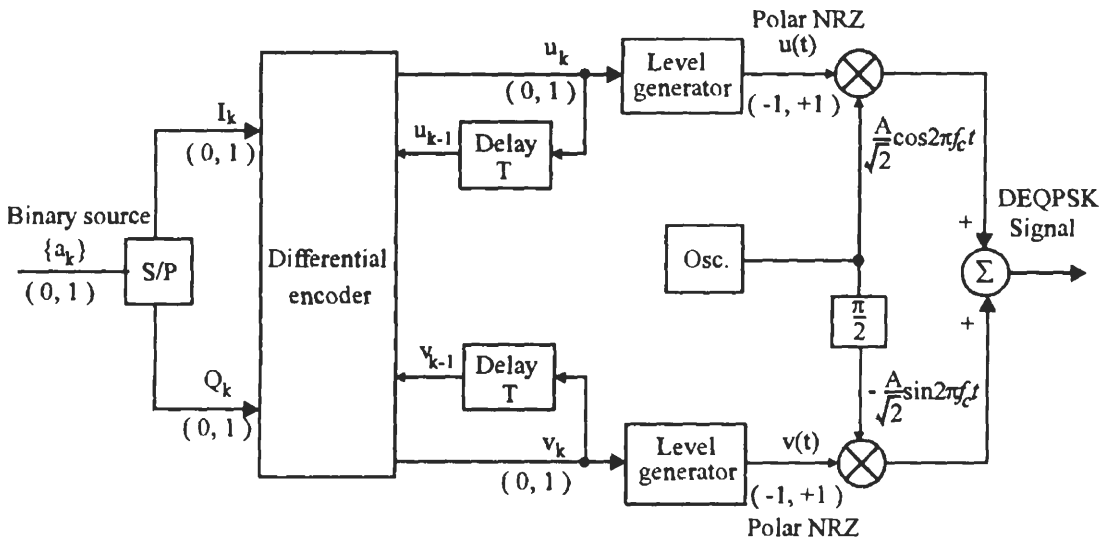


Figure 4.23 DEQPSK modulator.

probability can be approximately calculated using (4.25). Thus

$$P_b \approx Q \left(\sqrt{\frac{4E_b}{N_o}} \sin \frac{\pi}{4\sqrt{2}} \right), \text{ (Optimum DQPSK)} \quad (4.40)$$

which is plotted in Figure 4.21. It is about 2 to 3 dB inferior to coherent QPSK. Alternately, bit error probability of DQPSK can be evaluated using an expression given by [5] as

$$P_b = e^{-2\gamma_b} \sum_{k=0}^{\infty} (\sqrt{2} - 1)^k I_k(\sqrt{2}\gamma_b) - \frac{1}{2} I_0(\sqrt{2}\gamma_b) e^{-2\gamma_b} \quad (4.41)$$

where $\gamma_b = E_b/N_o$ and $I_\alpha(x)$ is the α th order modified Bessel function of the first kind which may be represented by the infinite series

$$I_\alpha(x) \triangleq \sum_{k=0}^{\infty} \frac{(x/2)^{\alpha+2k}}{k! \Gamma(\alpha + k + 1)}, \quad x \geq 0$$

and the gamma function is defined as

$$\Gamma(p) \triangleq \int_0^{\infty} t^{p-1} e^{-t} dt, \quad p > 0$$

Like in binary DPSK case, a suboptimum demodulator using previous symbols as references is shown in Figure 4.24 where the integrator can be replaced by a low-pass filter [6]. The front-end bandpass filter reduces noise power but preserves the phase of the signal. In the absence of noise, the I-channel integrator output is

$$\begin{aligned} & \int_{kT}^{(k+1)T} A^2 \cos(2\pi f_c t + \theta_k) \cos(2\pi f_c t + \theta_{k-1}) dt \\ &= \frac{1}{2} \int_{kT}^{(k+1)T} A^2 \{ \cos(4\pi f_c t + \theta_k + \theta_{k-1}) + \cos(\theta_k - \theta_{k-1}) \} dt \\ &= \frac{1}{2} A^2 T \cos \Delta\theta_k \end{aligned}$$

Similarly the Q-channel integrator output is $\frac{1}{2} A^2 T \sin \Delta\theta_k$. The arctangent operation extracts the $\hat{\Delta\theta}_k$ (estimate of $\Delta\theta_k$ with the presence of noise) and a comparator compares it to the four $\Delta\theta_i$ and chooses the closest. The dibit is then recovered from the detected $\Delta\theta_i$. For special dibits- $\Delta\theta_i$ assignment, such as the one for $\pi/4$ -QPSK, as will be seen in the next section, the angle detector can be replaced by two threshold detectors (see Figure 4.31). The bit error probability of the suboptimum demodulator

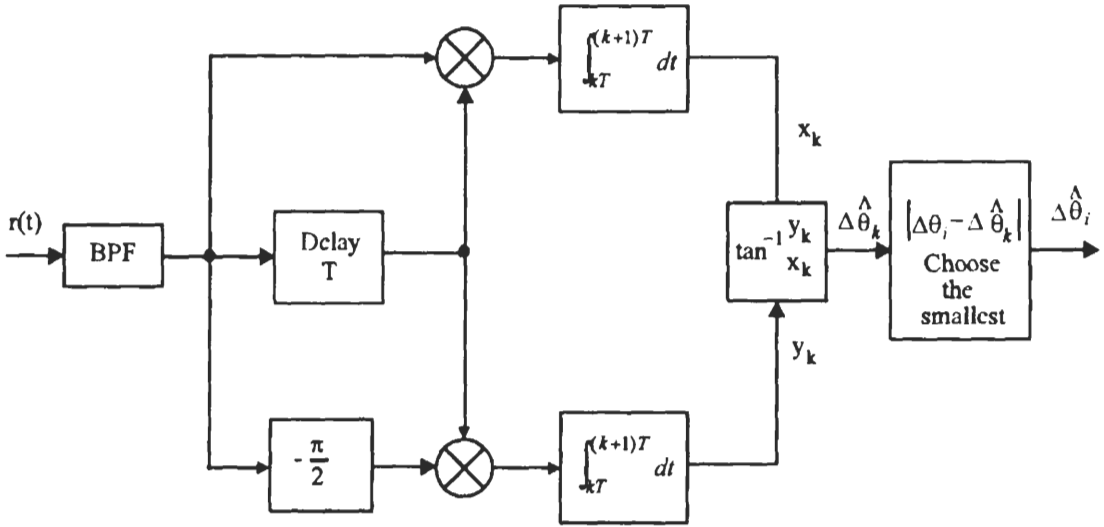


Figure 4.24 Suboptimum DQPSK demodulator (see Figure 4.16 for optimum demodulator).

in Figure 4.24 is given by [7, p.260]

$$P_b \approx e^{-(A^2/2\sigma^2)(1-1/\sqrt{2})} \tag{4.42}$$

where $A^2/2\sigma^2$ is the carrier-to-noise power ratio. In order to compare this to other error probabilities, we need to relate $A^2/2\sigma^2$ to E_b/N_o . In the derivation of this expression [7], the narrow-band noise has a variance of σ^2 for the inphase and quadrature component at the output of the front-end bandpass filter. The total noise variance is also equal to σ^2 [8, p.76]. The baseband signal is bandlimited to B . The bandwidth of the bandpass filter is just the same. Thus there is no intersymbol interference and the signal amplitude at sampling instances is A . So far in this chapter, the baseband pulse shape is always assumed as rectangular. For this pulse shape, the intersymbol interference free filter is the Nyquist filter which has a bandwidth of $B = 1/T$ at carrier frequency. Thus the noise power $\sigma^2 = N_o/T$. The signal symbol energy $E_s = \frac{1}{2}A^2T$. Thus

$$A^2/2\sigma^2 = \frac{2E_s/T}{2N_o/T} = \frac{E_s}{N_o} = \frac{2E_b}{N_o}$$

This is also stated in [2, p.444, eqn.(7.6)]. Thus (4.42) can be written as

$$P_b \approx e^{-\frac{2E_b}{N_o}(1-1/\sqrt{2})} = e^{-0.59 \frac{E_b}{N_o}}, \text{ (Suboptimum DQPSK)} \tag{4.43}$$

This is plotted in Figure 4.21. Seen from the figure, the degradation to the optimum

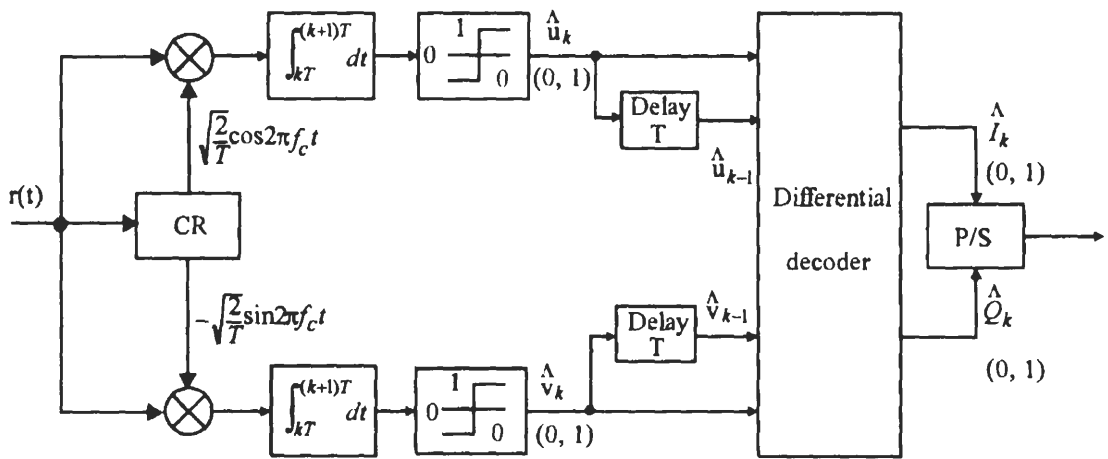


Figure 4.25 Coherent demodulation of DEQPSK.

DQPSK is less than 1 dB for high SNRs (>12 dB). But at the lower SNRs, the degradation is much larger. This is intuitively convincing since the reference signal is the previous signal which has noise. Compared to the suboptimum DBPSK, the degradation is about 1.75 dB for all SNRs.

For the purpose of phase ambiguity elimination, the DEQPSK signals are coherently demodulated. The demodulator is thus basically the same as QPSK demodulator except that a differential decoder must be inserted after demodulation. The demodulator can be in the form of Figure 4.17 where differential decoding is carried out on signal phases. However, since there are only two levels in the I- and Q-channels, the demodulator can be in a simpler form as shown in Figure 4.25, where the differential decoding is carried out on digital signal levels. The decoding rules are

$$\begin{aligned}
 \hat{I}_k &= \overline{(\hat{u}_k \oplus \hat{v}_k)}(\hat{u}_k \oplus \hat{u}_{k-1}) + (\hat{u}_k \oplus \hat{v}_k)(\hat{v}_k \oplus \hat{v}_{k-1}) \\
 \hat{Q}_k &= \overline{(\hat{u}_k \oplus \hat{v}_k)}(\hat{v}_k \oplus \hat{v}_{k-1}) + (\hat{u}_k \oplus \hat{v}_k)(\hat{u}_k \oplus \hat{u}_{k-1})
 \end{aligned}
 \tag{4.44}$$

Table 4.5 shows the decoding process assuming a phase ambiguity of $\pi/2$.

Note that the coherent demodulator for DEQPSK in Figure 4.25 is not suitable for $\pi/4$ -QPSK since its dibits- $\Delta\theta_i$ assignment is different (see the $\pi/4$ -QPSK section).

The symbol error probability has been given in (4.32). For Gray coded constel-

Transmitted absolute phases	$\frac{\pi}{4}$	$\frac{7\pi}{4}$	$\frac{\pi}{4}$	$\frac{7\pi}{4}$	$\frac{\pi}{4}$	$\frac{5\pi}{4}$	$\frac{3\pi}{4}$	$\frac{3\pi}{4}$	$\frac{7\pi}{4}$
Demodulation									
Estimated absolute phases	$\frac{3\pi}{4}$	$\frac{\pi}{4}$	$\frac{3\pi}{4}$	$\frac{\pi}{4}$	$\frac{3\pi}{4}$	$\frac{7\pi}{4}$	$\frac{5\pi}{4}$	$\frac{5\pi}{4}$	$\frac{\pi}{4}$
Detected digits	\hat{u}_k	0	1	0	1	0	1	0	1
	\hat{v}_k	1	1	1	1	0	0	0	1
Detected information digits	\hat{I}_k		1	0	1	0	1	1	0
	\hat{Q}_k		0	1	0	1	1	0	0

Table 4.5 Differential decoding for DEQPSK.

lation and at high SNR, this translates to a bit error probability of

$$P_b \approx 2Q \left(\sqrt{\frac{2E_b}{N_o}} \right), \quad (\text{DEQPSK}) \quad (4.45)$$

which is plotted in Figure 4.21. It is seen from the figure that DQPSK is less than 0.5 dB inferior to coherent QPSK.

4.8 OFFSET QPSK

Offset QPSK is essentially the same as QPSK except that the I- and Q-channel pulse trains are staggered. The modulator and the demodulator of OQPSK are shown in Figure 4.26, which differs from the QPSK only by an extra delay of $T/2$ seconds in the Q-channel. Based on the modulator, the OQPSK signal can be written as

$$s(t) = \frac{A}{\sqrt{2}} I(t) \cos 2\pi f_c t - \frac{A}{\sqrt{2}} Q\left(t - \frac{T}{2}\right) \sin 2\pi f_c t, \quad -\infty < t < \infty$$

Since OQPSK differs from QPSK only by a delay in the Q-channel signal, its power spectral density is the same as that of QPSK, and its error performance is also the same as that of QPSK.

The OQPSK waveforms are shown in Figure 4.27. We observe that due to the staggering of I- and Q-channels, the OQPSK signal has a symbol period of $T/2$. At any symbol boundary, only one of the two bits in the pair (I_k, Q_k) can change sign. Thus the phase changes at symbol boundaries can only be 0° and $\pm 90^\circ$. Whereas the QPSK signal has a symbol period of T , both two bits in the pair (I_k, Q_k) can change sign, and the phase changes at the symbol boundaries can be 180° in addition to 0° and $\pm 90^\circ$ (see Figure 4.19).

In comparison to QPSK, OQPSK signals are less susceptible to spectral side-lobe restoration in satellite transmitters. In satellite transmitters, modulated signals

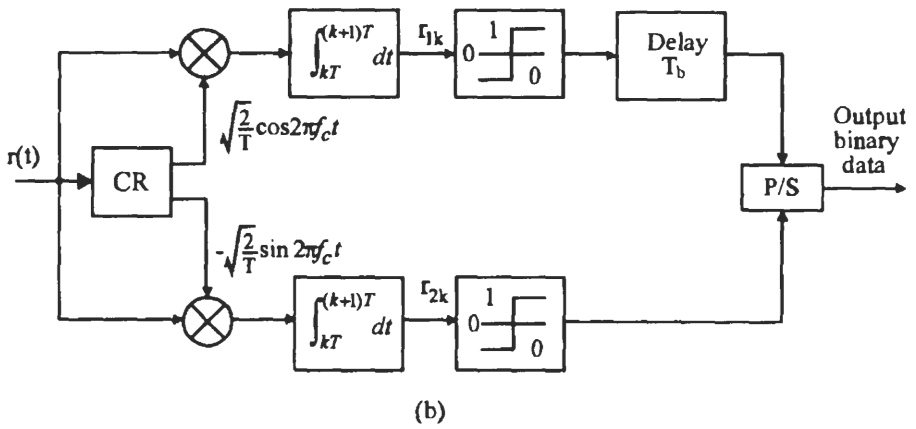
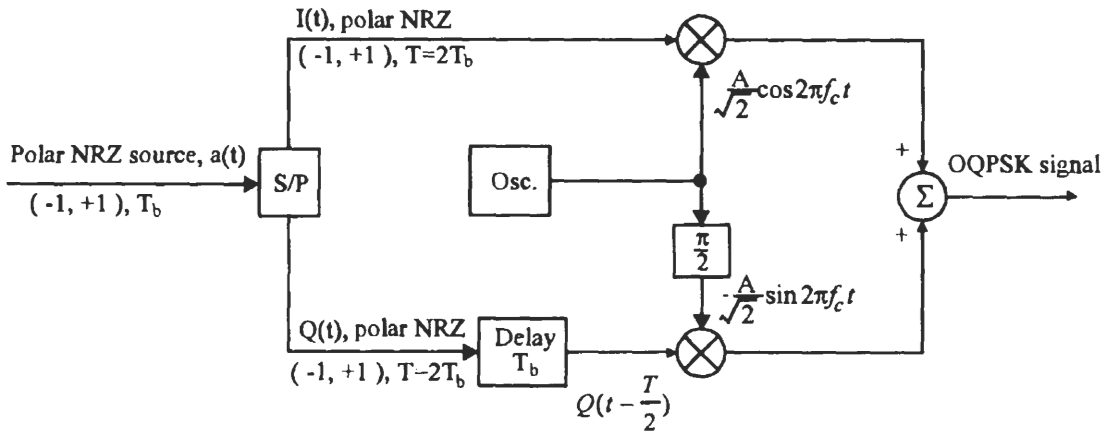


Figure 4.26 OQPSK modulator and demodulator.

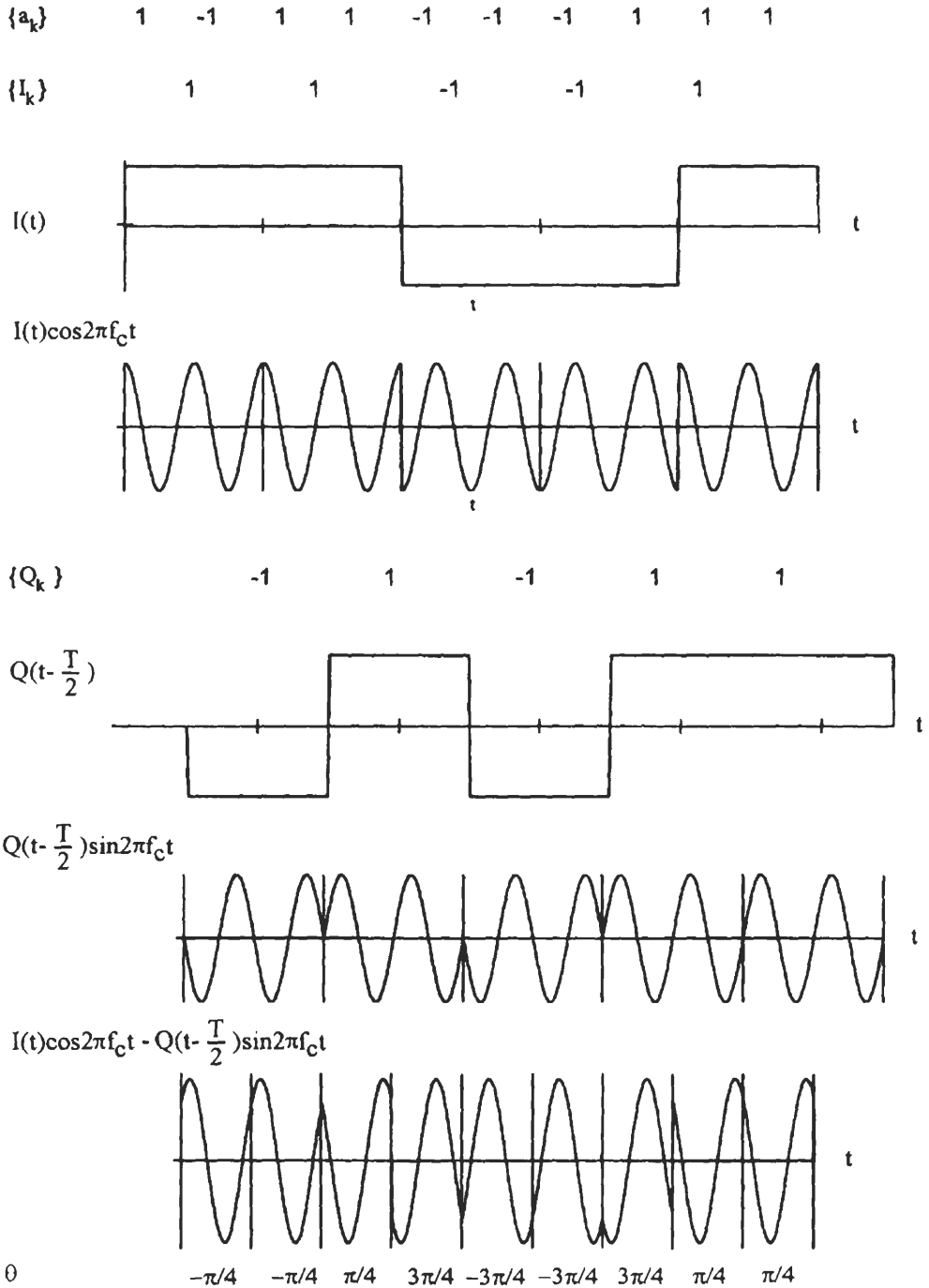


Figure 4.27 OQPSK waveforms.

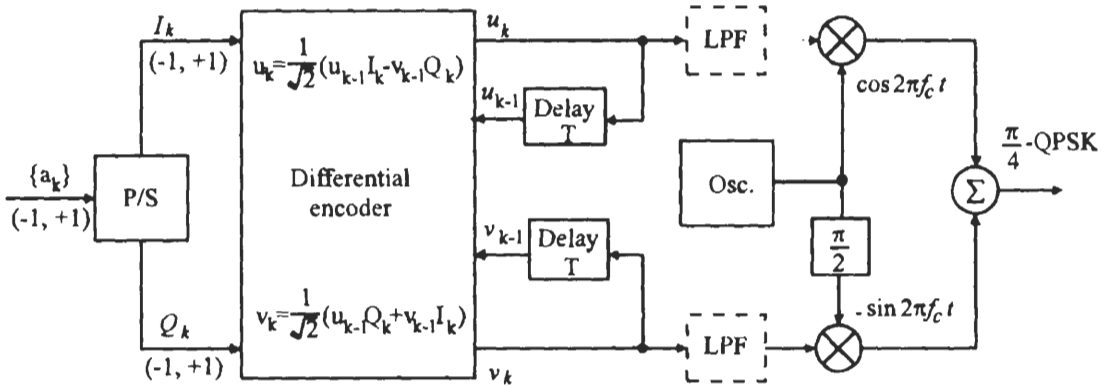


Figure 4.28 $\pi/4$ -QPSK modulator.

must be bandlimited by a bandpass filter in order to conform to out-of-band emission standards. The filtering degrades the constant-envelope property of QPSK, and the 180° phase shifts will cause the envelope to go to zero momentarily. When this signal is amplified by the final stage, usually a highly nonlinear power amplifier, the constant envelope will be restored. But at the same time the sidelobes will be restored. Note that arranging the bandpass filter after the power amplifier is not feasible since the bandwidth is very narrow compared with the carrier frequency, the Q-value of the filter must be extremely high such that it cannot be implemented by the current technology. In OQPSK, since the 180° phase shifts no longer exist, the sidelobe restoration is less severe [9].

4.9 $\pi/4$ -QPSK

Although OQPSK can reduce spectral restoration caused by nonlinearity in the power amplifier, it cannot be differentially encoded and decoded. $\pi/4$ -QPSK is a scheme which not only has no 180° phase shifts like OQPSK, but also can be differentially demodulated. These properties make it particularly suitable to mobile communications where differential demodulation can reduce the adversary effect of the fading channel. $\pi/4$ -QPSK has been adopted as the standard for the digital cellular telephone system in the United States and Japan.

$\pi/4$ -QPSK is first introduced by Baker in 1962 [10] and studied in [11, 12] and other articles.

The $\pi/4$ -QPSK is a form of differentially encoded QPSK. But it differs from the DEQPSK described in the previous section by the differential coding rules. Figure 4.28 is the $\pi/4$ -QPSK modulator. $(I(t), Q(t))$ and $(u(t), v(t))$ are the unencoded and

coded I-channel and Q-channel bits. The differential encoder of $\pi/4$ -QPSK modulator encodes $I(t)$ and $Q(t)$ into signals $u(t)$ and $v(t)$ according to the following rules

$$\left. \begin{aligned} u_k &= \frac{1}{\sqrt{2}}(u_{k-1}I_k - v_{k-1}Q_k) \\ v_k &= \frac{1}{\sqrt{2}}(u_{k-1}Q_k + v_{k-1}I_k) \end{aligned} \right\} \quad (4.46)$$

where u_k is the amplitude of $u(t)$ in the k th symbol duration and so on. We assume that I_k, Q_k takes values of $(-1, 1)$. If we initially specify that $u_0 = 1$ and $v_0 = 0$, then u_k and v_k can take the amplitudes of $\pm 1, 0$, and $\pm 1/\sqrt{2}$. The output signal of the modulator is

$$\begin{aligned} s(t) &= u_k \cos 2\pi f_c t + v_k \sin 2\pi f_c t \\ &= A \cos(2\pi f_c t + \Phi_k), \quad kT \leq t \leq (k+1)T \end{aligned}$$

where

$$\Phi_k = \tan^{-1} \frac{v_k}{u_k}$$

which depends on the encoded data, and

$$A = \sqrt{u_k^2 + v_k^2}$$

is independent of time index k , that is, the signal has a constant envelope. This can be easily verified by substituting (4.46) into the expression of A , it turns out $A_k = A_{k-1}$. In fact $A = 1$ for initial values $u_0 = 1$ and $v_0 = 0$. It can be proved that the phase relationship between two consecutive symbols is

$$\left. \begin{aligned} \Phi_k &= \Phi_{k-1} + \Delta\theta_k \\ \Delta\theta_k &= \tan^{-1} \frac{Q_k}{I_k} \end{aligned} \right\} \quad (4.47)$$

where $\Delta\theta_k$ is the phase difference determined by input data.

Proof: By definition

$$\begin{aligned} \tan \Phi_k &= \frac{v_k}{u_k} \\ &= \frac{u_{k-1}Q_k + v_{k-1}I_k}{u_{k-1}I_k - v_{k-1}Q_k} = \frac{Q_k + \frac{v_{k-1}}{u_{k-1}}I_k}{I_k - \frac{v_{k-1}}{u_{k-1}}Q_k} \\ &= \frac{Q_k + \tan \Phi_{k-1}I_k}{I_k - \tan \Phi_{k-1}Q_k} = \frac{Q_k \cos \Phi_{k-1} + I_k \sin \Phi_{k-1}}{I_k \cos \Phi_{k-1} - Q_k \sin \Phi_{k-1}} \end{aligned}$$

$I_k Q_k$	$\Delta\theta_k$	$\cos \Delta\theta_k$	$\sin \Delta\theta_k$
1 1	$\pi/4$	$1/\sqrt{2}$	$1/\sqrt{2}$
-1 1	$3\pi/4$	$-1/\sqrt{2}$	$1/\sqrt{2}$
-1 -1	$-3\pi/4$	$-1/\sqrt{2}$	$-1/\sqrt{2}$
1 -1	$-\pi/4$	$1/\sqrt{2}$	$-1/\sqrt{2}$

Table 4.6 $\pi/4$ -QPSK signal phase assignment.

Now let

$$\begin{aligned} I_k &= \sqrt{2} \cos \Delta\theta_k \\ Q_k &= \sqrt{2} \sin \Delta\theta_k \end{aligned} \quad (4.48)$$

then

$$\Delta\theta_k = \tan^{-1} \frac{Q_k}{I_k}$$

and we have

$$\begin{aligned} \tan \Phi_k &= \frac{\sin \Delta\theta_k \cos \Phi_{k-1} + \cos \Delta\theta_k \sin \Phi_{k-1}}{\cos \Delta\theta_k \cos \Phi_{k-1} - \sin \Delta\theta_k \sin \Phi_{k-1}} \\ &= \frac{\sin(\Phi_{k-1} + \Delta\theta_k)}{\cos(\Phi_{k-1} + \Delta\theta_k)} = \tan(\Phi_{k-1} + \Delta\theta_k) \end{aligned}$$

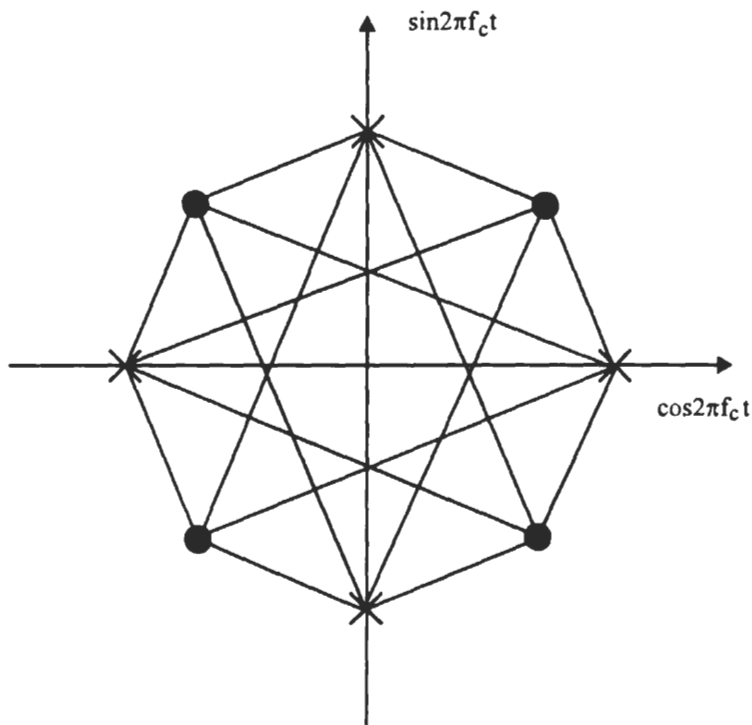
thus we have proved (4.47). Using (4.48) we can write (4.46) as

$$\begin{aligned} u_k &= u_{k-1} \cos \Delta\theta_k - v_{k-1} \sin \Delta\theta_k \\ v_k &= u_{k-1} \sin \Delta\theta_k + v_{k-1} \cos \Delta\theta_k \end{aligned} \quad (4.49)$$

Table 4.6 shows how $\Delta\theta_k$ is determined by the input data.

Referring to the values of $\Delta\theta_k$ in Table 4.6, we can see clearly from (4.47) that the phase changes are confined to odd-number multiples of $\pi/4$ (45°). There are no phase changes of 90° or 180° . In addition, information is carried by the phase changes $\Delta\theta_k$, not the absolute phase Φ_k . The signal constellation is shown in Figure 4.29. The angle of a vector (or symbol) with respect to the positive direction of axis u is the symbol phase Φ_k . The symbols represented by \bullet can only become symbols represented by \times , and vice versa. Transitions among themselves are not possible. The phase change from one symbol to the other is $\Delta\theta_k$.

Since information is carried by the phase changes $\Delta\theta_k$, differentially coherent demodulation can be used. However, coherent demodulation is desirable when higher power efficiency is required. There are four ways to demodulate a $\pi/4$ -QPSK

Figure 4.29 $\pi/4$ -QPSK signal constellation.

signal:⁶

1. Baseband differential detection,
2. IF band differential detection,
3. FM-discriminator detection,
4. Coherent detection.

The first three demodulators are reported to be equivalent in error performance [11]. The coherent demodulator is 2 to 3 dB better.

Figure 4.30 is the baseband differential demodulator which is just a special case of the DMPSK demodulator in Figure 4.16. The LPF in Figure 4.30 is equivalent to the integrator in Figure 4.16. The angle calculation and comparison stages in Figure 4.16 are equivalently replaced by two threshold detectors. The bandpass filter (BPF) at the front end is used to minimize the noise power. However, carrier phase must be preserved for the proper differential detection. A square-root raised-cosine roll-off BPF can achieve this goal [12]. The local oscillation has the same frequency as the

⁶ As a matter of fact, these methods are also applicable to other differential MPSK schemes.

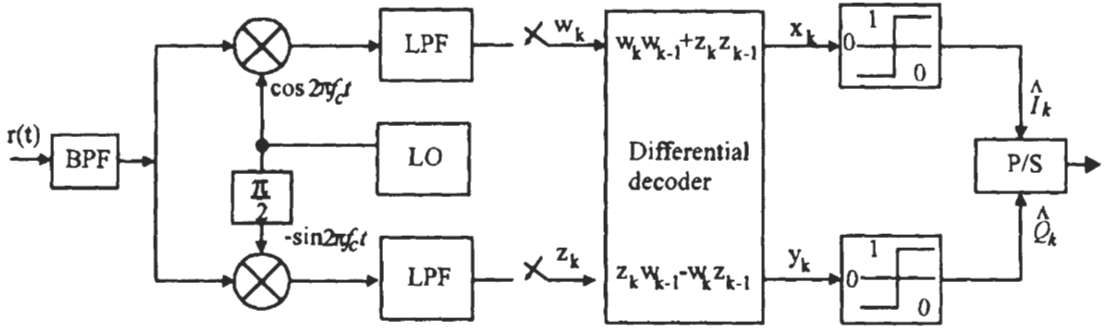


Figure 4.30 Baseband differential demodulator for $\pi/4$ -QPSK.

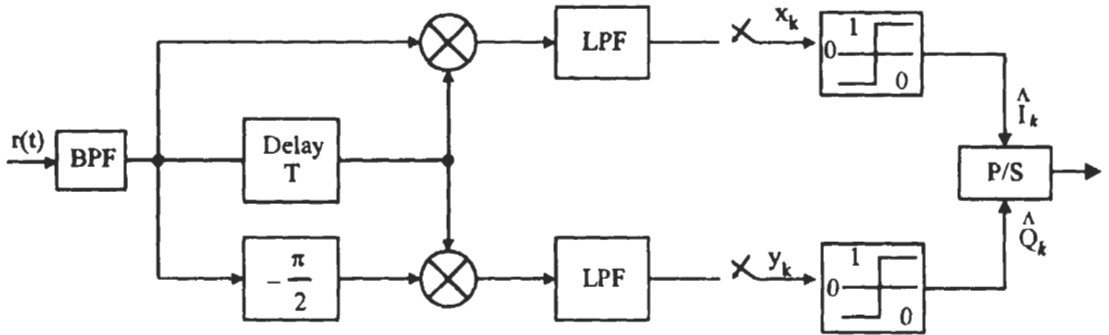


Figure 4.31 IF band differential demodulator for $\pi/4$ -QPSK.

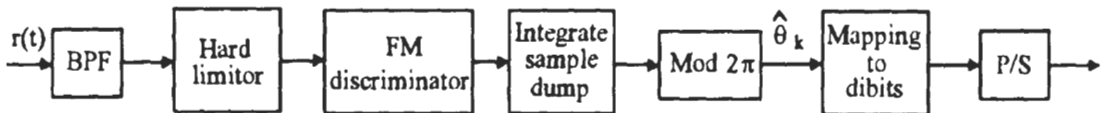


Figure 4.32 FM-discriminator demodulator for $\pi/4$ -QPSK.

unmodulated carrier but its phase is not synchronous with the received signal. It is assumed that the difference phase θ in the received signal remains essentially the same from the previous symbol duration to the current symbol duration. This phase difference will be cancelled in the baseband differential decoder.

In the absence of noise, the output of the BPF in the k th symbol duration is

$$r(t) = A_k \cos(2\pi f_c t + \Phi_k + \theta), \quad kT \leq t \leq (k+1)T \quad (4.50)$$

where θ is the random phase introduced by the channel. We assume that θ changes very slowly in comparison to the symbol rate so that it is considered constant in two consecutive symbols. The time-varying amplitude A_k has replaced the constant amplitude in the transmitted signal. The variation in amplitude might be due to channel fading or interference. In the k th symbol duration the I-channel multiplier output is

$$A_k \cos(2\pi f_c t) \cos(2\pi f_c t + \Phi_k + \theta) = \frac{1}{2} A_k [\cos(4\pi f_c t + \Phi_k + \theta) + \cos(\Phi_k + \theta)]$$

The low-pass filter (LPF) output for the I-channel is therefore (ignoring the factor $1/2$ and the LPF loss)

$$w_k = A_k \cos(\Phi_k + \theta)$$

Similarly the Q-channel LPF output is

$$z_k = A_k \sin(\Phi_k + \theta)$$

Since θ has not been changed from the previous symbol duration, then

$$w_{k-1} = A_{k-1} \cos(\Phi_{k-1} + \theta)$$

$$z_{k-1} = A_{k-1} \sin(\Phi_{k-1} + \theta)$$

The decoding rule is

$$x_k = w_k w_{k-1} + z_k z_{k-1}$$

$$y_k = z_k w_{k-1} - w_k z_{k-1}$$

which is

$$x_k = A_k A_{k-1} [\cos(\Phi_k + \theta) \cos(\Phi_{k-1} + \theta) + \sin(\Phi_k + \theta) \sin(\Phi_{k-1} + \theta)]$$

$$= A_k A_{k-1} \cos(\Phi_k - \Phi_{k-1}) = A_k A_{k-1} \cos \Delta\theta_k$$

$$y_k = A_k A_{k-1} [\sin(\Phi_k + \theta) \cos(\Phi_{k-1} + \theta) - \cos(\Phi_k + \theta) \sin(\Phi_{k-1} + \theta)]$$

$$= A_k A_{k-1} \sin(\Phi_k - \Phi_{k-1}) = A_k A_{k-1} \sin \Delta\theta_k$$

From Table 4.6, the decision devices decide⁷

$$\begin{aligned}\hat{I}_k &= 1, \text{ if } x_k > 0 \text{ or } \hat{I}_k = -1, \text{ if } x_k < 0 \\ \hat{Q}_k &= 1, \text{ if } y_k > 0 \text{ or } \hat{Q}_k = -1, \text{ if } y_k < 0\end{aligned}$$

The symbol error probability is given in (4.29) or (4.30), and P_b is given in (4.40).

The IF band differential demodulator (Figure 4.31) cancels the phase difference θ in the IF band. The I-channel multiplier output is

$$\begin{aligned}& A^2 \cos(2\pi f_c t + \Phi_k + \theta) \cos(2\pi f_c t + \Phi_{k-1} + \theta) \\ &= \frac{1}{2} A^2 [(\cos(4\pi f_c t + \Phi_k + \Phi_{k-1} + 2\theta) + \cos(\Phi_k - \Phi_{k-1}))]\end{aligned}$$

Again ignoring the factor $A^2/2$ and the LPF loss, LPF output is $\cos(\Phi_k - \Phi_{k-1}) = x_k$. Similarly the Q-channel LPF output is found to be $\sin(\Phi_k - \Phi_{k-1}) = y_k$. The rest is the same as the baseband differential detection. The advantage of this demodulator is that no local oscillator is needed.

The discriminator demodulator is shown in Figure 4.32. The ideal bandpass hard limiter keeps the envelope of the received signal constant without changing its phase. The ideal frequency discriminator output is proportional to the instantaneous frequency deviation of the input signal. That is

$$v(t) = \frac{d}{dt} (\Phi(t) + \theta)$$

The integrate-sample-dump (ISD) circuit output is

$$\begin{aligned}\int_{(k-1)T}^{kT} v(t) dt &= \Phi_k - \Phi_{k-1} \\ &= \Delta\theta_k + 2n\pi \\ &= \Delta\theta_k, (\text{mod } 2\pi)\end{aligned}$$

where $2n\pi$ is caused by click noise [13]. The modulo- 2π operation removes the $2n\pi$ term and the output is $\Delta\theta_k$ which in turn will be mapped to a corresponding dibit.

The error probabilities of the above three demodulators are reported to be equal [11].⁸ Like the DQPSK in the last section, the symbol error probability for the above three equivalent demodulators is given by (4.29) or (4.30). The bit error probability

⁷ In Figure 4.16, the decision rule is to choose the smallest $|\Delta\theta_i - \Delta\hat{\theta}_k|$. This rule is simplified for $\pi/4$ -QPSK as described here.

⁸ But it is not clear why the IF band differential demodulator could be equivalent to the baseband differential demodulator, because the latter is optimum and the former is not. according to our discussion in the section discussing DQPSK. The same doubt should arise regarding the discriminator demodulator.

can be approximately calculated using (4.25). Alternately, bit error probability can be evaluated using (4.40).

The coherent $\pi/4$ -QPSK demodulator can be in the form of Figure 4.17 where differential decoding is performed on the signal phases. The coherent demodulator of DEQPSK in Figure 4.25 is not suitable for $\pi/4$ -QPSK since its dibits- $\Delta\theta_i$ assignment is different. A novel coherent $\pi/4$ -QPSK demodulator (Figure 4.33) has been proposed in [11] where differential decoding is performed on the baseband signal levels. In $\pi/4$ -QPSK, assuming $A_k = 1$ in (4.50), the demodulated signals are two-level ($\pm 1/\sqrt{2}$) at every other sampling instant. In between, the signals are three-level ($0, \pm 1$). This can be seen from the signal constellation (Figure 4.29), where \bullet signals are two-level and \times signals are three-level, and a \bullet signal must be followed by a \times signal or vice versa. If three-level detection is employed, the performance degrades compared with two-level detection. The three-level signals are converted to two-level signals in Figure 4.33. The converted two-level signals are detected by a two-level threshold detector. When the signals are two-level, the switches are in position A, the detection is the same as in QPSK. When the signals are three-level, the switches are in position B, the signals are converted to two-level by the following simple operations

$$\begin{aligned}x_{2k} &= x_{1k} - y_{1k} \\y_{2k} &= x_{1k} + y_{1k}\end{aligned}\tag{4.51}$$

It is easy to verify that the conversions are (ignoring noise)

$$\begin{aligned}(x_{1k}, y_{1k}) &\longrightarrow (x_{2k}, y_{2k}) \\(+1, 0) &\longrightarrow (+1, +1) \\(-1, 0) &\longrightarrow (-1, -1) \\(0, +1) &\longrightarrow (-1, +1) \\(0, -1) &\longrightarrow (+1, -1)\end{aligned}$$

This is equivalent to rotate vector (x_{1k}, y_{1k}) by $+\pi/4$ and amplify its amplitude by $\sqrt{2}$. In other words, it is to rotate a \times vector to the next \bullet vector position with an amplitude gain of $\sqrt{2}$. This makes signal power doubled. However, the noise power is also doubled since the in-phase and quadrature channel noise are uncorrelated (see (4.51)). Thus the BER performance of the coherent $\pi/4$ -QPSK is the same as that of the coherent QPSK.

The detected signals \hat{u}_k and \hat{v}_k are decoded by a DEQPSK differential decoder as in (4.44). Then the signals must be passed through a special P/S converter. The circuit is shown in Figure 4.34. The clock is derived from the symbol clock by dividing the frequency by two. The phase of this clock is synchronous to the switch

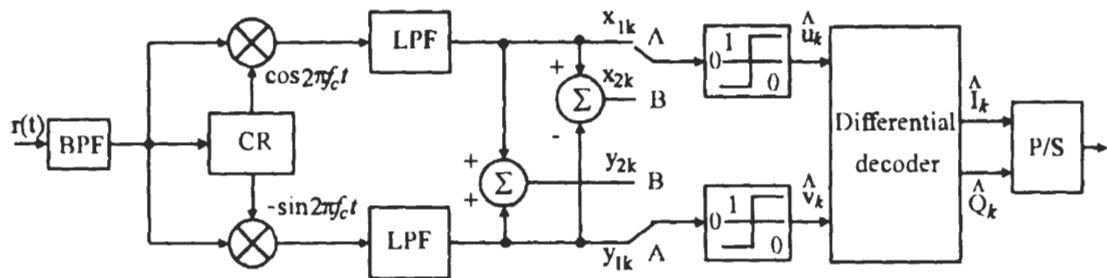


Figure 4.33 $\pi/4$ -QPSK coherent demodulator.

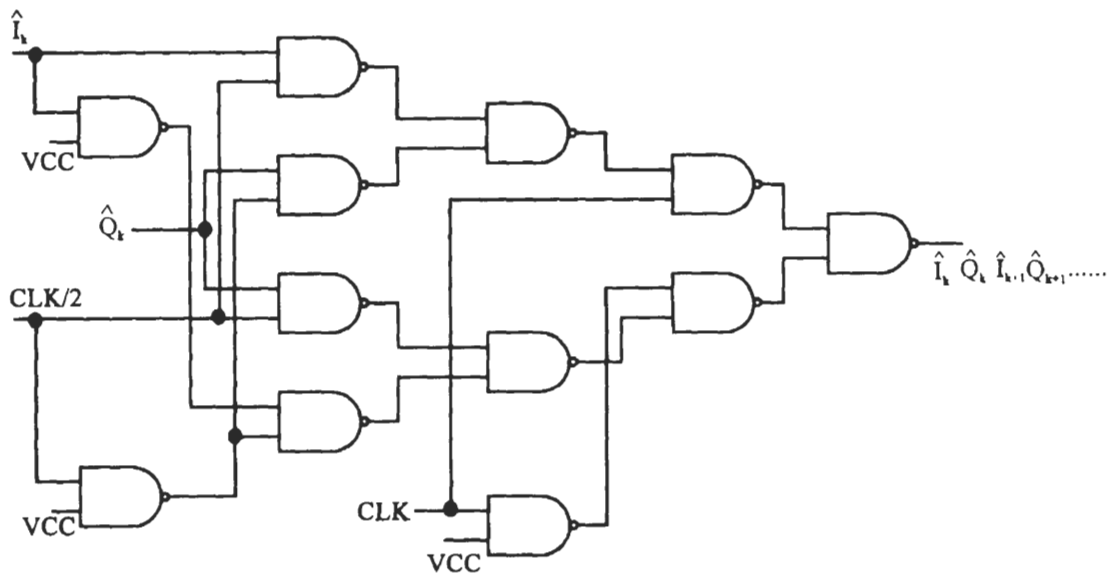


Figure 4.34 The parallel-to-serial converter of the $\pi/4$ -QPSK coherent demodulator.

for selecting sampled signals. The S/P converter delivers inphase and quadrature data alternately to the output. Refer to [11] for details.

As mentioned above in terms of error probability in the AWGN channel, the $\pi/4$ -QPSK is the same as ordinary DEQPSK or DQPSK. That is, the coherently demodulated $\pi/4$ -QPSK has the same BER as that of DEQPSK and the noncoherently demodulated $\pi/4$ -QPSK has the same BER as that of DQPSK (see Figure 4.21).

4.10 SYNCHRONIZATION

Coherent demodulation requires that the reference signal at the receiver be synchronized in phase and frequency with the received signal. Both coherent and noncoherent demodulations require symbol timing at the receiver to be synchronized in phase and frequency with the received signal.

Carrier synchronization can be achieved by sending a pilot tone before message signals. Because the pilot tone has a strong spectral line at the carrier frequency, the receiver can easily lock on it and generates a local coherent carrier. However, this requires extra transmission bandwidth.

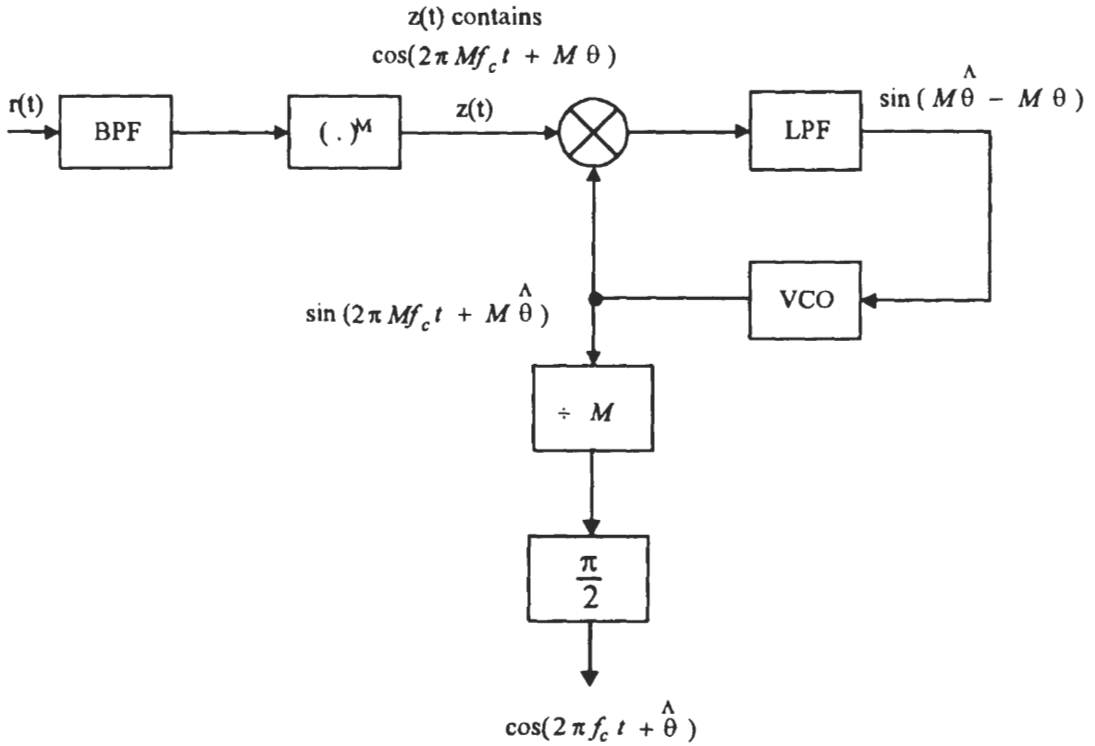
Carrier synchronization also can be achieved with a carrier recovery circuit which extracts the phase and frequency information from the noisy received signal and use it to generate a clean sinusoidal reference signal.

Symbol synchronization usually is achieved by a clock (symbol timing) recovery circuit which uses the received signal to control the local oscillator.

4.10.1 Carrier Recovery

The PSK signals have no spectral line at carrier frequency. Therefore a nonlinear device is needed in the carrier recovery circuit to generate such a line spectrum. There are two main types of carrier synchronizers, the M th power loop, and the Costas loop.

Figure 4.35 is the M th power loop for carrier recovery for M -ary PSK. For BPSK (or DEBPSK), $M = 2$, thus it is a squaring loop. For QPSK (or OQPSK, DEQPSK), $M = 4$, it is a quadrupling loop, and so on. It is the M th power device that produces the spectral line at Mf_c . The phase lock loop consisting of the phase detector, the LPF, and the VCO, tracks and locks onto the frequency and phase of the Mf_c component. The divide-by- M device divides the frequency of this component to produce the desired carrier at frequency f_c and with almost the same phase of the received signal. Before locking, there is a phase difference in the received signal relative to the VCO output signal. We denote the phase of the received signal as θ and the phase of the VCO output as $M\hat{\theta}$.

Figure 4.35 M th power synchronizer for carrier recovery.

For BPSK, using (4.5), setting $A = 1$, and noticing that $a^2(t) = 1$, we have

$$\begin{aligned}
 z(t) &= [s(t) + n(t)]^2 = a^2(t) \cos^2(2\pi f_c t + \theta) + \text{noise terms} \\
 &= \frac{1}{2}[1 + \cos(4\pi f_c t + 2\theta)] + \text{noise terms}
 \end{aligned}$$

which contains a spectral line at $2f_c$ that can be tracked by the phase lock loop (PLL). The VCO output is divided by two in frequency to provide the desired carrier. It is obvious that the loop will produce a carrier with the same phase when the phase θ is either 0 or π . Then the demodulator output could be $+a(t)$ or $-a(t)$. We say that the loop has a phase ambiguity of π . Differential coding can eliminate phase ambiguity, as we described in previous sections in this chapter.

For QPSK, using (4.35), setting $A = \sqrt{2}$, and noticing that $I^2(t) = Q^2(t) = 1$, we have

$$\begin{aligned}
 z(t) &= [s(t) + n(t)]^4 \\
 &= \{[I(t) \cos(2\pi f_c t + \theta) - Q(t) \sin(2\pi f_c t + \theta) + n(t)]^2\}^2
 \end{aligned}$$

$$\begin{aligned}
&= [1 - I(t)Q(t) \sin(4\pi f_c t + 2\theta)]^2 + \text{noise terms} \\
&= 1 - 2I(t)Q(t) \sin(4\pi f_c t + 2\theta) + \frac{1}{2} - \frac{1}{2} \cos(8\pi f_c t + 4\theta) + \text{noise terms}
\end{aligned}$$

The last signal term contains a spectral line at $4f_c$ which is locked onto by the PLL. A divide-by-four device is used to derive the carrier frequency. Note that the $I(t)Q(t) \sin(4\pi f_c t + 2\theta)$ term resulted from squaring operation cannot produce a line spectrum since $I(t)Q(t)$ has a zero mean value. Therefore fourth power operation is needed for QPSK (and OQPSK). The last term will have a 0 initial phase for $\theta = 0$, or $\pm\pi/2$. The demodulator output could be $\pm I(t)$ or $\pm Q(t)$. This is to say that there is a $\pi/2$ phase ambiguity in the carrier recovery. It can be eliminated by differential coding as we discussed before.

For general MPSK, where $M = 2^n$, the M th power operation will produce a spectral line at Mf_c and the phase ambiguity is $2\pi/M$.

The performance of the M th power loop is generally measured by the phase tracking error. Under the usual small angle approximation (i.e., the phase error is small so that $M\hat{\theta} - M\theta \approx \sin(M\hat{\theta} - M\theta)$), the variance of such error is given by [14]

$$\sigma_{\hat{\theta}}^2 = 2N_o B_L S_L \quad (4.52)$$

where B_L is the loop bandwidth defined in terms of the loop transfer function $H(f)$ as follows

$$B_L = \int_0^{\infty} |H(f)|^2 df, \quad (\text{Hz})$$

The parameter S_L is the upper bound of squaring loss in the BPSK case and quadrupling loss in the QPSK case. S_L is a number without unit that reflects the increase in the variance of phase error due to squaring or quadrupling operation in the phase tracking loop. They are given by [14]

$$S_L = 1 + \frac{1}{2\rho_i}, \quad \text{for } M = 2$$

and

$$S_L = 1 + \frac{9}{\rho_i} + \frac{6}{\rho_i^2} + \frac{3}{2\rho_i^3}, \quad \text{for } M = 4$$

where ρ_i is the input signal-to-noise ratio of the carrier recovery circuit. Observing (4.52), the unit of $\sigma_{\hat{\theta}}^2$ is seemingly watt instead of radian². This is due to the small-angle approximation in deriving the phase error variance where volt is replaced by radian. Therefore the unit of $\sigma_{\hat{\theta}}^2$ should be radian².

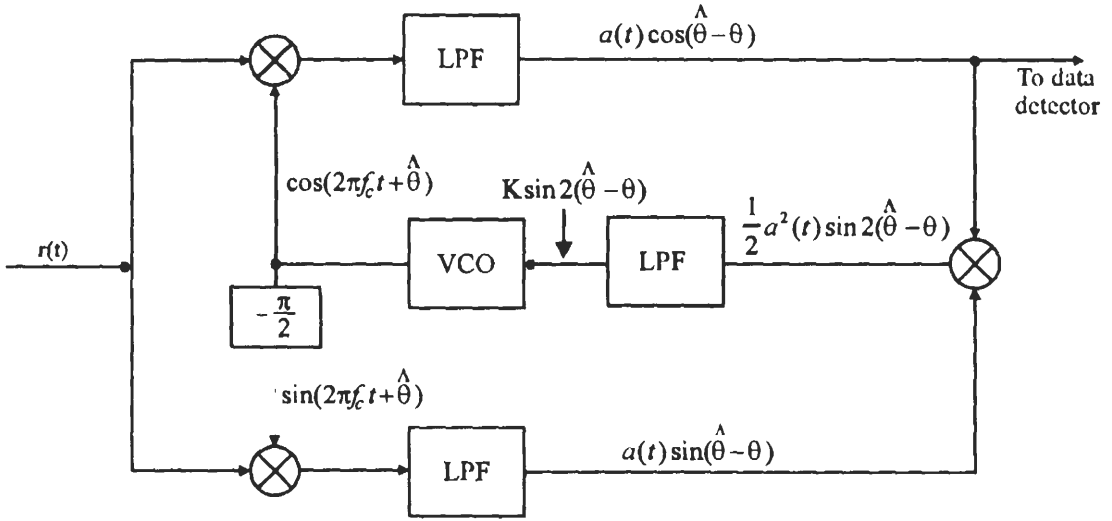


Figure 4.36 Costas loop for carrier recover for BPSK.

A difficulty in circuit implementation of the M th power loop is the M th power device, especially at high frequencies. Costas loop design avoids this device.

Figure 4.36 is the Costas loop for carrier recovery for BPSK. Initially the VCO generates a sinusoid with a frequency close to the carrier frequency f_c and some initial phase. The frequency difference and the initial phase are accounted for by the phase $\hat{\theta}$. The multipliers in the I- and Q-channels produce $2f_c$ terms and zero frequency terms. The LPFs attenuate the $2f_c$ terms and their outputs are proportional to $a(t) \cos(\hat{\theta} - \theta)$ or $a(t) \sin(\hat{\theta} - \theta)$. Then these two terms multiply again to give the term $\frac{1}{2}a^2(t) \sin 2(\hat{\theta} - \theta)$ which is low-pass filtered one more time to get rid of any amplitude fluctuation in $a^2(t)$, thus the control signal to the VCO is proportional to $\sin 2(\hat{\theta} - \theta)$, which drives the VCO such that the difference $\hat{\theta} - \theta$ becomes smaller and smaller. For sufficiently small $\hat{\theta} - \theta$, the I-channel output is the demodulated signal.

The Costas loop for QPSK is shown in Figure 4.37. The figure is self-explanatory and its working principle is similar to that of BPSK. The limiters are bipolar, which are used to control the amplitude of the two channels' signal to maintain balance. When the phase difference $\phi = \hat{\theta} - \theta$ is sufficiently small, the I- and Q-channel outputs are the demodulated signals.

A difficulty in Costas loop implementation is to maintain the balance between the I- and Q-channel. The two multipliers and low-pass filters in these two channels must be perfectly matched in order to achieve the theoretical performance.

Although the appearance of the M th power loop and the Costas loop are quite

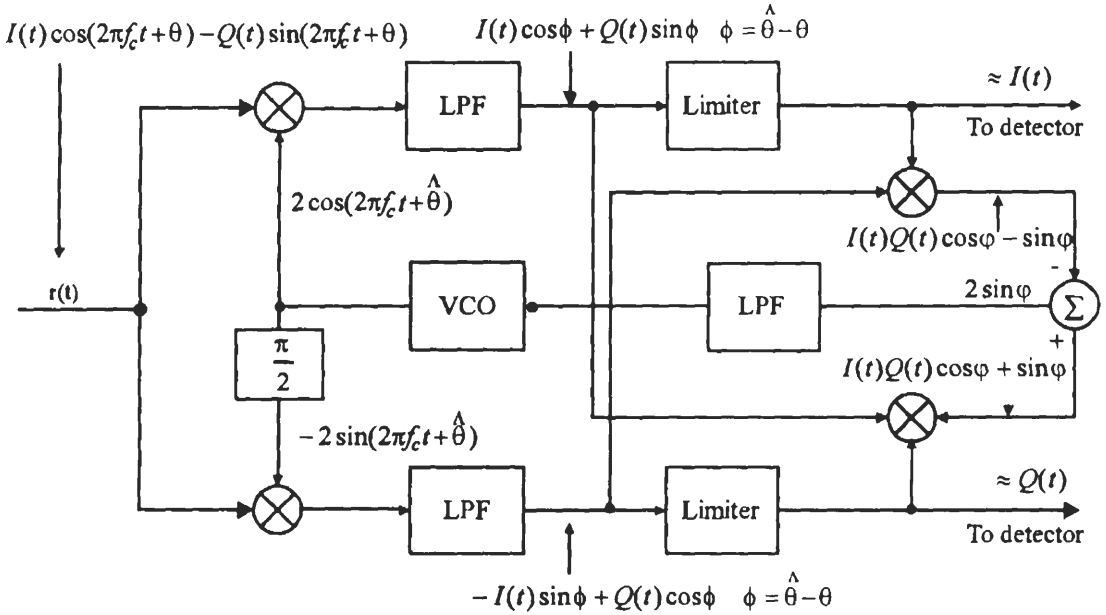


Figure 4.37 Costas loop for carrier recovery for QPSK.

different, their performance can be shown to be the same [14]. Therefore (4.52) is also applicable to Costas loops.

4.10.2 Clock Recovery

The clock or symbol timing recovery can be classified into two basic groups. One group is the open loop synchronizer which uses nonlinear devices. These circuits recover the clock signal directly from the data stream by nonlinear operations on the received data stream. Another group is the closed-loop synchronizers which attempt to lock a local clock signal onto the received data stream by use of comparative measurements on the local and received signals.

Two examples of the open-loop synchronizer are shown in Figure 4.38. The data stream that we use in the phase shift keying modulation is NRZ waveform. Recall in Chapter 2 we have shown that this waveform has no spectral energy at the clock frequency (see Figure 2.3(a)). Thus in the open-loop synchronizers in Figure 4.38, the first thing that one needs to do is to create spectral energy at the clock frequency. In the first example, a Fourier component at the data clock frequency is generated by the delay-and-multiply operation on the demodulated signal $m(t)$. This frequency component is then extracted by the BPF that follows and shaped into square wave by the final stage. The second example generates the clock frequency

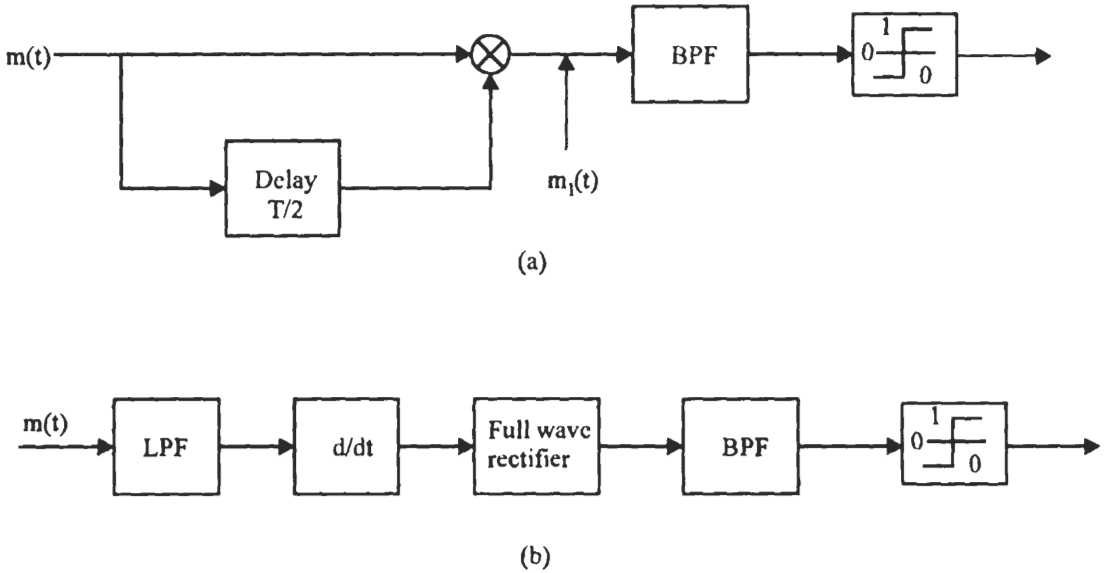


Figure 4.38 Two types of open-loop symbol synchronizers.

component by using the differentiator-rectifier combination. The differentiator is very sensitive to wideband noise, therefore a low-pass filter is placed in the front end of the synchronizer.

An early/late-gate circuit shown in Figure 4.39 is an example of the class of closed-loop synchronizers. The working principle is easily understood by referencing Figure 4.40. The time zero point is set by the square wave clock locally generated by the VCO. If the VCO square wave clock is in perfect synchronism with the demodulated signal $m(t)$, the early-gate integrator and the late-gate integrator will accumulate the same amount of signal energy so that the error signal $e = 0$. If the VCO frequency is higher than that of $m(t)$, then $m(t)$ is late by $\Delta < d$, relative to the VCO clock. Thus the integration time in the early-gate integrator will be $T - d - \Delta$, while the integration time in the late-gate integrator is still the entire $T - d$. The error signal will be proportional to $-\Delta$. This error signal will reduce the VCO frequency and retard the VCO timing to bring it back toward the timing of $m(t)$. If the VCO frequency had been lower and the timing had been late, the error signal would be proportional to $+\Delta$, and the reverse process would happen, that is, the VCO frequency would be increased and its timing would be advanced toward that of the incoming signal.

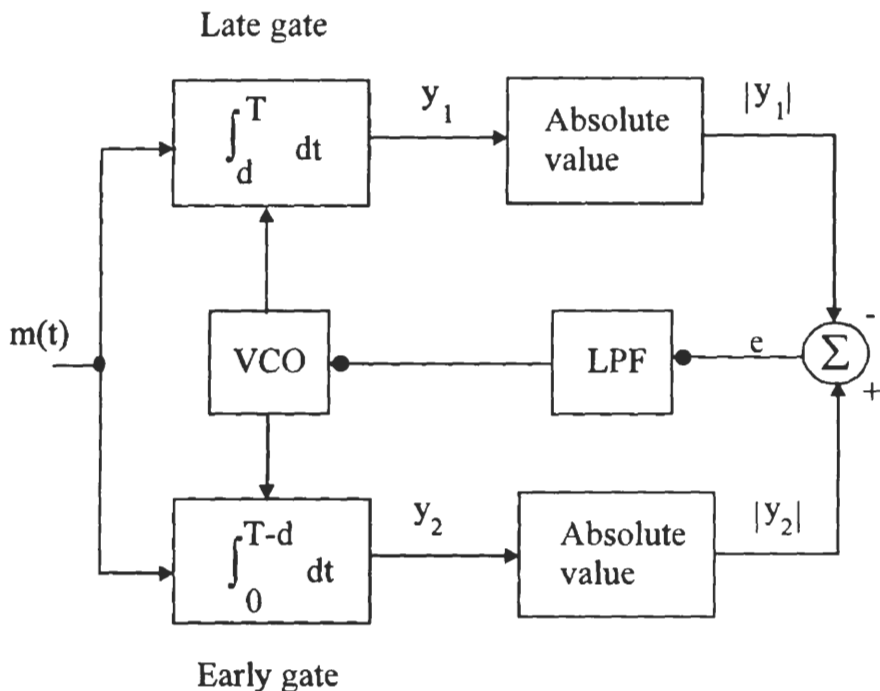


Figure 4.39 Early/late-gate clock synchronizer.

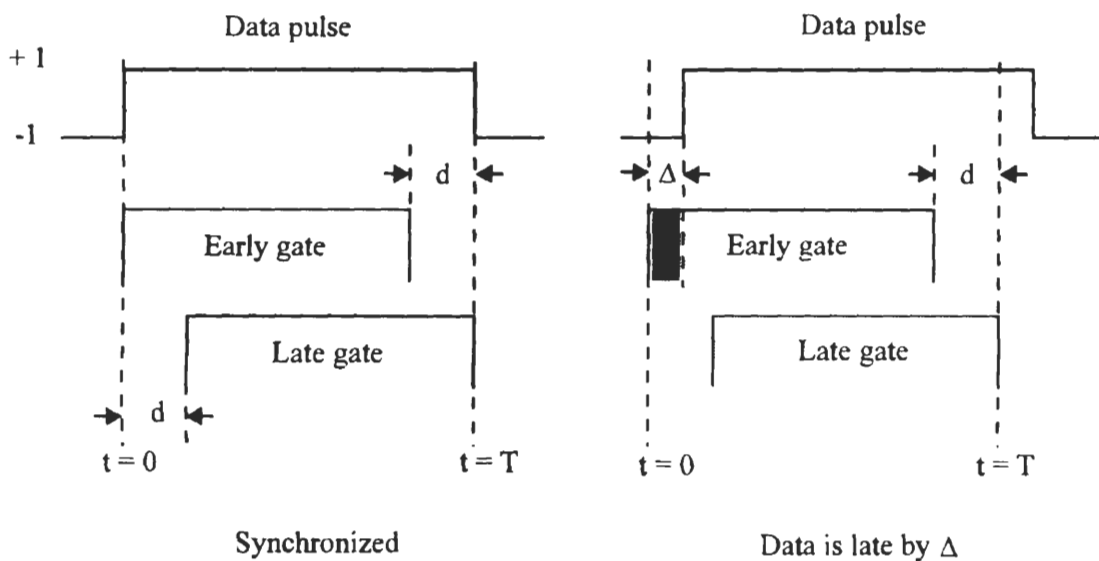


Figure 4.40 Early/late-gate timing illustration.

4.10.3 Effects of Phase and Timing Error

As an example, we want to check the effects of phase and timing error on the bit error probability of coherent BPSK in the AWGN channel.

If the local carrier is in error by ϕ radians, the correlator output amplitude will be reduced by a factor $\cos \phi$. Thus the conditional bit error probability of BPSK will be

$$P_b(\phi) = Q\left(\sqrt{\frac{2E_b}{N_o}} \cos \phi\right) \quad (4.53)$$

If ϕ is Gaussianly distributed with variance σ_ϕ^2 , the bit error probability is [15, p.270-271]

$$\begin{aligned} P_b &= \int_{-\infty}^{\infty} p(\phi) P_b(\phi) d\phi \\ &= \frac{2}{\sqrt{2\pi}\sigma_\phi} \int_0^{\infty} \exp\left(-\frac{\phi^2}{2\sigma_\phi^2}\right) Q\left(\sqrt{\frac{2E_b}{N_o}} \cos \phi\right) d\phi \end{aligned} \quad (4.54)$$

This is plotted in Figure 4.41 where different curves are labeled according to values of the standard deviation of the phase error σ_ϕ in radians. It is seen that when $\sigma_\phi < 0.2$, the degradation is not significant.

The effect of a symbol synchronization error on the bit error probability of BPSK depends on the presence or absence of a symbol transition. If two successive symbols are identical, an incorrect symbol reference will have no effect on the error probability. If two successive symbols differ, the magnitude of the correlator output is reduced by a factor of $1 - (2|\Delta|/T)$ where Δ is the timing error. Thus given a timing error, the conditional P_b is

$$\begin{aligned} P_b(\Delta) &= \Pr(\text{error} \mid \text{transition}, \Delta) \Pr(\text{transition} \mid \Delta) \\ &\quad + \Pr(\text{error} \mid \text{no transition}, \Delta) \Pr(\text{no transition} \mid \Delta) \end{aligned}$$

If the successive symbols are independent and equally likely to be either of the two binary symbols, the probability of transition is one-half, and, if the normalized timing error $\tau = \Delta/T$ is Gaussianly distributed, then

$$\begin{aligned} P_b &= \frac{1}{2\sqrt{2\pi}\sigma_\tau} \int_{-0.5}^{0.5} \exp\left(-\frac{\tau^2}{2\sigma_\tau^2}\right) Q\left(\sqrt{\frac{2E_b}{N_o}} (1 - 2|\tau|)\right) d\tau \\ &\quad + \frac{1}{2} Q\left(\sqrt{\frac{2E_b}{N_o}}\right) \end{aligned} \quad (4.55)$$

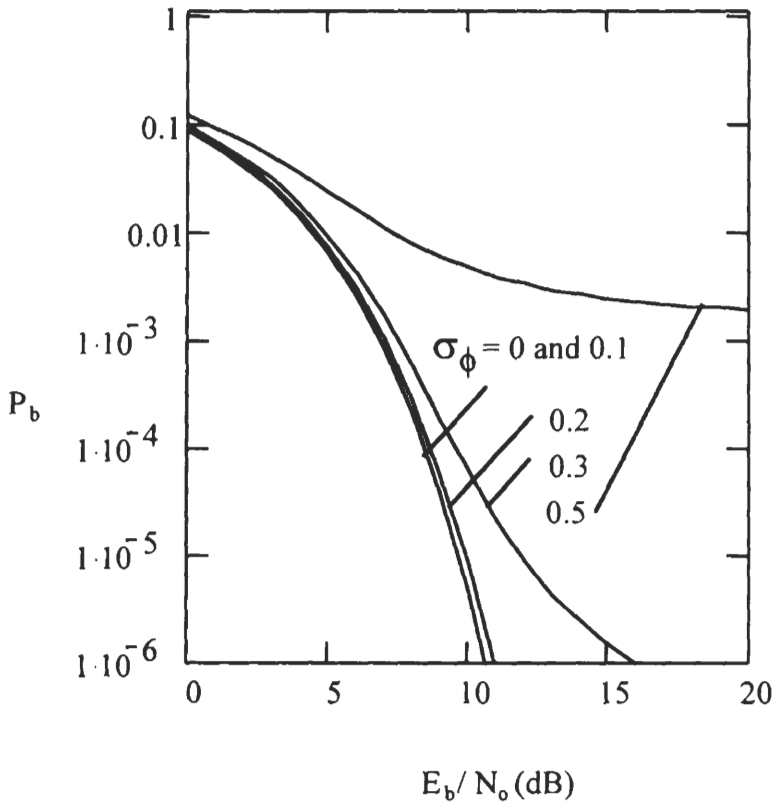


Figure 4.41 Effect of imperfect carrier synchronization on P_b of BPSK.

where the integration limits are 0.5 to -0.5 which is the range of the timing errors [16, section 6-4 and 9-4]. This is plotted in Figure 4.42, where different curves are labeled according to a value of the $\pi\sigma_\tau$ where σ_τ is the standard deviation of the timing error τ . When $\pi\sigma_\tau$ is less than 0.2, the degradation is not significant.

It should be pointed out that (4.54) and (4.55), consequently Figure 4.41 and 4.42, are based on the assumption that the errors are Gaussianly distributed [15, p.270-271], which may not be accurate, depending on the carrier and clock recovery systems. More accurate, but also more complicated, error distribution models and error probability results are given in [16, section 6-4 and 9-4].

4.11 SUMMARY

In this chapter we have covered all important PSK modulation schemes. We de-

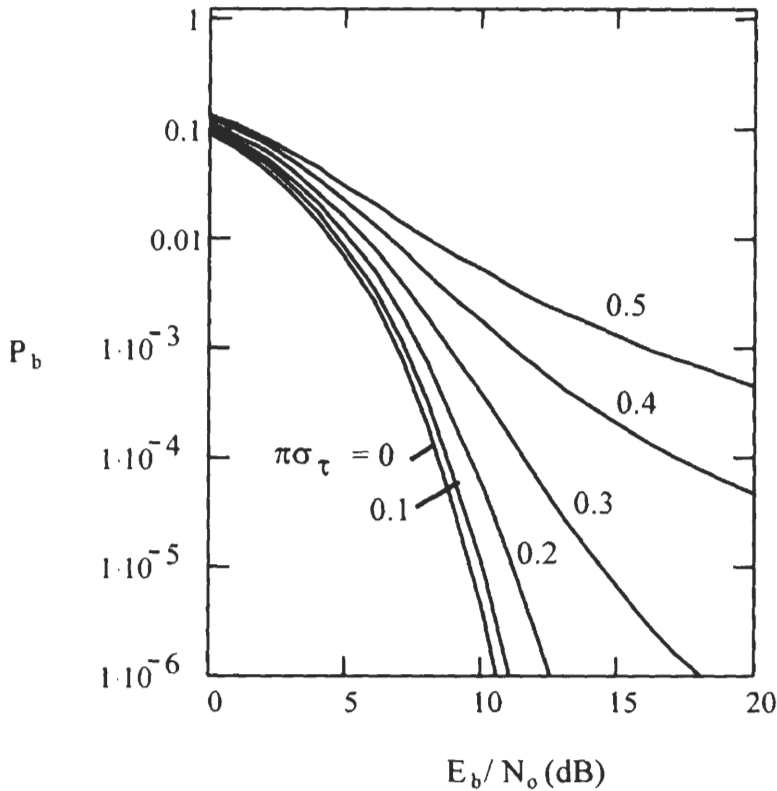


Figure 4.42 Effect of imperfect symbol synchronization on P_b of BPSK.

scribed all aspects, including signal expressions, waveforms, power spectral density, modulator, demodulator, and symbol or bit error probability. We started from the basic BPSK and its noncoherent version, DBPSK. Then we proceed to M-ary PSK and its differential version. For them we established general optimum demodulator block diagrams, error probability formulas, and PSD expressions. These results were later used for QPSK and DQPSK. However, QPSK and DQPSK are not merely special cases of MPSK and MDPSK. Their signal constellations allow for further simplification of the demodulators. Noticeably, phase calculation and comparison stages of the demodulators are replaced by level detectors. Offset QPSK, as a solution to suppress sidelobe spread after bandlimiting and nonlinear amplifications, was briefly described due to its historical value. $\pi/4$ -QPSK, as standard modulation in several digital cellular systems, was covered in great detail. Its modulator, base-band differential demodulator, IF-band differential demodulator, FM-discriminator demodulator, and coherent demodulator were described. Error performance was de-

Modulation	P_b	Degradation	PSD and B_{null}
BPSK	$Q\left(\sqrt{\frac{2E_b}{N_o}}\right)$	0 dB (ref.)	$A^2T_b \left(\frac{\sin \pi f T_b}{\pi f T_b}\right)^2$ $B_{null} = 2/T_b$
DEBPSK	$\approx 2Q\left(\sqrt{\frac{2E_b}{N_o}}\right)$	< 0.5 dB	
DBPSK (Optimum)	$\frac{1}{2}e^{-E_b/N_o}$	0.5-1 dB	
DBPSK (Suboptimum)	$\frac{1}{2}e^{-0.8E_b/N_o}$	1.5-2 dB	
QPSK	$Q\left(\sqrt{\frac{2E_b}{N_o}}\right)$	0 dB (ref.)	$2A^2T_b \left(\frac{\sin 2\pi f T_b}{2\pi f T_b}\right)^2$ $B_{null} = 1/T_b$
DEQPSK	$\approx 2Q\left(\sqrt{\frac{2E_b}{N_o}}\right)$	< 0.5 dB	
DQPSK (Optimum)	$\approx Q\left(\sqrt{\frac{4E_b}{N_o}} \sin \frac{\pi}{4\sqrt{2}}\right)$	2-3 dB	
DQPSK (Suboptimum)	$\approx e^{-0.59\frac{E_b}{N_o}}$	3-5 dB	
$\pi/4$ -QPSK	$\approx 2Q\left(\sqrt{\frac{2E_b}{N_o}}\right)$ (= DEQPSK)	< 0.5 dB	$2A^2T_b \left(\frac{\sin 2\pi f T_b}{2\pi f T_b}\right)^2$ $B_{null} = 1/T_b$
$\pi/4$ -DQPSK	$\approx Q\left(\sqrt{\frac{4E_b}{N_o}} \sin \frac{\pi}{4\sqrt{2}}\right)$ (= optimum DQPSK)	2-3 dB	
MPSK ($M > 4$) ($n = \log_2 M$)	$\approx \frac{2}{n}Q\left(\sqrt{\frac{2nE_b}{N_o}} \sin \frac{\pi}{M}\right)$	0 dB (ref.)	$nA^2T_b \left(\frac{\sin n\pi f T_b}{n\pi f T_b}\right)^2$ $B_{null} = 2/(nT_b)$
DEMPSK	Eqn.(4.31)	< 0.5 dB	
DMPSK (Optimum)	$\approx \frac{2}{n}Q\left(\sqrt{\frac{2nE_b}{N_o}} \sin \frac{\pi}{\sqrt{2}M}\right)$	3 dB (asympt.)	

Table 4.7 PSK schemes comparion.

scribed. Finally we covered the synchronization. Carrier synchronization is needed for coherent PSK schemes. Symbol synchronization is needed for any digital modulation schemes. Table 4.7 summarizes and compares the various aspects of PSK schemes described in this chapter. The error performance degradation is measured in increase of E_b/N_o for achieving the same error probability, reference to the coherent demodulation. BPSK and QPSK are the most widely used PSK schemes. This is due to their system simplicity and excellent power and bandwidth efficiency. Higher order MPSK can be used if higher bandwidth efficiency is desired and higher signal-to-noise ratio is available.

Up to this point, we have studied classical frequency and phase shift keying schemes. In the rest of this book, we will study more bandwidth efficient and/or power efficient modulation schemes. In the next chapter, a scheme with important practical applications, minimum shift keying (MSK), which can be considered as an development from OQPSK or a special continuous phase FSK, will be studied.

4.12 APPENDIX 4A

To derive the expression for $p(\varphi/H_i)$, we first complete the square in exponent of $p(\rho, \hat{\theta}/H_i)$ by writing

$$\begin{aligned}\rho^2 + E - 2\rho\sqrt{E}\cos\varphi &= (\rho - \sqrt{E}\cos\varphi)^2 - E\cos^2\varphi + E \\ &= (\rho - \sqrt{E}\cos\varphi)^2 + E\sin^2\varphi\end{aligned}$$

Then we integrate $p(\rho, \hat{\theta}/H_i)$ with respect to ρ to obtain the PDF of φ

$$\begin{aligned}p(\varphi/H_i) &= \int_0^\infty \frac{\rho}{\pi N_o} \exp\left\{-\frac{1}{N_o}[(\rho - \sqrt{E}\cos\varphi)^2 + E\sin^2\varphi]\right\} d\rho \\ &= \exp\left\{-\frac{E}{N_o}\sin^2\varphi\right\} \int_0^\infty \frac{\rho}{\pi N_o} \exp\left\{-\frac{1}{N_o}(\rho - \sqrt{E}\cos\varphi)^2\right\} d\rho\end{aligned}$$

Now change the variable to make the exponent be $-t^2$. This requires

$$t = \frac{1}{\sqrt{N_o}}(\rho - \sqrt{E}\cos\varphi)$$

or inversely

$$\rho = \sqrt{N_o}t + \sqrt{E}\cos\varphi$$

Noting that $d\rho = \sqrt{N_o}dt$, and when $\rho = 0$, $t = -\sqrt{E/N_o}\cos\varphi$, the integral

becomes

$$\begin{aligned}
 & p(\varphi/H_i) \\
 = & \exp\left\{-\frac{E}{N_o} \sin^2 \varphi\right\} \int_{-\sqrt{E/N_o} \cos \varphi}^{\infty} \frac{1}{\pi \sqrt{N_o}} \left[\sqrt{N_o} t + \sqrt{E} \cos \varphi \right] \exp\{-t^2\} dt
 \end{aligned} \tag{4.56}$$

The first term of the integral is

$$\begin{aligned}
 \int_{-\sqrt{E/N_o} \cos \varphi}^{\infty} \frac{t}{\pi} \exp\{-t^2\} dt &= -\frac{1}{2\pi} \exp\{-t^2\} \Big|_{-\sqrt{E/N_o} \cos \varphi}^{\infty} \\
 &= \frac{1}{2\pi} \exp\left\{-\frac{E}{N_o} \cos^2 \varphi\right\}
 \end{aligned} \tag{4.57}$$

The second term of the integral is

$$\begin{aligned}
 & \int_{-\sqrt{E/N_o} \cos \varphi}^{\infty} \frac{\sqrt{E} \cos \varphi}{\pi \sqrt{N_o}} \exp\{-t^2\} dt \\
 = & \frac{\cos \varphi}{2\sqrt{\pi}} \sqrt{\frac{E}{N_o}} \int_{-\sqrt{E/N_o} \cos \varphi}^{\infty} \frac{2}{\sqrt{\pi}} \exp\{-t^2\} dt \\
 = & \frac{\cos \varphi}{2\sqrt{\pi}} \sqrt{\frac{E}{N_o}} \left[1 + \operatorname{erf} \left(\sqrt{\frac{E}{N_o}} \cos \varphi \right) \right]
 \end{aligned} \tag{4.58}$$

where

$$\operatorname{erf}(x) \triangleq \frac{2}{\sqrt{\pi}} \int_0^x e^{-t^2} dt$$

is the *error function* which has the following properties

$$\operatorname{erf}(x) = 1 - \int_x^{\infty} \frac{2}{\sqrt{\pi}} \exp\{-t^2\} dt$$

and

$$\operatorname{erf}(-x) = -\operatorname{erf}(x)$$

We have used these properties in deriving (4.58). Substituting (4.57) and (4.58) into (4.56) we have

$$p(\varphi/H_i) = \exp\left\{-\frac{E}{N_o} \sin^2 \varphi\right\} \left\{ \frac{1}{2\pi} \exp\left\{-\frac{E}{N_o} \cos^2 \varphi\right\} + \frac{\cos \varphi}{2\sqrt{\pi}} \sqrt{\frac{E}{N_o}} \right\}$$

$$\cdot \left[1 + \operatorname{erf} \left(\sqrt{\frac{E}{N_o}} \cos \varphi \right) \right] \Bigg\}$$

Factorizing $\frac{1}{2\pi} \exp\{-\frac{E}{N_o} \cos^2 \varphi\}$ out of the bracket we obtain

$$\begin{aligned} p(\varphi/H_i) &= \frac{e^{-E/N_o}}{2\pi} \left\{ 1 + \sqrt{\frac{\pi E}{N_o}} (\cos \varphi) e^{(E/N_o) \cos^2 \varphi} \right. \\ &\quad \cdot \left. \left[1 + \operatorname{erf} \left(\sqrt{\frac{E}{N_o}} \cos \varphi \right) \right] \right\} \\ &= p(\varphi) \end{aligned}$$

References

- [1] Park, J. H., Jr., "On binary DPSK detection," *IEEE Trans. Commun.*, vol. 26, no. 4, April 1978, pp. 484-486.
- [2] Simon, K. M., S. M. Hinedi, and W. C. Lindsey, *Digital Communication Techniques, Signal Design and Detection*, Englewood Cliffs, New Jersey: Prentice Hall, 1995.
- [3] Van Trees, H. L., *Detection, Estimation, and Modulation Theory, Part I*, New York: John Wiley & Sons, Inc., 1968.
- [4] Benedetto, S., E. Biglieri, and V. Castellani, *Digital Transmission Theory*, Englewood Cliffs, New Jersey: Prentice Hall, 1987.
- [5] Proakis, J., *Digital Communications*, 2nd Ed., New York: McGraw-Hill, 1989.
- [6] Feher K., *Digital Communications: Satellite/Earth Station Engineering*, Englewood Cliffs, New Jersey: Prentice Hall, 1983.
- [7] Lucky, R., J. Salz, and J. Weldon, *Principles of Data Communications*, New York: McGraw-Hill, 1968.
- [8] Whalen, A. D., *Detection of Signals in Noise*, New York and London: Academic Press, 1971.
- [9] Pasupathy, S., "Minimum shift keying: a spectrally efficient modulation," *IEEE Communications Magazine*, July 1979.
- [10] Baker, P. A., "Phase Modulation Data Sets for Serial Transmission at 2000 and 2400 Bits per Second, Part I," *AIEE Trans. Comm. Electron.*, July 1962.
- [11] Liu, C. L. and K. Feher, " $\pi/4$ -QPSK Modems for Satellite Sound/Data Broadcast Systems," *IEEE Trans. Broadcasting*, March 1991.
- [12] Feher, K., "MODEMS for Emerging Digital Cellular-Mobile Radio System," *IEEE Trans. on Vehicular Technology*; vol. 40, no. 2, May 1991, pp. 355-365.
- [13] Roden, M., *Analog and Digital Communications*, 3rd Ed., Englewood Cliffs, New Jersey: Prentice Hall, 1991.

- [14] Gardner, F. M., *Phaselock Techniques*, 2nd Ed., New York: John Wiley, 1979.
- [15] Stiffler, J. J., *Theory of Synchronous Communications*. Englewood Cliffs, New Jersey: Prentice Hall, 1971.
- [16] Lindsay, W.C. and M. K. Simon, *Telecommunication Systems Engineering*. Englewood Cliffs, New Jersey: Prentice Hall, 1973.

Selected Bibliography

- Couch II, L. W., *Digital and Analog Communication Systems*, 3rd Ed., New York: Macmillan, 1990.
- Divsalar, D., and M. K. Simon, "On the implementation and performance of single and double differential detection schemes," *IEEE Trans. Commun.*, vol. 40, no. 2, Feb. 1992, pp. 278-291.
- Haykin, S., *Digital Communications*, New York: John Wiley, 1988.
- Haykin, S., *Communication Systems*, 3rd Ed., New York: John Wiley, 1994.
- Liu, C. L. and K. Feher, "Bit error performance of $\pi/4$ -DQPSK in a frequency-selective fast Rayleigh fading channel," *IEEE Trans. Vehicular Technology*, vol. 40, no. 3, August 1991.
- Sklar, B., *Digital Communications, Fundamentals and Applications*, Englewood Cliffs, New Jersey: Prentice Hall, 1988.
- Smith, D. R., *Digital Transmission Systems*, 2nd Ed., New York: Van Nostrand Reinhold, 1993.
- Ziemer R. E., R. L. Peterson, *Introduction to Digital Communication*. New York: Macmillan, 1992.

Chapter 5

Minimum Shift Keying and MSK-Type Modulations

In the previous chapter we have seen that the major advantage of OQPSK over QPSK is that it exhibits less phase changes at symbol transitions, thus out-of-band interference due to band limiting and amplifier nonlinearity is reduced. This suggests that further improvement is possible if phase transitions are further smoothed or even become completely continuous. Minimum shift keying (MSK) is such a continuous phase modulation scheme. It can be derived from OQPSK by shaping the pulses with half sinusoidal waveforms, or can be derived as a special case of continuous phase frequency shift keying (CPFSK).

MSK was first proposed by Doelz and Heald in their patent in 1961 [1]. DeBuda discussed it as a special case of CPFSK in 1972 [2]. Gronemeyer and McBride described it as sinusoidally weighted OQPSK in 1976 [3]. Amoroso and Kivett simplified it by an equivalent serial implementation (SMSK) in 1977 [4]. Now MSK has been used in actual communication systems. For instance, SMSK has been implemented in NASA's Advanced Communications Technology Satellite (ACTS) [5] and Gaussian MSK (GMSK) has been used as the modulation scheme of European GSM (global system for mobile) communication system [6].

This chapter is organized as follows: Section 5.1 describes the basic MSK (i.e., parallel MSK) in great detail in order for the readers to grasp the fundamental concept and important properties of MSK thoroughly. Section 5.2 discusses its power spectral density and bandwidth. MSK modulator, demodulator, and synchronization are presented in Sections 5.3, 5.4, and 5.5, respectively. MSK error probability is discussed in Section 5.6. Section 5.7 is devoted to SMSK in a great detail because of its importance in practical applications. MSK-type schemes which are modified MSK schemes for better bandwidth efficiency or power efficiency, are discussed in detail in Sections 5.8 through 5.13. However, GMSK is not covered in this chapter, instead, it is discussed in Chapter 6 in the context of continuous phase modulation. Finally, the chapter is concluded with a summary in Section 5.14.

5.1 DESCRIPTION OF MSK

5.1.1 MSK Viewed as a Sinusoidal Weighted OQPSK

In OQPSK modulation, $I(t)$ and $Q(t)$, the staggered data streams of the I-channel and Q-channel are directly modulated onto two orthogonal carriers. Now we weight each bit of $I(t)$ or $Q(t)$ with a half period of cosine function or sine function with a period of $4T$, $A \cos(\pi/2T)$ or $A \sin(\pi/2T)$, respectively, then modulate them onto one of two orthogonal carriers, $\cos 2\pi f_c t$ or $\sin 2\pi f_c t$, by doing these we create an MSK signal

$$s(t) = AI(t)\cos\left(\frac{\pi t}{2T}\right)\cos 2\pi f_c t + AQ(t)\sin\left(\frac{\pi t}{2T}\right)\sin 2\pi f_c t \quad (5.1)$$

where T is the bit period of the data.

Figure 5.1 shows the waveforms of MSK at each stage of modulation. Figure 5.1(a) is the $I(t)$ waveform for the sample symbol stream of $\{1, -1, 1, 1, -1\}$. Note that each $I(t)$ symbol occupies an interval of $2T$ from $(2n - 1)T$ to $(2n + 1)T$, $n = 0, 1, 2, \dots$. Figure 5.1(b) is the weighting cosine waveform with a period of $4T$, whose half period coincides with one symbol of $I(t)$. Figure 5.1(c) is the cosine weighted symbol stream. Figure 5.1(d) is the modulated I-channel carrier that is obtained by multiplying the waveform in Figure 5.1(c) by the carrier $\cos 2\pi f_c t$. This signal is the first term in (5.1).

Figure 5.1(e–h) shows the similar modulation process in Q-channel for the sample $Q(t)$ stream of $\{1, 1, -1, 1, -1\}$. Note that $Q(t)$ is delayed by T with respect to $I(t)$. Each symbol starts from $2nT$ and ends at $(2n + 2)T$, $n = 0, 1, 2, \dots$. The weighting signal is sine instead of cosine, thus each half period coincides with one symbol of $Q(t)$. Figure 5.1(h) is the second term in (5.1).

Figure 5.1(i) shows the composite MSK signal $s(t)$, which is the sum of waveforms of Figure 5.1(d) and Figure 5.1(h).¹

From Figure 5.1(i) we observe the following properties of MSK. First, its envelope is constant. Second, the phase is continuous at bit transitions in the carrier. There are no abrupt phase changes at bit transitions like in QPSK or OQPSK. Third, the signal is an FSK signal with two different frequencies and with a symbol duration

¹ The MSK defined in (5.1) and illustrated in Figure 5.1 is called Type I MSK where the weighting is alternating positive and negative half-sinusoid. Another type is called Type II MSK where the weighting is always a positive half-sinusoid [7]. These two types are the same in terms of power spectral density, which is determined by the shape of the half-sinusoid, and error probability, which is determined by the energy of the half-sinusoid. The only difference between them is the weighting signal in the modulator and the demodulator. Therefore it suffices to analyze Type I only in the rest of this chapter.

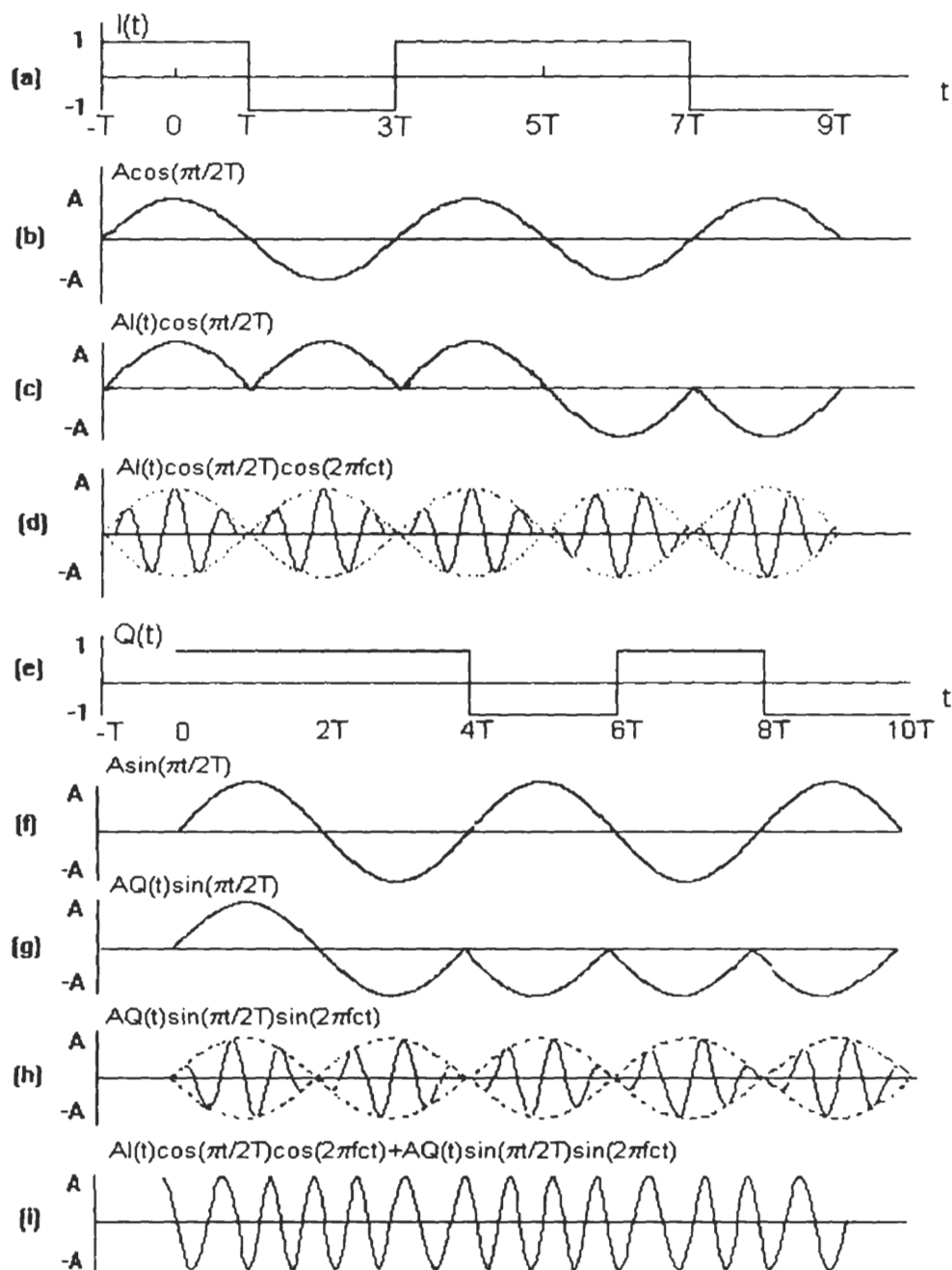


Figure 5.1 MSK waveforms.

of T .²

To better understand the above properties we rewrite (5.1) in a different form. In the k th bit period of T seconds, $I(t)$ and $Q(t)$ is either 1 or -1 , we denote them as I_k and Q_k , thus

$$\begin{aligned}
 s(t) &= \pm A \cos\left(\frac{\pi t}{2T}\right) \cos 2\pi f_c t \pm A \sin\left(\frac{\pi t}{2T}\right) \sin 2\pi f_c t \\
 &= \pm A \cos\left[2\pi f_c t + d_k \frac{\pi t}{2T}\right] \\
 &= A \cos\left[2\pi f_c t + d_k \frac{\pi t}{2T} + \Phi_k\right] \\
 &= A \cos\left[2\pi\left(f_c + d_k \frac{1}{4T}\right)t + \Phi_k\right], \quad kT \leq t \leq (k+1)T \quad (5.2)
 \end{aligned}$$

where $d_k = 1$ when I_k and Q_k have opposite signs (i.e., successive bits in the serial data stream are different), and $d_k = -1$ when I_k and Q_k have same signs (i.e., successive bits in the serial data stream are the same). Or equivalently

$$d_k = -I_k Q_k \quad (5.3)$$

$\Phi_k = 0$ or π corresponding to $I_k = 1$ or -1 . Or equivalently

$$\Phi_k = \frac{\pi}{2}(1 - I_k) \quad (5.4)$$

Both d_k and Φ_k are constant in a bit period of T seconds since I_k and Q_k are constant in T .

It is clear from (5.2) that MSK signal is a special FSK signal with two frequencies $f_+ = f_c + 1/4T$ or $f_- = f_c - 1/4T$, where f_+ is called space frequency, f_- mark frequency, and f_c apparent carrier frequency. The frequency separation is $\Delta f = 1/2T$. This is the minimum separation for two FSK signals to be orthogonal, hence the name "minimum shift keying."

Ordinary coherent FSK signal could have continuous phase or discontinuous phase at bit transitions (see Figure 3.3). MSK carrier phase is always continuous at bit transitions. To see this, we check the excess phase of the MSK signal, referenced to the carrier phase, which is given by

$$\Theta(t) = d_k \frac{\pi t}{2T} + \Phi_k = \pm \frac{\pi t}{2T} + \Phi_k, \quad kT \leq t \leq (k+1)T \quad (5.5)$$

Because Φ_k is constant in the interval $[kT, (k+1)T]$, $\Theta(t)$ is linear and continuous

² Note that the MSK signal has a symbol duration of T instead of $2T$ despite that the symbol durations are $2T$ for $I(t)$ and $Q(t)$. This property is the same as that of OQPSK since both of them have a staggered Q-channel symbol stream. QPSK has a symbol duration of $2T$.

in the interval $[kT, (k+1)T]$. However, to ensure phase continuity at bit transitions, at the end of the k th bit period, we must require

$$d_k \frac{\pi(k+1)T}{2T} + \Phi_k = d_{k+1} \frac{\pi(k+1)T}{2T} + \Phi_{k+1} \pmod{2\pi} \quad (5.6)$$

In the following we will show that this requirement is always satisfied for the MSK signal in (5.1).

Note that since $d_k = -I_k Q_k$, and $\Phi_k = (1 - I_k)\pi/2$, the left-hand side (LHS) and the right-hand side (RHS) of (5.6) become

$$LHS = -I_k Q_k (k+1) \frac{\pi}{2} + \frac{\pi}{2}(1 - I_k) \quad (5.7)$$

$$RHS = -I_{k+1} Q_{k+1} (k+1) \frac{\pi}{2} + \frac{\pi}{2}(1 - I_{k+1}) \quad (5.8)$$

Because I_k and Q_k each occupies $2T$ and are staggered, we can assume $I_k = I_{k+1}$ for odd k and $Q_k = Q_{k+1}$ for even k (or vice versa). Thus, if k is odd, $I_k = I_{k+1}$,

$$RHS = -I_k Q_{k+1} (k+1) \frac{\pi}{2} + \frac{\pi}{2}(1 - I_k) \quad (5.9)$$

Compare (5.9) to (5.7), we can see that to make them equal is to satisfy the requirement

$$-I_k Q_k (k+1) \frac{\pi}{2} = -I_k Q_{k+1} (k+1) \frac{\pi}{2}$$

This obviously is true when $Q_k = Q_{k+1}$. When $Q_k \neq Q_{k+1}$, then $Q_k = -Q_{k+1}$, the above requirement becomes

$$-I_k Q_k (k+1) \frac{\pi}{2} = I_k Q_k (k+1) \frac{\pi}{2} \pmod{2\pi}$$

Since k is odd, $(k+1)$ is even, and note that $I_k = \pm 1$ and $Q_k = \pm 1$, the above requirement becomes

$$-m\pi = m\pi \pmod{2\pi}$$

If m is odd, $\pm m\pi = \pi \pmod{2\pi}$. If m is even, $\pm m\pi = 0 \pmod{2\pi}$. Thus, in any case, the requirement is satisfied.

If k is even, $Q_k = Q_{k+1}$, again we have two cases. First case, $I_k = I_{k+1}$, it is easy to see that (5.7) is equal to (5.8). Second case, $I_k \neq I_{k+1}$ (i.e., $I_k = -I_{k+1}$), then

$$LHS = -I_k Q_k (k+1) \frac{\pi}{2} + \frac{\pi}{2}(1 - I_k)$$

I_k	Q_k	LHS	RHS
1	1	$-(k+1)\frac{\pi}{2}$	$(k+3)\frac{\pi}{2} = (k+2)\pi + LHS = LHS \pmod{2\pi}$
1	-1	$(k+1)\frac{\pi}{2}$	$(-k+1)\frac{\pi}{2} = -k\pi + LHS = LHS \pmod{2\pi}$
-1	1	$(k+1)\frac{\pi}{2}$	$(-k+1)\frac{\pi}{2}$ same as the second case
-1	-1	$(-k+1)\frac{\pi}{2}$	$(k+1)\frac{\pi}{2}$ same as the second case

Table 5.1 Possible cases (note that k is even).

$$RHS = I_k Q_k (k+1) \frac{\pi}{2} + \frac{\pi}{2} (1 + I_k)$$

Table 5.1 shows all possible cases of the above two expressions. As seen from Table 5.1, in all cases $LHS = RHS \pmod{2\pi}$.

The above proof shows that the excess phase $\Theta(t)$ is always continuous. The phase of the apparent carrier is $2\pi f_c t$ which is also continuous at any time. Therefore the total phase, $2\pi f_c t + \Theta(t)$, is always continuous at any time. Note that in the above discussion we did not specify any relationship between f_c and the symbol rate $1/T$. In other words, for the MSK signal phase to be continuous, no specific relation between f_c and $1/T$ is required. However, as we will show in Section 5.4, preferably f_c should be chosen as a multiple of $1/4T$, but it is for orthogonality of its I-channel and Q-channel signal components, not for continuous phase purpose.

From the above discussion we also can see that $\Theta(kT)$ is a multiple of $\pi/2$. However, the total phase at bit transitions (or initial phase of the bit), $2\pi f_c kT + \Theta(kT)$, is not necessarily a multiple of $\pi/2$. It could be any value depending on the value of f_c in relation to the bit period T . If f_c is a multiple of $1/4T$ (i.e., $f_c = m/4T$) for a positive integer m , then $2\pi f_c kT = mk\pi/2$, which is a multiple of $\pi/2$. Thus the total phase at bit transitions is also a multiple of $\pi/2$. If f_c is not a multiple of $1/4T$, then the total phase at bit transitions is usually not a multiple of $\pi/2$. As we have pointed out above, f_c is indeed usually chosen as a multiple of $1/4T$ for orthogonality of its I-channel and Q-channel signals. Consequently, the total phase at bit transitions is a multiple of $\pi/2$.

The excess phase $\Theta(t)$ increases or decreases linearly with time during each bit period of T seconds (see (5.5)). If $d_k = 1$ in the bit period, the carrier phase is increased by $\pi/2$ by the end of the bit period. This corresponds to an FSK signal at the higher frequency f_+ . If $d_k = -1$ in the bit period, the carrier phase is decreased by $\pi/2$ by the end of the bit period. This corresponds to an FSK signal at the lower frequency f_- . Figure 5.2 is the phase tree of MSK signal's excess phase $\Theta(t)$. The bold-faced path represents the data sequence $d_k = -I_k Q_k$ for I_k and Q_k in Figure 5.1. The excess phase values at bit transitions are always a multiple of $\pi/2$. If f_c happens to be a multiple of $1/T$, then the excess phase values at bit transitions in the phase tree are also the total phase values of the carrier at bit transitions. From (5.5)

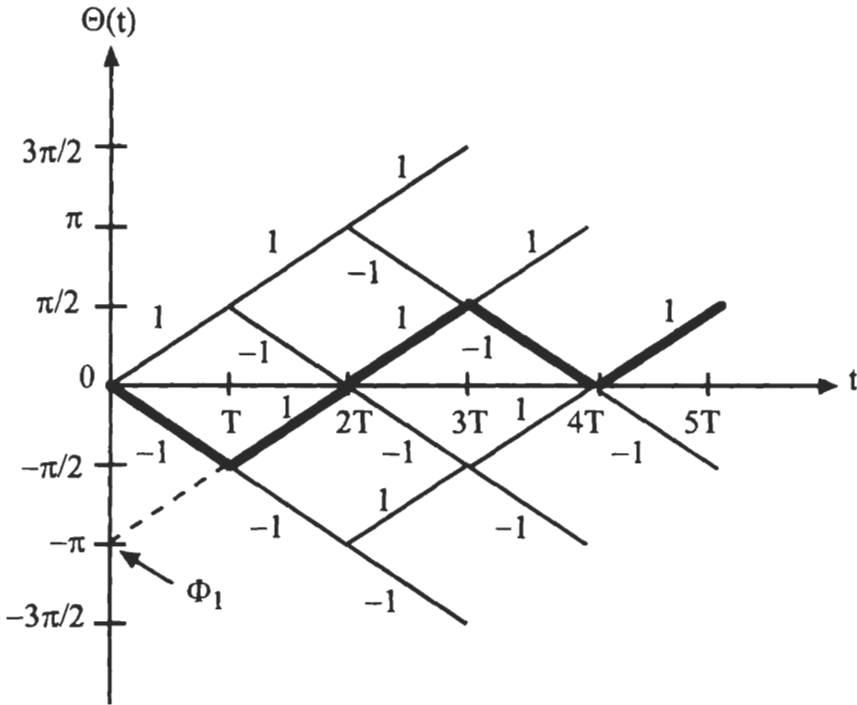


Figure 5.2 MSK excess phase tree.

we can infer that Φ_k is not the initial phase of the k th bit period, since $t \neq 0$ at the bit starting point. Rather it represents the ordinate intercept of the excess phase since $\Phi_k = \Theta(0)$. In Figure 5.2 we show $\Phi_1 = -\pi$ as an example, which is the ordinate intercept of the excess phase at time $t = T$ for the bold-face path.

Figure 5.3 is the phase trellis of $\Theta(t)$. A trellis is a tree-like structure with merged branches. In Figure 5.3 nodes with the same phases in a modulo- 2π sense are merged. The only possible phases at bit transitions are $\pm\pi/2$ and $\pm\pi$. The data sequence of Figure 5.1 is again shown as the bold-faced path.

5.1.2 MSK Viewed as a Special Case of CPFSK

MSK can also be viewed as a special case of CPFSK with modulation index $h = 0.5$. In Chapter 3 we express CPFSK signal as (see (3.3))

$$s(t) = A \cos\left(2\pi f_c t + \frac{\pi h d_k (t - kT)}{T} + \pi h \sum_{i=0}^{k-1} d_i\right), \quad kT \leq t \leq (k+1)T$$

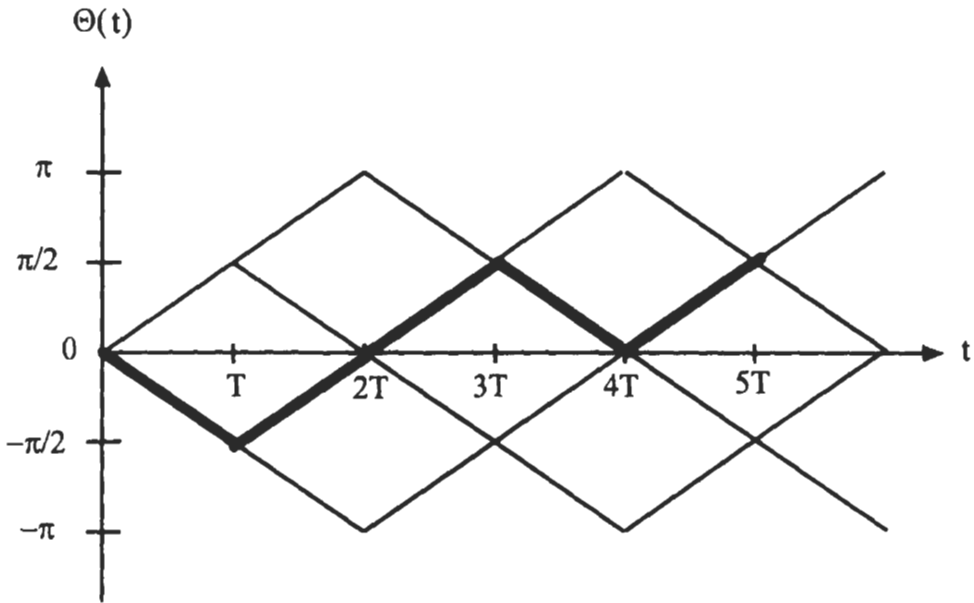


Figure 5.3 MSK excess phase trellis.

which can be written as

$$s(t) = A \cos\left[2\pi f_c t + h d_k \frac{\pi t}{T} + \Phi_k\right], \quad kT \leq t \leq (k+1)T \quad (5.10)$$

where

$$\Phi_k = \pi h \left(\sum_{i=0}^{k-1} d_i - k d_k \right) \quad (5.11)$$

where d_k is input data (± 1) transmitted at rate $R_b = 1/T$. h is modulation index which determines the frequency shift in the bit interval. In fact the frequency shift is $h d_k / 2T$. Φ_k is constant in the bit interval; but it is not the initial phase of the bit. It represents the ordinate intercept of the excess phase $\Theta(t) = h d_k \pi t / T + \Phi_k$, as we mentioned before.

With $h = 0.5$ the signal becomes

$$s(t) = A \cos\left[2\pi f_c t + d_k \frac{\pi t}{2T} + \Phi_k\right], \quad kT \leq t \leq (k+1)T \quad (5.12)$$

which is exactly the signal in (5.2).

To maintain continuous phase at bit transition $t = kT$, the following conditions

must be met

$$d_{k-1} \frac{\pi}{2} k + \Phi_{k-1} = d_k \frac{\pi}{2} k + \Phi_k \pmod{2\pi}$$

This is

$$\Phi_k = \Phi_{k-1} + \frac{\pi k}{2} (d_{k-1} - d_k) \pmod{2\pi}$$

or

$$\Phi_k = \begin{cases} \Phi_{k-1} \pmod{2\pi}, & d_k = d_{k-1} \\ \Phi_{k-1} \pm \pi k \pmod{2\pi}, & d_k \neq d_{k-1} \end{cases}$$

Assume that $\Phi_0 = 0$, then $\Phi_k = 0$ or π depending on the value of Φ_{k-1} and the relation between d_k and d_{k-1} .

In the previous section we have shown that when d_k is derived from the staggered I-channel and Q-channel bit streams by $d_k = -I_k Q_k$, then $\Phi_k = 0$ or π , and phase is continuous at any time, including bit transitions. Equivalently, d_k can be generated by differential encoding of the data stream [7]

$$d_k = d_{k-1} \oplus a_k$$

where $\{a_k\}$ is the original data stream, \oplus represents exclusive-OR (XOR) operation (refer to Section 4.2 discussing DPSK for differential encoding). This equivalence can be verified by examining some arbitrary examples. This fact implies that MSK signal can be generated as CPM signal with $h = 0.5$, and the sign of frequency shift of each bit is controlled by the differentially encoded input bit stream. The MSK signal realized in this manner is called fast frequency shift keying, or FFSK [2].

5.2 POWER SPECTRUM AND BANDWIDTH

5.2.1 Power Spectral Density of MSK

In Appendix A we have shown that the PSD of a bandpass signal is the shifted version of the equivalent baseband signal or complex envelope's PSD. Therefore it suffices to determine the PSD of the equivalent baseband signal $\tilde{s}(t)$. The MSK signal of (5.1) consists of the in-phase component and the quadrature component which are independent from each other. The PSD of the complex envelope is the sum of the PSDs of these two components (A.21).

$$\Psi_{\tilde{s}}(f) = \Psi_I(f) + \Psi_Q(f)$$

To find $\Psi_I(f)$ and $\Psi_Q(f)$, refer to (A.19). It shows that the PSD of a binary, bipolar (± 1), equiprobable, stationary, and uncorrelated digital waveform is just equal to the energy spectral density of the symbol shaping pulse divided by the symbol duration. In MSK, the symbol shaping pulses are

$$p(t) = \begin{cases} A \cos \frac{\pi t}{2T}, & -T \leq t \leq T \\ 0, & \text{elsewhere} \end{cases} \quad (5.13)$$

for I-channel and

$$q(t) = p(t - T) = \begin{cases} A \sin \frac{\pi t}{2T}, & 0 \leq t \leq 2T \\ 0, & \text{elsewhere} \end{cases}$$

for Q-channel. Note their durations are $2T$, not T . Since there is only a phase factor between their Fourier transforms, their energy spectral densities are the same. By taking a Fourier transform of either function, say, $p(t)$, and square the magnitude, divide by $2T$, we have

$$\Psi_I(f) = \Psi_Q(f) = \frac{1}{2T} \left(\frac{4AT[\cos 2\pi T f]}{\pi[1 - (4Tf)^2]} \right)^2$$

Therefore

$$\Psi_s(f) = 2\Psi_I(f) = \frac{16A^2T}{\pi^2} \left[\frac{\cos 2\pi T f}{1 - (4Tf)^2} \right]^2 \quad (5.14)$$

Figure 5.4 shows the $\Psi_s(f)$ of MSK along with those of BPSK, QPSK, and OQPSK. They are plotted as a function of f normalized to the data rate $R_b = 1/T$. The MSK spectrum falls off at a rate proportional to $(f/R_b)^{-4}$ for large values of f/R_b . In contrast, the QPSK or OQPSK spectrum falls off at a rate proportional to only $(f/R_b)^{-2}$. The BPSK spectrum also falls off at a rate proportional to $(f/R_b)^{-2}$ even though its spectral lobe widths are double that of QPSK or OQPSK. The main lobe of the MSK spectrum is narrower than that of BPSK spectrum and wider than that of the QPSK or OQPSK spectrum. The first nulls of BPSK, MSK, and QPSK or OQPSK spectrum fall at $f/R_b = 1.0, 0.75$, and 0.5 , respectively. Therefore the null-to-null bandwidth is $2.0R_b$ for BPSK, $1.5R_b$ for MSK, and $1.0R_b$ for QPSK or OQPSK.

5.2.2 Bandwidth of MSK and Comparison with PSK Schemes

Another useful measure of the compactness of a modulated signal's spectrum is the fractional out-of-band power, P_{ob} , defined by (2.21).

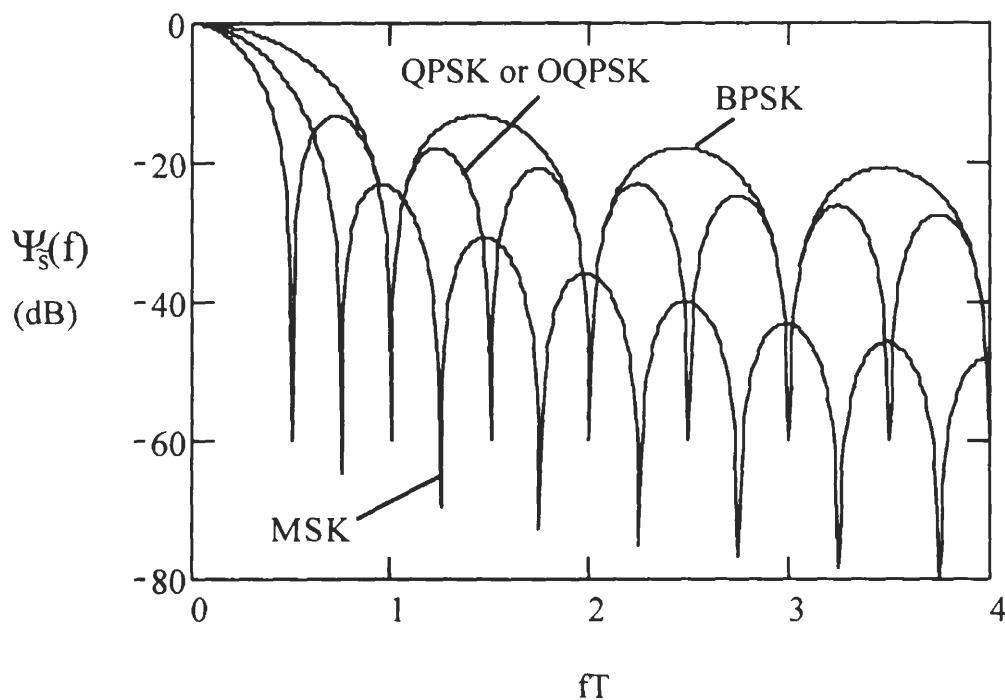


Figure 5.4 MSK power spectral density.

Figure 5.5 shows the $P_{ob}(B)$ for BPSK, QPSK or OQPSK, and MSK as a function of two-sided bandwidth $2B$ normalized to the binary data rate. From this figure we can see that MSK has a bit more out-of-band power than QPSK or OQPSK for $2B < 0.75R_b$, and less out-of-band power for $2B > 0.75R_b$. The bandwidths containing 90% of the power for these modulation schemes can be obtained by numerical calculations. The results are as follows

$$B_{90\%} \approx 0.76R_b \quad (\text{MSK})$$

$$B_{90\%} \approx 0.8R_b \quad (\text{QPSK, OQPSK})$$

$$B_{90\%} \approx 1.7R_b \quad (\text{BPSK})$$

These can also be approximately obtained by noting the bandwidths on the curves corresponding to $P_{ob} = -10 \text{ dB}$. Because the MSK spectrum falls off much faster, a more stringent in-band power specification, such as 99%, results in a much smaller

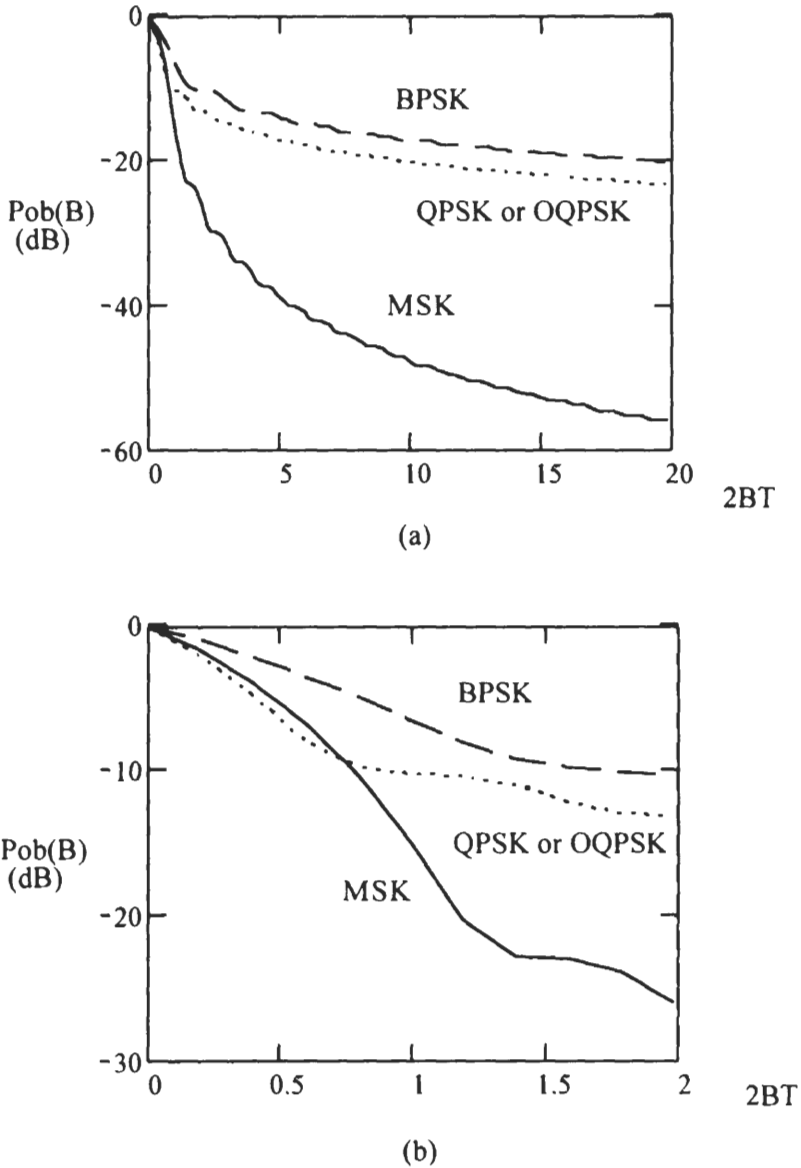


Figure 5.5 Fractional out-of-band power of MSK, BPSK, and QPSK or OQPSK.

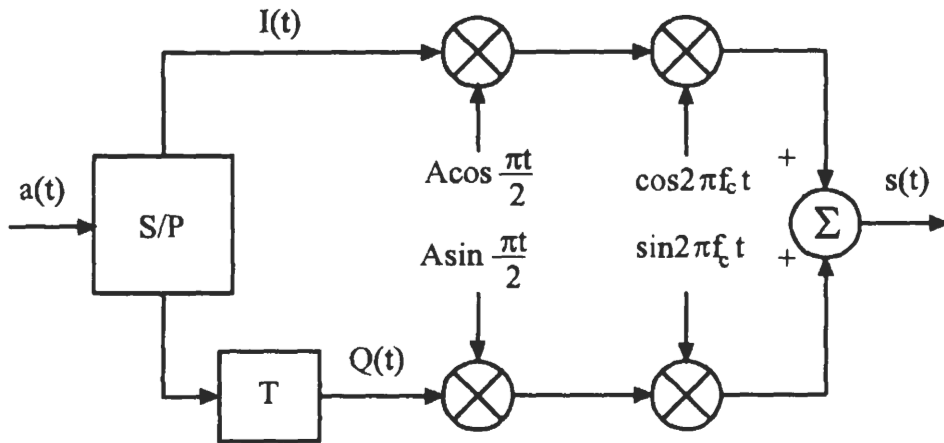


Figure 5.6 MSK modulator (I).

bandwidth for MSK than for BPSK, QPSK or OQPSK. The numerical results are

$$B_{99\%} \approx 1.2R_b \quad (\text{MSK})$$

$$B_{99\%} \approx 10R_b \quad (\text{QPSK or OQPSK})$$

$$B_{99\%} \approx 20R_b \quad (\text{BPSK})$$

These can also be obtained by noting the bandwidths on the curves corresponding to $P_{ob} = -20 \text{ dB}$.

These comparisons suggest that for system bandwidths exceeding about $1.2R_b$, MSK should provide lower BER performance than QPSK or OQPSK. However, as system bandwidths decrease to $0.75R_b$, their BER performance should be very close since all of them have 90% in-band power. As system bandwidths decrease below $0.75R_b$, the BER performance of QPSK or OQPSK should be better. As system bandwidth is increased, their BER performance converges to infinite bandwidth case, that is, they have the same BER performance. The precise boundaries of regions of superior performance for each modulation scheme are difficult to determine in practical situations, since the detailed channel characteristics must be considered.

5.3 MODULATOR

Figure 5.6 is the MSK modulator implemented as a sinusoidal weighted OQPSK. It

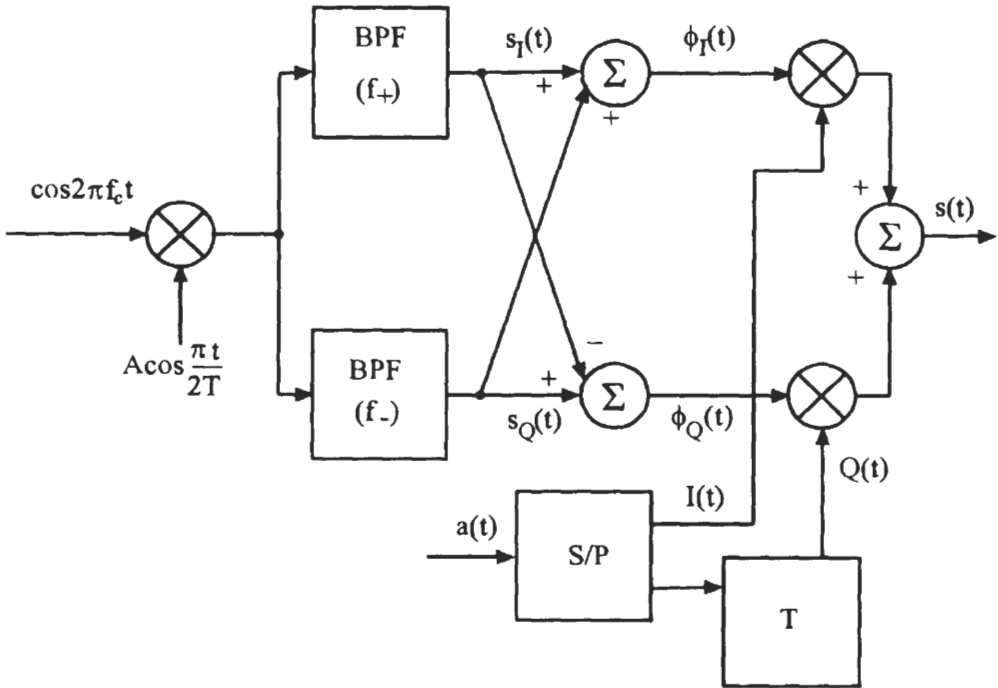


Figure 5.7 MSK modulator (II).

is directly based on (5.1). The data stream signal $a(t)$ is demultiplexed into $I(t)$ and $Q(t)$ by the serial-to-parallel converter (S/P). The in-phase channel signal $I(t)$ consists of even-numbered bits, and the quadrature channel signal $Q(t)$ consists of odd-numbered bits. Each bit in $I(t)$ and $Q(t)$ has a duration of $2T$. $Q(t)$ is delayed by T with respect to $I(t)$. $I(t)$ is multiplied by $A \cos \pi t/2T$ and $\cos 2\pi f_c t$ in the two subsequent multipliers in the I-channel. $Q(t)$ is multiplied by $A \sin \pi t/2T$ and $\sin 2\pi f_c t$ in the two subsequent multipliers in the Q-channel. $A \sin \pi t/2T$ and $\sin 2\pi f_c t$ are obtained through $\pi/2$ phase shifters from $A \cos \pi t/2T$ and $\cos 2\pi f_c t$, respectively. In the summer, the I-channel and Q-channel modulated signals are added to obtain the MSK signal. Previous discussion has shown that $A \cos \pi t/2T$ and $\cos 2\pi f_c t$ need not be synchronized. Therefore $A \cos \pi t/2T$ and $\cos 2\pi f_c t$ can be generated by two independent oscillators.

Figure 5.7 is an alternate implementation. The advantage of it is that carrier coherence and the frequency deviation ratio are largely unaffected by variations in the data rate [8]. The first stage is a high-frequency multiplier which produces two phase coherent frequency components

$$s_I(t) = \frac{1}{2} A \cos 2\pi f_+ t \quad (5.15)$$

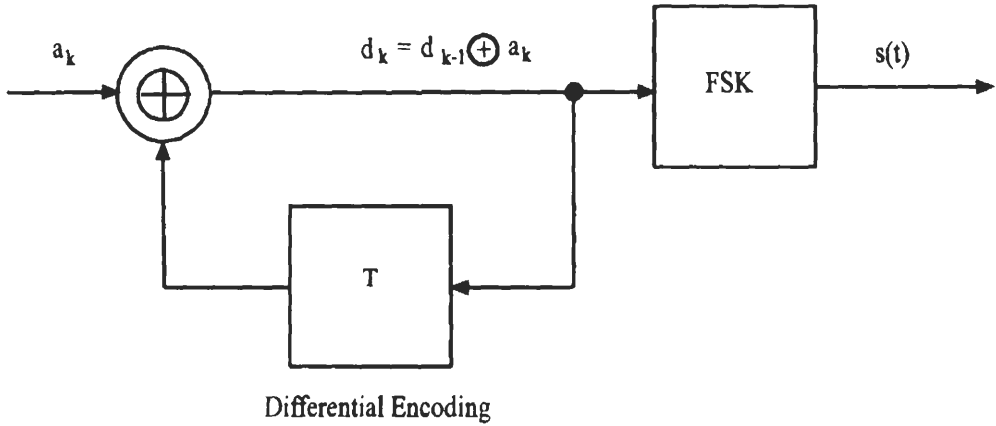


Figure 5.8 MSK modulator (III).

and

$$s_Q(t) = \frac{1}{2}A \cos 2\pi f_- t \quad (5.16)$$

where $f_+ = f_c + 1/4T$ and $f_- = f_c - 1/4T$. These two sinusoidal waves are separated from each other by two narrow-band filters centered at f_+ and f_- , respectively. At the two summers' outputs, the signals are

$$\begin{aligned} \phi_I(t) &= s_I(t) + s_Q(t) \\ &= \frac{1}{2}A \cos 2\pi f_+ t + \frac{1}{2}A \cos 2\pi f_- t \\ &= A \cos \pi t/2T \cos 2\pi f_c t \end{aligned} \quad (5.17)$$

for I-channel and

$$\begin{aligned} \phi_Q(t) &= s_I(t) - s_Q(t) \\ &= -\frac{1}{2}A \cos 2\pi f_+ t + \frac{1}{2}A \cos 2\pi f_- t \\ &= A \sin \pi t/2T \sin 2\pi f_c t \end{aligned} \quad (5.18)$$

for Q-channel. These two signals are the sinusoidally weighted carriers. They are further modulated by $I(t)$ and $Q(t)$, respectively, and then summed to form the final MSK signal.

Figure 5.8 is the MSK modulator implemented as a differentially encoded FSK with $h = 0.5$ (FFSK). The FSK modulator can be any type as described in Chapter 3. The only difference here is the differential encoder which consists of an exclusive

OR gate (XOR) plus a delay device of T seconds which returns the previous encoder output d_{k-1} to the XOR gate.

5.4 DEMODULATOR

Using the two basis functions defined in the previous section, the MSK signal in the k th bit interval can be written as

$$s(t) = I_k \phi_I(t) + Q_k \phi_Q(t), \quad kT \leq t \leq (k+1)T$$

It can be shown that $\phi_I(t)$ and $\phi_Q(t)$ are orthogonal for $f_c = n/4T$, n integer ($n \neq 1$), over a period of T .

Proof:

$$\begin{aligned} & \int_{kT}^{(k+1)T} \phi_I(t) \phi_Q(t) dt \\ &= \int_{kT}^{(k+1)T} A^2 \cos\left(\frac{\pi t}{2T}\right) \cos 2\pi f_c t \sin\left(\frac{\pi t}{2T}\right) \sin 2\pi f_c t dt \\ &= \frac{1}{4} A^2 \int_{kT}^{(k+1)T} \sin\left(\frac{\pi t}{T}\right) \sin 4\pi f_c t dt \\ &= \frac{1}{8} A^2 \int_{kT}^{(k+1)T} \left[\cos\left(4\pi f_c t - \frac{\pi t}{T}\right) - \cos\left(4\pi f_c t + \frac{\pi t}{T}\right) \right] dt \end{aligned}$$

The first term integrates to

$$\frac{A^2}{8} \frac{1}{4\pi f_c - \frac{\pi}{T}} \sin\left(\left(4\pi f_c - \frac{\pi}{T}\right)t\right) \Bigg|_{kT}^{(k+1)T} \quad (5.19)$$

This will be zero when³

$$4\pi f_c - \frac{\pi}{T} = \frac{m\pi}{T}, \quad m \text{ integer } (m \neq 0)$$

This is

$$f_c = \frac{(m+1)}{4T} = \frac{n}{4T}, \quad n \text{ integer } (n \neq 1)$$

This obviously also holds for the second term. This concludes the proof.

³ When $m = 0$, we have a limit $\lim_{x \rightarrow 0} \sin x/x = 1$ and the integral in (5.19) evaluates to $A^2/8$.

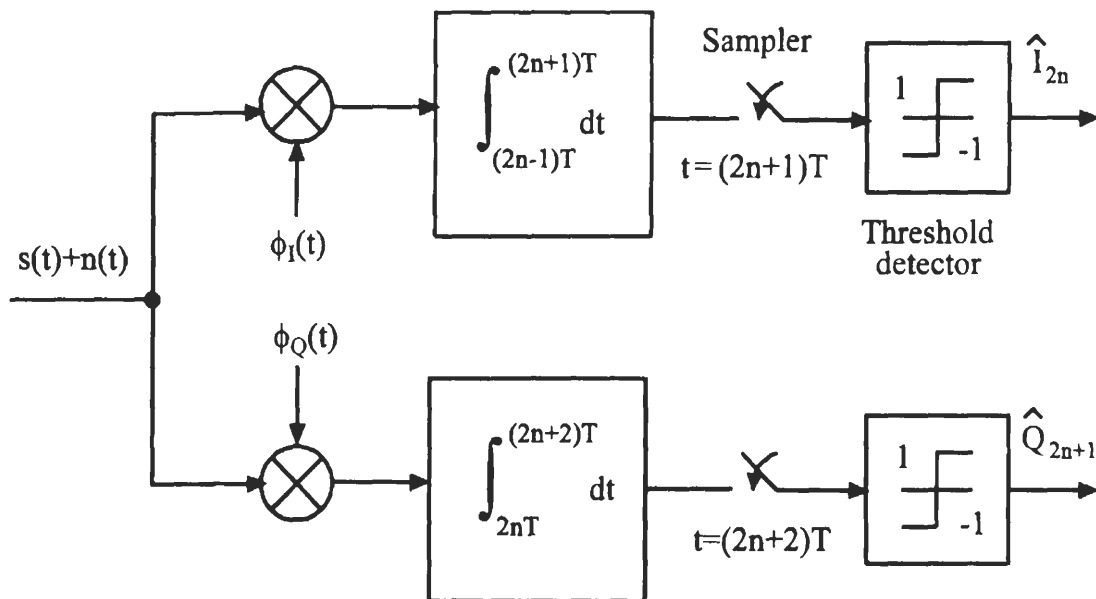


Figure 5.9 MSK demodulator (I).

When n is not an integer, $\phi_I(t)$ and $\phi_Q(t)$ are essentially orthogonal for $f_c \gg 1/T$, which is the usual case. This is because the coefficient in front of the sine function in (5.19) is very small when $f_c \gg 1/T$. From now on for all practical purposes, we consider that $\phi_I(t)$ and $\phi_Q(t)$ are orthogonal in a period of T . It follows that they are also orthogonal in a period of $2T$.

Since $\phi_I(t)$ and $\phi_Q(t)$ are orthogonal, the optimum coherent demodulation of MSK is very much similar to that of QPSK. Figure 5.9 is the optimum coherent MSK demodulator (the method of obtaining the reference signals and bit timing will be discussed in the next section). Since each data symbol in $I(t)$ or $Q(t)$ occupies a period of $2T$, the demodulator operates on a $2T$ basis. We now denote symbols as $\{I_k, k = 0, 2, 4, \dots\}$ and $\{Q_k, k = 1, 3, 5, \dots\}$. For k th symbol interval, the integration interval in the I-channel is from $(2n - 1)T$ to $(2n + 1)T$ and in the Q-channel is from $2nT$ to $(2n + 2)T$, where $n = 0, 1, 2, \dots$. These intervals correspond to the respective data symbol periods (see Figure 5.1). In I-channel the integrator output is

$$\begin{aligned} & \int_{(2n-1)T}^{(2n+1)T} s(t)\phi_I(t)dt \\ &= \int_{(2n-1)T}^{(2n+1)T} [I_k\phi_I(t) + Q_k\phi_Q(t)]\phi_I(t)dt \end{aligned}$$

$$\begin{aligned}
&= \int_{(2n-1)T}^{(2n+1)T} I_k \phi_I^2(t) dt, \quad (\text{the second term vanishes due to orthogonality}) \\
&= \int_{(2n-1)T}^{(2n+1)T} A^2 I_k \cos^2\left(\frac{\pi t}{2T}\right) \cos^2 2\pi f_c t dt \\
&= \int_{(2n-1)T}^{(2n+1)T} A^2 I_k \frac{1}{2} \left(1 + \cos\left(\frac{\pi t}{T}\right)\right) \frac{1}{2} (1 + \cos 4\pi f_c t) dt \\
&= \int_{(2n-1)T}^{(2n+1)T} \frac{1}{4} A^2 I_k [1 + \cos\left(\frac{\pi t}{T}\right) + \cos 4\pi f_c t + \cos\left(\frac{\pi t}{T}\right) \cos 4\pi f_c t] dt \\
&= \frac{1}{2} A^2 T I_k
\end{aligned}$$

Only the first term in the above integration produces a nonzero result. The integration of the second term is exactly zero. The integrations of the third term and the fourth term are exactly zero only when f_c is a multiple of $1/4T$ (i.e., when the carriers of two channels are orthogonal). Therefore we usually choose f_c as a multiple of $1/4T$. However, even if f_c is not a multiple of $1/4T$, the integrations of the third term and the fourth term are not exactly zero; but they are very small in comparison with the first term for $f_c \gg 1/T$, which is usually the case. Therefore we can conclude that the sampler output of I-channel is essentially $A^2 T I_k / 2$ regardless of the carrier orthogonality. Similarly we can show that the sampler output of Q-channel is $A^2 T Q_k / 2$. These two signals are detected by the threshold detectors to finally put out I_k and Q_k . The thresholds of detectors are set to zero.

Figure 5.10 is an alternate MSK demodulator where demodulation is accomplished in two steps (the method of obtaining the reference signals and bit timing will be discussed in the next section). It is equivalent to the one in Figure 5.9. In the absence of noise, in I-channel, the output of the first multiplier is

$$\begin{aligned}
&s(t) \cos 2\pi f_c t \\
&= A \left[I(t) \cos\left(\frac{\pi t}{2T}\right) \cos 2\pi f_c t + Q(t) \sin\left(\frac{\pi t}{2T}\right) \sin 2\pi f_c t \right] \cos 2\pi f_c t \\
&= \frac{1}{2} A I(t) \cos\left(\frac{\pi t}{2T}\right) + \frac{1}{2} A I(t) \cos\left(\frac{\pi t}{2T}\right) \cos 4\pi f_c t \\
&\quad + \frac{1}{2} A Q(t) \sin\left(\frac{\pi t}{2T}\right) \sin 4\pi f_c t
\end{aligned}$$

After the low-pass filter the two high-frequency terms are rejected and its output is only the first term. It is then multiplied by the weighting signal and integrated for $2T$ which is the symbol length of $I(t)$ and $Q(t)$. Since the symbols of $I(t)$ and $Q(t)$ are staggered, the integrations limits are also staggered. For I-channel, the output of

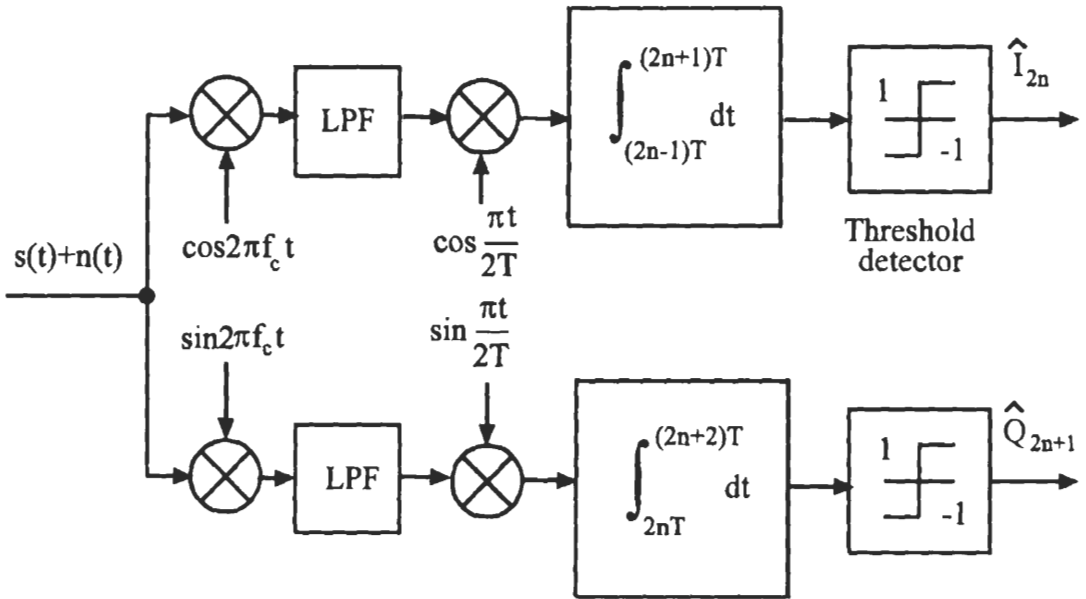


Figure 5.10 MSK demodulator (II).

the integrator at $t = (2n + 1)T$ is

$$\begin{aligned}
 & \int_{(2n-1)T}^{(2n+1)T} \frac{1}{2} A I_k \cos\left(\frac{\pi t}{2T}\right) \cos\left(\frac{\pi t}{2T}\right) dt \\
 &= \int_{(2n-1)T}^{(2n+1)T} \frac{1}{4} A [I_k + I_k \cos\left(\frac{2\pi t}{2T}\right)] dt \\
 &= \frac{1}{2} A T I_k
 \end{aligned}$$

which is proportional to the data bit I_k . It is then sent to the detector with a threshold of zero. Without noise or other channel impairment, the detector output is definitely the data bit I_k . Similarly the output of the Q-channel integrator is $\frac{1}{2} A T Q_k$. Thus Q_k can be recovered by the Q-channel detector. When noise or other channel impairment, such as bandlimiting and fading, are present, detection errors will occur. The bit error probability for an AWGN channel will be discussed in a later section.

Since MSK is a type of CPM, it can also be demodulated as a CPM scheme with trellis demodulation using the Viterbi algorithm [7]. This will be discussed in the next chapter. Since MSK is a type of FSK, it can be demodulated noncoherently with about 1 dB asymptotic loss in power efficiency. The demodulated sequence is $\{d_k\}$, which can be converted back to the original data $\{a_k\}$ by the decoding rule

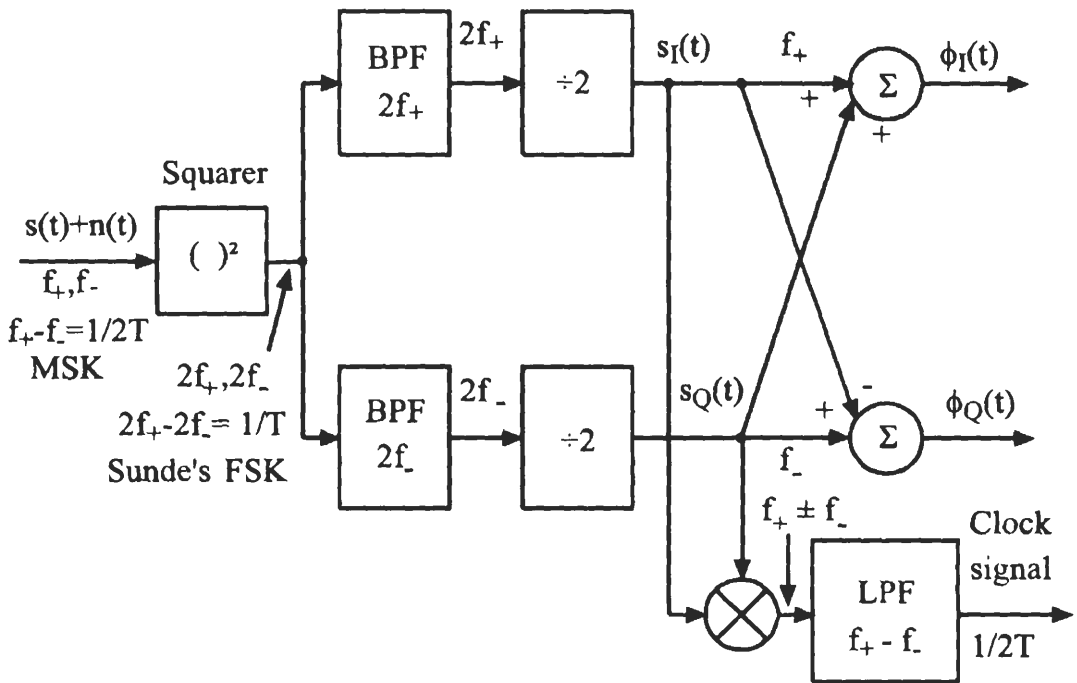


Figure 5.11 MSK carrier and symbol-timing recovery. From [9]. Copyright © 1979 IEEE.

$a_k = d_k \oplus d_{k-1}$. This possibility of noncoherent demodulation permits inexpensive demodulation of MSK when the received signal-to-noise ratio is adequate and provides a low-cost alternative in some systems.

5.5 SYNCHRONIZATION

For the demodulator in Figure 5.9, the reference carriers $\phi_I(t)$, $\phi_Q(t)$, and the clock signal at 1/2 the bit rate needed at the samplers, are recovered from the received signal by the synchronization circuits in Figure 5.11. (With a little extra circuit it can be used for carrier recovery for the demodulator in Figure 5.10 too. This will be shown shortly.) The MSK signal $s(t)$ has no discrete components which can be used for synchronization (Figure 5.4). However, it produces strong discrete spectral components at $2f_+$ and $2f_-$ when passed through a squarer.

$$\begin{aligned}
 s^2(t) &= A^2 \cos^2\left[2\pi f_c t \pm \frac{\pi t}{2T} + \Phi_k\right] \\
 &= \frac{1}{2} A^2 \left[1 + \cos\left(4\pi f_c t \pm \frac{\pi t}{T} + 2\Phi_k\right)\right]
 \end{aligned}$$

$$= \frac{1}{2}A^2\left[1 + \cos\left(4\pi f_c t \pm \frac{\pi t}{T}\right)\right]$$

where $2\Phi_k = 0 \pmod{2\pi}$. The second term is the so-called Sunde's FSK signal with $h = 1$ and the two frequencies are $2f_+$ and $2f_-$. This signal has two strong discrete spectral components at $2f_+$ and $2f_-$, which contain one-half of the total power of the FSK signal (refer to Chapter 3). These components are extracted by bandpass filters (in practice, by phase-lock loops) and then divided by two in frequency to give $s_I(t) = \cos 2\pi f_+ t$ and $s_Q(t) = \cos 2\pi f_- t$. (Suppose their amplitudes are scaled to 1.) The sum $s_I(t) + s_Q(t)$ and difference $s_I(t) - s_Q(t)$ produce the reference carriers $\phi_I(t)$ and $\phi_Q(t)$ (except a factor A), respectively, (see (5.17) and (5.18)).

By multiplying $s_I(t)$ and $s_Q(t)$ we have

$$\begin{aligned} s_I(t)s_Q(t) &= \cos 2\pi f_+ t \cos 2\pi f_- t \\ &= \frac{1}{2}\left[\cos \frac{\pi t}{T} + \cos 4\pi f_c t\right] \end{aligned} \quad (5.20)$$

By passing this signal through a low-pass filter, the output is $\frac{1}{2} \cos \pi t/T$, a sinusoidal signal at $1/2$ the bit rate, which can be easily converted into a square-wave timing clock for the integrators and the samplers in the demodulator.

By passing the product signal through a high-pass filter the output is $\frac{1}{2} \cos 4\pi f_c t$. Dividing its frequency by 2 and scaling up its amplitude, we can get $\cos 2\pi f_c t$ which is the carrier needed in the demodulator in Figure 5.10. The baseband sinusoidal weighting signal $\cos \pi t/2T$ needed in Figure 5.10 can also be extracted from the signal in (5.20) by a low-pass filter and a divide-by-two frequency divider. Thus the carrier and bit-timing recovery circuit in Figure 5.11 can be used for both demodulators in Figure 5.9 and 5.10, with little extra circuit for the one in Figure 5.10.

There is a 180° phase ambiguity in carrier recovery because of the squaring operation. Since $[\pm s(t)]^2 = s^2(t)$, both $s(t)$ and $-s(t)$ generate the same references $\phi_I(t)$ and $\phi_Q(t)$. This is the 180° phase ambiguity. Therefore the demodulator outputs in the I- and Q-channels will be $-I(t)$ and $-Q(t)$, respectively, if the received signal is $-s(t)$. One method to solve this problem is to differentially encode the data stream before modulation, as described in Chapter 4 for the DPSK.

Recall that if MSK is implemented as FFSK, a differential encoder is needed at modulation and a differential decoder is needed at demodulation. If MSK is implemented as weighted OQPSK, the differential encoder and decoder are not needed. However, due to the 180° phase ambiguity in the carrier recovery operation, differential encoding and decoding are needed in both cases. In this sense FFSK and MSK are essentially the same.

5.6 ERROR PROBABILITY

The derivation of MSK bit error rate is very similar to that of QPSK in the previous chapter.

Assume the channel is AWGN, the received signal is

$$r(t) = s(t) + n(t)$$

where $n(t)$ is the additive white Gaussian noise. Refer to the demodulator in Figure 5.9 or Figure 5.10. The MSK signal is demodulated in I-channel and Q-channel. Due to the orthogonality of the I and Q components of the MSK signal, they do not interfere with each other in the demodulation process. However, the noise will cause the detectors to put out erroneous bits. The probability of bit error (P_b) or bit error rate (BER) is of interest. Because of symmetry, the I- and Q-channels have the same probability of bit error (i.e., $P_{bI} = P_{bQ}$). In addition, the errors in the I-channel and Q-channel are statistically independent (it will be shown shortly) and the detected bits from both channels are *directly* multiplexed to form the final data sequence. Therefore it suffices to consider only P_{bI} and this P_{bI} is the P_b for the entire demodulator.⁴

Refer to Figure 5.10 (same results will be obtained by using Figure 5.9), at the threshold detector input the I-channel signal is

$$y_{Ik} = \frac{1}{2}AT I_k + n_{Ik}$$

where $k = 2n$ and the noise

$$n_{Ik} = \int_{(2n-1)T}^{(2n+1)T} n(t) \cos\left(\frac{\pi t}{2T}\right) \cos 2\pi f_c t dt$$

which is Gaussian with zero mean (Refer to Appendix A). Its variance is

$$\begin{aligned} \sigma^2 &= E\{n_{Ik}^2\} = E\left\{\left[\int_{(2n-1)T}^{(2n+1)T} n(t) \cos\left(\frac{\pi t}{2T}\right) \cos 2\pi f_c t dt\right]^2\right\} \\ &= \int_{(2n-1)T}^{(2n+1)T} \int_{(2n-1)T}^{(2n+1)T} E\{n(t)n(\tau)\} \end{aligned}$$

⁴ Some authors calculate the symbol error probability P_s first, then derive the bit error probability P_b from P_s . This is not necessary and strictly speaking, it is not right, since for MSK, we never detect symbols, instead, we detect bits in the demodulation process.

$$\begin{aligned}
& \cdot \cos\left(\frac{\pi t}{2T}\right) \cos 2\pi f_c t \cos\left(\frac{\pi \tau}{2T}\right) \cos 2\pi f_c \tau dt d\tau \\
= & \int_{(2n-1)T}^{(2n+1)T} \int_{(2n-1)T}^{(2n+1)T} \frac{N_o}{2} \delta(t - \tau) \\
& \cdot \cos\left(\frac{\pi t}{2T}\right) \cos 2\pi f_c t \cos\left(\frac{\pi \tau}{2T}\right) \cos 2\pi f_c \tau dt d\tau \\
= & \frac{N_o}{2} \int_{(2n-1)T}^{(2n+1)T} \cos^2\left(\frac{\pi t}{2T}\right) \cos^2 2\pi f_c t dt \\
= & \frac{N_o T}{4}
\end{aligned}$$

The detector has a threshold of zero. The probability of bit error in the I-channel is

$$\begin{aligned}
P_{bI} &= \Pr\left[\frac{1}{2}AT + n_{Ik} < 0 | I_k = +1\right] \\
&= \Pr\left[-\frac{1}{2}AT + n_{Ik} > 0 | I_k = -1\right] \\
&= \Pr\left[n_{Ik} > \frac{1}{2}AT\right] \\
&= \int_{\frac{1}{2}AT}^{\infty} \frac{1}{\sqrt{2\pi}\sigma} \exp\left(-\frac{u^2}{2\sigma^2}\right) du = \int_{\frac{AT}{2\sigma}}^{\infty} \frac{1}{\sqrt{2\pi}} \exp\left(-\frac{x^2}{2}\right) dx \\
&= Q\left(\frac{AT}{2\sigma}\right) = Q\left(\frac{AT}{2\sqrt{N_o T/4}}\right) = Q\left(\sqrt{\frac{A^2 T}{N_o}}\right) \quad (5.21)
\end{aligned}$$

The bit energy E_b of the transmitted MSK signal is

$$\begin{aligned}
E_b &= \int_{(k-1)T}^{kT} A^2 \cos^2\left[2\pi\left(f_c + d_k \frac{1}{4T}\right)t + \Phi_k\right] dt \\
&= \frac{1}{2} A^2 \int_{(k-1)T}^{kT} \left\{1 + \cos\left[4\pi\left(f_c + d_k \frac{1}{4T}\right)t + 2\Phi_k\right]\right\} dt \\
&= \frac{1}{2} A^2 T \quad (5.22)
\end{aligned}$$

since the integration of the second term is zero.⁵ Thus the P_{bI} expression can be

⁵ Note that in one-bit duration, the MSK signal energy is constant even though the signal may have different frequencies from bit to bit.

written as

$$P_{bI} = Q \left(\sqrt{\frac{2E_b}{N_o}} \right) \quad (5.23)$$

Similarly we can derive the expression of P_{bQ} . The result is identical to P_{bI} . Now it remains to show that errors on the I- and Q-channels are statistically independent so that the overall bit error probability is $P_b = (P_{bI} + P_{bQ})/2 = P_{bI} = P_{bQ}$. This requires that noise n_{Ik} and n_{Qk} are uncorrelated, for they are Gaussian and uncorrelated Gaussian random variables are statistically independent. The noise component at the input of the Q-channel threshold detector is defined similarly to n_{Ik}

$$n_{Qk} = \int_{2nT}^{(2n+2)T} n(t) \sin\left(\frac{\pi t}{2T}\right) \sin 2\pi f_c t dt$$

The correlation of n_{Ik} with n_{Qk} is given by

$$\begin{aligned} & E\{n_{Ik}n_{Qk}\} \\ = & E \left\{ \int_{(2n-1)T}^{(2n+1)T} n(t) \cos\left(\frac{\pi t}{2T}\right) \cos 2\pi f_c t dt \right. \\ & \cdot \left. \int_{2nT}^{(2n+2)T} n(t) \sin\left(\frac{\pi t}{2T}\right) \sin 2\pi f_c t dt \right\} \\ = & \int_{(2n-1)T}^{(2n+1)T} \int_{2nT}^{(2n+2)T} E\{n(t)n(\tau)\} \\ & \cdot \cos\left(\frac{\pi t}{2T}\right) \sin\left(\frac{\pi \tau}{2T}\right) \cos 2\pi f_c t \sin 2\pi f_c \tau dt d\tau \\ = & \frac{N_o}{2} \int_{(2n-1)T}^{(2n+1)T} \int_{2nT}^{(2n+2)T} \delta(t - \tau) \\ & \cdot \cos\left(\frac{\pi t}{2T}\right) \sin\left(\frac{\pi \tau}{2T}\right) \cos 2\pi f_c t \sin 2\pi f_c \tau dt d\tau \\ = & \frac{N_o}{2} \int_{2nT}^{(2n+1)T} \cos\left(\frac{\pi t}{2T}\right) \sin\left(\frac{\pi t}{2T}\right) \cos 2\pi f_c t \sin 2\pi f_c t dt \\ = & 0 \end{aligned}$$

where the limits of the last integral follow due to the fact that $\delta(t - \tau) = 0$ for $t \neq \tau$. Thus n_{Ik} and n_{Qk} are uncorrelated and hence independent since they are Gaussian.

As a result, the bit error probability of the entire demodulator $P_b = P_{bI}$ is given by

$$P_b = Q \left(\sqrt{\frac{2E_b}{N_o}} \right) \quad (5.24)$$

which is exactly the same as that of BPSK, QPSK, and OQPSK whose P_b curve can be found in Figure 4.21.

5.7 SERIAL MSK

The implementation of MSK modulation and demodulation discussed in Sections 5.3 and 5.4 is in a parallel fashion. That is, the serial data stream is demultiplexed into even- and odd-indexed bits which are modulated and demodulated in two parallel channels. The MSK modulation and demodulation can also be implemented in a serial fashion [4, 10]. These two techniques are equivalent in performance theoretically. However, the serial implementation has advantages over the parallel one at high data rates. Serial MSK modulation and demodulation have the advantage that all operations are performed serially. The precise synchronization and balancing required for the quadrature signals of the parallel structures are no longer needed. This is especially beneficial at high data rates. The serial technique is described in this section.

5.7.1 SMSK Description

Serial MSK modulator and demodulator are illustrated in Figure 5.12. The modulator consists of a BPSK modulator with carrier frequency of $f_- = f_c - 1/4T$ and a bandpass conversion filter with impulse response

$$h(t) = \begin{cases} \sin 2\pi f_+ t = \sin 2\pi (f_c + \frac{1}{4T})t, & 0 \leq t \leq T \\ 0, & \text{elsewhere} \end{cases} \quad (5.25)$$

which corresponds to a $\sin(x)/x$ -shaped transfer function. We will show shortly why these operations produce an MSK modulated signal.

The serial demodulator structure is essentially the reverse of that of the modulator. It consists of a bandpass matched filter followed by a coherent demodulator and a low-pass filter which eliminates the double-frequency component generated by the mixer. The matched filter is not necessary for demodulation, but it can improve the signal-to-noise ratio, hence the error performance [4].

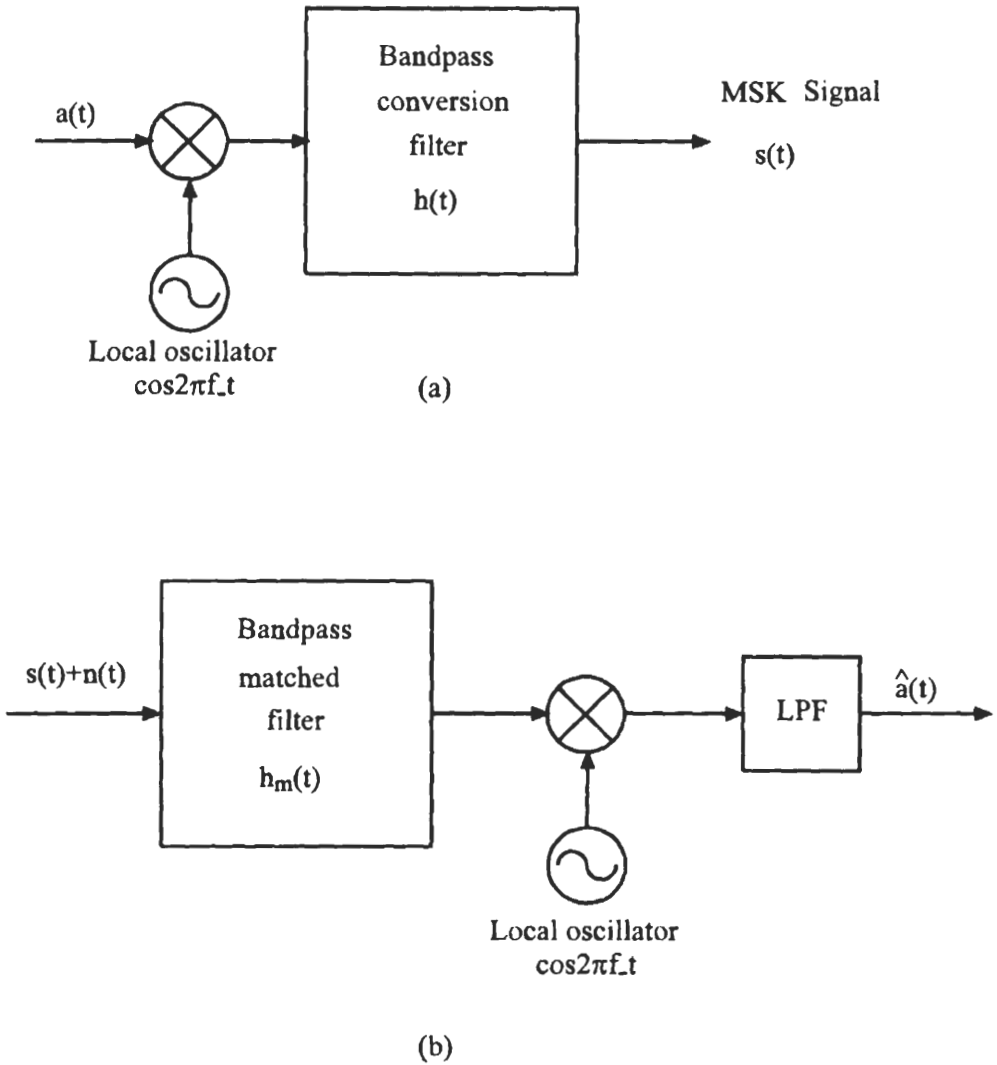


Figure 5.12 Serial modulator and demodulator for MSK (a) modulator, (b) demodulator.

The matched filter impulse response is

$$h_m(t) = \cos\left(\frac{\pi t}{2T}\right) \cos(2\pi f_c t) \quad 0 \leq t \leq 2T$$

which has a transfer function proportional to the square root of the power spectrum of the MSK signal. We will show shortly how $h_m(t)$ is determined.

5.7.2 SMSK Modulator

The following derivation basically follows that of Amoroso et al [4]. We will prove that the output of the conversion filter in Figure 5.12(a) is the MSK signal. In general we can assume the local oscillation is

$$f(t) = \sin(2\pi f_- t + \theta)$$

where θ represents the relative phase of f_- and the data transition ($\theta = \pi/2$ in Figure 5.12(a) since the oscillator output is $\cos(2\pi f_- t) = \sin(2\pi f_- t + \pi/2)$). The typical input burst for a bit to the conversion filter is thus

$$a_k f(t) = a_k \sin(2\pi f_- t + \theta), \quad kT \leq t \leq (k+1)T$$

where the $a_k \in (-1, +1)$ represents the data.

The output of the conversion filter is the convolution of $h(t)$ with $a_k f(t)$, which we denote as $a_k p_\theta(t)$ (it is denoted as $s(t)$ in Figure 5.12(a) for $\theta = \pi/2$ case).

$$\begin{aligned} a_k p_\theta(t) &= a_k \int_{-\infty}^{\infty} f(\tau) h(t - \tau) d\tau \\ &= \begin{cases} a_k \int_{kT}^t \sin(2\pi f_- \tau + \theta) \sin 2\pi f_+(t - \tau) d\tau, & kT \leq t \leq (k+1)T \\ a_k \int_{t-T}^{(k+1)T} \sin(2\pi f_- \tau + \theta) \sin 2\pi f_+(t - \tau) d\tau, & (k+1)T < t < (k+2)T \\ 0, & \text{elsewhere} \end{cases} \end{aligned}$$

which spans a duration of $2T$. The integration limits result from the fact that $f(\tau)$ and $h(t - \tau)$ are overlapped in $[kT, t]$ for $kT \leq t \leq (k+1)T$ and in $[t - T, (k+1)T]$ for $(k+1)T \leq t \leq (k+2)T$. We will see shortly that when $\theta = \pi/2$, $a_k p_\theta(t)$ becomes the MSK signal.

Working out the integrals, $p_\theta(t)$ can be reduced to the form

$$p_\theta(t) = \frac{1}{4\pi(f_+ - f_-)} [\sin(2\pi f_- t + \theta) - (-1)^k \sin(2\pi f_+ t + \theta)]$$

$$+ \frac{1}{4\pi(f_+ + f_-)} [\sin(2\pi f_- t + \theta) + (-1)^k \sin(2\pi f_+ t - \theta)],$$

$$kT \leq t \leq (k+2)T$$

For odd values of k ($k = 2n + 1$), this reduces to

$$p_{\theta_o}(t) = \frac{T}{\pi} \left[\cos \frac{\pi t}{2T} \sin(2\pi f_c t + \theta) - \frac{1}{4T f_c} \sin\left(\frac{\pi t}{2T} - \theta\right) \cos 2\pi f_c t \right] \quad (5.26)$$

where $f_c = (f_+ + f_-)/2$ is the apparent frequency. For even values of k ($k = 2n$), $p_{\theta}(t)$ reduces to

$$p_{\theta_e}(t) = \frac{T}{\pi} \left[-\sin \frac{\pi t}{2T} \cos(2\pi f_c t + \theta) + \frac{1}{4T f_c} \cos\left(\frac{\pi t}{2T} - \theta\right) \sin 2\pi f_c t \right] \quad (5.27)$$

Only when $\theta = \pi/2$, the above expressions become

$$p_o(t) = \frac{T}{\pi} \frac{4T f_c + 1}{4T f_c} \cos \frac{\pi t}{2T} \cos 2\pi f_c t, \quad (2n+1)T \leq t \leq (2n+3)T \quad (5.28)$$

and

$$p_e(t) = \frac{T}{\pi} \frac{4T f_c + 1}{4T f_c} \sin \frac{\pi t}{2T} \sin 2\pi f_c t, \quad 2nT \leq t \leq (2n+2)T \quad (5.29)$$

Note that both $p_o(t)$ and $p_e(t)$ spans $2T$. There is an overlap of T between them. In any one-bit interval, the final output of the conversion filter is one of the possible sums of these two components:

$$s(t) = \pm[p_o(t) + p_e(t)] = \pm \frac{T}{\pi} \frac{4T f_c + 1}{4T f_c} \cos 2\pi f_- t$$

and

$$s(t) = \pm[p_o(t) - p_e(t)] = \pm \frac{T}{\pi} \frac{4T f_c + 1}{4T f_c} \cos 2\pi f_+ t$$

These are exactly the MSK signals. It is clear from comparison that $p_o(t)$ and $p_e(t)$ are equivalent to the I- and Q-channel components of the parallel MSK. For $p_o(t)$ and $p_e(t)$ to be perfectly orthogonal, f_c must be a multiple of $1/4T$.

Now one can realize that the essence of serial MSK. The conversion filter spreads a burst of one bit of the BPSK signal over two-bit periods, weights the envelope by half cycle of cosine or sine, and modifies the carrier frequency from f_- to f_c . All these effects are accomplished through convolution. Due to the fact that the filter responds to odd bits and even bits differently, the final output can be viewed as the

superposition of these two outputs which are equivalent to I- or Q-channel signals in parallel MSK, respectively.

Note that the BPSK signal phase θ must be $\pi/2$ for SMSK to be accurate. If $\theta \neq \pi/2$, the terms

$$-\frac{1}{4Tf_c} \sin\left(\frac{\pi t}{2T} - \theta\right) \cos 2\pi f_c t$$

and

$$+\frac{1}{4Tf_c} \cos\left(\frac{\pi t}{2T} - \theta\right) \sin 2\pi f_c t$$

in (5.26) and (5.27), respectively, become undesirable. They cause the final SMSK signal envelope to fluctuate. However, for large ratio of f_c to data rate, the factor $1/4Tf_c$ causes the undesired terms to vanish, leaving the resulting SMSK signal independent of θ .

We can also verify the validity of SMSK in frequency-domain. The BPSK's single-sided spectrum is

$$\Psi_{BPSK}(f) = 2T \text{sinc}^2[(f - f_c)T + 0.25]$$

The conversion filter transfer function is

$$H(f) = T \text{sinc}[(f - f_c)T - 0.25] \exp(-j\pi f T)$$

The power spectrum of the output of the filter is the product of $\Psi_{BPSK}(f)$ and $|H(f)|^2$ which can be simplified to

$$\Psi_{MSK}(f) = \frac{8T^3}{\pi^4} \left[\frac{\cos 2\pi T(f - f_c)}{1 - (4T(f - f_c))^2} \right]^2$$

which is equivalent to the baseband power spectrum for MSK obtained earlier (5.14), except for a scaling factor.

5.7.3 SMSK Demodulator

The demodulation can be simply done by a coherent demodulator, that is, simply multiply the received signal with a local oscillation of frequency f_- and low-pass filter the mixer's output to remove the double-frequency component. This simple coherent demodulator is the one shown in Figure 5.12(b) without the matched filter. The result is the recovered data bits. This can be shown as follows.

Since the SMSK signal is the same as parallel MSK signal, the mixer input signal

expression is the one in (5.2). The mixer output is

$$\begin{aligned} & A \cos\left[2\pi f_c t + d_k \frac{\pi t}{2T} + \Phi_k\right] \cos 2\pi f_c t \\ = & A \cos\left[2\pi f_c t + d_k \frac{\pi t}{2T} + \Phi_k\right] \cos\left(2\pi f_c t - \frac{\pi t}{2T}\right) \\ = & \frac{1}{2} A \left[\cos\left(4\pi f_c t + d_k \frac{\pi t}{2T} + \Phi_k - \frac{\pi t}{2T}\right) + \cos\left(d_k \frac{\pi t}{2T} + \Phi_k + \frac{\pi t}{2T}\right) \right] \end{aligned}$$

The first term is the double-carrier-frequency term which will be eliminated by the low-pass filter. The second term (ignoring the constant $\frac{1}{2}A$) is

$$m(t) = \cos\left(d_k \frac{\pi t}{2T} + \Phi_k + \frac{\pi t}{2T}\right) = \begin{cases} \cos \frac{\pi t}{T}, & \text{for } d_k = 1, \Phi_k = 0 \\ -\cos \frac{\pi t}{T}, & \text{for } d_k = 1, \Phi_k = \pi \\ 1, & \text{for } d_k = -1, \Phi_k = 0 \\ -1, & \text{for } d_k = -1, \Phi_k = \pi \end{cases}$$

Recall that $d_k = -I_k Q_k$ and $\Phi_k = \frac{\pi}{2}(1 - I_k)$. In serial MSK, $I_k = a_k$ and $Q_k = a_{k-1}$. We can establish the following relations

$I_k = a_k$	$Q_k = a_{k-1}$	d_k	Φ_k	$m(t)$
1	1	-1	0	1
1	-1	1	0	$\cos \frac{\pi t}{T}$
-1	1	1	π	$-\cos \frac{\pi t}{T}$
-1	-1	-1	π	-1

It is clear that four different forms of the low-pass filter output $m(t)$, uniquely determines four different possible data pairs (a_k, a_{k-1}) , respectively, thus the demodulation is accomplished.

Figure 5.13 shows how a BPSK coherent demodulator recovers the data stream from an MSK signal [4]. Figure 5.13(a) is the data stream to be sent. Figure 5.13(b) is the frequency transmitted. Note that the frequency of each bit is determined by $d_k = -a_{k-1}a_k$. Figure 5.13(c) shows the MSK signal phase and the local oscillation phase referenced to the phase of f_c . Figure 5.13(d) shows the phase at mixer output which is the difference of the MSK signal phase and the local oscillation phase. Figure 5.13(e) is the final demodulated signal which is the cosine function of the phase difference at the mixer output and resembles the data stream transmitted.

Even though we discuss this demodulation method in the context of SMSK, it is apparent that it can be used for parallel MSK too since the MSK signals are the same regardless of how they are generated.

As mentioned earlier, the matched filter can improve the SNR even though it is not essential for SMSK demodulation. Now we determine its impulse response.

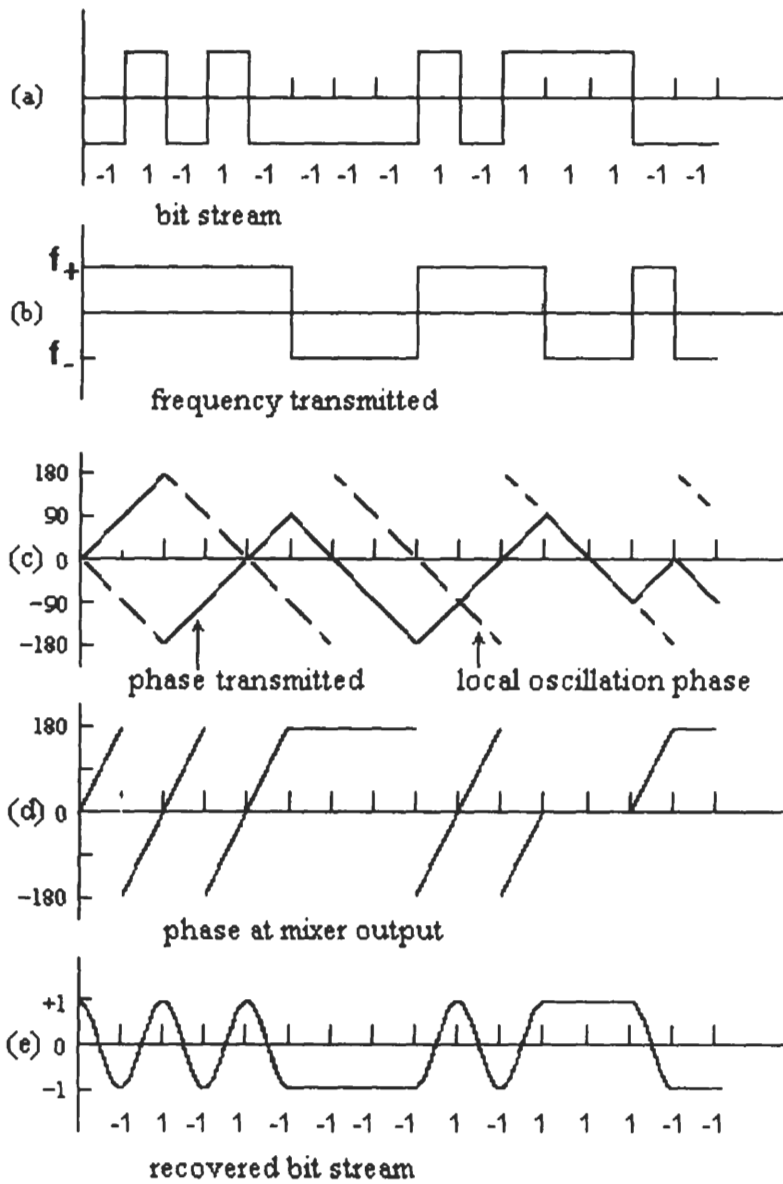


Figure 5.13 Demodulation of MSK signal by coherent BPSK demodulator. From [4]. Copyright © 1977 IEEE.

From the point of view of serial MSK, the MSK signal can be viewed as a sum of odd- and even-bit components, which are equivalent to I- and Q-channel components of the parallel MSK signal. The matched filter should match to the I- and Q-channel components at the same time. Consider a symbol of the MSK signal. As shown in (5.1) it is the result of superposition of the I- and the Q-channel component where

$$\varphi_I(t) = \cos\left(\frac{\pi t}{2T}\right) \cos(2\pi f_c t), \quad -T \leq t \leq T$$

and

$$\varphi_Q(t) = \sin\left(\frac{\pi t}{2T}\right) \sin(2\pi f_c t), \quad 0 \leq t \leq 2T$$

are the basic symbol functions for the I- and Q-channel, respectively. It seems that the matched filter can only be chosen to match to one of them. However, we now show that the matched filter chosen to match to $\varphi_I(t)$ also matches to $\varphi_Q(t)$ as far as the baseband output is concerned.

According to the matched filter theory, to match to the I-channel symbol, the matched filter impulse response should be the scaled mirror image of it, delayed by the signal duration $2T$:

$$\begin{aligned} h_m(t) &= \alpha \cos\left(\frac{\pi}{2T}(2T - t)\right) \cos(2\pi f_c(2T - t)), \\ &= \alpha \cos\left(\pi - \frac{\pi t}{2T}\right) \cos(m\pi - 2\pi f_c t), \\ &= \alpha(-1)^{m+1} \cos\left(\frac{\pi t}{2T}\right) \cos 2\pi f_c t, \\ &= \cos\left(\frac{\pi t}{2T}\right) \cos 2\pi f_c t, \quad T \leq t \leq 3T \end{aligned}$$

where $f_c = m/4T$ is assumed and $\alpha(-1)^{m+1}$ is merely a scaling constant which can be set to unity. The response of the matched filter to $\varphi_I(t)$ is

$$y_I(t) = \varphi_I(t) * h_m(t)$$

where $*$ denotes convolution. Then this signal is multiplied by the local carrier and low-pass filtered to give the final demodulated baseband symbol (detail omitted)

$$m_I(t) = \begin{cases} \frac{1}{4} \cos\left(\frac{\pi t}{2T}\right) \int_T^{T+t} \cos\left(\frac{\pi}{2T}\tau\right) \cos\left(\frac{\pi}{2T}(t-\tau)\right) d\tau, & 0 \leq t \leq 2T \\ \frac{1}{4} \cos\left(\frac{\pi t}{2T}\right) \int_{t-2T}^{3T} \cos\left(\frac{\pi}{2T}\tau\right) \cos\left(\frac{\pi}{2T}(t-\tau)\right) d\tau, & 2T \leq t \leq 4T \end{cases} \quad (5.30)$$

Working out the integrals (factor 1/4 omitted) the final demodulated baseband sym-

bol is

$$m_I(t) = \begin{cases} \cos \frac{\pi t}{2T} \left[\frac{1}{2} t \cos \frac{\pi t}{2T} - \frac{T}{\pi} \sin \frac{\pi t}{2T} \right], & 0 \leq t \leq 2T \\ \cos \frac{\pi t}{2T} \left[\frac{1}{2} (4T - t) \cos \frac{\pi t}{2T} + \frac{T}{\pi} \sin \frac{\pi t}{2T} \right], & 2T \leq t \leq 4T \end{cases}$$

which is shown in Figure 5.14(a). It is clear that matched filtering spreads the symbol to occupy $4T$ periods. Fortunately the output has zero values at all sampling instants except for at the center of the pulse. In other words, it introduces no intersymbol interference (ISI) if timing is accurately maintained.

By similar procedure, the Q-channel demodulated baseband symbol is found as (a constant factor $1/4$ is omitted)

$$m_Q(t) = \begin{cases} \sin \frac{\pi t}{2T} \left[\frac{1}{2} (t - T) \sin \frac{\pi t}{2T} + \frac{T}{\pi} \cos \frac{\pi t}{2T} \right], & T \leq t \leq 3T \\ \sin \frac{\pi t}{2T} \left[\frac{1}{2} (5T - t) \sin \frac{\pi t}{2T} - \frac{T}{\pi} \cos \frac{\pi t}{2T} \right], & 3T \leq t \leq 5T \end{cases}$$

which is also shown in Figure 5.14(a) (dotted line). It can be seen that it is merely a time shifted version of the I-channel demodulated symbol. It is easy to verify that $m_I(t - T) = m_Q(t)$.

Intuitively, why the matched filter treats I- and Q-channel symbols equally can be explained as follows. If we shift $\varphi_Q(t)$ to the left by T to coincide with $\varphi_I(t)$ on the time axis, it becomes

$$\varphi_Q(t + T) = \cos\left(\frac{\pi t}{2T}\right) \sin(2\pi f_c t + \theta),$$

where $\theta = 2\pi f_c T$. This means $\varphi_Q(t)$ and $\varphi_I(t)$ have the same envelope despite that their carriers may have phase difference. Therefore (5.30) is the same for the Q-channel since it only involves the convolution of envelopes. Consequently the results are the same except for a time delay of T .

Figure 5.14(b) shows the resultant demodulated signal for the same sequence in Figure 5.13.

The transfer function of the low-pass equivalent matched filter is

$$\tilde{H}_m(f) = \mathcal{F}\{\tilde{h}_m(t)\} = \mathcal{F}\left\{\cos\left(\frac{\pi t}{2T}\right)\right\} = \frac{4T[\cos 2\pi T f]}{\pi[1 - (4T f)^2]}$$

which is proportional to the square root of the PSD of the MSK signal.

5.7.4 Conversion and Matched Filter Implementation

The critical system components of the serial MSK are the biphase modulator, the bandpass conversion and matched filters, and the coherent demodulator (including carrier recovery). The modulator and the demodulator are no more special than the

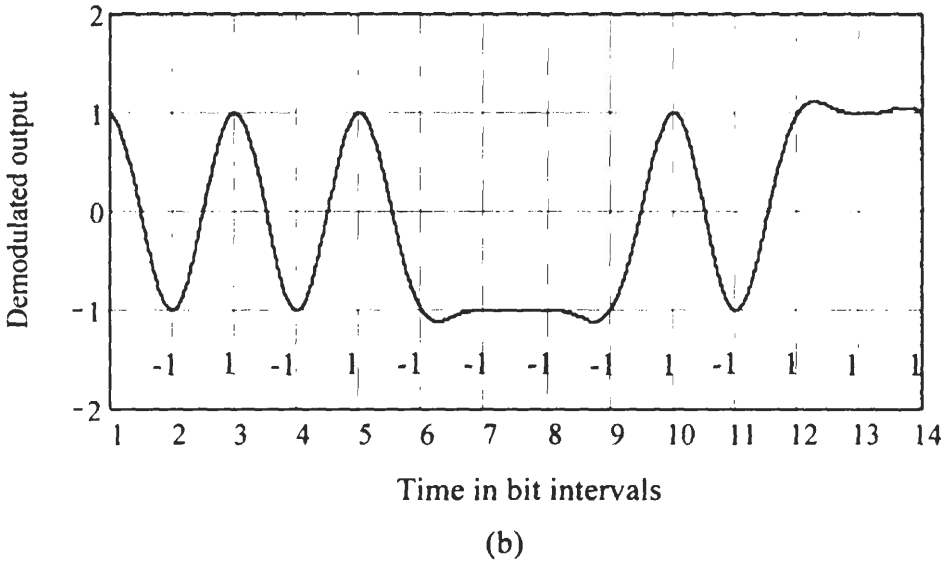
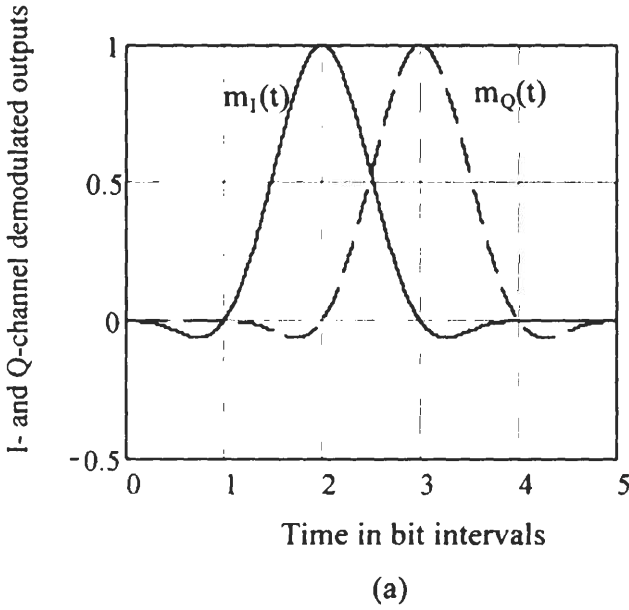


Figure 5.14 Demodulation of MSK signal with matched filter and coherent BPSK demodulator: (a) I-channel symbol, (b) Q-channel symbol, (c) demodulator output for the data sequence of Figure 5.13.

ones for BPSK. What are special here are the bandpass conversion and matched filters. They have been implemented with surface acoustic wave (SAW) devices. The maximum bandwidth of SAW devices is about 10% to 30% of the center frequency. For production SAW's, center frequencies of a few hundred MHz represent the upper limit, assuming normal fabrication techniques, with 1 GHz representing the upper limit if laser trimming and other special techniques are used. Thus the use of SAW filters implies an upper limit on data rate of about 100 Mbps, assuming the use of normal fabrication techniques [10].

An alternative to SAW implementation is the one utilizing baseband I/Q equivalents for the conversion and matched filters as shown in Figure 5.15. In Figure 5.15(a), data are demultiplexed into I/Q channels and filtered in baseband before being modulated onto two orthogonal carriers. Basically the reverse is done in the demodulator in Figure 5.15(b). Note that all reference signal frequencies in Figure 5.15 are the lower frequency of the two MSK frequencies: f_- .

The frequency responses of the baseband conversion and matched filters were derived in [10]. The frequency response of the conversion filter is

$$H_I(f) = \frac{T}{2} \left[\frac{\sin \pi(fT - 0.5)}{\pi(fT - 0.5)} + \frac{\sin \pi(fT + 0.5)}{\pi(fT + 0.5)} \right] \exp(-j\pi fT)$$

for I-channel and

$$H_Q(f) = j \frac{T}{2} \left[\frac{\sin \pi(fT - 0.5)}{\pi(fT - 0.5)} - \frac{\sin \pi(fT + 0.5)}{\pi(fT + 0.5)} \right] \exp(-j\pi fT)$$

for Q-channel. The overall equivalent low-pass transfer function of the conversion filter is

$$\begin{aligned} \tilde{H}(f) &= H_I(f) - jH_Q(f) \\ &= T \frac{\sin \pi(fT - 0.5)}{\pi(fT - 0.5)} \exp(-j\pi fT) \end{aligned}$$

These filter transfer functions are shown in Figure 5.16 (factor $\exp(-j\pi fT)$ or $j \exp(-j\pi fT)$ not included). From the figure we can see that the I-channel transfer function is low-pass and an even function of frequency and that the Q-channel transfer function is high-pass and an odd function of frequency. The total transfer function is a bandpass response with even symmetry about the frequency $f_+ = f_c + 1/4T$.

The frequency response of the matched filter is

$$H_{mI}(f) = \frac{T}{2} \left[\frac{2 \sin(2\pi fT)}{2\pi fT} + \frac{\sin(\pi(2fT - 1))}{\pi(2fT - 1)} + \frac{\sin(\pi(2fT + 1))}{\pi(2fT + 1)} \right]$$

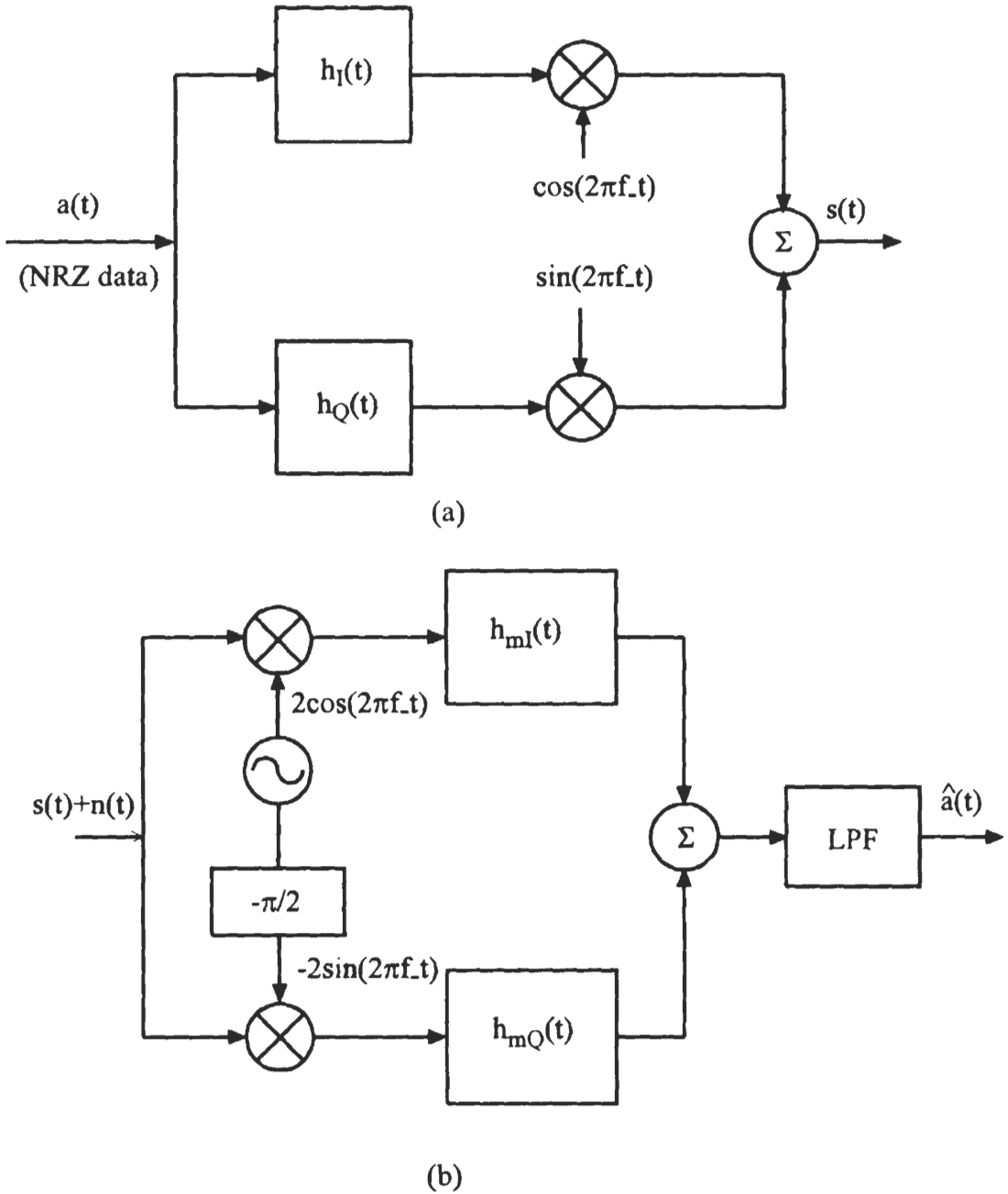


Figure 5.15 Baseband implementation of SMSK: (a) modulator, (b) demodulator.

for I-channel and

$$H_{mQ}(f) = -j \frac{T}{2} \left[\frac{\sin(\pi(2fT - 1))}{\pi(2fT - 1)} - \frac{\sin(\pi(2fT + 1))}{\pi(2fT + 1)} \right]$$

for Q-channel. The total response of the low-pass equivalent matched filter is

$$\begin{aligned} \tilde{H}_m(f) &= H_{mI}(f) + jH_{mQ}(f) \\ &= T \left[\frac{\sin(2\pi fT)}{2\pi fT} + \frac{\sin(\pi(2fT - 1))}{\pi(2fT - 1)} \right] \end{aligned}$$

The matched filters' responses are shown in Figure 5.17 (factor j not included). As in the case of the conversion filters, $H_{mI}(f)$ is even, low-pass, and $H_{mQ}(f)$ is odd, high-pass. The total transfer function $\tilde{H}_m(f)$ is a bandpass response with even symmetry about the frequency f_c .

These baseband filters can be implemented by transversal filter configuration as described in [10]. At very high data rates (e.g., 550 Mbps), these filters can be implemented by microwave stripline as reported in [10] for the advanced communications technology satellite of NASA.

5.7.5 Synchronization of SMSK

Two approaches can be used to recover the carrier for the SMSK signal. One is the synchronization circuit for the parallel MSK described in Section 5.1, which involves squaring the received signal to produce spectral components at $2f_-$ and $2f_+$. Since SMSK is mainly devised for high data rates, this approach is not satisfactory as it involves doubling the already high-frequency components.

Another approach is to use a Costas loop as shown in Figure 5.18. This structure is especially suitable for the I/Q demodulator structure in Figure 5.15(b), since the I- and Q-channel demodulated signals are already available for the matched filter implementation. The circuitry on the right of the dotted line in Figure 5.18 is the extra needed to form the Costas loop [10].

There exists a 180° phase ambiguity in the carrier acquisition loop due to the baseband multiplier [10]. One method to remove this ambiguity is to differentially encode the data before modulation, as described in Chapter 4.

5.8 MSK-TYPE MODULATION SCHEMES

After MSK was introduced, a lot of research effort was devoted to finding even more bandwidth-efficient modulation schemes. To improve bandwidth efficiency while

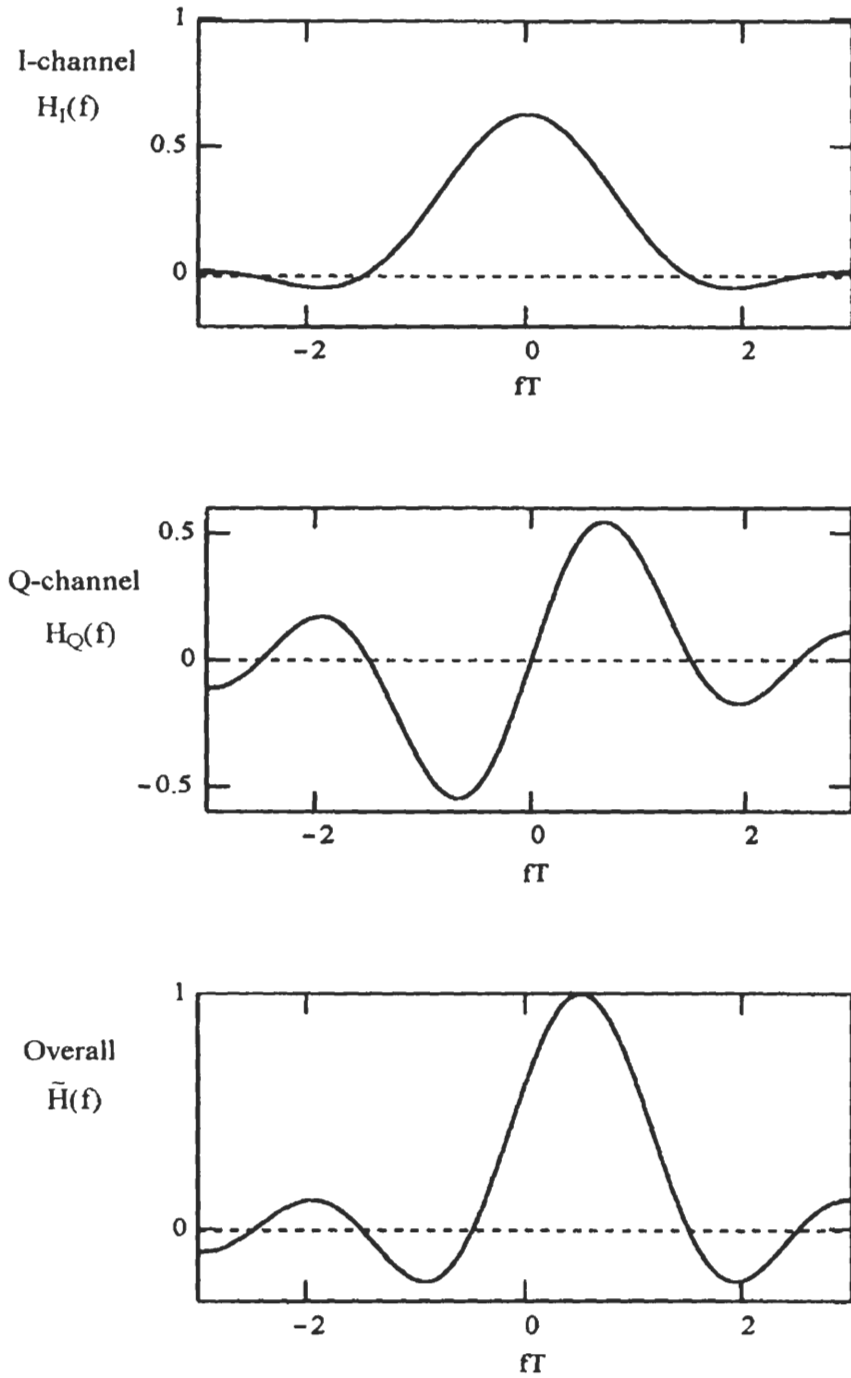


Figure 5.16 Baseband conversion filter frequency response.

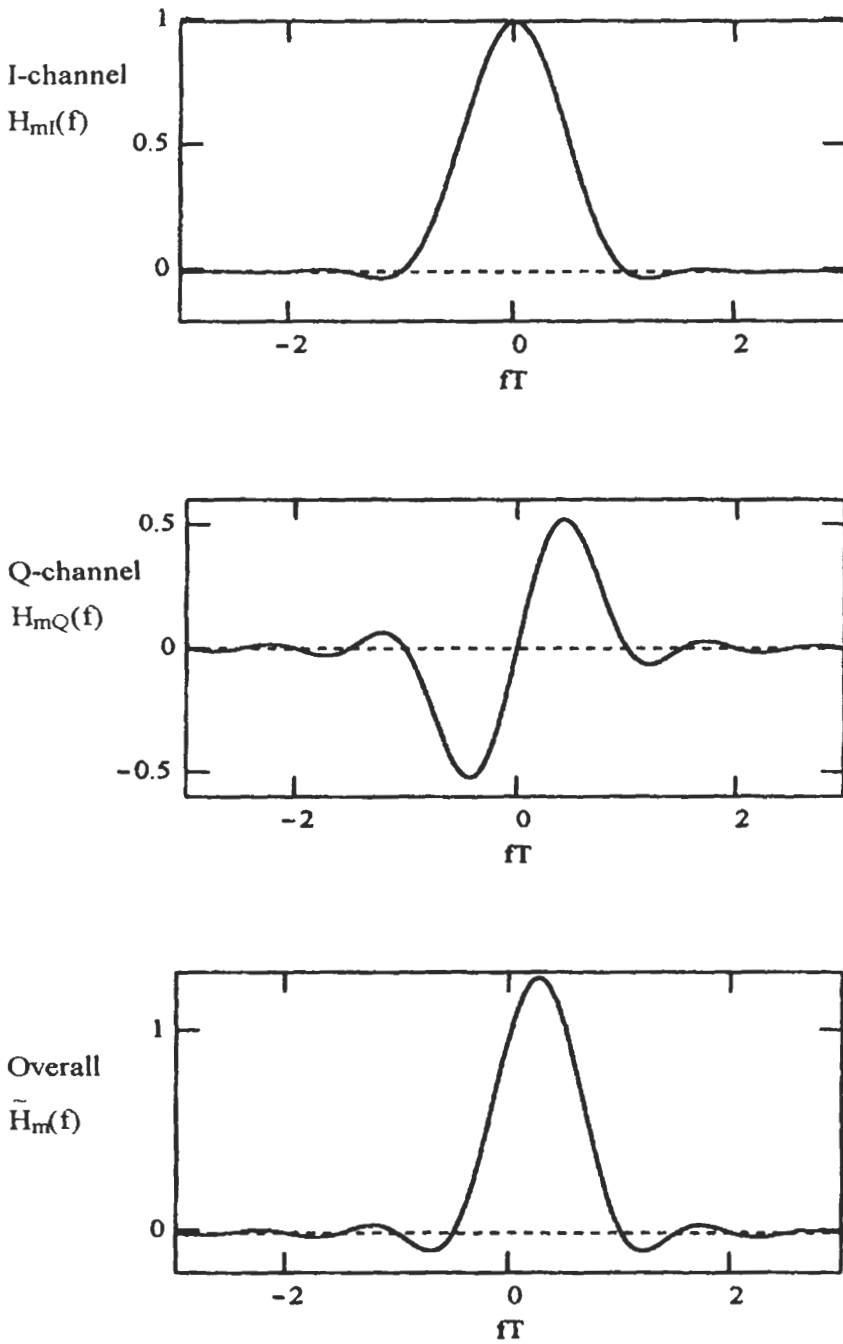


Figure 5.17 Baseband matched filter frequency response.

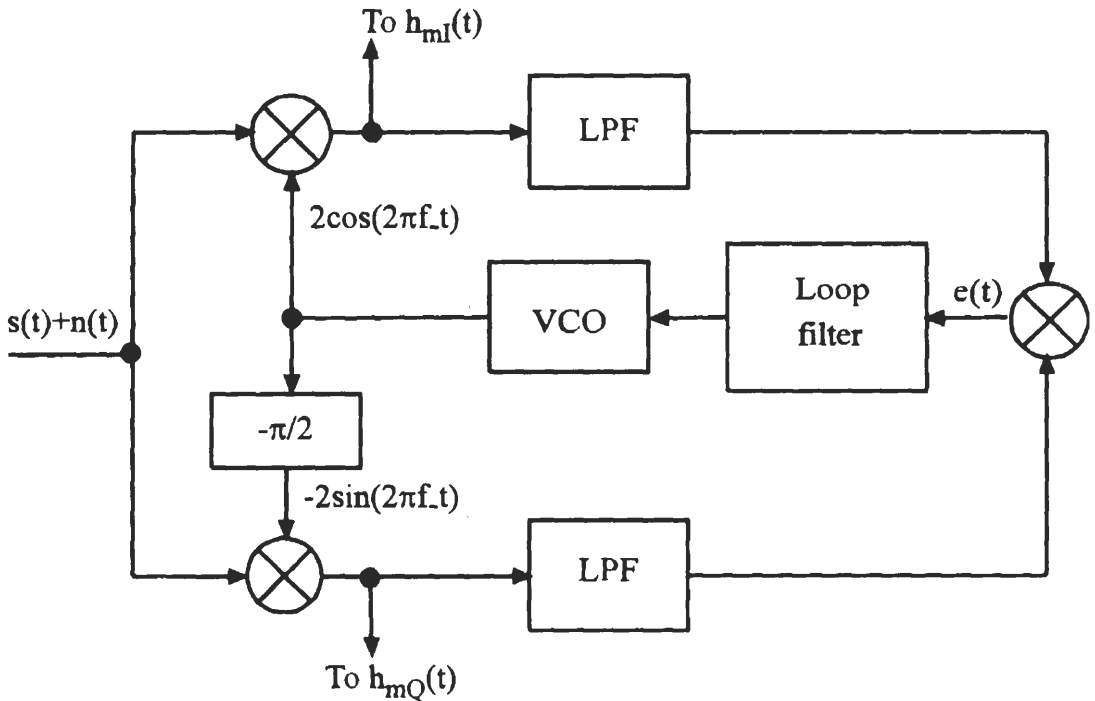


Figure 5.18 Costas loop for SMSK.

maintaining a constant envelope, one development direction is the continuous phase modulation with constant envelope, which has evolved into a large class of modulation schemes as we will study in Chapter 6 and 7. Another direction is to improve the spectra by using pulse shaping in quadrature modulation. In other words, new schemes are still based on two quadrature carriers like in MSK. However, the symbol shaping pulses are no longer half cosine. Instead, other pulse shapes are used. These schemes are sometimes called MSK-type schemes. All MSK-type signals can be expressed as

$$s(t) = s_I(t) \cos 2\pi f_c t + s_Q(t) \sin 2\pi f_c t, \quad -\infty \leq t \leq \infty \quad (5.31)$$

where $s_I(t)$ and $s_Q(t)$ are

$$s_I(t) = \sum_{k=-\infty}^{\infty} I_k p(t - 2kT) \quad (5.32)$$

$$s_Q(t) = \sum_{k=-\infty}^{\infty} Q_k p(t - 2kT - T) \quad (5.33)$$

where T is the bit time interval corresponding to the input data sequence $\{a_k \in (-1, +1)\}$ that has been demultiplexed into $\{I_k\}$ and $\{Q_k\}$. It is clear that each data symbol lasts for a duration of $2T$ in I- and Q-channels. Each data is weighted by a pulse-shaping function $p(t)$ which has a finite duration of $2T$. Just like MSK, a delay of T is introduced in the Q-channel, that is, the I- and Q-channel modulating signals are staggered. Also just like MSK, due to the staggering of the I- and Q-channels, the symbol duration of the MSK-type signal is T instead of $2T$ despite that the symbol durations are $2T$ for $s_I(t)$ and $s_Q(t)$. However, demodulation must be performed in a $2T$ duration.

For MSK-type schemes, the basic MSK modulator and demodulator in Figures 5.6 and 5.9 are applicable except that the pulse-shaping function must be replaced accordingly. Therefore for these schemes we will not repeat the description of the modulator and demodulator. Further, the serial MSK modulator and demodulator (Figure 5.12) can also be used for these MSK-type schemes, provided that the conversion filter in the modulator must be redesigned so that

$$\Psi_s(f) = |H(f)|^2 \Psi_{BPSK}(f) \quad (5.34)$$

where $\Psi_s(f)$ is the MSK-type signal spectrum, $H(f)$ is the conversion filter transfer function, and $\Psi_{BPSK}(f)$ is the spectrum of the BPSK signal which enters the filter. In the serial demodulator the matched filter must match to the pulse shape.

If the suboptimum receiver is acceptable, then all MSK-type schemes can be demodulated by a OQPSK-type demodulator where baseband correlation with $p(t)$ or matched filtering matched to $p(t)$ is omitted.

By choosing different $p(t)$, a variety of modulation schemes can be obtained. Sometimes $p(t)$ is indirectly determined by choosing the frequency pulse of the signal. The spectrum of the signal is determined by the pulse $p(t)$. In the following sections we will study a variety of pulse-shaping techniques that are primarily designed for satellite communications. What we are looking for from these modulation schemes are compact spectrum, low spectral spreading caused by nonlinear amplification, good error performance, and simple hardware implementation. We will describe a particular scheme or a class of schemes in each section. The emphasis is on the pulse shape and spectral properties. The error performance is also evaluated and often compared with that of MSK.

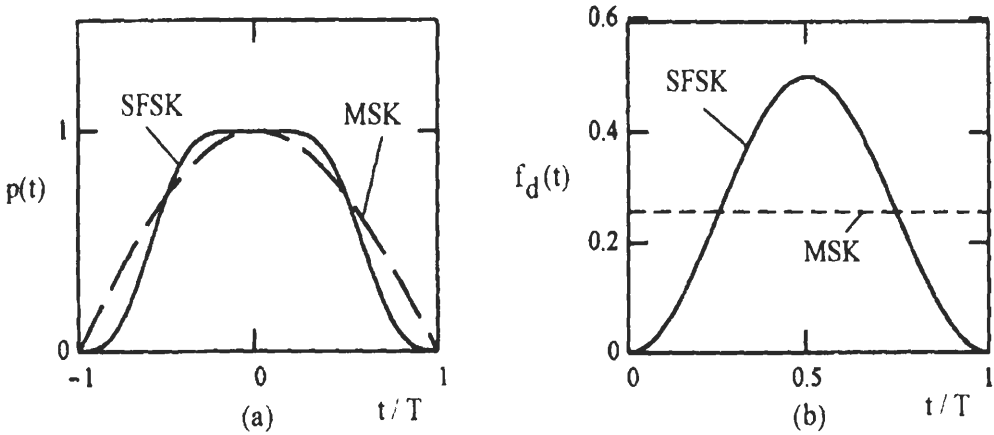


Figure 5.19 SFSK pulses: (a) amplitude pulse, (b) frequency deviation pulse.

5.9 SINUSOIDAL FREQUENCY SHIFT KEYING

Amoroso first proposed an alternate symbol shaping pulse as [11]

$$p(t) = \begin{cases} \cos \left[\frac{\pi t}{2T} - \frac{1}{4} \sin \frac{2\pi t}{T} \right], & -T \leq t \leq T \\ 0, & \text{elsewhere} \end{cases} \quad (5.35)$$

This scheme was named as sinusoidal frequency shift keying (SFSK) since the signal can be synthesized by applying a keyed sine wave to a linear integrator followed by a linear frequency modulator. Sensitivity of the spectrum to pulse shaping was examined by varying the factor value in front of the sine function. By comparing spectra for different factor values, it was found that $1/4$ is the value for the lowest sidelobes [11].

Figure 5.19(a) shows the pulse shape in comparison with that of MSK.

This scheme has a constant envelope, because in any symbol period, say $[0, T]$, the envelope

$$\begin{aligned} A(t) &= \sqrt{[I_0 p(t)]^2 + [Q_0 p(t - T)]^2} \\ &= \sqrt{p^2(t) + p^2(t - T)} \\ &= \sqrt{\cos^2 \left[\frac{\pi t}{2T} - \frac{1}{4} \sin \frac{2\pi t}{T} \right] + \sin^2 \left[\frac{\pi t}{2T} - \frac{1}{4} \sin \frac{2\pi t}{T} \right]} \\ &= 1 \end{aligned}$$

This scheme also has a continuous phase. Similar to the result for MSK (see (5.2)), in the duration $[kT, (k+1)T]$, the SFSK signal in (5.31) can be written as

$$s(t) = \cos[2\pi f_c t + d_k \phi(t) + \Phi_k] \quad (5.36)$$

where

$$d_k = -I_k Q_k$$

is determined by the staggered I- and Q-channel data, and

$$\phi(t) = \frac{\pi t}{2T} - \frac{1}{4} \sin \frac{2\pi t}{T} \quad (5.37)$$

which is the argument of the pulse-shaping function. The phase $\Phi_k = 0$ or π , corresponding to $I_k = 1$ or -1 . From (5.36) it is clear that the total phase in the duration is continuous. At the bit transition $\phi(kT) = \frac{k\pi}{2}$, the total excess phase is

$$\Theta(kT) = d_k \frac{k\pi}{2} + \Phi_k$$

This satisfies the same condition for phase continuity of MSK (see (5.6)). Thus like MSK, the phase of the SFSK signal is continuous at any time.

The frequency deviation is

$$f_d(t) = \frac{1}{2\pi} \frac{d}{dt} [d_k \phi(t)] = d_k \frac{1}{4T} (1 - \cos \frac{2\pi t}{T}) \quad (5.38)$$

which is shown in Figure 5.19(b).

Expression (5.36) shows that the SFSK can be generated by a frequency modulator with $\phi(t)$ as its phase deviation.⁶ Figure 5.20 is such a generator (modulator). Assuming the input is $d_k A \sin 2\pi t/T$, the output of the integrator is

$$\int_{kT}^{kT+t} d_k A \sin \frac{2\pi t}{T} dt = \frac{d_k AT}{2\pi} [1 - \cos \frac{2\pi t}{T}]$$

⁶ As we pointed out in the end of Section 5.1.2, having $d_k = -I_k Q_k$ is equivalent to having

$$d_k = d_{k-1} \oplus a_k$$

In other words, if we want the SFSK signal generated by the frequency modulator to be equivalent to the signal generated by a quadrature modulator, d_k must be differentially encoded using the original data sequence $\{a_k\}$. An SFSK signal so generated thus can be demodulated by the MSK-type quadrature demodulator. The outputs are directly I_k and Q_k . If d_k is the original data, the SFSK signal is a variation of the FFSK, which can still be quadraturely demodulated (first $\Theta(kT)$ is found and from which the data can be recovered) [2].

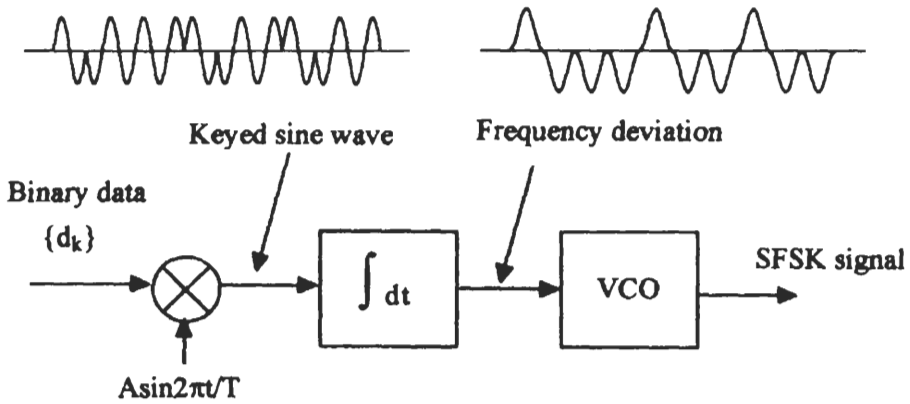


Figure 5.20 SFSK modulator.

This pulse is used as the control input to the VCO whose (radian) frequency deviation is proportional to the input voltage

$$\frac{d\Phi(t)}{dt} = \frac{d_k AK_V T}{2\pi} \left[1 - \cos \frac{2\pi t}{T} \right]$$

where K_V is the VCO sensitivity. The VCO output excess phase is

$$\begin{aligned} \Phi(t) &= \int_{kT}^{kT+t} \frac{d_k AK_V T}{2\pi} \left[1 - \cos \frac{2\pi t}{T} \right] dt \\ &= \frac{d_k AK_V T}{2\pi} \left[t - \frac{T}{2\pi} \sin \frac{2\pi t}{T} \right] \end{aligned}$$

Making $AK_V = \pi^2/T^2$, the above becomes

$$\begin{aligned} \Phi(t) &= d_k \left[\frac{\pi t}{2T} - \frac{1}{4} \sin \frac{2\pi t}{T} \right] \\ &= d_k \phi(t) \end{aligned}$$

Setting the VCO center frequency as f_c , the VCO output is then

$$s(t) = \cos [2\pi f_c t + d_k \phi(t) + \Phi_k] \quad (5.39)$$

The PSD of the modulated signal is determined by the pulse shape. The spectrum of the pulse shape can be analytically expressed as a sum of Bessel functions [11]. We only present the results here as shown in Figure 5.21. It can be seen that the sidelobes are considerably lower than those of MSK.

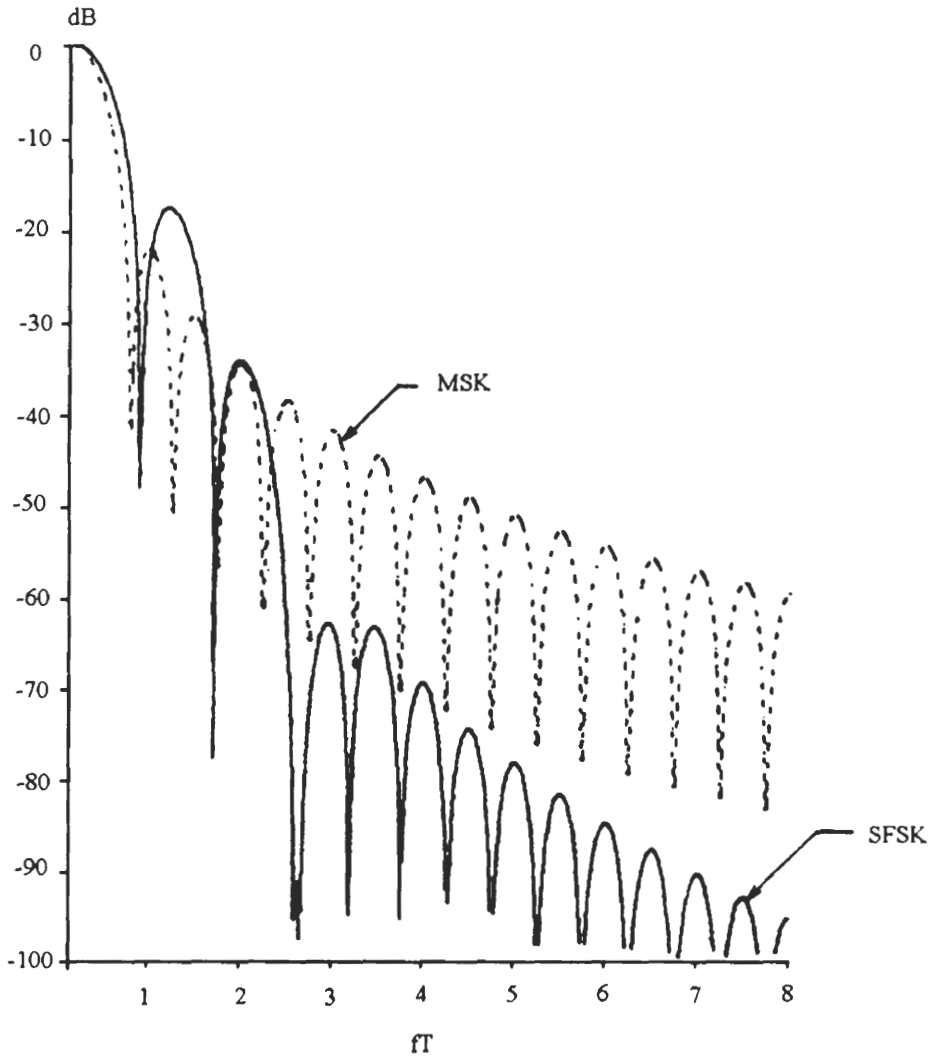


Figure 5.21 SFSK power spectral density. From [11]. Copyright © 1976 IEEE.

The error performance is the same as MSK since the bit energy of the SFSK signal is the same as that of MSK. This can be easily verified as follows (using MathCad, for example)

$$E_b = \int_0^T [p(t) \cos(2\pi f_c t) + p(t - T) \sin(2\pi f_c t)]^2 dt = \frac{1}{2}T$$

which is the same as (5.22) when $A = 1$.

In general, modulator and demodulator are the same as those of MSK except that baseband weighting pulse (which can be replaced by a matched filter in the receiver) is the one in (5.13). As we have shown above, the modulator can be implemented as the simple frequency modulator in Figure 5.20.

5.10 SIMON'S CLASS OF SYMBOL-SHAPING PULSES

When MSK is viewed as a special case of FSK, (5.10) implies that the data sequence $\{d_k\}$ is first translated into a binary data waveform with rectangular shaped pulses and then frequency modulated onto the carrier. A generalization of (5.10) which allows for other than rectangular frequency shaping pulses is proposed by Simon in [12] as

$$s(t) = A \cos[2\pi f_c t + \frac{\pi}{2T}(t - kT)f_k(t) + \Phi_k], \quad (k-1)T \leq t \leq (k+1)T \quad (5.40)$$

where

$$f_k(t) = \begin{cases} d_{k-1}g_1(t - (k-1)T), & (k-1)T \leq t \leq kT \\ d_k g_2(t - kT), & kT \leq t \leq (k+1)T \end{cases} \quad (5.41)$$

is the frequency shaping pulse which are nonzero only on the interval $[0, T]$. Note that since $s(t)$ is specified over a $2T$ interval, the phase Φ_k must remain constant over that interval and k is restricted to take on only-even or only-odd values. It is clear from (5.40) that the signal is of constant envelope.

It was found that for even symmetrical carrier envelopes in the I- and Q- channels, as is true in the original MSK, the two pulses $g_1(t)$ and $g_2(t)$ must be mirror images of each other around the point $t = T/2$, (i.e., $g_2(t) = g_1(T - t)$, $0 \leq t \leq T$). Thus only one of them need be specified. Suppose $g_2(t)$ is specified, then

$$\begin{aligned} f_0(t) &= \begin{cases} d_{-1}g_1(t + T), & -T \leq t \leq 0 \\ d_0 g_2(t), & 0 \leq t \leq T \end{cases} \\ &= \begin{cases} d_{-1}g_2(-t), & -T \leq t \leq 0 \\ d_0 g_2(t), & 0 \leq t \leq T \end{cases} \end{aligned} \quad (5.42)$$

and

$$f_k(t) = \begin{cases} d_{k-1}g_2(-t + kT), & (k-1)T \leq t \leq kT \\ d_k g_2(t - kT), & kT \leq t \leq (k+1)T \end{cases} \quad (5.43)$$

From this expression we can see that when $d_{k-1} = d_k$, the frequency pulses in the k th and $(k-1)$ th intervals are symmetrical about $t = kT$. Consider interval $[-T, T]$, the frequency deviation is

$$\begin{aligned} f_d(t) &= \frac{1}{2\pi} \left[\frac{d}{dt} \left(\frac{\pi}{2T} t f_k(t) \right) \right] \\ &= \frac{1}{4T} \left[t \frac{d}{dt} f_k(t) + f_k(t) \right] \\ &= \begin{cases} \frac{1}{4T} d_{k-1} \left[t \frac{d}{dt} g_2(-t) + g_2(-t) \right], & -T \leq t \leq 0 \\ \frac{1}{4T} d_k \left[t \frac{d}{dt} g_2(t) + g_2(t) \right], & 0 \leq t \leq T \end{cases} \end{aligned} \quad (5.44)$$

Excluding the data bits, the expressions of $f_d(t)$ in $[-T, 0]$ and $[0, T]$ are the same if $g_2(t)$ is even, or differ only by a negative sign if $g_2(t)$ is odd. In these cases we only need to consider interval $[0, T]$ or $[kT, (k+1)T]$ in general.

Further, since continuous rate of change of in-phase and quadrature envelopes leads to sharper spectral sidelobe roll-off, a constraint

$$g_1(T) = g_2(0) = 0 \quad (5.45)$$

may be imposed on $g_1(t)$ and $g_2(t)$ to ensure this desired property.

For identical I- and Q-channel envelopes further constraints are needed:

$$\left(1 - \frac{t}{T}\right)g_2(T-t) = 1 - \frac{t}{T}g_2(t), \quad 0 \leq t \leq T \quad (5.46)$$

or in terms of $g_1(t)$:

$$\left(1 - \frac{t}{T}\right)g_1(t) = 1 - \frac{t}{T}g_1(T-t), \quad 0 \leq t \leq T \quad (5.47)$$

Substituting $t = T/2$ into (5.46) and (5.47) we get

$$g_1\left(\frac{T}{2}\right) = g_2\left(\frac{T}{2}\right) = 1 \quad (5.48)$$

Based on these constraints we need only specify $g_2(t)$ in the interval $0 \leq t \leq T/2$ to determine $g_2(t)$ for $T/2 \leq t \leq T$. Similarly for $g_1(t)$. Assume

$$g_2(t) = \begin{cases} g_{21}(t), & 0 \leq t \leq T/2 \\ g_{22}(t), & T/2 \leq t \leq T \end{cases} \quad (5.49)$$

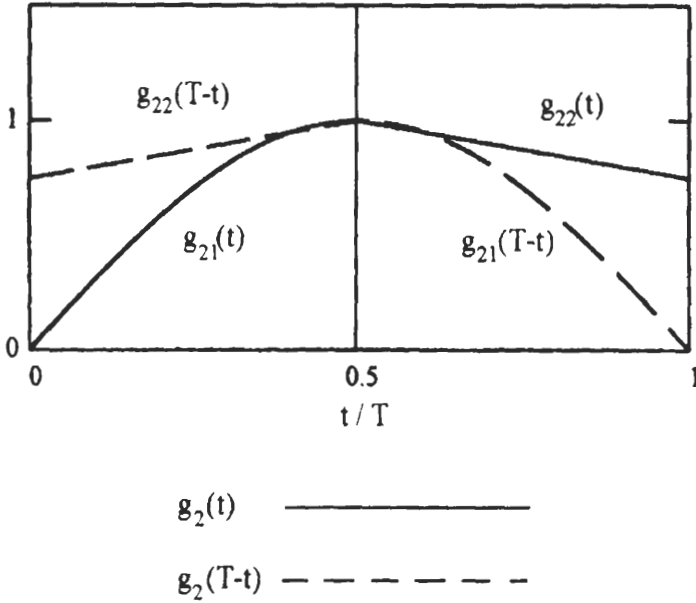


Figure 5.22 Relation between $g_2(T-t)$ and $g_2(t)$.

From Figure 5.22 we can see that

$$g_2(T-t) = \begin{cases} g_{22}(T-t), & 0 \leq t \leq T/2 \\ g_{21}(T-t), & T/2 \leq t \leq T \end{cases} \quad (5.50)$$

From (5.46) and (5.49) we can see that

$$\begin{aligned} g_2(T-t) &= \frac{T - t g_2(t)}{T-t} \\ &= \begin{cases} \frac{T - t g_{21}(t)}{T-t}, & 0 \leq t \leq T/2 \\ \frac{T - t g_{22}(t)}{T-t}, & T/2 \leq t \leq T \end{cases} \end{aligned}$$

Comparing to (5.50) we obtain

$$g_{21}(T-t) = \frac{T - t g_{22}(t)}{T-t}, \quad T/2 \leq t \leq T$$

or

$$g_{22}(t) = \frac{T - (T - t)g_{21}(T - t)}{t}, \quad T/2 \leq t \leq T \quad (5.51)$$

This changes (5.49) into

$$g_2(t) = \begin{cases} g_{21}(t), & 0 \leq t \leq T/2 \\ \frac{T - (T - t)g_{21}(T - t)}{t}, & T/2 \leq t \leq T \end{cases} \quad (5.52)$$

Thus the second part is found from the first part $g_{21}(t)$ using the above expression.

Under all the above constraints, we can express (5.41) in terms of $g_2(t)$, and expand (5.41) into I- and Q-channel summation, then we can easily identify the symbol shaping pulses as

$$p(t) = \begin{cases} \cos\left(\frac{\pi t}{2T}g_2(-t)\right), & -T \leq t \leq 0 \\ \cos\left(\frac{\pi t}{2T}g_2(t)\right), & 0 \leq t \leq T \end{cases} \quad (5.53)$$

for I-channel and

$$p(t - T) = \begin{cases} \sin\left(\frac{\pi t}{2T}g_2(t)\right), & 0 \leq t \leq T \\ \sin\left(\frac{\pi(2T - t)}{2T}g_2(2T - t)\right), & T \leq t \leq 2T \end{cases} \quad (5.54)$$

for Q-channel [12, 13], where $p(t - T)$ can be verified by use of (5.46). Note that when $g_2(t) = 1$, $p(t)$ falls back to that of the original MSK.

Several pulse shapes of $g_2(t)$ were examined in [12]. The first one is

$$g_2(t) = \begin{cases} 1 - \frac{\sin(2\pi t/T)}{(2\pi t/T)}, & 0 \leq t \leq T \\ 0, & \text{elsewhere} \end{cases} \quad (5.55)$$

which turns out to generate the SFSK. It can be easily verified that (5.55) satisfies (5.45) and (5.46). The corresponding frequency deviation pulse $f_d(t)$ and amplitude pulse are given earlier in (5.38) and (5.35) already.

The second is of polynomial-type

$$g_2(t) = \left(\frac{2t}{T}\right)^n, \quad 0 \leq t \leq T/2, \quad n = 1, 2, \dots \quad (5.56)$$

and it satisfies (5.45) and (5.46). The pulse in the interval $[T/2, T]$ can be determined by the relation given in (5.52). This pulse function is odd when n is odd, and even when n is even. The corresponding frequency deviation pulse $f_d(t)$ can be obtained

from (5.44) and is given by

$$f_d(t) = \begin{cases} \frac{d_k(n+1)}{4T} \left[\frac{2(t-kT)}{T} \right]^n, & kT \leq t \leq (k + \frac{1}{2})T \\ \frac{d_k(n+1)}{4T} \left[\frac{2[T-(t-kT)]}{T} \right]^n, & (k + \frac{1}{2})T \leq t \leq (k + 1)T \end{cases}$$

The amplitude pulse can be found from (5.53) and (5.54).

The third is

$$g_2(t) = \frac{1}{2} \frac{1 - \cos \pi t/T}{t/T}, \quad 0 \leq t \leq T/2 \quad (5.57)$$

and it satisfies (5.45) and (5.46). The pulse shape in the interval $[T/2, T]$ can be determined by the relation given in (5.52). This pulse function is odd. The corresponding frequency deviation pulse $f_d(t)$ can be obtained from (5.44) and is given by

$$f_d(t) = \frac{\pi d_k}{8T} \sin \frac{\pi(t - kT)}{T}, \quad kT \leq t \leq (k + 1)T$$

The amplitude pulse can be found from (5.53) and (5.54).

Figure 5.23 shows these frequency pulses, corresponding frequency deviation pulses, and amplitude pulse shapes (assuming $d_0 = 1$), where $n = 1$ for the second type. The frequency deviation pulse for the second type is a triangle and that for the third type is a half-sine function. The amplitude pulses are quite similar despite that the frequency deviation pulses are quite different.

The spectra (in the form of fractional out-of-band power P_{ob}) of these amplitude pulses are numerically computed in [12] and the results are shown in Figure 5.24. The results show that the $n = 1$ case polynomial-type pulse and the third type pulse have similar sidelobe roll-offs with the latter being slightly better. They roll off faster than SFSK within a bandwidth of approximately $BT = 2.0$, but slower thereafter. The roll-offs for higher values of n are significantly worse than SFSK. The $n = 1$ case polynomial-type pulse has spectral properties which are in a sense a compromise between those of MSK and SFSK. However, it has the practical advantage of offering easy transmitter implementation, that is, the transmitter oscillator is linearly swept in frequency.

One final comment is that when the receiver matched filters are matched over the $2T$ decision interval to the envelopes $p(t)$ and $p(t - T)$ of (5.53) and (5.54), the error performance is the same as that of MSK since the bit energy of the signals using the pulse shapes given in (5.55) to (5.57) is the same as that of MSK (checked using MathCad).

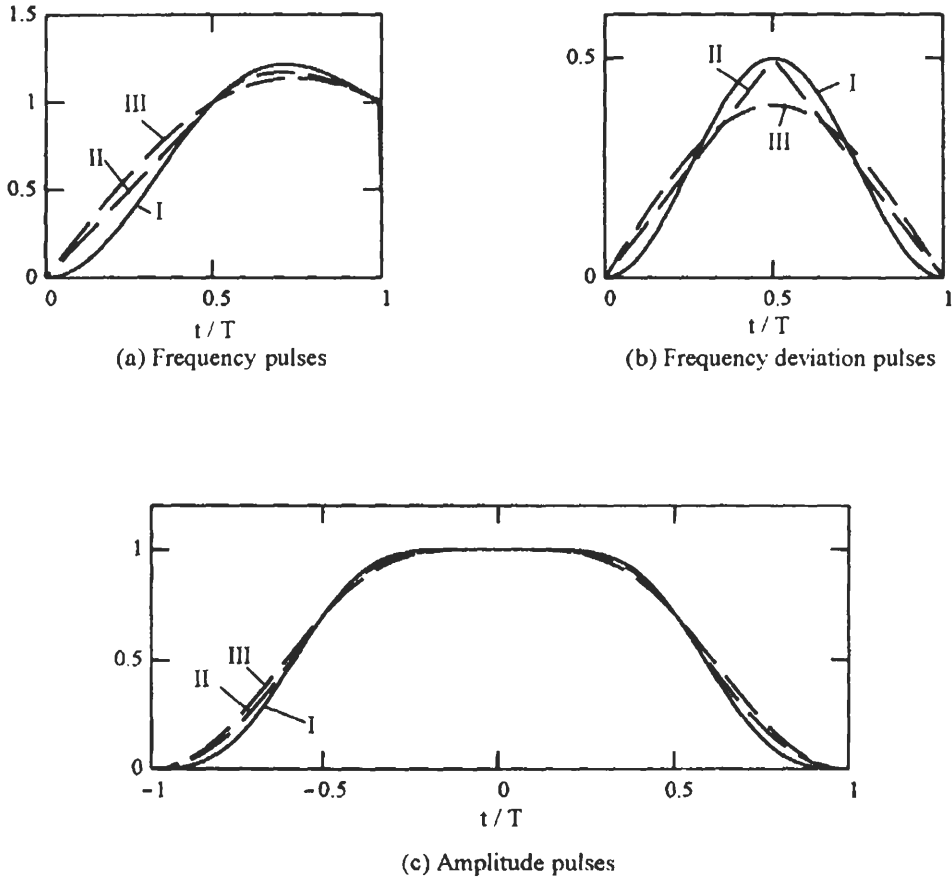


Figure 5.23 Simon's frequency pulses (a), frequency deviation pulses (b), and amplitude pulses (c).

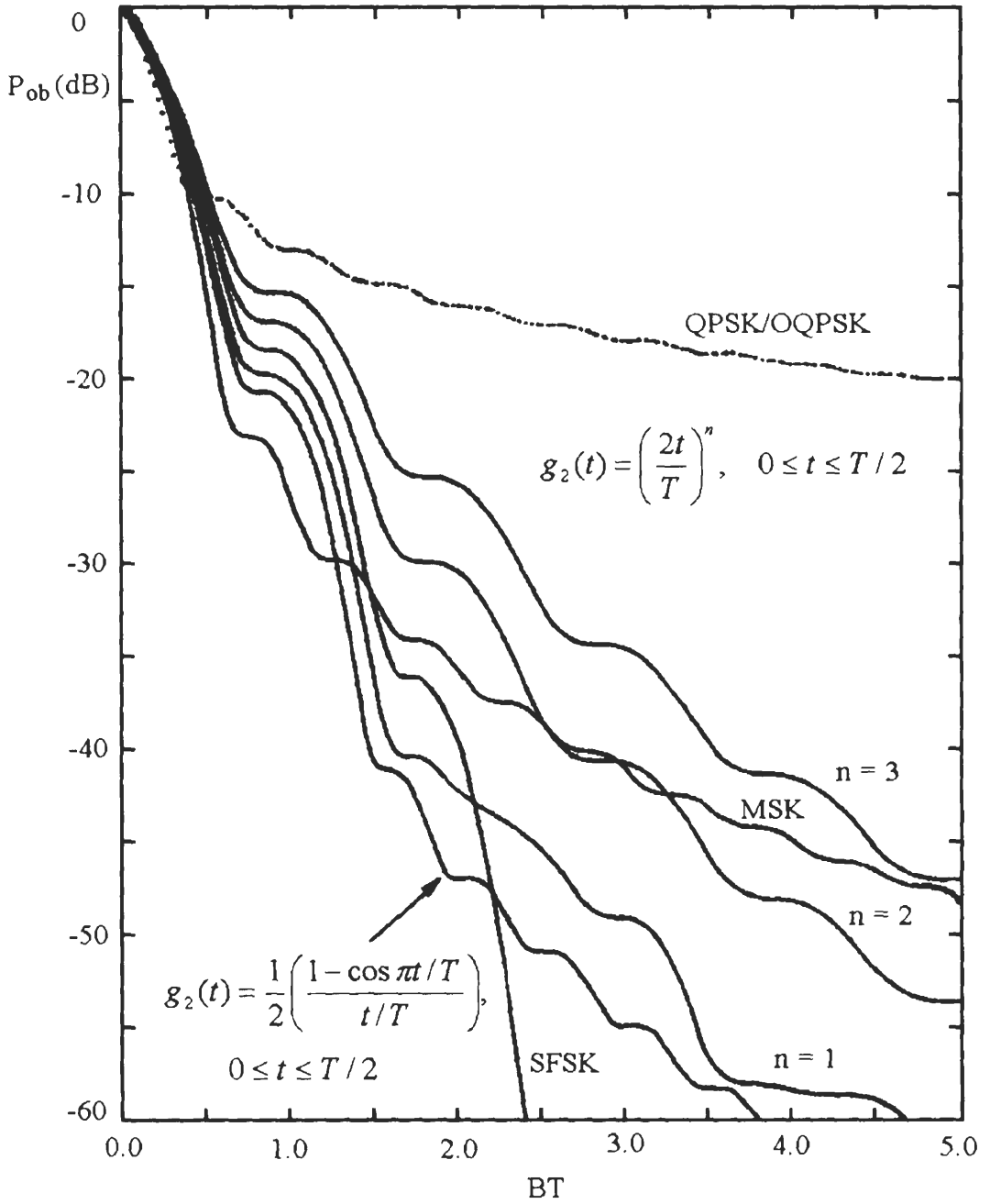


Figure 5.24 Fractional out-of-band behavior for several types of modulating pulses. From [12]. Copyright © 1976 IEEE.

5.11 RABZEL AND PASUPATHY'S SYMBOL-SHAPING PULSES

It is well known that if pulse $p(t)$ has $(N - 1)$ continuous derivatives which are equal to zero at the leading and trailing edges of the pulse, then its Fourier transform decays asymptotically as $f^{-(N+1)}$ and the power spectrum as $f^{-(2N+2)}$ [14]. (Only positive f need be considered since spectra are symmetrical about $f = 0$). Equivalent conditions on $g(t)$, which is denoted as $g_2(t)$ in (5.53) and (5.54), are derived in [13] as

$$g^{(i)}(T) = (-1)^i \frac{i!}{T^i}, \quad i = 0, 1, 2, \dots, N - 1$$

For an MSK-type signal, the above conditions are equivalent to

$$g^{(i-1)}(0) = 0, \quad i = 0, 1, 2, \dots, N - 1 \quad (5.58)$$

A general class of pulses was proposed by Rabzel and Pasupathy [13] as

$$g(t, \alpha, M) = 1 - \frac{\sum_{i=1}^M K_i \left[\sin\left(\alpha \frac{2\pi t}{T}\right) \right]^{2i-1}}{\left(\alpha \frac{2\pi t}{T}\right)}, \quad 0 \leq t \leq T \quad (5.59)$$

where

$$K_i = \frac{(2i - 2)!}{2^{2i-2} [(i - 1)!]^2 (2i - 1)}$$

and $\alpha = 1, 2, 3, \dots$. The K_i s are the coefficients of the series expansion of the inverse sine function, that is,

$$\sin^{-1}(x) = \sum_{j=1}^{\infty} K_j x^{2j-1}$$

The first 10 K_i s are 1, 0.167, 0.075, 0.045, 0.03, 0.022, 0.017, 0.014, 0.012, and 0.0097.

Note that an MSK-type signal using $g(t, \alpha, M)$ has a constant envelope since the signal is given in (5.40).

For finite M , it was shown in [13] that $g(t, \alpha, M)$ satisfies (5.46) and (5.58) with $N = 2M + 1$. Thus the power spectrum of an MSK-type signal employing this class of frequency shaping pulses will decay asymptotically as $f^{-(4M+4)}$. Some shaping pulses previously considered are special cases of (5.59). Specifically,

$$g(t, \alpha, 0) = 1$$

defines MSK, with an asymptotic decay rate of f^{-4} and

$$g(t, 1, 1) = 1 - \frac{\sin(2\pi t/T)}{(2\pi t/T)}$$

generates the SFSK with an asymptotic decay rate of f^{-8} . The shaping pulse defined in (5.57), which is not in the class, has an asymptotic decay rate of f^{-6} . These signals should be contrasted with the OQPSK signal which has an asymptotic decay rate of f^{-2} only.⁷

However, when $M = \infty$, the pulse is

$$g(t, 1, \infty) = \begin{cases} 0, & 0 \leq t \leq T/4 \\ 2 - \frac{T}{2t}, & T/4 \leq t \leq 3T/4 \\ \frac{T}{t}, & 3T/4 \leq t \leq T \end{cases}$$

which has a discontinuous first derivative (just like MSK) and hence its power spectrum decays as f^{-4} .

The plots of this class of frequency-shaping pulses and in-phase symbol-shaping pulses are given in Figures 5.25 and 5.26. The power spectra (in the form of out-of-band power P_{ob}) of corresponding MSK-type signals are given in Figure 5.27. For fixed $\alpha = 1$, the higher the values of M (except for $M = \infty$), the smoother the pulse shapes and the lower the out-of-band power. The $P_{ob(min)}$ in the figure refers to a lower bound on P_{ob} as calculated by Prabhu [16], using the optimum prolate spheroidal wave function for $p(t)$. The effect of α were also examined for fixed $M = 1$ case as shown in Figure 5.28. It was found that for large BT values the P_{ob} is smaller for $\alpha = 1$, and for small BT values the P_{ob} is smaller for larger α . However, using MSK at the small BT ranges is a better alternative since its P_{ob} is indistinguishable from that of SFSK but its system complexity is less.

The generation of the MSK-type signaling using $G(t, \alpha, M)$ is a straightforward extension of the scheme shown in Figure 5.20. The generator will use the frequency deviation function as an input to a VCO whose outputs are the I- and Q-channel symbol pulses $p(t)$ and $p(t-T)$. The generator is shown in Figure 5.29. The structure is based on the frequency deviation function.

$$f_d(t) = \frac{1}{4T} \frac{d}{dt} [tg(t)], \quad 0 \leq t \leq T$$

⁷ The symbol shaping pulse for OQPSK is $p(t) = 1, 0 \leq t \leq T$, and 0 elsewhere, which is discontinuous. Its integration (or -1 th derivative) is continuous. Thus $N = 0$, its power spectrum decays with an asymptotic decay rate of $|f|^{-(2N+2)} = |f|^{-2}$.

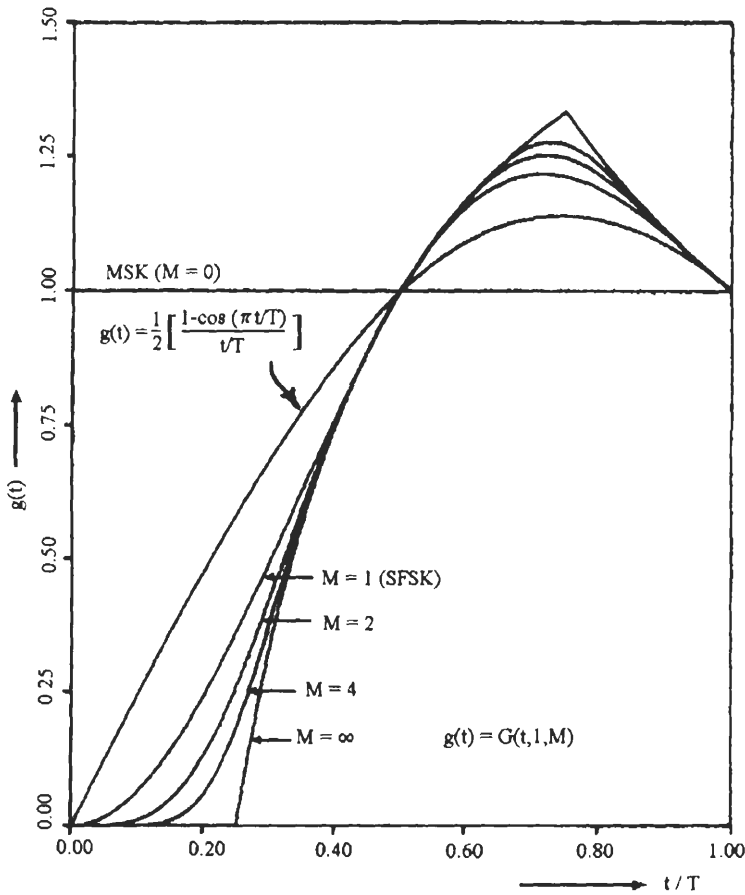


Figure 5.25 Rabzel and Pasupathy's symbol-shaping pulses. From [13]. Copyright © 1978 IEEE.

for which $g(t) = G(t, \alpha, M)$ yields

$$f_d(t) = \frac{1}{4T} \left\{ 1 - \cos \left(\frac{\alpha 2\pi t}{T} \right) \sum_{i=1}^M B_i \left[\sin \frac{\alpha 2\pi t}{T} \right]^{2i-2} \right\}$$

where

$$B_i = \frac{(2i-2)!}{2^{2i-2} [(i-1)!]^2}$$

The first four B_i s are 1, 1/2, 3/8, and 5/16. Note that the output of the VCO in Figure 5.20 is directly the modulated signal since the input is a keyed sine signal, whereas the outputs of the VCO in Figure 5.29 are baseband symbol pulses. Keying is performed

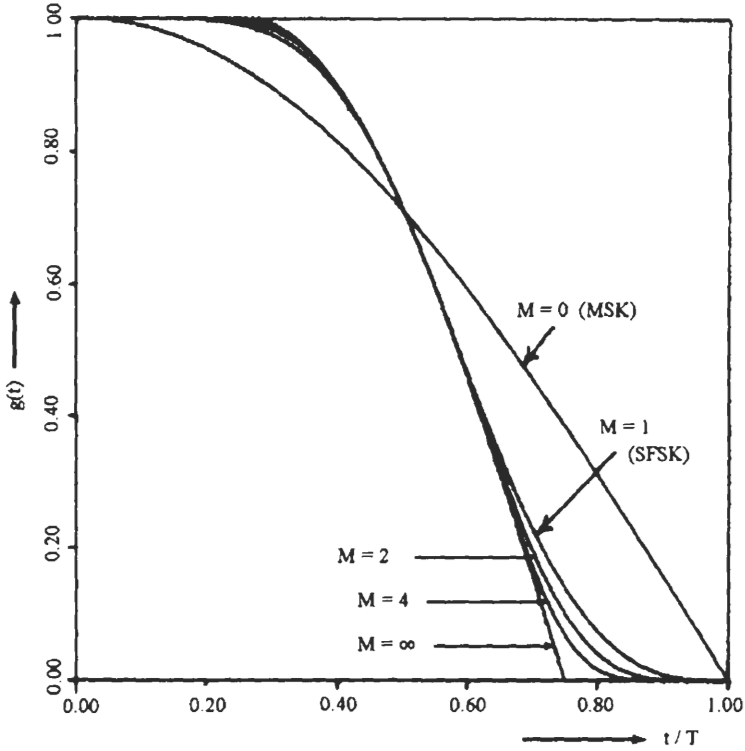


Figure 5.26 In-phase symbol weightings for $g(t) = G(t, 1, M)$. From [13]. Copyright © 1978 IEEE.

in the modulator.

Again the optimum demodulator is the same as that of MSK with the receiver matched filters matched over the $2T$ decision interval to the I- and Q-channel shaping pulses. The error performance is also the same since the bit energy of the signals using the pulse shapes given in (5.59) is the same as that of MSK (checked using MathCad).

5.12 BAZIN'S CLASS OF SYMBOL-SHAPING PULSES

A class of symbol-shaping pulses was proposed by Bazin [15] which includes the class of (5.59) as a subclass. Hence SFSK is also a element of the class. This class is defined to have up to N th continuous derivatives so that its power spectrum decays asymptotically as f^{-2N-4} and to produce a constant envelope of the MSK-type

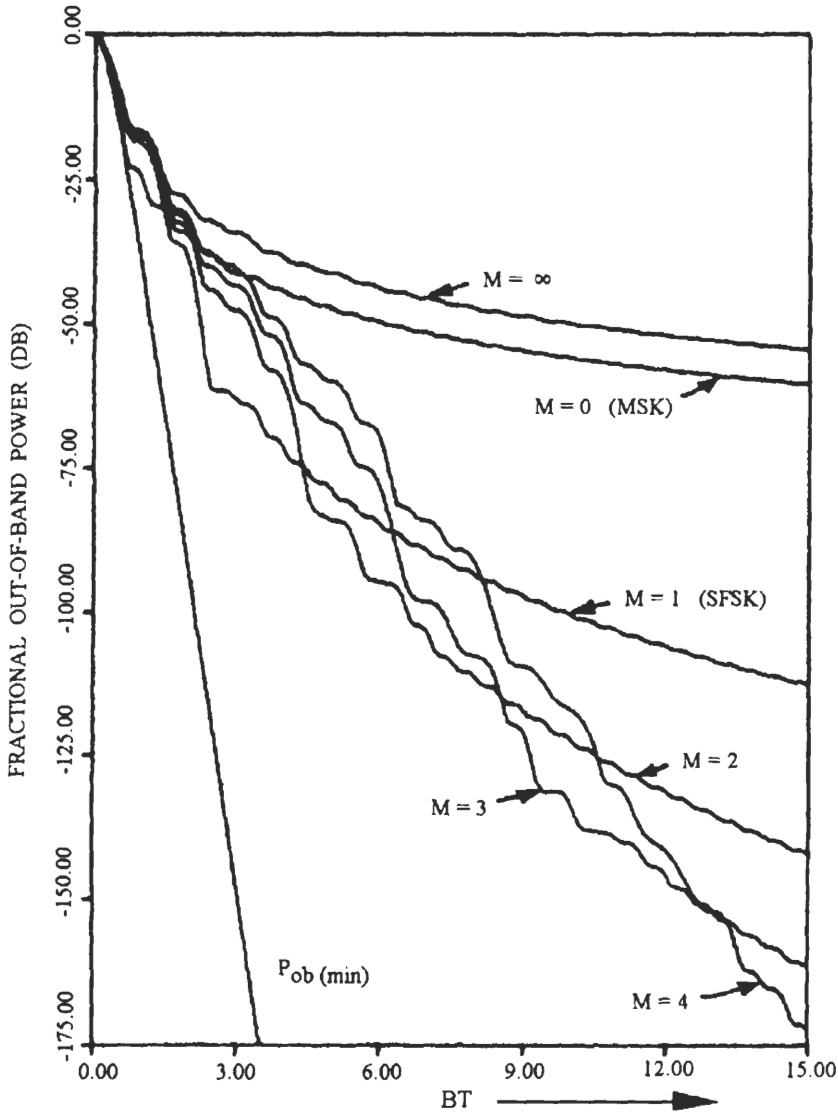


Figure 5.27 Fractional out-of-band powers for $G(t, 1, M)$. From [13]. Copyright © 1978 IEEE.

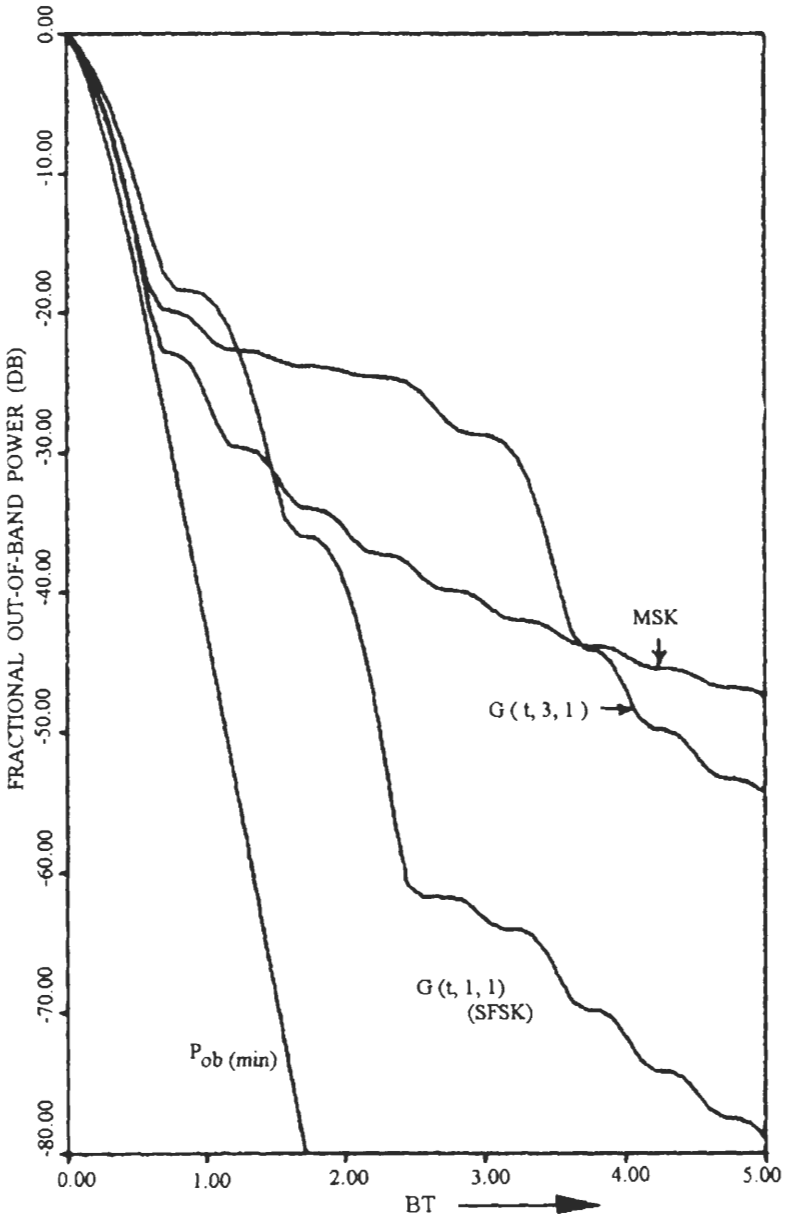


Figure 5.28 Effect of α in $G(t, \alpha, 1)$ on the fractional out-of-band power. From [13]. Copyright © 1978 IEEE.

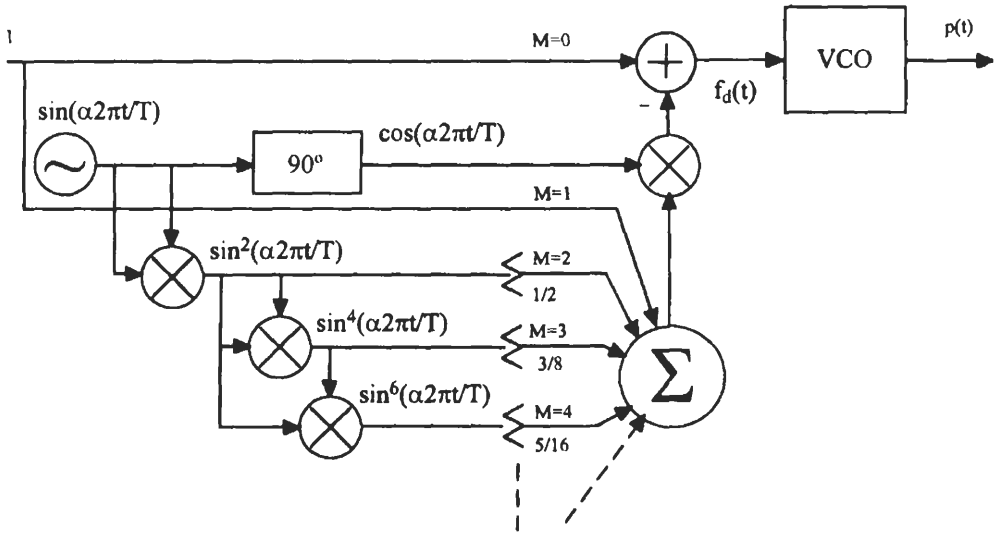


Figure 5.29 Generation of amplitude pulses. From [13]. Copyright © 1978 IEEE.

which generates:

$$p(t) = \cos \left[\frac{\pi t}{2T} - \sum_{k=1}^{N'} A_k \sin \frac{2\pi kt}{T} \right] \text{ and } N' \geq \frac{N}{2} \quad (5.60)$$

The A_k coefficients are solutions of the linear system:

$$\frac{d_i p(\pm T)}{dt^i} = 0, \quad i = 1, 2, \dots, N$$

Some A_k coefficients may be zero. The magnitude of the vector sum of the in-phase and quadrature pulse envelope is invariant since $p(t) = p(-t)$, and $p^2(t) + p^2(t - T) = 1$. SFSK is apparently an element of this class with $k = 1$ and $N = 2$ and $A_1 = 0.25$, hence the power spectrum asymptotically decays as f^{-8} . Another example of this class, called double SFSK (DSFSK) is defined by choosing $N' = 2$ and $N = 4$. The pulse is

$$p(t) = \cos \left[\frac{\pi t}{2T} - \frac{1}{3} \sin \frac{2\pi t}{T} + \frac{1}{24} \sin \frac{4\pi t}{T} \right]$$

Its power spectrum decays asymptotically as f^{-12} . It is interesting to compare this pulse to one of Rabzel's pulses which is close to it. By choosing $M = 2$ and $\alpha = 1$ in

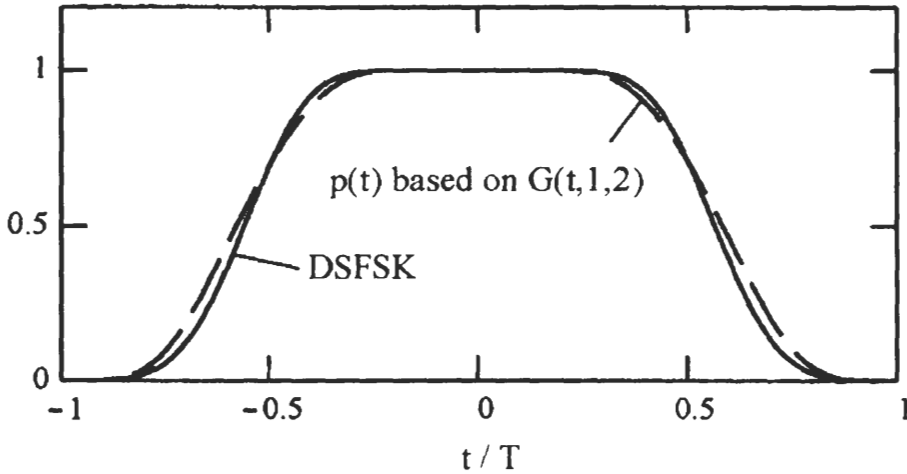


Figure 5.30 Bazin's pulse.

(5.59), Rabzel's frequency-shaping pulse leads to a symbol-shaping pulse as follows

$$p(t) = \cos \left[\frac{\pi t}{2T} - \frac{9}{32} \sin \frac{2\pi t}{T} + \frac{1}{96} \sin \frac{6\pi t}{T} \right] \quad (5.61)$$

The pulses are shown in Figure 5.30.

The comparison of power spectral densities in Figure 5.31 shows that the spectrum of DSFSK decays, on the average as f^{-12} beyond $f = 4.75/T$, and coincides with the SFSK spectrum near $f = 4/T$ and departs from the latter from $f = 1/T$ up to $f = 3.75/T$ where the power density is larger for DSFSK than for SFSK. The difference is maximum at $f = 3/T$ and equal to about 20 dB. The power spectrum of (5.61) is larger than SFSK and close to DSFSK before $f = 3.75/T$, and it approaches the SFSK spectrum beyond $f = 4.5/T$, but the effect of the asymptotic slope (as f^{-12}) does not happen before $f = 6/T$.

The error performance of above schemes is the same as MSK as long as the receiver uses matched filters which are matched to I- and Q-channel symbol-shaping pulses.

5.13 MSK-TYPE SIGNAL'S SPECTRAL MAIN LOBE

While above shaping techniques can reduce MSK spectral sidelobes considerably,

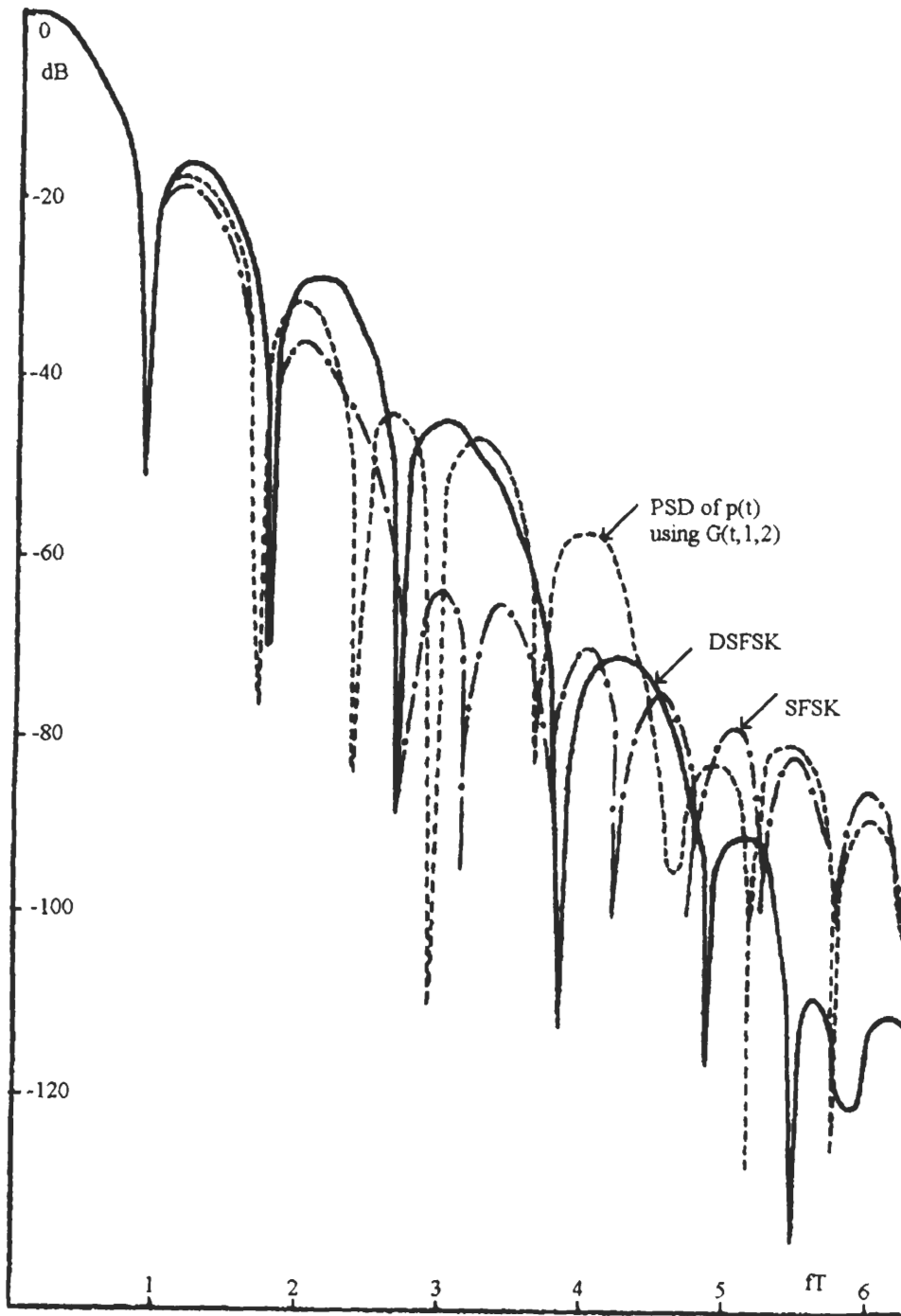


Figure 5.31 Power spectra. From [15]. Copyright © 1979 IEEE.

none of them can reduce the main lobe of MSK spectrum. A study of all these proposed symbol-shaping pulses $p(t)$ revealed the following common points: 1) All the proposed $p(t)$ are monotonic symmetrical pulses of finite duration $[-T, T]$, which is defined as follows: $p(t) = p(-t)$, $p'(t) \leq 0$ for $0 < t < T$. 2) The spectral main lobes of all of these $p(t)$ are always wider than that of a square pulse having the same time duration. In fact, it has been shown that an MSK-type signal generated by using a monotonic symmetrical pulse of finite duration $[-T, T]$ will always have a spectral main lobe wider than that of a conventional PSK signal generated by using an polar NRZ pulse of the same duration [17].

5.14 SUMMARY

In this chapter we first described the original MSK scheme which is implemented in a parallel fashion with I- and Q-channels in modulator and demodulator. It was described as a sinusoidally weighted OQPSK and as a special case of continuous phase modulation. Its properties of constant envelope and continuous phase were proved. Its power spectral density was derived and compared with those of BPSK, QPSK, and OQPSK. The comparison was in favor of MSK in terms of sidelobe roll-off speed. Then the MSK modulator, demodulator, and synchronization circuit were described. The error probability expression of MSK was derived, which turns out to be the same as that of BPSK, QPSK, and OQPSK. Next the serial MSK, which is suitable for high-speed transmission, was described in detail, including its principle, modulator, demodulator, conversion and matched filters, and synchronization. Finally, many MSK-type modulation schemes, which generally have better spectral sidelobe roll-offs or better error performances, but more complexity, were discussed.

Gaussian MSK (GMSK) is another spectral compact MSK-type scheme which passes the polar NRZ data waveform through a Gaussian filter before sending it to an FM modulator [18]. It also suffers loss in error performance depending on the filter bandwidth. This leads to a trade-off between error performance and bandwidth. It was shown that 0.7 dB loss for a filter bandwidth $B = 0.25/T$ is a good trade-off for mobile radio channels [18]. It has been chosen as the modulation scheme for European mobile GSM system. It will be discussed in Chapter 6 in the context of continuous phase modulation (CPM).

Efforts to improve the MSK error performance were also reported [19, 20]. Improvements are achieved by extending the observation interval from $2T$ for MSK to longer intervals. The improvements in E_b/N_o are on the order of 1 dB for $3T$ and 1.2 dB for $5T$ for an optimum value of $\Delta f = (f_+ - f_-) = 0.715/T$. For observation intervals longer than $5T$, improvements are minor. The complexity increase does not seem to favor these schemes over the simple yet efficient MSK.

We will revisit MSK and MSK-type schemes in the next chapter in the context of continuous phase modulation. In particular, one important MSK-type scheme, the GMSK, will be discussed in detail due to its application in the GSM system.

References

- [1] Doelz, M. L., and E. H. Heald, "Minimum-shift data communication system," Collins Radio Co., U.S. Patent 2977 417, March 28, 1961.
- [2] DeBuda, R., "Coherent demodulation of frequency-shift keying with low deviation ratio," *IEEE Trans. Commun.*, vol. 20, June 1972, pp. 429-435.
- [3] Gronemeyer, S. A., and A. L. McBride, "MSK and offset QPSK modulation," *IEEE Trans. Commun.*, vol. 24, August 1976, pp. 809-820.
- [4] Amoroso, F., and J. A. Kivett, "Simplified MSK signaling technique," *IEEE Trans. Commun.*, vol. 25, April 1977, pp. 433-441.
- [5] *System Handbook of Advanced Communications Technology Satellite (ACTS)*, NASA, Lewis Research Center, Cleveland, Ohio, 1993.
- [6] Steele, R., *Mobile Radio Communications*, New York: IEEE Press, 1995.
- [7] Bhargava, V. K., et al., *Digital Communications by Satellite*. New York: John Wiley and Sons, 1981.
- [8] Taylor, D. P., et al., "A high speed digital modem for experimental work on the communications technology satellite," *Canadian Electrical Engineering Journal*, vol. 2, no. 1, 1977, pp. 21-30.
- [9] Pasupathy, S., "Minimum shift keying: a spectrally efficient modulation," *IEEE Communications Magazine*, July 1979, pp. 14-22.
- [10] Ziemer, R. E., and C. R. Ryan, "Minimum-shift keyed modem implementations for high data rates," *IEEE Communications Magazine*, vol. 21, Oct. 1983, pp. 28-37.
- [11] Amoroso, F., "Pulse and spectrum manipulation in the minimum (frequency) shift keying (MSK) format," *IEEE Trans. Commun.*, vol. 24, March 1976, pp. 381-384.
- [12] Simon, M. K., "A generalization of minimum-shift-keying (MSK)-type signaling based upon input data symbol pulse shaping," *IEEE Trans. Commun.*, vol. 24, August 1976, pp. 845-856.
- [13] Rabzel, M., and S. Pasupathy, "Spectral shaping in MSK-type signals," *IEEE Trans. Commun.*, vol. 26, Jan. 1978, pp. 189-195.
- [14] Bennett, W. R., *Introduction of Signal Transmission*. New York: McGraw-Hill, 1970, p.17.
- [15] Bazin, B., "A class of MSK baseband pulse formats with sharp spectral roll-off," *IEEE Trans. Commun.*, vol. 27, May 1979, pp. 826-829.
- [16] Prabhu, V. K., "Spectral occupancy of digital angle-modulated signals," *Bell Syst. Tech. J.*, April 1976, pp. 429-453.
- [17] Boutin, N., and S. Morissette, "Do all MSK-type signaling waveforms have wider spectra than those of PSK?" *IEEE Trans. Commun.*, vol. 29, July 1981, pp. 1071-1072.
- [18] Murota, K., and K. Hirade, "GMSK modulation for digital mobile radio telephony," *IEEE Trans.*

Commun., vol. 29, July 1981, pp. 1044-1050.

- [19] Osborn, W. P. and M. B. Luntz, "Coherent and noncoherent detection of CPFSK," *IEEE Trans. Commun.*, vol. 22, August 1974, pp. 1023-1036.
- [20] De Buda, R., "About optimal properties of fast frequency-shift keying," *IEEE Trans. Commun.*, vol. 22, Oct. 1974, pp. 1726-1727.

Selected Bibliography

- Haykin, S., *Digital Communications*. New York, John Wiley, 1988.
- Sklar, B., *Digital Communications, Fundamentals and Applications*, Englewood Cliffs, New Jersey: Prentice Hall, 1988.
- Svensson, A., and C.-E. Sundberg, "Serial MSK-type detection of partial response continuous phase modulation," *IEEE Trans. Commun.*, vol. 33, Jan. 1985, pp. 44-52.
- Ziemer, R. E., and R. L. Peterson, *Introduction to Digital Communication*, 4th Ed., Boston: Houghton Mifflin, 1995.
- Ziemer, R. E., and W. H. Tranter, *Principles of Communications, Systems, Modulation, and Noise*, New York: Macmillan, 1992.

Chapter 6

Continuous Phase Modulation

From Chapter 5 we have learned that MSK signal has continuous phase. In fact MSK is just a special case of a large class of constant amplitude modulation schemes called continuous phase modulation (CPM). This class of modulation is jointly power and bandwidth efficient. With proper choice of pulse shapes and other parameters, CPM schemes may achieve higher bandwidth efficiency than QPSK and higher order MPSK schemes. Even though high-order QAM may outperform MPSK in terms of power or bandwidth efficiency (see Section 8.7 for comparison between QAM and MPSK), QAM's nonconstant envelope may hinder its use in channels with nonlinear power amplifiers. Therefore CPM has been getting a lot of attention in satellite channels and other channels. Some of the CPM schemes have been used in practical communication systems. For example, MSK has been used in NASA's Advanced Communication Technology Satellite (ACTS) system, GMSK (Gaussian MSK) has been used in the U.S. cellular digital packet data (CDPD) system and the European global system for mobile (GSM) system.

Significant contributions to CPM schemes, including signal design, spectral analysis, and error performance analysis were made by C-E. Sundberg, T. Aulin, A. Svensson and J. Anderson, among other authors [1-9]. Excellent treatment of CPM up to 1986 can be found in the book by J. Anderson, T. Aulin, and C-E. Sundberg [9] or the article by C-E. Sundberg [1]. In this chapter we will cover all basic aspects of CPM and present research results up to date. The treatment here is limited to the AWGN channel as we did for previous chapters. The multiple index continuous phase modulation (MHPM) will be covered in the next chapter.

We define CPM signal and study its phase properties in Section 6.1. Its power spectral density is studied in Section 6.2. The error probability of CPM schemes is determined by the Euclidean distances between signals. In Section 6.3, we derive the distance expression for CPM signals and compare distances for different CPM schemes. CPM modulators and demodulators are presented in Sections 6.4 and 6.5, respectively. Section 6.6 is for synchronization (carrier and symbol) of CPM signals.

Since it is currently used in practical systems, a comprehensive treatment on GMSK is given in Section 6.7. Section 6.8 summarizes this chapter.

6.1 DESCRIPTION OF CPM

CPM signal is defined by

$$s(t) = A \cos(2\pi f_c t + \Phi(t, \mathbf{a})), \quad -\infty \leq t \leq \infty \quad (6.1)$$

The signal amplitude is constant. Unlike signals of previously defined modulation schemes such as FSK and PSK, where signals are usually defined on a symbol interval, this signal is defined on the entire time axis. This is due to the continuous, time-varying phase $\Phi(t, \mathbf{a})$, which usually is influenced by more than one symbol. The transmitted M-ary symbol sequence $\mathbf{a} = \{a_k\}$ is imbedded in the *excess phase*

$$\Phi(t, \mathbf{a}) = 2\pi h \sum_{k=-\infty}^{\infty} a_k q(t - kT) \quad (6.2)$$

with

$$q(t) = \int_{-\infty}^t g(\tau) d\tau \quad (6.3)$$

The M-ary data a_k may take any of the M values: $\pm 1, \pm 3, \dots, \pm(M-1)$, where M usually is a power of 2. The phase is proportional to the parameter h which is called the *modulation index*.¹ Phase function $q(t)$, together with modulation index h and input symbols a_k , determine how the phase changes with time. The derivative of $q(t)$ is function $g(t)$, which is the *frequency shape pulse*. The function $g(t)$ usually has a smooth pulse shape over a finite time interval $0 \leq t \leq LT$, and is zero outside. When $L \leq 1$, we have a full-response pulse shape since the entire pulse is in a symbol time T . When $L > 1$, we have a partial-response pulse shape since only part of the pulse is in a symbol time T .

The modulation index h can be any real number in principle. However, for development of practical maximum likelihood CPM detectors, h should be chosen as a rational number. Rational h makes the number of the phase states finite, thus maximum likelihood detectors using the Viterbi algorithm can be used. The Viterbi algorithm will be discussed when CPM demodulation is addressed.

¹ If the modulation index h varies cyclically from symbol to symbol, we have a modulation scheme called multi-h phase modulation (MHPM). Due to its complexity and importance, we will study MHPM in Chapter 7.

We have stated that the phase $\Phi(t, \mathbf{a})$ is continuous without proof. We will prove its continuousness in Section 6.1.2.

6.1.1 Various Modulating Pulse Shapes

By choosing different pulses $g(t)$ and varying the modulation index h and size of symbol alphabet M , a great variety of CPM schemes can be obtained. Some of the popular pulse shapes are listed in the following [1]. All pulse functions in the list have been normalized such that

$$\int_{-\infty}^{\infty} g(t) dt = 1/2$$

This makes the maximum phase change of the signal to be $(M - 1)h\pi$ for the period of $g(t)$.

6.1.1.1 Rectangular (LREC), CPFSK, and MSK

LREC is the rectangular pulse with a length of L symbols. For example, 3REC has $L = 3$. LREC's $g(t)$ is defined by

$$g(t) = \begin{cases} \frac{1}{2LT}, & 0 \leq t \leq LT \\ 0, & \text{otherwise} \end{cases} \quad (6.4)$$

A special case is 1REC, which is most often referred to as CPFSK (continuous phase frequency shift keying). Further, if $M = 2$ and $h = 1/2$, 1REC becomes MSK. Substituting (6.4) with $L = 1$ into (6.3), we have

$$q(t) = \int_{-\infty}^t \frac{1}{2T} dt = \begin{cases} \int_0^t \frac{1}{2T} dt, & 0 < t < T \\ \int_0^T \frac{1}{2T} dt, & t > T \end{cases} = \begin{cases} \frac{t}{2}, & 0 < t < T \\ \frac{1}{2}, & t > T \end{cases}$$

Then substituting this into (6.2) we have in the interval $[kT, (k + 1)T]$

$$\begin{aligned} \Phi(t, \mathbf{a}) &= 2\pi h \left[\sum_{i=-\infty}^{k-1} a_i \frac{1}{2} + a_k \frac{1}{2T} (t - kT) \right] \\ &= \pi h \sum_{i=-\infty}^{k-1} a_i + ha_k \frac{\pi t}{T} - \pi ha_k k \\ &= ha_k \frac{\pi t}{T} + \Phi_k, \quad kT \leq t \leq (k + 1)T \end{aligned}$$

where

$$\Phi_k = \pi h \left(\sum_{i=-\infty}^{k-1} a_i - ka_k \right) \pmod{2\pi}$$

Thus

$$s(t) = A \cos(2\pi f_c t + ha_k \frac{\pi t}{T} + \Phi_k), \quad kT \leq t \leq (k+1)T$$

This is the expression of the CPFSK signal which we have mentioned in Chapter 5 (see Section 5.1.2). With $h = 0.5$, the above expression becomes

$$s(t) = A \cos(2\pi f_c t + a_k \frac{\pi t}{2T} + \Phi_k), \quad kT \leq t \leq (k+1)T$$

which is the MSK signal if a_k is binary (see Section 5.1.2).

Another special case is binary 2REC, also called duobinary MSK (DMSK). Thus for DMSK

$$g(t) = \begin{cases} \frac{1}{4T}, & 0 \leq t \leq 2T \\ 0, & \text{otherwise} \end{cases}$$

6.1.1.2 Raised Cosine (LRC)

LRC is the raised cosine with a length of L symbols. For example, 3RC has $L = 3$. LRC's $g(t)$ is defined by

$$g(t) = \begin{cases} \frac{1}{2LT} [1 - \cos(\frac{2\pi t}{LT})], & 0 \leq t \leq LT \\ 0, & \text{otherwise} \end{cases} \quad (6.5)$$

6.1.1.3 Spectrally Raised Cosine (LSRC)

LSRC is the spectrally raised cosine with length L . For example, 2SRC has $L = 2$. LSRC's $g(t)$ is defined by

$$g(t) = \frac{1}{LT} \frac{\sin(\frac{2\pi t}{LT}) \cos(\beta \frac{2\pi t}{LT})}{\frac{2\pi t}{LT} \left[1 - \left(\frac{4\beta t}{LT} \right)^2 \right]}, \quad 0 \leq \beta \leq 1 \quad (6.6)$$

6.1.1.4 Tamed Frequency Modulation (TFM)

TFM is the tamed frequency modulation. TFM's $g(t)$ is defined by

$$g(t) = \frac{1}{8}[ag_o(t-T) + bg_o(t) + ag_o(t+T)], \quad a = 1, b = 2 \quad (6.7)$$

$$g_o(t) \approx \sin\left(\frac{\pi t}{T}\right) \left[\frac{1}{\pi t} - \frac{2 - \frac{2\pi t}{T} \cot\left(\frac{\pi t}{T}\right) - \left(\frac{\pi t}{T}\right)^2}{\frac{24\pi t^3}{T^2}} \right]$$

6.1.1.5 Gaussian MSK (GMSK)

GMSK is the Gaussian minimum shift keying. GMSK's $g(t)$ is defined by

$$g(t) = \frac{1}{2T} \left[Q \left(2\pi B_b \frac{t - \frac{T}{2}}{\sqrt{\ln 2}} \right) - Q \left(2\pi B_b \frac{t + \frac{T}{2}}{\sqrt{\ln 2}} \right) \right], \quad 0 \leq B_b T \leq 1 \quad (6.8)$$

$$Q(t) = \int_t^\infty \frac{1}{\sqrt{2\pi}} \exp\left(-\frac{\tau^2}{2}\right) d\tau$$

Due to the importance of GMSK, we will describe it in more detail in Section 6.7.

Figure 6.1 shows the $g(t)$ pulse shapes and $q(t)$ pulse shapes defined in the above list. The time axis is normalized to T . The familiar rectangular pulse is defined on $[0, LT]$ and its phase function is linear, reaching the maximum (0.5) at the end of the period. The raised-cosine pulse is defined in $[0, LT]$, the corresponding phase function $q(t)$ is a nonlinear yet smooth curve in $[0, LT]$. The $q(t)$ reaches its maximum at the end of its period. The tamed frequency modulation pulse is defined in $[-\infty, \infty]$, however its major energy is within $[-2T, +2T]$. Its phase function $q(t)$ changes smoothly in the interval and reaches the maximum at about $2T$. The spectrally raised cosine pulse has similar properties of the TFM. However, the phase function exhibits small oscillation around 0 and 0.5. The GMSK $g(t)$ is also defined in $[-\infty, \infty]$, but the main energy is in $[-T, +T]$ (for $B_b T = 0.25$). The phase function changes smoothly in the same interval, reaching its maximum at T . Since the length of frequency pulse functions of TFM, SRC, and GMSK is infinite, they must be truncated in time-domain implementation.

As will be seen shortly, $g(t)$ and h can be chosen to enable the CPM schemes to outperform MSK in terms of power efficiency and bandwidth efficiency. The reason that this can happen is that memory has been introduced into the CPM signal by means of the continuous phase. Further memory can be built into the CPM signal by choosing a partial response $g(t)$ with $L > 1$.

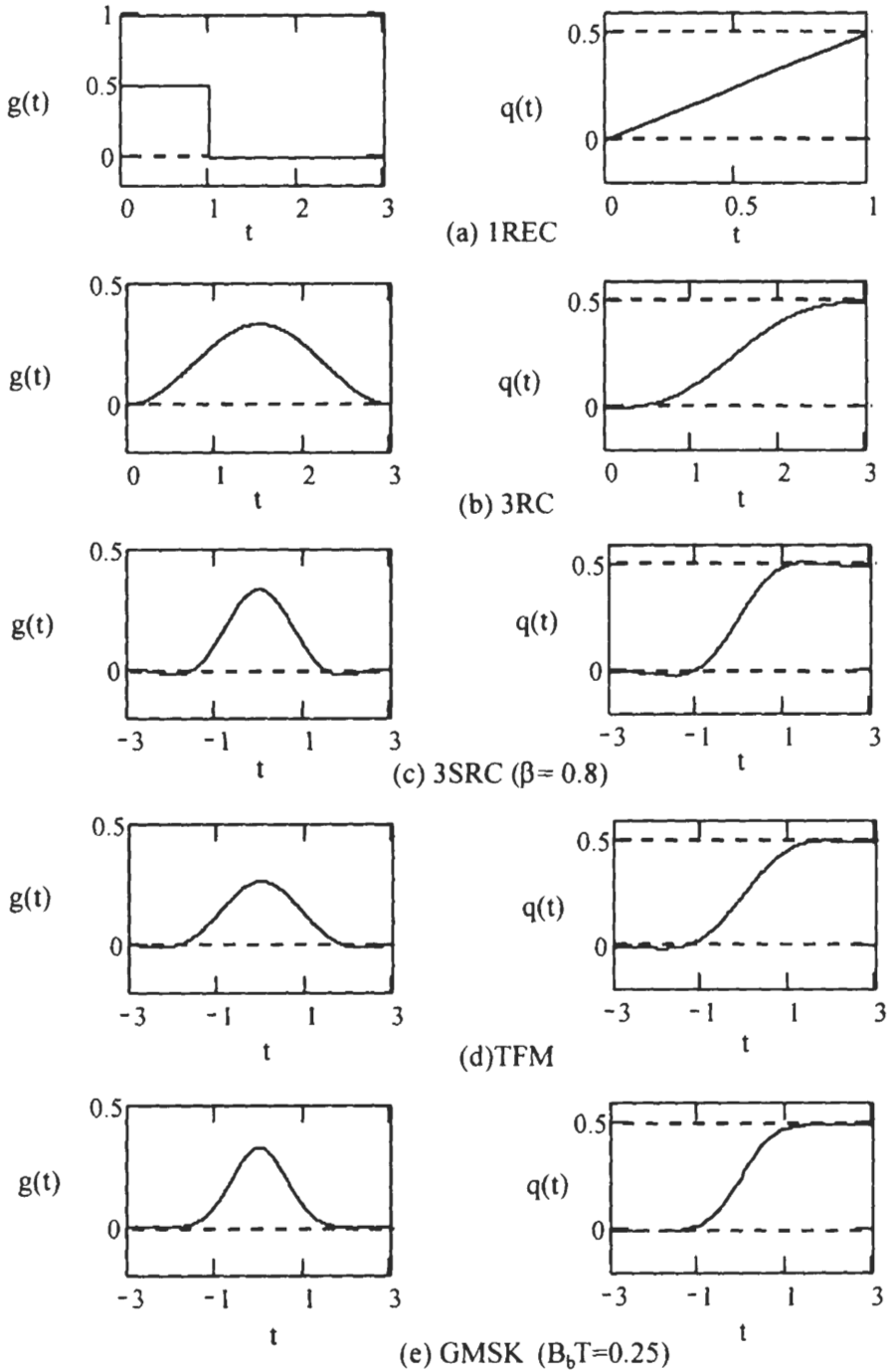


Figure 6.1 Frequency pulse shapes for CPM.

6.1.2 Phase and State of the CPM Signal

Since the information symbols are imbedded in the phase of the CPM signal, demodulation will be solely based on its phase. It is therefore very important that the phase behavior of CPM signals is fully understood.

First we examine an example shown in Figure 6.2 where phase $\Phi(t, \mathbf{a})$ of binary 3RC with $h = 2/3$ is shown for a particular data sequence. The unit of the phase is radian. We assume that the initial phase is zero, that is $\Phi(0, \mathbf{a}) = 0$. We have plotted the weighted $q(t - kT)$ for the first four data symbols and omitted the rest. The total phase $\Phi(t, \mathbf{a})$ (modulo 2π) for the sequence is shown on the bottom of the figure.

The continuousness of the phase $\Phi(t, \mathbf{a})$ can be easily proved with the help of Figure 6.2. Since $g(t)$ is a smooth function, its integral $q(t)$ is also a smooth function. The phase $\Phi(t, \mathbf{a})$ is a weighted sum of shifted versions of $q(t)$. Along the time axis, as t increases, a new weighted $q(t - kT)$ is added in at every symbol boundary. The value of $\Phi(t, \mathbf{a})$ will not change abruptly since $q(t)$ always starts from 0. Therefore the phase $\Phi(t, \mathbf{a})$ is continuous, even at the symbol boundaries.

From Figure 6.2 we can see that $q(t - kT)$ reaches its maximum at $t = (k + L)T$ and stays at the maximum for the rest of the time. Figure 6.2 is for 3RC which has a finite duration $L = 3$. For pulse shapes with infinite duration such as LSRC, TFM, and GMSK, the $q(t - kT)$ also reaches its maximum at $t = (k + L)T$, approximately (see Figure 6.1(c-e)). These maximum values are accumulated along the time axis. Thus we can separate the excess phase $\Phi(t, \mathbf{a})$ into two parts as follows.

The excess phase of a CPM signal during interval $kT < t < (k + 1)T$ can be written as

$$\begin{aligned}\Phi(t, \mathbf{a}) &= 2\pi h \sum_{i=k-L+1}^k a_i q(t - iT) + \theta_k \\ &= \theta(t, \mathbf{a}_k) + \theta_k\end{aligned}\quad (6.9)$$

where

$$\theta(t, \mathbf{a}_k) = 2\pi h \sum_{i=k-L+1}^k a_i q(t - iT) \quad (6.10)$$

is the *instant phase*, which represents the changing part of the total excess phase in $[kT, (k + 1)T]$, and

$$\theta_k = \left[h\pi \sum_{i=-\infty}^{k-L} a_i \right] \pmod{2\pi} \quad (6.11)$$

is the *cumulate phase*, which represents the constant part of the total excess phase in

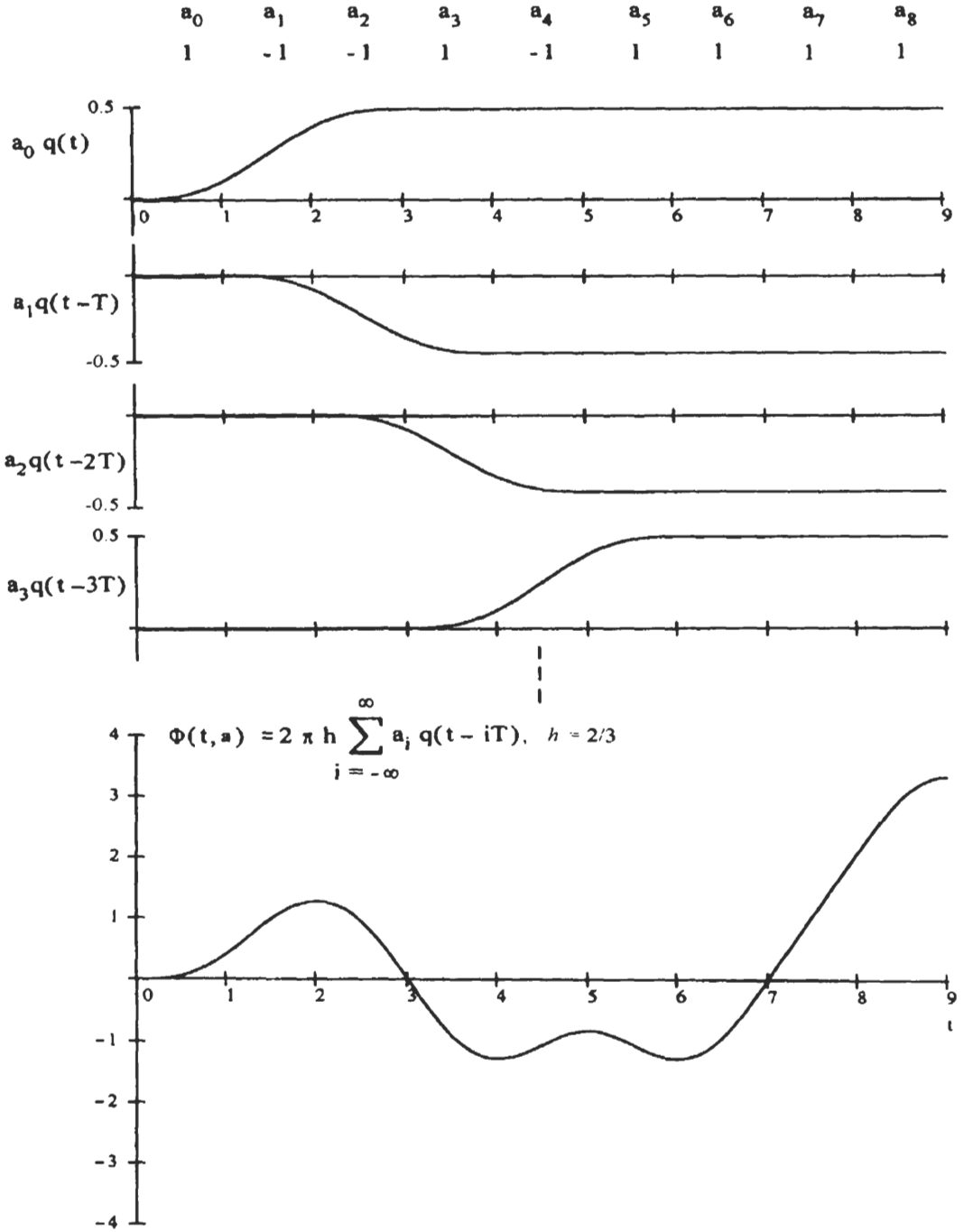


Figure 6.2 Phase $\Phi(t, \mathbf{a})$ of binary 3RC with $h = 2/3$.

$[kT, (k + 1)T]$, and is equal to the sum of the maximum phase changes contributed by each symbol, accumulated along the time axis up to the $(k - L)$ th symbol interval. It can be conveniently computed recursively as

$$\theta_{k+1} = \theta_k + h\pi a_{k-L+1} \quad (6.12)$$

The instant phase $\theta(t, \mathbf{a}_k)$ is determined by the data symbol a_k and previous $L - 1$ symbols. For example, if $L = 1$, then

$$\theta(t, \mathbf{a}_k) = 2\pi h a_k q(t - kT), \quad kT \leq t \leq (k + 1)T$$

which is a changing phase proportional to the current data and the phase function, where $q(t)$ is nonzero in $(0, T)$ and zero otherwise. If $L = 2$, then

$$\theta(t, \mathbf{a}_k) = 2\pi h [a_{k-1} q(t - kT + T) + a_k q(t - kT)], \quad kT \leq t \leq (k + 1)T$$

where $q(t)$ is nonzero in $(0, 2T)$ and zero otherwise. $\theta(t, \mathbf{a}_k)$ is a changing phase proportional to the weighted sum of the current phase function and the previous phase function. The weighting factors are the current data symbol and the previous data symbol, respectively.

The cumulate phase θ_k is the accumulated phase due to the data up to $t = (k - L)T$, not including the phase accumulated by the carrier, and also not including the phase accumulated in the instant phase due to the previous $L - 1$ symbols. Therefore it is in general not the initial phase at time kT (at first glance, it seems to be the initial phase). The initial phase at $t = kT$ is $2\pi f_c kT + \theta_k + \theta(kT, \mathbf{a}_k)$. However, if $L = 1$, then $\theta(kT, \mathbf{a}_k) = 0$, and in addition if f_c is an integer multiple of symbol rate, θ_k would become the initial phase of the k th symbol interval.

If h is rational, that is, $h = 2q/p$ where q and p have no common factors, the number of distinct values of θ_k is p .

Proof: Since $h = 2q/p$,

$$\theta_k = \frac{2q\pi}{p} \sum_{i=-\infty}^{k-L} a_i = \text{multiple of } \frac{2\pi}{p}$$

Thus the number of states is

$$2\pi / (2\pi/p) = p$$

For example, $h = 1/2 = 2/4$ for MSK, its number of phase states is four (see Figure 5.3). If h is a real number, the number of distinct values of θ_k is infinite.

We define a *state* of a CPM signal at $t = kT$ as the vector

$$\mathbf{s}_k = (\theta_k, a_{k-1}, a_{k-2}, \dots, a_{k-L+1})$$

which consists of the value of the cumulate phase θ_k and the previous $L - 1$ symbols. For rational h , since the number of distinct values of θ_k is p , the number of states is at most pM^{L-1} . However, for real h , the number of states is infinite. Each state corresponds to a specific function form of the excess phase $\Phi(t, \mathbf{a})$.

Using $3RC$ with $h = 2/3$ and binary symbols ($M = 2$) as an example, we have

$$\mathbf{s}_k = (\theta_k, a_{k-1}, a_{k-2}) \quad (6.13)$$

where

$$\theta_k = \left[\frac{2}{3}\pi \sum_{i=-\infty}^{k-L} a_i \right] \pmod{2\pi} = \begin{cases} 0 \\ \frac{2}{3}\pi \\ \frac{4}{3}\pi \end{cases} \quad (6.14)$$

The number of θ_k is 3. Thus the binary $3RC$ has a total of 12 states. The recursive expression for θ_k is

$$\theta_{k+1} = \theta_k + \frac{2}{3}\pi a_{k-2} \quad (6.15)$$

The information bearing phase $\Phi(t, \mathbf{a})$ for the binary $3RC$ is

$$\begin{aligned} \Phi(t, \mathbf{a}) &= \frac{4\pi}{3} [a_{k-2}q(t - kT + 2T) + a_{k-1}q(t - kT + T) \\ &\quad + a_kq(t - kT)] + \theta_k, \\ kT &\leq t \leq (k+1)T \end{aligned} \quad (6.16)$$

where

$$q(t) = \int_0^t \frac{1}{6T} \left[1 - \cos\left(\frac{2\pi t}{3T}\right) \right] dt$$

which is nonzero in $(0, 3T)$ and zero otherwise. At $t = kT$,

$$\Phi(kT, \mathbf{a}) = \frac{4\pi}{3} [a_{k-2}q(2T) + a_{k-1}q(T) + a_kq(0)] + \theta_k$$

where $q(0) = 0$, $q(T) = 0.098$, and $q(2T) = 0.402$. Thus

$$\Phi(kT, \mathbf{a}) = \frac{4\pi}{3} [0.402a_{k-2} + 0.098a_{k-1}] + \theta_k \quad (6.17)$$

Table 6.1 lists the 12 values of $\Phi(kT, \mathbf{a})$ corresponding to the 12 states. The fourth column contains the direct results from (6.17). The last column contains the results converted into $[0, 2\pi]$. These phase values can also be converted into $[-2\pi, 0]$, with the same array of absolute values. From the last column we can see that in fact there are only nine distinct values. Some of the phase values are produced by more than

State	θ_k	a_{k-1}	a_{k-2}	$\Phi(kT, \mathbf{a})$ direct results from (6.17)	$\Phi(kT, \mathbf{a})$ converted into $[0, 2\pi]$
1	0	-1	-1	$-\frac{2}{3}\pi$	$\frac{4}{3}\pi$
2	0	-1	+1	$\frac{1.22}{3}\pi$	$\frac{1.22}{3}\pi$
3	0	+1	-1	$-\frac{1.22}{3}\pi$	$\frac{4.78}{3}\pi$
4	0	+1	+1	$\frac{2}{3}\pi$	$\frac{2}{3}\pi$
5	$\frac{2}{3}\pi$	-1	-1	0	0
6	$\frac{2}{3}\pi$	-1	+1	$\frac{3.22}{3}\pi$	$\frac{3.22}{3}\pi$
7	$\frac{2}{3}\pi$	+1	-1	$\frac{0.78}{3}\pi$	$\frac{0.78}{3}\pi$
8	$\frac{2}{3}\pi$	+1	+1	$\frac{4}{3}\pi$	$\frac{4}{3}\pi$
9	$\frac{4}{3}\pi$	-1	-1	$\frac{2}{3}\pi$	$\frac{2}{3}\pi$
10	$\frac{4}{3}\pi$	-1	+1	$\frac{5.22}{3}\pi$	$\frac{5.22}{3}\pi$
11	$\frac{4}{3}\pi$	+1	-1	$\frac{2.78}{3}\pi$	$\frac{2.78}{3}\pi$
12	$\frac{4}{3}\pi$	+1	+1	2π	2π

Table 6.1 3RC states and phase values.

one state. $\frac{2}{3}\pi$ and $\frac{4}{3}\pi$ are repeated once, and 0 and 2π are the same. In this sense, these states are equivalent. That is, states 1 and 8, 4 and 9, 5 and 12 are equivalent.

6.1.3 Phase Tree and Trellis, State Trellis

For an arbitrary data sequence, the phases of the CPM signals will follow a unique continuous phase trajectory (or path). The collection of all possible phase paths forms a phase tree. When h is rational the number of phase states is finite and the phase tree can be collapsed into a trellis.

In Chapter 5 we have seen the phase tree and trellis of MSK, which is a 1REC with $M = 2$ and $h = 1/2$ (see Figures 5.2 and 5.3). Here we examine an additional example with nonlinear yet smooth phase function $q(t)$: binary 3RC with $h = 2/3$. Its phase tree is drawn in Figure 6.3 using (6.16). We assume that the initial phase is zero, that is, $\Phi(0, \mathbf{a}) = 0$. We also assume that the two symbols before $t = 0$ are +1. The ± 1 on a branch is the data symbol that, together with the previous two symbols and the phase θ_k , produces the phase trajectory (see (6.16)). It can be easily examined that all the phase values at $t = kT$ in the phase tree are included in Table 6.1.

As time increases, the tree will grow bigger. However, by using a modulo- 2π operation, this phase tree can be collapsed into a trellis. Figure 6.4 shows the trellis. The trellis is drawn by using a modulo 2π operation first, then converting those phases in $[0, -2\pi]$ into $[0, 2\pi]$ by simply adding 2π to the values. The trellis becomes fully developed only after $t = 4T$. This is because it takes $2T$ to have all possible

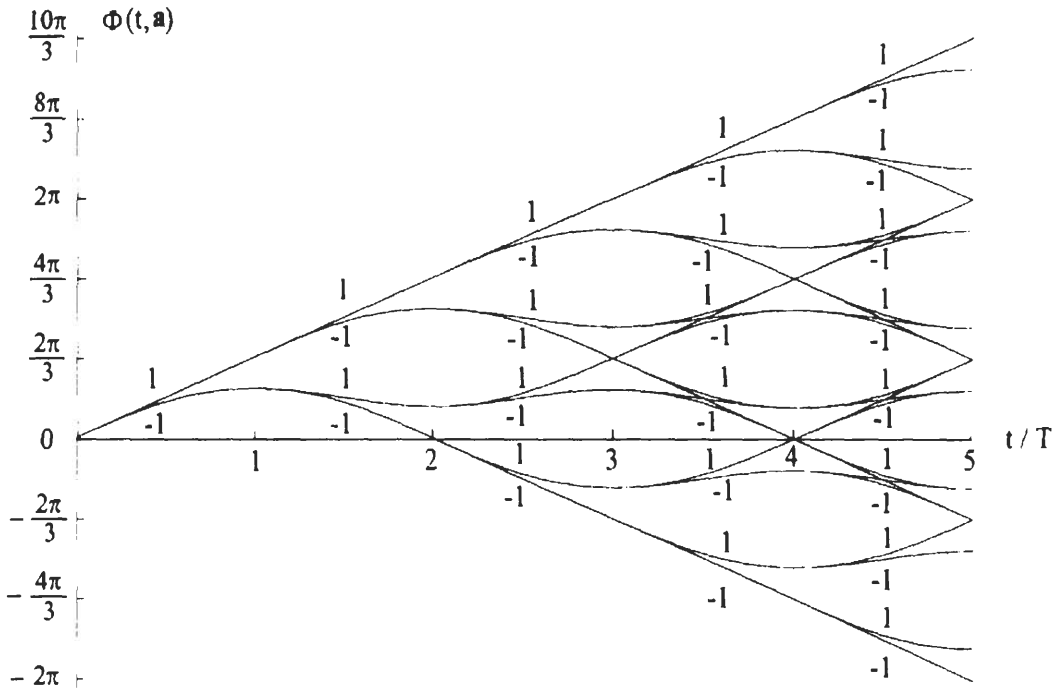


Figure 6.3 Phase tree of binary 3RC with $h = 2/3$. The phase starts with value zero at $t = 0$. After: [9].

θ_k (see (6.14)) and another $2T$ to have all possible instant phase values (see (6.16)). Now we examine the phase values at $t = 4T$ or $5T$. From the top to the bottom, those values correspond to states 12 (or 5), 10, 3, 1 (or 8), 6, 11, 4 (or 9), 2, 7, and 5 (or 12) in Table 6.1. At each node, there are two branches coming in and two branches going out except for those double-state nodes where four branches are coming in and going out. Each branch represents an input symbol (+1 or -1). Each branch is the phase trajectory from the previous node to the current node.

The phase tree and the phase trellis are very useful for understanding the phase behavior of the CPM signals. However, for demodulating CPM signals, a *state trellis* instead of phase trellis is more convenient. Figure 6.5 shows the state trellis of the 3RC example. The trellis is drawn using (6.13), (6.14), and (6.15). In the figure, each state is represented by a node, even for those states that produce the same phase

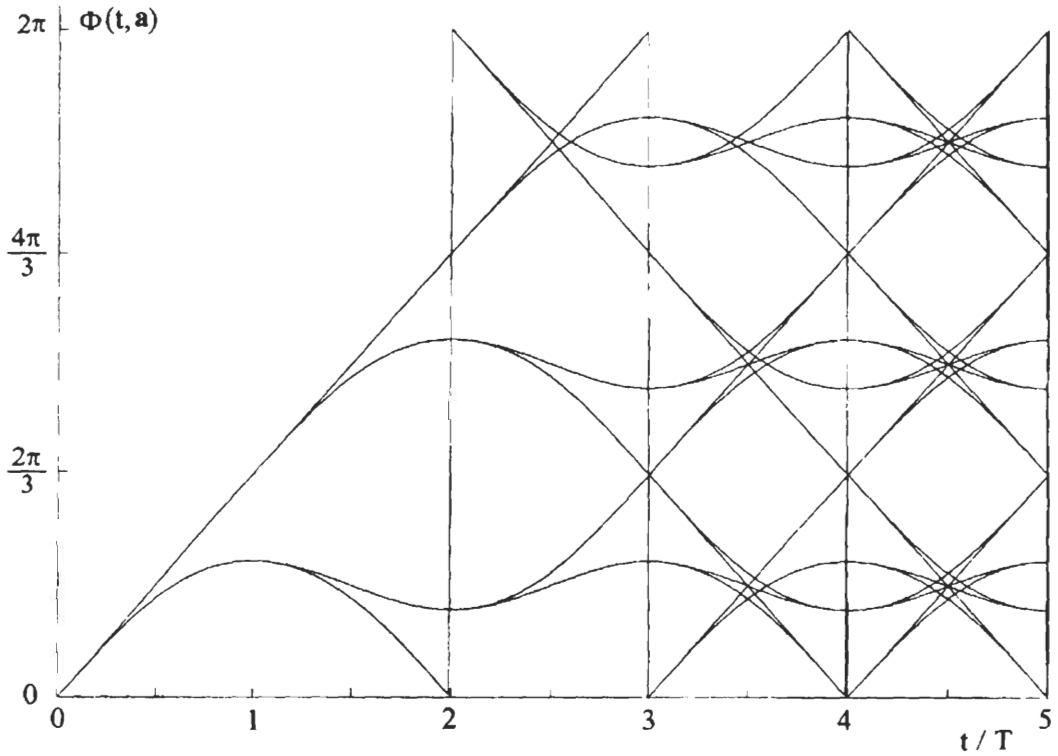


Figure 6.4 Phase trellis of binary 3RC with $h = 2/3$. The phase starts with value zero at $t = 0$.

values. In this way there are always two branches coming in and going out at a state. In general, there are always M branches in and out at a state for M -ary symbols. In addition, in the state trellis, the lines connecting states are not trajectories of the signal phases. They are there simply to show the transitions from one state to the other. Thus a state trellis is almost the same as a phase trellis except that the transition branches are not phase trajectories and the nodes are labeled by states instead of phases. However, we know that states can be mapped into phases even though the mapping may not be completely one-to-one (see Figures 6.4 and 6.5).

For full-response CPM, the state vector is just θ_k , thus the nodes of the state trellis are identical to the nodes of the phase trellis, but the branches are still different. For linear full-response CPM (CPFSK), even the branches of the phase trellis are straight lines, thus the appearance of the state trellis and the phase trellis are completely the same.

Another interesting fact is that the frequency pulse shape $g(t)$ does not affect the structure of the trellis as long as the convention $\int_{-\infty}^{\infty} g(t)dt = 1/2$ (or other constant) is observed. This is because the states are defined by $(\theta_k, a_{k-1}, a_{k-2}, \dots, a_{k-L+1})$, where data have nothing to do with $g(t)$, and θ_k also is independent of $g(t)$ provided $\int_{-\infty}^{\infty} g(t)dt = 1/2$ (or other constant). This fact makes a trellis applicable to many schemes with different frequency pulse shapes as long as their L and h are the same.

If h is irrational, $\Phi(t, \mathbf{a})$ will have an infinite number of possible values, depending on the current symbol and all previous symbols. The phase tree still exists, but the number of branches at each node for a specific input symbol will no longer be M . Rather it grows exponentially with the depth of the tree (M^N , N is the depth). This tree cannot be collapsed into a trellis.

6.2 POWER SPECTRAL DENSITY

The methods of calculating power spectral densities of CPM signals, or other digitally modulated signals, for that matter, basically fall into three classes: direct method [10], Markov method [11], and correlation method [12]. Computer simulation can also be used. Finally, measuring is always a method of finding CPM spectra, and is also the ultimate verification of the calculated spectra.

In the direct method one takes the Fourier transform $S_N(f, \mathbf{a}, \phi_o)$ of a truncated deterministic CPM signal $s_N(t) = s_N(t, \mathbf{a}, \phi_o)$ and then forms the average over data \mathbf{a} and initial phase ϕ_o which is distributed uniformly over $(0, 2\pi)$. That is

$$PSD = \lim_{N \rightarrow \infty} \frac{1}{NT} E\{|S_N(f, \mathbf{a}, \phi_o)|^2\}$$

where N is an integer. We have used this method to find out the PSD formulas of the baseband modulations in Appendix A. The results turned out to be quite simple. For CPM, however, the resultant equations are often complicated and two-dimensional numerical integrations are required.

In the Markov method, the random data are modeled as a Markov process characterized by a transition matrix. Then the autocorrelation function can be expressed in terms of this transition matrix and the matrix of the correlation between the basic baseband pulses. The Fourier transform of the autocorrelation function is the power spectral density of the modulated signal. We have used this method in Chapter 2 for finding the PSDs of Bi- Φ -M and the delay modulation line codes.

In the correlation method, the correlation function of a CPM signal is calculated first, then one takes the Fourier transform of the correlation function to get the PSD. The correlation is formed by first taking the average over data \mathbf{a} of the product of

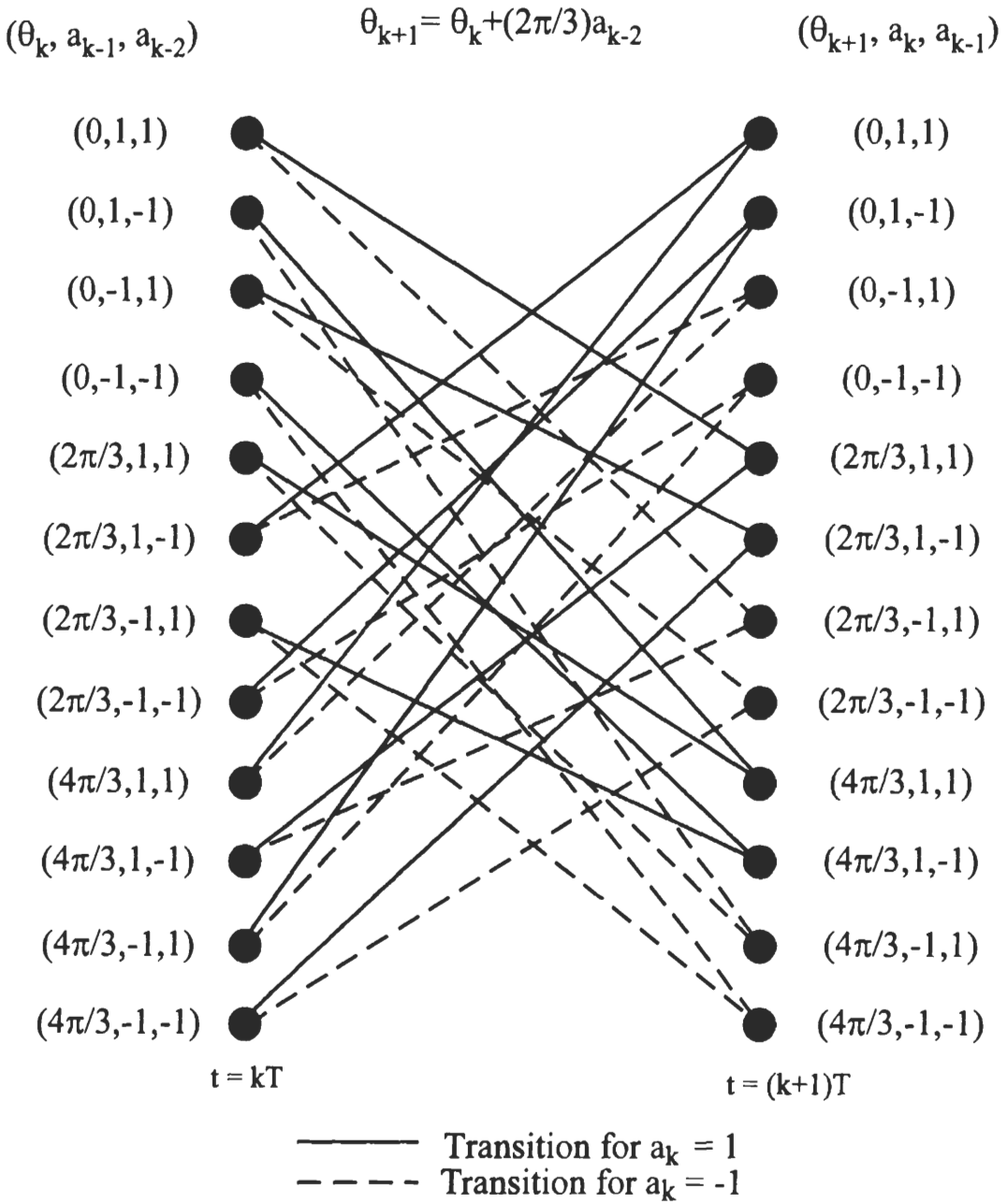


Figure 6.5 State trellis of binary 3RC with $h = 2/3$. After: [9]

the signal's complex envelopes $\tilde{s}(t + \tau, \mathbf{a})$ and $\tilde{s}(t, \mathbf{a})$:

$$R_{\tilde{s}}(t + \tau, t) = E\{\tilde{s}(t + \tau, \mathbf{a})\tilde{s}(t, \mathbf{a})\} \quad (6.18)$$

and then taking the time average over a period of T :

$$R_{\tilde{s}}(\tau) = \frac{1}{T} \int_0^T R_{\tilde{s}}(t + \tau, t) dt \quad (6.19)$$

A fast, relatively simple, numerical method first appeared in [13]. It also can be found in [9] and [14]. This method is a type of correlation method. The derivation of the method is presented in Appendix A together with methods of computing PSDs of other digitally modulated signals. Here we list the steps and formulas of the numerical calculation resulting from the two steps in (6.18) and (6.19). All PSD expressions are for CPM signals with a unit amplitude. For CPM signals with an amplitude A , their PSDs just need to be scaled up by A^2 .

6.2.1 Steps for Calculating PSDs for General CPM Signals

1. Calculate the autocorrelation function $R_{\tilde{s}}(\tau)$ over the interval $[0, (L + 1)T]$. Note that the time difference τ is written in the form $\tau = \xi + mT$ with $0 \leq \xi < T$ and $m = 0, 1, 2, \dots$

$$\begin{aligned} R_{\tilde{s}}(\tau) &= R_{\tilde{s}}(\xi + mT) \\ &= \frac{1}{T} \int_0^T \prod_{k=1-L}^{m+1} \left\{ \sum_{\substack{n=-(M-1) \\ n \text{ odd}}}^{M-1} P_n \exp\{j2\pi hn[q(t + \xi - (k - m)T) \right. \\ &\quad \left. - q(t - kT)]\} dt \right\} \end{aligned} \quad (6.20)$$

where P_n is the a priori probability of the n th symbol. The weighted (by P_n) sum is the result of averaging over M symbols. The product represents correlating over $L + m$ symbol periods. Finally, the integration is the result of averaging over the time for a symbol period.

2. Calculate

$$C_a = \sum_{\substack{n=-(M-1) \\ n \text{ odd}}}^{M-1} P_n \exp[j2\pi hnq(LT)] \quad (6.21)$$

The coefficient C_a will be used in the next step of computing. If h is not an integer, then $|C_a| < 1$, the PSD is purely continuous. If h is an integer, then $|C_a| = 1$, the PSD contains a continuous part as well as a discrete part (spectral lines).

3. IF $|C_a| < 1$, which is the common case when h is not an integer, usually rational, calculate the PSD using

$$\Psi_{\tilde{s}}(f) = 2 \operatorname{Re} \left\{ \int_0^{LT} R_{\tilde{s}}(\tau) e^{-j2\pi f\tau} d\tau + \frac{e^{-j2\pi fLT}}{1 - C_a e^{-j2\pi fT}} \int_0^T R_{\tilde{s}}(\tau + LT) e^{-j2\pi f\tau} d\tau \right\} \quad (6.22)$$

The PSD is continuous. A special case is when the data symbols are equally likely, which is also the most common case, then $P_n = 1/M$, for $n = \pm 1, \pm 3, \dots, \pm(M-1)$. For this case, the sum of the exponential functions in (6.20) becomes real-valued due to symmetry of the data symbols, we have

$$R_{\tilde{s}}(\tau) = \frac{1}{T} \int_0^T \prod_{k=1-L}^{\lceil \tau/T \rceil} \frac{1}{M} \frac{\sin 2\pi h M [q(t + \tau - kT) - q(t - kT)]}{\sin 2\pi h [q(t + \tau - kT) - q(t - kT)]} dt \quad (6.23)$$

and the PSD is

$$\Psi_{\tilde{s}}(f) = 2 \left\{ \int_0^{LT} R_{\tilde{s}}(\tau) \cos 2\pi f\tau d\tau + \frac{1 - C_a \cos 2\pi fT}{1 + C_a^2 - 2C_a \cos 2\pi fT} \int_{LT}^{(L+1)T} R_{\tilde{s}}(\tau) \cos 2\pi f\tau d\tau \right\} \quad (6.24)$$

and (6.21) becomes

$$C_a = \frac{1}{M} \frac{\sin M\pi h}{\sin \pi h} \quad (6.25)$$

4. IF $|C_a| = 1$, which is the rare case when h is an integer, the autocorrelation function contains an aperiodic part $R_{con}(\tau)$ and a periodical part $R_{dis}(\tau)$.

$$R_{\tilde{s}}(\tau) = R_{con}(\tau) + R_{dis}(\tau)$$

As a result, the PSD contains a continuous part and a discrete part.

$$\Psi_{\bar{s}}(f) = 2 \operatorname{Re} \left[\int_0^{LT} R_{con}(\tau) e^{-j2\pi f\tau} d\tau \right] + F_{dis}(f) \quad (6.26)$$

where $F_{dis}(f)$ is the discrete PSD which is the Fourier series coefficients of $R_{dis}(\tau)$. It is shown in Appendix A that when h is even the period of $R_{dis}(\tau)$ is T , and the discrete frequency components appear at $f = \pm k/T$, $k = 0, 1, 2, \dots$. When h is odd, $R_{dis}(\tau)$ is a periodic, *odd half-wave symmetrical* function with a period of $2T$. Its spectrum would only have odd harmonics at $f = \pm(2k + 1)/2T$, $k = 0, 1, 2, \dots$ [15, p.103]. The property that a CPM signal with integer index has discrete frequency components can be used to recover the carrier and symbol timing in CPM receivers.

6.2.2 Effects of Pulse Shape, Modulation Index, and A Priori Distribution

Many numerical results are given in [1, 7–9]. The results include the PSDs for CPM schemes with (1) different frequency pulses ($g(t)$), (2) different modulation indexes (h), (3) different a priori distributions (P_n). The results are often shown in comparison with the PSD of MSK since MSK is a bandwidth-efficient modulation scheme that appeared earlier than general CPM schemes. Here we quote some of the important results.

First we want to show the effect of the shape of $g(t)$. Figure 6.6 shows PSDs of some binary CPM schemes with different $g(t)$, with a fixed index $h = 1/2$, and a uniform a priori distribution. GMSK4 and 3SRC6 mean that the $g(t)$ is truncated symmetrically to a length of 4 and 6 symbols, respectively. All four CPM schemes have better PSDs than MSK in that their spectra fall faster with frequency. The PSD of 3RC, GMSK4 with $B_b T = 0.25$, and 3SRC6 with $\beta = 0.8$ are very similar. This is no surprise since their $g(t)$ s are similar (see Figure 6.1). Figure 6.7 shows PSDs for some quaternary CPM schemes for a fixed index $h = 1/3$. It is clear that 3RC is better than 2RC, which in turn is better than 1REC and MSK. The spectrum of TFM is not shown, however, it is reported that TFM has a PSD similar to binary 3.7RC or 3.7SRC or GMSK with $B_b T = 0.2$ [1]. The conclusion we can draw from Figures 6.6 and 6.7 is that the effect of pulse shape on PSDs is significant, a longer and smoother pulse $g(t)$ yields narrower power spectra for fixed h and M .

Next, the effect of modulation index difference is demonstrated in Figure 6.8 using binary 4RC as an example. It is seen that lower h values yield lower spectral side-lobes as we would expect, since h controls the frequency deviation from the carrier frequency. The effect of h on PSD is significant. However, as we will see shortly, h also affects bit error probability. So the choice of h is not simply based on

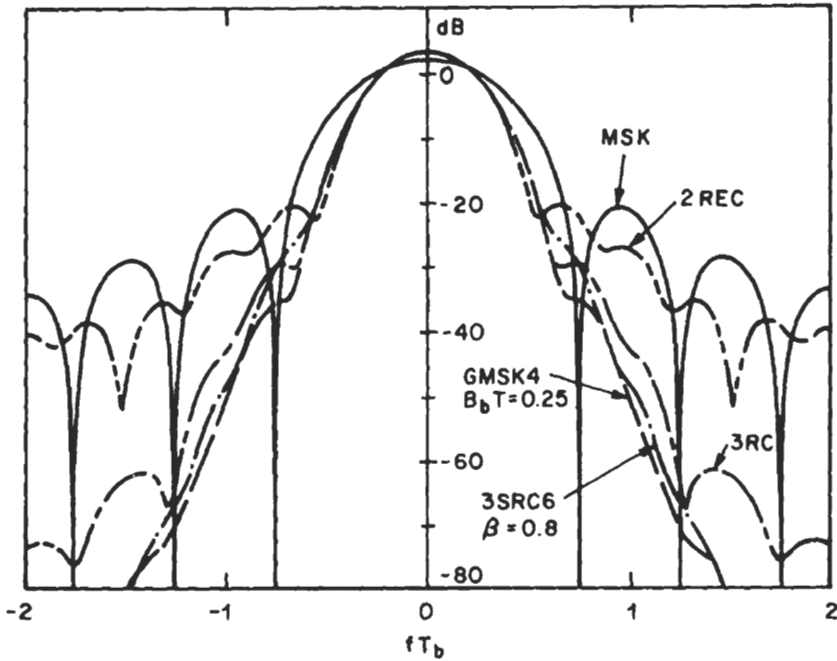


Figure 6.6 PSDs for some binary CPM schemes with $h = 1/2$, in comparison with MSK. From [1]. Copyright © 1986 IEEE.

PSD properties.

Finally, the effect of different a priori distributions (P_n) can be seen from Figure 6.9 where B_1 , B_2 , and B_3 are three a priori distributions (PDFs) defined as follows

$$(P_{-1}, P_{+1}) = \begin{cases} (\frac{1}{2}, \frac{1}{2}), & B_1 \\ (\frac{1}{4}, \frac{3}{4}), & B_2 \\ (\frac{1}{10}, \frac{9}{10}), & B_3 \end{cases}$$

From the figure we can see that the PSD of the symmetrical PDF is also symmetrical about $fT = 0$. The PSDs of the asymmetrical PDFs are also asymmetrical. However, all of them are very similar even for the very skewed distribution B_3 . Thus the conclusion is that the a priori distributions (P_n) do not affect the PDFs significantly.

6.2.3 PSD of CPFSK

For M-ary 1REC (CPFSK), the PSD has a closed form expression [9.10]. The expres-

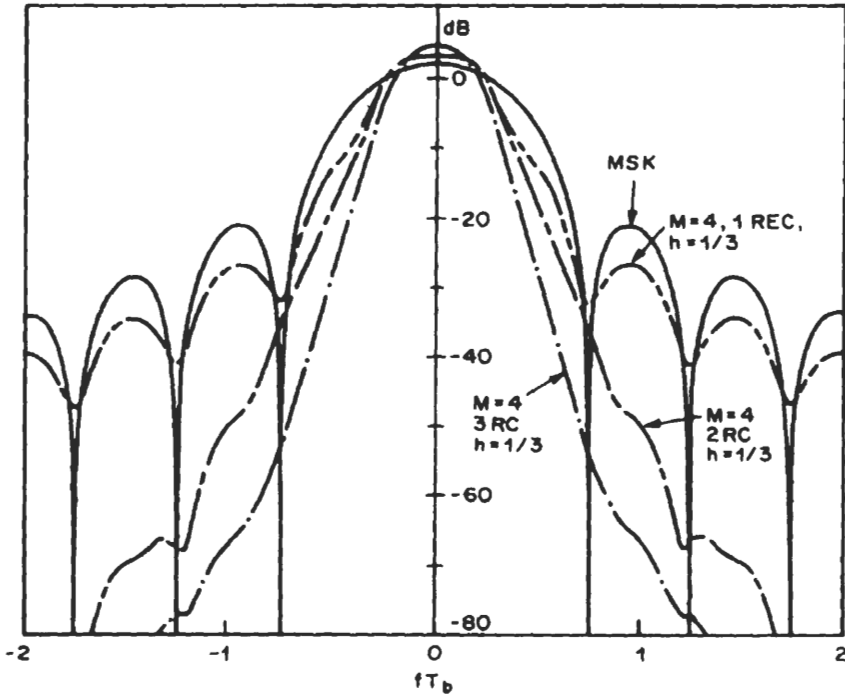


Figure 6.7 PSDs for some quaternary CPM schemes with $h = 1/3$, in comparison with MSK. From [1] Copyright © 1986 IEEE.

sion is

$$\Psi_{\bar{s}}(f) = \frac{A^2 T}{M} \sum_{i=1}^M \left[\frac{1}{2} \frac{\sin^2 \gamma_i}{\gamma_i^2} + \frac{1}{M} \sum_{j=1}^M A_{ij} \frac{\sin \gamma_i}{\gamma_i} \frac{\sin \gamma_j}{\gamma_j} \right] \quad (6.27)$$

where A is the signal amplitude. Other parameters are defined as

$$\gamma_i = (fT - (2i - M - 1) \frac{h}{2}) \pi, \quad i = 1, 2, \dots, M$$

$$A_{ij} = \frac{\cos(\gamma_i + \gamma_j) - C_a \cos(\gamma_i + \gamma_j - 2\pi fT)}{1 + C_a^2 - 2C_a \cos 2\pi fT}$$

$$C_a = \frac{1}{M} \frac{\sin M\pi h}{\sin \pi h}$$

This group of expressions has been presented in Chapter 3 in the context of M-ary

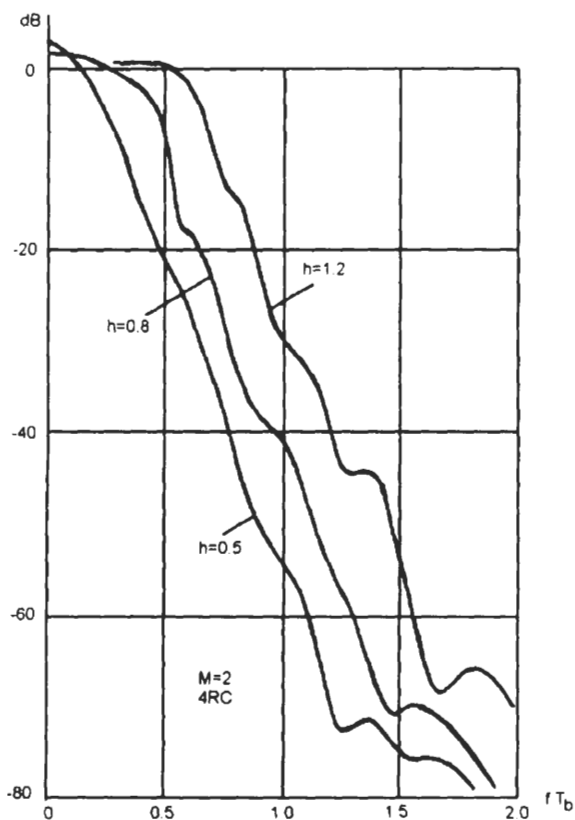


Figure 6.8 PSDs for binary 4RC for different h values. From [8]. Copyright © 1981 IEEE.

FSK.² PSD plots have also been given in Chapter 3 for $M = 2, 4,$ and 8 .

6.3 MLSD FOR CPM AND ERROR PROBABILITY

Unlike classic FSK and PSK modulation schemes, CPM signals have memory. The signal in one symbol duration is determined by the current input symbol and the state. The state vector consists of the previous $L - 1$ input symbols, and the phase θ_k , which is determined by all previous input symbols. Even when $g(t)$ has a finite length L , the length of phase function $q(t)$ is still infinite (see Figure 6.2). This is to say, CPM signals have an infinite long memory. It is for this reason that CPM signals can achieve better error performance than that of symbol-by-symbol modulation schemes. Since the memory length is infinite, for optimum detection, a receiver

² C_a has a different form in Chapter 3, but it can be reduced to the simpler form here.

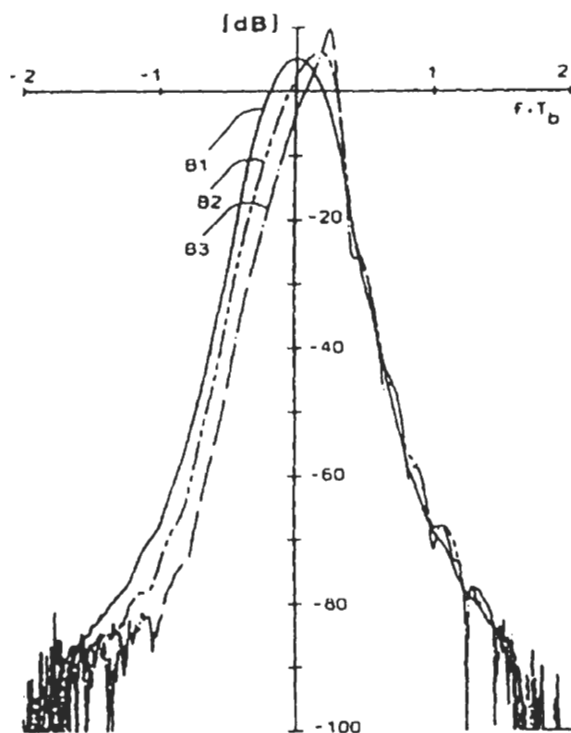


Figure 6.9 PSDs for binary 6RC with $h = 1/2$. PDFs are B_1 , B_2 , and B_3 . From [9]. Copyright 1986 Plenum.

must observe a transmitted waveform with infinite length and chooses the infinitely long sequence $\{a_k\}$ which minimizes the error probability. This can be achieved by the maximum likelihood sequence detection (MLSD). Of course this type of receiver does not exist in practice. The practical receivers can only observe a waveform with a finite length (N). As a result, the receiver is suboptimum. When $N \rightarrow \infty$, the receiver becomes optimum.

In this section we will analyze the error performance of the MLSD for CPM signals. The practical demodulator may, or may not use MLSD, depending on the trade-off between transmission power and system complexity. But the error performance of the MLSD can always serve as a bench mark. We will discuss various types of CPM receivers, optimum or nonoptimum, coherent or noncoherent, in Section 6.5. We will see that the error performance of the MLSD receiver and other receivers is determined by the Euclidean distances, especially the minimum distance, between signals. Therefore we will study the Euclidean distance of CPM signals in this sec-

tion in detail.

6.3.1 Error Probability and Euclidean Distance

Assuming the CPM receiver observes a sequence of N symbols. That is, the received signal is

$$r(t) = s_i(t) + n(t), \quad 0 \leq t \leq NT, \quad i = 1, 2, \dots, M^N$$

where $s_i(t)$ is the signal determined by the i th data sequence \mathbf{a}_i . For M -ary symbols there are a total of M^N different sequences. Therefore there are a total of M^N different $s_i(t)$. Viewing each $s_i(t)$ as a member of the M^N -ary signals, the results of detection of M -ary signals in Appendix B can be applied (M -ary becomes M^N -ary here). Since all $s_i(t)$ have the same energy and are equally likely, from Appendix B we know that the optimum detection is the MLSD which also achieves minimum sequence detection error probability. The MLSD receiver correlates the received signal with all possible signals

$$l_i = \int_0^{NT} r(t)s_i(t)dt, \quad i = 1, 2, \dots, M^N$$

and chooses the signal sequence which maximizes l_i .

The error probability that $s_i(t)$ is detected as any other sequence is bounded by the union bound (Appendix B, (B.43))

$$P_e(i) \leq \sum_{j \neq i} Q\left(\frac{D_{ij}}{\sqrt{2N_o}}\right) \quad (6.28)$$

where D_{ij} denotes the Euclidean distance between the two signals, which is defined as

$$D_{ij} = \left[\int_0^{NT} [s_i(t) - s_j(t)]^2 dt \right]^{\frac{1}{2}} \quad (6.29)$$

The squared distance is

$$\begin{aligned} D_{ij}^2 &= \int_0^{NT} [s_i(t) - s_j(t)]^2 dt \\ &= \int_0^{NT} [s_i^2(t) - 2s_i(t)s_j(t) + s_j^2(t)] dt \end{aligned}$$

$$\begin{aligned}
&= 2NE_s - \int_0^{NT} 2s_i(t)s_j(t)dt \\
&= 2NE_s - \int_0^{NT} 2A^2 \cos[2\pi f_c t + \Phi(t, \mathbf{a}_i)] \cos[2\pi f_c t + \Phi(t, \mathbf{a}_j)]dt \\
&= 2NE_s - \int_0^{NT} \frac{2E_s}{T} \{ \cos[\Phi(t, \mathbf{a}_i) - \Phi(t, \mathbf{a}_j)] \\
&\quad + \cos[4\pi f_c t + \Phi(t, \mathbf{a}_i) + \Phi(t, \mathbf{a}_j)] \} dt \\
&= 2NE_s - \int_0^{NT} \frac{2E_s}{T} \cos[\Phi(t, \mathbf{a}_i) - \Phi(t, \mathbf{a}_j)]dt + o(1/f_c)
\end{aligned}$$

where E_s is the symbol energy, and $o(1/f_c)$ denotes a term of order $1/f_c$, which means that the term is proportional to a factor $1/f_c$. This term is negligible when $f_c \gg 1$, which is the usual case in CPM. Thus the distance in the limit of high frequency is

$$D_{ij}^2 = 2NE_s - \int_0^{NT} \frac{2E_s}{T} \cos \Delta\Phi(t, \gamma_{ij})dt \quad (6.30)$$

where

$$\begin{aligned}
\Delta\Phi(t, \gamma_{ij}) &= \Phi(t, \mathbf{a}_i) - \Phi(t, \mathbf{a}_j) \\
&= 2\pi h \sum_{k=-\infty}^{\infty} (a_k^i - a_k^j)q(t - kT) \\
&= 2\pi h \sum_{k=-\infty}^{\infty} \gamma_k q(t - kT)
\end{aligned} \quad (6.31)$$

The superscript denotes the i th or j th data sequence and γ_{ij} is the *difference data sequence* between \mathbf{a}_i and \mathbf{a}_j .

Expression (6.30) is still not the most convenient one. The energy E_s is the symbol energy. In comparison modulation schemes, we must compare the error performance based on the same bit energy E_b . Since $E_s = (\log_2 M)E_b$, we normalize the distance to obtain

$$\begin{aligned}
d_{ij}^2 &= D_{ij}^2/2E_b \\
&= N(\log_2 M) - \int_0^{NT} \frac{(\log_2 M)}{T} \cos \Delta\Phi(t, \gamma_{ij})dt \\
&= \frac{\log_2 M}{T} \int_0^{NT} [1 - \cos \Delta\Phi(t, \gamma_{ij})]dt
\end{aligned}$$

$$= \frac{\log_2 M}{T} \sum_{k=0}^{N-1} \int_{kT}^{(k+1)T} [1 - \cos \Delta\Phi(t, \gamma_{ij})] dt \quad (6.32)$$

This shows that d_{ij}^2 is a nondecreasing function of the observation length N for a fixed pair of phase paths.

Now let us return to (6.28). Using an upper bound of the Q function [9, p. 21]

$$Q(x) < \frac{1}{2} e^{-x^2/2}, \quad x > 0 \quad (6.33)$$

we can write

$$P_e(i) \leq \frac{1}{2} \sum_{j \neq i} \exp\{-d_{ij}^2 (E_b/2N_o)\} \quad (6.34)$$

Each exponent contains the signal-to-noise ratio (SNR) E_b/N_o . For high SNR, the term with the smallest d_{ij}^2 will strongly dominate (6.34). Therefore at high SNR, we can approximate the bound as

$$P_e(i) \lesssim \frac{K_i}{2} \exp\{-\min_j [d_{ij}^2] (E_b/2N_o)\} \quad (6.35)$$

where K_i is the number of signals that have the minimum distance with $s_i(t)$. The total error probability can be bounded by

$$P_e \lesssim \frac{K}{2} \exp\{-\min_{\substack{i,j \\ i \neq j}} [d_{ij}^2] (E_b/2N_o)\} \quad (6.36)$$

where K is the number of signals that attain the minimum distances in all cases. A definition of minimum distance that applies to any signal set can be written as³

$$d_{\min}^2 \triangleq \frac{1}{2E_b} \min_{\substack{i,j \\ i \neq j}} \left[\int_0^{NT} [s_i(t) - s_j(t)]^2 dt \right] \quad (6.37)$$

For CPM signals it becomes

$$d_{\min}^2 = \frac{1}{2E_b} \min_{\substack{i,j \\ i \neq j}} \left\{ \frac{\log_2 M}{T} \int_0^{NT} [1 - \cos \Delta\Phi(t, \gamma_{ij})] dt \right\} \quad (6.38)$$

³ When the observation length N goes to infinity, the minimum distance is called *free distance*. That is

$$d_{free} = \lim_{N \rightarrow \infty} d_{\min}$$

Using d_{\min} notation (6.36) becomes

$$P_e \lesssim \frac{K}{2} \exp\{-d_{\min}^2 (E_b/2N_o)\} \quad (6.39)$$

or using (6.33) we have

$$P_e \lesssim KQ \left(d_{\min} \sqrt{E_b/N_o} \right) \quad (6.40)$$

Note P_e is the error probability of sequence detection, not the symbol or bit error probability. However, (6.39) and (6.40) are approximately equal to the symbol or bit error probability, since at high SNR a sequence error is most likely caused by one symbol error or one bit error. Even if a sequence error incurs multiple symbol or bit errors, the result is just an increase of the value of the factor K . This may cause a fraction of a dB increase in the error probability graph.

Since the error performance is primarily determined by the minimum distance d_{\min} , the error performance assessment of various CPM schemes can be replaced by assessment of d_{\min} or d_{\min}^2 . In other words, d_{\min}^2 will become the indicator for error performance evaluation and comparison.

To calculate d_{\min}^2 for an observation length of N symbols, all pairs of phase paths in the phase tree (or trellis, for rational h) over N symbol intervals must be considered. The phase paths must not coincide over the first symbol interval. The Euclidean distance is calculated according to (6.32) for all these pairs, and the minimum is the d_{\min}^2 over the observation of N symbols. The phrase "over the observation of N symbols" implies that d_{\min}^2 varies with N . Of course d_{\min}^2 varies with h and $g(t)$ too since $\Delta\Phi(t, \gamma_{ij})$ in (6.32) is a function of h and $g(t)$. But for the discussion below, we are only interested in its dependance on N and denote it as $d_{\min}^2(N)$.

A tight upper bound d_B^2 on $d_{\min}^2(N)$ is an important indicator of the error performance of the scheme since it gives the maximum achievable performance. To construct an upper bound on $d_{\min}^2(N)$ we can choose any pair of phase paths of length N . The distance of this pair must equal or exceed $d_{\min}^2(N)$. Since d_{\min}^2 is a nondecreasing function of N for a fixed pair of phase paths, $d_{\min}^2(\infty)$ must equal or exceed $d_{\min}^2(N)$ for any finite N . Thus we can choose any pair of phase paths of an infinite length to find an upper bound on $d_{\min}^2(N)$ for any N . Good candidates for a tight bound are infinitely long pairs of phase paths that merge as soon as possible. Some merges occur only for some specific h values. Others occur independent of h , which are called *inevitable*. The first inevitable merge is usually used for upper-bound calculation. The first inevitable merge occurs in general at $t = (L + 1)T$. The distances for all pairs of phase paths which give a first inevitable merger in the phase tree (for real h) or trellis (for rational h only) are calculated and compared.

The minimum of them is the upper bound d_B^2 . Sometimes the second, third or even deeper inevitable mergers may provide even tighter upper bound. For details about upper-bound calculation, refer to [7, 8].

6.3.2 Comparison of Minimum Distances

Efficient algorithms using the phase tree or trellis exist for computing d_{\min}^2 and its upper bound d_B^2 for different $g(t)$, L , h , and M [9, 16]. We will not attempt to describe the algorithms here since they are quite complicated. However, for the simple case of CPFSK (i.e., 1REC), an exact expression of d_{\min}^2 (in fact, d_{free}^2) has been found. First the upper bound for binary 1REC has been shown in [9] as $d_B^2 = 2[1 - \text{sinc}(2h)]$. Later, it was shown that this is in fact the exact value of d_{\min}^2 for $h < 1/2$ for binary 1REC [17]. Finally, this result was extended to more general cases in [18]. Specifically, d_{\min}^2 of M-ary CPFSK at any rational modulation index $h = p/q$, where p and q are relatively prime positive integers, is given by

$$d_{\min}^2 = \begin{cases} \log_2 M, & \text{integer } h \\ \min_{\gamma} \{2 \log_2 M [1 - \text{sinc}(\gamma h)]\}, & q \geq M \\ 2 \log_2 M [1 - \text{sinc}(2h)], & h < 0.3016773, q < M \\ \log_2 M, & h > 0.3016773, q < M \end{cases} \quad (6.41)$$

where $\gamma = 2, 4, 6, \dots, 2(M - 1)$. It is clear from the above expression that d_{\min}^2 is proportional to $\log_2 M$. In other words, larger M yields larger minimum distance.

We now present some results as examples in order to get an idea of the behavior of d_{\min}^2 and d_B^2 for more general cases. First we want to show how d_B^2 varies with h and how d_{\min}^2 varies with h and N . An example for a binary 3RC scheme is shown in Figure 6.10. The upper bound reaches its peak at an h value slightly smaller than one. The actual minimum distance d_{\min}^2 also generally increases with h for small h values and become oscillating for larger h values. For $N = 1$, d_{\min}^2 is very poor, but with $N = 2$, it already increases significantly. When $N = 4$, the upper bound is reached in the region $0 < h \lesssim 0.6$. For $h \approx 0.85$ the upper-bound value of 3.35 is reached with $N = 6$. Further increase of N does not increase d_{\min}^2 significantly. There are some weak points of h : $h = 2/3$ and $h = 1$, where the values of d_{\min}^2 are significantly lower. For practical design, we can approximate the optimum $h \approx 0.85$ by a rational number, for instance, $h = 7/8 = 0.875$. Then the scheme will have a state trellis and the MLSD can be performed by the Viterbi algorithm.

Figure 6.11 compares the d_B^2 for binary 1RC through 6RC. The linear vertical scale is the absolute distance and the dB scale is the relative distance normalized to that of MSK. The most important observation from this figure is that the distance increases with L for large h . For $h < 0.5$, the distance actually decreases with L .

But this comparison is not quite fair since the bandwidth also changes with L and h . A better comparison is given in Figure 6.12.

Figure 6.12 is a comparison of d_{\min}^2 between MSK and several schemes of CPM versus bandwidth. Each point represents a CPM scheme with its 99% double-sided normalized power bandwidth $2BT_b$ shown on the horizontal axis and the d_{\min}^2 difference relative to MSK shown on the vertical axis. If we draw a vertical line and a horizontal line through the MSK point, schemes to the left side of the vertical line are more bandwidth efficient than MSK and the ones to the right of the line; and the schemes above the horizontal line are more power efficient than MSK and those below the line. Those in the upper-left quadrant are both more bandwidth efficient and power efficient than MSK. It is evident that larger L and M yield more efficient schemes.

6.4 MODULATOR

A conceptual CPM modulator is shown in Figure 6.13. This is a direct implementation of (6.1). Data sequence $\{a_k\}$ passes through the filter and the multiplier to form the frequency pulse sequence $\{2\pi h a_k g(t - kT)\}$ which is used by the FM modulator to yield the required phase $\Phi(t, \mathbf{a})$. Note that an FM modulator instead of a phase modulation must be used since the input is $g(t)$, the frequency pulse, instead of $q(t)$, the phase pulse. If the FM modulator is a VCO (voltage-controlled oscillator), the VCO's control voltage is

$$v(t) = 2\pi h \sum_{k=-\infty}^{\infty} a_k g(t - kT)$$

But the VCO implementation is not practical since conventional free-running VCOs can not achieve either acceptable frequency stability or the linearity required for low distortion. Many practical solutions have been proposed. One solution is to use the quadrature structure proposed in [19] and also described in [9]. Other structures that use phase lock loop or bandpass filter and limiter are also described in [9]. Another method is to use all digital techniques, with the analog VCO replaced by a digital NCO (numerically controlled oscillator) [20]. We will describe these structures below.

6.4.1 Quadrature Modulator

The quadrature structure can be derived by rewriting the normalized CPM waveform

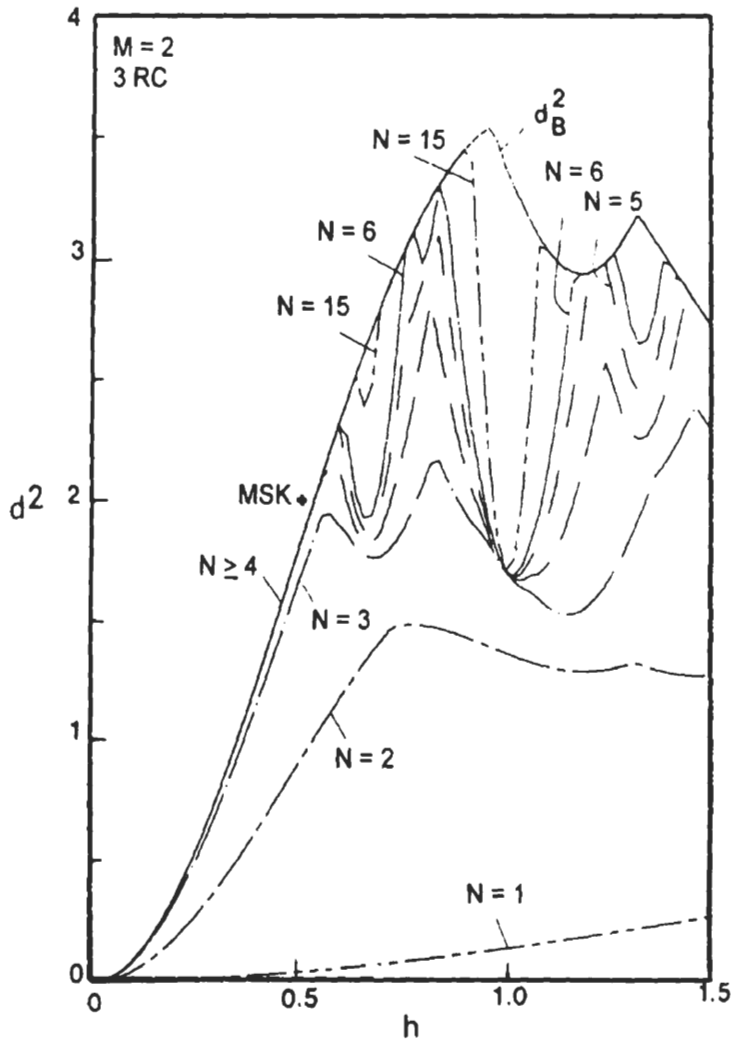


Figure 6.10 Minimum distance vs. h for binary 3RC scheme. From [9]. Copyright © 1986 Plenum.

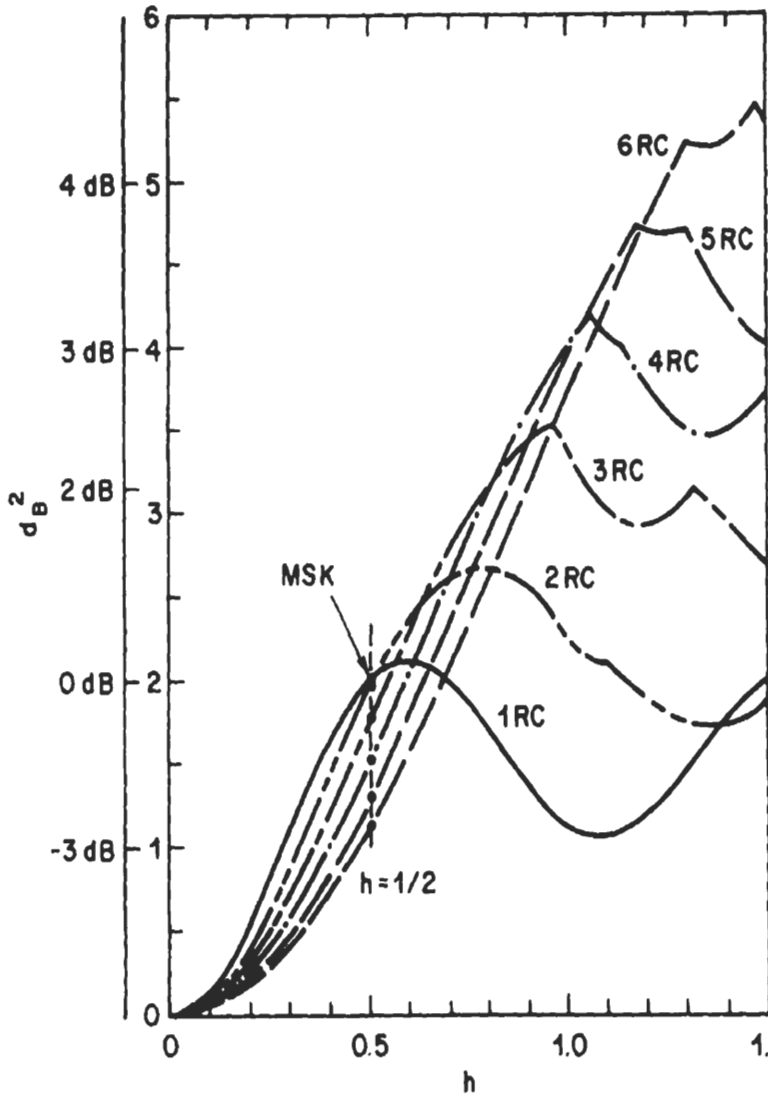


Figure 6.11 The upper bound d_B^2 as a function of h for LRC, $L = 1, 2, \dots, 6$. From [1]. Copyright © 1986 IEEE.

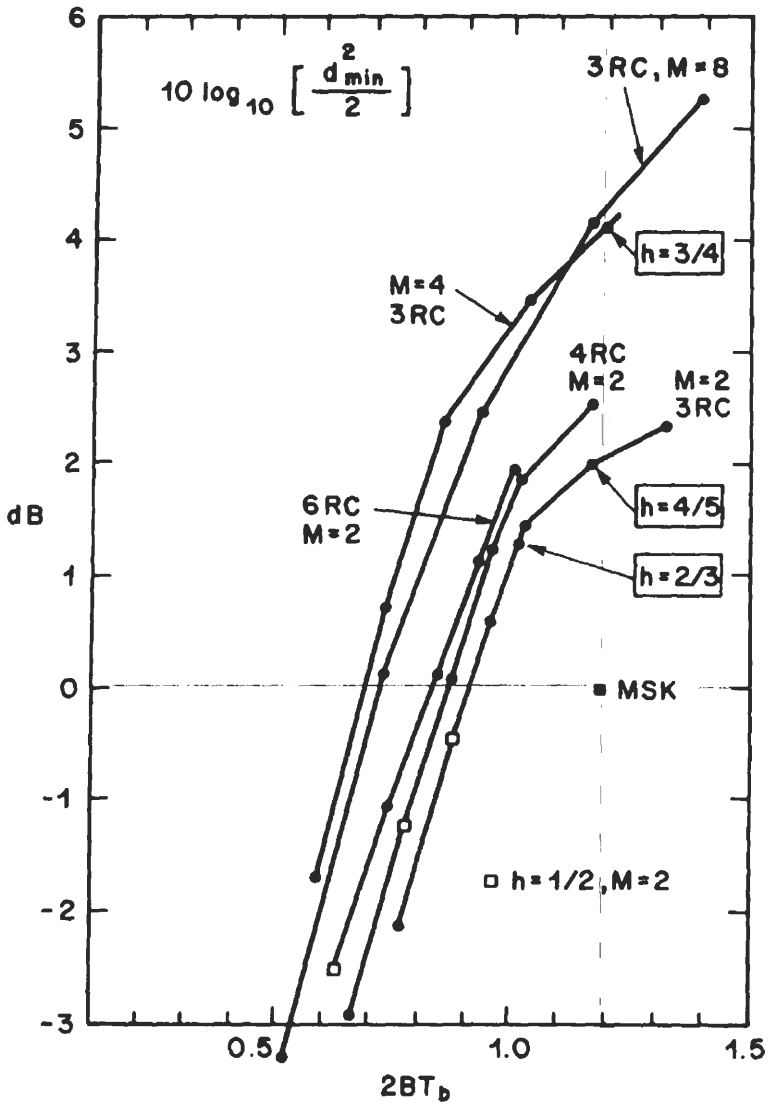


Figure 6.12 Power-bandwidth trade-off for CPM schemes using RC pulses. The bandwidth is defined with the 99%-power-in-band definition. The specific schemes are plotted as points and connected by straight lines. From [1]. Copyright © 1986 IEEE.

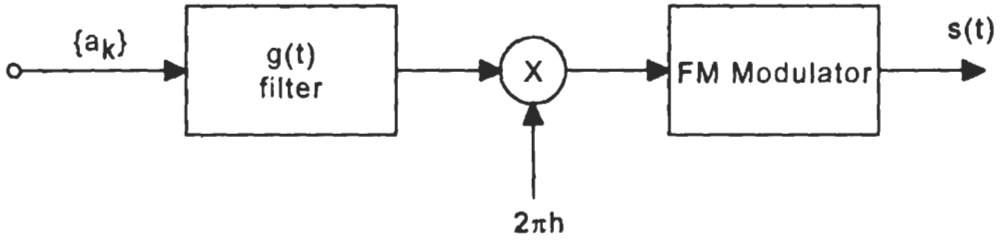


Figure 6.13 Conceptual CPM modulator [9]. Copyright © 1986 Plenum.

$s_o(t) = s(t)/A$ as:

$$s_o(t) = I(t) \cos(2\pi f_c t) - Q(t) \sin(2\pi f_c t), \quad (6.42)$$

where

$$I(t) = \cos \Phi(t, \mathbf{a}) = \cos[\theta(t, \mathbf{a}_k) + \theta_k] \quad (6.43)$$

and

$$Q(t) = \sin \Phi(t, \mathbf{a}) = \sin[\theta(t, \mathbf{a}_k) + \theta_k] \quad (6.44)$$

This expression is very similar to those of MPSK or MSK. The difference here lies in the generation of $I(t)$ and $Q(t)$. The most general and straightforward way is to use stored lookup tables for $I(t)$ and $Q(t)$. Figure 6.14 is the modulator based on (6.42) using ROM (read only memory) to store $I(t)$ and $Q(t)$ [7, 8]. Here we assume a rational h . Thus the number of shapes of $\Phi(t, \mathbf{a})$ in a symbol interval is finite (e.g., see Figure 6.4). So are the number of shapes of $I(t)$ and $Q(t)$ in a symbol interval. Therefore all possible shapes of $I(t)$ and $Q(t)$ in a symbol interval can be stored in ROMs. Since the shape of $\Phi(t, \mathbf{a})$ in a symbol interval is determined by the state $\mathbf{s}_k = (\theta_k, \mathbf{a}_{k-1}) = (\theta_k, a_{k-1}, a_{k-2}, \dots, a_{k-L+1})$ and the current input symbol a_k (again, refer to Figure 6.4), the shapes of $I(t)$ and $Q(t)$ in a symbol interval are addressed by the states \mathbf{s}_k and the current input symbol a_k .

In Figure 6.14, the data symbols are received by the shift register of length L . The output of the shift register is a symbol vector $\mathbf{a}_k = (a_k, a_{k-1}, a_{k-2}, \dots, a_{k-L+1})$. The phase states θ_k can be generated by a phase state ROM and a delay of T . At each symbol time, \mathbf{a}_k and θ_{k-1} are used as input to the state ROM to obtain θ_k . Preferably a phase state serial number ν_k instead of θ_k can be used. By doing this the phase state generation can be implemented as an up/down counter. One way to relate ν_k to θ_k is to use the relation

$$\theta_k = (h\pi\nu_k + \phi_o) \bmod (2\pi) \quad (6.45)$$

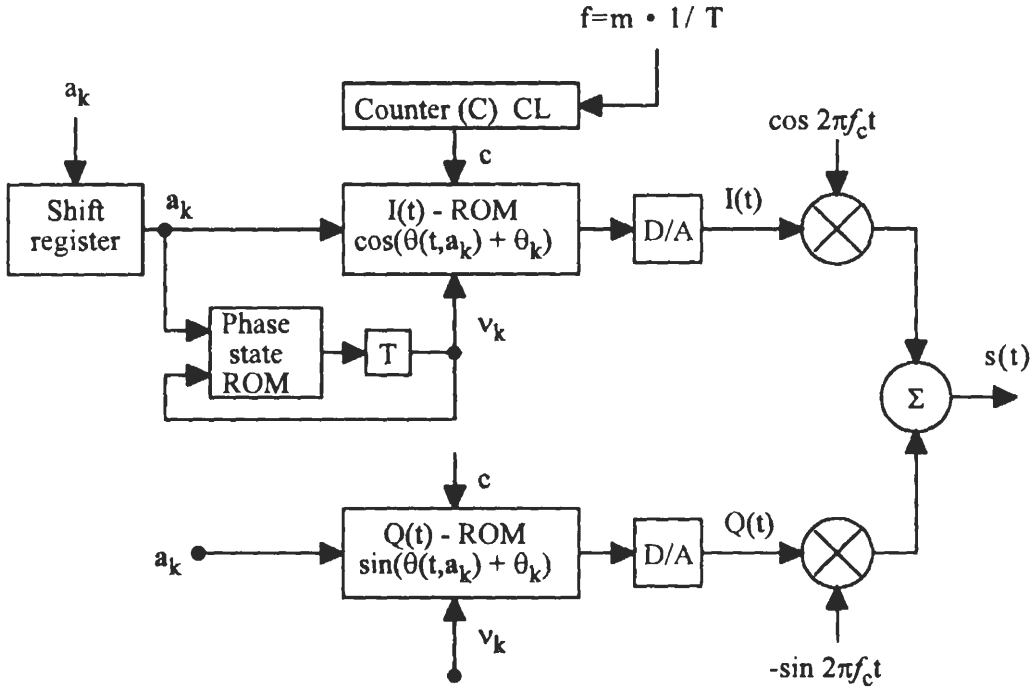


Figure 6.14 Quadrature modulator using phase state ROM. From [9]. Copyright © 1986 Plenum.

where ϕ_o is an arbitrary phase constant which is usually set to zero in analysis. For example, values of θ_k of the binary 3RC with $h = 2/3$ are $0, 2\pi/3$ and $4\pi/3$ (see (6.14)), which can be represented by $\nu_k = 0, 1, 2$.

The $I(t)$ and $Q(t)$ shapes are swept by a counter C at a speed m/T , where m is the number of stored samples per symbol interval. The symbol vector \mathbf{a}_k , the phase state serial number ν_k , and the counter output c are combined to form the addresses to obtain the samples of $I(t)$ and $Q(t)$ in the ROMs. These samples are converted to analog by the D/A converters. The rest of the modulator is the same as that of typical quadrature modulators.

The address field of the ROM is roughly $L \log_2 M + \lceil \log_2 p \rceil + 1$ bits. $L \log_2 M$ is for \mathbf{a}_k , and $\lceil \log_2 p \rceil + 1$ is for θ_k or ν_k , where $\lceil x \rceil$ denotes the smallest integer which is greater than x . Parameter p is the number of different θ_k and is related to index h by $h = 2q/p$ which we have stated before. The ROM size can be easily figured out. Since there are pM^{L-1} states, the current symbol has M different values, thus the number of $I(t)$ or $Q(t)$ shapes is $pM^{L-1}M = pM^L$. Each shape has m samples and each sample is quantized into m_q bits. Thus the ROM size is $pM^L m m_q$ bits. The above address length and ROM size are usually small. For example, for binary 3RC with $h = 2/3$, the ROM address length is only 5 bits and the ROM size is 1536 bits

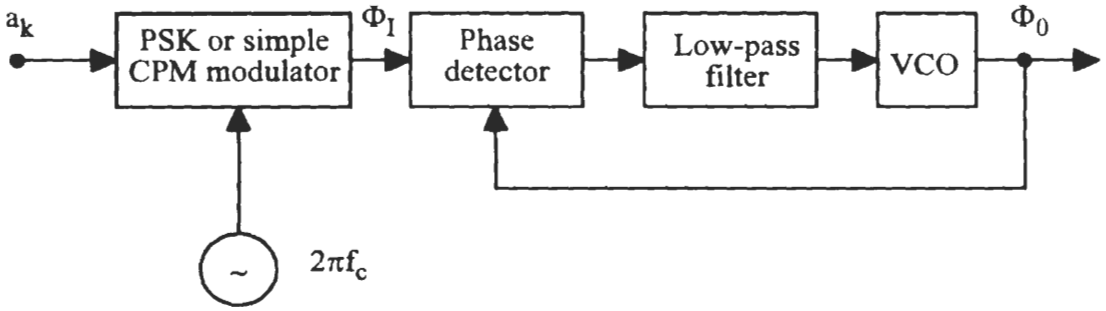


Figure 6.15 PLL implementation of CPM modulator. From [9] Copyright 1986 © Plenum.

assuming $m = 8$ and $m_q = 8$. For larger values of M , L , m , and m_q the ROM size is still very small in comparison to the capacity of ROMs that today's technology can achieve.

6.4.2 Serial Modulator

Similar to the technique used for serial MSK (SMSK) studied in Chapter 5, CPM modulator may be implemented serially. Figure 6.15 is a CPM modulator consisting of a PSK or simple CPM modulator and a PLL (phase locked loop). By replacing the PLL with a bandpass filter and a hard limiter one can implement a CPM modulator as in Figure 6.16. Like the SMSK case, the basic function of the PLL or bandpass filter is to smooth the incoming waveform, thus creating a signal with correlation over several symbol intervals and a narrower spectrum. By properly choosing the PLL or the filter, it is possible to approximately generate a signal very close to the desired CPM signal (in the SMSK case, the generated signal is exactly the MSK signal). The limiter in Figure 6.16 is used to keep the signal amplitude constant in case there is any amplitude variation after filtering. In the following we show how CPM modulation can be achieved by these two structures.

6.4.2.1 PLL Modulator

Refer to Figure 6.15. Assuming the phase detector is used in its linear region, the input phase from the simple CPM modulator is

$$\Phi_I(t, \mathbf{a}) = \sum_k 2\pi h a_k q_I(t - kT)$$

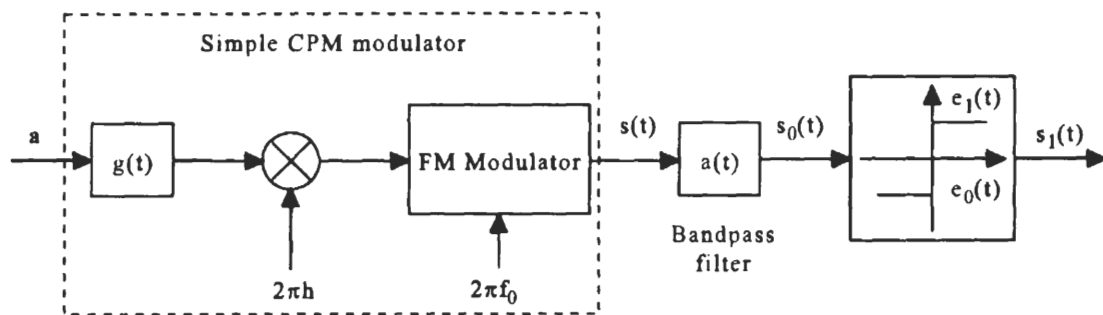


Figure 6.16 Bandpass filter and hard-limiter implementation of CPM modulator. From [9]. Copyright © 1986 Plenum.

Assuming the PLL impulse response is $h(t)$ then the output phase is

$$\Phi_o(t, \mathbf{a}) = \sum_k 2\pi h a_k q_I(t - kT) * h(t)$$

where $*$ denotes convolution. Comparing this to the CPM phase expression, we have

$$q(t - kT) = q_I(t - kT) * h(t)$$

Thus the desired $q(t)$ can be deconvolved into two simpler functions, $q_I(t)$ and $h(t)$, and the CPM modulator complexity is reduced. The deconvolution may be done easier in frequency domain since

$$Q(f) = Q_I(f)H(f)$$

The problem with the PLL modulator is the limit on modulation index h since the maximum of the phase deviation $\Phi_o(t, \mathbf{a}) - \Phi_I(t, \mathbf{a})$ is limited by the linear region of the PLL operation characteristic. The limit also depends on the phase pulse length L and number of levels M . A rough estimation is that [9, p.226]

$$h < \frac{2}{(L+1)(M-1)}$$

which is quite small for large L and M . For example, a binary 3RC CPM would have a maximum index of 0.5 and a quaternary 2RC a maximum index of 0.2.

6.4.2.2 BPF-Limiter Modulator

In Figure 6.16, the phase of the limiter output is the same as the input. That is

$$\Phi_1(t, \mathbf{a}) = \Phi_0(t, \mathbf{a}) = \arg\{\tilde{s}_0(t) * \tilde{a}(t)\}$$

where signal and filter are denoted by their complex envelopes, and $\arg\{z\}$ denotes the argument of the complex quantity z . The above expression can be written as

$$\Phi_1(t, \mathbf{a}) = \arg\{\exp[j\Phi(t, \mathbf{a})] * \tilde{a}(t)\}$$

where $\Phi(t, \mathbf{a})$ is the phase of the signal from the simple CPM stage which can be written as

$$\begin{aligned}\Phi(t, \mathbf{a}) &= 2\pi h \sum_{i=k-L+1}^k a_i q(t - iT) + \theta_k \\ &= \theta(t, \mathbf{a}_k) + \theta_k\end{aligned}$$

where we have assumed that $q(t)$ has a finite length L . For low modulation indexes, the time varying part of $\Phi(t, \mathbf{a})$ may be considered small enough to expand the exponential function into a Taylor series. That is

$$\theta_1(t, \mathbf{a}_k) = \arg\left\{\left[1 + j\theta(t, \mathbf{a}_k) - \frac{\theta^2(t, \mathbf{a}_k)}{2} + \dots\right] * \tilde{a}(t)\right\}$$

To a first-order approximation, we have

$$\theta_1(t, \mathbf{a}_k) = \arg\{[1 + j\theta(t, \mathbf{a}_k)] * \tilde{a}(t)\}$$

Now we assume the filter $a(t)$ is real (this requires the bandpass filter have a symmetrical frequency response), we have

$$\begin{aligned}\theta_1(t, \mathbf{a}_k) &= \arg\{[1 + j\theta(t, \mathbf{a}_k)] * a(t)\} \\ &= \arctan\left[\frac{\theta(t, \mathbf{a}_k) * a(t)}{1 * a(t)}\right]\end{aligned}$$

The denominator is a constant, denote it by A , and for small h values the arctan may be omitted, thus

$$\theta_1(t, \mathbf{a}_k) \approx \theta(t, \mathbf{a}_k) * \frac{a(t)}{A}$$

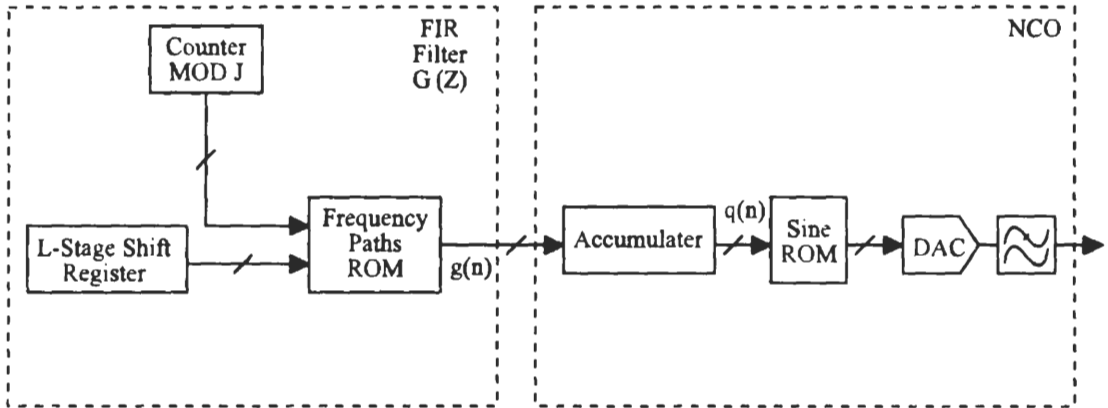


Figure 6.17 All digital CPM modulator. From [20]. Copyright © 1987 IEEE.

or

$$\theta_1(t, \mathbf{a}_k) \approx 2\pi h \sum_{i=k-L+1}^k a_i q(t - iT) * \frac{a(t)}{A}$$

When this expression is compared with the standard CPM phase, it is seen that the bandpass filter to a first-order approximation acts as a linear filter on the phase response. Thus one can synthesize the desired $q_1(t)$ from two simpler functions $q(t)$ and $a(t)$.

The problem of this approach is of course the imperfect linearity of the phase, which may cause some spectrum spread [9, p. 231].

The advantages of the two serial modulators in comparison with the quadrature modulator are faster speed and no need of balance between two channels.

6.4.3 All-Digital Modulator

A completely digital implementation of the CPM modulator is proposed in [20]. The structure is based on the conceptual CPM modulator in Figure 6.13, but all function blocks are implemented digitally. Filter $G(j\omega)$ (Fourier transform of $g(t)$) is replaced by a digital FIR filter $G(z)$, and the VCO by a numerically controlled oscillator (NCO). Figure 6.17 is the all-digital CPM modulator. Even though the ROM-based quadrature modulator (Figure 6.14) uses digital technique to generate $I(t)$ and $Q(t)$, the modulation stages are still analog. In this all-digital implementation, the modulation stage is realized by the NCO.

The NCO consists of an accumulator, a sine ROM, a DAC, and a low-pass filter. The low-pass filter is to filter out any high-frequency harmonics after the DAC. The

sine ROM stores samples of just *one* sinusoid so that the content of the n th memory location is

$$\langle n \rangle = \{2^{K-1} \cos(2\pi n/N)\}$$

where $\{\cdot\}$ means the nearest integer, and K is the number of bits per location in the ROM (i.e., the DAC converter resolution). N is an integer which is the discrete period of the sinusoid. The analog period or frequency is determined by N and the clock frequency f_s of the circuit. The accumulator is in fact a discrete integrator. At symbol interval j , it provides a number n_j as an address for the ROM. Assume the accumulator increases its output by 1 at each clock interval, the output of the sinusoid will repeat itself every N clock intervals. That is, the output signal will have a frequency of

$$K_{NCO} = \frac{f_s}{N}$$

which may be called the sensitivity of the NCO. K_{NCO} is usually an integer. Suppose now the accumulator accepts a number k at its input for each clock interval, the output of the accumulator in the j th interval of the clock is

$$n_j = \{k + n_{j-1}\} \bmod(N)$$

Thus the frequency of the signal at the output of the DAC is

$$f_{NCO} = kK_{NCO}$$

The constraint on k is that $k \leq N/2$ due to the sampling theorem. By changing k , different frequencies can be obtained. The highest is $f_s/2$ and the lowest is $f_s/N = K_{NCO}$.

For CPFSK, the only thing that the FIR filter in Figure 6.17 needs to do is put out different k values from the frequency paths ROM for different data symbols. In fact, M different values of k are needed for an M -ary CPFSK scheme. Since usually f_{NCO} is chosen as an integer multiple of the symbol rate ($1/T$), the number of periods of the sinusoid in T is an integer. Thus the signal can start with zero phase and also can end with zero phase in every symbol interval. In this way, the phase continuity can be achieved.

For more complex CPM schemes, the FIR must provide frequency pulse-shaping processing. In principle, this processing can always be provided by an FIR filter, but in practice it is usually much simpler to use the structure shown in Figure 6.17. The L -stage shifter register remembers the last L symbols and uses them as the addresses for samples of one of M^L possible frequency paths. The frequency paths can be

easily derived from the phase paths (see (6.9)):

$$f(t, \mathbf{a}) = \frac{d}{dt} \Phi(t, \mathbf{a}) = 2\pi h \sum_{i=j-L+1}^j a_i g(t - iT) \quad (6.46)$$

whose samples are stored in the frequency paths ROM.

This all-digital CPM modulator is extremely stable, with very low phase noise, and very flexible. For instance, by increasing N , the resolution can be increased. For more design details the reader is referred to [20] where simulation and experimental results are also available.

6.5 DEMODULATOR

The demodulator is sometimes referred to as the receiver in the literature, even though their meanings are slightly different. We will use them interchangeably.

An important parameter which dictates the structure of the receiver is the modulation index h . If h is rational, as we demonstrated in Section 6.1, there is a state trellis for this CPM scheme. Each path in the trellis uniquely corresponds to a data sequence. Some search algorithms (e.g., the Viterbi algorithm) can be used to search through the trellis to find the transmitted data sequence under certain criterion. If h is irrational, there are no state trellis that exists. In this case a sequence detection based on the phase tree is theoretically possible, but it is impractical since the number of branches at a node in the phase tree grows exponentially with the length of the path. Thus there exists no trellis for irrational h .

We will consider rational h only.

6.5.1 Optimum ML Coherent Demodulator

An optimum MLSD coherent demodulator structure was first developed for binary CPFSK in [21] and extended for M-ary CPFSK in [22]. However, their results are in fact applicable to any CPM scheme as pointed out by [9, p. 233]. The receiver is to detect the first symbol using an observation of N symbols. As we have pointed out previously, the phase produced by the first symbol (any symbol, in fact) lasts forever. Therefore, only when $N \rightarrow \infty$, the receiver is optimum in the sense that all phase information of the first symbol contained in the entire signal is used. When N is finite, the receiver is only suboptimum in the sense that not all phase information is used. However, if only N symbols are observed, the best we can do is to perform MLSD based on the given observation. In this sense, it is optimum. That is why it is called optimum ML demodulator.

We use a shorthand notation developed in [21] for the received signal

$$r(t) = s(t, a_1, A_k) + n(t), \quad 0 \leq t < NT$$

where $s(t, a_1, A_k)$ is a general CPM signal corresponding to the data symbol sequence $\{a_1, A_k\}$, a_1 is the first symbol to be detected, and $A_k = \{a_2, a_3, \dots, a_N\}$, $k = 1, 2, \dots, M^{N-1}$ are the all possible data sequences with $N - 1$ bits following a_1 . For coherent detection, the initial phase of the signal is known, and hence will be assumed to be zero without loss in generality.

The optimum receiver is a first-symbol detector [7.21, 22]. The receiver is only interested in finding an estimate of the first symbol a_1 , not the entire sequence. Thus we can partition all M^N sequences into M groups:

$$\left\{ \begin{array}{l} 1, a_2, a_3, \dots, a_N \\ -1, a_2, a_3, \dots, a_N \\ 3, a_2, a_3, \dots, a_N \\ -3, a_2, a_3, \dots, a_N \\ \vdots \\ (M-1), a_2, a_3, \dots, a_N \\ -(M-1), a_2, a_3, \dots, a_N \end{array} \right.$$

Note that each group contains M^{N-1} sequences since $\{a_2, a_3, \dots, a_N\}$ has M^{N-1} possible combinations. The receiver must find which group of sequences maximizes the likelihood function, and take the first symbol of that group as the estimate. This problem is the composite hypothesis problem treated in [23, 24] and other books. The main point about the composite hypothesis problem is that the observables pertaining to the symbol to be estimated (a_1 , here) are distributed according to certain probability density, and to estimate the symbol, the likelihood of the symbol must be averaged over the density. In our case (AWGN channel with a noise spectral density N_o), the likelihood conditioned on a specific A_k is $\exp\left(\frac{2}{N_o} \int_0^{NT} r(t)s(t, a_1, A_k)dt\right)$ [23, 24]. It must be averaged over the probability distribution density of A_k to obtain the unconditional likelihood of a_1 . Since A_k can have $m = M^{N-1}$ different possibilities, the discrete probability density function (PDF) of A_k is $f(A_k) = 1/M^{N-1}$ for each possible A_k . Thus the likelihoods for all M possible a_1 s are (ignoring factor $1/M^{N-1}$ since it is the same for all likelihoods)

$$l_1 = \sum_{j=1}^m \exp \left[\frac{2}{N_o} \int_0^{NT} r(t)s(t, 1, A_j)dt \right]$$

$$\begin{aligned}
 l_2 &= \sum_{j=1}^m \exp \left[\frac{2}{N_o} \int_0^{NT} r(t) s(t, -1, A_j) dt \right] \\
 &\vdots \\
 l_{M-1} &= \sum_{j=1}^m \exp \left[\frac{2}{N_o} \int_0^{NT} r(t) s(t, M-1, A_j) dt \right] \\
 l_M &= \sum_{j=1}^m \exp \left[\frac{2}{N_o} \int_0^{NT} r(t) s(t, -(M-1), A_j) dt \right] \quad (6.47)
 \end{aligned}$$

The receiver then chooses the data symbol a_1 that corresponds to the largest of l_1 to l_M . The receiver is shown in Figure 6.18. The correlators' outputs are denoted by $x_{\lambda j}$, $\lambda = 1, 2, \dots, M$, $j = 1, 2, \dots, m$ where

$$x_{\lambda j} = \begin{cases} \int_0^{NT} r(t) s(t, \lambda, A_j) dt, & \lambda \text{ odd} \\ \int_0^{NT} r(t) s(t, -(\lambda-1), A_j) dt, & \lambda \text{ even} \end{cases}$$

Then the M likelihoods can be written as

$$l_\lambda = \sum_{j=1}^m \exp \left(\frac{2}{N_o} x_{\lambda j} \right), \quad \lambda = 1, 2, \dots, M$$

It is impossible to analyze the exact error performance of the optimum receiver. However, for high SNR the receiver can be simplified to a suboptimum receiver whose error performance can be analyzed by means of union bound.

For large SNR,

$$l_\lambda = \sum_{j=1}^m \exp \left(\frac{2}{N_o} x_{\lambda j} \right) \approx \exp \left(\frac{2}{N_o} x_\lambda \right)$$

where x_λ is the largest of $x_{\lambda j}$. Furthermore, since $\exp(\cdot)$ is a monotonic function, x_λ is an equivalent parameter for decision making. Thus a suboptimum receiver does not need the $\exp(\cdot)$ blocks and the summers in Figure 6.18. The receiver directly checks the outputs of the correlators and makes the decision on a_1 that corresponds to the largest $x_{\lambda j}$. Its performance should be very close to that of the optimum receiver for high SNR.

The suboptimum receiver is in fact an ML sequence detector. As we pointed out before, if $N \rightarrow \infty$, the receiver is optimum. Therefore, the performance of the suboptimum receiver can be compensated for by increasing the observation length.

The error probability of the optimum first-symbol receiver is difficult to analyze.

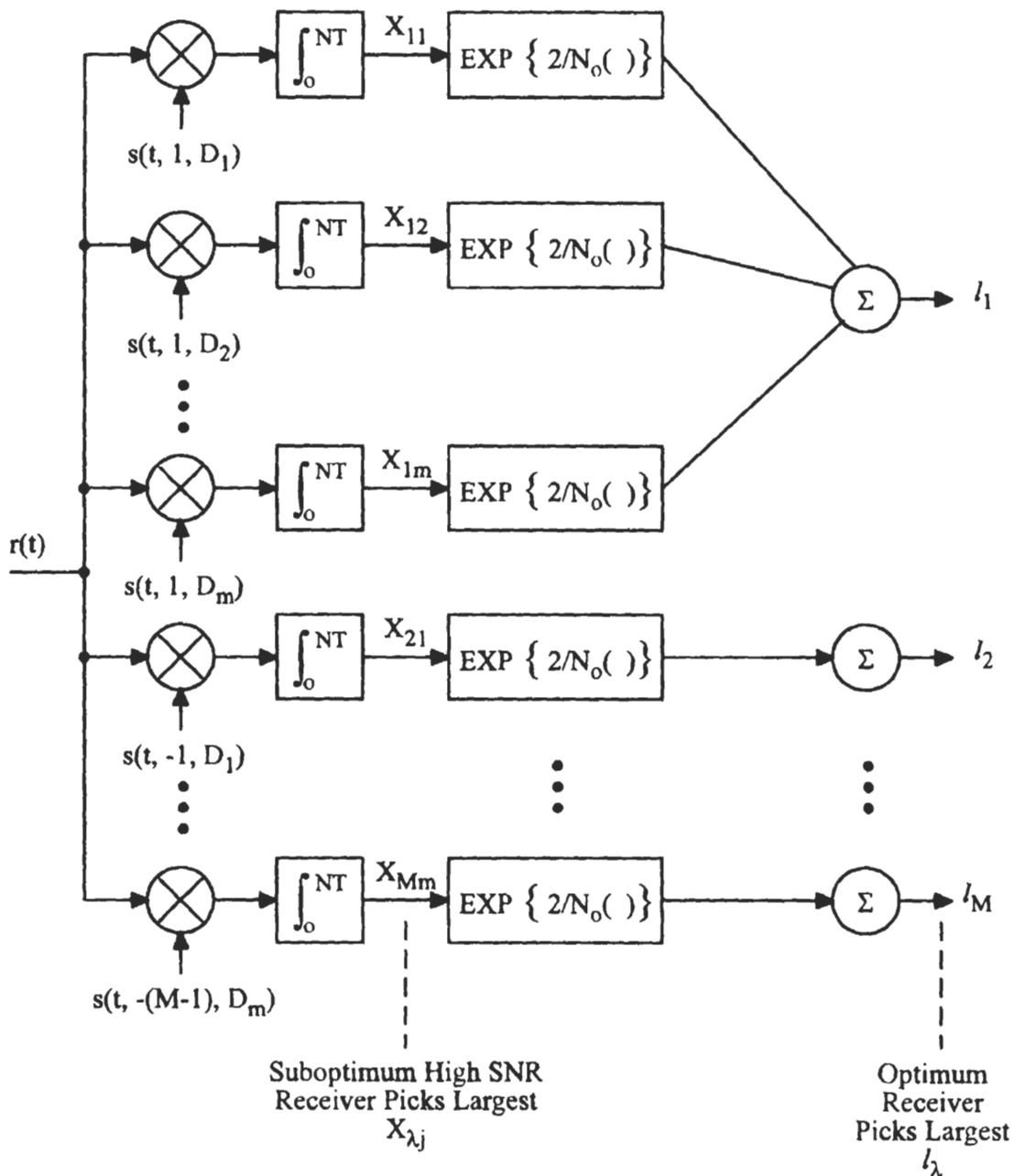


Figure 6.18 Optimum and high-SNR suboptimum CPM receivers. From [22] Copyright © 1976 IEEE.

However, for high SNR, the suboptimum receiver is just as good as the optimum one. The error performance thus can be evaluated by using the suboptimum receiver which is the ML sequence detector. Its performance has been analyzed in Section 6.3, and is dominated by the minimum distance between all sequences. That is

$$P_e \lesssim KQ \left(d_{\min} \sqrt{E_b/N_o} \right)$$

where K is the number of sequences that attain the minimum distances in all cases. Using the definitions of the distance and x , they can be related as $d^2 = \frac{1}{E_b} [NE_s - x]$ and $d_{\min}^2 = \frac{1}{E_b} [NE_s - x_{\Lambda}]$.

The error probability upper-bound curves for binary, quaternary, and octal CPFSK schemes with various h values are given in [22] (Figures 6.19 to 6.21). The h values used in the figures are the optimum values, that is, the values for which the upper bounds are the smallest. These values are found by trial-and-error numerically. The curves show that binary CPFSK ($h = 0.715$) offers up to 1.1 dB improvement for five-symbol detection with respect to coherent BPSK. Quaternary CPFSK offers a 2.5 dB improvement for two-symbol detection ($h = 1.75$) and a further 1 dB improvement for five-symbol detection ($h = 0.8$) over coherent QPSK. Octal CPFSK ($h = 0.879$) offers a 1.9 dB advantage over orthogonal signaling for two-symbol detection and a 2.6 dB improvement for three-symbol detection. The advantage over nonorthogonal coherent 8PSK is huge, in the neighborhood of 7.5 dB. Simulation results provided in [22] confirm the tightness of the upper bound at high SNR (> 4 dB).

Note that the above comparison is based on the assumption that no signal distortion exists at receiver. This implies the bandwidth of the communication system is, theoretically, infinite; and practically, wide enough to receive most of the signal spectrum. This in turn implies that the bandwidth requirement is generally higher for larger values of h (refer to Figures 3.12 to 3.14). Obviously this argument also applies to the noncoherent detection case in the next section.

6.5.2 Optimum ML Noncoherent Demodulator

The optimum ML noncoherent demodulator is also developed in [21, 22]. For noncoherent detection, the carrier initial phase ϕ is unknown. We assume a uniform PDF $f(\phi)$ from 0 to 2π , that is

$$f(\phi) = \frac{1}{2\pi}, \quad 0 \leq \phi \leq 2\pi$$

Different from the coherent case, the $r(t)$ is observed for $(2n + 1)$ symbols and the symbol to be detected is the middle symbol [21, 22] (according to [21], the magnitude

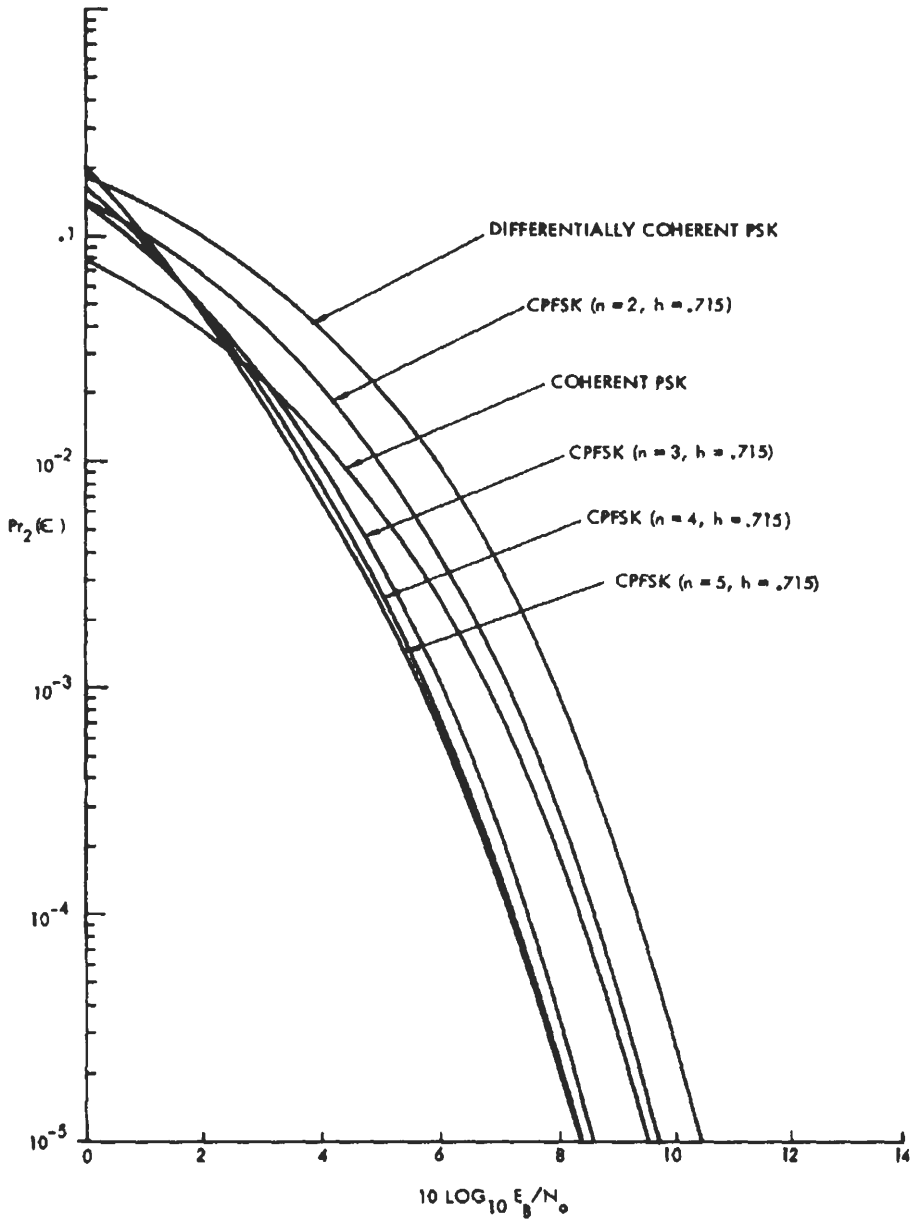


Figure 6.19 P_b for binary coherent CPFSK in comparison with coherent BPSK and differentially coherent BPSK. From [22]. Copyright © 1976 IEEE.

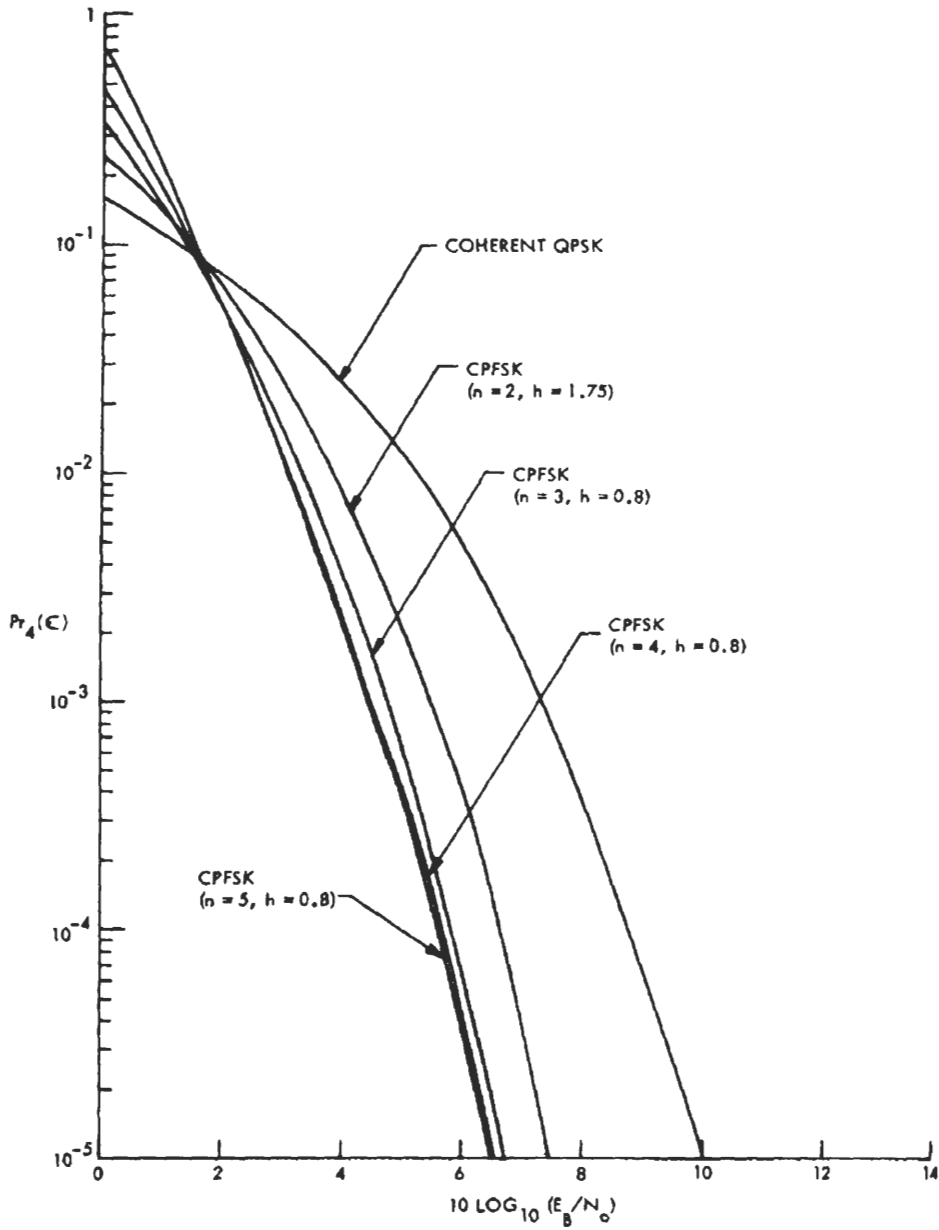


Figure 6.20 P_s for quaternary coherent CPFSK in comparison with coherent QPSK. From [22]. Copyright © 1976 IEEE.

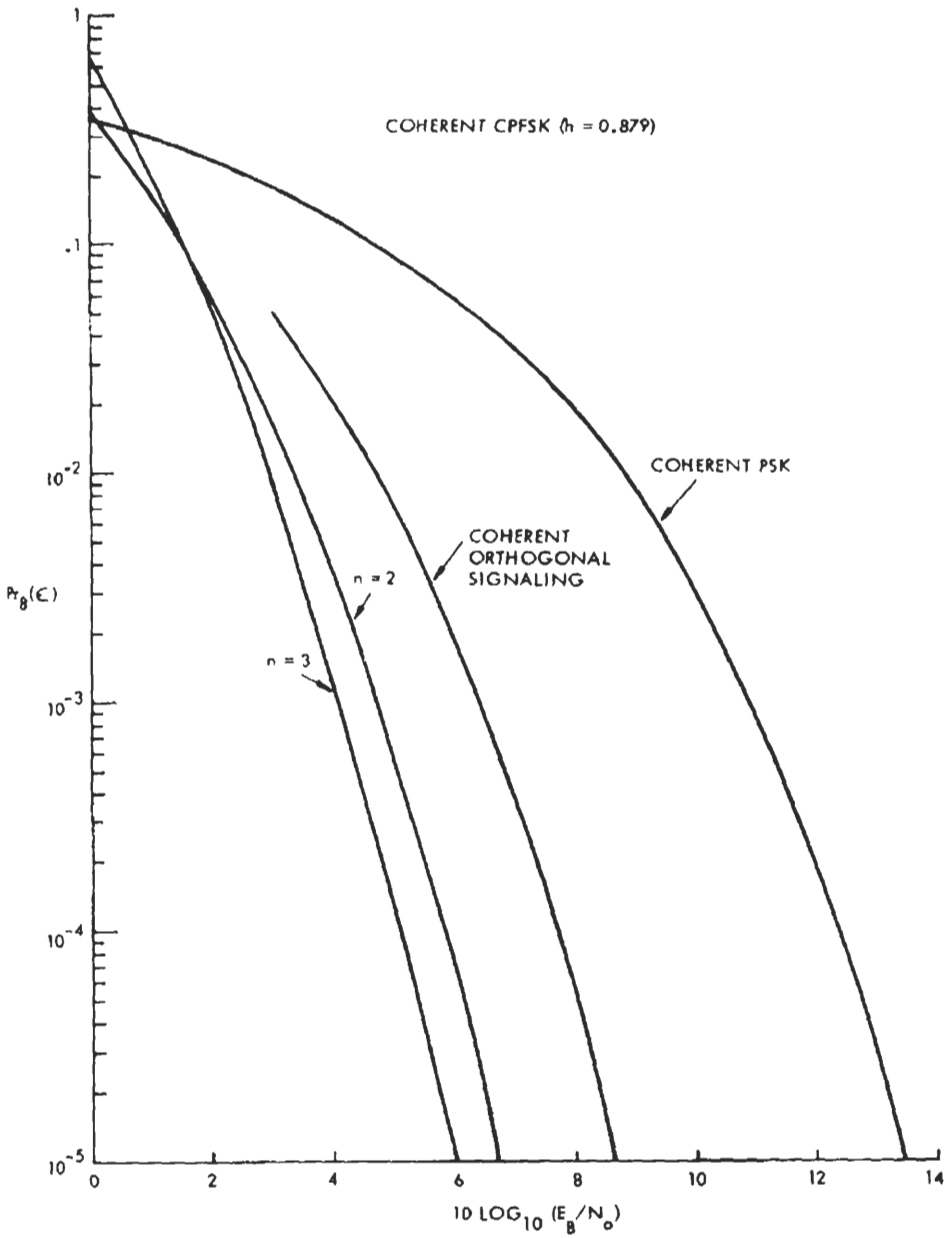


Figure 6.21 P_b for octal coherent CPFSK in comparison with coherent 8PSK and orthogonal signaling. From [22]. Copyright © 1976 IEEE.

of the complex correlation between two binary CPFSK waveforms corresponding to data sequences differing in only one bit is a minimum when the difference bit is in the middle). Using a shorthand notation for the signal we can write

$$r(t) = s(t, a_{n+1}, \Delta_k, \phi) + n(t), \quad 0 \leq t \leq (2n+1)T$$

where a_{n+1} is the middle symbol which is to be detected, Δ_k is a $2n$ -tuple defined as

$$\Delta_k = \{a_1, a_2, \dots, a_n, a_{n+2}, \dots, a_{2n+1}\}$$

There are a total of $\mu = M^{2n}$ sequences of Δ_k . All of them are equally likely, that is, the PDF of Δ is $f(\Delta) = 1/\mu$. The conditional likelihood

$$\exp\left(\frac{2}{N_o} \int_0^{(2n+1)T} r(t)s(t, a_{n+1}, \Delta_k, \phi)dt\right)$$

must be averaged over Δ and ϕ . That is

$$\begin{aligned} l_1 &= \frac{1}{\mu} \int_{\phi} \sum_{k=1}^{\mu} \exp\left[\frac{2}{N_o} \int_0^{(2n+1)T} r(t)s(t, 1, \Delta_k, \phi)dt\right] f(\phi)d\phi \\ l_2 &= \frac{1}{\mu} \int_{\phi} \sum_{k=1}^{\mu} \exp\left[\frac{2}{N_o} \int_0^{(2n+1)T} r(t)s(t, -1, \Delta_k, \phi)dt\right] f(\phi)d\phi \\ &\vdots \\ l_{M-1} &= \frac{1}{\mu} \int_{\phi} \sum_{k=1}^{\mu} \exp\left[\frac{2}{N_o} \int_0^{(2n+1)T} r(t)s(t, M-1, \Delta_k, \phi)dt\right] f(\phi)d\phi \\ l_M &= \frac{1}{\mu} \int_{\phi} \sum_{k=1}^{\mu} \exp\left[\frac{2}{N_o} \int_0^{(2n+1)T} r(t)s(t, -(M-1), \Delta_k, \phi)dt\right] f(\phi)d\phi \end{aligned} \quad (6.48)$$

The average over the phase leads to zeroth-order modified Bessel function (see Section B.3 of Appendix B, particularly (B.51) to (B.55)), so we have

$$\begin{aligned} l_1 &= \frac{1}{\mu} \sum_{k=1}^{\mu} I_0\left(\frac{2}{N_o} z_{1k}\right) \\ l_2 &= \frac{1}{\mu} \sum_{k=1}^{\mu} I_0\left(\frac{2}{N_o} z_{2k}\right) \end{aligned}$$

$$l_M = \frac{1}{\mu} \sum_{k=1}^{\mu} I_0\left(\frac{2}{N_o} z_{Mk}\right) \quad (6.49)$$

where

$$z_{ik}^2 = x_{ik}^2 + y_{ik}^2 \quad (6.50)$$

$$x_{ik} = \begin{cases} \int r(t)s(t, i, \Delta_k, 0)dt, & i \text{ odd} \\ \int r(t)s(t, -(i-1), \Delta_k, 0)dt, & i \text{ even} \end{cases}$$

and

$$y_{ik} = \begin{cases} \int r(t)s(t, i, \Delta_k, \pi/2)dt, & i \text{ odd} \\ \int r(t)s(t, -(i-1), \Delta_k, \pi/2)dt, & i \text{ even} \end{cases}$$

Since x_{ik} and y_{ik} are Gaussian with nonzero mean, z_{ik} is a Rician statistic variable.

The optimum noncoherent receiver structure is shown in Figure 6.22 where all integration intervals are from 0 to $(2n+1)T$. It is optimum independent of SNR. Unfortunately, its error performance is difficult to analyze, as in the coherent case. However, we can derive a suboptimum receiver for high SNR and its error performance bound can be determined.

For high SNR, we have with good approximation

$$\sum_{k=1}^{\mu} I_0\left(\frac{2}{N_o} z_{ik}\right) \approx I_0\left(\frac{2}{N_o} z_{i\Lambda}\right)$$

where $z_{i\Lambda}$ is the largest of the z_{ik} . In addition, the Bessel function is a monotonic function, thus the suboptimum receiver needs only to examine all the z_{ik} , $i = 1, 2, \dots, M$, and chooses the a_{n+1} corresponding to the largest. The suboptimum noncoherent receiver is also shown in Figure 6.22. The error performance of the suboptimum receiver can be analyzed using the union bound. The reader is referred to [22] for details.

The error probability upper-bound curves for noncoherent binary, quaternary, and octal CPFSK schemes with various h values are given in [22] (Figures 6.23 to 6.25). The h values used in the figure are the optimum h values that are similar to the coherent ones. The binary noncoherent CPFSK ($h = 0.715$) outperforms coherent BPSK up to 0.5 dB for $SNR > 7.5$ dB for five-symbol detection, while for three-symbol detection, it is inferior by about 1 dB at high SNR. Quaternary noncoherent CPFSK also achieves better performance than coherent QPSK, offers a 2 dB improvement for three-symbol detection ($h = 0.8$) and a further 0.8 dB improvement for five-symbol detection ($h = 0.8$). Noncoherent octal CPFSK ($h =$

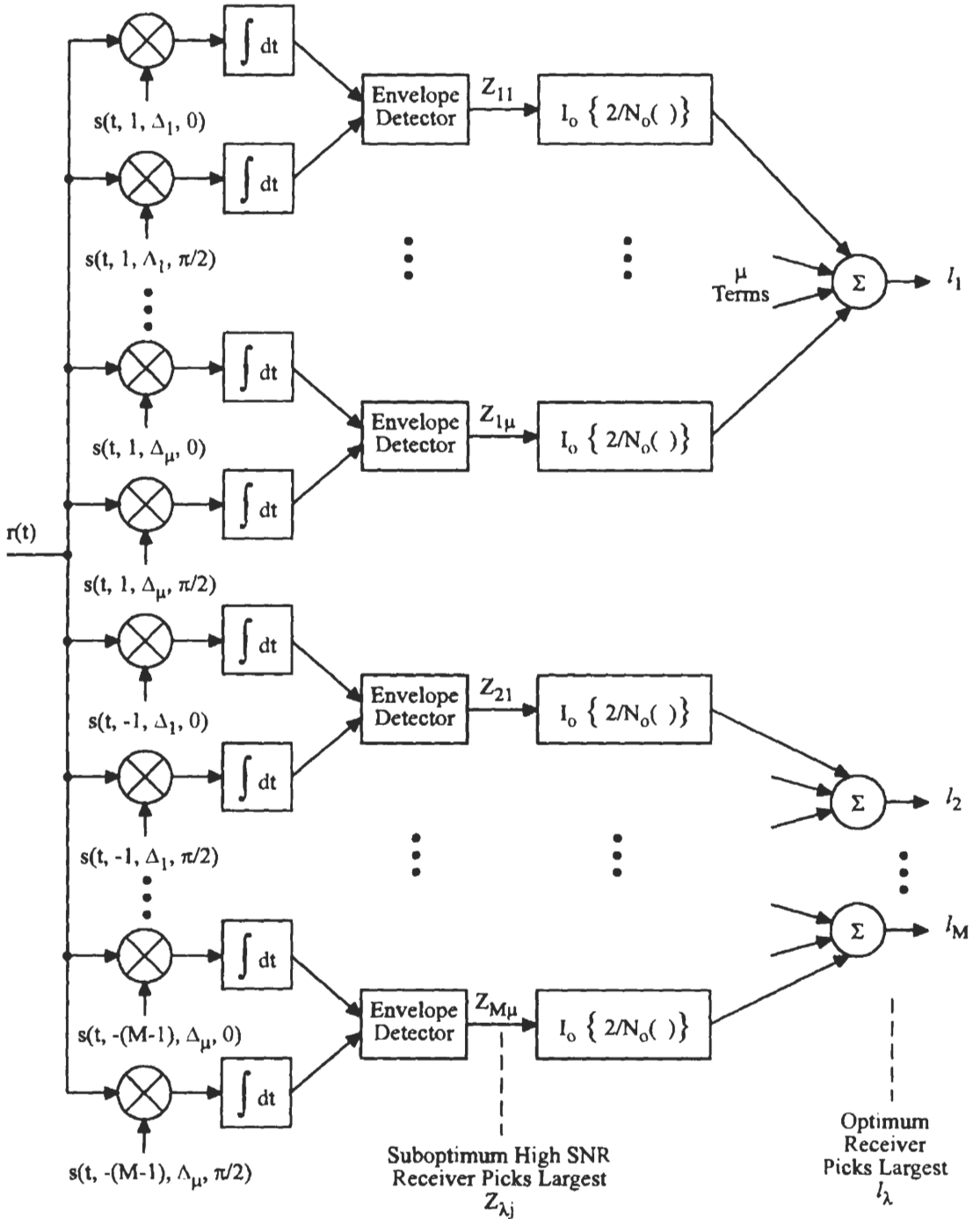


Figure 6.22 Optimum and high-SNR suboptimum CPM noncoherent receiver. From [22] Copyright © 1976 IEEE.

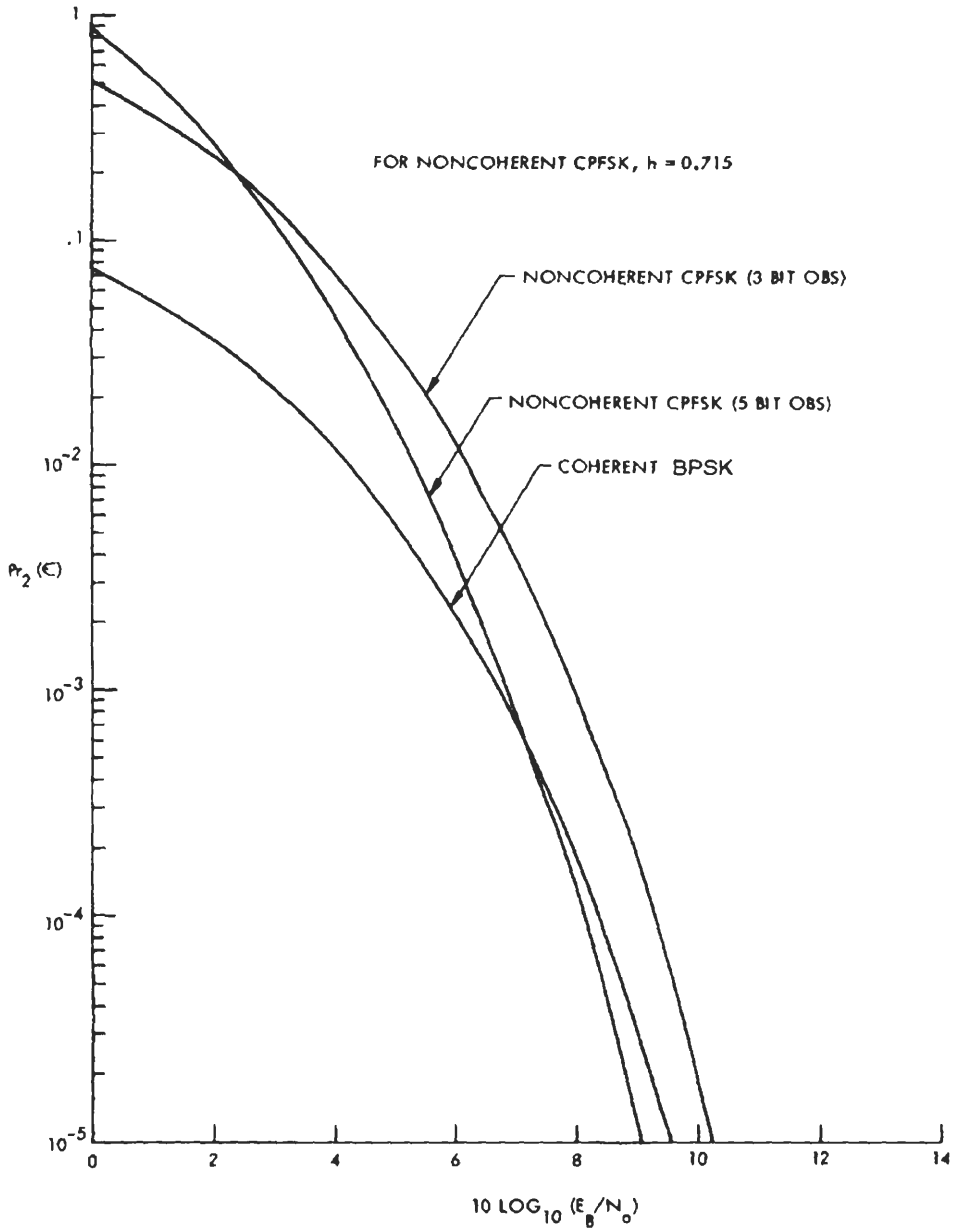


Figure 6.23 P_b of binary noncoherent CPFSK in comparison with coherent BPSK. From [22] Copyright © 1976 IEEE.

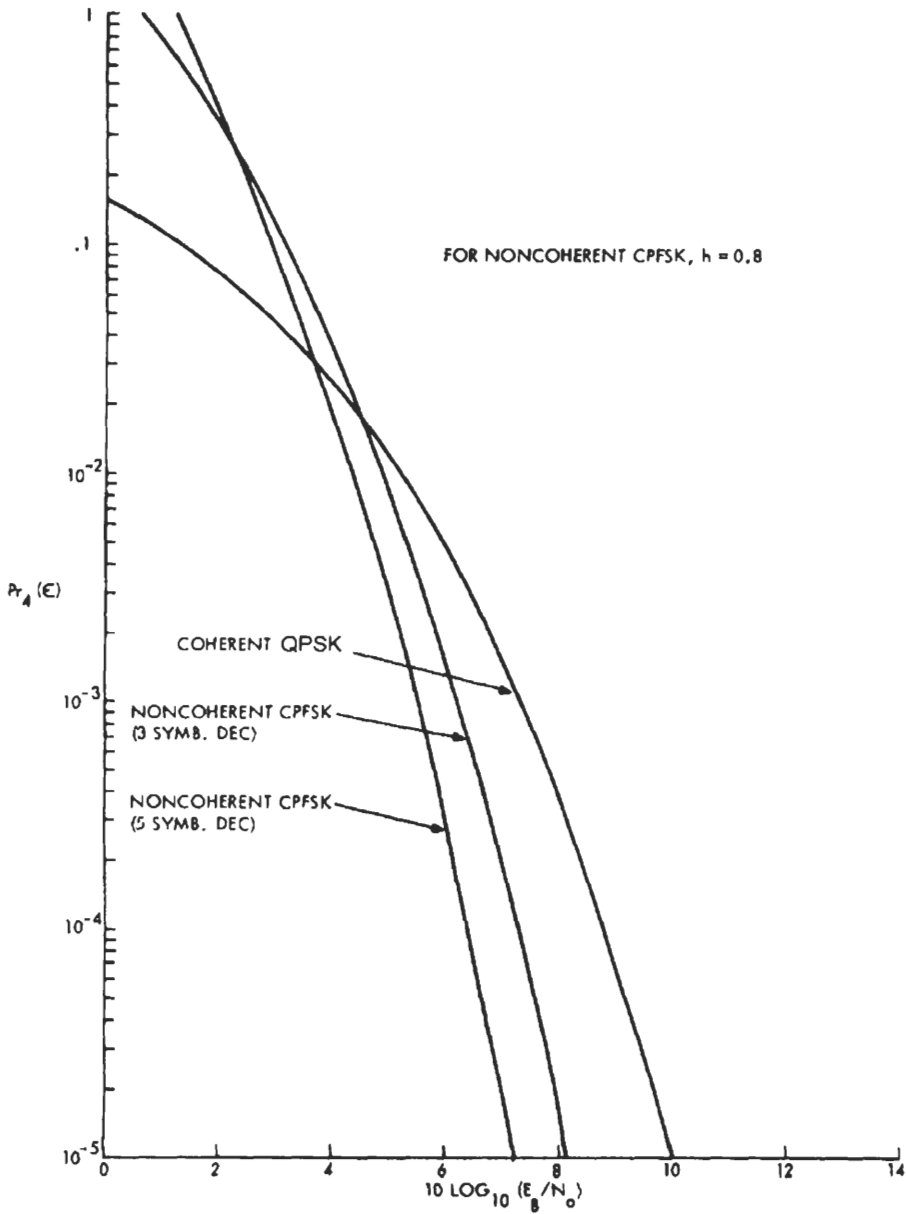


Figure 6.24 P_s of 4-ary noncoherent CPFSK in comparison with coherent QPSK. From [22]. Copyright © 1976 IEEE.

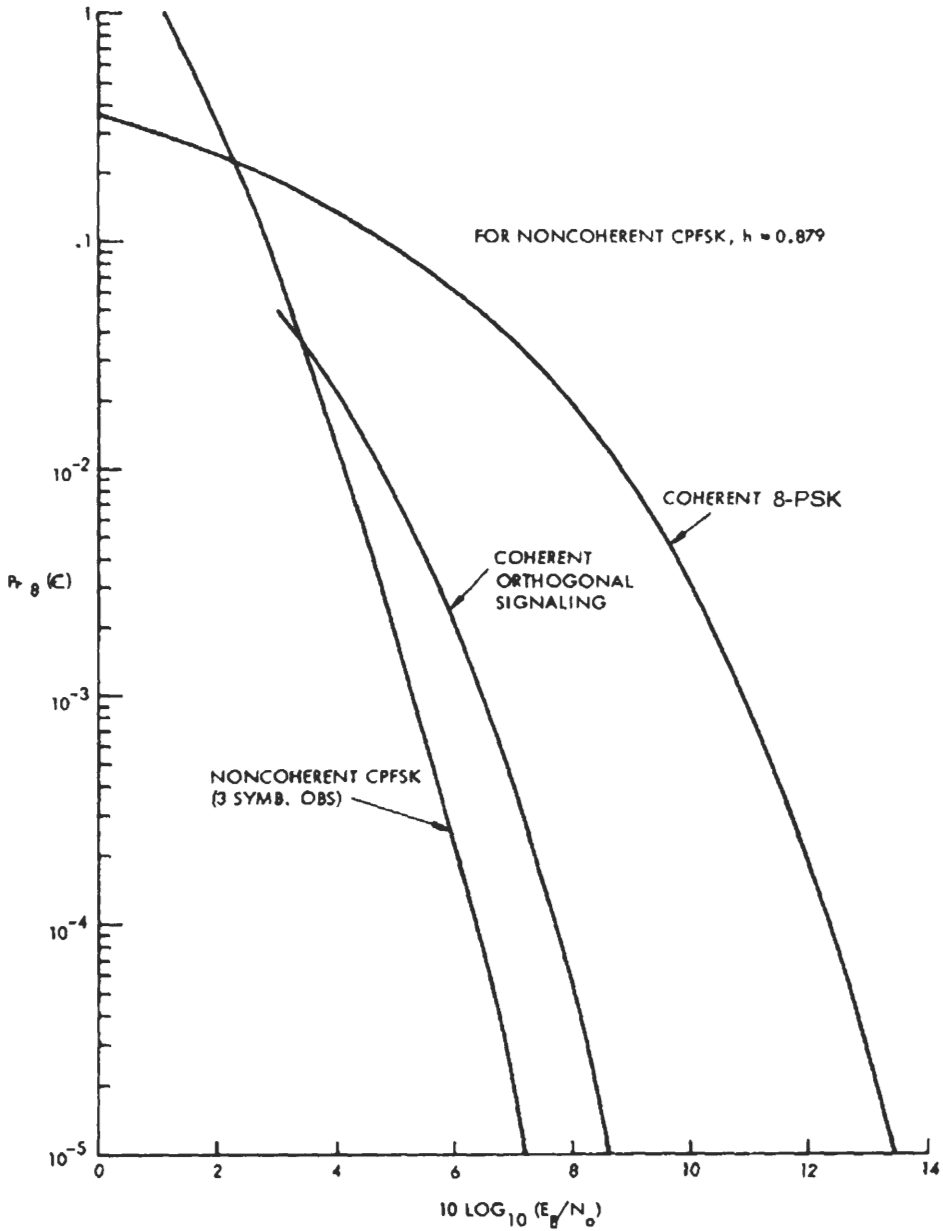


Figure 6.25 P_b of 8-ary noncoherent CPFSK in comparison with coherent 8PSK and coherent orthogonal signaling. From [22]. Copyright © 1976 IEEE.

0.879) offers a 1 dB advantage over orthogonal signaling for three-symbol detection and a significant advantage over nonorthogonal 8PSK, in the neighborhood of 6 dB. Simulation results provided in [22] confirm the tightness of the upper bound at high SNR (> 4 dB).

6.5.3 Viterbi Demodulator

Even though the above two receivers can be applied to general CPM, they become unreasonably complex. Also, it is not clear how successive symbol decisions can be made in a convenient way using the structures in Figures 6.18 and 6.22. An MLSD demodulator using the Viterbi processor was proposed in [8] for partial (and full) response CPM. We will study this structure in this Section. We will see that this structure can provide successive real-time symbol decisions in a convenient manner.

This structure is based on the state trellis that we developed in Section 6.1. As pointed out before, for CPM schemes to have a state trellis, the modulation index h must be a rational number. Thus in this section, we exclusively deal with rational h .

We have studied the state trellis of CPM schemes in Section 6.1, and an example is given in Figure 6.5. Here we briefly repeat the state development in Section 6.1. A state at $t = kT$ is defined by the vector

$$\mathbf{s}_k = (\theta_k, a_{k-1}, a_{k-2}, \dots, a_{k-L+1})$$

where L is the finite length of the frequency shape pulse $g(t)$. For rational $h = 2q/p$ (q, p integers), there are p different phase states with values $0, 2\pi/p, 2 \cdot 2\pi/p, \dots, (p-1)2\pi/p$. Thus the number of states is

$$S = pM^{L-1}$$

In the state trellis, there are M branches coming into a state and M branches leaving from a state. So the total number of in-branches is pM^L and number of out-branches is also pM^L .

The receiver observes the signal $r(t) = s(t, \mathbf{a}) + n(t)$, where the noise $n(t)$ is Gaussian and white. Here we explicitly show the data sequence \mathbf{a} as an argument of the signal. The MLSD receiver maximizes the log likelihood function, or equivalently, the correlation (see Appendix B, Detection of M-ary Signals)

$$l(\tilde{\mathbf{a}}) = \int_{-\infty}^{\infty} r(t)s(t, \tilde{\mathbf{a}})dt$$

where $\tilde{\mathbf{a}}$ is any possible data sequence which might be transmitted, one of them is \mathbf{a} , the actual transmitted one. A practical receiver can only observe signals for a finite

period. Thus we rewrite the above as

$$l_k(\tilde{\mathbf{a}}) = \int_0^{(k+1)T} r(t)s(t, \tilde{\mathbf{a}})dt$$

and it can be written in a recursive form

$$l_k(\tilde{\mathbf{a}}) = l_{k-1}(\tilde{\mathbf{a}}) + Z_k(\tilde{\mathbf{a}})$$

where

$$\begin{aligned} Z_k(\tilde{\mathbf{a}}) &= \int_{kT}^{(k+1)T} r(t)s(t, \tilde{\mathbf{a}})dt \\ &= \int_{kT}^{(k+1)T} r(t) \cos[2\pi f_c t + \theta(t, \tilde{\mathbf{a}}_k) + \tilde{\theta}_k]dt \end{aligned} \quad (6.51)$$

which is called the *metric* of the branch corresponding to the signal $s(t, \tilde{\mathbf{a}})$ in the k th symbol interval (the amplitude of $s(t, \tilde{\mathbf{a}})$ is normalized to 1 since it is the same for all signals). This metric is the correlation between the received signal and $s(t, \tilde{\mathbf{a}})$ over the k th symbol interval.

The Viterbi algorithm (VA) recursively accumulates the branch metrics up to the k th symbol interval for certain paths in the trellis and chooses those paths that have the maximum *path metrics*. Since the VA does not search all paths, the algorithm is much more efficient than the exhaustive search. Yet the VA can guarantee to find the maximum likelihood path. We will describe the VA in detail shortly.

Now we have to construct a receiver that can produce the branch metric $Z_k(\tilde{\mathbf{a}})$ in an efficient way. Since the number of branches (in or out) in the trellis is pM^L , there are pM^L different values of $Z_k(\tilde{\mathbf{a}})$. It is well known that a correlator can be implemented as a matched filter with its output sampled at the end of the integration period. Thus we want to realize (6.51) by matched filters. The signal can be written in quadrature form as (see (6.42) to (6.44))

$$s(t, \mathbf{a}) = AI(t, \mathbf{a}) \cos(2\pi f_c t) - AQ(t, \mathbf{a}) \sin(2\pi f_c t)$$

and the received noise is bandpass noise which can also be put in a quadrature form

$$n(t) = x(t) \cos(2\pi f_c t) - y(t) \sin(2\pi f_c t)$$

Thus $r(t)$ can be written as

$$\begin{aligned} r(t) &= s(t, \mathbf{a}) + n(t) \\ &= \hat{I}(t, \mathbf{a}) \cos(2\pi f_c t) - \hat{Q}(t, \mathbf{a}) \sin(2\pi f_c t) \end{aligned} \quad (6.52)$$

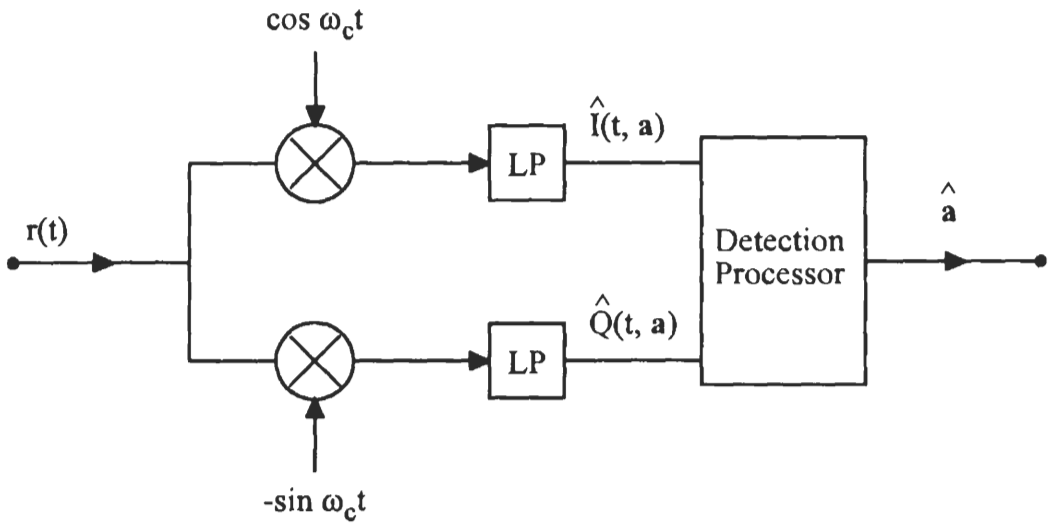


Figure 6.26 Basic quadrature receiver. From [9]. Copyright © 1986 Plenum.

where

$$\left. \begin{aligned} \hat{I}(t, \mathbf{a}) &= AI(t, \mathbf{a}) + x(t) \\ \hat{Q}(t, \mathbf{a}) &= AQ(t, \mathbf{a}) + y(t) \end{aligned} \right\}$$

These two quadrature components can be produced by the quadrature receiver in Figure 6.26. Using (6.52) in (6.51) and omitting double frequency terms and a constant of $1/2$, we have

$$\begin{aligned} Z_k(\tilde{\mathbf{a}}_k, \tilde{\theta}_k) &= \cos(\tilde{\theta}_k) \int_{kT}^{(k+1)T} \hat{I}(t, \mathbf{a}) \cos[\theta(t, \tilde{\mathbf{a}}_k)] dt \\ &\quad + \cos(\tilde{\theta}_k) \int_{kT}^{(k+1)T} \hat{Q}(t, \mathbf{a}) \sin[\theta(t, \tilde{\mathbf{a}}_k)] dt \\ &\quad + \sin(\tilde{\theta}_k) \int_{kT}^{(k+1)T} \hat{Q}(t, \mathbf{a}) \cos[\theta(t, \tilde{\mathbf{a}}_k)] dt \\ &\quad - \sin(\tilde{\theta}_k) \int_{kT}^{(k+1)T} \hat{I}(t, \mathbf{a}) \sin[\theta(t, \tilde{\mathbf{a}}_k)] dt \end{aligned} \quad (6.53)$$

This can be implemented by $4M^L$ baseband filters with the impulse responses

$$h_{c,i}(t, \tilde{\mathbf{a}}) = \begin{cases} \cos[\theta(T-t, \tilde{\mathbf{a}})] \\ 0, & \text{for } t \text{ outside } [0, T] \end{cases}$$

$$= \begin{cases} \cos[2\pi h \sum_{j=-L+1}^0 \tilde{a}_j q((1-j)T - t)] \\ 0 & \text{for } t \text{ outside } [0, T] \end{cases} \quad (6.54)$$

$$(i = 1, 2, \dots, 2M^L)$$

and

$$h_{s,i}(t, \tilde{\mathbf{a}}) = \begin{cases} \sin[\theta(T - t, \tilde{\mathbf{a}}_k)] \\ 0 & \text{for } t \text{ outside } [0, T] \end{cases}$$

$$= \begin{cases} \sin[2\pi h \sum_{j=-L+1}^0 \tilde{a}_j q((1-j)T - t)] \\ 0 & \text{for } t \text{ outside } [0, T] \end{cases} \quad (6.55)$$

$$(i = 1, 2, \dots, 2M^L)$$

There are M^L different $\tilde{\mathbf{a}}_k$ sequences. For each sequence a pair of matched filters is needed for $\hat{I}(t, \mathbf{a})$ and another pair is needed for $\hat{Q}(t, \mathbf{a})$. Thus total $2M^L$ cosine matched filters and $2M^L$ sine matched filters are needed. Realizing that every $\tilde{\mathbf{a}}_k$ sequence has a corresponding sequence with reversed sign, the number of matched filters can be reduced by a factor of 2. Figure 6.27, where $H = M^L$, is the optimum receiver based on (6.53) using $2M^L$ matched filters. The outputs of these filters are sampled at the end of the k th symbol interval, which produces the branch metrics $Z_k(\tilde{\mathbf{a}}_k, \tilde{\theta}_k)$. The processor in the figure is the Viterbi processor.

The Viterbi algorithm was discovered and analyzed by Viterbi [25] in 1967 for decoding convolutional codes. Later on it was extended to maximum likelihood sequence estimation (MLSE) for channels with intersymbol interference [26] and for partial response continuous phase modulation [8]. All of them have one thing in common: there is memory in the received signals. That is, the received signal values are determined by not only the current symbol, but also some or all previous symbols. Each of the possible combinations of the previous symbols constitutes a state. In the CPM case, the signal value is also affected by the cumulate phase θ_k (see Section 6.1.2). Assuming that $L - 1$ is the memory length, the symbol is M -ary, and θ_k has p different values, then there are total $S = pM^{L-1}$ states. Each of the possible transmitted sequence is a path in the S -state trellis. The MLSE receiver searches through the trellis to find the path which best matches to the transmitted sequence in the maximum likelihood sense. The Viterbi algorithm is an efficient algorithm to implement the ML search. The brutal-force search (i.e., test each path), is too time consuming. It needs to test M^N paths, where N is the number of symbols in a frame of data. To get an idea of the number of paths, let us assume $M = 2$ (binary), $N = 64$ (8 bytes), then $M^N = 1.89 \times 10^{19} = 1.89 \times 10^{10}$ billion paths. Searching this trellis is impossible in practice. However, with the Viterbi algorithm, as we will see shortly, the number of paths to be searched is only the number of states:

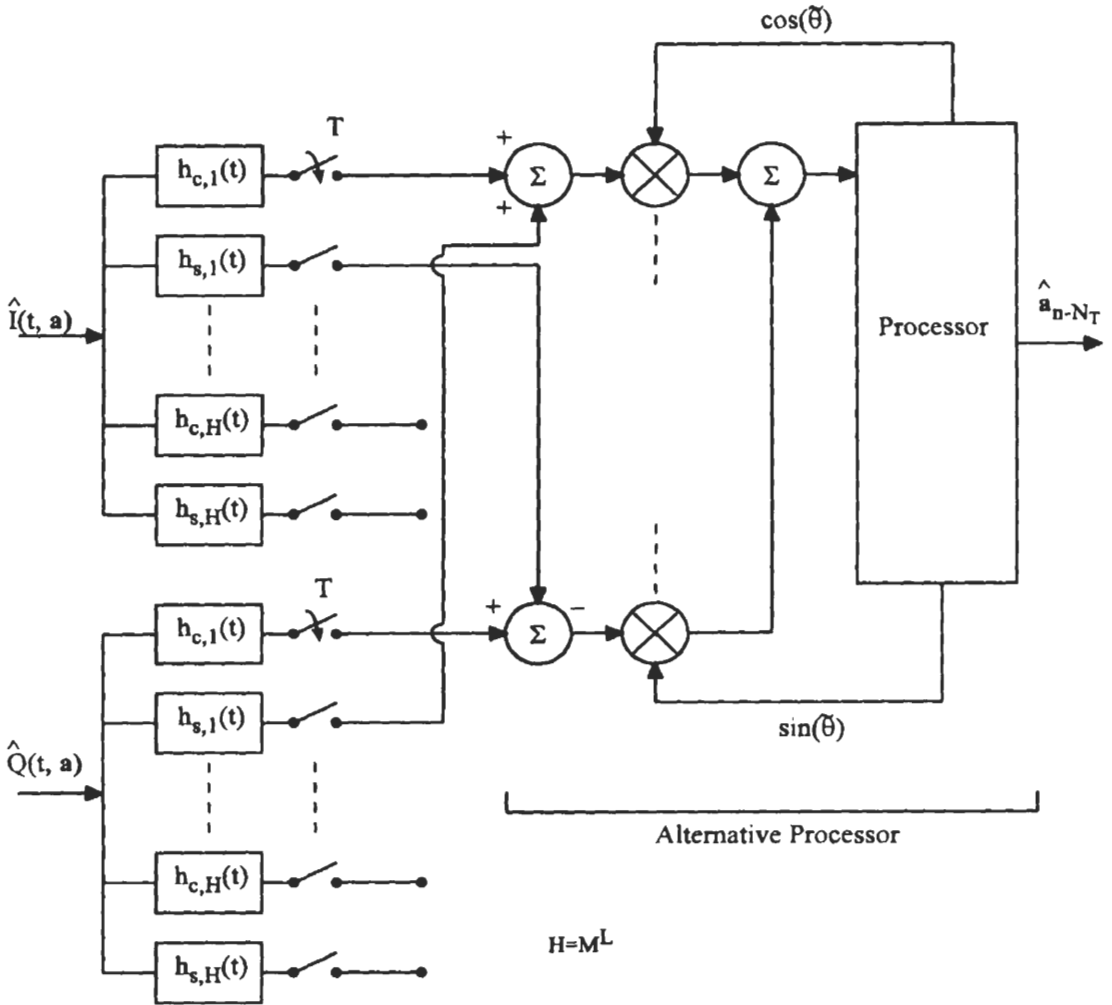


Figure 6.27 Matched filter bank. From [8]. Copyright © 1981 IEEE.

$S = pM^{L-1}$. Usually L and p are small integers. For example, if $L = 3$, $p = 3$, then $S = 12$ (Figure 6.5). The savings on the search time are tremendous, and the search time of the Viterbi algorithm is independent of the sequence length.

Now we describe the Viterbi algorithm for the partial response CPM case. Refer to Figure 6.5 while reading the following steps of the Viterbi algorithm.

1. At time $(k + 1)T$, for any state node, compute the M ($M = 2$ in Figure 6.5) branch metrics $Z_k(\tilde{\mathbf{a}}_k, \tilde{\theta}_k)$ for the incoming M branches using (6.53). This is done by the matched filter banks in Figure 6.27.
2. Add the M branch metrics to the M path metrics $l_{k-1}(\tilde{\mathbf{a}}_k)$ which are the path metrics for the M paths up to time kT and are connected with the M branches, respectively. Thus the path metrics are updated to time $(k + 1)T$. Denote them as $l_k^{(i)}(\tilde{\mathbf{a}}_{k+1})$, $i = 1, 2, \dots, M$.
3. Compare the M updated path metric $l_k^{(i)}(\tilde{\mathbf{a}}_{k+1})$ and choose the path with the largest path metric as the *survivor* path of the state node. Eliminate the other $M - 1$ paths. When step one to three are done for all states, there is only one survivor path for each state. The survivor paths' data and metrics must be stored.
4. Then advance time by T and repeat steps one to three until demodulation reaches the end of the sequence. Then choose the path with the largest path metric as the demodulated path, which is the maximum likelihood (ML) path. By retrieving the stored data of the ML path, we obtain the demodulated data.

We have asserted that the path found by the Viterbi algorithm is the ML path. This assertion is not difficult to prove. Assume that the ML path is eliminated by the algorithm at time t_i . This implies that the partial path metric of the survivor (denoted as $l(t_i)$) is larger than that of the ML path (denoted as $l_{ML}(t_i)$). That is

$$l(t_i) > l_{ML}(t_i)$$

Now if the remaining (future) portion of the ML path (denote its metric as $l_{ML}(t > t_i)$) is appended on to the survivor at time t_i , the total metric will be greater than the total metric of the ML path. That is

$$l(t_i) + l_{ML}(t > t_i) > l_{ML}(t_i) + l_{ML}(t > t_i)$$

However, this is impossible since the right-hand side is the ML path metric which is supposed to be the largest. Hence the ML path cannot be eliminated by the VA.

References on the Viterbi algorithm are widely available, such as [25], [27], and [28] or any coding book.

Since CPM signal is normally not in a block structure, a modified VA is used for the CPM, much the same way as a modified VA is used for decoding convolutional

codes [28]. It puts out one symbol at a time successively after a decoding delay that is the same for every symbol, and it accepts sequences of indefinite length. The surviving paths at each state of the trellis are saved only back to a certain point, a length called path memory N_T . The decision is made on the oldest symbol by certain criterion, such as taking the symbol that belongs to the majority of the surviving paths, or the symbol that belongs to the maximum likelihood path, or by simply choosing at random. The best criterion depends on conditions like SNR. The choice of N_T can be guided by the distance property of the CPM. If N_B is the length for the paths to reach the upper bound of the minimum distance, then the path memory N_T should be at least N_B , and experiment has shown that N_B is almost always enough [9].

The error probability of the perfect Viterbi demodulator, of course, is the one of the MLSD as given in Section 6.3.1, particularly, (6.39) and (6.40). The error probability of the modified Viterbi demodulator should be very close to the perfect one, especially at high SNR.

Simulation results of the error probability of the modified Viterbi receiver for some representative CPM schemes, such as 8-ary CPFSK and binary 3RC are shown in Figures 6.28 and 6.29 [9]. In Figure 6.28, the path memory has been set to 50 symbol intervals, which is more than enough for the minimum distance to occur. Twenty sample points per symbol interval have been used. Figure 6.28 shows two 8-ary CPFSK schemes, one with $h = 1/4$ and the other with $h = 5/11$. The 8-ary symbols are Gray coded. Figure 6.29 shows the results for binary 3RC with $h = 4/5$ when $N_T = 1, 2, \dots, 20$ and $N_T = \infty$. By increasing N_T the upper bound is improved at high SNR, but it is still loose at low SNR. The asymptotic gain is about 2 dB over QPSK, which can be fairly accurately predicted by $d_{\min}^2 = 3.17$ ($d_{\min}^2 = 2$ for QPSK). This conclusion holds for many schemes. That is, d_{\min} is sufficient for the characterization of performance in terms of symbol error probability.

More results have been obtained for a wide variety of CPM schemes in the literature, see for instance [29] and [30].

The complexity of the matched filter bank and the Viterbi algorithm limit the implementation of such an optimum receiver to small values of M and L . In the following sections, we will present some important research results on reduction of complexity of CPM receivers, sometimes at expenses of error performance.

6.5.4 Reduced-Complexity Viterbi Demodulator

A class of reduced-complexity Viterbi detectors for partial response CPM schemes has been proposed in [31]. The key concept is that the approximate receiver is based on a less complex CPM scheme than the transmitted scheme. The less complex scheme is a scheme with a shorter frequency pulse length and sometimes simpler frequency

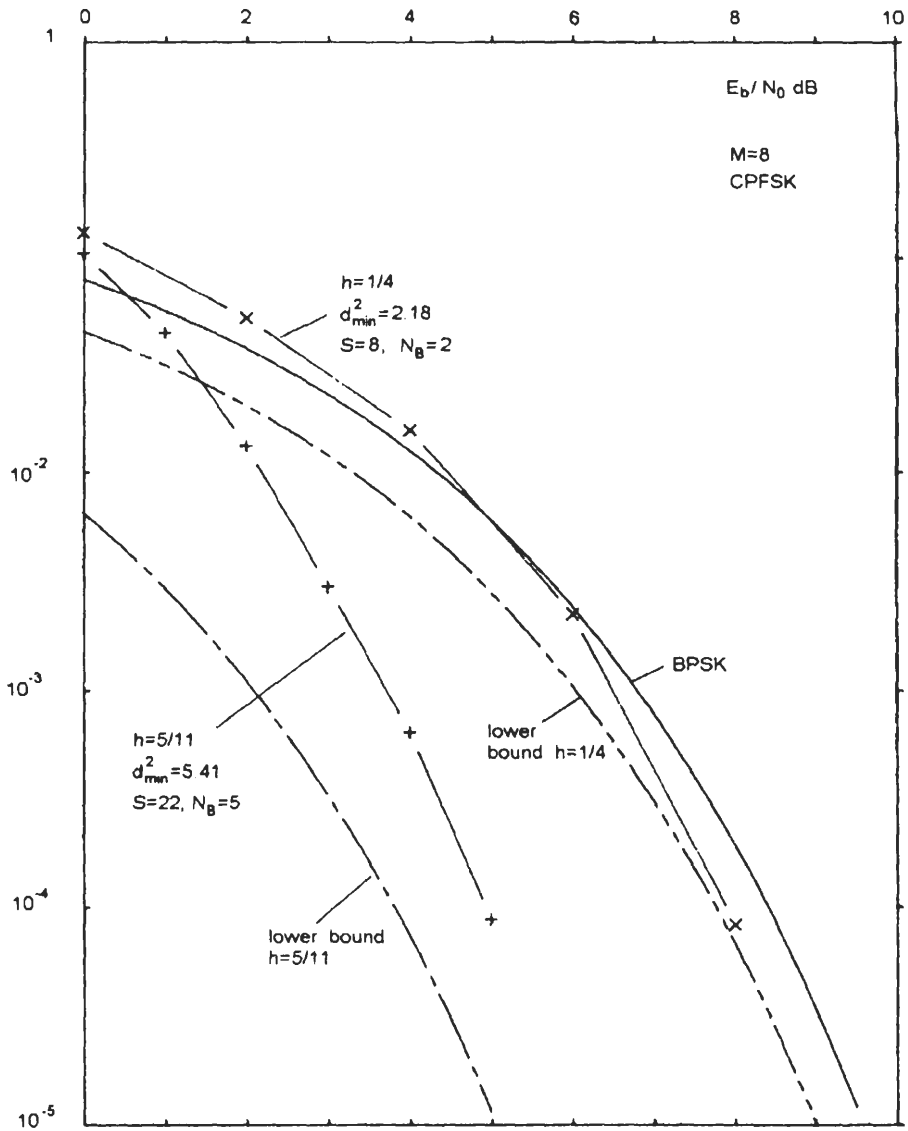


Figure 6.28 Simulated P_b for 8-ary CPFSK with comparisons with asymptotic lower bounds. Modified Viterbi receiver. From [9, p. 261]. Copyright © 1986 Plenum.

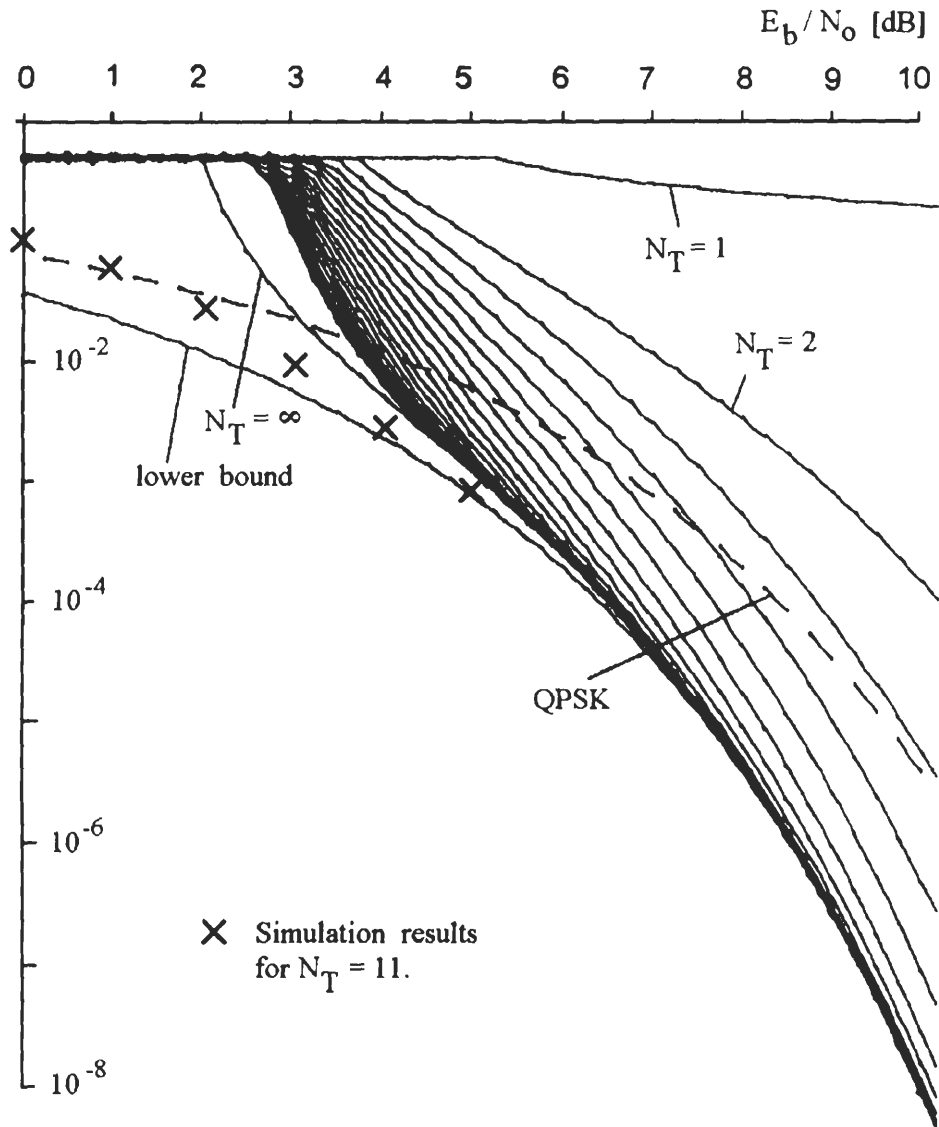


Figure 6.29 Simulated P_b for binary 3RC, $h = 4/5$, $N_T = 11$. Upper bounds for $N_T = 1, 2, \dots, 20$ and a lower bound are also shown. Modified Viterbi receiver. From [8]. Copyright © 1981 IEEE.

pulse. Figure 6.30 shows the transmitter phase tree for 3RC and the receiver phase tree for 2REC which is used to approximate the transmitter phase tree. The 2REC phase tree is shown with a small phase offset ($T/2$ in this case). From the figure we can see that the two trees are very close. Since all the data information is carried by the phase tree, we have reason to believe that using the approximate phase tree for demodulation can almost achieve the performance of the optimum receiver which uses the transmitter phase tree. If the transmitter pulse length is L_T and the receiver pulse length is L_R , the complexity reduction factor is $M^{(L_T - L_R)}$ in terms of both the number of receiver states and that of receiver filters.

For a particular transmitter frequency pulse $g_T(t)$, an optimum receiver frequency pulse $g_R(t)$ can be found so that the minimum distance of the receiver trellis is maximized. In particular, a piecewise linear function for $0 < t < L_RT$ is defined in [31] and used for optimization.

Simulation results reported in [31] are shown in Figures 6.31 and 6.32. In Figure 6.31, 4RC-4RC2 means the transmission is 4RC and the receiver is based on a 4RC pulse truncated to a length of two. 4RC-2T0.5 denotes the scheme with a transmitter of 4RC and a receiver based on the optimum piecewise linear function with $L_R = 2T$ and an index $h = 0.5$. The 2T0.5 receiver is optimum to the 4RC transmitter. The notations in Figure 6.32 are defined in the same manner. From the figures we can see that the loss of error performance is very small, which is about 0.1 dB at high SNR, while the receiver complexity reduction factor is two to four.

6.5.5 Reduction of the Number of Filters for LREC CPM

It has been shown that for LREC CPM, the size of the matched filter bank need only increase linearly with L [32]. In Section 6.5.3, we stated that there are $2M^L$ matched filters because there are M^L different values of $\theta(t, \tilde{\mathbf{a}}_k)$. Here we can show that there are only $L(M - 1) + 1$ different $\theta(t, \tilde{\mathbf{a}}_k)$ for LREC CPM. Thus the number of matched filters is only $2L(M - 1) + 2$ for LREC CPM.

The LREC phase pulse is given by

$$q(t) = \begin{cases} 0, & t < 0 \\ \frac{t}{2LT}, & 0 \leq t < T \\ \frac{1}{2}, & t \geq LT \end{cases}$$

In the interval $[0, T]$, it can be easily verified using an example (say 3REC),

$$a_0q(t) + a_{-1}q(t + T) + \cdots + a_{-(L-1)}q(t + (L - 1)T) = Aq(t) + B$$

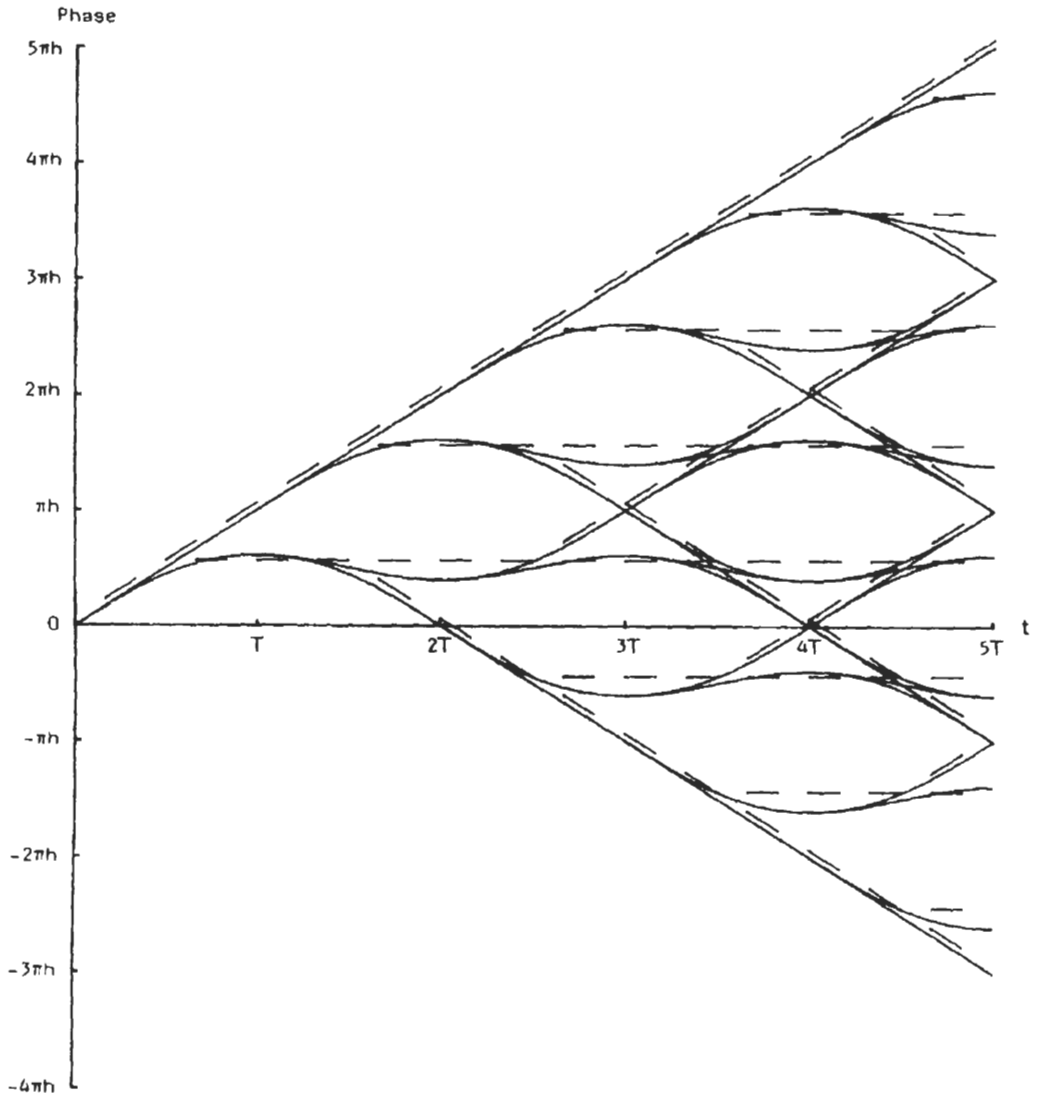


Figure 6.30 Transmitter phase tree (solid) for 3RC and receiver phase tree for 2REC. Correct timing, small phase offset ($T/2$). From [31]. Copyright © 1984 IEEE.

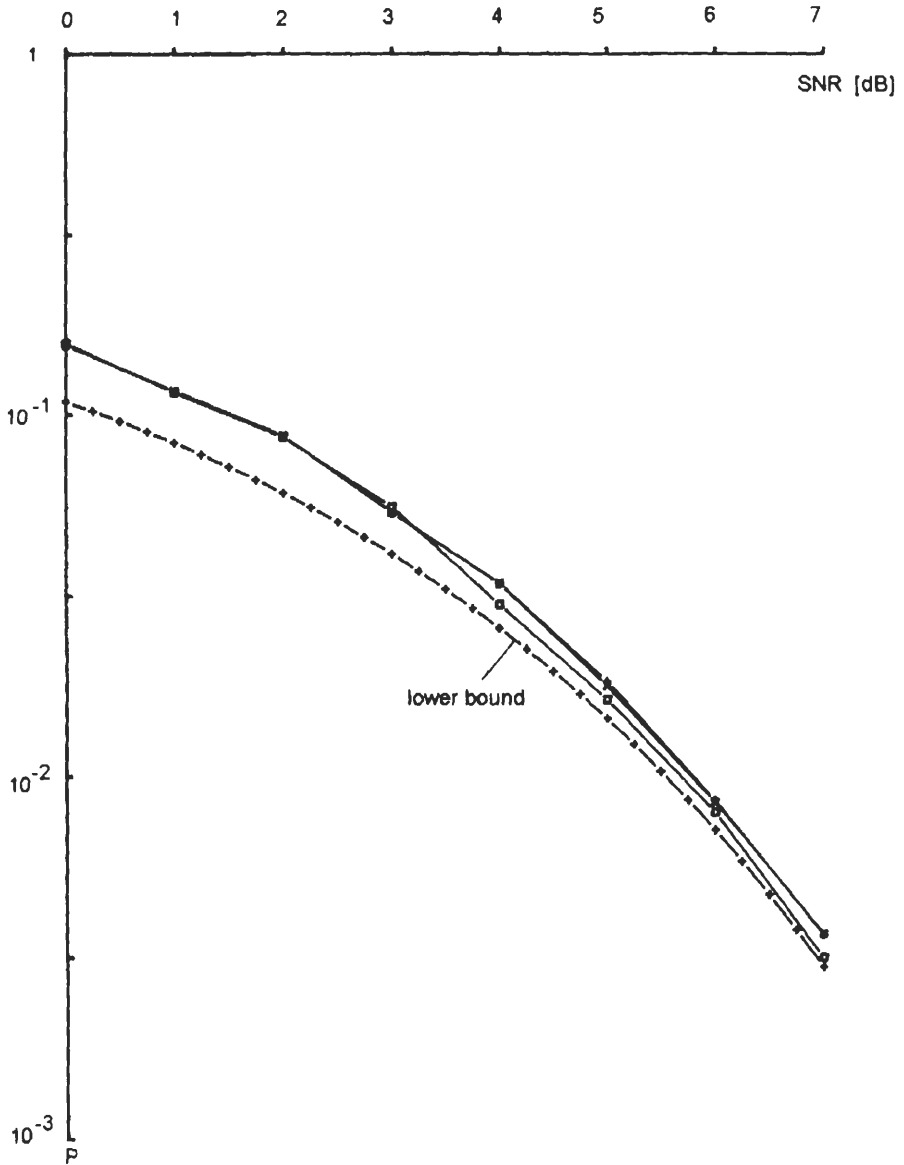


Figure 6.31 Simulated P_b for 4RC-4RC2 (+), 4RC-2T0.5 (x), and optimum 4RC (□) for $h = 1/2$. The lower bound for the optimum receiver is also shown. The results are based on 2500 errors. From [31]. Copyright © 1984 IEEE.

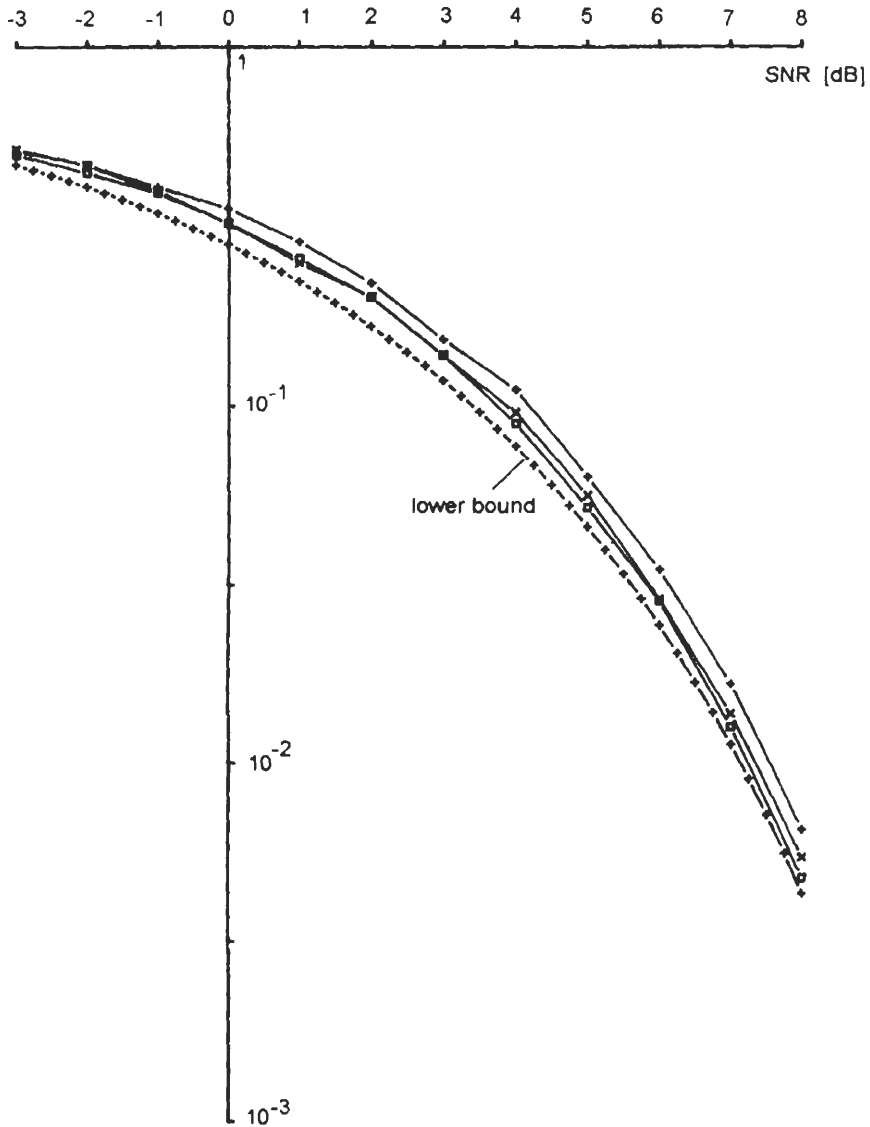


Figure 6.32 Simulated P_s for quaternary 2RC-2RC1 (+), 2RC-1T0.25 (x), and optimum 2RC (□) for $h = 1/4$. The lower bound for the optimum receiver is also shown. The results are based on 2500 errors. From [31]. Copyright © 1984 IEEE.

where

$$A = \sum_{i=0}^{L-1} a_{-i}, \quad B = \sum_{i=0}^{L-1} a_{-i} \left(\frac{i}{2L} \right)$$

During the interval $[kT, (k+1)T]$, the time-varying phase

$$\begin{aligned} \theta(t, \mathbf{a}_k) &= 2\pi h \sum_{i=k-L+1}^k a_i q(t - iT) \\ &= 2\pi h q(t - kT) \sum_{i=0}^{L-1} a_{k-i} + 2\pi h \sum_{i=0}^{L-1} a_{k-i} \left(\frac{i}{2L} \right) \end{aligned}$$

Where $a_j \in \{-(M-1), \dots, -1, 1, \dots, (M-1)\}$. We can write $a_j = 2u_j - (M-1)$ where $u_j \in \{0, 1, \dots, (M-1)\}$. Then

$$\theta(t, \mathbf{a}_k) = \theta_t(t, \mathbf{a}_k) + \theta_c(\mathbf{a}_k)$$

where

$$\theta_t(t, \mathbf{a}_k) = 4\pi h q(t - kT) \sum_{i=0}^{L-1} \left[u_{k-i} - \frac{M-1}{2} \right]$$

$$\theta_c(\mathbf{a}_k) = 4\pi h \sum_{i=0}^{L-1} \left[u_{k-i} - \frac{M-1}{2} \right] \left(\frac{i}{2L} \right)$$

Since $\sum_{i=0}^{L-1} u_{k-i} \in \{0, 1, \dots, L(M-1)\}$, there are only $L(M-1) + 1$ different $\theta_t(t, \mathbf{a}_k)$. Thus the ML demodulator only needs $2L(M-1) + 2$ matched filters to compute the metrics for all pM^L states as follows.

$$\begin{aligned} Z_k(\tilde{\mathbf{a}}_k, \tilde{\theta}_k) &= \cos[\tilde{\theta}_k + \theta_c(\tilde{\mathbf{a}}_k)] \int_{kT}^{(k+1)T} \hat{I}(t) \cos[\theta_t(t, \tilde{\mathbf{a}}_k)] dt \\ &\quad + \cos[\tilde{\theta}_k + \theta_c(\tilde{\mathbf{a}}_k)] \int_{kT}^{(k+1)T} \hat{Q}(t) \sin[\theta_t(t, \tilde{\mathbf{a}}_k)] dt \\ &\quad + \sin[\tilde{\theta}_k + \theta_c(\tilde{\mathbf{a}}_k)] \int_{kT}^{(k+1)T} \hat{Q}(t) \cos[\theta_t(t, \tilde{\mathbf{a}}_k)] dt \\ &\quad - \sin[\tilde{\theta}_k + \theta_c(\tilde{\mathbf{a}}_k)] \int_{kT}^{(k+1)T} \hat{I}(t) \sin[\theta_t(t, \tilde{\mathbf{a}}_k)] dt \end{aligned}$$

The complexity of the Viterbi processor remains unchanged since the number of states is still pM^L .

This simplified receiver also can be applied to any CPM with a piecewise linear pulse. For smoother pulses one can use a piecewise linear approximation to the pulse [32].

6.5.6 ML Block Detection of Noncoherent CPM

Maximum likelihood block detection of noncoherent full-response CPM is proposed in [33]. The derivation of this receiver starts with the likelihood function conditioned on the received signal phase. Then averaging it over the random phase leads to the likelihood function which in turn gives the sufficient statistics for decision making.

Assume the received signal $r(t)$ is observed for a N -symbol period. Denoting the M -ary symbol set as $\{\Delta_i = -M + (2i - 1); i = 1, 2, \dots, M\}$, let $\mathbf{i} = (i_1, i_2, \dots, i_N)$ be a sequence of indexes whose elements take on values from the set of integers $\{1, 2, \dots, M\}$. The detection rule is as follows. At n th symbol time, for each particular input data vector $\Delta = (\Delta_{i_1}, \Delta_{i_2}, \dots, \Delta_{i_N})$ compute

$$\beta_{\mathbf{i}} = \sum_{k=1}^N \Gamma_{i_k, N-k} C_k$$

where

$$\Gamma_{ij} = \int_{(n-j)T}^{(n-j+1)T} r(t) e^{-j2\pi h \Delta_{i,j} q(t-(n-j)T)} dt$$

and the C_i s are complex constants defined recursively as follows

$$C_1 = 1; \quad C_{k+1} = C_k e^{-j\pi h \Delta_{i_k}}; \quad k = 1, 2, \dots, N - 1$$

Then

$$\text{choose } a_{n-N+1} = \Delta_{i_1^*}, a_{n-N+2} = \Delta_{i_2^*}, \dots, a_n = \Delta_{i_N^*}, \text{ if } |\beta_{\mathbf{i}}|_{\max} = |\beta_{\mathbf{i}^*}|$$

where $\mathbf{i}^* = (i_1^*, i_2^*, \dots, i_N^*)$ is a particular value of \mathbf{i} and $\Delta^* = (\Delta_{i_1^*}, \Delta_{i_2^*}, \dots, \Delta_{i_N^*})$ is the corresponding input data vector.

The implementation of the above rule is straight forward in complex form (Figure 6.33). For MSK (IREC, $h = 1/2$), the receiver can be implemented in a real I-Q form as shown in Figure 6.34. The receiver has a front end (correlators to produce Γ_{ij}) analogous to that for a coherent CPM receiver. What is different from the coherent ML receiver is that the number of the correlators is M , not M^L . The complexity of the processor that follows depends on the length of the observation. This

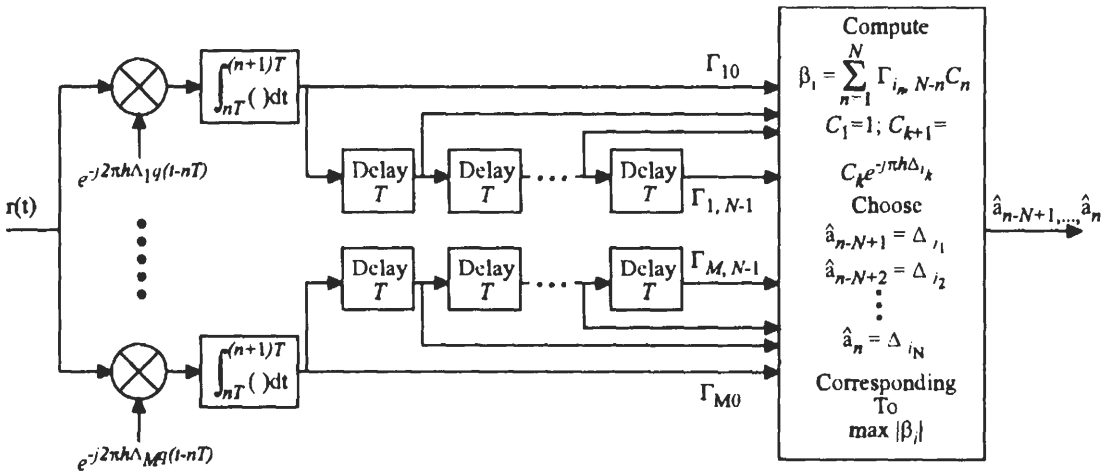


Figure 6.33 ML block estimator for noncoherent CPM based on an N -symbol observation. From [33]. Copyright © 1993 IEEE.

structure is much less complex than that of the coherent one.

The error performance analysis in [33] shows that large gain can be achieved by making block-by-block decisions in proportion to the length of the observation rather than making symbol-by-symbol decisions based on the same observation length. Figure 6.35 shows the P_b upper bounds for 1REC CPM with $h = 0.5$ (MSK) with N as a parameter. It is evident that dramatic improvement in P_b can be obtained with moderate values of N .

It should be pointed out that Figure 6.35 curves compare poorly with Figure 6.23 which is also for noncoherent CPM (not exactly MSK since $h = 0.715$). However, the noncoherent detector for Figure 6.23 detects only one symbol based on N (odd) observations, while the detector here detects a block of N symbols based on N observations. So the speed is N times faster here.

6.5.7 MSK-Type Demodulator

Recall that MSK is a member of the CPM class. It is a 1REC CPM with $h = 1/2$. Its demodulation can be performed by a parallel-type receiver (PMSK), or equivalently, by a serial-type receiver (SMSK), as studied in Chapter 5. Research shows that the MSK-type receiver works well for binary CPM schemes with $h = 1/2$ [9, 34–36]. Of course this receiver is not optimum in general, but the performance of this type of receiver is almost equal to the optimum Viterbi receiver for schemes with a moderate degree of smoothing, that is, overlapping frequency pulses of length L up to three to four symbol intervals, such as 3RC, 4RC, TFM, and some GMSK schemes.

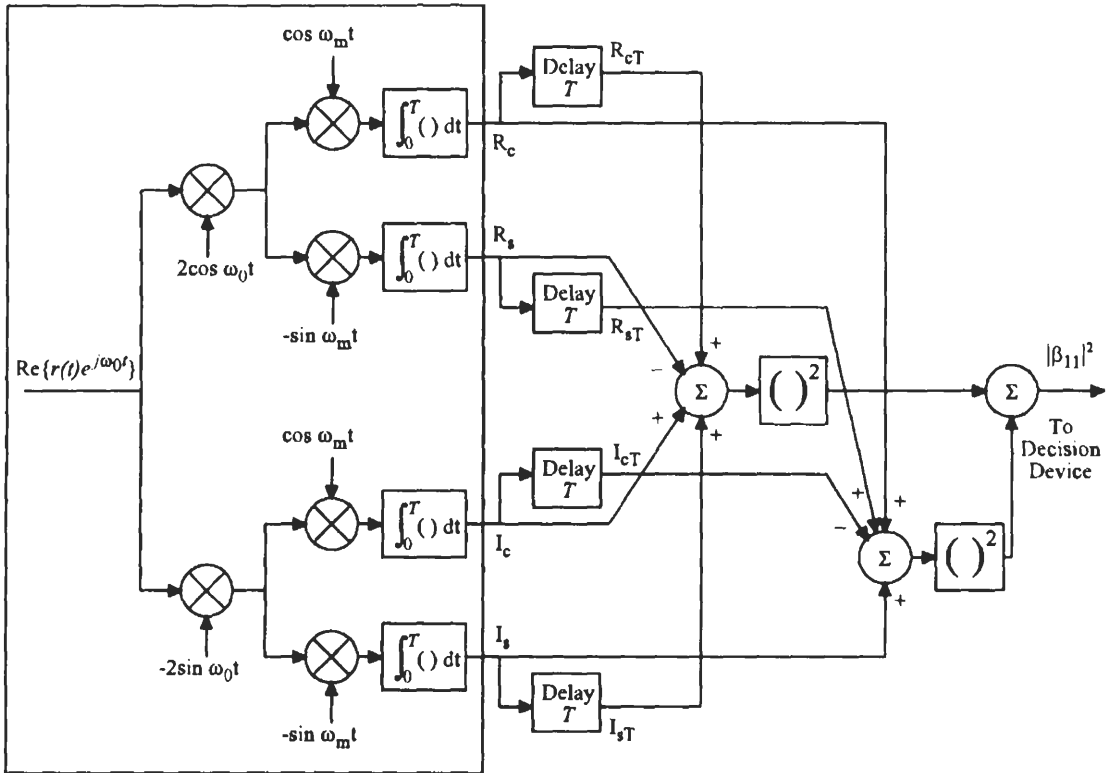


Figure 6.34 A real I-Q implementation of an ML block estimator for noncoherent MSK based on a two-symbol observation. From [33]. Copyright © 1993 IEEE.

Figure 6.36 is the structure of a parallel MSK-type receiver, where perfect carrier recovery and symbol timing are assumed, that is, the demodulation is coherent. This receiver works for binary CPM schemes with $h = 1/2$ because these schemes have $\cos[\Phi(t, \mathbf{a})]$ eye patterns that have maximum open at $t = (2n + 1)T, n = 0, 1, 2, \dots$. Figure 6.37 is the $\cos[\Phi(t, \mathbf{a})]$ eye pattern for 3RC, $h = 1/2$ CPM [36]. If the filter $a(t)$ is an ideal low-pass filter, the output of the upper arm of the receiver is exactly $\cos[\Phi(t, \mathbf{a})]$ and the output of the lower arm is exactly $\sin[\Phi(t, \mathbf{a})]$. The eye pattern of $\sin[\Phi(t, \mathbf{a})]$ is the same as $\cos[\Phi(t, \mathbf{a})]$ but shifted by T in time. Therefore the receiver samples the upper arm and lower arm at $t = (2n + 1)T$ and $t = 2nT$, alternatively. The “decision logic” observes the sampled signals for a length of N_T symbol intervals and makes an optimum decision on one symbol [9. p. 297]. The decision logic also performs differential decoding (for differential encoded data) and multiplexing. The filter $a(t)$ can be optimized to minimize the average symbol error probability [34, 37].

As in the MSK case, the parallel receiver in Figure 6.36 can be replaced by an

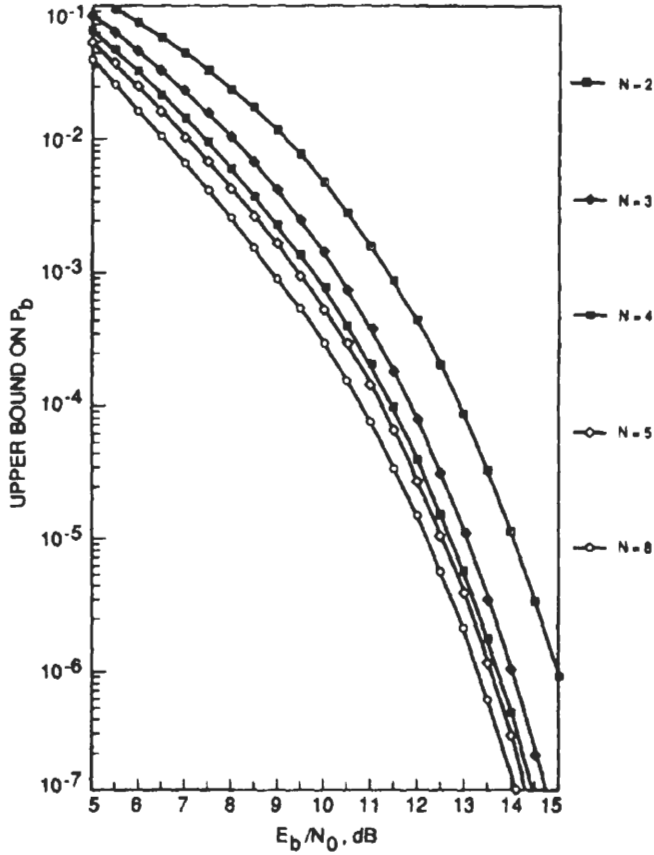


Figure 6.35 Upper bounds on P_b for MSK with multiple-symbol noncoherent detection. From [33]. Copyright © 1993 IEEE.

equivalent serial MSK-type receiver (Figure 6.38). For MSK, the filter $a(t)$ in the parallel receiver is [38]

$$a(t) = \begin{cases} \cos(\frac{\pi t}{2T}), & |t| \leq T \\ 0, & \text{otherwise} \end{cases}$$

and the corresponding serial filters are

$$h_1(t) = \begin{cases} \cos^2(\frac{\pi t}{2T}), & |t| \leq T \\ 0, & \text{otherwise} \end{cases}$$

$$h_2(t) = \begin{cases} -\frac{1}{2} \sin(\frac{\pi t}{T}), & |t| \leq T \\ 0, & \text{otherwise} \end{cases}$$

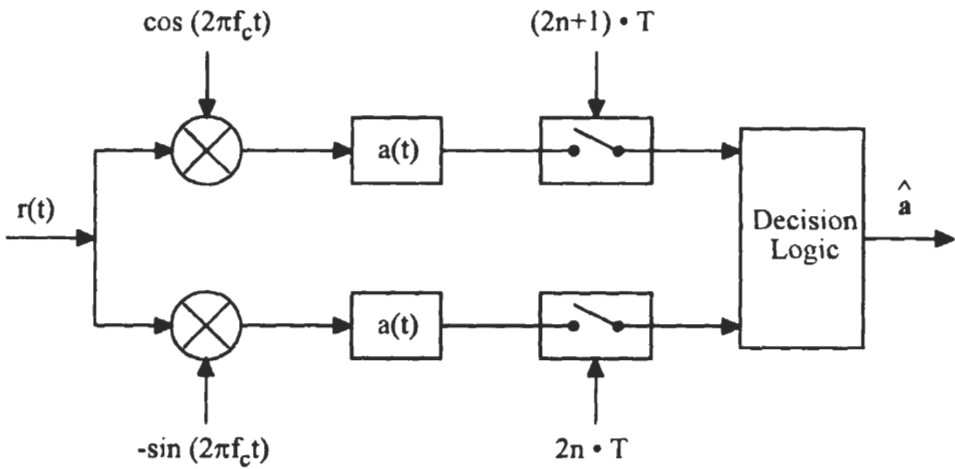


Figure 6.36 Parallel MSK-type receiver for binary CPM with $h = 1/2$. From [35]. Copyright © 1985 IEEE.

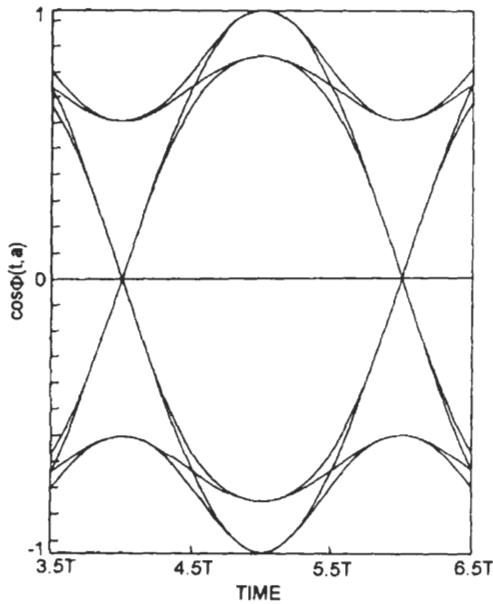


Figure 6.37 $\cos\Phi(t, a)$ eye pattern for parallel MSK-type receiver for binary 3RC, $h = 1/2$, scheme. From [36]. Copyright © 1982. AT&T. All rights reserved. Reprinted with permission.

(These two filters are denoted as $h_{mI}(t)$ and $h_{mQ}(t)$ in Figure 5.15, Chapter 5. Their frequency responses are shown in Figure 5.17.) The above filters in fact satisfy the following relations

$$\begin{cases} h_1(t) = a(t) \cos\left(\frac{\pi t}{2T}\right) \\ h_2(t) = -a(t) \sin\left(\frac{\pi t}{2T}\right) \end{cases} \quad (6.56)$$

It is therefore reasonable to assume that the serial receiver could also be used for general $h = 1/2$ binary CPM with the filters defined according to (6.56), and $a(t)$ the corresponding filter for the parallel receiver. Note that the local reference frequency of the serial receiver is $f_c - 1/4T$. Thus the lowpass signals in the quadrature arms of the serial receiver are $\cos[\Phi(t, \mathbf{a}) + \frac{\pi t}{2T}]$ and $\sin[\Phi(t, \mathbf{a}) + \frac{\pi t}{2T}]$ before the filters. The eye pattern of the sum of these two signals is shown in Figure 6.39 for binary, $h = 1/2$, 3RC scheme [35]. It can be seen that the serial eye pattern has open eyes at every $t = nT$. The sum of these signals are then sampled at every $t = nT$ and sent to the decision logic for decision making and differential decoding if needed.

It was shown that the serial and parallel receivers have equal performance, assuming perfect phase and time synchronization [35]. Figure 6.40 shows the error probability P in estimating the phase node θ_n for some binary CPM schemes with optimum filters in the MSK-type (parallel or serial) receiver. The bit error probability is about $2P$ [9, p. 299].

Serial and parallel MSK-type detection with phase errors and timing errors were compared for partial response CPM. It was found that the serial MSK-type receiver is less sensitive to phase errors while the parallel MSK-type receiver is less sensitive to symbol timing errors. Assuming that it is easier to obtain an accurate timing than phase synchronization, the serial receiver has advantage over the parallel one.

6.5.8 Differential and Discriminator Demodulator

Besides the optimum and suboptimum receivers described so far in this chapter, there exists simple noncoherent receivers. Figure 6.41 shows two such simple noncoherent receivers, differential and discriminator receivers for binary partial response CPM [9]. In the differential receiver the output of the filter $A(f)$ is a signal with time-varying amplitude $\mathcal{R}(t, \mathbf{a})$ and a distorted phase $\psi(t, \mathbf{a})$. The output of the differential detector would then become

$$y(t) \propto \mathcal{R}(t, \mathbf{a})\mathcal{R}(t - T, \mathbf{a}) \sin \Delta\psi(t, T, \mathbf{a})$$

where $\Delta\psi(t, T, \mathbf{a}) = \psi(t, \mathbf{a}) - \psi(t - T, \mathbf{a})$ is the phase difference between the current symbol and the previous symbol. The eye pattern of this signal has open eyes at every $t = kT$. This signal is sampled and a hard decision is made on the sample.

In the case of the discriminator, the output of the discriminator is the derivative of

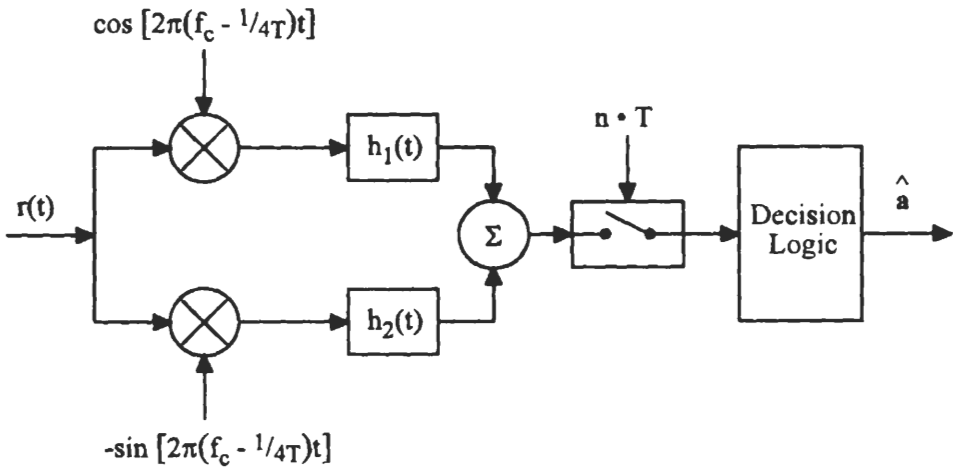


Figure 6.38 Serial MSK-type receiver for binary CPM with $h = 1/2$. From [35]. Copyright © 1985 IEEE.

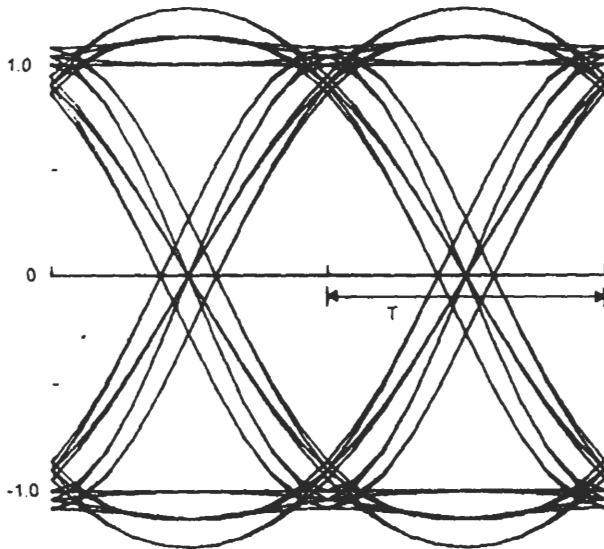


Figure 6.39 The eye pattern for serial MSK-type receiver for binary, $h = 1/2$, 3RC scheme. From [35]. Copyright © 1985 IEEE.

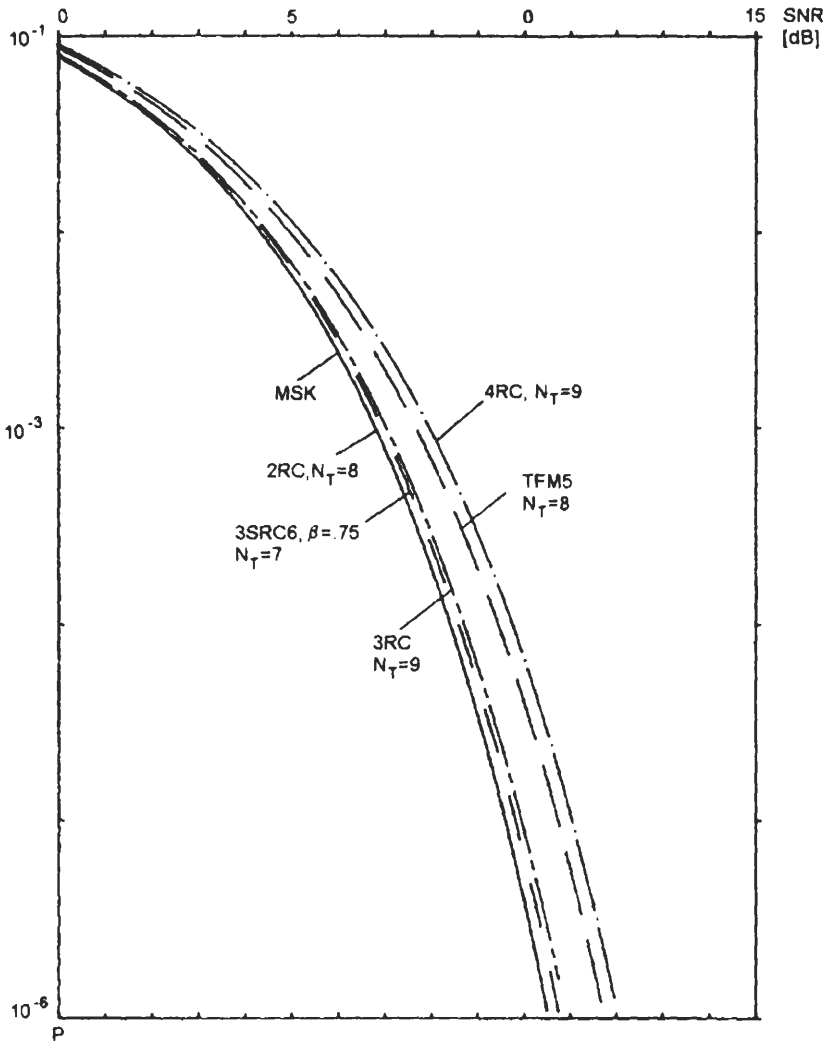


Figure 6.40 The error probability P for estimating phase node θ_n for some CPM schemes with optimum filters in the MSK-type (parallel or serial) receiver. The bit error probability is about $2P$. From [9, p. 320]. Copyright © 1986 Plenum.

the phase $\psi(t, \mathbf{a})$. An integrate-and-dump filter following the discriminator produces a phase difference $\Delta\Psi(t, T, \mathbf{a})$ which is slightly different from $\Delta\psi(t, T, \mathbf{a})$ [9, p. 269]. The hard decision detector decides $\tilde{\mathbf{a}}_{n-1} = 1$ if $\Delta\Psi(t, T, \mathbf{a}) > 0$, $\tilde{\mathbf{a}}_{n-1} = -1$ otherwise.

The filter $A(f)$ is chosen as a raised cosine (LRC) type in [9, p. 265]. As to the error performance of these two receivers, it is very difficult to analyze due to the nonlinearity. Some numerical results are available in [9, section 7.5.3]. It is expected that the simple receivers would have losses in error performance. However, for good combinations of modulations and differential detectors or discriminators, the loss at error rate 10^{-6} is only about 2 dB compared to coherent MSK. Figures 6.42 and 6.43 show some numerical results for binary CPM schemes, where 1RC/2RC means that the CPM scheme is 1RC and the receiver filter $A(f)$'s impulse response is 2RC (for LRC filter, the longer the L, the narrower the bandwidth required). Differential detection is best suited for schemes with $h \approx 1/2$, so that the index in Figure 6.42 is $1/2$. It is seen from Figure 6.42 that 1RC/3RC is quite poor and 1RC/2RC is the best, with a loss of about 2.5 dB over coherent MSK at $P_b = 10^{-4}$. The error performance of discriminator detection of $h = 1/2$ is very close to that of differential detector. Figure 6.43 shows some results for discriminator detection with $h = 0.62$. It turns out this index value makes the discriminator detection slightly better than differential detection: the loss of 1RC/2RC is about 2 dB over coherent MSK at $P_b = 10^{-4}$.

Sequence detection can also be applied to the differential and discriminator receivers since the memory in the continuous phase also can help in noncoherent reception. Receivers that use Viterbi processing following the discriminator [39–41, 43] or differential detector [3, 41–43] were proposed.

6.5.9 Other Types of Demodulators

In this section we present some less known, but maybe potentially useful CPM demodulators.

MSK and OQPSK are two well-known modulations that can be interpreted as a set of time/phase-shifted AM pulses. Laurent proved that any constant amplitude binary phase modulation can be expressed as a sum of a finite number of time limited amplitude modulated pulses (AMP) [44]. Based on this notion, Kaleh developed a coherent receiver using the Viterbi algorithm for binary partial response CPM [45]. The receiver's complexity is nearly the same as the old Viterbi receiver. However, the complexity can be reduced by using fewer matched filters and consequently smaller number of VA states while maintaining a near optimum error performance. A linear filter receiver can also be derived from the AMP representation. An example given in [45] is the binary GMSK with $BT = 0.25$ and $h = 0.5$, for which the simplified VA receiver only needs two matched filters and a four-state Viterbi processor, while

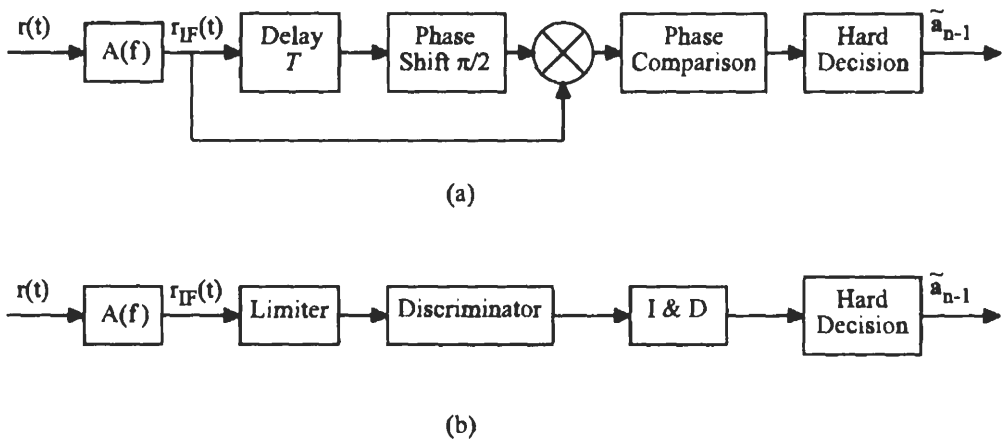


Figure 6.41 Differential (a) and discriminator (b) receiver for binary CPM schemes. From [9]. Copyright © 1986 Plenum.

the error performance loss is only about 0.24 dB. The error performance of the linear receiver is also only slightly worse than the simplified VA receiver.

The optimum ML coherent and noncoherent demodulators discussed in Sections 6.5.1 and 6.5.2 can be simplified. The idea is to use a matched filter that matches to the average of all signals having the same first symbol a_1 . Thus the total number of filters (or correlators) is reduced by a factor of M^{N-1} where N is the length in symbols of the observation. This suboptimum receiver is called average matched filter (AMF) receiver and is given in [46]. However, the error performance of this type of AMF receiver is not good since the received signal is poorly matched. For example, the loss of CPFSK at $P_b = 10^{-4}$ is about 3 dB [21, 46]. Another type of AMF receiver is proposed in [9] for partial response CPM. The impulse response of the filters is the average over all symbols except the prehistory and the decision symbol, where prehistory refers to the $L - 1$ symbols before the decision symbol.

In Section 6.5.4 we have explored the reduced state Viterbi demodulator. On the other hand, complexity reduction of the ML demodulator can be achieved by using search algorithms other than the Viterbi algorithm. Sequential algorithms are a class of suboptimum algorithms, which search through the state tree or trellis along only one path. The best known sequential algorithms are the Fano algorithm and the stack algorithm [28]. Other algorithms compromise between the Viterbi algorithm and the sequential algorithms, thus maintaining most of the optimum error performance while reducing the computational complexity. Refer to [47] for a survey of search algorithms.

In the above discussion, either we assume that the demodulation is coherent (i.e.,

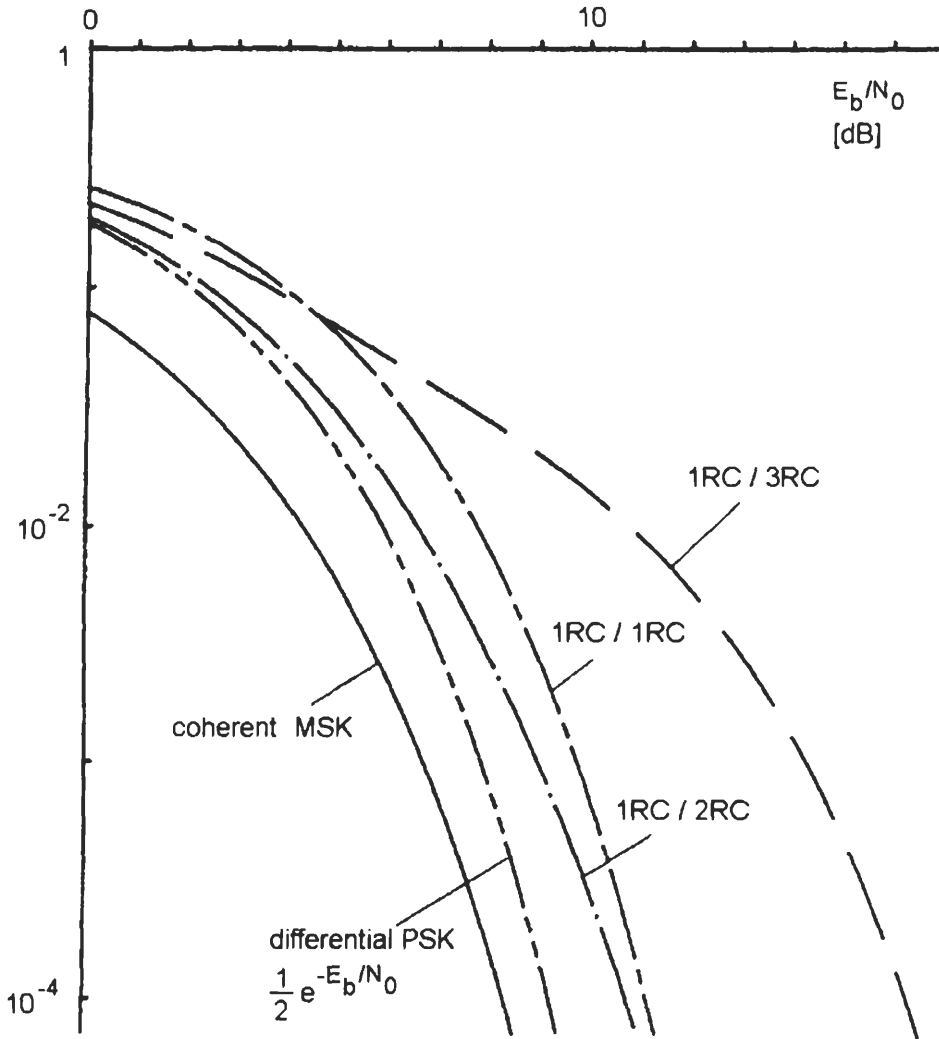


Figure 6.42 P_b for differential detection of 1RC with $h = 1/2$. From [9, p. 273]. Copyright © 1986 Plenum.

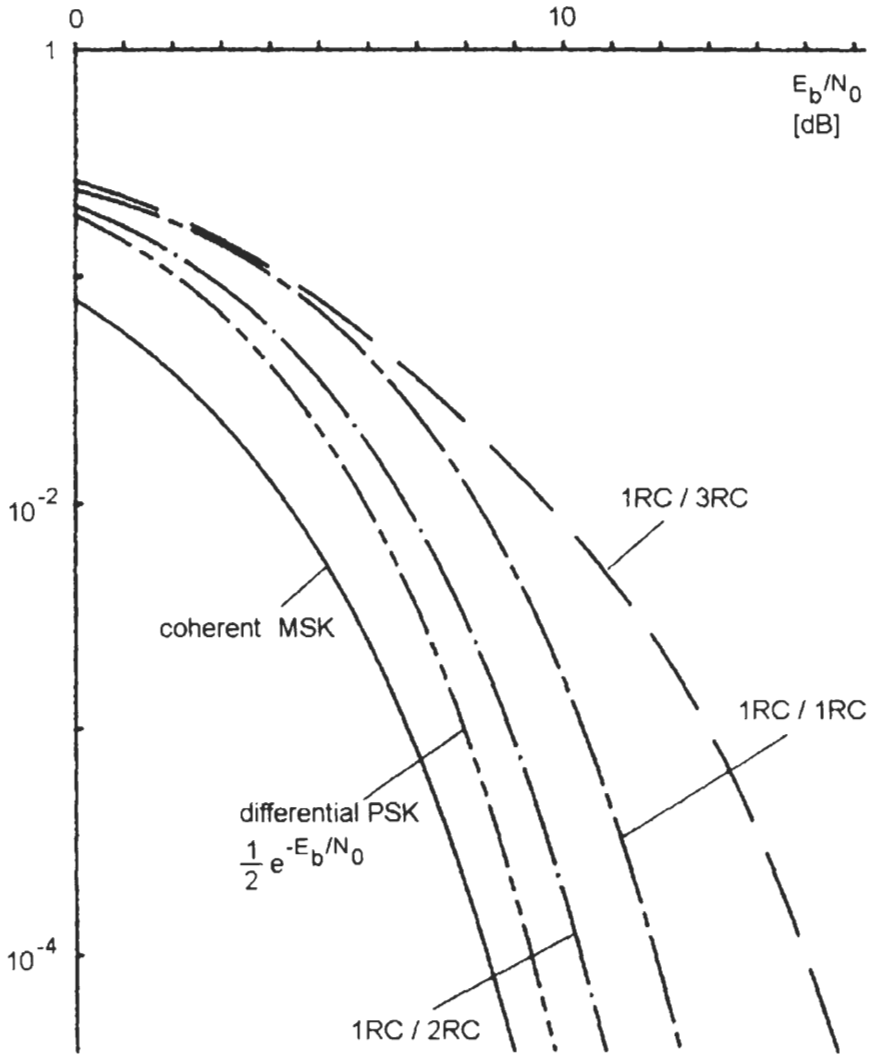


Figure 6.43 P_b for discriminator detection of 1RC with $h = 0.62$. From [9, p. 274]. Copyright © 1986 Plenum.

the received carrier phase is completely known (synchronized) to the receiver), or we assume that the demodulation is noncoherent (i.e., the received carrier phase is completely unknown (random) to the receiver). The complete randomness of the phase error in a noncoherent case is manifested by assuming it to have a uniform distribution in $[0, 2\pi]$. The practical situation of a coherent demodulator is in between. The best we can hope is that the carriers are synchronized with a phase error that fluctuates around a mean value zero. To deal with this situation, partial coherent receivers are considered in [9] where the phase error is assumed to have a PDF other than uniform, with various degrees of randomness.

Before we end this section, we would like to point out that demodulation for CPM has been, and still is, an active area of research. New ideas about CPM demodulator are expected to appear in the literature from time to time in the future.

6.6 SYNCHRONIZATION

Perhaps synchronization is the most difficult part of the CPM technique. Synchronization techniques for special CPM cases, like MSK, are relatively mature and in practical use. In this section we will discuss synchronizers for general CPM schemes. Some are extended from the MSK synchronizer and others are based on new ideas. Research on this subject is still active. New results are expected to appear in the future.

6.6.1 MSK-Type Synchronizer

The synchronization technique for MSK [48] (Figure 5.11) was first generalized by Lee [49] to include M-ary data and any rational modulation index, but the frequency pulse is still IREC. This synchronizer was further generalized by Sundberg [9] to be useful for any CPM schemes with rational index. Figure 6.44 is the generalized synchronizer. Now we explain how it works. The modulation index is assumed rational as $h = k_1/k_2$, where k_1, k_2 are nonzero integers. The nonlinearity in the synchronizer will raise the received signal to the power of k_2 .

$$[r(t)]^{k_2} = [s(t) + n(t)]^{k_2}$$

and one of the resultant components is [50]

$$\frac{[2E_s/T]^{k_2/2}}{2^{k_2-1}} \cos[2\pi k_2 f_c t + k_2 \Phi(t, \mathbf{a})]$$

The amplitude of this signal is not important in the following discussion. What is

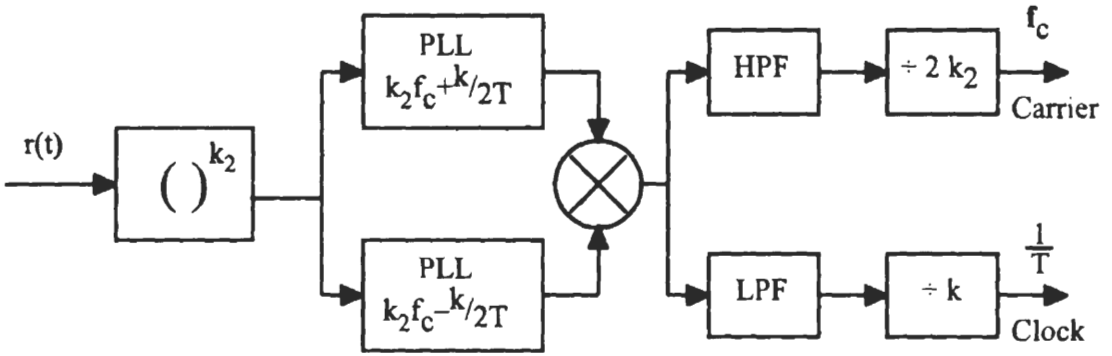


Figure 6.44 CPM synchronizer generalized from MSK synchronizer. After [9].

important is that this is a CPM signal with carrier frequency $k_2 f_c$ and phase

$$k_2 \Phi(t, \mathbf{a}) = k_2 2\pi \frac{k_1}{k_2} \sum_i a_i q(t - iT) = 2\pi k_1 \sum_i a_i q(t - iT)$$

which has an integer index $h' = k_1$. Recall that in Section 6.2.1, we state that when h' is an integer the PSD of the CPM signal contains a discrete part. The discrete frequency components appear at

$$f = \begin{cases} k_2 f_c \pm 2k/2T, & k = 0, 1, 2, \dots, \text{ for even } h' \\ k_2 f_c \pm (2k + 1)/2T, & k = 0, 1, 2, \dots, \text{ for odd } h' \end{cases} \quad (6.57)$$

Figure 6.45 illustrates such a scenario, where the spectrum is drawn in the baseband. Combining even and odd h' cases together, we can see

$$f = k_2 f_c \pm k/2T, \quad k = 0, 1, 2, \dots,$$

The two phase-lock loops (or narrow-band bandpass filters) in Figure 6.44 can select any pair of frequencies $k_2 f_c \pm k/2T$. The output of the mixer contains the sum and the difference of these two frequencies: $2k_2 f_c$ and k/T . Since in most cases the strongest components appear at $h'/2T$, thus the frequencies selected by the PLLs are usually $k_2 f_c \pm h'/2T$. The difference frequency would be $h'/T = k_1/T$. The high-pass filter and the low-pass filter pick up one of them. The frequency dividers divide two frequencies to produce f_c for the carrier and $1/T$ for the symbol timing.

The recovered carrier has a phase ambiguity of $2\pi/2k_2 = \pi/k_2$ because the received carrier frequency f_c has been multiplied by $2k_2$ in the recovery process. The symbol timing phase ambiguity is $2\pi/k_1$ for similar reasons. Recall that if $h = 2q/p$

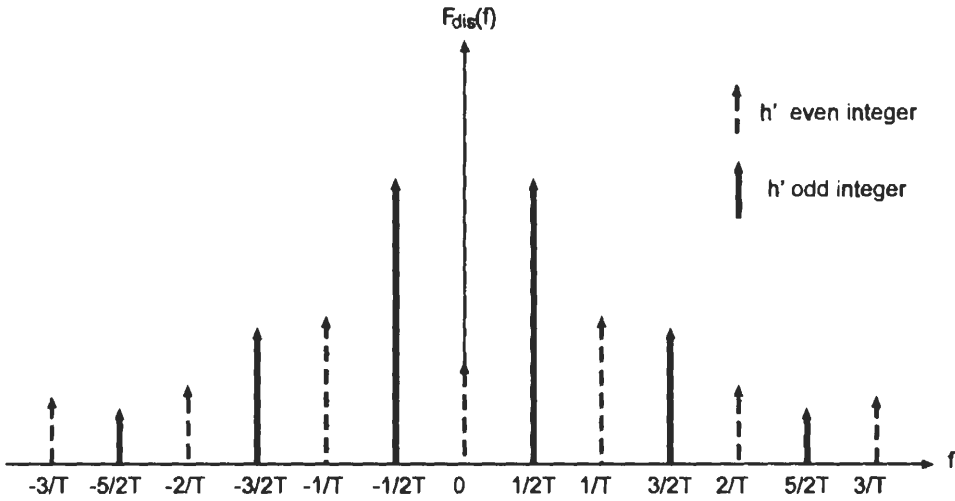


Figure 6.45 Discrete frequency components of CPM when h is an integer. From [9]. Copyright © 1986 Plenum.

where q and p are integers with no common factors, then there are p phase states in the signal. A phase shift of $2\pi/p$ merely renumbers the phases states. The trellis remains the same. Thus the phase of the carrier only has to be known modulo $2\pi/p$ if the Viterbi receiver is used. This greatly reduces and in most cases eliminates the effect of carrier phase ambiguity. For example, in MSK, $h = 1/2 = 2/4$, $p = 4$, $k_1 = 1$, $k_2 = 2$, the carrier phase ambiguity is $\pi/k_2 = \pi/2$, but the Viterbi processor can tolerate a phase shift of $2\pi/p = \pi/2$, thus the effect of carrier phase ambiguity is completely eliminated. However, optimum demodulation of MSK need not be performed by the Viterbi processor, rather, it can be performed by the quadrature receiver depicted in Figure 5.10. The carrier and the symbol timing are recovered by the circuit in Figure 5.11. It has a phase ambiguity of π which can be resolved by differentially encoding the data. The symbol phase ambiguity must be resolved in some way if $k_1 \neq 1$. If $k_1 = 1$, like in MSK, there is no phase ambiguity. Performance analysis results of the synchronizer are available in [9] and [51].

There are some problems with the MSK-type synchronizer. First, both carrier phase and symbol timing are recovered from the same outputs of the two tracking loops. As a result, the equivalent bandwidths for both carrier recovery and symbol-timing recovery are the same. For carrier recovery, the bandwidth of the PLLs cannot be made arbitrarily small due to factors such as phase noise and fading. As a result, the PLL bandwidth may be too wide for symbol-timing recovery. The recovered clock may suffer from a large level of phase jitter. Furthermore, since the mean time between cycle slips decreases as the PLL bandwidth is increased, the recovered

timing may have an undesirable rate of cycle slipping. The second problem of the MSK-type synchronizer is the difficulty of acquiring signals with a large Doppler shift with respect to the data rate. If the loops are to be swept, then particular care must be taken so that the two loops do not lock on to the same frequency. A signal dropout problem also exists in the MSK-type synchronizer. Certain data sequences may lead to the transmission of only one tone, so that one of the loops loses lock and returns to its rest frequency. This situation produces both carrier and clock tracking errors. Finally, the MSK-type synchronizer is not easy to be realized in VLSI, which reduces its practical significance.

6.6.2 Squaring Loop and Fourth-Power Loop Synchronizers

To overcome some of the shortcomings of the MSK-type synchronizer, a squaring loop and a fourth-power loop synchronizer were proposed by [52] for binary CPM schemes with $h = 1/2$ (Figure 6.46). These two synchronizers are for carrier recovery only. The timing recovery must be done separately. Thus its bandwidth can be selected independently of the carrier recovery bandwidth.

Figure 6.46(a) is the squaring loop synchronizer. Since we assume that the received CPM is binary with $h = 1/2 = k_1/k_2$, according to the argument in the previous subsection, the squaring operation generates a CPM signal at $2f_c$ with $h' = k_1 = 1$. This leads to discrete spectral lines at $2f_c \pm (2k + 1)/2T$, k integer, with $2f_c \pm 1/2T$ the strongest. The lines are shifted to $2f_c$ by multiplication with $\cos[\pi(t - T_d)/T]$, where T_d is the symbol timing delay (error). It is easy to see that when $T_d \neq 0$, the shifted spectral lines cannot be at $2f_c$ exactly. Therefore the prior knowledge of the symbol timing is essential to this synchronizer. It is shown in [52] that the phase error variance of this synchronizer increases with the increase of T_d . Other than that, the squaring loop's jitter performance is essentially the same as the MSK-type synchronizer, but the latter's practical limitations are eliminated. Most importantly, the squaring loop leaves the symbol timing to be recovered separately. The timing recovery bandwidth can be made much smaller than the carrier recovery bandwidth. Consequently the rate of clock slips can be reduced. The phase ambiguity of the squaring loop is π due to the squaring operation, which can be eliminated by differential encoding the data symbols.

Figure 6.46(b) is the fourth-power loop synchronizer. After the fourth-power nonlinearity, the signal contains a component $\cos[8\pi f_c t + 4\Phi(t, \mathbf{a})]$ which has an even index $h' = 2$. Thus the discrete lines are at $4f_c \pm k/T$, k integer. Setting $k = 0$, we obtain a line at $4f_c$ which is strong for most of the popular binary, $h = 1/2$ CPM schemes except MSK, for which the magnitude of this spectral line happens to be zero [52, Figure 4]. Thus this loop will not work for MSK. The advantage of the fourth-power loop is that it does not require prior knowledge of the symbol timing.

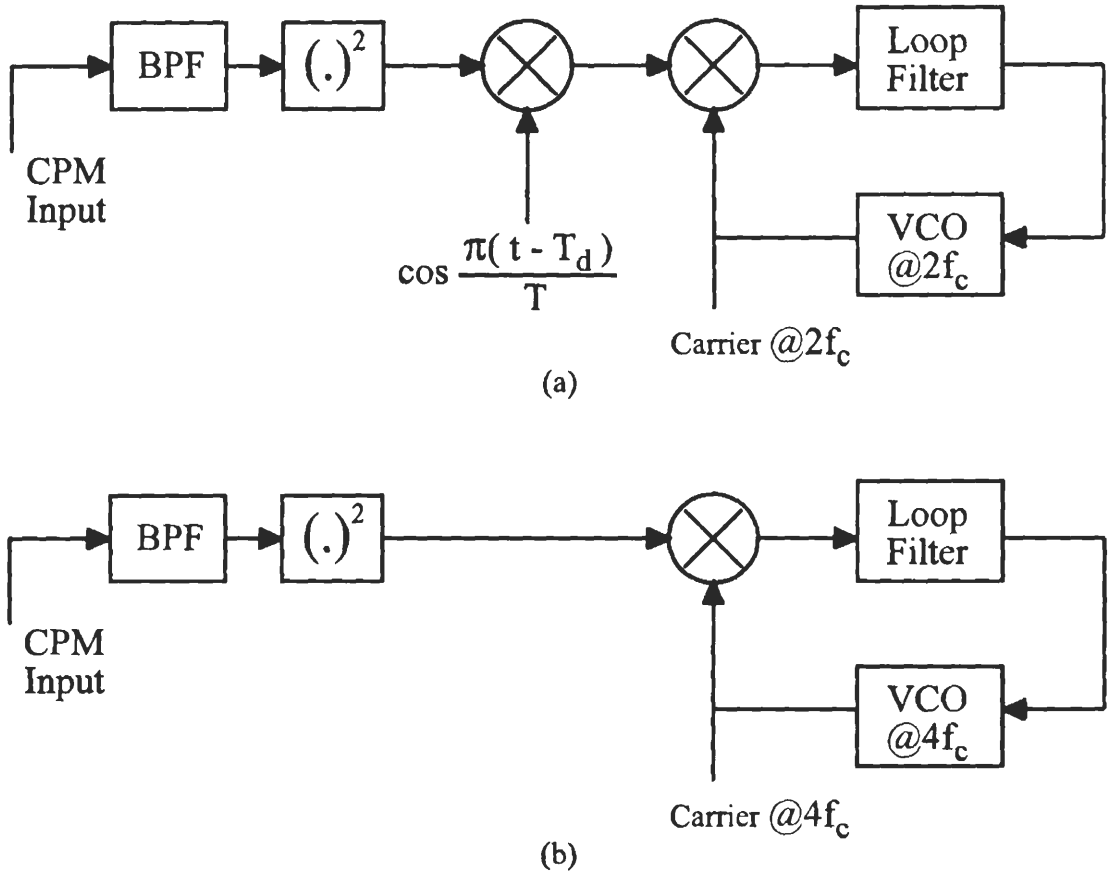


Figure 6.46 Squaring loop and fourth-power loop synchronizers for binary CPM with $h = 1/2$. From [52]. Copyright © 1989 IEEE.

As a result, it allows carrier phase and symbol timing to be recovered sequentially. A faster acquisition can be achieved.

The results in [52, Fig. 4] show that the fourth-power loop is inferior to the squaring loop at lower SNR and the situation is reversed at higher SNR. The two loops were evaluated with several popular binary $h = 1/2$ CPM schemes, including 2RC, 3RC, GMSK, TFM, and DMSK (duobinary MSK). It was found that the best performance (phase variance) is achieved with DMSK.

6.6.3 Other Types of Synchronizer

The synchronizers described above are relatively simple. More sophisticated synchronizers are reported in the literature. A synchronizer using the maximum a posteriori (MAP) technique to jointly estimate the carrier phase and symbol timing for

B_bT	90%	99%	99.9%	99.99%
0.2	0.52	0.79	0.99	1.22
0.25	0.57	0.86	1.09	1.37
0.5	0.69	1.04	1.33	2.08
MSK	0.78	1.20	2.76	6.00
TFM	0.52	0.79	1.02	1.37

Table 6.2 GMSK percentage bandwidth.

MSK is reported in [53]. A MAP symbol synchronizer for partial-response CPM is proposed in [54]. More synchronizers are mentioned in [9]. All these synchronizers are too complicated. More research is needed to make them easier to implement in practice.

6.7 GAUSSIAN MINIMUM SHIFT KEYING (GMSK)

GMSK was first proposed by Murota and Hirade for digital mobile radio telephony [3]. Currently GMSK is used in the U.S. cellular digital packet data (CDPD) system and European GSM system [55, p. 265]. The wide spread use is due to its compact power spectral density and excellent error performance.

GMSK, as its name suggests, is based on MSK and is developed to improve the spectral property of MSK by using a premodulation Gaussian filter. The transfer function of the filter is

$$H(f) = \exp \left\{ - \left(\frac{f}{B_b} \right)^2 \frac{\ln 2}{2} \right\} \quad (6.58)$$

where B_b is the 3-dB bandwidth. We have defined the frequency pulse $g(t)$ of GMSK in (6.8). This $g(t)$ can be generated by passing a rectangular pulse $rec(t/T)$ through this filter [56, p.183].

The power spectral density of GMSK is shown in Figure 6.47, where B_bT is a parameter. The spectrum of MSK ($B_bT = \infty$) is also shown for comparison. It is clear that the smaller the B_bT , the tighter the spectrum. However, the smaller the B_bT , the farther the GMSK is from the MSK. Then the degradation in error performance using an MSK demodulator will be larger. We will see this shortly. A fact that needs to be pointed out is that the spectrum of GMSK with $B_bT = 0.2$ is nearly equal to that of TFM. Table 6.2 shows the bandwidth (normalized to symbol rate) for the prescribed percentage of power within the bandwidth.

The modulator for GMSK currently used in CDPD and GSM systems is of the

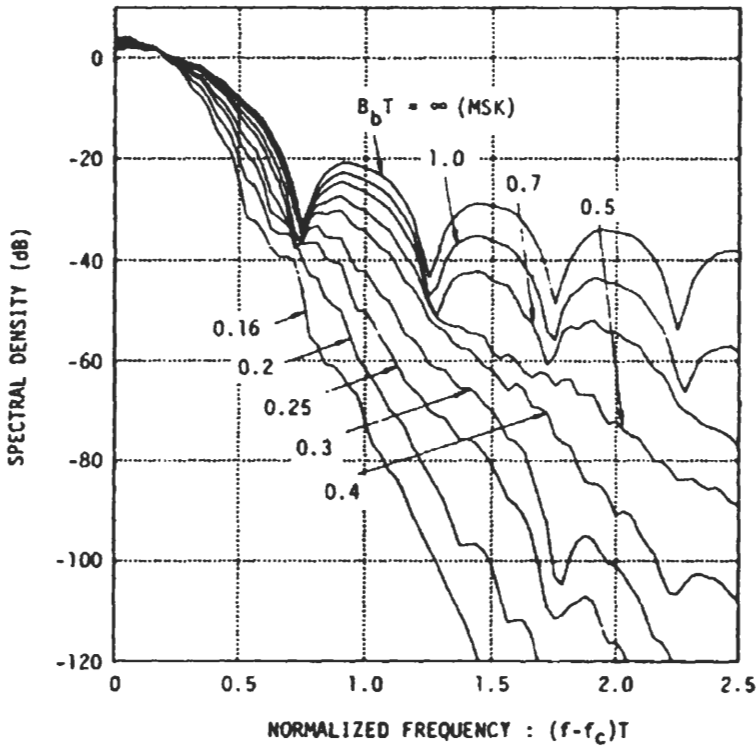


Figure 6.47 Power spectra of GMSK. From [3]. Copyright © 1981 IEEE.

type of Figure 6.13, where the filter must be a Gaussian filter and the FM modulator must be an MSK modulator (that is, an IREC modulator with $h = 0.5$). Of course other types of CPM modulators can also be used for GMSK.

The demodulation for GMSK of course can be done using all types of demodulators that we described in this chapter. The demodulator suggested in [3] is the Costas loop type shown in Figure 6.48 where demodulation and carrier recovery are combined. Clock recovery is still separated. Figure 6.49 is the digital implementation of Figure 6.48. In Figure 6.49, two D flip-flops act as the quadrature product demodulators and both the exclusive-or logic circuits are used for the baseband multipliers. The mutually orthogonal reference carriers are generated by the use of two D flip-flops. The VCO center frequency is then set equal to four times carrier center frequency. This circuit is considered to be especially suitable for mobile radio units which must be simple, small, and economical.

The theoretical BER performance of the coherent GMSK is of course described by the expressions given in Section 6.3.1. Figure 6.50 shows some measured BER

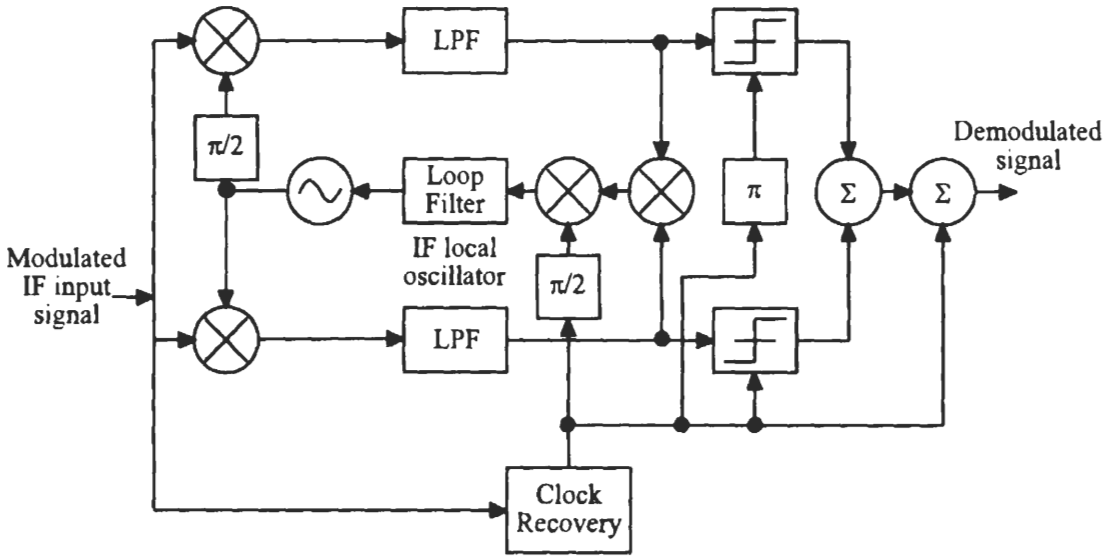


Figure 6.48 Block diagram of Costas loop demodulator for GMSK. From [3]. Copyright © 1981 IEEE.

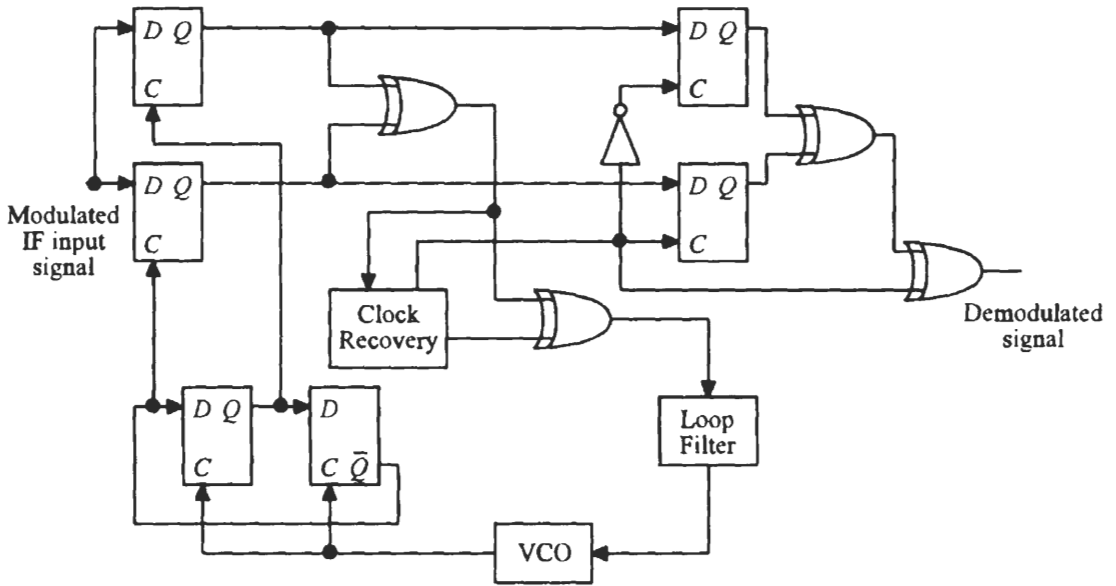


Figure 6.49 Digital circuit implementation of the Costas loop demodulator for GMSK. From [3]. Copyright © 1981 IEEE.

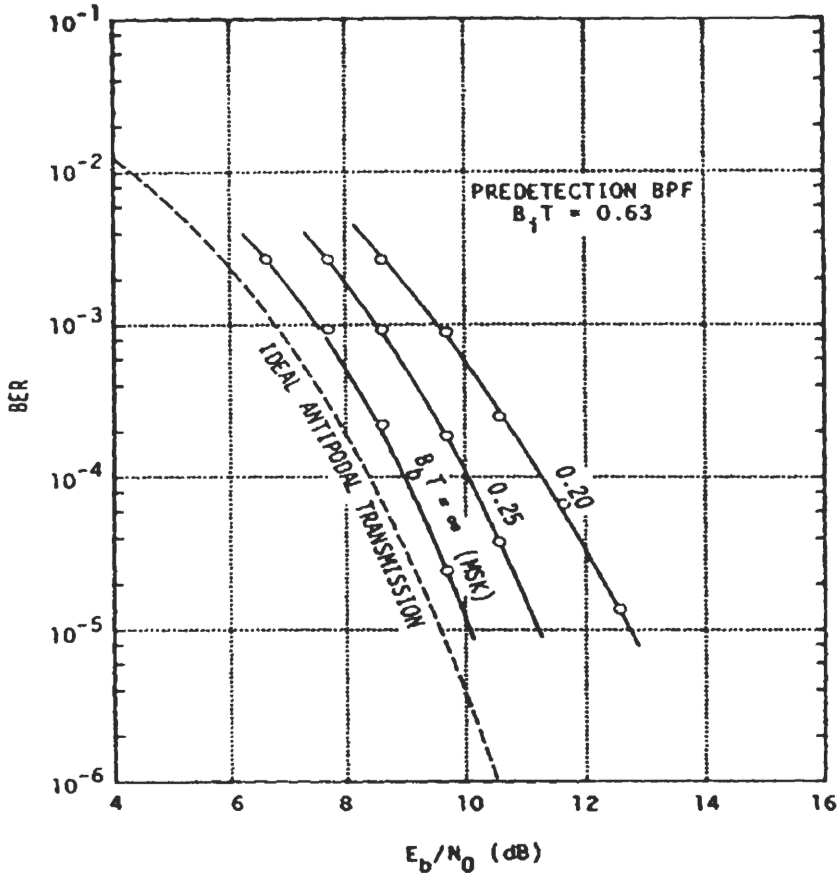


Figure 6.50 Measured BER of GMSK. From [3]. Copyright © 1981 IEEE.

results given in [3], where B_i is the 3-dB bandwidth of the predetection Gaussian filter. $B_i T = 0.63$ is the optimum value found. From the figure we can see that the degradation of GMSK relative to MSK is about 1 dB for $B_b T = 0.25$. Also the spectrum with $B_b T = 0.25$ is quite tight, so this bandwidth is considered a good choice. The measured BER curves can be approximated by the following equations

$$P_b \approx Q \left(\sqrt{\frac{2\alpha E_b}{N_o}} \right) \quad (6.59)$$

where

$$\alpha = \begin{cases} 0.68, & \text{for GMSK with } B_bT = 0.25 \\ 0.85, & \text{for simple MSK } (B_bT \rightarrow \infty) \end{cases}$$

6.8 SUMMARY

In this chapter we have studied the continuous phase modulation. We first defined the CPM signal. Then various important frequency pulses, including LREC, LRC, LSRC, TFM, and GMSK were presented. Both their mathematical expressions and waveforms were given. The phase, phase state, phase tree, phase trellis, state and state trellis of the CPM signal were studied in great detail since the information symbols are imbedded in the phase, and demodulation is based on the phase tree or the state trellis. Steps to calculate power spectral density of CPM were given, but the derivation was left in Appendix A. PSDs of some of the important CPM schemes were presented. The influence of pulse shape, modulation index, and a priori probability distribution on the PSD was demonstrated using examples. It was found that unlike pulse shape and modulation index, a priori probability distribution has no significant impact on the spectrum. The formula of the distance of CPM was derived. The error performance was related to the distance, particularly, the minimum distance of the CPM signal. It was found that the error performance is mainly determined by the minimum distance. Thus the minimum distance is often used as an indicator of the error performance of a CPM scheme. In the section on modulators, we covered direct modulator, quadrature modulator, serial modulator, and all-digital direct modulator. The great challenge of CPM lies in the design of demodulators. We studied optimum ML coherent and noncoherent demodulators which detect one symbol based on observation of several symbols. We described the Viterbi demodulator which is an ML detector based on the state trellis. The Viterbi demodulator detects the signal in a convenient recursive fashion, thus it allows the data stream to be continuous without frame structure. Demodulators that simplify the Viterbi detector, either based on a simpler trellis or based on a smaller number of matched filters were described. MSK-type demodulators, either parallel or serial, were discussed. They are very practical in terms of their simple structures, even though they offer slightly inferior error performance and are mainly suitable for binary CPM schemes with $h = 1/2$. The still simpler noncoherent differential and discriminator demodulators were also studied. Of course the price paid is the degradation in error performance, or power efficiency. However, when receiver complexity is a more severe problem than transmission power, they are not a bad choice. The synchronization problem is also a big challenge of CPM techniques. We described the popular MSK-

type synchronizer and newer squaring loop and fourth-power loop synchronizers. Other complex synchronizers were also mentioned. Finally, we discussed GMSK in detail in a dedicated section due to its importance in practical use.

Multi- h phase modulation is developed from single- h CPM that we have just studied. It offers even better performance, but with a greater complexity. We will study the multi- h phase modulation in the next chapter.

References

- [1] Sundberg, C-E, "Continuous phase modulation: a class of jointly power and bandwidth efficient digital modulation schemes with constant amplitude," *IEEE Communications Magazine*, vol. 24, no. 4, April, 1986, pp. 25-38.
- [2] de Jager, F., and C. B. Dekker, "Tamed frequency modulation, a novel method to achieve spectrum economy in digital transmission," *IEEE Trans. on Comm.*, vol. 26, no. 5, May 1978, pp. 534-542.
- [3] Murota, K., and K. Hirade, "GMSK modulation for digital mobile telephony," *IEEE Trans. on Comm.*, vol. 29, no. 7, July 1981, pp. 1044-1050.
- [4] Muilwijk, D., "Correlative phase shift keying—a class of constant envelope modulation techniques." *IEEE Trans. on Comm.*, vol. 29, no. 3, March 1981, pp. 226-236.
- [5] Deshpande, G. S. and P. H. Wittke, "Correlative encoded digital FM," *IEEE Trans. on Comm.*, vol. 29, no. 2, Feb. 1981, pp. 156-162.
- [6] Chung, K. S., "General tamed frequency modulation and its application for mobile radio communication," *IEEE Jour. on Selected Areas in Comm.*, vol. 2, no. 4, July 1984, pp. 487-497.
- [7] Aulin, T., and C-E. Sundberg, "Continuous phase modulation—Part I: Full response signaling." *IEEE Trans. on Comm.*, vol. 29, no. 3, March 1981, pp. 196-206.
- [8] Aulin, T., N. Rydbeck, and C-E. Sundberg, "Continuous phase modulation—Part II: Partial response signaling," *IEEE Trans. on Comm.*, vol. 29, no. 3, March 1981, pp. 210-225.
- [9] Anderson, J., T. Aulin, and C-E. Sundberg, *Digital Phase Modulation*, New York: Plenum Publishing Company, 1986.
- [10] Anderson, R. R., and J. Salz, "Spectra of digital FM," *Bell System Tech. J.*, vol. 44, 1965, pp. 1165-1189.
- [11] Prabhu, V. K. and H. E. Rowe, "Spectra of digital phase modulation by matrix methods." *Bell System Tech. J.*, vol. 53, 1974, pp. 899-935.
- [12] Greenstein, L. J., "Spectra of PSK signals with overlapping baseband pulses," *IEEE Trans. on Comm.*, vol. 25, 1977, pp. 523-530.
- [13] Aulin, T., and C-E. Sundberg, "An easy way to calculate power spectra for digital FM." *IEE proceedings*, Part F, vol. 130, no. 6, 1983, pp. 519-526.
- [14] Proakis, J.G., *Digital Communications*, 2nd Ed., New York: McGraw-Hill, 1989.
- [15] McGillem, C. and G. Cooper, *Continuous and Discrete Signal and System Analysis*, 3rd Ed., Philadelphia: Sanders College Publishing, 1991.

- [16] Wilson, S. G., and M. G. Mulligan. "An improved algorithm for evaluating trellis phase codes." *IEEE Trans. on Information Theory*; vol. 30, no. 6, Nov. 1984, pp. 846-851.
- [17] Rimoldi, B., "Exact formula for the minimum squared euclidean distance of CPFSK," *IEEE Trans. on Comm.*, vol. 39, no. 9, Sept., 1991, pp. 1280-1282.
- [18] Ekanayake, N., and R. Liyanapathirana, "On the exact formula for minimum squared distance of CPFSK," *IEEE Trans. on Comm.*, vol. 42, no. 11, Nov. 1994, pp. 2917-2918.
- [19] Aulin, T., N. Rydbeck, and C-E. Sundberg, "Transmitter and receiver structure for M-ary partial response FM," *IEEE Trans. on Comm.*, vol. 26, no. 3, May 1978, pp. 534-538.
- [20] Kopta, A., S. Budisin, and V. Jovanovic, "New universal all-digital CPM modulator," *IEEE Trans. on Comm.*, vol. 35, no. 4, April 1987, pp. 458-462.
- [21] Osborne, W. P., and M. B. Luntz, "Coherent and noncoherent detection of CPFSK," *IEEE Trans. on Comm.*, vol. 22, no. 8, Aug. 1974, pp. 1023-1036.
- [22] Schonhoff, T. A., "Symbol error probabilities for M-ary CPFSK: coherent and noncoherent detection," *IEEE Trans. on Comm.*, vol. 24, no. 6, June 1976, pp. 644-652.
- [23] Van Trees, H. L., *Detection, Estimation, and Modulation Theory, Part I*, New York: John Wiley & Sons, Inc., 1968.
- [24] Stiffler, J. J., *Theory of Synchronous Communications*, Englewood Cliffs, New Jersey: Prentice Hall, Inc., 1971.
- [25] Viterbi, A. J., "Error bounds for convolutional codes and an asymptotically optimum decoding algorithm," *IEEE Trans. on Inform. Theory*; vol. 13, April 1967, pp. 260-269.
- [26] Forney, G. D. Jr., "Maximum likelihood sequence estimation of digital sequences in the presence of intersymbol interference," *IEEE Trans. Inform. Theory*; vol. 18, May 1972, pp. 363-378.
- [27] Forney, G. D., "The Viterbi algorithm," *Proceedings of IEEE* vol. 61, 1973, pp. 268-278.
- [28] Viterbi, A. J. and J. K. Omura, *Principles of Digital Communication and Coding*, New York: McGraw-Hill, 1979.
- [29] Aulin, T., "Three papers on continuous phase modulation (CPM)," Thesis, University of Lund, November 1979.
- [30] Aulin, T., "Symbol error probability bounds for coherently Viterbi detected continuous phase modulated signals," *IEEE Trans. on Comm.*, vol. 29, 1981, pp. 1707-1715.
- [31] Svensson, A., C-E. Sundberg, and T. Aulin, "A class of reduced-complexity Viterbi detectors for partial response continuous phase modulation," *IEEE Trans. on Comm.*, vol. 32, no. 10, Oct. 1984, pp. 1079-1087.
- [32] Kramer, G. G., and E. Shwedyk, "On reducing the number of matched filters for optimum detection of LREC CPM," *Proceedings of Queen's University Symposium of Communications*, Canada, May 1992.
- [33] Simon, M., and D. Divsalar, "Maximum-likelihood block detection of noncoherent continuous phase modulation," *IEEE Trans. on Comm.*, vol. 41, no. 1, Jan. 1993, pp. 90-98.
- [34] Svensson, A., and C-E. Sunderberg, "Optimum MSK-type receivers for CPM on Gaussian and Rayleigh fading channels," *IEE proceedings*, Part F, vol.131, no. 5, 1984, pp. 480-490.

- [35] Svensson, A., and C-E. Sundberg, "Serial MSK-type detection of partial response continuous phase modulation," *IEEE Trans. on Comm.*, vol. 33, no. 1, January 1985, pp. 44-52.
- [36] Sundberg, C-E., "Error probability of partial response continuous phase modulation with coherent MSK-type receiver, diversity and slow Rayleigh fading in Gaussian noise." *The Bell System Technical Journal*, vol. 61, no. 8, 1982, pp. 1933-1963.
- [37] Galko, P., "Generalized MSK," Ph. D. thesis, University of Toronto, Canada, August, 1982.
- [38] Ziemer, R., C. Ryan, and J. Stilwell, "Conversion and matched filter approximations for serial minimum-shift keyed modulation," *IEEE Trans. on Comm.*, vol. 30, no. 3, March 1982, pp. 495-509.
- [39] Chung, K. S., and L. E. Zegers, "Generalized tamed frequency modulation," *Proc. IEEE International Conf. on Acoustics, Speech and Signal Processing*, vol. 3, Paris, May 1982, pp. 1805-1808.
- [40] Chung, K. S. "A noncoherent receiver for GTFM signals," *Proc. IEEE GLOBECOM '82*, Miami, December 1982, pp. B3.5.1-N3.5.5.
- [41] Stjernvall, J-E., and J. Uddenfeldt, "Gaussian MSK with different demodulators and channel coding for mobile telephony," *Proc. ICC '84*, Amsterdam, The Netherlands, May 14-17, 1984, pp. 1219-1222.
- [42] Hirade, K. M. et al., "Error-rate performance of digital FM with differential detection in mobile radio channels," *IEEE Trans. on Vehicular Technology*, vol. 28, 1979, pp. 204-212.
- [43] Svensson, A., and C-E. Sundberg, "On error probability for several types of noncoherent detection of CPM," *Proc. IEEE GLOBECOM '84*, Atlanta, Georgia, Nov. 1984, pp. 22.5.1-22.5.7.
- [44] Laurent, P., "Exact and approximate construction of digital phase modulations by superposition of amplitude modulated pulses (AMP)," *IEEE Trans. Commun.*, vol. 34, no. 2, Feb. 1986, pp. 150-160.
- [45] Kaleb, G., "Simple coherent receivers for partial response continuous phase modulation," *IEEE Journal on Selected Areas in Commun.*, vol. 7, no. 9, Dec. 1989, pp. 1427-1436.
- [46] Hirt, W., and S. Pasupathy, "Suboptimal reception of binary CPSK signals," *IEE proceedings*, Part F, vol.128, no. 3, pp. 125-134, 1981.
- [47] Anderson, J. B., and S. Mohan, "Sequential coding algorithms: a survey and cost analysis," *IEEE Trans. on Commun.*, vol. 32, 1984, pp. 169-176.
- [48] DeBuda, R., "Coherent demodulation of frequency-shift keying with low deviation ratio," *IEEE Trans. Commun.*, vol. 20, June 1972, pp. 429-435.
- [49] Lee, W. U., "Carrier synchronization of CPFSK signals," *Proc. NTC '77*, 1977, pp. 30.2.1-30.2.4.
- [50] Aulin, T., and C-E. Sundberg, "Synchronization properties of continuous phase modulation," *Proc. IEEE GLOBECOM '82*, Miami, Dec. 1982, pp. D7.1.1-D7.1.7.
- [51] D'andrea, A., U. Mengali, and R. Reggiannini, "Carrier phase and clock recovery for continuous phase modulated signals," *IEEE Trans. Commun.*, vol. 35, no. 10, Oct. 1972, pp.1095-1101.
- [52] El-tanany, M., and S. Mahmoud, "Analysis of two loops for carrier recovery in CPM with index 1/2," *IEEE Trans. Commun.*, vol. 37, no. 2, Feb. 1989, pp.164-176.
- [53] Booth, R., "An illustration of the MAP estimation for deriving closed-loop phase tracking topolo-

- gies: The MSK signal structure," *IEEE Trans. Commun.*, vol. 28, no. 8, August 1980, pp.1137-1142.
- [54] Glisic, S., "Symbol synchronization in digital communication systems using partial response CPM signaling," *IEEE Trans. Commun.*, vol. 37, no. 3, March 1989, pp.298-308.
- [55] Rappaport, T., *Wireless Communications*, Upper Saddle River, New Jersey: Prentice Hall, 1996.
- [56] Stüber, G., *Principle of Mobile Communication*, Boston: Kluwer Academic Publishers, 1996.

Chapter 7

Multi- h Continuous Phase Modulation

Multi- h continuous phase modulation (MHPM) is a special class of CPM where the modulation index h is cyclically changed for successive symbol intervals. Cyclically changing indexes leads to delayed merging of neighboring phase trellis paths, which in turn increases the minimum Euclidean distance and improves the error performance. Binary multi- h CPFSK schemes were first proposed by Miyakawa et al [1], and were generalized by Anderson, De Buda, and Taylor [2–4]. Recently, MHPM technique has received a great deal of attention for application in satellite communications due to its power and bandwidth efficiency which are even better than that of CPM [5].

In this chapter we will cover all basic aspects of MHPM in great detail. However, the treatment here is limited to an AWGN channel as we did for previous chapters. The application of MHPM in fading channels will be treated in Chapter 10. Combined MHPM and convolutional codes are beyond the scope of this book and are not covered.

We define MHPM signal and study its phase and phase trellis properties in Section 7.1. Its power spectral density is studied in Section 7.2. The Euclidean distances of MHPM signals and their error probabilities are discussed in Section 7.3. MHPM modulators are basically the same as those for CPM, which is briefly mentioned in Section 7.4. The MHPM demodulators and synchronizers are more complicated than those of CPM. They are presented in Section 7.5. New developments of MHPM are discussed in Section 7.6. Summary of this chapter is given in Section 7.7.

7.1 MHPM SIGNAL, PHASE TREE, AND TRELLIS

The expressions for MHPM are essentially the same as those for CPM ((6.1) to (6.3)) except that h is replaced by h_k . That is

$$s(t) = A \cos(2\pi f_c t + \Phi(t, \mathbf{a})), \quad -\infty < t < \infty \quad (7.1)$$

where the phase is

$$\Phi(t, \mathbf{a}) = 2\pi \sum_{k=-\infty}^{\infty} h_k a_k q(t - kT) \quad (7.2)$$

where T is the symbol period and

$$q(t) = \int_{-\infty}^t g(\tau) d\tau \quad (7.3)$$

The M -ary data a_k may take any of the M values: $\pm 1, \pm 3, \dots, \pm(M-1)$. The index h_k cyclically changes from symbol to symbol with a period of K , but only one index is used during one symbol interval, that is, $h_1, h_2, \dots, h_K, h_1, h_2, \dots, h_K$, and so on. It is normally assumed that the set of modulation index is rational with a common denominator

$$H_K = (h_1, h_2, \dots, h_K) = \left(\frac{p_1}{q}, \frac{p_2}{q}, \dots, \frac{p_K}{q} \right) \quad (7.4)$$

where $p_i, i = 1, \dots, K$ and q are small integers and all h_i values are multiples of $1/q$. Note that q in denominator of (7.4) has no relation to $q(t)$ in (7.3). For bandwidth considerations, h_i is usually chosen to be smaller than one. The index set H_K is also called a multi- h phase code since it controls the signal phase.

As in the case of single- h CPM, the frequency pulse $g(t)$ can be full response or partial-response. It can be any one of the smooth waveforms defined in Section 6.1.1. In addition, we still keep the convention that

$$\int_{-\infty}^{\infty} g(t) dt = 1/2 \quad (7.5)$$

This makes the maximum phase change of the signal to be $(M-1)h_i\pi$ for the period of $g(t)$. Usually $g(t)$ is a pulse defined in $[0, LT]$ and is zero outside this interval. Thus we have $q(LT) = \int_0^{LT} g(t) dt = 1/2$.

The definition of instant phase and cumulate phase of MHPM are similar to those of single- h CPM (see Section 6.1.2). During interval $kT < t < (k+1)T$ the instant phase of a MHPM signal with a $g(t)$ of length LT is

$$\theta(t, \mathbf{a}_k) = 2\pi \sum_{i=k-L+1}^k h_i a_i q(t - iT) \quad (7.6)$$

the cumulate phase is

$$\theta_k = \left[\pi \sum_{i=-\infty}^{k-L} h_i a_i \right] \pmod{2\pi} \quad (7.7)$$

and the total phase is the sum of the above two

$$\Phi(t, \mathbf{a}) = \theta(t, \mathbf{a}_k) + \theta_k \quad (7.8)$$

A simple but very important MHPM scheme is the 1REC MHPM. Since $g(t) = 1/2T$ for $[0, T]$ and zero elsewhere, $\theta(t, \mathbf{a}_k) = \pi h_k a_k (t - kT)/T$ and the signal in $[kT, (k+1)T]$ is

$$s(t) = A \cos\left(2\pi f_c t + \frac{a_k \pi h_k (t - kT)}{T} + \theta_k\right), \quad kT \leq t \leq (k+1)T \quad (7.9)$$

The phase change at the end of each interval is $a_k \pi h_k$.

As in the single- h CPM case, there exists a phase tree for MHPM whether the indexes are rational or irrational. If the indexes are rational, the phase tree can be collapsed into a periodic phase trellis. The difference of using multiple indexes lies in the phase changing slopes in the phase tree and delayed path merge in the trellis. Figure 7.1 compares the phase trees of two binary CPFSK schemes with single- h and $H_2 = (2/4, 3/4)$ side by side. The absolute value of the phase tree slope of the single- h CPFSK is constant, which is $h\pi/T$, whereas it is $\pi/2T$ and $3\pi/4T$ alternatively for the H_2 CPFSK. Figure 7.2 shows the phase trellises for $h = 1/2$ and $h = 3/4$ single- h binary CPFSK. The first merges happen at $t = 2T$ (see the bold line paths). Figure 7.3 shows the trellis of $H_2 = (2/4, 3/4)$ binary CPFSK scheme where the first merge occurs at $t = 3T$. It is this delayed merge that gives the MHPM larger minimum Euclidean distance between neighboring paths that in turn gives rise to a better error performance.

Recall that we defined state of CPM as

$$\mathbf{s}_k = (\theta_k, a_{k-1}, a_{k-2}, \dots, a_{k-L+1})$$

and the Viterbi demodulator relies on the state trellis (see, for example, Figure 6.5). This definition is also applicable to MHPM and a state trellis is generally needed for the Viterbi demodulator. However, as we state in Section 6.1.1, for full-response MHPM, the phase trellis is equivalent to the state trellis for explaining and designing the Viterbi demodulator. Therefore the phase trellis of full-response MHPM is often called state trellis in the literature. For partial-response MHPM, a state trellis like the one for single- h CPM is needed (see Figure 6.5).

Historically, multi- h CPFSK, which is full-response with a rectangular frequency

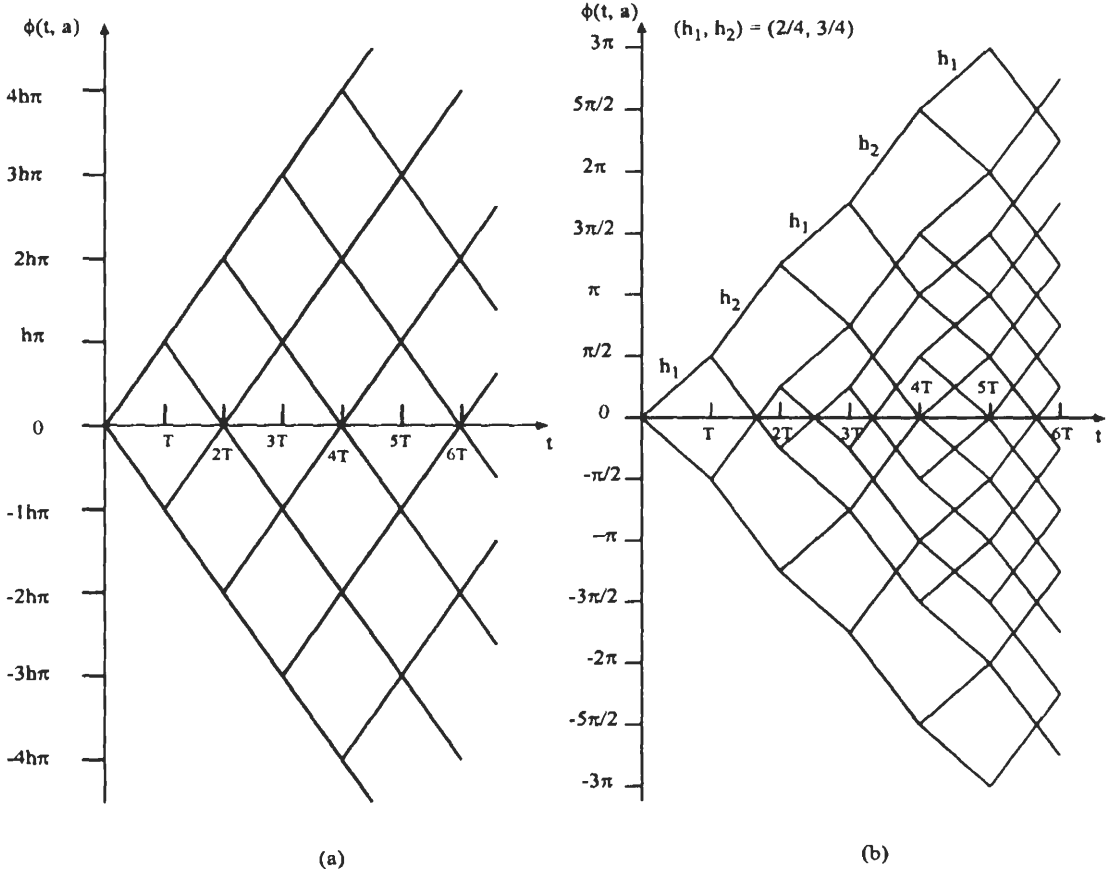


Figure 7.1 Phase trees for (a) single- h ($1/2$) binary CPFSK, (b) multi- h ($2/4, 3/4$) binary CPFSK. From [5]. Copyright © 1991 IEEE.

pulse, was first studied and the majority of the research results in the literature were about it. In the context of MHPM, we prefer to name it as IREC MHPM. In the following, we will present the results for both IREC MHPM and other full-response or partial-response MHPM with the emphasis on the IREC MHPM.

For MHPM with θ_k given in (7.7) and K indexes given in (7.4), we have

$$\theta_k = \left[\frac{\pi}{q} \sum_{i=-\infty}^{k-L} p_i a_i \right] \pmod{2\pi}$$

It is clear that cumulate phase θ_k is always some multiple of π/q . The maximum number of distinct phase states θ_k in the trellis is therefore $N_s = 2\pi/(\pi/q) = 2q$. However, it was shown that the number of phase states at any $t = kT$ is q , even

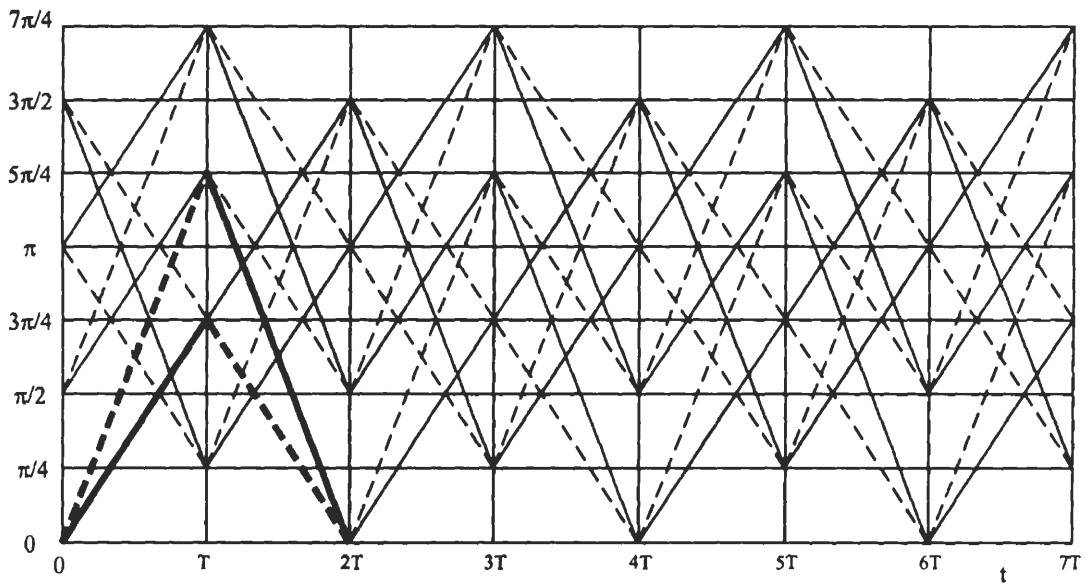
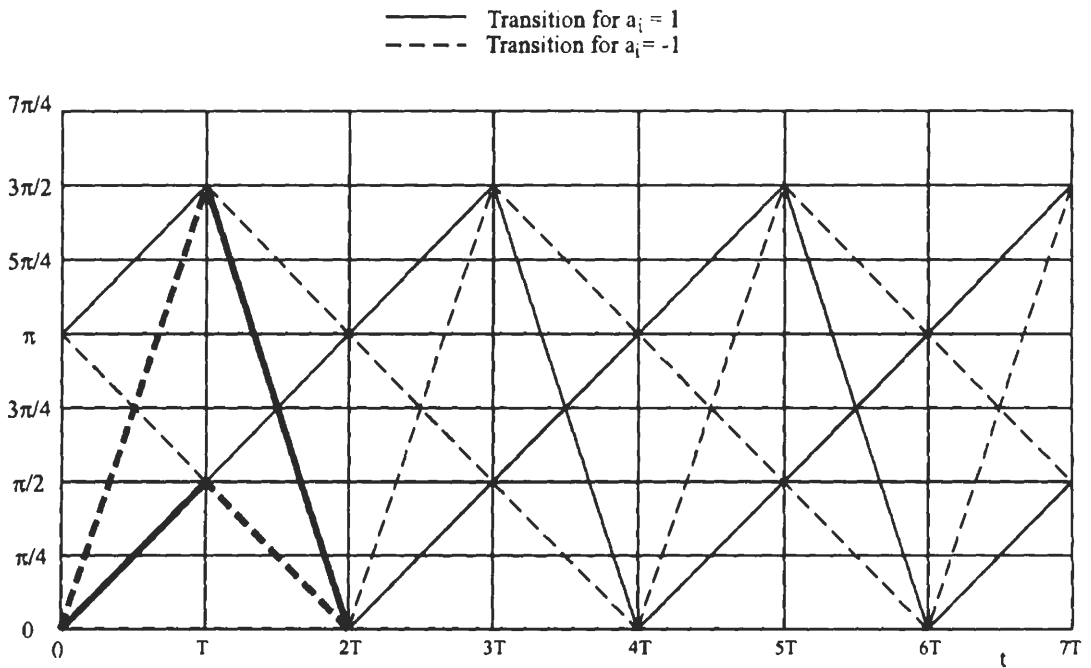


Figure 7.2 Phase trellis for (a) $h = 1/2$ binary CPFSK, (b) $h = 3/4$ binary CPFSK. From [5]. Copyright © 1991 IEEE.

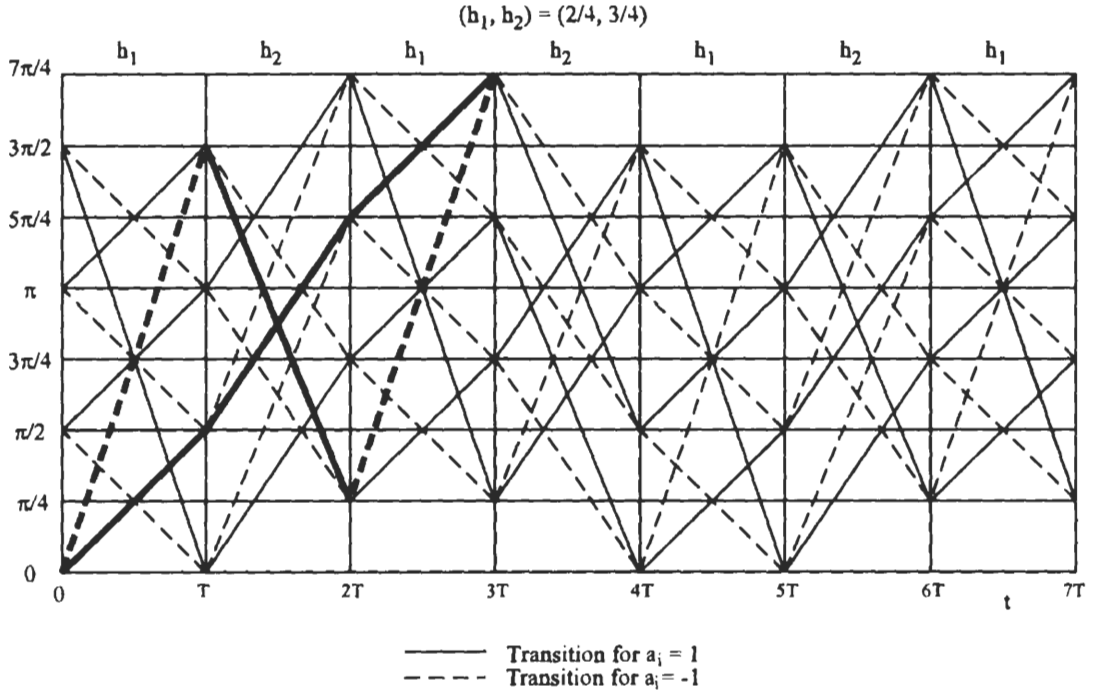


Figure 7.3 Phase trellis for $H_2 = (2/4, 3/4)$ binary CPFSK. From [5] Copyright © 1991 IEEE.

though the total number of phase states may be q or $2q$ [6, 7]. Here a rigorous proof is given. To simplify the proof without loss of generality, we assume that the time index i starts at $i = 1$

$$\theta_k = \left[\frac{\pi}{q} \sum_{i=1}^{k-L} p_i a_i \right] \pmod{2\pi}$$

where p_i could be an even or odd number.

First we prove that if $\sum_{i=1}^{k-L} p_i$ is odd, $\sum_{i=1}^{k-L} p_i a_i$ must be odd. This conclusion can be proved as follows. First this is apparently true for all $a_i = 1$ or all $a_i = -1$. In general, for any set of $a_i \in \{\pm 1, \pm 3, \dots, \pm(M-1)\}$, if $\sum_{i=1}^{k-L} p_i$ is odd, then there must be an odd number (say, N_{odd}) of odd p_i s and any number (odd or even, say, N_{even}) of even p_i s in $\sum_{i=1}^{k-L} p_i$. In the sum $\sum_{i=1}^{k-L} p_i a_i$, it is obvious that a term generated by an even p_i is always even. A term generated by an odd p_i is always odd since p_i and a_i are both odd. Thus in the sum $\sum_{i=1}^{k-L} p_i a_i$, the subsum of those N_{even} terms generated by even p_i s is even; the subsum of those N_{odd} terms generated by odd p_i s is always odd since each term is odd and the number of such terms is also odd. Thus the total sum $\sum_{i=1}^{k-L} p_i a_i$ is odd.

Likewise, we prove that if $\sum_{i=1}^{k-L} p_i$ is even, $\sum_{i=1}^{k-L} p_i a_i$ must be even. In this case, the number of odd p_i s (N_{odd}) must be even. The subsum of N_{odd} odd $p_i a_i$ terms is even since each term is odd but the number of terms is even. Thus the total sum $\sum_{i=1}^{k-L} p_i a_i$ is even.

When $\sum_{i=1}^{k-L} p_i a_i$ is odd, it takes values of $\pm 1, \pm 3, \dots$ and $\theta_k = \pm\pi/q, \pm 3\pi/q, \dots$; when $\sum_{i=1}^{k-L} p_i a_i$ is even, it takes values of $0, \pm 2, \pm 4, \dots$ and $\theta_k = 0, \pm 2\pi/q, \pm 4\pi/q, \dots$. We can convert the phases into $[0, 2\pi]$ and summarize the above results as follows.

$$\theta_k = \frac{\pi}{q}, \frac{3\pi}{q}, \frac{5\pi}{q}, \dots, \frac{(2q-1)\pi}{q}, \quad \Lambda_k = \sum_{i=1}^{k-L} p_i \text{ odd} \quad (7.10)$$

$$\theta_k = 0, \frac{2\pi}{q}, \frac{4\pi}{q}, \dots, \frac{2\pi(q-1)}{q}, \quad \Lambda_k = \sum_{i=1}^{k-L} p_i \text{ even} \quad (7.11)$$

In either case, the number of possible phases ($\text{mod } 2\pi$) is q with a distance of $2\pi/q$ between two adjacent phases. Thus at any $t = kT$, the number of possible phases is q .

The number of total phase states (N_s) in the phase trellis could be $2q$ or q . If not all p_i s are even, Λ_k is odd at some times and even at other times, then the phase can take values in (7.10) and (7.11) (i.e., $N_s = 2q$). If all p_i s are even, Λ_k is even all the time, then the phase can take values in (7.11) only, i.e., $N_s = q$. The first case is the usual case since usually q is chosen as a power of 2, thus not all p_i s are even. Otherwise if all p_i s are even, q can be reduced by a factor of two in defining H_K (see (7.4)), still resulting in the case that "not all p_i s are even." The second case, which is not the usual case, happens when q is an odd number. We summarize the conclusions as follows.

$$\text{If not all } p_i \text{ s are even, } N_s = 2q \quad (7.12)$$

$$\text{If all } p_i \text{ s are even, } N_s = q \quad (7.13)$$

Some examples which support the above theory are given here. An example for the first case (not all p_i s are even) is $H_2 = (2/4, 3/4)$, starting from $k = L + 2$. $\Lambda_k = 5, 7, 10, 12, 15, 17, \dots$. The values of Λ_k are odd or even. $N_s = 2q = 8$ (Figure 7.3). Another example for the first case is $H_3 = (1/8, 2/8, 3/8)$, starting from $k = L + 3$, $\Lambda_k = 6, 7, 9, 12, 13, \dots$. The values of Λ_k are odd or even, $N_s = 2q = 16$. The trellis is shown in Figure 7.4. Finally, an example for the second case (all p_i s are even) is $H_2 = (2/5, 4/5)$. Starting from $k = L + 2$, $\Lambda_k = 6, 8, 12, 14, 18, \dots$. All values of Λ_k are even in this case, thus $N_s = q = 5$. The trellis is in Figure 7.5.

$$(h_1, h_2, h_3) = (1/8, 2/8, 3/8)$$

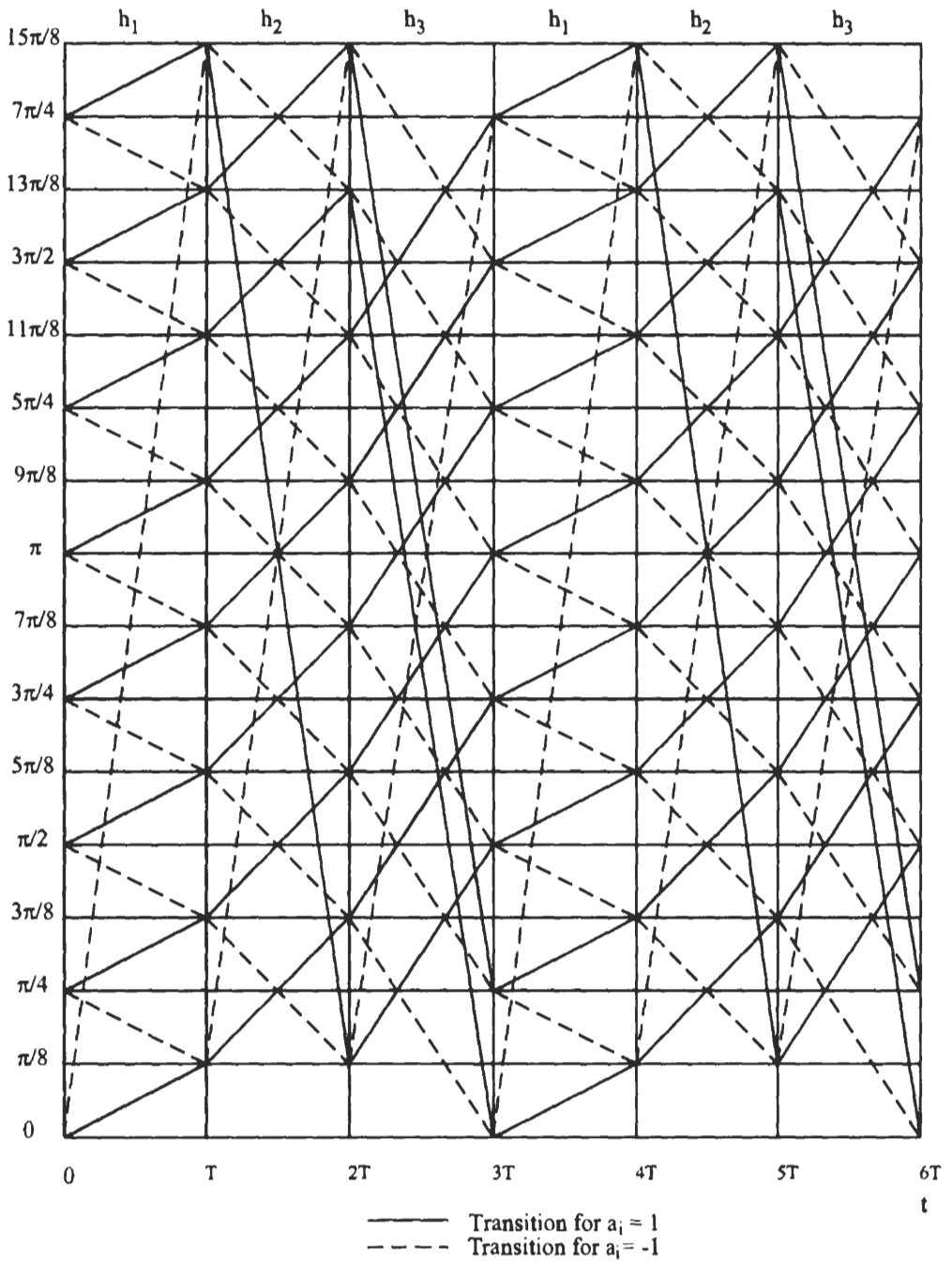


Figure 7.4 Phase trellis for $H_3 = (1/8, 2/8, 3/8)$ binary CPFSK.

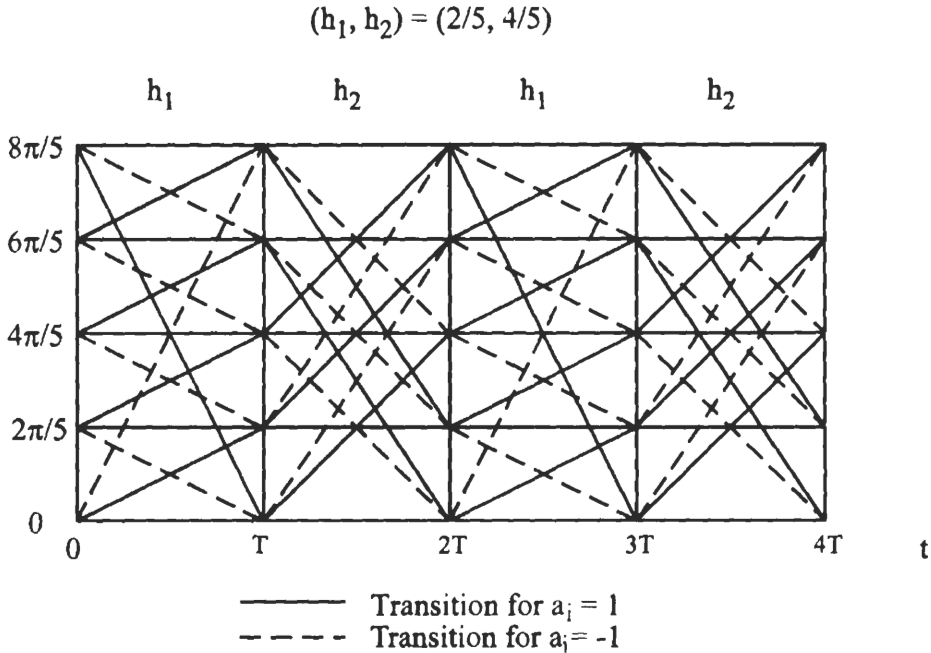


Figure 7.5 Phase trellis for $H_2 = (2/5, 4/5)$ binary CPFSK.

It is natural to think that the period of the trellis (T_p) is KT since K modulation indexes are cyclically rotated. In fact T_p could be KT or $2KT$, depending on a quantity related to the modulation indexes.

$$T_p = KT, \quad \Gamma = \sum_{i=1}^K p_i \text{ even} \tag{7.14}$$

$$T_p = 2KT, \quad \Gamma = \sum_{i=1}^K p_i \text{ odd} \tag{7.15}$$

Here is the proof. Assume the trellis starts from $k = 1$. When Γ is even, from (7.11) we can see that $\theta_K = 0, 2\pi/q, 4\pi/q, \dots, 2\pi(q - 1)/q$. Starting from this point, after K symbols, θ_K will increase to $\theta_{2K} = \theta_K + \sum_{i=1}^K p_i a_i$. Since Γ is even, from (7.11) we can see that the increment $\sum_{i=1}^K p_i a_i$ is one of the following values, $0, 2\pi/q, 4\pi/q, \dots, 2\pi(q - 1)/q$. The resulting θ_{2K} is also one of the same set of values ($\text{mod } 2\pi$). Thus the period is KT . When Γ is odd, from (7.10) we can see that $\theta_K = \pi/q, 3\pi/q, 5\pi/q, \dots, (2q - 1)\pi/q$. Starting from this point, after K symbols, θ_K will increase to $\theta_{2K} = \theta_K + \sum_{i=1}^K p_i a_i$. Since Γ is odd, from (7.10) we can see that

the increment $\sum_{i=1}^K p_i a_i$ is one of the following values, $\pi/q, 3\pi/q, 5\pi/q, \dots, (2q - 1)\pi/q$. The resulting θ_{2K} is one of the values in (7.11) ($\text{mod } 2\pi$). Only after next K symbols, the phases could become the values in (7.10). Thus the period is $2KT$.

Again we can use Figures 7.3, 7.4, and 7.5 to verify the periods of phase trellis. In Figure 7.3, $K = 2$, $\Gamma = 5$ (odd), the period $T_p = 2KT = 4T$. In Figure 7.4, $K = 3$, $\Gamma = 6$ (even), the period $T_p = KT = 3T$. In Figure 7.5, $K = 2$, $\Gamma = 6$ (even), the period $T_p = KT = 2T$.

Note that since in the derivation we did not put any constraint on L , the length of the frequency pulse, (7.11) to (7.15) are applicable to M-ary MHPM with any L values. In other words, they are applicable to both full-response and partial-response M-ary MHPM schemes. They are also applicable to single- h CPM since it is just a special case of MHPM. Figure 7.2 are two examples for single- h CPM. Their number of phases and length of periods also satisfy the above four expressions.

As we pointed out in Chapter 6, θ_k is in general not the total phase at time kT . However, if $L = 1$ and in addition f_c is an integer multiple of symbol rate, and θ_k is the total phase at $t = kT$, thus the initial phase of the k th symbol interval.

Another important parameter of the phase trellis is the *constraint length* which is the minimum number of symbol intervals over which any two paths remain unmerged. The constraint length determines the minimum Euclidean distance which in turn determines the error probability. A set H_K cannot have constraint length longer than $K + 1$, since a merge is always possible over $K + 1$ intervals. For instance, data $(K + 1)$ -tuples $(1, -1, \dots, -1)$ and $(-1, \dots, -1, 1)$, where $-1, \dots, -1$ indicates K successive -1 s and that corresponding modulation indexes are $(h_1, h_2, \dots, h_K, h_1)$, represent two paths which diverge at the first symbol and merge at the last symbol. The first merger that occurs independently of the values of modulation indexes is called the first *inevitable* merger. It is clear from above that the first inevitable merger occurs at $t = (K + 1)T$ for full-response MHPM schemes.

It was found that there exist sets H_K which can achieve the maximum attainable constraint length $(K + 1)$ [4, 14]. A necessary and sufficient condition for the set to achieve the upper limit $K + 1$ is that the weighted sum $(k_1 h_1 + k_2 h_2 + \dots + k_K h_K)$ must not be integer-valued for any integer K -tuple (k_1, k_2, \dots, k_K) with $k_i \in \{0, 1, 2, \dots, M - 1\}$. Furthermore, if h_i are multiples of $1/q$, then H_K can achieve the maximum constraint length only if $q \geq M^K$. However, it has been shown that MHPM schemes exist that do not satisfy $q \geq M^K$, but still offer significant gain over the best CPFSK schemes with comparable bandwidth and number of receiver states [8].

For partial-response MHPM with K indexes and a $g(t)$ of L symbol duration, the first inevitable merger in the phase trellis occurs at $t = (L + K)T$ [9]. Thus the constraint length of such a scheme cannot be longer than $L + K$.

7.2 POWER SPECTRAL DENSITY

Similar to the calculation of the power spectral density of single- h CPM, there are three methods for computing the power spectral density of MHPM schemes: the direct method, the Markov chain method, and the autocorrelation method. See Section 6.2 for general descriptions of these methods. For MHPM they need modifications.

First we consider binary 1REC MHPM (binary multi- h CPFSK). The autocorrelation function has been analytically found in [10]. It was shown in [11, pp. 377-378] that the autocorrelation function of a phase-modulated signal is the same as the real part of the characteristic function of the probability density function of the *phase changing variable* $\Phi(t + \tau, \mathbf{a}) - \Phi(t, \mathbf{a})$. Using this property, the autocorrelation function of binary 1REC MHPM was found as

$$R(x) = \begin{cases} \frac{1}{K} \sum_{i=1}^K \left[\frac{x}{2} D(-\pi h_i x, \pi h_{i+1} x) + \frac{x}{2} D(\pi h_i x, \pi h_{i+1} x) \right. \\ \left. + (1-x) \cos \pi h_i x \right], & \text{for } n = 0 \\ \frac{1}{K} \sum_{i=1}^K \left(\prod_{j=1}^{n-1} \cos h_{i+j} \right) \\ \left[\frac{x}{2} \cos h_{i+n} [D(-\pi h_i x, \pi h_{i+n+1} x) + \frac{x}{2} D(\pi h_i x, \pi h_{i+n+1} x)] \right. \\ \left. + \frac{(1-x)}{2} [D(\pi h_i + \pi h_{i+n} x, \pi h_i x + \pi h_{i+n}) \right. \\ \left. + D(\pi h_i - \pi h_{i+n} x, \pi h_i x - \pi h_{i+n})] \right], & \text{for } n = 1, 2, \dots \end{cases} \quad (7.16)$$

where x is the normalized time variable

$$\begin{aligned} x &= \Delta\tau/T \\ \tau &= nT + \Delta\tau \text{ and } 0 \leq \Delta\tau \leq T \end{aligned}$$

and

$$D(x, y) = \begin{cases} \cos x, & x = y \\ (\sin y - \sin x)/(y - x), & x \neq y \end{cases}$$

A special case is the MSK ($K = 1, h = 1/2$) for which (7.16) becomes

$$R(x) = \begin{cases} (1 - \frac{x}{2}) \cos(\frac{\pi}{2} x) + \frac{1}{\pi} \sin(\frac{\pi}{2} x), & \text{for } n = 0 \\ (\frac{x-1}{2}) \sin(\frac{\pi}{2} x) + \frac{1}{\pi} \cos(\frac{\pi}{2} x), & \text{for } n = 1 \\ 0, & \text{for } n > 1 \end{cases}$$

which is the same as that derived in [12].

An analytical expression for the power spectral density can be found by taking the Fourier transform of (7.16). Note that since $R(\tau)$ will rapidly approach zero as n increases, it is sufficient to consider only a few symbol intervals. Figure 7.6 shows the autocorrelation function and power spectral density of the binary 1REC MHPM scheme with $H_3 = \{4/8, 5/8, 6/8\}$, obtained using the above method.

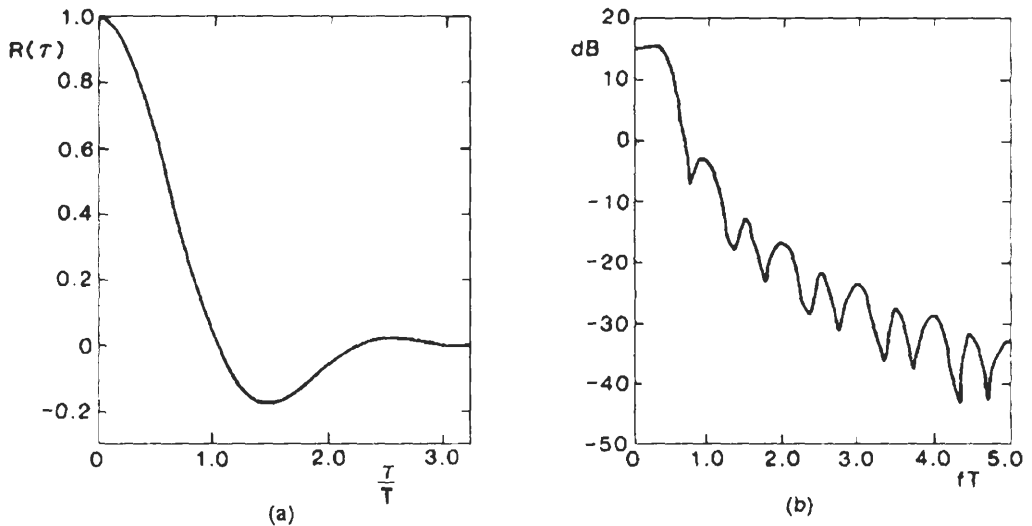


Figure 7.6 Autocorrelation function (a), and power spectral density (b), of the binary 1REC MHPM scheme with $H_3 = \{4/8, 5/8, 6/8\}$. From [10]. Copyright © 1985 IEEE.

The numerical autocorrelation method for single- h CPM described in Chapter 6 can also be generalized for MHPM. A guide line for this generalization is given in [13, p. 162]. However, no detailed results are available.

The direct method has been applied to binary 1REC MHPM [4] and M-ary full-response MHPM [14]. This method is general and has ability to provide exact (via numerical integration) power spectral density. In this method, the power spectral density is given by

$$\Psi_{\bar{s}}(f) = \lim_{N \rightarrow \infty} E\{|\Psi_{NT}(f)|^2 / NT\}$$

where $\Psi_{NT}(f)$ is the direct Fourier transform of a NT second segment of the MHPM signal. The expectation is over the data modulation and the random initial phase angle.

The work of [14] for PSD of M-ary full-response MHPM is based on the work for PSD of FSK in [15] where it is assumed that the random modulation waveform is selected in independent, identically distributed manner in each symbol interval. In attempting to apply the results of [15] to MHPM, one faces the difficulty that the selection of modulation is not identically distributed, though independent, in each interval. This is because the h_k index is cyclically chosen, and the allowable modulating signals form different sets for different time indexes. A way out of this dif-

difficulty is to view the modulation as having a basic signaling interval of $T' = KT$ seconds, thus the distribution on each super-interval is identical. Now there are M^K distinct waveforms to choose from. Based on this concept, the results of [15] can be applied directly to the M-ary full-response MHPM case. The one-side low-pass (or complex envelope) PSD is given by the following equations:

$$\Psi_{\bar{s}}(f) = \frac{2}{T'} [P(f) + 2 \operatorname{Re}\{F(f)F_b^*(f) \exp(-j2\pi fT') + F(f)F_b^*(f)\Lambda(f)\}] \quad (7.17)$$

where

$$\Lambda(f) = \exp(-j4\pi fT') \frac{C(T')}{1 - C(T') \exp(-j2\pi fT')} \quad (7.18)$$

To evaluate the above we define

$$b_n(t) = \pi \int_0^t \sum_{i=1}^K a_{in} h_i g(\tau - iT) d\tau, \quad n = 1, 2, \dots, M^K \quad (7.19)$$

where $\{a_{in}, i = 1, 2, \dots, K\}$ is one of the M^K distinct data vectors of length K . From $b_n(t)$ we obtain

$$B_n = b_n(T') \quad (7.20)$$

$$F_n(f) = \int_0^{T'} \exp(-j2\pi ft + jb_n(t)) dt \quad (7.21)$$

and from B_n we have

$$C(T') = E\{\exp(jB_n)\}$$

and using $F_n(f)$ we obtain

$$P(f) = E\{|F_n(f)|^2\} = M^{-K} \sum_n |F_n(f)|^2 \quad (7.22)$$

$$F(f) = E\{F_n(f)\} = M^{-K} \sum_n F_n(f) \quad (7.23)$$

Finally using $F_n(f)$ and B_n we define

$$F_b^*(f) = E\{F_n^*(f) \exp(jB_n)\} = M^{-K} \sum_n F_n^*(f) \exp(jB_n) \quad (7.24)$$

In the above series of equations, $E\{\cdot\}$ denotes the expectation with respect to the random index $n = 1, 2, \dots, M^K$.

The expression in (7.17) is valid only when $|C(T')| < 1$ [15]. This is also the condition for absence of discrete components in the PSD, and is always satisfied for those MHPM schemes of interest.

Computation of the spectrum of a particular frequency starts from (7.21) for all n . Then other quantities can be computed. The only difficult calculation is (7.21) where numerical integration must be performed. In the cases of LREC and LRC frequency pulses, analytical expressions may be obtained for (7.21), thus considerably simplifying the calculation. Programming efficiency may be increased by exploiting the symmetry in $b_n(t)$ and by utilizing the tree structure of the M^K signals. The entire computation effort is roughly proportional to M^K . For practical schemes K usually is a small number. The computation complexity should not be a problem.

As in the case of single- h CPM, when H_K is a set of integer indexes, $|C(T')| = 1$, line spectral components will appear in the PSD [14].

Figure 7.7 shows PSDs for several sets of indexes obtained using the above method. Figure 7.7(a) also shows the PSD of MSK for comparison. It is seen that the spectrum of the $\{2/4, 3/4\}$ binary IREC scheme is largely the same of MSK, but it has an asymptotic coding gain over MSK of about 1.4 dB. The spectrum for $\{4/9, 6/9\}$ binary IREC scheme is shown in Figure 7.7(b), which also is similar to MSK spectrum. The asymptotic coding gain over MSK is 2.3 dB. Both multi- h spectra in Figures 7.7(a, b) are absent from nulls. Multiple indexes appear to smear the spectra and fill the nulls in the MSK spectra. The roll-off rate of the two spectra is proportional to f^{-4} . Figure 7.7(c) is the PSD for $\{4/8, 5/8, 6/8\}$ binary IREC scheme. This spectrum is also shown in Figure 7.6 where the autocorrelation method is used. It can be seen that both methods produce the same PSD. Again the spectrum of this scheme is similar to those in Figure 7.7(a, b). This is not surprising since their minimum and maximum deviations (determined by the indexes) are equivalent or close. This scheme has a 2.8 dB asymptotic coding gain over MSK. PSD of the $\{4/9, 6/9\}$ binary RC scheme is shown in Figure 7.7(d). The roll-off rate is proportional to f^{-8} .

For phase modulation, it was shown that if the phase pulse $q(t)$ has $(N - 1)$ continuous derivatives which are equal to zero at the leading and trailing edges, then the power spectrum decays asymptotically as $f^{-2(N+1)}$ [16].¹ For IREC MHPM schemes, $N = 1$, thus their spectra decay as f^{-4} as shown in Figures 7.7 (a to c). For raised-cosine pulse, $N = 3$, and its spectrum decays as f^{-8} as shown in Figure 7.7(d).

There are two simple methods that approximate the spectrum of an MHPM

¹ Similar results are stated in Chapter 5, Section 5.11 for symbol shaping pulse.

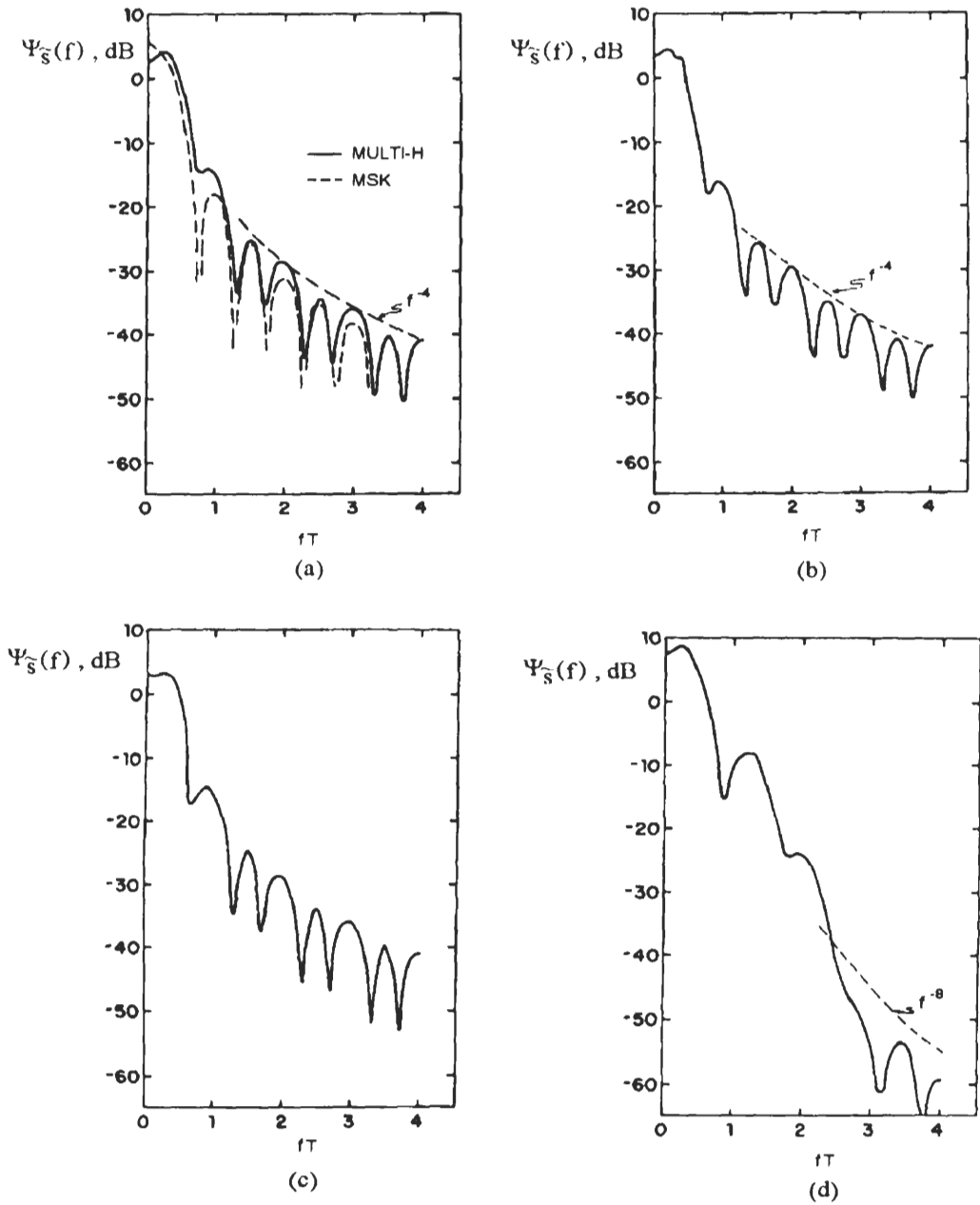


Figure 7.7 (a) PSD for $\{2/4, 3/4\}$ binary IREC MHPM in comparison with MSK, (b) PSD for $\{4/9, 6/9\}$ binary IREC MHPM, (c) PSD for $\{4/8, 5/8, 6/8\}$ binary IREC MHPM, (d) PSD for $\{2/4, 3/4\}$ binary RC MHPM. From [14]. Copyright © 1981 IEEE.

scheme [14]. Method one is to treat the spectrum as an average of constant- h spectra. That is

$$\Psi_{\bar{s}}(f) \approx \frac{1}{K} \sum_{i=1}^K \Psi_{h_i}(f)$$

where $\Psi_{h_i}(f)$ is the spectrum corresponding to index h_i . Method two is to average the indexes first

$$\bar{h} = \frac{1}{K} \sum_{i=1}^K h_i$$

then calculate the spectrum for the single- h CPM with $h = \bar{h}$. It is intuitive that the closer the indexes become, the more accurate the approximation is. It was reported in [14] that with “good” multi- h schemes, method one is generally quite accurate (i.e., ± 2 dB error in the spectrum). Good schemes appear to be those with indexes grouped near one value. Method two also gives the general spectrum shape, but it gives true nulls rather than local minima, and is somewhat misleading in that regard. Both methods are quite accurate in terms of describing out-of-band power behavior.

The spectra of some MHPM schemes with partial-response frequency pulse were obtained by simulations [9]. Figure 7.8 shows PSDs for several binary 4S MHPM schemes with various indexes. A 4S frequency pulse is obtained by convolving 3S with 1REC, while 3S is obtained by convolving 2TRI (2S) with 1REC, where 2TRI is a triangular pulse over two-symbol intervals. Figure 7.9 shows the LS pulses and some other pulses. In Figure 7.8, the average indexes are 0.5 and 0.8. The spectra of the 0.8 group is wider than that of 0.5 group. In each group, the spreading between the two indexes determines the spectral width. Generally, the wider the spread, the wider the spectrum. Also it is clear from the figure that the average index can be used to calculate approximately the MHPM spectra, especially when the spread is narrow.

7.3 DISTANCE PROPERTIES AND ERROR PROBABILITY

The distance equations of single- h CPM are still applicable to MHPM. Particularly we rewrite the normalized Euclidean distance (6.32) here

$$d_{ij}^2 = \frac{\log_2 M}{T} \int_0^{NT} [1 - \cos \Delta\Phi(t, \gamma_{ij})] dt \quad (7.25)$$

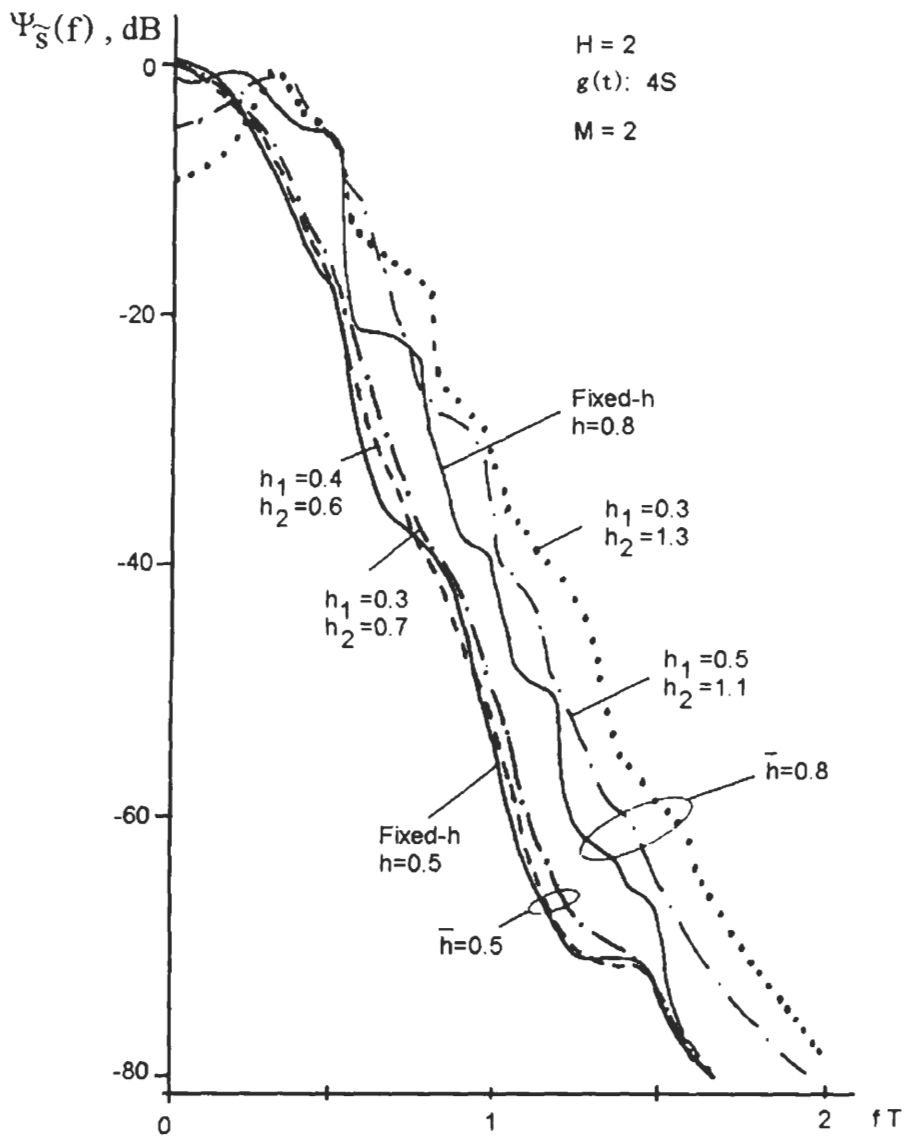


Figure 7.8 PSDs for several binary 4S MHPM schemes with various indexes. From [9]. Copyright © 1982 IEEE.

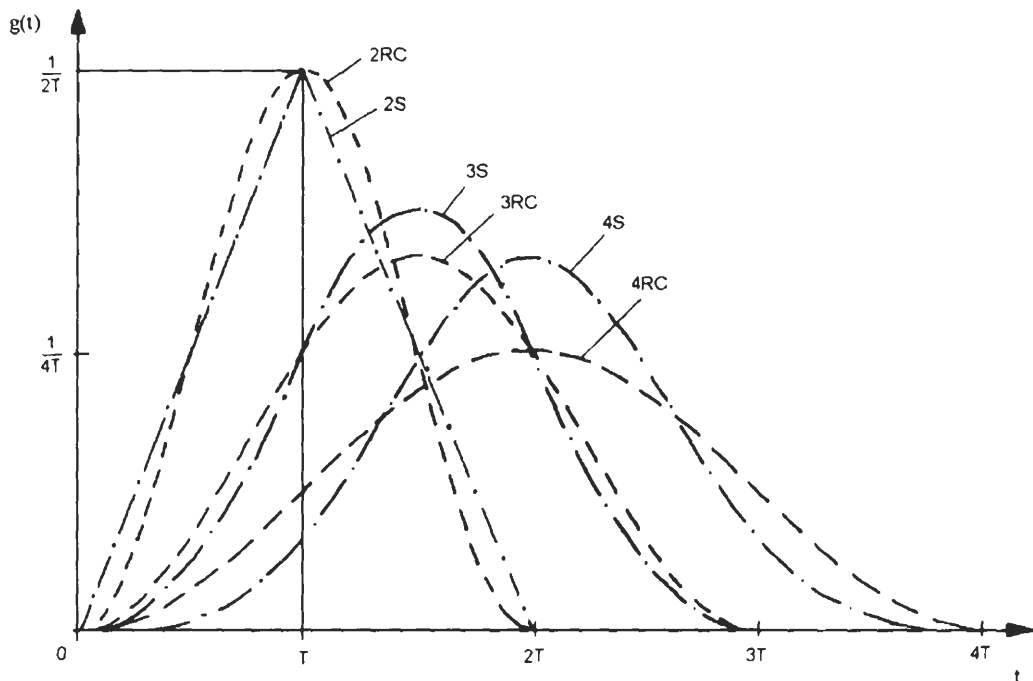


Figure 7.9 Some frequency pulse shapes. From [9], Copyright © 1982 IEEE.

where

$$\Delta\Phi(t, \gamma_{ij}) = 2\pi \sum_{k=-\infty}^{\infty} h_k \gamma_k q(t - kT) \tag{7.26}$$

is slightly different from (6.31). The difference is that h has been replaced by h_k .

The error probability is again largely determined by the minimum distance d_{\min} as in (6.39) and (6.40) when detected with the maximum likelihood sequence detector at high signal-to-noise ratios. We rewrite them here

$$P_e \lesssim \frac{K}{2} \exp\{-d_{\min}^2 (E_b/2N_o)\} \tag{7.27}$$

or

$$P_e \lesssim KQ \left(d_{\min} \sqrt{E_b/N_o} \right) \tag{7.28}$$

As we pointed out in Chapter 6, that even though P_e is the error probability of sequence detection, it is approximately equal to the symbol error probability at high

SNR.

Distance properties of M -ary IREC (or linear phase) MHPM schemes have been analyzed in [17]. Upper bounds on the minimum distances were calculated for binary IREC 2- h schemes, M -ary IREC 2- h schemes, binary IREC 3- h schemes, binary IREC 4- h schemes, quaternary and octal IREC MHPM schemes. An upper bound on the minimum distance is an important parameter of an MHPM scheme since it gives the maximum achievable minimum distance, hence the minimum achievable error probability of the scheme. The actual minimum distances were calculated for several different 2- h schemes and for various parameter combinations.

As we described in Chapter 6, upper bound on the d_{\min}^2 can be obtained by calculating the distances and choosing the minimum for all pairs of phase paths which give first, or deeper, inevitable mergers in the phase tree or trellis. As we already know from Chapter 6, upper bound d_B^2 is a function of h for fixed frequency pulse $g(t)$. For MHPM it is a function of H_K for fixed frequency pulse $g(t)$. Logically the upper bounds for multi- h schemes should be calculated against various sets of (h_1, h_2, \dots, h_K) . However, empirical results show that most of the good 2- h , 3- h , and 4- h schemes are those with low and moderate average \bar{h} values and the individual h_i values are close together. Thus it is of special interest to study the upper bound for the case $h_i = h$. This of course degenerates the multi- h schemes back to single- h schemes whose upper-bound expressions are different and upper-bound values are smaller. Typically, first merges of single- h schemes occur earlier and the upper bound is smaller. However, we can still pretend that the scheme is multi- h and the merges remain unchanged, thus the expressions also remain unchanged. Then we let all $h_i = \bar{h}$, the resulting expressions would become the approximate upper bounds for schemes with h_i close to each other but still different. Strictly speaking, these upper bounds are not upper bounds for any scheme, single- h or multi- h , since for single- h , bound expressions are different; for multi- h , there exist no such schemes where all h_i are equal. Nonetheless the upper bound for $h_i = \bar{h}$ is representative for schemes with h_i close to each other but still different [17]. Figure 7.10 is a summary of upper bounds on d_{\min}^2 for various M and K versus \bar{h} for multi- h schemes and versus h for single- h schemes, respectively. This figure is simple, clear, and representative due to the use of average index \bar{h} . Otherwise, if various index sets H_K were used, the figure would have been too complicated, and not representative.

Now let us examine Figure 7.10. For $M = 2$, the maximum increase of bound for $K \geq 2$ over the $K = 1$ case is 3 dB for $\bar{h} \leq 0.5$. For larger \bar{h} values slightly better bounds are obtained with increasing values of K . Further increase in K leads to smaller gain in bounds. On the other hand, increasing M gives significant gain in distance bounds. For instance, $M = 4$ single- h case has the same bound as that for $M = 2, K = 2, 3, 4$ cases for $\bar{h} \leq 0.5$. And $M = 8$ single- h case has the higher bound than that for $M = 2, K = 2, 3, 4$ cases for $\bar{h} \leq 0.5$. The conclusion from Fig-

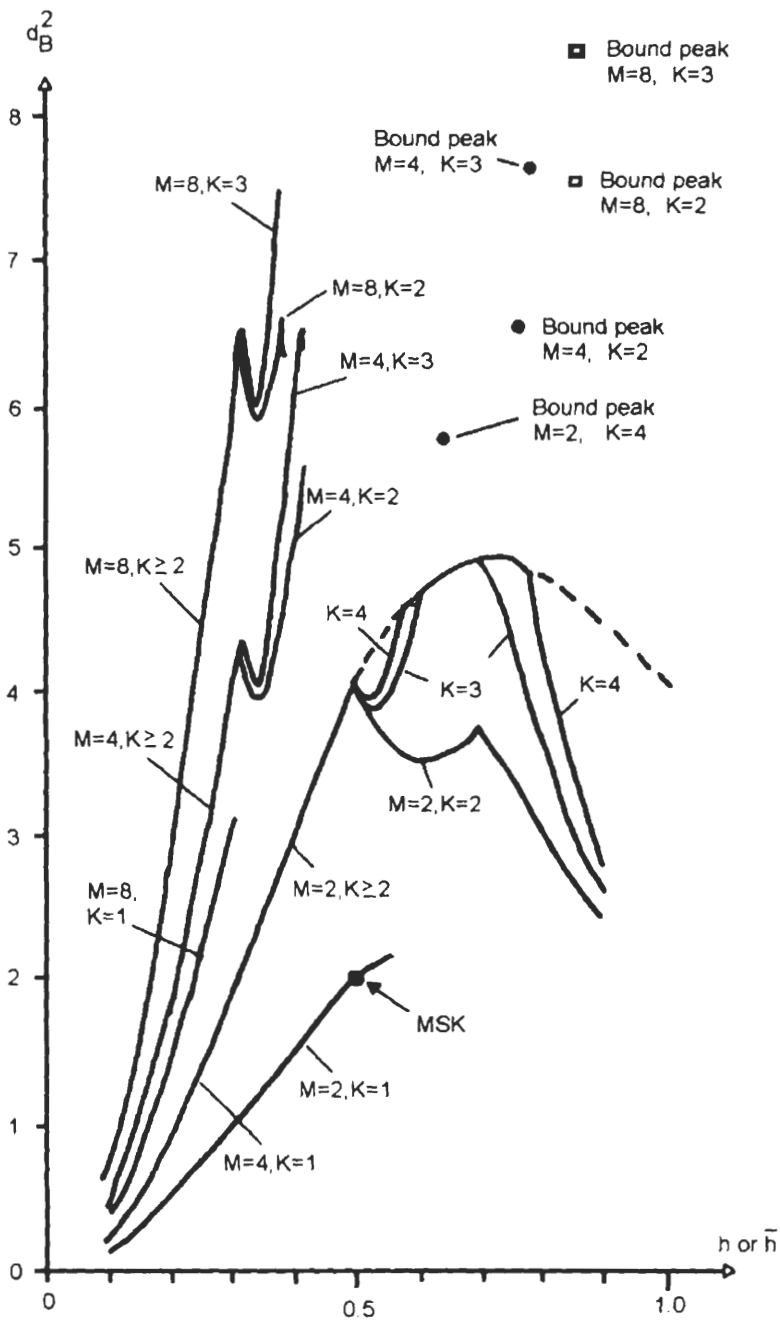


Figure 7.10 Summary of upper bounds d_B^2 on d_{min}^2 for various M and K values. From [17]. Copyright © 1982 IEEE.

ure 7.10 is that to keep system complexity down while achieving fairly large distance gain, the good choices are binary 2- h schemes and quaternary single- h schemes for $\bar{h} \leq 0.5$. Further increasing K and/or M will not increase distance gain significantly while the system complexity will increase significantly. In addition, using $\bar{h} > 0.5$ is not preferable since the signal bandwidth will be increased.

Actual d_{\min}^2 has been calculated in [17] for various schemes. Figure 7.11 shows d_{\min}^2 for binary 1REC 2- h schemes where $h_1 = 0.5$ is fixed and h_2 is allowed to change. The path length is $N = 30$ for calculating d_{\min}^2 . The dashed line is the upper bound. From the figure, it can be seen that the upper bound is tight in this h region except for those weak or catastrophic values of the modulation indexes. For these specific values of modulation indexes, merges occur earlier in the phase tree, leading to reduced minimum distances. In Figure 7.11, the weak indexes are $(1/2, 1/4)$, $(1/2, 1/3)$, $(1/2, 1/2)$, $(1/2, 3/4)$, and $(1/2, 1)$. More results of d_{\min}^2 for binary and quaternary 1REC MHPM schemes are available in [17].

By using partial-response frequency pulses, further gain of minimum distance can be obtained [9]. Of course the price is the increased system complexity.

The trade-offs between distance and bandwidth for full-response 1REC-MHPM schemes and partial-response 3RC MHPM schemes are considered in [9] and the results are summarized in Figures 7.12 and 7.13, respectively.

In Figure 7.12, the bandwidth is the two-sided normalized 99% in-band power bandwidth and the distance is relative to MSK. The MSK's two-sided 99% bandwidth is $1.2R_b$ (see Section 5.2.2). Among single- h schemes, $M = 4$ schemes outperform $M = 2$ schemes considerably. Slight further improvement can be obtained by increasing M to 8, especially at large h values (large $2BT_b$). The figure also shows the equal- h bounds for $K = 2$ schemes with $M = 2, 4$, and 8. Again we can see that going from $M = 2$ to $M = 4$ improves significantly and going from $M = 4$ to $M = 8$ does not make much difference. Specific schemes are shown for the $K = 2, M = 2$ and $K = 2, M = 4$ cases. It can be seen that these schemes are slightly below corresponding bounds. For $K = 3$, bound peak points are shown. The $M = 2, K > 2$ equal- h bound is also shown, which coincides with the $M = 2, K = 2$ bound in the first part of the curve (also see Figure 7.10). An overall comparison reveals that binary multi- h schemes perform roughly the same as single- h $M = 4$ or $M = 8$ schemes. In most cases M-ary single- h schemes are better. Considerable improvements are obtained by using $K = 2, M = 4$ schemes. Only minor further improvement can be obtained by further increasing K and/or M .

Figure 7.13 shows power-bandwidth trade-off for M-ary partial-response 3RC MHPM schemes. The bandwidth is defined as the bit rate normalized width of the smooth power spectra at the -60 dB level, not the fractional out-of-band power bandwidth used in Figure 7.12. The figure shows four cases: $M = 2, 4$ and $K = 1, 2$.

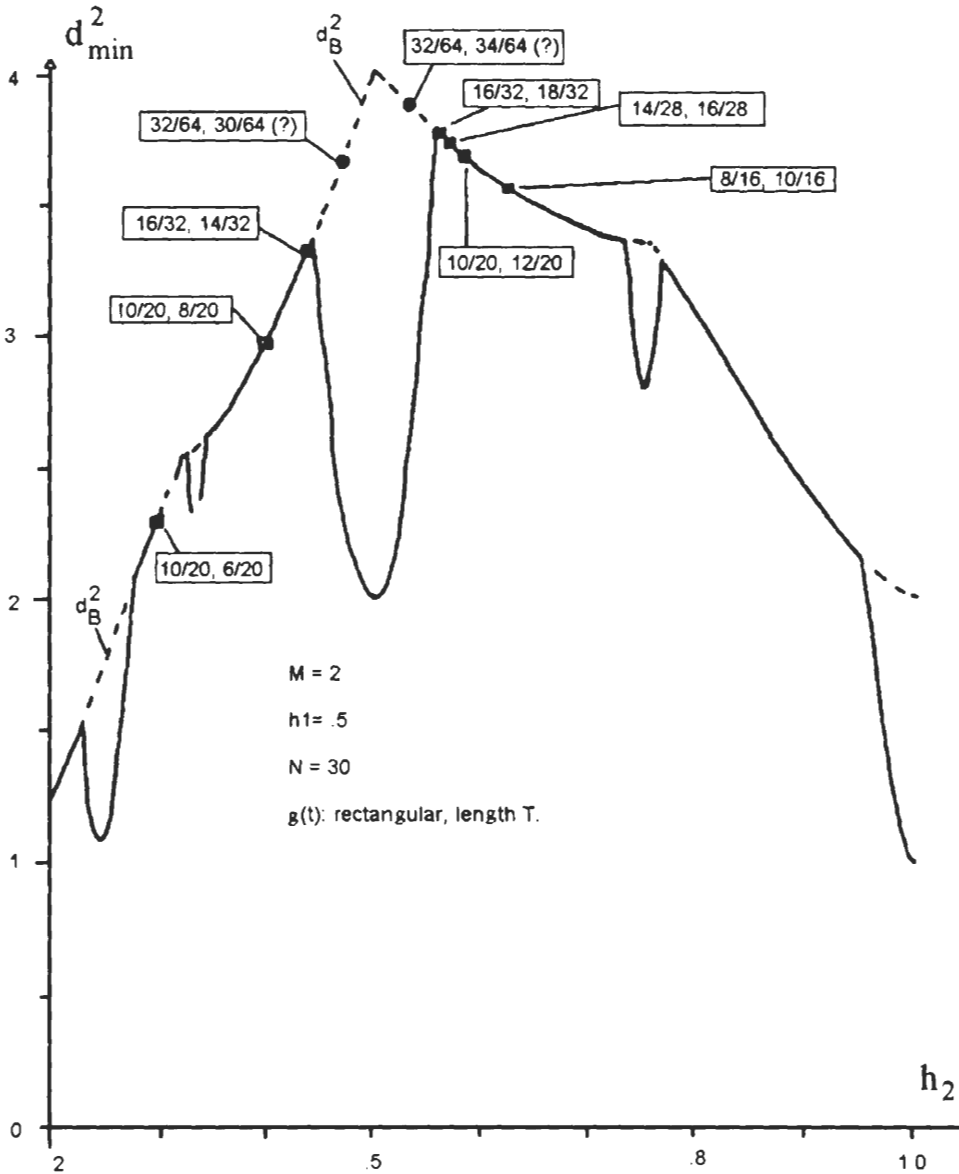


Figure 7.11 The minimum squared normalized Euclidean distance d_{\min}^2 for binary 1REC 2- h schemes with $h_1 = 0.5$ versus h_2 for $N = 30$. From [17]. Copyright © 1982 IEEE.

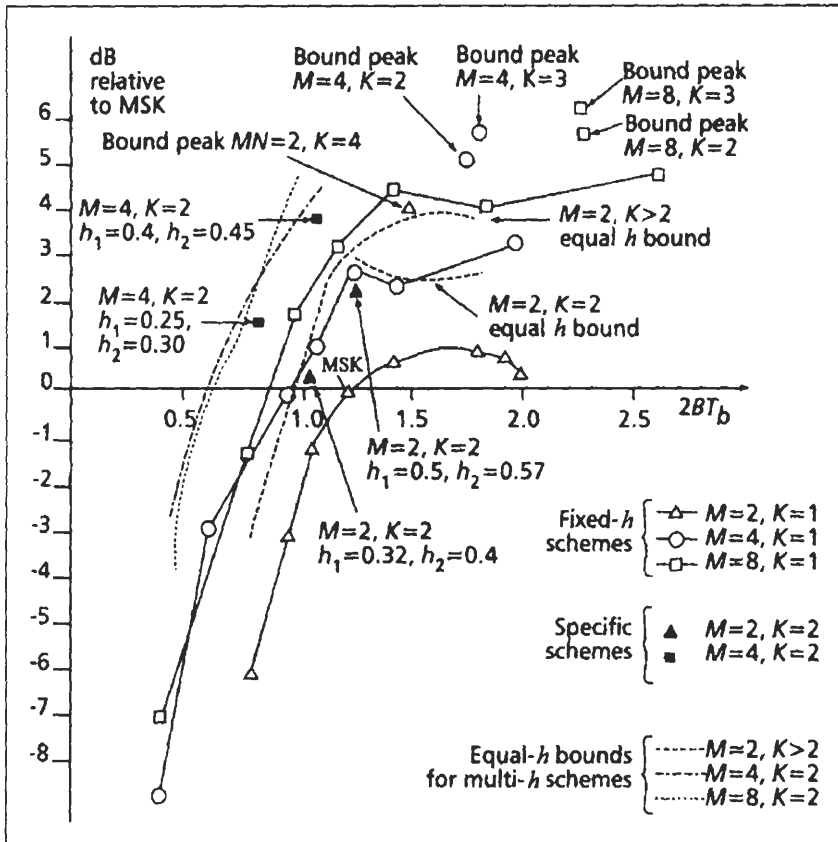


Figure 7.12 Power bandwidth trade-off for M -ary 1REC MHPM schemes. The bandwidth is the -20 dB (99%) out-of-band power bandwidth. All schemes are compared at equal bit rate. From [9]. Copyright © 1982 IEEE.

Again from this figure we can see that $M = 4$ schemes are considerably better than $M = 2$ schemes for the same h or H_K ; and 2- h schemes are slightly better than single- h schemes for the same M . There are two 2- h 3RC schemes that are considerably better than MSK: $M = 4$, $H_2 = (0.35, 0.40)$, and $(0.40, 0.45)$. They have 1.81 dB and 3.14 dB gain in distance over MSK.

Lereim investigated the coding gain and spectral properties of the various binary 1REC MHPM signals extensively and the results are summarized in Tables 7.1, 7.2, and 7.3 [6]. The modulation indexes are expressed in the form of $\{q/p_1, p_2, \dots, p_K\}$. The decision depth is the depth in the trellis beyond which all unmerged paths have distance exceeding d_{free} , the free distance,² and is a useful design parameter for

² d_{free} is defined as the distance from a given ("transmitted") path to its nearest neighbor of any

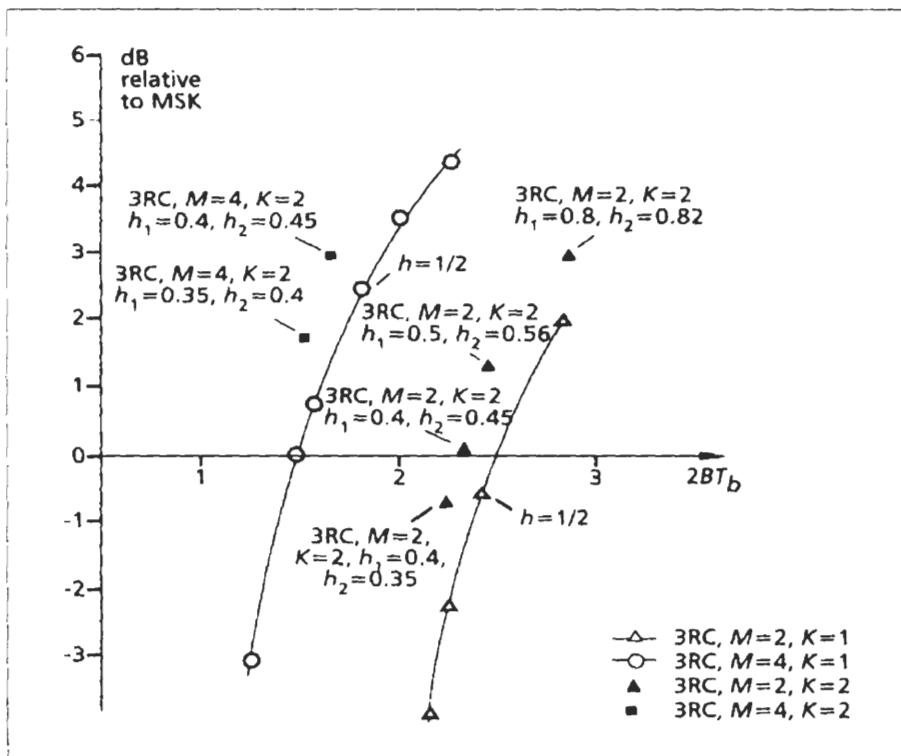


Figure 7.13 Power bandwidth trade-off for M-ary partial response 3RC MHPM schemes. The bandwidth is defined as the bit rate normalized width of the PSDs at the -60 dB level. From [9]. Copyright © 1982 IEEE.

the practical Viterbi demodulator. The coding gain is the gain in d_{\min}^2 over that of MSK. The bandwidths are the one-sided fractional out-of-band power bandwidths normalized to the bit rate. For MSK, we can easily find out (using (5.14) and (2.21)) $B_{95\%} \approx 0.45$, $B_{99\%} \approx 0.6$, $B_{99.5\%} \approx 0.81$. These are benchmarks for bandwidth comparison when reading the tables. Table 7.1 lists the schemes with high coding gains. But these schemes also need higher bandwidth than MSK; and the schemes have at least three indexes, which translate into high system complexity. Table 7.2 lists the schemes with moderate coding gain and less bandwidth needs than MSK, and some schemes have only two indexes. Table 7.3 lists the schemes with some coding loss and very high bandwidth savings with respect to MSK.

length. For linear codes, such as convolutional codes, d_{free} is independent of the transmitted path. For multi- h codes, d_{free} varies with the transmitted path. Thus there is a $d_{free, \min}$ which dominates the error performance. See [4] for more about d_{free} .

H_K	K	Coding gain (dB)	Bandwidth			Decision depth
			95.0%	99.0%	99.5%	
16/12 10 11 8	4	3.66	0.53	0.85	1.00	26-38
16/10 11 12	3	3.36	0.53	0.89	1.03	26-27
13/8 9 10	3	3.19	0.53	0.90	1.03	17-20
16/11 12 10 8	4	3.16	0.53	0.85	1.00	11-27
16/12 11 10 8	4	3.16	0.53	0.85	1.00	11-34
16/9 10 11	3	3.13	0.51	0.81	0.98	24-26
14/8 9 10	3	3.13	0.53	0.84	0.99	18-20
16/12 9 10 8	4	3.03	0.51	0.81	0.98	28
14/9 10 11	3	2.96	0.54	0.91	1.04	17-26
16/12 10 9 8	4	2.91	0.51	0.81	0.98	29-30
16/10 12 9 8	4	2.91	0.51	0.81	0.98	29
16/8 9 10	3	2.82	0.49	0.64	0.93	28
14/7 8 9	3	2.81	0.50	0.65	0.94	22
12/6 7 8	3	2.81	0.50	0.66	0.95	17
10/5 6 7	3	2.81	0.51	0.78	0.90	13
12/6 7 9	3	2.77	0.53	0.83	0.99	7-17
8/4 5 6	3	2.77	0.53	0.84	1.00	7-9
12/6 8 9	3	2.77	0.53	0.85	1.00	13-14
16/8 9	2	2.74	0.48	0.61	0.89	20
10/5 6 8	3	2.74	0.54	0.86	1.01	11-13

Table 7.1 Binary 1REC MHPM schemes with high coding gain over MSK. From [6].

H_K	K	Coding gain(dB)	Bandwidth			Decision depth
			95.0%	99.0%	99.5%	
16/78	2	2.19	0.45	0.59	0.68	21
16/678	3	2.10	0.43	0.59	0.66	20
14/67	2	2.07	0.44	0.59	0.68	19
14/567	3	1.96	0.43	0.58	0.65	16-18
10/45	2	1.72	0.44	0.59	0.66	11
15/67	2	1.67	0.43	0.58	0.65	20
16/6478	4	1.65	0.40	0.56	0.64	7-20
15/567	3	1.53	0.40	0.56	0.64	20
12/456	3	1.47	0.41	0.58	0.65	13
8/34	2	1.45	0.43	0.59	0.66	8
16/4678	4	1.45	0.40	0.58	0.65	20
13/56	2	1.44	0.41	0.58	0.65	15
14/57	2	1.28	0.43	0.59	0.66	11
16/67	2	1.28	0.40	0.56	0.64	21
16/4768	4	1.21	0.40	0.59	0.65	11-20
11/45	2	1.12	0.40	0.58	0.64	11
16/567	3	1.07	0.39	0.55	0.63	20
14/56	2	0.97	0.40	0.56	0.63	16
13/456	3	0.89	0.39	0.56	0.64	14
16/58	2	0.87	0.40	0.60	0.68	8

Table 7.2 Bandwidth efficient binary IREC MHPM schemes with moderate coding gain over MSK. From [6].

H_K	K	Coding gain(dB)	Bandwidth			Decision depth
			95.0%	99.0%	99.5%	
15/3 4 5	3	-2.40	0.29	0.46	0.54	11
14/3 4	2	-2.67	0.26	0.46	0.54	8
16/3 4 5	3	-2.92	0.26	0.46	0.53	11
16/3 5	2	-3.03	0.28	0.46	0.55	11
13/3 4	2	-2.08	0.29	0.48	0.56	8
15/3 5	2	-2.50	0.29	0.48	0.56	11
16/4 5	2	-1.57	0.30	0.49	0.56	12
11/2 3 4	3	-2.48	0.30	0.49	0.56	9-10
9/2 3	2	-2.54	0.30	0.49	0.58	6
15/4 5	2	-1.08	0.31	0.50	0.58	12
10/2 3 4	3	-1.70	0.33	0.50	0.56	9-10
14/3 4 5	3	-1.84	0.31	0.50	0.58	10
16/4 5 6	3	-0.68	0.33	0.51	0.58	15-16
13/3 4 5	3	-1.25	0.33	0.51	0.59	10
8/2 3	2	-1.62	0.33	0.51	0.59	6
14/3 5	2	-1.94	0.30	0.51	0.59	10
16/5 6	2	0.06	0.35	0.53	0.60	16
14/4 5	2	-0.56	0.34	0.53	0.59	12
11/3 4	2	-0.80	0.34	0.53	0.60	8
13/3 5	2	-1.35	0.33	0.53	0.61	10

Table 7.3 Bandwidth efficient binary IREC MHPM schemes (with negative coding gain over MSK). From [6].

So far we have been focusing on d_{\min}^2 and its upper bound d_B^2 . Even though d_{\min}^2 and d_B^2 are good performance indicators, it would be desirable to have the results of the symbol or bit error probability directly. Over bounds to probability of error event are given in [4] for binary 1REC MHPM. Bit error probabilities for the same class of schemes were found by simulation and presented in [18].³ Further improved results were reported in [19] where upper and lower bounds as well as simulation results for the bit error probabilities of the M-ary 1REC schemes were presented. Figures 7.14 to 7.16 are from [19]. Simulations were performed by the Viterbi demodulator.

Three schemes, binary $\{2/4, 3/4\}$, $\{4/8, 5/8, 6/8\}$, and 4-ary $\{3/16, 4/16\}$ were considered. The free distance calculations for these schemes project an asymptotic gain over coherent BPSK or QPSK by 1.4 dB, 2.8 dB and -0.8 dB, respectively. The first two have spectra comparable to that of CPFSK with $h = 5/8$, and the 99% bandwidth is about 1.67 times the bit rate. The 4-ary scheme has a narrower bandwidth. Its 99% bandwidth is about 0.7 times the bit rate.

The upper bounds and lower bounds and simulated bit error probabilities for the binary $\{2/4, 3/4\}$ scheme are shown in Figure 7.14 where N is the number of symbols of the observation (or path memory length). The decision depth is four for this scheme. Thus we expect that $N = 4$ should be adequate as a practical path memory length. From Figure 7.14 we can see that this indeed is true. For $P_b < 10^{-4}$, the upper bound for $N = 4$ case is only 0.2 dB or less higher than the unlimited path memory case. The simulation results for $N = 4$ and $N = \infty$ are very close. The upper and lower bounds for $N \geq 4$ are very tight at $E_b/N_o \geq 8$ dB. With $N = 2$, the performance is much poorer. It is essentially equal to that of BPSK (see the BPSK curve in Figure 4.4).

Figure 7.15 shows the bounds for the binary $\{4/8, 5/8, 6, 8\}$ scheme. Larger asymptotic coding gain with respect to coherent BPSK is observed. When compared with the $\{2/4, 3/4\}$ scheme, this stronger scheme needs longer path memory length to realize its potential. The decision depth for this scheme is nine. The upper bound for $N = 8$ is about 0.3 dB higher than the unlimited memory bound.

Figure 7.16 shows the bounds for the 4-ary $\{3/16, 4/16\}$ scheme. This scheme has a narrower bandwidth than the binary ones. However, the coding gain is negative with respect to coherent BPSK. The asymptotic loss is about 0.8 dB. Again the decision depth for this scheme is nine, the upper bound for $N = 8$ is about 0.3 dB higher than the unlimited memory bound.

³ The binary data symbols are $[0, 1]$ in [4, 18] instead of $[-1, 1]$ which is the common assumption in the literature and this book. The $[0, 1]$ symbol assumption does not change the distance property of the phase trellis, hence the error performance. However, it does reduce the number of distinct phases in the trellis to half. That is, the number of distinct phases is q instead of $2q$ [4].

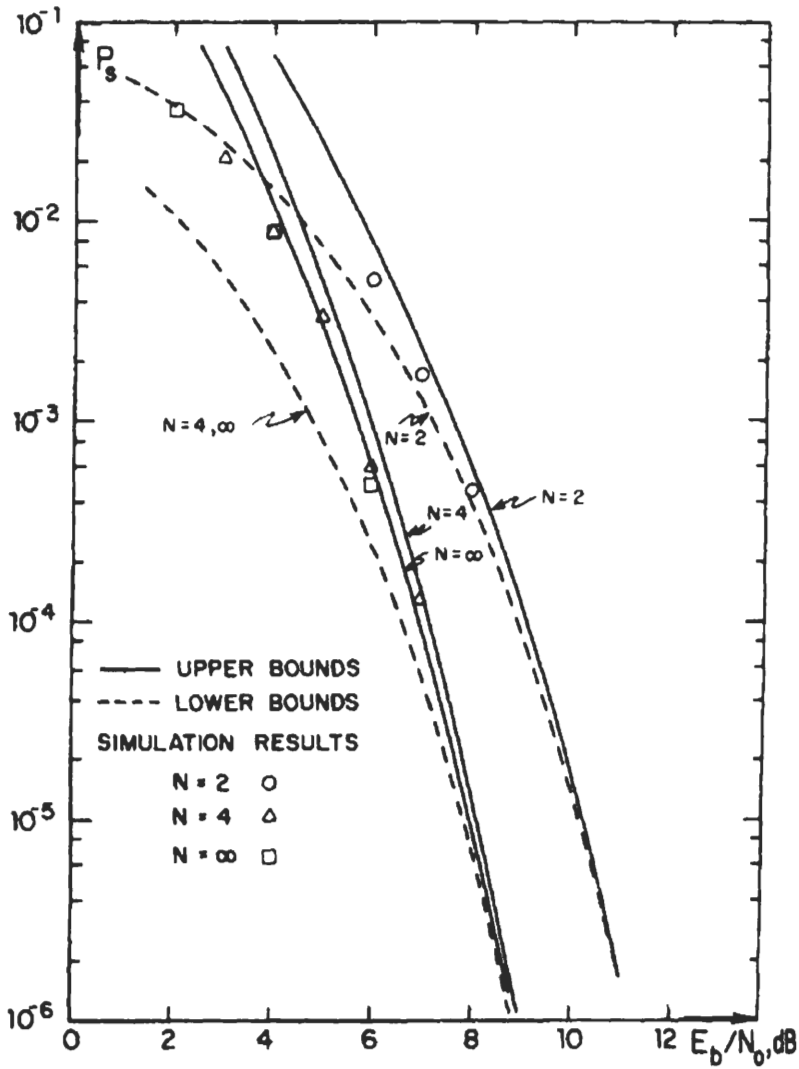


Figure 7.14 Bounds and simulated bit error probabilities for the binary IREC {2/4, 3/4} scheme. The decision depth of the Viterbi algorithm is four. From [19]. Copyright © 1982 IEEE.

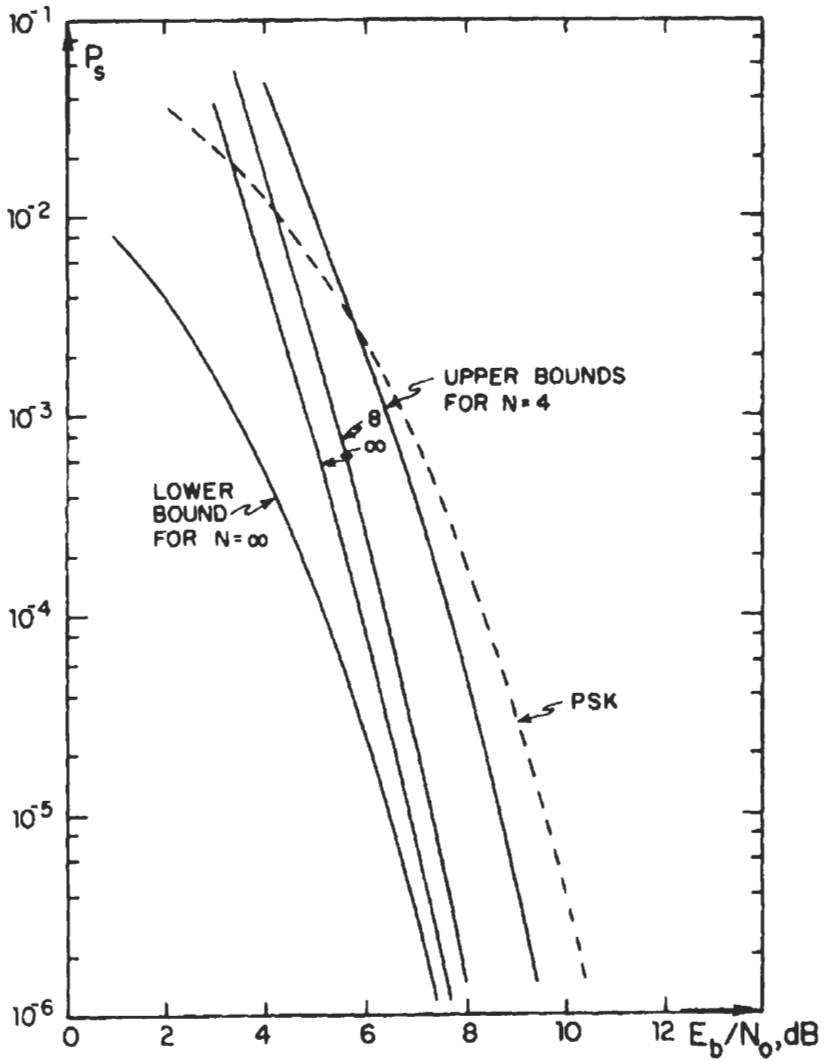


Figure 7.15 Bounds for the binary 1REC {4/8, 5/8, 6, 8} scheme. The decision depth of the Viterbi algorithm is nine. From [19]. Copyright © 1982 IEEE.

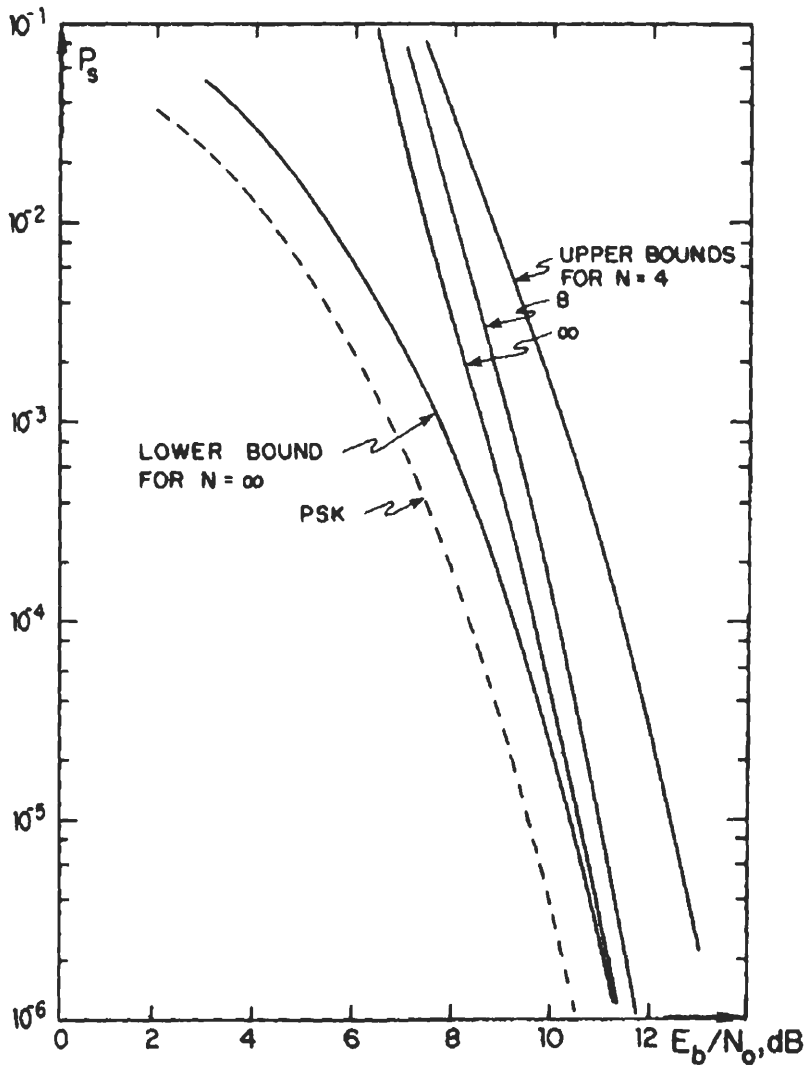


Figure 7.16 Bounds for the 4-ary 1REC {3/16, 4/16} scheme. The decision depth of the Viterbi algorithm is nine. From [19]. Copyright © 1982 IEEE.

7.4 MODULATOR

MHPM modulators are almost identical to those of single- h CPM except that the index h must be cyclically rotated when modulating. Specifically, Figures 6.13 to 6.17 all can be adapted to MHPM by cyclically changing the modulation indexes.

7.5 DEMODULATOR AND SYNCHRONIZATION

MHPM demodulators are also similar to single- h CPM demodulators except that the demodulator must have a prior knowledge of the sequence of indexes h_k employed at the transmitter. Thus in principle we can adapt all demodulators in Chapter 6 to MHPM. However, since the MLSE demodulator using the Viterbi algorithm is the most promising one and is explored the most in the literature, we will only consider this type of MHPM demodulators.

For MHPM schemes with rational indexes, MLSE demodulation is based on their state trellises using the Viterbi algorithm. For MHPM schemes with rational indexes and full-response frequency pulse, the phase trellis is equivalent to the state trellis, thus MLSE demodulation is based on their phase trellises using the Viterbi algorithm. Difference between various MLSE demodulators lie in the “front end” of the demodulator (i.e., the method of obtaining the branch metrics in the trellis).

MHPM demodulators reported in the literature so far are for full-response binary or M-ary CPFSK (i.e., 1REC-MHPM) schemes [4, 7, 18, 20–23]. Demodulators for partial-response MHPM schemes and frequency pulses other than 1REC have not been reported in the literature. In the following, we will first discuss the demodulator for binary multi- h CPFSK, which has a very simple structure. Then we will discuss the more complex demodulators for M-ary CPFSK with carrier and/or symbol synchronization.

7.5.1 A Simple ML Demodulator for Multi- h Binary CPFSK

Figure 7.17 is the simple ML multi- h binary CPFSK demodulator which employs four bandpass correlators. The reference signals must be updated for each symbol interval by cyclically switching indexes h_k . The coefficients $\{A'_1, A'_2, A'_3, A'_4\}$ are sufficient statistics for the signal. They are used to compute the branch metrics of the phase trellis for the Viterbi processor which eventually demodulates the signal. Factors $C_{1,k}$, $C_{2,k}$, and D_k are related to indexes too and must be cyclically changed.

This demodulator was first proposed in [4] and later in [18] as a means of simulating error performance. It was later presented as a formal demodulator in [7].

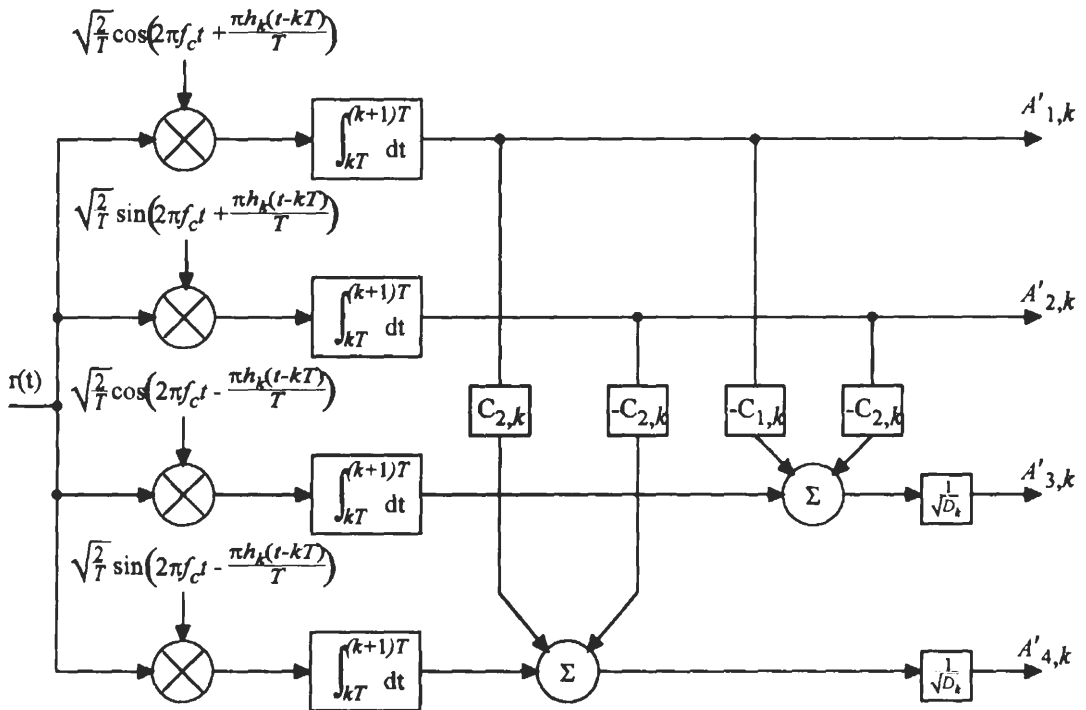


Figure 7.17 Multi- h binary CPFSK demodulation: determination of coefficients. From Bhargava et al., *Digital Communications by Satellite*, Copyright © 1981 John Wiley & Sons, Inc. Reprinted by permission of John Wiley & Sons, Inc.

Although this demodulator was proposed for multi- h CPFSK, we have no reason to believe that this demodulator cannot be used for single- h binary CPFSK. We need simply replace h_k by h . We have presented the Viterbi demodulator for the general CPM case in Chapter 6, Section 6.5.3. It needs a basic quadrature receiver (Figure 6.26) and a bank of $2M^L$ baseband matched filters (Figure 6.27). When applied to binary CPFSK (single- h or multi- h), the number of the matched filters in Figure 6.27 is four which is the same as the number of correlators in Figure 7.17. The structure of Figure 7.17 looks a bit simpler since no quadrature receiver is needed. However, it requires four coherent reference signals with not only the exact carrier frequency but also a linear phase $\pi h_k t/T$ which depends on the modulation index of the symbol interval. The four coherent reference signals in Figure 7.17 must be provided by a separate carrier recovery circuit.

We now derive the demodulator structure of Figure 7.17. It is obtained by the Gram-Schmidt procedure (which is also used in the discussion of detection of binary and M-ary signals in Appendix B).

Using trigonometric identities, we can expand the CPFSK signal in (7.9) as (ex-

pressing the amplitude in terms of the signal energy E : $A = \sqrt{2E/T}$)

$$\begin{aligned}
 s(t) &= \sqrt{\frac{2E}{T}} \cos\left(2\pi f_c t + \frac{a_k \pi h_k(t - kT)}{T} + \theta_k\right) \\
 &= \sqrt{\frac{2E}{T}} \left[\cos \theta_k \cos\left(2\pi f_c t + \frac{a_k \pi h_k(t - kT)}{T}\right) \right. \\
 &\quad \left. - \sin \theta_k \sin\left(2\pi f_c t + \frac{a_k \pi h_k(t - kT)}{T}\right) \right] \\
 &= \sqrt{\frac{2E}{T}} \left\{ \cos \theta_k \left[\cos(2\pi f_c t) \cos \frac{a_k \pi h_k(t - kT)}{T} \right. \right. \\
 &\quad \left. \left. - \sin(2\pi f_c t) \sin \frac{a_k \pi h_k(t - kT)}{T} \right] \right. \\
 &\quad \left. - \sin \theta_k \left[\sin(2\pi f_c t) \cos \frac{a_k \pi h_k(t - kT)}{T} \right. \right. \\
 &\quad \left. \left. + \cos(2\pi f_c t) \sin \frac{a_k \pi h_k(t - kT)}{T} \right] \right\}
 \end{aligned}$$

Realizing that if $a = \pm 1$, then $\cos(ax) = \cos x$ and $\sin(ax) = a \sin x$, the above can be reduced to

$$\begin{aligned}
 s(t) &= \sqrt{\frac{2E}{T}} \left\{ \cos \theta_k \left[\cos(2\pi f_c t) \cos \frac{\pi h_k(t - kT)}{T} \right. \right. \\
 &\quad \left. \left. - a_k \sin(2\pi f_c t) \sin \frac{\pi h_k(t - kT)}{T} \right] \right. \\
 &\quad \left. - \sin \theta_k \left[\sin(2\pi f_c t) \cos \frac{\pi h_k(t - kT)}{T} \right. \right. \\
 &\quad \left. \left. + a_k \cos(2\pi f_c t) \sin \frac{\pi h_k(t - kT)}{T} \right] \right\} \quad (7.29)
 \end{aligned}$$

Using trigonometric identities for $\cos u \cos v$, $\cos u \sin v$, $\sin u \sin v$, $\sin u \cos v$, the above can be converted to

$$\begin{aligned}
 s(t) &= \sqrt{\frac{2E}{T}} (\cos \theta_k) \left(\frac{1 + a_k}{2} \right) \cos \left(2\pi f_c t + \frac{\pi h_k(t - kT)}{T} \right) \\
 &\quad - \sqrt{\frac{2E}{T}} (\sin \theta_k) \left(\frac{1 + a_k}{2} \right) \sin \left(2\pi f_c t + \frac{\pi h_k(t - kT)}{T} \right)
 \end{aligned}$$

$$\begin{aligned}
& + \sqrt{\frac{2E}{T}} (\cos \theta_k) \left(\frac{1 - a_k}{2} \right) \cos \left(2\pi f_c t - \frac{\pi h_k (t - kT)}{T} \right) \\
& - \sqrt{\frac{2E}{T}} (\sin \theta_k) \left(\frac{1 - a_k}{2} \right) \sin \left(2\pi f_c t - \frac{\pi h_k (t - kT)}{T} \right) \quad (7.30)
\end{aligned}$$

Although each pair of terms with $\pi h_k(t - kT)/T$ and $-\pi h_k(t - kT)/T$ is orthogonal, terms in one pair are not orthogonal to terms in the second pair. By using the Gram-Schmidt procedure, however, we can transform (7.30) into a orthogonal expansion based on the following four orthonormal base functions (see Appendix 7A at the end of this chapter)

$$\psi_1(t) = \sqrt{\frac{2}{T}} \cos \left(2\pi f_c t + \frac{\pi h_k (t - kT)}{T} \right) \quad (7.31)$$

$$\psi_2(t) = \sqrt{\frac{2}{T}} \sin \left(2\pi f_c t + \frac{\pi h_k (t - kT)}{T} \right) \quad (7.32)$$

$$\psi_3(t) = \frac{1}{\sqrt{D_k}} \left[\sqrt{\frac{2}{T}} \cos \left(2\pi f_c t - \frac{\pi h_k (t - kT)}{T} \right) - C_{1,k} \psi_1(t) - C_{2,k} \psi_2(t) \right] \quad (7.33)$$

$$\psi_4(t) = \frac{1}{\sqrt{D_k}} \left[\sqrt{\frac{2}{T}} \sin \left(2\pi f_c t - \frac{\pi h_k (t - kT)}{T} \right) + C_{2,k} \psi_1(t) - C_{1,k} \psi_2(t) \right] \quad (7.34)$$

where

$$C_{1,k} = \frac{\sin 2\pi h_k}{2\pi h_k}$$

$$C_{2,k} = \frac{1 - \cos 2\pi h_k}{2\pi h_k}$$

$$D_k = 1 - C_{1,k}^2 - C_{2,k}^2$$

Using these four functions, the signal $s(t)$ can be written as

$$\begin{aligned}
s(t) &= \sqrt{E} (\cos \theta_k) \left(\frac{1 + a_k}{2} \right) \psi_1(t) \\
&\quad - \sqrt{E} (\sin \theta_k) \left(\frac{1 + a_k}{2} \right) \psi_2(t)
\end{aligned}$$

$$\begin{aligned}
& +\sqrt{E}(\cos \theta_k) \left(\frac{1-a_k}{2}\right) \left[C_{1,k}\psi_1(t) + C_{2,k}\psi_2(t) + \sqrt{D_k}\psi_3(t)\right] \\
& -\sqrt{E}(\sin \theta_k) \left(\frac{1-a_k}{2}\right) \left[-C_{2,k}\psi_1(t) + C_{1,k}\psi_2(t) + \sqrt{D_k}\psi_4(t)\right]
\end{aligned} \tag{7.35}$$

Rearranging terms in (7.35) gives

$$s(t) = \sqrt{E} [A_{1,k}\psi_1(t) + A_{2,k}\psi_2(t) + A_{3,k}\psi_3(t) + A_{4,k}\psi_4(t)] \tag{7.36}$$

where

$$A_{1,k} = (\cos \theta_k) \left(\frac{1+a_k}{2}\right) + C_{1,k}(\cos \theta_k) \left(\frac{1-a_k}{2}\right) + C_{2,k}(\sin \theta_k) \left(\frac{1-a_k}{2}\right) \tag{7.37}$$

$$A_{2,k} = -(\sin \theta_k) \left(\frac{1+a_k}{2}\right) + C_{2,k}(\cos \theta_k) \left(\frac{1-a_k}{2}\right) - C_{1,k}(\sin \theta_k) \left(\frac{1-a_k}{2}\right) \tag{7.38}$$

$$A_{3,k} = (\cos \theta_k) \left(\frac{1-a_k}{2}\right) \sqrt{D_k} \tag{7.39}$$

$$A_{4,k} = -(\sin \theta_k) \left(\frac{1-a_k}{2}\right) \sqrt{D_k} \tag{7.40}$$

The coefficients reflect the data, the cumulate phase, and the modulation index (contained in $C_{i,k}$ and D_k) in each symbol interval. They completely determine the signal $s(t)$. Due to the orthogonality of the base functions, these coefficients can be obtained by correlating $s(t)$ with each of the base functions

$$A_{i,k} = \frac{1}{\sqrt{E}} \int_{kT}^{(k+1)T} s(t)\psi_i(t)dt$$

which is equivalent to passing the signal $s(t)$ through the structure in Figure 7.19 (except for a factor \sqrt{E}). The reference signals for the correlators are not completely orthogonal, but with the additional multipliers and adders, it is equivalent to a structure with the four orthonormal base functions given in (7.31) to (7.34).

In the following we will show how the structure of Figure 7.19 is used in the Viterbi MLSE demodulator.

Recall the derivation of the Viterbi demodulator in Section 6.5.3 which is ap-

plicable to multi- h case too. The branch metric of the Viterbi processor is

$$Z_k(\tilde{\mathbf{a}}) = \int_{kT}^{(k+1)T} r(t)s(t, \tilde{\mathbf{a}})dt \quad (7.41)$$

where $\tilde{\mathbf{a}}$ is an estimate of the transmitted data sequence \mathbf{a} . For the estimate data sequence the signal in the k th interval is

$$s(t, \tilde{\mathbf{a}}) = \sqrt{E} \left[\tilde{A}_{1,k}\psi_1(t) + \tilde{A}_{2,k}\psi_2(t) + \tilde{A}_{3,k}\psi_3(t) + \tilde{A}_{4,k}\psi_4(t) \right] \quad (7.42)$$

where

$$\tilde{A}_{i,k} = \frac{1}{\sqrt{E}} \int_{kT}^{(k+1)T} s(t, \tilde{\mathbf{a}})\psi_i(t)dt \quad (7.43)$$

are determined by the sequence $\tilde{\mathbf{a}}$. These coefficients are computed using (7.37) to (7.40) given the sequence $\tilde{\mathbf{a}}$.

Substitute (7.42) into (7.41) we have

$$\begin{aligned} Z_k(\tilde{\mathbf{a}}) &= \int_{kT}^{(k+1)T} r(t)\sqrt{E} \left[\tilde{A}_{1,k}\psi_1(t) + \tilde{A}_{2,k}\psi_2(t) \right. \\ &\quad \left. + \tilde{A}_{3,k}\psi_3(t) + \tilde{A}_{4,k}\psi_4(t) \right] dt \\ &= \sum_{i=1}^4 \int_{kT}^{(k+1)T} \sqrt{E}r(t)\tilde{A}_{i,k}\psi_i(t)dt \\ &= \sqrt{E} \sum_{i=1}^4 \tilde{A}_{i,k}A'_{i,k} \end{aligned} \quad (7.44)$$

where

$$\begin{aligned} A'_{i,k} &= \int_{kT}^{(k+1)T} r(t)\psi_i(t)dt \\ &= \int_{kT}^{(k+1)T} [s(t, \mathbf{a}) + n(t)]\psi_i(t)dt \\ &= \int_{kT}^{(k+1)T} s(t, \mathbf{a})\psi_i(t)dt + \int_{kT}^{(k+1)T} n(t)\psi_i(t)dt \\ &= \sqrt{E}A_{i,k} + n_{i,k} \end{aligned} \quad (7.45)$$

are the coefficients obtained by passing $r(t)$ through the correlators in Figure 7.17. These are the coefficients of the transmitted signal and noise terms $n_{i,k}$ which are

white Gaussian.

Equation (7.44) shows that the branch metric is equal to the inner product of the received coefficients $\{A'_{1,k}, A'_{2,k}, A'_{3,k}, A'_{4,k}\}$ obtained by the correlators of Figure 7.17 and the locally available coefficients $\{\tilde{A}_{1,k}, \tilde{A}_{2,k}, \tilde{A}_{3,k}, \tilde{A}_{4,k}\}$. These local coefficients are based on the estimate sequence $\tilde{\mathbf{a}}$ and are updated for each symbol interval as the length of $\tilde{\mathbf{a}}$ grows in the Viterbi demodulation process. Particularly, from (7.37) to (7.40) we can see that to compute $\tilde{A}_{i,k}$, we need the symbol estimate \tilde{a}_k , cumulate phase estimate $\tilde{\theta}_k$, and the current modulation index h_k . The Viterbi processor is able to track the estimate sequence (path) $\tilde{\mathbf{a}}$ and related phase sequence $\tilde{\theta}$, and the modulation index h_k must be provided by a synchronizer.

7.5.2 Joint Demodulation and Carrier Synchronization of Multi- h CPFSK

Although the demodulator described above is simple, it requires separate circuits for carrier synchronization and symbol synchronization. A joint demodulation and carrier synchronization scheme was proposed by Mazur and Taylor [23] for binary multi- h CPFSK. The approach is to use the Viterbi algorithm for estimating the data and the carrier phase error. The estimated phase error is used in a closed phase-tracking loop to achieve carrier phase synchronization. The scheme is named decision-directed demodulator. The scheme is shown in Figure 7.18. The inner product calculator (IPC) is to produce the branch metrics needed in the Viterbi algorithm. As we discussed in Section 6.5.3 (see (6.51)), for the AWGN channel, the branch metrics are the correlations of the received signal $r(t)$ with the local carriers. For the j th signaling interval the metrics are

$$\begin{aligned}
 b(1, h_j, n) &= \int_{jT}^{(j+1)T} r(t) \cos \left[2\pi f_c t + \frac{\pi h_j}{T} (t - jT) + \frac{n\pi}{q} + \phi(0) \right] dt \\
 b(-1, h_j, n) &= \int_{jT}^{(j+1)T} r(t) \cos \left[2\pi f_c t - \frac{\pi h_j}{T} (t - jT) + \frac{n\pi}{q} + \phi(0) \right] dt \\
 n &= 0, 1, 2, \dots, 2q - 1
 \end{aligned} \tag{7.46}$$

for data symbol 1 and -1 , respectively. Recall $h_i = p_i/q$ and there are $2q$ phase states in the trellis for an even q which is the usual case. Therefore the phase state at the beginning of the interval is $n\pi/q$, $n = 0, 1, 2, \dots, 2q - 1$. The cosine functions are the local carriers, corresponding to 1 and -1 , respectively. $\phi(0)$ is the initial phase of the local carriers. To have coherent detection, $\phi(0)$ must be estimated from $r(t)$, that is, the carriers must be synchronized with the received signal.

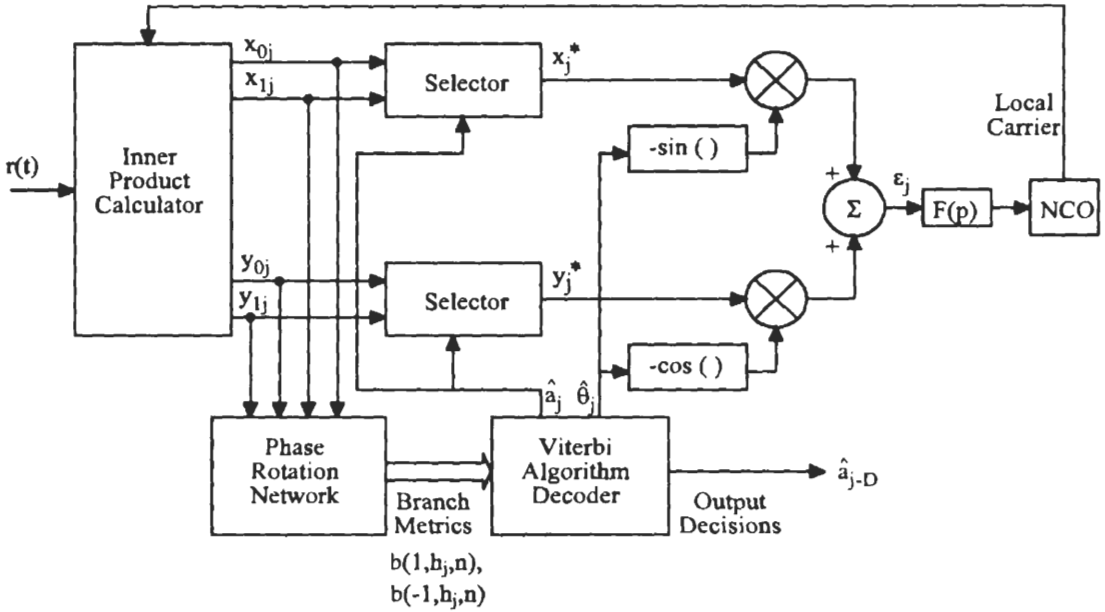


Figure 7.18 Receiver for binary multi-h CPFSK showing the decision-directed carrier recovery loop and the use of the Viterbi algorithm in phase error computation. From [23]. Copyright © 1981 IEEE.

The branch metrics can be rewritten as

$$\begin{aligned}
 b(1, h_j, n) &= X_{1j} \cos \frac{n\pi}{q} - Y_{1j} \sin \frac{n\pi}{q} \\
 b(-1, h_j, n) &= X_{0j} \cos \frac{n\pi}{q} - Y_{0j} \sin \frac{n\pi}{q} \\
 n &= 0, 1, 2, \dots, 2q - 1
 \end{aligned} \tag{7.47}$$

where

$$\begin{aligned}
 X_{1j} &= \int_{jT}^{(j+1)T} r(t) \cos \left[2\pi f_c t + \frac{\pi h_j}{T} (t - jT) + \phi(0) \right] dt \\
 Y_{1j} &= \int_{jT}^{(j+1)T} r(t) \sin \left[2\pi f_c t + \frac{\pi h_j}{T} (t - jT) + \phi(0) \right] dt \\
 X_{0j} &= \int_{jT}^{(j+1)T} r(t) \cos \left[2\pi f_c t - \frac{\pi h_j}{T} (t - jT) + \phi(0) \right] dt \\
 Y_{0j} &= \int_{jT}^{(j+1)T} r(t) \sin \left[2\pi f_c t - \frac{\pi h_j}{T} (t - jT) + \phi(0) \right] dt
 \end{aligned} \tag{7.48}$$

The benefit of converting (7.46) to (7.47) and (7.48) is that the local carriers in (7.48) no longer depend on $n\pi/q$, unlike the ones in (7.46). In addition, the computation of branch metrics are made more efficient by means of the two-step calculation depicted in (7.48) and (7.47).

Since $r(t) = s(t) + n(t)$, where $s(t)$ is the signal defined in (7.9) and $n(t)$ is the AWGN with zero mean and a single-sided power spectral density N_o , each of the above four correlations consists of a signal part and a noise part. In the following we will show how the phase error is extracted. For this purpose we assume that noise is absent. Under this assumption, we rewrite the received $r(t)$ in a different form

$$r(t) = s(t) = A \cos[2\pi f_c t + \theta(t, a_j) + \theta_j + \phi_j], \quad jT \leq t \leq (j+1)T$$

where

$$\begin{aligned} \theta(t, a_j) &= \pm \frac{\pi h_j}{T} (t - jT), \quad \text{for } a_j = \pm 1 \\ \theta_j &= \frac{n\pi}{q}, \quad n = 0, 1, 2, \dots, 2q - 1 \end{aligned}$$

and ϕ_j is the random phase introduced by the channel. Then when $a_j = 1$, using (7.48) we have

$$\begin{aligned} X_{1j} &= \int_{jT}^{(j+1)T} A \cos[2\pi f_c t + \theta(t, a_j) + \theta_j + \phi_j] \\ &\quad \cdot \cos[2\pi f_c t + \theta(t, a_j) + \phi(0)] dt \\ &= \frac{1}{2} \int_{jT}^{(j+1)T} A \cos[4\pi f_c t + 2\theta(t, a_j) + \theta_j + \phi_j + \phi(0)] dt \\ &\quad + \frac{1}{2} \int_{jT}^{(j+1)T} A \cos[\theta_j + \phi_j - \phi(0)] dt \\ &\approx \frac{1}{2} A \cos(\theta_j + \varepsilon_j), \quad a_j = 1 \end{aligned}$$

since the first integral is approximately zero for $f_c \gg 1/T$. In the above

$$\varepsilon_j = \phi_j - \phi(0)$$

is the difference between the signal random phase and the carrier initial phase which is the estimate of the signal random phase. Thus ε_j is the estimate error. Similarly we can find out others. In summary, we have

$$X_{1j} \approx \frac{1}{2} A \cos(\theta_j + \varepsilon_j), \quad a_j = 1 \quad (7.49)$$

$$Y_{1j} \approx -\frac{1}{2}A \sin(\theta_j + \varepsilon_j), \quad a_j = 1 \quad (7.50)$$

$$X_{0j} \approx \frac{1}{2}A \cos(\theta_j + \varepsilon_j), \quad a_j = -1 \quad (7.51)$$

$$Y_{0j} \approx -\frac{1}{2}A \sin(\theta_j + \varepsilon_j), \quad a_j = -1 \quad (7.52)$$

The nonmatched cases: X_{1j} , $a_j = -1$, Y_{1j} , $a_j = -1$, X_{0j} , $a_j = 1$, Y_{0j} , $a_j = 1$, are not listed above since they are irrelevant to the discussion that follows.

In Figure 7.18, the inner product calculator (IPC) is used to generate the primitive set of four correlations X_{1j} , Y_{1j} , X_{0j} , and Y_{0j} needed for each signaling interval, and a phase rotation network (PRN) uses these to realize the calculation in (7.47) (which is a phase rotation operation). Table lookup techniques may be used to implement the PRN. The outputs of the PRN are the branch metrics given in (7.47), which are used in the Viterbi algorithm detector. For bit interval j and state n , the PRN produces two branch metrics $b(1, h_j, n)$ and $b(-1, h_j, n)$ for $\hat{a}_j = 1$ and -1 , respectively. Based on these metrics, the Viterbi detector makes a tentative decision \hat{a}_j on the data symbol for the current interval (choosing the one with a larger branch metric). Based on a sequence of \hat{a}_j the Viterbi detector makes the final decision \hat{a}_{j-D} on the symbol back by D intervals, where D is the decision depth, typically 4 to 8 constraint lengths (see Section 6.5.3). The Viterbi detector also makes a tentative decision $\hat{\theta}_j$ on the cumulate phase θ_j . Assume that the data estimate \hat{a}_j and phase estimate $\hat{\theta}_j$ are correct, \hat{a}_j and $\hat{\theta}_j$ are used to estimate the phase error ε_j as follows

$$\text{If } \hat{a}_j = 1, \text{ choose } X_j^* = X_{1j}, Y_j^* = Y_{1j}$$

then in the absence of noise

$$\begin{aligned} & -X_j^* \sin \hat{\theta}_j - Y_j^* \cos \hat{\theta}_j \\ = & -X_{1j} \sin \hat{\theta}_j - Y_{1j} \cos \hat{\theta}_j \\ = & -\frac{1}{2}A \cos(\theta_j + \varepsilon_j) \sin \hat{\theta}_j + \frac{1}{2}A \sin(\theta_j + \varepsilon_j) \cos \hat{\theta}_j \\ = & \frac{1}{2}A \sin(\theta_j + \varepsilon_j - \hat{\theta}_j) \\ = & \frac{1}{2}A \sin \varepsilon_j \\ \approx & \frac{1}{2}A \varepsilon_j \propto \varepsilon_j, \text{ for small } \varepsilon_j \end{aligned}$$

Similarly

$$\text{If } \hat{a}_j = -1, \text{ choose } X_j^* = X_{0j}, Y_j^* = Y_{0j}$$

then

$$\begin{aligned} & -X_j^* \sin \hat{\theta}_j - Y_j^* \cos \hat{\theta}_j \\ = & -X_{0j} \sin \hat{\theta}_j - Y_{0j} \cos \hat{\theta}_j \\ = & \frac{1}{2} A \sin \varepsilon_j \\ \approx & \frac{1}{2} A \varepsilon_j \propto \varepsilon_j, \text{ for small } \varepsilon_j \end{aligned}$$

It is clear that if the Viterbi estimates \hat{a}_j and $\hat{\theta}_j$ are correct, the operation $-X_j^* \sin \hat{\theta}_j - Y_j^* \cos \hat{\theta}_j$ produces a quantity that is proportional to the phase estimation error (Figure 7.18). With noise present, the error signal is passed through the low-pass filter $F(p)$ in order to reduce the noise. The output is used to control the NCO (numerically controlled oscillator) to generate a carrier with a decreasing phase error as this phase lock loop converges.

A scheme of $(3/8, 4/8)$ and other schemes were simulated in [23]. It was found empirically that the minimum number of bits of quantization required for demodulation/decoding is given by $1 + \log_2 q$, and that rounding to the nearest quantization level, as opposed to truncating, leads to superior performance. It was reported that a digital word size of 5 to 6 bits appears sufficient and the expected coding gain of 1.45 dB for $(3/8, 4/8)$ was nearly reached. For the schemes tested, an rms phase error of $0.2(\pi/2q)$ rad is typically sufficient to achieve almost optimum (within 0.2 dB) error-rate performance. In order to achieve this phase error, a minimum loop SNR of 30 dB is required.

7.5.3 Joint Carrier Phase Tracking and Data Detection of Multi- h CPFSK

A joint demodulation and carrier phase tracking (not synchronization) receiver was proposed in [20] for binary multi- h CPFSK. In this receiver, the demodulator is of the correlator type shown in Figure 7.17. It is modified to take into consideration the carrier phase error. The demodulator is followed by the Viterbi algorithm, which maximizes the a posteriori path metric. Thus the receiver is called a MAP-VA receiver. The Viterbi algorithm estimates both data and phase error of the local carrier. The estimated phase error is not used to adjust the local carrier phase to achieve phase synchronization. Instead, it is used in the Viterbi algorithm to assist in demodulating the data. Because no carrier synchronization is really achieved, the error performance of this receiver appears inferior to the decision-directed receiver given in [23]

Based on the simulation in [20] we can make a comparison between this MAP-VA receiver with the decision-directed receiver. The rms phase error of $0.2(\pi/2q)$ rad mentioned above translates to a squared phase error of 0.16 rad^2 for the $(3/8, 4/8)$ scheme. According to the results given in [20], for this amount of phase error, the loss in error performance at $P_e = 10^{-3}$ is about 2.5 dB (Figure 4 in [20]), whereas the loss is only 0.2 dB in [23]. The advantage of this receiver is that its system complexity is simpler, no phase lock loop is utilized. The detail of this receiver is omitted here due to the highly mathematical derivation.

7.5.4 Joint Demodulation, Carrier Synchronization, and Symbol Synchronization of M-ary Multi- h CPFSK

A receiver which can jointly perform demodulation, carrier recovery, and symbol synchronization for 4-ary multi- h CPFSK was proposed by Premji and Taylor in [21]. The receiver is an extension of the work on binary multi- h CPFSK in [23], and again is based on maximum likelihood sequence estimation via the Viterbi algorithm.

The derivation of this receiver basically follows that in Section 7.5.2. Since carrier and symbol synchronization are considered, the signal model includes an unknown carrier phase θ_0 and an unknown symbol timing offset τ_0 as

$$s(t) = A \cos[2\pi f_c t + a_j \frac{\pi h_j}{T} (t - jT - \tau_0) + \theta_0 + \theta_j], \quad jT + \tau_0 \leq t \leq (j+1)T + \tau_0$$

where $\theta_j = n\pi/q$, $n = 0, 1, 2, \dots, 2q - 1$ is the accumulated phase due to previous data. For the j th signaling interval the branch metrics, corresponding to the branches of the phase trellis extending from the n th trellis node at time $t = jT + \hat{\tau}_0$, are the correlations between the $r(t)$ and the local carriers:

$$\begin{aligned} & b(a_k, h_j, n) \\ &= \int_{jT + \hat{\tau}_0}^{(j+1)T + \hat{\tau}_0} r(t) \cos \left[2\pi f_c t + a_k \frac{\pi h_j}{T} (t - jT - \hat{\tau}_0) + \hat{\theta}_0 + \frac{n\pi}{q} \right] dt \\ &= \cos\left(\frac{n\pi}{q}\right) X_j - \sin\left(\frac{n\pi}{q}\right) Y_j \\ n &= 0, 1, 2, \dots, 2q - 1, \quad k = 1, 2, 3, 4 \end{aligned} \tag{7.53}$$

where

$$\begin{aligned} X_j &= \int_{jT + \hat{\tau}_0}^{(j+1)T + \hat{\tau}_0} r(t) \cos \left[2\pi f_c t + a_k \frac{\pi h_j}{T} (t - jT - \hat{\tau}_0) + \hat{\theta}_0 \right] dt \\ Y_j &= \int_{jT + \hat{\tau}_0}^{(j+1)T + \hat{\tau}_0} r(t) \sin \left[2\pi f_c t + a_k \frac{\pi h_j}{T} (t - jT - \hat{\tau}_0) + \hat{\theta}_0 \right] dt \end{aligned}$$

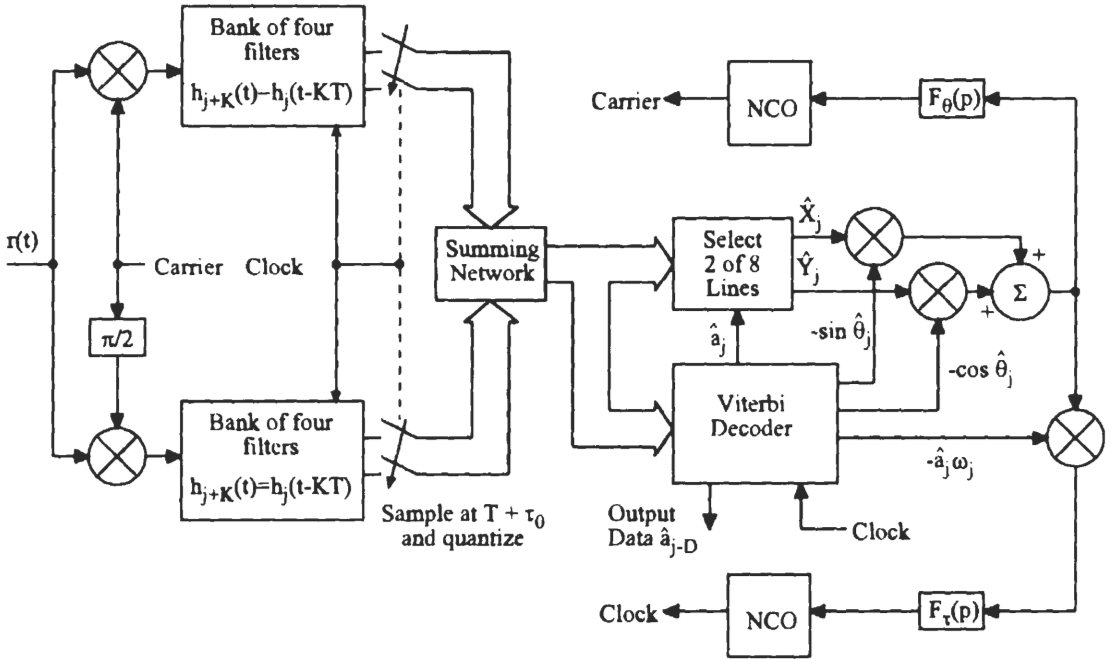


Figure 7.19 Joint demodulation, carrier synchronization, and symbol synchronization for 4-ary multi-*h* CPFSK. From [21]. Copyright © 1987 IEEE.

$$a_k = +1, -1, +3, \text{ or } -3 \text{ for } k = 1, 2, 3, 4 \tag{7.54}$$

where $\hat{\tau}_0$ and $\hat{\theta}_0$ are estimates of τ_0 and θ_0 , respectively. There are four a_k s, that is, $a_k = +1, -1, +3, \text{ or } -3$ for $k = 1, 2, 3, 4$, corresponding to four branches of a node in the trellis. The local carriers in (7.54) no longer depend on $n\pi/q$. Since $a_k = \pm 1, \pm 3$, during the j th interval four correlations operation are needed for X_j and another four correlation operations are needed for Y_j . The total number of correlations is eight in each interval.

The receiver is shown in Figure 7.19. The correlations of (7.54) are implemented by the two carrier-multipliers, two cycled banks of matched filters, and the summing network. The Viterbi decoder calculates the branch metric using (7.53) and performs the MLSE based on the phase trellis. In the following, we explain the correlation operation first and then the Viterbi decoder.

The correlations of (7.54) are actually implemented by matched filtering based on the well-known fact that correlation can be realized by matched filtering sampled at the end of the correlation period. Further, the received signal is down-converted to the baseband by the multipliers before filtering is performed. The equivalence of the operation in Figure 7.19 to (7.54) can be shown as follows. First, define a shorthand

notation $\alpha_j(t)$ for the linear phase term,

$$\alpha_j(t) = \frac{a_j \pi h_j}{T} (t - jT - \tau_0), \quad jT + \tau_0 \leq t \leq (j+1)T + \tau_0$$

Then the integrand of X_j can be written as

$$\begin{aligned} & \cos [2\pi f_c t + \alpha_j(t) + \theta_j + \theta_0] \cos [2\pi f_c t + \hat{\alpha}_j(t) + \hat{\theta}_0] \\ &= \frac{1}{2} \cos [4\pi f_c t + \alpha_j(t) + \theta_j + \theta_0 + \hat{\alpha}_j(t) + \hat{\theta}_0] \\ & \quad + \frac{1}{2} \cos [\alpha_j(t) - \hat{\alpha}_j(t) + \theta_j + \theta_0 - \hat{\theta}_0] \end{aligned}$$

Since the double frequency term integrates to zero, only the low-pass term of the above contributes to X_j (a factor of 1/2 is ignored and set $\varepsilon_{j\theta} = \theta_0 - \hat{\theta}_0$)

$$\begin{aligned} X_j &= \int_{jT+\hat{\tau}_0}^{(j+1)T+\hat{\tau}_0} \cos [\alpha_j(t) + \theta_j + \varepsilon_{j\theta} - \hat{\alpha}_j(t)] dt \\ &= \int_{jT+\hat{\tau}_0}^{(j+1)T+\hat{\tau}_0} \cos [\alpha_j(t) + \theta_j + \varepsilon_{j\theta}] \cos \hat{\alpha}_j(t) dt \\ & \quad + \int_{jT+\hat{\tau}_0}^{(j+1)T+\hat{\tau}_0} \sin [\alpha_j(t) + \theta_j + \varepsilon_{j\theta}] \sin \hat{\alpha}_j(t) dt \end{aligned} \quad (7.55)$$

Similarly Y_j can be shown as

$$\begin{aligned} Y_j &= - \int_{jT+\hat{\tau}_0}^{(j+1)T+\hat{\tau}_0} \sin [\alpha_j(t) + \theta_j + \varepsilon_{j\theta} - \hat{\alpha}_j(t)] dt \\ &= - \int_{jT+\hat{\tau}_0}^{(j+1)T+\hat{\tau}_0} \sin [\alpha_j(t) + \theta_j + \varepsilon_{j\theta}] \cos \hat{\alpha}_j(t) dt \\ & \quad + \int_{jT+\hat{\tau}_0}^{(j+1)T+\hat{\tau}_0} \cos [\alpha_j(t) + \theta_j + \varepsilon_{j\theta}] \sin \hat{\alpha}_j(t) dt \end{aligned} \quad (7.56)$$

Now assume that the carrier in Figure 7.19 is

$$C(t) = \cos(2\pi f_c t + \hat{\theta}_0)$$

where the estimated phase $\hat{\theta}_0$ is included. Then the I-channel (upper channel) multiplier output is

$$r(t)C(t) = \cos [2\pi f_c t + \alpha_j(t) + \theta_j + \theta_0] \cos(2\pi f_c t + \hat{\theta}_0)$$

the low-pass term of it is (a factor of 1/2 is ignored)

$$x_j(t) = \cos [\alpha_j(t) + \theta_j + \varepsilon_{j\theta}] \quad (7.57)$$

Similarly, the low-pass term of the output of the Q-channel (lower channel) multiplier is

$$y_j(t) = \sin [\alpha_j(t) + \theta_j + \varepsilon_{j\theta}] \quad (7.58)$$

By inspecting the expressions for $x_j(t)$, $y_j(t)$, X_j , and Y_j , we can see that

$$\begin{aligned} X_j &= \int_{jT+\hat{\tau}_0}^{(j+1)T+\hat{\tau}_0} x_j(t) \cos \hat{\alpha}_j(t) dt \\ &\quad + \int_{jT+\hat{\tau}_0}^{(j+1)T+\hat{\tau}_0} y_j(t) \sin \hat{\alpha}_j(t) dt \end{aligned} \quad (7.59)$$

$$\begin{aligned} Y_j &= - \int_{jT+\hat{\tau}_0}^{(j+1)T+\hat{\tau}_0} y_j(t) \cos \hat{\alpha}_j(t) dt \\ &\quad + \int_{jT+\hat{\tau}_0}^{(j+1)T+\hat{\tau}_0} x_j(t) \sin \hat{\alpha}_j(t) dt \end{aligned} \quad (7.60)$$

All the four integrations in (7.59) and (7.60) are now correlations in baseband. These correlations can be implemented by matched filtering. The filter impulse responses must match to

$$\cos \hat{\alpha}_j(t) = \cos \frac{a_j \pi h_j}{T} (t - jT - \hat{\tau}_0)$$

and

$$\sin \hat{\alpha}_j(t) = \sin \frac{a_j \pi h_j}{T} (t - jT - \hat{\tau}_0)$$

Since $a_j = \pm 1, \pm 3$ and by considering $\pm \sin \hat{\alpha}_j(t)$ as just one filter since the sign can be taken care of later when summing is done, the number of matched filter impulse responses is actually four. Recall that if the reference signal in the correlation is $s(t)$, then matched filter must be $h(t) = ks(T-t)$, k constant. Thus in the 0th interval the four matched filter impulse responses are (assuming symbol timing offset $\hat{\tau}_0 = 0$, since $\hat{\tau}_0$ is random and cannot be anticipated when filters are determined).

$$\{h_0(t)\} = \left\{ \cos \frac{\pi h_0(T-t)}{T}, \sin \frac{\pi h_0(T-t)}{T}, \cos \frac{3\pi h_0(T-t)}{T}, \sin \frac{3\pi h_0(T-t)}{T} \right\} \quad (7.61)$$

where h_0 is one of the K indexes, usually the first one. In the j th interval, the filter expressions can be obtained by replacing h_0 by h_j and t by $t - jT$ in the above expressions.

For a K -index CPFSK, there are K sets of four filters in the above forms, with each set using a different index. In the receiver these K sets are cyclically reused such that

$$\{h_{j+K}(t)\} = \{h_j(t - KT)\}$$

From (7.59) and (7.60) we also see that the I-channel alone cannot produce X_j and the Q-channel alone cannot produce Y_j . Thus a summing network is needed to perform the additions and subtractions in (7.59) and (7.60).

A selector in Figure 7.19 selects a pair of signals (\hat{X}_j, \hat{Y}_j) out of four pairs of (X_j, Y_j) based on the data estimate \hat{a}_j provided by the Viterbi decoder. This (\hat{X}_j, \hat{Y}_j) and the phase estimate $\hat{\theta}_j$ are used to generate the phase error estimate $\hat{\epsilon}_{j\theta}$ and timing offset estimate $\hat{\epsilon}_{j\tau}$ as follows

$$\begin{aligned}\hat{\epsilon}_{j\theta} &= -[\hat{X}_j \sin \hat{\theta}_j + \hat{Y}_j \cos \hat{\theta}_j] \\ \hat{\epsilon}_{j\tau} &= -\hat{a}_j \omega_j \hat{\epsilon}_{j\theta}\end{aligned}$$

where $\omega_j = \pi h_j / T$. These have been shown to be optimum under the condition that the tracking loop bandwidth is much smaller than the data rate [21]. These error signals are passed through loop filters and eventually are used to control two NCOs to produce a synchronous carrier and a synchronous symbol timing clock, respectively.

The performance analysis of this receiver is very complicated and is thus omitted here. The receiver was simulated for a (12/16, 13/16) multi- h CPFSK. The simulation used a six-bit quantization and a 15-symbol decision depth in the Viterbi decoder. The results showed that a coding gain of approximately 3.8 dB (over MSK) is already realized at a BER of 10^{-3} , while the expected asymptotic gain is about 4.52 dB for an ideal receiver. At values of E_s/N_o above 13 dB, a reasonable acquisition time/steady-state jitter trade-off may be attained through a suitable choice of loop SNRs. At lower E_s/N_o , however, some form of gear shifting of the loop bandwidth becomes necessary to ensure both a reasonable acquisition time and low steady-state jitter subsequent to acquisition. At an input E_s/N_o of 13 dB, satisfactory receiver performance mandates loop SNR values of approximately 35 dB for the carrier recovery loop and 33 dB for the clock loop.

A simplified suboptimum version of the above receiver is given in [22]. The major change of the receiver is that a fixed bank of filters has replaced the cyclically changing matched filters. The impulse responses of the fixed filters have the average h of the indexes. Thus they still have the forms given in (7.61) except that h_i is replaced by h . By using fixed filters, a complexity reduction of $1/K$ is

achieved while the penalty is a degradation in error-rate performance of 0.6 to 0.7 dB at $BER = 10^{-3}$ for the code (15/20, 17/20) that was simulated.

7.5.5 Synchronization of MHPM

Three levels of synchronization are required in a MHPM demodulator: carrier phase, symbol timing, and superbaud timing. Carrier phase and symbol-timing synchronization are common for all coherent phase modulations. What is unique here is the superbaud timing. The superbaud is the period of cyclic rotation of the K modulation indexes. A superbaud period is KT . Since symbol timing and superbaud timing are harmonically related, either one can be derived from the other easily. For example, if superbaud timing is established, a frequency multiplier of K times is sufficient to produce the symbol timing.

For the receiver in Section 7.5.4, carrier synchronization and symbol-timing synchronization are incorporated in the receiver already. For the receiver in Section 7.5.3, carrier phase synchronization is not needed and only symbol-timing synchronization is needed. For the receiver in Section 7.5.2, carrier phase synchronization is incorporated in the receiver, thus only symbol-timing synchronization is needed. For the receiver in Section 7.5.1, both carrier synchronization and symbol-timing synchronization are needed.

Recall that in Section 6.6.1 we discussed the MSK-type carrier and symbol synchronizer for single- h CPM (Figure 6.44). This synchronizer can also be used for MHPM [23]. First the received signal is raised to the power of q (recall $h_i = p_i/q$) by the nonlinear device in the synchronizer.

$$[r(t)]^q = [s(t) + n(t)]^q$$

and one of the resultant components is (the amplitude is immaterial, it is set to 1)

$$\cos[2\pi q f_c t + q\Phi(t, \mathbf{a})]$$

This is an MHPM signal with carrier frequency qf_c and phase

$$q\Phi(t, \mathbf{a}) = 2\pi \sum_i a_i p_i q(t - iT)$$

which has an integer index p_i . Recall that in Section 6.2.1, we state that when the index is an integer the PSD of the CPM signal contains a continuous part and a discrete part. Similarly, it can be shown [24] that when the index is an integer the PSD of the MHPM signal contains a continuous part and a discrete part. The discrete

frequency components appear at

$$f = \begin{cases} qf_c \pm \frac{2k}{2KT}, & k = 0, 1, 2, \dots, & \text{if } \Gamma = \sum_{i=1}^K p_i \text{ is even} \\ qf_c \pm \frac{2k+1}{2KT}, & k = 0, 1, 2, \dots, & \text{if } \Gamma = \sum_{i=1}^K p_i \text{ is odd} \end{cases} \quad (7.62)$$

which can be simplified as

$$f = qf_c \pm \frac{n}{2KT} \begin{cases} n \text{ is even if } \Gamma = \sum_{i=1}^K p_i \text{ is even} \\ n \text{ is odd if } \Gamma = \sum_{i=1}^K p_i \text{ is odd} \end{cases} \quad (7.63)$$

When $K = 1$, the above expression degenerates back to the expression for single- h CPM. Those spectral lines that contain significant power are few in number since their weights decay rapidly at higher harmonics (large n). For any given multi- h codes, however, there are always two or three adjacent lines near the peak (qf_c) of the spectrum which contain significant power. The spectral lines are separated by $1/KT$ Hz.

Based on (7.63), a synchronizer that is similar to the MSK-type carrier and symbol synchronizer for single- h CPM (Figure 6.44) can be constructed as shown in Figure 7.20. The two phase lock loops (or narrow-band bandpass filters) can select any pair of frequencies $qf_c \pm n/2KT$. The output of the mixer contains the sum and the difference of these two frequencies: $2qf_c$ and n/KT . The high-pass filter and the low-pass filter pick up one of them. The frequency dividers divide two frequencies to produce f_c for the carrier and $1/KT$ for the superbaud timing. The symbol timing is derived from the superbaud timing by a frequency multiplier.

If carrier recovery is already incorporated in the demodulator, like the one in Figure 7.18, the carrier recovery part of Figure 7.20 is not needed.

7.6 IMPROVED MHPM SCHEMES

Improvements on MHPM schemes have been made during the recent years. Techniques that combine MHPM with error control codes, such as convolutional codes, will be discussed in a later chapter. What we present here are techniques which make changes on the MHPM phase characteristic itself. These include MHPM schemes with asymmetrical modulation indexes, multi- T realization of multi- h , correlatively encoded MHPM, and nonlinear multi- h CPFSK. It should be pointed out that these improved MHPM schemes may require more complex receivers which have not been available in the published literature.

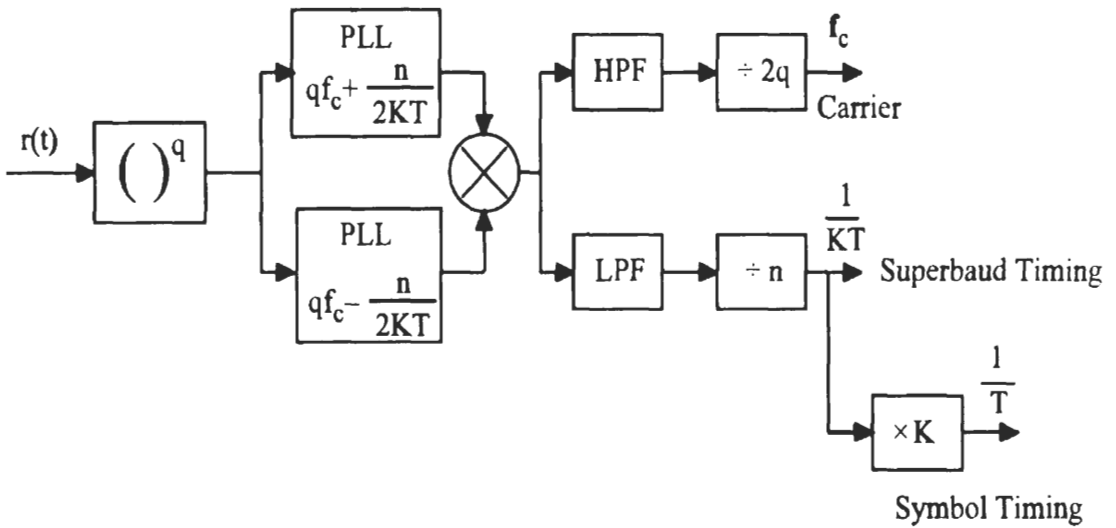


Figure 7.20 MHPM carrier, symbol and superbaud synchronizer.

7.6.1 MHPM With Asymmetrical Modulation Indexes

Binary MHPM schemes with asymmetrical modulation indexes are proposed in [25, 26]. They use a set of modulation indexes h_{+k} for data +1 and h_{-k} for data -1 during any k th signaling interval. One simple way of doing this is to use the same set of the modulation indexes for both h_{+k} and h_{-k} and simply shift h_{-k} with respect to h_{+k} . For example, let $\{h_a, h_b, h_c\}$ be the modulation index set for a 3- h binary scheme. The asymmetric modulation index sets can be arranged as follows.

$k :$	1	2	3	4	5	6	...
$h_{+k} :$	h_a	h_b	h_c	h_a	h_b	h_c	...
$h_{-k} :$	h_b	h_c	h_a	h_b	h_c	h_a	...

That is, $h_{+(k+1)} = h_{-k}$. This makes the index for the i th interval in the phase trellis, h_{+k} or h_{-k} , not necessarily equal for different paths, whereas in conventional MHPM it is fixed. As a result, the phase values at $t = kT$ for asymmetric MHPM may be a multiple of π/q , instead of $2\pi/q$ as in the conventional MHPM. This gives more flexibility to make the minimum Euclidean distance larger. Improvements over the symmetrical ones in the range of 0.5 to 1 dB in the upper bounds of error probability are reported. The spectral properties of the asymmetrical schemes are almost the same of the symmetrical ones.

7.6.2 Multi- T Realization of Multi- h Phase Codes

Binary and M-ary linear phase multi- T phase codes are investigated in [27,28]. The modulation index is effectively changed by cyclically varying the symbol interval with a constant frequency deviation (excluding the effect of the data symbol). For every multi- h code $\{h_1, h_2, \dots, h_K\}$ a set of symbol periods can be defined as

$$\{T_1, T_2, \dots, T_K\} = \{\lambda_1 T, \lambda_2 T, \dots, \lambda_K T\}$$

where T is the average period

$$T = (T_1 + T_2 + \dots + T_K)/K$$

and

$$\lambda_i = h_i/h$$

h is the average index

$$h = (h_1 + h_2 + \dots + h_K)/K$$

Imitating the signal form of the conventional CPFSK, this signal can be written as

$$s(t) = A \cos(2\pi f_c t + \frac{a_k \pi h (t - t_k)}{T} + \theta_k), \quad t_k \leq t \leq t_{k+1} \quad (7.64)$$

where

$$t_k = \sum_{i=-\infty}^{k-1} T_i$$

The phase change at the end of each interval is $a_k \pi h T_k / T$. Thus the effective index is $h_k = h T_k / T$ in terms of phase increment for each symbol interval. However, in terms of phase change slope, it is like a single- h CPM.

It is shown that multi- T codes are similar to multi- h codes in terms of minimum distance and spectral properties. However, the extraction of the synchronization information by means of a PLL seems to be easier for multi- T codes than multi- h codes since the spectrum for the q th power of the binary multi- T signal contains only two lines in the vicinity of $q f_c$, whereas there are more than two lines in the case of binary multi- h signals [28].

7.6.3 Correlatively Encoded Multi- h Signaling Technique

A correlatively encoded multi- h signaling technique was introduced by Fonseka et

al [29]. It was claimed that this scheme performed significantly better than partial-response MHPM. In this scheme, the MHPM signal is defined as

$$\begin{aligned} s(t) &= A \cos \left[2\pi f_c t + \frac{\pi h_k (a_k + a_{k-1} + \dots + a_{k-L+1})}{LT} (t - kT) + \theta_k \right] \\ &= A \cos [2\pi f_c t + \Phi(t, \mathbf{a})], \quad kT \leq t \leq (k+1)T \end{aligned} \quad (7.65)$$

This signal is a multi- h CPFSK signal with a depth of correlation L , is abbreviated by LCE-MH. Recall that the total phase of the partial-response multi- h CPFSK (LREC-MH) signal is

$$\Phi(t, \mathbf{a}) = \frac{\pi (a_k h_k + a_{k-1} h_{k-1} + \dots + a_{k-L+1} h_{k-L+1})}{LT} (t - kT) + \theta_k \quad (7.66)$$

Clearly, when h is constant, LCE-MH is identical to LREC-MH. LREC-MH signals are generated by first multiplying the information data by the modulation indexes and then correlative encoding, while LCE-MH signals are generated by first correlative encoding the information data and then multiplying by the modulation indexes. Thus the phase variation of LREC-MH during any signal interval is influenced not only by the modulation index used in that interval, but also by the modulation indexes used in the previous $(L - 1)$ intervals. The phase variation of LCEC-MH signals during any signal interval is influenced by only the modulation index used in that interval.

In addition to correlative coding as depicted in (7.65), modulation indexes can be arranged in certain patterns instead of simply cycling them. This can further increase the constraint length and the minimum distance. Two good patterns used in (7.65) are $2-h$ slots of $2T$ pattern

$$\{h_1, h_1, h_2, h_2, h_1, h_1, h_2, h_2, \dots\}$$

and $2-h$ slots of $3T$ pattern

$$\{h_1, h_1, h_1, h_2, h_2, h_2, h_1, h_1, h_1, h_2, h_2, h_2, \dots\}$$

Some numerical results in [29] are listed in Table 7.4, where comparisons are made between the correlatively encoded/ $2-h$ signals with partial-response/ $2-h$ signals at fixed modulation indexes. In the table, N_R is the receiver path memory length and is equal to the minimum number of intervals required to ensure that the distance between any two paths is less than the minimum distance of the signals. From the table, it is seen that significant coding gain can be achieved by correlative encoding over the conventional partial-response MHPM.

h_1, h_2	signal type	index pattern	d_{\min}^2	N_R	p.r./reg. 2-h		gain (dB)
					d_{\min}^2	N_R	
0.5,0.7	2CE-MH	slots of 2T	3.28	36	2.518	47	1.152
0.5,0.7	2CE-MH	slots of 2T	3.97	16	3.226	8	0.876
0.5,0.7	3CE-MH	regular 2-h	2.39	22	1.226	7	2.890
0.8,1.0	3CE-MH	regular 2-h	4.01	19	3.000	31	1.263
19/24,5/4	3CE-MH	regular 2-h	5.00	40	2.217	7	3.535
19/24,7/6	3CE-MH	slots of 3T	5.13	76	2.487	7	3.140

Table 7.4 Comparison of correlatively encoded 2- h signals with partial response 2- h signals. From [29]. Copyright © IEEE.

7.6.4 Nonlinear Multi- h CPFSK

A scheme called nonlinear multi- h CPFSK is proposed in [30]. In this scheme, the signals still have the same form of (7.9) except that the modulation index during any k th interval h_k is a function of signaling interval k and m previous symbols. The m previous symbols define 2^m states $S_i = 0, 1, 2, \dots, 2^m - 1$. The scheme uses 2^m modulation index patterns, and a pattern

$$H_{S_i} = \{h_{S_i}(0), h_{S_i}(1), \dots, h_{S_i}(K-1)\}$$

contains K distinct modulation indexes where H_{S_i} denotes the modulation index pattern selected for symbol state S_i . Once the modulation index pattern is selected, a modulation index is picked from it by cyclically shifting the modulation indexes with period K as in ordinary multi- h CPFSK. It is observed that the constraint length of this scheme is $m + K + 1$, whereas it is $K + 1$ for the ordinary multi- h CPFSK. By properly choosing the index pattern, increases in the minimum Euclidean distance of up to 2.7 dB over ordinary multi- h CPFSK and up to 1.8 dB over asymmetrical multi- h CPFSK have been observed.

7.7 SUMMARY

In this chapter we have studied the multi- h continuous phase modulation (MHPM). We first defined the MHPM signal. Then we studied the properties of its phase trellis, including the number of phase states, the period of the trellis. A direct method of computing the spectra of the MHPM schemes was described and spectra of some important MHPM schemes were presented. The calculation of the distances is similar to CPM. Many results of the minimum distance and its upper bound for various binary and M-ary MHPM schemes were presented. Three extensive tables compared many

multi- h codes in terms of their coding gain, bandwidth, and decision depth. Those are valuable design references. The modulator for MHPM is almost the same as that of the CPM except that the index must be cyclically rotated. Thus it is not repeated in this chapter. The demodulators for MHPM are also similar to single- h CPM demodulators except that the demodulator must have a prior knowledge of the sequence of indexes h_k employed at the transmitter. Thus in principle we can modify all demodulators in Chapter 6 for MHPM. However, since the MLSE demodulator using the Viterbi algorithm is the most promising one, several demodulators of this type were presented. Some of these receivers incorporate carrier and symbol synchronization in the receiver. For those that do not, a separate synchronizer is needed, which was discussed. Finally, we briefly described several improved MHPM schemes in the end of the chapter. These schemes manipulate the modulation indexes in a variety of ways in an attempt to increase the minimum distance, while maintaining a similar spectrum. The receivers for many of these schemes have not yet appeared in the literature.

In the next chapter we will study quadrature amplitude modulation (QAM) which is a nonconstant envelope modulation scheme with very high bandwidth efficiency, and is widely used in systems where constant envelope is not required.

7.8 APPENDIX 7A

By inspecting (7.30), two of the orthonormal functions can be assigned as

$$\psi_1(t) = \sqrt{\frac{2}{T}} \cos \left(2\pi f_c t + \frac{\pi h_k(t - kT)}{T} \right) \quad (7.67)$$

$$\psi_2(t) = \sqrt{\frac{2}{T}} \sin \left(2\pi f_c t + \frac{\pi h_k(t - kT)}{T} \right) \quad (7.68)$$

The orthogonal relationship can be verified by integration:

$$\begin{aligned} & \int_{kT}^{(k+1)T} \psi_1(t) \psi_2(t) dt \\ &= \frac{2}{T} \int_{kT}^{(k+1)T} \cos \left(2\pi f_c t + \frac{\pi h_k(t - kT)}{T} \right) \sin \left(2\pi f_c t + \frac{\pi h_k(t - kT)}{T} \right) dt \\ &= \frac{1}{T} \int_{kT}^{(k+1)T} \sin \left(4\pi f_c t + \frac{2\pi h_k(t - kT)}{T} \right) dt \end{aligned}$$

$$\begin{aligned}
&= \frac{-1}{T(4\pi f_c + 2\pi h_k/T)} \left[\cos \left(4\pi f_c t + \frac{2\pi h_k(t - kT)}{T} \right) \right]_{kT}^{(k+1)T} \\
&= \frac{-1}{T(4\pi f_c + 2\pi h_k/T)} [\cos(4\pi f_c(k+1)T + 2\pi h_k) - \cos(4\pi f_c kT)]
\end{aligned}$$

In most systems of practical interest $f_c \gg 1/T$, this means $2\pi f_c T \geq 2\pi$. The value in the bracket is between -2 and $+2$, thus the above is approximately equal to zero. The norm of $\psi_1(t)$ is

$$\begin{aligned}
\int_{kT}^{(k+1)T} \psi_1^2(t) dt &= \frac{2}{T} \int_{kT}^{(k+1)T} \cos^2 \left(2\pi f_c t + \frac{\pi h_k(t - kT)}{T} \right) dt \\
&= \frac{1}{T} \int_{kT}^{(k+1)T} \left[1 + \cos 2 \left(2\pi f_c t + \frac{\pi h_k(t - kT)}{T} \right) \right] dt \\
&= 1 + \frac{\sin 2(2\pi f_c t + \pi h_k(t - kT)/T)}{2T(2\pi f_c + \pi h_k/T)} \Big|_{kT}^{(k+1)T} \\
&\approx 1
\end{aligned}$$

Similarly we can show $\int_{kT}^{(k+1)T} \psi_2^2(t) dt \approx 1$. The remaining orthonormal functions are found as follows. Define

$$s_3(t) = \sqrt{\frac{2}{T}} \cos \left(2\pi f_c t - \frac{\pi h_k(t - kT)}{T} \right) \quad (7.69)$$

$$\begin{aligned}
s_{31} &= \int_{kT}^{(k+1)T} s_3(t) \psi_1(t) dt \\
&= \frac{2}{T} \int_{kT}^{(k+1)T} \cos \left(2\pi f_c t - \frac{\pi h_k(t - kT)}{T} \right) \\
&\quad \cdot \cos \left(2\pi f_c t + \frac{\pi h_k(t - kT)}{T} \right) dt \\
&= \frac{1}{T} \int_{kT}^{(k+1)T} \left(\cos 4\pi f_c t + \cos \frac{2\pi h_k(t - kT)}{T} \right) dt \\
&= \frac{1}{T} \left(\frac{\sin 4\pi f_c t}{4\pi f_c} + \frac{T \sin 2\pi h_k(t - kT)/T}{2\pi h_k} \right)_{kT}^{(k+1)T} \\
&\approx \frac{\sin 2\pi h_k}{2\pi h_k} \triangleq C_{1,k} \quad (7.70)
\end{aligned}$$

Similarly

$$\begin{aligned}
s_{32} &= \int_{kT}^{(k+1)T} s_3(t)\psi_2(t)dt \\
&= \frac{2}{T} \int_{kT}^{(k+1)T} \cos\left(2\pi f_c t - \frac{\pi h_k(t-kT)}{T}\right) \\
&\quad \cdot \sin\left(2\pi f_c t + \frac{\pi h_k(t-kT)}{T}\right) dt \\
&= \frac{1}{T} \int_{kT}^{(k+1)T} \left(\sin 4\pi f_c t + \sin \frac{2\pi h_k(t-kT)}{T}\right) dt \\
&= \frac{1}{T} \left(\frac{-\cos 4\pi f_c t}{4\pi f_c} - \frac{T \cos 2\pi h_k(t-kT)/T}{2\pi h_k}\right)_{kT}^{(k+1)T} \\
&\approx \frac{1 - \cos 2\pi h_k}{2\pi h_k} \triangleq C_{2,k}
\end{aligned} \tag{7.71}$$

According to Gram-Schmidt procedure, the third orthonormal function is

$$\psi_3(t) = \frac{f_3(t)}{\sqrt{E_3}}$$

where

$$f_3(t) = s_3(t) - s_{31}\psi_1(t) - s_{32}\psi_2(t)$$

and

$$\begin{aligned}
E_3 &= \int_{kT}^{(k+1)T} f_3^2(t)dt \\
&= \int_{kT}^{(k+1)T} [s_3(t) - s_{31}\psi_1(t) - s_{32}\psi_2(t)]^2 dt \\
&= 1 + s_{31}^2 + s_{32}^2 - 2s_{31}^2 - 2s_{32}^2 \\
&= 1 - C_{1,k}^2 - C_{2,k}^2 \triangleq D_k
\end{aligned} \tag{7.72}$$

Thus

$$\begin{aligned}
\psi_3(t) &= \frac{s_3(t) - C_{1,k}\psi_1(t) - C_{2,k}\psi_2(t)}{\sqrt{D_k}} \\
&= \frac{1}{\sqrt{D_k}} \left[\sqrt{\frac{2}{T}} \cos\left(2\pi f_c t - \frac{\pi h_k(t-kT)}{T}\right) \right. \\
&\quad \left. - C_{1,k}\psi_1(t) - C_{2,k}\psi_2(t) \right]
\end{aligned} \tag{7.73}$$

Finally

$$\psi_4(t) = \frac{f_4(t)}{\sqrt{E_4}}$$

where

$$f_4(t) = s_4(t) - s_{41}\psi_1(t) - s_{42}\psi_2(t) - s_{43}\psi_3(t)$$

where

$$s_4(t) = \sqrt{\frac{2}{T}} \sin\left(2\pi f_c t - \frac{\pi h_k(t - kT)}{T}\right) \quad (7.74)$$

The coefficients s_{4i} are determined as follows:

$$\begin{aligned} s_{41} &= \int_{kT}^{(k+1)T} s_4(t)\psi_1(t)dt \\ &= \frac{2}{T} \int_{kT}^{(k+1)T} \sin\left(2\pi f_c t - \frac{\pi h_k(t - kT)}{T}\right) \\ &\quad \cdot \cos\left(2\pi f_c t + \frac{\pi h_k(t - kT)}{T}\right) dt \\ &= \frac{1}{T} \left(\frac{-\cos 4\pi f_c t}{4\pi f_c} + \frac{T \cos 2\pi h_k(t - kT)/T}{2\pi h_k} \right)_{kT}^{(k+1)T} \\ &\approx \frac{\cos 2\pi h_k - 1}{2\pi h_k} = -C_{2,k} \end{aligned} \quad (7.75)$$

$$\begin{aligned} s_{42} &= \int_{kT}^{(k+1)T} s_4(t)\psi_2(t)dt \\ &= \frac{2}{T} \int_{kT}^{(k+1)T} \sin\left(2\pi f_c t - \frac{\pi h_k(t - kT)}{T}\right) \\ &\quad \cdot \sin\left(2\pi f_c t + \frac{\pi h_k(t - kT)}{T}\right) dt \\ &= \frac{1}{T} \left(\frac{T \sin 2\pi h_k(t - kT)/T}{2\pi h_k} - \frac{\sin 4\pi f_c t}{4\pi f_c} \right)_{kT}^{(k+1)T} \\ &\approx \frac{\sin 2\pi h_k}{2\pi h_k} = C_{1,k} \end{aligned} \quad (7.76)$$

$$\begin{aligned}
 s_{43} &= \frac{2}{T} \int_{kT}^{(k+1)T} \sin \left(2\pi f_c t - \frac{\pi h_k(t - kT)}{T} \right) \\
 &\quad \cdot \cos \left(2\pi f_c t - \frac{\pi h_k(t - kT)}{T} \right) dt \\
 &\approx 0
 \end{aligned} \tag{7.77}$$

$$\begin{aligned}
 E_4 &= \int_{kT}^{(k+1)T} f_4^2(t) dt \\
 &= \int_{kT}^{(k+1)T} [s_4(t) - s_{41}\psi_1(t) - s_{42}\psi_2(t)]^2 dt \\
 &= 1 - C_{1,k}^2 - C_{2,k}^2 = D_k
 \end{aligned} \tag{7.78}$$

Thus

$$\begin{aligned}
 \psi_4(t) &= \frac{s_4(t) + C_{2,k}\psi_1(t) - C_{1,k}\psi_2(t)}{\sqrt{D_k}} \\
 &= \frac{1}{\sqrt{D_k}} \left[\sqrt{\frac{2}{T}} \sin \left(2\pi f_c t - \frac{\pi h_k(t - kT)}{T} \right) \right. \\
 &\quad \left. + C_{2,k}\psi_1(t) - C_{1,k}\psi_2(t) \right]
 \end{aligned} \tag{7.79}$$

References

- [1] Miyakawa, H., H. Harashima, and Y. Tanaka, "A new digital modulation scheme, multi-code binary CPFSSK," *Proc. 3rd Int. Conf. on Digital Satellite Comm.*, Nov. 1975, pp. 105-112.
- [2] Anderson, J., and R. DeBuda, "Better phase-modulation error performance using trellis phase code," *Electron. Lett.*, vol. 12, no. 22, Oct. 1976, pp. 587-588.
- [3] Anderson, J., and D. P. Taylor, "Trellis phase-modulation coding: minimum distance and spectral results," *Proc. Electron. Aerospace Syst. Conf.*, Sept. 1977, pp. 29-1A-1G.
- [4] Anderson, J., and D. P. Taylor, "A bandwidth efficient class of signal space codes," *IEEE Trans. Inform. Theory*, vol. 24, no. 6, Nov. 1978, pp. 703-712.
- [5] Sasase, I., and S. Mori, "Multi- h phase-coded modulation," *IEEE Communications Magazine*, vol. 29, no. 12, Dec. 1991, pp. 46-56.
- [6] Lereim, A., "Spectral properties of multi- h codes," *M. Eng. Thesis, McMaster Univ Techn. Report*, no. CRL-57, Communications Research Laboratory, McMaster University, Hamilton, Ontario, Canada, July 1978.
- [7] Bhargava, V. R. et al., *Digital Communications by Satellite*, New York: John Wiley & Sons, 1981.
- [8] Holubowicz, W., "Optimum parameter combinations for multi- h phase codes," *IEEE Trans. on Comm.*, vol. 38, no. 11, Nov. 1990, pp. 1929-1931.

- [9] Aulin, T., and C-E. Sundberg, "Minimum Euclidean distance and power spectrum for a class of smoothed phase codes with constant envelope," *IEEE Trans. on Comm.*, vol. 30, no. 7, July 1982, pp. 1721-1729.
- [10] Maseng, T., "The autocorrelation function for multi- h coded signals," *IEEE Trans. on Comm.*, vol. 33, no. 5, May 1985, pp. 481-484.
- [11] Papoulis, A., *Probability; Random Variables, and Stochastic Processes*, Tokyo, Japan: McGraw-Hill Kogakusha, 1965.
- [12] Bennett, W., and S. Rice, "Spectral density and autocorrelation functions associated with binary frequency shift keying," *Bell Syst. Tech. J.*, vol. 42, 1963, pp. 2355-2385.
- [13] Anderson, J., T. Aulin, and C-E. Sundberg, *Digital Phase Modulation*, New York, Plenum Publishing Company, 1986.
- [14] Wilson, S., and R. Gaus, "Power spectra of multi- h phase codes," *IEEE Trans. on Comm.*, vol. 29, no. 3, Mar. 1981, pp. 250-256.
- [15] Mazo, J., and J. Salz, "Spectra of frequency modulation with random waveforms," *Inform. Contr.*, vol. 42, 1966, pp. 414-422.
- [16] Baker, T., "Asymptotic behavior of digital FM spectra," *IEEE Trans. on Comm.*, vol. 22, no. 10, Oct. 1974, pp. 1585-1594.
- [17] Aulin, T., and C-E Sundberg, "On the minimum Euclidean distance for a class of signal space codes," *IEEE Trans. Inform. Theory*, vol. 28, no. 1, Jan. 1982, pp. 43-55.
- [18] Anderson, J., "Simulated error performance of multi- h phase codes," *IEEE Trans. Inform. Theory*, vol. 27, no. 3, May 1981, pp. 357-362.
- [19] Wilson, S., J. Highfill III, and C-D. Hsu, "Error bounds for multi- h phase codes," *IEEE Trans. Information Theory*, vol. 28, no. 4, July 1982, pp. 650-665.
- [20] Liebetreu, J., "Joint carrier phase estimation and data detection algorithm for multi- h CPM data transmission," *IEEE Trans. on Comm.*, vol. 34, no. 9, Sept. 1986, pp. 873-881.
- [21] Premji, A., and D. Taylor, "Receiver structures for multi- h signaling formats," *IEEE Trans. on Comm.*, vol. 35, no. 4, April 1987, pp. 439-451.
- [22] Premji, A., and D. Taylor, "A practical receiver structures for multi- h signals," *IEEE Trans. on Comm.*, vol. 35, no. 9, Sept. 1987, pp. 901-908.
- [23] Mazur, B., and D. Taylor, "Demodulation and carrier synchronization of multi- h phase codes," *IEEE Trans. on Comm.*, vol. 29, no. 3, March. 1981, pp. 257-266.
- [24] Taylor D., and B. Mazur, "Research on self-synchronization of phase codes," *McMaster Univ Techn. Report*, no. CRL-63, Communications Research Laboratory, McMaster University, Hamilton, Ontario, Canada, Apr. 1979.
- [25] Hwang, H., L. Lee, and S. Chen, "Multi- h phase coded modulations with asymmetrical modulation indices," *IEEE Journal of Selected Areas in Communications*, vol. 7, no. 9, Dec. 1989, pp. 1450-1461
- [26] Hwang, H., L. Lee, and S. Chen, "Asymmetrical modulation indexes in full/partial-response multi- h phase-coded modulation with different phase pulse functions," *IEE Proc.*, vol. 139, Part I, Oct. 1992, pp. 508-514.

- [27] Holubowicz, W., and P. Szulakiwicz, "Multi- T realization of multi- h phase codes," *IEEE Trans. Inform. Theory*, vol. 31, no. 4, July 1985, pp. 528-529.
- [28] Szulakiwicz, P., " M -ary linear phase multi- T codes," *IEEE Trans. on Comm.*, vol. 37, no. 3, March 1989, pp. 197-199.
- [29] Fonseka, J., and G. Davis, "Correlatively encoded multi- h signals," *IEEE Trans. on Comm.*, vol. 41, no. 3, March 1993, pp. 444-446.
- [30] Mao, R., and J. Fonseka, "Nonlinear multi- h phase codes for CPFSK signaling," *IEEE Trans. on Comm.*, vol. 43, no. 8, August 1995, pp. 2350-2359.

Selected Bibliography

- Ziemer, R. and R. Peterson, *Introduction to Digital Communications*, New York: Macmillan, 1992.

Chapter 8

Quadrature Amplitude Modulation

At this point, all the passband modulation schemes we have studied, FSK, PSK, CPM, and MHPM, are constant envelope schemes. The constant envelope property of these schemes is specially important to systems with power amplifiers which must operate in the nonlinear region of the input-output characteristic for maximum power efficiency, like the satellite transponders. For some other communication systems, constant envelope may not be a crucial requirement, whereas bandwidth efficiency is more important. Quadrature amplitude modulation (QAM) is such a class of non-constant envelope schemes that can achieve higher bandwidth efficiency than MPSK with the same average signal power. QAM is widely used in modems designed for telephone channels. The CCITT telephone circuit modem standards V.29 to V.33 are all based on various QAM schemes ranging from uncoded 16-QAM to trellis coded 128-QAM. The research of QAM applications in satellite systems, point-to-point wireless systems, and mobile cellular telephone systems also has been very active.

In Chapter 1 we mentioned binary amplitude shift keying (ASK). ASK can also be made M-ary, called M-ary amplitude modulation (MAM). MAM is usually no longer a preferable choice due to its poor power efficiency. However, since QAM signal consists of two MAM components and they can be demodulated in two separate channels, it is necessary to understand MAM's behavior in order to understand QAM. We discuss MAM in Section 8.1. Then we move on to define QAM signal and constellation in Section 8.2. Various QAM constellations are introduced in Section 8.3, but only the square QAM constellations are described in detail. QAM's PSD, modulator, demodulator, error probability, synchronization, and differential coding are discussed in Sections 8.4 to 8.9. Section 8.10 summarizes the chapter.

8.1 M-ARY AMPLITUDE MODULATION

In this section we first introduce MAM in its most general form which is applicable to

baseband as well as bandpass signals. Then we focus our attention on the analysis of bandpass MAM signals which will serve as a foundation for analyzing QAM signals.

In its most general form, an M-ary amplitude modulation signal can be expressed as

$$s_i(t) = s_i \phi(t), \quad 0 \leq t \leq T \quad (8.1)$$

for $i = 1, 2, \dots, M$, $\phi(t)$ is any unit energy function of duration T , that is $\int_0^T \phi^2(t) dt = 1$. Consequently $s_i^2 = E_i$ is the energy of $s_i(t)$. If $\phi(t)$ is a baseband pulse, then $s_i(t)$ is the baseband M-ary amplitude modulation, which is usually called M-ary pulse amplitude modulation (PAM). The NRZ and RZ line codes are examples of baseband binary AM schemes. If $\phi(t)$ is a high frequency sinusoidal carrier, then $s_i(t)$ is the passband M-ary amplitude modulation. The passband MAM is also called amplitude shift keying (ASK). The OOK (on-off keying) is a binary passband AM scheme with one of the s_i being zero. The BPSK can be also viewed as a binary passband AM scheme with two antipodal s_i .

8.1.1 Power Spectral Density

On the entire time axis, we can write MAM signal as

$$s(t) = \sum_{k=-\infty}^{\infty} s_k \phi(t - kT), \quad -\infty < t < \infty \quad (8.2)$$

where amplitude s_k is determined by the message data which are random. Thus s_k is a random variable. Expression (8.2) is in the form of (A.14) in Appendix A. Further assuming that data are uncorrelated, the PSD of $s(t)$ is given by (A.18), that is

$$\Psi_s(f) = \frac{\sigma_s^2 |\Phi(f)|^2}{T} + \left(\frac{m_s}{T}\right)^2 \sum_{k=-\infty}^{\infty} |\Phi(\frac{k}{T})|^2 \delta(f - \frac{k}{T}) \quad (8.3)$$

where $\Phi(f) = \mathcal{F}\{\phi(t)\}$, σ_s^2 is the variance of s_k and m_s is the mean value of s_k . The first part of (8.3) is the continuous spectrum and the second part is the discrete spectral lines. Note that $\Phi(f)$ could be a baseband spectrum or a bandpass spectrum, depending on whether $\phi(t)$ is baseband or bandpass

For MAM, usually the amplitudes are uniformly spaced and symmetrically located around zero. Then $m_s = 0$, thus

$$\Psi_s(f) = \frac{\sigma_s^2 |\Phi(f)|^2}{T} \quad (8.4)$$

This tells us that the PSD of MAM is determined by the PSD of the basis function

$\phi(t)$. If the amplitude distribution is not symmetrical around zero, then $m_s \neq 0$, discrete spectral lines will be present.

Note that (8.3) and (8.4) are applicable to both baseband and bandpass $\phi(t)$. However, for bandpass $\phi(t)$, the spectrum $\Phi(f)$ has two parts, centered around f_c and $-f_c$. Thus (8.3) and (8.4) are not convenient to use. For bandpass random signal the PSD is completely determined by the PSD of its complex envelope or equivalent baseband signal (A.13). Thus it suffices to have the PSD of the complex envelope $\Psi_{\tilde{s}}(f)$ instead of $\Psi_s(f)$. Assuming the bandpass MAM signal is

$$s_i(t) = A_i p(t) \cos 2\pi f_c t, \quad 0 \leq t \leq T$$

where $p(t)$ is a pulse-shaping function, then the complex envelope of $s(t)$ on the entire time axis is

$$\tilde{s}(t) = \sum_{k=-\infty}^{\infty} A_k p(t - kT), \quad -\infty < t < \infty$$

which is in the form of (A.14). Thus for uncorrelated data, the PSD of bandpass MAM signal is

$$\Psi_{\tilde{s}}(f) = \frac{\sigma_A^2 |P(f)|^2}{T} + \left(\frac{m_A}{T}\right)^2 \sum_{k=-\infty}^{\infty} |P\left(\frac{k}{T}\right)|^2 \delta\left(f - \frac{k}{T}\right) \quad (8.5)$$

where $P(f) = \mathcal{F}\{p(t)\}$ is the spectrum of $p(t)$, σ_A^2 is the variance of A_k , and m_A is the mean value of A_k . Usually the amplitudes are uniformly spaced and symmetrically located around zero. Then $m_A = 0$, and

$$\Psi_{\tilde{s}}(f) = \frac{\sigma_A^2 |P(f)|^2}{T} \quad (8.6)$$

The above shows that the PSD of bandpass MAM is determined by the PSD of the pulse-shaping function $p(t)$. If the amplitude distribution is not symmetrical around zero, then $m_A \neq 0$, discrete spectral lines will be present, such as in the OOK case.

Now let us assume $p(t)$ is rectangular with unit amplitude then

$$|P(f)| = \left| T \frac{\sin \pi f T}{\pi f T} \right| \quad (8.7)$$

and

$$\Psi_{\tilde{s}}(f) = \sigma_A^2 T \left(\frac{\sin \pi f T}{\pi f T} \right)^2 \quad (8.8)$$

which has the same shape of the PSD of MPSK.

8.1.2 Optimum Detection and Error Probability

In the M-ary PAM signal set, there is only one basis function which is the $\phi(t)$. Geometrically, each signal can be represented by its projection on the $\phi(t)$

$$s_i = \int_0^T s_i(t)\phi(t)dt$$

Thus from (B.37), the optimum detector is a one-dimensional minimum distance detector. Assuming the received signal is

$$r(t) = s_i(t) + n(t)$$

the sufficient statistic is

$$r = \int_0^T r(t)\phi(t)dt \quad (8.9)$$

and the detector compares r to s_i and chooses the closest (minimum distance decision rule).

The error probability of the coherent detection for an M-ary PAM with equal amplitude spacings can be derived as follows. Assuming AWGN channel with two-sided noise PSD of $N_o/2$,

$$r = \int_0^T r(t)\phi(t)dt = \int_0^T [s_i(t) + n(t)]\phi(t)dt = s_i + n$$

where n is Gaussian with zero mean and a variance of $N_o/2$. Thus r is Gaussian with mean s_i and variance $N_o/2$. Figure 8.1 shows the probability distribution densities of r conditioned on s_i , where τ_i are thresholds. This figure can help us derive the error probability.

Assuming s_i is transmitted, a symbol error occurs when the noise n exceeds in magnitude one-half of the distance between two adjacent levels. This probability is the same for each s_i except for the two outside levels, where an error can occur in one direction only. Assuming all amplitude levels are equally likely, the average symbol error probability is

$$P_s = \frac{M-1}{M} \Pr \left(|r - s_i| > \frac{\Delta}{2} \right)$$

where Δ is the distance between adjacent signal levels, and also is the distance between adjacent thresholds. For equal amplitude spacing, the amplitudes may be ex-

$$f(r/x) = \frac{1}{\sqrt{\pi \cdot N_o}} \exp\left[-\frac{(r-x)^2}{N_o}\right]$$

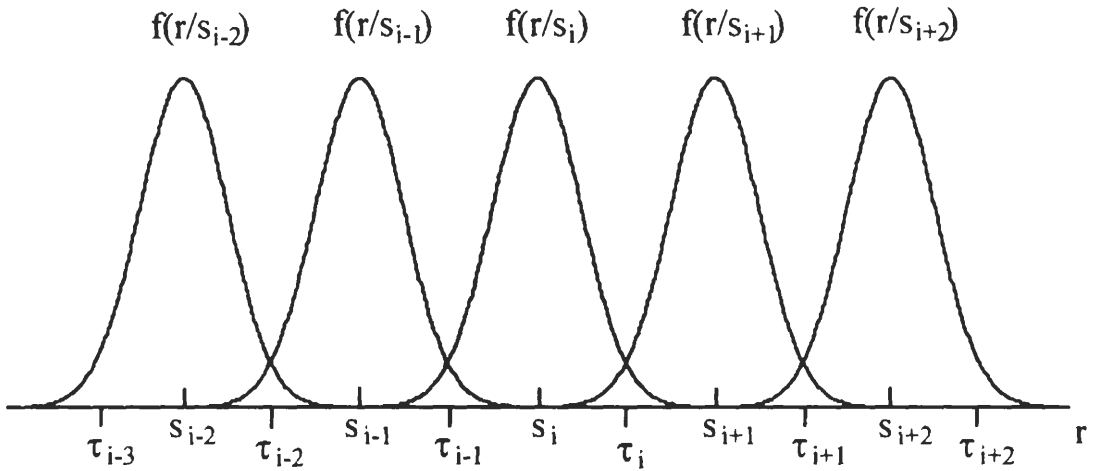


Figure 8.1 Thresholds and decision regions for M-ary PAM.

pressed as

$$s_i = (2i - 1 - M)A_o, \quad i = 1, 2, \dots, M \tag{8.10}$$

where A_o is the smallest amplitude. Then

$$\Delta = |s_i - s_{i-1}| = 2A_o$$

Thus

$$\begin{aligned} P_s &= \frac{M-1}{M} \Pr(|r - s_i| > A_o) = \frac{M-1}{M} \frac{2}{\sqrt{\pi N_o}} \int_{A_o}^{\infty} e^{-x^2/N_o} dx \\ &= \frac{M-1}{M} \frac{2}{\sqrt{2\pi}} \int_{A_o\sqrt{2/N_o}}^{\infty} e^{-x^2/2} dx = \frac{2(M-1)}{M} Q\left(\sqrt{\frac{2A_o^2}{N_o}}\right) \end{aligned} \tag{8.11}$$

The symbol error probability can be expressed in terms of the average energy or power of the signals. The average energy of the signals is

$$E_{avg} = \frac{1}{M} \sum_{i=1}^M E_i = \frac{1}{M} \sum_{i=1}^M s_i^2$$

$$\begin{aligned}
&= \frac{1}{M} \sum_{i=1}^M (2i - 1 - M)^2 A_o^2 = \frac{1}{M} \frac{M(M^2 - 1)A_o^2}{3} \\
&= \frac{1}{3}(M^2 - 1)A_o^2
\end{aligned} \tag{8.12}$$

As a result, (8.11) becomes

$$P_s = \frac{2(M - 1)}{M} Q \left(\sqrt{\frac{6E_{avg}}{(M^2 - 1)N_o}} \right) \tag{8.13}$$

or

$$P_s = \frac{2(M - 1)}{M} Q \left(\sqrt{\frac{6P_{avg}T}{(M^2 - 1)N_o}} \right) \tag{8.14}$$

where $P_{avg} = E_{avg}/T$ is the average power. Since the average energy per bit is $E_{bavg} = E_{avg}/\log_2 M$, (8.13) can be written as

$$P_s = \frac{2(M - 1)}{M} Q \left(\sqrt{\frac{6(\log_2 M)E_{bavg}}{(M^2 - 1)N_o}} \right) \tag{8.15}$$

Figure 8.2 shows the curves of the symbol error probability of the M-ary PAM versus E_{bavg}/N_o . We emphasize that (8.13) to (8.15) depend on only average energy or power of the signal symbols, not the function form of $\phi(t)$. This makes (8.13) to (8.15) applicable to both baseband and bandpass MAM signals. The $M = 2$ case corresponds to NRZ-L (baseband), or BPSK (bandpass), in this case (8.15) reduces to (2.48) or (4.6).

In comparison to MPSK, starting from $M = 4$, the error probability of M-ary PAM is inferior to that of the MPSK. In fact we can easily compare them. From the P_s of the MPSK (4.24) and (8.13), the ratio (MAM over MPSK) of the arguments inside the square root sign of the Q-function is

$$R_M = \frac{3}{(M^2 - 1) \sin^2 \frac{\pi}{M}} \tag{8.16}$$

and is tabulated in Table 8.1. If $M \geq 32$ the degradation is constantly 5.17 dB. This is easily seen from (8.16). For large M , $\sin \pi/M \cong \pi/M$, and $R_M \cong 3/\pi^2 \cong 0.304$. Another fact is that in both MAM and MPSK, for the same error probability, the power increase is 6 dB for doubling M for large M . This can be seen from (4.24) and (8.13). This means in terms of increasing bandwidth efficiency with increased M , both schemes pay the same penalty in BER performance. However, MAM still has a fixed 5.17 dB disadvantage against MPSK. This shows MAM is inferior to MPSK in

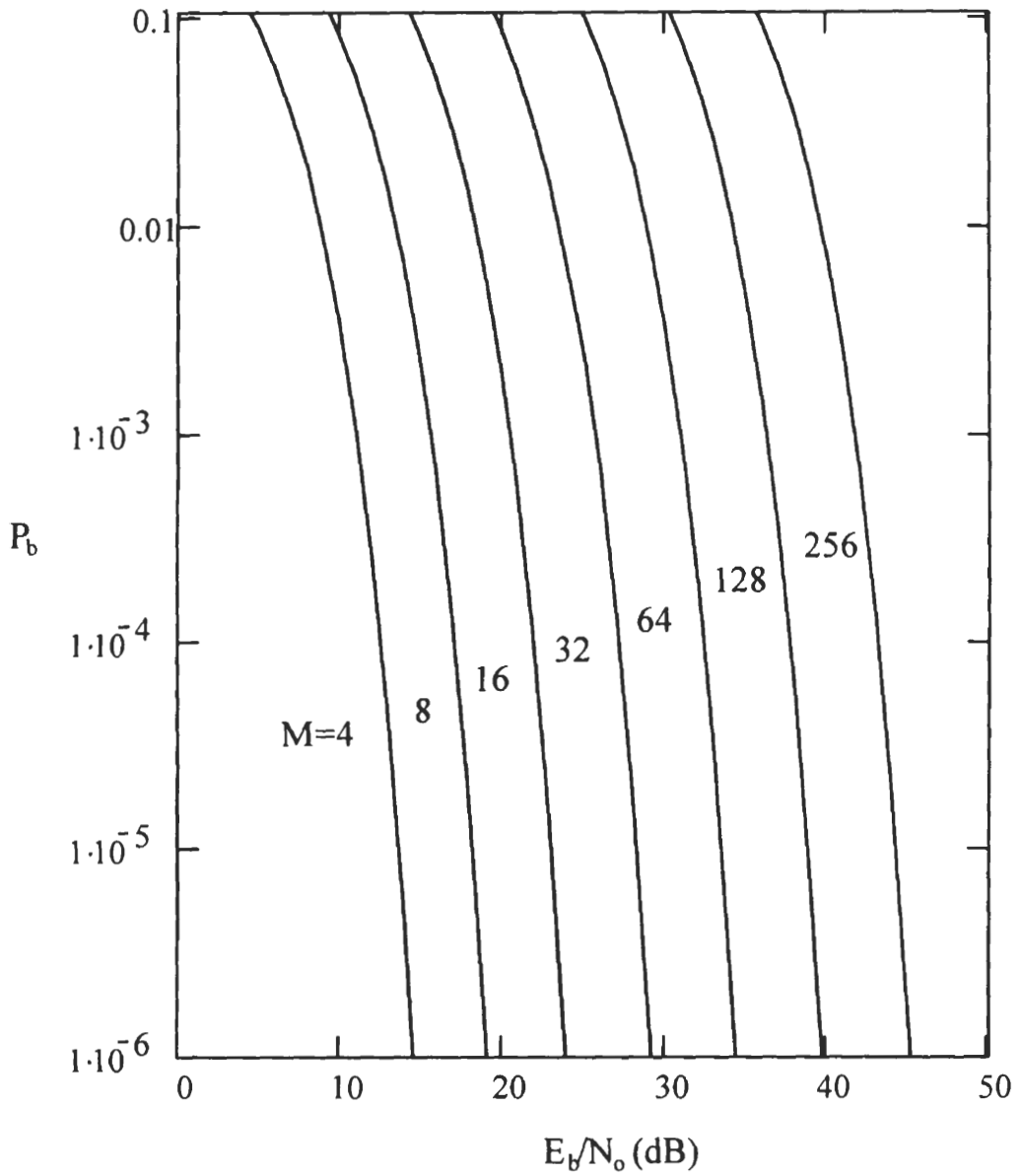


Figure 8.2 Symbol error probability of MAM.

M	R_M	$10 \log R_M$ (dB)
2	1	0
4	0.4	-3.98
8	0.325	-4.88
16	0.309	-5.10
32	0.305	-5.16
64	0.304	-5.17
128	0.304	-5.17
256	0.304	-5.17

Table 8.1 Power penalty of MAM over MPSK.

terms of error probability. However, we will see that going to two-dimensional AM, namely, QAM, improves error rate performance significantly. As a result, QAM is superior to MPSK when $M > 4$.

8.1.3 Modulator and Demodulator for Bandpass MAM

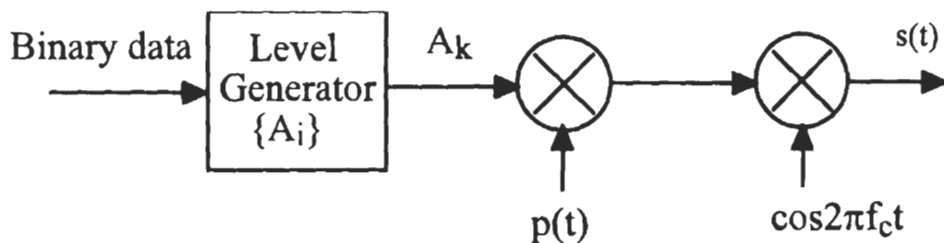
Now we focus on bandpass MAM. The bandpass MAM signal set is

$$s_i(t) = A_i p(t) \cos 2\pi f_c t, \quad 0 \leq t \leq T \quad (8.17)$$

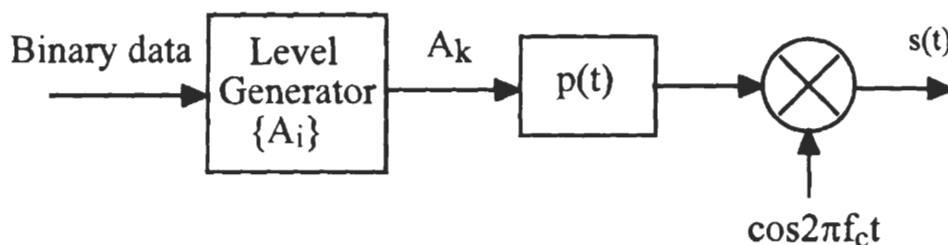
for $i = 1, 2, \dots, M$. It can be easily written in the form of (8.1) by defining $\phi(t) = \sqrt{2/E_p} p(t) \cos 2\pi f_c t$ where E_p is the energy of pulse-shaping signal $p(t)$ in $[0, T]$. Note that $\int_0^T \phi^2(t) dt \cong 1$ for $f_c \gg 1/T$. Thus for most practical cases, $s_i(t) = A_i \sqrt{E_p/2} \phi(t)$ and $s_i = A_i \sqrt{E_p/2}$.

The modulator is shown in Figure 8.3. Figure 8.3(a) is a direct implementation of (8.17). The level generator takes $n = \log_2 M$ bits from the binary data stream and maps them into an amplitude level $A_k \in \{A_i\}$, where the subscript k indicates the k th symbol interval. The mapping is preferably Gray coding so that the n -tuples representing the adjacent amplitudes differ only by one bit. The functions of the rest blocks are self-explanatory. The equivalent implementation is shown in Figure 8.3(b). It is more practical for hardware implementation. The $p(t)$ multiplier is replaced with a filter with an impulse response $p(t)$. In order to generate a pulse $A_i p(t)$, the input to the filter must be an impulse $A_i \delta(t)$. In practice, this can be realized by a very narrow pulse with amplitude A_i .

The optimum receiver implementing the minimum distance rule is shown in Figure 8.4 where the last block is a threshold detector. Figure 8.4(a) is a direct implementation of (8.9) and the minimum distance rule. In Figure 8.4(b), the correlation with $p(t)$ is replaced by a matched filter and a sampler. Figure 8.4(b) is more practical for



(a)



(b)

Figure 8.3 Bandpass MAM modulator.

hardware implementation. The equivalence between parts (a) and (b) in Figure 8.4 can be shown as follows. For the signal part in the noise-corrupted received signal, the output of the down-converter in both cases is

$$\begin{aligned} & A_i p(t) \cos 2\pi f_c t \sqrt{\frac{2}{E_p}} \cos 2\pi f_c t \\ &= \frac{1}{2} A_i \sqrt{\frac{2}{E_p}} p(t) [1 + \cos 4\pi f_c t] \end{aligned}$$

In Figure 8.4(a), the integrator output is

$$\frac{1}{2} A_i \sqrt{\frac{2}{E_p}} \int_0^T p^2(t) [1 + \cos 4\pi f_c t] dt = A_i \sqrt{\frac{E_p}{2}} = s_i$$

for $f_c \gg 1/T$. In Figure 8.4(b), the high-frequency term $\cos 4\pi f_c t$ is blocked by the low-pass filter $p(T-t)$. The output of the filter is

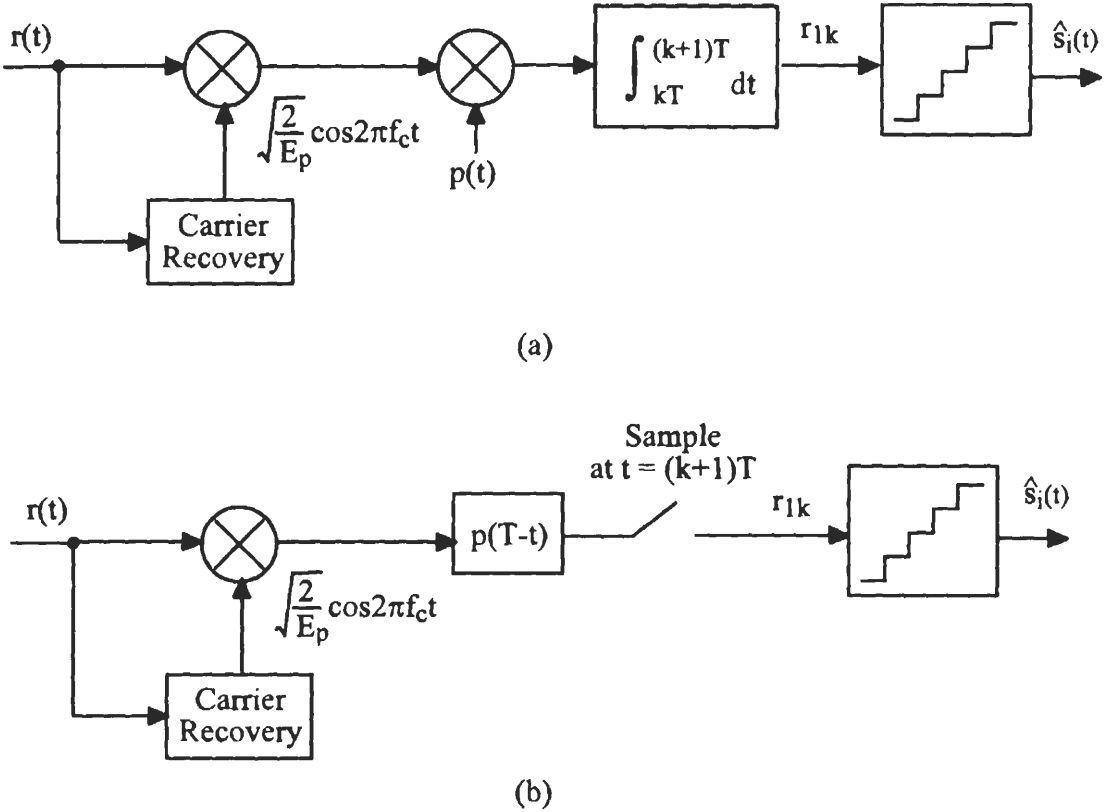


Figure 8.4 Optimum coherent demodulators for bandpass MAM.

$$\begin{aligned}
 & \frac{1}{2} A_i \sqrt{\frac{2}{E_p}} \int_0^t p(\tau) p(T - t + \tau) d\tau \Big|_{t=T} \\
 &= \frac{1}{2} A_i \sqrt{\frac{2}{E_p}} \int_0^T p(\tau) p(\tau) d\tau = A_i \sqrt{\frac{E_p}{2}} = s_i
 \end{aligned}$$

which is exactly the same as the output of the integrator in Figure 8.4(a). As to the noise in the received signal, parts (a) and (b) in Figure 8.4 are also equivalent. Assuming the noise in the received signal is $n(t)$. The output noise of the integrator in Figure 8.4(a) is $\int_0^T n(t)\phi(t)dt$. The output noise of the down-converter is

$$n_1(t) = n(t) \sqrt{\frac{2}{E_p}} \cos 2\pi f_c t = \frac{n(t)\phi(t)}{p(t)}$$

Then the output of the matched filter is

$$\begin{aligned} \int_0^t n_1(\tau)p(T-t+\tau)d\tau \Big|_{t=T} &= \int_0^t \frac{n(\tau)\phi(\tau)}{p(\tau)}p(T-t+\tau)d\tau \Big|_{t=T} \\ &= \int_0^T \frac{n(\tau)\phi(\tau)}{p(\tau)}p(\tau)d\tau \Big|_{t=T} \\ &= \int_0^T n(\tau)\phi(\tau)d\tau \end{aligned}$$

which is exactly the same as that of the correlator. Thus the equivalence between parts (a) and (b) in Figure 8.4 is established.

The threshold detector has $M - 1$ thresholds, each placed in the middle of two signal points (refer to Figure 8.1). The correlator computes the r and the threshold detector is actually computing the distance of r to the amplitudes s_i , $i = 1, 2, \dots, M$ and chooses the smallest. Note that the reference signal can be any scaled version of $\phi(t)$ as long as the thresholds are scaled accordingly.

The coherent carrier in the coherent demodulator can be generated using the synchronization methods described in Chapter 4, such as a squaring loop (Figure 4.35 with $M = 2$). The π phase ambiguity associated with the squaring loop can be solved by differential coding. The Costas loop (Figure 4.36) can also be used to demodulate MAM. The symbol timing clock can be recovered by using the methods described in Chapter 4.

8.1.4 On-Off Keying

The simplest MAM, is the OOK, which we mentioned in Chapter 1. The OOK signal set is

$$\begin{aligned} s_1(t) &= A \cos 2\pi f_c t, & \text{for } a = 1, & \quad 0 \leq t \leq T \\ s_2(t) &= 0, & \text{for } a = 0, & \quad 0 \leq t \leq T \end{aligned} \quad (8.18)$$

where a is the binary data which are assumed uncorrelated and equally likely. The complex envelope of the OOK signal $s(t)$ on the entire time axis is

$$\tilde{s}(t) = \sum_{k=-\infty}^{\infty} A_k p(t - kT), \quad -\infty < t < \infty$$

where $A_k \in \{0, A\}$, $p(t)$ is a rectangular pulse with unit amplitude whose $P(f)$ is given by (8.7). Since $m_A = A/2$ and $\sigma_A^2 = A^2/4$, $P(\frac{k}{T}) = 0$ except for $k = 0$,

from (8.5) we have the PSD for OOK as

$$\Psi_{\tilde{s}}(f) = \frac{A^2 T}{4} \left(\frac{\sin \pi f T}{\pi f T} \right)^2 + \frac{A^2}{4} \delta(f) \quad (8.19)$$

Note this is exactly the same as the PSD of the unipolar NRZ line codes (see (2.25) and Figure 2.3(b)).

The symbol error probability for coherent demodulation of OOK can be obtained from (8.13) with $E_{avg} = E_b$, or directly from (B.32), the BER expression for binary signaling. That is

$$P_b = Q \left(\sqrt{\frac{E_b}{2N_o}} \right) \quad (8.20)$$

where E_b is the average bit energy. When compared with BPSK, the PSD is the same except that it has a spectral line at f_c , which can be locked on by a phase lock loop to recover the carrier, but the BER performance of OOK is 3 dB inferior to that of BPSK. OOK is not usually preferred against BPSK.

8.2 QAM SIGNAL DESCRIPTION

Having studied MAM, we are ready to discuss QAM. In MAM schemes, signals have the same phase but different amplitudes. In MPSK schemes, signals have the same amplitude but different phases. Naturally, the next step of development is to consider using both amplitude and phase modulations in a scheme (QAM). That is

$$s_i(t) = A_i \cos(2\pi f_c t + \theta_i), \quad i = 1, 2, \dots, M \quad (8.21)$$

where A_i is the amplitude and θ_i is the phase of the i th signal in the M -ary signal set. Pulse shaping is usually used to improve the spectrum and for ISI control purpose in QAM. With pulse shaping, the QAM signal is

$$s_i(t) = A_i p(t) \cos(2\pi f_c t + \theta_i), \quad i = 1, 2, \dots, M \quad (8.22)$$

where $p(t)$ is a smooth pulse defined on $[0, T]$.¹ Expression (8.22) can be written as

$$s_i(t) = A_{i1}p(t) \cos 2\pi f_c t - A_{i2}p(t) \sin 2\pi f_c t \quad (8.23)$$

where

$$A_{i1} = A_i \cos \theta_i \quad (8.24)$$

$$A_{i2} = A_i \sin \theta_i \quad (8.25)$$

and

$$A_i = \sqrt{A_{i1}^2 + A_{i2}^2} \quad (8.26)$$

Similar to MPSK, QAM signal can be expressed as a linear combination of two orthonormal functions. Expression (8.23) can be written as

$$s_i(t) = s_{i1}\phi_1(t) + s_{i2}\phi_2(t) \quad (8.27)$$

where

$$\phi_1(t) = \sqrt{\frac{2}{E_p}} p(t) \cos 2\pi f_c t, \quad 0 \leq t \leq T \quad (8.28)$$

$$\phi_2(t) = -\sqrt{\frac{2}{E_p}} p(t) \sin 2\pi f_c t, \quad 0 \leq t \leq T \quad (8.29)$$

and

$$s_{i1} = \sqrt{\frac{E_p}{2}} A_{i1} = \sqrt{\frac{E_p}{2}} A_i \cos \theta_i \quad (8.30)$$

$$s_{i2} = \sqrt{\frac{E_p}{2}} A_{i2} = \sqrt{\frac{E_p}{2}} A_i \sin \theta_i \quad (8.31)$$

where E_p is the energy of $p(t)$ in $[0, T]$. That is $E_p = \int_0^T p^2(t) dt$. The factor $\sqrt{2/E_p}$ is to normalize the basis functions $\phi_1(t)$ and $\phi_2(t)$.

¹ Even if pulse shaping is not desired, there is still inevitably pulse shaping due to the limited bandwidth of the system. In fact, deliberate pulse shaping is usually achieved through filtering. That is to make $P(f) = H_T(f)H_C(f)H_R(f)$ or equivalently $p(t) = h_T(t) * h_C(t) * h_R(t)$, where $h_T(t)$, $h_C(t)$ and $h_R(t)$ are the impulse responses of the transmitter filter, channel, and receiver filter, respectively. $H_T(f)$, $H_C(f)$, and $H_R(f)$ are their transfer functions. A common choice of $P(f)$ is the raised-cosine, whose time domain function $p(t)$ has zero values at sampling instants except for at $t = 0$. Thus $p(t)$ incurs no ISI. However, the raised-cosine response is noncausal, only an approximate delayed version is realizable. See [1, pp. 100-102].

It can be easily verified that the basis functions $\phi_1(t)$ and $\phi_2(t)$ are virtually orthonormal for $f_c \gg 1/T$. When $f_c \gg 1/T$, $p(t)$ is a slow-varying envelope. First they are virtually normalized since

$$\begin{aligned} \int_0^T \phi_1^2(t) dt &= \frac{2}{E_p} \int_0^T p^2(t) \cos^2 2\pi f_c t dt \\ &= \frac{1}{E_p} \int_0^T p^2(t) [1 + \cos 4\pi f_c t] dt \\ &\cong 1, \quad \text{for } f_c \gg 1/T \end{aligned}$$

The same is true for $\phi_2(t)$. Second, they are virtually orthogonal since

$$\begin{aligned} \int_0^T \phi_1(t) \phi_2(t) dt &= -\frac{2}{E_p} \int_0^T p^2(t) \cos 2\pi f_c t \sin 2\pi f_c t dt \\ &= -\frac{2}{E_p} \int_0^T p^2(t) \sin 4\pi f_c t dt \\ &\cong 0, \quad \text{for } f_c \gg 1/T \end{aligned}$$

Thus for most practical cases, $\phi_1(t)$ and $\phi_2(t)$ are orthonormal. When there is no pulse shaping, that is, $p(t) = 1$ in $[0, T]$, $E_p = T$. Then (8.28) and (8.29) have the same forms of (4.2) and (4.3). They are precisely orthonormal.

The energy of the i th signal is

$$E_i = \int_0^T s_i^2(t) dt \cong \frac{1}{2} A_i^2 E_p \quad (8.32)$$

and the average signal energy is

$$E_{avg} = \frac{1}{2} E_p \cdot E\{A_i^2\} \quad (8.33)$$

The average power is

$$P_{avg} = \frac{E_{avg}}{T} \quad (8.34)$$

The average amplitude is

$$A_{avg} = \sqrt{2P_{avg}} \quad (8.35)$$

Similar to MPSK, a geometric representation called constellation is a very clear way of describing a QAM signal set. The horizontal axis of the constellation plane is $\phi_1(t)$ and the vertical axis is $\phi_2(t)$. A QAM signal is represented by a point (or

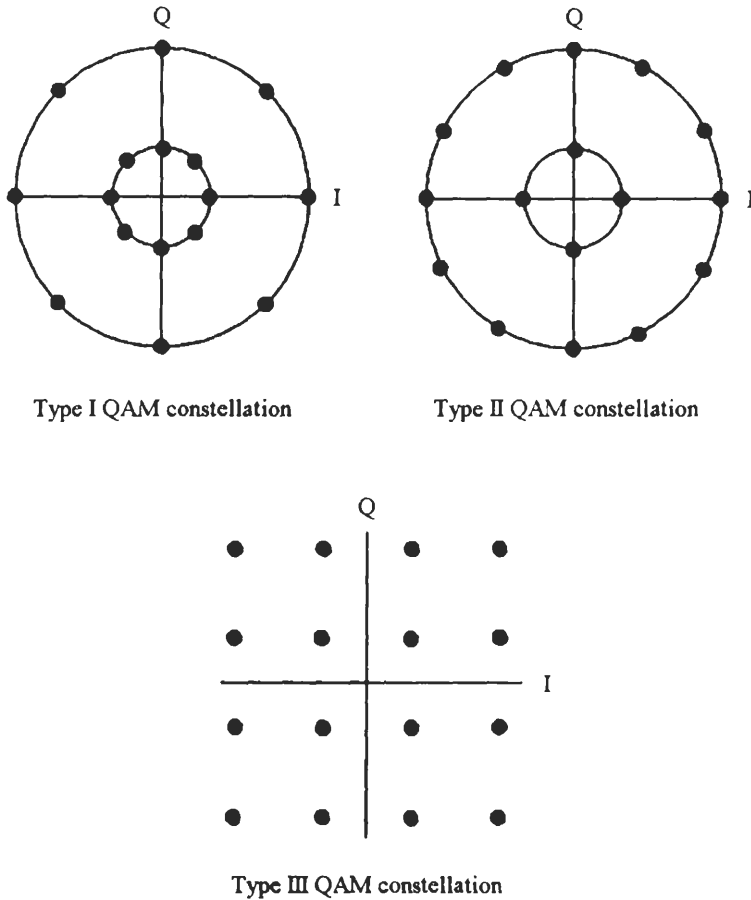


Figure 8.5 Examples of type I, II and III QAM constellations. From [8]. Copyright © 1994 IEEE.

vector, or phasor) with coordinates (s_{i1}, s_{i2}) . Alternatively, the two axes can be simply chosen as $p(t) \cos 2\pi f_c t$ and $-p(t) \sin 2\pi f_c t$. Then the signal coordinates are (A_{i1}, A_{i2}) . The two axes sometimes are simply labeled as I-axis and Q-axis, and sometimes are even left unlabeled. Figure 8.5 shows examples of three types of QAM constellations.

Now let us examine the properties of the QAM constellation. Assuming the axes are $\phi_1(t)$ and $\phi_2(t)$, then each signal is represented by the phasor

$$\mathbf{s}_i = (s_{i1}, s_{i2})$$

The magnitude of the phasor is

$$\|\mathbf{s}_i\| = \sqrt{s_{i1}^2 + s_{i2}^2} = \sqrt{E_i} \quad (8.36)$$

which is related to the signal amplitude by (from (8.32) and (8.36))

$$A_i = \sqrt{\frac{2}{E_p}} \|\mathbf{s}_i\| \quad (8.37)$$

The average energy is

$$E_{avg} = E\{E_i\} = E\{\|\mathbf{s}_i\|^2\} \quad (8.38)$$

The phase θ_i is the angle of the corresponding phasor

$$\theta_i = \tan^{-1} \frac{s_{i2}}{s_{i1}} \quad (8.39)$$

The distance between any pair of phasors is

$$\begin{aligned} d_{ij} &= \sqrt{\|\mathbf{s}_i - \mathbf{s}_j\|^2} \\ &= \sqrt{(s_{i1} - s_{j1})^2 + (s_{i2} - s_{j2})^2}, \quad i, j = 1, 2, \dots, M \end{aligned} \quad (8.40)$$

Depending what values (s_{i1}, s_{i2}) or (A_i, θ_i) are assigned with, a variety of QAM constellations can be realized.

8.3 QAM CONSTELLATIONS

The first QAM scheme was proposed by C. R. Cahn in 1960 [2]. He simply extended phase modulation to a multi-amplitude phase modulation. That is, there is more than one amplitude associated with an allowed phase. In the constellation, a fixed number of signal points (or phasors) are equally spaced on each of the N circles, where N is the number of amplitude levels (Figure 8.5(a)). This is called type I constellation in the literature. In a type I constellation, the points on the inner ring are closest together in distance and are most vulnerable to errors. To overcome this problem, type II constellation was proposed by Hancock and Lucky a few months later [3](Figure 8.5(b)). In a type II constellation, signal points are still on circles, but the number of points on the inner circle is less than the number of points on the outer circle, making the distance between two adjacent points on the inner circle approximately equal to that on the outer circle. Type III constellation is the square

QAM constellation shown in Figure 8.5(c), which was proposed by Campopiano and Glazer in 1962 [4]. Their analysis showed that the type III system offered a very small improvement in performance over the type II system, but its implementation would be considerably simpler than that of type I and II. Due to this, the type III constellation has been the most widely used system. Some other two dimensional constellations considered in the literature are given in Figure 8.6. The circular constellations are denoted by the notation (n_1, n_2, \dots) where n_1 is the number of signal points on the inner circle, n_2 is the number of signal points on the next circle, and so on. Figure 8.6 contains the type II and type III constellations.

When designing a constellation, consideration must be given to:

1. The minimum Euclidean distance d_{\min} among the phasors (signal points). It should be as large as possible under other constraints, since it determines the symbol error probability of the modulation scheme.
2. The phase differences among the phasors. It should be as large as possible under other constraints, since it determines the phase jitter immunity and hence the scheme's resilience against the carrier- and clock-recovery imperfections and channel phase rotations.
3. The average power of the phasors. It should be as small as possible under other constraints.
4. The ratio of the peak-to-average phasor power, which is a measure of robustness against nonlinear distortion caused by the power amplifier. It should be as close to unity as possible under other constraints.
5. The implementation complexity.
6. Other properties, such as resilience against fading.

Research results have shown that the square constellation (type III) is the most appropriate choice in AWGN channels. It can be easily generated as two MAM signals impressed on two phase-quadrature carriers. It can be easily demodulated to yield two quadrature components. Each component can be individually detected by comparing it to a set of thresholds. A few of the other constellations offer slightly better error performance, but with a much more complicated system implementation. Therefore we will concentrate on the square constellation in this chapter. The type I constellation (also called star constellation) is not optimum in terms of d_{\min} under the constraint of average phasor power. However, it allows efficient differential encoding and decoding methods to be used. This makes it suitable for fading channels. Its application in fading channels will be covered in Chapter 10.

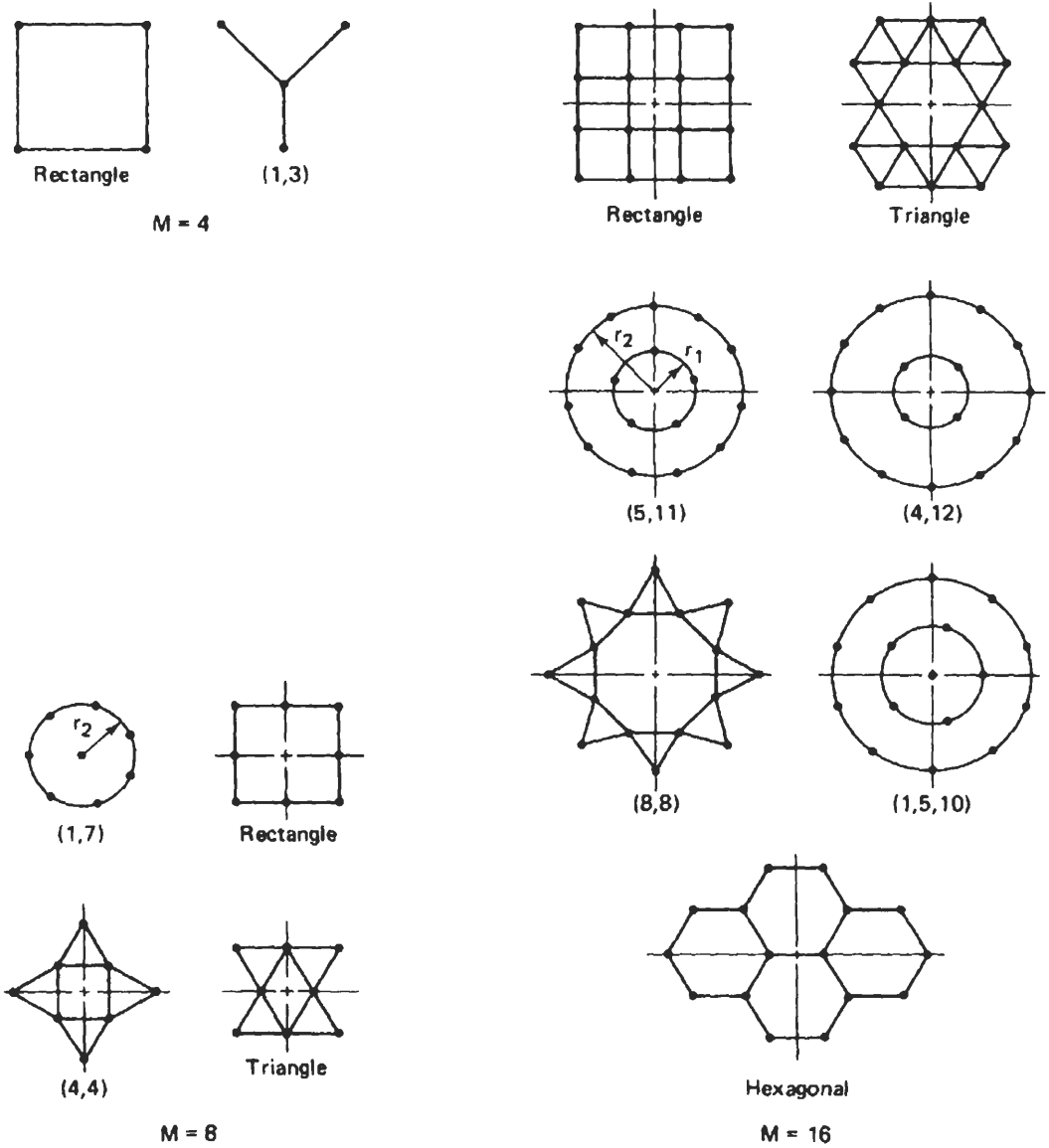


Figure 8.6 Various QAM constellations. From [5]. Copyright © 1974 IEEE.

8.3.1 Square QAM

For M-ary square QAM signals, (8.23) and (8.27) can be written in the following form

$$\begin{aligned} s_i(t) &= I_i \sqrt{\frac{E_0}{E_p}} p(t) \cos 2\pi f_c t - Q_i \sqrt{\frac{E_0}{E_p}} p(t) \sin 2\pi f_c t \\ &= I_i \sqrt{\frac{E_0}{2}} \phi_1(t) + Q_i \sqrt{\frac{E_0}{2}} \phi_2(t) \end{aligned} \quad (8.41)$$

where E_0 is the energy of the signal with the lowest amplitude, and (I_i, Q_i) are a pair of independent integers which determine the location of the signal point in the constellation. The minimum values of (I_i, Q_i) are $(\pm 1, \pm 1)$. The pair (I_i, Q_i) is an element of the $L \times L$ matrix:

$$[I_i, Q_i] = \begin{bmatrix} (-L+1, L-1) & (-L+3, L-1) & \cdots & (L-1, L-1) \\ (-L+1, L-3) & (-L+3, L-3) & \cdots & (L-1, L-3) \\ \vdots & \vdots & & \vdots \\ (-L+1, -L+1) & (-L+3, -L+1) & \cdots & (L-1, -L+1) \end{bmatrix} \quad (8.42)$$

where

$$L = \sqrt{M}, \quad M = 4^n, \quad n = 1, 2, 3, \dots$$

For example, for the 16-QAM in Figure 8.7, where $L = 4$, the matrix is

$$[I_i, Q_i] = \begin{bmatrix} (-3, 3) & (-1, 3) & (1, 3) & (3, 3) \\ (-3, 1) & (-1, 1) & (1, 1) & (3, 1) \\ (-3, -1) & (-1, -1) & (1, -1) & (3, -1) \\ (-3, -3) & (-1, -3) & (1, -3) & (3, -3) \end{bmatrix} \quad (8.43)$$

When $M = 2^n$ but not 4^n , L is not an integer, we cannot use the matrix (8.42) directly to define the QAM. However, we may use a modified matrix to define the QAM. For example, the 32-QAM can be defined by a 6×6 matrix without the four elements on the four corners.

The constellation can be conveniently expressed in terms of (I_i, Q_i) . The phasors for the square QAM are

$$\mathbf{s}_i = \left(I_i \sqrt{\frac{E_0}{2}}, Q_i \sqrt{\frac{E_0}{2}} \right) \quad i = 1, 2, \dots, M$$

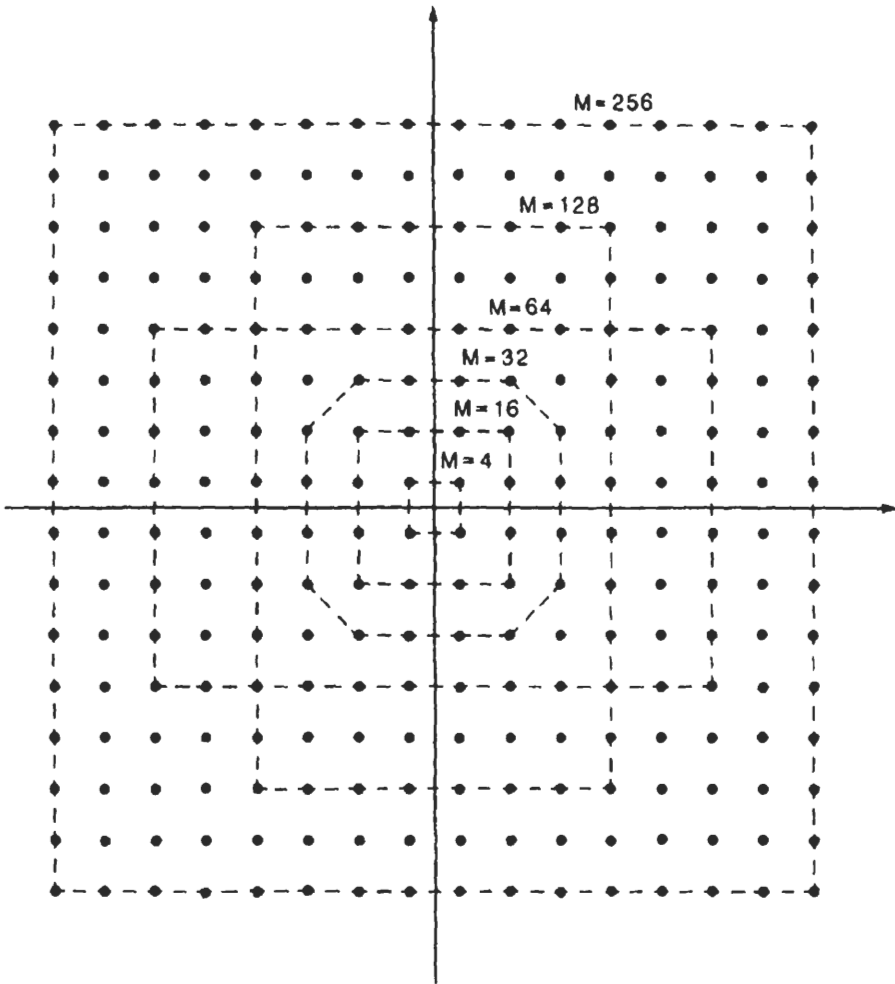


Figure 8.7 Square QAM constellations. From [6, p.224]. Copyright © 1987 Prentice Hall.

The magnitude of a phasor is

$$\|s_i\| = \sqrt{\frac{E_0}{2}(I_i^2 + Q_i^2)}$$

The QAM signal in (8.41) can also be written as

$$s_i(t) = A_i \cos(2\pi f_c t + \theta_i)$$

where the amplitude is

$$A_i = \sqrt{\frac{E_0}{E_p}(I_i^2 + Q_i^2)} = \sqrt{\frac{2}{E_p}} \|s_i\|$$

The phase θ_i is the angle of the corresponding phasor

$$\theta_i = \tan^{-1} \frac{Q_i}{I_i}$$

The distance between any pair of phasors is

$$\begin{aligned} d_{ij} &= \sqrt{|s_i - s_j|^2} \\ &= \sqrt{\frac{E_0}{2} [(I_i - I_j)^2 + (Q_i - Q_j)^2]}, \quad i, j = 1, 2, \dots, M \end{aligned}$$

The average energy is

$$E_{avg} = E\left\{\frac{E_0}{2}(I_i^2 + Q_i^2)\right\} = \frac{E_0}{2} [E\{I_i^2\} + E\{Q_i^2\}] = E_0 E\{I_i^2\}$$

and the average power is

$$P_{avg} = \frac{E_0}{T} E\{I_i^2\}$$

where for the strict square ($L \times L$) QAM

$$\begin{aligned} E\{I_i^2\} &= \frac{1}{L} [(-(L-1))^2 + (-(L-3))^2 + \dots + (L-3)^2 + (L-1)^2] \\ &= \frac{2}{L} [1^2 + 3^2 + \dots + (L-1)^2] \\ &= \frac{1}{3}(L^2 - 1) = \frac{1}{3}(M - 1) \end{aligned} \tag{8.44}$$

Thus

$$P_{avg} = \frac{E_0}{3T}(M-1) = P_0 \frac{1}{3}(M-1) \quad (8.45)$$

where P_0 is the power of the smallest signal.

8.4 POWER SPECTRAL DENSITY

Using the PSD formula for quadrature modulation (see (A.21) in Appendix A), the PSD of the square QAM can be computed as follows.

In order to include the most general case, we consider QAM with pulse shaping.

$$s_i(t) = A_i p(t) \cos(2\pi f_c t + \theta_i), \quad i = 1, 2, \dots, M$$

On the entire time axis, the QAM signal can be written as

$$s(t) = \operatorname{Re} \left\{ \left[\sum_{k=-\infty}^{\infty} A_k \exp(j\theta_k) p(t - kT) \right] \exp(j2\pi f_c t) \right\}, \quad -\infty < t < \infty \quad (8.46)$$

The complex envelope of the QAM signal is

$$\begin{aligned} \tilde{s}(t) &= \sum_{k=-\infty}^{\infty} A_k \exp(j\theta_k) p(t - kT) \\ &= \sum_{k=-\infty}^{\infty} A_k \cos \theta_k p(t - kT) + j \sum_{k=-\infty}^{\infty} A_k \sin \theta_k p(t - kT) \quad (8.47) \\ &= \sum_{k=-\infty}^{\infty} A_{k1} p(t - kT) + j \sum_{k=-\infty}^{\infty} A_{k2} p(t - kT) \end{aligned}$$

where

$$A_{k1} = A_k \cos \theta_k$$

$$A_{k2} = A_k \sin \theta_k$$

These are random variables with equal probability for each value. They have zero means for symmetrical constellations (Figures 8.5 to 8.7). The variances of them depend on the constellation shape.

$$\sigma_1^2 = E\{A_{k1}^2\}$$

$$\sigma_2^2 = E\{A_{k2}^2\}$$

From (8.38), the average power of the signal is

$$P_{avg} = \frac{1}{2T} E_p \cdot E\{A_i^2\} = \frac{1}{2T} E_p (\sigma_1^2 + \sigma_2^2)$$

Now we use the PSD formula (A.21) in Appendix A to compute the PSD of QAM. We rewrite it in the following

$$\Psi_{\bar{s}}(f) = \frac{\sigma_x^2 |P(f)|^2}{T} + \frac{\sigma_y^2 |Q(f)|^2}{T}$$

where $P(f)$ and $Q(f)$ are the spectra of the I-channel signal and Q-channel signal pulse shape, respectively. This is a very general formula, applicable to any quadrature modulated signal. For QAM schemes $P(f) = Q(f)$, $\sigma_x^2 = \sigma_1^2$ and $\sigma_y^2 = \sigma_2^2$, we have

$$\Psi_{\bar{s}}(f) = \frac{|P(f)|^2}{T} (\sigma_1^2 + \sigma_2^2) = \frac{2P_{avg}}{E_p} |P(f)|^2 \quad (8.48)$$

This equation tells us that the shape of the PSD of a QAM scheme is determined by the baseband pulse shape, and the magnitude of the PSD is determined by the average power (or average amplitude) of the QAM signal set. It is also worthwhile to point out that the shape of the PSD of a QAM scheme is independent of the constellation. In other words, no matter what the constellation is, be it square, circular or others, the PSD shape is the same as long as the $p(t)$ is the same, the PSD magnitude is also the same as long as the average signal power is also the same.

Without particular pulse shaping, $p(t)$ is just a rectangular pulse with unit amplitude. Then $E_p = T$ and

$$|P(f)| = \left| T \frac{\sin \pi f T}{\pi f T} \right|$$

Therefore

$$\begin{aligned} \Psi_{\bar{s}}(f) &= 2P_{avg} T \left(\frac{\sin \pi f T}{\pi f T} \right)^2 \\ &= A_{avg}^2 T \left(\frac{\sin \pi f T}{\pi f T} \right)^2 \\ &= A_{avg}^2 n T_b \left(\frac{\sin \pi f n T_b}{\pi f n T_b} \right)^2 \end{aligned} \quad (8.49)$$

where $n = \log_2 M$ and $T_b = T/n$ is the bit period. This PSD has the same shape of the PSD of MPSK (see (4.26)). The only difference lies in the magnitude. In the MPSK case, the PSD magnitude depends on the signal amplitude because there is only one signal amplitude. In the QAM case, the PSD magnitude depends on the average signal amplitude. Thus, the PSD curves for MPSK in Figure 4.15 are also applicable to QAM schemes as long as the average amplitude of the QAM is used. For example, for M-ary square QAM, from (8.49) and (8.45) we have

$$\begin{aligned}\Psi_{\bar{s}}(f) &= \frac{2E_0}{3}(M-1) \left(\frac{\sin \pi f T}{\pi f T} \right)^2 \\ &= \frac{2E_0}{3}(M-1) \left(\frac{\sin \pi f n T_b}{\pi f n T_b} \right)^2\end{aligned}\quad (8.50)$$

8.5 MODULATOR

The QAM modulator is almost identical to that of MPSK since both of them are quadrature schemes. We can write the QAM signal as

$$s(t) = s_1(t) \cos 2\pi f_c t - s_2(t) \sin 2\pi f_c t, \quad -\infty < t < \infty \quad (8.51)$$

where

$$\begin{aligned}s_1(t) &= \sum_{k=-\infty}^{\infty} A_{k1} p(t - kT) \\ s_2(t) &= \sum_{k=-\infty}^{\infty} A_{k2} p(t - kT)\end{aligned}$$

The modulator derived directly from (8.51) is shown in Figure 8.8. If pulse shaping is not desired, the $p(t)$ block will be absent. The data bit sequence is divided into n -tuples of n bits. There are $M = 2^n$ distinct n -tuples. Each n -tuple of the input bits is used to control the level generator. The level generator provides the I- and Q-channel the particular sign and level for a signal's horizontal and vertical coordinates (A_{k1}, A_{k2}) , respectively. The mapping from n -tuples to QAM points are usually Gray coded for minimizing bit errors. For square QAM, perfect Gray coding is possible. Figure 8.9 is a Gray coded square 16-QAM constellation. For some constellations, such as a circular QAM with four points on the inner ring and eight on the outer, it is not possible to have perfect Gray coding.

Digital synthesis techniques can be used to generate QAM signals. Each signal

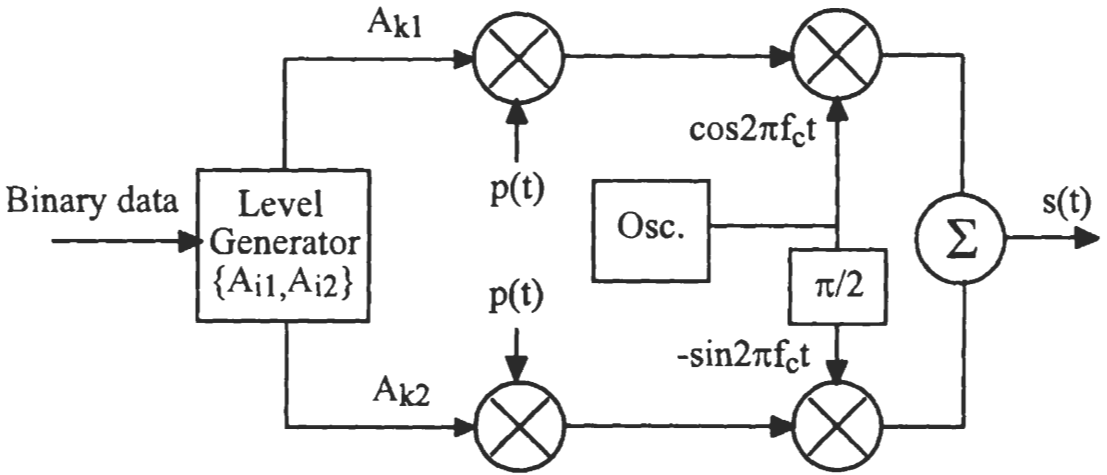


Figure 8.8 QAM modulator.

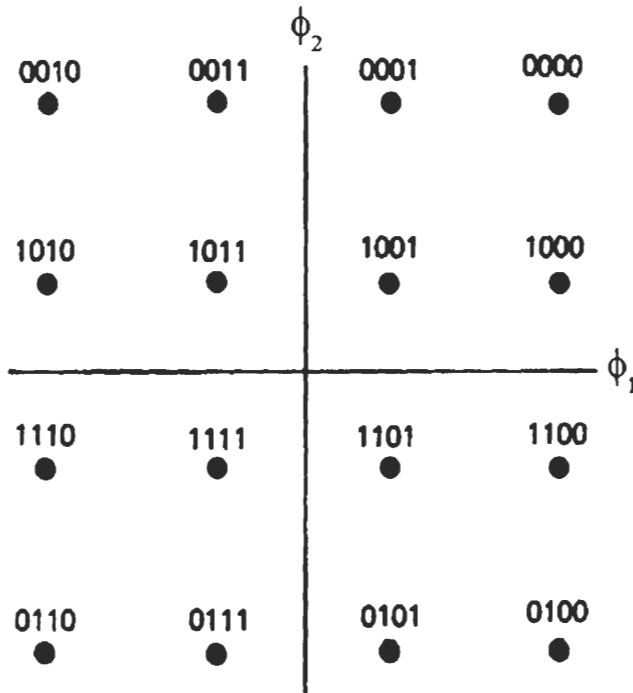


Figure 8.9 Gray coded square 16-QAM constellation. The signal points are labeled with 4-bit Gray codes.

in the constellation can be stored as a set of samples and the data n -tuple is used as the address to obtain the samples. The samples are fed to a D/A converter whose output is the desired QAM signal.

8.6 DEMODULATOR

Similar to MPSK, the coherent demodulation of QAM could be implemented by one of the coherent detectors for M -ary signals as described in Appendix B. Since the QAM signal set has only two basis functions, the simplest receiver is the one that uses two correlators (Figure B.8 with $N = 2$). Due to the special characteristic of the QAM signal, the general demodulator of Figure B.8 can be simplified.

The received signal is

$$r(t) = s_i(t) + n(t)$$

According to (B.37) in Appendix B, for QAM signal detection the sufficient statistic is the (squared) distance²

$$l_i = (r_1 - s_{i1})^2 + (r_2 - s_{i2})^2 \quad (8.52)$$

where

$$r_1 \triangleq \int_0^T r(t)\phi_1(t)dt = s_{i1} + n_1$$

$$r_2 \triangleq \int_0^T r(t)\phi_2(t)dt = s_{i2} + n_2$$

are independent Gaussian random variables with mean values s_{i1} and s_{i2} , respectively. Their variance is $N_o/2$. The pair (r_1, r_2) determines a point in the QAM constellation plane, representing the received noisy signal. The detector compares the distances from (r_1, r_2) to all pairs of (s_{i1}, s_{i2}) and chooses the closest one.

Figure 8.10 is the demodulator based on the above decision rule where subscript k indicates the k th symbol period. Note that the amplitude of the reference signals can be any value, which is $\sqrt{2/E_p}$ in the figure, as long as (s_{i1}, s_{i2}) are also scaled accordingly. As we have shown in Section 8.1.3, the integrators may be replaced by matched filters whose outputs are sampled at $t = (k + 1)T$ (Figure 8.11). The filter impulse responses match to the shaping pulse $p(t)$. For the square QAM, the r_{1k} and

² Note that this is different from the sufficient statistic of MPSK. In the case of MPSK, each signal has the same energy, thus (B.38) with B_j dropped instead of (B.37) is used, which leads to a decision rule that compares only angles not distances.

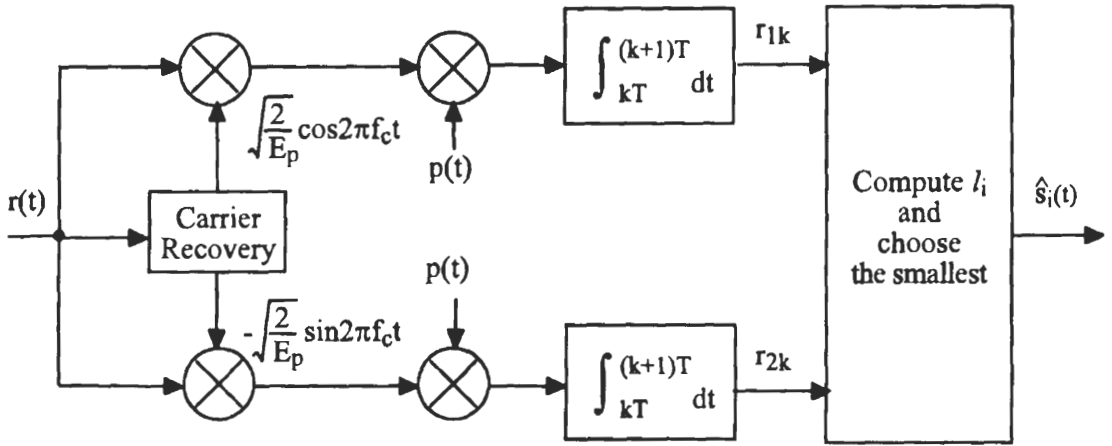


Figure 8.10 Coherent demodulator for QAM.

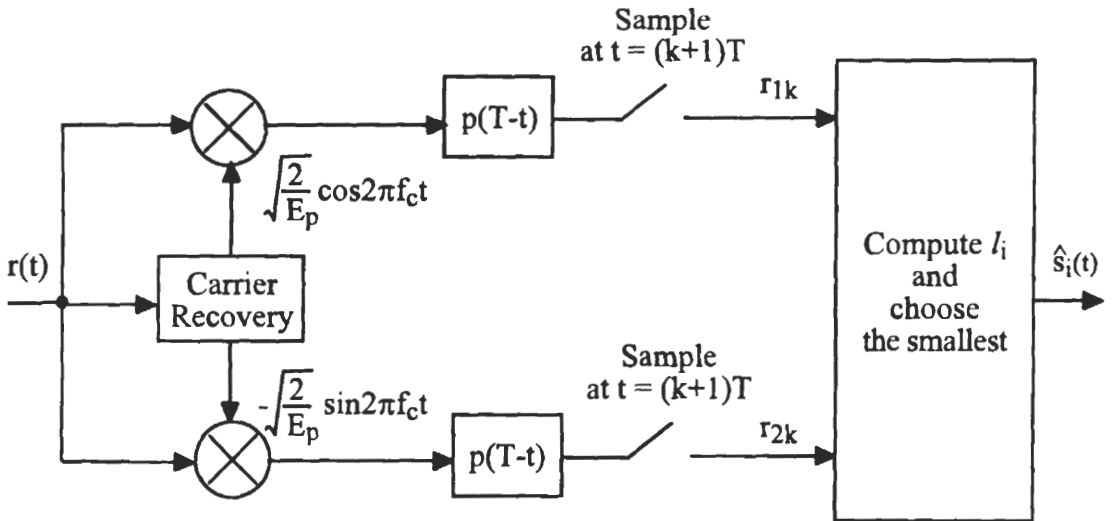


Figure 8.11 Coherent QAM demodulator using matched filters.

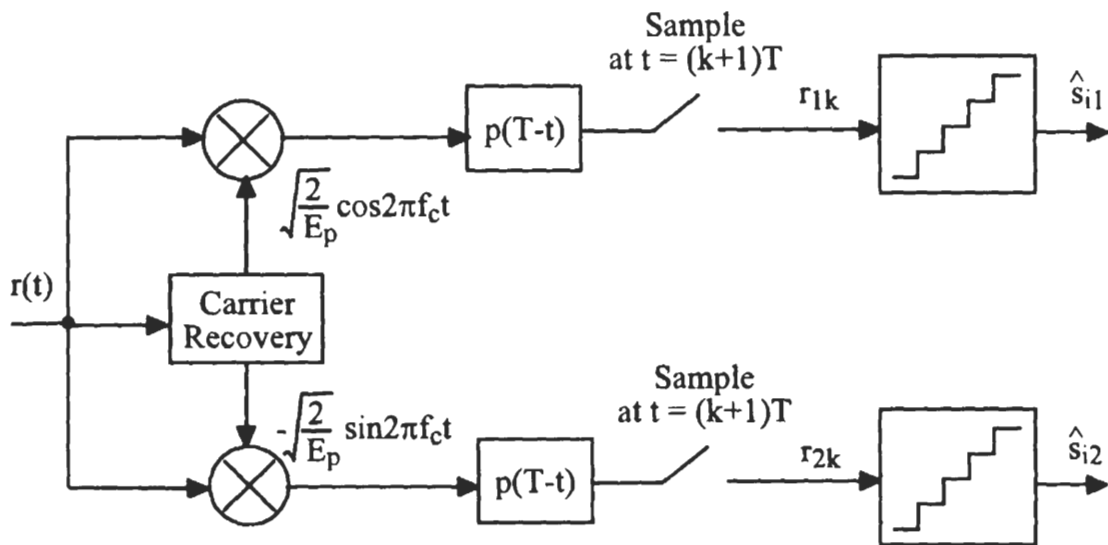


Figure 8.12 Coherent demodulator for square QAM using threshold detectors. I-channel and Q-channel are demodulated separately.

r_{2k} can be detected separately by two multi-threshold detectors to yield s_{i1} and s_{i2} , and then signal $s_i(t)$ can be determined (Figure 8.12).

8.7 ERROR PROBABILITY

For square QAM constellations with $M = 2^k$ where k is even, the QAM constellation is equivalent to two MAM signals on quadrature carriers, each having $L = \sqrt{M}$ signal points. As we have seen from the last section, each MAM signal can be demodulated separately. A QAM symbol is detected correctly only when two MAM symbols are detected correctly. Thus the probability of correct detection of a QAM symbol is

$$P_c = (1 - P_{\sqrt{M}})^2$$

where $P_{\sqrt{M}}$ is the symbol error probability of a \sqrt{M} -ary AM with one-half the average power of the QAM signal. From (8.13) we have

$$P_{\sqrt{M}} = \frac{2(\sqrt{M} - 1)}{\sqrt{M}} Q \left(\sqrt{\frac{3E_{avg}}{(M - 1)N_o}} \right) \quad (8.53)$$

where E_{avg}/N_o is the average SNR per symbol. The symbol error probability of the

square QAM is

$$P_s = 1 - (1 - P_{\sqrt{M}})^2 = 2P_{\sqrt{M}} - P_{\sqrt{M}}^2 \quad (8.54)$$

At high SNR,

$$P_s \cong 2P_{\sqrt{M}} = \frac{4(\sqrt{M} - 1)}{\sqrt{M}} Q \left(\sqrt{\frac{3E_{avg}}{(M-1)N_o}} \right) \quad (8.55)$$

Note that (8.54) is exact for square QAM with $M = 2^k$ where k is even. When k is odd there is no equivalent \sqrt{M} -ary AM system. However, we can find a tight upper bound [7, Page 655]

$$\begin{aligned} P_s &\leq 1 - \left[1 - 2Q \left(\sqrt{\frac{3E_{avg}}{(M-1)N_o}} \right) \right]^2 \\ &\leq 4Q \left(\sqrt{\frac{3kE_{bavg}}{(M-1)N_o}} \right) \end{aligned} \quad (8.56)$$

for any $k \geq 1$, where E_{bavg}/N_o is the average SNR per bit.

To obtain bit error probability from the symbol error probability, we observe that square QAM can be perfectly Gray coded. That is, there is only one bit difference between adjacent symbols. Each symbol error most likely causes one bit error at large SNR. Thus

$$P_b \cong \frac{P_s}{\log_2 M} \quad (8.57)$$

Figure 8.13 shows the P_b curves for $M = 4, 8, 16, 32, 64, 128$, and 256 where the curves for $M = 8, 32$, and 128 are tight upper bounds (dotted lines).

In the following we compare QAM with MPSK. From the P_s of MPSK (4.24) and (8.55) or (8.56), the ratio (QAM over MPSK) of the arguments inside the square root sign of the Q-function is

$$R_M = \frac{3}{2(M-1) \sin^2 \pi/M} \quad (8.58)$$

This reflects the ratio of the signal power. This ratio is tabulated in Table 8.2.

From the table we can see that for $M > 4$, the QAM is superior to MPSK. Furthermore, for large $M (\geq 32)$ the power savings increases 3 dB for doubling the number of signal points. This can be explained from (8.58) by observing that $R_M \cong 3M/2\pi^2$ for large M . This can also be looked at from another point of view. Examining (8.55) or (8.56) reveals that for large M , doubling M incurs 3 dB penalty

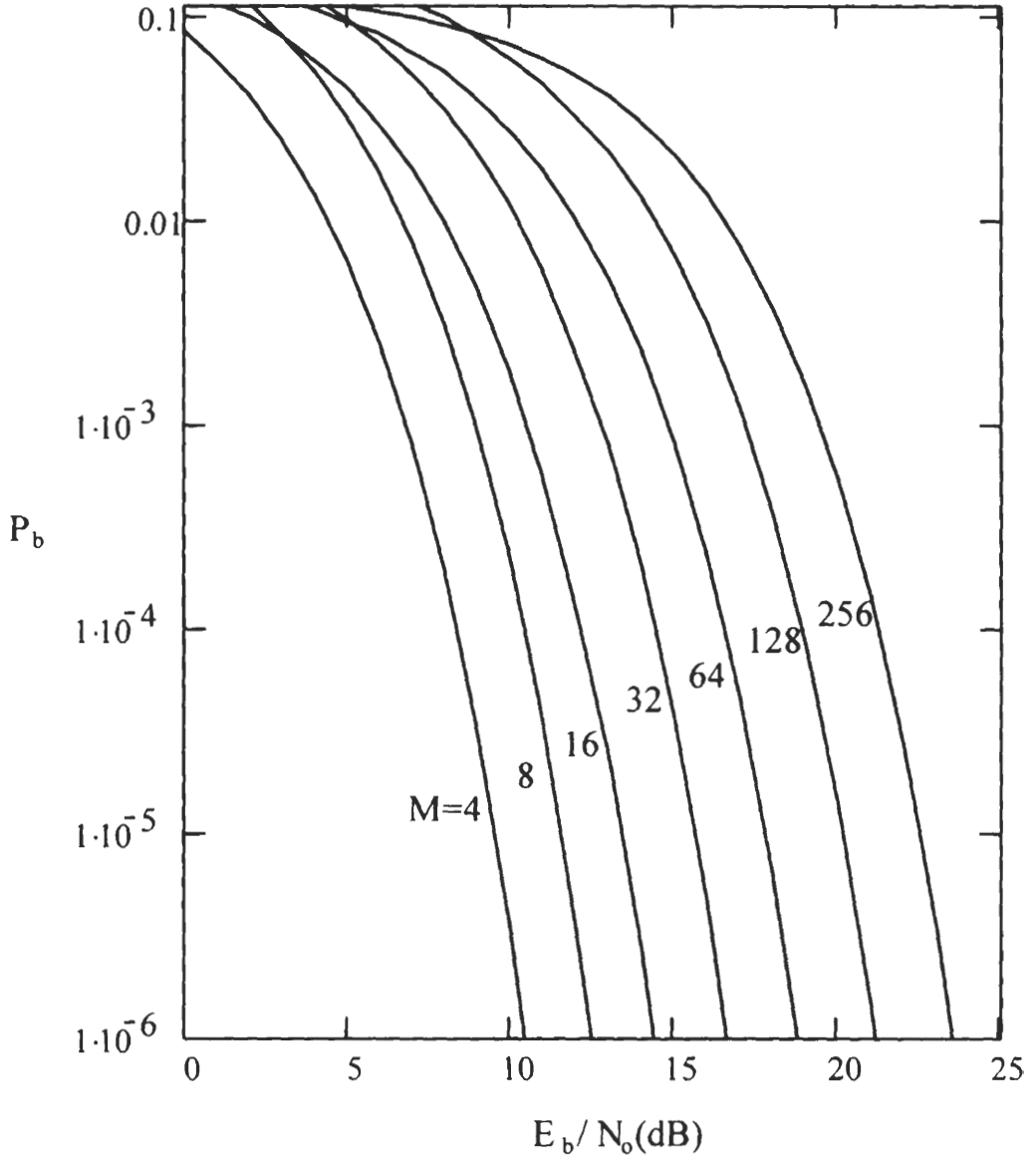


Figure 8.13 Square QAM bit error probability.

M	R_M	$10 \log R_M$ (dB)
4	1	0
8	1.463	1.65
16	2.627	4.20
32	5.036	7.02
64	9.889	9.95
128	19.61	12.92
256	39.06	15.92

Table 8.2 Power savings of QAM over MPSK.

in signal power, whereas the penalty for MPSK and MAM is 6 dB as we pointed out before. That is why Table 8.2 shows a 3 dB increase in power savings for doubling M when QAM is compared with MPSK (and it is also true compared with MAM).

8.8 SYNCHRONIZATION

Clock synchronization for QAM is usually achieved by clock recovery circuit which extracts the clock from the demodulated signal or uses the demodulated signal to control the local oscillator. Clock recovery techniques for QAM are the same as those for MPSK. The open-loop clock recovery circuits in Figure 4.37 and the early/late-gate clock recovery circuit in Figure 4.38 are all applicable to QAM. Refer to Chapter 4 for details.

Carrier synchronization is always necessary for square QAM constellations, even when differential coding is used. This is because differential coding for the square QAM is only for some of the bits in a symbol. Even though these bits can be determined by comparing two consecutive symbols (differential demodulation), the rest of the bits still must be determined by coherent demodulation. Thus the entire symbol might as well be coherently demodulated. For a description of differential coding for QAM, refer to the next section. Circular QAM constellations do not require carrier synchronization if differential encoding is used. We will discuss this in Chapter 10.

Carrier synchronization can be achieved by the pilot-tone technique or a separate synchronization channel, which requires extra bandwidth, as we mentioned in Chapter 4. Again we will not elaborate on this. Instead we focus on the carrier recovery techniques. There are two major types of carrier recovery techniques for QAM. One is the fourth-power loop (or times-four loop) and another is the decision-directed carrier recovery (DDCR). According to [8, Page 182], the decision-directed carrier recovery technique is one of the most popular carrier recovery schemes used in fixed-link

QAM systems. The fourth-power loop carrier recovery has been suggested for digital radio in fading environment [9]. In the following we first discuss the fourth-power loop technique and then the decision-directed carrier recovery technique.

Recall that the M th-power loop (Figure 4.35) is used for MPSK, but for M -ary QAM, the M th-power loop is not necessary, only the fourth-power loop is needed. Unfortunately the squaring loop does not work for symmetrical QAM since the average energy at $2f_c$ is zero. It is also known that for M greater than four, the data pattern effects lead to an increased amount of carrier phase jitter in an M th-power loop [9]. Thus the fourth-power loop is the right choice for QAM.

We show below that the squaring loop does not work for symmetrical QAM, but the fourth-power loop does. From Section 8.5 we see that A_{i1} and A_{i2} are generated by level generators using the input data which are random. Therefore A_{i1} and A_{i2} are random. We assume that their values are symmetrical about zero, that is, they have zero means. We further assume that the input data are ergodic random processes. Consequently A_{i1} and A_{i2} are ergodic random processes so that the time average is equal to the statistical average. All the above assumptions are the usual case in digital communications. We square the QAM signal given in (8.23) and take the average over all possible i to obtain

$$\begin{aligned} E\{s_i^2(t)\} &= E\{p^2(t)[A_{i1}^2 \cos^2 \omega_c t - 2A_{i1}A_{i2} \cos \omega_c t \sin \omega_c t + A_{i2}^2 \sin^2 \omega_c t]\} \\ &= E\{p^2(t)[A_{i1}^2 \cos^2 \omega_c t + A_{i2}^2 \sin^2 \omega_c t]\} \\ &= \frac{1}{2}p^2(t) [(E\{A_{i1}^2\} + E\{A_{i2}^2\}) + (E\{A_{i1}^2\} - E\{A_{i2}^2\}) \cos 2\omega_c t] \end{aligned}$$

where $\omega_c = 2\pi f_c$ and the middle term in the first expression vanishes since A_{i1} and A_{i2} are independent zero-mean random processes so that

$$E\{A_{i1}A_{i2}\} = E\{A_{i1}\}E\{A_{i2}\} = 0$$

For symmetrical QAM, $E\{A_{i1}^2\} = E\{A_{i2}^2\}$, the above becomes

$$E\{s_i^2(t)\} = p^2(t)E\{A_{i1}^2\}$$

which has no periodical component at f_c or its multiples. We can intentionally unbalance the QAM constellation to make carrier recovery possible, but this leads to inefficient signal constellations. A fourth-power nonlinearity can produce a nonzero component at $4f_c$ even if the QAM is symmetrical. Using trigonometrical identities we can show that (see Appendix 8A at the end of this chapter)

$$\begin{aligned} E\{s_i^4(t)\} &= \frac{1}{8}p^4(t)[E\{A_{i1}^4\}(3 + 4 \cos 2\omega_c t + \cos 4\omega_c t) \\ &\quad + E\{A_{i2}^4\}(3 - 4 \cos 2\omega_c t + \cos 4\omega_c t)] \end{aligned}$$

$$+\frac{3}{4}p^4(t)E\{A_{i1}^2\}E\{A_{i2}^2\}(1 - \cos 4\omega_c t) \quad (8.59)$$

For symmetrical QAM, since $E\{A_{i1}^2\} = E\{A_{i2}^2\}$, we have

$$\begin{aligned} E\{s_i^4(t)\} &= \frac{3}{4}p^4(t) [E\{A_{i1}^4\} + (E\{A_{i1}^2\})^2] \\ &+ \frac{1}{4}p^4(t) [E\{A_{i1}^4\} - 3(E\{A_{i1}^2\})^2] \cos 4\omega_c t \end{aligned} \quad (8.60)$$

There is a nonzero component at $4f_c$.

For the square QAM, $A_{i1} = I_i \sqrt{E_0/E_p}$, $A_{i2} = Q_i \sqrt{E_0/E_p}$ (see (8.41)).

$$E\{A_{i1}^2\} = \frac{E_0}{E_p} \frac{1}{3} (M - 1) \quad (8.61)$$

where the result of (8.44) is used, and

$$E\{A_{i1}^4\} = \left(\frac{E_0}{E_p}\right)^2 E\{I_i^4\}$$

where

$$\begin{aligned} E\{I_i^4\} &= \frac{1}{L} [(-(L-1))^4 + (-(L-3))^4 + \dots + (L-3)^4 + (L-1)^4] \\ &= \frac{2}{L} [1^4 + 3^4 + \dots + (L-1)^4] \\ &= \frac{1}{15} (3L^4 - 10L^2 + 7) = \frac{1}{15} (3M^2 - 10M + 7) \end{aligned} \quad (8.62)$$

Substitute (8.61) and (8.62) into (8.60), we have

$$E\{s_i^4(t)\} = \frac{1}{30} p^4(t) \left(\frac{E_0}{E_p}\right)^2 [(7M^2 - 20M + 13) - (M^2 - 1) \cos 4\omega_c t] \quad (8.63)$$

From (8.63) we can see that the $4f_c$ component always has a phase of π for the square QAM.

For the square 16-QAM we have

$$E\{s_i^4(t)\} = \frac{1}{2} p^4(t) \left(\frac{E_0}{E_p}\right)^2 (99 - 17 \cos 4\omega_c t)$$

M	r_M	$20 \log R_M$ (dB)
4	0.333	-9.54
16	0.172	-15.30
64	0.149	-16.51
256	0.144	-16.80

Table 8.3 Amplitude ratio.

If $p(t) = 1$, then $E_p = T$, then

$$E\{s_i^4(t)\} = \frac{1}{2} \left(\frac{E_0}{T} \right)^2 (99 - 17 \cos 4\omega_c t)$$

This shows that the $4f_c$ component has a phase of π and an amplitude of $17/99 \cong 17.2\%$ of the dc component. In fact we can calculate this ratio for a series of M , as listed in Table 8.3.

$$r_M = \frac{M^2 - 1}{7M^2 - 20M + 13} \quad (8.64)$$

Note that the above results (Table 8.3) are for ideal fourth-power devices and square QAM. For other types of constellations and nonideal devices, the results would be different. For some types of constellations, the $4f_c$ component may be too weak to be useful. Then other carrier recovery techniques, such as the decision-directed carrier recovery technique may be needed.

The block diagram in Figure 4.35 can be used for the fourth-power loop by letting $M = 4$. A slightly different version was proposed by Rustako et al [9] where the fourth-power loop was proposed for QAM digital radio receivers. Figure 8.14 is the diagram given in [9]. The VCO is working at f_c . A $\times 4$ block is inserted in the PLL loop to raise the VCO frequency to $4f_c$, which is then compared with the output of another $\times 4$ block whose input is the received signal. The $\times 4$ block is actually realized by a frequency-doubler whose nonlinearity generates a $4f_c$ component as a by-product at a level of about 20 dB below the $2f_c$ component. A detailed analysis of the times-four loop can be found in [9]. Rustako notes that in a fading environment, decision-directed carrier recovery suffers when occasional receiver outage destroys the accuracy of the data detections. This causes loss of carrier recovery and considerable time may be required to re-acquire the carrier. He notes that times-four carrier recovery does not depend on data decision. For this and other reasons, times-four carrier recovery was proposed for digital radio receivers.

As mentioned, the decision-directed carrier recovery technique is one of the most popular carrier recovery schemes used in fixed-link QAM systems. The mech-

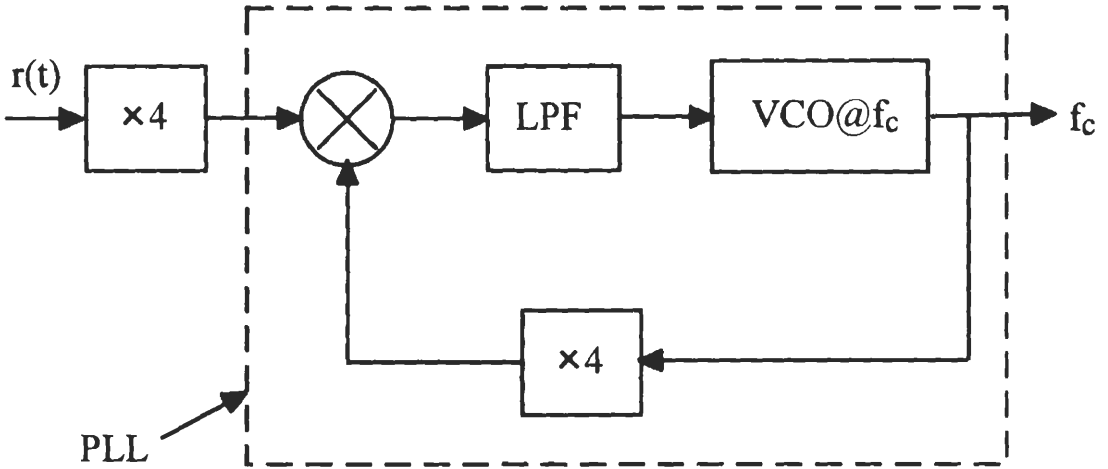


Figure 8.14 Times-four carrier recovery loop for QAM.

anism of DDCR is not based on nonlinearity. In this scheme, when a symbol is received, it is demodulated and a decision is made as to which was the most likely constellation point transmitted. Then it is assumed that the phase difference between the received symbol and the constellation point is due to carrier-recovery error, and the carrier recovery is updated accordingly. DDCR has the advantage that it can be used for all types of constellations. However, it exhibits a BER threshold. If the receiver BER is less than this threshold, it works extremely well since the “decisions” that assist the carrier recovery are correct almost all the time. If the receiver BER is higher than this threshold, the decisions on the constellation points are wrong more frequently. The update signal to the carrier recovery system therefore is erroneous more frequently, the cumulative effect can drive the carrier phase further and further away from the correct value. Whether DDCR is suitable for a particular application depends on this BER threshold.

Horikawa et al designed a DDCR system for a 200Mbps square 16-QAM [10]. In their design, the square 16-QAM constellation points are divided into two subgroups, called class I and class II phasors (Figure 8.15). The class II phasors are those on the second circle with a normalized amplitude of $\sqrt{10}$. The rest are the class I phasors, four are on the outer circle, with an amplitude of $\sqrt{18}$; four are on the inner circle, with an amplitude of $\sqrt{2}$. The quadrature components of the class I phasors are equal in magnitude (i.e., $|I| = |Q|$), whereas the quadrature components of the class II phasors have a 3 to 1 ratio (i.e., $|I| = 3|Q|$ or $|Q| = 3|I|$).

Horikawa’s DDCR system operates only on class I phasors. In other words, only class I phasors in the received signal are utilized by the DDCR system to recover the carrier. The DDCR system compares the values of the demodulated signal I and Q.

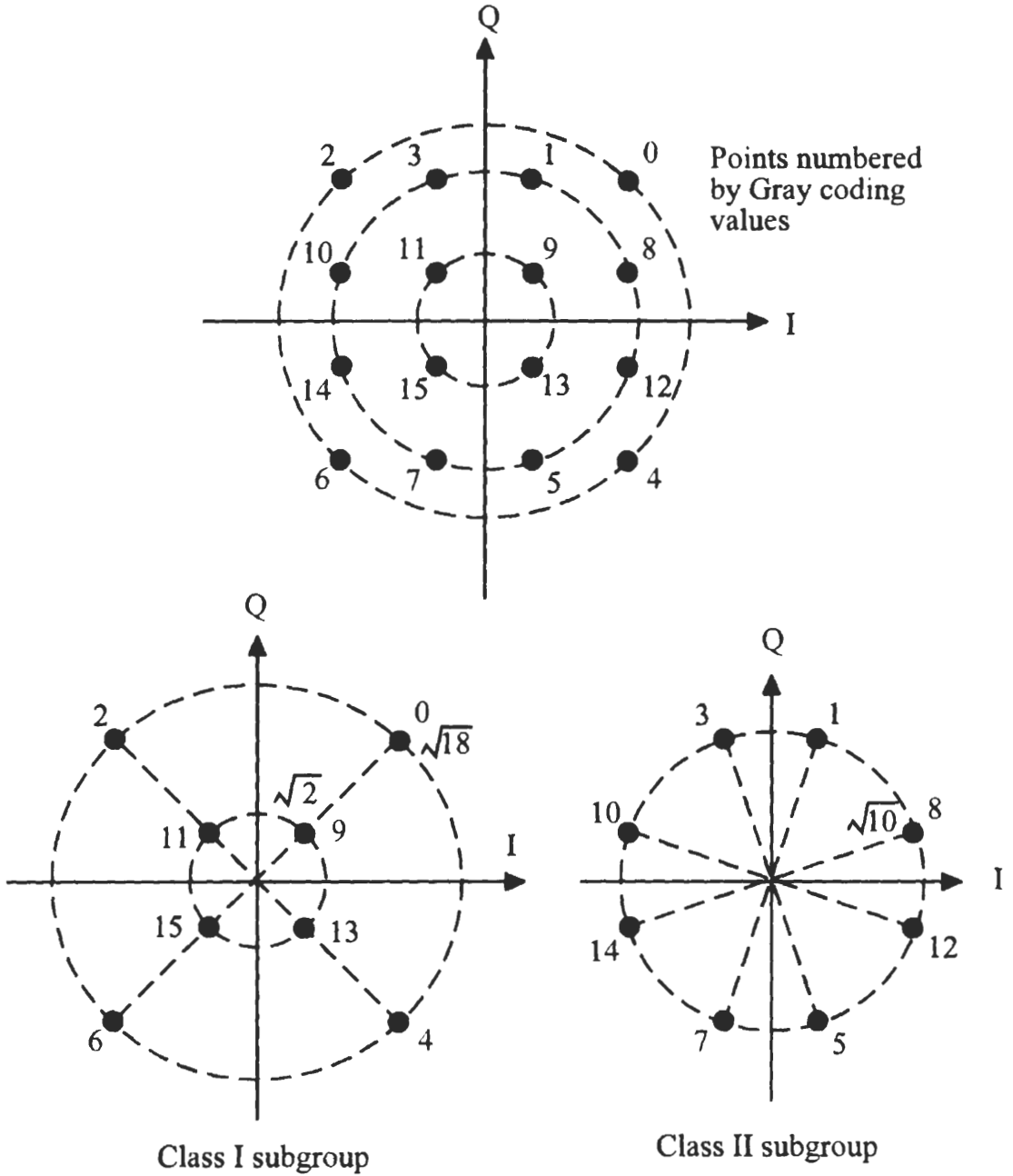


Figure 8.15 Square 16-QAM subgroups.

If they satisfy the relationship

$$\frac{|I|}{2} < |Q| < 2|I| \quad (8.65)$$

then the system decides that a class I phasor has been sent. This rule is designed to effectively reject class II phasors while detecting class II phasors in a noisy environment. Once a class I phasor is detected, its I and Q values are used to determine polarity of the carrier drift and subsequently to adjust the VCO. The algorithm is as follows [8]. First compute the quantities

$$\begin{aligned} a &= \text{pol}(I) \oplus \text{pol}(Q) \\ b &= \text{pol}(I + Q) \\ c &= \text{pol}(I - Q) \\ d &= (a \oplus b) \oplus c \end{aligned} \quad (8.66)$$

where \oplus denotes modulo-2 addition or XOR operation, and

$$\text{pol}(x) = \begin{cases} 1, & x > 0 \\ 0, & x < 0 \end{cases}$$

The d is used to control the VCO.

According to the above algorithm, the values of (abc) and d are shown in Figure 8.16 for each octant. As can be seen, the value of d changes between 0 and 1 alternately from an octant to the next. The quantity d is used to adjust the VCO frequency and phase. The demodulated signal is

$$r = LPF\{A_i \cos(\omega_c t + \theta_i) \cdot 2 \cos(\omega_c t + \Delta\theta)\} = A_i \cos(\theta_i - \Delta\theta) \quad (8.67)$$

where LPF denotes low-pass filtering. The VCO is assumed to have an amplitude of 2 and a phase error $\Delta\theta$ which is due to frequency error and initial phase error. From Figure 8.16, when $d = 0$, the angle of r is less than the transmitted phasor. From (8.67), this implies that the VCO has a positive phase error. Thus the VCO is instructed to run slower (reduce its frequency). When $d = 1$, the angle of r is greater than the transmitted phasor. From (8.67), this implies that the VCO has a negative phase error. Thus the VCO is instructed to run faster (increase its frequency). For example, assume $r = (I, Q) = (2.24, 3.6)$ is received (see Figure 8.16). Then $a = \text{pol}(2.24) \oplus \text{pol}(3.6) = 1 \oplus 1 = 0$, $b = \text{pol}(5.84) = 1$, $c = \text{pol}(-1.36) = 0$, and $d = 0 \oplus 1 \oplus 0 = 1$. Thus the VCO is instructed to increase its frequency.

The DDCR system is shown in Figure 8.17. The received signal $r(t)$ is demodulated by the I- and Q-branches to produce I and Q. Then I and Q are fed into four comparators to generate a , b , and c , which are fed into XORs to generate d . At the

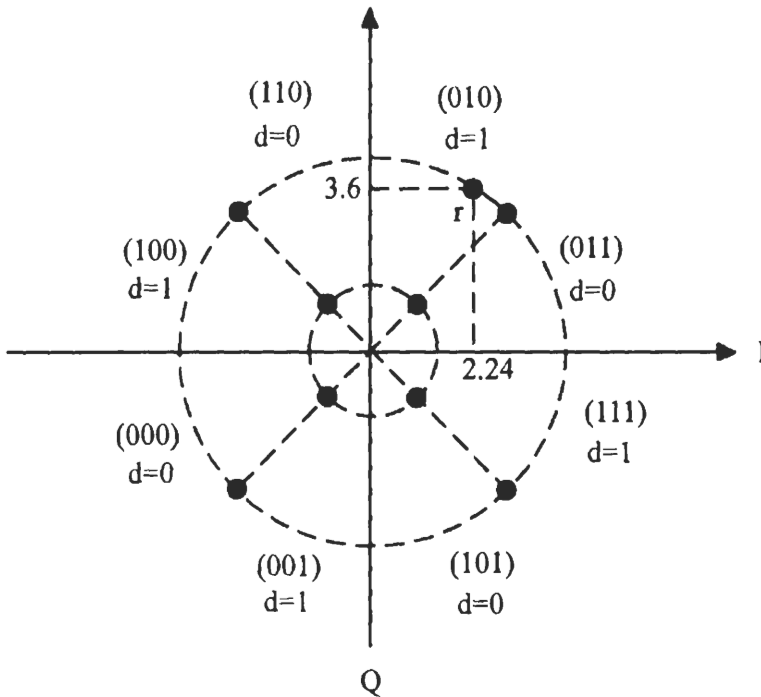


Figure 8.16 Distribution of the quantities in the DDCR algorithm.

same time, the I and Q are full-wave rectified to produce $|I|$ and $|Q|$, which are passed through the other two comparators to check whether they satisfy the relation (8.65). If they do, the selective gate will open, allowing signal d to pass the D flip-flop to control the VCO. Once synchronization is established in Figure 8.17, the I- and Q-channel outputs can be tapped by two threshold detectors to determine the transmitted symbol. Thus only two extra threshold detectors are needed to make Figure 8.17 a complete demodulator.

8.9 DIFFERENTIAL CODING IN QAM

In Chapter 4 we studied differential coding for MPSK signals. Similarly, differential coding is needed for QAM. It is needed for square QAM to resolve the phase ambiguity in carrier recovery. For circular QAM the use of differential coding can eliminate the need for carrier recovery, which is particularly attractive for fading channels. We will elaborate on this in Chapter 10. For now we focus on how differential coding is constructed in square QAM.

Weber proposed a scheme for differentially encoding the signals for QAM and

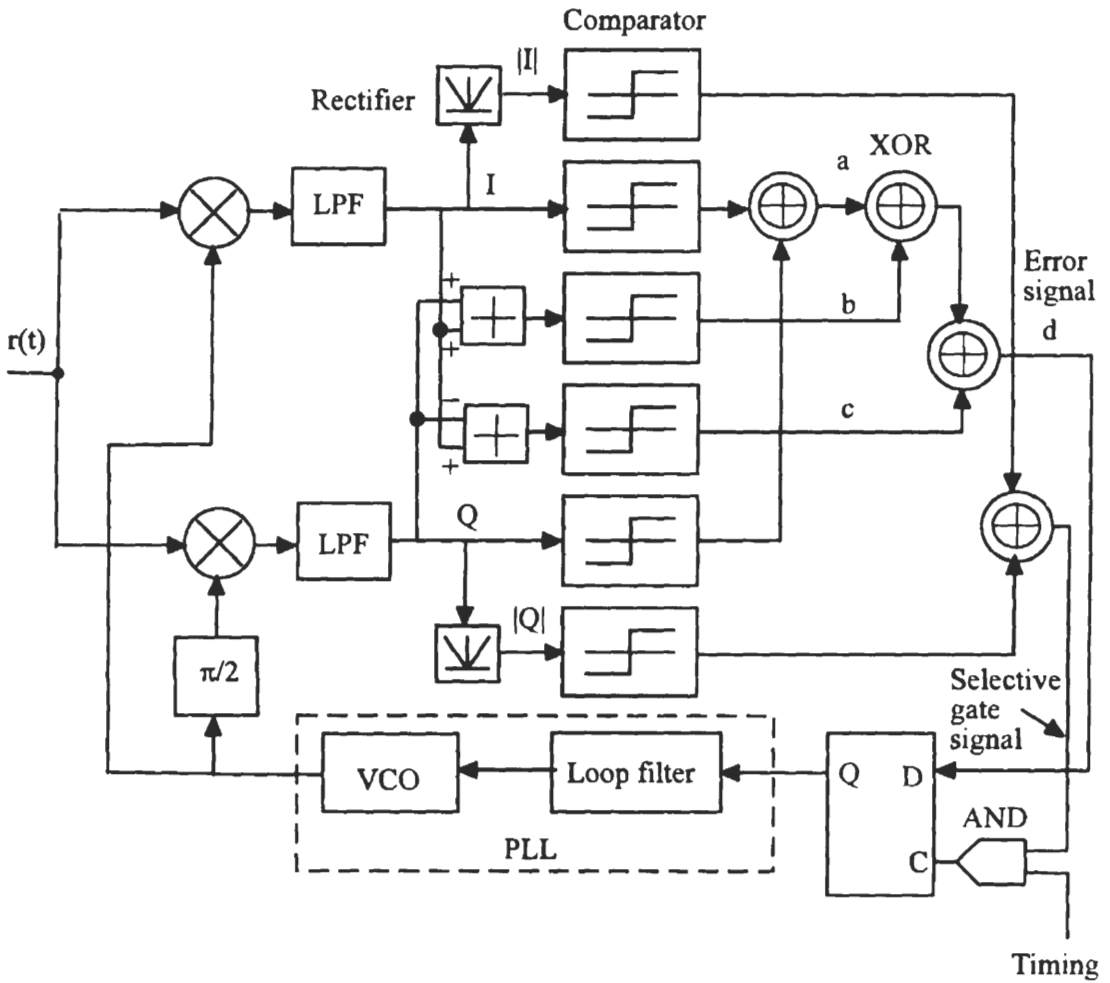


Figure 8.17 Implementation of a decision-directed carrier recovery system for square 16-QAM. From [10]. Copyright © 1979 IEEE.

MPSK [11]. We follow his paper here. First, a signal set has an L -fold rotational symmetry if the signal set pattern remains unchanged after a rotation of $\pm I \cdot (2\pi/L)$ radians, where I and L are integers. For example, in Figure 8.5, the type I constellation has an 8-fold symmetry, the type II constellation has a 4-fold symmetry, and the type III constellation has also a 4-fold symmetry. As a matter of fact, all square QAM schemes are 4-fold symmetrical. It is also clear that all MPSK schemes are M -fold symmetrical. The L -fold rotational symmetry causes a phase ambiguity of $2\pi/L$, that is, any phase rotation of $2\pi/L$ or its multiples in the received signal will cause the signal to be demodulated as another signal. For example, for the square QAM, times-four loop is used for carrier recovery. Any phase rotation of $\pi/2$ in the received signal will not change the constellation, thus the recovered carrier, which is based on the average of signals over the constellation (over a long period of time in practice), will always have the same phase. Thus the signals in the first quadrant may be demodulated as the signals in the second quadrant, or third quadrant, or fourth quadrant, depending on the actual amount of phase rotation. Differential coding is an efficient way to resolve the phase ambiguity. Other methods include sending a separate synchronizing signal or periodic insertion of a synchronizing sequence in the data sequence. The differential coding method does not require extra bandwidth like the other two, but increases the error probability slightly.

As discussed before, the QAM signal points are usually Gray coded in order to minimize bit error probability. Differential coding will violate the Gray code rule, thus increasing the bit error probability. However, the differential coding procedure should be carefully chosen such that it can remove the symmetrical ambiguities at a minimum increase of the error probability. The following is the differential coding procedure given by Weber for an $M = 2^K$ signal set for which $L = 2^N$.

1. Divide the signal space into L equal pie-shaped sectors. These sectors are differentially encoded using the first N bits of each K bits of data. That is, the first N bits determine the *change in sector*.
2. The remaining $K - N$ bits determine the signal point within the sector. The $2^{(K-N)}$ signal points within the sector must be Gray coded to reduce the probability of error. (However, perfect Gray coding may not be possible.)

We will see how this is done through an example. Figure 8.18 is the differential encoding for the square 16-QAM. In the figure, the signal space is divided by the I- and Q-axes into $L = 4$ pie-shaped sectors (quadrants in this case). Signal points are labeled with the last two bits in a 4-tuple. As far as these two bits are concerned, they are Gray coded in each sector. In addition they are arranged so that they are 4-fold symmetrical in terms of the last two bits. That is, a rotation of $\pi/2$ or its multiples of any signal will result in a signal having the same last two bits. The first two bits are used to determine the change of quadrant. Table 8.4 shows the encoding

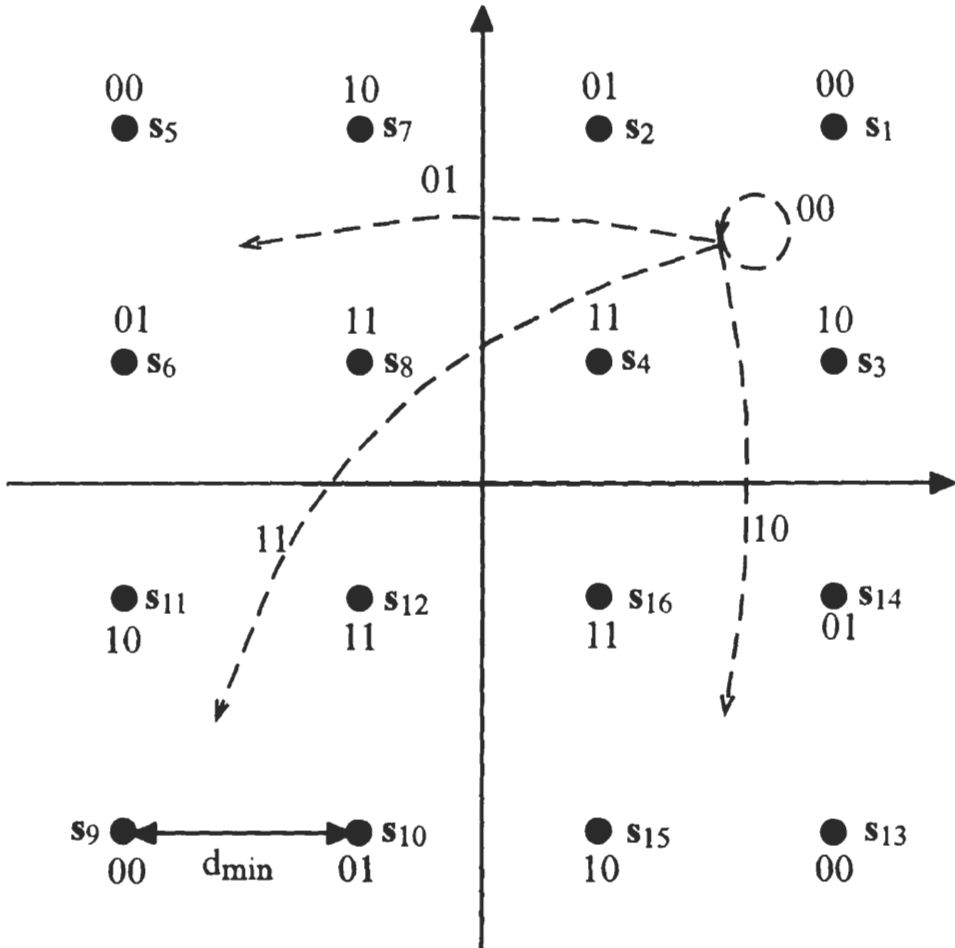


Figure 8.18 Differential encoding for square 16-QAM. From [11]. Copyright © 1978 IEEE.

and decoding procedure for Figure 8.18 through an example. The first quadrant is denoted as q_1 , the second q_2 , and so on. The change in quadrant (Δq) is denoted as 0 for no change, +1 for forwarding one quadrant, and so on. We assume the initial reference signal is s_1 , corresponding to bits 0000. Take the second four bits 1011 as an example. The first two bits are 10, which means the quadrant change is -1 according to Figure 8.18. Since the current quadrant is q_1 , the next will be q_4 , that is, the next signal must be in q_4 . Since the last two bits are 11, within q_4 , the signal labelled with 11 is signal s_{16} . Thus the signal point to be transmitted is s_{16} . When s_{16} is received without phase rotation ($\Delta\phi = 0$), which is compared with the previous signal (s_1) to determine the quadrant change (-1). This determines 10 as the first two bits. The last two bits then are determined as 11 by the fact that s_{16} is labeled 11. When s_{16} is received with phase rotation (say $\Delta\phi = \pi/2$), which becomes s_4 . At

Encoding	ref.				
Message	0000	1011	0001	1100	0110
Δq		-1	0	+2	+1
q_i	q_1	q_4	q_4	q_2	q_3
Transmitted signal	s_1	s_{16}	s_{14}	s_5	s_{11}
Decoding ($\Delta\phi = 0$)	ref.				
Received signal	s_1	s_{16}	s_{14}	s_5	s_{11}
Δq		-1	0	+2	+1
Decoded Message	0000	1011	0001	1100	0110
Decoding ($\Delta\phi = \pi/2$)					
Received signal	s_5	s_4	s_2	s_9	s_{15}
Δq		-1	0	+2	+1
Decoded Message	0000	1011	0001	1100	0110

Table 8.4 Examples of differential coding for square 16-QAM.

the same time the reference signal is also changed to s_5 due to the rotation. Signal s_4 is compared with the previous signal (s_5) to determine the quadrant change (-1). This determines 10 as the first two bits. The last two bits then are determined as 11 by the fact that s_4 is labeled 11. From the table we can see that phase rotation does not affect decoding of the signals. Thus the phase ambiguity is removed.

For general K -bit (K even) square QAM, again only the first two bits need to be differentially encoded for resolving the quadrant ambiguity, while the remaining $K - 2$ bits are Gray coded in each quadrant. For other constellations, such as circular QAM, the same encoding principles apply. The concrete encoding rules depend on the concrete constellation structure. See [11] for more examples.

In evaluating the error probability of the differentially coded QAM, a high SNR is assumed. This implies the errors are dominantly the errors made between points separated by the minimum distance d_{\min} . Thus we only consider this type of error in approximating the error probability. The above differential encoding schemes produce two types of symbol errors: those between symbols within the same sector and those between symbols of different sectors. In the first type of error, the first N bits are not affected since they are the same for all points in the sector. Thus only one or more of the $(K - N)$ bits will be in error, depending on how the symbols in the sector have been Gray coded. If the symbols in the sector are perfectly Gray coded, like in the square 16-QAM case, only one bit will be in error. If the symbols in the sector are not perfectly Gray coded, more than one bit on average will be in error. Then we say there is a Gray code penalty for the imperfect Gray coding. For this type of error, no error propagation exists since the differentially encoded bits are unaffected. In the second type of error, bit errors can arise from two sources. First, since the sec-

tor boundary has been crossed, a minimum of two bit errors will occur in the first N bits, one in each of two succeeding symbols (error propagation), due to the comparisons used in differential decoding. Additional bit errors may occur in the remaining $K - N$ bits depending on how these adjacent border symbols are encoded. While a perfect Gray code may be found for the symbols within a sector, a Gray code penalty may exist with symbols lying on the sector boundaries.

The relationship between the error probability of the differentially encoded system and that of the uncoded system can be given in the following general formula

$$P_{b,d} = F \cdot P_b$$

where $P_{b,d}$ is the bit error probability of the differentially coded system, and P_b is the bit error probability of the differentially uncoded system. The factor F is the penalty for differential encoding. For the differentially uncoded system,

$$P_b = \frac{g}{K} P_s$$

where P_s is the symbol error probability, $g \geq 1$ is the Gray code penalty, representing the average number of erroneous bits in a symbol error. For the perfect Gray coded system, $g = 1$. For the differentially encoded system,

$$P_{b,d} = \frac{f}{K} P_s$$

where f is the differentially encoded Gray code penalty, also representing the average number of erroneous bits in a symbol error. Thus the penalty for differential encoding is

$$F = \frac{f}{g} \quad (8.68)$$

The factor f can be found as follows.

1. Within a single sector draw lines between symbol points pairs separated by d_{\min} ; denote the total number of these lines by N_1 ;
2. Next to each line write the Hamming distance (number of bits which differ) between the two signal points; denote the sum of all such Hamming distances in the sector by H_1 ;
3. Draw lines between points lying on *one* of the sector boundaries with points in the adjacent sectors separated by d_{\min} ; denote the number of these lines by N_2 and denote the sum of their Hamming distances by H_2 .

Then the differential encoding penalty is

$$f = \frac{H_1 + H_2 + 2N_2}{N_1 + N_2} \quad (8.69)$$

where the third term in the numerator is due to error propagation in the differentially encoded bits. The numerator is in fact the total number of bit errors when all possible symbol errors are considered, and the denominator is in fact the total number of possible symbol errors. Thus f is the average bit errors per symbol. Note that H_1/N_1 is the Gray code penalty within a sector and H_2/N_2 is the Gray code penalty across the boundary.

For the differentially encoded square 16-QAM in Figure 8.18, $N_1 = 4$ and $H_1 = 4$ while $N_2 = 2$ and $H_2 = 2$, Thus $f = (4 + 2 + 4)/(4 + 2) = 10/6 = 1.67$. For general K -bit (K even) square QAM with the first two bits differentially encoded for resolving the quadrant ambiguity and the remaining $K - 2$ bits Gray coded, it can be shown that

$$\begin{aligned} N_1 &= 2^{K-1} - 2^{K/2} \\ H_1 &= 2^{K-1} - 2^{K/2} \\ N_2 &= 2^{(K/2-1)} \\ H_2 &= \left(\frac{K}{2} - 1\right) 2^{(K/2-1)} \end{aligned} \quad (8.70)$$

For the above general case $g = 1$ so that from (8.70) and (8.69)

$$F = 1 + \frac{K/2}{2^{K/2} - 1}, \quad (\text{square QAM, } K \text{ even})$$

Thus F goes from two for $K = 2$ (4-QAM or QPSK) to nearly one for very large K . This penalty of two or less is insignificant in term of increase in SNR, which is usually a fraction of a dB.

8.10 SUMMARY

We discussed M-ary amplitude modulation (MAM) in Section 8.1. In a concise fashion, we covered all aspects of MAM, including PSD, optimum detection, error probability, modulator and demodulator. The discussion was general in that the results are applicable to both baseband and bandpass cases, and in the case of bandpass MAM, pulse shaping was also included. We also showed the equivalence between the correlator receiver and matched filter receiver even when pulse shaping is involved. There was a subsection devoted to OOK. It is often the first modulation scheme introduced

in textbooks due to its historical importance. The discussion of MAM primarily served as a foundation for understanding QAM. However, at the same time MAM's properties were compared with MPSK, showing the superiority of MPSK. The bulk of this chapter of course is for QAM. We defined QAM signal and constellation in Section 8.2 where the orthogonality of the two components of the QAM was proved in the presence of the pulse-shaping function. Various QAM constellations were introduced in Section 8.3 in order to give the reader an overview of the QAM constellations. But only the square QAM constellations were described in detail since they are among the most efficient yet their implementations are the simplest. In Section 8.4, QAM's PSD was derived. It turned out that the shape of PSD of QAM is solely determined by the pulse-shaping function. This property is the same as that of MAM and MPSK. In Sections 8.5 and 8.6 we presented modulator and demodulator based on those of MAM. The modulator is almost identical to that of MPSK except that the level settings of the level generators are different. Gray coding is usually used for mapping from data n -tuples to QAM points for minimizing bit errors. The demodulator is also similar to the MPSK demodulator. The error probability of QAM was derived in Section 8.7 based on that of MAM. It was shown that QAM requires less signal-to-noise ratios than MPSK for achieving the same error performance. At $M = 4$ level, they are the same since 4-PSK is 4-QAM. Above $M = 4$, the signal power savings range from 1.65 to 16 dB for $M = 8, 16, \dots, 256$. The savings increase by approximately 3 dB for doubling the number of points in the constellation. This is what makes QAM very attractive. Synchronization for QAM was discussed in Section 8.8. The clock recovery of QAM is not a particular problem. The clock recovery techniques in Chapter 4 are applicable. The carrier recovery of QAM has its particular feature. It turned out that it does not require M th-power nonlinearity as in the MPSK case. It requires a fourth-power loop, but a squaring loop does not work. We showed in detail why this is true. We also described a decision-directed carrier recovery system which does not rely on nonlinearity at all. Finally in Section 8.9 we discussed differential coding for QAM for the purpose of phase ambiguity elimination.

The application of QAM, particularly the star QAM, to fading channels will be discussed in the Chapter 10.

8.11 APPENDIX 8A

We form the fourth power of $s_i(t)$:

$$\begin{aligned} E\{s_i^4(t)\} &= E\{[A_{i1}p(t)\cos\omega_c t - A_{i2}p(t)\sin\omega_c t]^4\} \\ &= p^4(t)E\{[A_{i1}\cos\omega_c t - A_{i2}\sin\omega_c t]^4\} \end{aligned} \quad (8.71)$$

To simplify the derivation we denote

$$x = A_{i1} \cos \omega_c t$$

$$y = -A_{i2} \sin \omega_c t$$

Note that $E\{x\} = E\{y\} = 0$ since $E\{A_{i1}\} = E\{A_{i2}\} = 0$. Using x and y notations we can write (8.71) as

$$\begin{aligned} E\{s_i^4(t)\} &= p^4(t)E\{[x + y]^4\} \\ &= p^4(t)E\{x^4 + 4x^3y + 6x^2y^2 + 4xy^3 + y^4\} \\ &= p^4(t)E\{x^4 + 6x^2y^2 + y^4\} \end{aligned} \quad (8.72)$$

where $E\{4x^3y\} = 4E\{x^3\}E\{y\} = 0$ and $E\{4xy^3\} = 4E\{x\}E\{y^3\} = 0$. Using trigonometrical identities we obtain

$$\begin{aligned} x^4 &= A_{i1}^4 \cos^4 \omega_c t = A_{i1}^4 [\cos^2 \omega_c t]^2 = A_{i1}^4 \left[\frac{1}{2}(1 + \cos 2\omega_c t) \right]^2 \\ &= \frac{1}{4} A_{i1}^4 (1 + 2 \cos 2\omega_c t + \cos^2 2\omega_c t) \\ &= \frac{1}{4} A_{i1}^4 \left[1 + 2 \cos 2\omega_c t + \frac{1}{2}(1 + \cos 4\omega_c t) \right] \\ &= \frac{1}{8} A_{i1}^4 [2 + 4 \cos 2\omega_c t + (1 + \cos 4\omega_c t)] \\ &= \frac{1}{8} A_{i1}^4 (3 + 4 \cos 2\omega_c t + \cos 4\omega_c t) \end{aligned} \quad (8.73)$$

$$\begin{aligned} y^4 &= A_{i2}^4 \sin^4 \omega_c t = A_{i2}^4 [\sin^2 \omega_c t]^2 = A_{i2}^4 \left[\frac{1}{2}(1 - \cos 2\omega_c t) \right]^2 \\ &= \frac{1}{4} A_{i2}^4 (1 - 2 \cos 2\omega_c t + \cos^2 2\omega_c t) \\ &= \frac{1}{4} A_{i2}^4 \left[1 - 2 \cos 2\omega_c t + \frac{1}{2}(1 + \cos 4\omega_c t) \right] \\ &= \frac{1}{8} A_{i2}^4 [2 - 4 \cos 2\omega_c t + (1 + \cos 4\omega_c t)] \\ &= \frac{1}{8} A_{i2}^4 (3 - 4 \cos 2\omega_c t + \cos 4\omega_c t) \end{aligned} \quad (8.74)$$

$$6x^2y^2 = 6A_{i1}^2 A_{i2}^2 \cos^2 \omega_c t \sin^2 \omega_c t$$

$$\begin{aligned}
&= 6A_{i1}^2 A_{i2}^2 \frac{1}{2}(1 + \cos 2\omega_c t) \frac{1}{2}(1 - \cos 2\omega_c t) \\
&= \frac{3}{2} A_{i1}^2 A_{i2}^2 (1 - \cos^2 2\omega_c t) = \frac{3}{2} A_{i1}^2 A_{i2}^2 \sin^2 2\omega_c t \\
&= \frac{3}{2} A_{i1}^2 A_{i2}^2 \frac{1}{2}(1 - \cos 4\omega_c t) = \frac{3}{4} A_{i1}^2 A_{i2}^2 (1 - \cos 4\omega_c t) \quad (8.75)
\end{aligned}$$

Substituting (8.73), (8.74), and (8.75) into (8.72), we obtain

$$\begin{aligned}
E\{s_i^4(t)\} &= \frac{1}{8} p^4(t) [E\{A_{i1}^4\} (3 + 4 \cos 2\omega_c t + \cos 4\omega_c t) \\
&\quad + E\{A_{i2}^4\} (3 - 4 \cos 2\omega_c t + \cos 4\omega_c t)] \\
&\quad + \frac{3}{4} p^4(t) E\{A_{i1}^2\} E\{A_{i2}^2\} (1 - \cos 4\omega_c t)
\end{aligned}$$

References

- [1] Sklar, B., *Digital Communications, Fundamentals and Applications*, Englewood Cliffs, New Jersey: Prentice Hall, 1988.
- [2] Cahn, C. R., "Combined digital phase and amplitude modulation communication system," *IRE Trans. Comms.*, vol. 8, Sept. 1960, pp. 150-155.
- [3] Hancock, J. C., and R. W. Lucky, "Performance of combined amplitude and phase modulated communications system," *IRE Trans. Comms.*, vol. 8, Dec. 1960, pp. 232-237.
- [4] Campopiano, C. N., and B. G. Glazer, "A coherent digital amplitude and phase modulation system," *IRE Trans. Comms.*, vol. 10, Mar. 1962, pp. 90-95.
- [5] Thomas, C. M., M. Y. Weidner, and S. H. Durrani, "Digital amplitude-phase keying with M-ary alphabets," *IEEE Trans. Comms.*, vol. 22, no. 2, Feb. 1974, pp. 168-180.
- [6] Benedetto, S., Biglieri, E., and Castellani, V., *Digital Transmission Theory*, Englewood Cliffs, New Jersey: Prentice Hall, 1987.
- [7] Proakis, J., and M. Salehi, *Communication Systems Engineering*, Englewood Cliffs, New Jersey: Prentice Hall, 1994.
- [8] Webb, W. T., and L. Hanzo, *Modern Quadrature Amplitude Modulation*, New York: IEEE Press, and London: Pentech Press, 1994.
- [9] Rustako, A., et al., "Using times four carrier recovery in M-QAM digital radio receivers," *IEEE Journal on Selected Areas in Comms.*, vol. 5, no. 3, April 1987, pp. 524-533.
- [10] Horikawa, I., T. Murase, and Y. Saito, "Design and performances of a 200 Mbit/s 16 QAM digital radio system," *IEEE Trans. Comms.*, vol. 27, no. 12, Dec. 1979, pp. 1953-1958.
- [11] Weber, W. J., "Differential encoding for multiple amplitude and phase shift keying systems," *IEEE Trans. Comms.*, vol. 26, no. 3, Mar. 1978, pp. 385-391.

Selected Bibliography

- Couch II, L. W., *Digital and Analog Communication Systems*, 3rd Ed., New York: Macmillan, 1990.
- Haykin, S., *Communication Systems*. 3rd Ed., New York: John Wiley, 1994.
- Simon, K. M., S. M. Hinedi, and W. C. Lindsey, *Digital Communication Techniques. Signal Design and Detection*, Englewood Cliffs, New Jersey: Prentice Hall, 1995.
- Smith, D. R., *Digital Transmission Systems*, 2nd Ed., New York: Van Nostrand Reinhold, 1993.
- Ziemer, R. E., R. L. Peterson, *Introduction to Digital Communication*, New York: Macmillan, 1992.

Chapter 9

Nonconstant-Envelope Bandwidth-Efficient Modulations

The schemes we studied in Chapters 5, 6, and 7 are all bandwidth-efficient modulation schemes with constant envelopes. The next natural step is to explore the possibility of obtaining high bandwidth efficiency using nonconstant-envelope schemes. QAM is very bandwidth efficient, but its amplitude can vary considerably. This makes it unsuitable for transmitters with power amplifiers that must operate in a nonlinear region for maximum efficiency. A lot of effort has been devoted to finding bandwidth-efficient schemes without too much amplitude variations. This can be achieved by using pulse shaping in quadrature modulation or other means.

In this chapter modulation schemes with compact spectrum, low spectral spreading caused by nonlinear amplification, good error performance, and simple hardware implementation are presented. In describing these nonconstant-envelope schemes, the emphasis is on the pulse shape and spectral properties. The eye diagram of each scheme is also presented since it is critical in demodulation if a conventional OQPSK-type demodulator is used. Even though the OQPSK-type demodulator is not optimum for these schemes, it is often suggested due to its simplicity and small loss in error performance. The error performance loss with respect to MSK is evaluated.

Since the majority of the schemes presented in this chapter are two-symbol-time($2T_s$) schemes, we have a general discussion of this type of scheme in Section 9.1. Particularly, an optimum receiver for the AWGN channel is developed in this section. Individual schemes are described in the sections that follow. Section 9.2 describes the quasi-bandlimited modulation (QBL) [1]. The quadrature overlapped raised-cosine modulation (QORC), and its staggered version (SQORC) proposed in [2] are described in Section 9.3. Later a scheme named modified QORC (MQORC) was proposed in [3]. MQORC uses a different pulse-shaping function which is similar to that of SFSK (sinusoidal frequency shift keying, see Section 5.9). This pulse improves the spectrum further, however the pulse involves Bessel functions and it is not easy to implement. We will not include this scheme here. But the quadrature

overlapped squared raised-cosine (QOSRC) modulation [4] is simple to realize. It is also described in Section 9.3. The research group led by Dr. Kamilo Feher developed a family of power-efficient coherent nonconstant-envelope modems. Prior to a hard limiter, the envelope of the modulated signals is not constant, but a hard limiter inserted into the transmission channel does not significantly spread the processed signal spectrum. Thus, these techniques are suitable for nonlinearly amplified satellite channels in a densely packed ACI (adjacent channel interference) environment. This family of modulation schemes include IJF (intersymbol-interference/jitter-free) OQPSK [5], TSI (two-symbol-interval) OQPSK [6], SQAM (superposed-QAM) [7], and XPSK (crosscorrelated QPSK) [8]. Among them, the XPSK is the most complex one. XPSK involves 16 different cross-correlated signal combinations using 14 different signal patterns. It can achieve almost constant signal envelope. Its spectrum is similar to that of TFM (tamed frequency modulation, see Chapter 6 for TFM). However, due to its complex signal format, it may not be a preferable choice over other schemes. We will not include it here. The other Feher's schemes all use one pulse pattern. IJF-OQPSK and TSI-OQPSK are discussed in Section 9.4. SQAM is discussed in Section 9.5. Section 9.6 describes a new approach of achieving compact spectrum, other than pulse shaping. The scheme is called quadrature quadrature phase shift keying (Q^2 PSK). Section 9.7 summarizes this chapter.

9.1 TWO-SYMBOL-PERIOD SCHEMES AND OPTIMUM DEMODULATOR

The majority of the schemes in this chapter are $2T_s$ schemes, they can be expressed as

$$s(t) = s_I(t) \cos 2\pi f_c t + s_Q(t) \sin 2\pi f_c t, \quad -\infty \leq t \leq \infty \quad (9.1)$$

where

$$s_I(t) = \sum_{k=-\infty}^{\infty} I_k p(t - 2kT_b) \quad (9.2)$$

$$s_Q(t) = \sum_{k=-\infty}^{\infty} Q_k p(t - 2kT_b - \tau) \quad (9.3)$$

where T_b is the bit time interval corresponding to the input data sequence $\{a_k \in (-1, +1)\}$ that has been demultiplexed into $\{I_k\}$ and $\{Q_k\}$. It is clear that each data symbol lasts for a duration of $T_s = 2T_b$ in I- and Q-channels. Each data is weighted by a pulse-shaping function $p(t)$ which has a duration of $2T_s = 4T_b$. If the delay

τ is zero we have a nonstaggered scheme, otherwise we have a staggered scheme. Usually, if a staggered scheme is desired, τ is set to be T_b . In this case, due to the staggering of the I- and Q-channels, the symbol duration of the modulated signal is T_b instead of $2T_b$ despite that the symbol durations are $2T_b$ for $s_I(t)$ and $s_Q(t)$. However, demodulation must be performed in a $2T_b$ duration.

The modulators for $2T_s$ schemes are the same as that of QPSK/OQPSK, except that a baseband signal processor (filter) is inserted in each channel prior to the carrier multiplier. The processor weights the data by the symbol pulse and overlaps them by T_s . This can be realized by using a filter with an impulse response of the pulse-shaping function ($p(t)$). In the following sections of $2T_s$ schemes, we will not repeat this statement again.

By a reasoning similar to that in Section 8.2 for QAM, the I- and Q-channel components in (9.1) are essentially orthogonal for $f_c \gg 1/T_s$. Thus the receiver will have the same quadrature structure as in MSK (Figure 5.9). That is, an inphase carrier in I-channel and a quadrature carrier in Q-channel are used to separate the I- and Q-channel data streams. However, the post-separation processing is different, which is based on the possible composite waveforms in a $2T_b$ -symbol duration in the I- or Q-channel data stream. In the detection interval $[0, 2T_b]$ (or any $[2kT_b, 2(k+1)T_b]$ interval), the I-channel baseband signal is (assuming $p(t)$ is defined on $[-2T_b, 2T_b]$)

$$s_I(t) = \pm p(t) \pm p(t - 2T_b), \quad 0 \leq t \leq 2T_b$$

Thus there are four possible waveforms of $s_I(t)$. But two are just negatives of the other two.

$$\begin{cases} f_1(t) = p(t) + p(t - 2T_b), & a_k = a_{k+1} = 1 \\ f_2(t) = p(t) - p(t - 2T_b), & a_k = 1, a_{k+1} = -1 \\ f_3(t) = -f_2(t), & a_k = -1, a_{k+1} = 1 \\ f_4(t) = -f_1(t), & a_k = a_{k+1} = -1 \end{cases} \quad (9.4)$$

The energy of each signal is

$$\mathcal{E}_i = \int_0^{2T_b} f_i^2(t) dt, \quad i = 1, 2, \dots, 4 \quad (9.5)$$

The Q-channel waveforms are just the delayed-by- τ version of the I-channel waveforms. The following discussion is based on the I-channel. The results are obviously applicable to the Q-channel provided proper symbol timing is maintained (delay τ with respect to I-channel, $\tau = 0$ for nonstaggered schemes).

The post-separation demodulator thus can be based on these four waveforms. As usual we assume the noise $n(t)$ at the input of the entire demodulator is AWGN

with zero mean and a two-sided PSD of $N_o/2$. The received signal at any moment is

$$r(t) = f_i(t) \cos 2\pi f_c t + f_j(t - \tau) \sin 2\pi f_c t + n(t), \quad i, j = 1, 2, \dots, 4$$

But as far as the detection of the I-channel signal is concerned, the Q-channel signal does not have any effect. Thus to the I-channel the received signal can be written as

$$r(t) = f_i(t) \cos 2\pi f_c t + n(t) = s_i(t) + n(t), \quad i = 1, 2, \dots, 4$$

where

$$s_i(t) = f_i(t) \cos 2\pi f_c t, \quad i = 1, 2, \dots, 4$$

The problem now becomes a 4-ary signal detection problem with different signal energies. From (B.38) the sufficient statistic is

$$l_i = r_i + c_i, \quad i = 1, 2, 3, 4$$

where

$$r_i = \int_0^{2T_b} r(t) s_i(t) dt = \int_0^{2T_b} r_I(t) f_i(t) dt$$

$$r_I(t) = r(t) \cos 2\pi f_c t$$

is the post-separation signal which is obtained by a down-converter with a reference signal of $\cos 2\pi f_c t$.

$$c_i = \frac{1}{2} (N_o \ln(P_i) - E_i)$$

where $P_i = 1/4$ for equally likely data.

$$E_i = \int_0^{2T_b} s_i^2(t) dt = \frac{1}{2} \mathcal{E}_i, \quad i = 1, 2, \dots, 4$$

Since the first term in c_i is the same for all four signals, it can be eliminated. The detector chooses the largest of l_i and the corresponding data pattern can be identified. From (9.4) we know that only two correlators for r_1 and r_2 are needed. That is

$$\begin{cases} l_1 = r_1 - E_1/2 \\ l_2 = r_2 - E_2/2 \\ l_3 = -r_2 - E_3/2 \\ l_4 = -r_1 - E_4/2 \end{cases}$$

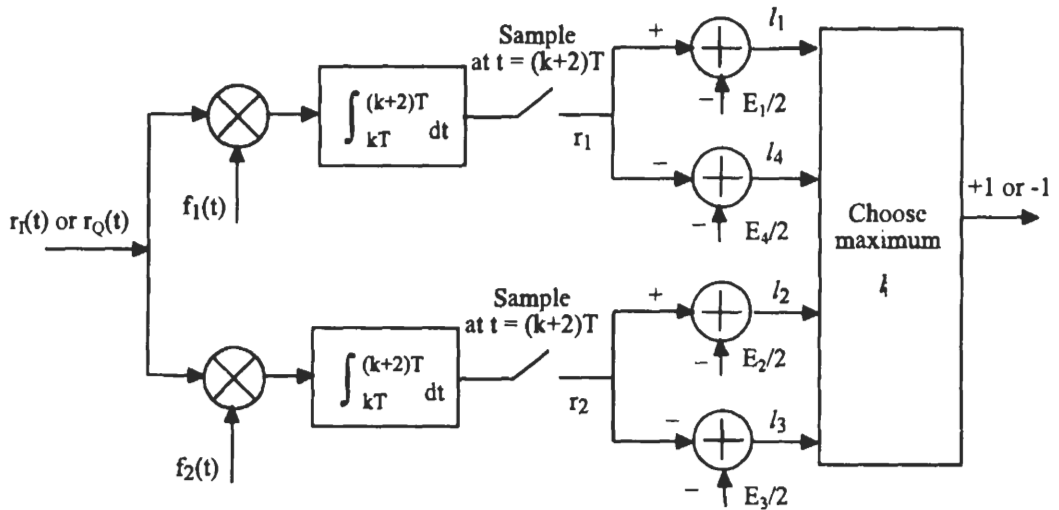
Figure 9.1 Correlation detector for $2T_s$ schemes with overlapping pulses.

Figure 9.1 shows the correlation detector which can be used for I- or Q-channel post-separation processing. The detector input is the post-separation signal $r_I(t)$ or $r_Q(t)$. The detector output is directly the first data symbol in the data pattern since once maximum l_i is determined the first data symbol is also determined.

The upper bound of the symbol error probability of this optimum receiver has been given in Appendix B (B.43), that is,

$$P_s \leq \sum_{j \neq i} Q \left(\sqrt{\frac{d_{ij}^2}{2N_o}} \right), \quad i, j = 1, 2, \dots, 4 \quad (9.6)$$

where

$$\begin{aligned} d_{ij}^2 &= \int_0^{2T_b} [s_i(t) - s_j(t)]^2 dt \\ &= \frac{1}{2} \int_0^{2T_b} [f_i(t) - f_j(t)]^2 dt \\ &= \frac{1}{2} \int_0^{2T_b} f_i^2(t) dt + \frac{1}{2} \int_0^{2T_b} f_j^2(t) dt - \int_0^{2T_b} f_i(t) f_j(t) dt \\ &= \mathcal{E}_i + \mathcal{E}_j - \int_0^{2T_b} f_i(t) f_j(t) dt, \quad i, j = 1, 2, \dots, 4 \end{aligned} \quad (9.7)$$

Usually the pulse $p(t)$ is symmetrical about $t = 0$ (if $p(t)$ is defined in $[-2T_b, 2T_b]$). Then $f_1(t)$ and $f_4(t)$ are even functions about $t = T_b$ and $f_2(t)$ and $f_3(t)$ are odd functions about $t = T_b$. As a result, $f_1(t)$ is orthogonal to $f_2(t)$ and $f_3(t)$ in $[0, 2T_b]$. So is $f_4(t)$ to $f_2(t)$ and $f_3(t)$. That is

$$\int_0^{2T_b} f_i(t)f_j(t)dt = 0, \quad \text{for } \begin{cases} i = 1, j = 2 \\ i = 1, j = 3 \\ i = 4, j = 2 \\ i = 4, j = 3 \end{cases} \quad (9.8)$$

We check one example:

$$\begin{aligned} \int_0^{2T_b} f_1(t)f_2(t)dt &= \int_0^{2T_b} [p(t) + p(t - 2T_b)][p(t) - p(t - 2T_b)]dt \\ &= \int_0^{2T_b} p^2(t)dt - \int_0^{2T_b} p^2(t - 2T_b)dt \\ &= \int_0^{2T_b} p^2(t)dt - \int_{-2T_b}^0 p^2(\tau)d\tau = 0 \end{aligned}$$

The last step holds because $p(t)$ is symmetrical about $t = 0$. The orthogonality of other pairs can be similarly verified. From (9.7) and (9.8), and noticing that $\mathcal{E}_4 = \mathcal{E}_1$ and $\mathcal{E}_3 = \mathcal{E}_2$, we have

$$[d_{ij}^2] = \frac{1}{2} \begin{bmatrix} 0 & \mathcal{E}_1 + \mathcal{E}_2 & \mathcal{E}_1 + \mathcal{E}_2 & 4\mathcal{E}_1 \\ \mathcal{E}_1 + \mathcal{E}_2 & 0 & 4\mathcal{E}_2 & \mathcal{E}_1 + \mathcal{E}_2 \\ \mathcal{E}_1 + \mathcal{E}_2 & 4\mathcal{E}_2 & 0 & \mathcal{E}_1 + \mathcal{E}_2 \\ 4\mathcal{E}_1 & \mathcal{E}_1 + \mathcal{E}_2 & \mathcal{E}_1 + \mathcal{E}_2 & 0 \end{bmatrix} \quad (9.9)$$

Since \mathcal{E}_i s are usually close, the distance $(\mathcal{E}_1 + \mathcal{E}_2)/2$ is the minimum (d_{\min}). At high signal-to-noise ratio, the larger distance terms may be ignored. If that is the case, only the four d_{\min} terms need be considered. They are d_{12}, d_{13}, d_{24} , and d_{34} . Their value is

$$d_{\min}^2 = (\mathcal{E}_1 + \mathcal{E}_2)/2 = E_1 + E_2 = 2E_{avg} = 4E_b$$

where E_{avg} and E_b are average symbol and bit energy, respectively. Thus the symbol error probability is approximately

$$P_s \lesssim 4Q \left(\sqrt{\frac{2E_b}{N_o}} \right)$$

Furthermore, among the four error events associated with the d_{\min} terms, two events

(events associated with d_{12} and d_{34}) actually do not cause bit errors (see (9.4) where $f_1(t)$ and $f_2(t)$ have the same first bit, so do $f_3(t)$ and $f_4(t)$). Thus we have the bit error probability

$$P_b \lesssim 2Q \left(\sqrt{\frac{2E_b}{N_o}} \right) \quad (9.10)$$

This is two times that of MSK. However, in terms of SNR required for the same P_b , this is only slightly inferior to MSK (about 0.3 dB at 10^{-5}). Sometimes the second smallest distance is too close to d_{\min} to be ignored. Then the error probability expression has to include the term associated with the second smallest distance.

The synchronization schemes for $2T_s$ schemes are in general the same as those of QPSK/OQPSK since all of them are quadrature modulations. Thus the carrier and symbol synchronization techniques described in Chapter 4 can be applied. Recall MSK has a combined carrier and symbol recovery circuit (Figure 5.11) due to its unique spectral components. It is also possible to exploit the spectral properties of $2T_s$ schemes to obtain better synchronization schemes.

9.2 QUASI-BANDLIMITED MODULATION

Amoroso proposed the use of quasi-bandlimited pulses in MSK-type modulation to improve the spectrum for the near-center region ($f \leq 1/T_b$), including reducing the main lobe width [1]. The proposed pulses are

$$p(t) = \begin{cases} \left[\frac{\sin \frac{\pi t}{2T_b}}{\frac{\pi t}{2T_b}} \right]^n, & -2T_b \leq t \leq 2T_b \\ 0, & \text{elsewhere} \end{cases} \quad (9.11)$$

$$n = 1, 2, 3, \dots$$

These pulses will not maintain a constant envelope for the MSK-type signal which they generate. But a bandpass hard limiter will be introduced just before transmission to ensure envelope constancy. The term “quasi-bandlimited” refers to the fact that the pulse duration is relaxed to $4T_b$ from $2T_b$ of the MSK, thus the bandwidth is somewhat more limited, but not completely limited as in the case where the duration is allowed to extend to $\pm\infty$.

Figure 9.2(a) shows $p(t)$ for $n = 3$ (denoted as QBL-3) in comparison with the pulse of MSK. The QBL pulse has a duration of $4T_b$. From (9.2) and (9.3), the adjacent pulses in each channel are overlapped by a length of $2T_b$. However, if sampled at center of each pulse (i.e., at $t = 2kT_b$ for the I-channel and $t = (2k + 1)T_b$ for the Q-channel), there is no intersymbol interference in the samples (Figure

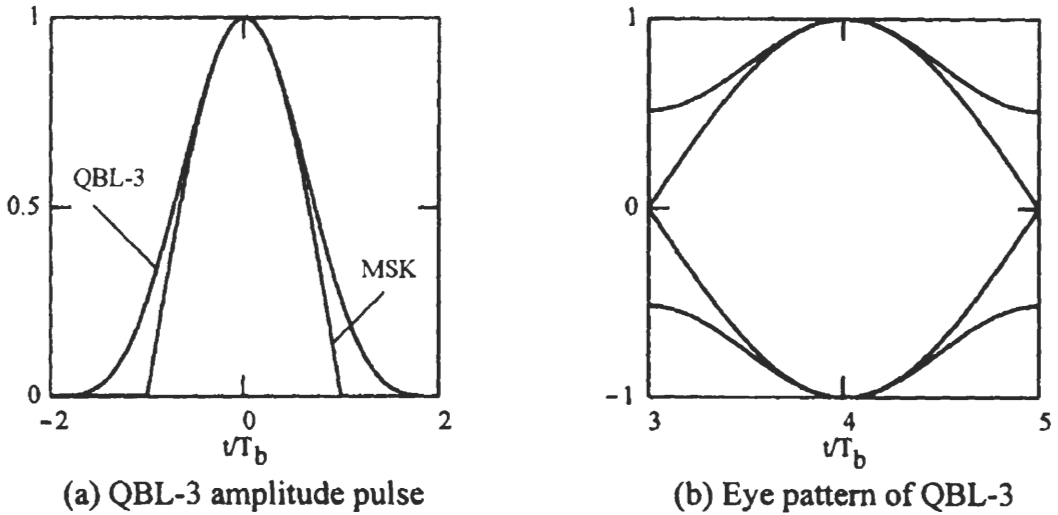


Figure 9.2 (a) QBL-3 amplitude pulse in comparison with MSK amplitude pulse, (b) eye pattern of QBL-3 for I-channel.

9.2(b)).

The modulated QBL signal is given by (9.1) to (9.3). The pulse sequences in the I- and Q-channel are staggered by a length of T_b . Since the pulse occupies a duration of $4T_b$, in any period of T_b , there are four segments of pulses which affect the envelope of the modulated signal. We can use any period of T_b , say, the period $[0, T_b]$, to compute the amplitude distribution. In $[0, T_b]$, the four pulse segments are from $p(t)$, $p(t - 2T_b)$, $p(t + T_b)$, $p(t - T_b)$. The first two affect the I-channel signal, and the last two affect the Q-channel signal. Thus the amplitude of the QBL signal is

$$A(t) = \sqrt{[I_0 p(t) + I_1 p(t - 2T_b)]^2 + [Q_{-1} p(t + T_b) + Q_0 p(t - T_b)]^2}$$

There are 16 different combinations of $[I_0, I_1, Q_{-1}, Q_0]$. However, one-half of them is just the negated version of another half. We only need to compute the amplitude for the first half. For $n = 3$, the possible envelopes found by numerical computation are shown in Figure 9.3. The minimum amplitude is $A_{\min} = 0.994$ and the maximum amplitude is $A_{\max} = 1.125$. The minimum to maximum ratio is

$$A_{\min}/A_{\max} = 0.884$$

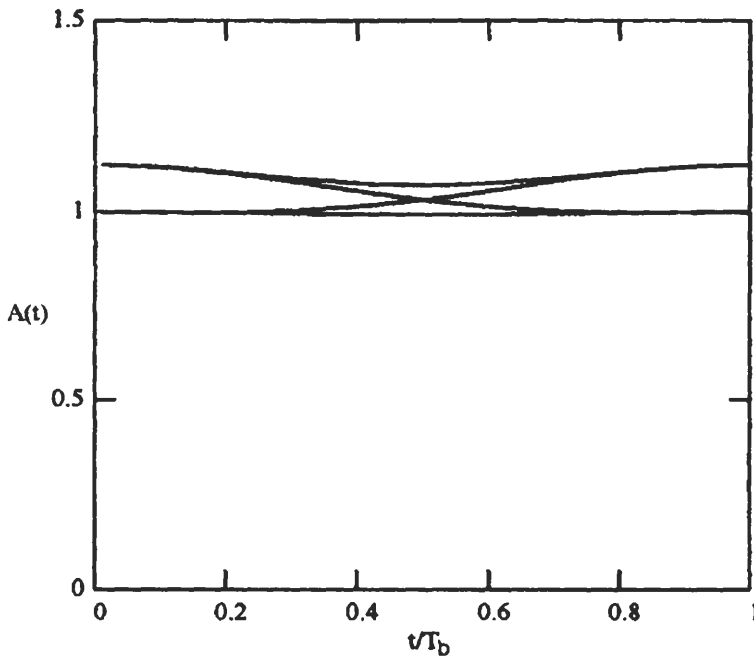


Figure 9.3 Possible envelopes of QBL-3 signal ($n = 3$).

Amoroso considered a hard limiter characterized by

$$y(t) = \frac{s(t)}{A(t)}$$

Then the amplitude of $y(t)$ is always one.

The spectral analysis is quite involved [1]. We only present the results here. Figure 9.4 shows the power spectral densities with hard limiting, for $n = 1, 2, 3, 4$. It is seen that $n = 3$ (QBL-3) is the best overall. Figure 9.5 compares the PSDs of QBL-3 with those of SFSK and MSK. It is seen that QBL-3 is much better in terms of having lower sidelobes. The hard limiting spreads the PSD slightly.

The implementation of QBL suggested in [1] is to use the serial MSK modulator and demodulator given in Figure 5.12. The only change is the conversion filter $H(f)$ in the transmitter, which must satisfy the following expression to produce the desired spectral shape

$$\Psi_s(f) = |H(f)|^2 \Psi_{BPSK}(f)$$

where $\Psi_s(f)$ is the QBL signal spectrum, $H(f)$ is the conversion filter transfer func-

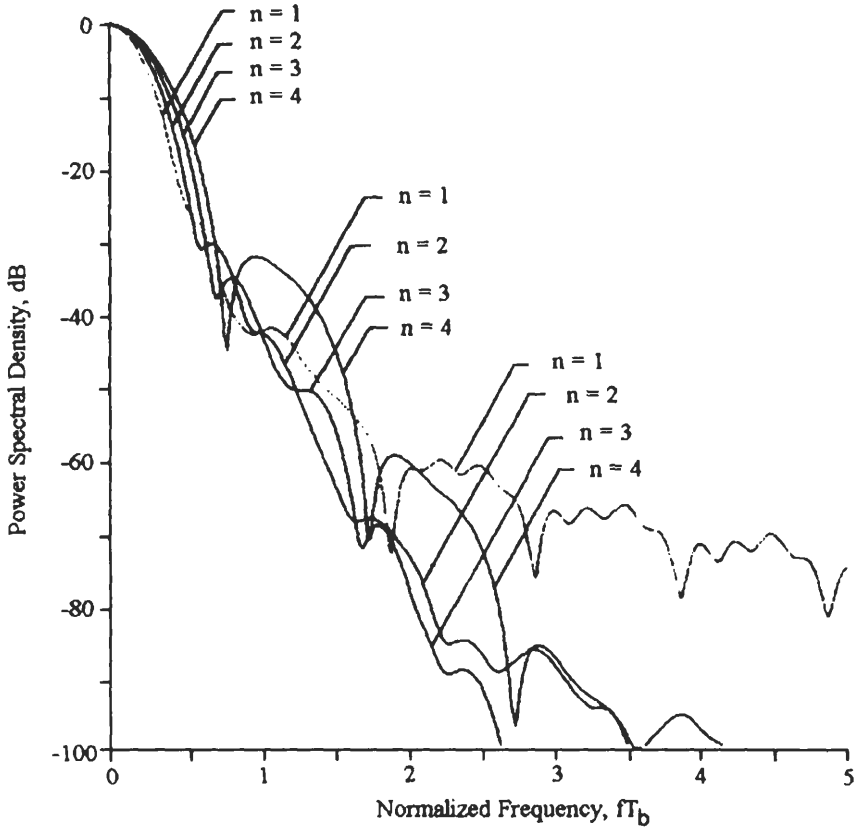


Figure 9.4 Power spectral densities of QBL- n with hard limiting, for $n = 1, 2, 3, 4$. From [1]. Copyright © 1979 IEEE.

n	Loss (dB) with hard limiting	Loss (dB) no limiting	Limiter loss (dB)	Eye Opening with hard limiting (%)	Eye Opening no limiting (%)
1	8.16	6.53	1.63	36	45
2	2.13	1.83	0.30	73	77
3	0.66	0.54	0.12	88	90
4	0.15	0.12	0.03	95	96

Table 9.1 Losses of power efficiency for QBL signals with respect to MSK.

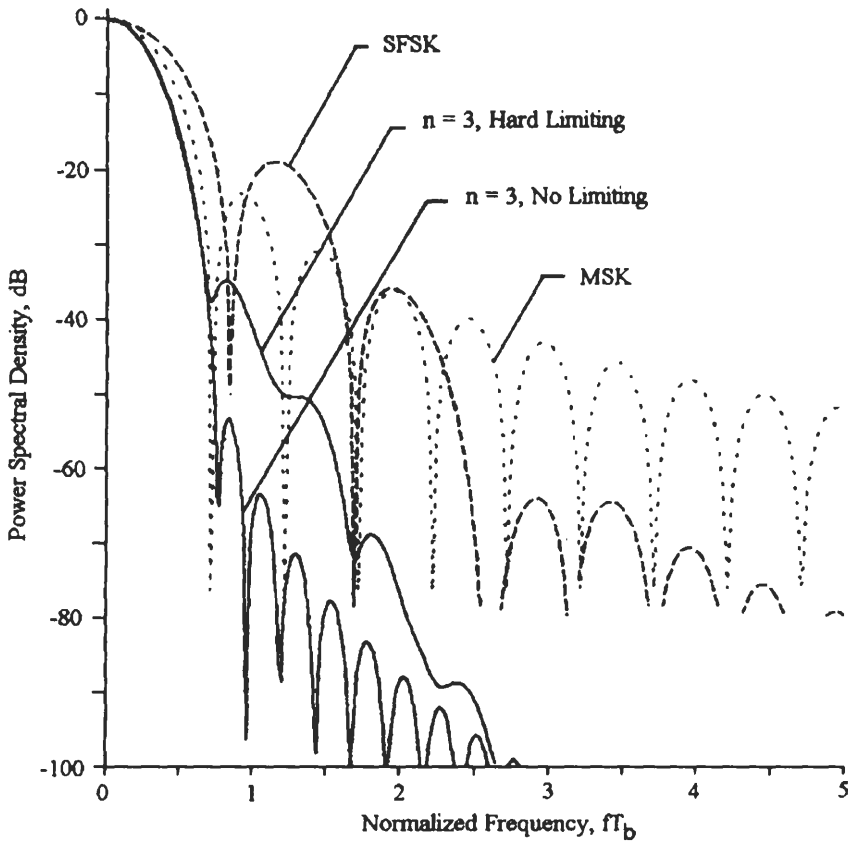


Figure 9.5 Power spectral densities for classical MSK, SFSK, and QBL- n for $n = 3$ with hard limiting, and $n = 3$ without limiting. From [1]. Copyright © 1979 IEEE.

tion, and $\Psi_{BPSK}(f)$ is the spectrum of the BPSK signal which enters the filter. At the receiver a filter matched to $p(t)$ is used. This receiver is not optimum since the matched filter does not match the envelopes of the received signal.

The loss in power efficiency in comparison with MSK is shown in Table 9.1. The eye opening is defined as the ratio of smallest detected voltage to mean detected voltage in I- or Q-channel baseband signal. A matched filter is assumed in the receiver, which introduces intersymbol interference. This accounts for the less than 100% eye openings even without hard limiting. The signal would always have 100% eye openings if there were no hard limiting and filtering (Figure 9.2(b)). The table shows that the losses range from a fraction of a dB to many dBs. It is clear that the $n = 3$ case is the best choice since its loss is only a fraction of a dB while its PSD is the most compact one. Its eye opening loss is also small, about 10%. According to [1], it appears

that much of the loss is due to intersymbol interference of the commonly encountered linear type, suggesting that a moderate amount of transversal filtering could reduce the loss considerably.

If QBL is used in an AWGN channel, the optimum demodulator is the one given in Section 9.1. The four waveforms are

$$\begin{cases} f_1(t) = \left[\frac{\sin \frac{\pi t}{2T_b}}{\frac{\pi t}{2T_b}} \right]^n + \left[\frac{\sin \frac{\pi(t-2T_b)}{2T_b}}{\frac{\pi(t-2T_b)}{2T_b}} \right]^n, & a_k = a_{k+1} = 1 \\ f_2(t) = \left[\frac{\sin \frac{\pi t}{2T_b}}{\frac{\pi t}{2T_b}} \right]^n - \left[\frac{\sin \frac{\pi(t-2T_b)}{2T_b}}{\frac{\pi(t-2T_b)}{2T_b}} \right]^n, & a_k = 1, a_{k+1} = -1 \\ f_3(t) = -f_2(t), & a_k = -1, a_{k+1} = 1 \\ f_4(t) = -f_1(t), & a_k = a_{k+1} = -1 \end{cases} \quad (9.12)$$

For $n = 3$ (QBL-3), the energies of these signal are

$$\mathcal{E}_i = \begin{cases} 1.206T_b, & i = 1, 4 \\ 0.994T_b, & i = 2, 3 \end{cases} \quad (9.13)$$

The energies of $s_i(t)$ are

$$E_i = \frac{1}{2}\mathcal{E}_i = \begin{cases} 0.603T_b, & i = 1, 4 \\ 0.497T_b, & i = 2, 3 \end{cases} \quad (9.14)$$

and the distances of $s_i(t)$ are

$$[d_{ij}^2] = T_b \begin{bmatrix} 0 & 1.1 & 1.1 & 2.411 \\ 1.1 & 0 & 1.988 & 1.1 \\ 1.1 & 1.988 & 0 & 1.1 \\ 2.411 & 1.1 & 1.1 & 0 \end{bmatrix} \quad (9.15)$$

The upper bound on the symbol error probability is

$$P_s \leq 4Q \left(\sqrt{\frac{1.1T_b}{2N_o}} \right) + Q \left(\sqrt{\frac{1.988T_b}{2N_o}} \right) + Q \left(\sqrt{\frac{2.411T_b}{2N_o}} \right) \quad (9.16)$$

At high signal-to-noise ratio, since $d_{\min}^2 = 1.1T_b$ is much smaller (2.6 dB) than the next smallest distance, the P_b given by (9.10) is applicable to QBL signals. That is,

$$P_b \lesssim 2Q \left(\sqrt{\frac{2E_b}{N_o}} \right) \quad (9.17)$$

This translates to a fraction of dB increase in SNR for the same P_b when compared with MSK.

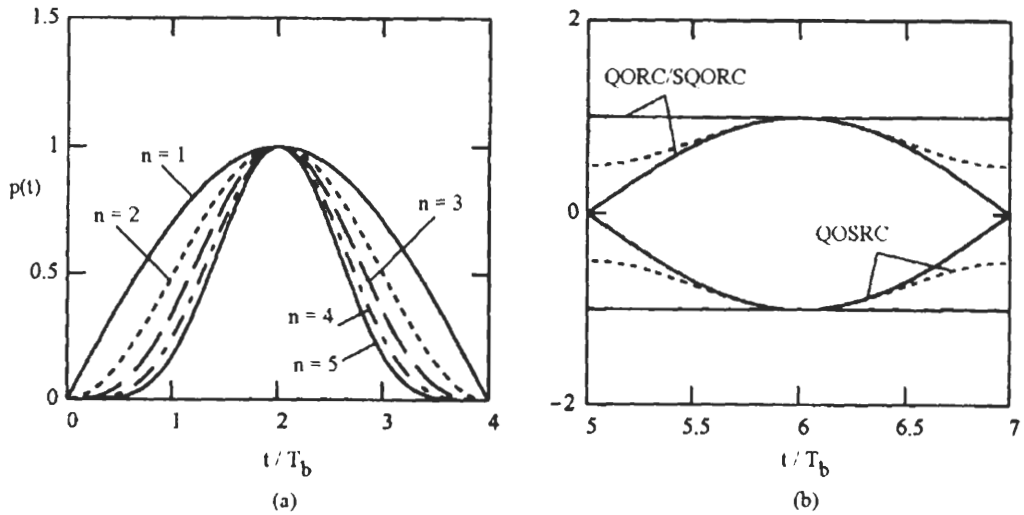


Figure 9.6 (a) Pulse shapes, (b) eye patterns for QORC/SQORC (solid line) and QOSRC (dotted line).

9.3 QORC, SQORC, AND QOSRC

Quadrature overlapped raised-cosine modulation (QORC) and its staggered version (SQORC) were proposed in [2]. The amplitude pulse-shaping function (or baseband pulse) is the raised-cosine pulse given by

$$p(t) = \frac{1}{2} \left(1 - \cos \frac{\pi t}{2T_b} \right), \quad 0 \leq t \leq 4T_b \quad (9.18)$$

The QORC/SQORC signal's I- and Q-channel data streams take the form of overlapping raised-cosine pulse shapes, that is, $s_I(t)$ and $s_Q(t)$ are given by (9.2) and (9.3). If $\tau = 0$, the signal is QORC. If $\tau = T_b$, the signal becomes SQORC.

Later the pulse shape in (9.18) was generalized to [4]

$$p(t) = \left[\sin \left(\frac{\pi t}{4T_b} \right) \right]^n, \quad 0 \leq t \leq 4T_b \quad (9.19)$$

Note that the $n = 2$ case is the pulse for QORC and that the $n = 4$ case is named as quadrature overlapped squared raised-cosine (QOSRC) modulation. The I- and Q-channel signals are staggered by T_b in QOSRC. The pulses for $n = 1, 2, \dots, 5$ are shown in Figure 9.6. Also shown are the eye patterns in $[4T_b, 8T_b]$ or any $[2kT_b, 2(k+1)T_b]$ interval. The inner eye of QOSRC coincides with that of QORC/SQORC. If sampled at $t = 2kT_b$, there is no ISI.

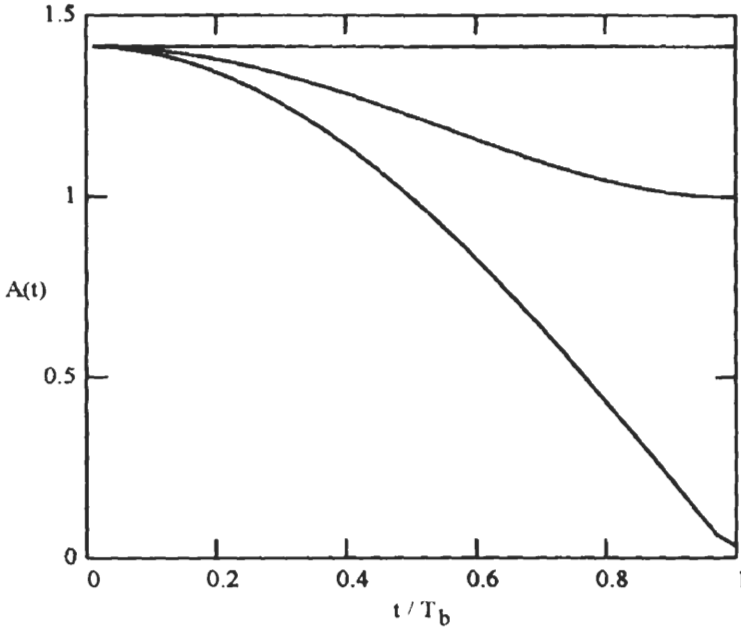


Figure 9.7 Possible envelopes for QORC.

Using the same technique for QBL, the amplitude variation of QORC, SQORC, and QOSRC can be found. For QORC, there is no staggering, the amplitude is given by

$$A(t) = \sqrt{[I_0p(t) + I_{-1}p(t + 2T_b)]^2 + [Q_0p(t) + Q_{-1}p(t + 2T_b)]^2}$$

It is found that $A_{\max} = \sqrt{2}$ and $A_{\min} = 0$. Figure 9.7 shows the three possible envelopes for QORC. It shows that the envelopes may descend down to zero at bit boundaries. For SQORC, there is staggering, the amplitude is

$$A(t) = \sqrt{[I_0p(t) + I_{-1}p(t + 2T_b)]^2 + [Q_{-1}p(t + T_b) + Q_{-2}p(t + 3T_b)]^2} \tag{9.20}$$

It is found that $A_{\max} = \sqrt{2}$ and $A_{\min} = 1$. Thus

$$A_{\min}/A_{\max} \approx 0.7$$

For QOSRC, there is staggering too, amplitude formula is again (9.20). It is found

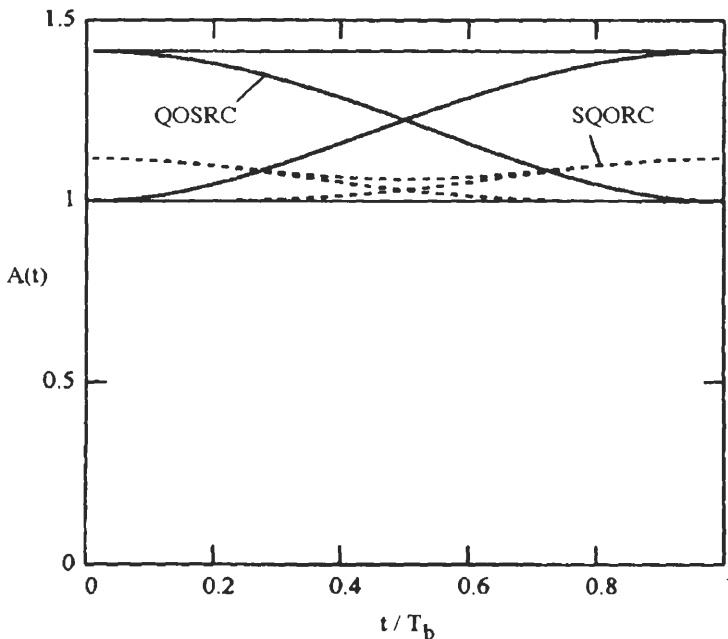


Figure 9.8 Possible envelopes for SQORC and QOSRC.

that $A_{\max} = 1.118$ and $A_{\min} = 1$. Thus

$$A_{\min}/A_{\max} \approx 0.9$$

Figure 9.8 shows the four possible envelopes for SQORC and QOSRC, respectively. The flat line $A(t) = 1$ is for both cases.

The power spectral density expression of QORC/SQORC derived in [2] is

$$\Psi_{\bar{s}}(f) = P_c T_b \left[\frac{\sin(2\pi f T_b)}{2\pi f T_b} \right]^2 \left[\frac{\cos(2\pi f T_b)}{1 - (4f T_b)^2} \right]^2 \quad (9.21)$$

where P_c is the power of the modulated signal. Comparing (9.21) with (4.38) and (5.14) reveals that except for a constant, the PSD of QORC/SQORC is the product of the PSDs of MSK and QPSK/OQPSK. The PSD is shown in Figure 9.9 in comparison with those of QPSK/OQPSK and MSK. The PSD of QORC/SQORC retains the same first null as QPSK/OQPSK. The remaining nulls occur twice as often as they do for QPSK/OQPSK. From the denominators of (9.21) we can see the sidelobe roll-off rate is proportional to f^{-6} which is the product of that of QPSK/OQPSK (f^{-2}) and that of MSK (f^{-4}).

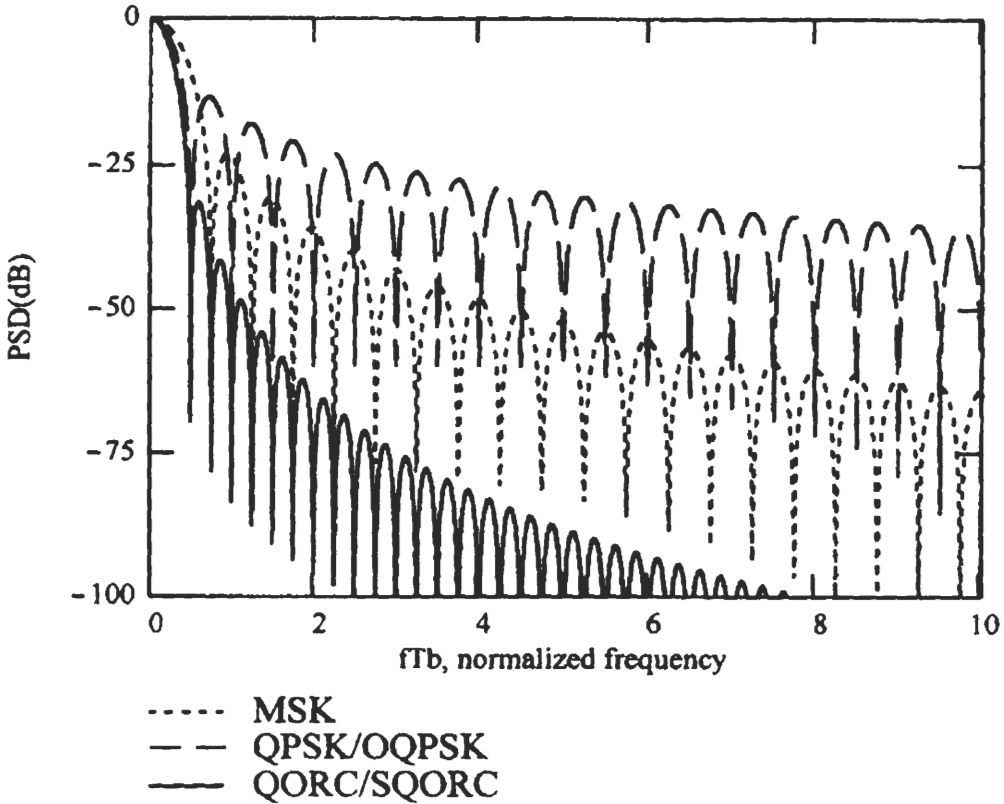


Figure 9.9 PSD of QORC/SQORC.

The PSDs for QOSRC and other pulses given in (9.19) were obtained by numerical Fourier transform in [4] and are shown in Figure 9.10. It is seen that all PSDs have almost the same characteristics in the region $0 \leq fT_b \leq 0.7$ while the side lobes of the $n = 4$ case (QOSRC) drop much faster than others, including that of QORC/SQORC.

The error performance of QORC/SQORC in a nonlinear channel was evaluated through computer simulation in [2]. The channel consists of an input filter followed by a TWT (traveling wave tube) amplifier. The two types of input filter are a seven-pole Chebyshev design with a 3 dB RF bandwidth of 56 MHz and a 56 MHz phase equalized filter. The demodulator is the QPSK/OQPSK type demodulator with a third-order Butterworth filter following the carrier multiplier in I- and Q-channel, respectively. The BT products were optimized as the data rate was varied. Simulation results show that QORC and QPSK perform equally well for the entire bit rate range

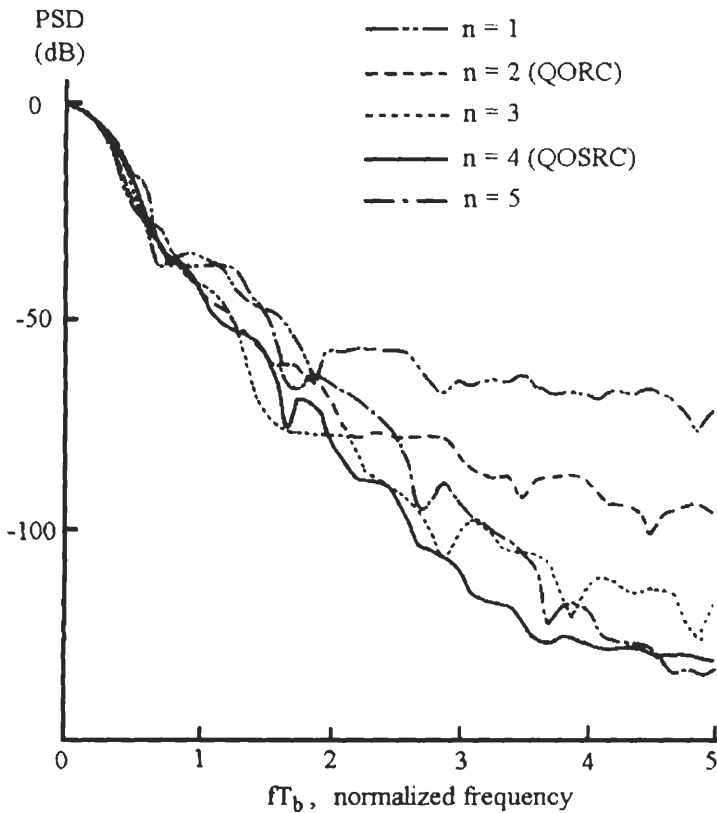


Figure 9.10 PSDs of modulated signals using the pulses in (9.19). From [4]. Copyright © 1985 IEEE.

(40 to 120 Mbps). MSK performs about 0.7 dB better at lower rates and 0.5 to 1.0 dB worse at higher rates. SQPSK performs equally well with QORC at lower rates but about 1.0 dB worse at high rates. The error performance of QOSRC is considered on a hard-limited satellite channel when both uplink and downlink additive Gaussian noise and intersymbol interference caused by transmitter filtering are present [4]. It was found that the error performance of QOSRC is better than that of QORC.

If QORC/SQORC is used in an AWGN channel, the optimum demodulator given in Figure 9.1 can be used. The four waveforms in $[0, 2T_b]$ (or $[T_b, 3T_b]$ for Q-channel

of SQORC) are

$$\begin{cases} f_1(t) = 1, & a_k = a_{k+1} = 1 \\ f_2(t) = \cos(\frac{\pi t}{2T_b}), & a_k = 1, a_{k+1} = -1 \\ f_3(t) = -f_2(t), & a_k = -1, a_{k+1} = 1 \\ f_4(t) = -f_1(t), & a_k = a_{k+1} = -1 \end{cases} \quad (9.22)$$

The energies of these signals are

$$\mathcal{E}_i = \begin{cases} 2T_b, & i = 1, 4 \\ T_b, & i = 2, 3 \end{cases} \quad (9.23)$$

The energies of $s_i(t)$ are

$$E_i = \frac{1}{2}\mathcal{E}_i = \begin{cases} T_b, & i = 1, 4 \\ 0.5T_b, & i = 2, 3 \end{cases} \quad (9.24)$$

and the distances of $s_i(t)$ are

$$[d_{ij}^2] = T_b \begin{bmatrix} 0 & 1.5 & 1.5 & 4 \\ 1.5 & 0 & 2 & 1.5 \\ 1.5 & 2 & 0 & 1.5 \\ 4 & 1.5 & 1.5 & 0 \end{bmatrix} \quad (9.25)$$

The upper bound on the symbol error probability is

$$P_s \leq 4Q\left(\sqrt{\frac{1.5T_b}{2N_o}}\right) + Q\left(\sqrt{\frac{2T_b}{2N_o}}\right) + Q\left(\sqrt{\frac{4T_b}{2N_o}}\right) \quad (9.26)$$

Since $d_{\min}^2 = 1.5T_b$ is only about 1.2 dB smaller than the second smallest distance, the P_b expression should include the second smallest distance. Among the four error events associated with the d_{\min} terms, two events (events associated with d_{12} and d_{34}) actually do not cause bit errors. The error event associated with the second smallest distance (d_{23}) does make one bit error. From (9.24) we see that $E_b = E_{avg}/2 = 0.375T_b$, thus

$$P_b \lesssim 2Q\left(\sqrt{\frac{2E_b}{N_o}}\right) + Q\left(\sqrt{\frac{2.67E_b}{N_o}}\right) \quad (9.27)$$

This is slightly higher than MSK and QBL.

For QOSRC we can find in $[0, 2T_b]$ for I-channel (or $[T_b, 3T_b]$ for Q-channel)

$$\begin{cases} f_1(t) = \left[\sin\left(\frac{\pi(t+2T_b)}{4T_b}\right) \right]^4 + \left[\sin\left(\frac{\pi t}{4T_b}\right) \right]^4, & a_k = a_{k+1} = 1 \\ f_2(t) = \left[\sin\left(\frac{\pi(t+2T_b)}{4T_b}\right) \right]^4 - \left[\sin\left(\frac{\pi t}{4T_b}\right) \right]^4, & a_k = 1, a_{k+1} = -1 \\ f_3(t) = -f_2(t), & a_k = -1, a_{k+1} = 1 \\ f_4(t) = -f_1(t), & a_k = a_{k+1} = -1 \end{cases} \quad (9.28)$$

The energy of each signal is

$$\mathcal{E}_i = \begin{cases} 1.188T_b, & i = 1, 4 \\ T_b, & i = 2, 3 \end{cases} \quad (9.29)$$

The energies of $s_i(t)$ are

$$E_i = \frac{1}{2}\mathcal{E}_i = \begin{cases} 0.594T_b, & i = 1, 4 \\ 0.5T_b, & i = 2, 3 \end{cases} \quad (9.30)$$

and the distances of $s_i(t)$ are

$$[d_{ij}^2] = T_b \begin{bmatrix} 0 & 1.094 & 1.094 & 2.375 \\ 1.094 & 0 & 2 & 1.094 \\ 1.094 & 2 & 0 & 1.094 \\ 2.375 & 1.094 & 1.094 & 0 \end{bmatrix} \quad (9.31)$$

The upper bound on the symbol error probability is

$$P_s \leq 4Q\left(\sqrt{\frac{1.094T_b}{2N_o}}\right) + Q\left(\sqrt{\frac{2T_b}{2N_o}}\right) + Q\left(\sqrt{\frac{2.375T_b}{2N_o}}\right) \quad (9.32)$$

At high signal-to-noise ratio, since $d_{\min}^2 = 1.094T_b$ is much smaller (2.6 dB) than the next smallest distance, the P_b given by (9.10) is applicable to QOSRC signal. That is,

$$P_b \lesssim 2Q\left(\sqrt{\frac{2E_b}{N_o}}\right) \quad (9.33)$$

Thus P_b of QOSRC is the same as that of QBL and is slightly higher than that of MSK.

9.4 IJF-OQPSK AND TSI-OQPSK

Intersymbol-interference/jitter-free OQPSK (IJF-OQPSK) was first proposed in [5]. An example of intersymbol-interference-free and jitter-free baseband signal and its generator are shown in Figure 9.10(a) and (b), respectively. When sampled at symbol boundaries, the sampled signal is clearly ISI-free. It is also jitter-free since there is no abrupt amplitude change at any sampling instant so that any symbol timing jitter essentially causes no errors in sampled signals. From the figure we can see that the filtered data stream consists of four pulse shapes: ± 1 and $\pm \sin(\pi t/T_s)$ defined in $[-T_s/2, T_s/2]$ where $T_s = 2T_b$ is the symbol duration.¹ Therefore we need only two pulse shapes to define an intersymbol-interference/jitter-free baseband signal. One is an even function $s_e(t)$ and the other is an odd function $s_o(t)$ with equal nonzero amplitude at the symbol boundaries, that is,

$$\begin{cases} s_e(t) = s_e(-t), & |t| \leq T_s/2 \\ s_o(t) = -s_o(t), & |t| \leq T_s/2 \\ s_e(t) = s_o(t) = 0, & |t| > T_s/2 \\ s_e(t) = s_o(t) \neq 0, & t = T_s/2 \end{cases} \quad (9.34)$$

The encoding of binary data stream $\{a_k\}$ into an IJF data stream $\{y_k(t)\}$ obeys the following rules

$$y_k(t) = \begin{cases} s_e(t - kT_s), & \text{if } a_k = a_{k-1} = 1 \\ -s_e(t - kT_s), & \text{if } a_k = a_{k-1} = -1 \\ s_o(t - kT_s), & \text{if } a_k = 1, a_{k-1} = -1 \\ -s_o(t - kT_s), & \text{if } a_k = -1, a_{k-1} = 1 \end{cases} \quad (9.35)$$

where $y_k(t)$ is the waveform in $[(k-1)T_s, kT_s]$. In Figure 9.11,

$$\begin{cases} s_e(t) = 1, & |t| \leq T_s/2 \\ s_o(t) = \sin(\frac{\pi t}{T_s}), & |t| \leq T_s/2 \end{cases} \quad (9.36)$$

and $s_e(t) = s_o(t) = 1$ for $t = T_s/2$. The encoding rules are clearly demonstrated by the example in Figure 9.11.

When I- and Q-channel data of an OQPSK modulator undergo the above data encoding and pulse shaping, we obtain the scheme named IJF-OQPSK in the literature.

This early IJF-OQPSK scheme was extended to a class of schemes called two-symbol-interval hard limited OQPSK (TSI-OQPSK) [6]. This class of two-symbol-

¹ In this section and the next section we use T_s instead of T_b as the basic time interval in order to be consistent with the literature that proposed the schemes. This enables the reader to refer to the literature without confusion caused by different basic time intervals.

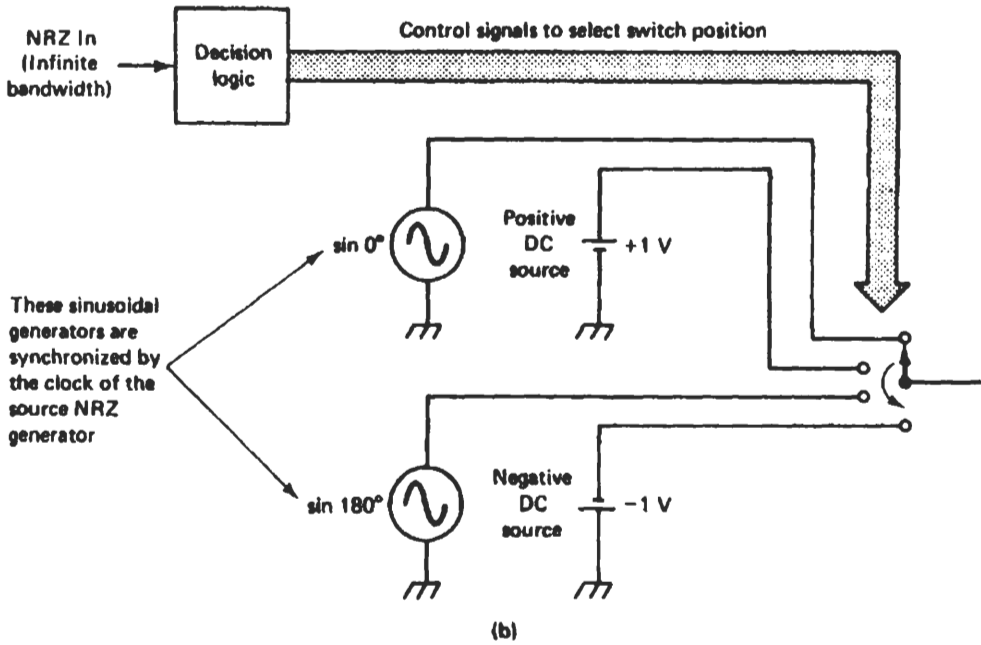
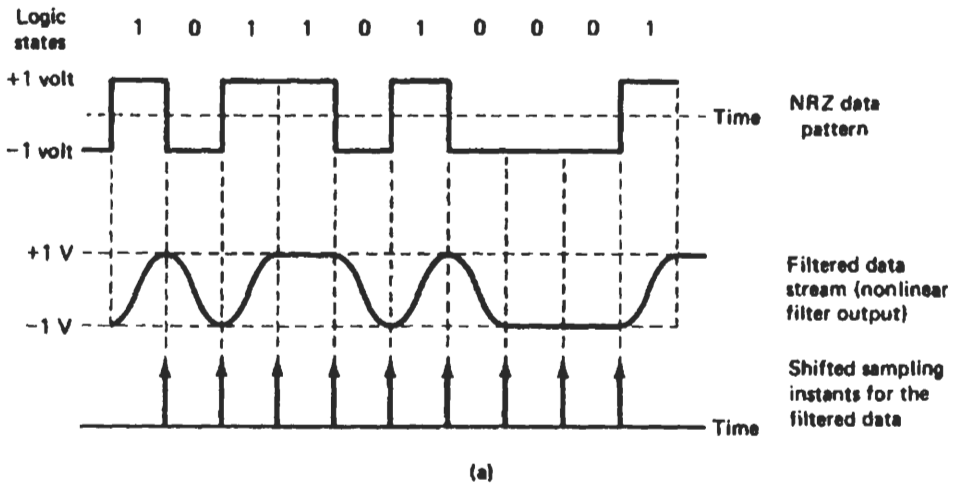


Figure 9.11 Intersymbol-interference/jitter-free signaling. From [9, p. 343]. Copyright © 1987 Kamilo Feher.

interval amplitude pulse-shaping functions is defined as

$$p^{(n)}(t) = \begin{cases} \frac{1}{2} \left[1 - \frac{\sin\{\frac{\pi}{nT_s}(|t| - T_s/2)\}}{\sin(\frac{\pi}{2n})} \right], & -T_s \leq t \leq T_s \\ 0, & \text{elsewhere} \end{cases} \quad n = 1, 2, \dots \quad (9.37)$$

The pulse lasts for two symbol durations in the I- and Q-channel. They are overlapped in the baseband signal streams. By choosing different values of n , a class of TSI-OQPSK schemes result. Figure 9.12(a) shows this class of pulses. When $n = 1$, (9.37) becomes a raised-cosine function

$$p^{(1)}(t) = \begin{cases} \frac{1}{2} \left[1 + \cos\left(\frac{\pi t}{T_s}\right) \right], & -T_s \leq t \leq T_s \\ 0, & \text{elsewhere} \end{cases} \quad (9.38)$$

This is the same pulse defined in (9.18). Therefore TSI-OQPSK ($n = 1$) is SQORC and as will be shown next, it is also the IJF-OQPSK defined in (9.36).

To show that this class of pulses can realize an IJF scheme, we notice that in the interval of $[0, T_s]$, the composite waveform is one of the four waveforms: $\pm p^{(n)}(t) \pm p^{(n)}(t - T_s)$. Using (9.37) we have

$$p^{(n)}(t) + p^{(n)}(t - T_s) = 1, \quad 0 \leq t \leq T_s$$

and

$$-p^{(n)}(t) + p^{(n)}(t - T_s) = \frac{\sin\{\frac{\pi}{nT_s}(t - T_s/2)\}}{\sin(\frac{\pi}{2n})}, \quad 0 \leq t \leq T_s$$

The other two waveforms are just their negatives, respectively. These waveforms are just the shifted-by- $T_s/2$ version of the odd and even functions required by the IJF property. That is, the odd and even functions that satisfy the IJF conditions in (9.34) are

$$s_e^{(n)}(t) = p^{(n)}\left(t + \frac{T_s}{2}\right) + p^{(n)}\left(t - \frac{T_s}{2}\right) = \begin{cases} 1, & |t| \leq T_s/2 \\ 0, & \text{elsewhere} \end{cases} \quad (9.39)$$

and

$$s_o^{(n)}(t) = -p^{(n)}\left(t + \frac{T_s}{2}\right) + p^{(n)}\left(t - \frac{T_s}{2}\right) = \begin{cases} \frac{\sin(\frac{\pi t}{nT_s})}{\sin(\frac{\pi}{2n})}, & |t| \leq T_s/2 \\ 0, & \text{elsewhere} \end{cases} \quad (9.40)$$

Thus the waveforms of the baseband data stream are similar to Figure 9.11(a) with the curved parts obeying the functions $\pm s_o^{(n)}(t)$. Figure 9.12(b, c) shows the even and odd functions given in (9.39) and (9.40). Note that when $n = 1$, the odd and

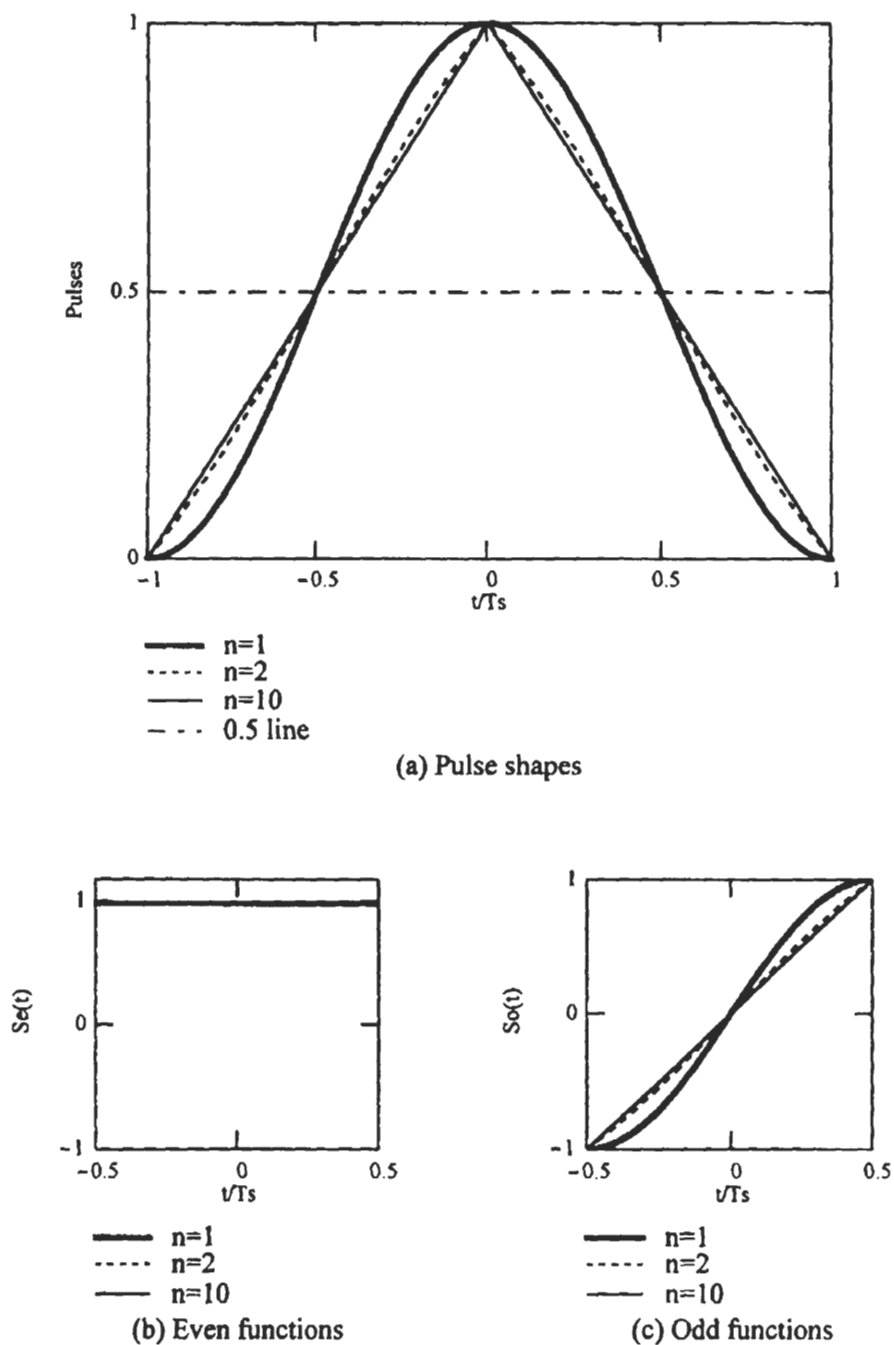


Figure 9.12 TSI pulses and odd and even functions.

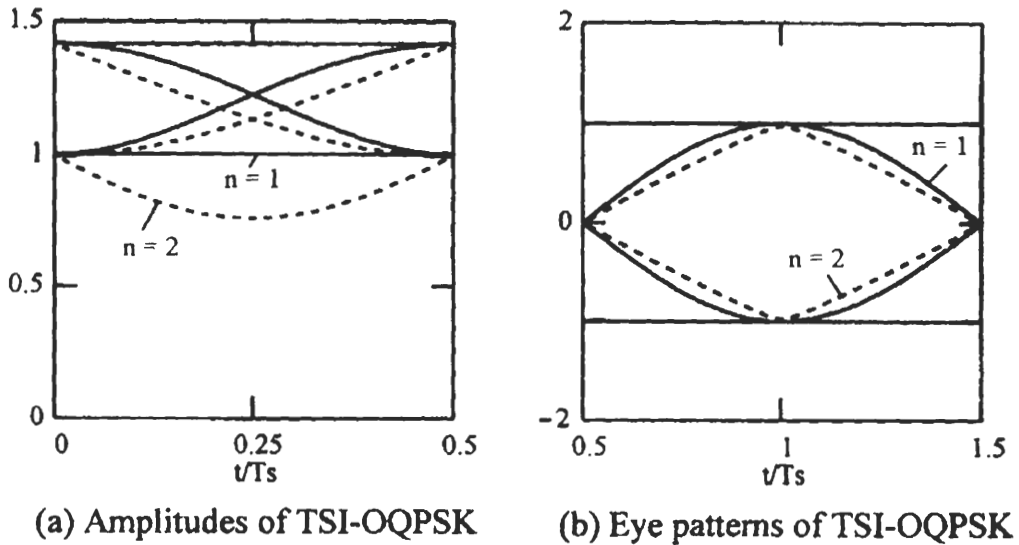


Figure 9.13 Amplitudes and eye patterns of TSI-OQPSK.

even pulses are the same as those in (9.36), that is, IJF-OQPSK is a special case of TSI-OQPSK. Its TSI pulse is a raised-cosine function given in (9.38).

This class of schemes are nonconstant envelope schemes. Figure 9.13 shows the possible amplitudes and the eye diagrams (the two flat lines in the eye diagrams are for any value of n). It is found that for $n = 1$, $A_{\max} = \sqrt{2}$ and $A_{\min} = 1$. Thus

$$A_{\min}/A_{\max} \approx 0.7$$

For $n = 2$, $A_{\max} = \sqrt{2}$ and $A_{\min} = 0.765$.

$$A_{\min}/A_{\max} \approx 0.54$$

When n increases further the amplitude and eye diagrams change very little since the pulse shapes change very little. From the eye patterns it is clear that this class of schemes is ISI-free and jitter-free if sampled at the center of the eye diagram.

The PSDs of TSI-OQPSK baseband signals are shown in Figure 9.14. It is seen that $n = 1$ case (IJF-OQPSK) has the lowest sidelobes. However, TSI signals with $n = 2, 3, \dots$ have a narrower main lobe than the one with $n = 1$. Figure 9.15 is the PSDs after nonlinear amplification. It is seen that the TSI's spectral components that cause significant ACI (adjacent channel interference) are about 10 dB lower than

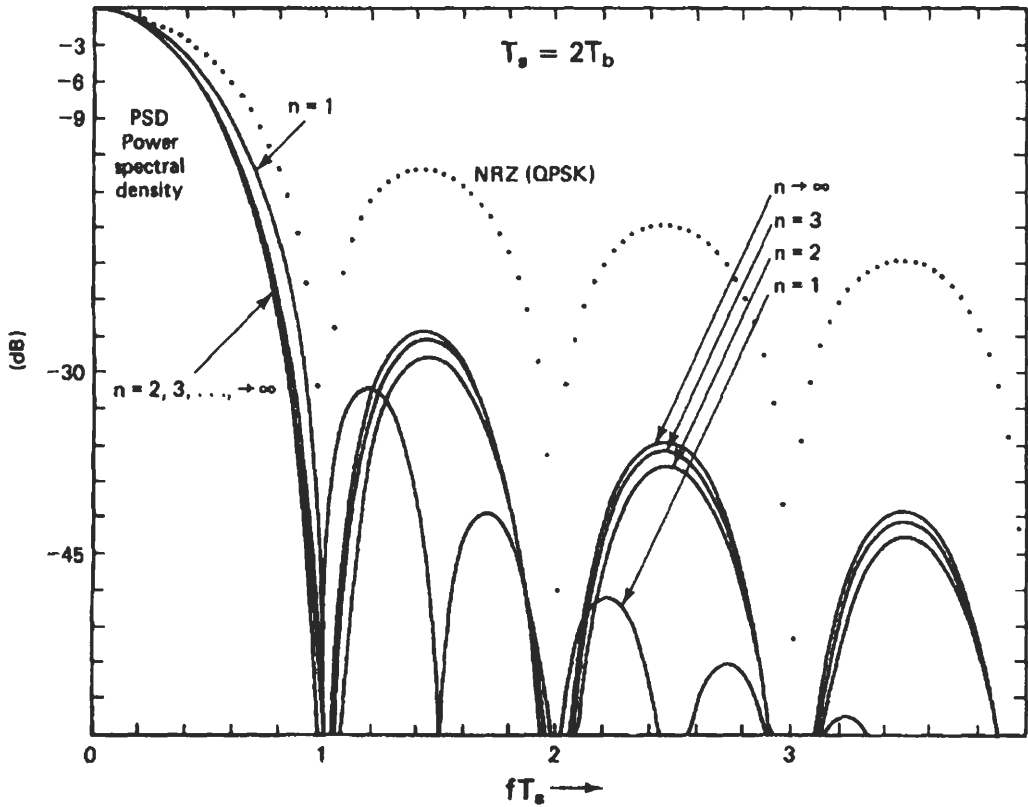


Figure 9.14 PSDs of TSI signals. From [6]. Copyright © 1983 IEEE.

QPSK and 5 dB lower than OQPSK.

Similar to QBL and QORC/SQORC, the optimum receiver of Section 9.1 can be used for TSI-OQPSK signals, including the IJF-OQPSK signal, in an AWGN channel. TSI-OQPSK ($n = 1$), IJF-OQPSK, and SQORC are identical. The bit error probability of SQORC has been proven to be essentially the same as that of MSK. Thus all of them have a bit error probability essentially equal to that of MSK.

For TSI-OQPSK ($n = 2$), substituting (9.37) into (9.4), we find in $[0, T_s]$ for I-channel (or $[T_s/2, 3T_s/2]$ for Q-channel)

$$\begin{cases} f_1(t) = 1, & a_k = a_{k+1} = 1 \\ f_2(t) = \sqrt{2} \sin\left\{\frac{\pi}{2T_s}(T_s/2 - t)\right\}, & a_k = 1, a_{k+1} = -1 \\ f_3(t) = -f_2(t), & a_k = -1, a_{k+1} = 1 \\ f_4(t) = -f_1(t), & a_k = a_{k+1} = -1 \end{cases} \quad (9.41)$$

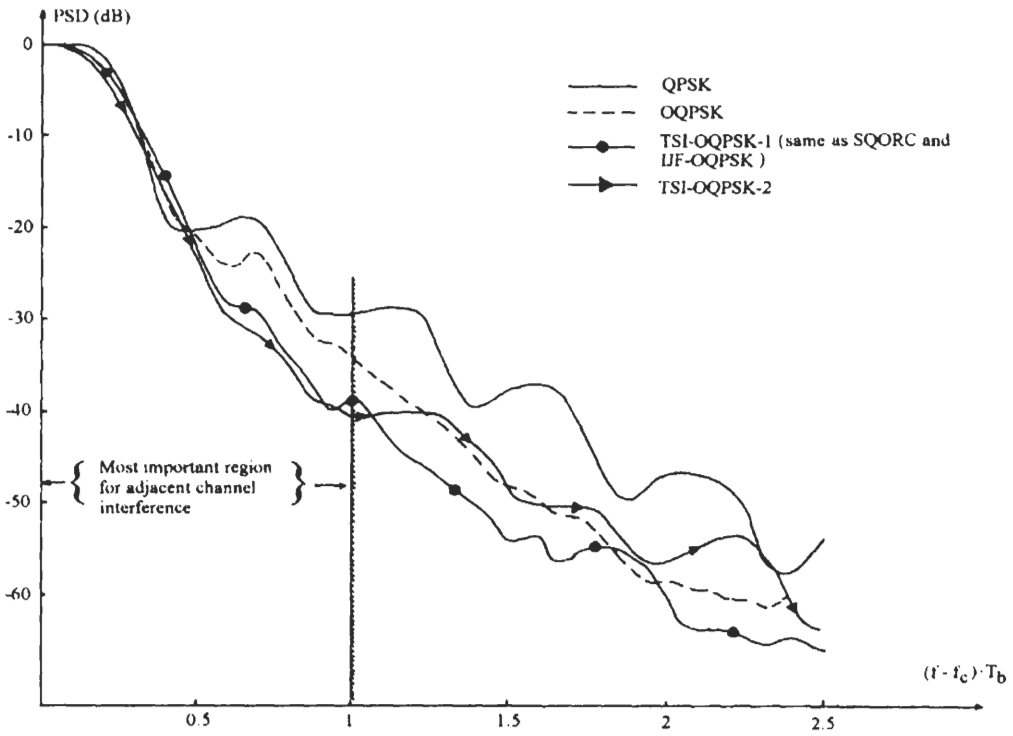


Figure 9.15 Nonlinearly amplified (saturated HPA with 0-dB input back off) PSDs of TSI signals. From [10]. Copyright © 1984 IEEE.

The energy of each signal is

$$\mathcal{E}_i = \begin{cases} 2T_b, & i = 1, 4 \\ 0.726T_b, & i = 2, 3 \end{cases} \tag{9.42}$$

Here we express \mathcal{E}_i in terms of T_b in order that they can be readily compared with those of previously described schemes. The energies of $s_i(t)$ are

$$E_i = \frac{1}{2}\mathcal{E}_i = \begin{cases} T_b, & i = 1, 4 \\ 0.363T_b, & i = 2, 3 \end{cases} \tag{9.43}$$

and the distances of $s_i(t)$ are

$$[d_{ij}^2] = T_b \begin{bmatrix} 0 & 1.363 & 1.363 & 4 \\ 1.363 & 0 & 1.454 & 1.363 \\ 1.363 & 1.454 & 0 & 1.363 \\ 4 & 1.363 & 1.363 & 0 \end{bmatrix} \quad (9.44)$$

The upper bound on the symbol error probability is

$$P_s \leq 4Q \left(\sqrt{\frac{1.363T_b}{2N_o}} \right) + Q \left(\sqrt{\frac{1.454T_b}{2N_o}} \right) + Q \left(\sqrt{\frac{4T_b}{2N_o}} \right) \quad (9.45)$$

Since $d_{\min}^2 = 1.363T_b$ is only about 0.28 dB smaller than the second smallest distance, the P_b expression should include the second smallest distance. Among the four error events associated with the d_{\min} terms, two events (events associated with d_{12} and d_{34}) actually do not cause bit errors. The error event associated with the second smallest distance ($d_{23} = 1.454T_b$) does make one bit error. From (9.43) we see that $E_b = E_{avg}/2 = 0.34075T_b$. The P_b is approximated as

$$P_b \approx 2Q \left(\sqrt{\frac{2E_b}{N_o}} \right) + Q \left(\sqrt{\frac{2.133E_b}{N_o}} \right) \quad (9.46)$$

This is slightly higher than MSK and QBL.

The error performance of TSI-OQPSK signals was evaluated through simulation for satellite channels with saturated HPA (high power amplifier) or cascaded hard-limiter and HPA in an ACI environment with AWGN [10]. The demodulator in the simulation is just the ordinary OQPSK demodulator with proper filtering (see [10] for details). Due to the more compact PSDs of the TSI-OQPSK signals, it was found that in the ACI environment the degradation with respect to ideal channel is less for TSI-OQPSK signals than for conventional QPSK and OQPSK (Figures 9.16 to 9.18). In the figures, Δf is the carrier frequency spacing between two adjacent channels. The effect of the spectral advantages of TSI-OQPSK schemes becomes even more evident when the received modulated carrier power of the main channel is below that of the adjacent channels. This situation occurs in the case of an uplink fade of the desired channel in satellite communications. Figure 9.19 presents examples of E_b/N_o degradation as a function of the fade depth of the desired channel. As the main channel is attenuated, the ACI becomes predominant and for this reason the modulation technique which creates less ACI provides better performance. As an example, at a spacing of 92% of the bit rate, with a fade depth of 12 dB, the TSI-OQPSK-2 only has a degradation of 2 dB, whereas the degradation of QPSK is more than 7 dB (Figure 9.19(a)). With tighter spacing, the differences are even more

E_b/N_o degradation
(dB)

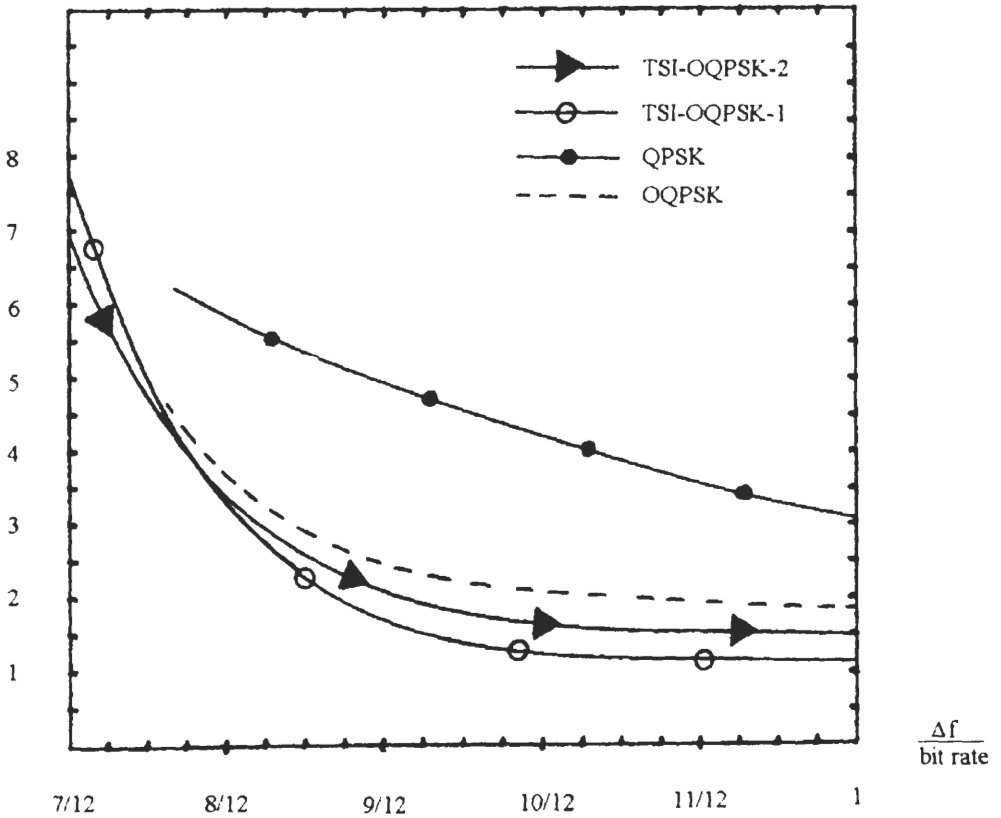


Figure 9.16 E_b/N_o degradation (at $P_b = 10^{-6}$) of ideal hard-limited QPSK, OQPSK, and TSI-OQPSK schemes in an ACI and AWGN environment. From [10]. Copyright © 1984 IEEE.

E_b/N_o degradation
(dB)

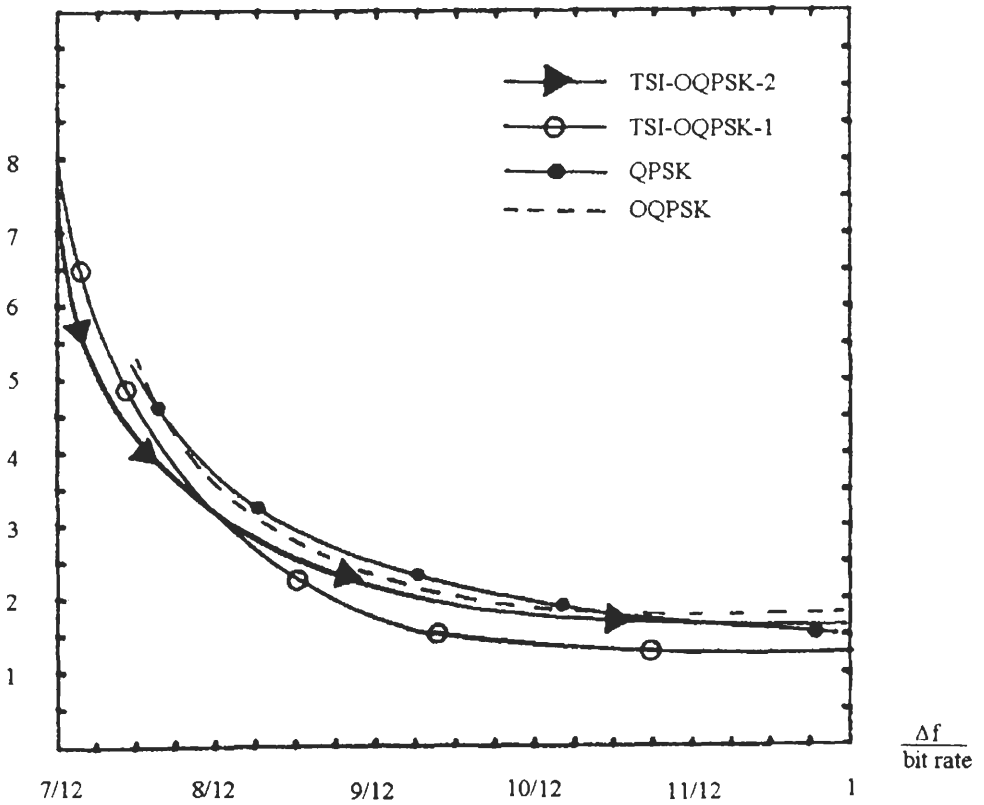


Figure 9.17 E_b/N_o degradation (at $P_b = 10^{-6}$) of saturated HPA-QPSK, OQPSK, and TSI-OQPSK schemes in an ACI and AWGN environment. From [10]. Copyright © 1984 IEEE.

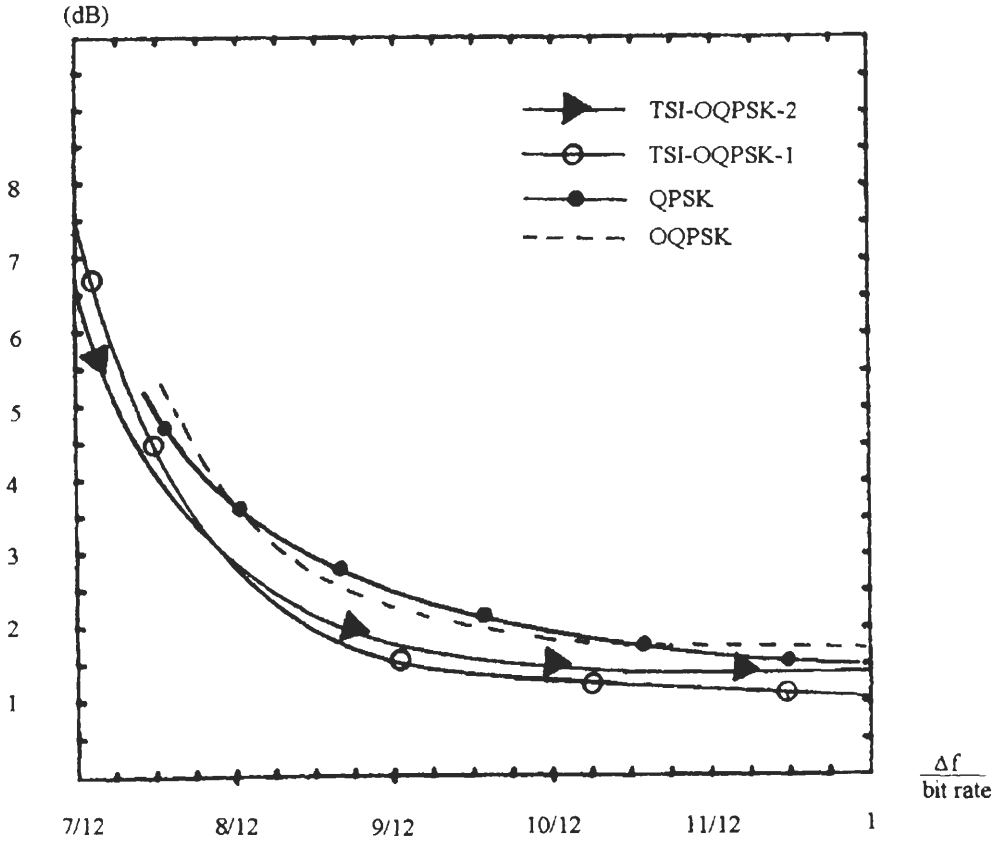
E_b/N_o degradation

Figure 9.18 E_b/N_o degradation (at $P_b = 10^{-6}$) of a saturated HPA-QPSK, OQPSK, and cascaded hard-limiter-HPA TSI-OQPSK schemes in an ACI and AWGN environment. From [10]. Copyright © 1984 IEEE.

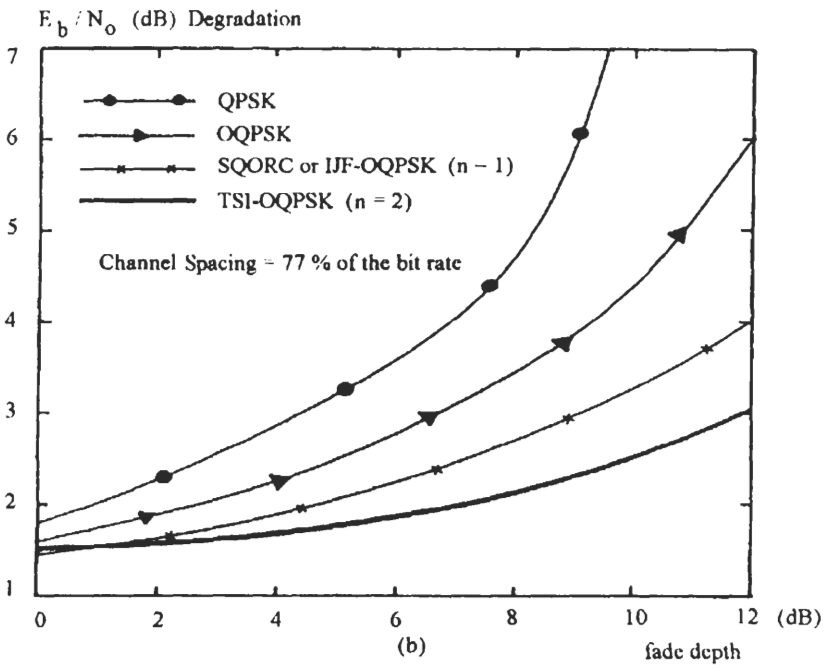
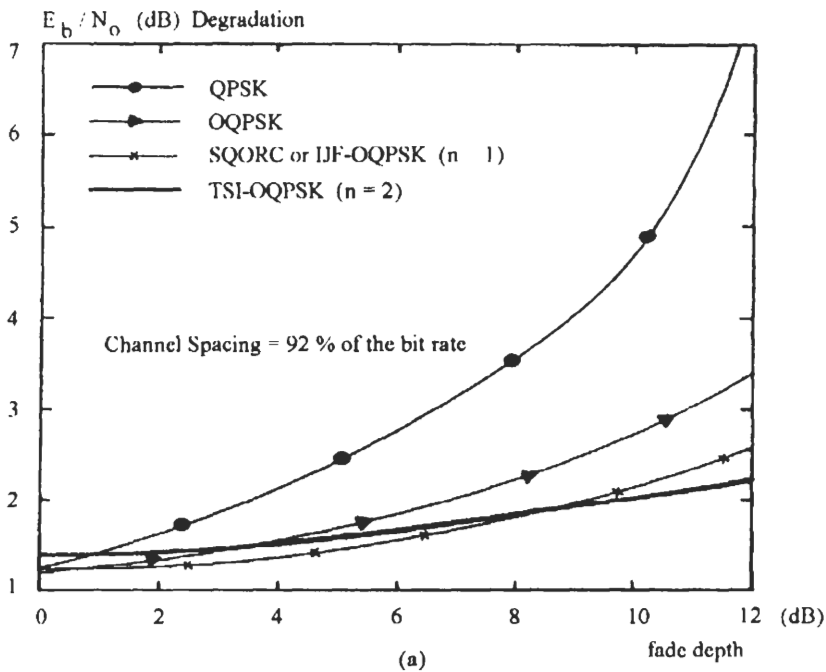


Figure 9.19 E_b/N_o degradation versus fade depth of the desired channel: (a) spacing of 92% of the bit rate, compared to $E_b/N_o = 8.4$ dB for $P_s = 10^{-4}$, (b) spacing of 77% of the bit rate, compared to $E_b/N_o = 8.4$ dB for $P_s = 10^{-4}$. From [10]. Copyright © 1984 IEEE.

evident and TSI-OQPSK-2 is better than the others at all fade depth (Figure 9.19(b) where the spacing is 77%).

9.5 SUPERPOSED-QAM

The superposed-QAM (SQAM) is proposed in [7]. The amplitude pulse-shaping function consists of two superposed raised-cosine functions and is given by

$$p(t) = \frac{1}{2} \left(1 + \cos \frac{\pi t}{T_s} \right) - \frac{1-A}{2} \left(1 - \cos \frac{2\pi t}{T_s} \right), \quad -T_s \leq t \leq T_s \quad (9.47)$$

where A is a constant within $[0.5, 1.5]$. When $A = 1$, the SQAM is equal to IJF-OQPSK or SQORC. But by choosing different values of A we can obtain a better spectrum than that of IJF-OQPSK or SQORC. Figure 9.20 shows the SQAM pulse shapes and the eye patterns. The inner curves of all three eye patterns coincide. Figure 9.21 shows amplitudes for different values of A . The flat line $A = 1$ is for both cases. It is found that

$$A_{\min} = 1, A_{\max} = 1.077, A_{\min}/A_{\max} = 0.93, \text{ for } A = 0.7$$

$$A_{\min} = 1, A_{\max} = 1.166, A_{\min}/A_{\max} = 0.86, \text{ for } A = 0.8$$

$$A_{\min} = 1, A_{\max} = 1.281, A_{\min}/A_{\max} = 0.78, \text{ for } A = 0.9$$

When $A = 1$, the scheme is equal to SQORC, we recall that $A_{\max} = \sqrt{2}$ and $A_{\min} = 1$, the ratio is 0.7.

The normalized PSD expression of the equiprobable SQAM baseband signal is given by [7.11]

$$\Psi_{\bar{s}}(f) = \frac{1}{A^2} \left(\frac{1}{1 - 4T_s^2 f^2} + \frac{A-1}{1 - T_s^2 f^2} \right) \left(\frac{\sin 2\pi f T_s}{2\pi f T_s} \right)^2 \quad (9.48)$$

Figure 9.22 shows the PSD of SQAM ($A = 0.8$) in comparison with others in a hard-limited channel. Figure 9.23 shows the fractional out-of-band power of SQAM with various A values and others in a hard-limited channel. From Figure 9.23 we can see that a decrease of A leads to a faster spectral roll-off at higher frequencies at the expense of a slightly wider main lobe. SQAM has spectral advantages over QPSK and MSK, and comparable spectral properties to TFM and QBL.

The error performance of SQAM was evaluated for a hard-limited channel by simulation in [7]. The demodulator in the simulation is the same as an OQPSK demodulator where a fourth-order Butterworth low-pass filter is used after the carrier

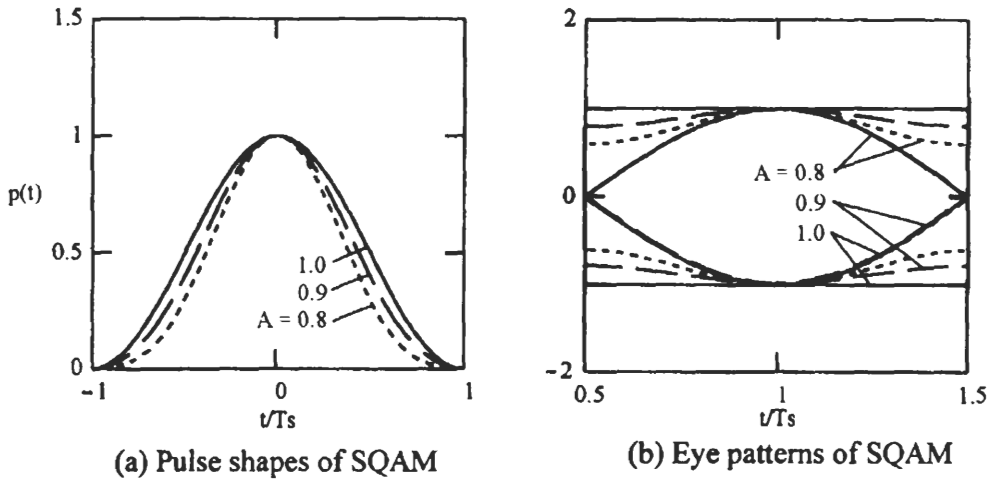


Figure 9.20 Pulse shapes and eye patterns of SQAM.

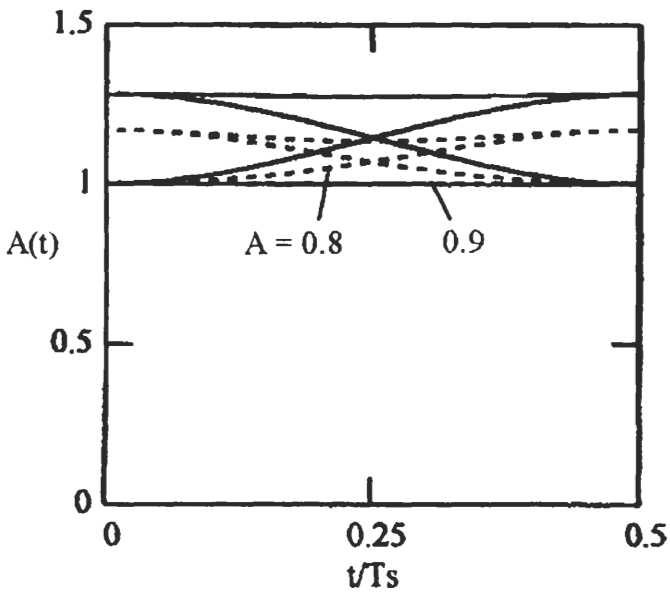


Figure 9.21 Amplitudes of SQAM.

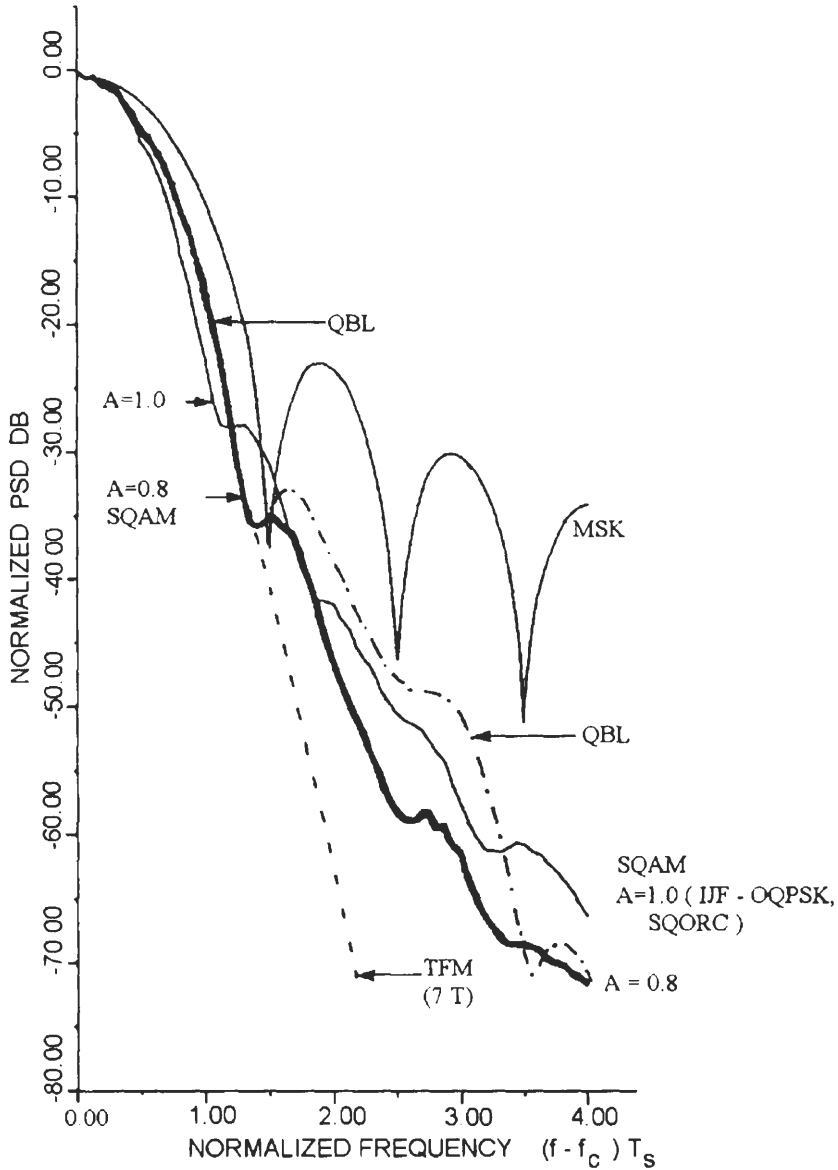


Figure 9.22 PSDs of SQAM, MSK, QBL, IJF-OQPSK (SQORC), and TFM in a nonlinear (hard-limited) channel. From [7]. Copyright © 1985 IEEE.

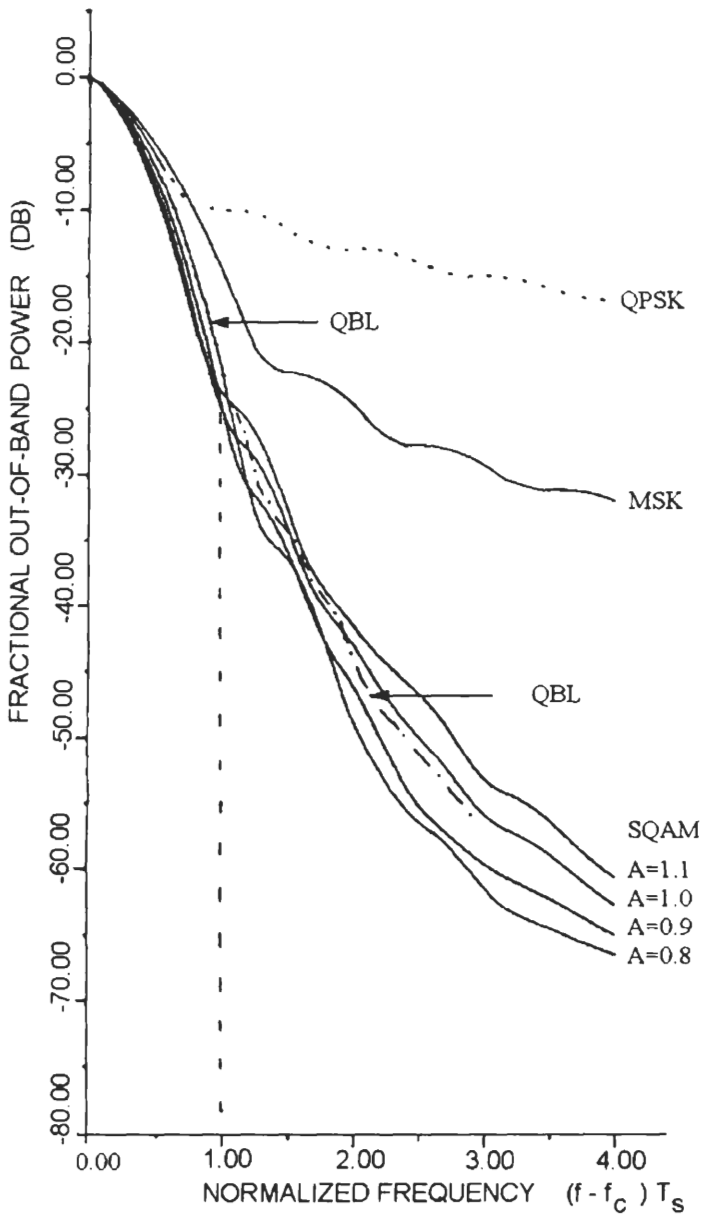


Figure 9.23 Out-of-band to total power ratio of SQAM, MSK, QBL, IJF-OQPSK (SQORC), and QPSK in a nonlinear (hard-limited) channel. From [7]. Copyright © 1985 IEEE.

multiplier. The filter's 3 dB bandwidth is $f_{3dB} = 1.1f_N$ where f_N is the Nyquist bandwidth which in turn is one-half of the symbol rate. The simulation results are given in Figure 9.24. It can be seen that the performance is the best when $A = 0.8$. It was reported that $A = 0.8$ is also the best for a linear channel [7]. It is also shown that the performance of SQAM is 0.5 to 2 dB inferior to that of QPSK in a linear channel.

Error performance of SQAM in a nonlinearly amplified multichannel interference environment was studied in [11]. Again the demodulator is the OQPSK demodulator. In the simulation model, there is a transmitter filter (Tx filter) after the modulator and a receiver filter (Rx filter) before the demodulator. The Tx and Rx filters used in the simulation are fourth-order Butterworth bandpass filter with an equivalent 3 dB low-pass bandwidth $BT_s = 0.5$ (i.e., the bandpass filter has a 3 dB bandwidth of $1/T_s$). Figure 9.25 shows the degradation (compared to $E_b/N_o = 8.4$ dB at $P_b = 10^{-4}$) against channel spacing for hard-limited multichannel with two equal-power ACIs. It is seen that SQAM ($A = 0.85$) has the least degradation. Figure 9.26 shows the degradation (compared to the same E_b/N_o) against fade-depth of the desired channel in a hard-limited multichannel system. Again SQAM ($A=0.85$) shows a significant improvement over other schemes.

The optimum demodulator in Figure 9.1 can be applied to SQAM. The four possible composite baseband signals in a symbol duration ($[0, T_s]$ for I-channel or $[T_s/2, 3T_s/2]$ for Q-channel) are

$$\left\{ \begin{array}{ll} f_1(t) = A + (1 - A) \cos(2\pi t/T_s), & a_k = a_{k+1} = 1 \\ f_2(t) = -\cos(\pi t/T_s), & a_k = 1, a_{k+1} = -1 \\ f_3(t) = \cos(\pi t/T_s), & a_k = -1, a_{k+1} = 1 \\ f_4(t) = -A - (1 - A) \cos(2\pi t/T_s), & a_k = a_{k+1} = -1 \end{array} \right. \quad (9.49)$$

The energy of each signal is

$$\mathcal{E}_i = \begin{cases} 2[A^2 + (1 - A)^2/2]T_b, & i = 1, 4 \\ T_b, & i = 2, 3 \end{cases} \quad (9.50)$$

The energies of $s_i(t)$ are

$$E_i = \frac{1}{2}\mathcal{E}_i = \begin{cases} [A^2 + (1 - A)^2/2] T_b, & i = 1, 4 \\ 0.5T_b, & i = 2, 3 \end{cases} \quad (9.51)$$

and the distances of $s_i(t)$ can be calculated by (9.9). The distances for $A = 0.8$ and

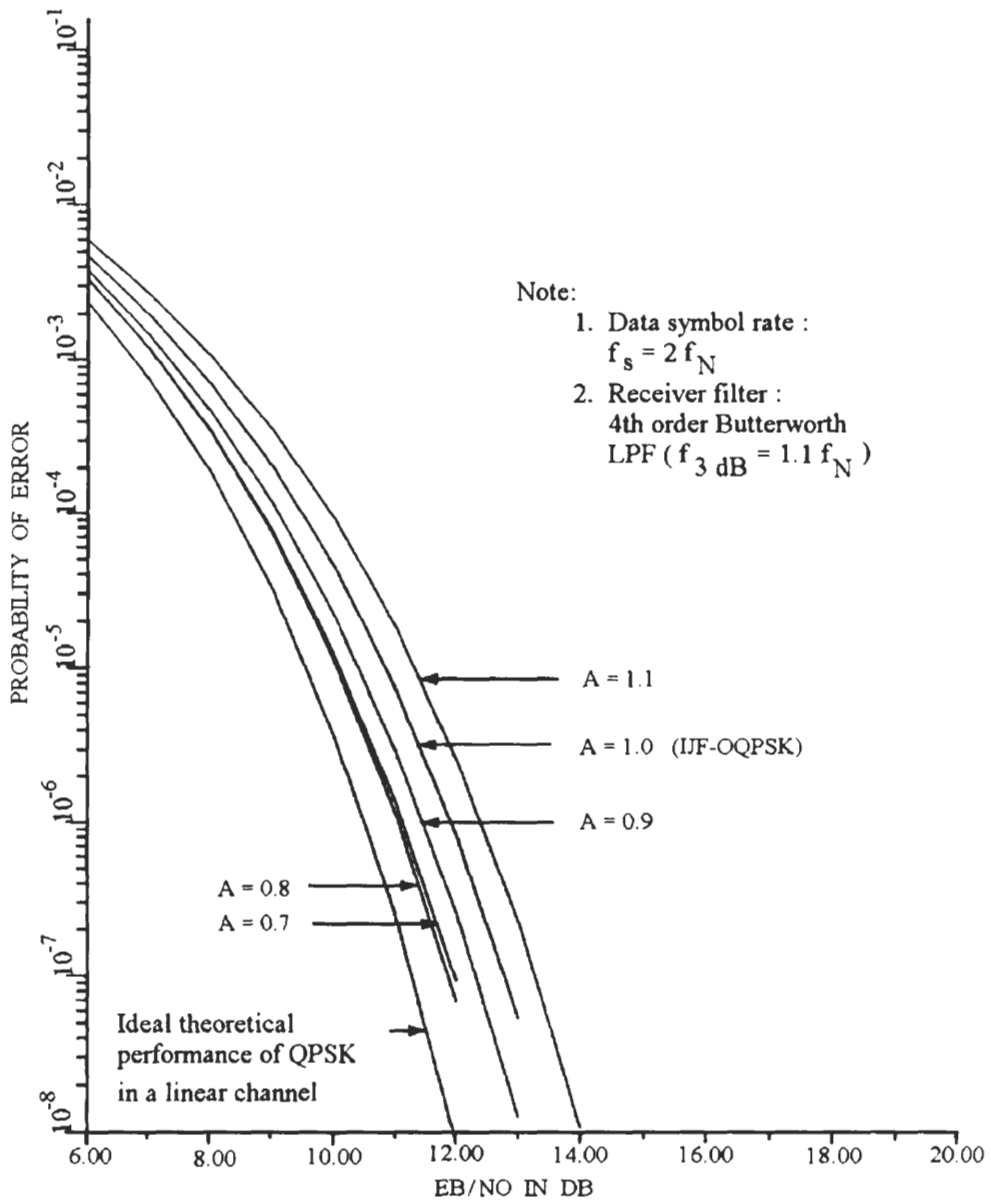


Figure 9.24 Error performance (P_b) of SQAM in a nonlinear (hard-limited) channel. From [7]. Copyright © 1985 IEEE.

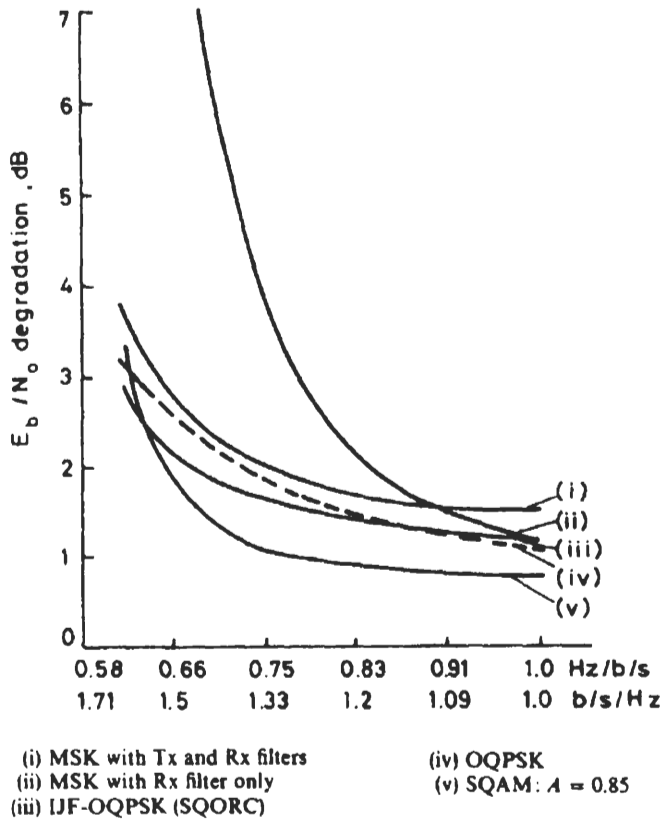


Figure 9.25 E_b/N_o degradation (compared to $E_b/N_o = 8.4$ dB at $P_b = 10^{-4}$) against channel spacing for hard-limited multichannel system with two equal-power ACIs. From [11], Copyright © 1985 IEE.

0.9 are as follows:

$$[d_{ij}^2] = T_b \begin{bmatrix} 0 & 1.16 & 1.16 & 2.64 \\ 1.16 & 0 & 2 & 1.16 \\ 1.16 & 2 & 0 & 1.16 \\ 2.64 & 1.16 & 1.16 & 0 \end{bmatrix}, \quad \text{for } A = 0.8 \quad (9.52)$$

$$[d_{ij}^2] = T_b \begin{bmatrix} 0 & 1.315 & 1.315 & 3.26 \\ 1.315 & 0 & 2 & 1.315 \\ 1.315 & 2 & 0 & 1.315 \\ 3.26 & 1.315 & 1.315 & 0 \end{bmatrix}, \quad \text{for } A = 0.9 \quad (9.53)$$

The symbol error probability upper bound can be found accordingly using (9.6).

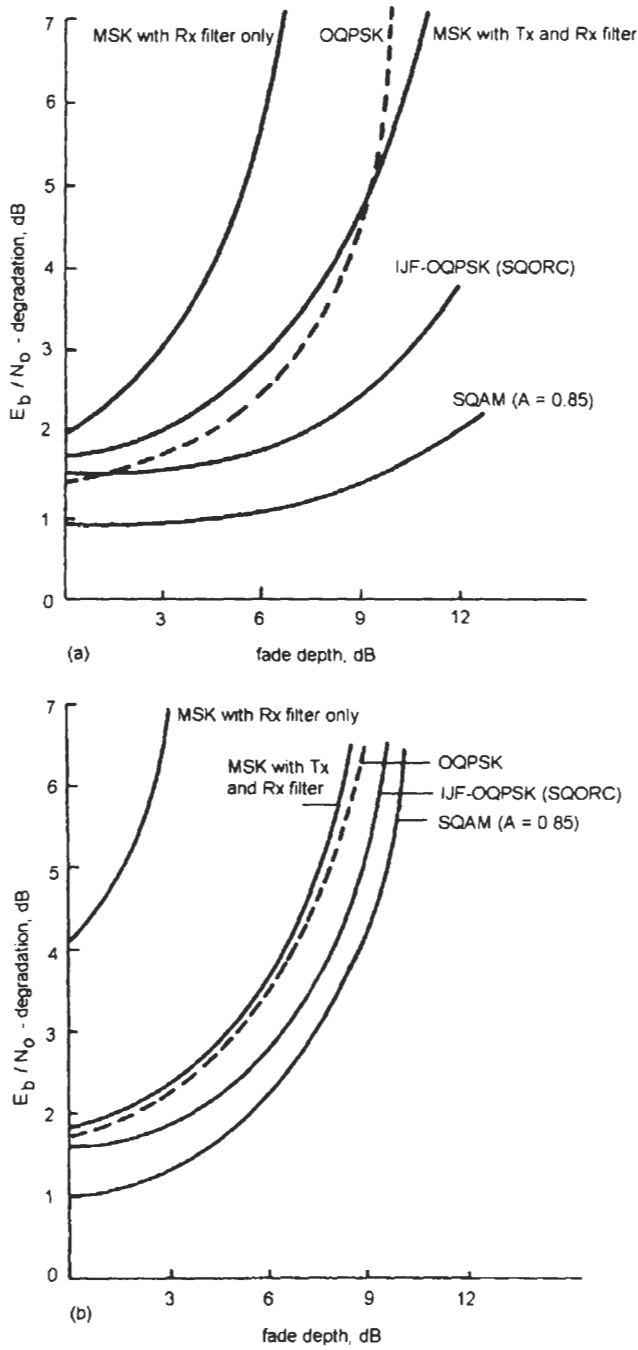


Figure 9.26 E_b/N_0 degradation (compared to $E_b/N_0 = 8.4$ dB at $P_b = 10^{-4}$) against fade depth of the desired channel in hard-limited multichannel system. (a) $\Delta f = 0.83 f_b$ (b) $\Delta f = 0.75 f_b$. From [11]. Copyright © 1985 IEE.

For both cases d_{\min}^2 is not too far away from the second smallest distance. This makes the error probability of SQAM slightly higher than that of MSK and QBL. It is clear that when A value decreases the distances decrease in general. Thus error performance degradation is expected. But this is not the case in an ACI channel as we have discussed already.

9.6 QUADRATURE QUADRATURE PSK

Q^2 PSK is proposed in [12], which is a nonconstant-envelope spectrally efficient modulation scheme. We know that QPSK is more bandwidth efficient than BPSK. The increase of bandwidth efficiency is achieved by increasing the number of dimensions of the signal basis. That is, the number of basis signals is one for BPSK and two for QPSK. The Q^2 PSK uses four basis signals. Four is considered to be the maximum number of dimensions achievable [12, Section III].

The signal set of Q^2 PSK is

$$\begin{cases} s_1(t) = \cos\left(\frac{\pi t}{2T}\right) \cos 2\pi f_c t, & |t| \leq T \\ s_2(t) = \sin\left(\frac{\pi t}{2T}\right) \cos 2\pi f_c t, & |t| \leq T \\ s_3(t) = \cos\left(\frac{\pi t}{2T}\right) \sin 2\pi f_c t, & |t| \leq T \\ s_4(t) = \sin\left(\frac{\pi t}{2T}\right) \sin 2\pi f_c t, & |t| \leq T \\ s_i(t) = 0, & i = 1, 2, 3, 4, \quad |t| > T \end{cases} \quad (9.54)$$

where $2T$ is the duration of the signals. The signal set can be considered as consisting of two carriers $\cos 2\pi f_c t$ and $\sin 2\pi f_c t$ and two pulse-shaping functions:

$$p_1(t) = \begin{cases} \cos\left(\frac{\pi t}{2T}\right), & |t| \leq T \\ 0, & |t| > T \end{cases} \quad (9.55)$$

and

$$p_2(t) = \begin{cases} \sin\left(\frac{\pi t}{2T}\right), & |t| \leq T \\ 0, & |t| > T \end{cases} \quad (9.56)$$

The two carriers are orthogonal and the two pulse-shaping functions are also orthogonal. Note that between any two signals in the set $\{s_i(t)\}$, there is a common factor which is either a pulse-shaping function or a carrier; the remaining factor in one signal is in quadrature with the remaining factor in the other. This makes $\{s_i(t)\}$ a set of four equal-energy orthogonal signals under the restriction that

$$f_c = \frac{n}{4T}, \quad n = \text{integer} \geq 2$$

However, the signal set is not normalized. Each signal has an energy of 0.5 in

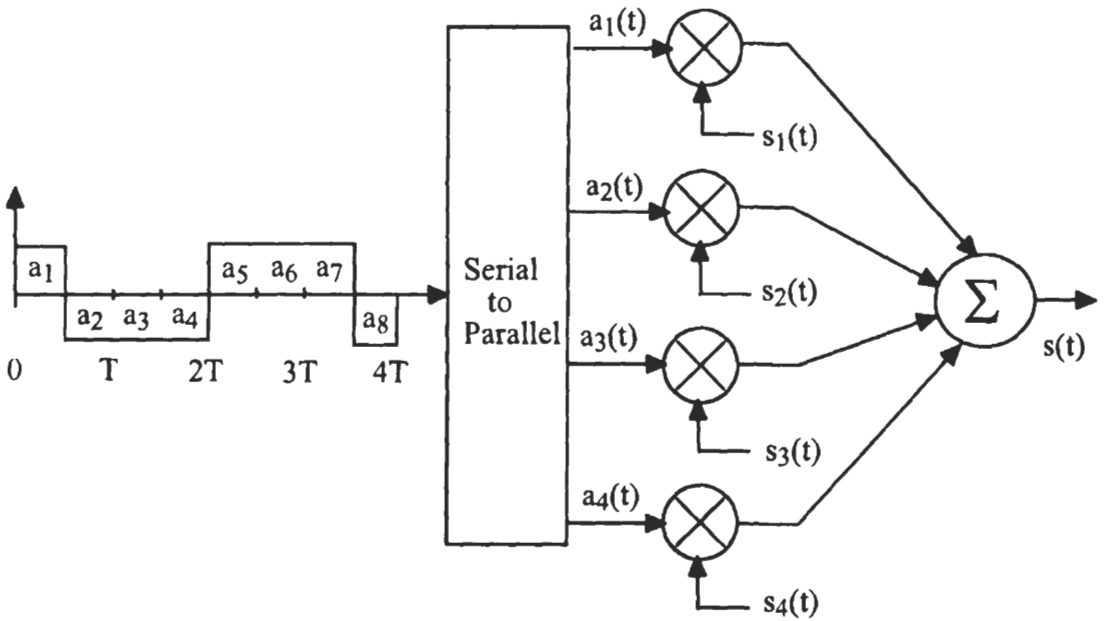


Figure 9.27 Q²PSK modulator.

$[-T, T]$. The orthogonality remains invariant with the shift of time origin by multiples of $2T$. This is to say that if $\{s_i(t)\}$ is defined by (9.54) for $|t| \leq \infty$ instead of $|t| \leq T$, then one will get orthogonality over every interval of $2T$ centered around $t = 2mT, m$ being an integer. This orthogonality suggests a modulation scheme shown in Figure 9.27. Data $\{a_i \in (\pm 1)\}$ from a binary source at a bit rate $R_b = 2/T$ is demultiplexed into four streams $\{a_i(t)\}$. Duration of each pulse in the streams is

$$T_s = 2T = 4T_b$$

which is four times the bit duration. If the symbol rate is the same, the bit rate of the Q²PSK is twice that of QPSK and MSK. This is the fundamental reason why the bandwidth efficiency can be doubled with Q²PSK with respect to MSK, as we will see shortly.

The modulated signal is

$$\begin{aligned} s(t) &= a_1(t) \cos\left(\frac{\pi t}{2T}\right) \cos(2\pi f_c t) + a_2(t) \sin\left(\frac{\pi t}{2T}\right) \cos(2\pi f_c t) \\ &\quad + a_3(t) \cos\left(\frac{\pi t}{2T}\right) \sin(2\pi f_c t) + a_4(t) \sin\left(\frac{\pi t}{2T}\right) \sin(2\pi f_c t) \\ &= \cos \left[2\pi \left(f_c + \frac{b_{14}(t)}{4T} \right) t + \phi_{14}(t) \right] \end{aligned}$$

$$+ \sin \left[2\pi \left(f_c + \frac{b_{23}(t)}{4T} \right) t + \phi_{23}(t) \right] \quad (9.57)$$

$$|t| \leq T$$

where

$$b_{14}(t) = -a_1(t)a_4(t)$$

$$\phi_{14}(t) = 0 \text{ or } \pi \text{ depending on } a_1(t) = +1 \text{ or } -1$$

and

$$b_{23}(t) = +a_2(t)a_3(t)$$

$$\phi_{23}(t) = 0 \text{ or } \pi \text{ depending on } a_1(t) = +1 \text{ or } -1$$

At first glance, the two parts of the signal in (9.57) are like two MSK signals. However, there is a key difference between them and the MSK signal. In the MSK signal the I- and Q-channel signals are offset by T , which makes phase continuous at symbol boundaries, whereas there is no offset in Q²PSK. Thus the Q²PSK cannot be thought of as consisting of two MSK signals, rather it can be thought of as consisting of two FSK-BPSK signals whose phase is not always continuous at symbol boundaries as in MSK. Noting that there are two distinct frequencies and two distinct phases in each of the two components, the total number of distinct signals in Q²PSK is 16.

This signal has a nonconstant envelope. Using trigonometrical identities and noting that $a_i = \pm 1$, (9.57) can easily be written as

$$s(t) = A(t) \cos(2\pi f_c t + \theta(t)) \quad (9.58)$$

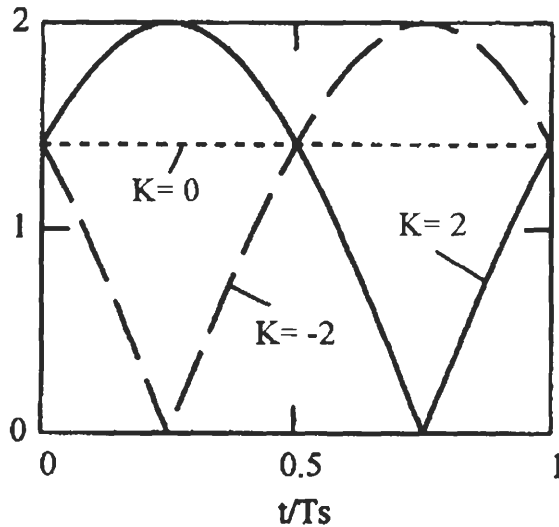
where $\theta(t)$ is the carrier phase and $A(t)$ is the carrier amplitude given by

$$A(t) = \left[2 + (a_1 a_2 + a_3 a_4) \sin \frac{\pi t}{T} \right]^{1/2} \quad (9.59)$$

It is clear that the amplitude varies with time in general. Without any constraint on the data, $K = a_1 a_2 + a_3 a_4 = 0, \pm 2$. The possible amplitude variation in a symbol period ($T_s = 2T$) is shown in Figure 9.28. The amplitude can dip to zero at times. This is not a desired property for applications in nonlinear channels. However, when $K = 0$, the amplitude is constant. A coding scheme can be designed such that K is always zero, making the amplitude constant. We will discuss this shortly.

To find the PSD of the Q²PSK signal we write (9.57) for $|t| \leq \infty$ as

$$s(t) = [x_1(t) \cos 2\pi f_c t + y_1(t) \sin 2\pi f_c t] + [x_2(t) \cos 2\pi f_c t + y_2(t) \sin 2\pi f_c t] \quad (9.60)$$

Figure 9.28 Possible amplitudes of Q^2PSK .

where

$$x_1(t) = \sum_{k=-\infty}^{\infty} a_{1k} p_1(t - kT_s)$$

$$x_2(t) = \sum_{k=-\infty}^{\infty} a_{2k} p_2(t - kT_s)$$

$$y_1(t) = \sum_{k=-\infty}^{\infty} a_{3k} p_1(t - kT_s)$$

$$y_2(t) = \sum_{k=-\infty}^{\infty} a_{4k} p_2(t - kT_s)$$

The complex envelope of the signal is

$$\tilde{s}(t) = x_1(t) + x_2(t) - jy_1(t) - jy_2(t)$$

The autocorrelation is

$$\begin{aligned} R_{\tilde{s}}(\tau) &= E\{\tilde{s}(t)\tilde{s}^*(t-\tau)\} = R_{x_1}(\tau) + R_{x_2}(\tau) + R_{y_1}(\tau) + R_{y_2}(\tau) \\ &= 2R_{x_1}(\tau) + 2R_{x_2}(\tau) \end{aligned}$$

where the cross terms are all zero since the data are independent and $R_{x_1}(\tau) = R_{y_1}(\tau)$, $R_{x_2}(\tau) = R_{y_2}(\tau)$ since their signals have the same pulse shape and the data have the same statistics. Taking the Fourier transform of $R_{\tilde{s}}(\tau)$ and using (A.18) we obtain the PSD of Q²PSK as

$$\Psi_{\tilde{s}}(f) = \frac{2}{T_s} [|P_1(f)|^2 + |P_2(f)|^2]$$

where $P_1(f)$ and $P_2(f)$ are Fourier transforms of $p_1(t)$ and $p_2(t)$, respectively.

$$P_1(f) = \frac{4T}{\pi} \left(\frac{\cos 2\pi fT}{1 - 16f^2T^2} \right)$$

$$P_2(f) = \frac{-j16T}{\pi} \left(\frac{fT \cos 2\pi fT}{1 - 16f^2T^2} \right)$$

Thus

$$\Psi_{\tilde{s}}(f) = \frac{16T}{\pi^2} (1 + 16f^2T^2) \left(\frac{\cos 2\pi fT}{1 - 16f^2T^2} \right)^2 \quad (9.61)$$

From this expression we can observe that the term in the squared parentheses is of the same form as that of MSK (see (5.14)) except that $T = 2T_b$. Thus the first null is at $f = 0.75/T = 0.375/T_b$, which is only one-half of that of MSK. Thus the bandwidth efficiency of Q²PSK is twice as much as that of MSK as far as the main lobe is concerned. Figure 9.29 shows the PSD of Q²PSK in comparison with those of OQPSK and MSK. Figure 9.30 is the fractional out-of-band power of the Q²PSK. The main lobe of the Q²PSK PSD is narrower than that of MSK (Figure 9.29), as a result, its roll-off within $2BT_b = 0.8$ is faster than that of MSK and QPSK/OQPSK (Figure 9.30(b)). Beyond $2BT_b = 0.8$ its roll-off rate is slower than that of MSK, and is the same as that of QPSK/OQPSK, however at a lower level (Figure 9.30(a)). The reason that the side lobes in Q²PSK are higher than that of MSK are as follows. Q²PSK uses two different pulses; one is $p_1(t)$ having a cosinusoidal shape as in MSK, the other is $p_2(t)$ having a sinusoidal shape. The shape of $p_1(t)$ is smoother than $p_2(t)$ in the sense that $p_2(t)$ has jumps at $t = \pm T$. As a result, for large f , the spectral roll-off associated with $p_2(t)$ is proportional to f^{-2} , while that with $p_1(t)$ varies as f^{-4} .

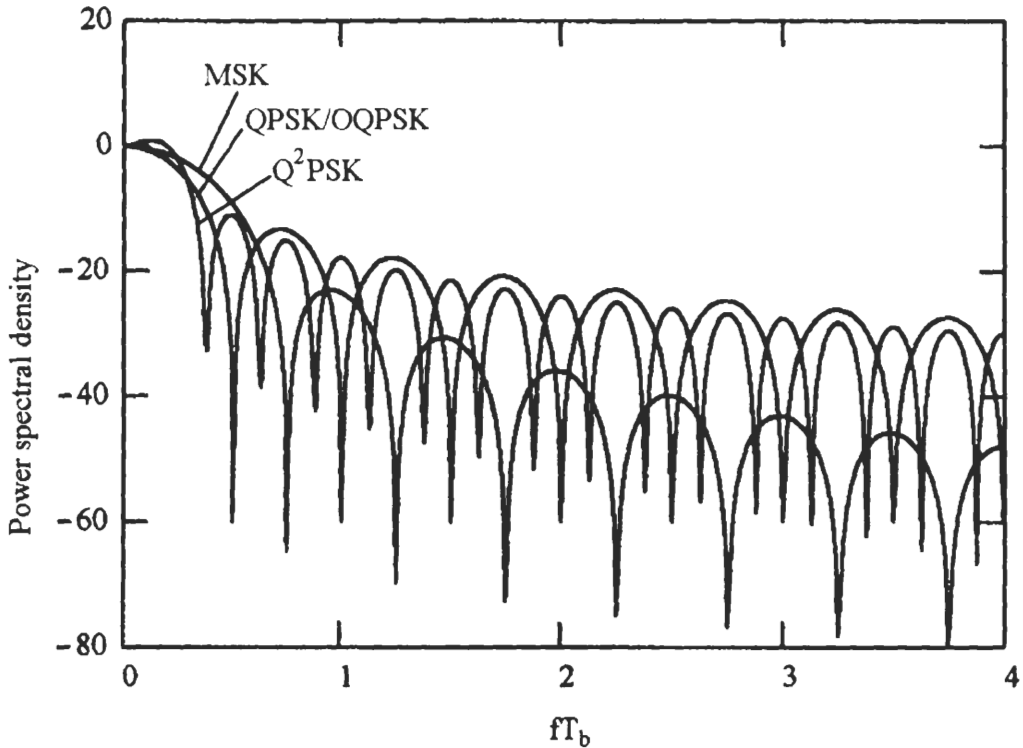
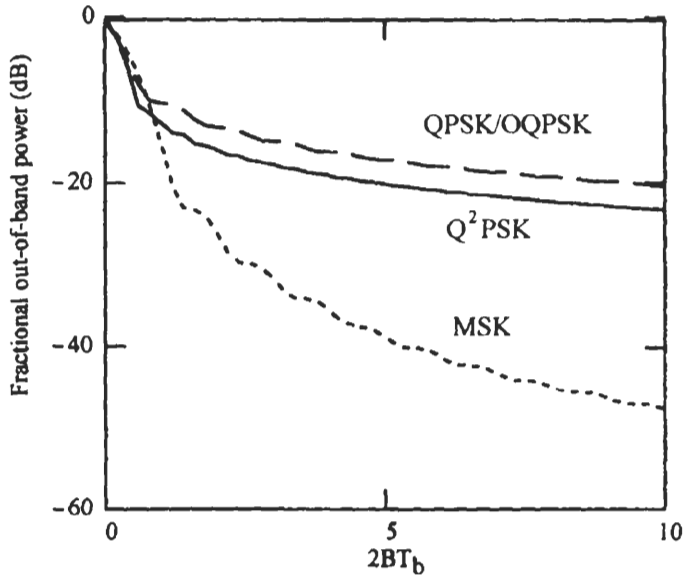


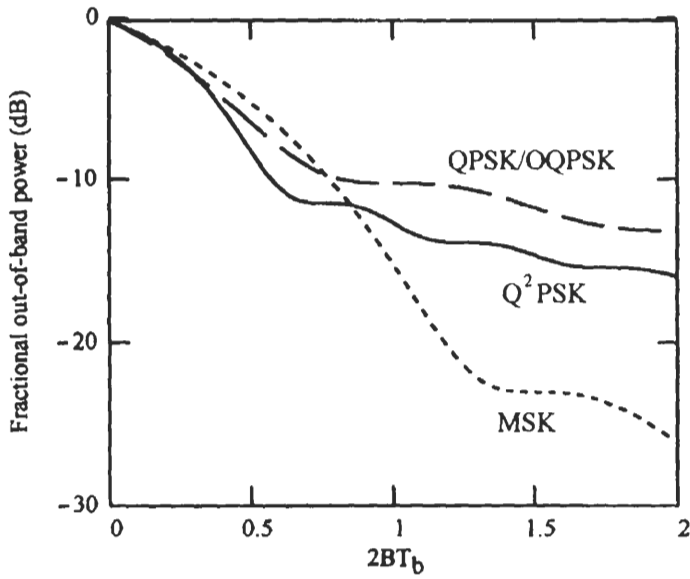
Figure 9.29 PSD of Q^2 PSK in comparison with MSK, QPSK/OQPSK.

Since Q^2 PSK signals are linear combinations of four orthogonal basis signals $\{s_i(t)\}$, the optimum demodulator is of the type given in Figure B.8 or B.9 with four correlators. Each signal is determined by a data four-tuple $\{a_1, a_2, a_3, a_4\}$. The total number of signals is $M = 2^4 = 16$. The bias terms $\{B_j\}_{j=1}^{16}$ can be eliminated since signals are equally likely and of same energy. The weighting matrix consists of the 16 distinct data four-tuples. Each data four-tuple is a column of it.

However, we are not really interested in detecting any one of the 16 signals. Instead we are interested in detecting the data bits $\{a_1, a_2, a_3, a_4\}$ which are imbedded in the signal. Since each bit a_i is associated with only one of the four orthogonal carriers, each data bit can be detected independently. Thus the demodulator can be simplified as shown in Figure 9.31. This is very much similar to the detection of I- and Q-channel bits in MSK. The bit error probability of this receiver is easy to determine. For any channel i in Figure 9.31, due to orthogonality, the correlator output caused by other three component signals other than $a_i s_i(t)$ is zero. As far as detection of $a_i s_i(t)$ is concerned, the other three signals do not have any effect. Thus the

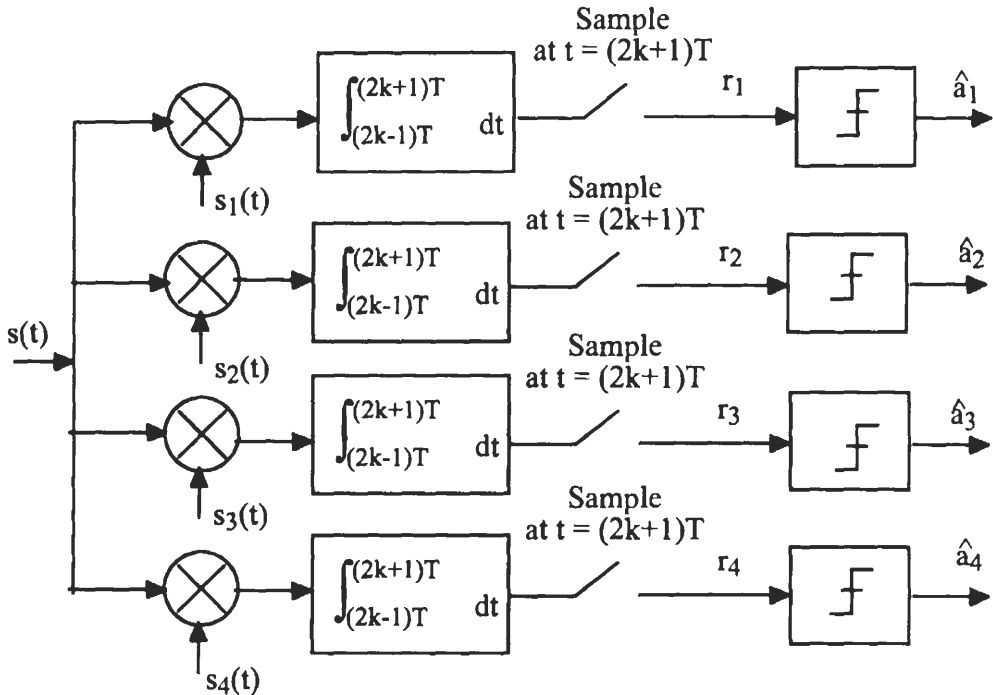


(a)



(b)

Figure 9.30 Fractional out-of-band power of Q^2 PSK in comparison with MSK and QPSK/OQPSK.

Figure 9.31 Q^2 PSK demodulator.

detection becomes just a detection of antipodal binary data a_i , modulated on a carrier $s_i(t)$. This detection problem is identical to that of I- or Q-channel detection of MSK (see Section 5.6). Therefore the bit error probability of Q^2 PSK is the same as that of MSK. That is

$$P_b = Q\left(\sqrt{\frac{2E_b}{N_o}}\right) \quad (9.62)$$

It is interesting to note that the bit error probability is proved to be the same as in (9.62) if the symbols are detected using the demodulator depicted in Figure B.8 [12]. Thus the demodulator in Figure 9.31 is optimum as far as bit detection is concerned. The performance coincidence is due to the fact that each bit a_i is associated with only one of the four orthogonal carriers. We have seen similar phenomena in QPSK and MSK.

While Q^2 PSK has the same error performance as those of BPSK, QPSK, and MSK in an AWGN channel, for bandlimited channels, they behave differently due to their different spectra. Figure 9.32 is a comparison of their bit error probabilities. The performance evaluation assumed a sixth-order Butterworth filter with 3 dB band-

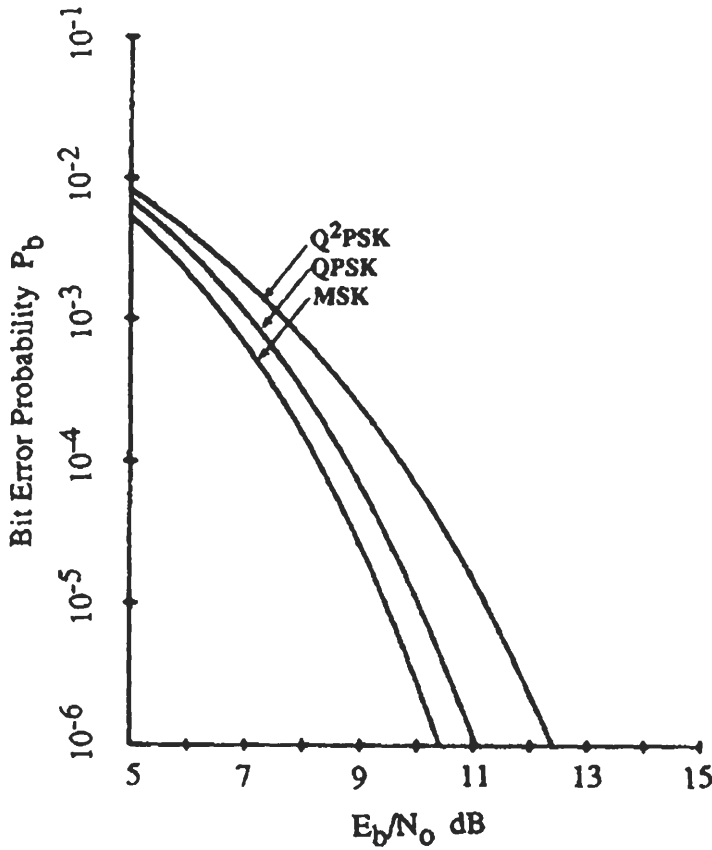


Figure 9.32 Bit error probability of Q^2PSK , QPSK and MSK in a bandlimited channel. Bandlimiting filter is six-order Butterworth with 3 dB bandwidth equal to $1.2/T$. From [12]. Copyright © 1989 IEEE.

width W equal to $1.2/T$. The E_b/N_0 requirement of Q^2PSK is approximately 1.6 dB higher than that of MSK for $P_b = 10^{-5}$. The bit rate and bandwidth efficiency for MSK in this situation are $R_{b(MSK)} = 1/T$ and $R_{b(MSK)}/W = 0.83$. For Q^2PSK these values are $R_{b(Q^2PSK)} = 2/T$ and $R_{b(Q^2PSK)}/W = 1.66$ bits/s/Hz. Thus Q^2PSK achieves twice the bandwidth efficiency of MSK at the expense of 1.6 dB increase in the average bit energy.

The synchronization scheme for Q^2PSK is derived as follows. If the Q^2PSK signal passes through a squaring device, we get

$$s^2(t) = 1 + \frac{1}{2}(a_1a_2 + a_3a_4) \sin\left(\frac{\pi t}{T}\right)$$

$$\begin{aligned}
& + \frac{1}{2}(a_1 a_2 - a_3 a_4) \sin\left(\frac{\pi t}{T}\right) \cos(4\pi f_c t) \\
& + \cos(\theta_{12} - \theta_{34}) \sin(4\pi f_c t) \\
& + \cos(\theta_{12} + \theta_{34}) \cos\left(\frac{\pi t}{T}\right) \sin(4\pi f_c t) \\
& + \sin(\theta_{12} + \theta_{34}) \sin\left(\frac{\pi t}{T}\right) \sin(4\pi f_c t)
\end{aligned} \tag{9.63}$$

where

$$\begin{aligned}
\theta_{12}(t) &= \tan^{-1} \left(\frac{a_2(t)}{a_1(t)} \right) \\
\theta_{34}(t) &= \tan^{-1} \left(\frac{a_4(t)}{a_3(t)} \right)
\end{aligned}$$

There are five components in (9.63) which carry carrier- or symbol-timing information. The expected value of each component is zero. Filtering and further nonlinearity are needed in order to recover the carrier and symbol timing. By a low-pass and a bandpass filtering of the squared signal, we can obtain two signals

$$x_1(t) = \frac{1}{2}(a_1 a_2 + a_3 a_4) \sin\left(\frac{\pi t}{T}\right)$$

$$x_2(t) = \cos(\theta_{12} - \theta_{34}) \sin(4\pi f_c t)$$

After squaring $x_1(t)$ and $x_2(t)$ and taking the expectation, we obtain

$$E\{x_1^2(t)\} = \frac{1}{4} \left(1 - \cos \frac{2\pi t}{T}\right)$$

$$E\{x_2^2(t)\} = \frac{1}{4} (1 - \cos 8\pi f_c t)$$

Thus on the average $x_1^2(t)$ and $x_2^2(t)$ contain spectral lines at $1/T$ and $4f_c$. We can use these lines to lock phase-lock loops and carry out frequency division to recover the symbol-timing clock and carrier as

$$x_{c1}(t) = \cos(\pi t/T)$$

$$x_c(t) = \cos 2\pi f_c t$$

Figure 9.33 is the block diagram of the synchronization scheme.

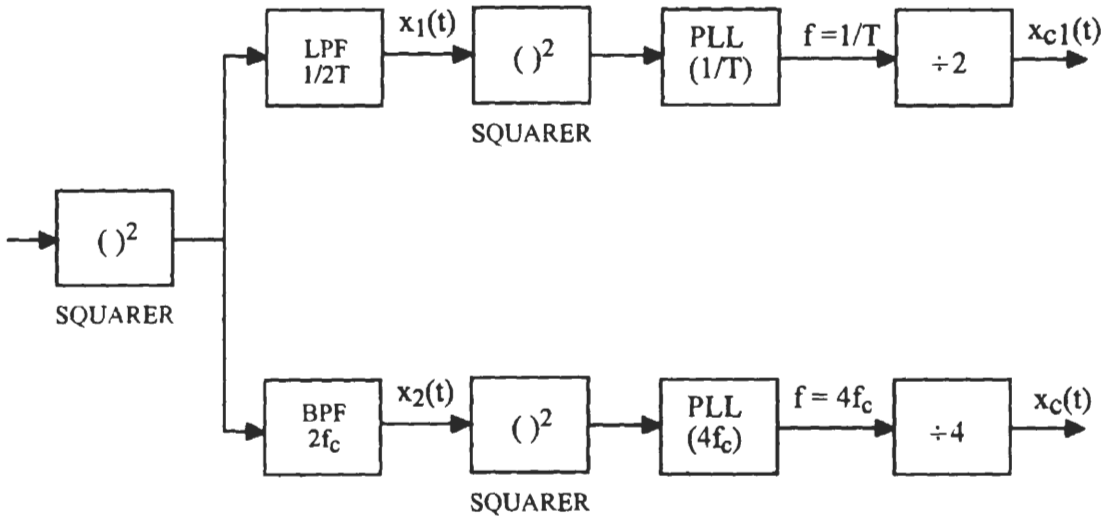


Figure 9.33 Synchronization scheme for coherent demodulation of Q^2PSK . From [12]. Copyright © 1989 IEEE.

The realization of modulator is shown in Figure 9.34. The basis signal set $\{s_i(t)\}$ is generated by a single oscillator of f_c and a bank of four bandpass filters and four adders.

The constant envelope version of Q^2PSK can be obtained by a simple coding scheme. From $K = a_1a_2 + a_3a_4 = 0$ we see that

$$a_4 = -\frac{a_1a_2}{a_3} \quad (9.64)$$

The encoder accepts serial data and for every three information bits $\{a_1, a_2, a_3\}$, it generates a codeword $\{a_1, a_2, a_3, a_4\}$ where a_4 satisfies (9.64). The rate of the code is $3/4$. The constant envelope feature is achieved at the expense of bandwidth efficiency. The information transmission rate is reduced from $R_b = 2/T$ to $3/2T$. But this is still 50% more than that of MSK ($R_b = 1/2T$ for MSK).

The modulator of the constant envelope Q^2PSK is the same as that of Q^2PSK except that an encoder must be added to the input to perform the coding given in (9.64).

Due to coding, the number of distinct signals is reduced from 16 to 8. Four of the eight possible codewords $\{C_i\}_{i=1}^8$ are as follows:

$$\begin{aligned} C_1 &= (+++-) \\ C_2 &= (++-+) \end{aligned}$$

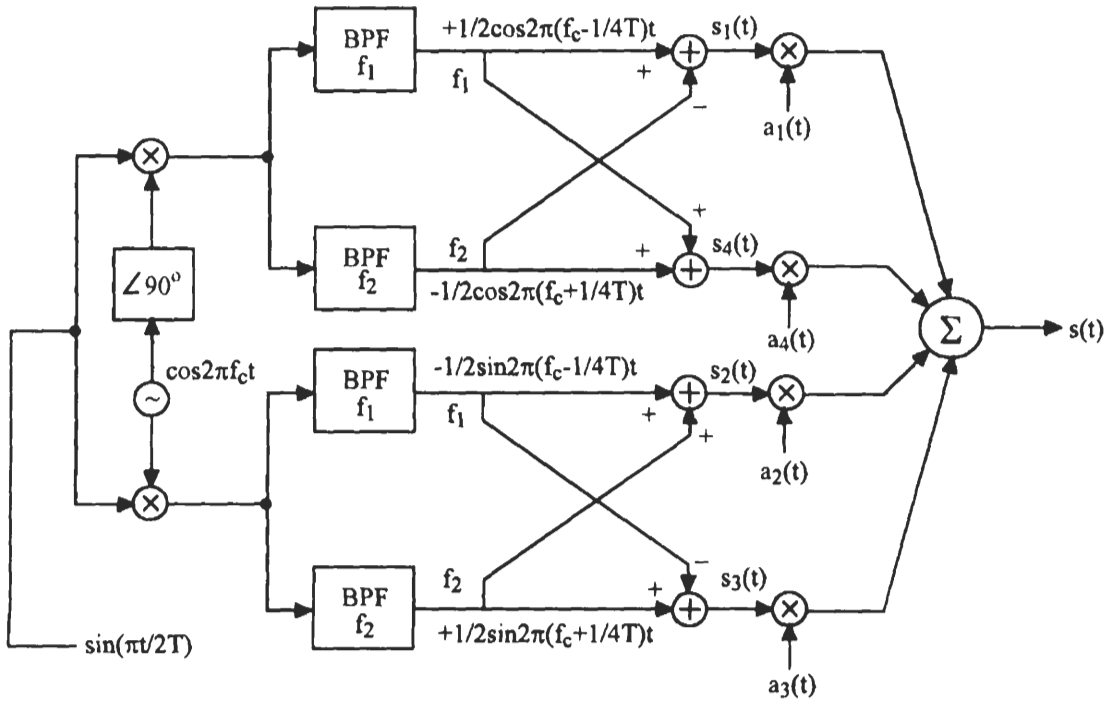


Figure 9.34 Realization of Q²PSK modulator. From [12]. Copyright © 1989 IEEE.

$$C_3 = (+ - ++)$$

$$C_4 = (+ - --)$$

where + and - represent +1 and -1, respectively. The remaining four codewords are just the negatives of these. This is a set of eight biorthogonal codewords with a minimum Hamming distance of two.² The code cannot be used for error correction, but the redundancy can be used to improve the error performance. The minimum Euclidean distance of the uncoded Q²PSK is due to one different bit in the four-tuple, say a_j , then the squared minimum Euclidean distance is

$$\int_{-T}^T (s_j(t) + s_j(t))^2 dt = 4 \int_{-T}^T s_j^2(t) dt = 4E_b$$

The minimum Euclidean distance of the coded Q²PSK is due to two different bits in

² Hamming distance between two codewords is defined as the number of bits in which they differ.

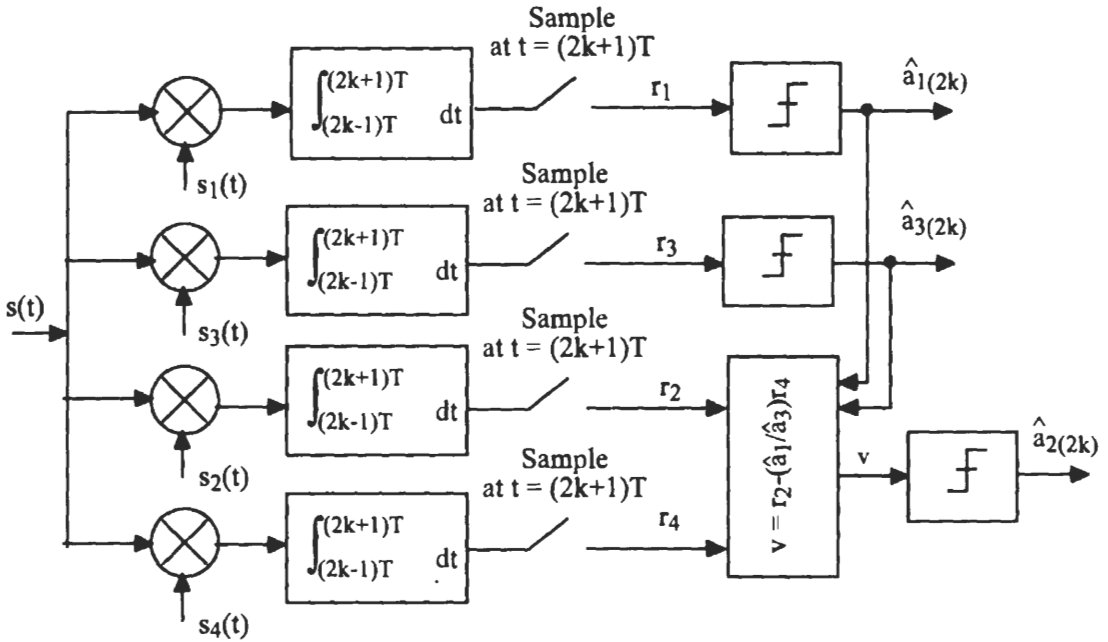


Figure 9.35 Constant envelop Q²PSK demodulator. From [12]. Copyright © 1989 IEEE.

the four-tuple, say a_i and a_j , then the squared minimum Euclidean distance is

$$\int_{-T}^T [(s_i(t) + s_i(t))^2 + (s_j(t) + s_j(t))^2] dt = 8 \int_{-T}^T s_i^2(t) dt = 6E_b$$

where $\int_{-T}^T s_i^2(t) dt = \frac{3}{4} E_b$ since a four-bit codeword represents three information bits. The coded Q²PSK has a minimum Euclidean distance $\sqrt{1.5} = 1.22$ times greater than that of uncoded Q²PSK. This provides a coding gain of 1.76 dB if the optimum demodulator (Figure B.8) is used.

From an implementation point of view, a nonoptimum demodulator based on hard decision may be of interest. Figure 9.35 is a nonoptimum demodulator for the coded Q²PSK which is basically the same as Figure 9.31 except for the decoding part. According to [12], the pulses associated with $s_1(t)$ and $s_3(t)$ are relatively less distorted in a bandlimiting channel as compared to those associated with $s_2(t)$ and $s_4(t)$. Thus \hat{a}_1 and \hat{a}_3 are directly determined from the correlator outputs r_1 and r_3 , while \hat{a}_2 is determined from \hat{a}_1 , \hat{a}_3 , r_2 , and r_4 . The sufficient statistic for decision on \hat{a}_2 is

$$V = r_2 - \frac{\hat{a}_1}{\hat{a}_3} r_4$$

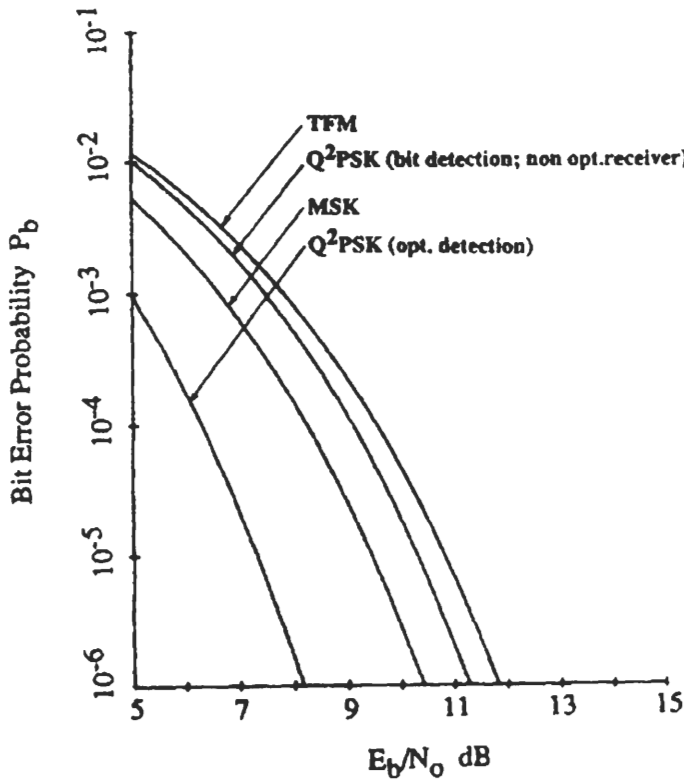


Figure 9.36 Bit error probabilities for constant envelope Q²PSK, MSK, and TFM. From [12]. Copyright © 1989 IEEE.

The decoder decides \hat{a}_2 as +1 or -1 according as $V \geq 0$ or $V < 0$. The correct decision on \hat{a}_2 relies on the correct decision on \hat{a}_1 and \hat{a}_3 . Figure 9.36 shows the performance of the constant envelope Q²PSK in a bandlimited channel where a sixth-order Butterworth filter with 3 dB bandwidth of $1.2/T$ is used in both transmitter and receiver. It is seen that for $P_b = 10^{-5}$, the constant envelope Q²PSK with nonoptimum demodulation requires an $E_b/N_o = 10.3$ dB while the MSK requires an $E_b/N_o = 9.6$ dB. Thus there is a 50% increase in bandwidth efficiency over MSK at a cost of 0.7 dB increase in the average bit energy. The error performance of the optimum demodulator shown in the figure does not assume band limitation.

The synchronization system for the uncoded Q²PSK is no longer applicable for the constant envelope Q²PSK. Substituting (9.64) into (9.63), we get

$$s^2(t) = 1 + \frac{1}{2}(a_1 a_3 + a_1 a_2) \sin \left(2\pi t \left(2f_c + \frac{1}{2T} \right) \right)$$

$$+ \frac{1}{2}(a_1 a_3 - a_1 a_2) \sin \left(2\pi t \left(2f_c - \frac{1}{2T} \right) \right) \quad (9.65)$$

There are two components in (9.65) which carry the carrier and clock information. But their expectations are zero. Further filtering and nonlinearity are needed to recover the carrier and clock information. By bandpass filtering we can get

$$x_1(t) = \frac{1}{2}(a_1 a_3 + a_1 a_2) \sin \left(2\pi t \left(2f_c + \frac{1}{2T} \right) \right)$$

$$x_2(t) = \frac{1}{2}(a_1 a_3 - a_1 a_2) \sin \left(2\pi t \left(2f_c - \frac{1}{2T} \right) \right)$$

It can be shown that $x_1^2(t)$ and $x_2^2(t)$, on the average, contain spectral lines at $4f_c \pm \frac{1}{T}$. We can use phase-locked loops to lock on these lines and carry out frequency division to get

$$x_3(t) = \cos \left(2\pi t \left(f_c + \frac{1}{4T} \right) \right)$$

$$x_4(t) = \cos \left(2\pi t \left(f_c - \frac{1}{4T} \right) \right)$$

Then a multiplication of these two followed by bandpass filtering and frequency division gives the desired carrier and clock signal

$$x_{c1}(t) = \cos \left(\frac{\pi t}{T} \right)$$

$$x_c(t) = \cos 2\pi f_c t$$

The block diagram of this synchronization scheme is shown in Figure 9.37.

To further improve the bandwidth efficiency of Q²PSK, pulse shapes other than the ones in (9.55) and (9.56) can be used [12]. A few of transmitter baseband filter pairs that can achieve zero intersymbol interference and zero cross-correlation are given in Figure 9.38. These filters have a two-sided bandwidth of $1/T$, thus can achieve a bandwidth efficiency of 2 bits/s/Hz which is better than the 1.66 bits/s/Hz as previously demonstrated for (9.55) and (9.56). The filter pair in Figure 3.38(a) is a Hilbert transform pair. The rectangular frequency responses of this pair of filters are difficult to realize. Besides, a Hilbert transform pair has an additional problem because of the finite dc content. The pair in Figure 3.38(b) has no problem of dc content but it still has the problem of sharp cutoff at the band edge of $P_2(f)$. From the realization point of view, the pair in Figure 3.38(c) is specially convenient; one

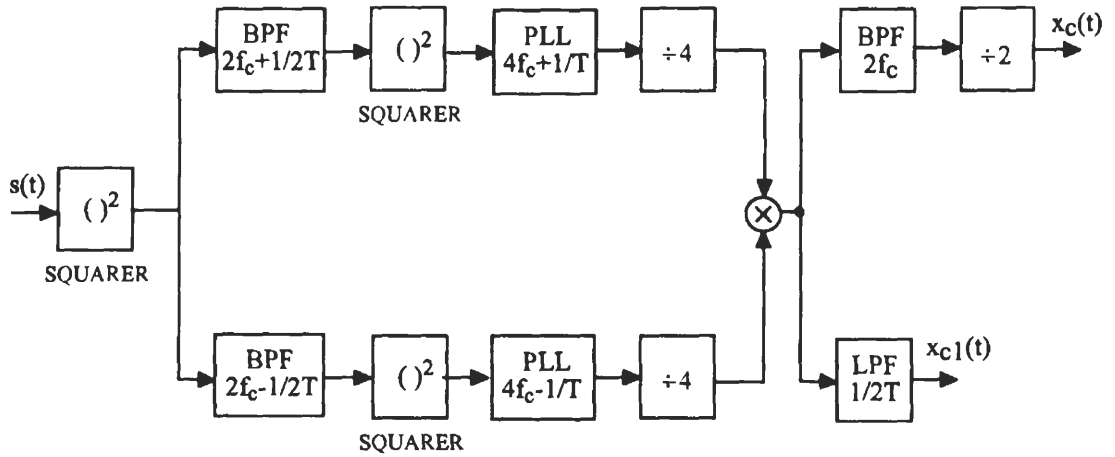


Figure 9.37 Synchronization scheme for coherent demodulation of constant envelope Q²PSK. From [12]. Copyright © 1989 IEEE.

of the two filters is a cosine shape $P_1(f)$ and the other $P_2(f)$ is just a bandlimited differentiator. Note that $P_2(f)$ still has sharp cutoff edges at $f = \pm 1/2T$. However, if a Butterworth filter is incorporated with the ideal differentiator, the realization problem is greatly reduced. The bit error performance has been studied for $P_1(f) = \sqrt{2T} \cos \pi fT$ and $P_2(f) = jfB(f)$ where $B(f)$ is a Butterworth low-pass filter of second order with 3 dB bandwidth $W = 0.5R_b$. The corresponding transfer function is given by

$$P_2(s) = \frac{s}{s^2 + \sqrt{2}s + 1}$$

where s is the complex frequency (normalized with respect to 3 dB bandwidth). This transfer function is realizable. With this pair of filters, not only the bandwidth efficiency is improved to 2 bits/s/Hz, but also the energy efficiency is improved from 11.2 dB to 10.8 dB for a bit error probability of 10^{-5} .

A generalized Q²PSK signaling format has been proposed for differential encoding and differential detection [13]. It is suitable for mobile and fixed radio links with multipath and fading problems. Differential detection of Q²PSK requires approximately 3 dB extra E_b/N_o . However, the 3 dB loss can be fully or partially recovered if maximum likelihood decoding is used based on multiple (more than two) symbol observations.

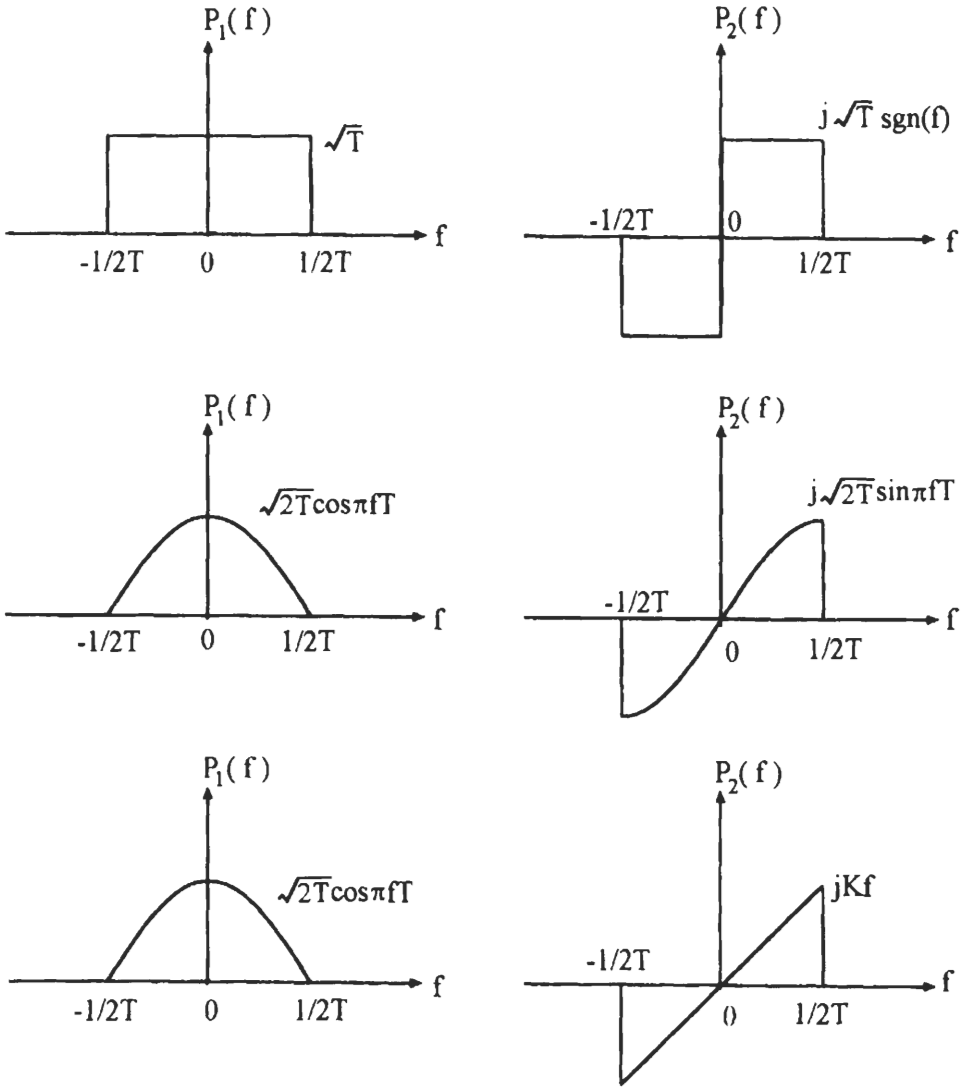


Figure 9.38 Transmitter filter pairs for Q²PSK transmission with zero intersymbol interference and cross-correlation. From [12]. Copyright © 1989 IEEE.

9.7 SUMMARY

In this chapter we have covered the main research results on nonconstant-envelope bandwidth-efficient modulation schemes during the last twenty years. We have studied eight different schemes, namely, QBL, QORC, SQORC, QOSRC, IJF-OQPSK, TSI-OQPSK, SQAM, and Q²PSK. The first seven are all similar in that each of them consists of two quadrature carriers weighted by pulses of a length of $2T_b$ or $4T_b$. The last one consists of four carriers weighted by sinusoidal or cosinusoidal pulses of a length of, again, $4T_b$.

By relaxing the constant envelope constraint, these proposed schemes are able to shrink the spectrum of the signal while maintaining a bit error probability close to MSK. The envelope fluctuations are not significant for staggered schemes. But the nonstaggered scheme QORC exhibits a big envelope variation. All of the eight schemes studied have spectral main lobes comparable to or smaller than that of QPSK and a faster spectral roll-off of the sidelobes. Therefore they provide low spectral spreading caused by nonlinear amplification.

Some schemes, namely the IJF-OQPSK, TSI-OQPSK, and SQAM have been examined against the ACI environment and found to have less degradation in error probability than QPSK/OQPSK. Other schemes have not been examined against the ACI environment and the study can be done in the future as research topics.

For the $2T_b$ schemes we have developed an optimum demodulator which uses two correlators in each of I- and Q-channel. For all the $2T_b$ schemes, the bit error probability of the optimum demodulator is slightly higher than that of MSK. However, all these schemes can be demodulated by a conventional QPSK/OQPSK demodulator with small loss in error performance. For Q²PSK, noncoherent demodulation is impossible and a coherent demodulator is developed. The Q²PSK can also be made constant-envelope by a simple coding scheme. But the improvement of bandwidth efficiency over MSK is reduced from 100% to 50%.

References

- [1] Amoroso, F., "The use of quasi-bandlimited pulses in MSK transmission," *IEEE Trans. Commun.*, vol. 27, no. 10, Oct. 1979, pp. 1616-1624.
- [2] Austin, M. C., and M. V. Chang, "Quadrature overlapped raised-cosine modulation," *IEEE Trans. on Comm.* vol. 29, no. 3, March 1981, pp. 237-249.
- [3] Sasase, I., Y. Harada, and S. Mori, "Bandwidth efficient quadrature overlapped modulation," *IEEE Trans. on Comm.* vol. 32, no. 5, Jan. 1984, pp. 638-640.
- [4] Sasase, I., R. Nagayama and S. Mori, "Bandwidth efficient quadrature overlapped squared raised-cosine modulation," *IEEE Trans. on Comm.* vol. 33, no. 1, Jan. 1985, pp. 101-103.
- [5] Le-Ngoc, T., K. Feher, and H. P. Van, "New modulation techniques for low-cost power and band-

- width efficient satellite stations," *IEEE Trans. on Comm.* vol. 30, no. 1, July 1982, pp. 275-283.
- [6] Van, H. P, and K. Feher, "A class of two symbol interval modems for nonlinear radio systems," *IEEE Trans. on Comm.* vol. 31, no. 3, Mar. 1983, pp. 433-441.
- [7] Seo, J., and K. Feher, "SQAM: a new superposed QAM modem technique," *IEEE Trans. on Comm.* vol. 33, no. 3, March 1985, pp. 296-300.
- [8] Kato, S., and K. Feher, "XPSK: a new cross-correlated phase-shift-keying modulation technique," *IEEE Trans. on Comm.* vol. 31, no. 5, May 1983, pp. 701-706.
- [9] Feher et al, *Advanced Digital Communications: Systems and Signal Processing Techniques*, Englewood Cliffs, New Jersey: Prentice Hall, 1987.
- [10] Van, H. P and K. Feher, "TSI-OQPSK for multiple carrier satellite systems," *IEEE Trans. on Comm.* vol. 32, no. 7, July 1984, pp. 818-825.
- [11] Seo, J. and K. Feher, "Performance of SQAM systems in a nonlinearly amplified multichannel interference environment," *IEE Proceedings*. vol. 132. Pt. F. no. 3, June 1985, pp. 175-180.
- [12] Saha, D. and T. G. Birdsall, "Quadrature-quadrature phase-shift keying," *IEEE Trans. on Comm.* vol. 37, no. 5, May 1989, pp. 437-448.
- [13] El-Ghandour, O. and D. Saha, "Differential detection in quadrature-quadrature phase shift keying (Q^2 PSK) systems," *IEEE Trans. On Comm.*, vol. 39, no. 5, May 1991, pp. 703-712.

Chapter 10

Performance of Modulations in Fading Channels

In wireless radio channels, a signal from the transmitter may arrive at the receiver's antenna through several different paths. The transmitted electromagnetic wave may be reflected, diffracted, and scattered by surrounding buildings and the terrain in the case of mobile radio communications, or by troposphere and ionosphere in the case of long-distance radio communications. As a result, the signal picked up by the receiver's antenna is a composite signal consisting of these *multipath signals*. Sometimes a line-of-sight (LOS) signal may exist. The multipath signals arrive at the receiver at slightly different delays and have different amplitudes. The different delays translate to different phases. This results in a composite signal which can vary widely and rapidly in amplitude and phase. This phenomena is called *fading*. Variations in the property of the propagation medium, such as the occurrence of rain or snow, also can cause fading. However, this type of fading is long-term fading, which we will not consider here. Multipath also causes intersymbol interference for digital signals. For mobile radio channels (ground and satellite), there is also the Doppler frequency shift. Doppler shift causes carrier frequency drift and signal bandwidth spread. All these adversaries cause degradation in performance of modulation schemes in comparison with that in AWGN channels. In this chapter we study performances of modulation schemes in fading channels. To do that we need to briefly study the characteristics of fading channels (Section 10.1). After that we first study flat-fading-channel performances of common binary and quaternary schemes, namely, BFSK, BPSK, DBPSK, QPSK, OQPSK, and MSK including GMSK in Section 10.2. In Section 10.3, their performances in frequency-selective channels are studied. The fading-channel performance of $\pi/4$ -DQPSK, which is especially important since it is the standard in the United States and Japanese cellular telephone systems, is covered in great detail in Section 10.4. Then we move on to cover IREC-MHPM or multi- h CPFSK in Section 10.5 and QAM in Section 10.6. Section 10.7 provides a brief discussion of remedial measures against fading. An in-

depth discussion of remedial measures is beyond the scope of this book. The reader is provided with relevant references. Section 10.8 is a brief summary of this chapter.

10.1 FADING CHANNEL CHARACTERISTICS

10.1.1 Channel Characteristics

A fading-multipath channel is characterized by several parameters:

- Delay spread.* In a multipath channel, the signal power at the receiver spreads over a certain range of time. The delay of the i th signal component in excess of the delay of the first arriving component is called excess delay, denoted as τ_i . Since τ is a random variable, the average $\bar{\tau}$ is the *mean excess delay*, the square root of the variance σ_τ is called *rms excess delay*, and *excess delay spread* (X dB) is defined as the longest time delay during which multipath energy falls to X dB below the maximum. In other words, the maximum excess delay is defined as $\tau_X - \tau_0$, where τ_0 is the delay of the first arriving signal and τ_X is the maximum delay at which a multipath component is within X dB of the strongest signal which is not necessarily the first arriving signal. Figure 10.1 is an example of an indoor power delay profile, showing the definitions of delay spread parameters. The typical σ_τ values are on the order of microseconds (μs) in outdoor mobile radio channels and on the order of nanoseconds (ns) in indoor channels.
- Coherence bandwidth.* The coherence bandwidth B_c is defined as the range of frequencies over which the channel can be considered “flat,” meaning the channel passes all spectral components with approximately equal gain and linear phase. Frequency components in this bandwidth have a strong correlation in amplitude, hence the name “coherence bandwidth.” On the other hand, two sinusoidal signals with frequency separation greater than B_c are affected quite differently. To derive a value of B_c , we define an envelope correlation coefficient between two signals as

$$\rho(\Delta f, \Delta t) = \frac{E\{a_1 a_2\} - E\{a_1\}E\{a_2\}}{\sqrt{(E\{a_1^2\} - (E\{a_1\})^2)(E\{a_2^2\} - (E\{a_2\})^2)}}$$

where $E\{\cdot\}$ denote the ensemble average and a_1 and a_2 represent the amplitudes of signals at frequencies f_1 and f_2 , respectively, and at times t_1 and t_2 , respectively, where $|f_2 - f_1| = \Delta f$ and $|t_2 - t_1| = \Delta t$. Next we employ the approximation that in the mobile radio environment the amplitude of each

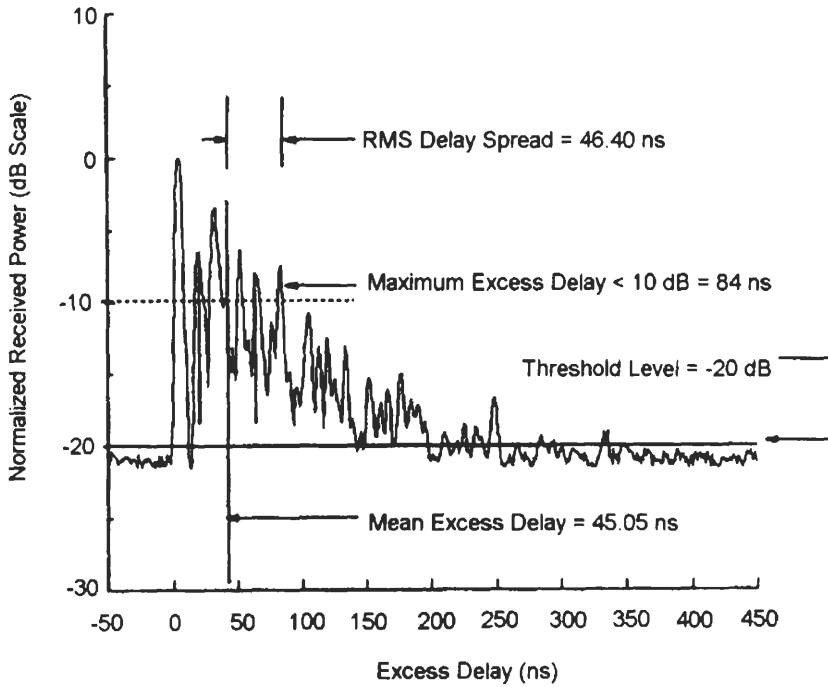


Figure 10.1 Delay spread parameters. From [1]. Copyright © 1996 Prentice Hall.

received signal is unity and that the probability of receiving a signal with delay τ is given by

$$p(\tau) = \frac{1}{2\pi\sigma_\tau} \exp\left(\frac{-\tau}{\sigma_\tau}\right) \quad (10.1)$$

Then it can be shown [2, 3] that the envelope correlation coefficient for two signals separated by Δf Hz and Δt seconds is equal to

$$\rho(\Delta f, \Delta t) = \frac{J_0^2(2\pi f_m \Delta t)}{1 + (2\pi \Delta f)^2 \sigma_\tau^2} \quad (10.2)$$

where $J_0(\cdot)$ is the zeroth order Bessel function of the first kind and $f_m = v/c$ is the maximum Doppler shift for a velocity of v , with c representing the velocity of light. If $\Delta t = 0$, the envelope correlation coefficient becomes the frequency correlation coefficient

$$\rho(\Delta f, 0) = \frac{1}{1 + (2\pi \Delta f)^2 \sigma_\tau^2} \quad (10.3)$$

Now from (10.3) we can relate coherence bandwidth to the rms delay spread inversely as follows

$$B_c = \frac{1}{2\pi\sigma_\tau} \sqrt{\frac{1 - \rho(B_c, 0)}{\rho(B_c, 0)}} \quad (10.4)$$

Usually the coherence bandwidth is defined as the frequency separation at which $\rho(B_c, 0) = 0.5$. Thus from (10.4) we have

$$B_c = \frac{1}{2\pi\sigma_\tau} \quad (10.5)$$

However, we can determine a coherence bandwidth for any value of frequency correlation $\rho(B_c, 0)$. For example if $\rho(B_c, 0) = 0.9$, we have

$$B_c = \frac{1}{6\pi\sigma_\tau} \quad (10.6)$$

Note that the relations given in (10.4) to (10.6) are based on (10.1) which is an approximation. Thus the above relations between B_c and σ_τ are just coarse estimates.

- *Doppler spread.* Doppler spread B_D is a measure of the spectral broadening caused by the relative movement of the mobile and base station, or by movement of objects in the channel. It is obvious that the Doppler spread is equal to the maximum Doppler frequency (i.e., $B_D = f_m$). The total bandwidth of the received signal is determined by the bandwidth of the baseband signal and the Doppler spread. If the baseband bandwidth is much greater than B_D , the effects of Doppler spread is negligible at the receiver.
- *Coherence time.* Similar to the definition of the coherence bandwidth, we can define a coherence time which is an estimate of at what transmitted signal duration distortion becomes noticeable. The coherence time T_c is defined as the time difference between two signals with the same frequency, whose envelope correlation is 0.5. That is

$$\rho(0, T_c) = 0.5$$

which implies from (10.2)

$$\rho(0, T_c) = J_0^2(2\pi f_m T_c) = 0.5$$

This makes

$$T_c \approx \frac{9}{16\pi f_m} = \frac{9}{16\pi B_D} \quad (10.7)$$

Some authors simply use a more coarse estimate, that is,

$$T_c \approx \frac{1}{B_D} \quad (10.8)$$

This actually corresponds to $\rho(0, T_c) \approx J_0^2(2\pi) = 0.048$. Equation (10.8) is a much less restrictive definition than (10.7). According to [1], a popular rule of thumb for modern digital communications is to define the coherence time as the geometric mean of (10.7) and (10.8). That is

$$T_c = \sqrt{\frac{9}{16\pi B_D^2}} = \frac{0.423}{B_D} \quad (10.9)$$

10.1.2 Channel Classification

We use the above parameters to classify fading channels.

- *Flat fading.* Flat fading is also called frequency nonselective fading. If a wireless channel has a constant gain and linear phase response over a bandwidth which is greater than the signal bandwidth, then the signal will undergo flat or frequency nonselective fading. This type of fading is historically the most common fading model used in the literature. In flat fading, the multipath structure is such that the spectral characteristics of the transmitted signal is preserved at the receiver. However, the strength of the signal changes with time, due to the variation of the gain of the channel caused by multipath. In terms of the parameters we just defined, the flat fading channel is characterized by

$$B_c \gg B_s$$

or equivalently

$$\sigma_\tau \ll T_s$$

where B_s is the signal bandwidth and T_s is the symbol period of the signal. *That is, a fading channel is flat or frequency nonselective if the channel coherence bandwidth is much greater than the signal bandwidth, or equivalently, the rms delay spread is much smaller than the signal symbol period.* Since the frequency response is flat, the impulse response of a flat fading channel can be modeled as a delta function without delay. The strength of the delta function changes with time.

- *Frequency selective fading.* If the channel has a constant gain and a linear phase

response over a bandwidth which is smaller than the signal bandwidth, then the signal undergoes frequency selective fading. This is caused by such a multipath structure that the received signal contains multiple versions of the transmitted signal with different attenuations and time delays. Due to the time dispersion of the transmitted signal, the received signal has intersymbol interference. Thus the received signal is distorted. Viewed in the frequency domain, some frequency components have greater gains than others. Frequency selective fading channels are much more difficult to model than flat fading channels. Each multipath signal must be modeled and the channel is considered as a linear filter. Models are usually developed based on wideband measurement. In terms of the parameters, the frequency selective fading channel is characterized by

$$B_c < B_s$$

or equivalently

$$\sigma_\tau > T_s$$

That is, a fading channel is frequency selective if the channel coherence bandwidth is smaller than the signal bandwidth, or equivalently, the rms delay spread is greater than the signal symbol period. This rule may be too stringent for identifying a channel as frequency selective. A common rule of thumb is that a channel is frequency selective if $\sigma_\tau > 0.1T_s$, although this depends on the specific type of modulation used [1].

- *Fast fading.* If the channel impulse response changes rapidly within a signal symbol duration, the channel is classified as a fast fading channel, otherwise it is classified as a slow fading channel. The fast change of the channel impulse response is caused by the motion, or equivalently, the Doppler spreading. *Quantitatively, when the channel coherence time is smaller than the symbol duration, or equivalently, the Doppler spreading is greater than the signal bandwidth, a signal undergoes fast fading.* That is, if

$$T_s > T_c$$

or equivalently

$$B_s < B_D$$

the channel is a fast fading channel.

- *Slow fading.* In a slow fading channel, the channel impulse response changes at a much slower rate than the symbol rate. *The channel coherence time is much greater than the symbol duration, or equivalently, the Doppler spreading is much smaller than the signal bandwidth.* That is, a signal undergoes slow

Based on multipath time delay spread	
Flat Fading $B_c \gg B_s$ $\sigma_\tau \ll T_s$	Frequency Selective Fading $B_c < B_s$ $\sigma_\tau > T_s$
Based on Doppler frequency spread	
Fast Fading $B_D > B_s$ $T_c < T_s$	Slow Fading $B_D \ll B_s$ $T_c \gg T_s$

Table 10.1 Fading channel classification.

fading if

$$T_s \ll T_c$$

or equivalently

$$B_s \gg B_D$$

In a slow fading channel, the channel impulse response can be considered static within one or several symbol durations.

Table 10.1 is a summary of the channel classifications.

A combination of the low data rate (i.e., T_s is large) and the high speed of the mobile unit corresponds to fast fading since the mobile experiences rapid electromagnetic field changes in a very short time (i.e., T_c is small). In the contrary, a combination of high data rate and low speed corresponds to slow fading. Of course, when the mobile unit is not moving, the channel is a slow fading channel regardless of the data rate.

It should be pointed out that when a channel is classified as a fast or slow fading channel, it does not classify whether the channel is flat fading or frequency selective fading. A *flat fading, fast fading* channel is a channel whose impulse response is a delta function with a strength that varies faster than the symbol rate. In a *frequency selective, fast fading* channel, the amplitude, phase and time delay of any of the multipath components vary faster than the symbol rate. The other two combinations are the *flat, slow fading* channel and *frequency selective, slow fading* channel. As a matter of fact, these two are the common models in practice since fast fading only occurs for very low data rates at which the mobile can move a long distance and experiences a wide range of signal strength change in a symbol period. We will focus on the *flat, slow fading* channel and *frequency selective, slow fading* channel in the rest of this chapter.

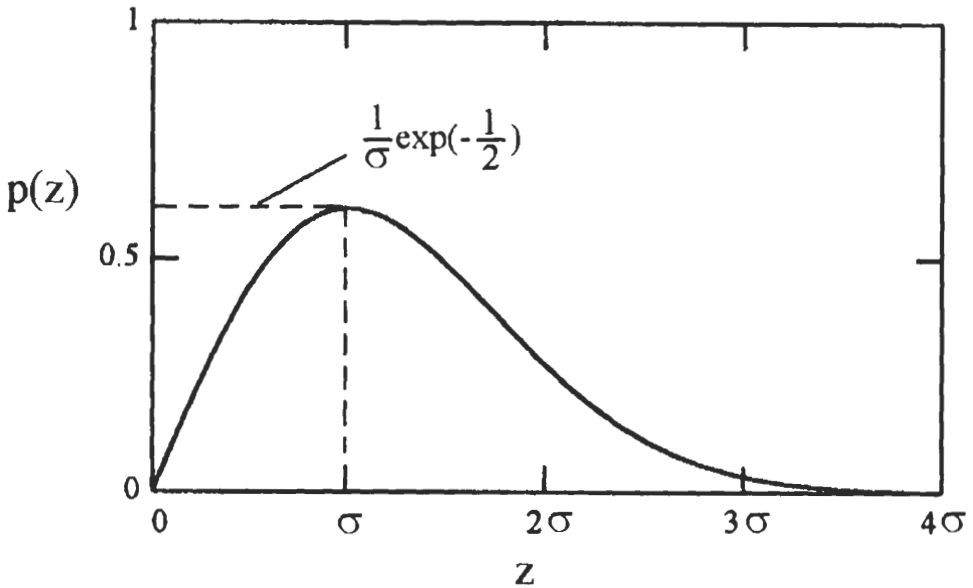


Figure 10.2 Rayleigh distribution density.

10.1.3 Fading Envelope Distributions

In a multipath channel, the received signal consists of a large number of plane waves, whose complex low-pass signal

$$\tilde{r}(t) = r_I(t) + jr_Q(t)$$

can be modeled as a Gaussian random process. If none of the multipath components is dominant, $r_I(t)$ and $r_Q(t)$ are Gaussian processes with zero mean and a variance of σ^2 . The envelope $z(t) = |\tilde{r}(t)|$ obeys the *Rayleigh distribution*. The probability density function (PDF) of the Rayleigh envelope is given by

$$p(z) = \frac{z}{\sigma^2} \exp\left(-\frac{z^2}{2\sigma^2}\right), \quad z \geq 0 \quad (10.10)$$

and $p(z) = 0$ for $z < 0$. Rayleigh fading agrees very well with empirical observations for macrocellular applications. The plot of $p(z)$ is given in Figure 10.2. The maximum $p(z)$ occurs at $z = \sigma$.

The probability that the envelope does not exceed a specific value Z is given by

the cumulative distribution function (CDF)

$$P(Z) = \Pr(z \leq Z) = \int_0^Z p(z) dz = 1 - \exp\left(-\frac{Z^2}{2\sigma^2}\right)$$

The mean value of the Rayleigh envelope is

$$E\{z\} = \int_0^\infty zp(z) dz = \sqrt{\frac{\pi}{2}}\sigma = 1.2533\sigma$$

The average power of the Rayleigh envelope is

$$E\{z^2\} = \Omega = 2\sigma^2$$

The ac power of the envelope is the variance

$$\begin{aligned}\sigma_z^2 &= E\{z^2\} - (E\{z\})^2 = 2\sigma^2 - \left(\sqrt{\frac{\pi}{2}}\sigma\right)^2 \\ &= \left(2 - \frac{\pi}{2}\right)\sigma^2 = 0.4292\sigma^2\end{aligned}$$

The Rayleigh density can be written in terms of the average power Ω as

$$p(z) = \frac{2z}{\Omega} \exp\left(-\frac{z^2}{\Omega}\right), \quad z \geq 0 \quad (10.11)$$

If a dominant component, such as the LOS or specular component, is present in the multipath channel, $r_I(t)$ and $r_Q(t)$ have nonzero mean and the envelope has a *Rician distribution*

$$p(z) = \frac{z}{\sigma^2} \exp\left(-\frac{z^2 + A^2}{2\sigma^2}\right) I_0\left(\frac{Az}{\sigma^2}\right), \quad z \geq 0 \quad (10.12)$$

and $p(z) = 0$ for $z < 0$, where A is the peak amplitude of the dominant signal and $I_0(\cdot)$ is the zeroth modified Bessel function of the first kind. Rician fading is very often observed in microcellular applications. A parameter K is often defined for a Rician channel

$$K = \frac{A^2}{2\sigma^2} \quad (10.13)$$

which is the ratio of the power of the specular signal over the power of the scattered components. In terms of dB, we have

$$K(\text{dB}) = 10 \log \frac{A^2}{2\sigma^2}$$

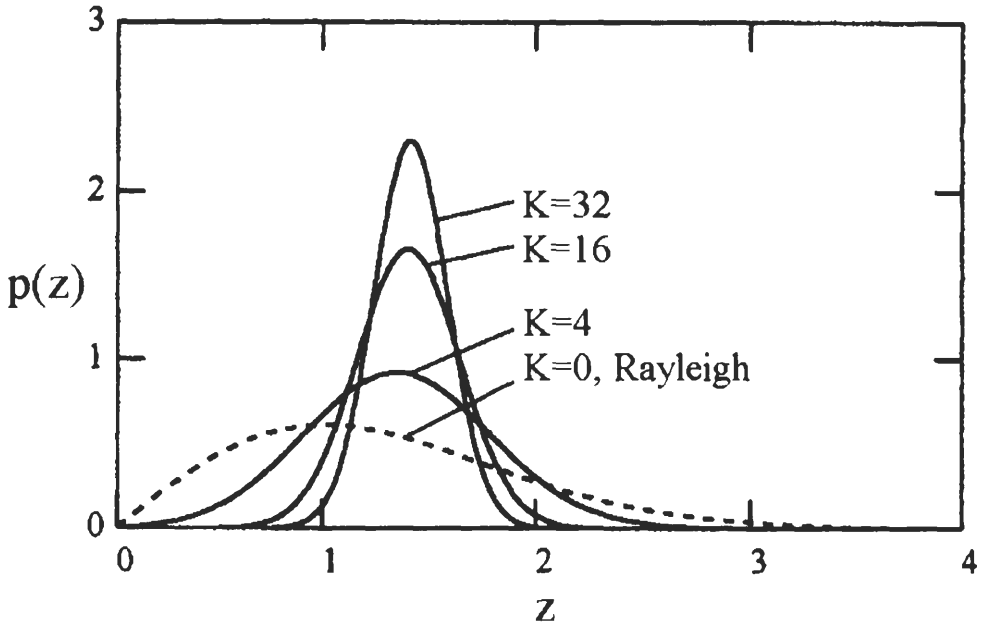


Figure 10.3 Rician distribution density curves for a fixed average power $\Omega = 2$ so that when $K = 0$, the Rayleigh curve is exactly the same as in Figure 10.2.

The average power

$$E\{z^2\} = \Omega = A^2 + 2\sigma^2 = 2\sigma^2(1 + K)$$

The Rician density can be written in terms of K and Ω ,

$$p(z) = \frac{2z(K+1)}{\Omega} \exp\left(-K - \frac{(K+1)z^2}{\Omega}\right) I_0\left(2z\sqrt{\frac{K(K+1)}{\Omega}}\right), \quad z \geq 0 \quad (10.14)$$

Figure 10.3 shows the Rician distribution density for some values of K . When $K = 0$, the Rician distribution becomes the Rayleigh distribution. When $K = \infty$ the channel does not exhibit any fading. The curves are for a fixed average power $\Omega = 2$, so that when $K = 0$, $\Omega = 2\sigma^2$ and $p(z)$ is identical to that given in (10.11).

Another model of envelope distribution is the Nakagami distribution which was selected to fit empirical data for long-distance HF channels. The Nakagami distribution is given by [4]

$$p(z) = \frac{2m^m z^{2m-1}}{\Gamma(m)\Omega^m} \exp\left\{-\frac{mz^2}{\Omega}\right\}, \quad m \geq \frac{1}{2} \quad (10.15)$$

where $\Omega = E\{z^2\}$. When $m = 1$, the Nakagami distribution becomes the Rayleigh distribution. It is claimed to provide a closer match to some experimental data than Rayleigh or Rician distributions. However, the claims were based on fitting envelope statistics around the mean or median, rather than the near-zero region which is fundamental to system performance over fading channels [5]. Therefore, the results based on a Nakagami distribution appear questionable for practical use, and they will not be discussed further in this chapter.

10.2 DIGITAL MODULATION IN SLOW, FLAT FADING CHANNELS

In a flat fading channel, the signal undergoes a multiplicative variation. In general this multiplicative factor is complex, that is, the signal amplitude as well as phase are affected. If we further assume that the fading is slow, then the amplitude attenuation and phase shift of the received signal can be considered constant over at least a symbol duration. Therefore, if the transmitted equivalent low-pass complex signal is $\tilde{s}(t)$, the received equivalent low-pass complex signal can be written as

$$\tilde{r}(t) = ze^{-j\phi}\tilde{s}(t) + \tilde{n}(t) \quad (10.16)$$

where z is the amplitude of the signal (assuming $\tilde{s}(t)$ has a unit amplitude), ϕ is the phase shift of the signal caused by the channel, and $\tilde{n}(t)$ is the equivalent low-pass complex additive Gaussian noise.

The received signal may be coherently detected or noncoherently detected, depending on whether it is possible to accurately estimate the phase shift ϕ . In either case, the average error probability can be evaluated by averaging the error probability for a fixed amplitude z over the entire range of z . That is

$$P_e = \int_0^\infty P_e(\gamma_b)p(\gamma_b)d\gamma_b \quad (10.17)$$

where

$$\gamma_b = z^2 E_b/N_o$$

is the signal-to-noise ratio with fading for a particular value of z , $P_e(\gamma_b)$ is the symbol or bit error probability conditioned on a fixed γ_b , and $p(\gamma_b)$ is the probability density function of γ_b , and P_e is the average symbol or bit error probability.

10.2.1 Rayleigh Fading Channel

For Rayleigh fading channel, z has a Rayleigh distribution, thus z^2 and γ_b have a

chi-square distribution with two degree of freedom. That is

$$p(\gamma_b) = \frac{1}{\Gamma} \exp\left(-\frac{\gamma_b}{\Gamma}\right), \quad \Gamma \geq 0 \quad (10.18)$$

where

$$\Gamma = E\{z^2\} \frac{E_b}{N_o}$$

is the average value of the signal-to-noise ratio.¹

Substituting the error probability expression of a specific modulation in the AWGN channel and (10.18) into (10.17), we can obtain the error probability expression of the modulation in a slow, flat, Rayleigh fading channel. For many important modulation schemes, the P_e expression in the AWGN channel is in the form of Q function or exponential function. Fortunately, for these two function forms, the P_e expressions in the fading channel are in closed forms. For other schemes numerical calculation is needed to obtain the error probabilities in the fading channel.

For many schemes, the symbol or bit error rate in the AWGN channel can be expressed in one of the two general forms as

$$P_e = CQ\left(\sqrt{\frac{\delta E_b}{N_o}}\right)$$

$$P_e = C \exp\left(-\frac{\delta E_b}{N_o}\right)$$

where C and δ are constants (see Table 4.7 for many examples). In the fading channel, the signal-to-noise ratio E_b/N_o becomes $\gamma_b = z^2 E_b/N_o$. Correspondingly the conditional error probabilities are

$$P_e(\gamma_b) = CQ\left(\sqrt{\delta\gamma_b}\right) \quad (10.19)$$

$$P_e(\gamma_b) = C \exp(-\delta\gamma_b) \quad (10.20)$$

Substituting (10.19) or (10.20) and (10.18) into (10.17), we can obtain the corresponding symbol or bit error probabilities.

¹ From Section 10.1.3 we know that $z^2(t) = r_I^2(t) + r_Q^2(t)$ where $r_I(t)$ and $r_Q(t)$ are Gaussian random processes. It is well known that the sum of n Gaussian random variables obeys a distribution called chi-square (χ^2) distribution with n degrees of freedom. See [6, p. 109]

For the exponential function $P_e(\gamma_b)$, (10.17) can be evaluated easily. The result is

$$P_e = \frac{C}{1 + \delta\Gamma} \quad (10.21)$$

For the Q function $P_e(\gamma_b)$, (10.17) is evaluated using the following two formulas. The first is from the integral table [7]

$$\int_0^{\infty} [1 - \operatorname{erf}(\beta x)] e^{-\mu x^2} \cdot x dx = \frac{1}{2\mu} \left(1 - \frac{\beta}{\sqrt{\mu + \beta^2}} \right) \quad (10.22)$$

and the second is the well-known relation between the error function and the Q function

$$1 - \operatorname{erf}(x) = 2Q(\sqrt{2}x) \quad (10.23)$$

which is used to convert the Q function into the error function in order to use (10.22). Substituting (10.19) and (10.18) into (10.17), using (10.23), and making a variable change $\gamma_b = x^2$, we have

$$P_e = \int_0^{\infty} \frac{C}{\Gamma} [1 - \operatorname{erf}(\sqrt{\frac{\delta}{2}}x)] e^{-\frac{x^2}{\Gamma}} \cdot x dx$$

Recognizing $\sqrt{\delta/2} = \beta$ and $1/\Gamma = \mu$ in (10.22), the above is equal to

$$P_e = \frac{C}{2} \left[1 - \sqrt{\frac{\delta\Gamma}{2 + \delta\Gamma}} \right] \quad (10.24)$$

Using general expressions (10.21) and (10.24), error rates of many modulation schemes in the slow, flat, Rayleigh channel can be easily found out.

For *coherent BPSK, QPSK, OQPSK, and MSK*, their P_b expressions are the same in the AWGN channel. That is, $P_b = Q\left(\sqrt{2E_b/N_o}\right)$. This means $C = 1$ and $\delta = 2$ in (10.24). The result is

$$P_b = \frac{1}{2} \left[1 - \sqrt{\frac{\Gamma}{1 + \Gamma}} \right], \quad (\text{coherent BPSK, QPSK, OQPSK, and MSK}) \quad (10.25)$$

For *optimum differential BPSK* (Figure 4.7 and (4.10)), $P_b = \frac{1}{2} \exp(-\frac{E_b}{N_o})$ in

the AWGN channel, which makes $C = 1/2$ and $\delta = 1$. From (10.21) we have

$$P_b = \frac{1}{2(1 + \Gamma)}, \quad (\text{optimum DBPSK}) \quad (10.26)$$

For *coherent binary FSK*, $P_b = Q\left(\sqrt{E_b/N_o}\right)$ in the AWGN channel. This implies $C = 1$ and $\delta = 1$. From (10.24) we obtain

$$P_b = \frac{1}{2} \left[1 - \sqrt{\frac{\Gamma}{2 + \Gamma}} \right], \quad (\text{coherent BFSK}) \quad (10.27)$$

For *noncoherent orthogonal BFSK*, $P_b = \frac{1}{2} \exp(-\frac{E_b}{2N_o})$ in the AWGN channel. This leads to $C = 1/2$ and $\delta = 1/2$, thus

$$P_b = \frac{1}{2 + \Gamma}, \quad (\text{noncoherent orthogonal BFSK}) \quad (10.28)$$

For large signal-to-noise ratios, the above error probability expressions can be approximated as

$$P_b \approx \frac{1}{4\Gamma}, \quad (\text{coherent BPSK, QPSK/OQPSK, MSK})$$

$$P_b \approx \frac{1}{2\Gamma}, \quad (\text{coherent BFSK and optimum DBPSK})$$

$$P_b \approx \frac{1}{\Gamma}, \quad (\text{noncoherent orthogonal BFSK})$$

For *GMSK*, the AWGN channel bit error rate is $P_b = Q\left(\sqrt{2\varepsilon E_b/N_o}\right)$. Thus $C = 1$, $\delta = 2\varepsilon$ and

$$P_b = \frac{1}{2} \left[1 - \sqrt{\frac{\varepsilon\Gamma}{1 + \varepsilon\Gamma}} \right] \approx \frac{1}{4\varepsilon\Gamma}, \quad (\text{coherent GMSK}) \quad (10.29)$$

where

$$\varepsilon = \begin{cases} 0.68, & \text{for } BT_s = 0.25 \\ 0.85, & \text{for } BT_s = \infty \end{cases}$$

For $\pi/4$ -*DQPSK*, the AWGN channel bit error rate is

$$P_b \approx Q\left(\sqrt{4E_b/N_o} \sin(\pi/4\sqrt{2})\right) = Q\left(\sqrt{1.112E_b/N_o}\right)$$

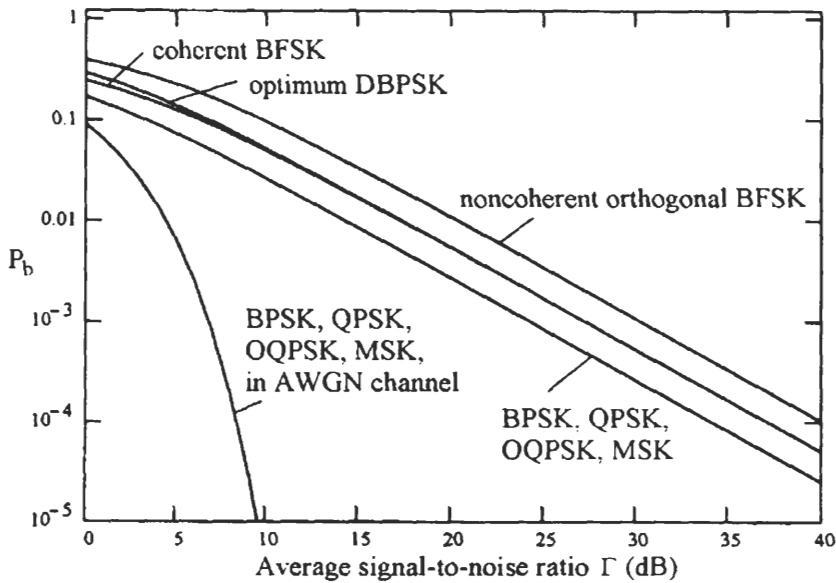


Figure 10.4 Bit error rates of several common modulation schemes in a slow, flat, Rayleigh fading channel.

(see Table 4.7). Thus $C = 1$ and $\delta = 1.112$. From (10.24) we have

$$P_b = \frac{1}{2} \left[1 - \sqrt{\frac{0.556\Gamma}{1 + 0.556\Gamma}} \right] \approx \frac{1}{2.224\Gamma}, \quad (\text{optimum } \pi/4 - \text{DQPSK}) \quad (10.30)$$

The list can go on for many other schemes whose error rate expressions have the forms in (10.19) or (10.20).

Figures 10.4 and 10.5 illustrate the error performance of the above schemes in the slow, flat, Rayleigh channel. It is seen that Rayleigh fading causes a significant loss in signal-to-noise ratio for the same bit error probability, in comparison with the AWGN channel. For example at $P_b = 10^{-3}$, which is considered to be adequate for voice communications, the increase in the average signal-to-noise ratio is about 15 to 20 dB, depending on the particular modulation scheme used. The losses can be significantly reduced by using diversity techniques and error-control coding techniques.

10.2.2 Rician Fading Channel

For the Rician fading channel the amplitude z of the received signal $r(t)$ in (10.16)

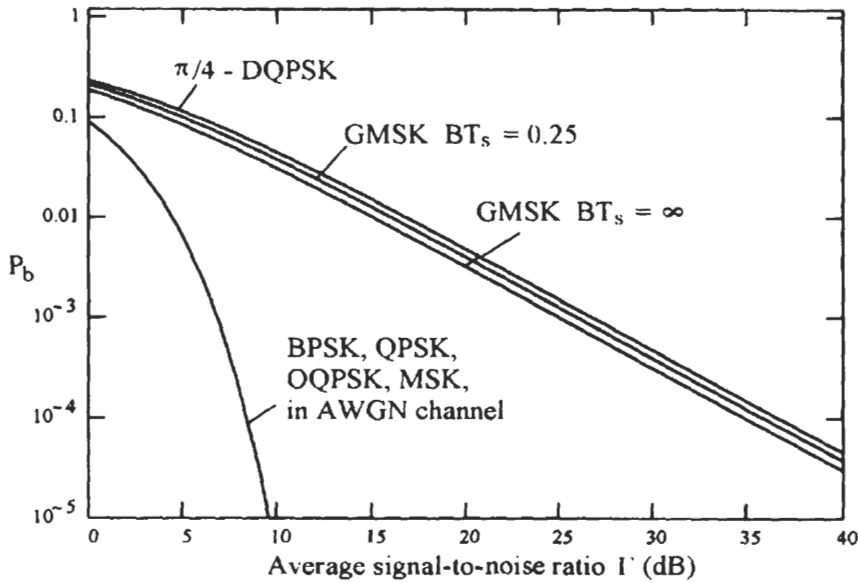


Figure 10.5 Bit error rates of GMSK and $\pi/4$ -DQPSK in a slow, flat, Rayleigh fading channel.

has a density function given in (10.12). Closed-form expressions for the error probabilities of DPSK and orthogonal FSK in Rician fading channels are found in [8]. First the Rician density in (10.12) is transformed to an expression where the random variable is the instantaneous signal-to-noise ratio $\gamma_b = z^2 E_b/N_o$ instead of the signal amplitude z .

$$p(\gamma_b) = \frac{K+1}{\Gamma} \exp\left(-\frac{\gamma_b(K+1) + K\Gamma}{\Gamma}\right) I_0\left(\sqrt{\frac{4(K+1)K\gamma_b}{\Gamma}}\right) \quad (10.31)$$

where K is the ratio of the power of the specular signal over the power of the scattered components defined in (10.13). Using (10.31) and appropriate $P_e(\gamma_b)$ in (10.17) and again using the appropriate entry in the integral table [7], we obtain

$$P_b = \frac{K+1}{2(K+1+\Gamma)} \exp\left(-\frac{K\Gamma}{K+1+\Gamma}\right), \quad (\text{optimum DBPSK}) \quad (10.32)$$

and

$$P_b = \frac{K+1}{2(K+1)+\Gamma} \exp\left(-\frac{K\Gamma}{2(K+1)+\Gamma}\right), \quad (\text{noncoherent BFSK}) \quad (10.33)$$

Figures 10.6 and 10.7 show the plots from (10.32) and (10.33).

For other modulation schemes, we can substitute (10.31) and the appropriate AWGN error rate expressions into (10.17) and numerically evaluate their error performance in the slow, flat, Rician channel. Figures 10.8 to 10.12 are the numerical results. Figure 10.8 is for BPSK, QPSK/OQPSK, and MSK. Figure 10.9 is for BFSK. Figure 10.10 is for GMSK ($BT = \infty$) and Figure 10.11 is for GMSK ($BT = 0.25$). Figure 10.12 is for $\pi/4$ -DQPSK. It is seen from Figures 10.8 to 10.12 that the curves are more compact and more evenly spaced than those in Figures 10.6 and 10.7.

10.3 DIGITAL MODULATION IN FREQUENCY SELECTIVE CHANNELS

In a frequency selective fading channel, the received signal contains multiple delayed versions of the transmitted signal. The multipath signals cause intersymbol interference (ISI) which results in an irreducible BER floor. The BER falls initially with the increase of the signal-to-noise ratio (E_b/N_o), and stops falling when the signal-to-noise ratio is sufficiently high at which the errors are almost exclusively caused by the ISI. From the cause of the error floor, it is clear that the BER floor is directly related to the delays of the multipath components.

Simulation is the main tool of studying BER behavior in frequency selective fading channels. Chuang [9] simulated the error performance of unfiltered BPSK, QPSK, OQPSK, and MSK schemes in frequency selective fading channels. Chuang also simulated the error performance of GMSK with various BT_b of the premodulation filter and QPSK with a raised-cosine Nyquist pulse (RC-QPSK)² using various roll-off factors α .

Chuang found through simulation that coherent detection performs better than differential detection in frequency selective fading channels. So his study was concentrated on coherent detection.

Figure 10.13 presents the irreducible BER performance for unfiltered BPSK, QPSK, OQPSK, and MSK with coherent detection for a channel with a Gaussian-shaped power delay profile. The parameter d is the rms delay spread normalized

² The pulse shape of RC-QPSK is obtained by filtering the baseband NRZ pulse with a raised-cosine frequency response

$$H(f) = \begin{cases} 1, & \text{for } |f| < 2W_0 - W \\ \cos^2\left(\frac{\pi}{4} \frac{|f| + W - 2W_0}{W - W_0}\right), & \text{for } 2W_0 - W < |f| < W \\ 0, & \text{for } |f| > W \end{cases}$$

where W is the absolute bandwidth of the filter and $W_0 = 1/2T_s$ is the Nyquist bandwidth. The roll-off factor is defined as $\alpha = (W - W_0)/W_0$. The larger the α , the larger the bandwidth W .

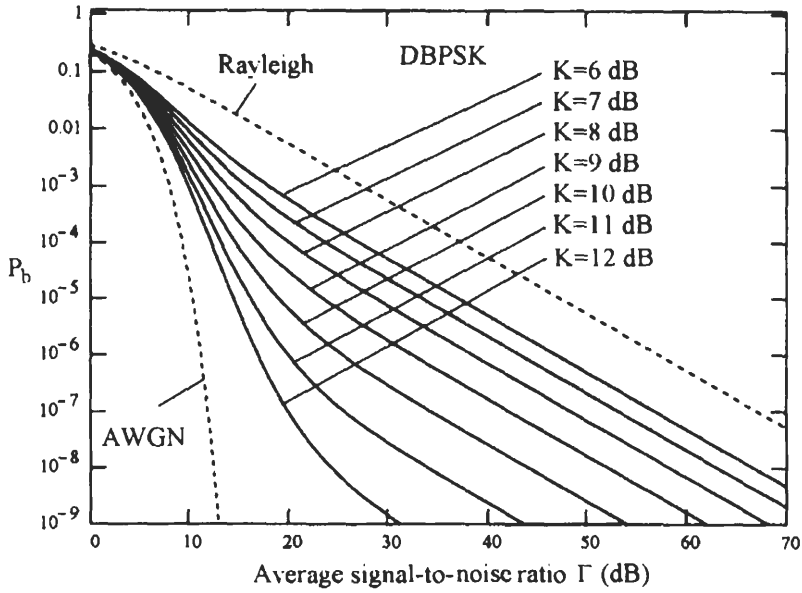


Figure 10.6 Bit error rate of optimum DBPSK in Rician fading channel.

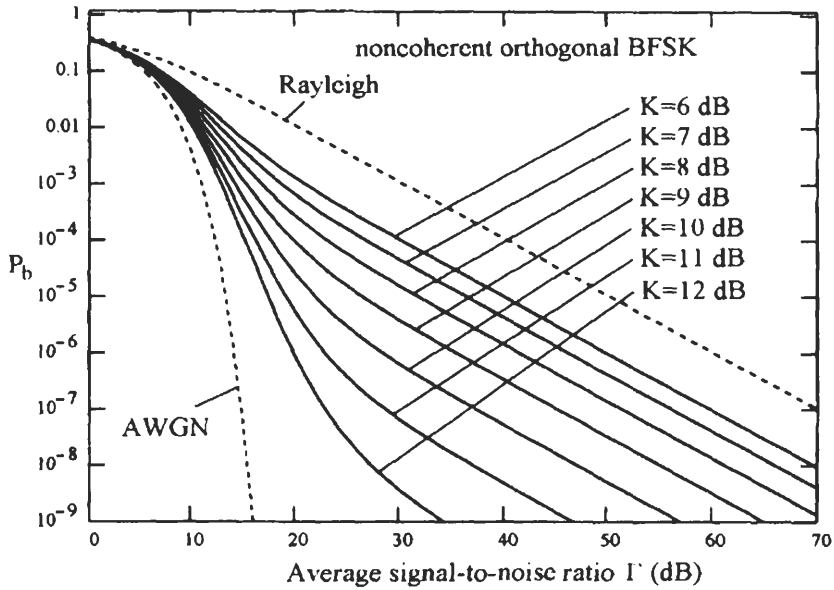


Figure 10.7 Bit error rate of noncoherent orthogonal BFSK in Rician fading channel.

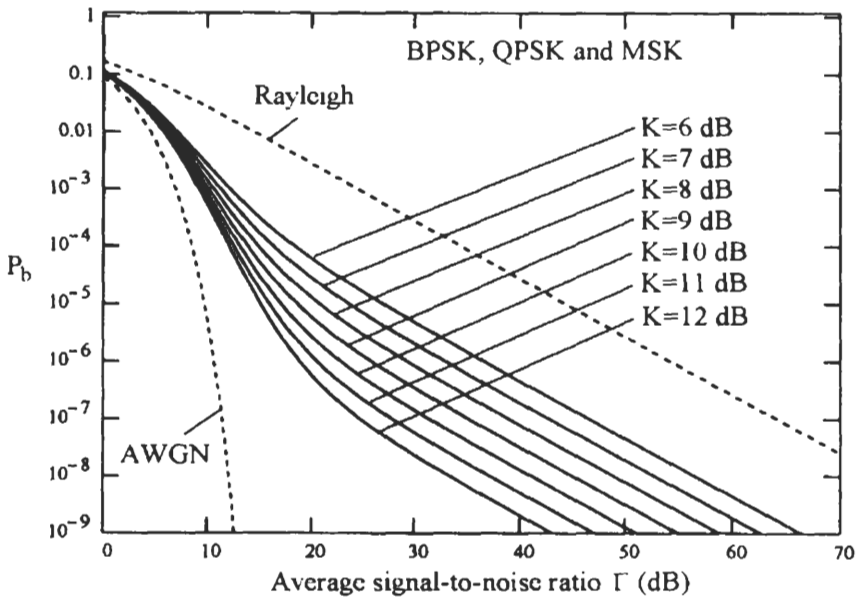


Figure 10.8 Bit error rate of BPSK, QPSK/OQPSK, MSK in Rician fading channel.

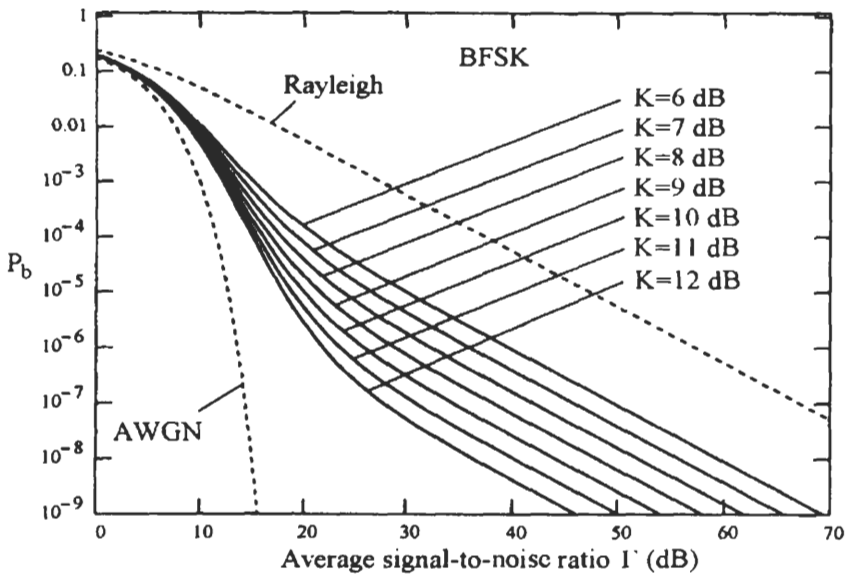


Figure 10.9 BER of BFSK in Rician fading channel.

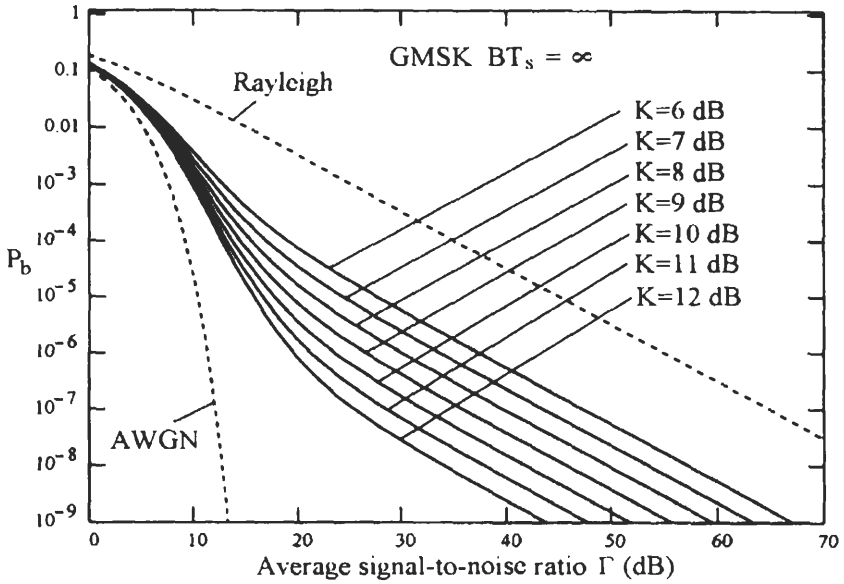


Figure 10.10 BER of GMSK ($BT = \infty$) in slow, flat, Rician fading channel.

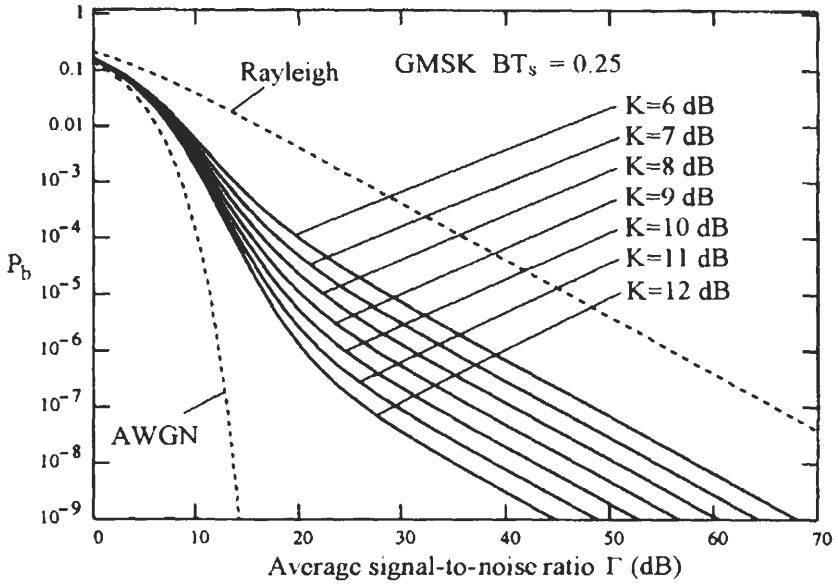


Figure 10.11 BER of GMSK ($BT = 0.25$) in slow, flat, Rician fading channel.

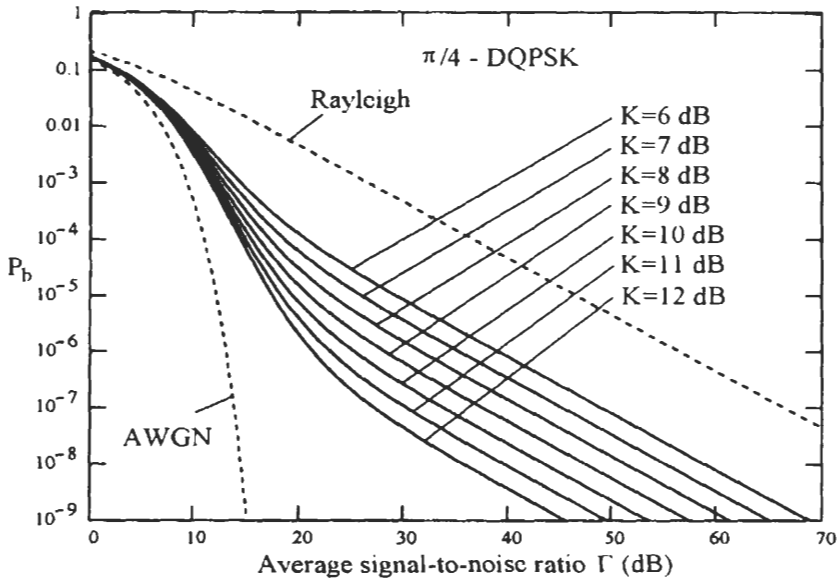


Figure 10.12 BER of $\pi/4$ -DQPSK in slow, flat, Rician fading channel.

by the symbol period (i.e., $d = \sigma_\tau/T_s$). This figure indicates the performance is ranked in the following order: 1) BPSK, 2) QPSK, 3) OQPSK, 4) MSK. The performance of BPSK is the best because cross-rail interference does not exist. Cross-rail interference exists in quadrature modulations (QPSK, OQPSK, and MSK), where the modulator has two rails (I- and Q- channels). The two bit sequences will have no interference to each other if ideal channel condition is maintained and coherent demodulation is used. However, in multipath fading channels, these two sequences cannot be completely separated at the demodulator due to the multipath fading condition. Both OQPSK and MSK have a $T_s/2$ timing offset between two bit sequences, hence the cross-rail ISI is more severe. Therefore their performances are inferior to that of QPSK.

The normalization factor for parameter d in Figure 10.13 is the symbol period T_s , during which two bits are transmitted in QPSK, OQPSK, and MSK, whereas only one bit is transmitted in BPSK. In other words, the comparison of error floor in Figure 10.13 is based on different bit rate or information throughput. A fairer comparison should be based on $d' = \sigma_\tau/T_b$, that is, on the same bit rate. Figure 10.14 is the same set of curves as in Figure 10.13 plotted against d' . It is clear from the figure that four-level modulations are more resistant to delay spread than BPSK for the same information throughput. The intuitive reason for this is that for the same bit rate the four-level modulations have twice the length of the symbol period of that

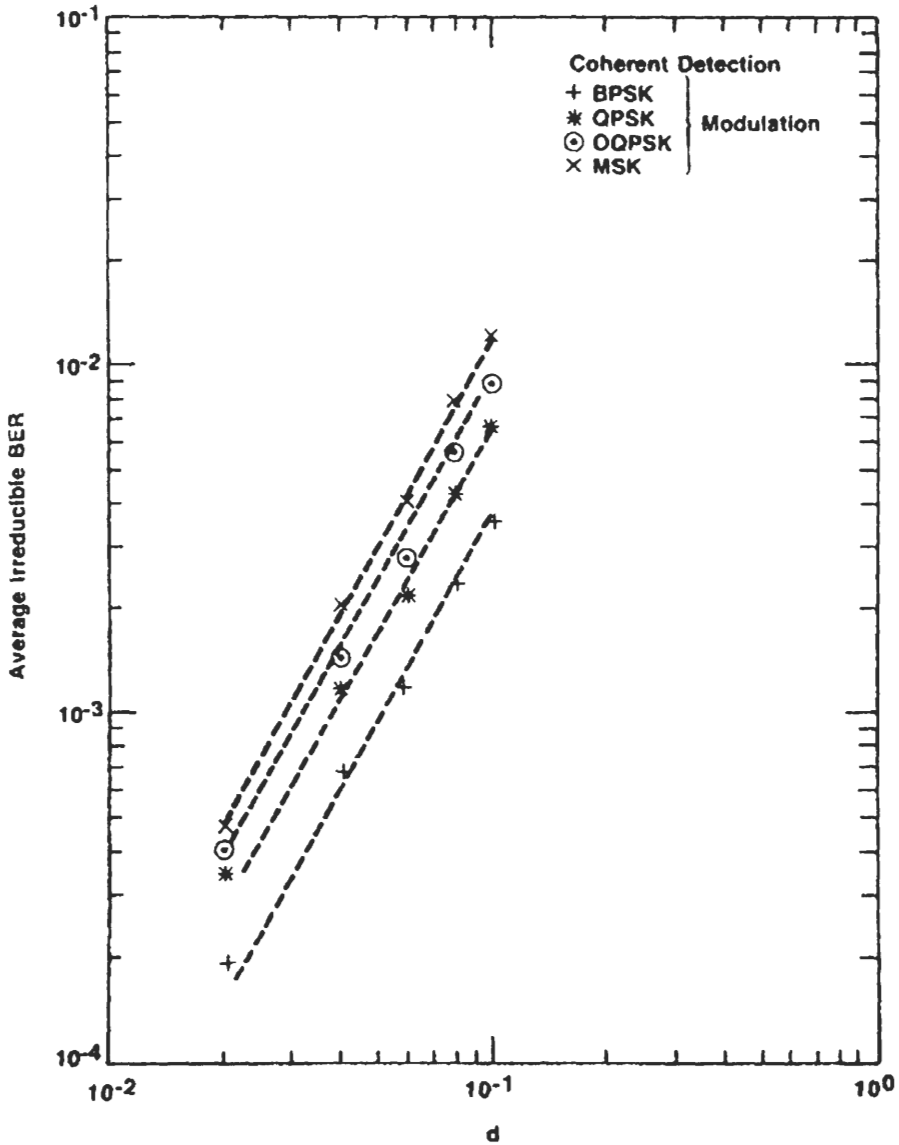


Figure 10.13 The irreducible BER performance for different modulations with coherent detection for a channel with a Gaussian-shaped power delay profile. The parameter d is the rms delay spread normalized by the symbol period. From [9]. Copyright © 1987 IEEE.

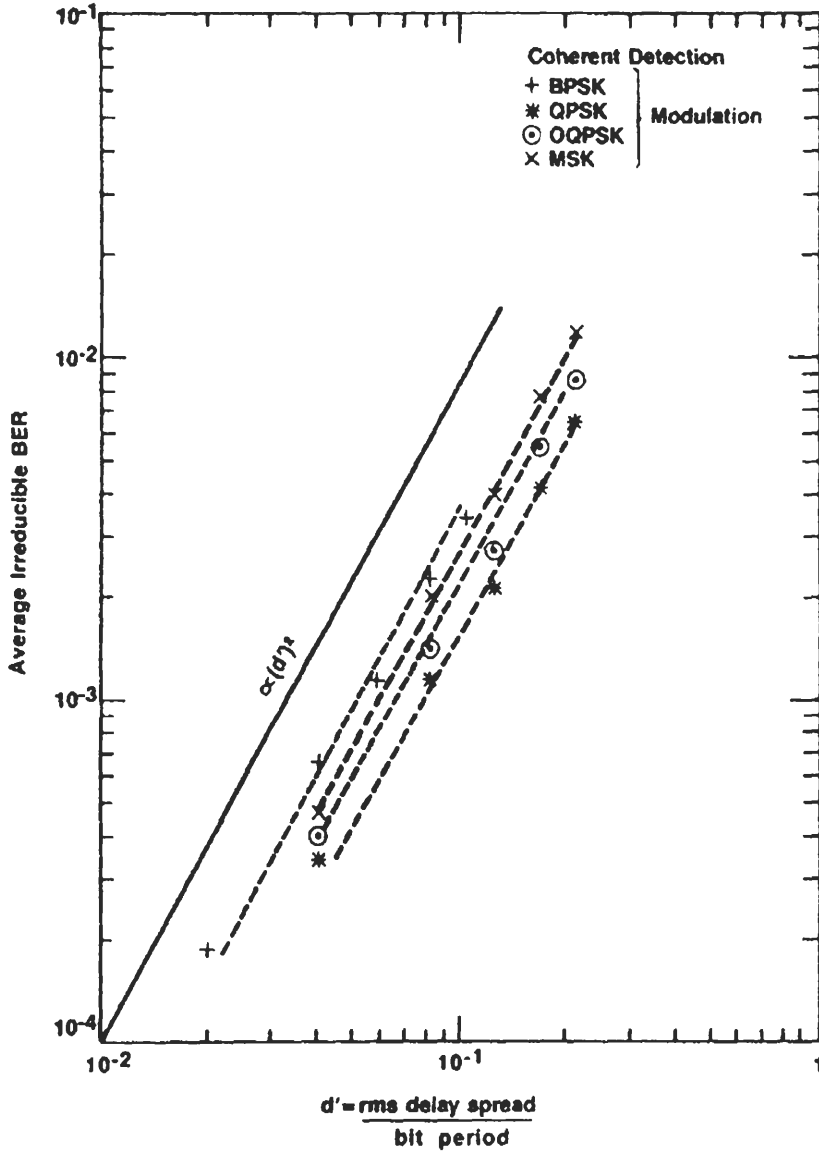


Figure 10.14 The same set of curves as in Figure 10.13, plotted against rms delay spread normalized by the bit period instead of symbol period. From [9]. Copyright © 1987 IEEE.

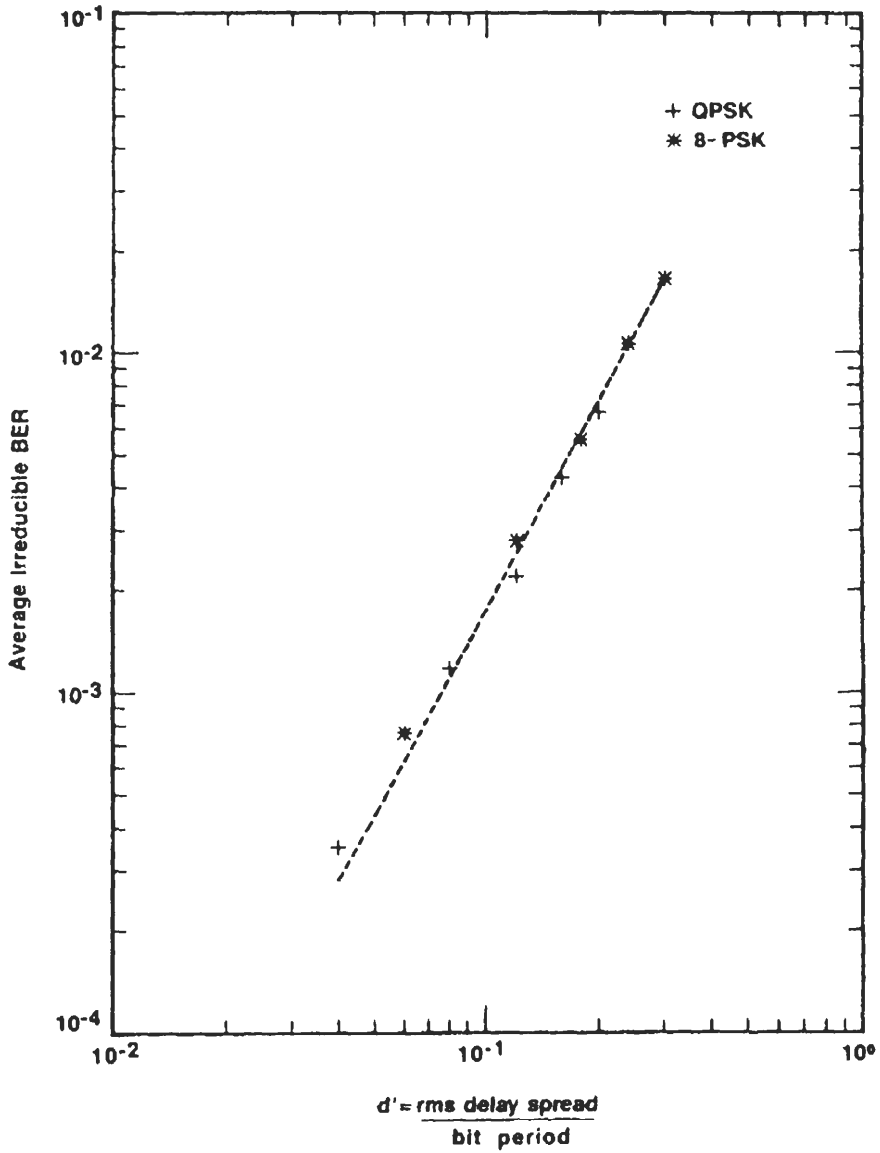


Figure 10.15 The irreducible BER performance for QPSK and 8-PSK. The parameter d' is the rms delay spread normalized by the bit period. From [9]. Copyright © 1987 IEEE.

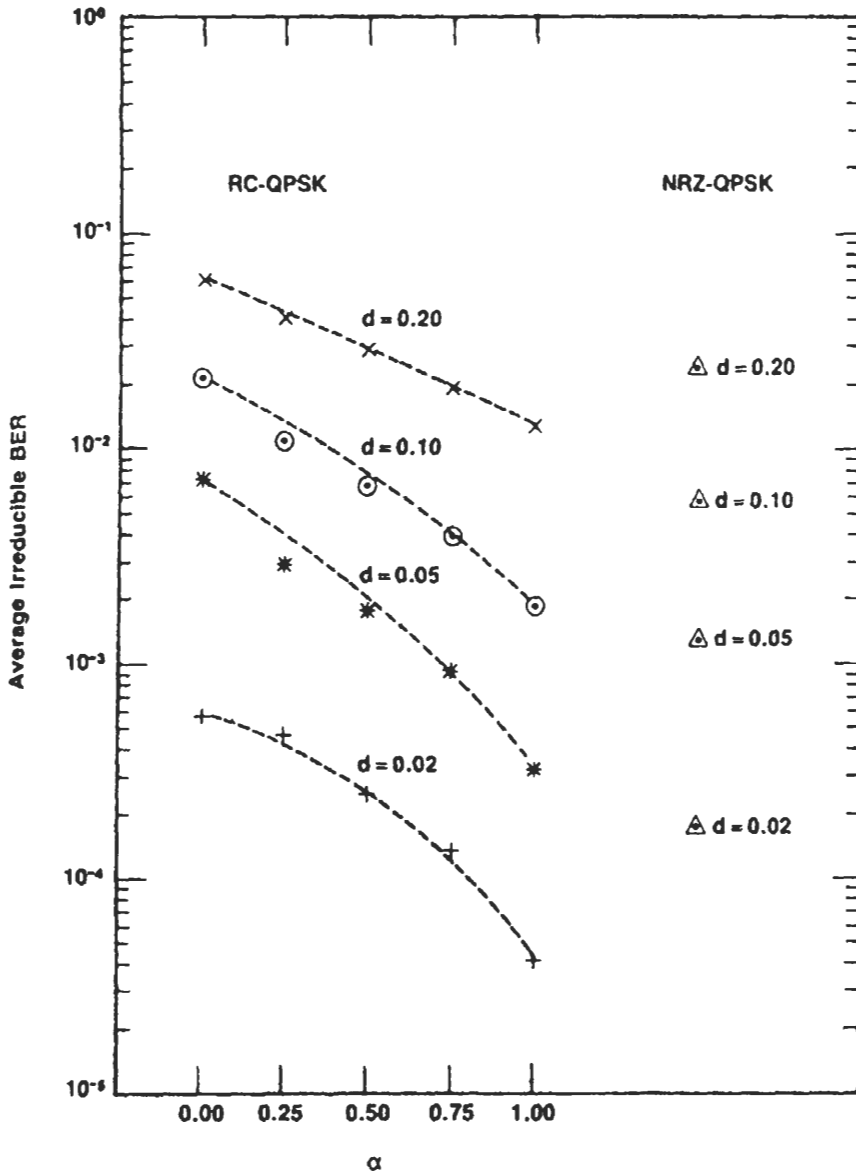


Figure 10.16 The irreducible BER performance for RC-QPSK with coherent detection for a channel with a measured power delay profile in Figure 10.18. Results for the unfiltered QPSK are also shown for comparison. The parameter α is the roll-off factor in raised-cosine filter. The parameter d is the rms delay spread normalized by the symbol period. From [9]. Copyright © 1987 IEEE.

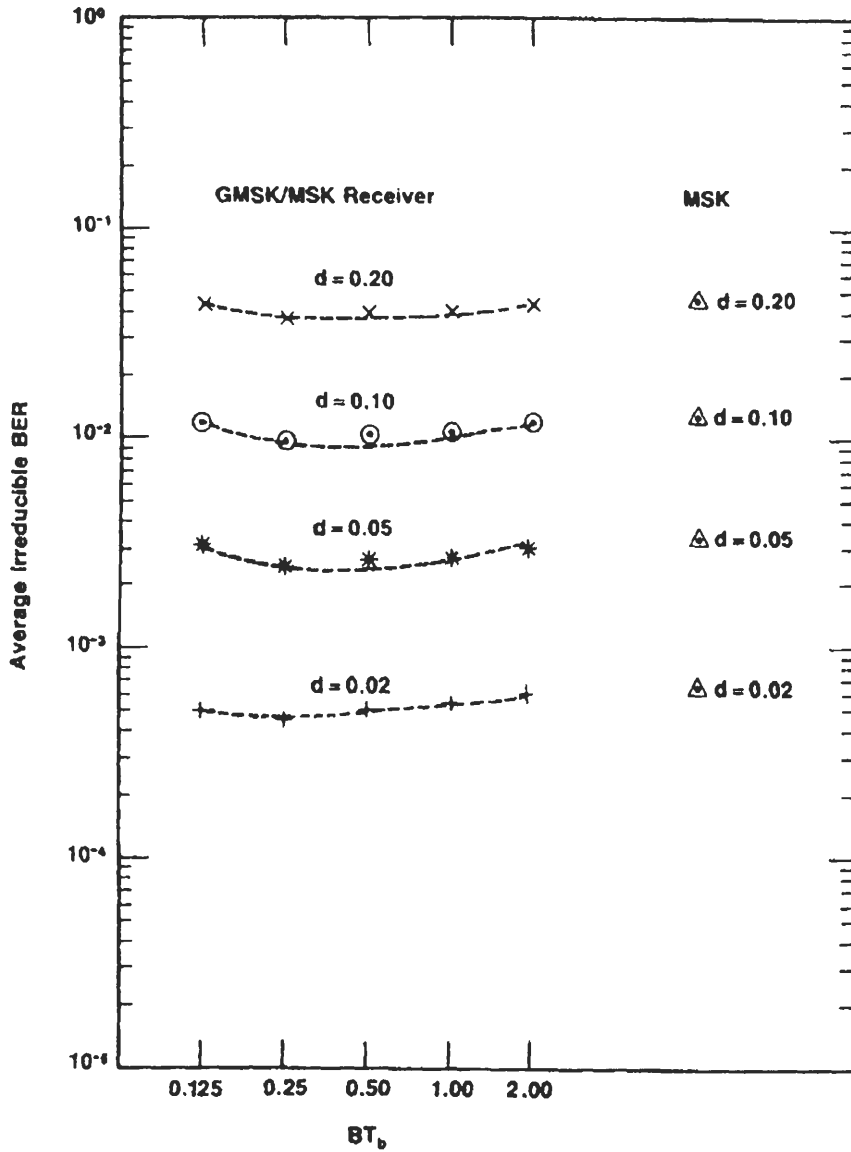


Figure 10.17 The irreducible BER performance for GMSK with coherent detection for a channel with a measured power delay profile as shown in Figure 10.18. Results for the unfiltered MSK are also shown for comparison. The parameter BT_b is the 3 dB bandwidth of the premodulation Gaussian filter normalized by bit rate. The parameter d is the rms delay spread normalized by the symbol period. From [9] Copyright © 1987 IEEE.

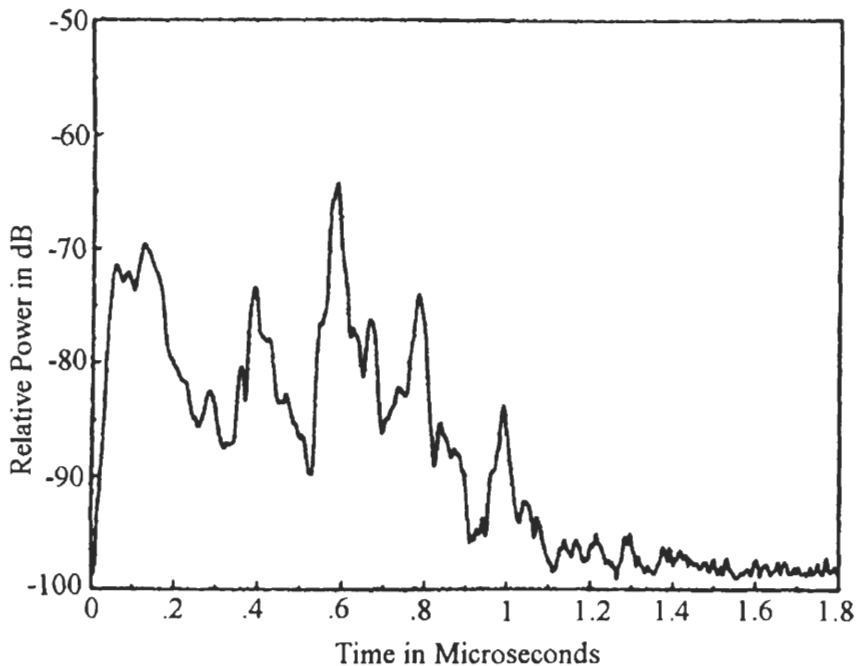


Figure 10.18 A power delay profile obtained from measurements done in an office building; the rms delay spread is approximately 250 ns. From [9]. Copyright © 1987 IEEE.

of BPSK; therefore for the same d' , the relative delay spread d is only one-half of that of BPSK for four-level modulations. It is d , not d' that influences the detection of a bit.

Higher level modulations were also simulated. Figure 10.15 indicates that the performance of 8-PSK is not superior to that of QPSK as SNR approaches infinity, even though it has 3 bits per symbol. This is not surprising since BER of 8-PSK is much higher than that of QPSK in an AWGN channel (see Figure 4.13 where symbol error rate is shown, however it can be easily converted to BER using (4.25)). The advantage of smaller d' is offset by this disadvantage. This is why four-level modulations are chosen for all third-generation wireless standards.

It is also interesting to note that all curves in Figures 10.13, 10.14 and 10.15 are nearly parallel to a straight line of slope two. That is, an order of magnitude increase in delay spread results in about two orders of magnitude increase in the irreducible BER within the range of d simulated. These simulation results are consistent with an earlier theoretical finding given in [10].

Figure 10.16 shows the irreducible BER of RC-QPSK as a function of α , the roll-off factor in raised-cosine filter, for different values of rms delay spread. The

delay spread profile is a measured one shown in Figure 10.18. Results for the unfiltered QPSK are also shown for comparison. As α increases, the irreducible BER decreases monotonically due to decrease in ISI. However, the spectral occupancy also increases. It is seen from the figure that the RC-QPSK with $\alpha \geq 0.75$ has lower irreducible BER than the unfiltered NRZ-QPSK.

Figure 10.17 shows the irreducible BER of GMSK as a function of BT_b , the 3 dB bandwidth of the premodulation Gaussian filter normalized by bit rate. The delay spread profile of the channel is again the one shown in Figure 10.18. Results for the unfiltered MSK are also shown for comparison. The GMSK is demodulated by an MSK receiver which is not matched to the GMSK signal. It is seen from the figure that the best BER performance is obtained by choosing $BT_b = 0.25$; however, the performance is not very sensitive to BT_b until BT_b is too small (< 0.25).

10.4 $\pi/4$ -DQPSK IN FADING CHANNELS

Since $\pi/4$ -DQPSK is the standard of the third-generation mobile telephone systems in the United States and Japan, its performance in the mobile fading channel is of great interest. Its performance in a slow, flat, Rayleigh or Rician fading channel has been discussed in Section 10.2. The research groups led by Dr. Feher and Dr. Rappaport investigated its BER performance for other important channel conditions and results were published in references [11–13].

In [12], the channel model is the flat-fading indoor radio channel model based on measurements. The BER results of the simulation are based on the channel characteristics of 50 simulated measurement locations and narrow-band flat fading characteristics seen by a mobile at each location. Twenty-five of those 50 simulated channels are in LOS topography and 25 of them are in OBS (obstructed) topography. Figure 10.19 shows the results for $\pi/4$ -DQPSK as well as BPSK and FSK. BPSK has a 3 dB advantage over $\pi/4$ -DQPSK at low E_b/N_o values, and a 2.8 dB advantage at higher signal levels. But this is offset by the 3 dB advantage on the spectral efficiency offered by $\pi/4$ -DQPSK. This suggests that among the three schemes compared, $\pi/4$ -DQPSK is the most appropriate choice for indoor flat fading radio channels.

The error performance of $\pi/4$ -DQPSK is analyzed for a two-ray Rayleigh fading mobile channel with a co-channel interference (CCI) in [11]. This is considered to be the model for the cellular mobile communication. The channel is modeled by the following expression.

$$\tilde{r}(t) = R_1(t)e^{-j\phi_1(t)}\tilde{s}_T(t) + R_2(t)e^{-j\phi_2(t)}\tilde{s}_T(t - \tau) + R_3(t)e^{-j\phi_3(t)}\tilde{s}_C(t) + \tilde{n}(t) \quad (10.34)$$

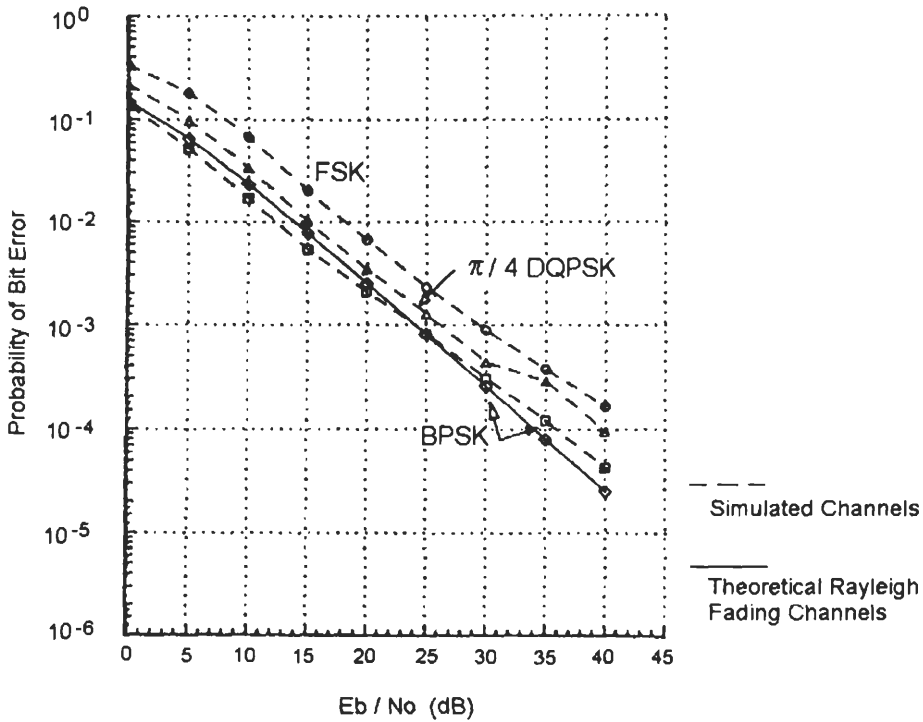


Figure 10.19 Comparison of simulated BER performance for various modulation schemes in the 50 combined simulated channels. From [12]. Copyright © 1991 IEEE.

where $\tilde{r}(t)$ is the equivalent low-pass received signal. $\tilde{s}_T(t)$ is the transmitted low-pass signal and $\tilde{s}_T(t - \tau)$ is the second ray with a delay τ . $\tilde{s}_C(t)$ is the low-pass co-channel interference. $\tilde{n}(t)$ is the low-pass AWGN. $R_i(t)$, $i = 1, 2, 3$, are Rayleigh envelopes and $\phi_i(t)$, $i = 1, 2, 3$, are random phases with uniform distribution. The combination of $s_T(t)$ and $s_T(t - \tau)$ accounts for the frequency-selective fading. If $R_2(t) = 0$, the channel is not frequency-selective fading, it is flat fading. If $R_3(t) = 0$, there is no CCI. The channel could be slow fading or fast fading, depending on the speed of the mobile and the data rate. In terms of the received signal, this is reflected by the Doppler spread, or equivalently, the correlation of the signal samples.

In the analysis, to avoid ISI, a raised-cosine filter with roll-off factor α is used in the transmitter and a brick-wall filter with bandwidth (baseband) equal to $(1 + \alpha)f_N + f_{D,\max}$ is used in the receiver, where f_N is the Nyquist bandwidth ($f_N = 1/2T_s$ in baseband, see Section 1.4.2), and $f_{D,\max}$ is maximum Doppler spread. The receiver passes the received signal without distortion. The system is ISI-free. This causes

0.57 dB ($= 10\log(1 + \alpha)(1 - 0.25\alpha)$)³ E_b/N_o degradation for $\alpha = 0.2$. However, when CCI is the dominant interference as in cellular systems, the performance is the same as the matched filtering system.

The analytical BER expressions for DBPSK, DQPSK, and $\pi/4$ -DQPSK are derived in [11]. However, these expressions are quite complicated. We would rather not list them here, instead, some representative numerical results for several sets of important parameters are presented. First we define the parameters.

1. C/N denotes the average carrier-to-noise power ratio with noise power measured in receiver bandwidth ($2(1 + \alpha)f_N$), if $f_{D,\max} \ll f_N$. Recall that we usually draw BER curves against E_b/N_o instead of C/N . The relation between them is simple. We know that $C = E_b f_b$ and $N = N_o W_n$, where f_b is the data bit rate and W_n is the equivalent noise bandwidth, then

$$\frac{C}{N} = \frac{f_b}{W_n} \cdot \frac{E_b}{N_o} \quad (10.35)$$

For $\pi/4$ -DQPSK using the Nyquist filter, at the carrier band $W_n = 2f_N = f_s = f_b/2$. Thus $C/N = 2E_b/N_o$. That is, C/N is greater than E_b/N_o by 3 dB in a $\pi/4$ -DQPSK system with matched Nyquist filters in the transmitter and the receiver. Since E_b/N_o and C/N are proportional to each other, the degradation caused by the raised-cosine filter is the same in C/N and E_b/N_o .

2. C/I denotes the average carrier-to-interference power ratio.
3. C/D denotes the average power ratio between the main-path signal and the delayed-path signal.
4. τ/T_s denotes the delay of the secondary path normalized to the symbol period.

Figures 10.20 to 10.23 show some representative numerical results. Figure 10.20 shows the BER ($P(e)$) versus C/N of $\pi/4$ -DQPSK in a flat, slow, Rayleigh fading channel corrupted by AWGN and co-channel interference. No Doppler spread and time dispersion are assumed. That is, the mobile speed is zero and there is no second ray of signal. The filter roll-off factor $\alpha = 0.2$. The numbered curves are for different values of carrier-to-interference ratio.⁴ Inspecting these curves carefully, we can

³ This is the ratio between the equivalent noise bandwidths of the simulated system and the matched filtering system where a Nyquist filter is used in the transmitter and the receiver. The Nyquist filter is the most narrow-banded filter without ISI. But Nyquist filter is susceptible to timing jitters and more difficult to implement. It can be easily shown that the equivalent noise bandwidth of a raised-cosine filter is $f_N(1 - 0.25\alpha)$. Thus the total equivalent noise bandwidth of the simulated system is $(1 + \alpha)(1 - 0.25\alpha)f_N$.

⁴ Curve (5) corresponds to a flat, slow, Rayleigh fading channel without CCI. So this curve should be equivalent to that in Figure 10.5. Recall that we just argued that C/N is greater than E_b/N_o by 3 dB and there is also a 0.57 dB degradation due to the filtering, then the C/N curve should be shifted to the right by 3.57 dB compared with the E_b/N_o curve. By comparing them we can see this is true.

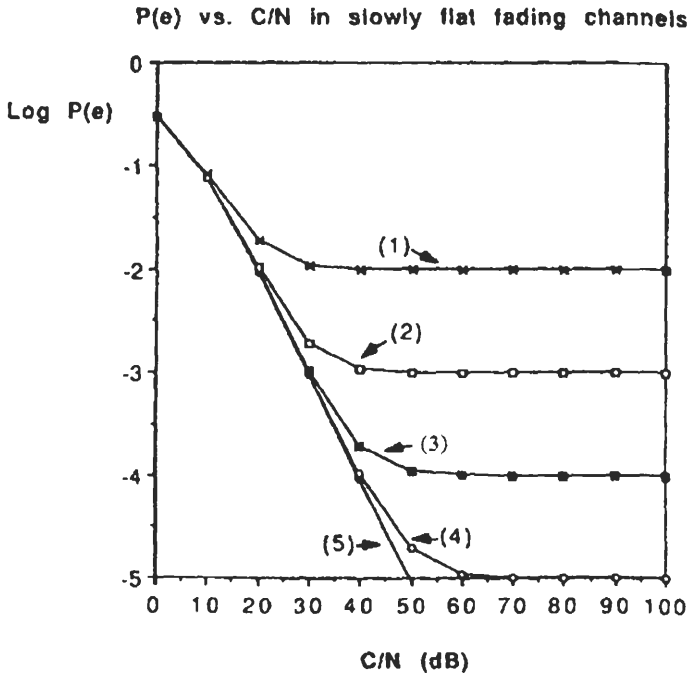


Figure 10.20 BER ($P(e)$) versus C/N of $\pi/4$ -DQPSK in a flat, slow, Rayleigh fading channel corrupted by AWGN and co-channel interference. $f_c = 850$ MHz, $f_s = 24$ kbps, $\alpha = 0.2$. No Doppler spread and time dispersion. $C/I = (1) 20, (2) 30, (3) 40, (4) 50, (5) \infty$ dB. From [11]. Copyright © 1991 IEEE.

see that when C/N is approximately equal to C/I , the effect of the CCI begins to become dominant. When C/N is much greater than C/I , the effect of the CCI is an irreducible error floor. This is no surprise since the co-channel signal is just another noise to the main channel signal.

Figure 10.21 shows the effect of mobile speed, or equivalently, the Doppler spread. No CCI and time dispersion are assumed. Again $\alpha = 0.2$. The curves are for speed from 0 to 75 miles per hour (mph). It is seen that even when there are no CCI and no noise ($C/N \rightarrow \infty$), there are still errors as long as the mobile speed is not zero. The errors are caused by the random phase modulation of the fast channel (due to motion of the mobile).

Figure 10.22 illustrates the BER of $\pi/4$ -DQPSK in a frequency-selective slow fading channel. There are no AWGN, CCI, and Doppler spread. The curves are drawn versus C/D , using τ/T_s as a parameter. Comparing Figure 10.22 to 10.21, it is seen that for small τ/T_s , the system can tolerate stronger delayed signal than CCI. For τ that approaches T_s , the BER caused by delayed signal approaches that caused

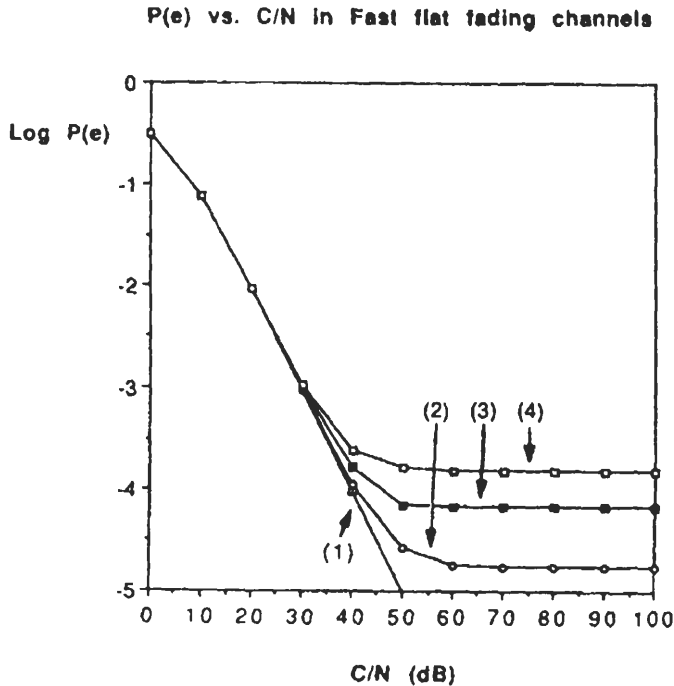


Figure 10.21 BER versus C/N of $\pi/4$ -DQPSK in a flat, fast, Rayleigh fading channel corrupted by AWGN. No CCI and time dispersion. $f_c = 850$ MHz, $f_s = 24$ kbps, $\alpha = 0.2$. $v = (1) 0, (2) 25, (3) 50, (4) 75$ mph. From [11]. Copyright © 1991 IEEE.

by a CCI as we expect since the information source is assumed uncorrelated.

Figure 10.23 illustrates the BER of $\pi/4$ -DQPSK in a frequency-selective fast fading channel. No AWGN or CCI are present in the channel. This figure shows that when the delayed signal is comparable to the main-path signal (C/D close to 0 dB), the error rate is controlled by the frequency selectivity (τ/T_s). When delayed signal power is small, BER is controlled by fast fading (speed v).

The simulation in [13] is for a two-ray Rayleigh fading model and measurement-based models. The two-ray model is the same as that given in (10.34) and the filtering strategy is also the same as in [11]. The simulation results confirm the analytical results by Liu and Feher [11].

10.5 MHPM IN FADING CHANNELS

The performance of the rectangular frequency pulse multi- h modulation scheme (IREC-MHPM, also known as multi- h CPFSK) is evaluated for slow, flat or fre-

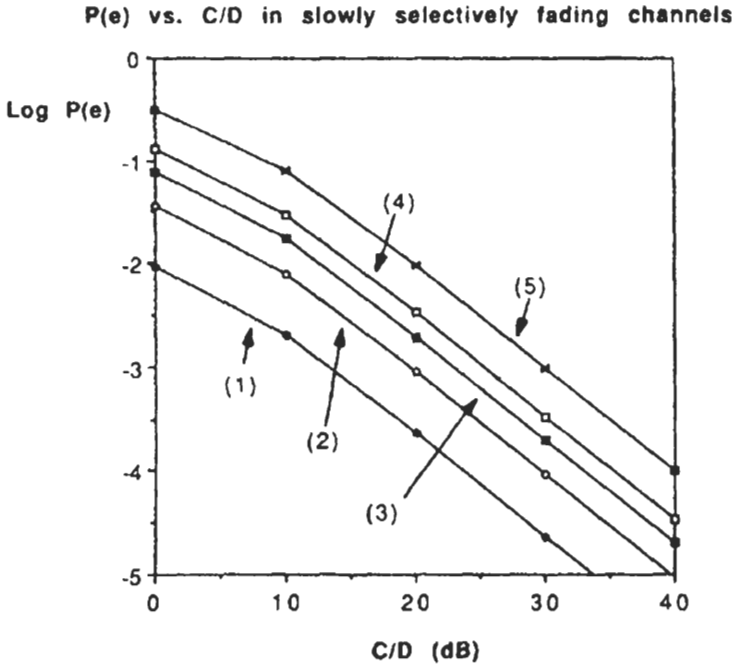


Figure 10.22 BER versus C/D of $\pi/4$ -DQPSK in a frequency-selective slowly fading channel. No AWGN, CCI and Doppler spread. $f_c = 850$ MHz, $f_s = 24$ kbps, $\alpha = 0.2$. $\tau/T_s =$ (1) 0.1, (2) 0.2, (3) 0.3, (4) 0.4, (5) 1.0. From [11]. Copyright © 1991 IEEE.

quency selective Rician and Rayleigh channels with Doppler frequency shift [14]. The evaluation is performed with a method combining analysis and simulation. Performance degradations are evaluated for various direct-to-reflected signal ratio, Doppler shifts, and relative time delays in Rician fading channels. The channel model is a two-ray model consisting of a direct signal without fading, and a reflected signal with Rayleigh fading. AWGN is also included. The satellite-to-ground vehicle channel and the airplane-to-ground channel, where MHPM schemes are likely to be used, are of this type. The received signal is

$$r(t) = r_d(t) + r_r(t) + n(t)$$

where

$$r_d(t) = \sqrt{\frac{2E}{T_s}} \cos \left(\omega_c t + \frac{a_i \pi h_i t}{T_s} + \phi_i \right); 0 \leq t \leq T_s$$

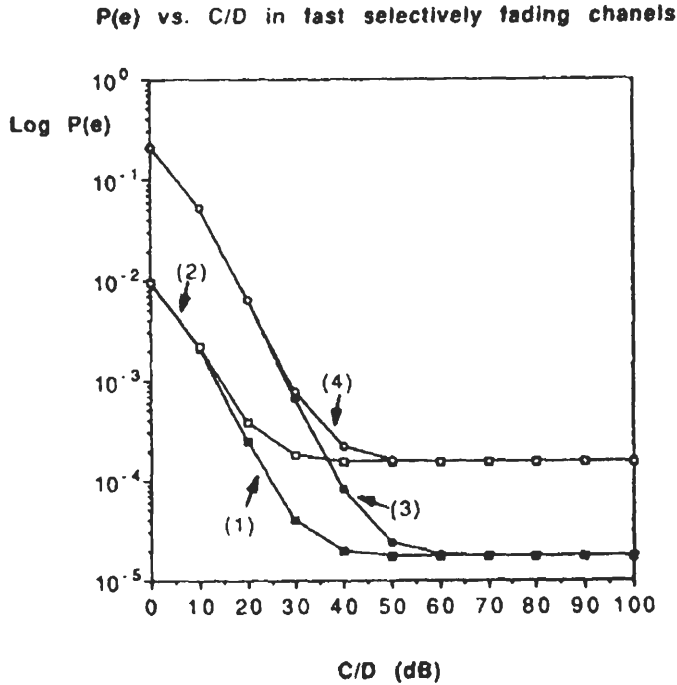


Figure 10.23 BER versus C/D of $\pi/4$ -DQPSK in a frequency-selective fast fading channel. No AWGN, CCI. $f_c = 850$ MHz, $f_s = 24$ kbps, $\alpha = 0.2$. (1) $\tau/T_s = 0.1$, $v = 25$ mph, (2) $\tau/T_s = 0.1$, $v = 75$ mph, (3) $\tau/T_s = 0.5$, $v = 25$ mph, (4) $\tau/T_s = 0.5$, $v = 75$ mph. From [11]. Copyright © 1991 IEEE.

is the direct component,

$$r_r(t) = v_i \sqrt{\frac{2E}{T_s}} \cos \left((\omega_c + \Delta\omega)(t - \tau) + \frac{a_i \pi h_i (t - \tau)}{T_s} + (\phi_i + \varphi_i) \right)$$

is the reflected component, and $n(t)$ is the AWGN. The parameters are defined as follows:

- E = symbol energy;
- ω_c = carrier angular frequency;
- a_i = information data, $a_i \in [+1, -1]$;
- M = even constant and a power of 2;
- h_i = one of a set of modulation indexes (h_1, h_2, \dots, h_K);
- ϕ_i = the phase at the beginning of the i th interval;
- v_i = Rayleigh envelope;
- φ_i = uniformly distributed phase in $(0, 2\pi)$;

τ = delay of the Rayleigh signal with respect to the direct signal.

The direct component of signal experiences a Doppler shift $\Delta\omega$ due to the relative motion between the transmitter and the receiver. For the coherent detection of 1REC-MHPM, the carrier needs to be recovered at the receiver. Since the direct signal is usually dominant, the recovered local carrier frequency is the same as the direct signal frequency, which is denoted as ω_c . Note that it is different from the transmitted frequency by $\Delta\omega$. The Doppler shift is not explicitly included in the Rayleigh fading signal model since its effect is modeled by the Rayleigh envelope and the random phase. Therefore Rayleigh signal has the same carrier frequency as the transmission, but it is different from ω_c by $\Delta\omega$. There is also a delay τ in $r_r(t)$ with respect to the direct component $r_d(t)$.

Recall that 1REC-MHPM can be demodulated by an MLSE demodulator using four correlators and the Viterbi algorithm (see Section 7.5.1). The simulation in [14] is based on the analytical results of the correlators' outputs and the Viterbi algorithm. A similar method was used for the AWGN channel [15].

In the simulation the two independent Gaussian processes which produce the Rayleigh fading envelopes are bandlimited by a 6th order Butterworth low-pass filter. It has a bandwidth of the fading process determined by the Doppler spread of the channel which, in turn, is determined by the mobile speed.

In the simulation it is found that P_b increases with the increase of Doppler shift f_d slightly, where $f_d = \Delta f T_s$ is the Doppler shift normalized to the symbol rate. However, the effect of f_d is not as significant as that of other parameters. Therefore when we examine the effect of other parameters, we set $f_d = 0.2$ which gives an average value of P_b in the practical range of f_d . The simulation results are summarized in the following figures.

Figure 10.24 shows various P_b plots of Rician fading for different K , the direct-to-reflected signal power ratio, and normalized delay $t_d = \tau/T_s$ for the 1REC-MHPM scheme with $H_2 = (2/4, 3/4)$. When $K = 0$ we arrive at Rayleigh fading. It is seen from the plot of Rayleigh fading that the bit error rate P_b is very high (0.25 – 0.26). This is due to the fact that the simulated receiver is not synchronized to the reflected component.⁵ When the content of P_d is increased, that is, when a carrier is recovered at the receiver from the direct signal component, a significant improvement in P_b is observed (see plots for $K = 0, 5, 10$, and 20 dB). The P_b at $K = 20$ dB is comparable to that in the presence of only AWGN. For $P_b = 10^{-6}$,

⁵ In the simulation, the Rayleigh channel is obtained as a special case of the Rician channel where carrier synchronization is established for the direct signal. When the power of the direct signal is reduced to zero, the channel becomes pure Rayleigh without carrier synchronization. If synchronization was established for the Rayleigh signal, the BER performance would be improved and BER curve would be similar to that of BPSK or QPSK (see Figure 10.4) since the BER expression of MHPM is also of the form of a Q function (see (7.28)).

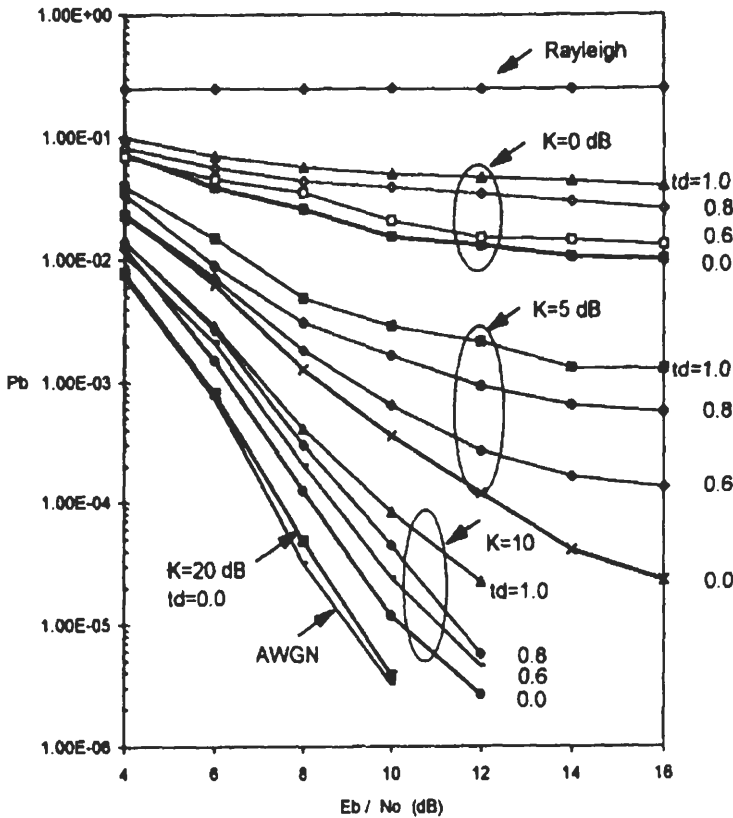


Figure 10.24 Performance of 1REC-MHPM $H_2 = (2/4, 3/4)$ in Rayleigh, Rician, and AWGN channels for various values of K and t_d ($f_d = 0.2$). Rayleigh channel is approximated by $K = -200$ dB, and no synchronization is done for the Rayleigh fading signal. From [14]. Copyright © 1997 IEEE.

the performance degradation at $K = 10$ dB and $t_d = 0$, with respect to the AWGN channel, is about 2 dB. Due to the Rayleigh component in the signal these plots show error floors. Figure 10.24 also shows the effect of t_d on the P_b . It is seen that when t_d increases P_b increases steadily, especially when $t_d \geq 0.6$. This is due to the fact that when t_d is much larger than 0, the channel becomes frequency-selective, which causes additional distortion of the signal on top of fading and AWGN. This in turn increases the P_b . However, they can be largely removed if a channel state tracking mechanism is incorporated.

Figure 10.25 is similar to Figure 10.24 except that it is for $H_3 = (4/8, 5/8, 6/8)$. Again we see that the direct-to-reflected signal ratio K and t_d have significant impact on P_b .

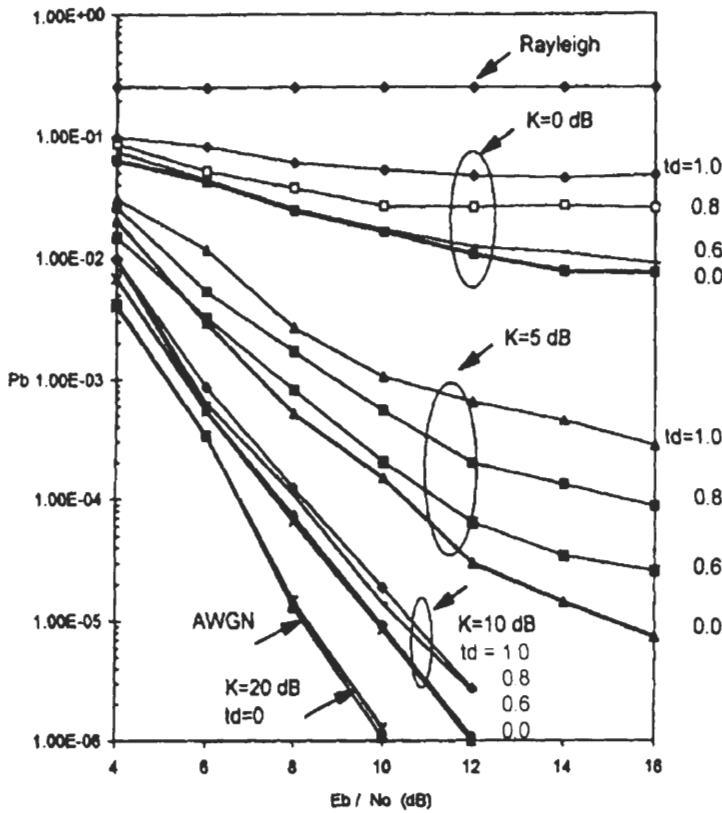


Figure 10.25 Performance of 1REC-MHPM $H_3 = (4/8, 5/8, 6/8)$ in Rayleigh, Rician, and AWGN channels for various values of K and t_d ($f_d = 0.2$). Rayleigh channel is approximated by $K = -200$ dB, and no synchronization is done for the Rayleigh fading signal. From [14]. Copyright © 1997 IEEE.

The performance comparison of MSK and 1REC-MHPM schemes in Rician fading is plotted in Figure 10.26, for $K = 10$ dB and $t_d = 0$ and 1.0. This figure compares the MSK, $H_2 = (2/4, 3/4)$, and $H_3 = (4/8, 5/8, 6/8)$. The solid lines are for the $t_d = 0$ case, and the dotted lines are for the $t_d = 1.0$ case. The performance of $H_2 = (2/4, 3/4)$ is found to be superior to MSK by about 2 dB for $t_d = 0$ throughout the E_b/N_o range. This coding gain is slightly larger than that in the AWGN channel (1.4 dB)[16]. Comparing $H_3 = (4/8, 5/8, 6/8)$ with MSK, the coding gain is around 3 dB for $t_d = 0$ which is slightly larger than that of AWGN channel (2.8 dB). For $t_d = 1.0$, MSK suffers from more loss in P_b than MHPM schemes. This indicates that these 1REC-MHPM schemes have retained their coding gain over MSK in fading channels and are subject to less loss in error performance when delay spread

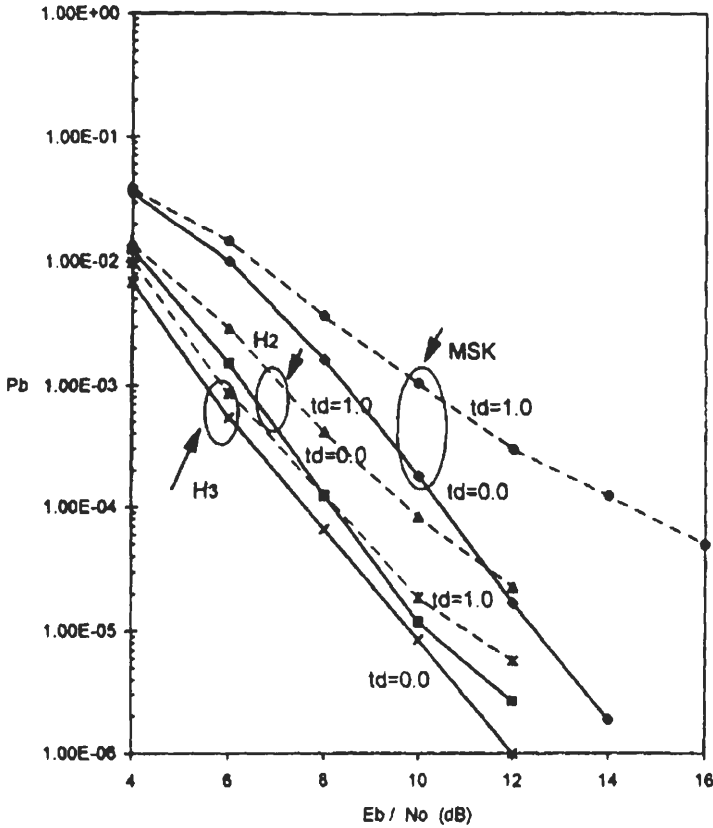


Figure 10.26 Comparison of MSK, $H_2 = (2/4, 3/4)$, and $H_3 = (4/8, 5/8, 6/8)$ in Rician channel ($K = 10dB$, $f_d = 0.2$). From [14]. Copyright © 1997 IEEE.

increases.

10.6 QAM IN FADING CHANNELS

Because of its great bandwidth efficiency, applications of QAM in fading channels have always been attracting interest. In this section, we first evaluate the error performance of the square M-ary QAM in a slow, flat Rayleigh or Rician fading channel, using the technique developed in Section 10.2. Then we present the star-QAM which is particularly suitable for fading channels.

10.6.1 Square QAM

Substituting the P_s expression for square M-ary QAM and corresponding fading distributions into (10.17), we can easily evaluate the symbol error probability of the square M-ary QAM in fading channels. If the bit-symbol mapping is Gray coded, as usually it is, the bit error probability can be found using the P_s - P_b relation expression (8.57).

At high SNRs, the P_s expression is (8.55) which is in Q-function form. We can directly use (10.24) to obtain the result. Note that in (8.55) E_{avg} is the energy per symbol, that is $E_{avg} = E_b \log_2 M$, then in fading channel (8.55) can be written as,

$$P_s \cong \frac{4(\sqrt{M} - 1)}{\sqrt{M}} Q \left(\sqrt{\frac{3 \log_2 M}{M - 1} \gamma_b} \right) \quad (10.36)$$

Comparing (10.36) with (10.19) we can recognize

$$C = \frac{4(\sqrt{M} - 1)}{\sqrt{M}}$$

and

$$\delta = \frac{3 \log_2 M}{M - 1}$$

Substituting them into (10.24) we have

$$P_s = \frac{2(\sqrt{M} - 1)}{\sqrt{M}} \left[1 - \sqrt{\frac{3 \Gamma \log_2 M}{2(M - 1) + 3 \Gamma \log_2 M}} \right], \quad (10.37)$$

(for square QAM at high SNR)

Note that when $M = 4$, square QAM degenerates to QPSK. In this case, we can easily check that (10.37) reduces to (10.25) except for a factor of two, since one is P_s and the other is P_b .

At low SNRs, (10.37) can induce big inaccuracy just as (8.55) would for an AWGN channel. Therefore we need to use (8.53) and (8.54) in conjunction with (10.18) in (10.17) to obtain the results numerically. Equation (8.53) must be rewritten in terms of γ_b as

$$P_{\sqrt{M}} \cong \frac{2(\sqrt{M} - 1)}{\sqrt{M}} Q \left(\sqrt{\frac{3 \log_2 M}{M - 1} \gamma_b} \right) \quad (10.38)$$

Figure 10.27 shows the numerical results which are accurate at both low and high

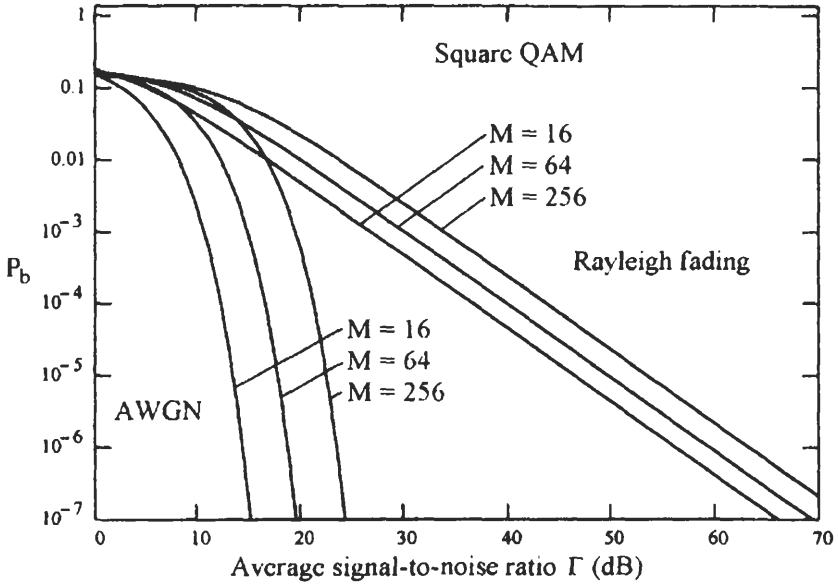


Figure 10.27 Bit error rates of square QAM in a slow, flat, Rayleigh fading channel.

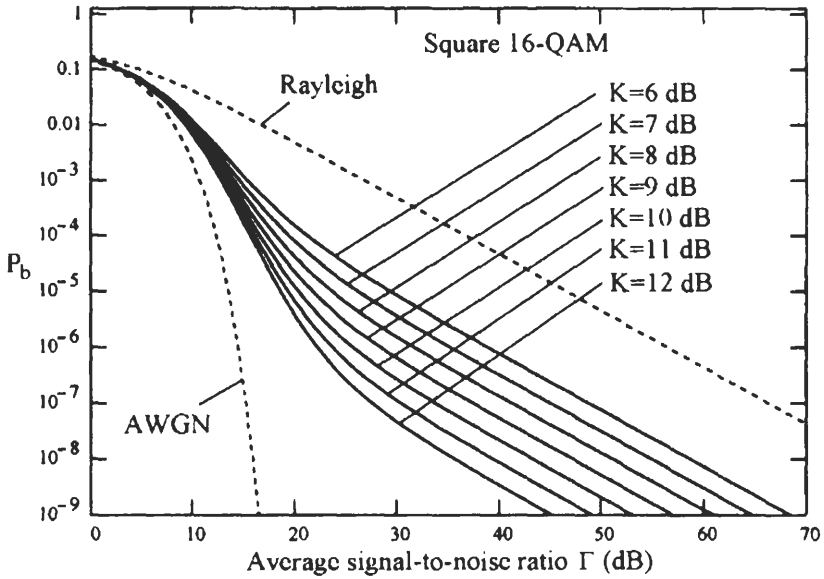


Figure 10.28 Bit error rates of square QAM in a slow, flat, Rician fading channel. $M = 16$.

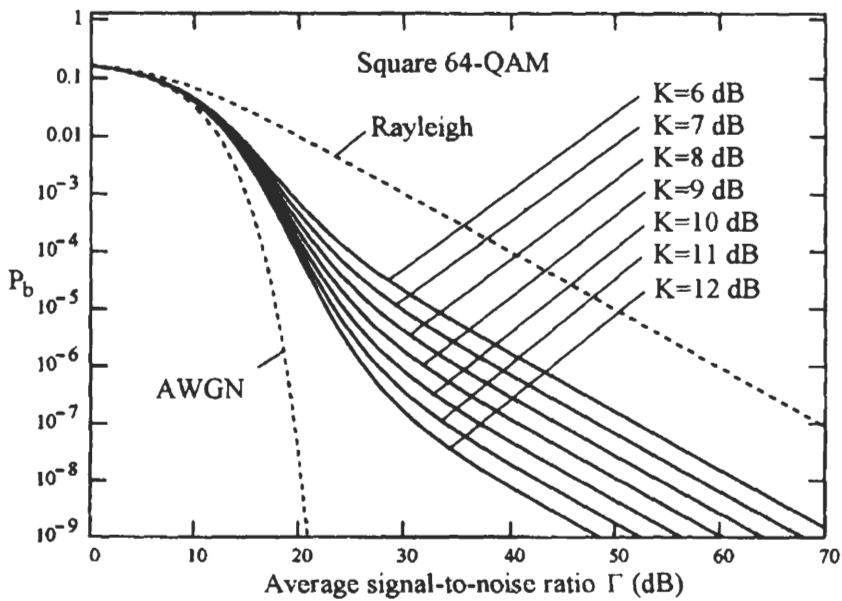


Figure 10.29 Bit error rates of square QAM in a slow, flat, Rician fading channel. $M = 64$.

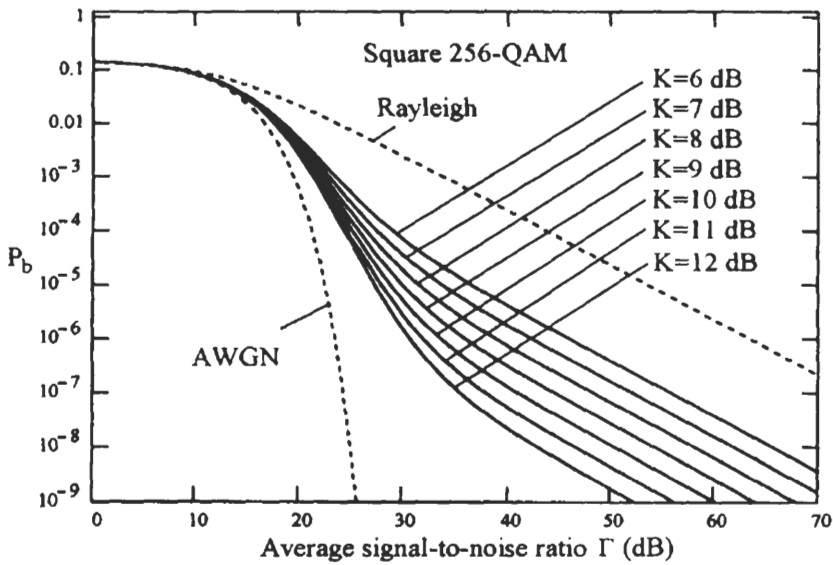


Figure 10.30 Bit error rates of square QAM in a slow, flat, Rician fading channel. $M = 256$.

SNRs.

For slow, flat, Rician fading channel, we can numerically find out the error performance using the same set of formulas except that the distribution density is (10.31) instead of (10.18). Figures 10.28 to 10.30 show the numerical results for $M = 16, 64,$ and 256 .

10.6.2 Star QAM

In Chapter 8 we have stated that star QAM is not optimum in terms of d_{\min} under the constraint of average phasor power. Therefore it is not a preferable choice in an AWGN channel. However, it allows efficient differential encoding and decoding, which makes it suitable for fading channels. Recall that we have discussed differential coding for square QAM in Chapter 8. That is for the purpose of resolving phase ambiguity in carrier recovery. The method of differential coding for star QAM is different and the purpose is different too: to avoid carrier recovery and enable differential detection of signals.

For the M -ary star constellations, such as the one in Figure 8.5(a), assume $M = 2^n$, there are $M_1 = 2^{n_1}$ amplitudes (cycles) and there are $M_2 = 2^{n_2}$ phases (points on a cycle), where $n_1 + n_2 = n$ and $M = M_1 M_2$. For example, when $n_1 = 1, n_2 = 3$, we have the 16 star QAM in Figure 8.5(a).

For the star QAM, since there are M_1 amplitudes, the average power is

$$P_{avg} = E\{A_i^2/2\} = \frac{1}{2M_1} \sum_{i=1}^{M_1} A_i^2 \quad (10.39)$$

where A_i is the amplitude of the i th phasor in the constellation. From (10.39) and (8.49) we have the PSD of the star QAM as

$$\begin{aligned} \Psi_s(f) &= \frac{T_s}{M_1} \left(\sum_{i=1}^{M_1} A_i^2 \right) \left(\frac{\sin \pi f T_s}{\pi f T_s} \right)^2 \\ &= \frac{nT_b}{M_1} \left(\sum_{i=1}^{M_1} A_i^2 \right) \left(\frac{\sin \pi f n T_b}{\pi f n T_b} \right)^2 \end{aligned} \quad (10.40)$$

The signal points in the star QAM can be easily encoded differentially [17, p. 325]. Use the star 16-QAM as an example. Of the four bits in each symbol, $b_1, b_2, b_3,$ and b_4 , the first bit is used to encode the amplitude change. For example, a 1 denotes the signal amplitude is changed and a 0 denotes no change. The rest of the four bits are Gray coded to denote the phase changes. For example we can code 000 as no phase change, 001 as $\pi/4$ change, etc. Table 10.2 shows the coding scheme. The Hamming

Pattern no.	Bit pattern ($b_2b_3b_4$)	Phase change ($\Delta\theta_i$)
1	000	0
2	001	$\pi/4$
3	011	$2\pi/4$
4	111	$3\pi/4$
5	010	$4\pi/4$
6	010	$5\pi/4$
7	110	$6\pi/4$
8	100	$7\pi/4$

Table 10.2 Gray-coded phase changes.

distance between two adjacent bit patterns (including no. 1 and no. 8) is one and the corresponding phase changes differ by $\pi/4$ which is the smallest increment. These patterns are not mapped into transmitted symbols, instead they are mapped into the phase differences of two consecutive transmitted symbols. When two symbols are received, first their amplitude is detected and b_1 is determined. Next their phases are compared to determine what is the $\Delta\theta_i$. From $\Delta\theta_i$, using a lookup table like Table 10.2, bit pattern $b_2b_3b_4$ can be determined. When $\Delta\theta_i$ is corrupted by noise and fading, and a detection error is made, most likely the error is made by taking one of the adjacent bit patterns. This leads to only one bit error because of Gray coding.

In the fading channel, the signal amplitude varies. Thus the threshold for amplitude detection is made adaptive. Let A_1 and A_2 denote the amplitudes of the two rings in the star 16-QAM constellation. Assume the received phasor amplitudes are Z_k and Z_{k+1} at time $t = kT_s$ and $(k + 1)T_s$. The algorithm used in [17, p. 325] is as follows. If

$$\frac{Z_{k+1}}{Z_k} \geq \frac{A_1 + A_2}{2}$$

or if

$$\frac{Z_{k+1}}{Z_k} < \frac{2}{A_1 + A_2}$$

then a significant change in amplitude is deemed to have occurred and bit b_1 is set to logic 1 at time $(k + 1)T_s$. This detection rule does not rely on the absolute value of the received signal amplitude, rather it depends on the relative amplitudes of the two consecutive signal amplitudes. This is exactly what is needed in a fading channel.

Figure 10.31 shows some simulation results for various 16-QAM schemes. The simulation parameters are as follows. The carrier frequency is 1.9 GHz, the symbol rate is 16 k symbol/s, the mobile's speed is 30 mph and the channel exhibits Rayleigh fading with AWGN. Both transmitter and receiver use a fourth-order Butterworth

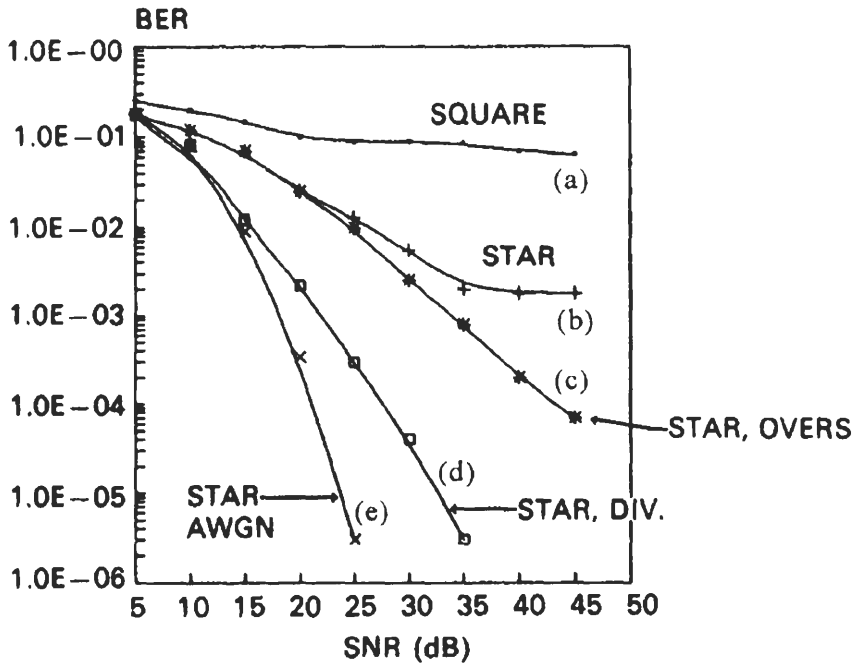


Figure 10.31 BER for various 16-QAM schemes using different demodulations. From [17]. Copyright © 1994 IEEE.

low-pass filter with a 3 dB point at 1.5 times that Baud rate. Curve (a) is the square 16-QAM performance, which is worse than that given in Figure 10.27 where no filtering is assumed. Curve (b) is the performance of the differential star 16-QAM, which is largely enhanced compared with square 16-QAM. Curve (c) is again for star 16-QAM, but an oversampling technique is used. By this technique, $n = 8$ samples equally spaced in time are made per symbol period. The variations observed in these samples are used to modify Z_k and Z_{k+1} , hence improve the amplitude detection (see [17, p. 325] for detail). Curve (d) is for star 16-QAM with two-antenna switched diversity where the larger of the two signals received are selected. Curve (e) is the performance of star 16-QAM in an AWGN channel. From this figure it is seen that differential star QAM improves BER performance in fading channels significantly.

10.7 REMEDIAL MEASURES AGAINST FADING

From the above discussion we can see that fading, especially Rayleigh fading, can

reduce the BER performance of a modulation scheme significantly. Remedial measures against fading must be adopted in order to preserve or at least partially preserve the BER performance. In this section, we just briefly point out these measures. A detailed discussion is beyond the scope of this book. The purpose of this brief discussion is to provide a general idea of remedial measures against fading and references.

The first, also simplest, measure against fading is to use a differential modulation scheme where carrier phase synchronization is not required. Up to 3 dB loss in error performance is expected. In the above discussion, the performance of DBPSK and $\pi/4$ -DQPSK in fading channels has been addressed. Additional references exist for DBPSK and differential MSK in Rician fast fading environment [18], differential GMSK in land mobile channel [19], narrow-band $\pi/4$ -DQPSK in Rayleigh fading channel [20], and multiple-symbol differential detection of $\pi/4$ -DQPSK in land mobile satellite communications channels [21].

If the loss due to differential coding is not allowed, then coherent demodulation is required. To help the receiver establish carrier phase synchronization in a fading environment, a pilot tone or pilot symbols can be used. A technique called transparent tone in band (TTIB) is proposed for various mobile applications by McGeehan, Bateman et al [22,23], and is also described in [17]. In TTIB systems for mobile radio applications, a spectral gap of a certain bandwidth is allocated in the center of the signal spectrum to allow insertion of the pilot tone. The frequency of the pilot tone is usually the carrier frequency in order that it can assist the receiver in carrier recovery. An alternative to TTIB is the pilot symbol assisted modulation (PSAM) [24–27]. In this method, known phasors are inserted into the data stream. The receiver extracts channel attenuation and phase rotation information from the received known symbols and uses it for fading envelope and phase compensation.

Another efficient remedial measure is the diversity technique [1,4]. The concept of diversity is to enable the receiver to receive more than one signal at any moment. It is very unlikely that all signals are in deep fade. Therefore the receiver can usually receive adequate signal power by choosing the strongest signal, or combining them together. There are five major categories of diversity techniques.

1. *Space diversity*. It is usually achieved by using more than one receiver antennas. The spacing between antenna is choosing so that the received signals experience uncorrelated fading. A spacial separation of a half-wavelength is usually enough for two-dimensional isotropic scattering. This is called microscopic diversity. Another type of space diversity is achieved by selecting different base stations. Shadowing due to variations in terrain and the nature of surroundings causes large-scale fading. By selecting a base station which is not shadowed, the mobile can improve its signal-to-noise ratio in the forward link significantly. This is called macroscopic diversity. Macroscopic diversity can also be used in the

base station receiver. By using multiple base station antennas, the base station receiver can choose the strongest signal from the mobile.

2. *Polarization diversity.* A scattering environment tends to depolarize a signal. Receiver antennas having different polarizations can be used to obtain diversity. An example is the use of vertical monopole and patch antennas in cellular telephone user units. Another application of polarization diversity is at the base station. At base station space diversity is less practical because the narrow angle of incident fields requires large antenna separation. However, orthogonal polarization diversity is possible since many users are using portable units and the signal polarizations are no longer pure vertical due to hand-tilting.
3. *Frequency diversity.* This is achieved by transmitting the same signal on multiple carriers. These carrier frequencies are separated by at least the coherent bandwidth of the channel. Thus each signal does not experience the same fading. Frequency diversity is often used in microwave line-of-sight links using frequency division multiplexing (FDM). In these links deep fading may occur due to tropospheric propagation and resulting refraction. A spare frequency channel is usually provided for several frequency channels, each carrying an independent traffic. If any one of the frequency channels is experiencing deep fading, its traffic can be switched to the spare channel.
4. *Time diversity.* Signals are transmitted in multiple time slots separated by at least the coherence time of the channel. For example, repetition codes transmit a symbol in several time slots. Other sophisticated error control codes encode a message sequence into a longer coded sequence. This is also a type of time diversity because the information is distributed on the entire code so if a part of it is erased the information can still be recovered. Interleaving is usually used in combination with error control codes. When an interleaved sequence is deinterleaved at the receiver, bursty errors are spread out and become isolated errors which can be easily corrected by the error control code. Interleaving effectively separates the symbols corresponding to a message by more than the channel coherence time.
5. *Multipath diversity.* Using a tapped delay line the energy in the multipath components can be collected and their weighted sum becomes a stronger signal. This type of receiver is called a RAKE receiver since the block diagram is just like a garden rake. Multipath diversity is also sometimes considered as time diversity since signal components at different times are collected.

There are also other diversity techniques. The *angle diversity* or *direction diversity* uses several directional antennas. Each antenna receives plane waves arriving from a narrow range of angles. Signals received by different antennas are thus uncorrelated. A new technique is called *diversity transform* [28] which transforms the

message sequence into another sequence for transmission. However, unlike error control coding, it does not increase the length of the sequence.

It is not enough to just have diverse signal sources (called diversity branches) for the receiver. It is important how the receiver processes these signals. The processing techniques are called *diversity combining* techniques. The *predetection selective combining* technique selects the signal with the highest signal-to-noise ratio. The *predetection and postdetection maximal ratio combining* technique combines weighted signals from all diversity branches. Each signal is weighted by its complex fading gain which must be estimated at the receiver. This technique gives the best possible performance among the diversity combining techniques. If the signals are not weighted, then the process is called *predetection and postdetection coherent equal gain combining*. The *predetection switched combining* technique uses a scanner to scan through the diversity branches until it finds one that has a signal-to-noise ratio that is above specified threshold. This branch is used until the signal-to-noise ratio drops below the threshold, then the scan process starts again.

Refer to [1.4] for detailed treatment of diversity techniques and diversity combining techniques.

Finally we need to point out that *equalization* is also an important remedial measure against fading. Equalization eliminates the intersymbol interference caused by the multipath propagation as well as bandlimiting of the channel. Refer to [1.4] for detailed discussion of equalization techniques for fading channels.

10.8 SUMMARY

In this chapter we studied the error performance of modulation schemes in fading channels. First we briefly studied the characteristics of fading channels in terms of four important parameters: delay spread, coherence bandwidth, Doppler shift, and coherence time. Using these parameters, we classified fading channels into slow or fast, frequency-nonselective (flat) or frequency-selective. We observed that slow channels are more common than fast channels which occur only when data rate is very low. We described the major fading envelope distributions: Rayleigh and Rician. The flat-fading-channel (Rayleigh and Rician) performances of common binary and quaternary schemes, namely, BFSK, BPSK, DBPSK, QPSK, OQPSK, $\pi/4$ -DQPSK, and MSK including GMSK were treated in great details. Error probability expressions were derived and plots were given. It was observed that Rayleigh fading and low- K Rician fading cause substantial degradation in error performance. The rapid exponential roll-off of the AWGN channel performance curves become slow reciprocal roll-off in fading channels. The performances of above schemes in frequency-selective channel were studied through simulation and the results were

presented in Section 10.3. Irreducible error floors are the feature of the performances in frequency-selective channels. The error floor increases with increasing delay spread, and decreasing filter bandwidth. The fading-channel performance of $\pi/4$ -DQPSK was covered in great detail in Section 10.4. This coverage included the performance in a flat-fading indoor channel, and performance in a two-ray Rayleigh fading channel (slow or fast) with CCI and Doppler shift. As expected, performance degrades with increase in CCI and Doppler shift. The plots given can be valuable reference resources for design engineers. The simulation results of the performance of 1REC-MHPM or multi- h CPFSK in slow, flat or frequency-selective Rician and Rayleigh channel were presented in Section 10.5. The fading channel performance of square QAM was discussed in Section 10.6. We also introduced the star QAM in Section 10.6. The star constellation can be easily differentially coded and decoded, releasing the requirement of carrier phase synchronization. Finally, in Section 10.7 we briefly introduced remedial measures against fading. These including differential coding, pilot tone or pilot symbol techniques, and most importantly, the diversity techniques.

References

- [1] Rappaport, T. S., *Wireless Communications: Principles and Practice*, Upper Saddle River, New Jersey: Prentice Hall PTR, 1996.
- [2] Lee, W. C. Y., *Mobile Communications Engineering*, New York: MacGraw-Hill, 1982.
- [3] Jakes, W. C., ed. *Microwave Mobile Communications*, New York: Wiley, 1974.
- [4] Stüber, G. L., *Principles of Mobile Communication*, Boston: Kluwer Academic Publishers, 1996.
- [5] Stein, S. "Fading channel issues in system engineering." *IEEE Journal on Selected Areas in Communications*, vol. 5, no. 2, Feb. 1987, pp. 68-89.
- [6] Whalen, A. D., *Detection of Signals in Noise*, New York and London: Academic Press, 1971.
- [7] Gradshteyn, I. S., and I. M. Ryzhik, *Table of Integrals, Series and Products*, New York and London: Academic Press, 1980, p.649.
- [8] Roberts, J., and J. Bargallo, "DPSK performance for indoor wireless Rician fading channels." *IEEE Trans. Communications*, vol. 42, no. 2/3/4, Feb./Mar./Apr. 1994, pp. 592-596.
- [9] Chuang, J., "The effects of time delay spread on the portable radio communications channels with digital modulation." *IEEE Journal on Selected Areas in Communications*, vol. 5, no. 5, June 1987, pp. 879-889.
- [10] Anderson, J. B., and S. L. Lauritzen, and C. Thommesen, "Statistics of phase derivatives in mobile communications," *Proc. 1986 IEEE VT Conference*, May 20-22, 1986.
- [11] Liu, C., and K. Feher, "Bit error rate performance of $\pi/4$ -DQPSK in a frequency-selective fast Rayleigh fading channel." *IEEE Trans. on Vehicular Technology*, vol. 40, no. 3, August 1991, pp. 558-568.

- [12] Rappaport, T., and V. Fung, "Simulation of bit error performance of FSK, BPSK, and $\pi/4$ -DQPSK in flat fading indoor radio channels using a measurement-based channel model," *IEEE Trans. on Vehicular Technology*, vol. 40, no.4, Nov. 1991, pp. 731-740.
- [13] Fung, V., T. Rappaport, and B. Thoma, "Bit error simulation for $\pi/4$ -DQPSK mobile radio communications using two-ray and measurement-based impulse response channel models." *IEEE Journal on Selected Areas in Communications*, vol. 11, no. 3, April 1993, pp. 393-405.
- [14] Xiong, F., and S. Bhatmuley, "Performance of MHPM in Rician and Rayleigh fading mobile channels," *IEEE Trans. Communications*, vol. 45, no. 3, March 1997, pp. 279-282.
- [15] Anderson, J. B., "Simulated error performance of Multi- h phase codes," *IEEE Trans. Inform. Theory*, vol. IT-27, no. 3, May 1981, pp. 357-362.
- [16] Wilson, S. G., J. H. Highfill, III, and C-D, Hsu, "Error bounds for multi- h phase codes." *IEEE Trans. Information Theory*, vol. 28, no. 4, pp. 650-665, July 1982.
- [17] Webb, W. T. and L. Hanzo, *Modern Quadrature Amplitude Modulation*, New York: IEEE Press, and London: Pentech Press, 1994.
- [18] Mason, L., "Error probability evaluation for systems employing differential detection in a Rician fast fading environment and Gaussian noise," *IEEE Trans. Communications*, vol. 35, no. 1, Jan. 1987, pp. 39-46.
- [19] Varshney, P., J. Salt, and S. Kumar, "BER analysis of GMSK with differential detection in a land mobile channel," *IEEE Trans. on Vehicular Technology*, vol. 42, no. 4, Nov. 1993, pp. 683-689.
- [20] Ng, C., T. Tjhung, F. Adachi, and K. Lye, "On the error rates of differentially detected narrowband $\pi/4$ -DQPSK in Rayleigh fading and Gaussian noise," *IEEE Trans. on Vehicular Technology*, vol. 42, no. 3, August 1993, pp. 259-265.
- [21] Xiong, F., and D. Wu, "Multiple-symbol differential detection of $\pi/4$ -DQPSK in land mobile satellite communications channels," to appear in *IEE Proc. Communications*.
- [22] McGeehan J., and A. Bateman, "Phase-locked transparent tone in band (TTIB): A new spectrum configuration particularly suited to the transmission of data over SSB mobile radio networks," *IEEE Trans. on Communications*, vol. 32, 1984, pp. 81-87.
- [23] McGeehan J., and A. Bateman, "Theoretical and experimental investigation of feedforward signal regeneration," *IEEE Trans. on Vehicular Technology*, vol. 32, 1983, pp. 106-120.
- [24] Lodge, J., and M. Moher, "Time diversity for mobile satellite channels using trellis coded modulations," *IEEE Global Telecommun. Conf.*, Tokyo, 1987
- [25] Moher, M., and J. Lodge, "TCMP - A modulation and coding strategy for Rician fading channels," *IEEE J. Select. Areas Commun.*, vol. 7, Dec. 1989, pp. 1347-1355.
- [26] Sampei, S., and T. Sunaga, "Rayleigh fading compensation method for 16-QAM in digital land mobile radio channels," *Proc. IEEE Veh. Technol. Conf.*, San Francisco, CA, May 1989, pp. 640-646.
- [27] Hanzo, L., et al., "Transmission of digitally encoded speech at 1.2 K Baud for PCN." *IEE-Proc. Part-L* vol. 139, no. 4, Aug. 1992, pp. 437-447.
- [28] Rainish, D., "Diversity transform for fading channels," *IEEE Trans. on Communications*, vol. 44, no. 12, Dec. 1996, pp. 1653-1661.

Selected Bibliography

- Lee, W. C. Y., *Mobile Cellular Telecommunications: Analog and Digital Systems*, 2nd Ed., New York: MacGraw-Hill, 1995.
- Sklar, B., *Digital Communications, Fundamentals and Applications*, Englewood Cliffs, New Jersey: Prentice Hall, 1988.
- Steele, Raymond, *Mobile Radio Communications*, London: Pentech Press Publishers, and New York: IEEE Press, 1992.

Appendix A

Power Spectral Densities of Signals

In this appendix we deal with the problem of finding spectra of signals and power spectral densities (PSDs) of noise and modulated signals. The reader is assumed to have an understanding of the characteristics of deterministic signals and their Fourier transform or series, characteristics of random processes, their correlation functions, and their power spectral densities. Based on this knowledge, we concentrate on finding spectra of bandpass signals and PSDs of bandpass random processes, and PSDs of digitally modulated signals in baseband or passband. Specifically, formulas of PSDs of baseband digital signals (line codes), quadrature modulations (MPSK, MSK, etc.), and continuous phase modulations (CPM) are derived.

A.1 BANDPASS SIGNALS AND SPECTRA

Consider a signal in the form

$$s(t) = a(t) \cos[2\pi f_c t + \theta(t)] \quad (\text{A.1})$$

where $a(t)$ is the amplitude (envelope), $\theta(t)$ is the phase, and f_c is the carrier frequency of $s(t)$. For signals of practical interest, $a(t)$ and $\theta(t)$ are slow-changing functions of t , compared with the carrier frequency. Thus the bandwidth occupied by the signal is small relative to the carrier frequency. Such a signal $s(t)$ is called a narrowband bandpass signal, or simply, a bandpass signal. The signal can be rewritten as

$$\begin{aligned} s(t) &= a(t) \cos \theta(t) \cos 2\pi f_c t - a(t) \sin \theta(t) \sin 2\pi f_c t \\ &= x(t) \cos(2\pi f_c t) - y(t) \sin(2\pi f_c t) \end{aligned}$$

where

$$x(t) = a(t) \cos \theta(t)$$

$$y(t) = a(t) \sin \theta(t)$$

are called inphase and quadrature component, respectively. We will show that the frequency components of $x(t)$ and $y(t)$ are concentrated near $f = 0$. Thus these two signal components are called low-pass signals.

By defining the *complex envelope* of $s(t)$ as

$$\tilde{s}(t) = x(t) + jy(t)$$

we can write

$$s(t) = \text{Re}[\tilde{s}(t)e^{j2\pi f_c t}]$$

where $\text{Re}[\]$ denotes the real part of the content of the brackets.

The Fourier transform of the signal $s(t)$ is

$$\begin{aligned} S(f) &= \int_{-\infty}^{\infty} s(t)e^{-j2\pi ft} dt \\ &= \int_{-\infty}^{\infty} \text{Re}[\tilde{s}(t)e^{j2\pi f_c t}]e^{-j2\pi ft} dt \\ &= \frac{1}{2} \int_{-\infty}^{\infty} [\tilde{s}(t)e^{j2\pi f_c t} + \tilde{s}^*(t)e^{-j2\pi f_c t}]e^{-j2\pi ft} dt \\ &= \frac{1}{2} [\tilde{S}(f - f_c) + \tilde{S}^*(-f - f_c)] \end{aligned} \quad (\text{A.2})$$

where $*$ denotes conjugate, and $\tilde{S}(f)$ is the Fourier transform of the complex envelope $\tilde{s}(t)$. Note that $S(f)$ is in general a complex function. Its magnitude $|S(f)|$ is called the amplitude spectrum and its argument is called the phase spectrum.

Since the frequency components in the spectrum of $s(t)$ are concentrated around f_c , the above expression indicates that the frequency components of $\tilde{S}(f)$ must be in the neighborhood of zero frequency. In other words, the complex envelope $\tilde{s}(t)$ is a low-pass (or baseband) signal. Complex envelope is also called equivalent baseband or low-pass signal. Equation (A.2) is a very important expression which shows that the spectrum of a bandpass signal is the frequency-shifted version of the spectrum of its complex envelope. Therefore in many cases it suffices to determine the spectrum of the complex envelope.

The PSD of a signal is defined as the signal power in a unit frequency bandwidth (i.e., watts per Hz). The PSD definition is

$$\Psi_s(f) \triangleq |S(f)|^2$$

Note that PSD is always a real function. Since $|S(f)|$ is the amplitude spectrum and

is in the unit of volts per Hz, $|S(f)|^2$ is in the unit of watts per Hz (on a resistance of 1Ω , so called normalized power).

For the bandpass signal, (A.2) can be converted into power spectral density form. Since $\tilde{S}(f - f_c)$ and $\tilde{S}^*(-f - f_c)$ do not overlap, the PSD of $s(t)$ is

$$\begin{aligned}
 \Psi_s(f) &= |S(f)|^2 = S(f)S^*(f) \\
 &= \frac{1}{2}[\tilde{S}(f - f_c) + \tilde{S}^*(-f - f_c)] \cdot \frac{1}{2}[\tilde{S}^*(f - f_c) + \tilde{S}(-f - f_c)] \\
 &= \frac{1}{4}[\tilde{S}(f - f_c)\tilde{S}^*(f - f_c) + \tilde{S}^*(-f - f_c)\tilde{S}(-f - f_c)] \\
 &= \frac{1}{4}[|\tilde{S}(f - f_c)|^2 + |\tilde{S}(-f - f_c)|^2] \\
 &= \frac{1}{4}[\Psi_{\tilde{s}}(f - f_c) + \Psi_{\tilde{s}}(-f - f_c)] \tag{A.3}
 \end{aligned}$$

where

$$\Psi_{\tilde{s}}(f) = |\tilde{S}(f)|^2$$

is the PSD of the equivalent baseband signal.

We will see in the next section that for a random process we cannot define a spectrum, but the power spectral density can be defined for characterizing its frequency domain characteristics.

A.2 BANDPASS STATIONARY RANDOM PROCESS AND PSD

The major noises, thermal noise and shot noise, in an electronic system are white noise. That is, their power spectral densities are flat over a wide range of frequencies. In bandpass systems, due to filters in the system, the noise entering the system becomes bandlimited.

Many bandpass signals of practical interest, such as FSK, PSK signals, binary or M-ary, may well be represented by (A.1). However, either $a(t)$ or $\theta(t)$ or both of them may be modulated by information-carrying symbols. Due to the random nature of the information symbols, signal $s(t)$ is a random process instead of a deterministic signal.

Thus the description and properties of a bandpass random process, be it noise or signal, and its spectral density are of interest. In this section we will establish the relation between the bandpass stationary random process and its equivalent baseband stationary random process, and the relation between their power spectral densities.

Consider a wide-sense stationary random process $n(t)$ with zero mean and a PSD of $\Psi_n(f)$. The PSD is concentrated about $\pm f_c$, and is zero outside a certain

interval, where f_c is called the carrier frequency. The process is called a narrow-band bandpass process if the width of the spectral density is much smaller than f_c . Similar to narrow-band bandpass signals, a narrow-band bandpass process can be represented by any one of the three different forms [1,2]

$$\begin{aligned} n(t) &= a(t) \cos[2\pi f_c t + \theta(t)] \\ &= x(t) \cos(2\pi f_c t) - y(t) \sin(2\pi f_c t) \\ &= \operatorname{Re}[\tilde{n}(t)e^{j2\pi f_c t}] \end{aligned} \quad (\text{A.4})$$

where $a(t)$ and $\theta(t)$ are the random amplitude and phase, $x(t)$ and $y(t)$ are the in-phase and quadrature components which are also random, and $\tilde{n}(t)$ is the complex envelope of $n(t)$,

$$\tilde{n}(t) = x(t) + jy(t)$$

which is random too.

The autocorrelation function of $n(t)$ is

$$\begin{aligned} R_{nn}(\tau) &= E[n(t)n(t-\tau)] \\ &= E\{[x(t) \cos(2\pi f_c t) - y(t) \sin(2\pi f_c t)] \\ &\quad \cdot [x(t-\tau) \cos(2\pi f_c(t-\tau)) - y(t-\tau) \sin(2\pi f_c(t-\tau))]\} \\ &= R_{xx}(\tau) \cos(2\pi f_c t) \cos(2\pi f_c(t-\tau)) \\ &\quad + R_{yy}(\tau) \sin(2\pi f_c t) \sin(2\pi f_c(t-\tau)) \\ &\quad - R_{xy}(\tau) \cos(2\pi f_c t) \sin(2\pi f_c(t-\tau)) \\ &\quad - R_{yx}(\tau) \sin(2\pi f_c t) \cos(2\pi f_c(t-\tau)) \\ &= \frac{1}{2}[R_{xx}(\tau) + R_{yy}(\tau)] \cos 2\pi f_c \tau \\ &\quad + \frac{1}{2}[R_{xx}(\tau) - R_{yy}(\tau)] \cos 2\pi f_c(2t - \tau) \\ &\quad - \frac{1}{2}[R_{yx}(\tau) - R_{xy}(\tau)] \sin 2\pi f_c \tau \\ &\quad - \frac{1}{2}[R_{yx}(\tau) + R_{xy}(\tau)] \sin 2\pi f_c(2t - \tau) \end{aligned}$$

where

$$R_{xx}(\tau) = E\{x(t)x(t-\tau)\}$$

$$R_{yy}(\tau) = E\{y(t)y(t-\tau)\}$$

$$R_{xy}(\tau) = E\{x(t)y(t-\tau)\}$$

$$R_{yx}(\tau) = E\{y(t)x(t - \tau)\}$$

Since $n(t)$ is stationary, its autocorrelation function must not be a function of time t . Therefore the second and fourth term in the above expression must be zero. This leads to

$$R_{xx}(\tau) = R_{yy}(\tau) \quad (\text{A.5})$$

and

$$R_{yx}(\tau) = -R_{xy}(\tau) \quad (\text{A.6})$$

and

$$R_{nn}(\tau) = R_{xx}(\tau) \cos 2\pi f_c \tau + R_{xy}(\tau) \sin 2\pi f_c \tau \quad (\text{A.7})$$

Using the definitions one can check that the autocorrelation functions $R_{xx}(\tau)$ and $R_{yy}(\tau)$ are even functions. From (A.6) we can derive an important property of the cross-correlation function of $x(t)$ and $y(t)$

$$R_{yx}(-\tau) = E[y(t)x(t + \tau)] = E[x(\xi)y(\xi - \tau)] = R_{xy}(\tau) = -R_{yx}(\tau) \quad (\text{A.8})$$

Thus $R_{yx}(\tau)$ is an odd function of τ . Due to the relation of (A.6), $R_{xy}(\tau)$ is also an odd function of τ . This in turn verifies that $R_{nn}(\tau)$ is an even function of τ , as it should be from its definition.

The autocorrelation function of the complex envelope $\tilde{n}(t)$ is

$$\begin{aligned} R_{\tilde{n}\tilde{n}}(\tau) &= \frac{1}{2} E[\tilde{n}(t)\tilde{n}^*(t - \tau)] \\ &= \frac{1}{2} E[[x(t) + jy(t)][x(t - \tau) - jy(t - \tau)]] \\ &= \frac{1}{2} [R_{xx}(\tau) + R_{yy}(\tau) - jR_{xy}(\tau) + jR_{yx}(\tau)] \end{aligned}$$

Using (A.5) and (A.6) we have

$$R_{\tilde{n}\tilde{n}}(\tau) = R_{xx}(\tau) + jR_{yx}(\tau) \quad (\text{A.9})$$

This relates the autocorrelation function of the complex envelope to the autocorrelation functions of the quadrature components. Further, from (A.9) and (A.8) we can see that

$$R_{\tilde{n}\tilde{n}}(\tau) = R_{\tilde{n}\tilde{n}}^*(-\tau) \quad (\text{A.10})$$

The power spectral density of it is the Fourier transform of the autocorrelation func-

tion (Wiener-Khinchine relation):

$$\begin{aligned}\Psi_{\tilde{n}}(f) &= \int_{-\infty}^{\infty} R_{\tilde{n}\tilde{n}}(\tau)e^{-j2\pi f\tau} d\tau = \int_{-\infty}^{\infty} R_{\tilde{n}\tilde{n}}^*(-\tau)e^{-j2\pi f\tau} d\tau \\ &= \left[\int_{-\infty}^{\infty} R_{\tilde{n}\tilde{n}}(-\tau)e^{j2\pi f\tau} d\tau \right]^* = \Psi_{\tilde{n}}^*(f)\end{aligned}\quad (\text{A.11})$$

This means that $\Psi_{\tilde{n}}(f)$ is a real-valued function of f .

Using (A.7) and (A.9) we have

$$R_{nn}(\tau) = \text{Re}[R_{\tilde{n}\tilde{n}}(\tau)e^{j2\pi f_c\tau}] \quad (\text{A.12})$$

This indicates that the autocorrelation function of the bandpass stationary random process is completely determined by the autocorrelation function of its complex envelope. Consequently the power spectral density of $n(t)$ is also completely determined by the power spectral density of $\tilde{n}(t)$ as follows.

$$\begin{aligned}\Psi_n(f) &= \mathcal{F}\{\text{Re}[R_{\tilde{n}\tilde{n}}(\tau)e^{j2\pi f_c\tau}]\} \\ &= \mathcal{F}\left\{\frac{1}{2}[R_{\tilde{n}\tilde{n}}(\tau)e^{j2\pi f_c\tau} + R_{\tilde{n}\tilde{n}}^*(\tau)e^{-j2\pi f_c\tau}]\right\} \\ &= \frac{1}{2}\{\Psi_{\tilde{n}}(f - f_c) + \Psi_{\tilde{n}}^*(-f - f_c)\}\end{aligned}$$

where we have used the frequency shifting and conjugate function properties of the Fourier transform (\mathcal{F}) (see [1]). Further, since $\Psi_{\tilde{n}}(f)$ is real-valued (see (A.11)), the above equation can be finalized as

$$\Psi_n(f) = \frac{1}{2}[\Psi_{\tilde{n}}(f - f_c) + \Psi_{\tilde{n}}(-f - f_c)] \quad (\text{A.13})$$

This equation indicates that the PSD of a bandpass stationary random process, be it noise or signal, is completely determined by the PSD of its complex envelope or equivalent baseband signal. It consists of frequency shifted (also scaled by 1/2) $\Psi_{\tilde{n}}(f)$ centered at f_c and $-f_c$ respectively. Thus when we examine the PSD of a bandpass stationary random process, it is sufficient to examine the PSD of its complex envelope or equivalent baseband signal.

A.3 POWER SPECTRAL DENSITIES OF DIGITAL SIGNALS

Digital signals are essentially random in nature. For example, in digital telephony the digital signals are digitized voice, which are random. In digital television the digital signals are digitized image and voice, which are also random. The bandwidth

occupied by a digital signal is of the most concern to system design engineers. In this section we derive a general formula for the PSD of digital signals. This general formula includes cases of correlated data and uncorrelated data. Therefore it can be used for a wide range of applications involving baseband signals and bandpass signals.

Let the baseband digital signal be represented by

$$s(t) = \sum_{n=-\infty}^{\infty} a_n g(t - nT) \quad (\text{A.14})$$

where a_n are discrete random data symbols, $g(t)$ is a signal of duration T (i.e., nonzero only in $[0, T]$). Let us name $g(t)$ as the *symbol function*. It could be any signal with a Fourier transform. For example it could be a baseband symbol-shaping pulse or a burst of carrier at passband. The random sequence $\{a_n\}$ could be binary or nonbinary.

Now to find out the power spectral density of the signal in (A.14), we first truncate the signal to get

$$s_N(t) = \sum_{n=-N}^N a_n g(t - nT) \quad (\text{A.15})$$

Next we assume it is not random and take Fourier transform of both sides of (A.15), the spectrum of this truncated signal is found as

$$A_N(f) = G(f) \sum_{n=-N}^N a_n e^{-j\omega nT}$$

where $\omega = 2\pi f$. The power spectral density of the original signal in (A.14) is obtained by taking the statistical average and time limit of $|A_N(f)|^2$ as follows.

$$\begin{aligned} \Psi_s(f) &= \lim_{N \rightarrow \infty} \frac{1}{(2N+1)T} E\{|A_N(f)|^2\} \\ &= \lim_{N \rightarrow \infty} \frac{|G(f)|^2}{(2N+1)T} E\left\{\left|\sum_{n=-N}^N a_n e^{-j\omega nT}\right|^2\right\} \\ &= \lim_{N \rightarrow \infty} \frac{|G(f)|^2}{(2N+1)T} E\left\{\left(\sum_{n=-N}^N a_n e^{-j\omega nT}\right)\left(\sum_{n=-N}^N a_n e^{-j\omega nT}\right)^*\right\} \\ &= |G(f)|^2 \lim_{N \rightarrow \infty} \frac{1}{(2N+1)T} \sum_{n=-N}^N \sum_{m=-N}^N E\{a_n a_m\} e^{j(m-n)\omega T} \end{aligned}$$

$$= |G(f)|^2 \lim_{N \rightarrow \infty} \frac{1}{(2N+1)T} \sum_{n=-N}^N \sum_{k=n+N}^{n-N} R(k) e^{-jk\omega T}$$

where $k = n - m$, $E\{a_n a_m\} = E\{a_n a_{n-k}\} = R(k)$ is the autocorrelation function of the data bits. Note that $R(-k) = R(k)$. Realizing the inner summations become the same regardless of the value of index n when $N \rightarrow \infty$, we obtain

$$\begin{aligned} \Psi_s(f) &= \frac{|G(f)|^2}{T} \lim_{N \rightarrow \infty} \left(\frac{2N+1}{(2N+1)} \sum_{k=n+N}^{n-N} R(k) e^{-jk\omega T} \right) \\ &= \frac{|G(f)|^2}{T} \sum_{k=-\infty}^{\infty} R(k) e^{-jk\omega T} \end{aligned}$$

Equivalently this is

$$\Psi_s(f) = \frac{|G(f)|^2}{T} \sum_{k=-\infty}^{\infty} R(k) e^{-jk\omega T} \quad (\text{A.16})$$

Now we discuss two possible cases of $R(k)$.

A.3.1 Case 1: Data Symbols Are Uncorrelated

Assume a_n has a mean of $E\{a_n\} = m_a$ and a variance of σ_a^2 , then

$$\begin{aligned} R(k) &= \begin{cases} E\{a_n^2\}, & k = 0 \\ E\{a_n\}E\{a_{n-k}\}, & k \neq 0 \end{cases} \\ &= \begin{cases} \sigma_a^2 + m_a^2, & k = 0 \\ m_a^2, & k \neq 0 \end{cases} \end{aligned}$$

Substitute this for $R(k)$ in (A.16) we have

$$\Psi_s(f) = \frac{|G(f)|^2}{T} \left(\sigma_a^2 + m_a^2 \sum_{k=-\infty}^{\infty} e^{-jk\omega T} \right)$$

By revoking the Poisson sum formula ([1] p.62)

$$\sum_{k=-\infty}^{\infty} e^{-jk\omega T} = \frac{1}{T} \sum_{k=-\infty}^{\infty} \delta\left(f - \frac{k}{T}\right)$$

where $\delta(f)$ is the impulse function, we have

$$\Psi_s(f) = \frac{|G(f)|^2}{T} \left(\sigma_a^2 + \frac{m_a^2}{T} \sum_{k=-\infty}^{\infty} \delta(f - \frac{k}{T}) \right) \quad (\text{A.17})$$

That is, for uncorrelated data

$$\Psi_s(f) = \underbrace{\frac{\sigma_a^2 |G(f)|^2}{T}}_{\text{continuous spectrum}} + \underbrace{\left(\frac{m_a}{T} \right)^2 \sum_{k=-\infty}^{\infty} |G(\frac{k}{T})|^2 \delta(f - \frac{k}{T})}_{\text{discrete spectrum}} \quad (\text{A.18})$$

The first term is the continuous part of the spectrum which is a scaled version of the PSD of the symbol-shaping pulse. The second term is the discrete part of the spectrum which has spectral lines at frequencies k/T (i.e., multiples of the data rate). The spectral lines have an envelope of the shape of the PSD of the symbol-shaping pulse. Each spectral line has a strength of $(m_a/T)^2 |G(k/T)|^2$.

In digital communications, the most common case is that the data bits are binary (± 1), equiprobable, stationary, and uncorrelated. That is

$$s(t) = \sum_{n=-\infty}^{\infty} a_n g(t - nT)$$

where $a_n = +1$ or -1 with equal probabilities, and $E\{a_n a_m\} = E\{a_n\}E\{a_m\}$ for $n \neq m$. It is easy to see that its mean is zero:

$$m_a = E\{a_n\} = 0.5(1) + 0.5(-1) = 0$$

and its variance is

$$\sigma_a^2 = E\{a_n^2\} + m_a^2 = E\{a_n^2\} = 0.5(+1)^2 + 0.5(-1)^2 = 1$$

Further, since a_n are uncorrelated and stationary, then

$$\begin{aligned} R(k) &= E\{a_n a_{n-k}\} \\ &= \begin{cases} E\{a_n^2\} = \sigma_a^2 = 1, & k = 0 \\ E\{a_n a_{n-k}\} = E\{a_n\}E\{a_{n-k}\} = 0 \cdot 0 = 0, & k \neq 0 \end{cases} \end{aligned}$$

Now refer to (A.18), note that $m_a = 0$ and $\sigma_a^2 = 1$, the second term becomes 0 and the PSD of the signal is

$$\Psi_s(f) = \frac{|G(f)|^2}{T} \quad (\text{A.19})$$

This is a very important expression which will be used often in evaluating PSD of digital modulated signals. It shows that the PSD of a binary (± 1), equiprobable, stationary, and uncorrelated data sequence is just equal to the energy spectral density $|G(f)|^2$ of the symbol-shaping pulse $g(t)$ divided by the symbol duration.

Example 1 Data bits are binary (± 1), equiprobable, stationary, and uncorrelated. The symbol-shaping pulse is the rectangular pulse: $g(t) = 1$ for $(-T/2, T/2)$ and 0 elsewhere. Then from a Fourier transform table,

$$G(f) = T \left(\frac{\sin \pi fT}{\pi fT} \right)$$

From (A.19) its PSD is

$$\Psi_s(f) = \frac{|G(f)|^2}{T} = T \left(\frac{\sin \pi fT}{\pi fT} \right)^2$$

A.3.2 Case 2: Data Symbols Are Correlated

For the general case where there is correlation between that data, let \tilde{a}_n be the corresponding data that have been normalized to have unity variance and zero mean, that is $\tilde{a}_n = (a_n - m_a)/\sigma_a$, thus $a_n = \sigma_a \tilde{a}_n + m_a$, then

$$\begin{aligned} R(k) &= E\{a_n a_{n-k}\} = E\{(\sigma_a \tilde{a}_n + m_a)(\sigma_a \tilde{a}_{n-k} + m_a)\} \\ &= \sigma_a^2 E\{\tilde{a}_n \tilde{a}_{n-k}\} + \underbrace{E\{\sigma_a m_a \tilde{a}_n\}}_0 + \underbrace{E\{\sigma_a m_a \tilde{a}_{n-k}\}}_0 + E\{m_a^2\} \\ &= \sigma_a^2 \rho(k) + m_a^2 \end{aligned}$$

where

$$\rho(k) = E\{\tilde{a}_n \tilde{a}_{n-k}\}$$

is the autocorrelation coefficient. Thus for correlated data

$$\begin{aligned} \Psi_s(f) &= \frac{|G(f)|^2}{T} \left(\sigma_a^2 \sum_{k=-\infty}^{\infty} \rho(k) e^{-jk\omega T} + m_a^2 \sum_{k=-\infty}^{\infty} e^{-jk\omega T} \right) \\ &= \underbrace{\sigma_a^2 R_d |G(f)|^2 w_p(f)}_{\text{continuous spectrum}} + \underbrace{(m_a R_d)^2 \sum_{k=-\infty}^{\infty} |G(kR_d)|^2 \delta(f - kR_d)}_{\text{discrete spectrum}} \end{aligned}$$

where $R_d = 1/T$ is the data rate, and Poisson sum formula is used for the second term conversion and

$$w_p(f) = \sum_{k=-\infty}^{\infty} \rho(k) e^{-jk\omega T} = \mathcal{F} \left\{ \sum_{k=-\infty}^{\infty} \rho(k) \delta(\tau - kT) \right\}$$

is a spectral weight function which can be obtained from the Fourier transform (\mathcal{F}) of the autocorrelation coefficient impulse train. Comparing (A.20) with (A.18) shows that the PSD of the correlated digital signal has the same discrete spectral part of the uncorrelated one. However, its continuous spectral part has an additional weight function which is determined by the autocorrelation coefficient impulse train of the data sequence.

In this section we have derived the PSD of a baseband digital signal by using time and statistical average of the Fourier transform of the truncated signal. Another method is to use the Wiener-Khinchine relation (Section A.2). That is, we first find the autocorrelation function of the digital signal $g(t)$. Then we take the Fourier transform to find the PSD expression. See reference [2, p.191] for detail.

A.4 POWER SPECTRAL DENSITIES OF DIGITAL BANDPASS SIGNALS

We have mentioned that symbol function $g(t)$ could be any function with a Fourier transform defined on $[0, T]$. Even though the spectral density expressions derived in the previous section are used mainly for a variety of baseband digital signals, they can also be used for some bandpass signals. For example, $g(t)$ could be a burst of carrier, sinusoidal, or square waveform. If $g(t)$ is a burst of sinusoidal signal, the signal $s(t)$ would be an ASK signal. The spectrum of $g(t)$ can be easily found as

$$\begin{aligned} G(f) &= \mathcal{F}\{\cos(2\pi f_c t)\}, \quad 0 \leq t \leq T \\ &= \frac{1}{2}T[\text{sinc}(f - f_c)T + \text{sinc}(f + f_c)T]e^{-j\pi f T} \end{aligned}$$

and the PSD of the ASK signal is

$$\begin{aligned} \Psi_s(f) &= \frac{|G(f)|^2}{T} = \frac{1}{T} \left(\frac{1}{2}T[\text{sinc}(f - f_c)T + \text{sinc}(f + f_c)T] \right)^2 \\ &\approx \frac{1}{4}T\{\text{sinc}^2(f - f_c)T + \text{sinc}^2(f + f_c)T\} \end{aligned}$$

which appears as two squared sinc functions centered at f_c and $-f_c$, respectively.

For bandpass signals with data symbols embedded in the phase or frequency of the carrier, the signal cannot be written as the form of (A.14). We must find another way to compute the spectra.

Many bandpass signals of practical interest, such as FSK, PSK signals, binary or M-ary, can be considered as a sum of an inphase component and a quadrature component. There is a rather easy way to compute the PSD of such a signal. We will discuss the method here. For other bandpass signals, such as a continuous phase modulation (CPM) signal, finding the PSD is much more complicated. We will discuss the method in the next section.

Now consider a carrier modulated bandpass signal in the form of

$$s(t) = x(t) \cos(2\pi f_c t) - y(t) \sin(2\pi f_c t)$$

where $x(t)$ and $y(t)$ are the inphase and quadrature components, determined by data symbol sequences $\{x_k\}$ and $\{y_k\}$, respectively.

$$x(t) = \sum_{k=-\infty}^{\infty} x_k p(t - kT)$$

$$y(t) = \sum_{k=-\infty}^{\infty} y_k q(t - kT)$$

The signals $p(t)$ and $q(t)$ are baseband pulse-shaping functions defined on $[0, T]$, whose Fourier transforms,

$$P(f) = \mathcal{F}\{p(t)\}$$

and

$$Q(f) = \mathcal{F}\{q(t)\}$$

exist.

We assume that $\{x_k\}$ and $\{y_k\}$ are independent, identically distributed random sequences with zero means

$$m_x = m_y = 0$$

and each sequence member has mean square value

$$E\{x_k^2\} = \sigma_x^2$$

and

$$E\{y_k^2\} = \sigma_y^2$$

respectively. Thus $\{x_k\}$ and $\{y_k\}$ are discrete stationary random processes. According to (A.13), it suffices to find the PSD of the complex envelope. The complex envelope of the signal $s(t)$ is

$$\tilde{s}(t) = x(t) + jy(t)$$

To calculate the PSD of $\tilde{s}(t)$, we calculate its autocorrelation function first.

$$\begin{aligned} R_{\tilde{s}}(\tau) &= E\{\tilde{s}(t)\tilde{s}^*(t-\tau)\} \\ &= E\{[x(t) + jy(t)][x(t-\tau) - jy(t-\tau)]\} \\ &= R_x(\tau) + R_y(\tau) \end{aligned}$$

where

$$R_x(\tau) = E\{x(t)x(t-\tau)\}$$

and

$$R_y(\tau) = E\{y(t)y(t-\tau)\}$$

and the cross-correlation terms vanished since they are zero. From the Wiener-Khintchine theorem, we have

$$\begin{aligned} \Psi_{\tilde{s}}(f) &= \mathcal{F}\{R_{\tilde{s}}(\tau)\} = \mathcal{F}\{R_x(\tau)\} + \mathcal{F}\{R_y(\tau)\} \\ &= \Psi_x(f) + \Psi_y(f) \end{aligned}$$

where $\Psi_x(f)$ and $\Psi_y(f)$ are PSD of the inphase and quadrature component, respectively. Comparing the expressions of $x(t)$ and $y(t)$ with (A.14) we realize that we can use (A.18) to find $\Psi_x(f)$ and $\Psi_y(f)$. That is

$$\Psi_x(f) = \frac{\sigma_x^2 |P(f)|^2}{T}$$

and

$$\Psi_y(f) = \frac{\sigma_y^2 |Q(f)|^2}{T}$$

thus

$$\Psi_{\tilde{s}}(f) = \frac{\sigma_x^2 |P(f)|^2}{T} + \frac{\sigma_y^2 |Q(f)|^2}{T} \quad (\text{A.21})$$

This expression can be used for all quadrature modulated signals, including M-ary PSK, MSK, QAM, etc.

A.5 POWER SPECTRAL DENSITIES OF CPM SIGNALS

CPM signal is defined by

$$s(t) = A \cos(2\pi f_c t + \Phi(t, \mathbf{a})), \quad -\infty \leq t \leq \infty \quad (\text{A.22})$$

The transmitted M-ary symbols a_i are embedded in the phase

$$\Phi(t, \mathbf{a}) = 2\pi h \sum_{k=-\infty}^{\infty} a_k q(t - kT), \quad (\text{A.23})$$

with

$$q(t) = \int_{-\infty}^t g(\tau) d\tau. \quad (\text{A.24})$$

The M-ary data a_k may take any of the M values: $\pm 1, \pm 3, \dots, \pm(M-1)$, where M usually is a power of 2. The phase is proportional to the parameter h which is called the modulation index. Function $g(t)$ is the *frequency shape pulse*. The function $g(t)$ usually has a smooth pulse shape over a finite time interval $0 \leq t \leq LT$, and is zero outside. Function $q(t)$ is the *phase function*. For $g(t)$ defined on $[0, LT]$, $q(t) = 0$ for $t < 0$, and $q(t)$ reaches the maximum at $t = LT$ and remains at the maximum thereafter. Usually $g(t)$ is normalized to have $q(t \geq LT) = 1/2$.

We assume that symbols $\{a_k\}$ are statistically independent and identically distributed with prior probabilities $\Pr(a_n) = P_n$, $n = \pm 1, \pm 3, \dots, \pm(M-1)$, where $\sum P_n = 1$.

The CPM signal can be written as

$$\begin{aligned} s(t) &= A \operatorname{Re}\{\exp[j2\pi f_c t + j\Phi(t, \mathbf{a})]\} \\ &= A \operatorname{Re}\{\exp[j\Phi(t, \mathbf{a})] \exp[j2\pi f_c t]\} \end{aligned}$$

The complex envelope of the CPM signal is (omitting the constant amplitude A , which will not affect the shape of the autocorrelation function and the power spectral density)

$$\tilde{s}(t) = \exp[j\Phi(t, \mathbf{a})]$$

We now present a simple, fast, and reliable general numerical method of computing the PSD of the general CPM signal. This method was first given in [3] and appeared in [2] and [4] as well.

First we find the autocorrelation of $\tilde{s}(t)$.

$$R_{\tilde{s}}(t + \tau; t) = E\{\exp[j\Phi(t + \tau, \mathbf{a})][\exp[j\Phi(t, \mathbf{a})]]^*\}$$

$$\begin{aligned}
 &= E\{\exp[j\Phi(t + \tau, \mathbf{a}) - j\Phi(t, \mathbf{a})]\} \\
 &= E\left\{\exp\left[j2\pi h \sum_{k=-\infty}^{\infty} a_k[q(t + \tau - kT) - q(t - kT)]\right]\right\}
 \end{aligned}$$

The sum in the exponent can be expressed as a product of exponents

$$R_{\bar{s}}(t + \tau; t) = E\left\{\prod_{k=-\infty}^{\infty} \exp[j2\pi h a_k[q(t + \tau - kT) - q(t - kT)]]\right\}$$

Now we carry out the expectation over the data symbols. Since they are statistically independent, we have

$$R_{\bar{s}}(t + \tau; t) = \prod_{k=-\infty}^{\infty} \left\{ \sum_{\substack{n=-(M-1) \\ n \text{ odd}}}^{M-1} P_n \exp[j2\pi h n[q(t + \tau - kT) - q(t - kT)]] \right\} \quad (\text{A.25})$$

where P_n is the a priori probability of the symbol n . Then we take the time-average of the autocorrelation function in $[0, T]$. (In fact averaging over any time interval of duration T would give the same result.)

$$R_{\bar{s}}(\tau) = \frac{1}{T} \int_0^T R_{\bar{s}}(t + \tau; t) dt \quad (\text{A.26})$$

Seemingly, there are an infinite number of factors in the product of (A.25), but in fact there are only a finite number of terms that have nonzero exponents. Note that the integration interval is only in $[0, T]$. Since $q(t)$ is 0 for $t < 0$ and equal to $1/2$ for $t \geq LT$, for most k , the two terms in the exponent in (A.25) will both be zero or both be $1/2$. That is, they cancel to zero for all but a finite number of factors.

Suppose $\tau \geq 0$ and let $\tau = \xi + mT$ where $0 \leq \xi < T$ and $m = 0, 1, 2, \dots$, then for the exponent to be unconditionally zero, we have to have

$$\begin{cases} t + \xi + mT - kT < 0 \\ t - kT < 0 \end{cases} \quad (\text{A.27})$$

or

$$\begin{cases} t + \xi + mT - kT > LT \\ t - kT > LT \end{cases} \quad (\text{A.28})$$

Notice that $0 \leq t < T$ and $0 \leq \xi < T$, then $0 \leq t + \xi < 2T$. From (A.27) we have $k > m + 2$. From (A.28) we obtain $k < -L$. Thus for the exponent to be nonzero

we need

$$1 - L \leq k \leq m + 1 \quad (\text{A.29})$$

For other values of the index k , the exponent is zero, the sum of P_n becomes 1. Thus (A.26) reduces to

$$\begin{aligned} R_{\bar{s}}(\tau) &= R_{\bar{s}}(\xi + mT) \\ &= \frac{1}{T} \int_0^T \prod_{k=1-L}^{m+1} \left\{ \sum_{\substack{n=-(M-1) \\ n \text{ odd}}}^{M-1} P_n \exp[j2\pi hnq_d(t, m, k, \xi)] \right\} dt \end{aligned} \quad (\text{A.30})$$

where

$$q_d(t, m, k, \xi) = q(t + \xi - (k - m)T) - q(t - kT)$$

Note that we have assumed that $\tau \geq 0$ in deriving the above expression. However, we can use a property of autocorrelation functions to find $R_{\bar{s}}(\tau)$ for $\tau \leq 0$. It is well known that [5]

$$R_{\bar{s}}(-\tau) = R_{\bar{s}}^*(\tau) \quad (\text{A.31})$$

This property can be used to find $R_{\bar{s}}(\tau)$ for $\tau \leq 0$ from values of $R_{\bar{s}}(\tau)$ for $\tau \geq 0$.

Before we proceed to find the PSD of the CPM signal by taking the Fourier transform of $R_{\bar{s}}(\tau)$, we need to study (A.30) for $\tau = \xi + mT \geq LT$. The results will be used in finding the PSD.

We divide the range of k , in which the exponent is nonzero, given in (A.29), into two segments: $1 - L \leq k \leq 0$ and $1 \leq k \leq m + 1$. For $1 - L \leq k \leq 0$, we have $t + \tau - kT > LT$ for $t \in [0, T]$. Then $q(t + \tau - kT) = q(LT)$ which is a constant. For $1 \leq k \leq m + 1$ we have $t - kT \leq 0$, then $q(t - kT) = 0$ always. Thus we have

$$\begin{aligned} R_{\bar{s}}(\tau) &= R_{\bar{s}}(\xi + mT) \\ &= \frac{1}{T} \int_0^T \prod_{k=1-L}^0 \left\{ \sum_{\substack{n=-(M-1) \\ n \text{ odd}}}^{M-1} P_n \exp[j2\pi hn[q(LT) - q(t - kT)]] \right\} \\ &\quad \times \prod_{k=1}^{m+1} \left\{ \sum_{\substack{n=-(M-1) \\ n \text{ odd}}}^{M-1} P_n \exp[j2\pi hnq(t + \tau - kT)] \right\} dt \end{aligned} \quad (\text{A.32})$$

Now notice that

$$\begin{aligned}
 & \exp [j2\pi hnq(t + \tau - kT)] \\
 = & \exp [j2\pi hnq(t + \xi + mT - kT)] \\
 = & \exp [j2\pi hnq(t + \xi - (k - m)T)] \\
 = & \exp [j2\pi hnq(t + \xi - iT)]
 \end{aligned}$$

where $i = k - m$. Using index i , $\prod_{k=1}^{m+1}$ becomes $\prod_{i=1-m}^1 = \prod_{i=1-m}^{-L} \prod_{i=-L+1}^1$. For indexes $1 - m \leq i \leq -L$, $q(t + \xi - iT) = q(LT)$ always. Thus (A.32) becomes

$$\begin{aligned}
 R_{\bar{s}}(\tau) &= \frac{1}{T} \int_0^T \prod_{k=1-L}^0 \left\{ \sum_{\substack{n=-(M-1) \\ n \text{ odd}}}^{M-1} P_n \exp [j2\pi hn[q(LT) - q(t - kT)]] \right\} \\
 &\quad \times C_a^{m-L} \prod_{k=-L+1}^1 \left\{ \sum_{\substack{n=-(M-1) \\ n \text{ odd}}}^{M-1} P_n \exp [j2\pi hnq(t + \xi - kT)] \right\} dt. \\
 (\text{for } m &\geq L) \tag{A.33}
 \end{aligned}$$

where

$$C_a = \sum_{\substack{n=-(M-1) \\ n \text{ odd}}}^{M-1} P_n \exp [j2\pi hnq(LT)] \tag{A.34}$$

is a constant, independent of τ and C_a^{m-L} represents the product $\prod_{i=1-m}^{-L}$. The integrand in (A.33) is independent of m , and only depends on ξ . We can write the autocorrelation function as

$$R_{\bar{s}}(\tau) = R_{\bar{s}}(\xi + mT) = C_a^{m-L} \psi(\xi), \quad m \geq L, \quad 0 \leq \xi < T \tag{A.35}$$

where $\psi(\xi)$ denotes the integral in (A.33) which only need be computed in $[0, T]$. Thus $R_{\bar{s}}(\tau)$ is separable in the arguments ξ and m . To compute $R_{\bar{s}}(\tau)$ one only needs to compute $\psi(\xi)$ in $[0, T]$ and multiply it with the constant C_a^{m-L} which is the geometrical decaying factor from symbol interval to symbol interval.

Now we proceed to find the power spectral density of the CPM signal by taking the Fourier transform of $R_{\bar{s}}(\tau)$

$$\Psi_{\bar{s}}(f) = \mathcal{F}\{R_{\bar{s}}(\tau)\} = \int_{-\infty}^{\infty} R_{\bar{s}}(\tau) e^{-j2\pi f\tau} d\tau$$

Using (A.31), this can be simplified as

$$\Psi_{\bar{s}}(f) = 2 \operatorname{Re} \left[\int_0^{\infty} R_{\bar{s}}(\tau) e^{-j2\pi f\tau} d\tau \right] \quad (\text{A.36})$$

in which $\tau \geq 0$. Therefore $R_{\bar{s}}(\tau)$ need be computed only for positive τ values. The integral in the above equation can be divided into two parts

$$\int_0^{\infty} R_{\bar{s}}(\tau) e^{-j2\pi f\tau} d\tau = \int_0^{LT} R_{\bar{s}}(\tau) e^{-j2\pi f\tau} d\tau + \int_{LT}^{\infty} R_{\bar{s}}(\tau) e^{-j2\pi f\tau} d\tau \quad (\text{A.37})$$

where the second integral is

$$\begin{aligned} \int_{LT}^{\infty} R_{\bar{s}}(\tau) e^{-j2\pi f\tau} d\tau &= \sum_{m=L}^{\infty} \int_0^T C_a^{m-L} \psi(\xi) e^{-j2\pi f(\xi+mT)} d\xi \\ &= \sum_{m=L}^{\infty} e^{-j2\pi fmT} \int_0^T C_a^{m-L} \psi(\xi) e^{-j2\pi f\xi} d\xi \\ &= \left(\sum_{m=L}^{\infty} e^{-j2\pi fmT} C_a^{m-L} \right) \int_0^T \psi(\xi) e^{-j2\pi f\xi} d\xi \\ &= e^{-j2\pi fLT} \left(\sum_{n=0}^{\infty} e^{-j2\pi fnT} C_a^n \right) \int_0^T \psi(\xi) e^{-j2\pi f\xi} d\xi \end{aligned} \quad (\text{A.38})$$

From (A.34) we know $|C_a| \leq 1$. Consider $|C_a| < 1$ first. The sum in (A.38) is geometric and converges (the well-known sum formula for a geometric series $\sum_{n=0}^{\infty} x^n = 1/(1-x)$, $|x| < 1$, is used)

$$\sum_{n=0}^{\infty} e^{-j2\pi fnT} C_a^n = \frac{1}{1 - C_a e^{-j2\pi fT}} \quad (\text{A.39})$$

Further, let $m = L$ in (A.35) we have

$$\psi(\xi) = R_{\bar{s}}(\xi + LT)$$

Then (A.38) can be expressed in terms of $R_{\bar{s}}(\tau)$ as

$$\int_{LT}^{\infty} R_{\bar{s}}(\tau) e^{-j2\pi f\tau} d\tau = \frac{e^{-j2\pi fLT}}{1 - C_a e^{-j2\pi fT}} \int_0^T R_{\bar{s}}(\tau + LT) e^{-j2\pi f\tau} d\tau \quad (\text{A.40})$$

Then (A.36) can be expressed in the following final form

$$\Psi_{\bar{s}}(f) = 2 \operatorname{Re} \left\{ \int_0^{LT} R_{\bar{s}}(\tau) e^{-j2\pi f\tau} d\tau + \frac{e^{-j2\pi fLT}}{1 - C_a e^{-j2\pi fT}} \int_0^T R_{\bar{s}}(\tau + LT) e^{-j2\pi f\tau} d\tau \right\} \quad (\text{A.41})$$

From this expression we see that $R_{\bar{s}}(\tau)$ only has to be computed over the interval $[0, (L + 1)T]$. The $R_{\bar{s}}(\tau)$ is most easily computed numerically by using (A.30). Then using (A.34) and (A.41) the PSD of a general CPM signal can be found for the case $|C_a| < 1$.

A special case is that $P_n = 1/M, n = \pm 1, \pm 3, \dots, \pm(M - 1)$. For this case, all quantities are real-valued, we have

$$R_{\bar{s}}(\tau) = \frac{1}{T} \int_0^T \prod_{k=1-L}^{\lceil \tau/T \rceil} \frac{1}{M} \frac{\sin 2\pi h M [q(t + \tau - kT) - q(t - kT)]}{\sin 2\pi h [q(t + \tau - kT) - q(t - kT)]} \quad (\text{A.42})$$

and

$$\Psi_{\bar{s}}(f) = 2 \int_0^{LT} R_{\bar{s}}(\tau) \cos 2\pi f\tau d\tau + \frac{2(1 - C_a \cos 2\pi fT)}{1 + C_a^2 - 2C_a \cos 2\pi fT} \int_{LT}^{(L+1)T} R_{\bar{s}}(\tau) \cos 2\pi f\tau d\tau \quad (\text{A.43})$$

Now consider $|C_a| = 1$ case. The analysis here basically follows the one given in [3]. First we note that when $q(LT) = 0$, then $C_a = 1$. But this is not our case since we have normalized $q(t)$ so that $q(LT) = 1/2$ in the above analysis. For $q(LT) = 1/2$,

$$C_a = \sum_{\substack{n=-(M-1) \\ n \text{ odd}}}^{M-1} P_n \exp[j\pi hn]$$

When h is not an integer, there are M cases that make $|C_a| = 1$ for M -ary symbols. That is, if the a priori probability of one symbol is 1 and the a priori probability of other symbols is 0, then

$$C_a = e^{jhn\pi}, \quad \operatorname{Pr}(n) = 1 \quad (\text{A.44})$$

These are extreme cases that have very little practical value. When h is an integer,

for M-ary symbols,

$$\begin{aligned}
 C_a &= \sum_{\substack{n=-(M-1) \\ n \text{ odd}}}^{M-1} P_n \exp[j\pi hn] \\
 &= \begin{cases} -1, & h \text{ odd integer} \\ +1, & h \text{ even integer} \end{cases} \quad (\text{A.45})
 \end{aligned}$$

These two cases make $R_{\bar{s}}(\tau)$ periodical outside $|\tau| = LT$, see (A.35). It is clear from (A.35) and (A.45) that when h is odd, the period is $2T$, when h is even, the period is T .

Extend the periodic part of $R_{\bar{s}}(\tau)$ to also cover the interval $[-LT, LT]$, and call this part $R_{dis}(\tau)$, then the rest of $R_{\bar{s}}(\tau)$ can be called $R_{con}(\tau)$, thus

$$R_{\bar{s}}(\tau) = R_{con}(\tau) + R_{dis}(\tau)$$

where $R_{dis}(\tau)$ is strictly periodical and $R_{con}(\tau)$ is not. It is obvious that $R_{con}(\tau) \equiv 0$, for $|\tau| \geq LT$ from the above definition. Thus $R_{con}(\tau)$ yields the continuous part of the PSD and $R_{dis}(\tau)$ yields the discrete part of the PSD.

$$\Psi_{\bar{s}}(f) = 2 \operatorname{Re} \left[\int_0^{LT} R_{con}(\tau) e^{-j2\pi f\tau} d\tau \right] + F_{dis}(f) \quad (\text{A.46})$$

where $F_{dis}(f)$ is the discrete PSD of $R_{dis}(\tau)$ that should be computed using formulas of Fourier coefficients instead of (A.41). When h is even since the period of $R_{dis}(\tau)$ is T , the discrete frequency components appear at $f = \pm k/T$, $k = 0, 1, 2, \dots$. When h is odd, $R_{dis}(\tau) = \pm\psi(\xi)$ alternatively for every T seconds, that is, it is a periodic function with *odd half-wave symmetry* [6, p. 104]. Its spectrum would only have odd harmonics at $f = \pm(2k + 1)/2T$, $k = 0, 1, 2, \dots$.

The property that a CPM signal with integer index has discrete frequency components can be used to recover the carrier and symbol timing in CPM receivers. However, some of the components may have zero amplitude depending on the specific shape of the frequency pulse.

References

- [1] Haykin, S., *Communication Systems*, 3rd Ed., New York: John Wiley, 1994.
- [2] Proakis, J.G., *Digital Communications*, 2nd Ed., New York: McGraw-Hill, 1989.
- [3] Aulin, T. and C-E. Sundberg, "An easy way to calculate the power spectrum for digital FM." *Proceedings of the IEE, Part F: Communication, Radar and Signal Processing*, vol. 130(6), 1983, pp. 519-526.

- [4] Anderson, J., T. Aulin, and C-E. Sundberg, *Digital Phase Modulation*, New York: Plenum Publishing Company, 1986.
- [5] Whalen, A. D., *Detection of Signals in Noise*, New York and London: Academic Press, 1971.
- [6] McGillem, C., and G. Cooper, *Continuous and Discrete Signal and System Analysis*, 3rd Ed., Philadelphia: Sanders College Publishing, 1991.

Appendix B

Detection of Signals

B.1 DETECTION OF DISCRETE SIGNALS

Detection of discrete signals can be modeled by the classical hypothesis test problem. In this section we first examine the binary hypothesis test problem. We will address the M-ary hypothesis problem in later sections.

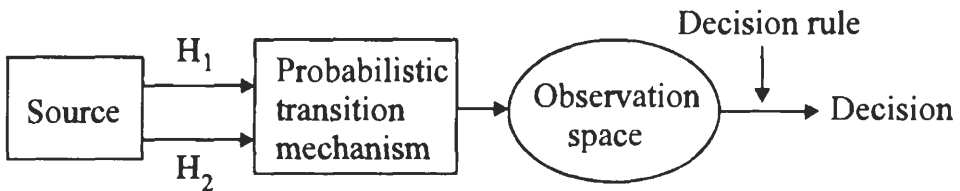


Figure B.1 Binary hypothesis test model.

B.1.1 Binary Hypothesis Test

The binary hypothesis model is shown in Figure B.1. The source generates an output which is one of two possible choices. We refer to them as *hypotheses*, H_1 and H_2 . In binary digital communications, these two outputs of the source are data 1 and 0. Therefore H_1 and H_2 can be associated with 1 and 0 being transmitted, respectively. The signal passes through a *probabilistic transition mechanism* which generates a point in the *observation space* based on the hypothesis and according to some probability law. In digital communications, it is the noisy channel which transports the signal but also adds noise to the signal. The observation space in general is N -dimensional. Each hypothesis maps into a point in the observation space. Each

point is an N -dimensional vector:

$$\mathbf{r} \triangleq \begin{bmatrix} r_1 \\ r_2 \\ \vdots \\ r_N \end{bmatrix}$$

The probabilistic transition mechanism generates points in accord with the two known conditional probability densities $p(\mathbf{r}/H_1)$ and $p(\mathbf{r}/H_2)$.¹ The object is to use this information to develop a suitable decision rule, based on which the two observations are compared and one of the hypotheses is chosen. To do this we must examine various criteria for making decisions.

B.1.2 Decision Criteria

With the binary hypothesis problem we know that either H_1 or H_2 is true. When we make decisions we could choose H_1 or H_2 . But a third choice is possible, that is, don't know. The third choice is actually used in digital communications. That is called *erasure*. However, we confine our discussion here to decision rules that require a choice of two hypotheses. In this case, there are four actions:

1. H_1 true; choose H_1 (correct);
2. H_1 true; choose H_2 (erroneous);
3. H_2 true; choose H_2 (correct);
4. H_2 true; choose H_1 (erroneous).

The first and third are correct choices. The second and the fourth are erroneous choices. The decision criterion should attach some relative importance to the four possible actions. The method of processing the received data (\mathbf{r}) will depend on the criterion we select.

B.1.2.1 Bayes Criterion

Bayes criterion is based on the average cost of four actions. We first define four costs as

1. $C_{11} \triangleq$ cost of action 1;

¹ $p(\mathbf{r}/H_i)$, $i = 1, 2$ are the probability densities of \mathbf{r} under the hypotheses H_i , $i = 1, 2$. Note that these two densities both are represented by the same function name p , but they are actually two different functions. The difference is indicated by the arguments. We will use this type of notation in the rest of this appendix.

2. $C_{21} \triangleq$ cost of action 2;
3. $C_{22} \triangleq$ cost of action 3;
4. $C_{12} \triangleq$ cost of action 4.

Note that C_{ij} denotes the cost of choosing hypothesis i while hypothesis j is true. Then we define the total cost as

$$\begin{aligned} \mathcal{R} \triangleq & C_{11}P_1 \Pr(\text{choose } H_1/H_1 \text{ is true}) \\ & + C_{21}P_1 \Pr(\text{choose } H_2/H_1 \text{ is true}) \\ & + C_{22}P_2 \Pr(\text{choose } H_1/H_2 \text{ is true}) \\ & + C_{12}P_2 \Pr(\text{choose } H_2/H_2 \text{ is true}) \end{aligned} \quad (\text{B.1})$$

where $P_1 = \Pr(H_1)$ and $P_2 = \Pr(H_2)$ are *a priori probabilities* of the hypotheses.

For each observation \mathbf{r} we must choose H_1 or H_2 . This is equivalent to divide the entire observation space Z into two subspaces Z_1 and Z_2 . If \mathbf{r} falls into Z_1 we say H_1 is true. If \mathbf{r} falls into Z_2 we say H_2 is true. Thus the cost can be written as

$$\begin{aligned} \mathcal{R} &= C_{11}P_1 \int_{Z_1} p(\mathbf{r}/H_1) d\mathbf{r} + C_{21}P_1 \int_{Z_2} p(\mathbf{r}/H_1) d\mathbf{r} \\ &+ C_{22}P_2 \int_{Z_2} p(\mathbf{r}/H_2) d\mathbf{r} + C_{12}P_2 \int_{Z_1} p(\mathbf{r}/H_2) d\mathbf{r} \\ &= P_1 C_{11} \int_{Z_1} p(\mathbf{r}/H_1) d\mathbf{r} + P_1 C_{21} \int_{Z-Z_1} p(\mathbf{r}/H_1) d\mathbf{r} \\ &+ P_2 C_{22} \int_{Z-Z_1} p(\mathbf{r}/H_2) d\mathbf{r} + P_2 C_{12} \int_{Z_1} p(\mathbf{r}/H_2) d\mathbf{r} \end{aligned} \quad (\text{B.2})$$

Observing that

$$\int_Z p(\mathbf{r}/H_1) d\mathbf{r} = \int_Z p(\mathbf{r}/H_2) d\mathbf{r} = 1$$

therefore

$$\begin{aligned} \mathcal{R} &= P_1 C_{21} + P_2 C_{22} \\ &+ \int_{Z_1} \{P_2(C_{12} - C_{22})p(\mathbf{r}/H_2) - P_1(C_{21} - C_{11})p(\mathbf{r}/H_1)\} d\mathbf{r} \end{aligned} \quad (\text{B.3})$$

We assume that the cost of a wrong decision is higher than the cost of a correct decision, that is,

$$C_{21} > C_{11}$$

$$C_{12} > C_{22}$$

In (B.3), to minimize \mathcal{R} we should assign all the values of \mathbf{r} which make the integral $\int_{Z_1}(\cdot) d\mathbf{r} < 0$ to Z_1 and assign all the values of \mathbf{r} which make the integral $\int_{Z_1}(\cdot) d\mathbf{r} > 0$ to Z_2 . Values of \mathbf{r} which make $\int_{Z_1}(\cdot) d\mathbf{r} = 0$ have no effect on the cost and may be assigned arbitrarily (they are assigned to H_1 here). Thus the decision regions are defined by: If

$$P_2(C_{12} - C_{22})p(\mathbf{r}/H_2) \geq P_1(C_{21} - C_{11})p(\mathbf{r}/H_1) \quad (\text{B.4})$$

assign \mathbf{r} to Z_2 (i.e., H_2 is true), otherwise assign \mathbf{r} to Z_1 (i.e., H_1 is true). Expression (B.4) can be written as

$$\frac{p(\mathbf{r}/H_2)}{p(\mathbf{r}/H_1)} \underset{H_1}{\overset{H_2}{\geq}} \frac{P_1(C_{21} - C_{11})}{P_2(C_{12} - C_{22})}$$

The left-hand-side quantity is called *likelihood ratio*:

$$\Lambda(\mathbf{r}) \triangleq \frac{p(\mathbf{r}/H_2)}{p(\mathbf{r}/H_1)} \quad (\text{B.5})$$

and the right-hand-side quantity is called *threshold*:

$$\eta \triangleq \frac{P_1(C_{21} - C_{11})}{P_2(C_{12} - C_{22})} \quad (\text{B.6})$$

Then the Bayes test becomes

$$\Lambda(\mathbf{r}) \underset{H_1}{\overset{H_2}{\geq}} \eta \quad (\text{B.7})$$

or

$$\ln \Lambda(\mathbf{r}) \underset{H_1}{\overset{H_2}{\geq}} \ln \eta \quad (\text{B.8})$$

since $\ln(\cdot)$ is a monotonic function. In the following we study several cases which are important in digital communication.

B.1.2.2 Minimum Probability of Error Criterion

A reasonable assignment of costs would be like this: let the costs for errors be equal and the costs for correct decisions be zero. Then we have $C_{12} = C_{21} = 1$ and

$C_{11} = C_{22} = 0$. The total cost from (B.2) is

$$\mathcal{R} = P_1 \int_{Z_2} p(\mathbf{r}/H_1) d\mathbf{r} + P_2 \int_{Z_1} p(\mathbf{r}/H_2) d\mathbf{r} \quad (\text{B.9})$$

which is the total error probability. Since the Bayes test minimizes \mathcal{R} , this set of cost assignments is called *minimum error probability criterion*. Under this criterion, the Bayes test becomes

$$\Lambda(\mathbf{r}) \underset{H_1}{\overset{H_2}{\geq}} \frac{P_1}{P_2} \quad (\text{B.10})$$

or

$$\ln \Lambda(\mathbf{r}) \underset{H_1}{\overset{H_2}{\geq}} \ln \frac{P_1}{P_2} \quad (\text{B.11})$$

B.1.2.3 Maximum A Posteriori Probability Criterion (MAP)

The minimum error probability criterion is also the *maximum a posteriori probability* (MAP) criterion.

Proof: The a posteriori probabilities are $\Pr(H_1/\mathbf{r})$ and $\Pr(H_2/\mathbf{r})$. Denote the probability density of \mathbf{r} as $p(\mathbf{r})$. The MAP test is

$$\begin{aligned} \frac{\Pr(H_2/\mathbf{r})}{\Pr(H_1/\mathbf{r})} &= \frac{\Pr(H_2/\mathbf{r})p(\mathbf{r})}{\Pr(H_1/\mathbf{r})p(\mathbf{r})} \\ &= \frac{p(H_2, \mathbf{r})}{p(H_1, \mathbf{r})} \\ &= \frac{p(\mathbf{r}/H_2) \Pr(H_2)}{p(\mathbf{r}/H_1) \Pr(H_1)} \\ &= \frac{p(\mathbf{r}/H_2) P_2}{p(\mathbf{r}/H_1) P_1} \underset{H_1}{\overset{H_2}{\geq}} 1 \end{aligned}$$

or

$$\Lambda(\mathbf{r}) \underset{H_1}{\overset{H_2}{\geq}} \frac{P_1}{P_2}$$

which is the minimum error probability test.

B.1.2.4 Maximum Likelihood Criterion

Now we further assume that $P_1 = P_2$, that is, the two hypotheses are equally likely. This case is the most frequent in digital communications. The minimum error probability test becomes

$$\Lambda(\mathbf{r}) \underset{H_1}{\overset{H_2}{\gtrless}} 1$$

which is

$$p(\mathbf{r}/H_2) \underset{H_1}{\overset{H_2}{\gtrless}} p(\mathbf{r}/H_1)$$

This means the decision rule is to compare likelihood functions and choose the largest: *maximum likelihood criterion*.

B.1.3 M Hypotheses

Now we consider M hypotheses. For M hypotheses, the risk is

$$\mathcal{R} = \sum_{i=1}^M \sum_{j=1}^M P_j C_{ij} \int_{Z_i} p(\mathbf{r}/H_j) d\mathbf{r} \quad (\text{B.12})$$

where the first summation is over choices and the second summation is over hypotheses. The optimum Bayes detector is the one that partitions the observation space Z into regions Z_i such that the risk is minimized. The risk expression can be written as

$$\begin{aligned} \mathcal{R} &= \sum_{i=1}^M \sum_{j=1}^M C_{ij} \int_{Z_i} p(\mathbf{r}/H_j) P_j d\mathbf{r} \\ &= \sum_{i=1}^M \sum_{j=1}^M C_{ij} \int_{Z_i} \Pr(H_j/\mathbf{r}) p(\mathbf{r}) d\mathbf{r} \\ &= \sum_{i=1}^M \int_{Z_i} \left(\sum_{j=1}^M C_{ij} \Pr(H_j/\mathbf{r}) \right) p(\mathbf{r}) d\mathbf{r} \end{aligned}$$

Let

$$\beta_i(\mathbf{r}) = \sum_{j=1}^M C_{ij} \Pr(H_j/\mathbf{r})$$

Then

$$\begin{aligned}\mathcal{R} &= \sum_{i=1}^M \int_{Z_i} \beta_i(\mathbf{r})p(\mathbf{r})d\mathbf{r} \\ &= \int_{Z_1} \beta_1(\mathbf{r})p(\mathbf{r})d\mathbf{r} + \int_{Z_2} \beta_2(\mathbf{r})p(\mathbf{r})d\mathbf{r} + \cdots + \int_{Z_M} \beta_M(\mathbf{r})p(\mathbf{r})d\mathbf{r}\end{aligned}$$

Each particular \mathbf{r} will be included in only one integral. The Bayes detector is supposed to assign it to the region Z_i where it will make the smallest contribution to the risk. Clearly this is done by choosing the smallest $\beta_i(\mathbf{r})$ and assigning \mathbf{r} to that region. Thus the detection rule becomes: compute $\beta_i(\mathbf{r})$ and choose the smallest.

Now consider the costs, $C_{ii} = 0$ and $C_{ij} = C, i \neq j$. Then

$$\beta_i(\mathbf{r}) = C \sum_{\substack{j=1 \\ j \neq i}}^M \Pr(H_j/\mathbf{r})$$

or

$$\beta_i(\mathbf{r}) = C[1 - \Pr(H_i/\mathbf{r})]$$

It is clear that choosing the largest $\Pr(H_i/\mathbf{r})$ is equivalent to choosing the smallest $\beta_i(\mathbf{r})$. So now the test becomes a maximum a posteriori probability test. If we further let $C = 1$, looking at the risk expression (B.12) we see that \mathcal{R} now is equal to the average error probability. So this is also a minimum error probability test.

Since

$$\Pr(H_i/\mathbf{r}) = \frac{p(\mathbf{r}/H_i)P_i}{p(\mathbf{r})}$$

and $p(\mathbf{r})$ is the same to all hypothesis, the alternative of this test is to compute $p(\mathbf{r}/H_i)P_i$ and choose the largest. In the following we apply this result to the general Gaussian problem [1, pp. 96-97] [2, pp. 91-92].

For a general Gaussian problem, there are M hypotheses and the observations are N -dimensional vectors which are Gaussian random variables. The density of the vector under the hypothesis H_i is

$$p(\mathbf{r}/H_i) = \frac{1}{(2\pi)^{N/2}|\mathbf{K}_i|^{1/2}} \exp\left[-\frac{1}{2}(\mathbf{r}^T - \boldsymbol{\mu}_i^T)\mathbf{K}_i^{-1}(\mathbf{r} - \boldsymbol{\mu}_i)\right] \quad (\text{B.13})$$

where $\boldsymbol{\mu}_i$ is the mean vector of \mathbf{r} under hypothesis H_i .

$$\boldsymbol{\mu}_i \triangleq E\{\mathbf{r}/H_i\} = \begin{bmatrix} \mu_{1i} \\ \mu_{2i} \\ \vdots \\ \mu_{Ni} \end{bmatrix}, \quad i = 1, 2, \dots, M$$

and \mathbf{K}_i is the covariance matrix under hypothesis H_i , defined as

$$\mathbf{K}_i = \begin{bmatrix} E\{(r_1 - \mu_{1i})^2\} & \cdots & E\{(r_1 - \mu_{1i})(r_N - \mu_{Ni})\} \\ \vdots & & \vdots \\ E\{(r_N - \mu_{Ni})(r_1 - \mu_{1i})\} & \cdots & E\{(r_N - \mu_{Ni})^2\} \end{bmatrix} \quad (\text{B.14})$$

which is an $N \times N$ matrix.

From above the optimum detector computes

$$P_i p(\mathbf{r}/H_i) = \frac{P_i}{(2\pi)^{N/2} |\mathbf{K}_i|^{1/2}} \exp\left[-\frac{1}{2} (\mathbf{r}^T - \boldsymbol{\mu}_i^T) \mathbf{K}_i^{-1} (\mathbf{r} - \boldsymbol{\mu}_i)\right]$$

and choose the largest. Taking the logarithm and neglecting common terms we have this decision rule: Compute

$$l_i = \ln P_i - \frac{1}{2} \ln |\mathbf{K}_i| - \frac{1}{2} (\mathbf{r}^T - \boldsymbol{\mu}_i^T) \mathbf{K}_i^{-1} (\mathbf{r} - \boldsymbol{\mu}_i) \quad (\text{B.15})$$

and choose the largest.

B.2 DETECTION OF CONTINUOUS SIGNALS WITH KNOWN PHASES

Binary signals are the most common type of signals, both in baseband modulation and carrier modulation. M-ary signals are also used in modulation, especially in carrier modulation. In this section we derive the optimum receiver and its error performance for binary signals first. Then we progress to address the issues for M-ary signals.

B.2.1 Detection of Binary Signals

B.2.1.1 Receiver Structure

A digital signal waveform with binary signaling consists of two kinds of signals $s_1(t)$

and $s_2(t)$ for $nT \leq t \leq (n+1)T$, $n = 0, 1, 2, \dots$. To simplify analysis without loss of generality, we set time duration as $0 \leq t \leq T$. From the point of view of detection theory, we say we have two hypotheses:

$$\begin{aligned} H_1 &: s_1(t), & 0 \leq t \leq T, \text{ is sent} \\ H_2 &: s_2(t), & 0 \leq t \leq T, \text{ is sent} \end{aligned}$$

The energy of them are

$$E_1 = \int_0^T s_1^2(t) dt$$

and

$$E_2 = \int_0^T s_2^2(t) dt$$

In general these two signals may be correlated. We define

$$\rho_{12} \triangleq \frac{1}{\sqrt{E_1 E_2}} \int_{-\infty}^{\infty} s_1(t) s_2(t) dt = \rho_{21}$$

as the *correlation coefficient* of $s_1(t)$ and $s_2(t)$. $|\rho_{12}| \leq 1$.

The received signal is

$$r(t) = s_i(t) + n(t), \quad i = 1, 2, \quad 0 \leq t \leq T$$

where $s_i(t)$ is one of the two possible signals, and $n(t)$ is the additive white Gaussian noise with zero mean and a two-sided spectral density of $N_o/2$. This implies that the autocorrelation function of $n(t)$ is

$$E\{n(t)n(\tau)\} = \frac{N_o}{2} \delta(t - \tau)$$

(see [2, p.156]), where $\delta(t)$ is the Dirac delta function.

Since $n(t)$ is a Gaussian process, the received signal $r(t)$ is also a Gaussian process with $s_i(t)$ as its mean value. In order to use the hypothesis test results described above, we need to represent $r(t)$ by a set of discrete quantities. Similar to the concept of Fourier series, we expand $r(t)$ as a weighted sum of a set of orthonormal basis functions [1, p. 178]

$$r(t) = \sum_{i=1}^N r_i \phi_i(t) \tag{B.16}$$

where $\phi_i(t)$ are orthonormal basis functions and

$$r_i = \int_0^T r(t)\phi_i(t)dt \quad (\text{B.17})$$

This can be verified by simply plugging in the sum expression of $r(t)$ into the integral and using the orthonormal property of the basis functions. The vector $[r_1, r_2, \dots, r_N]$ is the desired set of discrete quantities, called projections of $r(t)$ onto $\phi_i(t)$. It can be shown that since $\phi_i(t)$ are orthogonal, r_i is Gaussian and independent of each other. The orthogonal basis functions $\phi_i(t)$ can be found by the *Gram-Schmidt* procedure.

In this procedure, we choose the normalized first signal as the first coordinate or basis function

$$\phi_1(t) = \frac{s_1(t)}{\sqrt{E_1}}$$

Clearly $\phi_1(t)$ has unit energy, that is, it is *normalized*.

$$s_1(t) = \sqrt{E_1}\phi_1(t) = s_{11}\phi_1(t)$$

where coefficient $s_{11} = \sqrt{E_1}$ is the *projection* of $s_1(t)$ on the coordinate $\phi_1(t)$. Next we define the second basis function as

$$\phi_2(t) = c_2[s_2(t) - c_1\phi_1(t)]$$

where c_1 must be chosen to satisfy orthogonality of $\phi_2(t)$ with $\phi_1(t)$ and c_2 must be chosen to satisfy normality of $\phi_2(t)$. It is easy to find that

$$c_2 = \frac{1}{\sqrt{E_2 - s_{21}^2}} \quad (\text{B.18})$$

$$c_1 = s_{21} = \int_0^T s_2(t)\phi_1(t)dt \quad (\text{B.19})$$

The remaining $\phi_i(t)$ consist of an arbitrary orthonormal set whose members are orthogonal to $\phi_1(t)$ and $\phi_2(t)$. However, only the first two coefficients $[r_1, r_2]$ depend on transmitted signals. Therefore we only need to check these two *sufficient statistics*

$$\begin{aligned} r_i &= \int_0^T r(t)\phi_i(t)dt \\ &= \begin{cases} \int_0^T [s_1(t) + n(t)]\phi_i(t)dt, & H_1 \\ \int_0^T [s_2(t) + n(t)]\phi_i(t)dt, & H_2 \end{cases} \end{aligned}$$

$$= \begin{cases} s_{i1} + n_i, & H_1 \\ s_{i2} + n_i, & H_2 \end{cases}, \quad i = 1, 2$$

where

$$n_i = \int_0^T n(t)\phi_i(t)dt, \quad i = 1, 2$$

They are Gaussian random variables with zero-means and independent of each other. Their variances are identical, that is,

$$\begin{aligned} E\{n_i^2\} &= E\left\{\left(\int_0^T n(t)\phi_i(t)dt\right)^2\right\} \\ &= E\left\{\int_0^T n(t)\phi_i(t)dt \int_0^T n(\tau)\phi_i(\tau)d\tau\right\} \\ &= \int_0^T \int_0^T E\{n(t)n(\tau)\}\phi_i(t)\phi_i(\tau)dtd\tau \\ &= \int_0^T \int_0^T \frac{N_o}{2}\delta(t-\tau)\phi_i(t)\phi_i(\tau)dtd\tau \\ &= \frac{N_o}{2}, \quad i = 1, 2 \end{aligned}$$

The mean values of $[r_1, r_2]$ are²

$$H_1 : E\{r_i/H_1\} = \int_0^T s_1(t)\phi_i(t)dt = s_{i1}, \quad i = 1, 2$$

$$H_2 : E\{r_i/H_2\} = \int_0^T s_2(t)\phi_i(t)dt = s_{i2}, \quad i = 1, 2$$

and their covariance matrixes are (from (B.14))

$$\begin{aligned} \mathbf{K}_i &= \begin{bmatrix} E\{n_1^2\} & E\{n_1n_2\} \\ E\{n_2n_1\} & E\{n_2^2\} \end{bmatrix}, \quad i = 1, 2 \\ &= \begin{bmatrix} \frac{N_o}{2} & 0 \\ 0 & \frac{N_o}{2} \end{bmatrix}, \quad i = 1, 2 \end{aligned}$$

which are identical regardless of H_i . Substituting this into (B.13), we can form the

² Note that we use μ_{ij} for mean values in general cases. Here symbol s_{ij} instead of μ_{ij} is used to indicate that they are projections of signals onto the basis functions.

likelihood ratio

$$\Lambda[r(t)] = \frac{p(\mathbf{r}/H_1)}{p(\mathbf{r}/H_2)} = \frac{\frac{1}{\pi N_o} \exp\left\{-\frac{1}{N_o} [(r_1 - s_{11})^2 + (r_2 - s_{21})^2]\right\}}{\frac{1}{\pi N_o} \exp\left\{-\frac{1}{N_o} [(r_1 - s_{12})^2 + (r_2 - s_{22})^2]\right\}}$$

Taking the logarithm and canceling common terms we have the likelihood ratio test

$$\ln \Lambda[r(t)] = -\frac{1}{N_o} \sum_{i=1}^2 (r_i - s_{i1})^2 + \frac{1}{N_o} \sum_{i=1}^2 (r_i - s_{i2})^2 \underset{H_2}{\overset{H_1}{\gtrless}} \ln \eta$$

where the initial threshold $\eta = P_2/P_1$ for minimum error probability criterion. Realizing that each sum is just the squared magnitude of the difference vector, the above expression can be written as

$$\ln \Lambda[r(t)] = -\frac{1}{N_o} |\mathbf{r} - \mathbf{s}_1|^2 + \frac{1}{N_o} |\mathbf{r} - \mathbf{s}_2|^2 \underset{H_2}{\overset{H_1}{\gtrless}} \ln \eta$$

or

$$\mathbf{r}^T (\mathbf{s}_1 - \mathbf{s}_2) \underset{H_2}{\overset{H_1}{\gtrless}} \frac{N_o}{2} \ln \eta + \frac{1}{2} (|\mathbf{s}_1|^2 - |\mathbf{s}_2|^2) \triangleq \gamma \quad (\text{B.20})$$

The left-hand side is the sufficient statistic and the right-hand side is the final threshold.

From Parseval's theorem [3, p. 32],

$$\begin{aligned} l &\triangleq \mathbf{r}^T (\mathbf{s}_1 - \mathbf{s}_2) = \mathbf{r}^T \mathbf{s}_1 - \mathbf{r}^T \mathbf{s}_2 \\ &= \int_0^T r(t) s_1(t) dt - \int_0^T r(t) s_2(t) dt \end{aligned} \quad (\text{B.21})$$

and

$$\gamma = \frac{N_o}{2} \ln \eta + \frac{1}{2} (E_1 - E_2) \quad (\text{B.22})$$

Thus the receiver can be implemented as in Figure B.2 using two correlators. A single correlator implementation is shown in Figure B.3. The threshold γ can be reduced to simpler form for special cases. When the two signals have the same energy

$$\gamma = \frac{N_o}{2} \ln \frac{P_2}{P_1}$$

which is simply determined by the a priori probabilities and the noise spectral density. Further, if the two a priori probabilities are equal, then $\gamma = 0$. This is the familiar threshold used in binary communication systems.

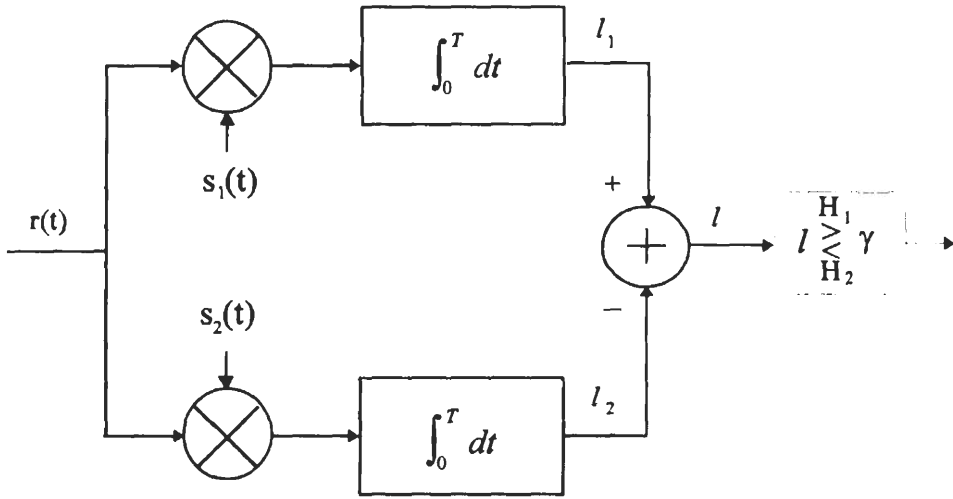


Figure B.2 Optimum binary receiver: two correlator implementation.

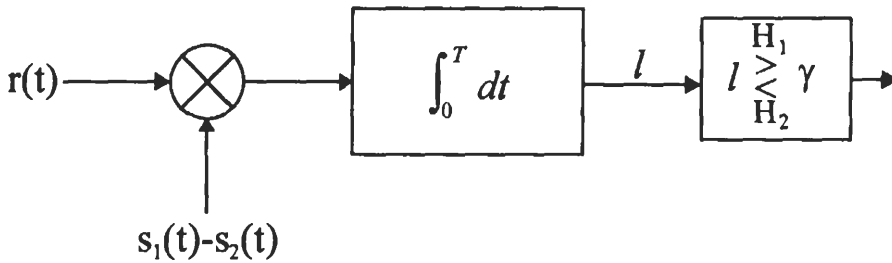


Figure B.3 Optimum binary receiver: one correlator implementation.

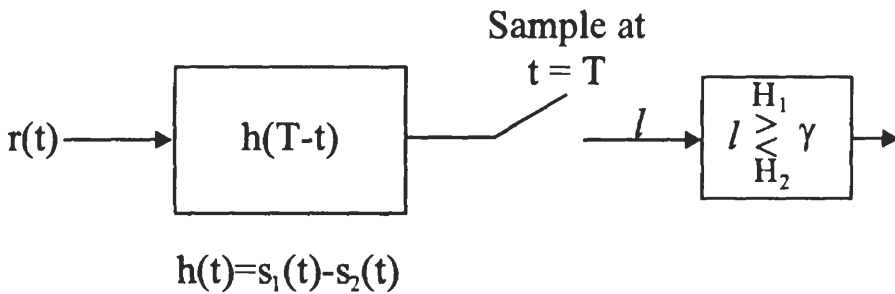


Figure B.4 Optimum binary receiver: matched filter implementation.

A correlator with reference signal $s(t)$ can be implemented as a matched filter with an impulse response

$$h(t) = s(T - t)$$

and sampled at time T . This can be verified by simply checking the output of the matched filter at $t = T$. The output of the matched filter is

$$\begin{aligned} z(t) &= r(t) * h(t) = \int_0^t r(\tau)h(t - \tau)d\tau \\ &= \int_0^t r(\tau)s[T - (t - \tau)]d\tau \\ &= \int_0^t r(\tau)s(T - t + \tau)d\tau \end{aligned}$$

When $t = T$,

$$\begin{aligned} z(T) &= \int_0^T r(\tau)s(T - T + \tau)d\tau \\ &= \int_0^T r(\tau)s(\tau)d\tau \end{aligned}$$

This is exactly the correlation between $r(t)$ and $s(t)$. From the derivation we can see that the correlator output is equivalent to the matched filter output *only* at $t = T$, the sampling moment. Figure B.4 shows the matched filter implementation of the optimum binary receiver. Note that the matched filter impulse response is

$$h(t) = s_1(T - t) - s_2(T - t) \quad (\text{B.23})$$

B.2.1.2 Matched Filter Maximizes Signal-to-Noise Ratio

We derived the matched filter receiver from the correlator receiver which, in turn, is derived from the minimum error probability criterion. One would naturally relate minimum error probability with maximum signal-to-noise ratio. It is indeed true that the optimum receiver's output has the maximum signal-to-noise ratio. This can be proved by checking the matched-filter receiver.

For an arbitrary signal $s(t)$, we want to choose a filter which can maximize the output signal-to-noise ratio at sampling time $t = T$. Assume the filter transfer

function is $H(f)$, and the signal spectrum is $S(f)$, then the output signal is

$$a(t) = \int_{-\infty}^{\infty} H(f)S(f)e^{j2\pi ft} df$$

The output noise spectral density is $|H(f)|^2 \frac{N_o}{2}$ (see [2, p. 47]) and the output noise autocorrelation function is

$$R(\tau) = \int_{-\infty}^{\infty} |H(f)|^2 \frac{N_o}{2} e^{j2\pi f\tau} df$$

The noise variance is therefore

$$\sigma^2 = R(0) = \frac{N_o}{2} \int_{-\infty}^{\infty} |H(f)|^2 df$$

The output signal power to average noise power ratio at $t = T$ is

$$\left(\frac{S}{N}\right)_T = \frac{\left| \int_{-\infty}^{\infty} H(f)S(f)e^{j2\pi fT} df \right|^2}{\frac{N_o}{2} \int_{-\infty}^{\infty} |H(f)|^2 df}$$

By using *Schwartz's inequality* [3, p. 618] it is easy to see

$$\begin{aligned} \left(\frac{S}{N}\right)_T &\leq \frac{\int_{-\infty}^{\infty} |H(f)|^2 df \int_{-\infty}^{\infty} |S(f)|^2 df}{\frac{N_o}{2} \int_{-\infty}^{\infty} |H(f)|^2 df} \\ &= \frac{2}{N_o} \int_{-\infty}^{\infty} |S(f)|^2 df \end{aligned}$$

Equality of Schwartz's inequality holds only when

$$H(f) = kS^*(f)e^{-j2\pi fT}$$

or

$$h(t) = \begin{cases} ks(T-t), & 0 \leq t \leq T \\ 0, & \text{elsewhere} \end{cases}$$

This is the matched filter.

B.2.1.3 Error Probability

Next we proceed to derive the error probability of the optimum receiver. It is conveniently done using the one correlator receiver. We need to check the probability

density of output l first. Denote

$$s_d(t) \triangleq s_1(t) - s_2(t)$$

which is called the difference signal. Its energy is

$$\begin{aligned} E_d &= \int_0^T s_d^2(t) dt \\ &= \int_0^T s_1^2(t) dt - 2 \int_0^T s_1(t) s_2(t) dt + \int_0^T s_2^2(t) dt \\ &= E_1 - 2\rho_{12} \sqrt{E_2 E_1} + E_2 \end{aligned} \quad (\text{B.24})$$

Under hypothesis H_1

$$\begin{aligned} l &= \int_0^T r(t) s_d(t) dt \\ &= \int_0^T [s_1(t) + n(t)] s_d(t) dt \\ &= \int_0^T s_1(t) s_d(t) dt + \int_0^T n(t) s_d(t) dt \\ &= \int_0^T s_1^2(t) dt - \int_0^T s_1(t) s_2(t) dt + \int_0^T n(t) s_d(t) dt \\ &= E_1 - \rho_{12} \sqrt{E_1 E_2} + n = \mu_1 + n \end{aligned}$$

where

$$\mu_1 \triangleq E_1 - \rho_{12} \sqrt{E_1 E_2} \quad (\text{B.25})$$

and $n = \int_0^T n(t) s_d(t) dt$ is a zero-mean Gaussian random variable. Its variance is

$$\begin{aligned} \sigma^2 &= E\{n^2\} = E\left\{\left[\int_0^T n(t) s_d(t) dt\right]^2\right\} \\ &= \int_0^T \int_0^T E\{n(t) n(\tau)\} s_d(t) s_d(\tau) dt d\tau \\ &= \frac{N_o}{2} \int_0^T \int_0^T \delta(t - \tau) s_d(t) s_d(\tau) dt d\tau \\ &= \frac{N_o}{2} \int_0^T s_d^2(t) dt = \frac{N_o}{2} E_d \end{aligned} \quad (\text{B.26})$$

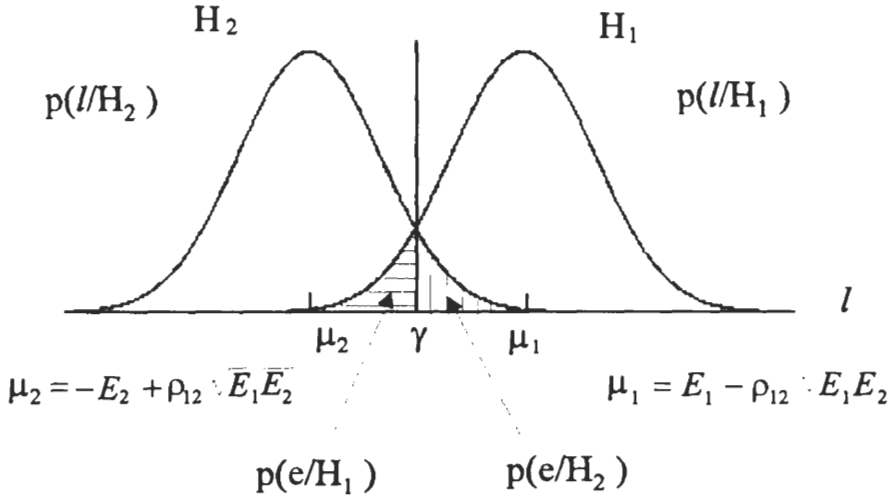


Figure B.5 Decision space.

Similarly under hypothesis H_2

$$l = -E_2 + \rho_{12}\sqrt{E_1E_2} + n = \mu_2 + n$$

where

$$\mu_2 \triangleq -E_2 + \rho_{12}\sqrt{E_1E_2} \quad (\text{B.27})$$

and n has the same density as before.

Having seen $l = \mu_i + n$, $i = 1, 2$, and n is a Gaussian random variable with zero mean and a variance of $E_d N_o / 2$, we can see that l is a Gaussian random variable with mean μ_i and a variance of $E_d N_o / 2$. Thus the conditional densities of l are

$$p(l/H_1) = \frac{1}{\sqrt{\pi N_o E_d}} \exp\left\{-\frac{(l - \mu_1)^2}{N_o E_d}\right\}$$

$$p(l/H_2) = \frac{1}{\sqrt{\pi N_o E_d}} \exp\left\{-\frac{(l - \mu_2)^2}{N_o E_d}\right\}$$

where l is a value of the random variable l . Figure B.5 shows these two densities (assuming $\rho_{12} \leq 0$). When H_2 is true the receiver will make an error if l is on the right side of the threshold and vice versa. The average bit error probability is

$$P_b = P_1 P(e/H_1) + P_2 P(e/H_2)$$

where

$$\begin{aligned}
 P(e/H_2) &= \Pr(l > \gamma/H_2) = \int_{\gamma}^{\infty} p(l/H_2) dl \\
 &= \int_{\gamma}^{\infty} \frac{1}{\sqrt{\pi N_o E_d}} \exp\left\{-\frac{(l - \mu_2)^2}{N_o E_d}\right\} dl \\
 &= \int_{(\gamma - \mu_2)/\sqrt{N_o E_d/2}}^{\infty} \frac{1}{\sqrt{2\pi}} \exp\left\{-\frac{x^2}{2}\right\} dx \\
 &= Q\left(\frac{\gamma - \mu_2}{\sqrt{N_o E_d/2}}\right)
 \end{aligned} \tag{B.28}$$

where

$$Q(x) \triangleq \int_x^{\infty} \frac{1}{\sqrt{2\pi}} \exp\left\{-\frac{u^2}{2}\right\} du$$

is called Marcum's *Q-function*.³

Similarly

$$\begin{aligned}
 P(e/H_1) &= \Pr(l < \gamma/H_1) = 1 - \Pr(l > \gamma/H_1) \\
 &= 1 - Q\left(\frac{\gamma - \mu_1}{\sqrt{N_o E_d/2}}\right)
 \end{aligned} \tag{B.29}$$

Now we discuss an important case where two signals are equally likely. Then $\eta = 1$

³ Van Trees [1, p. 37] denoted this as $\text{erfc}_*(x)$. But it is not the same as $\text{erfc}(x)$ which is called *complementary error function*.

$$\text{erfc}(x) \triangleq 1 - \text{erf}(x)$$

where $\text{erf}(x)$ is the *error function* defined as

$$\text{erf}(x) \triangleq \frac{2}{\sqrt{\pi}} \int_0^x \exp(-u^2) du$$

which is usually tabulated in mathematics handbooks. Thus $Q(x)$ is related to $\text{erfc}(x)$ by

$$Q(x) = \frac{1}{2} \text{erfc}\left(\frac{x}{\sqrt{2}}\right)$$

or

$$\text{erfc}(x) = 2Q(\sqrt{2}x)$$

and

$$\gamma = \frac{N_o}{2} \ln \eta + \frac{1}{2}(E_1 - E_2) = \frac{1}{2}(E_1 - E_2) = \frac{1}{2}(\mu_1 + \mu_2) \quad (\text{B.30})$$

The threshold is in the midway between the two mean values in Figure B.5. $P(e/H_1)$ and $P(e/H_2)$ are the small shaded areas. From the symmetry of the figure we can easily see that

$$P(e/H_1) = P(e/H_2)$$

It can also be verified from the error probability expressions using a property of the Q function: $Q(x) = 1 - Q(-x)$. Thus

$$P_b = \frac{1}{2}(P(e/H_1) + P(e/H_2)) = P(e/H_2) = P(e/H_1)$$

Thus substituting (B.30) into (B.28) we have

$$P_b = Q\left(\frac{\mu_1 - \mu_2}{\sqrt{2N_o E_d}}\right) \quad (\text{B.31})$$

Now substituting (B.25), (B.27), and (B.24) into (B.31) we obtain the final result

$$P_b = Q\left(\sqrt{\frac{E_d}{2N_o}}\right) \quad (\text{B.32})$$

This expression shows that the larger the distance (E_d) between the two signals $s_1(t)$ and $s_2(t)$, the smaller the P_b . This is intuitively convincing since the larger the distance, the easier for the detector to distinguish them. It is also important to note that the error probability *only* depends on the difference signal's energy, not its shape.

It is also revealing to see the relation between P_b with the individual signal energies. Substituting (B.24) into (B.32),

$$P_b = Q\left(\sqrt{\frac{E_1 + E_2 - 2\rho_{12}\sqrt{E_2 E_1}}{2N_o}}\right) \quad (\text{B.33})$$

This expression indicates that P_b depends not only on the individual signal energies, but also on the correlation between them. It is interesting to discover that when $\rho_{12} = -1$ (i.e., when two signals are *antipodal*), P_b is the minimum. If $\rho_{12} = 0$, the signals are *orthogonal*. P_b is not minimum for orthogonal signals.

Now we consider a common case in digital communications. Two signals are

equally likely, have equal energies (E_b) and are antipodal. Then (B.33) becomes

$$P_b = Q\left(\sqrt{\frac{2E_b}{N_o}}\right) \quad (\text{B.34})$$

If these two signals are equiprobable and equal energy, but orthogonal, then

$$P_b = Q\left(\sqrt{\frac{E_b}{N_o}}\right) \quad (\text{B.35})$$

B.2.2 Detection of M-ary Signals

B.2.2.1 Receiver Structure

Assume M hypotheses, the received signal under hypothesis H_i is

$$H_i : r(t) = s_i(t) + n(t), \quad 0 \leq t \leq T, \quad i = 1, 2, \dots, M$$

where $s_i(t)$ is the signal and $n(t)$ is the white Gaussian noise with zero mean and a PSD of $N_o/2$. The signal energy is

$$\int_0^T s_i^2(t) dt = E_i, \quad i = 1, 2, \dots, M$$

and M signals are correlated

$$\frac{1}{\sqrt{E_i E_j}} \int_0^T s_i(t) s_j(t) dt = \rho_{ij}, \quad i, j = 1, 2, \dots, M \quad (\text{B.36})$$

We have shown in Section B.2.1.1 that $r(t)$ can be represented by a vector $[r_1, r_2, \dots, r_N]$ whose elements are projections of $r(t)$ onto a set of orthonormal functions $\phi_i(t)$, $i = 1, 2, \dots, N$. r_i will be Gaussian and independent of each other. Like in the binary case, the orthogonal basis functions $\phi_i(t)$ can be found by the *Gram-Schmidt procedure*. They are

$$\phi_1(t) = s_1(t) / \sqrt{E_1}$$

$$\phi_2(t) = c_2[s_2(t) - c_1\phi_1(t)]$$

where c_2, c_1 are given in (B.18) and (B.19), respectively. We can find $\phi_3(t)$ similarly by defining

$$\phi_3(t) = c_3[s_3(t) - c_1\phi_1(t) - c_2\phi_2(t)]$$

where c_1 and c_2 are determined by requiring orthogonality and c_3 is determined by requiring $\phi_3(t)$ to be normalized. The resulting $\phi_i(t)$ are orthogonal and normalized. They are *orthonormal* functions. We proceed this way until one of two things happens:

1. M orthonormal functions are obtained;
2. $N (< M)$ orthonormal functions are obtained and the remaining signals can be represented by linear combinations of these orthonormal functions.⁴

Then we use this set of orthonormal functions to generate N coefficients

$$r_i = \int_0^T r(t)\phi_i(t)dt, \quad i = 1, 2, \dots, N$$

r_i are statistically independent Gaussian random variables with variance of $N_o/2$. Their mean values depend on hypotheses,

$$\begin{aligned} s_{ij} &= E\{r_i/H_j\} = \int_0^T s_j(t)\phi_i(t)dt \\ i &= 1, 2, \dots, N; j = 1, 2, \dots, M \end{aligned}$$

This is the general Gaussian problem with equal $|\mathbf{K}_i|$ for all i and also $\mathbf{K}_i^{-1} = \frac{2}{N_o}\mathbf{I}$, where \mathbf{K}_i is defined in (B.14). When the criterion is minimum error probability, using (B.15) and dropping the term $\frac{1}{2} \ln |\mathbf{K}_i|$ which is independent of any hypothesis, we have this sufficient statistic

$$l'_j = \ln P_j - \frac{1}{N_o} \sum_{i=1}^N (r_i - s_{ij})^2, \quad j = 1, 2, \dots, M \quad (\text{B.37})$$

and determine H_j is true when l'_j is the largest. Expanding the above we have

$$l'_j = \ln P_j - \frac{1}{N_o} \left[\sum_{i=1}^N r_i^2 + \sum_{i=1}^N s_{ij}^2 - \sum_{i=1}^N 2r_i s_{ij} \right]$$

The term $\sum_{i=1}^N r_i^2$ is independent of any hypothesis, which can be dropped. From

⁴ In many cases the signal set is in the form of linear combinations of orthonormal functions already, such as MPSK, QAM, and M-ary PAM, then the Gram-Schmidt procedure is unnecessary.

Parseval's theorem

$$\sum_{i=1}^N s_{ij}^2 = \int_0^T s_j^2(t) dt = E_j$$

$$\sum_{i=1}^N r_i s_{ij} = \int_0^T r(t) s_j(t) dt$$

Thus the new sufficient statistic is

$$l_j = \int_0^T r(t) s_j(t) dt + B_j \quad (\text{B.38})$$

where the bias term

$$B_j = \frac{N_o}{2} \ln P_j - \frac{1}{2} E_j \quad (\text{B.39})$$

The detection rule is to choose the largest of l_j . The receiver is shown in Figure B.6. Its matched filter equivalence is shown in Figure B.7. It is worthwhile to point out that the decision rule of (B.38) does not require that the M signals are orthogonal. When signals are equally likely and have the same energy, then the bias term in l_j can be dropped.

If $N < M$, the optimum receiver can be implemented using N correlators [4, pp. 185-186]. This is due to the fact [1, p. 169]

$$s_j(t) = \sum_{i=1}^N s_{ij} \phi_i(t)$$

Then

$$\begin{aligned} \int_0^T r(t) s_j(t) dt &= \int_0^T r(t) \sum_{i=1}^N s_{ij} \phi_i(t) dt \\ &= \sum_{i=1}^N s_{ij} \int_0^T r(t) \phi_i(t) dt = \sum_{i=1}^N s_{ij} r_i \end{aligned}$$

where s_{ij} are known. Thus the receiver only needs to compute r_i using N correlators and weight the output with the signal coefficients s_{ij} to form the correlation (Figure B.8). The matched filter equivalence is shown in Figure B.9.

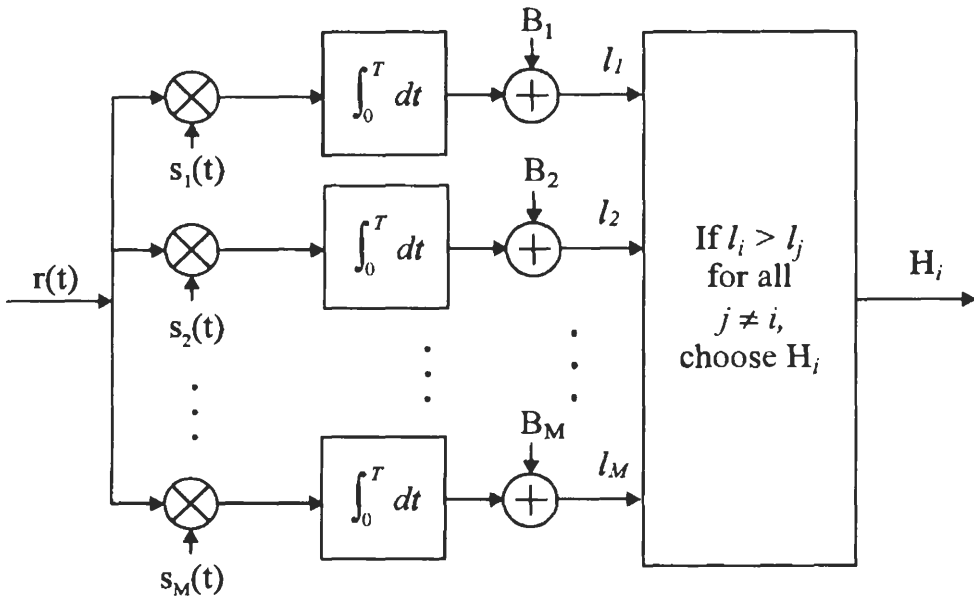


Figure B.6 Coherent M-ary detector using M correlators.

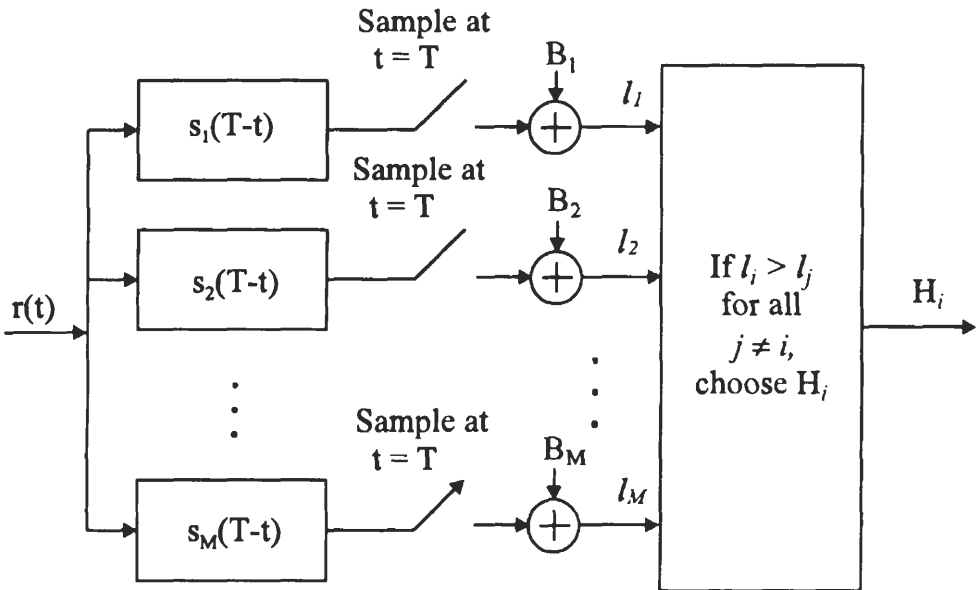
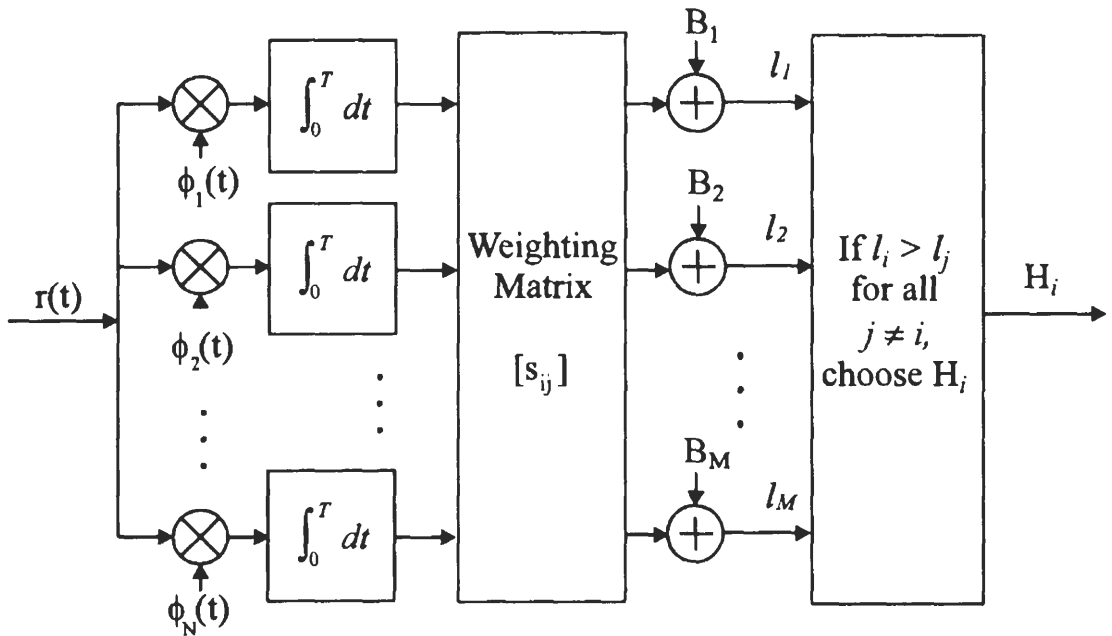
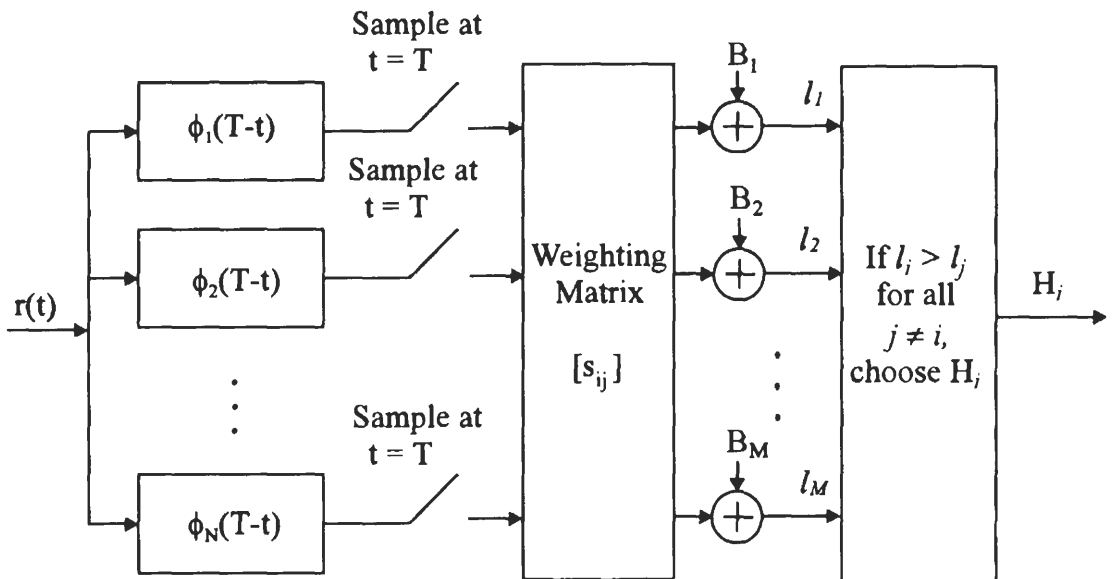


Figure B.7 Coherent M-ary detector using M matched filters.

Figure B.8 Coherent M-ary detector using N correlators.Figure B.9 Coherent M-ary detector using N matched filters.

B.2.2.2 Error Probability

Now we will derive the error probability of this important receiver for the symmetrical case: M signals are orthogonal to each other, each signal has the same symbol energy and a priori probability. That is, $P_j = P$ and $E_j = E_s$ for all j . In this case the bias term in (B.38) can be dropped and

$$l_j = \int_0^T r(t)s_j(t)dt$$

Since the problem is symmetrical we can assume that H_1 is true. An error occurs if $l_j > l_1, j \neq 1$.

$$P(e/H_1) = 1 - \Pr(\text{all } l_j < l_1 : j \neq 1/H_1) \quad (\text{B.40})$$

Because of symmetry, the average symbol error probability is equal to the above probability. Note that the $l_j (j \neq 1)$ have the same density conditioned on H_1 , and also independent of each other. Thus

$$\begin{aligned} P_s &= P(e/H_1) \\ &= 1 - \int_{-\infty}^{\infty} p(l_1/H_1) \left[\int_{-\infty}^{l_1} p(l_j/H_1) dl_2 \right]^{M-1} dl_1 \quad (\text{B.41}) \end{aligned}$$

To find the densities of l_1 and l_j under hypothesis H_1 , we note that

$$\begin{aligned} l_j &= \int_0^T r(t)s_j(t)dt \\ &= \int_0^T [s_1(t) + n(t)]s_j(t)dt \\ &= \int_0^T s_1(t)s_j(t)dt + \int_0^T n(t)s_j(t)dt \\ &= \begin{cases} E_s + n, & j = 1 \\ n, & j \neq 1, \end{cases} \end{aligned}$$

where n is a Gaussian random variable with zero mean and a variance $\frac{N_o}{2} E_s$ (see (B.26)).

Thus the densities are

$$p(l_1/H_1) = \frac{1}{\sqrt{\pi N_o E_s}} \exp\left\{-\frac{(l_1 - E_s)^2}{N_o E_s}\right\}$$

and

$$p(l_j/H_1) = \frac{1}{\sqrt{\pi N_o E_s}} \exp\left\{-\frac{l_j^2}{N_o E_s}\right\}$$

Substituting these densities into (B.41) and normalizing the variables we obtain

$$P_s = 1 - \int_{-\infty}^{\infty} \frac{1}{\sqrt{2\pi}} \exp\left\{-\frac{1}{2} \left(x - \sqrt{\frac{2E_s}{N_o}}\right)^2\right\} \cdot \left[\int_{-\infty}^x \frac{1}{\sqrt{2\pi}} \exp\left\{-\frac{y^2}{2}\right\} dy \right]^{M-1} dx$$

(for orthogonal equal energy signal set) (B.42)

This expression cannot be analytically integrated. However, we can derive a very simple bound. In order to obtain a bound for more general cases, we assume the signal set is not symmetrical. Then we replace l_1 in B.40 with l_i and rewrite the P_s as

$$P_s = \Pr(\text{any } l_j > l_i : j \neq i/H_i)$$

Now several l_j can be greater than l_i . The events are not mutually exclusive. Thus

$$P_s \leq \sum_{j \neq i} \Pr(l_j > l_i)$$

where each term in the sum is just the probability of error for two signals, which can be written in terms of their Euclidean distance as in (B.32). Thus

$$P_s \leq \sum_{j \neq i} Q\left(\frac{d_{ij}}{\sqrt{2N_o}}\right) \quad (\text{B.43})$$

where

$$d_{ij}^2 = \int_{-\infty}^{\infty} [s_i(t) - s_j(t)]^2 dt$$

For an *orthogonal and equal energy* signal set, all distances between any two signals are equal. The distance $d = \sqrt{2E_s}$, thus (B.43) becomes

$$P_s \leq (M-1)Q\left(\sqrt{\frac{E_s}{N_o}}\right)$$

(for equal energy and orthogonal signal set) (B.44)

For fixed M this bound becomes increasingly tight as E_s/N_o is increased. In fact, it becomes a good approximation for $P_s \leq 10^{-3}$. For $M = 2$, it becomes the exact expression.

B.3 DETECTION OF CONTINUOUS SIGNALS WITH UNKNOWN PHASES

In the above discussion of detection of M-ary signals (binary signal is just a special case), we have made a fundamental assumption: the signal phases are known to the receiver. This requires that the receiver has the mechanism to track the carrier phase so that the local reference signal phase is synchronized with that of the received signal. This is called *coherent* detection which is optimum in an AWGN channel. In practical channels, such as fading channels, multipath channels, the received signal phase is very difficult or even impossible to track. Thus the detection process may have to disregard the phase information to avoid complex circuits, at some expenses of performance degradation. This is called *noncoherent* detection. When the received signal phase is not tracked by the receiver, the signal phase is unknown to the receiver. The results of this section can be applied to binary and M-ary noncoherent FSK and DPSK.

B.3.1 Receiver Structure

Assume M hypotheses with priori probabilities $P_i = \Pr(H_i)$, the received signal under hypothesis H_i is

$$H_i : r(t) = s_i(t, \theta) + n(t), \quad 0 \leq t \leq T, \quad i = 1, 2, \dots, M$$

where $s_i(t, \theta)$ is the signal with an unknown phase θ and $n(t)$ is the white Gaussian noise with zero mean and a PSD of $N_o/2$. We assume the unknown phase is random with a PDF $p_\theta(\theta)$.

The procedure of deriving the optimum receiver for M-ary signals with unknown phases is similar to that of the known signals. First we use the Gram-Schmidt procedure to find a set of orthonormal basis functions and expand $r(t)$ onto these basis functions. The resultant vector \mathbf{r} will be used to form the likelihood function $p(\mathbf{r}/H_i)$. The decision rule for minimum error probability criterion is to compute $P_i p(\mathbf{r}/H_i)$ and choose the largest. The only new feature here is that the signal phase is random. Therefore the likelihood function is conditioned on the random phase θ ,

and the unconditional likelihood is

$$p(\mathbf{r}/H_i) = \int_{-\infty}^{\infty} p_{\theta}(\theta)p(\mathbf{r}/H_i, \theta)d\theta \quad (\text{B.45})$$

Because components of \mathbf{r} are independent Gaussian variables with equal variance, therefore $|\mathbf{K}_i|$ are all equal for all i , and in addition $\mathbf{K}_i^{-1} = \frac{2}{N_o}\mathbf{I}$, \mathbf{I} is the identity matrix. Thus the likelihood of (B.13) can be denoted simply as

$$\begin{aligned} p(\mathbf{r}/H_i, \theta) &= K \exp\left[-\frac{1}{N_o}(\mathbf{r}^T - \mathbf{s}_i^T(\theta))(\mathbf{r} - \mathbf{s}_i(\theta))\right] \\ &= K \exp\left[-\frac{1}{N_o} \sum_{j=1}^N (r_j - s_{ji}(\theta))^2\right] \\ &= K \exp\left\{-\frac{1}{N_o} \sum_{j=1}^N [r_j^2 + s_{ji}^2(\theta) - 2r_j s_{ji}(\theta)]\right\} \\ &= K' \exp\left\{-\frac{1}{N_o} \sum_{j=1}^N [s_{ji}^2(\theta) - 2r_j s_{ji}(\theta)]\right\} \end{aligned} \quad (\text{B.46})$$

where K and K' are constants. The term $\exp[-\frac{1}{N_o} \sum_{j=1}^N r_j^2]$ is common to all hypotheses, thus is included in the constant K' . The two sum terms in the exponent can be written as two integrals by using Parseval's theorem as we did from (B.37) through (B.38). Thus

$$p(\mathbf{r}/H_i, \theta) = K' \exp\left\{-\frac{1}{N_o} \left[\int_0^T s_i^2(t, \theta)dt - 2 \int_0^T r(t)s_i(t, \theta)dt \right]\right\} \quad (\text{B.47})$$

The unconditional likelihood is

$$p(\mathbf{r}/H_i) = K' \int_{-\infty}^{\infty} p_{\theta}(\theta)d\theta \exp\left\{-\frac{1}{N_o} \left[\int_0^T s_i^2(t, \theta)dt - 2 \int_0^T r(t)s_i(t, \theta)dt \right]\right\} \quad (\text{B.48})$$

Now we assume that θ is uniformly distributed on $[0, 2\pi]$, that is

$$p_{\theta}(\theta) = \frac{1}{2\pi}, \quad 0 \leq \theta \leq 2\pi$$

The decision rule is to maximize $P_i p(\mathbf{r}/H_i)$ over all i . From above it is seen that

this is to maximize

$$\begin{aligned}
 & P_i \int_0^{2\pi} \frac{1}{2\pi} d\theta \exp \left\{ -\frac{1}{N_o} \left[\int_0^T s_i^2(t, \theta) dt - 2 \int_0^T r(t) s_i(t, \theta) dt \right] \right\} \\
 = & P_i e^{-\frac{E_i}{N_o}} \int_0^{2\pi} \frac{1}{2\pi} d\theta \exp \left\{ \frac{2}{N_o} \int_0^T r(t) s_i(t, \theta) dt \right\} \quad (\text{B.49})
 \end{aligned}$$

where $E_i = \int_0^T s_i^2(t, \theta) dt$ is the energy of the i th signal. Now we assume that $s_i(t)$ is the *carrier-modulated* signal, that is,

$$s_i(t) = A_i(t) \cos[2\pi f_c t + \varphi_i(t)]$$

where $A_i(t)$ is the amplitude modulation and $\varphi_i(t)$ is the phase modulation. If the signal is frequency modulated, we can embed it into the phase modulation term. The received signal with unknown phase will be

$$s_i(t, \theta) = A_i(t) \cos[2\pi f_c t + \varphi_i(t) + \theta]$$

Thus (B.49) can be written as

$$\begin{aligned}
 & P_i e^{-\frac{E_i}{N_o}} \int_0^{2\pi} \frac{1}{2\pi} d\theta \exp \left\{ \frac{2}{N_o} \int_0^T r(t) s_i(t, \theta) dt \right\} \\
 = & P_i e^{-\frac{E_i}{N_o}} \int_0^{2\pi} \frac{1}{2\pi} d\theta \exp \left\{ \frac{2}{N_o} \int_0^T r(t) A_i(t) \cos[2\pi f_c t + \varphi_i(t) + \theta] dt \right\} \quad (\text{B.50})
 \end{aligned}$$

Now we define

$$\begin{aligned}
 z_{c_i} &= \int_0^T r(t) A_i(t) \cos[2\pi f_c t + \varphi_i(t)] dt \\
 &= \int_0^T r(t) s_i(t) dt \quad (\text{B.51})
 \end{aligned}$$

and

$$\begin{aligned}
 z_{s_i} &= \int_0^T r(t) A_i(t) \sin[2\pi f_c t + \varphi_i(t)] dt \\
 &= \int_0^T r(t) s_i(t, \frac{\pi}{2}) dt
 \end{aligned}$$

where

$$\begin{aligned} s_i(t, \frac{\pi}{2}) &= A_i(t) \sin[2\pi f_c t + \varphi_i(t)] \\ &= A_i(t) \cos[2\pi f_c t + \varphi_i(t) - \frac{\pi}{2}] \end{aligned}$$

Then (B.50) becomes

$$\begin{aligned} &P_i e^{-\frac{E_i}{N_o}} \int_0^{2\pi} \frac{1}{2\pi} \exp\left(\frac{2}{N_o} [z_{c_i} \cos \theta - z_{s_i} \sin \theta]\right) d\theta \\ = &P_i e^{-\frac{E_i}{N_o}} \int_0^{2\pi} \frac{1}{2\pi} \exp\left[\frac{2}{N_o} z_i \cos(\theta + \delta)\right] d\theta \end{aligned} \quad (\text{B.52})$$

where

$$z_i = \sqrt{z_{c_i}^2 + z_{s_i}^2}$$

and

$$\delta = \tan^{-1} \left(\frac{z_{s_i}}{z_{c_i}} \right)$$

The integral in (B.52) is related to the zeroth-order modified Bessel function defined as

$$I_0(x) = \int_0^{2\pi} \frac{1}{2\pi} \exp[x \cos(\theta + \delta)] d\theta, \quad \delta \text{ is any constant}$$

By using this function (B.52) can be written as

$$P_i e^{-\frac{E_i}{N_o}} I_0\left(\frac{2z_i}{N_o}\right)$$

Taking the logarithm we can equivalently state the rule as maximizing

$$l_i \triangleq \ln I_0\left(\frac{2z_i}{N_o}\right) - \frac{E_i}{N_o} + \ln P_i \quad (\text{B.53})$$

Because for fixed E_i/N_o , $\ln(\cdot)$ and $I_0(\cdot)$ both are monotonic functions, this is to maximize

$$l_i \triangleq \frac{2z_i}{N_o} - \frac{E_i}{N_o} + \ln P_i \quad (\text{B.54})$$

Figure B.10 is the receiver realizing the above decision rule. Figure B.11 is the matched filter-envelope detector version.

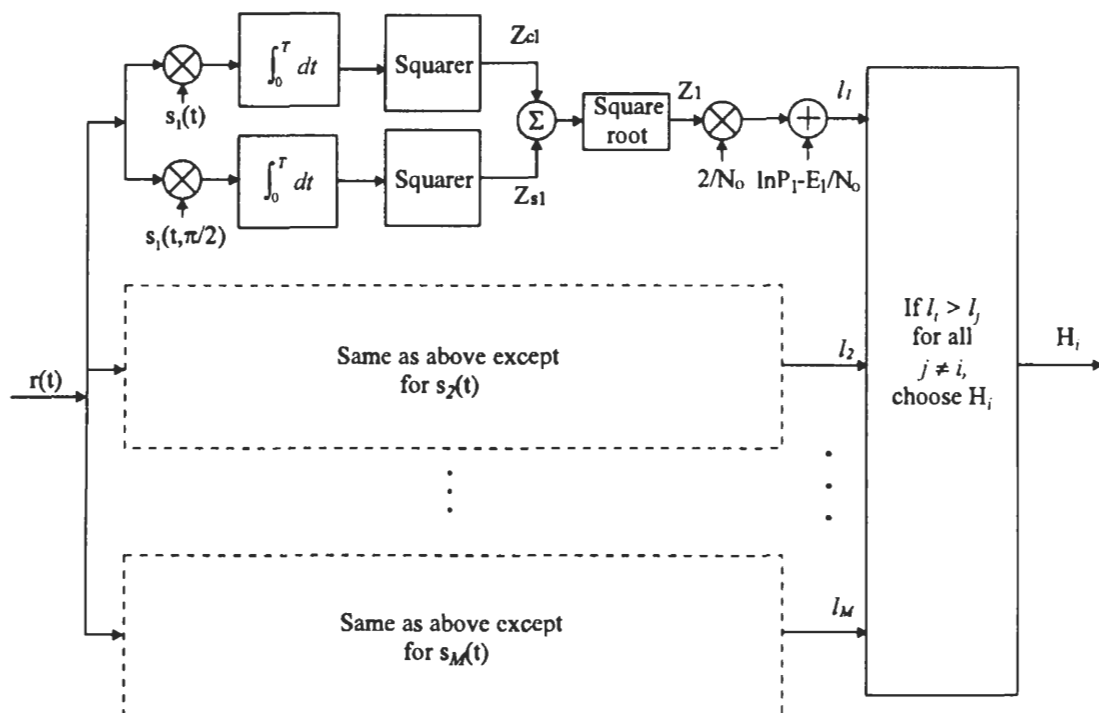


Figure B.10 Optimum detector for M-ary signals with unknown phases: correlator form.

If we further assume that the signals are equally likely and have the same energy, which is common in noncoherent communications, then the decision rule is to maximize z_i or z_i^2 :

$$\begin{aligned}
 l_i^2 &\triangleq z_i^2 = z_{c_i}^2 + z_{s_i}^2 \\
 &= \left(\int_0^T r(t) s_i(t) dt \right)^2 + \left(\int_0^T r(t) s_i(t, \frac{\pi}{2}) dt \right)^2 \quad (\text{B.55})
 \end{aligned}$$

The block diagram is shown in Figure B.12. Note that the two reference signals $s_i(t)$ and $s_i(t, \frac{\pi}{2})$ are orthogonal. Figure B.13 is the matched filter-envelope detector version, where

$$h_i(t) = s_i(T - t), \quad 0 \leq t \leq T$$

Proof: The output of the matched filter is

$$z_i(t) = \int_0^t r(\tau) s_i(T - t + \tau) d\tau$$

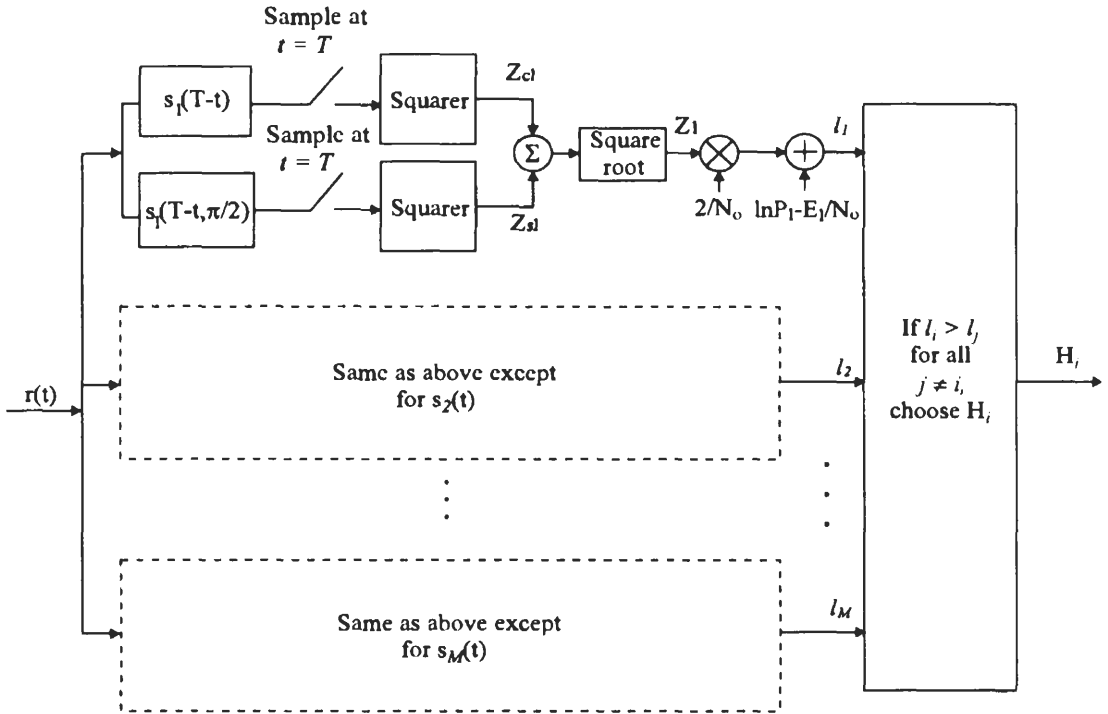


Figure B.11 Optimum detector for M-ary signals with unknown phases: matched filter form.

Substituting the expression of $s_i(\tau)$ into the above equation we have

$$\begin{aligned}
 & z_i(t) \\
 = & \int_0^t r(\tau) A_i(T-t+\tau) \cos[2\pi f_c(T-t+\tau) + \varphi_i(T-t+\tau)] d\tau \\
 = & \int_0^t r(\tau) A_i(T-t+\tau) \cos 2\pi f_c(T-t) \cos[2\pi f_c\tau + \varphi_i(T-t+\tau)] d\tau \\
 & - \int_0^t r(\tau) A_i(T-t+\tau) \sin 2\pi f_c(T-t) \sin[2\pi f_c\tau + \varphi_i(T-t+\tau)] d\tau \\
 = & \int_0^t r(\tau) A_i(T-t+\tau) \cos[2\pi f_c\tau + \varphi_i(T-t+\tau)] d\tau \cos 2\pi f_c(T-t) \\
 & - \int_0^t r(\tau) A_i(T-t+\tau) \sin[2\pi f_c\tau + \varphi_i(T-t+\tau)] d\tau \sin 2\pi f_c(T-t)
 \end{aligned}$$

The envelope at $t = T$ is

$$\begin{aligned}
 & \left\{ \left[\int_0^t r(\tau) A_i(T-t+\tau) \cos[2\pi f_c \tau + \varphi_i(T-t+\tau)] d\tau \right]^2 \right. \\
 & \left. + \left[\int_0^t r(\tau) A_i(T-t+\tau) \sin[2\pi f_c \tau + \varphi_i(T-t+\tau)] d\tau \right]^2 \right\}_{t=T}^{1/2} \\
 = & \left\{ \left[\int_0^T r(\tau) A_i(\tau) \cos[2\pi f_c \tau + \varphi_i(\tau)] d\tau \right]^2 \right. \\
 & \left. + \left[\int_0^T r(\tau) A_i(\tau) \sin[2\pi f_c \tau + \varphi_i(\tau)] d\tau \right]^2 \right\}^{1/2} \\
 = & \left\{ \left[\int_0^T r(\tau) s_i(\tau) d\tau \right]^2 + \left[\int_0^T r(\tau) s_i\left(\tau, \frac{\pi}{2}\right) d\tau \right]^2 \right\}^{1/2}
 \end{aligned}$$

which is exactly the output of the correlator version.

B.3.2 Receiver Error Performance

B.3.2.1 Binary Orthogonal Signals

We first derive the symbol error probability $P_s = P_b$ for the binary case. Then the results can be easily extended to the M-ary case.

The noncoherent receiver for binary signals is symmetrical in structure. The error probability of choosing $s_1(t)$ when $s_2(t)$ is actually transmitted is the same as that of choosing $s_2(t)$ when $s_1(t)$ is actually transmitted. For equally likely signals the average P_b is equal to either one of these two probabilities. Therefore in the following analysis we assume that $s_1(t)$ is transmitted.

Note that the receiver in Figure B.10 or Figure B.11 is for any signal sets with equal energy, equal a priori probability; orthogonality is not required. Here we further assume that the two signals are *orthogonal*. This is due to the fact that binary orthogonal signals have the smallest error probability among the class of binary signals with constrained peak energy and unknown phase [5].

Since $s_1(t)$ is orthogonal to $s_2(t)$ (also to $s_2(t, \frac{\pi}{2})$) the integrator outputs z_{c_2} and z_{s_2} are Gaussian random variables with zero mean and a variance of $\sigma^2 = \frac{N_0}{2} E_s$

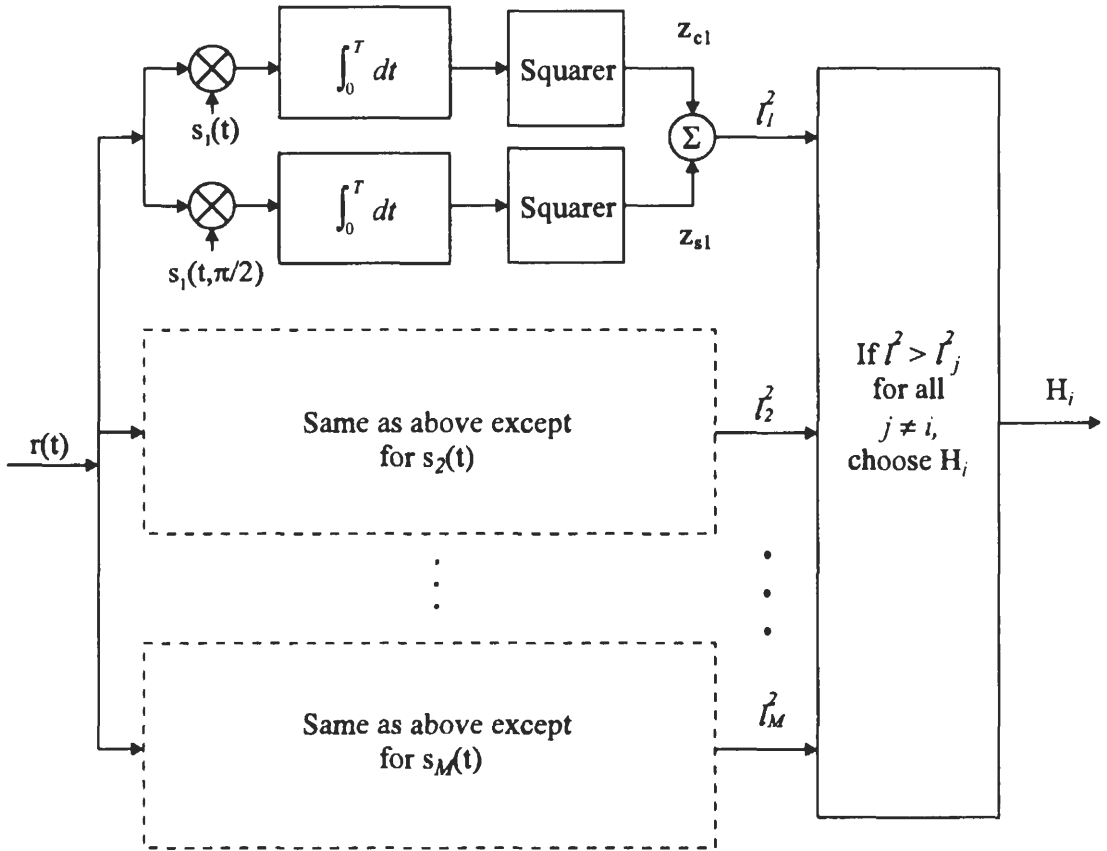


Figure B.12 Correlator receiver for M-ary signals with unknown phases. Signals are equally likely and with equal energy.

(refer to (B.26)). z_{c2} and z_{s2} are independent of each other since $s_i(t)$ and $s_i(t, \frac{\pi}{2})$ are orthogonal [1]. $l_2 = \sqrt{z_{c2}^2 + z_{s2}^2}$. It is well known that the PDF of the root-sum square of two independent Gaussian random variables is Rayleigh. That is

$$p(l_2/H_1) = \frac{l_2}{\sigma^2} e^{-l_2^2/2\sigma^2}, \quad l_2 \geq 0$$

z_{c1} and z_{s1} are also independent Gaussian random variables with the same variance, but their mean values are $\mu = E_s = E_b$. The PDF of $l_1 = \sqrt{z_{c1}^2 + z_{s1}^2}$ is the well-known Rician distribution

$$p(l_1/H_1) = \frac{l_1}{\sigma^2} I_0\left(\frac{\mu l_1}{\sigma^2}\right) e^{-(l_1^2 + \mu^2)/2\sigma^2}, \quad l_1 \geq 0$$

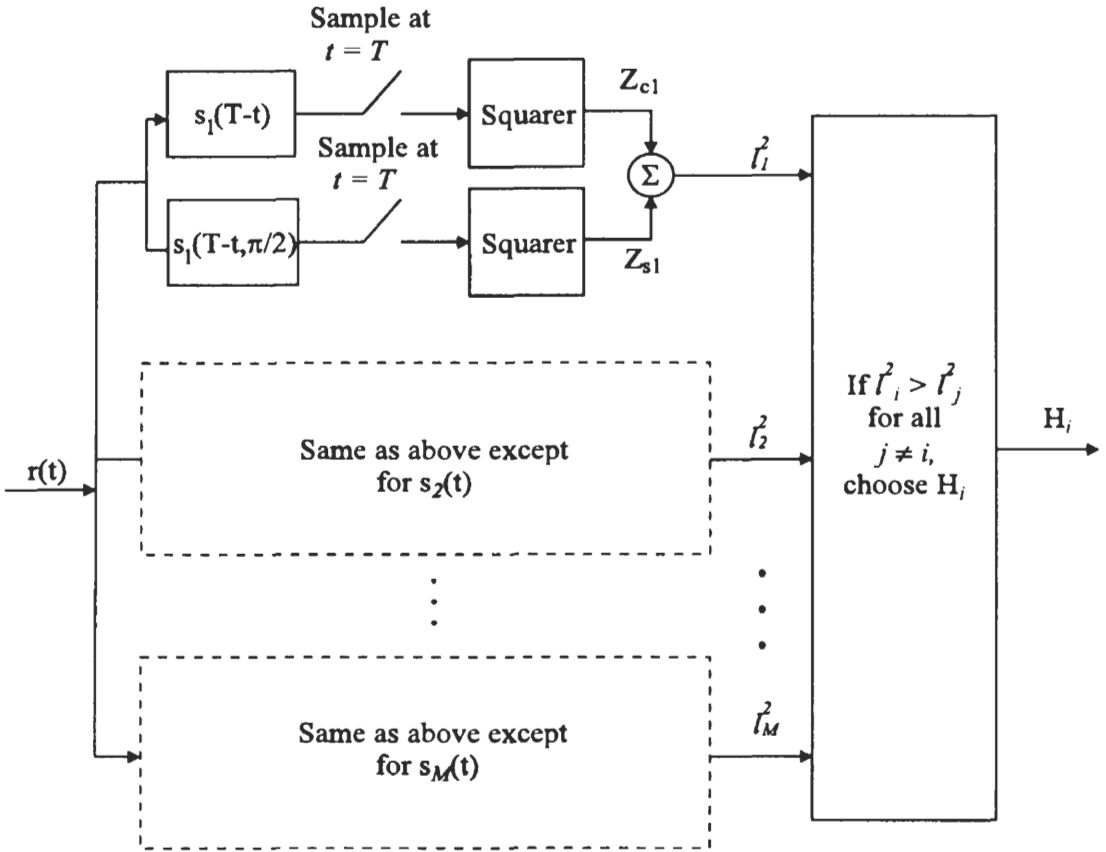


Figure B.13 Matched-filter receiver for M-ary signals with unknown phases. Signals are equally likely and with equal energy.

The probability of error, given that $s_1(t)$ is sent, is

$$\begin{aligned}
 P(e/H_1) &= \Pr(l_2 \geq l_1/H_1) \\
 &= \int_0^\infty \int_{l_1}^\infty p(l_1, l_2/H_1) dl_2 dl_1
 \end{aligned}$$

The random variables l_1, l_2 are independent because their noise parts are independent, which in turn follows the orthogonality of the two signals. Therefore

$$\begin{aligned}
 P(e/H_1) &= \int_0^\infty p(l_1/H_1) \left[\int_{l_1}^\infty p(l_2/H_1) dl_2 \right] dl_1 \\
 &= \int_0^\infty p(l_1/H_1) \left[\int_{l_1}^\infty \frac{l_2}{\sigma^2} e^{-l_2^2/2\sigma^2} dl_2 \right] dl_1
 \end{aligned}$$

$$= \int_0^\infty \frac{l_1}{\sigma^2} I_0\left(\frac{\mu l_1}{\sigma^2}\right) e^{-(l_1^2 + \mu^2)/2\sigma^2} [e^{-l_1^2/2\sigma^2}] dl_1$$

Combine the exponents, let $y = \sqrt{2}l_1$ and $\xi = \mu/\sqrt{2}$, the above integration can be written as

$$\begin{aligned} P(e/H_1) &= \frac{1}{2} e^{-\mu^2/4\sigma^2} \int_0^\infty \frac{y}{\sigma^2} I_0\left(\frac{\xi y}{\sigma^2}\right) e^{-(y^2 + \xi^2)/2\sigma^2} dy \\ &= \frac{1}{2} e^{-\mu^2/4\sigma^2} \end{aligned}$$

where the integration is one since the integrand is exactly the Rician density. We have already stated that this error probability is equal to the average symbol error probability which in binary case is also the bit error probability. Substituting values of μ and σ^2 into the above expression, we have the bit error probability for noncoherent detection of binary orthogonal signals in an AWGN channel as

$$P_b = \frac{1}{2} e^{-E_b/2N_o} \quad (\text{B.56})$$

B.3.2.2 M-ary Orthogonal Signals

For M-ary signals, the noncoherent receiver will produce M sufficient statistics: $l_i, i = 1, 2, \dots, M$. The decision device will compare them and choose the largest. We again assume that $s_1(t)$ is transmitted. With M-ary orthogonal signals, l_1 will be Rician and the rest will be Rayleigh. All l_i are independent. Again due to symmetry of the problem the symbol error probability will be the same as the error probability of losing detection of $s_1(t)$ when it is sent.

$$P_s = P(e/H_1) = 1 - P(c/H_1)$$

where $P(c/H_1)$ is the probability of correct detection. If we fix l_1 , the conditional probability is

$$\begin{aligned} P(c/H_1, l_1) &= \Pr(\text{all } l_i \leq l_1, i = 2, 3, \dots, M/H_1) \\ &= \left(\int_0^{l_1} \frac{l}{\sigma^2} e^{-l^2/2\sigma^2} dl \right)^{M-1} \\ &= [1 - e^{-l_1^2/2\sigma^2}]^{M-1} \end{aligned}$$

Now averaging this over the Rician distribution of l_1 , we have

$$P(c/H_1) = \int_0^\infty \frac{l_1}{\sigma^2} I_0\left(\frac{\mu l_1}{\sigma^2}\right) \exp\left[\frac{l_1^2 + \mu^2}{2\sigma^2}\right] [1 - e^{-l_1^2/2\sigma^2}]^{M-1} dl_1$$

Expanding the term raised to power $M - 1$ by binomial theorem and integrating term by term, we obtain the symbol error probability of noncoherent detection for M-ary orthogonal signals as

$$P_s = 1 - P(c/H_1) = \sum_{k=1}^{M-1} \frac{(-1)^{k+1}}{k+1} \binom{M-1}{k} \exp\left[-\frac{kE_s}{(k+1)N_o}\right] \quad (\text{B.57})$$

where $\binom{M-1}{k}$ is the binomial coefficient, defined by

$$\binom{M-1}{k} = \frac{(M-1)!}{(M-1-k)!k!}$$

The leading term of (B.57) provides an upper bound as

$$P_s \leq \frac{M-1}{2} \exp\left[-\frac{E_s}{2N_o}\right] \quad (\text{B.58})$$

For fixed M this bound becomes increasingly close to the actual value of P_s as E_s/N_o is increased. In fact when $M = 2$, the upper bound becomes the exact expression.

References

- [1] Van Trees, H. L., *Detection, Estimation, and Modulation Theory; Part I*, New York: John Wiley & Sons, Inc., 1968.
- [2] Whalen, A. D., *Detection of Signals in Noise*, New York and London: Academic Press, 1971.
- [3] Ziemer, R. E., and W. H. Tranter, *Principles of Communications, Systems, Modulations, and Noise*, 4th Ed., Boston and Toronto: Houghton Mifflin Company, 1995.
- [4] Simon, K. M., S. M. Hinedi, and W. C. Lindsey, *Digital Communication Techniques, Signal Design and Detection*, Englewood Cliffs, New Jersey: Prentice Hall, 1995.
- [5] Viterbi, A. J., *Principles of Coherent Communications*, New York: McGraw-Hill Book Company, 1966.

Glossary

ac	alternate current
ACI	adjacent channel interference
ACTS	Advanced Communications Technology Satellite (of NASA)
A/D	analog-to-digital (converter)
ADC	analog-to-digital converter
AM	amplitude modulation
AMF	average matched filter
AMI	alternative mark inversion
AMI-NRZ	alternative mark inversion-nonreturn-to-zero
AMI-RZ	alternative mark inversion-return-to-zero
AMPS	advance mobile phone service
ASK	amplitude shift keying
AT&T	American Telephone and Telegraph
AWGN	additive white Gaussian noise
BER	bit error rate
Bi- Φ -L	biphase level
Bi- Φ -M	biphase mark
Bi- Φ -S	biphase space
BFSK	binary frequency shift keying
BNZS	binary n zero substitution
BPF	bandpass filter
BPSK	binary phase shift keying
CCI	co-channel interference
CCITT	Consultative Committee for International Telephone and Telegraph
C/D	power ratio between the main-path signal and the delayed signal
CDPD	cellular digital packet data (system)
CHDB	compatible high density bipolar
C/I	carrier-to-interference ratio

CMI	coded mark inversion
C/N	carrier-to-noise ratio
CPFSK	continuous phase frequency shift keying
CPM	continuous phase modulation
CR	carrier recovery
CSMA/CD	carrier sense multiple access/collision detection
D/A	digital-to-analog (converter)
DAC	digital-to-analog converter
dB	decibel
DBPSK	differential binary phase shift keying (differentially encoded and differentially demodulated binary phase shift keying)
dc	direct current
DDCR	decision-directed carrier recovery
DEBPSK	differentially encoded binary phase shift keying (demodulation may not be differential)
DEMPSK	differentially encoded M-ary phase shift keying
DEQPSK	differentially encoded quadrature phase shift keying
DM	delay modulation
DmB1M	differential m binary with 1 mark inversion
DMI	differential mode inversion
DMPSK	differential M-ary phase shift keying
DMSK	duobinary minimum shift keying
DPSK	differential phase shift keying (usually it refers to DBPSK, but can be used as a generic name for all differential phase shift keying schemes)
DQPSK	differential quadrature phase shift keying
DS	digital sum
DSFSK	double sinusoidal frequency shift keying
DSV	digital sum variation
ETACS	European total access communication system
FDM	frequency division multiplexing
FFSK	fast frequency shift keying
FIR	finite impulse response (filter)
FM	frequency modulation
FSK	frequency shift keying
GMSK	Gaussian minimum shift keying
GSM	global system for mobile communication
HDB	high density bipolar
HF	high frequency
Hz	Hertz
IBM	International Business Machines (Corporation)
IF	intermediate frequency

IJF-OQPSK	intersymbol-interference/jitter-free OQPSK
IPC	inner product calculator
ISD	integrate-sample-dump (circuit)
ISI	intersymbol interference
LCE-MH	multi- h signal with a depth of correlation of L
LO	local oscillator
LOS	line of sight
LPF	low-pass filter
LRC	raised cosine pulse of length L
LRFC	rectangular pulse of length L
LSRC	spectrally raised cosine pulse of length L
MAM	M -ary amplitude modulation
MAP	maximum a posteriori probability
MASK	M -ary amplitude shift keying
MFSK	M -ary frequency shift keying
MHPM	multi- h phase modulation
ML	maximum likelihood
MLSD	maximum likelihood sequence detection
MLSE	maximum likelihood sequence estimation
MPSK	M -ary phase shift keying
MQORC	modified quadrature overlapped raised-cosine (modulation)
MSK	minimum shift keying
NASA	National Aeronautics and Space Administration
NCO	numerically-controlled oscillator
NRZ	nonreturn-to-zero
NRZ-L	nonreturn-to-zero-level
NRZ-M	nonreturn-to-zero-mark
NRZ-S	nonreturn-to-zero-space
OOK	binary on-off keying (binary ASK)
OQPSK	offset quadrature phase shift keying
PAM	pulse amplitude modulation
PCM	pulse code modulation
PDF	probability density function
$\pi/4$ -QPSK	$\pi/4$ quadrature phase shift keying
PFD m B $(m+1)$ B	Partially-flipped differential m bits with $(m+1)$ th check bit
PLL	phase lock loop
PPM	pulse position modulation
PSAM	pilot symbol assisted modulation
PSD	power spectral density
PSK	phase shift keying
PT	pseudoternary
QAM	quadrature amplitude modulation

QBL	quasi-bandlimited (modulation)
QORC	quadrature overlapped raised cosine (modulation)
QOSRC	quadrature overlapped squared raised cosine (modulation)
QPSK	quadrature phase shift keying
Q ² PSK	quadrature quadrature phase shift keying
RCA	Radio Corporation of America
RC-QPSK	raised-cosine quadrature phase shift keying
ROM	read only memory
RZ	return to zero
SFSK	sinusoidal frequency shift keying
SHPM	single-h phase modulation
SMSK	serial minimum shift keying
SNR	signal-to-noise ratio
SQAM	superposed quadrature amplitude modulation
SQORC	staggered quadrature overlapped raised cosine (modulation)
TFM	tamed frequency shift keying
TSI-OQPSK	two-symbol-interval offset quadrature phase shift keying
TTIB	transparent tone in band
TWTA	traveling wave tube amplifier
USDC	United States digital cellular (system)
VA	Viterbi algorithm
VCO	voltage-controlled oscillator
WSS	wide sense stationary
XPSK	cross-correlated quadrature phase shift keying

About the Author

Dr. Fuqin Xiong received his B.Sc. degree in communication engineering in 1970 and M.Sc. degree in communication and electronic system engineering in 1982 from Tsinghua University, Beijing, China, and a Ph.D. degree in 1989 from the Department of Electrical Engineering, University of Manitoba, Winnipeg, Canada.

From 1970 to 1978 Dr. Xiong was an assistant lecturer, and from 1983 to 1984 a lecturer in the Department of Radio-Electronics Engineering, Tsinghua University, Beijing, China. From 1984 to 1985 he was a visiting scholar at the Department of Electrical Engineering, University of Manitoba. Dr. Xiong joined the Department of Electrical Engineering, Cleveland State University, in 1990 as an assistant professor. He was promoted to associate professor with tenure in 1995. In 1997, while on sabbatical leave, he spent the spring semester at City University of Hong Kong and the summer in Tsinghua University, Beijing, China.

Dr. Xiong's research interests are in communication engineering, particularly in modulation and coding techniques for digital communications, including satellite and mobile communications. He has published numerous articles in technical journals such as IEEE Transactions and IEE Proceedings. He also served as a reviewer for IEEE Transactions and IEE Proceedings.

Dr. Xiong has been directing several research projects on digital modulation techniques sponsored by NASA Glenn Research Center, Cleveland, Ohio.

Dr. Xiong is a senior member of IEEE.

Index

Numbers

1REC MHPM

- 4-ary, bounds, 381
- autocorrelation function, 361, 362
- bandwidth efficiency, 376-77
- bit error probabilities, 378, 379
- bounds, 380
- direct method applied to, 362
- distance properties, 369
- distance vs. bandwidth tradeoffs, 371
- with higher coding gain over MSK, 375
- minimum squared normalized Euclidean distance, 372
- performance in Rayleigh, Rician, and AGWN channels, 552
- power bandwidth trade-off, 373
- PSD, 362, 365
- spectra decay, 364
- See also* Multi-h phase modulation (MHPM)

2B3B dc-constrained code, 74, 75

3RC MHPM

- M-ary partial-response, 371, 374
- power bandwidth trade-off, 374
- See also* Multi-h phase modulation (MHPM)

4B3T code, 79

6B4T code, 80-81

$\pi/4$ -DQPSK, 544-48

- BER vs. C/D, 549, 550
- BER vs. C/N, 547, 548
- error performance, 544-45
- in fading channels, 544-48
- in flat, fast Rayleigh fading channel, 548
- in flat, slow Rayleigh fading channel, 547
- in frequency-selective fast fading channel, 550
- in frequency-selective slowly fading channel, 549
- in Rician fading channel, 537
- spectral efficiency, 544

$\pi/4$ -QPSK, 12, 13, 170-79

- baseband differential demodulator, 174
- BER performance, 177
- bit error probability, 176-77, 179
- coherent demodulator, 177, 178
- decoding rule, 175
- defined, 170
- demodulation, 172-73
- differential encoder, 171
- FM-discriminator demodulator, 174, 176
- IF band differential demodulator, 174
- integrate-sample-dump (ISD) circuit output, 176
- modulator, 170-71
- parallel-to-serial converter, 178
- signal constellation, 173
- signal phase assignment, 172
- standard, 170

A

- Additive white Gaussian noise (AWGN) channel, 4-6
 - 1REC-MHPM performance in, 552, 553
 - $\pi/4$ -DQPSK, 530-31
 - autocorrelation function, 4
 - binary signal detection, 17
 - BPSK, 529
 - coherent binary FSK, 530
 - defined, 4
 - GMSK, 530
 - modulation schemes, 6
 - MSK, 529
 - noise power, 5
 - noncoherent orthogonal BFSK, 530
 - optimum differential BPSK, 529-30
 - OQPSK, 529
 - performance, 6
 - QBL, 470
 - QORC/SQORC, 475-76
 - QPSK, 529
 - symbol/bit error rate, 528
 - variance, 5
 - with zero mean, 44
- Adjacent channel interference (ACI), 460
- All-digital modulator, 295-97
 - defined, 295-96
 - illustrated, 295
 - stability, 297
 - See also* Modulators
- Alternative mark inversion (AMI) codes, 26, 82
 - AMI-NRZ, 26, 51-53
 - AMI-RZ, 26, 53
 - bandwidth, 36
 - BER, 51-53
 - efficiency, 63
 - PSD, 35-36
 - PSD illustration, 33
 - synchronization, 57
 - See also* Line codes
- Amplitude modulated pulses (AMP), 333
- Amplitude shift keying (ASK), 8, 13, 412
 - defined, 8
 - M-ary, 411-22
 - nonconstant envelope, 15
 - PSD, 11
- Analog-to-digital (A/D) converter, 1
- Angle diversity, 562
- Asymmetric MHPM, 400
- Autocorrelation coefficient, 576-77
- Autocorrelation function
 - 1REC MHPM, 362

Autocorrelation function (*continued*)

- AWGN, 4
- calculating, 274
- of complex envelope, 571
- Fourier transform of, 571-72
- periodic part, 275
- Q2PSK, 502

Average bit error probability, 605-6

Average matched filter (AMF) receiver, 334

B

Bandlimited channel, 6

Bandpass MAM

- demodulator, 418-21
- modulator, 418-21
- PSD, 413
- signal, 413
- signal set, 418
- See also* M-ary amplitude modulation (MAM)

Bandpass stationary random process, 569-72

Bandwidth

- AMI, 36
- biphase codes, 40
- coherence, 518-20
- dicode, 37
- DM, 43
- equivalent noise, 118
- IF filter, 119
- loop, 181
- MSK, 204-7
- noncoherent FSK, 101
- NRZ, 34
- null-to-null, 204
- Nyquist, 545
- PLL, 339
- RZ code, 25, 35
- tracking loop, 397

Bandwidth efficiency, 10-11

- 1REC MHPM, 376-77
- defined, 10
- MPSK, 148
- null-to-null, 11
- Nyquist, 11

Bandwidth efficiency (*continued*)

- percentage, 11
- Q2PSK, 502, 512

Baseband formats, 17

Baseband modulation, 17-83

Bayes criterion, 590-92

Bazin's symbol-shaping pulses, 250-54

- class elements, 253

- Bazin's symbol-shaping pulses (*continued*)
 - defined, 250-53
 - frequency-shaping, 254
 - illustrated, 254
 - PSDs, 254
 - SFSK, 253
 - See also* Symbol-shaping pulses
- Bessel function, 305
- Bi-F-M
 - BER, 54-57
 - defined, 27
 - matrices, 41
 - optimum receiver and decision regions, 56
 - See also* Biphase codes
- Binary codes
 - BER, 46-49
 - minimum error probability criterion, 46
 - optimum receiver for, 45
 - signals, 44
- Binary FSK (BFSK), 13, 87-94
 - baseband PSD, 93
 - demodulator, 118
 - in Rician fading channel, 534, 535
 - signals, 87
 - See also* Frequency shift keying (FSK)
- Binary N-zero substitution (BNZS) code, 58-60
 - bit error probability, 59
 - defined, 58
 - modal, 58-59
 - nonmodal, 58
 - spectrum calculation, 59
 - See also* Substitution line codes
- Binary PSK (BPSK), 9, 13, 123-29
 - antipodal signals, 123
 - bit error probability, 127
 - carrier recovery loop, 182
 - coherent, 128
 - coherent demodulator, 126, 224, 225
 - differential (DBPSK), 129-36
 - differential encoded (DEBPSK), 129-36
 - fractional out-of-band power, 206
 - imperfect symbol synchronization effect on, 188
 - modulator, 126
 - null-to-null bandwidth, 204
 - PSD, 127-29
 - in Rician fading channel, 535
 - signal constellation, 124
 - single-sided spectrum, 223
 - squaring loss, 181
 - waveforms, 124-25
 - See also* Phase shift keying

- Binary signal detection, 596-608
 - error probability, 603-8
 - matched filter maximizes SNR, 602-3
 - noncoherent receiver for, 621
 - receiver structure, 596-602
- Biphase codes, 22, 27, 82
 - bandwidth, 40
 - BER, 54-57
 - biphase-level, 27, 54
 - biphase-mark, 27, 41, 54-57
 - biphase-space, 27, 54
 - conditioned biphase-level, 27, 54
 - matrices, 41
 - PSD, 37-40
 - PSD illustration, 33
- Bipolar violation, 57
- Bit error rate (BER), 6
 - $\pi/4$ -QPSK, 177
 - AMI codes, 51-53
 - BFSK, 535
 - binary codes, 44-49
 - biphase codes, 54-57
 - BPSK, 535
 - CMI, 66
 - delay modulation, 57
 - dicodes, 53-54
 - frequency selective channels, 533
 - GMSK, 345
 - of line codes, 43-57
 - MSK, 535
 - noncoherent orthogonal BFSK in Rician fading channel, 534
 - NRZ codes, 46-48
 - OOK, 422
 - optimum DBPSK in Rician fading channel, 534
 - performance for different modulations, 538-42
 - pseudoternary codes, 49-54
 - QPSK/OQPSK, 535
 - RZ codes, 48-49
 - star QAM, 560
- Block codes, 62-81, 83
 - alphabetic, 62
 - CMI, 63-69
 - DmB1M, 76-77
 - DMI, 69-71
 - efficiency, 62-63
 - kBnT, 78-81
 - mB1C, 74-76
 - mBnB, 71-74
 - nonalphabetic, 62
 - PFmB(m+1)B, 77-78
 - See also* Line codes

BPF-limiter modulator, 294-95
 Butterworth filter, 505-6, 511, 513, 559-60

C

Carrier-modulated signal, 617

Carrier recovery, 179-83

- Costas loop, 182
- decision-directed (DDCR), 441
- MSK-type synchronizer, 339
- Mth power synchronizer for, 180
- phase ambiguity, 215
- QAM, 441-42
- signal-to-noise ratio, 181
- times-four, 445

Carrier synchronization, 179

- in 4-ary multi-h CPFSK, 394
- circular QAM and, 441
- in M-ary multi-h CPFSK, 393-98
- MSK-type, 399
- in multi-h CPFSK, 388-92
- square QAM, 441

Carter code, 71-72

- Circular QAM, 441
- Clock recovery, 183-85
- closed-loop synthesizer, 183
- early/late-gate synthesizer, 185
- groups, 183
- open-loop synchronizer, 183

Closed-loop synthesizer, 183

Coded mark inversion (CMI) codes, 63-69

- average bit error probability, 67
- BER, 66-69
- correlations and spectrum, 65
- decision space, 67
- defined, 63
- edge-detected, BER, 69
- signal format, 64
- spectrum calculation, 64-66
- transition density, 63
- waveform, 64
- See also* Block codes

Coherence bandwidth, 518-20

Coherence time, 520-21

Coherent detection, 615

Coherent FSK, 88-89

- demodulation, 95-98
- demodulator: matched filter implementation, 97
- demodulator: one correlator implementation, 96
- demodulator; correlator implementation, 96
- modulator, 89
- waveform, 90-91

- Coherent FSK (*continued*)
 - See also* Frequency shift keying (FSK)
- Communication channels, 4-7
 - AWGN, 4-6
 - bandlimited, 6
 - fading, 7, 516-64
 - LOS, 6
- Compatible high density bipolar n (CHDBn), 60
- Complex envelope
 - autocorrelation function, 571
 - defining, 568
 - MPSK, 146-47
 - Q2PSK, 501
- Constant envelope Q2PSK
 - bit error probabilities, 511
 - demodulator, 510
 - obtaining, 508
 - synchronization scheme, 513
- Constraint length, 360
- Continuous phase FSK (CPFSK), 13, 92
 - 4-ary noncoherent, comparison, 309
 - 8-ary, simulated, 318
 - 8-ary noncoherent, comparison, 310
 - binary coherent, comparison, 302
 - binary noncoherent, comparison, 308
 - defined, 91
 - differential and discriminator demodulator, 330-33
 - K-index, 397
 - M-ary multi-h, 393-98
 - MSK viewed as special case of, 201-3
 - multi-h schemes, 351
 - octal coherent, comparison, 304
 - phase trellis, 355-56, 358-59
 - PSD, 277-79
 - quaternary coherent, comparison, 303
 - signal form, 91
 - spectral expression, 93
 - See also* Frequency shift keying (FSK)
- Continuous phase modulation (CPM), 11, 259-347
 - binary partial response, 330
 - constant envelope, 15
 - CPFSK, 261-62
 - cumulate phase, 267, 268
 - defined, 259
 - demodulators, 297-337
 - description, 260-72
 - discrete frequency components, 339
 - distance property, 317
 - error probability, 259, 281-85
 - excess phase, 265-67
 - eye pattern, 331

Continuous phase modulation (CPM) (*continued*)

- frequency pulses, 15
 - full-response, 271
 - GMSK, 263-64
 - inevitable merge, 284
 - information bearing phase, 268
 - initial phase, 267
 - instant phase, 265-67
 - LRC, 262
 - LREC, 261-62
 - LSRC, 262
 - minimum distance comparison, 285-86
 - MLSD, 279-81
 - modulating pulse shapes, 261-64
 - modulation index effect, 276-77
 - modulator, 286-97
 - MSK, 261
 - MSK-type demodulator, 326-30
 - noncoherent, ML block detection, 325-26
 - optimum ML coherent demodulator, 297-301
 - optimum ML noncoherent demodulator, 301-11
 - parallel MSK-type receiver for, 329
 - phase tree, 269-70
 - phase trellis, 270, 271
 - power-bandwidth trade-off, 289
 - a priori distributions, 277
 - PSD calculation, 274-76
 - PSD illustrations, 277
 - PSDs, 272-79, 580-86
 - pulse shape effect, 276
 - quaternary, PSDs for, 278
 - schemes, 13, 259
 - signal, 260
 - signal definition, 580
 - signal phase, 265
 - signal state, 267-69
 - SMSK receiver for, 330, 331
 - state trellis, 270-72
 - state vector, 271
 - synchronization, 337-42
 - TFM, 263
 - Viterbi demodulator, 311-20
- Continuous signal detection (unknown phases), 615-25
- error performance, 621-25
 - receiver structure, 615-21
- Continuous signal detection, 596-615
- Conversion filter transfer function, 223
- Correlation coefficient, 44, 597
- Correlatively encoded multi-h signaling technique, 401-3
- defined, 401-2
 - signal comparison, 403

- Correlatively encoded multi-h signaling technique (*continued*)
 - signal definition, 402
- Costas loop, 182-83
 - for BPSK, 182
 - for GMSK, 344
 - for QPSK, 182, 183
 - for SMSK, 234
- Covariance matrixes, 599
- Crosscorrelated QPSK (XPSK), 13, 460

D

- Data detection, 392-93
 - Decision criteria, 590-94
 - Bayes criterion, 590-92
 - MAP criterion, 593
 - maximum likelihood criterion, 594
 - minimum probability of error criterion, 592-93
- Decision-directed carrier recovery (DDCR), 441
 - for 200Mbps square 16-QAM, 445
 - advantage, 445
 - implementation, 449
 - quantity distribution, 448
- Decision-directed demodulator, 388
- Decision space, 605
- Delay modulation (DM), 27, 82
 - bandwidth, 43
 - BER, 57
 - matrices, 42
 - PSD, 40-43
 - PSD illustration, 33
- Delay spread
 - defined, 518
 - four-level modulations and, 537
 - rms, 542, 543
- Demodulation
 - $\pi/4$ -QPSK, 172-73
 - BPSK, 126
 - coherent FSK, 95-98
 - DEQPSK, 166
 - digital communication system model for, 3
 - with discriminator, 115-20
 - joint, 388-92
 - with limiter-discriminator detection, 120
 - MFSK, 104-15
 - MSK, 211, 224, 225, 228
 - multi-h binary CPFSK, 383
 - noncoherent FSK, 98-101
- Demodulators
 - $\pi/4$ -QPSK
 - baseband differential, 174
 - coherent, 177, 178

Demodulators (*continued*)

pi/4-QPSK

FM-discriminator, 174, 176

IF band differential, 174

BFSK, 118

BPSK, 126, 224, 225

coherent FSK

correlator implementation, 96

matched filter implementation, 97

one correlator implementation, 96

CPM, 297-337

DBPSK, 131, 134

decision-directed, 388

differential, 330

differential QPSK, 161, 165

discriminator, 330-33

DMPSK, 152, 153

GMSK, 343

MAM, 418-21

MFSK, 104, 108, 109, 110, 113

MHPM, 382-92

MPSK, 141

MSK, 210-14

MSK-type, 235, 326-30

noncoherent FSK

bandpass filter implementation, 100

correlator implementation, 99

matched filter implementation, 99

noncoherent MFSK, 110

correlator-squarer implementation, 113

matched filter-envelope detector implementation, 115

matched filter-squarer detector implementation, 114

optimum ML coherent, 297-301

optimum ML noncoherent, 301-11

OQPSK-type, 459

post-separation, 461-62

Q2PSK, 503-5

QAM, 436-38

QPSK, 156, 158, 159

SFSK, 240

SMSK, 220, 223-27

SQAM, 494

synchronization, 398-99

two-symbol-period schemes, 461-62

Viterbi, 311-20

Detection of signals, 589-625

binary, 596-608

coherent, 615

continuous, 596-615

continuous, with unknown phases, 615-25

discrete, 589-96

Detection of signals (*continued*)

- M-ary, 608-15
- noncoherent, 615
- theory, 597

Dicodes

- bandwidth, 37
- BER, 53-54
- decoding, 26
- NRZ, 26
- PSD, 36
- RZ, 26

See also Bandwidth

Difference data sequence, 282

Difference signal, 604

Differential BPSK (DBPSK), 129-36

- bit error probability, 134, 136
 - demodulator, 131
 - encoded (DEBPSK), 129-36
 - integrator output, 129
 - modulator, 131
 - optimum demodulator, 134
 - PSD, 135, 136
 - receiver implementation, 132
 - in Rician fading channel, 534
 - symbols, 133
- See also* Binary PSK (BPSK)

Differential coding, 18-22, 24

- data distribution, 20
- decoding, 22
- decoding rule, 18
- defined, 18
- DEQPSK, 163
- encoding, 18-21
- examples, 19, 132
- performing, 18
- phase ambiguity and, 180
- QAM, 448-54
- star QAM, 558
- types, 21

Differential encoder/decoder, 20, 21

Differential mode inversion (DMI) codes, 69-71

- bipolar, 70
- defined, 69-70
- unipolar, 71
- waveform, 64

See also Block codes

Differential MPSK (DMPSK), 148-54

- coherent demodulator, 152, 153
- defined, 148
- encoded (DEMPSK), 148, 153
- PSD, 153-54

- Differential MPSK (DMPSK) (*continued*)
 - symbol error probability, 152-53
 - See also* M-ary PSK (MPSK)
- Differential QPSK, 160-67
 - bit error probability, 164
 - coding rules, 160
 - coherent demodulation, 166
 - demodulator, 161
 - differential coding, 163
 - differential decoding, 167
 - differentially encoded (DEQPSK), 161, 163, 166-67
 - modulator, 163
 - Pb of, 161
 - signal phase assignment, 163
 - suboptimum demodulator, 165
 - symbol error probability, 166-67
 - See also* Quadrature phase shift keying (QPSK)
- Digital bandpass signals PSDs, 577-79
- Digital communication systems, 1-4
 - block diagram, 2
 - modulation/demodulation model, 3
- Digital signal PSDs, 572-77
 - data symbols are correlated, 576-77
 - data symbols are uncorrelated, 574-76
- Digital sum (DS)
 - defined, 62
 - variation (DSV), 62, 78
- Digital-to-analog (D/A) converter, 2
- Dirac delta function, 4
- Discrete signal detection, 589-96
 - binary hypothesis test, 589-90
 - decision criteria, 590-94
 - M hypotheses, 594-96
 - See also* Detection of signals
- Discriminator demodulator, 330-33
 - filter, 333
 - illustrated, 334
 - output, 330-33
 - sequence detection, 333
 - Viterbi processing, 333
 - See also* Demodulators
- Diversity branches, 563
- Diversity techniques, 561-63
 - angle, 562
 - defined, 561
 - frequency, 562
 - multipath, 562
 - polarization, 562
 - space, 561-62
 - time, 562
 - transform, 562-63

- DmB1M codes, 76-77
 - consecutive identical digits, 77
 - defined, 76
 - See also* Block codes
- Doppler shift, 7, 133
 - effects, 517
 - Rayleigh fading and, 551
- Doppler spread
 - defined, 520
 - maximum, 545
- Double SFSK (DSFSK), 253, 254
- Duobinary MSK (DMSK), 262

E

- Early/late-gate clock synthesizer, 185
- Equalization, 563
- Equivalent noise bandwidth, 118
- Erasure, 590
- Error function, 142
 - complementary, 145
 - defined, 142, 191
 - properties, 192
- Error probability
 - $\pi/4$ -QPSK, 176-77, 179
 - binary signal, 603-8
 - BNZS code, 59
 - BPSK, 127
 - continuous signals with unknown phases, 621-25
 - CPM, 259, 281-85
 - DBPSK, 134, 136
 - DMPSK, 152-53
 - DQPSK, 164, 166-67
 - line codes, 24
 - MAM, 414-18
 - M-ary signal, 613-15
 - MFSK, 113-14
 - minimum, 46, 49, 592-93, 595
 - MPSK, 140
 - MSK, 216-19
 - OOK, 422
 - optimum ML demodulator, 299, 301, 306
 - optimum receiver, 603-8
 - PAM, 414, 416
 - PMSK, 330, 332
 - Q2PSK, 503, 505, 511
 - QAM, 438-41
 - QBL, 470
 - QORC, 476
 - QOSRC, 477
 - QPSK, 159
 - SMSK, 330, 332

Error probability (*continued*)
 SQAM, 496-98
 SQORC, 476
 square QAM, 438-39, 440, 452
 TSI-OQPSK, 485
 two-symbol-period schemes, 464, 465
 Viterbi demodulator, 317

Excess delay spread, 518

Excess phase, 260

F

Fading

defined, 517
 envelope distributions, 524-27
 remedial measures against, 560-63

Fading channels, 517-64

pi/4-DQPSK, 517, 544-48
 amplitude fluctuations, 7
 characteristics, 518-21
 classification, 521-23
 classification table, 523
 coherence bandwidth, 518-20
 coherence time, 520-21
 combinations, 523
 defined, 7
 delay spread, 518
 Doppler spread, 520
 fast, 522
 flat, 521
 frequency selective, 521-22, 533-44
 QAM in, 554-60
 Rayleigh, 527-31
 Rician, 531-33
 slow, 522-23
 slow, flat, 527-33

Fano algorithm, 334

Fast fading channel, 522

Flat fading channel, 521

Fourth-power loop synchronizer, 340-41, 444

defined, 340

illustrated, 341

Fractional out-of-band power, 206

Frequency diversity, 562

Frequency selective channel, 533-44

BER, 533

defined, 521-22

digital modulation in, 533-44

See also Fading channels

Frequency shape pulse, 260

Frequency shift keying (FSK), 8, 87-122

binary, 12

Frequency shift keying (FSK) (*continued*)

- coherent, 88-89, 90-91
- coherent demodulation, 95-98
- continuous phase, 91-92
- defined, 8-9
- demodulation using discriminator, 115-20
- generic, 12
- noncoherent, 87-88, 98-101
- PSD, 92-94
- schemes, 13
- summary, 121-22
- symbol timing, 121
- synchronization, 121

G

Gaussian MSK (GMSK), 13, 15, 195, 256, 342-46

- BER, 345, 532
- in CDPD systems, 259
- Costas loop, 344
- defined, 263, 342
- degradation, 345
- demodulator, 343
- frequency pulse, 342
- illustrated, 264
- irreducible BER performance for, 542
- modulator, 342-43
- percentage bandwidth, 342
- PSD, 342, 343
- in Rician fading channel, 536
- transfer function, 342

Gaussian probability function, 5

Gaussian random variables, 599, 604, 605, 613, 622

Gram-Schmidt procedure, 385, 406, 598, 608, 615

Gray coding, 137-38

- imperfect, 452
- square QAM, 434, 435, 452

Griffiths code, 72-73

- 3B4B translation table, 74
- 5B6B translation table, 73
- defined, 72
- See also* mBnB codes

H

High density bipolar n (HDBn) codes, 60-62

- commonly used, 62
- compatible (CHDBn), 60
- defined, 60-62
- See also* Substitution line codes

Hypotheses

- a priori probabilities, 591

Hypotheses (*continued*)

- decision criteria, 590-94
- defined, 589
- M, 594-96
- mapping, 589
- vector, 595-96

I

- IF filters, 119
- Inner product calculator (IPC), 388, 391
- Intersymbol interference (ISI), 6, 17-18, 227
- Intersymbol-interference/jitter-free OQPSK (IJF-OQPSK), 13, 478-90
 - defined, 478
 - out-of-band to total power ratio, 493
 - signaling illustration, 479
- Intersymbol-interference/jitter-free OQPSK (IJF-OQPSK) *See also* Offset QPSK

J

- Joint carrier phase tracking, 392-93
- Joint demodulation, 388-92
 - 4-ary multi-h CPFSK, 394
 - M-ary multi-h CPFSK, 393-98

K

- kBnT codes, 78-81
 - 4B3T, 79-80
 - 6B4T, 80-81
 - MS43, 80
 - defined, 78
 - efficiencies, 78

L

- LCE-MH, 402
- L-fold rotational symmetry, 450
- Likelihood ratio, 592
- Limiter-discriminator detection, 115-18, 120
- Line codes, 17
 - AMI, 26
 - bandwidth, 22-24
 - BER of, 43-57
 - biphase codes, 22, 27, 37-40, 54-57
 - bit sequence independence, 24
 - block, 22, 62-81
 - classes, 22
 - delay modulation, 27, 40-43, 57
 - description of, 22-27
 - differential coding, 24
 - error detection capability, 24
 - error probability, 24
 - features, 22-24
 - illustrated, 23

Line codes (*continued*)

- NRZ, 22, 25, 30-34, 46-48
- PSD of, 28-43
- pseudoternary codes, 26, 35-37, 49-54
- PT, 22
- RZ, 22, 25-26, 34-35, 48-49
- spectrum, 22
- substitution, 22, 57-62
- timing information, 22

Line-of-sight (LOS) channels, 6

Loop transfer function, 181

M

Manchester codes, 82

- BER, 54
- defined, 27
- efficiency, 63
- PSD, 37
- See also* Biphase codes

MAP

- criterion, 593
- symbol synchronizer, 341-42

MAP-VA receiver, 392, 393

Marcum's Q-function, 606

Markov method, 272

M-ary amplitude modulation (MAM), 411-22

- amplitudes, 412
- bandpass, 413, 416, 418-21
- baseband, 416
- behavior, 411
- demodulator, 418-21
- error probability, 414-18
- modulator, 418-21
- MPSK inferiority, 416-18
- on-off keying, 421-22
- optimum detection, 414-18
- passband, 412
- power efficiency, 411
- power penalty, 418
- PSD, 412-14
- signals, 412
- symbol error probability, 417

M-ary ASK (MASK), 13

M-ary FSK (MFSK), 13, 102-15

- coherent demodulator, 104, 108, 109
- coherent modulator, 108
- defined, 102
- equal-energy, 110, 111, 112, 116, 117
- equiprobable, 110, 111, 112, 116, 117
- for equiprobable messages, 102-3
- frequency separation, 102

- M-ary FSK (MFSK) (*continued*)
 - noncoherent demodulator, 110, 113
 - noncoherent modulator, 104-7
 - for non-equiprobable messages, 103
 - orthogonal, 110, 111, 112, 116, 117
 - PSD, 103-4
 - PSD illustration, 104, 105, 106
 - signal, 102
 - symbol error probability, 113-14
 - See also* Frequency shift keying (FSK)
- M-ary multi-h CPFSK, 393-98
 - carrier synchronization, 393-98
 - joint modulation, 393
 - phase trellis, 393
 - symbol synchronization, 393-98
- M-ary PSK(MPSK), 13, 136-48
 - bit rate, 147-48
 - coherent demodulation, 139
 - coherent demodulator using two correlators, 141
 - complex envelope, 146-47
 - decision regions, 146
 - differential (DMPSK), 148-54
 - Gray coded, 145
 - linear PSD, 149
 - logarithmic PSD, 149
 - MAM inferiority to, 416-18
 - maximum bandwidth efficiency, 148
 - modulator, 138-39
 - out-of-band power PSD, 149
 - PSD, 146-48
 - QAM superiority to, 418, 439
 - schemes, 136
 - signal constellation, 137
 - signal set, 136-37
 - symbol error probability, 140
 - symbol rate, 147
 - two-dimensional signals, 138
- M-ary signal detection, 608-15
 - coherent receiver for, 622
 - error probability, 613-15
 - matched-filter receiver for, 623
 - with M correlators, 611
 - with M matched filters, 611
 - with N correlators, 612
 - with N matched filters, 612
 - optimum, 619, 620
 - orthogonal, 624-25
 - receiver structure, 608-12
 - See also* Detection of signals
- Matched filters, 396
 - coherent QAM demodulator using, 437

- Matched filters (*continued*)
 - equivalence, 610
 - frequency response, 229
 - low-pass equivalent, 227, 231
 - maximizes SNR, 602-3
 - receiver, 244
 - theory, 226
 - total response, 231
- Maximum likelihood block detection
 - error performance, 326
 - illustrated, 326
 - noncoherent CPM, 325-26
 - real I-Q implementation, 327
- Maximum likelihood criterion, 594
- Maximum likelihood sequence detection (MLSD)
 - for CPM, 279-81
 - defined, 280
 - demodulator use of, 280
 - error performance, 280, 281-85
 - receiver, 281, 311
 - with Viterbi algorithm, 285
- Maximum likelihood sequence estimation (MLSE), 314
- mB1C codes, 74-76
 - defined, 76
 - scrambling, 76
 - spectral, 76
 - See also* Block codes
- mBnB codes, 71-74
 - 2B3B dc-constrained code, 74, 75
 - Carter code, 71-72
 - defined, 71
 - Griffiths code, 72-73
 - PAM-PPM code, 73-74, 75
 - See also* Block codes
- Mean excess delay, 518
- Metrics
 - branch, 312, 387-88, 389
 - defined, 312
 - path, 312
 - M hypotheses, 594-96
- Miller code *See also* Delay modulation (DM)
- Minimum error probability, 49
 - criterion, 592-93
 - test, 595
- Minimum shift keying (MSK), 13, 195-257
 - bandwidth, 204-7
 - bit energy, 217
 - bit error probability, 219
 - bit error rate, 216
 - carrier and symbol-timing recovery, 214
 - carrier phase, 198

Minimum shift keying (MSK) (*continued*)

- composite signal, 196
- continuous phase, 90
- demodulation, 211, 224, 225, 228
- demodulator, 210-14
- derivation, 195
- description of, 196-203
- duobinary (DMSK), 262
- error performance, 256
- error probability, 216-19
- excess phase, 198, 200
- FFSK implementation, 215
- fractional out-of-band power, 206
- LHS, 199, 200
- main lobe spectrum, 204
- ML block estimator implementation, 325-26
- modulator, 207-10
- modulator illustration, 207, 208, 209
- with multiple-symbol noncoherent detection, 328
- noncoherent demodulation, 214
- null-to-null bandwidth, 204
- optimum coherent demodulation, 211
- out-of-band to total power ratio, 493
- parallel (PMSK), 222, 223, 326
- phase tree, 200, 201
- phase trellis, 201, 202
- properties, 196-98
- PSD, 203-4
- PSD illustration, 205
- RHS, 199, 200
- Rician channel, 535, 554
- schemes, 195
- serial (SMSK), 219-31, 326
 - as set of time/phase-shifted AM pulses, 333
 - as sinusoidal weighted OQPSK, 196-201
 - as special case of CPFSK, 201-3
- spectrum fall-off rate, 204, 205
- symbol, 226
- symbol shaping pulses, 204
- synchronization, 214-15
- waveforms, 196, 197

See also Frequency shift keying (FSK)

Modified QORC (MQORC), 459

Modulation, 7-15

- $\pi/4$ -QPSK, 12, 13, 170-79
- ASK, 8, 13, 15
- AWGN, 6
- bandwidth efficiency, 10-11
- baseband, 8, 17-83
- basic, 12
- BFSK, 13

Modulation (*continued*)

- BPSK, 9, 13, 123-29
- choice criteria, 9-12
- classes, 12
- CPFSK, 13
- CPM, 11, 13, 15, 259-347
- digital communication system model for, 3
- in fading channels, 517-64
- FSK, 8-9, 13, 87-122
- GMSK, 13, 195, 256, 263, 342-46
- IJF-OQPSK, 13, 478-90
- LRC, 13, 262
- LREC, 13, 261-62
- LSRC, 13, 262
- MAM, 411-22
- MASK, 13
- MFSK, 13, 102-15
- MHPM, 13, 15, 351-408
- MPSK, 13, 136-48
- MQORC, 459
- MSK, 13, 195-257
- nonconstant-envelope bandwidth-efficient, 459-515
- NRZ-L, 7-8
- OOK, 8, 13, 421-22
- OQPSK, 13
- power efficiency, 10
- PSAM, 561
- PSK, 8, 9, 13, 15, 123-92
- Q2PSK, 13, 15, 498-514
- QAM, 9, 13, 15, 411-57
- QBL, 459, 465-71
- QORC, 13, 459, 471-77
- QOSRC, 13, 460, 471-77
- QPSK, 9, 13, 154-70
- scheme overview, 12-15
- SHPM, 13
- SMSK, 13, 195, 219-31
- SQAM, 13, 490-98
- SQORC, 13, 459, 471-77
- system complexity, 11-12
- TFM, 13, 263, 460
- tree, 14
- TSI-OQPSK, 13, 478-90
- XPSK, 13

Modulation index

- defined, 260
- effect, 276-77

Modulators

- $\pi/4$ -QPSK, 170-71
- all-digital, 295-97
- BPR-limiter, 294-95

Modulators (*continued*)

- BPSK, 126
 - coherent FSK, 89
 - CPM, 286-97
 - DBPSK, 131
 - differential QPSK, 163
 - FM, 286
 - GMSK, 342-43
 - MAM, 418-21
 - MFSK, 108
 - MHPM, 382
 - MPSK, 138-39
 - MSK, 207-10
 - noncoherent FSK, 88
 - noncoherent MFSK, 104-7
 - OQPSK, 168
 - PLL, 292-93
 - Q2PSK, 499, 508-9
 - QAM, 434-36
 - QPSK, 156, 158
 - quadrature, 286-92
 - serial, 292-95
 - SFSK, 238, 240
 - SMSK, 220, 221-23
 - two-symbol-period schemes, 461
- Modulo-2 addition, 18, 447
- MS43 code, 80
- MSK-type demodulators, 326-30
- MSK-type schemes, 231-36
- defined, 234
 - demodulator, 235
 - error performance, 235
 - modulator, 235
 - signaling generation, 248
 - signals, 234-35
 - signal spectral main lobe, 254-56
 - symbol duration, 235
 - See also* Minimum shift keying (MSK)
- MSK-type synchronizer, 337-40
- carrier, 399
 - carrier recovery, 339
 - defined, 337
 - illustrated, 338
 - phase-lock loops, 338
 - problems, 339-40
 - realization in VLSI, 340
 - signal dropout problem, 340
 - symbol, 399
- Multi-h phase modulation (MHPM), 13, 351-408
- 1REC *See also* 1REC MHPM
 - 3RC *See also* 3RC MHPM

Multi-h phase modulation (MHPM) (*continued*)

- application, in fading channels, 351
 - with asymmetrical modulation indexes, 400
 - asymptotic coding gain, 364
 - autocorrelation function, 362
 - bandwidth efficiency, 376-77
 - branch metrics, 389
 - carrier phase synchronization, 398-99
 - carrier synchronization, 388-92
 - correlatively encoded signaling techniques, 401-3
 - CPFSK schemes, 351
 - cumulate phase, 353
 - data detection, 392-93
 - defined, 351
 - demodulator, 382-92
 - distance properties, 366-81
 - error performance, 15
 - error probability, 368
 - frequency pulse, 352
 - full-response, 360, 362
 - with high coding gain over MSK, 375
 - improved, schemes, 399-403
 - index, 352, 354, 360
 - instant phase, 352
 - joint carrier phase tracking, 392-93
 - joint demodulation, 388-92
 - M-ary, 360, 362, 393-98
 - maximum increase of bounds, 369
 - modulator, 382
 - multi-T realization, 401
 - nonlinear, 403
 - partial response, 360, 366, 402
 - phase, 352
 - phase characteristic, 399
 - phase trees, 354
 - phase trellis, 355-56, 358-59
 - PSD, 361-66
 - PSD illustration, 367
 - receiver, 389
 - signal, 351-52
 - spectra decay, 364
 - superbaud period, 398-99
 - symbol-timing synchronization, 398-99
 - synchronization, 398-99
 - synchronizers, 400
 - total phase, 353
 - total phase states, 357
 - upper bounds, 369
 - upper bounds summary, 370
- Multipath diversity, 562
- Multipath interference, 7

Multipath signals, 517
 Multiple index continuous phase modulation (MHPM), 259
 Multi-T phase codes, 401

N

Nakagami distribution, 526-27

Noncoherent detection, 615

Noncoherent FSK

bandwidth, 101

defined, 87

demodulation, 98-101

demodulator: bandpass filter implementation, 100

demodulator: correlator implementation, 99

demodulator: matched filter implementation, 99

error performance, 119

modulator, 88

orthogonal signals, 101

received signal, 98

See also Frequency shift keying (FSK)

Noncoherent MFSK

demodulator: correlator-squarer implementation, 113

demodulator: matched filter-envelope detector implementation, 115

demodulator: matched filter-squarer detector implementation, 114

modulator, 104-7

symbol error probability, 113-14

See also M-ary FSK

Nonconstant-envelope bandwidth-efficient modulations, 459-515

Nonlinear multi-h CPFSK, 403

Nonreturn-to-zero codes (NRZ) codes, 22, 25, 82

bandwidth, 34

BER, 46-48

dicode, 26, 36

efficiency, 63

NRZ-L, 7-8, 25, 30, 46-47

NRZ-M, 25, 30, 47-48

NRZ-S, 25, 30, 47-48

polar, 31

PSD, 30-34

PSD illustration, 32

unipolar, 31, 47

See also Line codes

Normalized Euclidean distance, 366-68, 372

Null-to-null bandwidth efficiency, 11

Numerically controlled oscillator (NCO), 295

elements, 295

sensitivity, 296

Nyquist bandwidth efficiency, 11

Nyquist filter, 165

O

Observation space, 589

- Odd half-wave symmetry, 276, 586
- Offset QPSK (OQPSK), 13, 167-70
 - defined, 167
 - demodulator, 168
 - fractional out-of-band power, 206
 - I-/Q-channel data, 478
 - modulator, 168
 - MSK as sinusoidal weighted, 196-201
 - null-to-null bandwidth, 204
 - as set of time/phase-shifted AM pulses, 333
 - waveforms, 167, 169
 - See also* Quadrature phase shift keying (QPSK)
- On-off keying (OOK), 8, 13, 421-22
 - BER, 422
 - envelope, 421
 - preference, 422
 - PSD, 422
 - signal set, 421
 - symbol error probability, 422
- Open-loop synthesizer, 183-84
- Optimum binary receiver, 601
- Optimum ML coherent demodulator, 297-301
 - complexity reduction, 334
 - defined, 297
 - error probability, 299, 301
 - illustrated, 300
 - M likelihoods, 299
 - receiver, 298-99
 - See also* Demodulators
- Optimum ML noncoherent demodulator, 301-11
 - complexity reduction, 334
 - defined, 301
 - error probability, 306
 - illustrated, 307
 - structure, 306, 307
 - See also* Demodulators
- OQPSK-type demodulator, 459
- Orthogonal MFSK, 110, 111, 112, 116, 117
- Orthonormal functions, 405-7, 609

P

- PAM-PPM code, 73-74, 75
- Parallel MSK (PMSK), 222, 223, 326
 - bit error probability, 330, 332
 - eye pattern, 329
 - filter, 328
 - with phase and timing errors, 330
 - receiver for binary CPM, 329
 - receiver replacement, 327-28
 - structure, 327
 - See also* Minimum shift keying (MSK)

- Parseval's theorem, 600, 610, 616
- Path metrics, 312
- PCM waveforms, 17
- Percentage bandwidth efficiency, 11
- PFmB(m+1)B codes, 77-78
 - block synchronization, 78
 - defined, 77
 - stages, 77-78
 - See also* Block codes
- Phase function, 260
- Phase lock loop (PLL), 180, 338, 392
 - bandwidth, 339
 - modulator, 292-93
- Phase rotation network (PRN), 391
- Phase shift keying (PSK), 8, 123-92
 - carrier recovery, 179-83
 - clock recovery, 183-85
 - constant envelope, 13
 - defined, 9, 123
 - phase and timing error effects, 186-87
 - scheme comparison, 189
 - summary, 187-90
 - synchronization, 179-87
 - types of, 123
- Phase trees
 - 2REC receiver, 320, 321
 - 3RC transmitter, 320, 321
 - CPM, 269-70
 - MHPM, 354
 - MSK, 200, 201
- Phase trellis
 - constraint length, 360
 - CPM, 270, 271
 - M-ary multi-h CPFSK, 393
 - MHPM, 355-56, 358-59
 - MSK, 201, 202
 - periods, 360
- Pilot symbol assisted modulation (PSAM), 561
- PLL modulator, 292-93
 - impulse response, 293
- problem, 293
- Poisson sum formula, 29, 574-75
- Polarization diversity, 562
- Polar RZ
 - BER, 48
 - defined, 26
 - PSD, 34
 - See also* Return-to-zero codes
- Post-separation demodulator, 461-62
- Power efficiency, 10

- Power spectral densities (PSDs), 4, 10, 567-86
 - ASK, 11, 577
 - bandpass signal, 92, 567-69
 - bandpass stationary random process and, 569-72
 - biphase codes, 37-40
 - BPSK, 127-29
 - CPFSK, 277-79
 - CPM, 272-79, 580-86
 - DBPSK, 135, 136
 - DEBPSK, 153-54
 - delay modulation, 40-43
 - digital bandpass signals, 577-79
 - digital signals, 572-77
 - FSK, 92-94
 - general formula, 29
 - GMSK, 342, 343
 - line codes, 28-43
 - MAM, 412-13
 - MFSK, 103-4, 105, 106
 - MHPM, 361-66
 - MPSK, 146-48
 - MSK, 203-4
 - NRZ codes, 30-34
 - OOK, 422
 - pseudoternary codes, 35-37
 - QAM, 432-34
 - QBL, 468, 469
 - QORC, 473
 - QOSRC, 474, 475
 - QPSK, 160
 - Rayleigh envelope, 524
 - RZ codes, 34-35
 - SFSK, 238-39
 - SQAM, 490, 492
 - SQORC, 473
 - star QAM, 558
 - substitution line codes, 61
 - TSI-OQPSK, 482-83
- Predetection and postdetection coherent equal gain combining, 563
- Predetection and postdetection maximal ratio combining, 563
- Predetection selective combining, 563
- Predetection switched combining, 563
- Priori probability, 44
- Probabilistic transition mechanism, 589
- Pseudoternary codes, 26, 82
 - BER, 49-54
 - PSD, 35-37
- Pulse amplitude modulation (PAM), 412
 - decision regions, 415
 - error probability, 414, 416
 - signal set, 414

- Pulse amplitude modulation (PAM) (*continued*)
 - thresholds, 415
- Pulse code modulation (PCM), 17

Q

- Quadrature amplitude modulation (QAM), 9, 13, 259, 411-57
 - 16-QAM, 411, 434, 435
 - 32-QAM, 429
 - 128-QAM, 411
 - average amplitude, 424
 - average power, 424
 - average signal energy, 424, 426
 - carrier recovery, 441-42
 - circular, 441
 - constellation design consideration, 427
 - constellation illustrations, 428
 - constellations, 426-32
 - defined, 411, 422
 - demodulator, 436-38
 - differential coding in, 448-54
 - digital synthesis techniques for, 434-36
 - envelope, 424, 432
 - error probability, 438-41
 - in fading channels, 554-60
 - fixed-link, 444
 - modulator, 434-36
 - MPSK inferiority to, 418, 439
 - nonconstant envelope, 15
 - on time axis, 432
 - phasor magnitude, 426
 - power savings, 441
 - PSD, 432-34
 - pulse shaping in, 422
 - schemes, 411
 - signal description, 422-26
 - square, 429-32
 - star, 558-60
 - superposed (SQAM), 460
 - symmetrical, 442, 443
 - synchronization, 441-48
 - times-four carrier recovery loop, 445
 - type I, II, III constellations, 425, 426-27
 - use of, 15, 411
- Quadrature modulators, 286-92
 - defined, 286-87
 - with phase state ROM, 291
- Quadrature overlapped raised cosine modulation (QORC), 13, 459, 471-77
 - amplitude, 472
 - envelopes for, 472
 - error performance, 474-75
 - eye patterns, 471

- Quadrature overlapped raised cosine modulation (QORC) (*continued*)
 - PSD, 473
 - pulse shapes, 471
 - symbol error probability, 476
- Quadrature overlapped squared raised cosine modulation (QOSRC), 13, 460, 471-77
 - amplitude formula, 472
 - envelopes, 473
 - eye patterns, 471
 - PSDs, 474, 475
 - pulse shapes, 471
 - signal energy, 477
 - symbol error probability, 477
- Quadrature phase shift keying (QPSK), 9, 13, 154-70
 - Costas loop, 182, 183
 - crosscorrelated (XPSK), 460
 - data bits, 155
 - demodulator, 156, 158
 - demodulator bit error probability, 159
 - differential (DQPSK), 160-67
 - fractional out-of-band power, 206
 - irreducible BER performance for, 540
 - level generator, 139
 - linear PSD, 162
 - logarithmic PSD, 162
 - modulator, 156, 158
 - null-to-null bandwidth, 204
 - offset (OQPSK), 167-70
 - out-of-band power PSD, 162
 - out-of-band to total power ratio, 493
 - Pb, 160, 161
 - PSD, 160
 - in Rician fading channel, 535
 - signal constellation, 156
 - signal coordinates, 155
 - symbol interval, 156
 - waveforms, 155-56, 157
 - See also* M-ary PSK (MPSK)
- Quadrature quadrature phase shift keying (Q2PSK), 13, 498-514
 - amplitudes, 501
 - autocorrelation, 502
 - bandwidth efficiency, 502, 512
 - basis, 15
 - basis signals, 498
 - bit error probability, 503, 505, 511
 - bit rate, 499
 - complex envelope, 501
 - constant envelope, 508, 510, 511, 513
 - defined, 498
 - demodulator, 503-5
 - error performance, 505-6
 - fractional out-of-band power, 504

Quadrature quadrature phase shift keying (Q2PSK) (*continued*)

- generalized signaling format, 513
- modulated signal, 499-500
- modulator, 499, 508-9
- PSDs, 500-503
- pulses, 502
- pulse-shaping functions, 498
- signal set, 498
- synchronization, 506-8
- synchronization block diagram, 508
- transmitter filter pairs, 514
- uncoded, Euclidean distance, 509-10
- uncoded, synchronization, 511-12

Quadrature receiver, 313

Quasi-bandlimited modulation (QBL), 459, 465-71

- 3-amplitude pulse, 466
- in AWGN channel, 470
- defined, 465
- envelopes, 467
- hard limiter, 467
- implementation, 467
- out-of-band to total power ratio, 493
- power efficiency losses, 468, 469
- PSDs, 468, 469
- pulse duration, 465
- signal, 466
- spectral analysis, 467
- symbol error probability, 470

R

Rabzel and pasupathy's symbol-shaping pulses, 247-50

- amplitude pulse generation, 253
- baseband, 249-50
- defined, 247
- fractional out-of-band powers, 251, 252
- frequency-shaping, 248
- illustrated, 249
- in-phase, 250
- See also* Symbol-shaping pulses

Raised cosine pulse of length L (LRC), 13

- 1RC differential detection, 335
- 1RC discriminator detection, 336
- 3RC minimum distance, 287
- 3RC states/phases, 269
- 3RC state trellis, 273
- 3RC transmitter phase tree, 320, 321
- defined, 262
- illustrated, 264
- power-bandwidth trade-off, 289
- PSDs, 279, 280
- upper bound, 288

- Rayleigh distribution, 524
- Rayleigh envelope
 - ac power, 525
 - average power, 525
 - CDF, 525
 - mean value, 525
 - PSD, 524
- Rayleigh fading channel, 527-31
 - 1REC-MHPM performance in, 552, 553
 - for $\pi/4$ -DQPSK, 530-31
 - chi-square distribution, 528
 - for coherent binary FSK, 530
 - for coherent BPSK/QPSK/OQPSK/MSK, 529
 - Doppler shift and, 551
 - for GMSK, 530
 - for noncoherent orthogonal BFSK, 530
 - for optimum differential BPSK, 529-30
- Rayleigh distribution, 527
 - See also* Fading channels
- Rectangular pulse of length L (LREC), 13, 261-62
 - 1REC MHPM, 353, 362, 371-73, 376-79
 - 2REC, receiver phase tree, 320, 321
 - defined, 261
 - illustrated, 264
 - phase pulse, 320
 - reduction of number of filters for, 320-25
- Reduced-complexity Viterbi demodulator, 317-20
- Return-to-zero codes, 22, 25-26, 82
 - bandwidth, 25, 35
 - BER, 48-49
 - dicode, 26, 36
 - polar, 26, 34, 48
 - PSD, 34-35
 - PSD illustration, 32
 - unipolar, 25-26, 34, 48-49
 - See also* Line codes
- Rician distribution, 525
 - average power, 526
 - density curves, 526
- Rician fading channel, 531-33
 - 1REC-MHPM performance in, 552, 553
 - $\pi/4$ -DQPSK in, 537
 - amplitude, 531-32
 - BFSK in, 535
 - BPSK in, 535
 - error performance, 533
 - error probabilities in, 532
 - GMSK in, 436
 - MSK comparison, 554
 - MSK in, 535
 - noncoherent orthogonal BFSK in, 534

Rician fading channel (*continued*)

optimum DBPSK, 534

QPSK/OQPSK in, 535

See also Fading channels

Rms excess delay, 518

S

Schwartz's inequality, 603

Serial modulator, 292-95

BPF-limiter, 294-95

PLL, 292-93

Serial MSK (SMSK), 13, 195, 219-31, 326

advantages, 219

baseband conversion filter frequency response, 232

baseband implementation, 230-31

baseband matched filter frequency response, 233

bit error probability, 330, 332

conversion and matched filter implementation, 227-31

Costas loop, 234

critical components, 227

demodulator, 220, 223-27

description, 219-21

essence, 222-23

filters, 328, 330

local oscillation, 221

mixer output, 224

modulator, 220, 221-23

with phase and timing errors, 330

receiver for binary CPM, 330, 331

synchronization, 231

validity, in frequency-domain, 223

See also Minimum shift keying (MSK)

Serial-to-parallel (S/P) converter, 208

Signal detection, 589-625

Signal-to-noise ratio (SNR), 283

average, per symbol, 438

high, 283, 284, 306

loop, 397

low, 555

matched filter maximizes, 602-3

Simon's symbol-shaping pulses, 240-46

amplitude, 244, 245

fractional out-of-band behavior, 246

frequency derivation, 245

illustrated, 245

polynomial-type, 243

pulse functions, 243, 244

shapes, 243-44

spectra, 244

See also Symbol-shaping pulses

Sinc function, 31

- Single-h phase modulation (SHPM), 13
- Sinusoidal FSK (SFSK), 236-40
 - continuous phase, 237
 - defined, 236
 - demodulator, 240
 - double (DSFSK), 253, 254
 - envelope, 236
 - error performance, 240
 - frequency derivation, 237
 - modulator, 238, 240
 - PSD, 238-39
 - signal, 237
- Slow fading channel, 522-23
- Space diversity, 561-62
- Spectrally raised cosine pulse of length L (LSRC), 13
 - defined, 262
 - illustrated, 264
- Square QAM, 429-32
 - average energy, 431
 - BERs, 556-57, 560
 - bit error probability, 440
 - carrier synchronization, 441
 - coherent demodulator for, 438
 - differential coding, 448-54
 - differential coding examples, 452
 - differential encoding penalty, 454
 - differentially-coded, error probability, 452
 - distance between phasors, 431
 - in fading channels, 555-58
 - Gray coding, 434, 435
 - illustrated, 430
 - M-ary, 434
 - phase ambiguities, 448
 - phasor magnitude, 431
 - phasors, 429
 - PSD, 432
 - in slow, flat Rayleigh fading channel, 556
 - in slow, flat Rician fading channel, 556-57
 - subgroups, 446
 - symbol error probability, 438-39
 - See also* Quadrature amplitude modulation (QAM)
- Squaring loop synchronizer, 340-41
 - defined, 340
 - illustrated, 341
- Stack algorithm, 334
- Staggered QORC (SQORC), 13, 459, 471-77
 - amplitude, 472
 - envelopes, 473
 - error performance, 474-75
 - eye patterns, 471
 - PSD, 473

- Staggered QORC (SQORC) (*continued*)
 - pulse shapes, 471
 - symbol error probability, 476
- Star QAM, 558-60
 - average power, 558
 - BER, 560
 - differential coding, 558
 - Gray coded phase changes, 559
 - PSD, 558
 - signal points, 558
 - See also* Quadrature amplitude modulation (QAM)
- State trellis, 270-72
 - branch metric, 312
 - defined, 270
 - illustrated, 273
 - M branches, 311
 - number of branches, 312
 - phase trellis vs., 271
 - Viterbi demodulator, 353
- Substitution line codes, 57-62, 83
 - BNZS, 58-60
 - CHDBn, 60
 - HDBn, 60-62
 - illustrated, 59, 60
 - PSDs, 61
 - types of, 57
 - See also* Line codes
- Sunde's FSK signal, 215
- Superbaud period, 398-99
- Superposed-QAM (SQAM), 13, 460, 490-98
 - amplitudes, 491
 - defined, 490
 - degradation, 496, 497
 - demodulator, 494
 - error performance, 490-94, 495
 - eye patterns, 491
 - normalized PSD expression, 490
 - out-of-band to total power ratio, 493
 - PSDs, 490, 492
 - pulse shapes, 491
 - QPSK performance comparison, 494
 - signal energy, 494
 - symbol error probability, 496-98
- Surface acoustic wave (SAW) devices, 229
- Symbol function, 573
- Symbol-shaping pulses, 240-54
 - Bazin's, 250-54
 - common points, 256
 - Rabzel and Pasupathy's, 247-50
 - Simon's, 240-46
- Symbol synchronization, 186, 190

Symbol timing, 121

Symmetrical QAM, 442, 443

Synchronization

AMI code, 57

carrier, 179, 388-92, 393-98

carrier-phase, 398-99

CPM, 337-42

FSK, 121

imperfect, 187

MHPM, 398-99

MSK, 214-15

PSK, 179-87

Q2PSK, 506-8

QAM, 441-48

SMSK, 231

superbaud, 398-99

symbol, 186, 190, 393-98

symbol-timing, 398-99

two-symbol-period schemes, 465

Synchronizers

fourth-power loop, 340-41

MAP symbol, 341-42

MHPM, 400

MSK-type, 337-40, 399

squaring loop, 340-41

System complexity, 11-12

T

Tamed frequency modulation (TFM), 13, 460

defined, 263

illustrated, 264

Threshold, 592

Time diversity, 562

Timing error, 186-87

Transfer function, 513

conversion filter, 229

GMSK, 342

loop, 181

low-pass equivalent matched filter, 227

Transparent tone in band (TTIB), 561

Traveling wave tube amplifier (TWTA), 12, 15

Twinned binary, 26

Two-symbol-interval OQPSK (TSI-OQPSK), 13

amplitudes, 482

defined, 478-80, 480

degradation, 486, 487, 488

degradation vs. fade depth, 489-90

error performance, 485

eye patterns, 482

nonlinearly amplified PSDs, 484

odd and even functions, 481

Two-symbol-interval OQPSK (TSI-OQPSK) (*continued*)

- PSDs, 482-83
- pulses, 481
- signal energy, 484
- spectral advantages, 485
- symbol error probability, 485
- See also* Offset QPSK

Two-symbol-period schemes, 460-65

- bit error probability, 465
- correlation detector, 463
- modulators, 461
- post-separation demodulator, 461-62
- symbol error probability, 464
- synchronization, 465

U

Unconditional likelihood, 616

Unipolar RZ

- BER, 48-49
- defined, 26-27
- PSD, 34
- See also* Return-to-zero codes

V

Viterbi algorithm, 260, 285, 392

- for binary partial response CPM, 333
- branch metrics and, 312
- complexity, 317
- efficiency, 314
- for partial response CPM case, 316
- references, 316
- search time, 316

Viterbi decoder, 394, 397

Viterbi demodulator, 311-17

- branch metric, 387
- defined, 311
- error probability, 317
- implementation limitation, 317
- modified, 317
- reduced-complexity, 317-20
- state trellis, 353

Viterbi estimates, 392

Voltage-controlled oscillators (VCOs)

- adjustment, 447
- amplitude, 447
- control voltage, 286
- implementation, 286
- phase error, 447

W

White Gaussian noise, 597, 608, 615

Wiener-Khinchine theorem, 4, 572

telecommunications

In this single volume, **Fuqin Xiong** explains the full range of today's digital modulation techniques and their practical application to conventional, fixed microwave terrestrial communications, satellite communications, mobile wireless, mobile satellite, and fiber-optic communications. Covering traditional techniques such as FSK, BPSK, QPSK, and QAM, and state-of-the-art techniques including MSK, CPM, and MHPM, *Digital Modulation Techniques* is a one-stop resource that helps you save time and money.

After a brief overview of the history of digital modulation, this book delves into a comprehensive examination of operation principles, symbol and bit error performance, and spectral characteristics. It includes detailed explanations of block diagrams and/or circuits of modulators, demodulators, carrier recovery, clock recovery, and comparisons with other schemes.

An associate professor in the department of electrical and computer engineering at Cleveland State University, **Fuqin Xiong** received his B.Sc. and M.Sc. in electrical engineering from Tsinghua University in Beijing, China, and his Ph.D. from the University of Manitoba, Winnipeg, Canada.

ISBN 0-89006-970-0



90000

9 780890069707



Artech House Publishers BOSTON • LONDON